STATE OF THE CLIMATE IN 2024

Special Supplement to the
Bulletin of the American Meteorological Society
Vol. 106 No. 8, August 2025

Unauthenticated | Downloaded 11/23/25 11:52 AM UTC

Cover Credit:
Photo: The receding Swannanoa River along Highway 70 in Asheville, North Carolina, on 29 September 2024, two days after the passage of Hurricane Helene. Many lives were lost and homes were swept down this part of the river due to extreme flooding.

Photo credit: Deborah J. Misch, former Graphics team member for the BAMS State of the Climate.

Background image: NOAA GOES satellite Geocolor image of Hurricane Helene making landfall over the big bend region of Florida on 26 September 2024. Courtesy of CIRA/NOAA.

How to cite this document:
Special Supplement to the Bulletin of the American Meteorological Society, Vol. 106, No. 8, August 2025 https://doi.org/10.1175/2025BAMSStateoftheClimate.1. Compiled by NOAA's National Centers for Environmental Information, State of the Climate in 2024 is based on contributions from scientists from around the world. It provides a detailed update on global climate indicators, notable weather events, and other data collected by environmental monitoring stations and instruments located on land, water, ice, and in space.

Citing the complete report:
Blunden, J. and J. Reagan, Eds., 2025: "State of the Climate in 2024". Bull. Amer. Meteor. Soc., 106 (8), Si–S513 https://doi.org/10.1175/2025BAMSStateoftheClimate.1.

Corresponding author: Full Report: Jessica Blunden / jessica.blunden@noaa.gov

©2025 American Meteorological Society
For information regarding reuse of this content and general copyright information, consult the AMS Copyright Policy.

Unauthenticated | Downloaded 11/21/25 11:34 AM UTC

STATE OF THE CLIMATE IN 2024

Table of Contents

Unauthenticated | Downloaded 11/21/25 11:34 AM UTC

Abstract

—J. BLUNDEN, J. REAGAN, AND R. J. H. DUNN

In 2024, a strong El Niño at the beginning of the year transitioned to neutral conditions in boreal spring and then to La Niña-like conditions by year's end. Atmospheric concentrations of Earth's major greenhouse gases—carbon dioxide, methane, and nitrous oxide—continued to climb to record-high levels. The annual global average carbon dioxide concentration in the atmosphere rose to 422.8±0.1 ppm, which is a 52% increase over the pre-industrial level of ~278 ppm. The growth from 2023 to 2024 was 3.4 ppm, equal to the observed change between 2015 and 2016, which is the highest in the record since the 1960s.

The annual global temperature across land and ocean was the highest recorded in the observational record dating back to 1850, breaking the record just recently set in 2023. The warmth was widespread. Of the countries that report annual temperature rankings, dozens across the world observed record warmth for the year, including India, China, South Africa, and Brazil. Regions—including North America, the Caribbean, Africa, Oceania, and Europe as a whole—also experienced record warmth. Extreme temperature records were set in individual locations as well. On 7–8 October, Villamontes, Bolivia, recorded a new national record maximum temperature of 47.0°C. In central Myanmar, 48.2°C was recorded at Chank on 28 April, setting a new maximum temperature record for the country and breaking the previous record of 47.4°C set just 22 days earlier at the same location.

Across the Arctic, the annual surface air temperature was the second highest in the 125-year record. An intense August heatwave brought all-time record-high temperatures to parts of the northwest North American Arctic, and record-high August monthly mean temperatures at Svalbard Airport reached more than 11°C. In September, temperatures above 30°C were observed in Norway, marking the latest time of the year in the observational record that such high temperatures have occurred there.

Arctic maximum sea ice extent in 2024 was the second smallest in the 46-year satellite record, while minimum sea ice extent was the sixth smallest. The Northern Sea Route, which runs along the northern coast of Russia, opened later than recent years' average due to persistent ice in the southwest Chukchi Sea. The Northwest Passage's southern route through northwestern Canada opened again this year and, quite unusually considering past climatology, its northern route was also almost entirely ice-free at the end of September. In Antarctica, following record lows in 2023, net sea ice extent was larger than last year but continued to be well below average during much of 2024. The Antarctic daily minimum and maximum sea ice extents for the year were each the second lowest on record behind 2023, marking a continuation of low and record-low sea ice extent since 2016.

Significant weather events impacted Antarctica in 2024. A major warming event in the stratosphere in July and another at the surface in August led to numerous high-pressure and temperature records. Reanalysis estimates indicated that temperatures were 6°C–10°C above average across much of the interior during this two-month period, consistent with available but sparse observations. In terms of area, the Antarctic ozone hole was the seventh smallest in the 32-year record, appearing later than average and reaching its peak of 22.4 million square kilometers on 28 September.

Also within the cryosphere, the annual average snow cover extent was the smallest in the 55-year record for North America, and third smallest for the Northern Hemisphere overall. Glaciers lost a record amount of their mass in 2024; all 58 reference glaciers across the globe reported loss, marking only the second year—along with 2023—that this has occurred since the start of the record in 1970. In Colombia, the Conejeres Glacier was declared extinct, joining a growing number of glaciers on this list. In Venezuela, all glaciers have now officially disappeared.

Across the global oceans, record-breaking temperatures in 2023 persisted into 2024, with daily mean sea surface temperatures at record-high levels until late June. The annual sea surface temperature was the highest in the 171-year record, marking the second year in a row that the global ocean set such a record. Approximately 91% of the ocean surface experienced at least one marine heatwave in 2024, while only 26% experienced at least one cold spell. The surface-to-2000-m depth global ocean heat content was also a record high in 2024. Global mean sea level reached 105.8 mm above the average for 1993—when satellite measurements began—marking a new record high for the 13th consecutive year, with an increase of 4.6±1.4 mm over 2023.

A total of 82 named tropical cyclones were observed during the Northern and Southern Hemispheres' storm seasons, below the 1991–2020 average of 87 and equal to the number recorded in 2023. Hurricane Helene brought destruction from Florida far inland to the southern Appalachian Mountains. Helene caused devastating record flooding that contributed to over 200 deaths, the most in the United States since Hurricane Katrina in 2005. Hurricane Milton impacted Florida's Gulf Coast just 12 days after Helene affected the region, marking the shortest time between major hurricane landfalls in Florida. In the northwest Pacific basin, Super Typhoon Yagi became one of the most destructive storms to affect China and Vietnam in recent years, causing more than 800 fatalities.

Unauthenticated | Downloaded 11/21/25 11:34 AM UTC

The record-warm temperatures in 2024 created conditions that helped intensify the hydrological cycle. The annual global mean precipitation total for 2024 was the third highest since 1983; precipitation over land areas was near-normal while it was fourth highest over the oceans. This is likely associated with warm sea surface temperatures that enhanced regional evaporation. One-day maximum totals measured across the globe were also record high, indicating an increase in rainfall intensity.

Exceptionally heavy rainfall in early January caused the Congo River in Africa to rise to 6.26 m, marking its highest level since 1961. In April, Dubai in the southern Persian Gulf recorded 250 mm of rain in 24 hours—nearly three times its annual average. The torrential downpour submerged highways and paralyzed Dubai International Airport, where floodwaters halted operations for 48 hours. In South America, widespread rainfall totals of 400 mm or more from late April to early May in the state of Rio Grande do Sul triggered the worst flooding event on record in Brazil. Storm Boris brought record rainfall to eastern Central Europe in mid-September. The storm led to 24 fatalities and several billion dollars in damage; however, the death toll was significantly lower than in past major floods, highlighting the effectiveness of early warning systems and emergency management. Record rainfall led to major flooding in Valencia, Spain, on 29 October, with 720 mm recorded in a 12-hour period. At least 223 people were killed, and the economic damage exceeded $14 billion U.S. dollars.

Global drought decreased in 2024, both in intensity and extent, compared to 2023. Even so, Canada experienced both its driest and hottest year on record, contributing to one of its worst national wildfire seasons on record. Both Peru and Brazil reported their third driest year on record, with large swathes of the Amazon basin impacted by extreme drought conditions. By mid-October, the Rio Negro at Manaus, a major tributary of the Amazon River, recorded its lowest water levels since records began in 1902, surpassing the previous low in October 2023. Northwest Africa also saw exceptionally dry conditions as did Greece, Romania, and Bulgaria in Europe. The El Niño teleconnection patterns contributed to widespread drought across many countries of southern Africa. The resulting food and water shortages affected over 25 million people.

Unauthenticated | Downloaded 11/21/25 11:34 AM UTC

Editor and Author Affiliations (alphabetical by name)

Ades, Melanie, European Centre for Medium-Range Weather Forecasts, Reading, United Kingdom

Adjou, Mohamed, ISEN Engineering School, LaBISEN, Knowledge Learning and Information Modeling (KLaIM), Brest, France; University of Brest, Institut Universitaire Européen de la Mer (IUEM) UAR3113, Plouzané, France

Adler, Robert, Earth System Science Interdisciplinary Center, University of Maryland, College Park, Maryland

Adusumilli, Susheel, Scripps Institution of Oceanography, University of California, San Diego, La Jolla, California

Agyakwah, W., ERT, Inc., College Park, Maryland

Aldeco, Laura S., Servicio Meteorológico Nacional, Buenos Aires, Argentina

Alexe, Mihai, European Centre for Medium-Range Weather Forecasts, Bonn, Germany

Alfaro, Eric J., Center for Geophysical Research, University of Costa Rica, San José, Costa Rica; Center for Research in Marine Sciences and Limnology, University of Costa Rica, San José, Costa Rica; School of Physics, University of Costa Rica, San José, Costa Rica

Allan, Richard P., Department of Meteorology, University of Reading, Reading, United Kingdom; National Centre for Earth Observation (NCEO), University of Leicester, Leicester, United Kingdom

Allen, Teddy, Caribbean Institute for Meteorology and Hydrology, Bridgetown, Barbados

Allgood, Adam, NOAA/NWS National Centers for Environmental Prediction Climate Prediction Center, College Park, Maryland

Alves, Lincoln. M., National Institute for Space Research (INPE), São Paulo, Brazil

Amador, Jorge A., Center for Geophysical Research, University of Costa Rica, San José, Costa Rica; School of Physics, University of Costa Rica, San José, Costa Rica

Amory, Charles, Université Grenoble Alpes, Institut des Géosciences de l'Environnement, IRD, CNRS, Grenoble INP, Grenoble, France

Anderson, John, Hampton University, Hampton, Virginia

Andrade, B., Seychelles Meteorological Authority, Mahe, Seychelles

Anneville, Orlane, National Research Institute for Agriculture, Food and Environment (INRAE), CARRTEL, Université Savoie Mont Blanc, Thonon les Bains, France

Aono, Yasuyuki, Graduate School of Agriculture, Osaka Metropolitan University, Sakai, Japan

Arguez, Anthony, NOAA/NESDIS National Centers for Environmental Information, Asheville, North Carolina

Armenteras-Pascual, Dolors, Science Faculty, Universidad Nacional de Colombia, Bogotá, Colombia

Arosio, Carlo, University of Bremen, Bremen, Germany

Asgharzadeh, Parvaneh, Climate Department, Iran National Meteorological Organization, Tehran, Iran

Asher, Elizabeth, Cooperative Institute for Research in Environmental Sciences, University of Colorado Boulder, Boulder, Colorado; NOAA Global Monitoring Laboratory, Boulder, Colorado

Askjaer, Thomas G., Danish Meteorological Institute, Copenhagen, Denmark

Augustine, John A., NOAA Global Monitoring Laboratory, Boulder, Colorado

Avalos, Grinia, Servicio Nacional de Meteorología e Hidrología del Perú, Lima, Perú

Azorin-Molina, Cesar, Centro de Investigaciones sobre Desertificación – Spanish National Research Council (CSIC-UV-GVA), Valencia, Spain

Baez-Villanueva, Oscar M., Hydro-Climate Extremes Lab (H-CEL), Ghent University, Ghent, Belgium

Bahrami, Mahsa, Department of Geography, Pennsylvania State University, State College, Pennsylvania

Baiman, Rebecca, Department of Atmospheric and Oceanic Sciences, University of Colorado Boulder, Boulder, Colorado

Ballinger, Thomas J., International Arctic Research Center, University of Alaska Fairbanks, Fairbanks, Alaska

Bandgar, Arti, India Meteorological Department, Pune, India

Banwell, Alison F., Earth Science and Observation Center, Cooperative Institute for Research in Environmental Sciences (ESOC/CIRES), University of Colorado Boulder, Boulder, Colorado

Bardin, M. Yu., Yu. A. Izrael Institute of Global Climate and Ecology, Institute of Geography, Russian Academy of Sciences, Moscow, Russia

Barichivich, Jonathan, Laboratoire des Sciences du Climat et de l'Environnement (LSCE), LSCE/IPSL, CEA-CNRS-UVSQ, Gif-sur-Yvette, France

Baron, Alexandre, Cooperative Institute for Research in Environmental Sciences, University of Colorado Boulder, Boulder, Colorado; NOAA Chemical Sciences Laboratory, Boulder, Colorado

Barreira, Sandra, Argentine Naval Hydrographic Service, Buenos Aires, Argentina

Basckenstrass, Claire, Meteo France, Direction Interregionale Pour L'Ocean Indien, Réunion

Beadling, Rebecca L., Department of Earth and Environmental Science, Temple University, Philadelphia, Pennsylvania

Beauchemin, Marc, Environment and Climate Change Canada, Montreal, Canada

Beck, Hylke E., Physical Science and Engineering Division, King Abdullah University of Science and Technology, Thuwal, Saudi Arabia

Becker, Emily J., Rosenstiel School of Marine, Atmospheric, and Earth Science, University of Miami, Miami, Florida

Beckley, Brian, KBR, Inc., Greenbelt, Maryland; NASA Goddard Space Flight Center, Greenbelt, Maryland

Bekele, E., NOAA/NWS National Centers for Environmental Prediction Climate Prediction Center, College Park, Maryland

Bellas-Manley, Ashley, Colorado Center for Astrodynamics Research, Cooperative Institute for Research in Environmental Sciences, University of Colorado Boulder, Boulder, Colorado

Bellouin, Nicolas, University of Reading, Reading, United Kingdom; Institute Pierre Simon Laplace (IPSL), Guyancourt, France

Benedetti, Angela, European Centre for Medium-Range Weather Forecasts, Reading, United Kingdom

Berne, Christine, Météo-France, Toulouse, France

Berner, Logan T., School of Informatics, Computing, and Cyber Systems, Northern Arizona University, Flagstaff, Arizona

Bernhard, Germar H., Biospherical Instruments Inc., San Diego, California

Bhatt, Uma S., Geophysical Institute, University of Alaska Fairbanks, Fairbanks, Alaska

Bigalke, Siiri, Department of Geography, Portland State University, Portland, Oregon

Bilotta, Rocky, NOAA/NESDIS National Centers for Environmental Information, Asheville, North Carolina

Bissolli, Peter, Deutscher Wetterdienst, WMO RA VI Regional Climate Centre Network, Offenbach, Germany

Bjerke, Jarle W., Norwegian Institute for Nature Research, Trondheim, Norway; FRAM – High North Research Centre for Climate and the Environment, Tromsø, Norway

Blake, Eric S., NOAA/NWS National Hurricane Center, Miami, Florida

Blannin, Josh, Met Office Hadley Centre, Exeter, United Kingdom

Blenkinsop, Stephen, School of Engineering, Newcastle University, Newcastle-upon-Tyne, United Kingdom; Tyndall Centre for Climate Change Research, Norwich, United Kingdom

Bliss, Angela, NASA Goddard Space Flight Center, Greenbelt, Maryland

Blunden, Jessica, NOAA/NESDIS National Centers for Environmental Information, Asheville, North Carolina

Bochníček, Oliver, Slovak Hydrometeorological Institute, Bratislava, Slovakia

Bock, Olivier, Université Paris Cité, Institut de physique du globe de Paris, CNRS, IGN, Paris, France; Univ Gustave Eiffel, ENSG, IGN, Marne-la-Vallée, France

Bodin, Xavier, Laboratoire EDYTEM, CNRS/Université Savoie Mont-Blanc, Le Bourget-du-Lac, France

Unauthenticated | Downloaded 11/21/25 11:34 AM UTC

Bonte, Olivier, Hydro-Climate Extremes Lab (H-CEL), Ghent University, Ghent, Belgium
Bosilovich, Michael G., Global Modeling and Assimilation Office, NASA Goddard Space Flight Center, Greenbelt, Maryland
Boucher, Olivier, Institute Pierre Simon Laplace (IPSL), Guyancourt, France
Bowman, Kevin, Jet Propulsion Laboratory, California Institute of Technology, Pasadena, California
Box, Jason E., Geological Survey of Denmark and Greenland (GEUS), Copenhagen, Denmark
Brady, Mike, Climate Research Division, Environment and Climate Change Canada, Toronto, Canada
Brettschneider, Brian, NOAA/NWS Alaska Region, Anchorage, Alaska
Brittain, Kyle, Environment and Climate Change Canada, Calgary, Canada
Buehler, Sarah A., Universität Hamburg, Hamburg, Germany
Bukunt, Brandon, NOAA/NWS Weather Forecast Office, Tiyan, Guam
Bunno, Ayaka, Japan Meteorological Agency, Tokyo, Japan
Butler, Amy H., Chemical Sciences Laboratory, Boulder, Colorado
Byrne, Michael, P., School of Earth and Environmental Sciences, University of St Andrews, St Andrews, United Kingdom
Calderón, Blanca, Center for Geophysical Research, University of Costa Rica, San José, Costa Rica
Camargo, Suzana J., Lamont-Doherty Earth Observatory, Columbia University, Palisades, New York; Columbia Climate School, Columbia University, New York, New York
Campbell, Jayaka, Department of Physics, The University of the West Indies, Kingston, Jamaica
Campos, Diego, Barcelona Supercomputing Centre, Barcelona, Spain
Cappucci, Fabrizio, Joint Research Centre, European Commission, Ispra, Italy
Carter, Brendan R., Cooperative Institute for Climate, Ocean, and Ecosystem Studies, University of Washington, Seattle, Washington; NOAA/OAR Pacific Marine Environmental Laboratory, Seattle, Washington
Casella, Ana, Instituto Nacional de Meteorología e Hidrología de Venezuela (INAMEH), Caracas, Venezuela
Cetinić, Ivona, NASA Goddard Space Flight Center, Greenbelt, Maryland; Universities Space Research Association, Columbia, Maryland
Chambers, Don P., College of Marine Science, University of South Florida, St. Petersburg, Florida
Chan, Duo, School of Ocean and Earth Science, University of Southampton, Southampton, United Kingdom
Chandler, Elise, Bureau of Meteorology, Melbourne, Australia
Charlton, Candice S., Department of Physics, The University of the West Indies, Kingston, Jamaica
Chen, Hua, Nanjing University of Information Science and Technology, Nanjing, China
Chen, Lin, Institute for Climate and Application Research (ICAR)/KLME/ILCEC/CIC-FEMD, Nanjing University of Information Science and Technology, Nanjing, China
Cheng, Lijing, International Center for Climate and Environment Sciences, Institute of Atmospheric Physics, Chinese Academy of Sciences, Beijing, China
Cheng, Vincent Y. S., Environment and Climate Change Canada, Toronto, Canada
Christiansen, Hanne H., Arctic Geophysics Department, University Centre in Svalbard, Longyearbyen, Norway
Christy, John R., University of Alabama in Huntsville, Huntsville, Alabama
Chung, Eui-Seok, Korea Polar Research Institute, Incheon, South Korea
Ciasto, Laura M., NOAA/NWS National Centers for Environmental Prediction, Climate Prediction Center, College Park, Maryland
Clarke, Leonardo, Department of Physics, The University of the West Indies, Kingston, Jamaica
Clem, Kyle R., School of Geography, Environment and Earth Sciences, Victoria University of Wellington, Wellington, New Zealand
Clingan, Scott, Cooperative Institute for Research in Environmental Sciences, University of Colorado Boulder, Boulder, Colorado; NOAA Global Monitoring Laboratory, Boulder, Colorado
Coelho, Caio A.S., Centro de Previsão do Tempo e Estudos Climáticos/National Institute for Space Research, Center for Weather Forecasts and Climate Studies, Cachoeira Paulista, Brazil
Coldewey-Egbers, Melanie, German Aerospace Center (DLR), Oberpfaffenhofen, Germany
Colwell, Steve, British Antarctic Survey, Cambridge, United Kingdom
Cooley, Sarah, Duke University, Durham, North Carolina
Cooper, Owen R., NOAA Chemical Sciences Laboratory, Boulder, Colorado
Cornes, Richard C., National Oceanography Centre, Southampton, United Kingdom
Correa, Kris, Servicio Nacional de Meteorología e Hidrología del Perú, Lima, Perú
Costa, Felipe, Centro Internacional para la Investigación del Fenómeno de El Niño (CIIFEN), Guayaquil, Ecuador
Covey, Curt, Lawrence Livermore National Laboratory, Livermore, California
Coy, Lawrence, Science Systems and Applications, Inc., Lanham, Maryland; NASA Goddard Space Flight Center, Greenbelt, Maryland
Crawford, Alex, Department of Environment and Geography, University of Manitoba, Winnipeg, Canada
Crétaux, Jean-Francois, LEGOS (CNES/CNRS/IRD/UPS), Université de Toulouse, Toulouse, France
Crimmins, Theresa, USA National Phenology Network, School of Natural Resources and the Environment, University of Arizona, Tucson, Arizona
Crotwell, Molly, Cooperative Institute for Research in Earth Science, University of Colorado Boulder, Boulder, Colorado; NOAA Global Monitoring Laboratory, Boulder, Colorado
Culpepper, Joshua, Department of Biology, York University, Toronto, Canada
Cunha, Ana P., Centro Nacional de Monitoramento e Alertas de Desastres Naturais CEMADEN, São Paulo, Brazil
Cusicanqui, Diego, Institut de Géosciences de l'Environnement (IGE), Université Grenoble Alpes, INRAE, CNRS, IRD, Grenoble INP, ISTerre, Grenoble, France
Datta, Rajashree T., Department of Civil Engineering and Geosciences, TU Delft, The Netherlands
Davis, Sean M., NOAA Chemical Sciences Laboratory, Boulder, Colorado
De Bock, Veerle, Royal Meteorological Institute of Belgium, Brussels, Belgium
de Jeu, Richard A. M., Transmissivity B.V., Haarlem, The Netherlands
De Laat, Jos, Royal Netherlands Meteorological Institute (KNMI), DeBilt, The Netherlands
Decharme, Bertrand, Centre National de Recherches Météorologiques, Météo-France/CNRS, Toulouse, France
Degenstein, Doug, University of Saskatchewan, Saskatoon, Canada
Delaloye, Reynald, Department of Geosciences, University of Fribourg, Fribourg, Switzerland
Derksen, Chris, Climate Research Division, Environment and Climate Change Canada, Toronto, Canada
Di Tomaso, Enza, European Centre for Medium-Range Weather Forecasts, Bonn, Germany
Diamond, Howard J., NOAA/OAR Air Resources Laboratory, College Park, Maryland
Dindyal, S., Mauritius Meteorological Service, Vacoas, Mauritius
Divine, Dmitry, Norwegian Polar Institute, Fram Centre, Tromsø, Norway
Dokulil, Martin T., Research Institute for Limnology, University of Innsbruck, Mondsee, Austria
Donat, Markus G., Barcelona Supercomputing Centre, Barcelona, Spain; Catalan Institution for Research and Advanced Studies (ICREA), Barcelona, Spain
Dong, Shenfu, NOAA/OAR Atlantic Oceanographic and Meteorological Laboratory, Miami, Florida
Dorigo, Wouter A., Department of Geodesy and Geoinformation, TU Wien, Vienna, Austria

Unauthenticated | Downloaded 11/21/25 11:34 AM UTC

Druckenmiller, Matthew L., National Snow and Ice Data Center, Cooperative Institute for Research in Environmental Sciences, University of Colorado, Boulder, Colorado

du Plessis, Marcel, Department of Marine Sciences, University of Gothenburg, Sweden

Dugan, Hilary, Center of Limnology, University of Wisconsin-Madison, Madison, Wisconsin

Dulamsuren, Dashkhuu, Information Research Institute of Meteorology, Hydrology and Environment, Ulaanbaatar, Mongolia

Dunn, Robert J. H., Met Office Hadley Centre, Exeter, United Kingdom

Durre, Imke, Climate Science and Services Division, NOAA/NESDIS National Centers for Environmental Information, Asheville, North Carolina

Dutton, Geoff, Cooperative Institute for Research in Earth Science, University of Colorado Boulder, Boulder, Colorado

Echeverría Garcés, Paola, Instituto Nacional de Meteorología e Hidrología de Ecuador (INAMHI), Quito, Ecuador

Effertz, Peter, Cooperative Institute for Research in Environmental Sciences, University of Colorado Boulder, Boulder, Colorado; NOAA Global Monitoring Laboratory, Boulder, Colorado

Ekici, Mithat, Turkish State Meteorological Service, Ankara, Türkiye

Elias Chereque, Alesksandra, Department of Physics, University of Toronto, Toronto, Canada

ElKharrim, M., General Directorate of Meteorology, Rabat, Morocco

Enno, Sven-Erik, EUMETSAT, Darmstadt, Germany

Epstein, Howard E., Department of Environmental Sciences, University of Virginia, Charlottesville, Virginia

Espinoza, Jhan-Carlo, Université Grenoble Alpes, Institut des Géosciences de l'Environnement, IRD, CNRS, Grenoble INP, Grenoble, France

Estilow, Thomas W., Rutgers University, Piscataway, New Jersey

Estrella, Nicole, Ecoclimatology, Department of Life Science Systems, TUM School of Life Sciences, Technical University of Munich, Freising, Germany

Farrell, Sinead, Department of Geographical Sciences, University of Maryland, College Park, Maryland

Fauchereau, Nicolas, National Institute of Water and Atmospheric Research, Ltd., Auckland, New Zealand

Fausto, Robert S., Geological Survey of Denmark and Greenland (GEUS), Copenhagen, Denmark

Feely, Richard A., NOAA/OAR Pacific Marine Environmental Laboratory, Seattle, Washington

Fenimore, Chris, NOAA/NESDIS National Centers for Environmental Information, Asheville, North Carolina

Fereday, David, Met Office Hadley Centre, Exeter, United Kingdom

Fettweis, Xavier, SPHERES Research Unit, University of Liège, Liège, Belgium

Fioletov, Vitali E., Environment and Climate Change Canada, Toronto, Canada

Flemming, Johannes, European Centre for Medium-Range Weather Forecasts, Bonn, Germany

Fogarty, Chris, Canadian Hurricane Centre, Dartmouth, Canada

Fogt, Ryan L., Department of Geography, Ohio University, Athens, Ohio

Forbes, Bruce C., Arctic Centre, University of Lapland, Rovaniemi, Finland

Forde, Brendan, Environment and Climate Change Canada, Toronto, Canada

Formanek, Maud, Department of Geodesy and Geoinformation, TU Wien, Vienna, Austria

Foster, Michael J., Cooperative Institute for Meteorological Satellite Studies, Space Science and Engineering Center, University of Wisconsin-Madison, Madison, Wisconsin

Franz, Bryan A., NASA Goddard Space Flight Center, Greenbelt, Maryland

Frederikse, Thomas, Planet Labs, Haarlem, The Netherlands

Fricker, Helen A., Scripps Institution of Oceanography, University of California, San Diego, La Jolla, California

Frith, Stacey M., Science Systems and Applications, Inc, Lanham, Maryland; NASA Goddard Space Flight Center, Greenbelt, Maryland

Froidevaux, Lucien, Jet Propulsion Laboratory, California Institute of Technology, Pasadena, California

Frost, Gerald V. (JJ), Alaska Biological Research, Inc., Fairbanks, Alaska

Fuhrman, S., ERT, Inc., College Park, Maryland

Füllekrug, Martin, University of Bath, Bath, United Kingdom

Gallemann, Thomas, Bavarian Environment Agency, Augsburg, Germany

Ganter, Catherine, Bureau of Meteorology, Melbourne, Australia

Gao, Meng, NASA Goddard Space Flight Center, Greenbelt, Maryland; Science Systems and Applications, Inc., Lanham, Maryland

Garforth, Judith, Woodland Trust, Grantham, United Kingdom

Garg, Jay, ADNET Systems, Inc., Hampton, Virginia

Gerland, Sebastian, Norwegian Polar Institute, Fram Centre, Tromsø, Norway

Gevorgyan, Artur, Hydrometeorology and Monitoring Center, Yerevan, Armenia

Ghent, Darren, National Centre for Earth Observation (NCEO), University of Leicester, Leicester, United Kingdom; School of Physics and Astronomy, University of Leicester, Leicester, United Kingdom

Giglio, Donata, Department of Atmospheric and Oceanic Sciences, University of Colorado Boulder, Boulder, Colorado

Gleason, Karin, NOAA/NESDIS National Centers for Environmental Information, Asheville, North Carolina

Gobron, Nadine, Joint Research Centre, European Commission, Ispra, Italy

Goldenberg, Stanley B., NOAA/OAR Atlantic Oceanographic and Meteorological Laboratory, Miami, Florida

Gollop, Amee, Climatic Research Unit, School of Environmental Sciences, University of East Anglia, Norwich, United Kingdom

Good, Elizabeth, Met Office, Exeter, United Kingdom

Goodman, Steven, Thunderbolt Global Analytics, Huntsville, Alabama

Goto, Atsushi, Japan Meteorological Agency, Tokyo, Japan

Graham, Garrett, North Carolina Institute for Climate Studies, North Carolina State University, Asheville, North Carolina

Grimaldi, Stefania, Joint Research Centre, European Commission, Ispra, Italy

Grooß, Jens-Uwe, Forschungszentrum Jülich (ICE-4), Jülich, Germany

Gruber, Alexander, Department of Geodesy and Geoinformation, TU Wien, Vienna, Austria

Gu, Guojun, Earth System Science Interdisciplinary Center, University of Maryland, College Park, Maryland

Guglielmin, Mauro, Department of Theoretical and Applied Sciences, Insubria University, Varese, Italy

Haghdoost, Shekoofeh, Hydro-Climate Extremes Lab (H-CEL), Ghent University, Ghent, Belgium

Hahn, Sebastian, Department of Geodesy and Geoinformation, TU Wien, Vienna, Austria

Haimberger, Leopold, Department of Meteorology and Geophysics, University of Vienna, Austria

Hakmi, S., General Directorate of Meteorology, Rabat, Morocco

Hall, Brad D., NOAA Global Monitoring Laboratory, Boulder, Colorado

Hamlington, Benjamin D., Center for Coastal Physical Oceanography, Old Dominion University, Norfolk, Virginia

Hancock, Alyce M., Southern Ocean Observing System (SOOS), Institute for Marine and Antarctic Studies (IMAS), University of Tasmania, Hobart, Australia

Hanna, Edward, Department of Geography and Lincoln Climate Research Group, Lincoln, United Kingdom

Harlan, Merritt E., U.S. Geological Survey, Denver, Colorado

Harnos, Daniel S., NOAA/NWS National Centers for Environmental Prediction Climate Prediction Center, College Park, Maryland

Unauthenticated | Downloaded 11/21/25 11:34 AM UTC

Harris, Bethan L., National Centre for Earth Observation (NCEO), University of Leicester, Leicester, United Kingdom; United Kingdom Centre for Ecology & Hydrology, Wallingford, United Kingdom

Harris, Ian, National Centre for Atmospheric Science (NCAS), University of East Anglia, Norwich, United Kingdom; Climatic Research Unit, School of Environmental Sciences, University of East Anglia, Norwich, United Kingdom

He, Qiong, Earth System Modeling Center, Nanjing University of Information Science and Technology, Nanjing, China

Hemming, Deborah L., Met Office Hadley Centre, Exeter, United Kingdom; Birmingham Institute of Forest Research, Birmingham University, Birmingham, United Kingdom

Hendricks, Stefan, Alfred Wegener Institute, Helmholtz Centre for Polar and Marine Research, Bremerhaven, Germany

Hidalgo, Hugo G., Center for Geophysical Research, Center for Research in Pure and Applied Mathematics; University of Costa Rica, San José, Costa Rica; School of Physics, University of Costa Rica, San José, Costa Rica

Ho, Shu-peng (Ben), NOAA/NESDIS Center for Satellite Applications and Research, College Park, Maryland

Hobbs, Will, Australian Antarctic Program Partnership, Institute for Marine and Antarctic Studies, University of Tasmania, Hobart, Tasmania; Australian Research Council Centre of Excellence for Climate Extremes, University of Tasmania, Hobart, Tasmania

Holliday, Rebecca, Met Office, Exeter, United Kingdom

Holzworth, Robert, University of Washington, Seattle, Washington

Horton, Radley M., Columbia Climate School, Columbia University, New York, New York

Howell, Stephen, Climate Research Division, Environment and Climate Change Canada, Toronto, Canada

Hrbáček, Filip, Department of Geography, Masaryk University, Brno, Czech Republic

Hu, Guojie, Cryosphere Research Station on Qinghai-Tibet Plateau, Northwestern Institute of Eco-Environment and Resources, CAS, Lanzhou, China

Hu, Zeng-Zhen, NOAA/NWS National Centers for Environmental Prediction Climate Prediction Center, College Park, Maryland

Huang, Boyin, NOAA/NESDIS National Centers for Environmental Information, Asheville, North Carolina

Ialongo, Iolanda, Finnish Meteorological Institute, Helsinki, Finland

Inness, Antje, European Centre for Medium-Range Weather Forecasts, Reading, United Kingdom

Isaksen, Ketil, Norwegian Meteorological Institute, Oslo, Norway

Jersild, Annika, Earth System Science Interdisciplinary Center/Cooperative Institute for Satellite Earth System Studies, University of Maryland, College Park, Maryland

Jevrejeva, Svetlana, National Oceanography Centre, Liverpool, United Kingdom

Jha, B., ERT, Inc., College Park, Maryland

Jia, Gensuo, Institute of Atmospheric Physics, Chinese Academy of Sciences, Beijing, China

John, Viju O., EUMETSAT, Darmstadt, Germany

Johns, William E., Rosenstiel School of Marine and Atmospheric Science, University of Miami, Miami, Florida

Johnsen, Bjørn, Norwegian Radiation and Nuclear Safety Authority, Østerås, Norway

Johnson, Bryan, NOAA/OAR Earth System Research Laboratory, Global Monitoring Division, Boulder, Colorado; University of Colorado Boulder, Boulder, Colorado

Jones, Philip D., Climatic Research Unit, School of Environmental Sciences, University of East Anglia, Norwich, United Kingdom

Johnson, Gregory C., School of Oceanography, University of Washington, Seattle, Washington ; NOAA/OAR Pacific Marine Environmental Laboratory, Seattle, Washington (retired)

Josey, Simon A., National Oceanography Centre, Southampton, United Kingdom

Jumaux, G., Meteo France, Direction Interregionale Pour L'Ocean Indien, Réunion

Junod, Robert, Earth System Science Center, University of Alabama in Huntsville, Huntsville, Alabama

Kääb, Andreas, Department of Geosciences, University of Oslo, Norway

Kabidi, K., General Directorate of Meteorology, Rabat, Morocco

Kaiser, Johannes W., Norwegian Institute for Air Research (NILU), Kjeller, Norway

Kaleschke, Lars, Alfred Wegener Institute, Helmholtz Centre for Polar and Marine Research, Bremerhaven, Germany

Kaufmann, Viktor, Institute of Geodesy, Working Group Remote Sensing and Photogrammetry, Graz University of Technology, Graz, Austria

Kazemi, Amin Fazl, Climate Department, Iran National Meteorological Organization, Tehran, Iran

Keller, Linda M., Antarctic Meteorological Research and Data Center, Space Science and Engineering Center, University of Wisconsin-Madison, Madison, Wisconsin

Kellerer-Pirklbauer, Andreas, Department of Geography and Regional Science, Cascade—The Mountain Processes and Mountain Hazards Group, University of Graz, Graz, Austria

Kendon, Michael, Met Office Hadley Centre, Exeter, United Kingdom

Kennedy, John, Independent Researcher, Verdun, France

Kent, Elizabeth C., National Oceanography Centre, Southampton, United Kingdom

Khalatyan, Yelena, Hydrometeorology and Monitoring Center, Yerevan, Armenia

Khan, Valentina, Hydrometeorological Centre of Russia, World Meteorological Organization (WMO) North EurAsia Climate Center, Moscow, Russia

Khaykin, Sergey, Laboratoire Atmosphères, Observations Spatiales (LATMOS), UVSQ, Sorbonne Université, CNRS, IPSL, Guyancourt, France

Khiem, Mai Van, National Center of Hydro-Meteorological Forecasting, Vietnam Meteorological and Hydrological Administration, Hanoi, Vietnam

Kidd, Richard, EODC GmbH, Vienna, Austria

Killick, Rachel. E., Met Office Hadley Center, Exeter, United Kingdom

Kim, Seong-Joong, Korea Polar Research Institute, Incheon, South Korea

Kipling, Zak, European Centre for Medium-Range Weather Forecasts, Reading, United Kingdom

Kirkpatrick, Sarah, Fenner School of Environment and Society, Australian National University, Canberra, Australia

Kittel, Christoph, Department of Geography, University of Liège, Liège, Belgium; Physical Geography Research Group, Department of Geography, Vrije Universiteit Brussel, Brussels, Belgium

Klotzbach, Philip J., Department of Atmospheric Science, Colorado State University, Fort Collins, Colorado

Kondragunta, Shobha, NOAA/NESDIS, College Park, Maryland

Korshunova, Natalia N., All-Russia Research Institute of Hydrometeorological Information, World Data Center, Obninsk, Russia

Kovács, Dávid D., Department of Geodesy and Geoinformation, TU Wien, Vienna, Austria

Kowal, K., NOAA/NWS National Centers for Environmental Prediction Climate Prediction Center, College Park, Maryland

Kraemer, Benjamin M., University of Freiburg, Freiburg, Germany

Kramarova, Natalya A., NASA Goddard Space Flight Center, Greenbelt, Maryland

Kruger, A. C., Climate Service, South African Weather Service, Pretoria, South Africa

Kumar, Arun, NOAA/NWS National Centers for Environmental Prediction Climate Prediction Center, College Park, Maryland

Kuusela, Mikael, Department of Statistics and Data Science, Carnegie Mellon University, Pittsburg, Pennsylvania

L'Heureux, Michelle, NOAA/NWS National Centers for Environmental Prediction Climate Prediction Center, College Park, Maryland

Laas, Alo, Estonian University of Life Sciences, Tartumaa, Estonia

Labe, Zachary M., Geophysical Fluid Dynamics Laboratory, Princeton, New Jersey

Lader, Rick, International Arctic Research Center, University of Alaska Fairbanks, Fairbanks, Alaska

Lait, Leslie R., NASA Ames Research Center, Moffett Field, California

Unauthenticated | Downloaded 11/21/25 11:34 AM UTC

Lakatos, Mónika, Climatology Unit, Hungarian Meteorological Service, Budapest, Hungary
Lakkala, Kaisa, Finnish Meteorological Institute, Sodankylä, Finland
Lam, Hoang Phuc, National Center of Hydro-Meteorological Forecasting, Vietnam Meteorological and Hydrological Administration, Hanoi, Vietnam
Lamont, Tarron, Department of Forestry, Fisheries and the Environment, Cape Town, South Africa
Lan, Xin, Cooperative Institute for Research in the Environmental Sciences, University of Colorado Boulder, Boulder, Colorado; NOAA Global Monitoring Laboratory, Boulder, Colorado
Landerer, F. W., Jet Propulsion Laboratory, California Institute of Technology, Pasadena, California
Landschützer, Peter, Flanders Marine Institute, InnovOcean Campus, Ostend, Belgium
Landsea, Chris W., NOAA/NWS National Hurricane Center, Miami, Florida
Lantz, Kathleen O., NOAA Global Monitoring Laboratory, Boulder, Colorado
Lara, Mark J., Department of Plant Biology, University of Illinois, Urbana, Illinois; Department of Geography, University of Illinois, Urbana, Illinois
Lavado-Casimiro, Waldo, Servicio Nacional de Meteorología e Hidrología del Perú, Lima, Perú
Lavers, David A., European Centre for Medium-Range Weather Forecasts, Reading, United Kingdom
Lazzara, Matthew A., Department of Physical Sciences, School of Arts and Sciences, Madison Area Technical College; Antarctic Meteorological Research and Data Center, Space Science and Engineering Center, University of Wisconsin-Madison, Madison, Wisconsin
Le Hénaff, Matthieu, NOAA/OAR Atlantic Oceanographic and Meteorological Laboratory, Miami, Florida
Lee, Simon H., School of Earth and Environmental Sciences, University of St Andrews, St Andrews, United Kingdom
Leibensperger, Eric, Department of Physics and Astronomy, Ithaca College, Ithaca, New York
Lems, Johanna, Department of Geodesy and Geoinformation, TU Wien, Vienna, Austria
Lennard, Chris, Department of Environmental and Geographical Science, University of Cape Town, Cape Town, South Africa
Leuliette, Eric, NOAA/NWS NCWCP Laboratory for Satellite Altimetry, College Park, Maryland
Levenson, Eric S., University of Oregon, Eugene, Oregon
Libonati, R., Federal University of Rio de Janeiro, Rio de Janeiro, Brazil
Lieser, Jan L., Bureau of Meteorology, Hobart, Australia; Institute for Marine and Antarctic Studies (IMAS), University of Tasmania, Hobart, Australia
Liley, Ben, National Institute of Water and Atmospheric Research (NIWA), Lauder, New Zealand
Lin, I-I., National Taiwan University, Taipei, Taiwan
Liu, Xuefeng, Nanjing University of Information Science and Technology, Nanjing, China
Lo, Y. T. Eunice, Cabot Institute for the Environment; University of Bristol, Bristol, United Kingdom; Elizabeth Blackwell Institute for Health Research, University of Bristol, Bristol, United Kingdom
Locarnini, Ricardo, NOAA/NESDIS National Centers for Environmental Information, Silver Spring, Maryland
Loeb, Norman G., NASA Langley Research Center, Hampton, Virginia
Long, Lindsey N., NOAA/NWS National Centers for Environmental Prediction Climate Prediction Center, College Park, Maryland
Loomis, Bryant D., NASA Goddard Space Flight Center, Greenbelt, Maryland
Lopez, Hosmay, NOAA/OAR Atlantic Oceanographic and Meteorological Laboratory, Miami, Florida
Lorrey, Andrew M., National Institute of Water and Atmospheric Research, Ltd., Auckland, New Zealand
Loyola, Diego, German Aerospace Center (DLR), Oberpfaffenhofen, Germany
Lu, Rui, Nanjing University of Information Science and Technology, Nanjing, China
Lui, Yuk Sing, Hong Kong Observatory, Hong Kong, China
Lumpkin, Rick, NOAA/OAR Atlantic Oceanographic and Meteorological Laboratory, Miami, Florida
Lunagomez Cruz, Daniela Paola, National Meteorological Service of Mexico, Mexico City, Mexico
Luo, Jing-Jia, Institute for Climate and Application Research, Nanjing University of Information Science and Technology, Nanjing, China
Luojus, Kari, Arctic Research Centre, Finnish Meteorological Institute, Helsinki, Finland
Lyman, John M., Cooperative Institute for Marine and Atmospheric Research, University of Hawai' i, Honolulu, Hawai' i; NOAA/OAR Pacific Marine Environmental Laboratory, Seattle, Washington
Macander, Matthew J., Alaska Biological Research, Inc., Fairbanks, Alaska
Macara, Gregor, National Institute of Water and Atmospheric Research (NIWA), Lauder, New Zealand
MacFerrin, Michael, Earth Science and Observation Center, Cooperative Institute for Research in Environmental Sciences (ESOC/CIRES), University of Colorado Boulder, Boulder, Colorado
MacLennan, Michelle L., British Antarctic Survey, Cambridge, United Kingdom
Magee, Andrew D., School of Environmental and Life Sciences, University of Newcastle, Callaghan, New South Wales, Australia
Magnin, Florence, Laboratoire EDYTEM, CNRS/Université Savoie Mont-Blanc, Le Bourget-du-Lac, France
Magnússon, Rúna Í., Plant Ecology and Nature Conservation Group, Wageningen University & Research, Wageningen, Netherlands
Mamen, Jostein, Climate Division, Norwegian Meteorological Institute, Oslo, Norway
Mankoff, Ken D., Business Integra, New York, New York; NASA Goddard Institute for Space Studies, New York, New York
Marengo, Jose A., Centro Nacional de Monitoramento e Alertas de Desastres Naturais CEMADEN, São Paulo, Brazil
Martinez, Rodney, World Meteorological Organization, San Jose, Costa Rica
Massom, Robert A., Australian Antarctic Division, Australian Antarctic Program Partnership (AAPP) and Australian Centre for Excellence in Antarctic Science (ACEAS), Hobart, Australia
Matsuzaki, Shin-Ichiro, National Institute for Environmental Studies, Tsukuba, Japan
Matthews, Tom, Department of Geography, King's College London, London, United Kingdom
Mayer, Michael, Department of Meteorology and Geophysics, University of Vienna, Vienna, Austria; Research Department, European Centre for Medium-Range Weather Forecasts, Bonn, Germany
McBride, C., Climate Service, South African Weather Service, Pretoria, South Africa
McClelland, James W., Marine Biological Laboratory, Woods Hole, Massachusetts
McVicar, Tim R., CSIRO Environment, Canberra, Australia; Australian Research Council Centre of Excellence for Climate Extremes, Sydney, Australia
Mears, Carl A., Remote Sensing Systems, Santa Rosa, California
Medley, Brooke, Cryospheric Sciences Laboratory, NASA Goddard Space Flight Center, Greenbelt, Maryland
Meier, Walter N., National Snow and Ice Data Center, Cooperative Institute for Research in Environment Sciences, University of Colorado, Boulder, Colorado
Mekonnen, Ademe, North Carolina A&T University, Greensboro, North Carolina
Menzel, Annette, Ecoclimatology, Department of Life Science Systems, TUM School of Life Sciences, Technical University of Munich, Freising, Germany; Institute for Advanced Study, Technical University of Munich, Garching, Germany
Merchant, Christopher J., University of Reading, Reading, United Kingdom
Merrifield, Mark A., Integrative Oceanography Division, Scripps Institution of Oceanography, La Jolla, California

Unauthenticated | Downloaded 11/21/25 11:34 AM UTC

Meyer, Michael F., U.S. Geological Survey, Madison, Wisconsin
Mikolajczyk, David E., Antarctic Meteorological Research and Data Center, Space Science and Engineering Center, University of Wisconsin-Madison, Madison, Wisconsin
Milward, James, Department of Earth and Environmental Science, Temple University, Philadelphia, Pennsylvania
Minney, Caitlin, Bureau of Meteorology, Melbourne, Australia
Miralles, Diego G., Hydro-Climate Extremes Lab (H-CEL), Ghent University, Ghent, Belgium
Mishonov, Alexey, Earth System Science Interdisciplinary Center/Cooperative Institute for Satellite Earth System Studies, University of Maryland, College Park, Maryland; NOAA/NESDIS National Centers for Environmental Information, Silver Spring, Maryland
Mitchum, Gary T., College of Marine Science, University of South Florida, St. Petersburg, Florida
Moat, Ben I., National Oceanography Centre, Southampton, United Kingdom
Mohammadi, Marjan, Climate Department, Iran National Meteorology Organization, Tehran, Iran
Moise, Aurel, Centre for Climate Research Singapore, Meteorological Service Singapore, Singapore
Molina-Carpio, Jorge, Universidad Mayor de San Andrés, La Paz, Bolivia
Montenegro, Martin, Centro Internacional para la Investigación del Fenómeno de El Niño (CIIFEN), Guayaquil, Ecuador
Montesano, Paul M., NASA Goddard Space Flight Center, Greenbelt, Maryland
Montzka, Stephan A., NOAA Global Monitoring Laboratory, Boulder, Colorado
Moody, Ronald, Meteorological Service of Jamaica, Kingston, Jamaica
Moon, Twila A., National Snow and Ice Data Center, Cooperative Institute for Research in Environmental Sciences, University of Colorado, Boulder, Colorado
Mora, Natali, Center for Geophysical Research, University of Costa Rica, San José, Costa Rica
Morata Gasca, Ana, Agencia Estatal de Meteorología, Madrid, Spain
Morice, Colin, Met Office Hadley Centre, Exeter, United Kingdom
Morino, Isamu, National Institute for Environmental Studies Tsukuba, Ibaraki, Japan
Morris, Gary A., NOAA Global Monitoring Laboratory, Boulder, Colorado
Mostafa, A. E., Department of Seasonal Forecast and Climate Research, Cairo Numerical Weather Prediction, Egyptian Meteorological Authority, Cairo, Egypt
Mote, Thomas L., Department of Geography, University of Georgia, Athens, Georgia
Motrøen Gjelten, Herdis, Norwegian Meteorological Institute, Oslo, Norway
Mrekaj, Ivan, Technical University in Zvolen, Zvolen, Slovakia
Mudryk, Lawrence, Climate Research Division, Environment and Climate Change Canada, Toronto, Canada
Mühle, Jens, Scripps Institution of Oceanography, San Diego, California
Müller, Rolf, Forschungszentrum Jülich (IEK-7), Jülich, Germany
Nance, D., Cooperative Institute for Research in Environmental Sciences, University of Colorado Boulder, Boulder, Colorado
Neigh, Christopher S. R., NASA Goddard Space Flight Center, Greenbelt, Maryland
Nerem, R. Steven, Colorado Center for Astrodynamics Research, Cooperative Institute for Research in Environmental Sciences, University of Colorado Boulder, Boulder, Colorado
Newman, Paul A., NASA Goddard Space Flight Center, Greenbelt, Maryland
Nicolas, Julien P., European Centre for Medium-Range Weather Forecasts, Bonn, Germany
Noetzli, Jeannette, WSL Institute for Snow and Avalanche Research SLF, Davos Dorf, Switzerland; Climate Change, Extremes and Natural Hazards in Alpine Regions Research Centre (CERC), Davos Dorf, Switzerland
Nomenjanahary, T., Seychelles Meteorological Authority, Mahe, Seychelles
Norton, Taylor, Antarctic Meteorological Research and Data Center, Space Science and Engineering Center, University of Wisconsin-Madison, Madison, Wisconsin
Nyland, Kelsey E., George Washington University, Washington, DC
O'Keefe, John, The Harvard Forest, Harvard University, Petersham, Massachusetts
Oe, Mitsuho, Japan Meteorological Agency, Tokyo, Japan
Ollinik, Jessica Erin, Department of Chemistry and Biochemistry, University of Regina, Regina, Canada
Osborn, Timothy J., Climatic Research Unit, School of Environmental Sciences, University of East Anglia, Norwich, United Kingdom
Overland, James E., NOAA/OAR Pacific Marine Environmental Laboratory, Seattle, Washington
Pan, Y., International Desks, NOAA/NWS National Centers for Environmental Prediction Climate Prediction Center, College Park, Maryland; ERT, Inc., College Park, Maryland
Parrington, Mark, European Centre for Medium-Range Weather Forecasts, Bonn, Germany
Pasch, Richard J., NOAA/NWS National Hurricane Center, Miami, Florida
Pascual Ramírez, Reynaldo, National Meteorological Service of Mexico, Mexico City, Mexico
Pellet, Cécile, Department of Geosciences, University of Fribourg, Fribourg, Switzerland
Pelto, Mauri, Nichols College, Dudley, Massachusetts
Pennington, Elyse, Jet Propulsion Laboratory, California Institute of Technology, Pasadena, California
Perez, Renellys C., NOAA/OAR Atlantic Oceanographic and Meteorological Laboratory, Miami, Florida
Perovich, Donald K., Dartmouth College, Hanover, New Hampshire
Petersen, Kyle, Cooperative Institute for Research in Environmental Sciences, University of Colorado Boulder, Boulder, Colorado; NOAA Global Monitoring Laboratory, Boulder, Colorado
Petropavlovskikh, Irina, NOAA/OAR Earth System Research Laboratory, Global Monitoring Division, Boulder, Colorado; University of Colorado Boulder, Boulder, Colorado
Petty, Alek, NASA Goddard Space Flight Center, Greenbelt, Maryland
Pezza, Alexandre B., Greater Wellington Regional Council, Wellington, New Zealand
Pezzi, Luciano P., Laboratory of Ocean and Atmosphere Studies (LOA), Earth Observation and Geoinformatics Division (DIOTG), National Institute for Space Research (INPE), São José dos Campos, Brazil
Phillips, Coda, Cooperative Institute for Meteorological Satellite Studies, Space Science and Engineering Center, University of Wisconsin-Madison, Madison, Wisconsin
Phoenix, Gareth K., School of Biosciences, University of Sheffield, Sheffield, United Kingdom
Pierson, Don, Department of Ecology and Genetics, Uppsala University, Uppsala, Sweden
Pinto, Izidine, Royal Netherlands Meteorological Institute (KNMI), De Bilt, The Netherlands
Po-Chedley, Stephen, Lawrence Livermore National Laboratory, Livermore, California
Pogliotti, Paolo, Environmental Protection Agency of Valle d'Aosta, Saint Christophe, Italy
Poinar, Kristin, University at Buffalo, Buffalo, New York
Polvani, Lorenzo, Columbia University, New York, New York
Preimesberger, Wolfgang, Department of Geodesy and Geoinformation, TU Wien, Vienna, Austria
Price, Colin, Tel Aviv University, Tel Aviv, Israel
Pulkkanen, Merja, Finnish Environment Institute (SYKE), Helsinki, Finland
Randel, William J., National Center for Atmospheric Research, Boulder, Colorado
Raphael, Marilyn N., Department of Geography, University of California, Los Angeles, Los Angeles, California
Raymond, Colin, Joint Institute for Regional Earth System Science and Engineering, University of California, Los Angeles, Los Angeles, California

Unauthenticated | Downloaded 11/21/25 11:34 AM UTC

Reagan, James, NOAA/NESDIS National Centers for Environmental Information, Silver Spring, Maryland
Reid, Phillip, Bureau of Meteorology, Hobart, Australia; Australian Antarctic Program Partnership (AAPP), Hobart, Tasmania, Australia
Remy, Samuel, HYGEOS, Lille, France
Ricciardulli, Lucrezia, Remote Sensing Systems, Santa Rosa, California
Richardson, Andrew D., School of Informatics, Computing, and Cyber Systems, Northern Arizona University, Flagstaff, Arizona; Center for Ecosystem Science and Society, Northern Arizona University, Flagstaff, Arizona
Ricker, Robert, NORCE Norwegian Research Centre, Tromsø, Norway
Rivera, P. P., Servicio Nacional de Meteorología e Hidrología del Perú, Lima, Perú
Robinson, David A., Rutgers University, Piscataway, New Jersey
Robjhon, M., ERT Inc., College Park, Maryland; NOAA/NWS National Centers for Environmental Prediction Climate Prediction Center, NOAA, College Park, Maryland
Rodell, Matthew, Earth Sciences Division, NASA Goddard Space Flight Center, Greenbelt, Maryland
Rodriguez-Fernandez, Nemesio, CESBIO, Université de Toulouse, CNES/CNRS/INRAe/IRD/UPS, Toulouse, France
Roebeling, Maarit, Deutscher Wetterdienst, WMO RA VI Regional Climate Centre Network, Offenbach, Germany
Rogers, Cassandra D.W., Bureau of Meteorology, Melbourne, Australia
Rohini, P., India Meteorological Department, Ministry of Earth Sciences, Pune, India
Romanovsky, Vladimir E., Geophysical Institute, University of Alaska Fairbanks, Fairbanks, Alaska
Ronchail, Josyane, Laboratoire LOCEAN-IPSL, Paris, France
Rosencrans, Matthew, NOAA/NWS National Centers for Environmental Prediction Climate Prediction Center, College Park, Maryland
Rosenlof, Karen H., NOAA Chemical Sciences Laboratory, Boulder, Colorado
Rozanov, Alexei, University of Bremen, Bremen, Germany
Rozkošný, Jozef, Slovak Hydrometeorological Institute, Bratislava, Slovakia
Rubek, Frans, Danish Meteorological Institute, Copenhagen, Denmark
Rusanovskaya, Olga O., Institute of Biology, Irkutsk State University, Irkutsk, Russia
Rutishauser, This, Swiss Academy of Sciences (SCNAT), Bern, Switzerland
Ryan-Keogh, Thomas J., Southern Ocean Carbon-Climate Observatory, Council for Scientific and Industrial Research (CSIR), Cape Town, South Africa
Sabeerali, C. T., India Meteorological Department, Ministry of Earth Sciences, Pune, India
Sakai, Tetsu, Meteorological Research Institute, Japan Meteorological Agency, Tsukuba, Ibaraki, Japan
Salamon, Peter, Joint Research Centre, European Commission, Ispra, Italy
Salazar, Iliana, Centro Internacional para la Investigación del Fenómeno de El Niño (CIIFEN), Guayaquil, Ecuador
Salinas, Roberto, Dirección de Meteorología e Hidrología, Asunción, Paraguay; Dirección Nacional de Aeronáutica Civil, Asunción, Paraguay
Sánchez-Lugo, Ahira, NOAA/NESDIS National Centers for Environmental Information, Asheville, North Carolina
Santee, Michelle L., NASA Jet Propulsion Laboratory, Pasadena, California
Sato, Hirotaka, Tokyo Climate Center, Japan Meteorological Agency, Tokyo, Japan
Sawaengphokhai, Parnchai, ADNET Systems, Inc., Hampton, Virginia
Scambos, Theodore, Earth Science and Observation Center, Cooperative Institute for Research in Environmental Sciences (ESOC/CIRES), University of Colorado Boulder, Boulder, Colorado
Scheller, Johan H., Department of Ecoscience, Arctic Research Centre Aarhus University, Roskilde, Denmark
Schenzinger, Verena, Medical University of Innsbruck, Innsbruck, Austria
Schlegal, Robert W., Laboratoire d'Océanographie de Villefranche, Sorbonne Université, Villefranche-sur-mer, France
Schmid, Claudia, NOAA/OAR Atlantic Oceanographic and Meteorological Laboratory, Miami, Florida
Schmid, Martin, Eawag, Department Surface Waters—Research and Management, Kastanienbaum, Switzerland
Schreck, Carl J., Cooperative Institute for Satellite Earth System Studies, North Carolina Institute for Climate Studies, North Carolina State University, Asheville, North Carolina
Schulz, Cristina, Department of Marine and Environmental Sciences, Northeastern University, Boston, Massachussetts
Segele, Z. T., NOAA/NWS National Centers for Environmental Prediction Climate Prediction Center, College Park, Maryland
Sensoy, Serhat, Turkish State Meteorological Service, Ankara, Türkiye
Seong, Ji-In, Climate Change Monitoring Division, Korea Meteorological Administration, Seoul, South Korea
Serna Cuenca, Julieta, Instituto de Hidrología, Meteorología y Estudios Ambientales de Colombia (IDEAM), Bogotá, Colombia
Serreze, Mark C., National Snow and Ice Data Center, Cooperative Institute for Research in Environmental Sciences, University of Colorado, Boulder, Colorado
Sezaki, Fumi, Japan Meteorological Agency, Tokyo, Japan
Shao, Xi, Earth System Science Interdisciplinary Center, University of Maryland, College Park, Maryland
Sharma, Sapna, Department of Biology, York University, Toronto, Ontario, Canada
Shi, Jia-Rui, Courant Institute of Mathematical Sciences, New York University, New York City, New York
Shi, Lei, NOAA/NESDIS National Centers for Environmental Information, Asheville, North Carolina
Shiklomanov, Alexander I., University of New Hampshire, Durham, New Hampshire; Arctic and Antarctic Research Institute, St. Petersburg, Russia
Shiklomanov, Nikolay I., George Washington University, Washington, DC
Shimaraeva, Svetlana V., Institute of Biology, Irkutsk State University, Irkutsk, Russia
Shinohara, Ryuichiro, Regional Environment Conservation Division, National Institute for Environmental Studies, Tsukuba, Ibaraki, Japan
Shukla, R., NOAA/NWS National Centers for Environmental Prediction Climate Prediction Center, College Park, Maryland; ERT Inc., College Park, Maryland;
Silow, Eugene A., Institute of Biology, Irkutsk State University, Irkutsk, Russia
Sima, F., Retired, Banjul, The Gambia
Simmons, Adrian J., European Centre for Medium-Range Weather Forecasts, Reading, United Kingdom
Singh, B., University Corporation for Atmospheric Research Cooperative Programs for the Advancement of Earth System Science (CPAESS), College Park, Maryland
Smeed, David A., National Oceanography Centre, Southampton, United Kingdom
Smith, Adam, NOAA/NESDIS National Centers for Environmental Information, Asheville, North Carolina
Smith, Benjamin E., Polar Science Center, Applied Physics Laboratory, University of Washington, Seattle, Washington
Smith, Katie, Cooperative Institute for Research in Environmental Sciences, University of Colorado Boulder, Boulder, Colorado; NOAA Chemical Sciences Laboratory, Boulder, Colorado
Smith, Ryan H., NOAA/OAR Atlantic Oceanographic and Meteorological Laboratory, Miami, Florida
Smith, Sharon L., Geological Survey of Canada, Natural Resources Canada, Ottawa, Canada
Soden, Brian J., University of Miami, Miami, Florida
Sofieva, Viktoria, Finnish Meteorological Institute, Helsinki, Finland
Soldo, Logan, Cooperative Institute for Research in Environmental Sciences, University of Colorado Boulder, Boulder, Colorado; NOAA Global Monitoring Laboratory, Boulder, Colorado
Souza, Everaldo, Federal University of Pará (UFPA), Belém, Brazil
Speich, Sabrina, Laboratoire de Météorologie Dynamique, Institut Pierre-Simon Laplace, ENS-PSL, Paris, France

Unauthenticated | Downloaded 11/21/25 11:34 AM UTC

Spence-Hemmings, Jacqueline, Meteorological Service of Jamaica, Kingston, Jamaica
Spencer, Robert G. M., Florida State University, Tallahassee, Florida
Spillane, Sandra, Met Éireann, Dublin, Ireland
Sreejith, O. P., India Meteorological Department, Ministry of Earth Sciences, Pune, India
Srivastava, A. K., India Meteorological Department, Pune, India
Stackhouse, Jr., Paul W., NASA Langley Research Center, Hampton, Virginia
Stammerjohn, Sharon, Institute of Arctic and Alpine Research, University of Colorado Boulder, Boulder, Colorado
Stauffer, Ryan M., Atmospheric Chemistry and Dynamics Laboratory, NASA Goddard Space Flight Center, Greenbelt, Maryland
Steinbrecht, Wolfgang, Deutscher Wetterdienst, Hohenpeissenberg, Germany
Steiner, Andrea K., Wegener Center for Climate and Global Change, University of Graz, Graz, Austria
Stella, Jose L., Servicio Meteorológico Nacional, Buenos Aires, Argentina
Stephenson, Tannecia S., Department of Physics, The University of the West Indies, Kingston, Jamaica
Stevens, Laura, Cooperative Institute for Satellite Earth System Studies, North Carolina State University, Asheville, North Carolina
Stevens, Thea, Department of Meteorology, University of Reading, Reading, United Kingdom
Stoy, Paul C., College of Agricultural and Life Sciences, University of Wisconsin-Madison, Madison, Wisconsin
Streletskiy, Dmitry A., George Washington University, Washington, DC
Sukianto, Thea, Department of Statistics and Data Science, Carnegie Mellon University, Pittsburg, Pennsylvania
Suslova, Anya, Woodwell Climate Research Center, Falmouth, Massachusetts
Svendby, Tove, The Climate and Environmental Research Institute NILU, Kjeller, Norway
Sweet, William, NOAA/NOS Center for Operational Oceanographic Products and Services, Silver Spring, Maryland
Syafrianno, Alif Akbar, BMKG, Jakarta, Indonesia
Taha, Ghassan, Morgan State University, Baltimore, Maryland; NASA Goddard Flight Center, Greenbelt, Maryland
Takahashi, Kiyotoshi, Tokyo Climate Center, Japan Meteorological Agency, Tokyo, Japan
Takemura, Kazuto, Tokyo Climate Center, Japan Meteorological Agency, Tokyo, Japan
Tank, Suzanne E., University of Alberta, Edmonton, Canada
Taylor, Michael A., Department of Physics, The University of the West Indies, Kingston, Jamaica
Tedesco, Marco, Lamont-Doherty Earth Observatory, Columbia University, Palisades, New York
Thackeray, Stephen J., United Kingdom Centre for Ecology & Hydrology, Lancaster, United Kingdom
Thiaw, W., NOAA/NWS National Centers for Environmental Prediction Climate Prediction Center, College Park, Maryland
Thibert, Emmanuel, Institut de Géosciences de l'Environnement (IGE), Université Grenoble Alpes, INRAE, CNRS, IRD, Grenoble INP, IGE, Grenoble, France
Thomalla, Sandy, Southern Ocean Carbon-Climate Observatory, Council for Scientific and Industrial Research (CSIR), Cape Town, South Africa; Marine and Antarctic Research Centre for Innovation and Sustainability, Department of Oceanography, University of Cape Town, Cape Town, South Africa
Thoman, Richard L., International Arctic Research Center, University of Alaska Fairbanks, Fairbanks, Alaska
Thompson, Philip R., Cooperative Institute for Marine and Atmospheric Research, University of Hawai' i, Honolulu, Hawai' i
Tian-Kunze, Xiangshan, Alfred Wegener Institute, Helmholtz Centre for Polar and Marine Research, Bremerhaven, Germany
Timmermans, Mary-Louise, Yale University, New Haven, Connecticut
Timofeyev, Maxim A., Institute of Biology, Irkutsk State University, Irkutsk, Russia
Tømmervik, Hans, Norwegian Institute for Nature Research, Trondheim, Norway; FRAM – High North Research Centre for Climate and the Environment, Tromsø, Norway
Tourpali, Kleareti, Aristotle University, Thessaloniki, Greece
Tretiakov, Mikhail, Arctic and Antarctic Research Institute, St. Petersburg, Russia
Trewin, Blair C., Bureau of Meteorology, Melbourne, Australia
Triñanes, Joaquin A., Laboratory of Systems, Technological Research Institute, Universidad de Santiago de Compostela, Campus Universitario Sur, Santiago de Compostela, Spain; Cooperative Institute for Marine and Atmospheric Studies, Rosenstiel School of Marine and Atmospheric Science, University of Miami, Miami, Florida; NOAA/OAR Atlantic Oceanographic and Meteorological Laboratory, Miami, Florida
Tronquo, Emma, Hydro-Climate Extremes Lab (H-CEL), Ghent University, Ghent, Belgium; Department of Geoscience and Remote Sensing, TU Delft, Delft, The Netherlands
Trotman, Adrian, Caribbean Institute for Meteorology and Hydrology, Bridgetown, Barbados
Truchelut, Ryan E., WeatherTiger, Tallahassee, Florida
Trusel, Luke, Department of Geography, Pennsylvania State University, State College, Pennsylvania
Tuchen, Franz Philip, Cooperative Institute for Marine and Atmospheric Studies, University of Miami, Miami, Florida; NOAA/OAR Atlantic Oceanographic and Meteorological Laboratory, Miami, Florida
Turňa, Maroš, Slovak Hydrometeorological Institute, Bratislava, Slovakia
Tye, Mari R., National Center for Atmospheric Research, Boulder, Colorado
Uehling, John, Cooperative Institute Satellite Earth System Studies, North Carolina Institute for Climate Studies, North Carolina State University, Asheville, North Carolina
Urraca, Ruben, Joint Research Centre, European Commission, Ispra, Italy
van der A, Ronald, Royal Netherlands Meteorological Institute (KNMI), DeBilt, The Netherlands
van der Linden, Roderick, Deutscher Wetterdienst, Offenbach, Germany
van der Schrier, Gerard, Royal Netherlands Meteorological Institute (KNMI), De Bilt, The Netherlands
Van Meerbeeck, Cédric J., Caribbean Institute for Meteorology and Hydrology, Bridgetown, Barbados
van Vliet, Arnold J. H., Earth Systems and Global Change Group, Wageningen University & Research, The Netherlands
VanScoy, Greta, The Harvard Forest, Harvard University, Petersham, Massachusetts
Vazifeh, Ahad, Climate Department, Iran National Meteorological Organization, Tehran, Iran
Veal, Karen, National Centre for Earth Observation (NCEO), University of Leicester, Leicester, United Kingdom; School of Physics and Astronomy, University of Leicester, Leicester, United Kingdom
Verburg, Piet, National Institute of Water and Atmospheric Research (NIWA), Hamilton, New Zealand
Vernier, Jean-Paul, NASA Langley Research Center, Hampton, Virginia
Vimont, Isaac J., NOAA Global Monitoring Laboratory, Boulder, Colorado
Virasami, R., Mauritius Meteorological Service, Vacoas, Mauritius
Viticchie, Bartolomeo, EUMETSAT, Darmstadt, Germany
Vivero, Sebastián, Department of Geosciences, University of Fribourg, Fribourg, Switzerland
Volkov, Denis L., Cooperative Institute for Marine and Atmospheric Studies, University of Miami, Miami, Florida; NOAA/OAR Atlantic Oceanographic and Meteorological Laboratory, Miami, Florida
Vömel, Holger, National Center for Atmospheric Research, Boulder, Colorado
Vose, Russell S., NOAA/NESDIS National Centers for Environmental Information, Asheville, North Carolina

Unauthenticated | Downloaded 11/21/25 11:34 AM UTC

Editor and Author Affiliations (continued)

Waigl, Christine F., Geophysical Institute, University of Alaska Fairbanks, Fairbanks, Alaska

Walker, Donald (Skip) A., Institute of Arctic Biology, University of Alaska Fairbanks, Fairbanks, Alaska

Walsh, John E., International Arctic Research Center, University of Alaska Fairbanks, Fairbanks, Alaska

Wang, Bin, School of Ocean and Earth Science and Technology, Department of Meteorology, University of Hawaii at Manoa, Honolulu, Hawaii; International Pacific Research Center, Honolulu, Hawaii

Wang, Donqian, Climate Change Division, National Climate Center, China Meteorological Administration, Beijing, China

Wang, Hui, NOAA/NWS National Centers for Environmental Prediction Climate Prediction Center, College Park, Maryland

Wang, Muyin, NOAA/OAR Pacific Marine Environmental Laboratory, Seattle, Washington; Cooperative Institute for Climate, Ocean, and Ecosystem Studies, University of Washington, Seattle, Washington

Wang, Ray H. J., Georgia Institute of Technology, Atlanta, Georgia

Wanninkhof, Rik, NOAA/OAR Atlantic Oceanographic and Meteorological Laboratory, Miami, Florida

Waring, Abigail Marie, National Centre for Earth Observation (NCEO), University of Leicester, Leicester, United Kingdom; School of Physics and Astronomy, University of Leicester, Leicester, United Kingdom

Warnock, Taran, University of Saskatchewan, Saskatoon, Canada

Weber, Mark, University of Bremen, Bremen, Germany

Webster, Melinda, Polar Science Center, Applied Physics Laboratory, University of Washington, Seattle, Washington

Wei, Zigang, Science and Technology Corporation (STC), College Park, Maryland

Weller, Robert A., Department of Physical Oceanography, Woods Hole Oceanographic Institution, Woods Hole, Massachusetts

Westberry, Toby K., Oregon State University, Corvallis, Oregon

Widlansky, Matthew J., Cooperative Institute for Marine and Atmospheric Research, University of Hawai‘ i, Honolulu, Hawai‘ i

Wiese, David N., Jet Propulsion Laboratory, California Institute of Technology, Pasadena, California

Wild, Jeannette D., Earth System Science Interdisciplinary Center, University of Maryland, College Park, Maryland; NOAA/NESDIS Center for Satellite Applications and Research, College Park, Maryland

Wille, Jonathan D., Institute for Atmospheric and Climate Science, ETH Zürich, Zürich, Switzerland; Institut des Géosciences de l’Environnement, IRD, CNRS, Grenoble INP, Saint Martin d’Hères, France

Willems, An, Royal Meteorological Institute, Brussels, Belgium

Willett, Kate M., Met Office Hadley Centre, Exeter, United Kingdom

Williams, Earle, Massachusetts Institute of Technology, Cambridge, Massachusetts

Willis, Joshua K., Jet Propulsion Laboratory, California Institute of Technology, Pasadena, California

Wong, Takmeng, NASA Langley Research Center, Hampton, Virginia

Wood, Kimberly M., Department of Hydrology and Atmospheric Sciences, University of Arizona, Tucson, Arizona

Wood, Tom, Department of Geography, King’s College London, London, United Kingdom

Woolway, Richard Iestyn, School of Ocean Sciences, Bangor University, Bangor, United Kingdom

Worden, John, Jet Propulsion Laboratory, California Institute of Technology, Pasadena, California

Yang, Dedi, Environmental Sciences Division, Oak Ridge National Laboratory, Oak Ridge, Tennessee

Yang, Kai, Department of Atmospheric and Oceanic Sciences, University of Maryland, College Park, Maryland

Yang, Ying, Jiangsu Meteorological Observatory, Nanjing, China

Yin, Xungang, NOAA/NESDIS National Centers for Environmental Information, Asheville, North Carolina

Yu, Lisan, Department of Physical Oceanography, Woods Hole Oceanographic Institution, Woods Hole, Massachusetts

Zeng, Zhenzhong, School of Environmental Science and Engineering, Southern University of Science and Technology, Shenzhen, China

Zhang, Huai-Min, NOAA/NESDIS National Centers for Environmental Information, Asheville, North Carolina

Zhang, Peiqun, Beijing Climate Center, China Meteorological Administration, Beijing, China

Zhao, Lin, School of Geographical Sciences, Nanjing University of Information Science and Technology, Nanjing, China

Zhu, Zhiwei, Nanjing University of Information Science and Technology, Nanjing, China

Ziemke, Jerry R., Goddard Earth Sciences Technology and Research, Morgan State University, Baltimore, Maryland; NASA Goddard Space Flight Center, Greenbelt, Maryland

Ziese, Markus, Global Precipitation Climatology Centre, Deutscher Wetterdienst, Offenbach, Germany

Zolkos, Scott, Woodwell Climate Research Center, Falmouth, Massachusetts

Zotta, Ruxandra-Maria, TU Wien, Vienna, Austria

Zou, Cheng-Zhi, George Mason University, Fairfax, Virginia

Editorial and Production Team

Allen, Jessicca, Graphics Support, Cooperative Institute for Satellite Earth System Studies, North Carolina State University, Asheville, North Carolina

Camper, Amy V., Graphics Support, Innovative Consulting and Management Services, LLC, NOAA/NESDIS National Centers for Environmental Information, Asheville, North Carolina

Carroll, Lauren, Content Team Lead, Communications and Outreach, NOAA/NESDIS National Centers for Environmental Information, Asheville, North Carolina

Haley, Bridgette O., Graphics Support, NOAA/NESDIS National Centers for Environmental Information, Asheville, North Carolina

Love-Brotak, S. Elizabeth, Lead Graphics Production, NOAA/NESDIS National Centers for Environmental Information, Asheville, North Carolina

Ohlmann, Laura, Technical Editor, Innovative Consulting and Management Services, LLC, NOAA/NESDIS National Centers for Environmental Information, Asheville, North Carolina

Noguchi, Lukas, Technical Editor, Innovative Consulting and Management Services, LLC, NOAA/NESDIS National Centers for Environmental Information, Asheville, North Carolina

Riddle, Deborah B., Graphics Support, NOAA/NESDIS National Centers for Environmental Information, Asheville, North Carolina

Veasey, Sara W., Visual Communications Team Lead, Communications and Outreach, NOAA/NESDIS National Centers for Environmental Information, Asheville, North Carolina

Unauthenticated | Downloaded 11/21/25 11:34 AM UTC

STATE OF THE CLIMATE IN 2024

INTRODUCTION

J. Blunden, J. Reagan, and R. J. H. Dunn

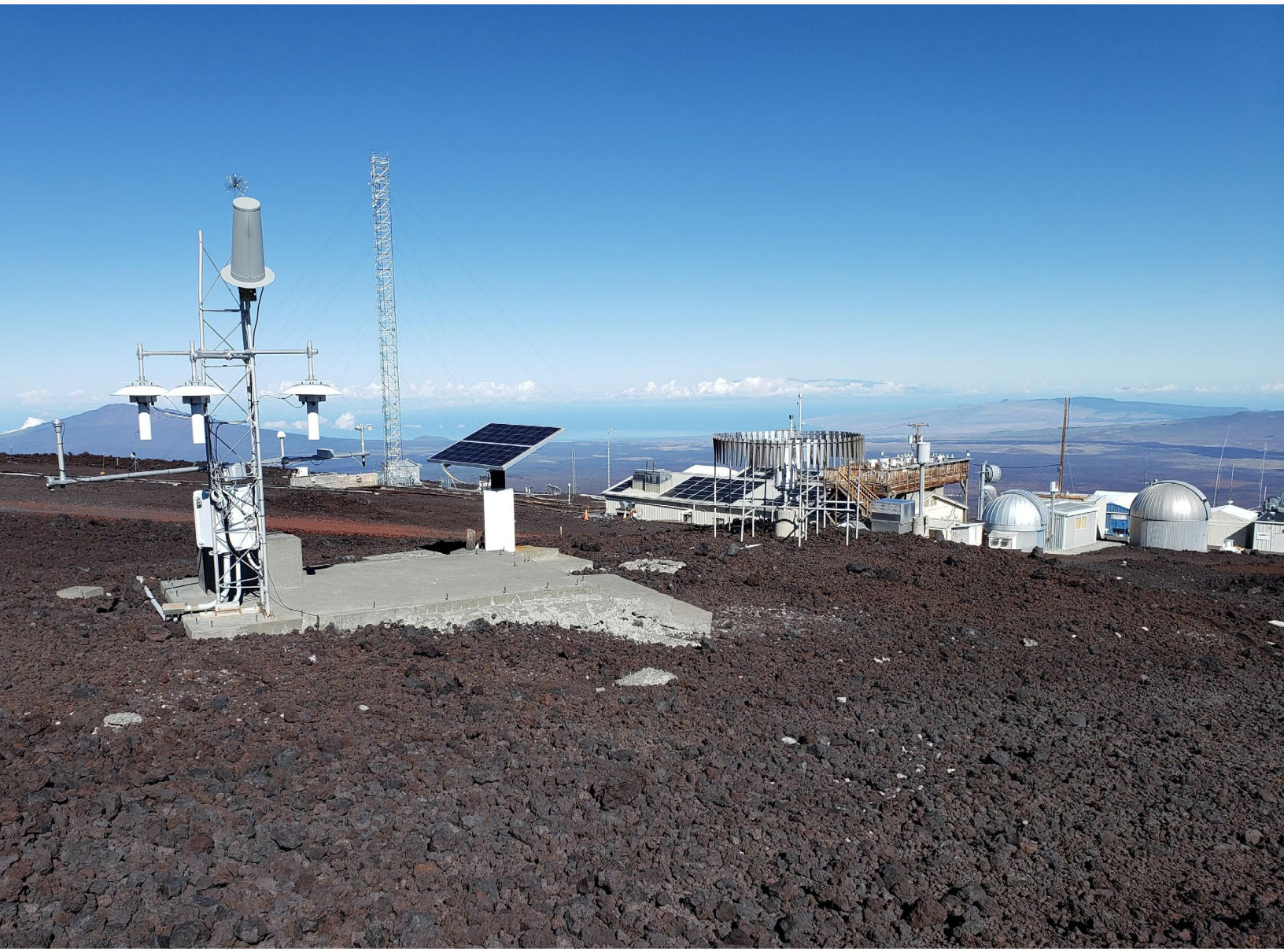

Special Online Supplement to the *Bulletin of the American Meteorological Society* Vol. 106, No. 8, August, 2025

https://doi.org/10.1175/2025BAMSStateoftheClimate_Intro.1
Corresponding author: Jessica Blunden / jessica.blunden@noaa.gov
©2025 American Meteorological Society
For information regarding reuse of this content and general copyright information, consult the AMS Copyright Policy.

Unauthenticated | Downloaded 11/21/25 11:34 AM UTC

STATE OF THE CLIMATE IN 2024
Introduction

Editors

Jessica Blunden
James Reagan

Chapter Editors

Anthony Arguez
Josh Blannin
Peter Bissolli
Kyle R. Clem
Howard J. Diamond
Matthew L. Druckenmiller
Robert J. H. Dunn
Catherine Ganter
Nadine Gobron
Gregory C. Johnson
Rick Lumpkin
Rodney Martinez
Ademe Mekonnen
Twila A. Moon
Gary A. Morris
Marilyn N. Raphael
Carl J. Schreck III
Laura Stevens
Richard L. Thoman
Kate M. Willett
Zhiwei Zhu

Technical Editor

Lukas Noguchi

BAMS Special Editor for Climate

Timothy DelSole

American Meteorological Society

Unauthenticated | Downloaded 11/21/25 11:34 AM UTC

Cover Credit:
The U.S. Climate Reference Network (USCRN) station at the NOAA Global Monitoring Laboratory's Mauna Loa Observatory, located on the north flank of Mauna Loa Volcano on the Big Island of Hawaii at an elevation of 3397 meters above sea level. The USCRN program is managed and led by NOAA's Air Resources Laboratory (ARL), in partnership with NOAA's National Centers for Environmental Information.

Photo credit: Mark Hall, ARL's Atmospheric Turbulence and Diffusion Division, Oak Ridge, Tennessee.

How to cite this document:
Introduction is one chapter from the *State of the Climate in 2024* annual report and is available from https://doi.org/10.1175/2025BAMSStateoftheClimate_Intro.1. Compiled by NOAA's National Centers for Environmental Information, *State of the Climate in 2024* is based on contributions from scientists from around the world. It provides a detailed update on global climate indicators, notable weather events, and other data collected by environmental monitoring stations and instruments located on land, water, ice, and in space. The full report is available from https://doi.org/10.1175/2025BAMSStateoftheClimate.1.

Citing the complete report:
Blunden, J. and J. Reagan, Eds., 2025: "State of the Climate in 2024". Bull. Amer. Meteor. Soc., 106 (8), Si–S514 https://doi.org/10.1175/2025BAMSStateoftheClimate.1.

Citing this chapter:
Blunden, J., J. Reagan, and R. J. H. Dunn, 2025: Introduction [in "State of the Climate in 2024"]. Bull. Amer. Meteor. Soc., 106 (8), S1–S10, https://doi.org/10.1175/2025BAMSStateoftheClimate_Intro.1.

Unauthenticated | Downloaded 11/21/25 11:34 AM UTC

Editor and Author Affiliations (alphabetical by name)

Blunden, Jessica, NOAA/NESDIS National Centers for Environmental Information, Asheville, North Carolina

Dunn, Robert J. H., Met Office Hadley Centre, Exeter, United Kingdom

Reagan, James, NOAA/NESDIS National Centers for Environmental Information, Silver Spring, Maryland

Editorial and Production Team

Allen, Jessicca, Graphics Support, Cooperative Institute for Satellite Earth System Studies, North Carolina State University, Asheville, North Carolina

Camper, Amy V., Graphics Support, Innovative Consulting and Management Services, LLC, NOAA/NESDIS National Centers for Environmental Information, Asheville, North Carolina

Carroll, Lauren, Content Team Lead, Communications and Outreach, NOAA/NESDIS National Centers for Environmental Information, Asheville, North Carolina

Haley, Bridgette O., Graphics Support, NOAA/NESDIS National Centers for Environmental Information, Asheville, North Carolina

Love-Brotak, S. Elizabeth, Lead Graphics Production, NOAA/NESDIS National Centers for Environmental Information, Asheville, North Carolina

Ohlmann, Laura, Technical Editor, Innovative Consulting and Management Services, LLC, NOAA/NESDIS National Centers for Environmental Information, Asheville, North Carolina

Noguchi, Lukas, Technical Editor, Innovative Consulting and Management Services, LLC, NOAA/NESDIS National Centers for Environmental Information, Asheville, North Carolina

Riddle, Deborah B., Graphics Support, NOAA/NESDIS National Centers for Environmental Information, Asheville, North Carolina

Veasey, Sara W., Visual Communications Team Lead, Communications and Outreach, NOAA/NESDIS National Centers for Environmental Information, Asheville, North Carolina

Unauthenticated | Downloaded 11/21/25 11:34 AM UTC

1. INTRODUCTION

J. Blunden, J. Reagan, and R. J. H. Dunn

This is the thirty-fifth issuance of the annual assessment now known as the *State of the Climate*, published in the Bulletin since 1996. Each year the report documents the status and trajectory of many components of the climate system across land, oceans, and cryosphere, and throughout Earth's atmosphere. Every year, authors of this report introduce new datasets (often with new variables), improved measurement and analysis methodologies, and an additional year of data that helps bring our understanding of Earth's system into sharper focus. Data are collected in a variety of ways, often in remote areas and sometimes in challenging conditions. This year's cover for the "Antarctica and the Southern Ocean" chapter depicts two researchers installing instrumentation in February 2024 near Crane Glacier on the Antarctic Peninsula to track glacier response to the 2022 loss of decadal fast ice in the Larsen B embayment. The cover of the Global Oceans chapter features a NEMO float, which is part of the global Argo array of ocean observing platforms that measure variables such as temperature and salinity from the surface of the ocean to depths of two kilometers. This chapter's cover highlights the Mauna Loa Observatory, which is set in a pristine environment on the Big Island of Hawaii and has been operational since 1958, where variables such as long-lived greenhouse gases, tropospheric ozone, and aerosols are continuously measured. These, and all datasets in this report, are documented in appendices at the end of each chapter, providing readers and researchers alike easy access to the data used in each section.

Several analyses informed us that 2024 began where 2023 ended—with a strong El Niño that helped elevate the annual global temperature to a record high in the more-than-170-year record for the second consecutive year. This new record occurred despite the El Niño quickly decaying to neutral conditions by the boreal spring of 2024. Most of the annual global surface high temperature records have occurred when the El Niño–Southern Oscillation (ENSO) is in its warm El Niño phase for at least part of the year. The last time the global temperature record was set two years in a row was in 2015 and 2016, which was also the last time a strong El Niño straddled two years.

The anomalous warmth in 2024 occurred across most of the world and contributed to many of the continued changes in key climate indicators that are documented throughout this report. Year-over-year changes and trends over each variable's period of record can be gleaned from the time series shown in Plate 1.1, which now features 39 variables, an increase of 3 from last year's report.

Annual, seasonal, monthly, and even daily climate data at scales ranging from local to global are of utmost importance for tracking changes and trends in our climate system. These changes can have direct impacts on ecosystems and the human population. For example, Canada—along with North America as a whole—reported its warmest year on record. Record-high maximum temperatures were set in northwest North America during August. The heat, along with dry conditions, contributed to substantial wildfire activity in the region that caused community evacuations and smoke-related health impacts.

For the second consecutive year, all 58 global reference glaciers across five continents lost mass in 2024, setting a new record for ice loss. In South America, Venezuela became the first Andes country to register the loss of all glaciers. In Colombia, the Conejeras Glacier was declared extinct, joining the list of glaciers that have disappeared in recent years. The continuing loss of these glaciers here and around the world affect people and surrounding ecosystems who depend on their meltwater during the warm season.

Unauthenticated | Downloaded 11/21/25 11:34 AM UTC

Across the globe, there were 82 named tropical cyclones, slightly below the annual average of 87 that occurred between 1991 and 2020. This statistic, while important for tracking such events at the global level, only tells part of a story. Several of these storms reached land and wreaked havoc, bringing heavy rains, strong winds, and destruction to places that were in and near their path. The impacts can be felt far inland from the location of the storm's landfall.

Our full report cover this year is a personal one for several of the authors, editors, and technical staff of this report. The photo, taken by one of our former colleagues who provided graphics support to this series for many years, depicts the aftermath of debris that was carried away by floodwaters and slammed into a bridge over the Swannanoa River in Asheville, North Carolina, on 27 September 2024, as Hurricane Helene decimated much of the area. Similarly, the cover for The Tropics chapter shows a broader aerial view of widespread flooding from the French Broad River that inundated homes and businesses a few miles away in another part of Asheville in the immediate aftermath of Helene. More than 100 people were killed and tens of billions of dollars in damage occurred in the western North Carolina region alone.

Many other extreme rainfall events occurred in other parts of the world during 2024, including unprecedented rainfall from late April to early May in the Brazilian state of Rio Grande do Sul, which is considered to be the worst climate disaster in Brazil's history in terms of damage and loss. The cover of the Regional Climates chapter captures a snapshot of this flooding in Canoas, one of many cities that were submerged in the region. On the other end of precipitation extremes, northern Ghana in Africa experienced its worst drought in four decades, which led to significant crop loss. These are only a few highlights of the many extreme events included throughout this year's report.

The compilation of the *State of the Climate* is possible due to the dedication of the 590 authors and editors from 58 countries. It would be an impossible feat for one country to perform this sort of comprehensive analysis on the state of today's climate, and we express our sincere appreciation to those who volunteer their time and expertise to provide a well-rounded and scientifically sound view of our climate system as well as to those who provide thoughtful feedback and peer review. The sequence of the *State of the Climate* in 2024 is similar to previous years: Chapter 1—Introduction (i.e., this chapter); Chapter 2—Global Climate; Chapter 3—Global Oceans; Chapter 4—The Tropics; Chapter 5—The Arctic; Chapter 6—Antarctica and the Southern Ocean; and Chapter 7—Regional Climates, which covers the seven regions of North America, Central America and the Caribbean, South America, Africa, Europe and the Middle East, Asia, and Oceania.

Unauthenticated | Downloaded 11/21/25 11:34 AM UTC

Selected Significant Climate Anomalies and Events: Annual 2024

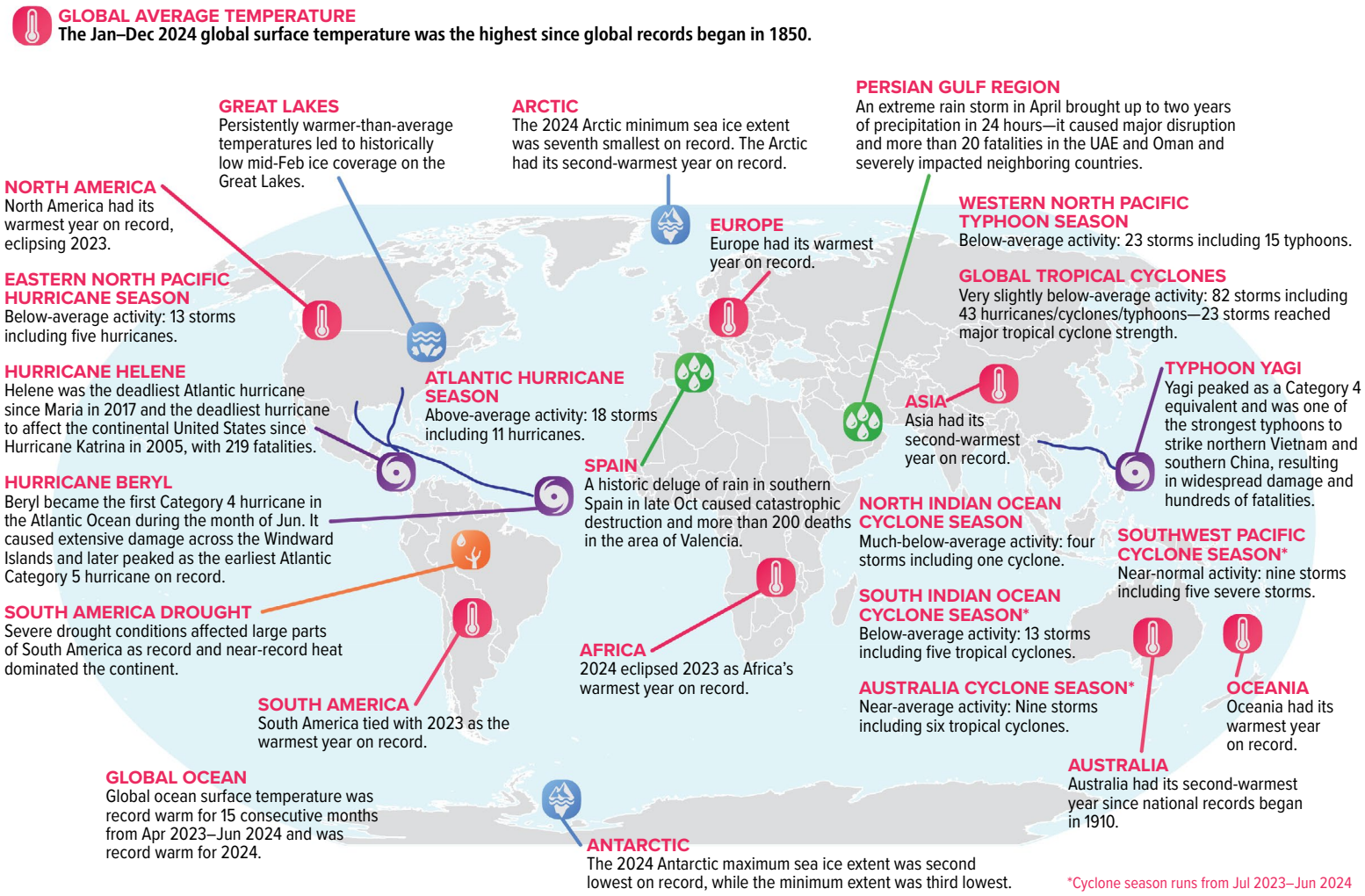

Fig. 1.1. Geographical distribution of selected notable climate anomalies and events in 2024.

Plate 1.1. (Next page.) Global (or representative) average time series for essential climate variables through 2024. Anomalies are shown relative to the base period in parentheses, although base periods used in other sections of the report may differ. The numbers in the parentheses in the lower left or right side of each panel indicate how many in situ (red), reanalysis (blue), and satellite (orange) datasets are used to create each time series, in that order. (a) Northern Hemisphere (NH) polar stratospheric ozone (Mar); (b) Southern Hemisphere polar stratospheric ozone (Oct); (c) surface temperature; (d) night marine air temperature; (e) lower-tropospheric temperature; (f) lower-stratospheric temperature; (g) land surface temperature extremes (warm days [TX90p, solid] and cool nights [$TN_{10}p$, dotted]); (h) equivalent temperature; (i) Arctic sea ice extent (max [solid] and min [dotted]); (j) Antarctic sea ice extent (max [solid] and min [dotted]); (k) glacier cumulative mean specific balance; (l) NH snow cover extent; (m) NH lake ice duration; (n) Mauna Loa apparent transmission; (o) lower-stratospheric water vapor; (p) cloud area fraction; (q) total column water vapor—land; (r) total column water vapor—ocean; (s) upper-tropospheric humidity; (t) specific humidity—land; (u) specific humidity—ocean; (v) relative humidity—land; (w) relative humidity—ocean; (x) humid heat extreme frequency (days per year exceeding the 90th percentile of the climatological daily maximum wet-bulb temperature [TwX90p; solid] and days per year below the 10th percentile of the climatological daily-minimum wet-bulb temperature [$TwN_{10}p$ [dotted]); (y) precipitation—land; (z) precipitation—ocean; (aa) ocean heat content (0 m–700 m); (ab) sea level rise; (ac) tropospheric ozone; (ad) tropospheric wind speed at 850 hPa; (ae) land wind speed; (af) ocean wind speed; (ag) biomass burning; (ah) land evaporation; (ai) soil moisture; (aj) terrestrial groundwater storage; (ak) fraction of absorbed photosynthetically active radiation (FAPAR); (al) land surface albedo—visible (solid) and infrared (dotted); (am) vegetation optical depth.

Unauthenticated | Downloaded 11/21/25 11:34 AM UTC

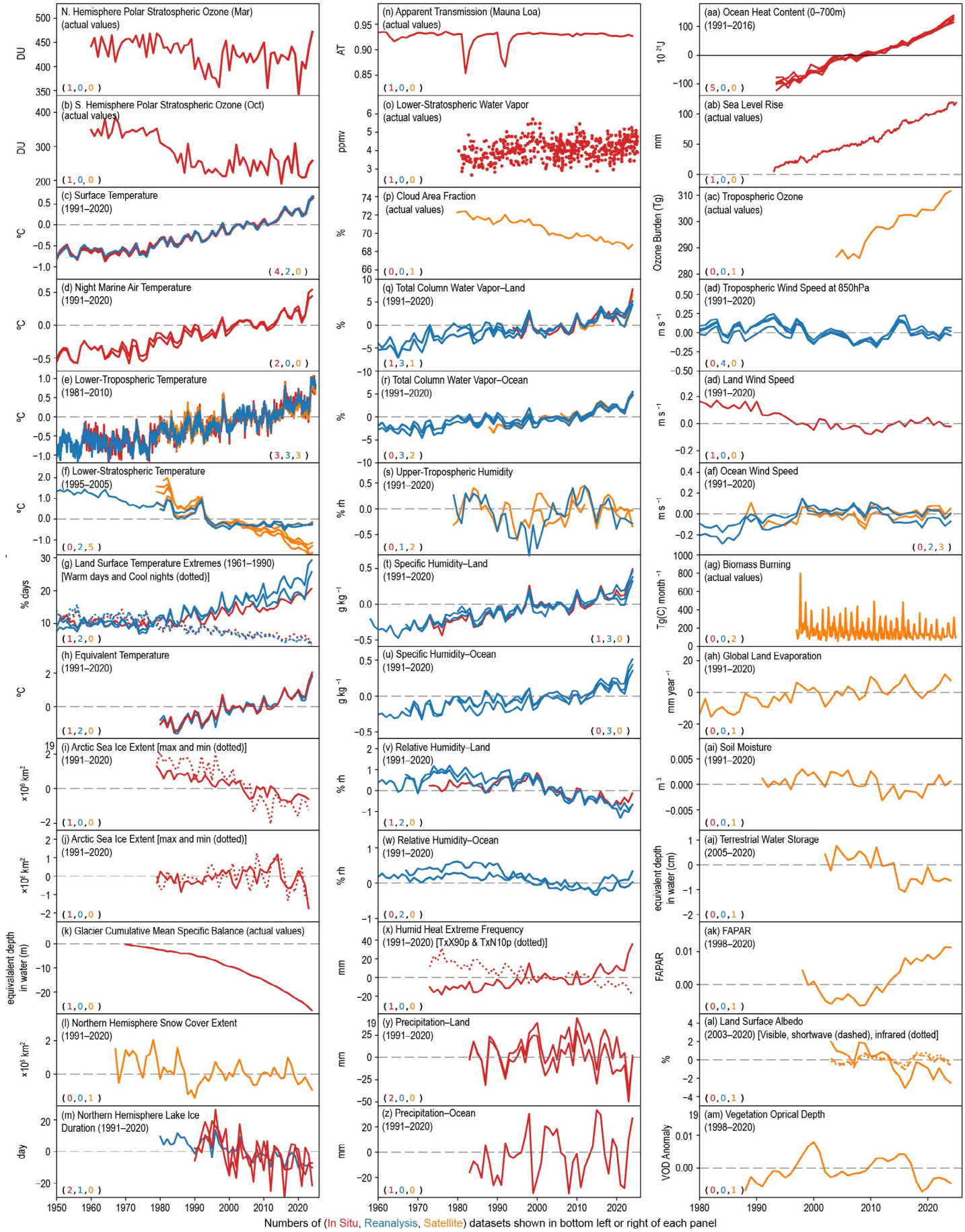

Unauthenticated | Downloaded 11/21/25 11:34 AM UTC

Essential Climate Variables

J. BLUNDEN, J. REAGAN, AND R. J. H. DUNN

The following variables are considered fully monitored in this report, in that there are sufficient spatial and temporal data, with peer-reviewed documentation to characterize them on a global scale:

- Surface atmosphere: air pressure, precipitation, temperature, water vapor, wind speed and direction
- Upper atmosphere: Earth radiation budget, temperature, water vapor, wind speed and direction
- Atmospheric composition: carbon dioxide, methane and other greenhouse gases, ozone
- Ocean physics: ocean surface heat flux, sea ice, sea level, surface salinity, sea surface temperature, subsurface salinity, subsurface temperature, surface currents, surface stress
- Ocean biogeochemistry: ocean color
- Ocean biogeosystems: plankton
- Land: albedo, river discharge, snow

The following variables are considered partially monitored, in that there is systematic, rigorous measurement found in this report, but some coverage of the variable in time and space is lacking due to observing limitations or limited availability of data or authors:

- Atmospheric composition: aerosols properties, cloud properties, precursors of aerosol and ozone
- Upper atmosphere: lightning
- Ocean physics: subsurface currents
- Ocean biogeochemistry: inorganic carbon
- Land: above-ground biomass, anthropogenic greenhouse gas fluxes, fire, fraction of absorbed photosynthetically active radiation, glaciers, groundwater, ice sheets and ice shelves, lakes, permafrost, soil moisture, land surface temperature
- Surface atmosphere: surface radiation budget

The following variables are not yet covered in this report, or are outside the scope of it.

- Ocean physics: sea state
- Ocean biogeochemistry: nitrous oxide, nutrients, oxygen, transient tracers
- Ocean biogeosystems: marine habitat properties
- Land: anthropogenic water use, land cover, latent and sensible heat fluxes, leaf area index, soil carbon

Unauthenticated | Downloaded 11/21/25 11:34 AM UTC

Acknowledgments

The editors thank the BAMS editorial staff, in particular Bryan Hanssen, who provided technical guidance and oversaw publication of the report; Andrea Herbst, who provided peer review support; Jess LaPointe, who oversaw the hundreds of citations and references this year; and the NCEI Graphics team for facilitating the construction of the report and executing the countless number of technical edits needed. We thank our technical editor Lukas Noguchi for his dedication and attention to detail. We also express our gratitude to Dr. Timothy DelSole, who served as the AMS special editor for this report. Finally, we thank all of the authors and chapter editors who provide these valuable contributions each year—always with an aim to improve and expand their analyses for the readers—as well as the many peer reviewers who dedicate their time and expertise to provide thoughtful feedback that continually helps evolve the report. Several authors and chapter editors retired prematurely and unexpectedly this year, many with multiple decades of contributions to this report. We thank them for their unwavering dedication to expanding our scientific knowledge and for sharing their work with us.

Unauthenticated | Downloaded 11/21/25 11:34 AM UTC

STATE OF THE CLIMATE IN 2024

GLOBAL CLIMATE

R. J. H. Dunn, J. Blannin, K. M. Willett, N. Gobron, and G. A. Morris, Eds.

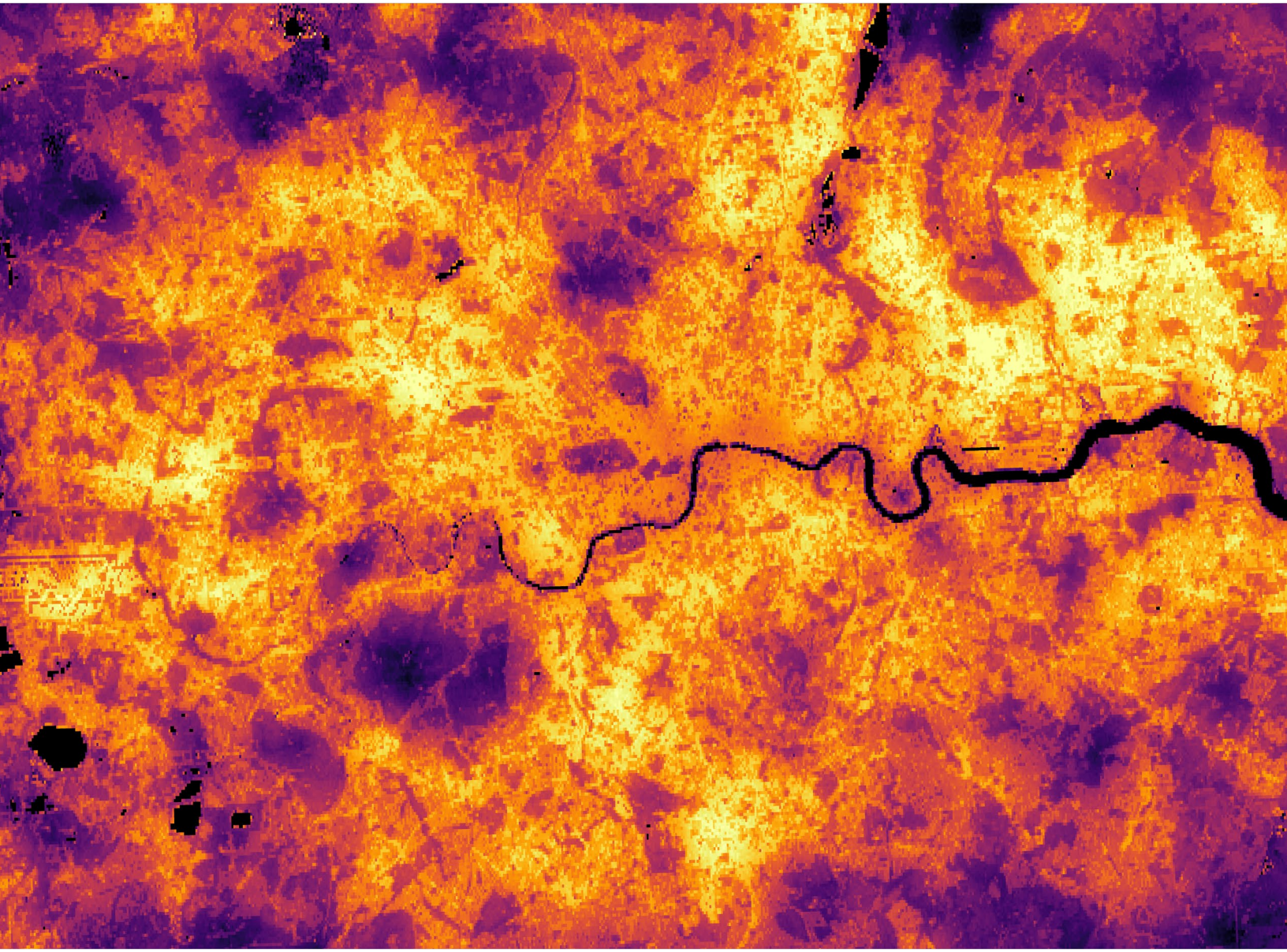

Special Online Supplement to the *Bulletin of the American Meteorological Society* Vol. 106, No. 8, August, 2025

https://doi.org/10.1175/BAMS-D-25-0102.1

Corresponding author: Robert Dunn / robert.dunn@metoffice.gov.uk

©2025 American Meteorological Society
For information regarding reuse of this content and general copyright information, consult the AMS Copyright Policy.

Unauthenticated | Downloaded 11/21/25 11:34 AM UTC

STATE OF THE CLIMATE IN 2024
Global Climate

Editors

Jessica Blunden
James Reagan

Chapter Editors

Anthony Arguez
Josh Blannin
Peter Bissolli
Kyle R. Clem
Howard J. Diamond
Matthew L. Druckenmiller
Robert J. H. Dunn
Catherine Ganter
Nadine Gobron
Gregory C. Johnson
Rick Lumpkin
Rodney Martinez
Ademe Mekonnen
Twila A. Moon
Gary A. Morris
Marilyn N. Raphael
Carl J. Schreck III
Laura Stevens
Richard L. Thoman
Kate M. Willett
Zhiwei Zhu

Technical Editor

Lukas Noguchi

BAMS Special Editor for Climate

Timothy DelSole

American Meteorological Society

Unauthenticated | Downloaded 11/21/25 11:34 AM UTC

Cover Credit:
Land Surface Temperature (LST) view of London, UK, on 30 July 2024 from Sentinel 3a. The LST data have been downscaled using Vis/SWIR inputs from Landsat 9 and Sentinel 2a and a bottom-of-atmosphere optimal estimation methodology to refine the estimates from 1 km data to 100 m.

Credit: M. Perry, C. Paton, B. Courtier, D, Ghent, NCEO, University of Leicester

How to cite this document:
Global Climate is one chapter from the *State of the Climate in 2024* annual report and is available from https://doi.org/10.1175/BAMS-D-25-0102.1. Compiled by NOAA's National Centers for Environmental Information, *State of the Climate in 2024* is based on contributions from scientists from around the world. It provides a detailed update on global climate indicators, notable weather events, and other data collected by environmental monitoring stations and instruments located on land, water, ice, and in space. The full report is available from https://doi.org/10.1175/2025BAMSStateoftheClimate.1.

Citing the complete report:
Blunden, J. and J. Reagan, Eds., 2025: "State of the Climate in 2024". Bull. Amer. Meteor. Soc., 106 (8), Si–S513 https://doi.org/10.1175/2025BAMSStateoftheClimate.1.

Citing this chapter:
Dunn, R. J. H., J. Blannin, K. M. Willett, N. Gobron, and G. A. Morris, Eds., 2025:
Global Climate [in "State of the Climate in 2024"]. Bull. Amer. Meteor. Soc., 106 (8), S11–S172, https://doi.org/10.1175/BAMS-D-25-0102.1.

Citing a section (example):
Fereday, D., D. Campos, and G. Macara, 2025: Mean sea level pressure and related modes of variabiity [in "State of the Climate in 2024"]. Bull. Amer. Meteor. Soc., 106 (8), S80–S81, https://doi.org/10.1175/BAMS-D-25-0102.1.

Unauthenticated | Downloaded 11/21/25 11:34 AM UTC

Editor and Author Affiliations (alphabetical by name)

Ades, Melanie, European Centre for Medium-Range Weather Forecasts, Reading, United Kingdom

Adler, Robert, Earth System Science Interdisciplinary Center, University of Maryland, College Park, Maryland

Alexe, Mihai, European Centre for Medium-Range Weather Forecasts, Bonn, Germany

Allan, Richard P., Department of Meteorology, University of Reading, Reading, United Kingdom; National Centre for Earth Observation (NCEO), University of Leicester, Leicester, United Kingdom

Anderson, John, Hampton University, Hampton, Virginia

Anneville, Orlane, National Research Institute for Agriculture, Food and Environment (INRAE), CARRTEL, Université Savoie Mont Blanc, Thonon les Bains, France

Aono, Yasuyuki, Graduate School of Agriculture, Osaka Metropolitan University, Sakai, Japan

Arguez, Anthony, NOAA/NESDIS National Centers for Environmental Information, Asheville, North Carolina

Armenteras-Pascual, Dolors, Science Faculty, Universidad Nacional de Colombia, Bogotá, Colombia

Arosio, Carlo, University of Bremen, Bremen, Germany

Asher, Elizabeth, Cooperative Institute for Research in Environmental Sciences, University of Colorado Boulder, Boulder, Colorado; NOAA Global Monitoring Laboratory, Boulder, Colorado

Augustine, John A., NOAA Global Monitoring Laboratory, Boulder, Colorado

Azorin-Molina, Cesar, Centro de Investigaciones sobre Desertificación – Spanish National Research Council (CSIC-UV-GVA), Valencia, Spain

Baez-Villanueva, Oscar M., Hydro-Climate Extremes Lab (H-CEL), Ghent University, Ghent, Belgium

Barichivich, Jonathan, Laboratoire des Sciences du Climat et de l'Environnement (LSCE), LSCE/IPSL, CEA-CNRS-UVSQ, Gif-sur-Yvette, France

Baron, Alexandre, Cooperative Institute for Research in Environmental Sciences, University of Colorado Boulder, Boulder, Colorado; NOAA Chemical Sciences Laboratory, Boulder, Colorado

Beck, Hylke E., Physical Science and Engineering Division, King Abdullah University of Science and Technology, Thuwal, Saudi Arabia

Bellouin, Nicolas, University of Reading, Reading, United Kingdom; Institute Pierre Simon Laplace (IPSL), Guyancourt, France

Benedetti, Angela, European Centre for Medium-Range Weather Forecasts, Reading, United Kingdom

Blannin, Josh, Met Office Hadley Centre, Exeter, United Kingdom

Blenkinsop, Stephen, School of Engineering, Newcastle University, Newcastle-upon-Tyne, United Kingdom; Tyndall Centre for Climate Change Research, Norwich, United Kingdom

Bock, Olivier, Université Paris Cité, Institut de physique du globe de Paris, CNRS, IGN, Paris, France; Univ Gustave Eiffel, ENSG, IGN, Marne-la-Vallée, France

Bodin, Xavier, Laboratoire EDYTEM, CNRS/Université Savoie Mont-Blanc, Le Bourget-du-Lac, France

Bonte, Olivier, Hydro-Climate Extremes Lab (H-CEL), Ghent University, Ghent, Belgium

Bosilovich, Michael G., Global Modeling and Assimilation Office, NASA Goddard Space Flight Center, Greenbelt, Maryland

Boucher, Olivier, Institute Pierre Simon Laplace (IPSL), Guyancourt, France

Bowman, Kevin, Jet Propulsion Laboratory, California Institute of Technology, Pasadena, California

Buehler, Sarah A., Universität Hamburg, Hamburg, Germany

Bunno, Ayaka, Japan Meteorological Agency, Tokyo, Japan

Byrne, Michael, P., School of Earth and Environmental Sciences, University of St Andrews, St Andrews, United Kingdom

Campos, Diego, Barcelona Supercomputing Centre, Barcelona, Spain

Cappucci, Fabrizio, Joint Research Centre, European Commission, Ispra, Italy

Carrea, Laura, University of Reading, Reading, United Kingdom

Casado-Rodríguez, Jesús, Joint Research Centre, European Commission, Ispra, Italy

Chang, Kai-Lan, Cooperative Institute for Research in Environmental Sciences, University of Colorado Boulder, Boulder, Colorado; NOAA Chemical Sciences Laboratory, Boulder, Colorado

Christiansen, Hanne H., Arctic Geophysics Department, University Centre in Svalbard, Longyearbyen, Norway

Christy, John R., University of Alabama in Huntsville, Huntsville, Alabama

Chung, Eui-Seok, Korea Polar Research Institute, Incheon, South Korea

Ciasto, Laura M., NOAA/NWS National Centers for Environmental Prediction, Climate Prediction Center, College Park, Maryland

Clingan, Scott, Cooperative Institute for Research in Environmental Sciences, University of Colorado Boulder, Boulder, Colorado; NOAA Global Monitoring Laboratory, Boulder, Colorado

Coldewey-Egbers, Melanie, German Aerospace Center (DLR), Oberpfaffenhofen, Germany

Cooley, Sarah, Duke University, Durham, North Carolina

Cooper, Owen R., NOAA Chemical Sciences Laboratory, Boulder, Colorado

Cornes, Richard C., National Oceanography Centre, Southampton, United Kingdom

Covey, Curt, Lawrence Livermore National Laboratory, Livermore, California

Crétaux, Jean-Francois, LEGOS (CNES/CNRS/IRD/UPS), Université de Toulouse, Toulouse, France

Crimmins, Theresa, USA National Phenology Network, School of Natural Resources and the Environment, University of Arizona, Tucson, Arizona

Crotwell, Molly, Cooperative Institute for Research in Earth Science, University of Colorado Boulder, Boulder, Colorado; NOAA Global Monitoring Laboratory, Boulder, Colorado

Culpepper, Joshua, Department of Biology, York University, Toronto, Canada

Cusicanqui, Diego, Institut de Géosciences de l'Environnement (IGE), Université Grenoble Alpes, INRAE, CNRS, IRD, Grenoble INP, ISTerre, Grenoble, France

Davis, Sean M., NOAA Chemical Sciences Laboratory, Boulder, Colorado

de Jeu, Richard A. M., Transmissivity B.V., Haarlem, The Netherlands

de Laat, Jos, Royal Netherlands Meteorological Institute (KNMI), DeBilt, The Netherlands

Degenstein, Doug, University of Saskatchewan, Saskatoon, Canada

Delaloye, Reynald, Department of Geosciences, University of Fribourg, Fribourg, Switzerland

Di Tomaso, Enza, European Centre for Medium-Range Weather Forecasts, Bonn, Germany

Dokulil, Martin T., Research Institute for Limnology, University of Innsbruck, Mondsee, Austria

Donat, Markus G., Barcelona Supercomputing Centre, Barcelona, Spain; Catalan Institution for Research and Advanced Studies (ICREA), Barcelona, Spain

Dorigo, Wouter A., Department of Geodesy and Geoinformation, TU Wien, Vienna, Austria

Dugan, Hilary, Center of Limnology, University of Wisconsin-Madison, Madison, Wisconsin

Dunn, Robert J. H., Met Office Hadley Centre, Exeter, United Kingdom

Durre, Imke, Climate Science and Services Division, NOAA/NESDIS National Centers for Environmental Information, Asheville, North Carolina

Dutton, Geoff, Cooperative Institute for Research in Earth Science, University of Colorado Boulder, Boulder, Colorado

Effertz, Peter, Cooperative Institute for Research in Environmental Sciences, University of Colorado Boulder, Boulder, Colorado; NOAA Global Monitoring Laboratory, Boulder, Colorado

Enno, Sven-Erik, EUMETSAT, Darmstadt, Germany

Estilow, Thomas W., Rutgers University, Piscataway, New Jersey

Estrella, Nicole, Ecoclimatology, Department of Life Science Systems, TUM School of Life Sciences, Technical University of Munich, Freising, Germany

Fereday, David, Met Office Hadley Centre, Exeter, United Kingdom

Unauthenticated | Downloaded 11/21/25 11:34 AM UTC

Fioletov, Vitali E., Environment and Climate Change Canada, Toronto, Canada
Flemming, Johannes, European Centre for Medium-Range Weather Forecasts, Bonn, Germany
Formanek, Maud, Department of Geodesy and Geoinformation, TU Wien, Vienna, Austria
Foster, Michael J., Cooperative Institute for Meteorological Satellite Studies, Space Science and Engineering Center, University of Wisconsin-Madison, Madison, Wisconsin
Frederikse, Thomas, Planet Labs, Haarlem, The Netherlands
Frith, Stacey M., Science Systems and Applications, Inc, Lanham, Maryland; NASA Goddard Space Flight Center, Greenbelt, Maryland
Froidevaux, Lucien, Jet Propulsion Laboratory, California Institute of Technology, Pasadena, California
Füllekrug, Martin, University of Bath, Bath, United Kingdom
Gallemann, Thomas, Bavarian Environment Agency, Augsburg, Germany
Garforth, Judith, Woodland Trust, Grantham, United Kingdom
Garg, Jay, ADNET Systems, Inc., Hampton, Virginia
Ghent, Darren, National Centre for Earth Observation (NCEO), University of Leicester, Leicester, United Kingdom; School of Physics and Astronomy, University of Leicester, Leicester, United Kingdom
Gobron, Nadine, Joint Research Centre, European Commission, Ispra, Italy
Gollop, Amee, Climatic Research Unit, School of Environmental Sciences, University of East Anglia, Norwich, United Kingdom
Good, Elizabeth, Met Office, Exeter, United Kingdom
Goodman, Steven, Thunderbolt Global Analytics, Huntsville, Alabama
Goto, Atsushi, Japan Meteorological Agency, Tokyo, Japan
Grimaldi, Stefania, Joint Research Centre, European Commission, Ispra, Italy
Gruber, Alexander, Department of Geodesy and Geoinformation, TU Wien, Vienna, Austria
Gu, Guojun, Earth System Science Interdisciplinary Center, University of Maryland, College Park, Maryland
Guglielmin, Mauro, Department of Theoretical and Applied Sciences, Insubria University, Varese, Italy
Haghdoost, Shekoofeh, Hydro-Climate Extremes Lab (H-CEL), Ghent University, Ghent, Belgium
Hahn, Sebastian, Department of Geodesy and Geoinformation, TU Wien, Vienna, Austria
Haimberger, Leopold, Department of Meteorology and Geophysics, University of Vienna, Austria
Hall, Brad D., NOAA Global Monitoring Laboratory, Boulder, Colorado
Harlan, Merritt E., U.S. Geological Survey, Denver, Colorado
Harris, Bethan L., National Centre for Earth Observation (NCEO), University of Leicester, Leicester, United Kingdom; United Kingdom Centre for Ecology & Hydrology, Wallingford, United Kingdom
Harris, Ian, National Centre for Atmospheric Science (NCAS), University of East Anglia, Norwich, United Kingdom; Climatic Research Unit, School of Environmental Sciences, University of East Anglia, Norwich, United Kingdom
Hemming, Deborah L., Met Office Hadley Centre, Exeter, United Kingdom; Birmingham Institute of Forest Research, Birmingham University, Birmingham, United Kingdom
Ho, Shu-peng (Ben), NOAA/NESDIS Center for Satellite Applications and Research, College Park, Maryland
Holliday, Rebecca, Met Office, Exeter, United Kingdom
Holzworth, Robert, University of Washington, Seattle, Washington
Horton, Radley M., Columbia Climate School, Columbia University, New York, New York
Hrbáček, Filip, Department of Geography, Masaryk University, Brno, Czech Republic
Hu, Guojie, Cryosphere Research Station on Qinghai-Tibet Plateau, Northwestern Institute of Eco-Environment and Resources, CAS, Lanzhou, China
Inness, Antje, European Centre for Medium-Range Weather Forecasts, Reading, United Kingdom
Isaksen, Ketil, Norwegian Meteorological Institute, Oslo, Norway
John, Viju O., EUMETSAT, Darmstadt, Germany
Jones, Philip D., Climatic Research Unit, School of Environmental Sciences, University of East Anglia, Norwich, United Kingdom
Junod, Robert, Earth System Science Center, University of Alabama in Huntsville, Huntsville, Alabama
Kääb, Andreas, Department of Geosciences, University of Oslo, Norway
Kaiser, Johannes W., Norwegian Institute for Air Research (NILU), Kjeller, Norway
Kaufmann, Viktor, Institute of Geodesy, Working Group Remote Sensing and Photogrammetry, Graz University of Technology, Graz, Austria
Kellerer-Pirklbauer, Andreas, Department of Geography and Regional Science, Cascade—The Mountain Processes and Mountain Hazards Group, University of Graz, Graz, Austria
Kent, Elizabeth C., National Oceanography Centre, Southampton, United Kingdom
Khaykin, Sergey, Laboratoire Atmosphères, Observations Spatiales (LATMOS), UVSQ, Sorbonne Université, CNRS, IPSL, Guyancourt, France
Kidd, Richard, EODC GmbH, Vienna, Austria
Kipling, Zak, European Centre for Medium-Range Weather Forecasts, Reading, United Kingdom
Kirkpatrick, Sarah, Fenner School of Environment and Society, Australian National University, Canberra, Australia
Kondragunta, Shobha, NOAA/NESDIS, College Park, Maryland
Kovács, Dávid D., Department of Geodesy and Geoinformation, TU Wien, Vienna, Austria
Kraemer, Benjamin M., University of Freiburg, Freiburg, Germany
Laas, Alo, Estonian University of Life Sciences, Tartumaa, Estonia
Lan, Xin, Cooperative Institute for Research in the Environmental Sciences, University of Colorado Boulder, Boulder, Colorado; NOAA Global Monitoring Laboratory, Boulder, Colorado
Lantz, Kathleen O., NOAA Global Monitoring Laboratory, Boulder, Colorado
Lavers, David A., European Centre for Medium-Range Weather Forecasts, Reading, United Kingdom
Leibensperger, Eric, Department of Physics and Astronomy, Ithaca College, Ithaca, New York
Lems, Johanna, Department of Geodesy and Geoinformation, TU Wien, Vienna, Austria
Lennard, Chris, Department of Environmental and Geographical Science, University of Cape Town, Cape Town, South Africa
Levenson, Eric S., University of Oregon, Eugene, Oregon
Liley, Ben, National Institute of Water and Atmospheric Research (NIWA), Lauder, New Zealand
Lo, Y. T. Eunice, Cabot Institute for the Environment; University of Bristol, Bristol, United Kingdom; Elizabeth Blackwell Institute for Health Research, University of Bristol, Bristol, United Kingdom
Loeb, Norman G., NASA Langley Research Center, Hampton, Virginia
Loyola, Diego, German Aerospace Center (DLR), Oberpfaffenhofen, Germany
Macara, Gregor, National Institute of Water and Atmospheric Research (NIWA), Lauder, New Zealand
Magnin, Florence, Laboratoire EDYTEM, CNRS/Université Savoie Mont-Blanc, Le Bourget-du-Lac, France
Matsuzaki, Shin-Ichiro, National Institute for Environmental Studies, Tsukuba, Japan
Matthews, Tom, Department of Geography, King's College London, London, United Kingdom
Mayer, Michael, Department of Meteorology and Geophysics, University of Vienna, Vienna, Austria; Research Department, European Centre for Medium-Range Weather Forecasts, Bonn, Germany

Unauthenticated | Downloaded 11/21/25 11:34 AM UTC

McVicar, Tim R., CSIRO Environment, Canberra, Australia; Australian Research Council Centre of Excellence for Climate Extremes, Sydney, Australia
Mears, Carl A., Remote Sensing Systems, Santa Rosa, California
Menzel, Annette, Ecoclimatology, Department of Life Science Systems, TUM School of Life Sciences, Technical University of Munich, Freising, Germany; Institute for Advanced Study, Technical University of Munich, Garching, Germany
Merchant, Christopher J., University of Reading, Reading, United Kingdom
Meyer, Michael F., U.S. Geological Survey, Madison, Wisconsin
Miralles, Diego G., Hydro-Climate Extremes Lab (H-CEL), Ghent University, Ghent, Belgium
Montzka, Stephan A., NOAA Global Monitoring Laboratory, Boulder, Colorado
Morice, Colin, Met Office Hadley Centre, Exeter, United Kingdom
Morino, Isamu, National Institute for Environmental Studies Tsukuba, Ibaraki, Japan
Morris, Gary A., NOAA Global Monitoring Laboratory, Boulder, Colorado
Mrekaj, Ivan, Technical University in Zvolen, Zvolen, Slovakia
Mühle, Jens, Scripps Institution of Oceanography, San Diego, California
Nance, D., Cooperative Institute for Research in Environmental Sciences, University of Colorado Boulder, Boulder, Colorado
Nicolas, Julien P., European Centre for Medium-Range Weather Forecasts, Bonn, Germany
Noetzli, Jeannette, WSL Institute for Snow and Avalanche Research SLF, Davos Dorf, Switzerland; Climate Change, Extremes and Natural Hazards in Alpine Regions Research Centre (CERC), Davos Dorf, Switzerland
O'Keefe, John, The Harvard Forest, Harvard University, Petersham, Massachusetts
Ollinik, Jessica Erin, Department of Chemistry and Biochemistry, University of Regina, Regina, Canada
Osborn, Timothy J., Climatic Research Unit, School of Environmental Sciences, University of East Anglia, Norwich, United Kingdom
Parrington, Mark, European Centre for Medium-Range Weather Forecasts, Bonn, Germany
Pellet, Cécile, Department of Geosciences, University of Fribourg, Fribourg, Switzerland
Pelto, Mauri, Nichols College, Dudley, Massachusetts
Pennington, Elyse, Jet Propulsion Laboratory, California Institute of Technology, Pasadena, California
Petersen, Kyle, Cooperative Institute for Research in Environmental Sciences, University of Colorado Boulder, Boulder, Colorado; NOAA Global Monitoring Laboratory, Boulder, Colorado
Phillips, Coda, Cooperative Institute for Meteorological Satellite Studies, Space Science and Engineering Center, University of Wisconsin-Madison, Madison, Wisconsin
Pierson, Don, Department of Ecology and Genetics, Uppsala University, Uppsala, Sweden
Pinto, Izidine, Royal Netherlands Meteorological Institute (KNMI), De Bilt, The Netherlands
Po-Chedley, Stephen, Lawrence Livermore National Laboratory, Livermore, California
Pogliotti, Paolo, Environmental Protection Agency of Valle d'Aosta, Saint Christophe, Italy
Polvani, Lorenzo, Columbia University, New York, New York
Preimesberger, Wolfgang, Department of Geodesy and Geoinformation, TU Wien, Vienna, Austria
Price, Colin, Tel Aviv University, Tel Aviv, Israel
Pulkkanen, Merja, Finnish Environment Institute (SYKE), Helsinki, Finland
Randel, William J., National Center for Atmospheric Research, Boulder, Colorado
Raymond, Colin, Joint Institute for Regional Earth System Science and Engineering, University of California, Los Angeles, Los Angeles, California
Remy, Samuel, HYGEOS, Lille, France
Ricciardulli, Lucrezia, Remote Sensing Systems, Santa Rosa, California
Richardson, Andrew D., School of Informatics, Computing, and Cyber Systems, Northern Arizona University, Flagstaff, Arizona; Center for Ecosystem Science and Society, Northern Arizona University, Flagstaff, Arizona
Robinson, David A., Rutgers University, Piscataway, New Jersey
Rodell, Matthew, Earth Sciences Division, NASA Goddard Space Flight Center, Greenbelt, Maryland
Rodriguez-Fernandez, Nemesio, CESBIO, Université de Toulouse, CNES/CNRS/INRAe/IRD/UPS, Toulouse, France
Rogers, Cassandra D.W., Bureau of Meteorology, Melbourne, Australia
Rohini, P., India Meteorological Department, Ministry of Earth Sciences, Pune, India
Rosenlof, Karen H., NOAA Chemical Sciences Laboratory, Boulder, Colorado
Rozanov, Alexei, University of Bremen, Bremen, Germany
Rozkošný, Jozef, Slovak Hydrometeorological Institute, Bratislava, Slovakia
Rusanovskaya, Olga O., Institute of Biology, Irkutsk State University, Irkutsk, Russia
Rutishauser, This, Swiss Academy of Sciences (SCNAT), Bern, Switzerland
Sabeerali, C. T., India Meteorological Department, Ministry of Earth Sciences, Pune, India
Sakai, Tetsu, Meteorological Research Institute, Japan Meteorological Agency, Tsukuba, Ibaraki, Japan
Salamon, Peter, Joint Research Centre, European Commission, Ispra, Italy
Sánchez-Lugo, Ahira, NOAA/NESDIS National Centers for Environmental Information, Asheville, North Carolina
Sawaengphokhai, Parnchai, ADNET Systems, Inc., Hampton, Virginia
Schenzinger, Verena, Medical University of Innsbruck, Innsbruck, Austria
Schmid, Martin, Eawag, Department Surface Waters—Research and Management, Kastanienbaum, Switzerland
Sezaki, Fumi, Japan Meteorological Agency, Tokyo, Japan
Shao, Xi, Earth System Science Interdisciplinary Center, University of Maryland, College Park, Maryland
Sharma, Sapna, Department of Biology, York University, Toronto, Ontario, Canada
Shi, Lei, NOAA/NESDIS National Centers for Environmental Information, Asheville, North Carolina
Shimaraeva, Svetlana V., Institute of Biology, Irkutsk State University, Irkutsk, Russia
Shinohara, Ryuichiro, Regional Environment Conservation Division, National Institute for Environmental Studies, Tsukuba, Ibaraki, Japan
Silow, Eugene A., Institute of Biology, Irkutsk State University, Irkutsk, Russia
Simmons, Adrian J., European Centre for Medium-Range Weather Forecasts, Reading, United Kingdom
Smith, Katie, Cooperative Institute for Research in Environmental Sciences, University of Colorado Boulder, Boulder, Colorado; NOAA Chemical Sciences Laboratory, Boulder, Colorado
Smith, Sharon L., Geological Survey of Canada, Natural Resources Canada, Ottawa, Canada
Soden, Brian J., University of Miami, Miami, Florida
Sofieva, Viktoria, Finnish Meteorological Institute, Helsinki, Finland
Soldo, Logan, Cooperative Institute for Research in Environmental Sciences, University of Colorado Boulder, Boulder, Colorado; NOAA Global Monitoring Laboratory, Boulder, Colorado
Sreejith, O. P., India Meteorological Department, Ministry of Earth Sciences, Pune, India
Stackhouse, Jr., Paul W., NASA Langley Research Center, Hampton, Virginia
Stauffer, Ryan M., Atmospheric Chemistry and Dynamics Laboratory, NASA Goddard Space Flight Center, Greenbelt, Maryland
Steinbrecht, Wolfgang, Deutscher Wetterdienst, Hohenpeissenberg, Germany
Steiner, Andrea K., Wegener Center for Climate and Global Change, University of Graz, Graz, Austria
Stevens, Thea, Department of Meteorology, University of Reading, Reading, United Kingdom

Unauthenticated | Downloaded 11/21/25 11:34 AM UTC

Editor and Author Affiliations (continued)

Stoy, Paul C., College of Agricultural and Life Sciences, University of Wisconsin-Madison, Madison, Wisconsin

Streletskiy, Dmitry A., George Washington University, Washington, DC

Taha, Ghassan, Morgan State University, Baltimore, Maryland; NASA Goddard Flight Center, Greenbelt, Maryland

Thackeray, Stephen J., United Kingdom Centre for Ecology & Hydrology, Lancaster, United Kingdom

Thibert, Emmanuel, Institut de Géosciences de l'Environnement (IGE), Université Grenoble Alpes, INRAE, CNRS, IRD, Grenoble INP, IGE, Grenoble, France

Timofeyev, Maxim A., Institute of Biology, Irkutsk State University, Irkutsk, Russia

Tourpali, Kleareti, Aristotle University, Thessaloniki, Greece

Tronquo, Emma, Hydro-Climate Extremes Lab (H-CEL), Ghent University, Ghent, Belgium; Department of Geoscience and Remote Sensing, TU Delft, Delft, The Netherlands

Tye, Mari R., National Center for Atmospheric Research, Boulder, Colorado

Urraca, Ruben, Joint Research Centre, European Commission, Ispra, Italy

van der A, Ronald, Royal Netherlands Meteorological Institute (KNMI), DeBilt, The Netherlands

van der Schrier, Gerard, Royal Netherlands Meteorological Institute (KNMI), DeBilt, The Netherlands

VanScoy, Greta, The Harvard Forest, Harvard University, Petersham, Massachusetts

van Vliet, Arnold J. H., Earth Systems and Global Change Group, Wageningen University & Research, The Netherlands

Veal, Karen, National Centre for Earth Observation (NCEO), University of Leicester, Leicester, United Kingdom; School of Physics and Astronomy, University of Leicester, Leicester, United Kingdom

Verburg, Piet, National Institute of Water and Atmospheric Research (NIWA), Hamilton, New Zealand

Vernier, Jean-Paul, NASA Langley Research Center, Hampton, Virginia

Vimont, Isaac J., NOAA Global Monitoring Laboratory, Boulder, Colorado

Viticchie, Bartolomeo, EUMETSAT, Darmstadt, Germany

Vivero, Sebastián, Department of Geosciences, University of Fribourg, Fribourg, Switzerland

Vömel, Holger, National Center for Atmospheric Research, Boulder, Colorado

Vose, Russell S., NOAA/NESDIS National Centers for Environmental Information, Asheville, North Carolina

Wang, Donqian, Climate Change Division, National Climate Center, China Meteorological Administration, Beijing, China

Wang, Ray H. J., Georgia Institute of Technology, Atlanta, Georgia

Waring, Abigail Marie, National Centre for Earth Observation (NCEO), University of Leicester, Leicester, United Kingdom; School of Physics and Astronomy, University of Leicester, Leicester, United Kingdom

Warnock, Taran, University of Saskatchewan, Saskatoon, Canada

Weber, Mark, University of Bremen, Bremen, Germany

Wei, Zigang, Science and Technology Corporation (STC), College Park, Maryland

Wiese, David N., Jet Propulsion Laboratory, California Institute of Technology, Pasadena, California

Wild, Jeannette D., Earth System Science Interdisciplinary Center, University of Maryland, College Park, Maryland; NOAA/NESDIS Center for Satellite Applications and Research, College Park, Maryland

Willett, Kate M., Met Office Hadley Centre, Exeter, United Kingdom

Williams, Earle, Massachusetts Institute of Technology, Cambridge, Massachusetts

Wong, Takmeng, NASA Langley Research Center, Hampton, Virginia

Wood, Tom, Department of Geography, King's College London, London, United Kingdom

Woolway, Richard Iestyn, School of Ocean Sciences, Bangor University, Bangor, United Kingdom

Worden, John, Jet Propulsion Laboratory, California Institute of Technology, Pasadena, California

Yang, Kai, Department of Atmospheric and Oceanic Sciences, University of Maryland, College Park, Maryland

Yin, Xungang, NOAA/NESDIS National Centers for Environmental Information, Asheville, North Carolina

Zeng, Zhenzhong, School of Environmental Science and Engineering, Southern University of Science and Technology, Shenzhen, China

Zhao, Lin, School of Geographical Sciences, Nanjing University of Information Science and Technology, Nanjing, China

Ziemke, Jerry R., Goddard Earth Sciences Technology and Research, Morgan State University, Baltimore, Maryland; NASA Goddard Space Flight Center, Greenbelt, Maryland

Ziese, Markus, Global Precipitation Climatology Centre, Deutscher Wetterdienst, Offenbach, Germany

Zotta, Ruxandra-Maria, TU Wien, Vienna, Austria

Zou, Cheng-Zhi, George Mason University, Fairfax, Virginia

Editorial and Production Team

Allen, Jessicca, Graphics Support, Cooperative Institute for Satellite Earth System Studies, North Carolina State University, Asheville, North Carolina

Camper, Amy V., Graphics Support, Innovative Consulting and Management Services, LLC, NOAA/NESDIS National Centers for Environmental Information, Asheville, North Carolina

Carroll, Lauren, Content Team Lead, Communications and Outreach, NOAA/NESDIS National Centers for Environmental Information, Asheville, North Carolina

Haley, Bridgette O., Graphics Support, NOAA/NESDIS National Centers for Environmental Information, Asheville, North Carolina

Love-Brotak, S. Elizabeth, Lead Graphics Production, NOAA/NESDIS National Centers for Environmental Information, Asheville, North Carolina

Ohlmann, Laura, Technical Editor, Innovative Consulting and Management Services, LLC, NOAA/NESDIS National Centers for Environmental Information, Asheville, North Carolina

Noguchi, Lukas, Technical Editor, Innovative Consulting and Management Services, LLC, NOAA/NESDIS National Centers for Environmental Information, Asheville, North Carolina

Riddle, Deborah B., Graphics Support, NOAA/NESDIS National Centers for Environmental Information, Asheville, North Carolina

Veasey, Sara W., Visual Communications Team Lead, Communications and Outreach, NOAA/NESDIS National Centers for Environmental Information, Asheville, North Carolina

Unauthenticated | Downloaded 11/21/25 11:34 AM UTC

2. Table of Contents

Unauthenticated | Downloaded 11/21/25 11:34 AM UTC

2. Table of Contents

Unauthenticated | Downloaded 11/21/25 11:34 AM UTC

2. GLOBAL CLIMATE

R. J. H. Dunn, J. Blannin, K. M. Willett, N. Gobron, and G. A. Morris, Eds.

a. Overview

—R. J. H. Dunn, J. Blannin, K. M. Willett, N. Gobron, and G. A. Morris

For the second year in a row, record-high global surface temperatures were set in 2024, according to all six global temperature datasets assessed in this report (Berkeley Earth, GISTEMP, HadCRUT5, the NOAA Merged Land Ocean Global Surface Temperature Analysis [NOAAGlobalTemp], ERA5, and the Japanese Reanalysis for Three Quarters of a Century [JRA-3Q]). The last time consecutive years set records was in 2015 and 2016 when a strong El Niño similarly boosted global temperatures. The last 10 years (2015–24) are now the warmest 10 in the instrumental record—warmer than the 2011–20 average—and hence "more likely than not warmer than any multi-century period after the last interglacial period, roughly 125,000 years ago" (Gulev et al. 2021). The increased energy within the climate system is detectable at the top of the atmosphere, with the outgoing longwave radiation anomaly continuing to be above the range of natural variability.

During 2024, El Niño conditions that had been present since the middle of 2023 faded to neutral by the end of the year. The warm conditions observed around the globe over the last two years had impacts across the climate system, as demonstrated by many of the metrics presented in this chapter. Other temperature metrics also reached record levels over the instrumental periods assessed in this chapter: over the oceans at night, on the surfaces of lakes, and in the lower troposphere as well as measures of equivalent temperature (which considers the moisture contribution to heat), and high and low temperature extremes.

The frozen parts of Earth responded with permafrost temperatures continuing to reach record-high levels in many locations, and the active-layer thickness (the portion that melts and refreezes annually) also increasing at most sites. Repeated high temperatures over the European Alps during recent summers has led to large increases in rock glacier velocities in that region. The Great Lakes had much-below-average ice cover over the 2023/24 winter, and there was below-average snow cover extent in the Northern Hemisphere. All 58 reference glaciers across five continents lost ice during 2024, resulting in the greatest average ice loss in the record, which began in 1970. One more glacier was also declared extinct during 2024.

Higher global temperatures impacted the water cycle. Although lower than 2023 values, water evaporation from land in the Northern Hemisphere reached one of the highest annual values on record, in line with the long-term increasing trend. Specific humidity reached record levels over land and ocean, and relative humidity over both domains was higher than 2023. There was little relief from high humid-heat conditions, with the frequency of high humid-heat days at a record level and intensity at the second-highest level in the record—only a fraction of a degree cooler than that of 2023. The global atmosphere contained the greatest amount of water vapor in the record, and over one-fifth of the globe recorded their highest values. This far exceeded 2023, where only one-tenth of the globe experienced record-high total column water vapor. Rainfall was globally high; 2024 was the third-wettest year since records began in 1983. However, rainfall over land was close to average, while over the ocean it was the fourth-wettest year on record (following 2015, 2016, and 1998). Extreme rainfall, as characterized by the annual maximum daily rainfall over land, was the wettest on record. Averaged globally (4190 lakes), lakes had a small increase in water storage, and regionally, over 40% of monitored lakes showed significant changes in storage and level.

Unauthenticated | Downloaded 11/21/25 11:34 AM UTC

The effects of ongoing droughts in southern Africa and in North and South America can be seen in the soil moisture and water storage patterns. They are also apparent in the river discharge and runoff levels, which are topics that will be covered in the chapter after a few years of absence. Globally, however, drought severity and extent decreased from the record set in 2023.

Atmospheric concentrations of the three main greenhouse gases (carbon dioxide [CO_2], methane [CH_4], nitrous oxide [N_2O]) again all reached record levels, with a record-equal annual increase in the annual change of CO_2 concentrations. However, concentrations of ozone-depleting substances continued to decline, corroborated by stratospheric ozone columns well above the 1998–2008 average, especially in the Northern Hemisphere. In contrast, stratospheric aerosols remained high because of the Ruang eruption in April 2024, affecting the atmospheric transmission of solar radiation over Hawaii later in the year, and the ongoing effects from the Hunga eruption in 2022. The latter eruption also caused the ongoing elevated stratospheric water vapor concentrations.

Our planet's surface albedo continued to darken with increased plant growth and decreased snow and ice cover. Plants responded to the warmer temperatures with some of the earliest starts to spring in the record over Europe—one to two weeks earlier than the 2000–20 baseline—and a warm autumn resulted in a much longer leaf-on season. Severe wildfire seasons occurred in South America (the worst since 2010), Canada (for the second consecutive year), and the Arctic, contributing to the second-highest atmospheric carbon monoxide concentrations since 2003 and the highest tropospheric aerosol optical depth since 2019, at 550 nm.

This year's iteration of the Global Climate chapter features two Sidebars, both of which present new topics that have not yet been explored in the report. The first covers the ability of satellite products to monitor changes in land surface temperature extremes and identify hotspots where regions of Earth are becoming uninhabitable. This Sidebar also discusses the importance of dataset stability for climate studies, as well as the correlation of land surface temperature and air temperature anomalies. The second Sidebar complements the section on greenhouse gas concentrations by examining short-lived climate forcers—compounds that have lifetimes ranging from a few hours to a few decades.

As usual in the Global Climate chapter, Plate 2.1 shows maps of global annual anomalies for many of the variables and metrics presented herein. Many of these variables are also presented as time series in Plate 1.1. Most sections now use the 1991–2020 climatological reference period, in line with the World Meteorological Organization's (WMO) recommendations, although this reference period is not possible for all datasets due to their length or legacy processing methods.

Unauthenticated | Downloaded 11/21/25 11:34 AM UTC

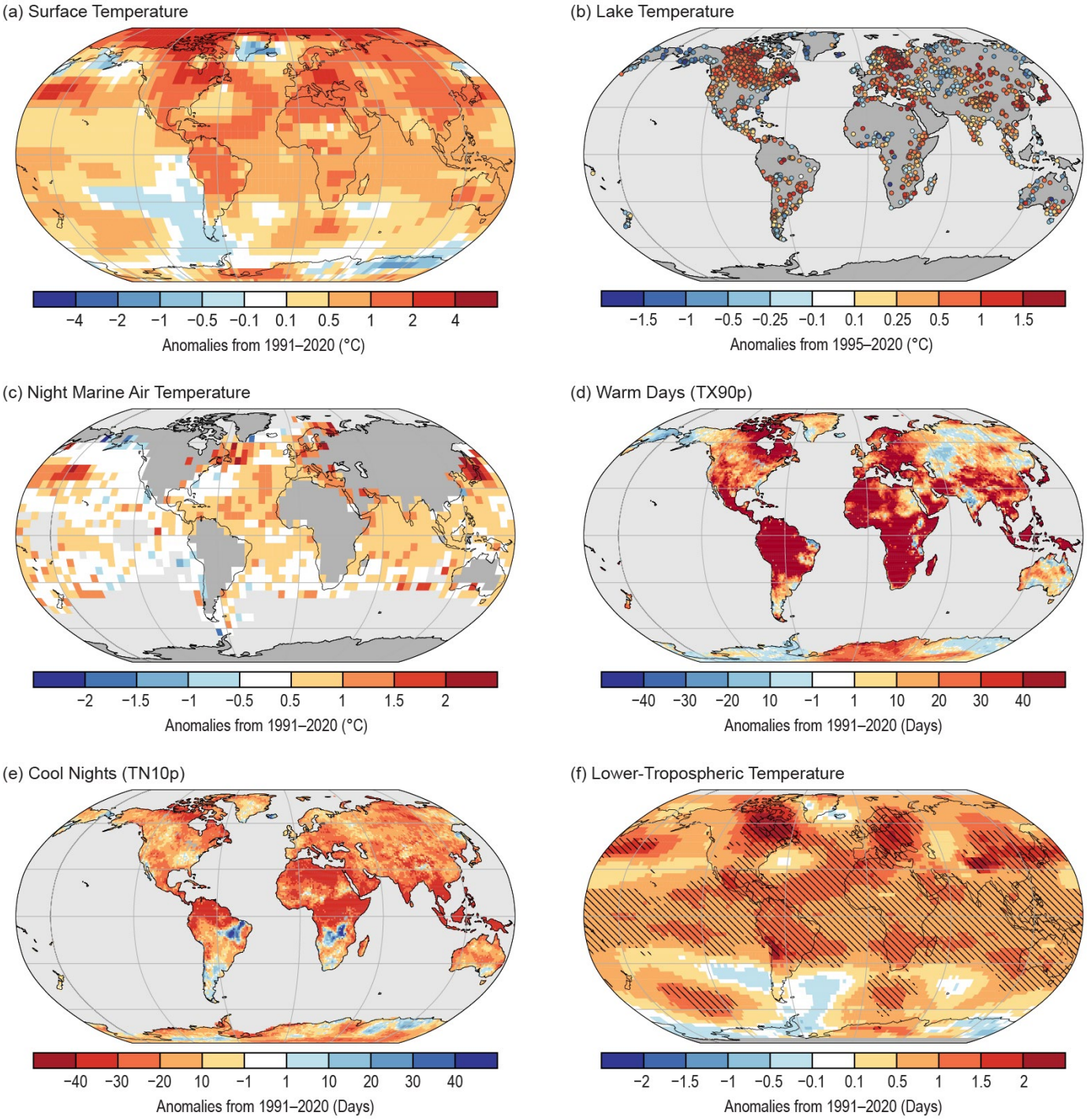

Plate 2.1. (a) NOAA NCEI Global land and ocean surface annual temperature anomalies (°C); (b) Satellite-derived lake surface water temperature annual anomalies, from European Space Agency (ESA) Climate Change Initiative (CCI) LAKES/Copernicus Climate Change Service (C3S) / Earth Observation Climate Information Service (EOCIS) (°C); (c) Climate Linked Atlantic Sector Science Night Marine Air Temperature (CLASSnmat) night marine air temperature annual average anomalies (°C); (d) ERA5 warm day threshold exceedance (TX90p); (e) ERA5 cool night threshold exceedance (TN10p); (f) Average of Remote Sensing Systems (RSS) and University of Alabama in Huntsville (UAH) lower-tropospheric annual temperature anomalies (°C). Hatching denotes regions in which 2024 was the warmest year on record; (g) ERA5 annual equivalent temperature anomalies (°C);

Unauthenticated | Downloaded 11/21/25 11:34 AM UTC

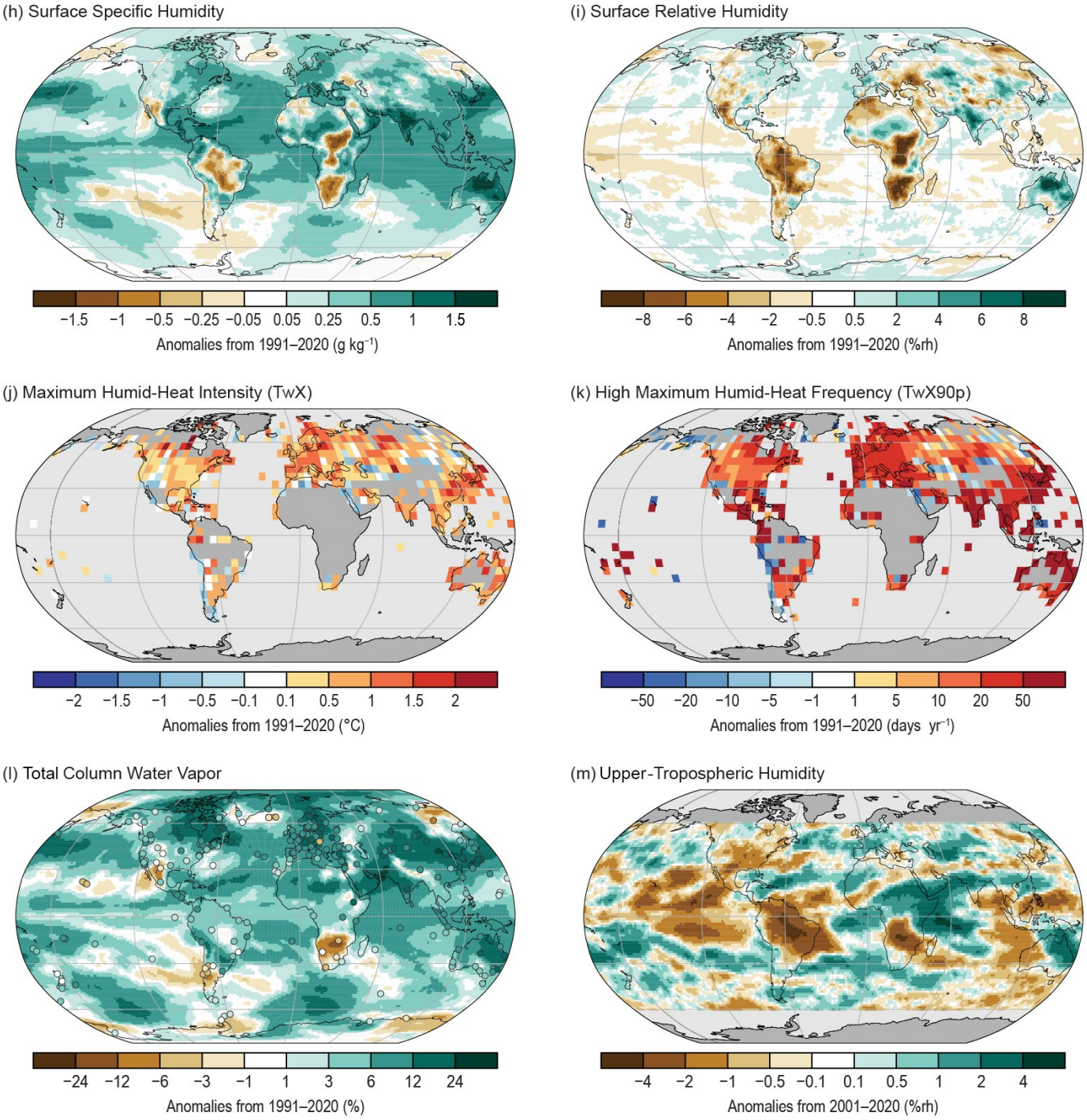

Plate 2.1 (cont.) (h) ERA5 surface specific humidity anomalies (g kg^{-1}); (i) ERA5 surface relative humidity anomalies (%rh); (j) Met Office Hadley Centre International Surface Dataset of Humidity extremes (HadISDH.extremes) humid heat intensity (T_wX), measured by the annual median anomaly of daily maximum wet-bulb temperature (°C). Gray background (over land) represent regions with insufficient data; (k) HadISDH.extremes humid heat frequency anomalies (T_wX90p), measured by the number of days where the daily maximum wet-bulb temperature exceeds the local daily 90th percentile (days yr^{-1}). Gray background (over land) represent regions with insufficient data; (l) JRA-3Q Total column water vapor (TCWV) anomalies (%). Data from Global Navigation Satellite System (GNSS) stations are plotted as filled circles; (m) Annual microwave-based upper-tropospheric humidity (UTH) anomalies (%rh); (n) Global Precipitation Climatology Centre (GPCC) annual mean precipitation anomalies (mm yr^{-1});

Unauthenticated | Downloaded 11/21/25 11:34 AM UTC

(o) Rx5day Anomalies

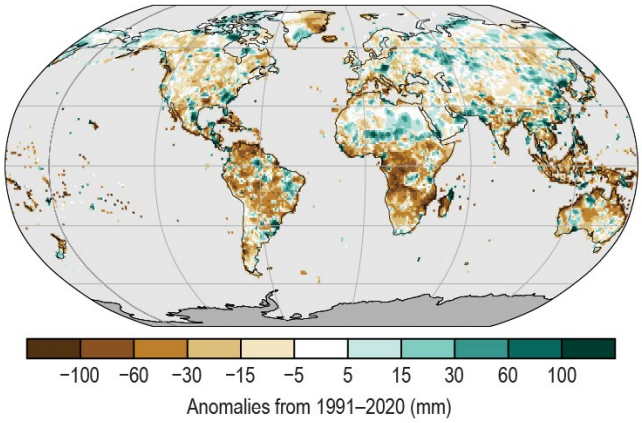

(p) Cloudiness

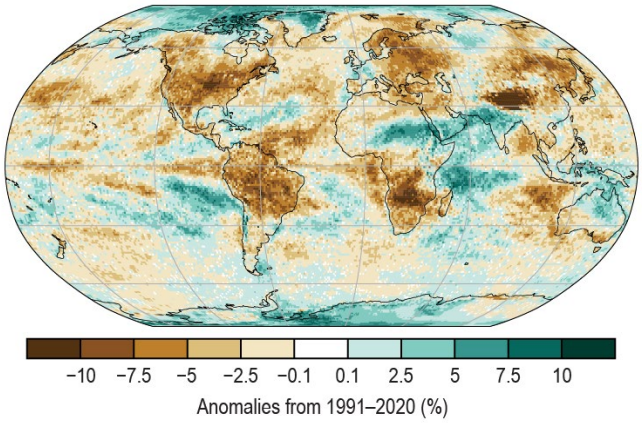

(q) Lake Water Storage

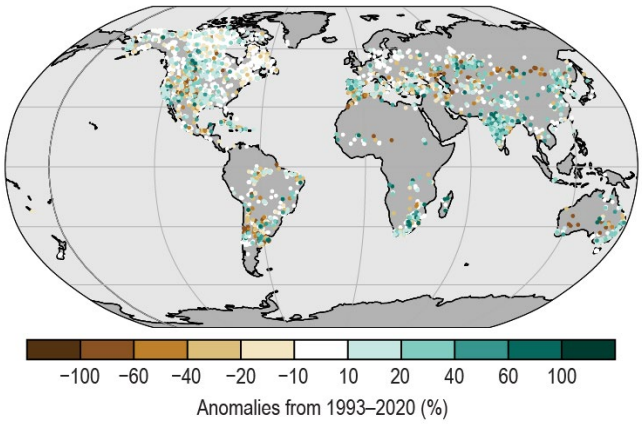

(r) Runoff

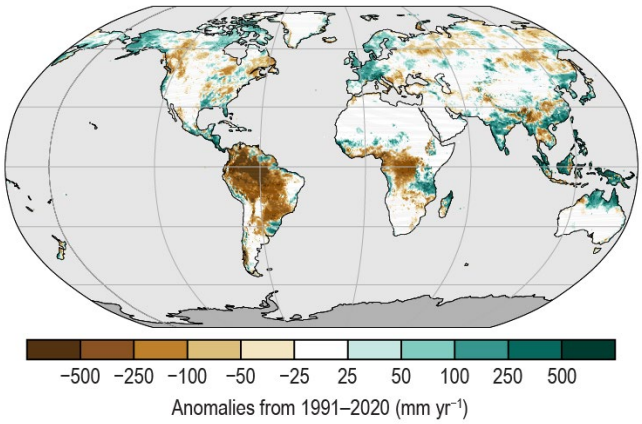

(s) River Discharge

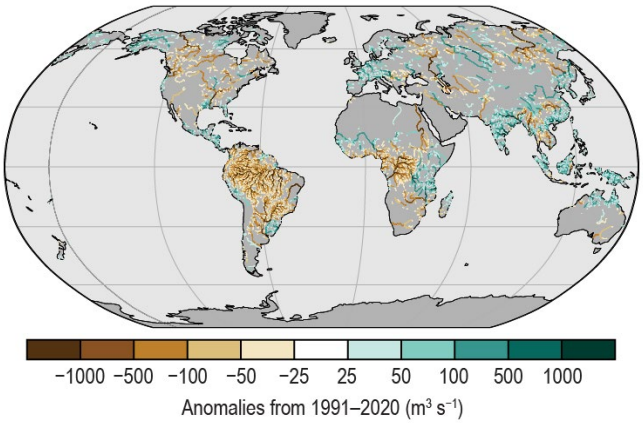

(t) Terrestrial Water Storage Difference

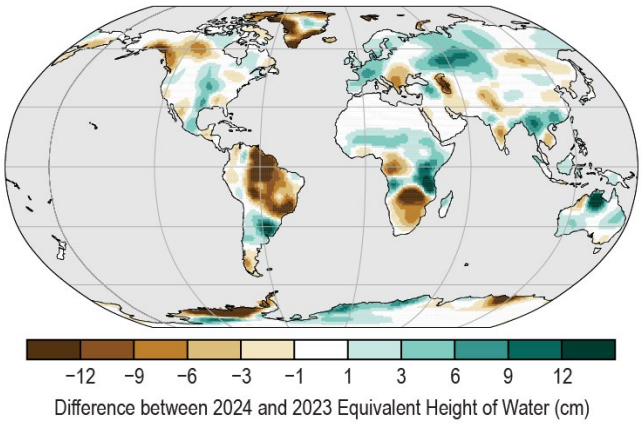

(u) Terrestrial Water Storage

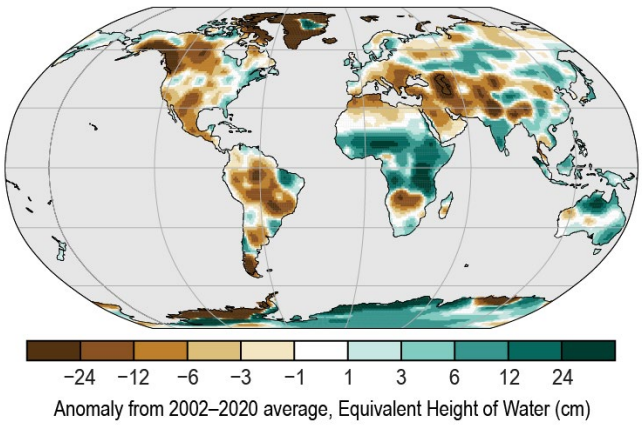

Plate 2.1 (cont.) (o) GPCC maximum five-day (Rx5day) annual precipitation anomalies (mm); (p) PATMOS-x 6.0 cloud fraction annual anomalies (%); (q) GloLakes lake water storage anomalies (%); (r) Global Flood Awareness System version 4 (GloFASv4) runoff anomalies (mm yr^{-1}); (s) GloFASv4 river discharge anomalies (m^3 s^{-1}); (t) Gravity Recovery and Climate Experiment Follow-On (GRACE-FO) difference in annual-mean terrestrial water storage between 2023 and 2024 (cm); (u) GRACE-FO terrestrial water storage anomalies (cm);

Unauthenticated | Downloaded 11/21/25 11:34 AM UTC

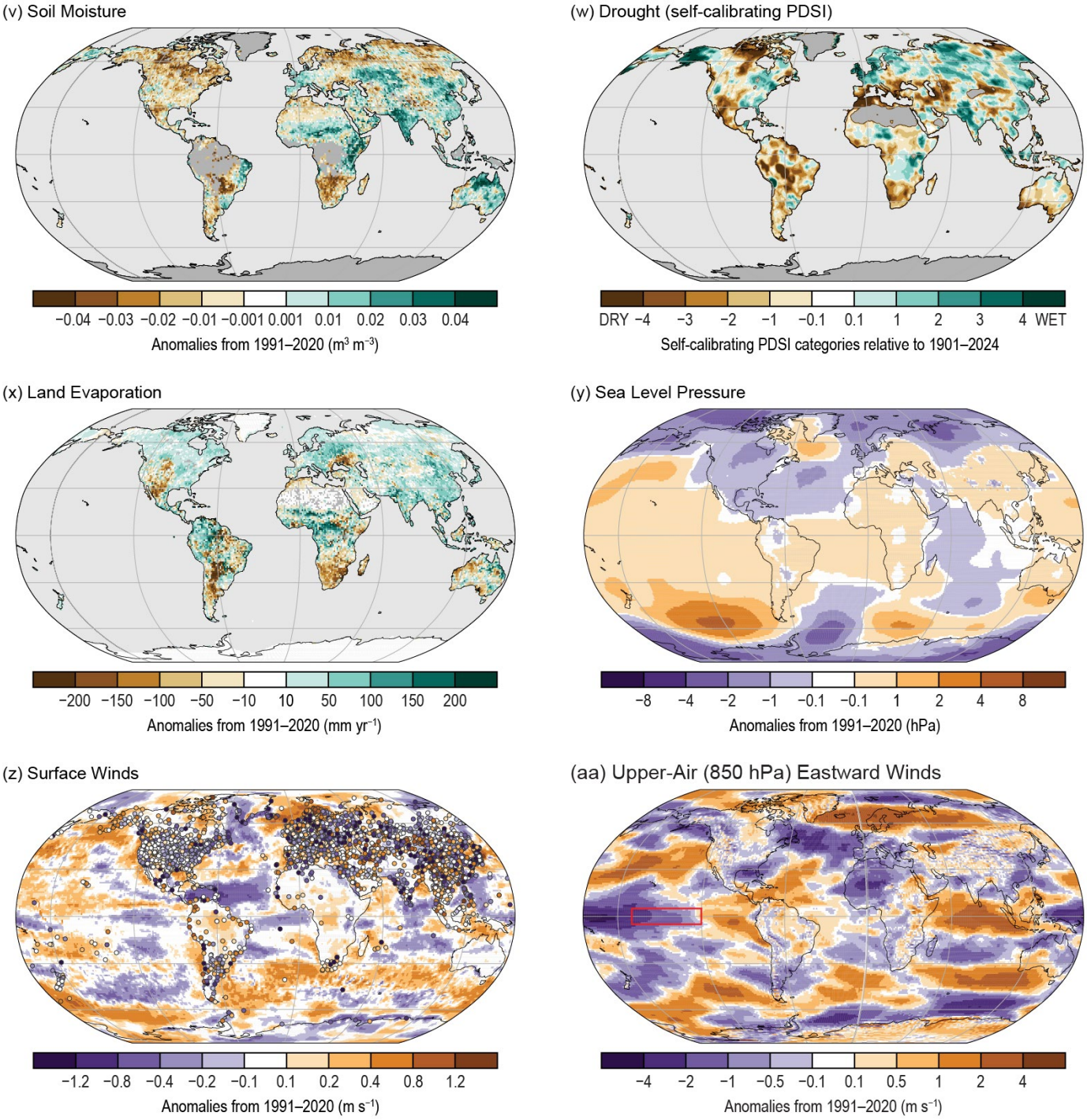

Plate 2.1 (cont.) (v) Copernicus Climate Change Service (C3S) average surface soil moisture anomalies ($m^3\ m^{-3}$). Data are masked where no retrieval is possible or where the quality is not assured and flagged, for example due to dense vegetation, frozen soil, or radio frequency interference; (w) Mean self-calibrating Palmer Drought Severity Index (scPDSI). Droughts are indicated by negative values (brown), wet episodes by positive values (green). No calculation is made where a drought index is meaningless (gray areas: ice sheets or deserts with approximately zero mean precipitation); (x) Great Lakes Environmental Assessment and Mapping Project (GLEAM) land evaporation anomalies (mm yr^{-1}); (y) ERA5 mean sea level pressure anomalies (hPa); (z) Surface wind speed anomalies (m s^{-1}) from the observational HadISD3 dataset (land, circles), the ERA5 reanalysis output (land, shaded areas), and RSS satellite observations (ocean, shaded areas); (aa) ERA5 850-hPa eastward wind speed anomalies for Oct–Dec (m s^{-1}); (ab) Copernicus Atmosphere Monitoring Service (CAMS) reanalysis total aerosol optical depth (AOD) anomalies at 550 nm;

Unauthenticated | Downloaded 11/21/25 11:34 AM UTC

(ac) PM2.5

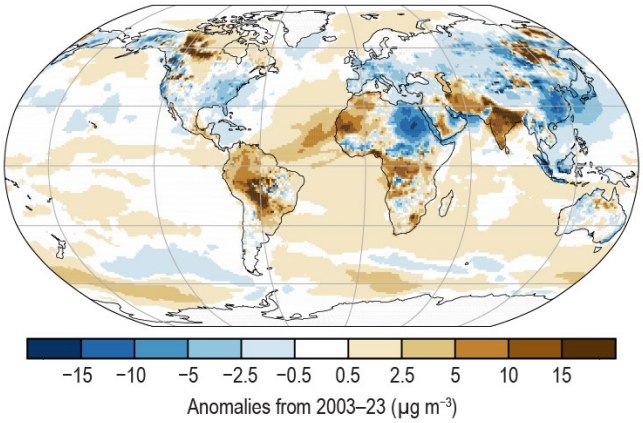

(ad) Extreme Aerosol Days

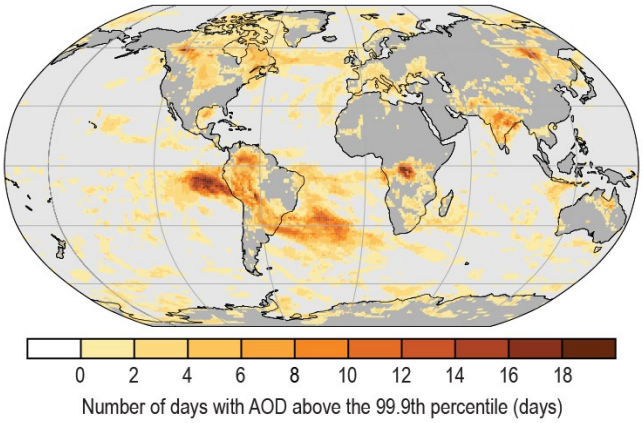

(ae) OMI/MLS Tropospheric Column Ozone

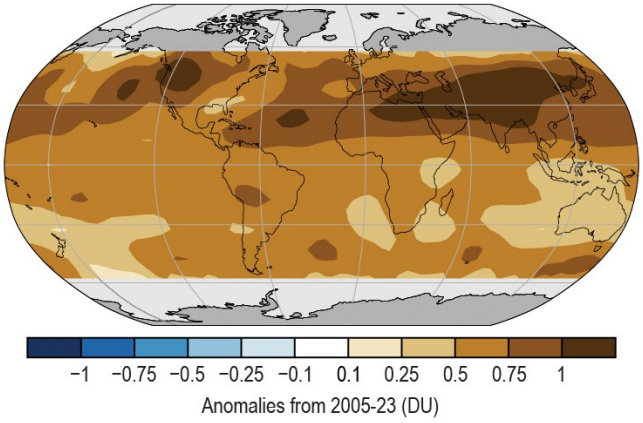

(af) Stratospheric (Total Column) Ozone

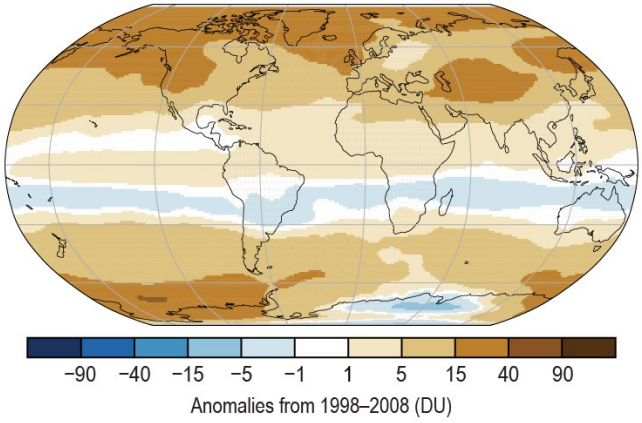

(ag) Carbon Monoxide

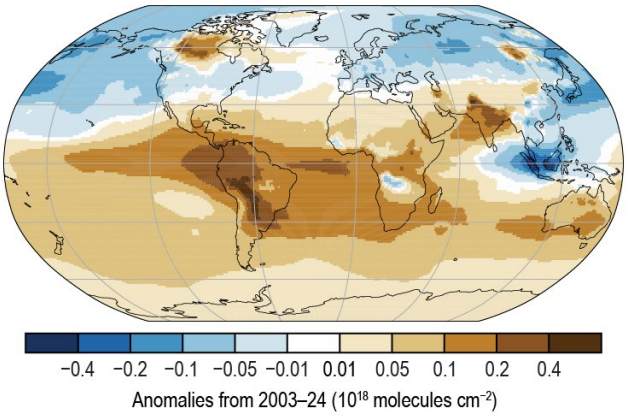

(ah) Visible Land Surface Albedo

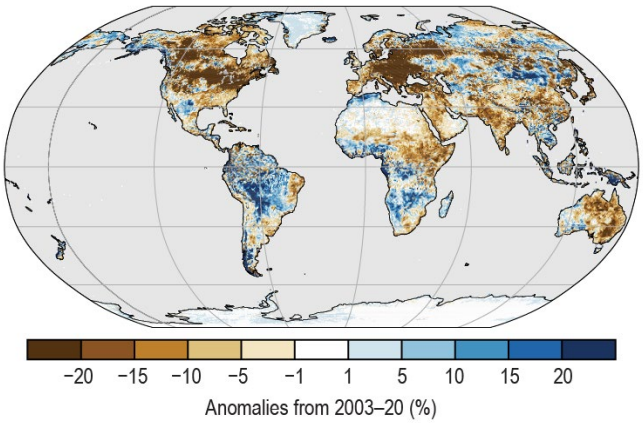

(ai) Near Infrared Land Surface Albedo

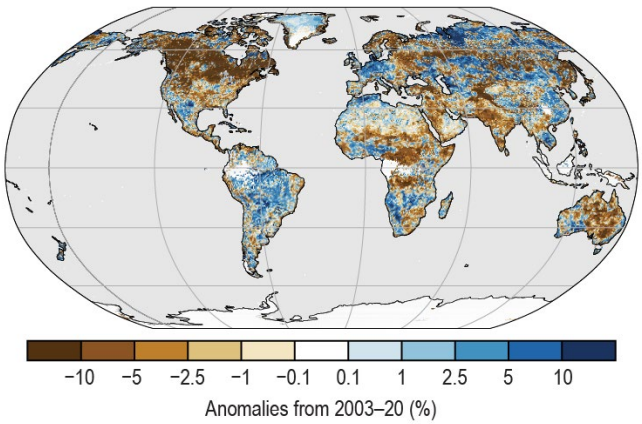

Plate 2.1 (cont.) (ac) CAMS reanalysis PM2.5 anomalies (μg m^{-3}); (ad) Number of days with AOD above the 99.9th percentile from CAMS reanalysis. Areas with zero days appear as the white/gray background; (ae) Ozone Monitoring Instrument (OMI)/Microwave Limb Sounder (MLS) tropospheric ozone column anomalies for 60°S–60°N (DU); (af) total column ozone anomalies determined from Tropospheric Monitoring Instrument (TROPOMI) aboard Sentinel-5 Precursor (S5P; DU); (ag) CAMS reanalysis total column carbon monoxide anomalies (× 10^{18} molecules cm^{-2}); (ah) Visible Infrared Imaging Radiometer Suite (VIIRS) land surface visible broadband albedo anomalies (%); (ai) VIIRS land surface near-infrared albedo anomalies (%);

Unauthenticated | Downloaded 11/21/25 11:34 AM UTC

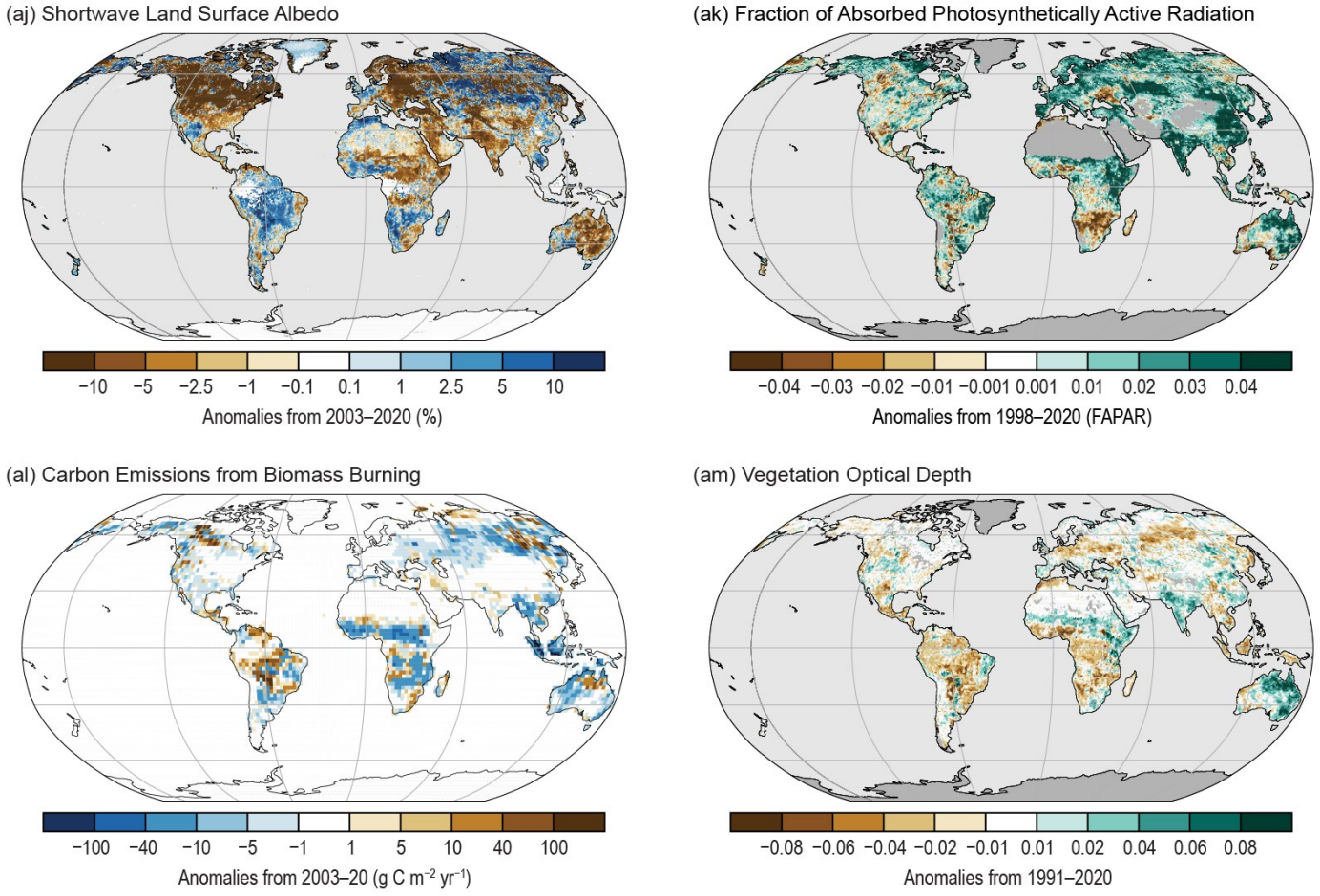

Plate 2.1 (cont.) (aj) VIIRS land surface shortwave broadband albedo anomalies (%); (ak) Fraction of absorbed photosynthetically active radiation (FAPAR) anomalies; (al) Global Fire Assimilation System version 1.4 (GFASv1.4) carbonaceous emission anomalies (g C m^{-2} yr^{-1}) from biomass burning; (am) Vegetation Optical Depth Climate Archive (VODCA) CXKu-band vegetation optical depth (VOD) anomalies.

Unauthenticated | Downloaded 11/21/25 11:34 AM UTC

b. Temperature

1. SURFACE TEMPERATURE

—A. Arguez, A. Bunno, A. Goto, C. Morice, J. P. Nicolas, A. Sánchez-Lugo, and F. Sezaki

For the second consecutive year, a new global surface temperature record was set. According to six global temperature datasets, the global surface temperature for 2024 was 0.63°C–0.72°C above the 1991–2020 average, (Table 2.1; Fig. 2.1). This was the highest value since global records began in the mid-1800s to mid-1900s, surpassing the previous warmest year on record set only last year (2023) by a margin of +0.08°C to +0.12°C.

According to all six global datasets, the last 10 years (2015–24) were the 10 warmest years on record. The datasets consist of four global in situ surface temperature analyses (GISTEMP, Lenssen et al. 2019; HadCRUT5, Morice et al. 2021; the NOAA Merged Land Ocean Global Surface Temperature Analysis [NOAAGlobalTemp], Vose et al. 2021; Berkeley Earth, Rhode and Hausfather 2020) and two global atmospheric reanalyses (ERA5, Hersbach et al. 2020, Soci et al. 2024; the Japanese Reanalysis for Three Quarters of a Century [JRA-3Q], Kosaka et al. 2024).

The global surface temperature for 2024 was also 1.46°C–1.62°C above the 1850–1900 average (a period commonly used to represent pre-industrial conditions). The pre-industrial temperature anomaly range was computed using the three datasets that extend back to 1850 (NOAAGlobalTemp, HadCRUT5, Berkeley Earth) using each dataset's own 1850–1900 baseline. Two of the three datasets indicated that the yearly temperature anomaly surpassed +1.5°C, the most ambitious limit set by the Paris Agreement (Paris Agreement 2015). Of note, exceeding +1.5°C in a single year does not represent a failure to achieve the Paris Agreement limit; this would require breaching +1.5°C over a longer period (WMO 2025a).

The global trends are within 0.20°C–0.22°C decade^{-1} for the short-term (1981–2024) and are within 0.08°C–0.09°C decade^{-1} for the long-term (1880–2024). Following the Arguez et al. (2020) approach, 2024 was 0.23°C–0.29°C above the value derived from the linear trend

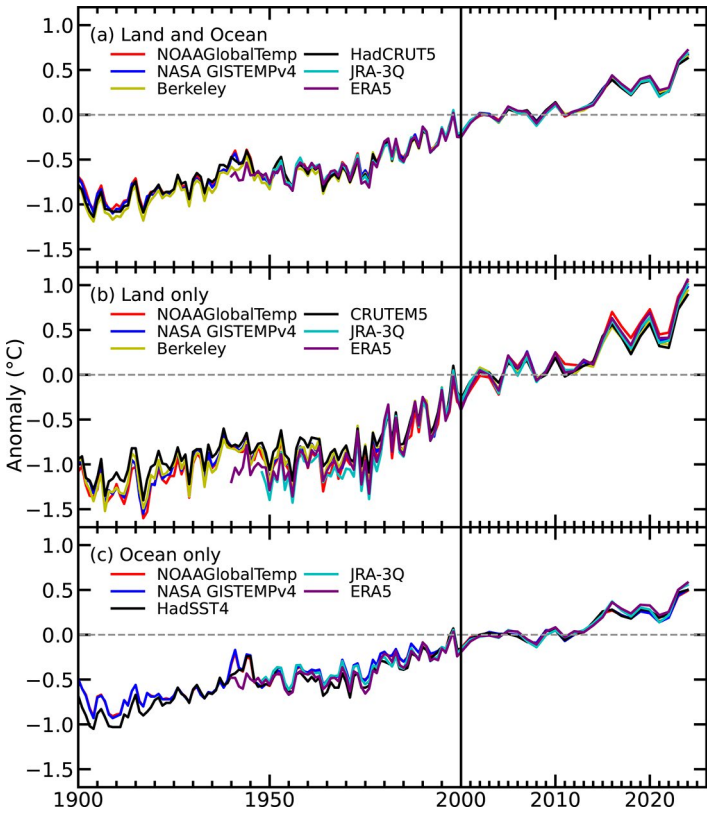

Fig. 2.1. Global average surface air temperature anomalies (°C; 1991–2020 base period). In situ estimates are shown from the NOAA Merged Land Ocean Global Surface Temperature Analysis (NOAAGlobalTemp; Vose et al. 2021), NASA Goddard Institute for Space Studies Surface Temperature Analysis version 4 (GISTEMPv4; Lenssen et al. 2019), Hadley Centre/Climatic Research Unit Temperature version 5 (HadCRUT5; Morice et al. 2021), Climatic Research Unit temperature version 5 (CRUTEM5; Osborn et al. 2021), Hadley Centre Sea Surface Temperature Dataset version 4 (HadSST4; Kennedy et al. 2019), and Berkeley Earth (Rhode and Hausfather 2020). Reanalysis estimates are shown from ERA5 (Hersbach et al. 2020; Bell et al. 2021) and the Japanese Reanalysis for Three Quarters of a Century (JRA-3Q; Kosaka et al. 2024).

Table 2.1. Global temperature anomalies (°C; 1991–2020 base period) for 2024. Note that for the HadCRUT5 column, land values were computed using the Climatic Research Unit Temperature version 5 (CRUTEM.5.0.2.0) dataset (Osborn et al. 2021), ocean values were computed using the Hadley Centre Sea Surface Temperature Dataset version 4 (HadSST.4.0.1.0) dataset (Kennedy et al. 2019), and global land and ocean values were computed using the HadCRUT.5.0.2.0 dataset (Morice et al. 2021).

Global	NASA-GISTEMPv4	HadCRUT5	NOAA GlobalTemp	Berkeley Earth	ERA5	JRA-3Q
Land	+0.98	+0.89	+1.04	+0.94	+1.06	+1.01
Ocean	+0.50	+0.50	+0.49	-	+0.58	+0.56
Land and Ocean	+0.67	+0.63	+0.67	+0.65	+0.72	+0.69

Unauthenticated | Downloaded 11/21/25 11:34 AM UTC

calculated over the last 50 years (1975–2024), registering the highest departures above the trend lines in all six global datasets.

The annual global land-only and ocean-only surface temperatures were also record high, at 0.89°C–1.06°C and 0.49°C–0.58°C above the 1991–2020 average, respectively (Table 2.1). The year was characterized by much-warmer-than-average conditions across most of the world's surface (Plate 2.1a; Appendix Figs. A2.1–A2.4), with record-high annual temperatures observed across parts of each continent and across large areas in the North and tropical Atlantic Ocean, North Indian Ocean, western Pacific Ocean, Arctic Ocean, and the Southern Ocean. In contrast, below-average annual temperatures were observed across Iceland, southern Greenland, the Bering Sea, the Okhotsk Sea, and parts of the eastern South Pacific, Southern Ocean, and Antarctica.

Monthly global surface temperatures were exceptionally high throughout the year, with each month ranking either as the warmest or the second-warmest on record. A strong El Niño event, which began during boreal summer 2023, continued into early 2024 before ending in boreal spring. The ensuing El Niño–Southern Oscillation (ENSO)-neutral conditions persisted through the remainder of the year until La Niña-like conditions emerged at the end of 2024. While several factors may have contributed to the record-high temperature in 2024, the influence of El Niño together with unusually warm oceans across many basins were key contributors to the high monthly global surface temperature records observed, especially during the first half of the year, adding warmth on top of the long-term warming caused by anthropogenic greenhouse gas emissions. The last time at least two consecutive years reached a new global surface temperature record was in 2015 and 2016, when a strong El Niño developed during the latter half of 2015 and dissipated by May 2016.

2. LAKE SURFACE TEMPERATURE

—L. Carrea, C. J. Merchant, R. I Woolway, J.-F. Creatux, T. M. Dokulil, H. Dugan, A. Laas, E. Leibensperger, S.-I. Matsuzaki, D. Pierson, M. Pulkkanen, O. O. Rusanovskaya, S. V. Shimaraeva, E. A. Silow, M. Schmid, M. A. Timofeyev, and P. Verburg

In 2024, the global average lake surface water temperature (LSWT) anomaly derived from satellite data during the warm season was +0.52°C with respect to the 1995–2020 baseline; the anomalies were positive for 79% and negative for 21% of the 1944 studied lakes. The 2024 anomaly is the largest since the record began in 1995. The mean LSWT trend during 1995 to 2024 was 0.22±0.01°C decade^{-1}, broadly consistent with previous analyses even though the number of lakes analyzed has doubled since 2022 (Woolway et al. 2017, 2018; Carrea et al. 2019, 2020, 2021, 2022a, 2023b, 2024; Fig. 2.2). The warm-season lake-mean LSWT anomalies for each lake are shown in Plate 2.1b.

In 2024, 56% of all observed lakes showed LSWT anomalies in excess of +0.5°C, and extensive regions with consistently large LSWT anomalies were detected. (Plate 2.1b). The largest positive anomalies were reported for lakes situated in Canada, China, Japan, the Tibetan area, eastern Europe, and the Middle East, while in Patagonia, Greenland, Alaska, and northeast Russia, lakes were found to be cooler than average.

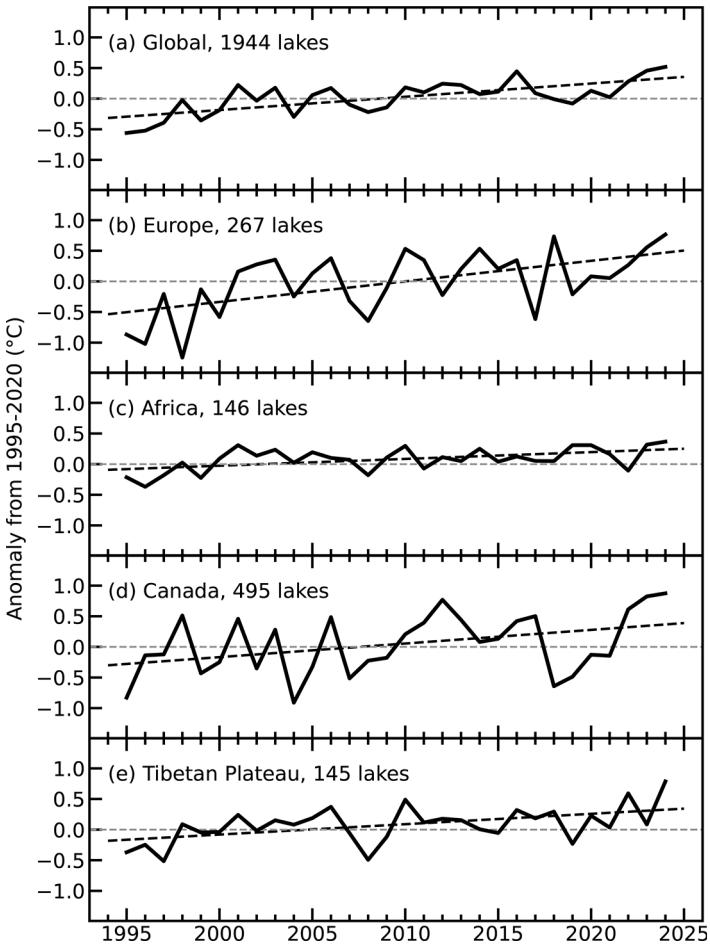

Fig. 2.2. Annual time series of satellite-derived warm-season lake surface water temperature anomalies (°C; 1995–2020 base period) from 1995 to 2024 for lakes distributed (a) globally, and regionally in (b) Europe, (c) Africa, (d) Canada, and (e) the Tibetan Plateau.

Unauthenticated | Downloaded 11/21/25 11:34 AM UTC

As in previous reports (see for example Carrea et al. 2023b, 2024), four regions were studied in more detail: Europe (number of lakes, n = 267, Figs. 2.2b, 2.3a), Africa (n =146, Figs. 2.2c, 2.3b), Tibet (n = 145, Figs. 2.2e, 2.3d), and Canada (n = 495, Figs. 2.2d, 2.3c). In these areas, the warm-season LSWT anomalies generally align with the air temperature anomalies extracted at the locations of the lakes from the dataset compiled by NASA's Goddard Institute for Space Studies (GISS; Hansen et al. 2010; GISTEMP Team 2025). The average LSWT trend was +0.34±0.03°C decade^{-1} in Europe (Fig. 2.2b) and +0.22±0.03°C decade^{-1} in Canada (Fig. 2.2d). In Canada, 96% of observed lakes were warmer than average, with only 4% being cooler than average, and the mean LSWT anomaly was +0.87°C in 2024. In Europe, the average anomaly was +0.77°C, and 86% of lakes presented positive anomalies. In Africa and Tibet, the long-term change in LSWT is comparatively smaller, at +0.11±0.01°C decade^{-1} and +0.17±0.02°C decade^{-1}, respectively (Figs. 2.2c,e). In Africa, 77% of the 146 lakes had positive LSWT anomalies, and the average anomaly in 2024 was +0.37°C. In Tibet, the average anomaly was +0.79°C, and the LSWT anomaly was positive for 143 lakes and negative for 2. In all these regions, the 2024 mean anomaly was the largest since the record began in 1995.

In situ single-point observations from 38 lakes were used to compute the warm-season temperature anomalies depicted in Fig. 2.4. Among these lakes, 27 have measurements for 2024, with an average anomaly of +1.25°C. Only three lakes experienced negative anomalies (average −0.59°C) and 24 lakes had positive anomalies (average +1.48°C) in 2024; Fig. 2.4 clearly shows that lakes are warming, especially after the year 2000. It is important to note that anomalies based on in situ measurements, which are point measurements, generally differ from those derived from satellite data, which instead represent lake-wide averages, and therefore are more representative of the lake response than single point. On the other hand, in situ measurements can offer high coverage in time while satellite data are sparser in time.

The period 1995–2020 is used as a baseline to compute the anomalies for both in situ (unless data were not available for the full period) and satellite temperature. The warm-season averages for midlatitude lakes were calculated

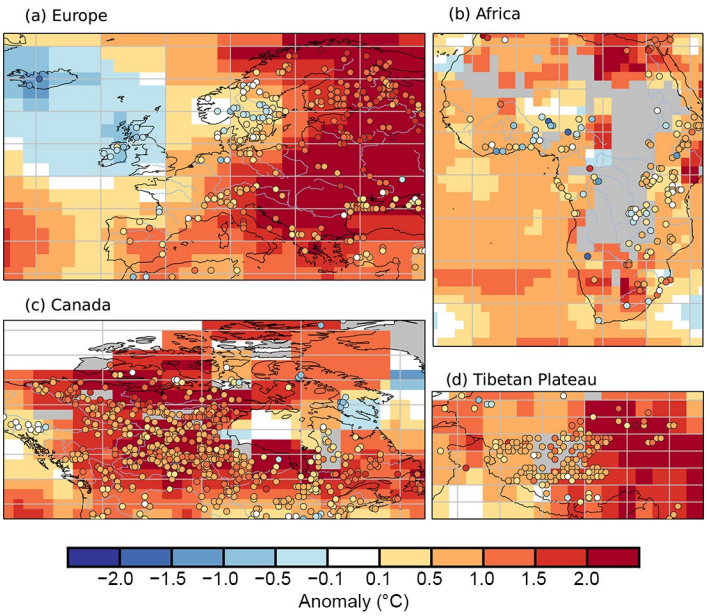

Fig. 2.3. Lake temperature anomalies (°C, colored dots) and 2-m air temperature anomalies (°C; NASA Goddard Institute for Space Studies [GISS]; Hansen et al. 2010, GISS Surface Temperature Analysis [GISTEMP] Team 2025) in 2024 for lakes in (a) Europe, (b) Africa, (c) Canada, and (d) the Tibetan Plateau. These values were calculated for the warm season (Jul–Sep in the extratropical Northern Hemisphere; Jan–Mar in the extratropical Southern Hemisphere; Jan–Dec in the tropics) with reference to the 1995–2020 base period.

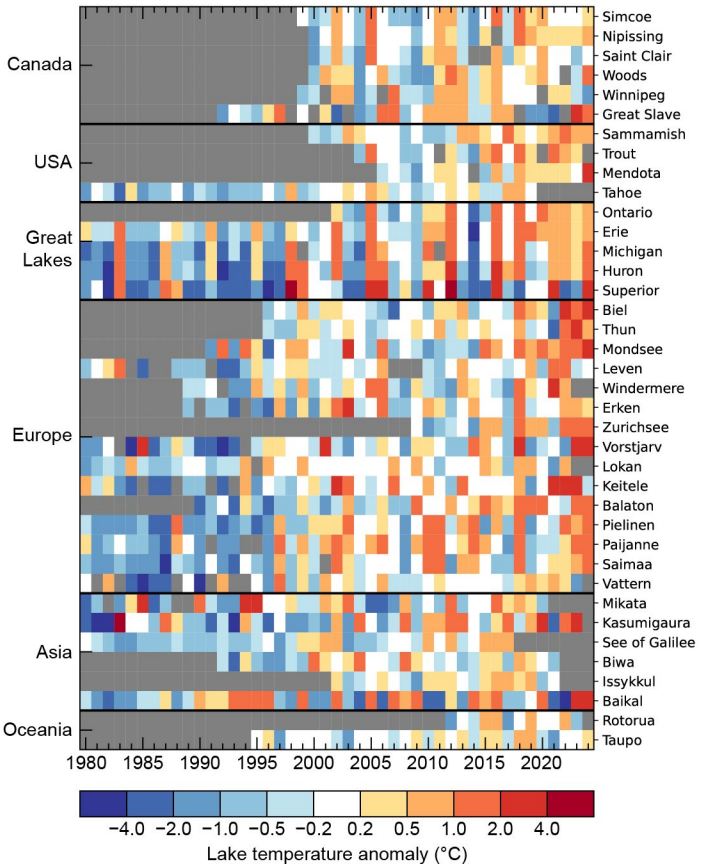

Fig. 2.4. In situ lake surface water temperature (LSWT) observations from 38 globally distributed lakes, showing the annually averaged warm season (Jul–Sep in the Northern Hemisphere; Jan–Mar in the Southern Hemisphere) anomalies (°C; 1995–2020 base period).

Unauthenticated | Downloaded 11/21/25 11:34 AM UTC

for the summer months (July–September in the Northern Hemisphere and January–March in the Southern Hemisphere), while annual averages are used for tropical lakes located within 23.5° of the equator. For global averages, an unweighted mean of all the lake LSWT anomalies was computed. LSWT time series were derived from the Copernicus Climate Change Service (until 2022) and the Earth Observation Climate Information Service climate data record (Carrea et al. 2022b, 2023a), which was based on the European Space Agency Climate Change Initiative LAKES v2.1 dataset and subsequently extended. For 2024, LSWT was retrieved from satellite observations from Sea and Land Surface Temperature Radiometers (SLSTR) onboard Sentinel3A and 3B. The retrieval method of MacCallum and Merchant (2012) was applied on image pixels filled with water according to both the inland water dataset of Carrea et al. (2015) and a reflectance-based water detection scheme (Carrea et al. 2023a).

The satellite-derived LSWT data were validated with in situ measurements with an average satellite minus in situ temperature difference of less than 0.5°C (Carrea et al. 2023a). The satellite-derived LSWT data were averaged spatially for each of a total of 1944 lakes, and lake-wide average surface temperatures have been shown to give a more representative picture of LSWT responses to climate change than single-point measurements (Woolway and Merchant 2018).

The averaged surface air temperature was calculated from the Global Historical Climatology Network version 4 (GHCNv4; 250-km smoothing radius) data of the NASA GISS surface temperature analysis (Hansen et al. 2010; GISTEMP Team 2025).

3. NIGHT MARINE AIR TEMPERATURE

—R. C. Cornes, R. Junod, and E. C. Kent

The global annual average night marine air temperature (NMAT) for 2024 was 0.44°C above the 1991–2020 baseline in the University of Alabama in Huntsville Night Marine Air Temperature (UAHNMAT; Junod and Christy 2020) dataset and 0.54°C in the Climate Linked Atlantic Sector Science Night Marine Air Temperature (CLASSnmat; Cornes et al. 2020) dataset. These values represent the highest in the record dating to 1900 and are 0.04°C higher than those of 2023 in both datasets.

Between 1900 and 2024, annual global average NMAT increased at a rate of 0.07°C decade^{-1} in UAHNMAT and 0.08°C decade^{-1} in CLASSnmat. As noted in previous *State of the Climate* reports (e.g., Cornes et al. 2023), sea surface temperatures (SSTs) have been increasing faster than NMAT for reasons that are not fully understood. For example, over the same 1900–2024 period, global annual averages in the Hadley Centre Sea Surface Temperature Dataset version 4 (HadSST4; Kennedy et al. 2019) increased at a rate of 0.09°C decade^{-1}. As a result, SST anomalies have consistently been higher than NMAT anomalies over the past decade (Fig. 2.5). The differences between SST and NMAT for individual years over that period have generally not been statistically significant due to the size

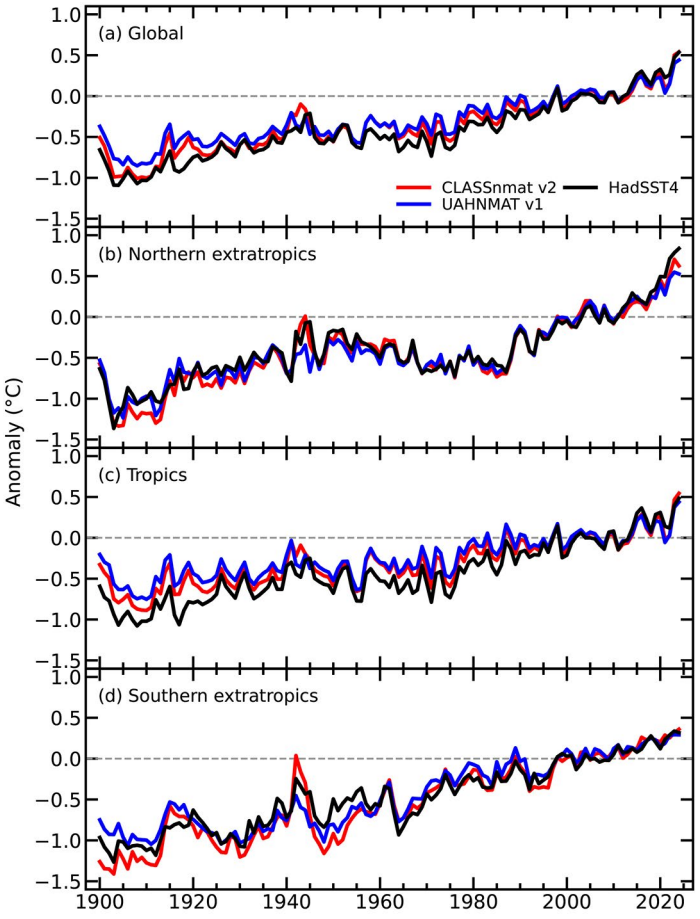

Fig. 2.5. Annual average night marine air temperature anomalies (°C; 1991–2020 base period) calculated from the Climate Linked Atlantic Sector Science Night Marine Air Temperature (CLASSnmat), University of Alabama in Huntsville Night Marine Air Temperature (UAHNMAT), and Hadley Centre Sea Surface Temperature Dataset version 4 (HadSST4) datasets averaged over the (a) globe, (b) northern extratropics, (c) tropics, and (d) southern extratropics. The tropics is defined as the latitude range 30°S–30°N and the northern (southern) extratropics as >30°N (<30°S). The averages only include values that are common to all three datasets for a given year; since UAHNMAT starts in 1900, only values for the period 1900–2024 are plotted.

Unauthenticated | Downloaded 11/21/25 11:34 AM UTC

of uncertainty estimates in the datasets (with 2-σ uncertainty around 0.1°C), although the large differences seen in 2021/22 have not been observed over the last two years.

Record temperatures were observed across the tropics in 2024, with anomalies of +0.54°C in CLASSnmat and +0.44°C in UAHNMAT. In the northern extratropics, however, NMAT values in 2024 were slightly lower than in 2023 (c.f. +0.71 in 2023 and +0.63°C in 2024 in CLASSnmat and +0.55 versus +0.53°C in UAHNMAT), making 2024 the second-warmest year in the record. In contrast, HadSST4 recorded 2024 as the warmest year in the northern extratropics, with an anomaly of +0.84°C. To prevent unequal spatial sampling affecting these results, all three datasets have been masked to ensure common coverage.

Regional differences in NMAT anomalies are further illustrated in Plate 2.1c. Temperature anomalies above +0.5°C were widespread across the globe in 2024, with especially large anomalies of up to +1.5°C relative to the 1991–2020 baseline observed across certain areas and notably across the northwestern Pacific. Negative temperature anomalies were present in the southeastern Pacific—and to a lesser extent, the northeastern Pacific—linked to the weakening El Niño conditions throughout 2024 and the switch to La Nina-like conditions at the end of the year (see section 4b for details). This change is reflected in the global monthly averages for NMAT and SST (Fig. 2.6). Starting in June 2023, exceptional temperature anomalies were recorded in these data (Cornes and Junod 2024) and continued into early 2024, with the highest anomalies peaking in January. While temperature anomalies slightly reduced in the second half of 2024 compared to 2023, they remained notably higher than previous years, with anomalies still 0.4°C above 1991–2020 levels.

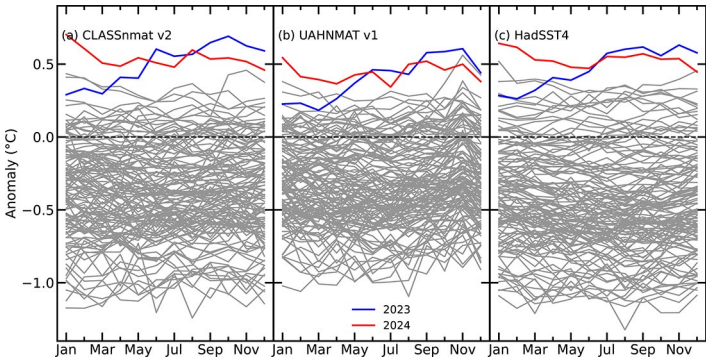

Fig. 2.6. Global monthly average night marine air temperature anomalies (°C; 1991–2020 base period) in the (a) Climate Linked Atlantic Sector Science Night Marine Air Temperature (CLASSnmat), (b) University of Alabama in Huntsville Night Marine Air Temperature (UAHNMAT), and (c) Hadley Centre Sea Surface Temperature Dataset version 4 (HadSST4) datasets. Each line represents a year of data, and the results for 2023 and 2024 are shown in blue and red, respectively.

The causes of these anomalously high temperatures in 2023 and 2024 have been variously discussed in the literature (see also section 2b1). Cattiaux et al. (2024) suggest that a combination of long-term anthropogenic warming and a significant peak in internal variability accounts for the observed conditions. Gettelman et al. (2024) propose that the anomalies in 2022/23 are due to an increase in net radiative forcing, driven by mandated reductions in ship-based sulfur emissions that came into effect in 2020. Further analysis is needed to understand the relative contributions of these factors to NMAT versus SST. However, based on the results presented here, no distinct difference is observed between NMAT and SST in terms of large-scale averages over the past two years. The fact that global and tropical average anomalies from CLASSnmat are now comparable to those from HadSST4 for the first time in 10 years may suggest an external forcing mechanism. However, the differences between UAHNMAT and CLASSnmat—despite using essentially the same input data, but undergoing different quality control and bias adjustment processes—are of the same magnitude as the differences between SST and NMAT. This suggests that structural uncertainties in dataset preparation may obscure any potential external forcing mechanisms.

4. SURFACE TEMPERATURE EXTREMES

—R. J. H. Dunn, M. G. Donat, S. Kirkpatrick, and M. G. Bosilovich

Ongoing record-breaking average global surface temperatures in 2024 (section 2b1) again was accompanied by further record-high numbers of warm days (TX90p; Table 2.2) and record-low numbers of cool nights (TN10p; Table 2.2) across all datasets assessed herein.

The globally averaged number of warm days indicated by the Global Historical Climatology Network Daily Extremes (GHCNDEX) dataset of gridded in situ observations (Donat et al. 2013) was 75±7 days, four days more than the value for 2023 (Fig. 2.7a; Table 2.2). At the other end of

Unauthenticated | Downloaded 11/21/25 11:34 AM UTC

the scale, there were only 13±8 cool nights, the lowest in this dataset (starting 1951; Fig. 2.7b) and substantially less than half the expected number (36.5 days by definition). As outlined in previous reports (e.g., Dunn et al. 2024a), GHCNDEX has severely limited spatial coverage for recent years (Appendix Fig. A2.5); thus three reanalysis products (ERA5, Hersbach et al. 2020, Bell et al. 2021, Soci et al. 2024; JRA-3Q, Kosada et al. 2024; MERRA-2, Gelaro et al. 2017) were used to give a globally complete (including Antarctica) assessment of the land surface extreme temperatures following Dunn et al. (2022b). As shown in Fig. 2.7c and Table 2.2, all these products show record-high and record-low values in 2024 for the number of warm days and cool nights, respectively, in the global average over land. The large differences between the GHCNDEX values in Table 2.2 and those from ERA5 and JRA-3Q using a 1961–90 reference period are likely due to the low spatial coverage of GHCNDEX (Appendix Fig. A2.5).

Especially high numbers of warm days were experienced across almost all of Africa and Central and South America as well as in northeastern Canada, eastern and southern Europe, and parts of the Middle East, China, and Southeast Asia. Some of these areas experienced twice as many warm days as would be expected on average within a year during the baseline period (Plate 2.1d). During 2024, many of these areas had the regionally highest number of warm days on record (Fig. 2.8a), often associated also with the highest absolute temperatures, particularly in parts of Central and South America and Africa (Fig. 2.8e). Moreover, areas in South America broke records in numbers of warm days (TX90p), which were only set last year (Fig. 2.8 in Dunn et al. 2024a).

Figure 2.8b shows the time series from calculating the land fraction setting record-high numbers of warm days sequentially in each year, i.e., the land area fraction in Fig. 2.8a categorized as “highest” but working through each year in turn to determine the area setting new records of TX90p per year. The first year will by default set a record value across the entire globe, but in a stable climate, records should become rarer over time. Therefore, the values from the first 20 years of each reanalysis are not shown. JRA-3Q has the largest land area experiencing record numbers of warm days in 2024, but a lower fraction than ERA5 which, along with MERRA-2, has the second largest (ERA5 has most in 2010 and MERRA-2 in 2002). For TN10p, in 2024 MERRA-2 has the largest area with new record-fewest numbers of cool nights, with JRA-3Q and ERA5 tied for second in 1998. The fraction of land with the highest annual maximum temperature (TXx; Fig. 2.8f; Table 2.2) is greatest in MERRA-2 and a close second to 1983 in JRA-3Q.

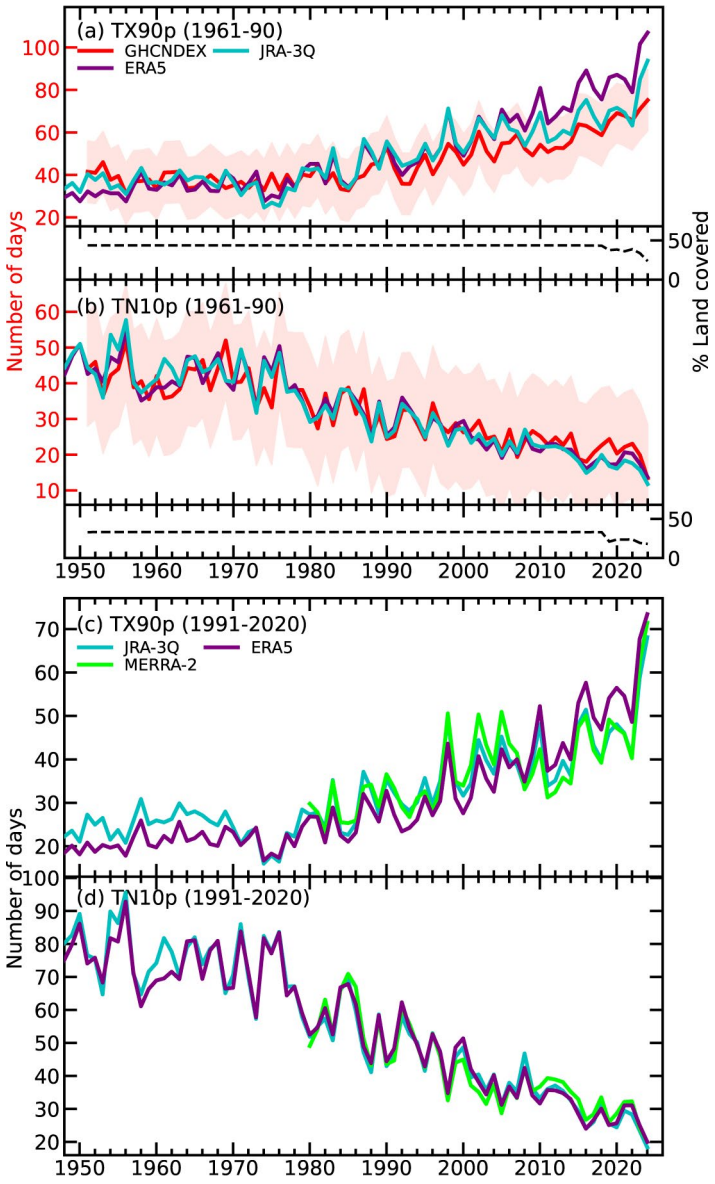

Fig. 2.7. (a),(b) Time series of the (a) annual number of warm days (TX90p) and (b) cool nights (TN10p) averaged over global land regions based on gridded station data from Global Historical Climatology Network Daily Extremes dataset (GHCNDEX), ERA5, and the Japanese Reanalysis for Three Quarters of a Century (JRA-3Q) reanalyses using 1961–90 as the reference period. The spatial coverage in GHCNDEX is limited; the black dashed lines show the percentage of land area covered (right y-axis). The 2-σ coverage uncertainty (following Brohan et al. 2006; Dunn et al. 2020) is shown by the light red bands in (a),(b). (c),(d) As in (a),(b), for three atmospheric reanalyses (ERA5, MERRA-2, and JRA-3Q) using 1991–2020 as the reference period.

Unauthenticated | Downloaded 11/21/25 11:34 AM UTC

Lower-than-expected numbers (36.5) of cool nights (TN10p) were found almost globally, with only parts of the Amazon basin and central-southern Africa experiencing higher-than-expected numbers (Plate 2.1e). This index is zero bounded (there cannot be fewer than zero cool nights, an anomaly of –36.5 days), in contrast to TX90p, which is bounded to zero for cold anomalies but asymmetrically bounded to 100% of days (i.e., 365 per year) for warm anomalies; with our choice of reference period in the current climate, we are far from this upper bound. Therefore, the magnitude of the anomalies in TN10p appear smaller as this index asymptotically reduces to zero as the temperature distribution moves farther from the 10% threshold (Dunn and Morice 2022).

Regionally, the record-lowest numbers of cool nights (TN10p) were found across much of tropical and northern Africa, Southeast Asia, eastern Europe, and northern South America (Fig. 2.8c), and the global area with record-low values is largest (in MERRA-2) or second largest (in ERA5 and JRA-3Q, both record in 1998) within the periods of the respective datasets (Fig. 2.8d).

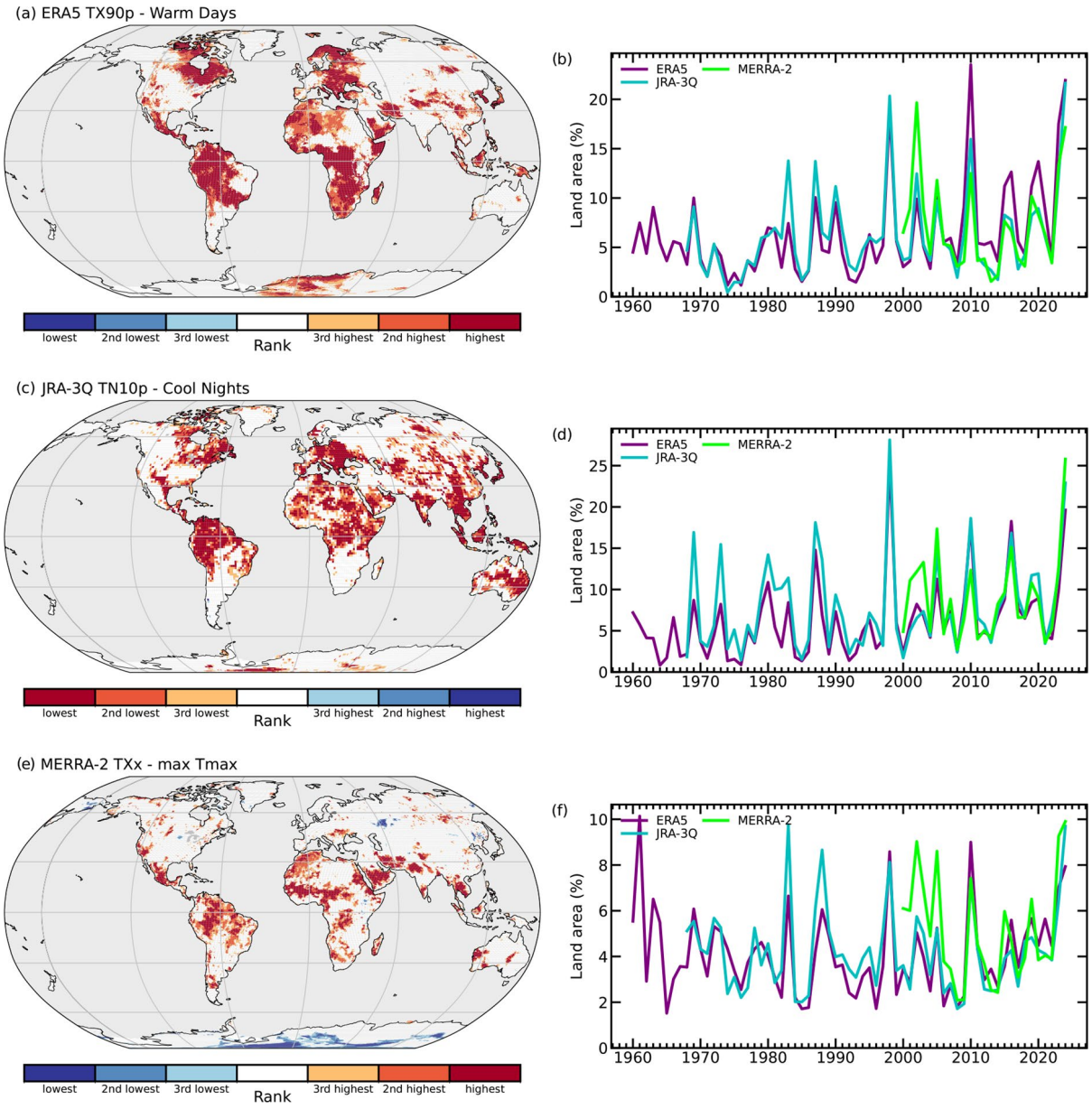

Fig. 2.8. Maps indicating grid cells where (a) the warm day index (TX90p) from ERA5 (since 1940), (c) the cool night index (TN10p) from the Japanese Reanalysis for Three Quarters of a Century (JRA-3Q; since 1948), and (e) the annual maximum temperature (TXx) from MERRA-2 (since 1980) for 2024 ranked in the three highest (orange to red) or three lowest (blue) values. Time series of the percent of land area ranked as the highest value for (b) TX90p, (d) TN10p, and (f) TXx sequentially in each year for ERA5 (from 1960), JRA-3Q (from 1968), and MERRA-2 (from 2000). The ranks from the first 20 years of each reanalysis are not calculated.

Unauthenticated | Downloaded 11/21/25 11:34 AM UTC

A number of indices have been recommended by the World Meteorological Organization to characterize temperature and precipitation extremes (Zhang et al. 2011; Dunn et al. 2024b), of which we present three here (Table 2.2). Dunn et al. (2022b) show there is good agreement between the observation-based and reanalysis products, especially for the two percentile-based indices used in this section. See Donat et al. (2013) and Dunn et al. (2022b) for details of indices from the observation-based and reanalyses datasets, respectively.

The indices shown here use fixed reference periods, and an intercomparison between these is not trivial (Dunn et al. 2020; Yosef et al. 2021; Dunn and Morice 2022); we show versions using both 1961–90 (for GHCNDEX, ERA5, and JRA-3Q) and 1991–2020 (for ERA5, MERRA-2, and JRA-3Q).

Table 2.2. Definitions of indices used for land surface temperature extremes, their globally averaged values (days) for 2024, and ranks from the four datasets. Coverage uncertainties are shown for GHCNDEX.

Index	Name	Definition	GHCNDEX (1951–2024) Value, [rank] Ref. Period 1961–90	ERA5 (1940–2024) Value, [rank] Ref. Period 1961–90	JRA-3Q (1948–2024) Value, [rank] Ref. Period 1961–90	ERA5 (1940–2024) Value, [rank] Ref. Period 1991–2020	JRA-3Q (1948–2024) Value, [rank] Ref. Period 1991–2020	MERRA-2 (1980–2024) Value, [rank] Ref. Period 1991–2020
TX90p	Warm days	Annual count of days when the daily maximum temperature exceeds the 90th percentile	75±7 [highest]	107 [highest]	94 [highest]	73 [highest]	68 [highest]	72 [highest]
TN10p	Cool nights	Annual count of nights when the daily minimum temperature falls below the 10th percentile	13±8 [lowest]	13 [lowest]	12 [lowest]	20 [lowest]	18 [lowest]	20 [lowest]
TXx	Warmest T-max	Annual maximum of the maximum temperature	36.5±0.3 [highest]	-	-	31.1 [highest]	30.6 [highest]	31.7 [highest]

Unauthenticated | Downloaded 11/21/25 11:34 AM UTC

Sidebar 2.1: **Super extreme land surface temperature hotspots**

—E. GOOD, J. BLANNIN, A. WARING, K. VEAL, AND D. GHENT

It is well documented that as Earth's climate warms, the frequency of extreme heat events is increasing (IPCC 2021; Dunn 2024a; Willett 2023b). Evidence suggests that the fraction of land becoming uninhabitable due to extreme heat will also increase with global warming (Matthews et al. 2025). Surface temperatures are traditionally monitored using data from weather stations measuring near-surface air temperature at ~1.5m–2m above the surface (T2m). However, station density and location limit spatial coverage and, therefore, knowledge of how extreme temperature frequency and intensity are evolving in many regions of the world (section 2b4; Dunn et al. 2024).

An alternative, independent source of information can be obtained from satellite observations of land surface temperature (LST) derived from sensors operating in the infrared (IR) and microwave regions of the electromagnetic spectrum. An advantage of using LST from satellites over ground-based T2m is in the global provision of data. However, a disadvantage is that the LST cannot be measured directly, as it relies on modeling of the impact of the atmosphere between the satellite and the surface to estimate it; furthermore, in the case of IR LSTs, only cloud-free observations are available. Additionally, although strongly correlated, LST and T2m are different variables. Over bare surfaces, LST represents how hot Earth's surface is to the touch, whereas over dense vegetation, it more closely represents the canopy surface temperature. Therefore, simultaneous LST–T2m differences often reach several °C and may exceed 20°C in some conditions (Good 2016). However, studies have shown that the long-term signal of change observed in LST and T2m datasets is similar

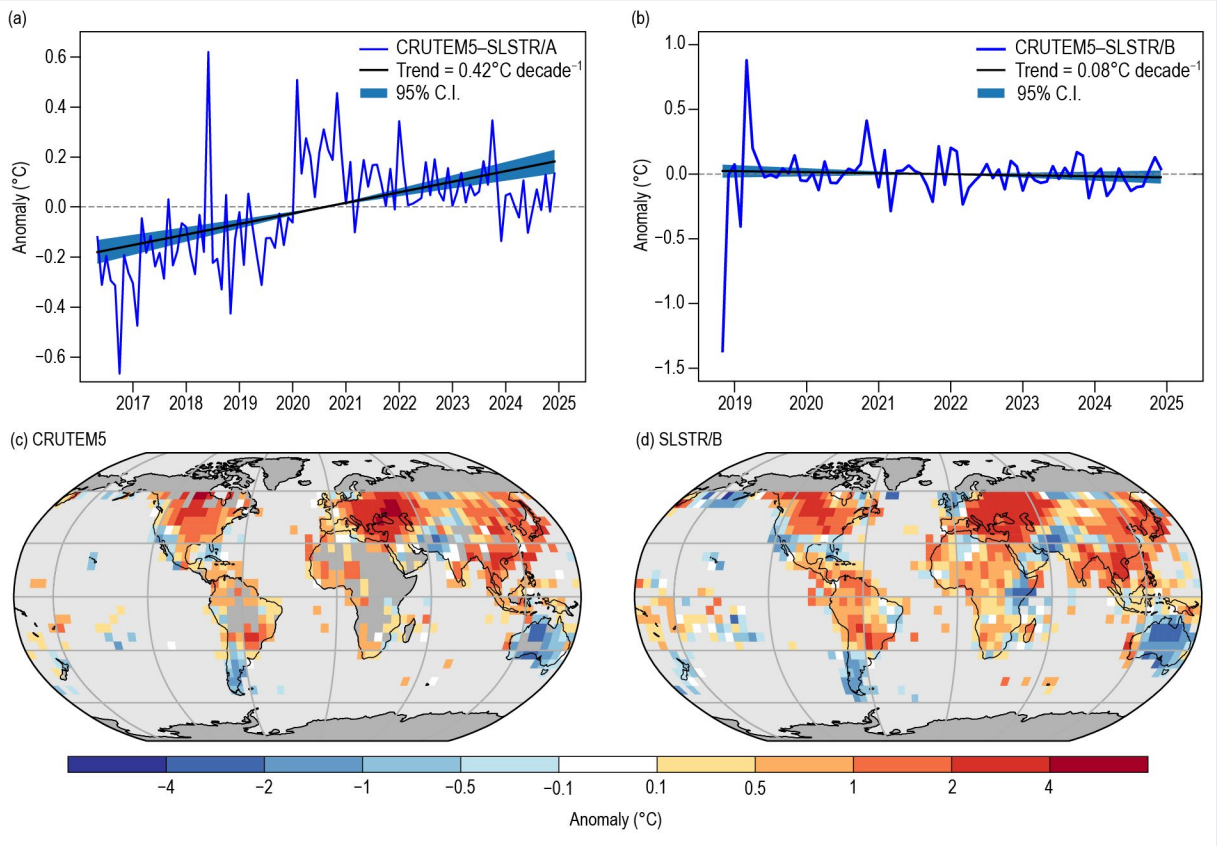

Fig. SB2.1. Time series for spatially matched 5° latitude–longitude data between ±60° latitude for (a) Sea and Land Surface Temperature Radiometer onboard the Sentinel-3A platform (SLSTR/A) land surface temperature (LST)-Climatic Research Unit temperature version 5 (CRUTEM5) anomalies of near-surface air temperature at ~1.5m–2m above the surface (T2m; reference baseline period is May 2016 to Dec 2024; the CRUTEM5 anomalies have been adjusted from the 1961–90 baseline period following Good et al. [2017]) and (b) Sea and Land Surface Temperature Radiometer onboard the Sentinel-3B platform (SLSTR/B) LST-CRUTEM5 T2m anomalies (baseline period Nov 2018 to Dec 2024). Trends have been calculated using the Theil-Sen/median of pairwise slopes method (Sen 1968). The Mar 2019 outlier in the SLSTR/B time series is due to 19 days of missing SLSTR/B data. The Nov 2018 outlier is outside the super extreme hotspot analysis period. Example 5° latitude–longitude anomaly maps for April 2024 for (c) SLSTR/B LST and (d) CRUTEM5 are also shown. All units are °C.

Unauthenticated | Downloaded 11/21/25 11:34 AM UTC

(Good et al. 2017, 2022). The objective of this analysis is to demonstrate how LST may be used to map and monitor super extreme hotspots (SEHs)—where Earth may already be, or is becoming, uninhabitable under climate change. Using LST is advantageous as many of these SEHs occur in regions with few T2m observations.

The data used are from the Sea and Land Surface Temperature Radiometer onboard the Sentinel-3B platform (SLSTR/B), which has been in polar orbit since April 2018. LST data for November 2018 to December 2024 have been obtained from the European Space Agency (ESA) Climate Change Initiative for LST (LST_cci; https://climate.esa.int/en/projects/land-surface-temperature/; version 4.00) and, for recent months in 2024, from the U.K. Earth Observation Climate Information Service (https://eocis.org/). The data from both sources are consistent and have been processed using the same approach (Ghent et al. 2024). The SLSTR/B instrument images Earth at ~1-km spatial resolution, providing a near-global view each day. However, as the SLSTR/B operates in the IR, only cloud-free LSTs are available. This dataset was selected as it is the only climate-quality LST dataset currently available for 2024. The widely-used LSTs from the Moderate Resolution Imaging Spectroradiometer (MODIS) sensors (2000–present) cannot be used, as these data are temporally unstable from around 2021 due to a changing observation time (https://modis-land.gsfc.nasa.gov/news.html). Similarly, data from the SLSTR onboard Sentinel-3A (SLSTR/A: 2016–24) cannot be used, as this dataset is unstable due to a variation in the processing by the ESA of the raw satellite data time series. Establishing temporal stability of LST datasets is crucial due to its often strong diurnal variation (Good 2016); a changing overpass time or any other non-climatic discontinuity in the dataset can have a critical effect on time series analysis.

Following the approach used by Good et al. (2017, 2022), the stability of SLSTR/A and /B between ±60° latitude is assessed using Climatic Research Unit temperature version 5 (CRUTEM5; Osborn et al. 2021). CRUTEM5 is a monthly 5° latitude–longitude T2m dataset based on homogenized global station data and provides a stable reference for assessing LST stability. There is a statistically significant slope in the mean daily SLSTR/A-minus-CRUTEM5 anomaly time series (Fig. SB2.1a, 0.42°C decade^{-1}; 95% confidence interval [CI] 0.31°C decade^{-1} to 0.54°C decade^{-1}) as well as a non-climatic discontinuity. By contrast, the SLSTR/B dataset (Fig. SB2.1b) appears stable (–0.08°C decade^{-1}; 95% CI –0.24°C decade^{-1} to 0.09°C decade^{-1}) and the monthly SLSTR/B and CRUTEM5 anomalies are similar and well correlated (Pearson correlation coefficient r = 0.81). Also shown in Figs. SB2.1c,d are examples of the SLSTR/B and CRUTEM5 anomaly maps for April 2024. The spatial pattern of the anomalies shows a high degree of spatial consistency (r = 0.84), confirming the overall similarity between the clear-sky LST and all-sky T2m signals and the more complete spatial coverage of the LST data.

With the stability of the SLSTR/B LSTs assured, the occurrence and temporal evolution of SEHs can be characterized. For context, Fig. SB2.2 shows the maximum SLSTR/B LST observed during 2024. The hottest regions occur in western North America, North Africa, the Arabian Peninsula, parts of South and Central Asia, and Australia, where LSTs of >60°C can occur. Using only full-year daytime data between 2019 and 2024, thresholds of 50°C and 55°C are used to identify SEHs; for context, 55°C is above the 99th percentile for the 2019–24 SLSTR-B data (53.2°C), thus these are globally extreme LSTs. Fig. SB2.3a shows the locations of SEHs in 2024; together with exceedances of other LST thresholds, SEHs are prevalent in the Arabian peninsula, Iran (Lut desert), across central Asia, parts of North Africa, western North America, and Australia, which is generally consistent with Mildrexler et al. (2006) and Zhao et al. (2021), who used MODIS to map global LST hotspots. Figure SB2.3b shows the annual time series of the number of SEH locations. Figure SB2.3c shows the fraction of valid observations across all grid cells exceeding each threshold, essentially representing the accumulated global frequency of SEHs each year. Both time series have small negative trends, although the p values indicate these are statistically insignificant. This is not surprising given the relatively short six-year period of data compared to the 30+ year record often used for climate applications. For all SEH metrics, 2019 is ranked as the most extreme year, followed by 2023, while

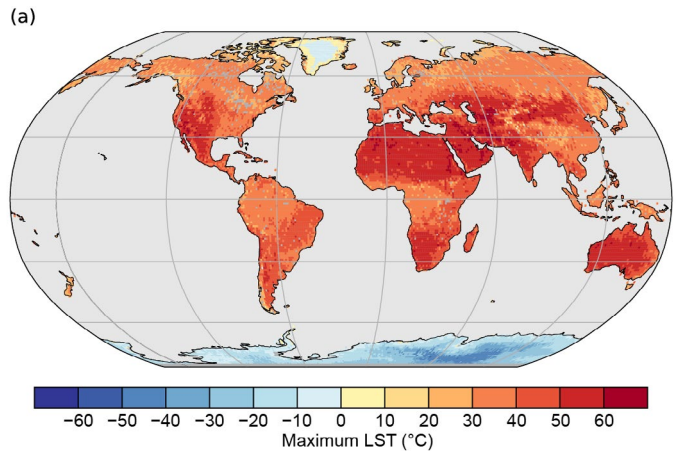

Fig. SB2.2. Maximum land surface temperature (LST; °C) observed during 2024 by the Sea and Land Surface Temperature Radiometer onboard the Sentinel-3B platform (SLSTR/B) at 0.1° latitude–longitude. The percentiles from the 2024 distribution of maximum LSTs at the native 0.01° spatial resolution are: 50.5°C (95th), 57.7°C (99th), and 62.3°C (99.9th). The hottest LSTs above ~62°C often occur in isolated grid cells and are associated with lava flows or wildfires.

Unauthenticated | Downloaded 11/21/25 11:34 AM UTC

2024 is third for both 50°C metrics and fourth for both 55°C metrics (i.e., both for the number of locations and total fraction per year). With a longer stable LST time series, this analysis demonstrates how LST could be used to monitor global heat extremes and the occurrence of SEHs, which may not be observable using T2m data.

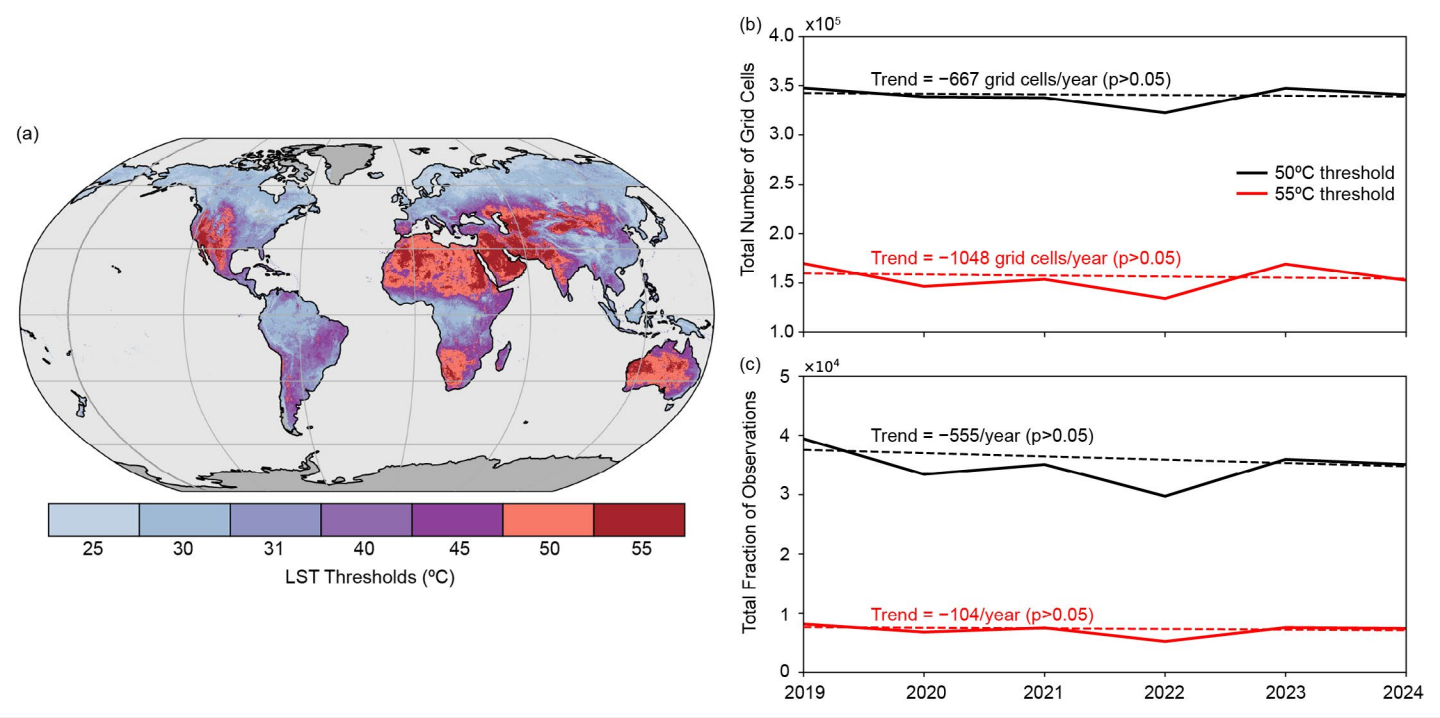

Fig. SB2.3. (a) Map showing where two or more valid Sea and Land Surface Temperature Radiometer onboard the Sentinel-3B platform (SLSTR/B) land surface temperature (LST) observations in 2024 exceed selected LST thresholds (25°C, 30°C, 35°C, 40°C, 45°C, 50°C, and 55°C); the SLSTR/B data have been resampled to 0.1° latitude–longitude. The time series of the number of (b) 0.1° grid cells for each year that exceed the 50°C (black) and 55°C (red) thresholds and (c) sum of the annual fraction of valid observations in each year that exceed these thresholds across all grid cells. The linear trends and p values are shown for information.

Unauthenticated | Downloaded 11/21/25 11:34 AM UTC

5. TROPOSPHERIC TEMPERATURE

—S. Po-Chedley, J. R. Christy, C.-Z. Zou, C. Mears, and L. Haimberger

Record-high global lower tropospheric temperature (LTT) values in the second half of 2023 persisted through boreal summer in 2024 (Fig. 2.9), producing a 2024 global-mean LTT that was 0.84°C (0.77°C–0.92°C depending on dataset) above the 1991–2020 climatological mean (Fig. 2.10). All nine tropospheric temperature datasets considered here (Table 2.3) ranked 2024 as the warmest year for global LTT, making 2023 the second-warmest year in most datasets.

Some of the recent tropospheric warmth is attributable to the strong El Niño event that peaked in the boreal winter of 2023/24. During El Niño events, tropical and global tropospheric temperatures lag behind warm central and eastern Pacific sea surface temperatures by three to five months, which helps to explain the exceptional warmth in the first half of 2024 (Fig. 2.10). Although the ENSO relaxed to neutral conditions by April–June and approached La Niña conditions by the end of the year (see section 4b for details), global LTT remained close to the record-breaking warmth in the final months of 2024 (Fig. 2.9). Most of the tropics and roughly half of Earth overall experienced record-warm LTT conditions in 2024 (Plate 2.1f).

Although the warmth seen over 2023/24 was above normal, it is consistent with long-term, greenhouse gas-driven warming that is evident in both global LTT and tropical tropospheric temperatures (TTTs) across a variety of tropospheric temperature datasets (Table 2.3); this is the fourth time in the last 10 years that record-warm global tropospheric temperatures have been reported in the *State of the Climate* (Po-Chedley et al. 2024, 2021; Christy 2017). Tropospheric temperature time series are derived from sparse weather balloon-based radiosonde records that measure temperatures as a function of height, satellite-borne microwave measurements that provide near-global observations over broad atmospheric layers, and reanalysis models that ingest and combine many observations to produce horizontally and vertically resolved estimates and forecasts of numerous

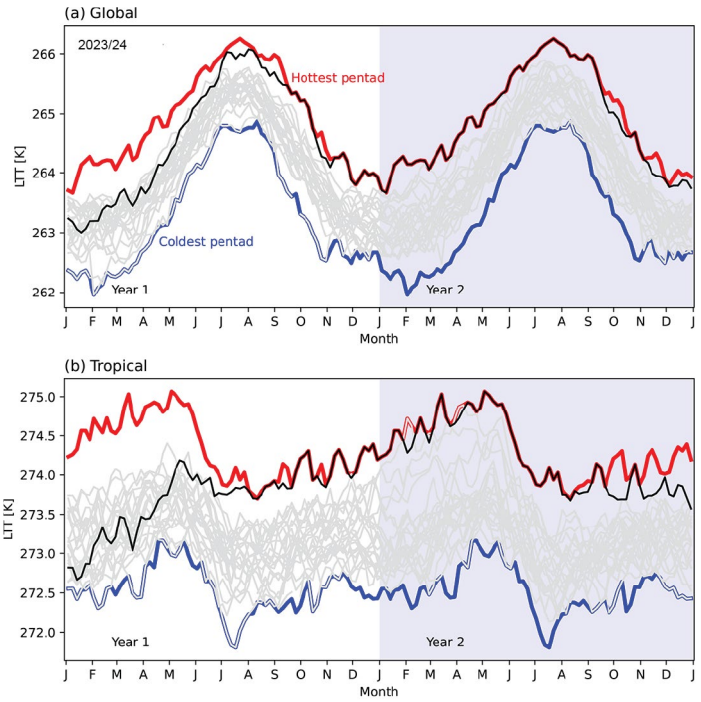

Fig. 2.9. (a) Global and (b) tropical (20°S–20°N) lower-tropospheric temperature (LTT) pentad averages over two-year segments (gray lines) from the University of Alabama in Huntsville (UAH) dataset. Each year is shown only once: odd (even) years are on the left (right) side of the figure. The most recent segment (2023/24) is shown in black and the hottest and coldest pentad values (of all years) are shown in red and blue, respectively.

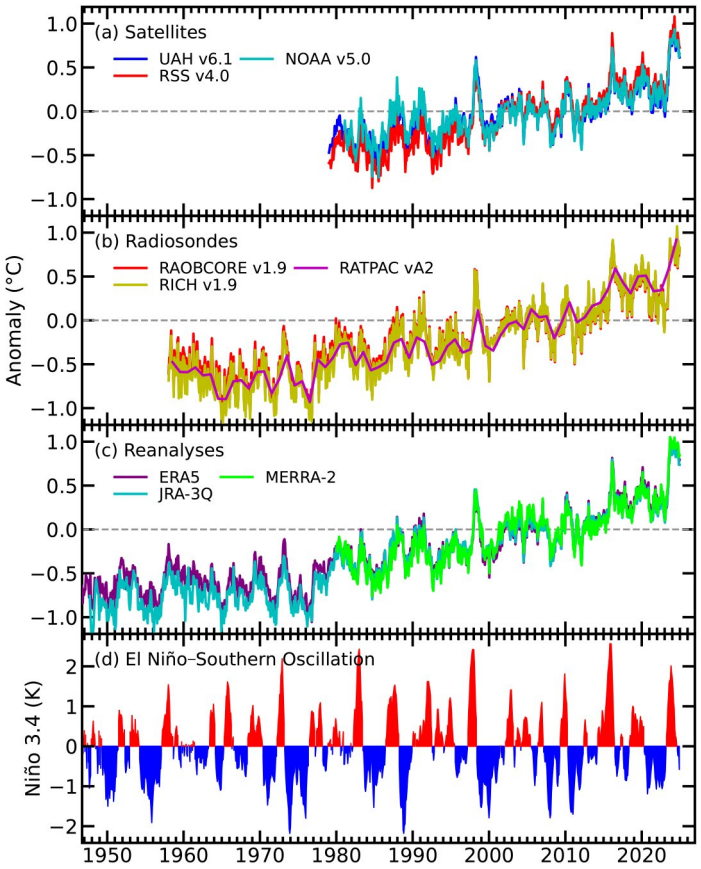

Fig. 2.10. Monthly average global lower-tropospheric temperature (LTT) anomalies for (a) satellite, (b) radiosonde, and (c) reanalysis datasets. In panel (d), red (blue) denotes positive (negative) values in the Niño-3.4 index. Annual averages are displayed for the Radiosonde Atmospheric Temperature Products for Assessing Climate (RATPAC)-A dataset. Anomalies are with respect to a 1991–2020 base period.

Unauthenticated | Downloaded 11/21/25 11:34 AM UTC

geophysical variables, including atmospheric temperature. In this report, the vertically resolved atmospheric temperature data from radiosondes and reanalyses are converted into a satellite-equivalent LTT time series, which represents the average temperature over a layer from the surface to ~10 km, and a TTT time series, which spans the surface to the tropical tropopause. Despite diversity in measurement methods and calibration procedures, all of the datasets exhibit similar variability and long-term trends (Fig. 2.10; Table 2.3).

The annual-mean tropospheric temperature was above the 1991–2020 climatological mean over more than 90% of Earth's surface (Plate 2.1f). Record-setting values covered about half of Earth's surface, including the deep tropics (20°S–20°N), Europe, eastern Canada, East Asia, and parts of the Southern Ocean. Below-average tropospheric temperatures were observed over less than 5% of Earth's surface (Plate 2.1f).

The recent surge in global temperatures in the past two years deserves continued scrutiny. While the contributions of internal variability and greenhouse gas-driven warming are key components of the record LTT values over 2023 and 2024, other factors including the solar cycle, reductions in ship-based aerosol emissions, and multi-year trends in planetary albedo have also likely played a role (e.g., Raghuraman et al. 2024; Goessling et al. 2025; Gettelman et al. 2024). The evolution of the global climate beyond 2024 will be of significant scientific interest as we strive to better understand the factors that contributed to the recent exceptional tropospheric warmth.

Table 2.3. Temperature trends (°C decade^{-1}) for global lower-tropospheric temperature (LTT) and tropical (20°S–20°N) tropospheric temperature (TTT) over the periods 1958–2024 and 1979–2024. NASA MERRA-2 data begin in 1980 and NOAA v5.0 LTT begins in 1981. Cells marked with a dash signify that the data do not extend back to 1958.

Method	Dataset	LTT (90°S–90°N) 1958	LTT (90°S–90°N) 1979	TTT (20°S–20°N) 1958	TTT (20°S–20°N) 1979
Radiosonde	NOAA RATPAC vA2 (Free et al. 2005)	0.19	0.24	0.18	0.20
Radiosonde	RAOBCORE v1.9 (Haimberger et al. 2012)	0.17	0.19	0.15	0.17
Radiosonde	RICH v1.9 (Haimberger et al. 2012)	0.19	0.21	0.19	0.21
Satellite	UAH v6.1 (Spencer et al. 2017)	-	0.15[1]	-	0.15
Satellite	RSS v4.0 (Mears and Wentz, 2016)	-	0.23	-	0.19
Satellite	NOAA v5.0 (Zou et al. 2023)	-	0.15[1]	-	0.13
Reanalysis	ERA5 (Hersbach et al. 2020)	0.17	0.20	0.17	0.19
Reanalysis	JRA-3Q (Kosaka et al. 2024)	0.19	0.20	0.19	0.18
Reanalysis	NASA MERRA-2 (Gelaro et al. 2017)	-	0.21	-	0.21
Median	N/A	0.19	0.20	0.18	0.19

[1] The vertical sampling in UAH and NOAA LTT is slightly different from other datasets and results in temperature trends that are approximately 0.01°C decade^{-1} smaller than in other datasets.

Unauthenticated | Downloaded 11/21/25 11:34 AM UTC

6. STRATOSPHERIC TEMPERATURE

—W. J. Randel, C. Covey, L. Polvani, and A. K. Steiner

Global-mean temperatures in the lower, middle, and upper stratosphere increased slightly during 2024, mainly reflecting a recovery from anomalous cooling due to the Hunga volcanic eruption in early 2022. The long-term trends during the satellite era of 1979–2024, however, show multi-decadal cooling of the stratosphere due to ozone depletion in the first two decades as well as anthropogenic CO_2 increases over the whole period. The Arctic stratospheric polar vortex was disturbed by two major stratospheric warming events during early 2024, while the Antarctic polar vortex was strong and persistent during the year. The stratospheric quasi-biennial oscillation (QBO) progressed normally in 2024, with equatorial westerly zonal wind shears and positive temperature anomalies descending from the middle to lower stratosphere during the year.

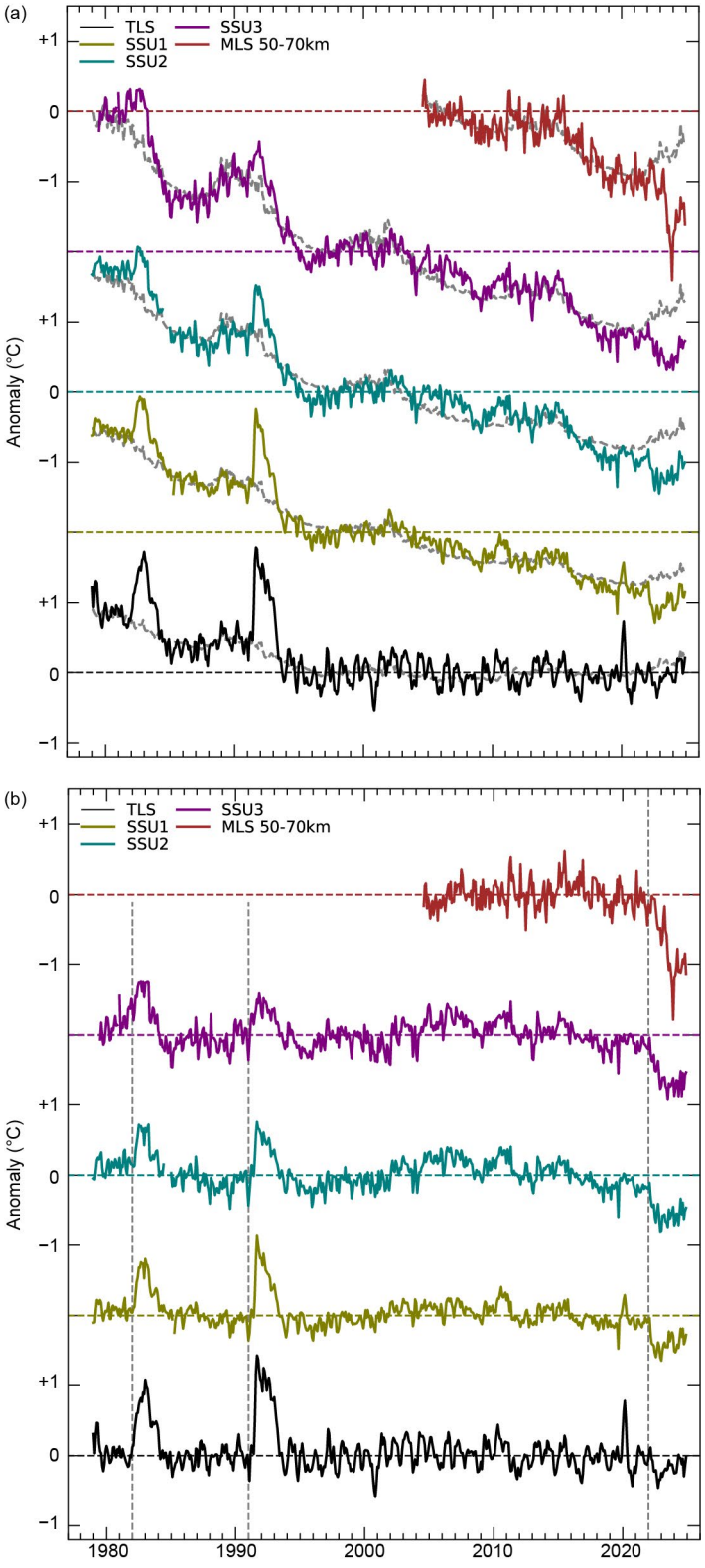

Global stratospheric temperatures have been monitored from satellite observations for over 40 years, and Fig. 2.11a shows time series of global monthly temperature anomalies spanning the lower to upper stratosphere and mesosphere from merged satellite data. In addition to long-term stratospheric cooling (due to CO_2 increases and stratospheric ozone changes), transient variations arise from the 11-year solar cycle and effects of large volcanic eruptions: El Chichón (1982), Pinatubo (1991), and Hunga (2022). Transient warming of the lower stratosphere is also evident following the Australian wildfires in early 2020 (Yu et al. 2021; Stocker et al. 2021). Effects of the volcanic eruptions and wildfires are more easily seen in Fig. 2.11b, which shows global temperature anomalies after removing the decadal-scale trends and solar cycle effects. The time series show anomalous cooling of the middle to upper stratosphere by 0.5°C–1.0°C in 2022/23, caused by radiative impacts of the unusually large quantities of water vapor (H_2O) injected directly to the stratosphere by the January 2022 Hunga volcanic eruption (Millan et al. 2022; Stocker et al. 2024; Randel et al. 2024).

Fig. 2.11. (a) Time series of monthly global average temperature anomalies (°C) for thick-layer averages spanning the lower to upper stratosphere and mesosphere (bottom to top). Middle and upper stratosphere data are from the Stratospheric Sounding Unit (SSU) updated with Microwave Limb Sounder (MLS) measurements, representing thick-layer averages centered near 30 km, 38 km, and 45 km (SSU1, SSU2 and SSU3, respectively). Lower-stratosphere temperatures (TLS) are ~13 km–22 km layer averages from satellite microwave measurements. These datasets are discussed in Steiner et al (2020). Mesosphere temperatures are 50-km–70-km averages from MLS data. (b) Global average temperature anomalies (°C) for each level, derived by subtracting linear trend and solar cycle fits to the time series in (a). These fits for each level are shown as dashed lines in panel (a). The vertical lines in (b) denote the El Chichón (1982), Pinatubo (1991), and Hunga (2022) volcanic eruptions. Figure updated from Randel et al (2024).

Unauthenticated | Downloaded 11/21/25 11:34 AM UTC

The Hunga water vapor anomalies have been diffusing globally and decreasing over time (e.g., Zhou et al. 2024), resulting in smaller stratospheric radiative impacts and a partial recovery from the anomalous cooling during 2024. The 11-year solar cycle was also near a maximum during 2024 (https://www.swpc.noaa.gov/products/solar-cycle-progression), contributing to slightly higher temperatures in the middle and upper stratosphere.

We note that the observed Hunga cooling over 2022–24 in the middle stratosphere is comparable in magnitude, but opposite in sign, to warm anomalies tied to the El Chichón (1982) and Pinatubo (1991) volcanic eruptions. The difference in sign is due to the stratospheric cooling effects of large water vapor anomalies from Hunga, whereas the El Chichón and Pinatubo warmings arise from sulfate aerosol-dominated warming effects. While the magnitude of the cooling anomalies due to Hunga increases with altitude, the magnitude of warming anomalies due to El Chichón and Pinatubo decreases with altitude. In the mesosphere, the Hunga cooling is a result of H_2O-induced ozone depletion (Randel et al. 2024).

Variations in polar vortex temperatures contribute little to global temperature anomalies but provide context for regional variability. Time series of Arctic and Antarctic polar vortex temperatures in 2024 are shown in Fig. 2.12, highlighting strong variability in the Arctic, with two separate stratospheric warming events in early 2024 (Lee et al. 2025). These events were caused by enhanced planetary wave forcing from the troposphere; the occurrence of two major warming events in the same year is unusual but has been observed several times in the past and has little to do with long-term climate change. In contrast, the Antarctic polar vortex shows a larger annual cycle with relatively little variability, although a series of weak wave-induced warming events were observed during austral mid-winter 2024.

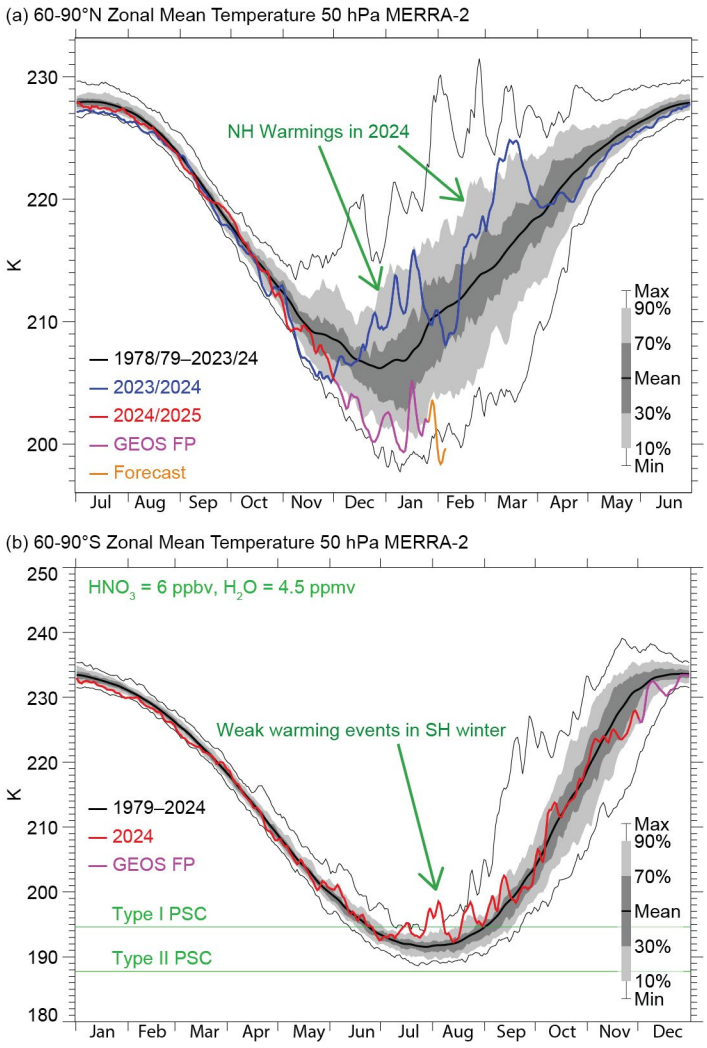

Fig. 2.12. (a) Time series of Arctic polar cap (60°N–90°N) temperatures in the lower stratosphere (50 hPa) during 2024, compared with the historical distribution of temperatures since 1978/79. Green arrows denote two stratospheric major warming events in early 2024. (b) Similar time series over the Antarctic (60°S–90°S) at 50 hPa. Note the different vertical axes between (a) and (b), and that the time axes are shifted by six months. (Data are from https://acd-ext.gsfc.nasa.gov/Data_services/met/ann_data.html.)

7. EQUIVALENT TEMPERATURE

—T. Matthews, T. Wood, P. Stoy, and M. Byrne

Global-mean equivalent temperature (*Teq*) reached its highest level in 2024 since at least 1979 according to reanalyses data, breaking its previous record (set in 2023) by 0.35°C–0.38°C.

Teq was introduced last year in the *State of the Climate in 2023* (Matthews et al. 2024). It is a more complete metric than air temperature (T) for tracking heat accumulation in the atmosphere:

$$Teq = T + qL/C_p$$

where T is the (dry-bulb) air temperature, q is the specific humidity (kg kg^{-1}), L is the latent heat of vaporization, and C_p is the specific heat capacity of the air. Note that Teq/C_p thus yields the 'moist static energy' that has also the subject of trend assessments (e.g., Peterson et al. 2011). *Teq* is therefore also closely related to wet-bulb temperature (T_w; section 2d2), but it has the advantage

Unauthenticated | Downloaded 11/21/25 11:34 AM UTC

of being linearly related to atmospheric heat accumulation; by comparison successive 1°C increments in T_w require progressively more heat accumulation.

The second term comprising *Teq* (the 'latent temperature', *Tq*) grows exponentially with *T* if relative humidity (*RH*) remains constant (due to the non-linearity in saturation vapor pressure as described by the Clausius Clapeyron equation). Hence, using *T* alone increasingly downplays the magnitude of changes in *Tq* and, accordingly, total heat content as the climate warms. This problem is not spatially uniform and is greater in regions with higher baseline *Tq* (such as within the tropics), where in some regions *Tq* is already rising faster than *T* (Matthews et al. 2022). Not only is *Teq* therefore more theoretically appropriate to track atmospheric heat accumulation as the climate changes, it is also more closely related to some key societal impacts. For example, extreme precipitation and human heat stress should be expected to scale more with *Teq* than *T* (Matthews et al. 2022; Song et al. 2022; Stoy et al. 2022). Note, however, that the closely related T_w remains much more widely used in the study of heat extremes (section 2d2).

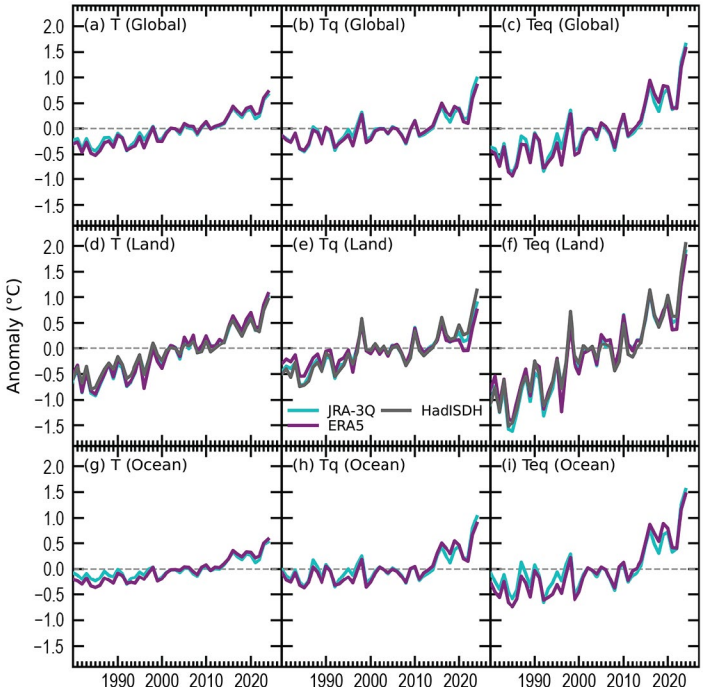

Fig. 2.13. (a),(d),(g) 2-m air temperature (*T*), (c),(f),(i) equivalent temperature (*Teq*), and (b),(e),(h) latent temperature (*Tq*) for (a),(b),(c) ocean + land, (d),(e),(f) land-only, and (g),(h),(i) ocean-only spatial mean anomalies versus the 1991–2020 baseline (°C). Each dataset is shown by colored lines: ERA5 (purple) and the Japanese Reanalysis for Three Quarters of a Century (JRA-3Q; cyan). Land-only sub-figures (d),(e),(f) also show Met Office Hadley Centre Integrated Surface Dataset of Humidity (HadISDH) anomalies (dark gray).

Teq anomalies for 2024 are assessed here using ERA5 (Hersbach et al. 2020) and JRA-3Q (Kosaka et al. 2024) reanalyses, along with the land-only station-based Met Office Hadley Centre Integrated Surface Dataset of Humidity over land (HadISDH.land; Willett et al. 2013, 2014). Globally (over land and ocean), *Teq* in 2024 was the highest on record according to both reanalyses datasets (Fig. 2.13), exceeding the previous records set in 2023 with departures of +1.57°C and +1.65°C above the 1991–2020 baseline for ERA5 and JRA-3Q, respectively (Table 2.4). Both datasets also rank the constituent parts of *Teq* (T and *Tq*) in the global series highest in 2024 (Appendix Tables A2.1–A2.3).

Across ERA5 and JRA-3Q, the mean 2024 global *Teq* anomaly (1.61±0.06°C, where uncertainty is one standard deviation across datasets) is much larger than that of *T* (0.70±0.04°C).

Table 2.4. Global equivalent temperature (*Teq*) anomalies and their constituent parts (*T*, *Tq*) in °C (1991–2020 base period) for 2024 and [rank] since 1979 (the earliest year common to all datasets). The uncertainty in the ensemble mean column represents one standard deviation.

Dataset	ERA5 *Teq*	ERA5 *T*	ERA5 *Tq*	JRA-3Q *Teq*	JRA-3Q *T*	JRA-3Q *Tq*	HadISDH *Teq*	HadISDH *T*	HadISDH *Tq*	Ensemble Mean *Teq*	Ensemble Mean *T*	Ensemble Mean *Tq*
Land + Ocean	1.57 [1]	0.72 [1]	0.85 [1]	1.65 [1]	0.67 [1]	0.98 [1]	-	-	-	1.61±0.06	0.70±0.04	0.92±0.09
Land only	1.80 [1]	1.06 [1]	0.73 [1]	1.90 [1]	1.01 [1]	0.89 [1]	2.04 [1]	0.96 [1]	1.13 [1]	1.91±0.12	1.01±0.05	0.92±0.20
Ocean only	1.46 [1]	0.58 [1]	0.88 [1]	1.55 [1]	0.52 [1]	1.02 [1]	-	-	-	1.51±0.06	0.55±0.04	0.95±0.10

Unauthenticated | Downloaded 11/21/25 11:34 AM UTC

This amplification is consistent with expectations of global-mean *RH* remaining approximately constant: the (exponential) increase in saturation vapor pressure with warming means that *Teq* must increase by more than *T* unless *RH* decreases sufficiently to leave *Tq* unchanged.

Considering spatial variation, both reanalyses agree that 2024 was the highest on record for *Teq*, *Tq*, and *T* over the oceans and over land (Table 2.4). For these datasets, the 2024 *T* anomaly was larger over land (1.01±0.05°C) than the ocean (0.55±0.04°C), whereas the *Tq* anomaly was more similar between land and ocean (0.92±0.20°C versus 0.95±0.10°C). As *Teq* is a combination of *T* and *Tq*, the land–ocean contrast for the 2024 anomaly (1.91±0.12°C versus 1.51±0.06°C) was also muted compared to *T*. Latitudinally, *Teq* anomalies in 2024 exhibited a more complex pattern than *T* (characterized by strong amplification in the Arctic; Figs. 2.14i–l). *Teq* had anomalies in the tropics and northern subtropics almost equal to those in the Arctic due to the much larger *Tq* anomalies at lower latitudes.

In general, 2024 *Tq* anomalies were therefore more likely to exceed *T* over the oceans and towards the equator (Figs. 2.14g,h,l). This pattern is consistent with theoretical expectations of *Tq* increasing by greater amounts relative to *T* in regions of higher baseline specific humidity

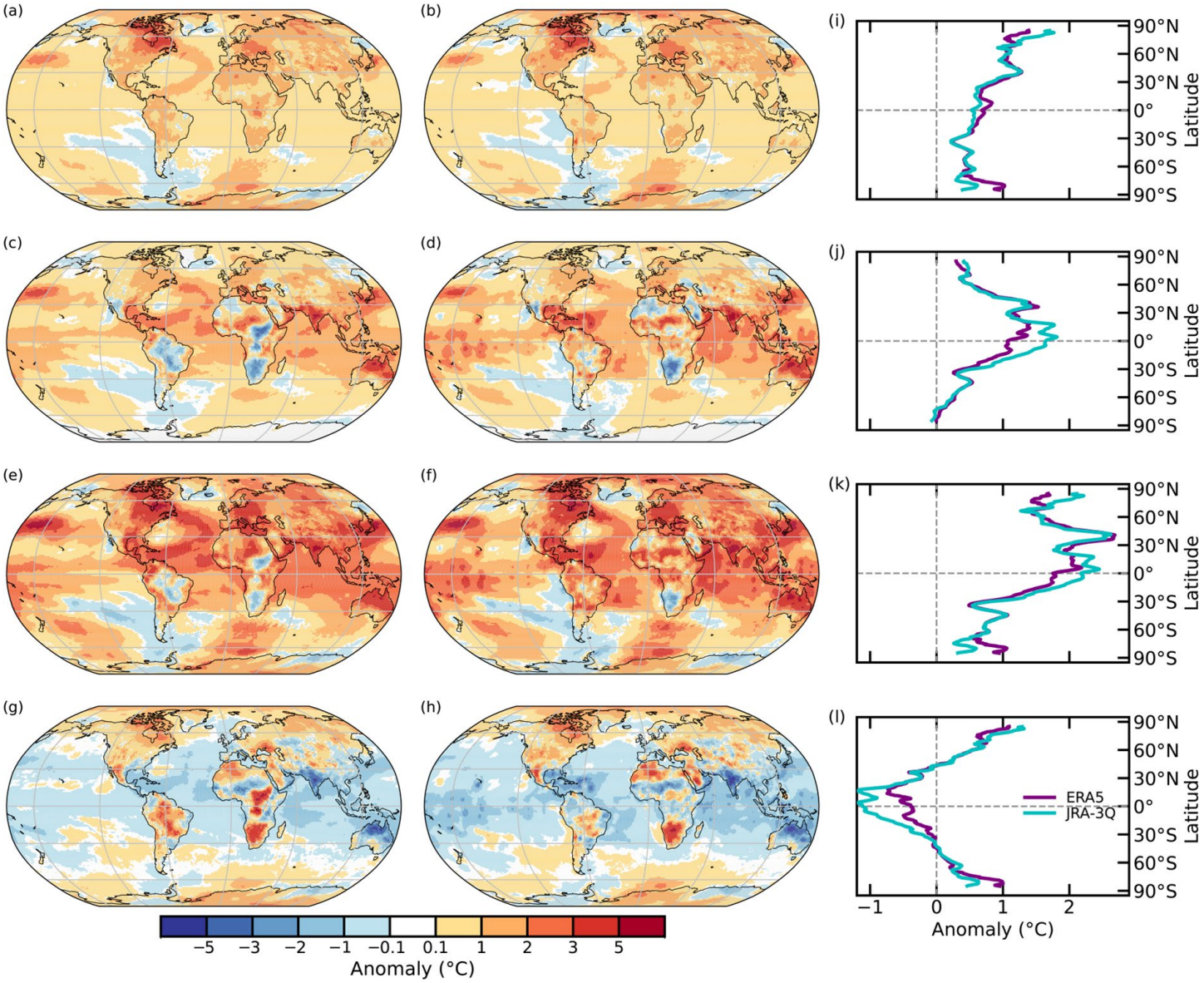

Fig. 2.14. Anomalies for (top to bottom): 2-m air temperature (*T*), latent temperature (*Tq*), equivalent temperature (*Teq*), and *T*–*Tq* according to ERA5 (left; [a],[c],[e],[g]) and the Japanese Reanalysis for Three Quarters of a Century (JRA-3Q) (right; [b],[d],[f],[h]) global (land and ocean). Zonal means for each variable are shown in the rightmost column (i)–(l) restricted to 85°S–85°N. Blue regions in the bottom row (*T*–*Tq*) experienced a larger 2024 anomaly in the latent heat term (*Tq*); red regions had a larger *T* anomaly.

Unauthenticated | Downloaded 11/21/25 11:34 AM UTC

(Matthews et al. 2022). It also highlights the importance of using *Teq* alongside *T* if hotspots in total atmospheric heat accumulation are to be correctly identified.

There were, however, exceptions in 2024 to the patterns of change in *T* and *Tq* expected from the baseline climates, with perhaps the most notable in Amazonia and North Africa (Figs. 2.14g,h). Under the assumption of constant *RH*, Amazonia (with relatively high baseline *Tq*) is one of the regions anticipated to experience larger changes in *Tq* than *T* under warming; the expectation is reversed for the relatively dry climate of North Africa (Matthews et al. 2022). The larger 2024 *T* anomalies in Amazonia and greater *Tq* anomalies in parts of North Africa are therefore consistent with reported drought conditions in Amazonia in 2024 (Maciel et al. 2024) and the extreme wet season rainfall in the Sahel (Pinto et al. 2024).

In summary, 2024 was a record-breaking year for *Teq*, with all datasets unanimous in their agreement that it was easily the highest over land and ocean since at least 1979.

Unauthenticated | Downloaded 11/21/25 11:34 AM UTC

c. Cryosphere

1. PERMAFROST TEMPERATURE AND ACTIVE-LAYER THICKNESS

—J. Noetzli, H. H. Christiansen, T. Gallemann, M. Gugliemin, F. Hrbáček, G. Hu, K. Isaksen, F. Magnin, P. Pogliotti, S. L. Smith, L. Zhao, and D. A. Streletskiy

Ground remaining at or below 0°C for two or more years—known as permafrost—occurs in polar and high mountain regions. Its warming and degradation can have important impacts on the landscape, ecosystems, infrastructure, and natural hazards. Widespread permafrost warming, thickening of the active layer (i.e., the seasonally thawed layer above the permafrost), and ground ice loss continued to be observed in 2024. Globally, permafrost warming rates at 10-m–20-m depth in cold permafrost (<–2°C) reach up to 1°C decade^{-1}. Warming rates are significantly reduced (<0.3°C decade^{-1}) in warm ice-bearing permafrost due to latent heat effects (Noetzli et al. 2024a; Smith et al. 2022; Zhao et al. 2024). Therefore, ground temperatures close to 0°C in ice-rich permafrost can remain nearly stable for years as ground ice is melting. Ground ice loss was observed in the Arctic (O'Neill et al. 2023; Streletskiy et al. 2025), European mountains (Etzelmüller et al. 2020; Mollaret et al. 2019), and the Qinghai–Tibet Plateau (QTP; Wang et al. 2023; Zou et al. 2024). Decadal active-layer thickening ranges from centimeters in continuous permafrost in Arctic sediments, to tens of centimeters in discontinuous bedrock permafrost in polar regions (Smith et al. 2024), southern Scandinavia (Etzelmüller et al. 2023), and the QTP (Zhao 2024; Hu 2024), to meters in bedrock or talus (scree) slopes in the European Alps (PERMOS 2024; Magnin et al. 2023).

Arctic permafrost has warmed by <0.3°C decade^{-1} in warmer permafrost to 0.8°C decade^{-1} in cold permafrost (Smith et al. 2024; see section 5j). Permafrost temperatures in 2024 were generally higher than in 2023. They were the highest on record at 8 of 25 sites reporting (7 in North America and 1 on Svalbard). In the Beaufort–Chukchi region (northern Alaska and Canadian Mackenzie Valley), higher permafrost temperatures in 2024 reflect higher surface air temperature (SAT) in 2023 that followed a short cooling period. Permafrost temperatures in high Arctic Svalbard increased again in 2024 following a cooling period after 2019 (Isaksen et al. 2022) and were close to previous values. Arctic permafrost is described in detail in section 5j.

On the Antarctic Peninsula, the annual shallow ground temperature in 2024 was 0.3°C below the 2011–20 mean on James Ross Island (Hrbáček et al. 2023) and within 0.1°C in the South Shetlands (de Pablo et al. 2024).

Permafrost in European mountains changed at rates between −0.01°C decade^{-1} and +1.77°C decade^{-1} (mean 0.41°C decade^{-1}) at 10-m depth during 2013–22 based on 50 time series, where permafrost was present at this depth for at least part of the decade (Noetzli et al. 2024b). Warming was >0.7°C decade^{-1} at 20% of these sites, which are in cold polar or high-elevation locations or where permafrost has recently disappeared. At 20-m depth, rates are generally lower (up to 0.7°C decade^{-1}) due to the delayed warming with increasing depth. In 2024, permafrost temperatures in the European Alps reached record highs at 10-m depth for most of the sites reporting (Fig. 2.15). This resulted from three consecutive exceptionally warm years and an early snow cover in winter 2024 following a warm autumn (MeteoSwiss 2025; PERMOS 2025). In northern Scandinavia, a record-warm summer 2024 led to strong permafrost warming at 10-m depth.

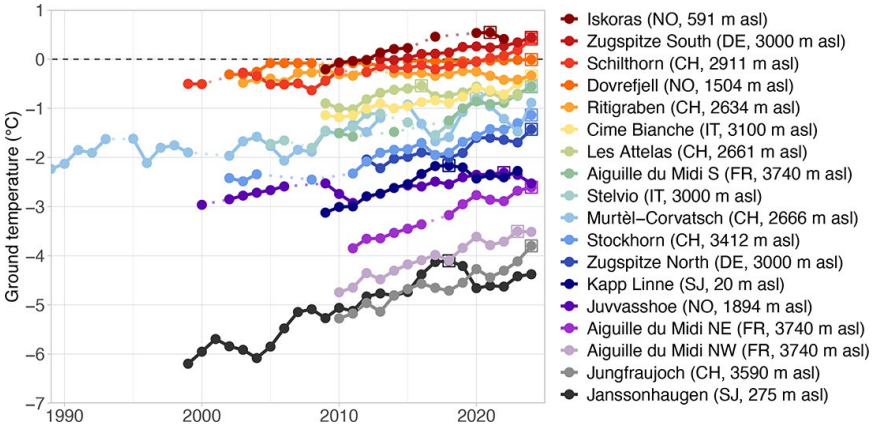

Fig. 2.15. Mean annual ground temperature (°C) measured in European permafrost boreholes in the Alps, Scandinavia, and Svalbard at a depth of ~10 m. Maximum values for each time series are highlighted by a square. (Data sources: Norway [NO] and Svalbard [SJ]: Norwegian Meteorological Institute and the University Centre in Svalbard [UNIS]; Switzerland [CH]: Swiss Permafrost Monitoring Network [PERMOS]; France [FR]: Updated from Magnin et al. 2023; Italy [IT]: Updated from Pogliotti et al. 2023 and Guglielmin, M. unpublished data. Germany [DE]: Bavarian Environment Agency.)

Unauthenticated | Downloaded 11/21/25 11:34 AM UTC

At Iskoras in northern Norway, permafrost thawed to a depth of 24 m, with >15 m of permafrost lost since 2008 (Etzelmüller et al. 2023).

In the central Asian QTP, significant permafrost warming for 2005–23 is reported for six sites at rates between 0.04°C decade^{-1} and 0.4°C decade^{-1} at 10-m depth (Fig. 2.16) and between 0.02°C decade^{-1} and 0.25°C decade^{-1} at 20-m depth.

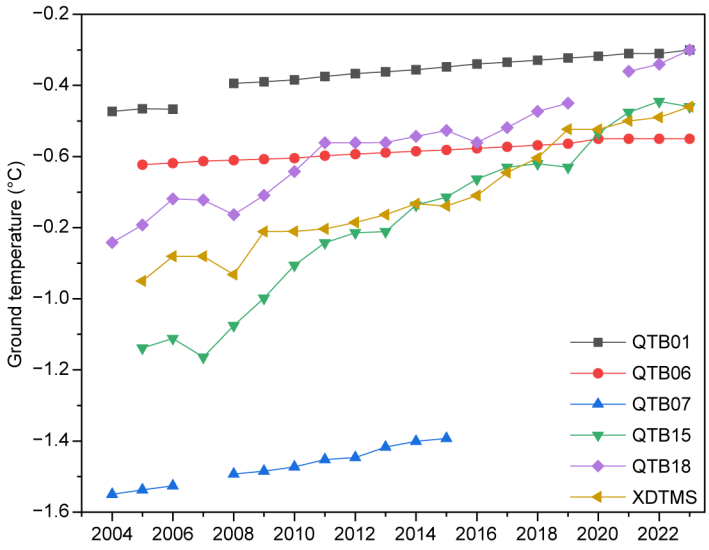

Fig. 2.16. Ground temperature (°C) measured at 10-m depth in the Qinghai–Tibet Plateau (QTP) in the period 2005–23. (Data source: Cryosphere Research Station on Qinghai-Xizang Plateau, Chinese Academy of Sciences [CAS].)

Active-layer thickness (ALT) increase in the Arctic continued in 2024 and was more pronounced in areas of discontinuous permafrost than in areas of continuous permafrost (Fig. 2.17; section 5j). In Interior Alaska and Mackenzie Valley, ALT was larger in 2023 and 2024 than in 2022. In Greenland, it was larger than average in 2024. In Svalbard, ALT reached an all-time high, following the third summer in a row with unprecedented high summer SAT. ALT in the European North and West Siberia was lower in 2024 than in 2023, but substantially above the 2000–20 mean. For the limited sites reporting in East Siberia and Chukotka, the ALT decrease over the past five years continued, with values that were lower in 2024 than in 2023 and below the 2000–24 mean.

On the Antarctic Peninsula, the maximum ALT since the start of measurements in 2014 was registered in 2023. In 2024, ALT was only slightly above the long-term mean and the lowest observed since 2020.

In Europe's mountains, ALT reached or exceeded the 2022/23 record values and continued the marked thickening of the past three years. During the period 2000–20, ALT increased by meters at several sites, reaching values beyond the climatic variability (Fig. 2.17b). At Schilthorn, Swiss Alps, ALT tripled to >13 m during 1998–2022, and the ground did not re-freeze in winter 2024 (PERMOS 2025).

ALT near Kunlun mountain pass (QTP) increased by 20.2 cm decade^{-1} during 1981–2023 at 10 sites, following a significant SAT increase during that period.

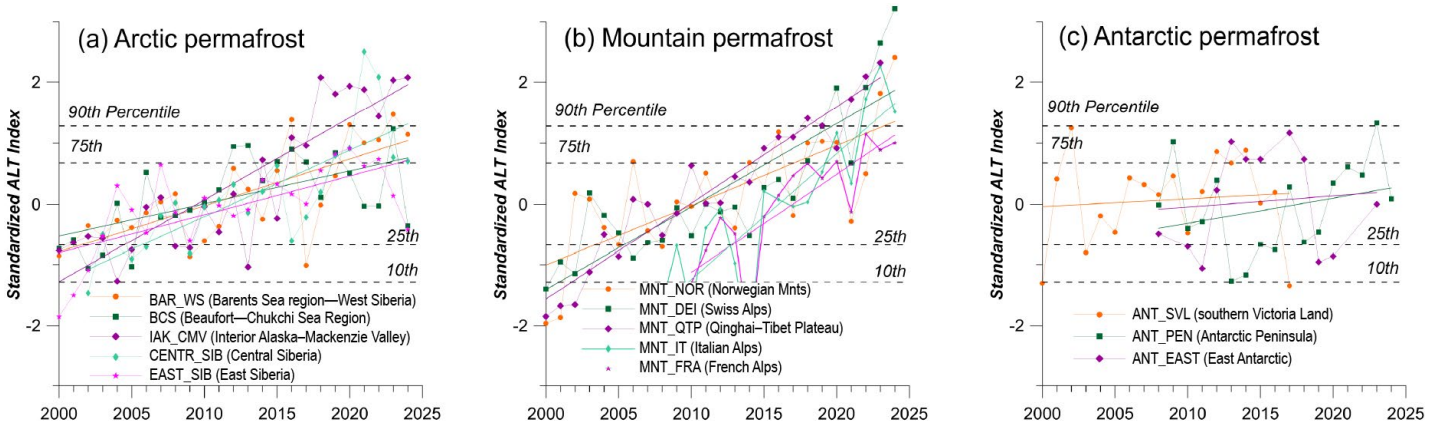

Fig. 2.17. Standardized index of active-layer thickness (ALT) relative to 2000–20. (a) Arctic regions: Beaufort–Chukchi Sea–Arctic Alaska and Mackenzie Delta region (BCS), Interior Alaska and central Mackenzie Valley, Northwest Territories (IAK_CMV), Barents Sea region–West Siberia (BAR_WS), Central Siberia (CENT_SIB), East Siberia (EAST_SIB); (b) Mountain regions: Norwegian mountains (MNT_NOR), Swiss Alps (MNT_SWI), Italian Alps (MNT_IT), French Alps (MNT_FRA), Qinghai-Tibet Plateau (MNT_QTP); and (c) Antarctic: southern Victoria Land (ANT_SVL), Antarctic Peninsula (ANT_PEN), East Antarctic (ANT_EAST). Note that only data from 30% of the Russian sites are reported. (Data source: Circumpolar Active Layer Monitoring [CALM].)

Unauthenticated | Downloaded 11/21/25 11:34 AM UTC

2. ROCK GLACIER VELOCITY

—C. Pellet, X. Bodin, D. Cusicanqui, R. Delaloye, A. Kääb, V. Kaufmann, E. Thibert, S. Vivero, and A. Kellerer-Pirklbauer

Rock glaciers are debris landforms generated by the creep of perennially frozen ground (permafrost). Their velocity evolutions are indicative of changes in the thermal state of permafrost and associated ground hydrological characteristics (RGIK 2023a). An overall increasing trend of rock glacier velocity (RGV) has been observed in mountain ranges worldwide since the 1950s (Pellet et al. 2024). In 2024, RGVs consistently increased in the European Alps compared to 2023, and in the Dry Andes, RGVs remained at a high level, with values similar to 2020. RGVs recently compiled in the United States further confirm this general trend of RGV increase (Kääb and Røste 2024), which is consistent with the increase of permafrost temperatures (section 2c1) to which RGV respond more or less synchronously (e.g., Staub et al. 2016).

In the European Alps, 2024 was the second-warmest hydrological year on record based on the average of five high-elevation stations (+1.52°C; Fig. 2.18a) yielding a general increase of RGVs. Compared to 2023, the highest RGV increase occurred in the Swiss Alps (+80.8% at Gemmi/Furggentälti and +80.7% at Grosses Gufer), whereas a +16.9% increase was observed in the French Alps at Laurichard as well as +3.4% and +5.1% increases in the Austrian Alps at Dösen and Hinteres Langtalkar, respectively (Fig. 2.18b). These observations are consistent with the permafrost temperature observations (section 2c1) as confirmed by the increasing temperatures measured in 2024 at 10-m depth on the rock glacier Murtèl in eastern Switzerland (Fig. 2.18a). The regional differences in magnitude of velocity increase is related to landform-specific characteristics combined with the spatial variability of snow conditions, namely early onset and well-above-average snow height throughout the winter in Switzerland and France (preventing any cooling of the ground; PERMOS 2025) as well as early onset followed by below-average snow heights in Austria (enabling limited cooling). The reported RGV observations in 2024 in the European Alps are consistent with the general acceleration trend observed at all sites since the 1950s (Kellerer-Pirklbauer et al. 2024).

In the Dry Andes, RGVs observed during 2023/24 show increases of +13.7% and +1.3% on El Cachito and Las Tolas, respectively, whereas a –15.9% decrease is observed on Tapado compared to 2019/20 (Fig. 2.18c). Velocities reached maximum values at El Cachito and remained at a high level compared to the entire time series on Las Tolas and Tapado. The overall increase observed since the 2000s is further confirmed by a recent study on Largo rock glacier (Fig. 2.18c; Cusicanqui et al. 2024) and is consistent with the slight air temperature increase observed in the region since 1976 (Vivero et al. 2021).

In Central Asia, RGVs observed on four landforms since the 1950s exhibit a general increase, with a marked acceleration in the period 2010–20 (Fig. 2.18d). This evolution is consistent with increasing air temperatures in the region (Azisov et al. 2022; Sorg et al. 2015).

In the United States, RGVs compiled on six rock glaciers show an overall increase since the first available measurements in the 1950s (Fig. 2.18e; Kääb and Røste 2024). This trend is consistent with the strongly increasing air temperature observed in that region (Kääb and Røste 2024).

RGV refers to velocities related to permafrost creep, which has to be understood as a combination of internal deformation of the frozen ground (creep stricto sensu) and shearing in one or more layers at depth (shear horizon; RGIK 2023b). RGVs are mostly related to the evolution of ground temperature and liquid water content between the upper surface of permafrost and the shear horizon (Cicoira et al. 2019; Staub et al. 2016). RGV increase and decrease positively correlates with temperature change. Despite differences in size, morphology, topographical, climatic, and geological settings, as well as velocity ranges, consistent regional RGV evolutions have been highlighted in several studies (see Hu et al. 2025). RGV time series are produced using both in situ and optical remote sensing (airborne and spaceborne) measurements. Surface displacements are computed based on matching between images or digital elevation models taken at different times, with the resulting accuracy strongly depending on the characteristics of the input data (Kääb et al. 2021; Vivero et al. 2021). Surface displacements are averaged for a cluster of points/pixels selected within areas considered as representative of the downslope movement

Unauthenticated | Downloaded 11/21/25 11:34 AM UTC

of the rock glacier (RGIK 2023b). The in situ measurements consist of annually repeated terrestrial geodetic surveys of the positions of selected boulders (10–100 per landform), yielding displacement observation with an average accuracy of mm to cm (Lambiel and Delaloye 2004; Thibert and Bodin 2022).

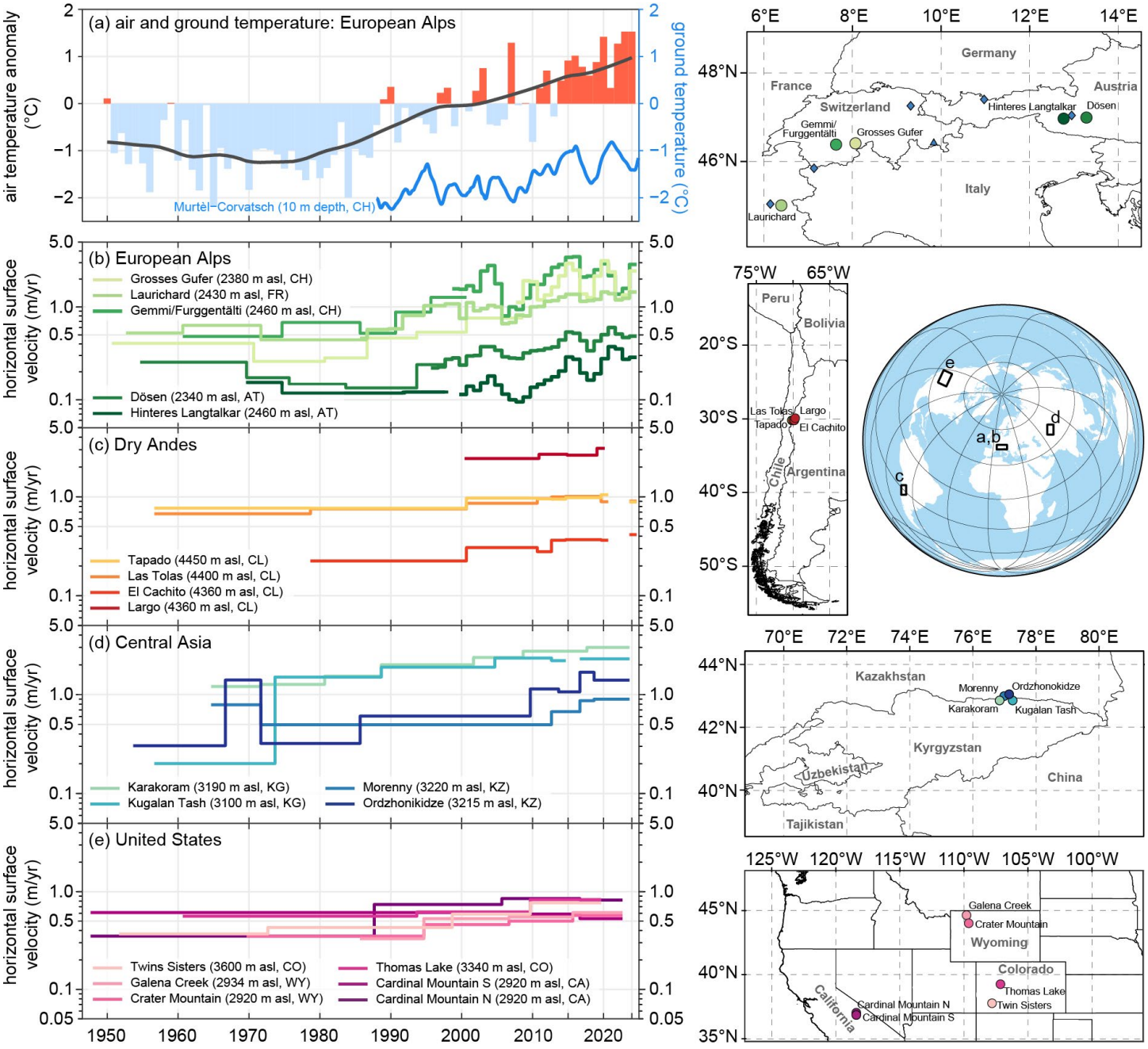

Fig. 2.18. Rock glacier velocity and climate: (a) air temperature in the European Alps and ground temperature in the Swiss Alps (°C), (b)–(e) rock glacier velocities (m yr^{-1}) at selected sites in the (b) European Alps, (c) Dry Andes (updated from Vivero et al. 2021 and Cusicanqui et al. 2024), (d) Central Asia (updated from Kääb et al. 2021), and (e) United States (adapted from Kääb and Røste 2024). Rock glacier velocities are based on in situ geodetic surveys ([b], since 2000s) or photogrammetry ([b]–[e]) in the context of long-term monitoring. In situ hydrological mean annual permafrost temperature measured at 10-m depth (blue line) at Murtèl Corvatsch (blue triangle on Europe map) and air temperature: composite anomaly to the 1991–2020 base period (bars) and composite 20-year running mean (solid line) at Besse (France [FR]), Grand Saint-Bernard (Switzerland [CH]), Saentis (CH), Sonnblick (Austria [AT]), and Zugspitze (Germany [D], blue diamonds on Europe map). (Sources: Météo-France, Deutscher Wetterdienst [DWD], MeteoSwiss, GeoSphere Austria, Swiss Permafrost Monitoring Network [PERMOS], University of Fribourg, University of Graz, Graz University of Technology, Université Grenoble Alpes National Institute of Agricultural Research [INRAE], University of Oslo).

Unauthenticated | Downloaded 11/21/25 11:34 AM UTC

3. ALPINE GLACIERS

—M. Pelto

In 2024, all 58 global reference glaciers reported a negative annual mass balance. This is only the second year in the 1970–2024 period with all negative annual balances, following 2023. The global average annual mass balance based on equal weighting of 19 regions is –1.30 m water equivalent (w.e.), the most negative value in the record (Fig. 2.19).

The 2024 dataset of submitted glaciological observations includes 142 glaciers from six continents and 27 nations, with 140 reporting a negative balance and 2 a positive balance. In 2024, the mean annual mass balance of the 58 global reference glaciers was –1.44 m w.e. and –1.36 m w.e. for all 142 reporting glaciers. This is a similar result to 2023, which saw a mean reference glacier balance of –1.62 m w.e. and –1.35 m w.e. for all 116 reporting glaciers.

The 2024 regionalized global average of –1.30 m w.e. exceeds the previous most negative year in 2023, which saw a regionalized global average of –1.25 m w.e. This makes 2024 the 37th consecutive year with a global alpine mass balance loss and the 15th consecutive year with a regionalized global mass balance below –0.5 m w.e. The acceleration of mass balance loss indicates that alpine glaciers are not approaching equilibrium. The acceleration of mass balance loss is apparent regardless of datasets used to determine it, including glaciological, geodetic, altimetry, and gravimetric observations (The GlaMBIE Team 2025). The intercomparison assessment identified that global glaciers annually lost 273±26 gigatons (Gt) in mass from 2000 to 2023, with loss having been 36% greater in the second half than in the first half of this period (The GlaMBIE Team 2025).

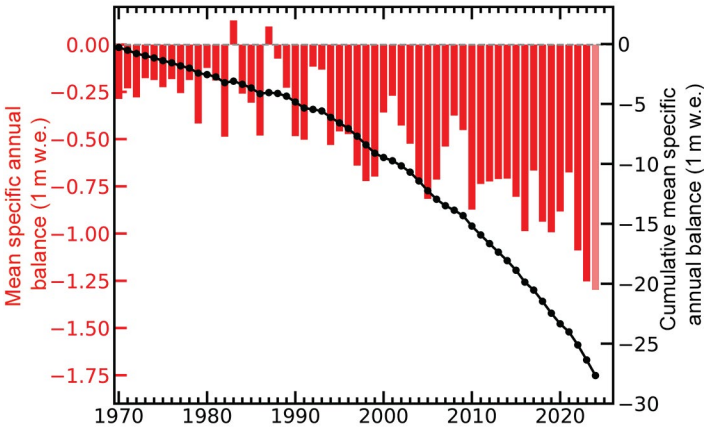

Fig. 2.19. Time series of regionalized average global mean annual glacier mass balance of alpine glaciers from 1970–2024 in m w.e., as determined by the World Glacier Monitoring Service. Annual mass balance is shown in red bars and annual cumulative mass balance is indicated by black dots.

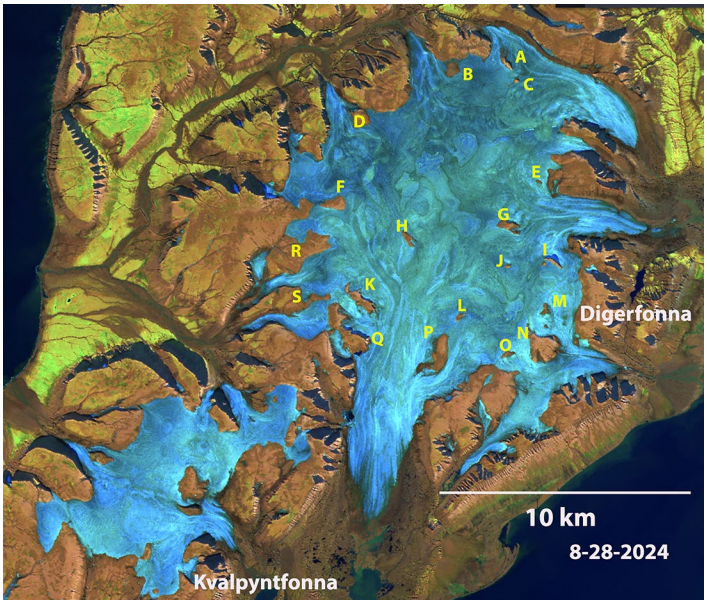

Fig. 2.20. Snow-free ice caps on Edgeoya Island, Svalbard, in Sentinel-2 Short-Wave Infrared RGB Composite imagery from 28 August 2024. Green represents vegetation, brown represents rock and soil, black represents water, white to very light blue represents snow, and darker grays and blues represent ice and firn. Glaciers across Svalbard were largely snow-free, leading to consistent mass balance losses exceeding –1.25 m w.e.

In the European Alps, all 49 glaciers reported negative mass balances, with 45 losing over 1 m w.e. All 10 Icelandic glaciers had negative balances. In Svalbard, all seven had negative balances exceeding an exceptional loss of 1.25 m w.e. This was the result of near complete snow cover loss across most glaciers (Fig. 2.20) following record temperatures in August (see section 7f5 for details). Twelve of the 13 glaciers from Norway and Sweden had mass losses of more than 1.0 m w.e.

Across High Mountain Asia, 20 of 21 glaciers, reporting from seven nations, had negative balances. The highest average losses were in the Himalayas of Nepal and the lowest in the Pamir Range of Tajikistan.

In the Andes Mountains of South America, all 14 glaciers, reporting from five nations, had negative balances. Conejeras Glacier (Colombia), following a 5.04 m w.e. loss in 2023, was declared extinct in 2024. The daily hydrograph below this glacier changed from a predominance

Unauthenticated | Downloaded 11/21/25 11:34 AM UTC

of days with a purely melt-driven hydrograph from 2006 to 2016 to an increase in the frequency of days with flows less influenced by melt after 2016 (Morán-Tejeda et al. 2018).

All 16 glaciers in North America had negative balances. All four glaciers in Arctic Canada had mass balance losses under 1 m w.e. In western Canada and Washington and Montana (United States), all 16 glaciers reporting had losses exceeding 1 m w.e. The Ice Worm Glacier (Washington) was listed as extinct in 2023 after 40 years of continuous observations (Pelto 2024). In 2024, loss from the relict ice (ice that is no longer moving or part of a glacier) was 2.4 m and melt runoff below the glacier had decreased similar to Conejeras Glacier (Pelto and Pelto 2025). In Alaska, all three glaciers had mass balance losses. Davies et al. (2024) examined the Juneau Icefield, the most observed icefield in Alaska in terms of mass balance, and found an acceleration of mass loss with a doubling after 2010 compared to 1979–2010.

Alpine annual mass balance glaciological observations are reported to the World Glacier Monitoring Service (WGMS) by national representatives with a 1 December annual submission deadline. WGMS reference glaciers have at least 30 continuous years of mass balance observation. Benchmark glaciers have at least a 10-year mass balance record and are in regions that lack sufficient reference glaciers. The combination of benchmark and reference glaciers is used to generate regional averages (WGMS 2023). Global values are calculated using a single averaged value for each of 19 mountain regions, limiting bias from observed regions (WGMS 2023). As this dataset expands, the annual values are reanalyzed and updated.

4. LAKE ICE COVER

—J. Culpepper, S. Sharma, R. I. Woolway, and J. E. Ollinik

Northern Hemisphere (NH) lakes tended toward later ice formation, earlier ice breakup, and shorter duration during the winter of 2023/24, similar to long-standing trends (Sharma et al. 2021). However, there was regional variability in ice patterns between North America and Europe, likely resulting from stronger warm anomalies in winter air temperatures in North America (see section 7b).

On average, NH lakes froze 3.6 days later, broke up 6.1 days earlier, and ice duration was 10 days shorter, based on ERA5 reanalysis data and compared to the 1991–2020 base period (Figs. 2.21a–c). Most regions experienced shorter ice duration, with the exception of Scandinavia, which saw longer duration owing partially to colder winter air temperature anomalies, particularly in the late autumn and early winter (October–January; Figs. 2.21c,d).

On average, during the 2023/24 winter, in situ lake ice observations (n = 123) revealed that ice-on was 7.6 days later, ice-off was 17.5 days earlier, and ice duration was 24 days shorter relative to the 1991–2020 base period (Figs. 2.22a–c). The lakes in North America had on average 42.4 fewer days of ice cover, whereas lakes in Finland and Sweden experienced 13.5 more days

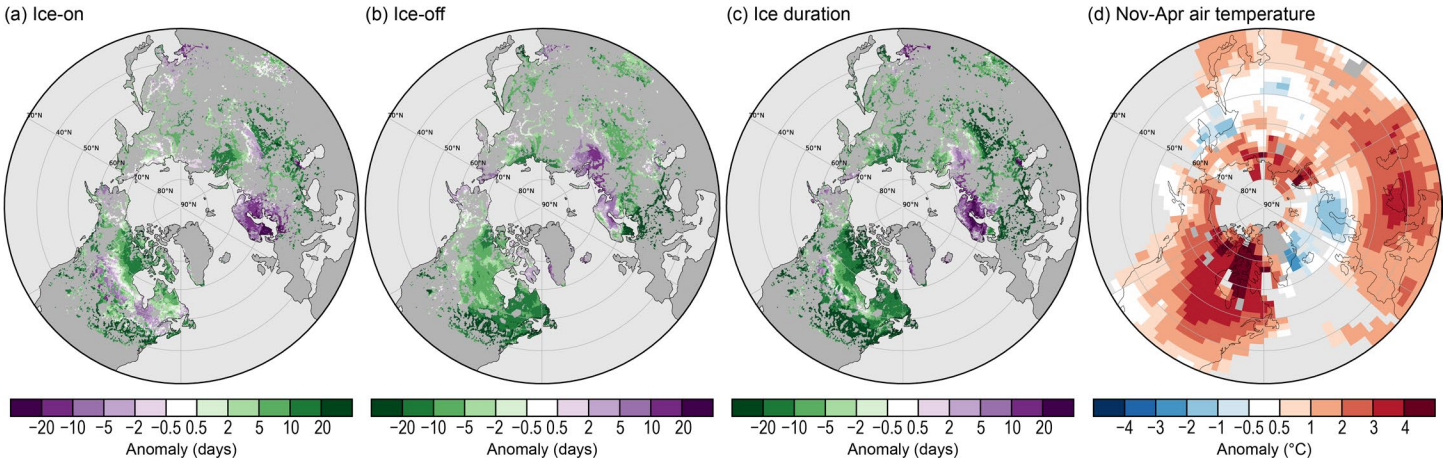

Fig. 2.21. Anomalies (days) compared to 1991–2020 base period in lake ice cover across the Northern Hemisphere during the winter of 2023/24 for the (a) ice formation period (negative [positive] values indicate earlier [later] ice formation), (b) ice breakup period (negative [positive] values indicate earlier [later] ice breakup), and (c) ice duration period. For duration (c), negative (positive) values indicate shorter (longer) ice cover. (d) The surface temperature anomalies (°C) for average temperatures between Nov 2023 and Apr 2024, where negative (positive) values are colder (warmer) temperatures.

Unauthenticated | Downloaded 11/21/25 11:34 AM UTC

of ice cover. El Niño-related temperature pattern conditions (Fig. 2.21d) strongly decreased ice coverage in North American lakes. Furthermore, Lake Suwa in Japan (36.0499°N, 138.0857°E) did not freeze, continuing a pattern of intermittent freezing. Lake Suwa has frozen in only 17 of the last 30 years, but has frozen every year between 2021 and 2023. Notably, Lake Suwa froze in 87 years in the twentieth century, although the majority of the ice-free years occurred after the 1970s.

Mountain lakes in North America and Europe experienced an average of 6.8 fewer days of ice cover (n = 13), resulting from ice formation (n = 14) that was 0.8 days earlier and ice breakup (n = 13) that was 6.9 days earlier (Fig. 2.22). Mountain lakes are a separate subset of in situ lakes identified using digital elevation models, which have an elevation of at least 300 m a.s.l. Ice loss can be more extreme in these lakes. For example, Lake Lunz only experienced 2 days of ice cover in 2024, compared to an average of 62 days between 1990 and 2019 (Kainz et al. 2017). Despite warmer temperatures during November through April, ice breakup was later in North American mountain lakes. Anomalously high snow cover (section 2c5) in the western United States likely drove delayed ice breakup in the California (Chandra et al. 2023) and Colorado (Caine et al. 2024) lakes included in this dataset.

The Laurentian Great Lakes had 31.8% less maximal ice coverage during the 2023/24 winter relative to the winters of 1991–2020. Lake Superior had 42.5% less ice coverage, followed by Lakes Erie (40.3%), Huron (37.3%), Ontario (20.9%), and Michigan (18.1%; Fig. 2.23). The Great Lakes reached their maximal ice coverage of 16% on 22 January, 31 days earlier than average. Notably, there was only 2.7% ice coverage across all of the Great Lakes on 11 February, the lowest ice coverage measured in mid-February since 1973. The Great Lakes region was characterized by generally warm winter air temperatures in 2023/24, with only a brief period of cold air temperatures in January 2024 (NOAA 2024). After the year 2000, an oscillatory pattern figures prominently in the time series (Fig. 2.23). Research suggests that a combination of the El Niño–Southern Oscillation (ENSO) and North Atlantic Oscillation (NAO) contribute to the variability in ice cover conditions in the Laurentian Great Lakes. For example, the Great Lakes have lower ice cover during strong La Niña events and the positive phase of the NAO (Bai et al. 2012). Moreover, NAO and ENSO can also interact to influence ice cover in a winter (Bai et al. 2012).

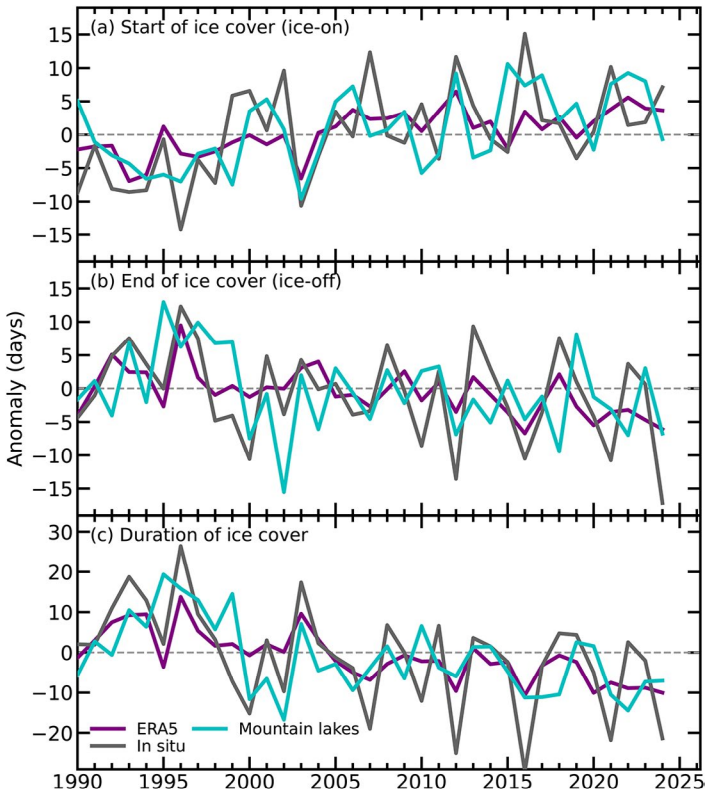

Fig. 2.22. The (a) ice-on, (b) ice-off, and (c) ice duration anomalies (days) for Northern Hemisphere lakes from 1990 to 2024 compared to the 1991–2020 base period for in situ observations (gray), mountain lake observations (blue), and ERA5 (black). Negative (positive) values indicate earlier (later) ice-on, earlier (later) ice-off, and shorter (longer) ice duration.

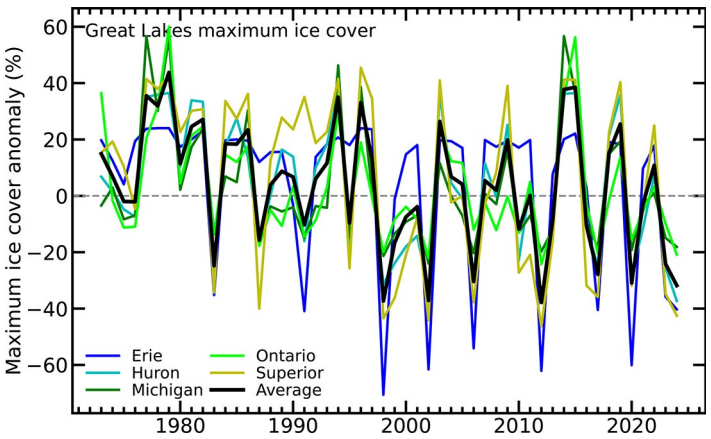

Fig. 2.23. Anomalies of the maximum ice cover extent (%) of the Laurentian Great Lakes for the period of 1973 to 2024 in relation to the 1991–2020 base period. The colored lines indicate individual lake anomalies (e.g., Erie anomaly in blue), while the black line shows the average anomaly. Negative (positive) values indicate less (more) maximum ice cover extent.

Unauthenticated | Downloaded 11/21/25 11:34 AM UTC

Established monitoring networks and citizen scientists contributed in situ observations for 123 lakes across Canada (n = 5 lakes), the United States (n = 88), Finland (n = 27), Sweden (n = 1), and Japan (n = 1) (Sharma et al. 2022). Mountain lake ice cover was derived from a similar network of scientists through the NH in North America (n = 8 lakes) and Europe (n = 10; Caine et al. 2024; Chandra et al. 2023; Kainz et al. 2017). Anomalies for each in situ lake were calculated as the difference between the 2023/24 ice value (i.e., ice-on, ice-off, duration) and the average of the 1991–2020 base period. Information on lake ice phenology was downloaded from ERA5 (Hersbach et al. 2020). Annual maximum ice coverage (%) data for each of the Laurentian Great Lakes were acquired for 1973–2024 from the NOAA Great Lakes Environmental Research Laboratory. Notably, the definitions of ice-on and ice-off varied by lake (e.g., complete ice cover, the date most of the lake is frozen [90%] or when most of the lake is ice-free [10%], the first or last time a boat could travel through two points), but did not vary over time for each lake (Sharma et al. 2022).

5. NORTHERN HEMISPHERE CONTINENTAL SNOW COVER EXTENT

—D. A. Robinson and T. W. Estilow

Annual snow cover extent (SCE) over Northern Hemisphere (NH) land averaged 23.9 million km² in 2024. This was 1.0 million km² less than the 1991–2020 mean and 1.2 million km² below the mean of the full period of record (1967–2024; Table 2.5). Overall, 2024 had the third-least-extensive cover on record. Twelve-month running mean SCE departures over all NH lands have not been as low as they were at the end of 2024 since June 2007, and before then July 1990 (Fig. 2.24a). Monthly SCE in 2024 ranged from a maximum of 46.9 million km² in January to a minimum of 2.6 million km² in August. Annual-mean SCE in North America (NA) was the least extensive on record in 2024, 0.1 million km² less than that of 1990; 2024 is now the second-least-extensive year on record. In terms of 12-month running means, the June 2024 value was the lowest since May 1968. Weekly NH SCE in 2024 was below long-term means for all but a few weeks from a winter maximum SCE in early January through the melt season. Autumn SCE was close to normal to begin the season, later becoming more erratic week to week from November into December (Fig. 2.24b).

In January, the NH SCE was in the middle tercile of the 58-year record. From February onward through spring, NH ranked in the lower tercile, from 1st to 19th least-extensive, with April having been record low. NA SCE in January was the 16th most extensive in January, while Eurasia was 18th least extensive. Both continents ranked from 3rd to 20th least extensive in each month from February to June. NA SCE was the third least extensive in both February and April. The 2024 snow season began in autumn with the 17th-most-extensive SCE over Europe in September and 18th in October. Meanwhile, snow was slow to appear over NA, with the 5th- and 13th-least-extensive SCE in September and October, respectively.

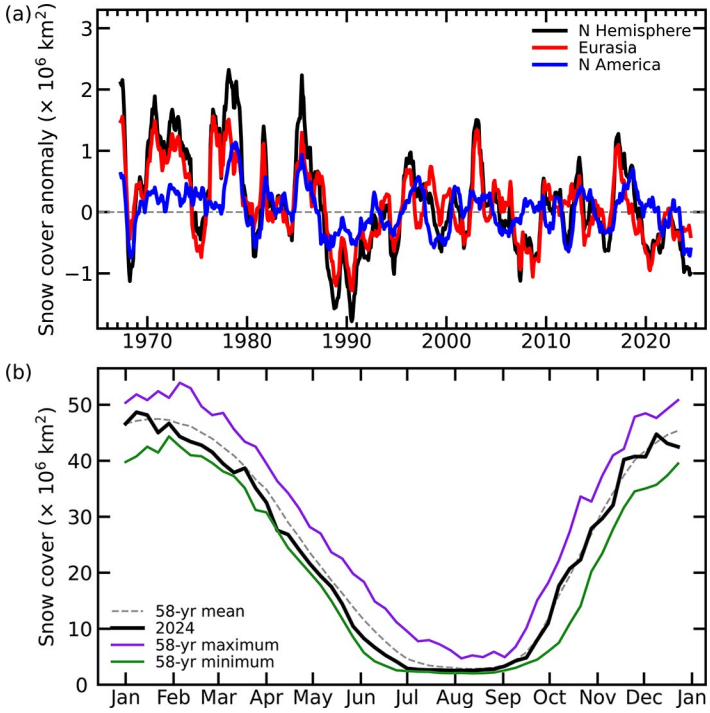

Fig. 2.24. (a) Twelve-month running anomalies of monthly snow cover extent (SCE) over Northern Hemisphere (NH) lands as a whole and Europe (EUR) and North America (NA) separately plotted on the seventh month using values from Nov 1966 to Dec 2024. Anomalies are calculated from NOAA snow maps. Mean NH SCE is 25.1 million km² for the full period of record. Monthly means for the period of record are used for nine missing months during 1968, 1969, and 1971 to create a continuous series of running means. Missing months fall between Jun and Oct. (b) Weekly NH SCE for 2024 (black) plotted with the mean (gray dashed line), maximum (purple), and minimum (green) SCE for each week. Mean weekly SCE and extremes are calculated using the 58-year record from Jan 1967 to Dec 2024. Weekly means for the period of record are used for 4, 21, and 12 missing weeks during 1968, 1969, and 1971 respectively. Weekly data granules represent SCE for each seven-day period ending on Monday.

Unauthenticated | Downloaded 11/21/25 11:34 AM UTC

NH SCE was the 19th least extensive in September and 25th most extensive in October. November and December SCE was 27th and 12th least extensive, respectively.

The contiguous United States' (U.S.) SCE was above normal, 16th most extensive, to start 2024, then rapidly fell to the 2nd least extensive in February. March through May ranged from 26th to 14th least extensive. Across Canada (CAN), the highest ranking for the winter and spring was 22nd least extensive in January, with each month from February through June ranging from 4th to 10th least extensive. In September, CAN ranked fourth least extensive and the U.S. was almost snow free. The U.S. and CAN SCE ranked, respectively, as the 17th and 16th least extensive in October. CAN also observed the 16th-least-extensive SCE in November, while the U.S. SCE increased to 24th most extensive. Snow conditions for the two nations reversed in December, with the U.S. seeing its 8th-least-extensive ranking and CAN its 15th most extensive.

SCE is calculated at the Rutgers Global Snow Lab (GSL) from daily SCE maps produced by meteorologists at the U.S. National Ice Center, who rely primarily on visible satellite imagery to construct the maps (Estilow et al. 2015). Maps depicting daily, weekly, and monthly conditions, anomalies, and climatologies may be viewed at the GSL website (https://snowcover.org).

Table 2.5. Monthly and annual climatological information for Northern Hemisphere (NH), Eurasia (EUR), and North America (NA) snow cover extent (SCE) between Nov 1966 and Dec 2024. Included are the numbers of years with data used in the calculations, NH anomalies, NH means, NH standard deviations (Std. Dev.), and ranks. Areas are in millions of square kilometers. 1968, 1969, and 1971 have one, five, and three missing months, respectively, and thus are not included in the annual (Ann) calculations. NA includes Greenland. Ranks are from most to least extensive (least to most in parentheses).

Time Period	Yrs	NH Anomaly	NH Mean	NH Std. Dev.	2024 NH Rank	2024 EUR Rank	2024 NA Rank
Jan	58	–0.2	47.1	1.5	32 (27)	41 (18)	16 (43)
Feb	58	–2.1	45.9	1.8	50 (9)	39 (20)	56 (3)
Mar	58	–2.0	40.4	1.8	51 (8)	46 (13)	45 (14)
Apr	58	–2.6	30.4	1.7	58 (1)	49 (10)	56 (3)
May	58	–1.9	19.0	2.0	45 (14)	40 (19)	53 (6)
Jun	57	–2.6	9.2	2.5	46 (12)	44 (14)	48 (10)
Jul	55	–1.1	3.8	1.2	45 (11)	45 (11)	44 (12)
Aug	56	–0.3	2.9	0.7	33 (24)	51 (6)	23 (34)
Sep	56	–0.5	5.4	0.9	40 (17)	17 (40)	54 (3)
Oct	57	+0.3	18.6	2.6	25 (33)	18 (40)	47 (11)
Nov	59	0.0	34.4	2.1	32 (28)	30 (30)	33 (27)
Dec	59	–1.0	43.7	1.8	47 (13)	39 (21)	44 (16)
Ann	55	–1.2	25.1	0.8	53 (3)	47 (9)	55 (1)

Unauthenticated | Downloaded 11/21/25 11:34 AM UTC

d. Hydrological cycle (atmosphere)

1. SURFACE HUMIDITY

—K. M. Willett, A. J. Simmons, M. Bosilovich, and D. A. Lavers

Global near-surface humidity remained exceptionally high in 2024, with a record-wet annual-mean specific humidity (q) anomaly over both land and ocean (Fig. 2.25; Table 2.6). This was the case for all data products, with record anomalies ranging from 0.32 g kg^{-1} (ERA5) to 0.58 g kg^{-1} (MERRA-2 masked to Met Office Hadley Centre Integrated Surface Dataset of Humidity [HadISDH] coverage) over land and 0.35 g kg^{-1} (ERA5) to 0.56 g kg^{-1} (HadISDH) over ocean. In all cases, 2024 land and ocean q was at least 0.1 g kg^{-1} wetter than in 2023. Global-mean relative humidity (*RH*), excluding MERRA-2, remained below the 1991–2020 baseline over land, between −0.13%rh to −0.71%rh (note that %rh is the unit for relative humidity, which is a percentage of how saturated the air is), meaning that air saturation is still low. However, land *RH* was not as dry as recent years in ERA5 and HadISDH, including 2023. Ocean near-surface *RH* was at or above the long-term mean in 2024. It showed a greater level of saturation than in 2023 in all data products, continuing a moistening tendency from 2020/21 and becoming a record-humid year for HadISDH and the Japanese Reanalysis for Three Quarters of a Century (JRA-3Q). Unlike land and ocean q, as well as land *RH*, there is little temporal agreement between any of the data products. Hence, uncertainty in ocean *RH* is large.

The recent ocean *RH* increase was consistent with the large increase in ocean near-surface water vapor, as inferred by q. This was related to the presence of El Niño from June 2023 to May 2024, which pumped extra moisture into the air in response to the warmer air and sea temperatures. Additional potential drivers of the extraordinarily warm near-surface air temperature in 2023/24 are still being explored (Goessling et al. 2025), including ongoing greenhouse gas emissions, reduced aerosol emissions, unusual heat in the North Atlantic Ocean, reduced low-cloud cover (Goessling et al. 2025), approach to solar maximum (NASA 2024), and additional stratospheric water vapor from the Hunga eruption. If these factors have been sufficient to contribute to global mean temperature, then they will likely also be contributing to the large amount of water vapor (q) and greater saturation (*RH*) compared to recent years.

Notably, previous El Niño events of 1972/73, 1977/78, 1982/83, 1986/87, 1991/92, 1997/98, 2009/10, 2015/16, and even the weak 2020 event are detectable in the global mean land and ocean q records (Figs. 2.25a–d, 2.26a). Associated peaks in *RH* are present but less clear, especially for ocean *RH*, with some events apparent in some data products but not others (Figs. 2.25e–h, 2.26c). Other sources of variability, including observational errors and biases, also contribute to *RH* variability. The 2023/24 El Niño was weaker and shorter (in terms of Niño-3.4 region temperatures) than the 1982/83, 1997/98, and 2015/16 events, making the q and *RH* anomalies even more noteworthy. The 1977/78, 1986/87, 2009/10, and 2023/24 El Niños were preceded by protracted periods of La Niña, which likely suppressed humidity somewhat, resulting in apparently larger increases thereafter. This was evident

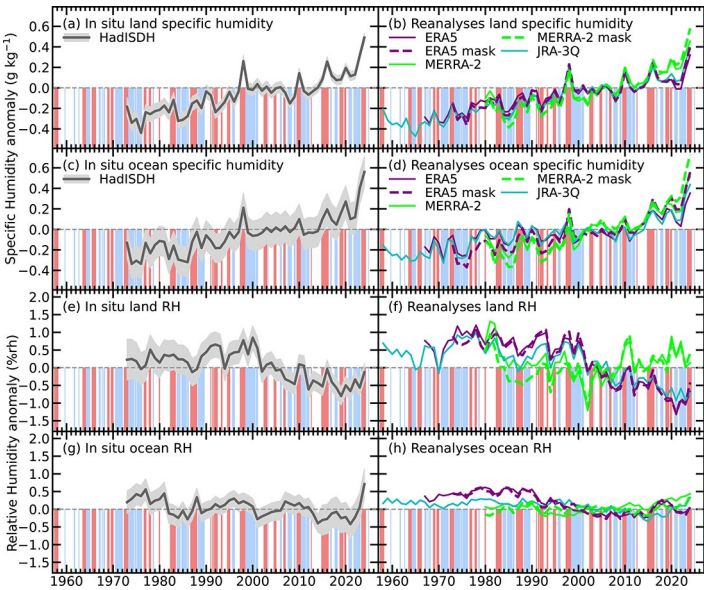

Fig. 2.25. Global average surface humidity annual anomalies (g kg^{-1} for [a]–[d] and %rh for [e]–[h]; 1991–2020 base period). For the in situ datasets, 2-m surface humidity is used over land, and ~10-m surface humidity over the oceans. For the reanalysis, 2-m humidity is used over the whole globe. For ERA5, ocean-series-only points over open sea are selected. ERA5 mask is a version of ERA5 limited to the spatial coverage of the Met Office Hadley Centre Integrated Surface Dataset of Humidity (HadISDH). 2-sigma uncertainty is shown for HadISDH capturing the observation, gridbox sampling, and spatial coverage uncertainty. Pink and blue shading highlights El Niño and La Niña years respectively, as identified by the NOAA Physical Sciences Laboratory Nino-3.4 index using the ±0.5°C threshold. (Sources: HadISDH [Willett et al. 2013, 2014, 2020]; ERA5 [Hersbach et al. 2020]; the Japanese Reanalysis for Three Quarters of a Century [JRA-3Q; Kosaka et al. 2024]; MERRA-2 [Gelaro et al. 2017].)

Unauthenticated | Downloaded 11/21/25 11:34 AM UTC

for q land and ocean but inconsistent for *RH* land and ocean, with differences between data products. Masked versions of MERRA-2 and ERA5, matching HadISDH coverage, show consistently higher q anomalies for recent years than their full-coverage equivalents (Table 2.6). This suggests that HadISDH is undersampling regions with lower q anomalies, which tend to be the drier regions (Simpson et al. 2024). Note that MERRA-2 land *RH* is quite different from that of the other estimates; the reasons for this are an active area of investigation.

Gaps over the drier land regions in HadISDH are clear in Appendix Figs. A2.6 and A2.8, as is the limited ocean coverage, leaving the Southern Ocean and central and eastern tropical Pacific barely sampled. Widespread wet anomalies in q exceeded 1 g kg^{-1} over northern Australia, South and North Korea, Japan, and their surrounding seas, as well as over India, the Caribbean and Central America, part of the North Pacific, and parts of northern tropical Africa. These were common to all data products (Plate 2.1h; Appendix Fig. A2.7) but with slight divergence over the North Pacific region. Anomalously large water vapor amounts were more widespread than

Table 2.6. Global mean surface-specific (q) and relative humidity (RH) anomalies (g kg^{-1} and %rh, respectively) for 2024 and 2023. Note that no previous record is reported for ocean RH because a long-term trend has not been robustly established. Values with a thermometer icon (🌡) identify new record-high values and year of previous highest.

Dataset	q (g kg^{-1}) 2024 Global Mean Anomaly	q (g kg^{-1}) 2023 Global Mean Anomaly	RH (%rh) 2024 Global Mean Anomaly	RH (%rh) 2023 Global Mean Anomaly	RH (%rh) Record low (Year of Record Low)
HadISDH.land	0.49 (2023) 🌡	0.31	–0.13	–0.56	–0.79 (2019)
ERA5 Over Land	0.32 (2016) 🌡	0.17	–0.67	–1.05	–1.32 (2021)
ERA5 Over Land Masked	0.40 (2023) 🌡	0.22	–0.43	–1.02	–1.26 (2021)
MERRA-2 Over Land	0.46 (2023) 🌡	0.33	0.14	0.01	–1.21 (2002)
MERRA-2 Over Land Masked	0.58 (2023) 🌡	0.40	0.40	0.04	–1.10 (2002)
JRA-3Q Over Land	0.38 (2023) 🌡	0.26	–0.71	–0.91	–0.93 (2021)
HadISDH.marine	0.56 (2023) 🌡	0.4	0.71 (1977) 🌡	0.06	-
ERA5 Over Ocean	0.35 (2023) 🌡	0.24	0.03	–0.08	-
ERA5 Over Ocean Masked	0.56 (2023) 🌡	0.39	0.07	–0.18	-
MERRA-2 Over Ocean	0.52 (2023) 🌡	0.42	0.44	0.37	-
MERRA-2 Over Ocean Masked	0.73 (2023) 🌡	0.55	0.39	0.14	-
JRA-3Q Over Ocean	0.44 (2023) 🌡	0.34	0.33 (1959) 🌡	0.10	-

Unauthenticated | Downloaded 11/21/25 11:34 AM UTC

in 2023. Then, the El Niño warm tongue pattern, strong positive Indian Ocean dipole, and high North Atlantic sea surface temperature (SST) patterns were clear. This spreading of positive *q* anomalies is common to many El Niño years. However, the 2023/24 *q* anomalies, in the context of the historical record, were unusually widespread and large (Fig. 2.26a). Despite this, some dry anomalies persisted from 2023 over the Amazon, central and southern Africa, and Mexico, and were actually more widespread and intense.

Positive, more-saturated-than-normal *RH* anomalies were more widespread and stronger than in recent years (Fig. 2.26; Plate 2.1i; Appendix Figs. A2.7, A2.9). Northern and eastern Australia, India, eastern Mongolia and northeastern China, Kazakhstan, and northeastern North America over land were more humid than normal. The positive anomalies over the eastern tropical Pacific, northeast Atlantic, and North Pacific were also notable. As for *q*, more-arid-than-normal anomalies strengthened relative to 2023 over the Amazon, central and southern Africa, and Mexico. HadISDH differs from ERA5 and MERRA-2 by showing less intense negative *RH* anomalies.

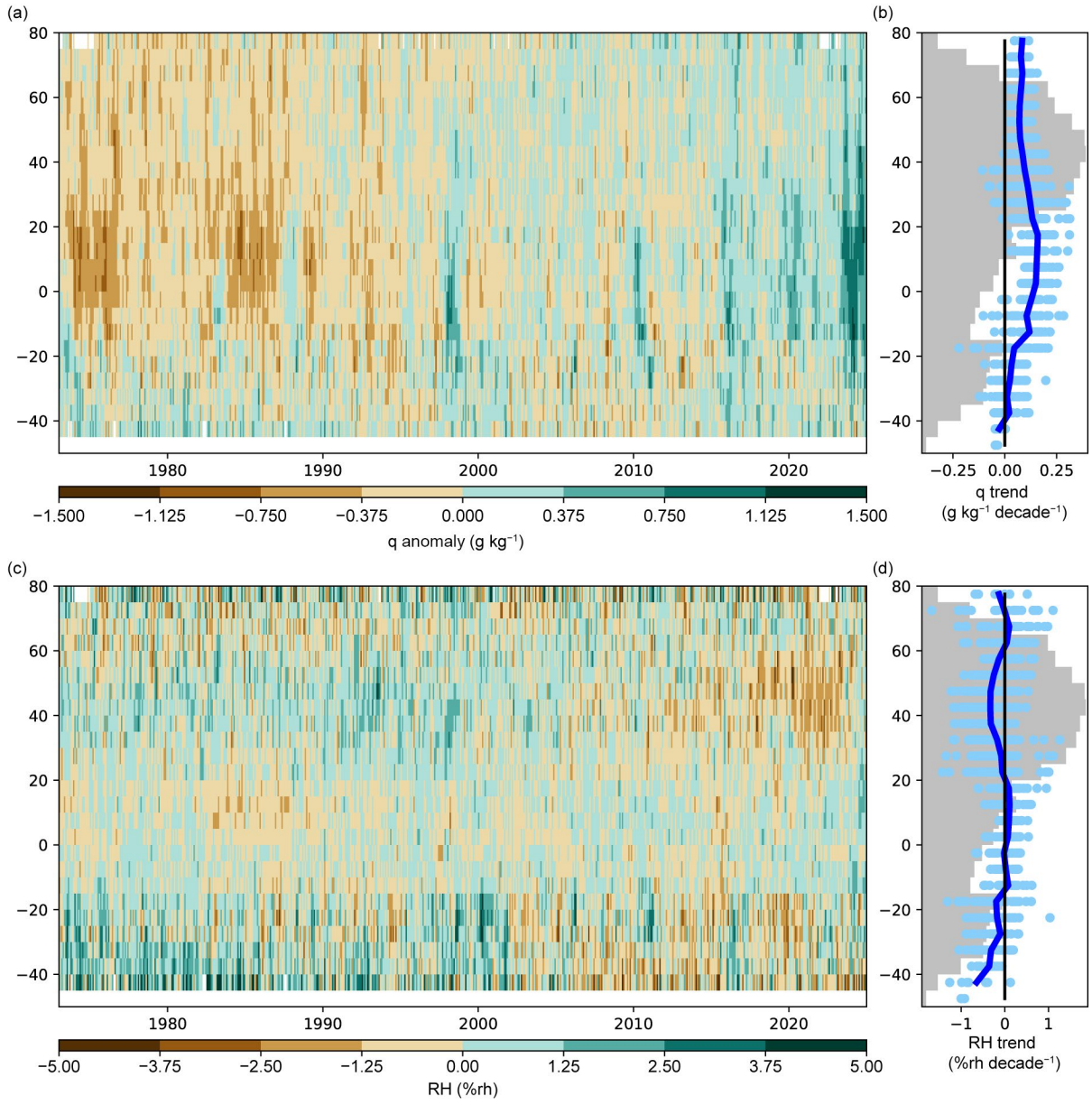

Fig. 2.26. Latitudinal monthly mean anomalies of (a) specific humidity (g kg⁻¹) and (c) relative humidity (%rh) by month from Met Office Hadley Centre Integrated Surface Dataset of Humidity over Land and Ocean (HadISDH.blend). (b),(d) Decadal trends for each gridbox (dots) and latitude band mean (line) are fitted using an ordinary least-squares (OLS) linear regression with an autoregressive (1) correction following Santer et al. (2008), with gray shading representing the percentage of globe covered by observations (in gridboxes) at each latitude band. Latitude band means are only calculated where there are at least five gridboxes (5° × 5°).

Unauthenticated | Downloaded 11/21/25 11:34 AM UTC

2. HUMID-HEAT EXTREMES OVER LAND

—K. M. Willett, R. M. Horton, Y. T. E. Lo, C. Raymond, C. D. W. Rogers, and D. Wang

Following an exceptional increase in the intensity and frequency of high humid heat in 2023, 2024 continued the upward trajectory (Fig. 2.27; Table 2.7). Maximum humid-heat intensity (T_wX; Table 2.7) was 0.5°C higher than the 1991–2020 average and only slightly lower than that of 2023 (0.6°C); where maximum humid-heat intensity is the annual median of the global land median monthly maximum wet-bulb temperature. Remarkably, high daily maximum humid-heat frequency (T_wX90p; Table 2.7) far exceeded the previous record, at 35.6 days above average versus 26.1 days in 2023; where high daily maximum humid-heat frequency is the annual sum of global-mean days per month with daily maximum wet-bulb temperature exceeding the local 90th percentile. These values are based on the gridded HadISDH Extremes (HadISDH.extremes.1.2.0.2024f; Willett 2023a,b,c; Willett et al. 2024) dataset, where monthly indices of daily maximum and minimum wet-bulb temperature are used as a measure of humid heat. Note that for the purposes of this review, "humid heat" is used as an energetic term that includes the contribution of temperature and moisture over the entire globe and annual cycle, rather than a term that focuses exclusively on regions and seasons where temperature and moisture are high.

For all specific thresholds of T_wX exceedance (Fig. 2.27d; Table 2.7), 2024 had record-high frequencies for the second consecutive year. For T_wX25, T_wX27, and T_wX29, these anomalies (with respect to the 1991–2020 base period) were 11.0 days, 13.8 days, and 1.7 days, respectively. T_wX31 anomalies were tied for record most frequent with both 2023 and 1998, at 0.2 days. In much of the tropics, almost every day of the year exceeds the T_w = 25°C threshold. Hence, the maximum possible globally averaged anomaly for T_wX25 is constrained and, therefore, can be less than the anomalies for T_wX27.

In 2024, most global land regions experienced more intense (T_wX) and more frequent (T_wX90p) high daily maximum humid-heat days than the 1991–2020 average (Plates 2.1j,k). High daily maximum humid heat was particularly frequent over India, Southeast Asia, East Asia, Australia, the Caribbean, Central America, and Europe (Plate 2.1k). There were several small regions of negative anomalies, which are mostly consistent between T_wX and T_wX90p; these occurred notably east of the Caspian Sea, in Mongolia, around the Red Sea,

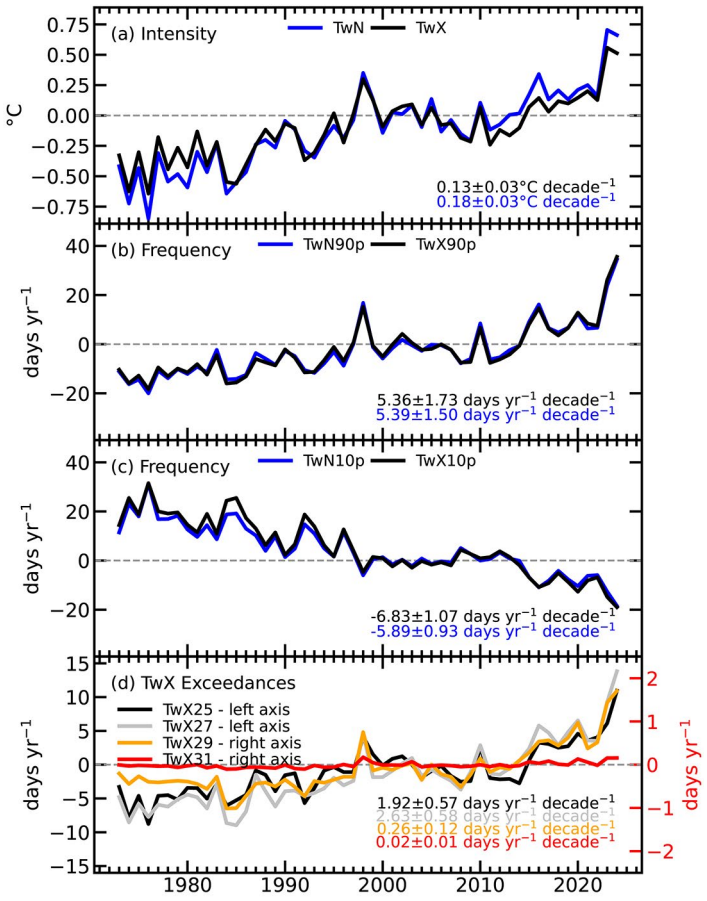

Fig. 2.27. Global land annual anomaly time series of various daily maximum and minimum humid-heat indices from Met Office Hadley Centre Integrated Surface Dataset of Humidity Extremes (HadISDH.extremes), relative to a 1991–2020 base period. Decadal trends (significant at p<0.01) are also shown. Trends were fitted using an ordinary least-squares linear regression with an autoregressive (1) correction following Santer et al. (2008). (a) Anomaly of the annual median of the global median monthly maximum (black) and minimum (blue) wet-bulb temperature (°C). (b) Anomaly of the annual sum of days where maximum (black) and minimum (blue) wet-bulb temperature exceeds the locally defined daily 90th percentile. (c) Anomaly of the annual sum of days where maximum (black) and minimum (blue) wet-bulb temperature is lower than the locally defined daily 10th percentile. (d) Anomalies of the annual sums of days where the maximum wet-bulb temperature ≥25°C, 27°C, 29°C, and 31°C thresholds. Note that coverage is skewed towards the northern extratropical latitudes with large data gaps over Africa, as well as considerable gaps over South America, Australia, and parts of Central Asia (see Plates 2.1j,k for spatial coverage).

Unauthenticated | Downloaded 11/21/25 11:34 AM UTC

in western portions of South America, and in the Sonoran Desert of northwestern Mexico and the southwestern United States.

Figure 2.28 presents 2024 indices by their decile relative to the historical record. Southeast Asia, eastern China, southern Japan, India, and northern Australia stood out as regions where T_wX25 and T_wX27 exceedances were "very unusually frequent" (top decile; Figs. 2.28a,b). This was similar to 2023, but 2024 also had more widespread "very unusually frequent" exceedances for the threshold of T_wX29 (Fig. 2.28c)—notably over eastern China and southern Japan, reflecting a record-setting high-humid-heat event in July and early August. Counting only gridboxes where exceedances of the respective thresholds occurred climatologically (≥15 years within the 1991–2020 period), 24%–37% of the 2024 gridbox-level high-humid-heat frequency fell in the "very unusually frequent" category and just 0%–4% in the "very unusually infrequent" category (not shown).

High humid heat is of particular concern to human health (Xu et al. 2025), including its daily maximum values (Matthews et al. 2025) and nighttime values (Okamoto-Mizuno et al. 1999). This year, four new indices are introduced (Table 2.7). The minimum humid-heat intensity (T_wN) and high daily minimum humid-heat frequency (T_wN90p) are presented. Low humid-heat (i.e., fresh-cool) day frequencies (T_wX10p, T_wN10p) are also introduced, defined in Table 2.7 (Figs. 2.27a–c). Daily minimum wet-bulb temperatures are not always representative of nighttime wet-bulb temperatures, and so that distinction is avoided here.

The time series of T_wN indices closely follow the T_wX equivalents. T_wN in 2024 was well above average (+0.7°C) and only a fraction of a degree cooler than in 2023. T_wN90p was 34.4 days above average in 2024, breaking the record set in 2023 (23.8 days). Overall, 1973–2024 trends in maximum and minimum humid-heat intensity (T_wX = 0.13±0.03 decade^{-1}; T_wN = 0.18±0.03°C decade^{-1}) and

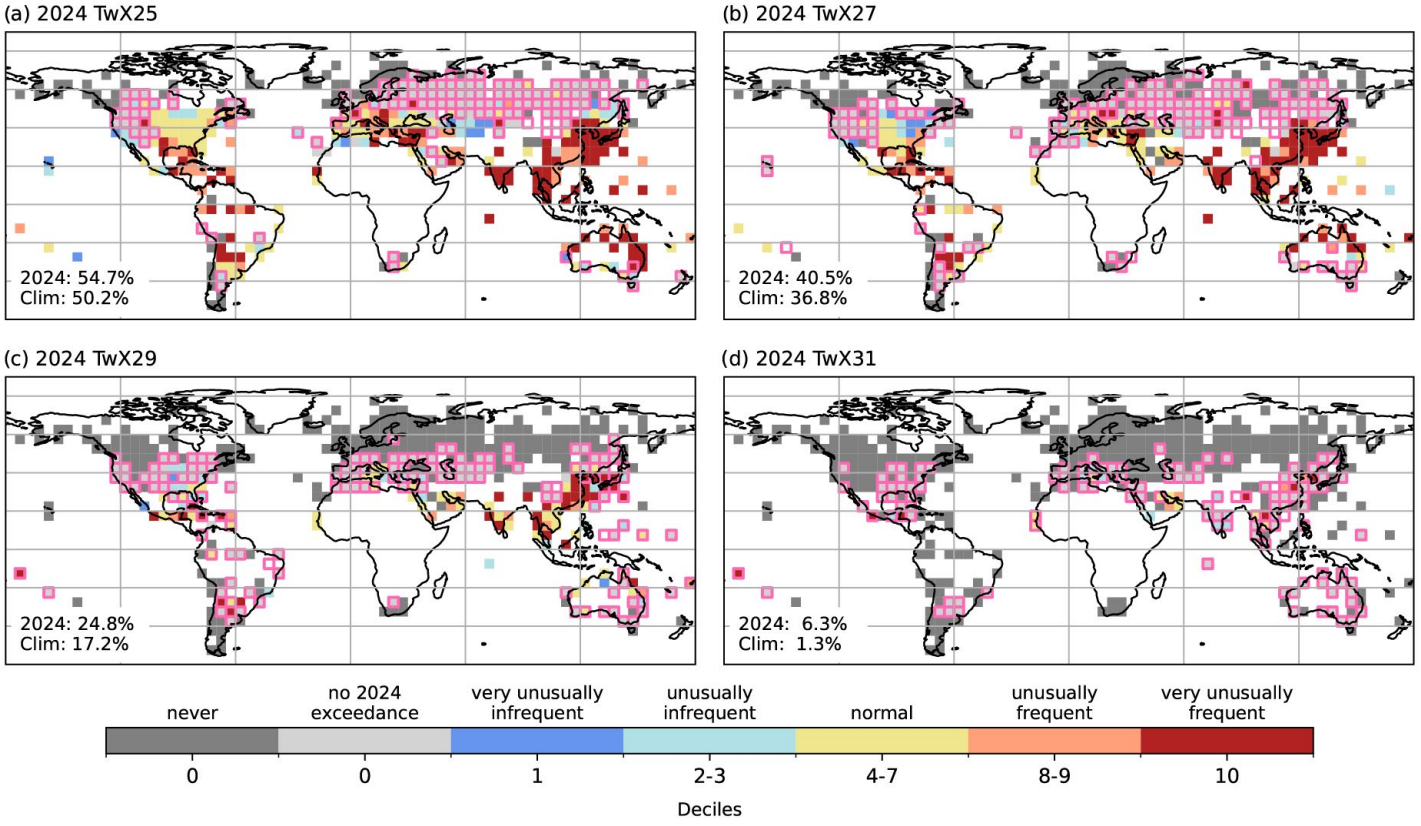

Fig. 2.28. High humid-heat extremes of 2024 as deciles over the period 1973–2024, ranking the number of days with maximum wet-bulb temperature (T_w)≥(a) 25°C (T_wX25), (b) 27°C (T_wX27), (c) 29°C (T_wX29), and (d) 31°C (T_wX31). Gridboxes bounded in pink indicate <15 years within the 1991–2020 period when exceedances occur. These panels are annotated with the percentage of observed gridbox area where an exceedance occurred in 2024 and climatologically (including only gridboxes with ≥15 years of at least one exceedance between 1991 and 2020). Data have been screened to remove gridboxes where temporal completeness is less than 70% (<36 years in 52), with whole years removed if one or more months are missing. White gridboxes (over land) represent regions with insufficient data.

Unauthenticated | Downloaded 11/21/25 11:34 AM UTC

high humid-heat frequency (T_wX90p = 5.36±1.73 days year^{-1} decade^{-1}; T_wN90p = 5.39±1.50 days year^{-1} decade^{-1}) were similar, robustly portraying increasing humid heat. Positive trends for daily minimum humid-heat anomalies for T_wN and T_wN90p (Appendix Figs. A2.10, A2.11) were marginally more ubiquitous than for T_wX and T_wX90p (Plates 2.1j,k).

As for the equivalent dry-bulb temperature extremes (section 2b4; Figs 2.7b,d), frequencies of low humid-heat days (Fig. 2.27c) have decreased substantially, with the rate being slightly stronger than for high humid-heat days, but with the opposite sign. T_wX10p and T_wN10p were 19 days and 18.4 days below the 1991–2020 average in 2024, respectively, both of which were new record lows.

Table 2.7. Definitions of 10 humid-heat indices and their respective recent global land annual anomalies (1991–2020 base period). The global annual anomalies for the exceedance indices (not T_wX or T_wN) are the sum of the monthly spatial means over the globe. For T_wX and T_wN, the median is used as a more robust measure in the presence of outliers, finding the median first over space for each month and then over time.

Index	Description	Meaning	2021 Global Anomaly	2022 Global Anomaly	2023 Global Anomaly	2024 Global Anomaly
T_wX	Annual median of monthly maximum of the daily-maximum wet-bulb temperature	Intensity of maximum humid heat	0.2°C	0.1°C	0.6°C	0.5°C
T_wN	Annual median of monthly minimum of the daily-minimum wet-bulb temperature	Intensity of minimum humid heat	0.3°C	0.2°C	0.7°C	0.7°C
T_wX90p	Days per year exceeding the 90th percentile of the climatological daily-maximum wet-bulb temperature (seasonally varying)	Frequency of high daily-maximum humid-heat days relative to local climatology	8.4 days	7.5 days	26.1 days	35.6 days
T_wX10p	Days per year below the 10th percentile of the climatological daily-maximum wet-bulb temperature (seasonally varying)	Frequency of low daily-maximum humid-heat days relative to local climatology	–8.1 days	–6.8 days	–14.8 days	–19 days
T_wN90p	Days per year exceeding the 90th percentile of the climatological daily-minimum wet-bulb temperature (seasonally varying)	Frequency of high daily-minimum humid-heat days relative to local climatology	6.4 days	6.7 days	23.8 days	34.4 days
T_wN10p	Days per year below the 10th percentile of the climatological daily-minimum wet-bulb temperature (seasonally varying)	Frequency of low daily-minimum humid-heat days relative to local climatology	–6.2 days	–5.9 days	–12.6 days	–18.4 days
T_wX25	Days per year where the daily-maximum wet-bulb temperature was ≥25°C	Frequency of moderately high humid-heat days	3.6 days	4.1 days	6.1 days	11.0 days
T_wX27	Days per year where the daily-maximum wet-bulb temperature was ≥27°C	Frequency of high humid-heat days	3.6 days	3.5 days	9.3 days	13.8 days
T_wX29	Days per year where the daily-maximum wet-bulb temperature was ≥29°C	Frequency of very high humid-heat days	0.4 days	0.5 days	1.4 days	1.7 days
T_wX31	Days per year where the daily-maximum wet-bulb temperature was ≥31°C	Frequency of severe humid-heat days	0.1 days	–0.0 days	0.2 days	0.2 days

Unauthenticated | Downloaded 11/21/25 11:34 AM UTC

3. TOTAL COLUMN WATER VAPOR

—O. Bock, C. A. Mears, S. P. Ho, and X. Shao

In 2024, the global (60°S–60°N) mean total column water vapor (TCWV) was approximately 5% above the 1991–2020 climatological average (Table 2.8), with little difference between ocean and land, according to three global reanalyses (ERA5, MERRA-2, and JRA-3Q) and three observational datasets (Microwave Radiometer [MWR], satellite Global Navigation Satellite System Radio Occultation [GNSS-RO], and ground-based GNSS). It was the wettest year on record across all six datasets and for all three domains (global, ocean, and land), surpassing 2023, which had already set records in some datasets (Fig. 2.29). This remarkable positive anomaly is associated with the unprecedented high global-mean surface temperature (GMST; section 2b1), making 2024 the warmest year in a multi-dataset record dating back to the mid-1800s. The strong correlation between temperature and TCWV anomalies again highlights how tightly the Clausius–Clapeyron relation constrains the global climate system (O'Gorman and Muller 2010). The relation predicts that a GMST anomaly of 0.7°C (actual range was 0.63°C–0.72°C; section 2b1) corresponds to a TCWV anomaly of 4.9%, assuming a scaling factor of 7% per °C. Interestingly, there was a contrast between land and ocean GMST anomalies in 2024, with land slightly warmer than the ocean. This is also reflected in units of kg m^{-2} of TCWV, with ocean TCWV anomalies greater than for land, but not in percentage (Table 2.8). This result suggests a substantial moisture transport from ocean to land on interannual timescales (Trenberth and Fasullo 2013).

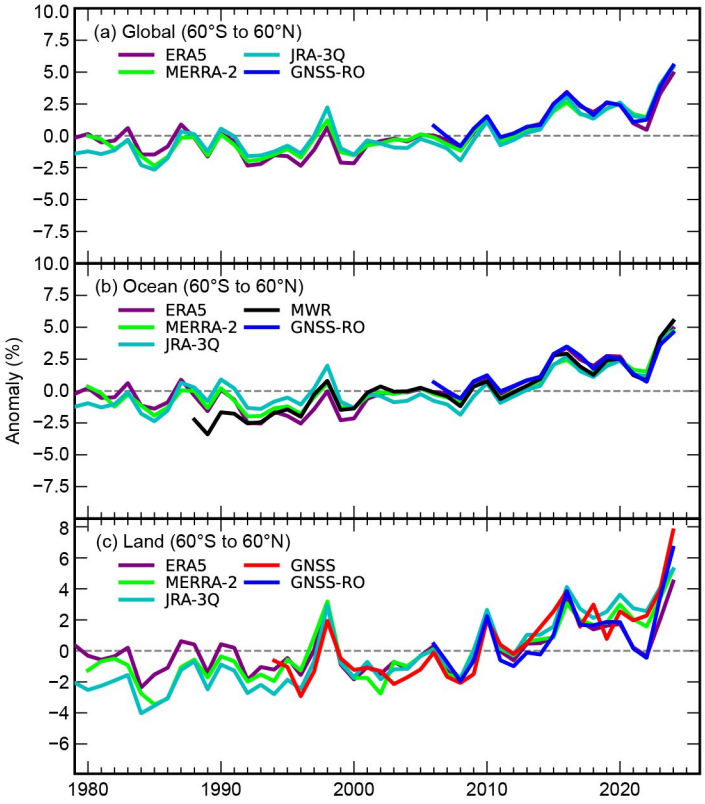

Fig. 2.29. Global mean (60°S–60°N) total column water vapor annual anomalies (%; 1991–2020 base period) over (a) land and ocean, (b) ocean-only, and (c) land-only from observations and reanalyses. The shorter time series from the observations have been adjusted, so there is zero mean difference relative to the ERA5 results during their respective periods of record.

The spatial distribution of TCWV anomalies in 2024 differs markedly from that of 2023, which exhibited a strong El Niño pattern, as well as from the La Niña years of 2021 and 2022 (Bock et al. 2024; Mears et al. 2023). In 2024, the moisture excess was nearly ubiquitous (Plate 2.1l). Almost 90% of the global atmosphere was wetter than the 1991–2020 climatological mean, with approximately 65% of the increase occurring over the oceans and 25% over land. Some regions experienced extreme positive TCWV anomalies reaching 15%–20%, including northeastern Canada, Europe, the Middle East, eastern Asia, and northeastern Australia. Most of these regions are adjacent to oceans that recorded exceptionally high temperature anomalies in 2024, notably the Indian and Atlantic Oceans, polar seas, and the extratropical Pacific.

Figure 2.30a shows the year of record-high TCWV anomaly across the globe from 1988 to 2024 for the JRA-3Q reanalysis, which is consistent with other datasets. Strong moistening (and warming) has particularly been observed in recent years, especially in 2023 and 2024, over the Indian and Atlantic Oceans and most land areas in the Northern Hemisphere. In contrast, the central-eastern Pacific experienced its strongest moist anomaly in 1998 during the exceptional 1997/98 El Niño event. The lower tropospheric temperature set a record in 2024 across most of the tropics, including the tropical Pacific as a whole (Plate 2.1f). Figure 2.30b shows that more than 20% of the globe recorded its highest TCWV anomaly in 2024—far exceeding 2023 (which ranks

Unauthenticated | Downloaded 11/21/25 11:34 AM UTC

Table 2.8. Global mean (60°S–60°N) total column water vapor (TCWV) anomalies (kg m^{-2} (%); 1991–2020 base period) for 2024 and linear trends (kg m^{-2} decade^{-1}) over the period 1991–2024 for reanalyses and Microwave Radiometer (MWR), (*) 2006–24 for Global Navigation Satellite System Radio Occultation (GNSS-RO), (**) 1995–2024 for ground-based GNSS (including 166 stations over land). Note that the inconsistency (ocean anomaly smaller than land) between GNSS-RO anomalies and those from reanalyses and satellites is likely due to the shorter base period.

TCWV Anomalies in 2024, Units in kg m^{-2} (%)						
Dataset	ERA5	MERRA-2	JRA-3Q	MWR	GNSS-RO*	GNSS**
Global	1.32 (4.9%)	1.50 (5.4%)	1.50 (5.5%)		1.45 (5.5%)	
Ocean	1.40 (4.9%)	1.38 (4.7%)	1.59 (5.5%)	1.63 (5.5%)	1.28 (4.6%)	
Land	1.04 (4.5%)	1.26 (5.2%)	1.19 (5.4%)		1.49 (6.6%)	1.48 (7.8%)
Trends over 1991–2024, Units in kg m^{-2} (% decade^{-1})						
Dataset	ERA5	MERRA-2	JRA-3Q	MWR	GNSS-RO*	GNSS**
Global	0.42 ± 0.06 (1.55 ± 0.23)	0.41 ± 0.07 (1.48 ± 0.25)	0.37 ± 0.10 (1.37 ± 0.35)		0.57 ± 0.17 (2.15 ± 0.63)	
Ocean	0.49 ± 0.06 (1.71 ± 0.22)	0.44 ± 0.07 (1.49 ± 0.24)	0.36 ± 0.12 (1.25 ± 0.40)	0.48 ± 0.07 (1.64 ± 0.25)	0.53 ± 0.16 (1.89 ± 0.58)	
Land	0.23 ± 0.07 (0.98 ± 0.29)	0.34 ± 0.08 (1.45 ± 0.35)	0.43 ± 0.06 (1.90 ± 0.28)		0.53 ± 0.20 (2.38 ± 0.90)	0.39 ± 0.08 (2.03 ± 0.47)

second at ~10%) and all previous years, including the three strongest El Niño years within the period (1997/98, 2009/10, and 2015/16).

The pronounced wet anomaly in 2024 significantly impacts the linear trend estimated from 1991 onward. The global-mean linear trend in ERA5 increases from 0.38 kg m^{-2} to 0.42 kg m^{-2} decade^{-1} (1.40% decade^{-1} to 1.55% decade^{-1}) between 2023 (Bock et al. 2024) and 2024 (Table 2.8). This increase is observed over ocean and land and is consistent across all datasets. Over the 34-year period, the total atmospheric water vapor content has increased by nearly 1.4 kg m^{-2} (or 5.1%), assuming an average trend value of 0.4 kg m^{-2} decade^{-1} (1.5% decade^{-1}).

This assessment is based on observations from satellite-borne MWRs over the oceans (Remote Sensing Systems [RSS] satellite; Mears et al. 2018), GNSS-RO data from the Constellation Observing System for Meteorology, Ionosphere, and Climate (COSMIC), Meteorological Operational satellite (MetOp)-A, -B, -C, COSMIC-2, PlanetIQ, Korea Multi-Purpose Satellite-5 (KOMPSAT-5), PAZ, TerraSAR-X (TSX), TerraSAR-X add-on for Digital Elevation Measurement (TDX), and Spire missions (Ho et al. 2020; Shao et al.

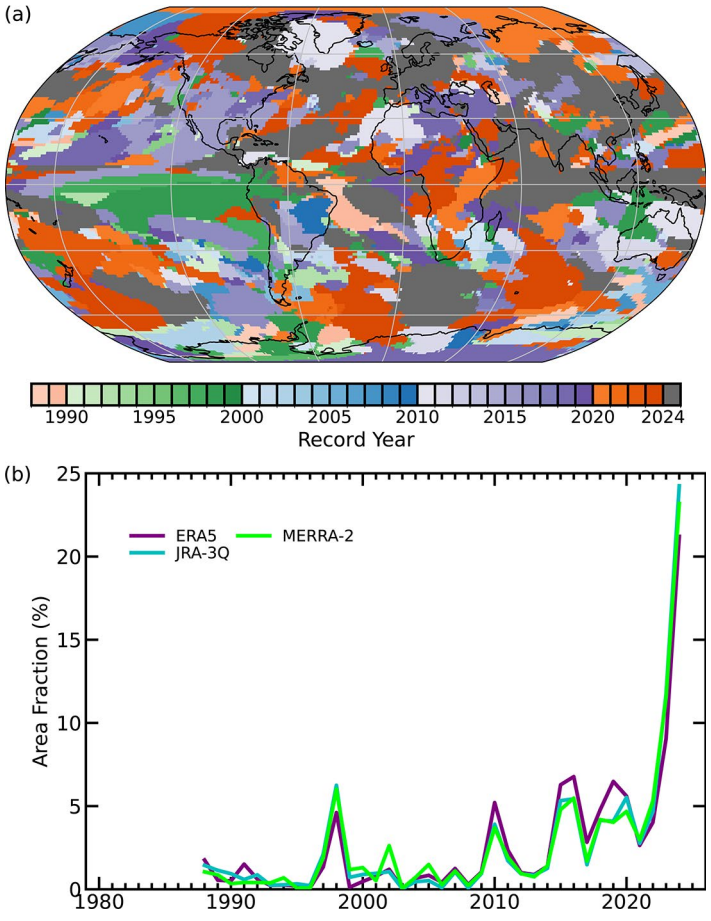

Fig. 2.30. (a) Record years in annual total column water vapor anomalies for the Japanese Reanalysis for Three Quarters of a Century (JRA-3Q) from 1988 to 2024. (b) Fraction of the globe for each year in (a).

Unauthenticated | Downloaded 11/21/25 11:34 AM UTC

2023), covering both land and ocean, as well as ground-based GNSS observations over land and islands (Bock 2025). Three global reanalysis products were used: ERA5 (Hersbach et al. 2020), MERRA-2 (Gelaro et al. 2017), and JRA-3Q (Kosaka et al. 2024). All three reanalyses assimilate satellite microwave radiometer data (as radiances) and GNSS-RO data (as bending angles) but not ground-based GNSS measurements, which serve as an independent validation dataset.

4. UPPER-TROPOSPHERIC HUMIDITY

—V. O. John, L. Shi, E.-S. Chung, T. Stevens, R. P. Allan, S. A. Buehler, and B. J. Soden

The global-mean upper-tropospheric humidity (UTH; %rh) anomalies, shown using relative humidity in Plate 2.1m (based on microwave data) and Fig. 2.31a, were slightly below normal in 2024, especially during the first half of the year (note that %rh is the unit for relative humidity, which is a percentage of how saturated the air is). This is expected during El Niño, which ended in boreal spring 2024, associated with large drier-than-average relative humidity anomalies at tropical and subtropical latitudes over the Pacific Ocean (McCarthy and Toumi 2004). As shown in Plate 2.1m, an annual average anomaly map of UTH in 2024, these drier areas are almost balanced by more humid-than-average anomalies in other areas of the tropics, unlike in 2023 (John et al. 2024). In 2023, there were slightly more areas in the tropics that were more humid than average (central and eastern Pacific, tropical Atlantic, and central Africa), but in 2024 the only substantial areas with above-average humidity were east Africa, the Arabian Sea, central India, northeast Australia, and adjacent areas of the western Pacific.

UTH anomalies, in general, reflect the large-scale circulation patterns. A strong positive phase of the Indian Ocean dipole (IOD) can be seen. Here, the cooler-than-normal eastern Indian Ocean and warmer-than-normal western Indian Ocean led to reduced convection in the east and enhanced convection in the west. There were generally dry conditions over northern South America and moist signatures over central India and the Horn of Africa. Very dry patches over southern Africa indicate ongoing drought in those regions, which began in late 2023. Despite 2023 and 2024 both being dominated by El Niño and a positive IOD, the spatial patterns are different. There were more widespread negative anomalies over North and South America and the western tropical Pacific in 2024 compared to 2023, as well as over eastern Asia and western Australia.

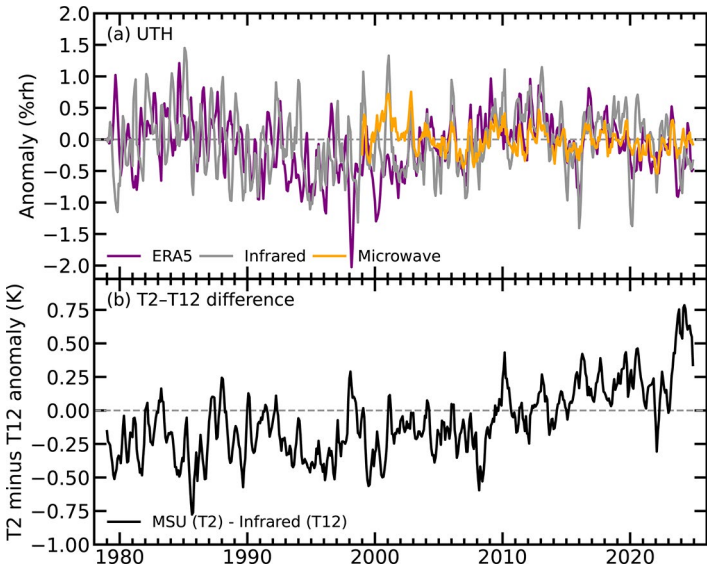

Fig. 2.31. Time series of (a) global monthly-mean anomaly upper-tropospheric humidity (UTH) for the three datasets (%rh; see text for details) and (b) the difference between upper-tropospheric temperature (T2) and water vapor channel (T12) brightness temperatures (K). Anomalies are with respect to the 2001–20 base period.

The mean and standard deviation (1-sigma) of the global monthly anomaly time series (Fig. 2.31) in 2024 were −0.10±0.22 %rh for the microwave based data (Chung et al. 2013), −0.47±0.44 %rh for the infrared based data (Shi and Bates 2011), and −0.31±0.44 %rh for ERA5 data (Hersbach et al. 2020). There is no significant long-term trend in any of the datasets. This is in line with the theoretical consideration that the large-scale relative humidity in the upper troposphere remains roughly unchanged (Ingram 2010). However, the absolute humidity (amount of water vapor) in the upper troposphere has increased. This is illustrated in Fig. 2.31b, which shows the difference between mid-to-upper-tropospheric mean layer temperature (Microwave Sounding Unit [MSU] T2; Zou et al. 2023) and the measured brightness temperature of the 6-μm water vapor channel (High-resolution Infrared Radiation Sounder [HIRS] T12), which is sensitive to the upper-tropospheric relative humidity. As the amount of water vapor in the upper troposphere (UT) increased, the emission level of the water vapor channel shifted higher in the troposphere. This resulted in water vapor emissions being associated with a lower temperature. Therefore, the positive trend in the difference (T2 – T12) time

Unauthenticated | Downloaded 11/21/25 11:34 AM UTC

series indicates moistening of the upper troposphere (Chung et al. 2014; Simmons 2022; John et al. 2024). The differences (T2 – T12) in 2024 were the largest in the series, implying record-high UT absolute humidity in 2024. These strikingly large anomalies are consistent with the presence of El Niño (for a portion of the year) as well as the record-high surface and lower tropospheric temperatures, near-surface specific humidity, and TCWV. The monthly anomalies became substantially less extreme late in 2024 as El Niño dissipated.

5. PRECIPITATION

—M. Ziese, R. S. Vose, R. Adler, G. Gu, and X. Yin

Precipitation is the primary source of fresh water needed for drinking, agriculture, hydropower, human wellbeing, and many other purposes. Both a lack (drought) and excess (e.g., flood) of water can have a large impact on human activities. The analyses presented here are based on data from two datasets: in situ from the Global Precipitation Climatology Centre (GPCC; Becker et al. 2013) and gauge-adjusted (including GPCC) satellite data from GPCP Version 3.2 (Huffman et al. 2023).

In 2024, excess precipitation (relative to the 1991–2020 baseline) was observed across much of the tropics (land and ocean; Fig. 2.32), Asia, and the northwestern Pacific, as well as the northern and southern subtropical Atlantic. A precipitation deficit occurred over southern Africa, the southeast Indian Ocean, the subtropical Pacific, South America, and the North Atlantic.

Globally, 2024 was the third-wettest year since 1983 (Fig. 2.33c; GPCP dataset only). While global land precipitation was around normal, precipitation over the oceans was far above normal, only exceeded by that of 1998, 2015, and 2016. The unusual high precipitation totals over the oceans (shown across the seasons in Fig. 2.32 but not in the land-only Plate 2.1n), were likely associated with above-normal sea surface temperatures (Plate 2.1a), which produced more regional evaporation (Plates 2.1h,l) and water for rainfall. This can be seen, for example, over the Gulf of America/Gulf of Mexico, Caribbean, and adjacent western Atlantic (Fig. 2.32) as well as over the Indian Ocean, western Pacific and South Pacific Convergence Zone, and northwestern Pacific. High ocean precipitation could be associated with the 2023/24 El Niño event; previous large El Niño events of 1997/98 and 2015/16 also preceded precipitation excess over the oceans.

Spatial variability of precipitation is higher compared to other atmospheric parameters such as air temperature. Therefore, precipitation totals as well as anomalies show a patchy pattern, where

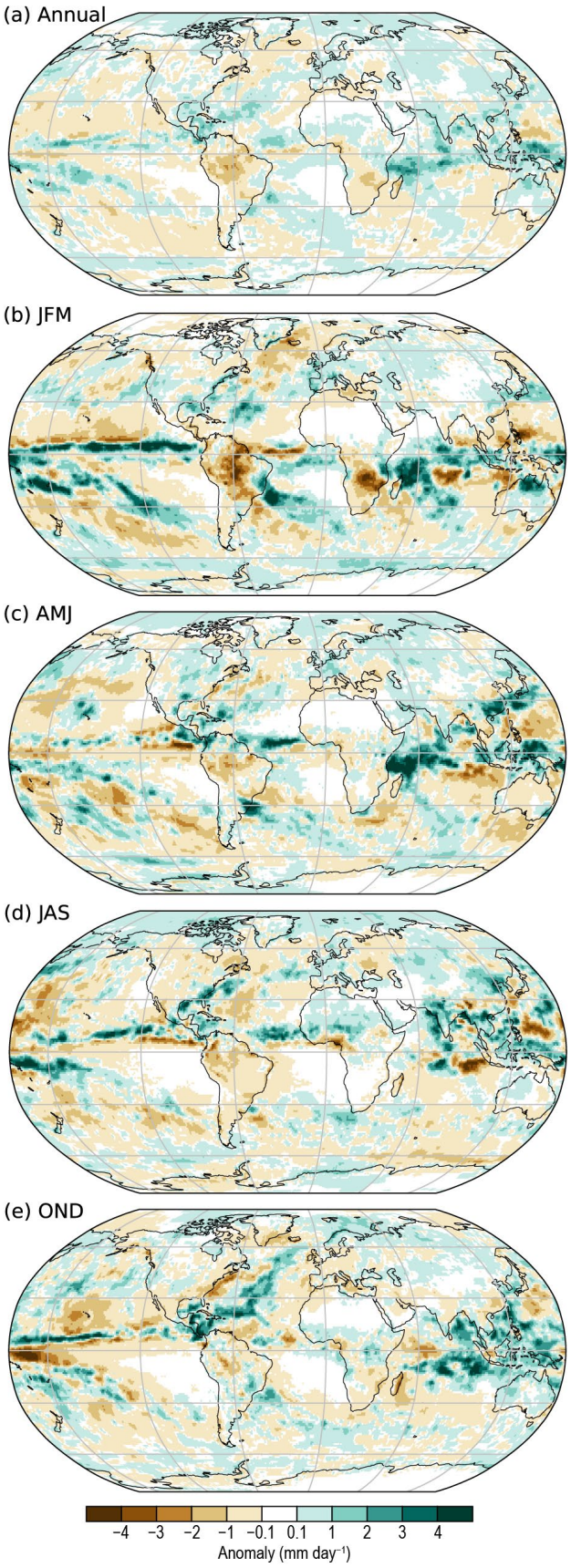

Fig. 2.32. 2024 annual and seasonal precipitation anomalies (mm day^{-1}; 1991–2020 base period) for (a) annual, (b) Jan–Mar (JFM), (c) Apr–Jun (AMJ), (d) Jul–Sep (JAS), and (e) Oct–Dec (OND). (Data source: Global Precipitation Climatology Project [GPCP].)

Unauthenticated | Downloaded 11/21/25 11:34 AM UTC

regions with excess precipitation (above the long-term mean) can be close to those with a precipitation deficit (below the long-term mean).

Focusing on land regions (Plate 2.1n), excess rainfall was observed in many parts of central and eastern Africa as well as in the Sahel region. Lower-than-usual rainfall was measured in southern Africa and western central Africa, reflecting drier-than-usual wet seasons. Madagascar and northwest Africa were also drier, having experienced multi-year drought (since 2020 and 2019, respectively; Fig. 2.32). These correspond with negative soil moisture anomalies (section 2d11).

Conditions were drier than usual in the Hindu Kush, parts of Southeast Asia, the Philippines, around the Laptev Sea in the Arctic, and also around the Himalayas. The latter was associated with a dry early monsoon season. Above-normal annual precipitation was mainly observed in the east, southeast, southwest, and northwest of Asia. All seasons were wetter than usual in northwestern and eastern Asia. Southern Asia exhibited strong wet anomalies in July, August, and September, but was otherwise mostly drier than usual.

In the Amazon basin, the drought that began in 2023 continued in 2024; all seasons were drier than usual (Fig. 2.33). While the majority of South America was drier than usual, some spots in the north, southeast, and south, such as western Patagonia, received excess precipitation (see section 7d for details).

Excess precipitation occurred across North America from the central Rocky Mountains to Florida (Plate 2.1n). Also, southern Central America and parts of the Caribbean, as well as some spots in north and northwest North America, were wetter than normal. Northern Central America, the northern Caribbean, and northeast and northern central North America were drier than usual.

The coastal regions in southern (including Tasmania), northwestern, and northeastern Australia had below-normal precipitation, as did smaller islands in the Pacific Ocean. The Maritime Continent, parts of northern, eastern, and western Australia, and some spots in New Zealand were wetter than normal.

Western and Central Europe as well as Scandinavia received more precipitation than the long-term mean. Eastern and southeastern Europe, the Middle East, and the region northward of the Black Sea were drier than normal.

The state of ENSO (El Niño–Southern Oscillation) influences regional precipitation patterns. El Niño conditions were present at the beginning of the year, then decreased and reached neutral conditions by April–June, which prevailed until the end of the year when weak La Niña-like conditions emerged. Associated with the El Niño conditions in the first months of the year are the below-normal precipitation totals in southern Africa and above-normal totals in eastern Africa, along with the wet conditions in East Asia, in southwestern North America, and northward of the Gulf of America/Gulf of Mexico (Fig. 2.32). These conditions dissipated by the latter half of 2024. Due to the ENSO-neutral conditions later in the year, corresponding seasonal anomalies were attributed to regional circulation and year-to-year variability.

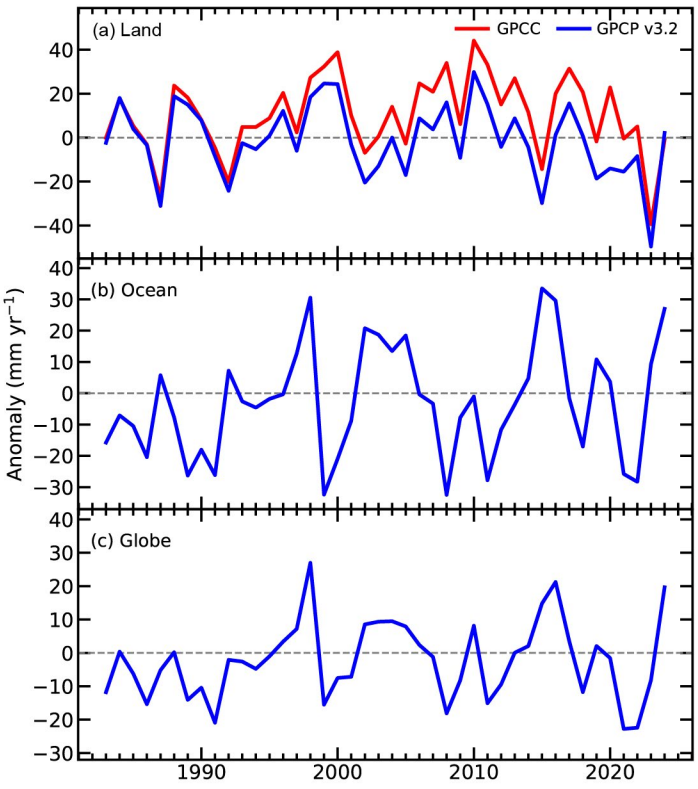

Fig. 2.33. 2024 globally averaged annual precipitation anomalies (mm yr^{-1}) relative to the 1991–2020 baseline period for (a) land areas, (b) ocean areas, and (c) globally (land and ocean).

Unauthenticated | Downloaded 11/21/25 11:34 AM UTC

6. LAND SURFACE PRECIPITATION EXTREMES

—M. R. Tye, S. Blenkinsop, M. G. Bosilovich, I. Durre, C. Lennard, I. Pinto, A. J. Simmons, and M. Ziese

Globally, 2024 was the wettest year on record with respect to extreme precipitation. The global-mean annual maximum daily precipitation total (Rx1day) from station and reanalysis records surpassed the previous record years of 2010 and 2020 (Fig. 2.34a).

More than two-thirds of the globe experienced unusually high precipitation (section 2d5), with attendant record-breaking extremes mostly occurring within the tropical belt. Many extremes occurred anomalously within extended droughts (sections 2d11, 2d12) or were seasonally unusual (e.g., during a dry season or during winter).

The strong El Niño in the first quarter, as well as the La Niña-like pattern that it transitioned to in the last quarter, both supported intensified precipitation extremes due to the accumulated atmospheric moisture associated with higher temperatures. Coupled with record ocean temperatures (see sections 2b1, 3b; Cheng et al. 2025), these conditions drove abnormally intense and clustered typhoons in the western Pacific (Cassidy 2024) and increased the distance of inland moisture transport into China (WWA 2024a). Cut-off lows across the North Atlantic spurred increased convective activity, which resulted in several record short-duration (sub-daily) rainfall totals. This activity included Storm Boris, which affected a large area in central Europe in September (see Sidebar 7.2; Magnusson et al. 2025), and intense rainfall that resulted in catastrophic flooding in Valencia, Spain, in October (see section 7f4; Pucik 2024). ENSO-associated shifts in the Intertropical Convergence Zone also impacted the locations of monsoonal systems and contributed to longer-duration precipitation extremes. A more-intense-than-normal hydrological cycle was apparent through connected mechanisms: above-normal air temperatures (section 2b1) and SSTs (sections 2b1, 3b), above-average seasonal precipitation (section 2d5), high soil moisture anomalies (section 2d11), high evaporation over land (section 2d13), high water vapor content (sections 2d1, 2d3), and the resultant precipitation maxima.

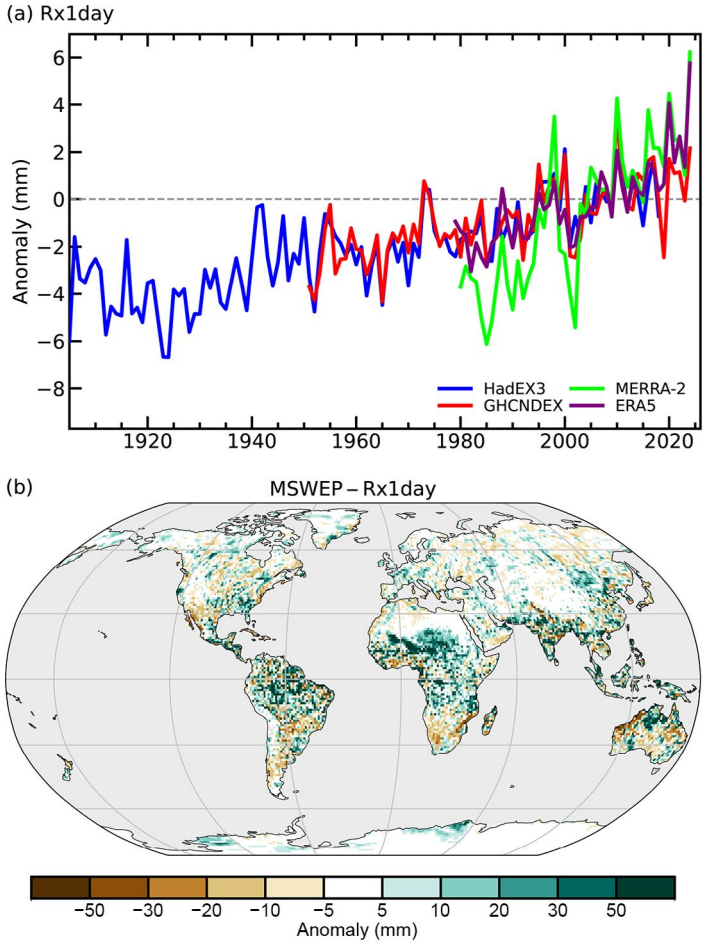

Fig. 2.34. (a) Global mean anomaly (with respect to 1991–2020) of one-day maxima (Rx1day) over land from the Met Office Hadley Centre Extremes dataset version 3 (HadEX3; Dunn et al. 2020), Global Historical Climatology Network Daily Extremes dataset (GHCNDEX; Donat et al. 2013), ERA5 (Hersbach et al. 2020), and MERRA-2 (Gelaro et al. 2017). (b) Global Rx1day anomalies in 2024 with respect to the 1991–2020 mean from Multi-Source Weighted-Ensemble Precipitation (MSWEP; Beck et al. 2019) highlighting a band of wet anomalies across the tropics.

Plate 2.1o and Figs. 2.34b, 2.35 show similar regions of wetter-than-normal one-day/accumulated five-day maxima (Rx1day, Rx5day) in a band between 30°S and 30°N. Higher latitudes experienced pockets of abnormal extreme precipitation within larger areas of drought conditions. Record-breaking accumulations, where noted, are limited by the availability of reliable long-duration observations.

At the continental scale, Australia experienced one of its wettest years on record (see section 7h4) with accompanying wetter-than-average precipitation maxima over the Northern Territory. Following record-breaking Rx1day/Rx5day in January, the transition to La Niña-like conditions

Unauthenticated | Downloaded 11/21/25 11:34 AM UTC

later in the year resulted in less severe precipitation extremes over Australasia compared with the rest of the globe (WMO 2024).

Despite fewer-than-normal typhoons in the western North Pacific (see section 4g4 for details), the season brought exceptionally heavy Rx1day/Rx5day and induced extensive flooding across the Philippines and surrounding countries in Southeast Asia in July and September (Tandon 2024). An exceptional clustering of six active typhoons occurred in the basin in less than a month in late October and November, further compounding the impacts of previous extreme precipitation (Cassidy 2024). As part of an active North Atlantic hurricane season (see section 4g2), a series of tropical cyclones developed in September and October. Notably, Hurricanes Helene and Milton each rapidly intensified, with Rx5day totals doubling previous records over parts of the eastern United States.

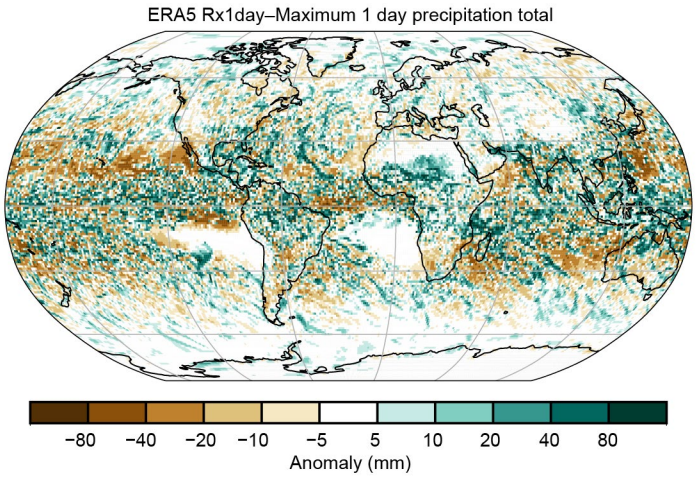

Fig. 2.35. 2024 accumulated one-day maxima (Rx1day; mm) anomalies from 1991–2020 from ERA5.

Precipitation extremes in southwestern Asia arose from the wetter-than-average monsoon and pre-monsoon (April–June), as the Indian Ocean experienced a below-average year for cyclones (see sections 4f, 4g5). Widespread heavy precipitation and flash floods over Pakistan and Afghanistan in April (Pakistan Meteorological Department 2025) were succeeded by record-breaking sub-daily precipitation in Lahore, Pakistan, in August (DW 2024). The highest multi-day precipitation in over 50 years occurred over northeast India and Bangladesh in August (Pandey and Sengupta 2024; Kamal et al. 2024), and Nepal in September (WWA 2024b).

A series of unusual Rx1day/Rx5day values occurred in otherwise arid or drought-affected countries surrounding the Mediterranean, the Persian Gulf, northeastern Africa, and the Sahel (section 2d5), all connected to active convection systems from cut-off lows. These included: the heaviest Rx1day in 75 years over northern Oman and the United Arab Emirates in April (Zhang et al. 2025); a series of heavy events that together generated the highest July rainfall total (since records began in 1956) at Cape Town International Airport in South Africa, triple its monthly climatology (South African Weather Service 2024); Rx1day and Rx5day each exceeding the monthly climatology in Morocco, Niger, and Nigeria in September; and historic hourly precipitation in southeastern Spain in late October (Kothari 2024). Torrential rain also occurred over Kenya and Tanzania in April, South Africa in June, and central Africa throughout July and August (NOAA NCEI 2025a).

Europe was affected by heavy precipitation throughout the year (ECMWF 2025). Geographic clusters of record-breaking Rx1day and Rx5day include France in April, Germany and the Netherlands in May and June, Poland and Czechia in September, and the United Kingdom and Ireland in November (see section 7f for details).

While much of Central and South America were in extended drought, isolated intense precipitation occurred across southwestern Brazil, Uruguay, and Argentina in March. Rio Grande do Sul experienced record-breaking Rx1day in April and May (see Sidebar 7.1; Zhang et al. 2025). Near-record precipitation also fell over Colombia and Bolivia during November (NOAA NCEI 2024; see section 7d).

7. CLOUDINESS

—C. Phillips and M. Foster

Cloud area fraction increased in 2024 compared to the record low observed in 2023. According to PATMOS-x observations (Foster et al. 2023; Fig. 2.36), global-mean cloud area fraction was significantly higher (0.4%) than in 2023. This is consistent with the Clouds and the Earth's Radiant Energy System (CERES) EBAF-TOA Ed4.2.1 cloud radiative effect data (Loeb et al. 2018). Compared to 2023, the global-mean shortwave cloud radiative effect (SWCRE) was 0.66 W m^{-2} more

Unauthenticated | Downloaded 11/21/25 11:34 AM UTC

"reflective", and in the longwave, global-mean cloud radiative effect (LWCRE) was 0.07 W m^{-2} more "insulating" in 2024. Combining shortwave and longwave changes (–0.59 W m^{-2}), the global-mean net cloud radiative effect corrected from the large 2023 anomaly such that 2024 was only 0.02 W m^{-2} above the 2000–20 average (–17.81 W m^{-2}).

Plate 2.1p shows the annual anomalies of cloud area fraction in 2024 compared to the 1991–2020 average. In 2023, the tropical Indian Ocean had an extremely low cloud area fraction, but it returned to normal levels in 2024. Southern Africa and South America saw below-average cloud area fraction, which aligns with observations of below-average water vapor and precipitation in these regions (Plates 2.1l,n).

Although cloud area fraction increased from 2023 to 2024, it remained well below the long-term average (–1.49% relative to 1991–2020) and was the second lowest since records began in 1980 (Fig. 2.36). Similarly, although greater than 2023, the CERES shortwave cloud radiative effect was both less reflective (SWCRE: –0.57 W m^{-2}) and less insulating (LWCRE: –0.55 W m^{-2}) than the long-term 2000–20 average. These findings of below-average cloud area fraction are consistent with the theory of a long-term trend of decreasing cloud cover discussed in previous reports (Phillips and Foster 2024). For example, global-mean shortwave cloud radiative effect has been trending towards less "reflective" (–0.44 W m^{-2} $decade^{-1}$), and the global-mean longwave cloud radiative effect has been trending towards less "insulating" since 2000 (–0.39 W m^{-2} $decade^{-1}$).

As an experiment, a GEO-Ring composite of Geostationary Operational Environmental Satellites (GOES)—namely GOES-16 and GOES-18—along with Himawari-9, Meteosat-9, and Meteosat-10, was processed for every six hours in 2024. Figure 2.37a shows the diurnal range of annual average cloud area fraction for 2024, in other words the difference in cloud between the peak and the trough time of day. The diurnal range of cloud area fraction for any given location is low, with an average value of 7.8%. Figure 2.37b shows the diurnal cycle of global-mean cloud area fraction for 2024. This is even smaller because some regions cancel each other out when the global mean is calculated. However, there are some regions with much higher diurnal variability. Most salient are the regions of stratocumulus clouds off the west coasts of continents. These

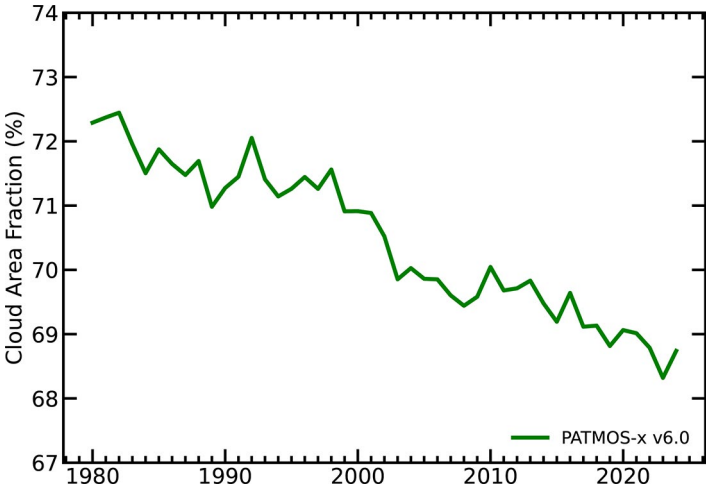

Fig. 2.36. Global annual mean cloud area fraction (%) from PATMOS-x v6.0.

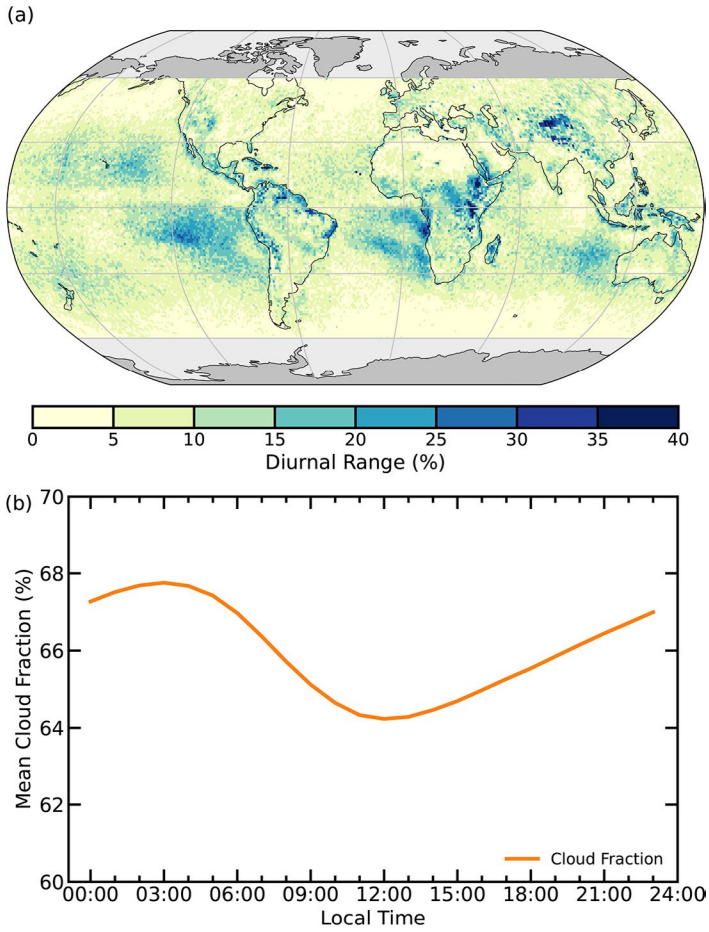

Fig. 2.37. The annual mean (a) diurnal range over the globe and (b) annual global mean diurnal cycle of average cloud area fraction (%) for 2024, as observed by the GEO-Ring composite of Geostationary Operational Environmental Satellite (GOES)-16, GOES-18, Himawari-9, Meteosat-9, and Meteosat-10.

Unauthenticated | Downloaded 11/21/25 11:34 AM UTC

regions should be considered carefully when performing cloud climatological studies, as the timing of observation can have a large impact on the results. The PATMOS-x observations used here (Plate 2.1p; Fig. 2.36) come from satellites with drifting observation times and must be corrected for such diurnal effects, though corrections to the 2024 global mean are negligible. Between 2023 and 2024, the NOAA-18 satellite drifted from 10:31 to 10:41 local time for morning equatorial crossing, NOAA-19 drifted from 08:37 to 09:17, and NOAA-15 drifted from 07:28 to 07:21 local time. Drift in the morning overpass is mostly cancelled by drift in the afternoon overpass such that the expected ensemble-mean effect is −0.03%, much smaller than the observed increase in cloud area fraction (0.4%).

Unauthenticated | Downloaded 11/21/25 11:34 AM UTC

d. Hydrological cycle (land)

8. LAKE WATER STORAGE AND LEVEL

—M. E. Harlan, M. F. Meyer, E. S. Levenson, S. Cooley, and B. M. Kraemer

In 2024, water storage and levels across 4487 lakes exhibited slight overall increases compared to a 1993–2020 baseline period based on two global datasets. Lake storage analysis was based on the GloLakes dataset (Hou et al. 2024; 4190 lakes, median area 5.52 km^2), and lake level was analyzed using the Global Reservoirs and Lakes Monitor (GREALM) dataset (Birkett et al. 2011; 297 lakes, median area 449.2 km^2). Relative to the 1993–2020 baseline, median storage increased by 1.61% in 2024, representing a median rise of 0.295 million cubic meters (MCM). The median lake level increased by 0.12 m, with anomalies ranging between −53 m and +28.9 m. However, marginal global changes obscured more substantial regional changes. After combining both datasets, level or storage increased in 57.8% and decreased in 42.2% of lakes relative to the baseline. A Welch's t-test comparing level and storage observations in 2024 relative to the baseline identified some of these trends as statistically robust (25.6% increased and 16.5% decreased; p<0.05). Long-term trends from these two datasets sometimes diverged (Fig. 2.38) and may not be representative of all lakes globally.

Regional patterns in lake storage were observed. Countries with the largest mean increases relative to the baseline included Syria, Senegal, Belize, Cambodia, Angola, Bangladesh, Sudan, and Libya (+23.4% to +84%), while decreases were most prominent in Niger, Chad, Mongolia, Algeria, Namibia, Argentina, Botswana, and Bosnia and Herzegovina (–20% to –74.8%). For lakes with substantial storage anomalies (>±20%), a weak positive correlation (r^2 = 0.11) between increased storage and higher ERA5 precipitation in 2024 was found, suggesting partial climatic influence (Hersbach et al. 2020). However, it is not advisable to overinterpret these country-level trends given the limited and uneven sampling of lakes, which may not capture broader hydrologic dynamics.

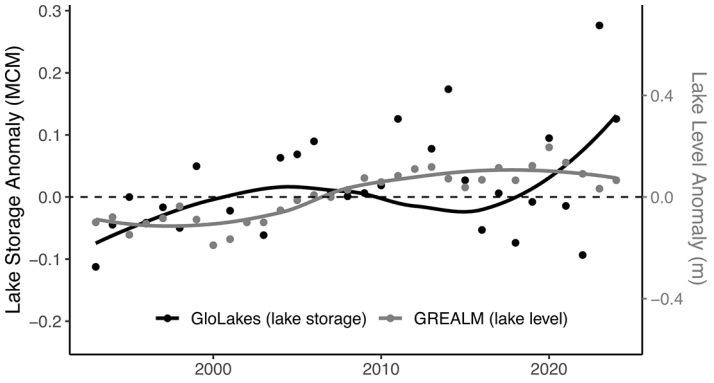

Fig. 2.38. Lake water storage and level anomalies relative to a baseline averaged period of 1993–2020 across each year from 1993 to 2024. Yearly median water storage (black) and level (gray) anomalies averaged across each water body are shown on dual y axes, expressed in million cubic meters (MCM) for lake water storage anomalies and meters (m) for lake water level anomalies. Local regression (loess) smoothing is applied to the annual median anomalies represented by the two curves.

Storage anomaly variance across binned lake sizes and between lakes classified as 'natural' or 'reservoir' was also analyzed using the Global Reservoir and Dam Database (Lehner et al. 2011). Statistically robust differences in storage variance were found across area bins and classifications (p<0.05; Levene's test for homogeneity of variance; Levene 1960), with smaller lakes and reservoirs showing higher anomaly variability (Fig. 2.39). The prevalence of both increasing and decreasing lake trends aligns with previous studies (Kraemer et al. 2020; Y. Feng et al. 2022). Discrepancies in global storage trends compared to more recent work (Yao et al. 2023) are likely a reflection of dataset differences. Continual monitoring of lake anomalies is critical for more accurately predicting dynamics in water availability, ecosystem resilience, and flood and drought risk (e.g., Weyhenmeyer et al. 2024; Han et al. 2024).

Both lake datasets incorporate remote sensing data to estimate storage (GloLakes) or level (GREALM). GloLakes combines Ice, Cloud, and land Elevation Satellite 2 (ICESat-2)

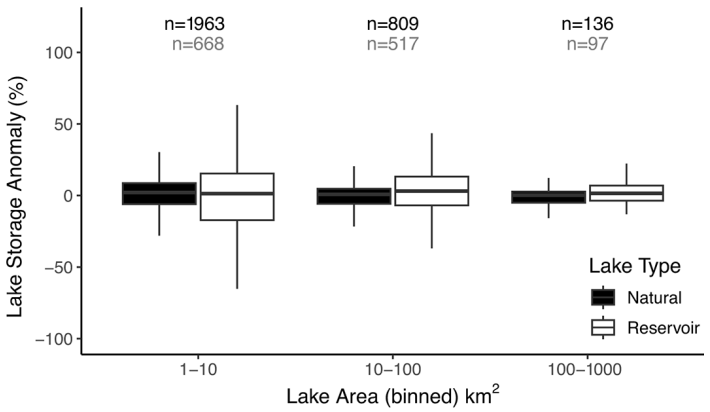

Fig. 2.39. Annual lake storage anomalies (%) for 2024 relative to 1993–2020 binned by lake size, and categorized as "natural" or "reservoir" based on inclusion in the Global Reservoir and Dam Database (Lehner et al. 2011). Lake bin counts (n) are displayed on top (black font) and reservoir counts are shown on bottom (gray font).

Unauthenticated | Downloaded 11/21/25 11:34 AM UTC

laser altimetry (Jasinski et al. 2023), GREALM radar altimetry data, and optical imagery from Landsat and Sentinel-2. The GloLakes dataset was refined by selecting lakes with at least 20 years of data, no data gaps longer than three years, and at least three observations in 2024. These 4190 lakes represent just 0.89% of global lake volume (HydroLAKES; Messager et al. 2016). To improve volume coverage, GREALM lake level data (Birkett et al. 2011) is also incorporated, adding an additional 297 lakes covering 88.7% of HydroLAKES volume. Anomalies are reported relative to a 1993–2020 baseline, consistent with GREALM availability. Both datasets are limited in spatiotemporal coverage globally, with overrepresentation in North America (Plate 2.1q) and underrepresentation in small (<1 km^2) lakes (Fig. 2.39), which dominate global lake area and storage variability (Pi et al. 2022; Xu et al. 2024). Further, satellite-based estimates of storage may not fully capture fine-scale temporal dynamics. Among the 85 lakes shared between GloLakes and GREALM, the median correlation coefficient (r^2) across each lake between storage and level anomalies was 0.361, yet 82.3% of lakes agree on 2024 anomaly direction. For the lakes present in both datasets, only anomalies for GREALM are provided, given the denser interannual record. Future integration of data from the recently launched Surface Water and Ocean Topography (SWOT) satellite mission or data from longer missions such as the Moderate Resolution Imaging Spectroradiometer (MODIS) may help increase spatiotemporal coverage.

9. RIVER DISCHARGE AND RUNOFF

—J. Casado-Rodríguez, S. Grimaldi, and P. Salamon

From the perspective of river discharge and runoff, 2024 was another dry year, continuing a trend of four consecutive years of below-normal global runoff (Fig. 2.40) and six years with below-normal global river discharge (Fig. 2.41).

Globally, runoff in 2024 exhibited drier-than-usual conditions compared with the reference period 1991–2020 (Fig. 2.40). However, this anomaly was not as pronounced as in 2023, which remains the driest year in the time series. A shift towards normal conditions was observed, likely associated with the transition from El Niño at the beginning of the year to a neutral phase (Oceanic Niño Index in Fig. 2.40; see section 4b for details). Additionally, 2024 was characterized by an intense negative phase of the Pacific Decadal Oscillation (PDO), which was the most negative since 1980. Despite this overarching pattern, significant regional differences were observed (Plate 2.1r). The Amazon, La Plata, and Congo basins experienced an extremely dry year (Toreti et al. 2024c). The anomaly in the Congo is partially attributed to an erroneous negative trend in the ERA5 precipitation over this region (section 2d5; Lavers et al. 2022; Liu et al. 2024). Drought conditions also affected the Atlantic and Pacific coasts of North America,

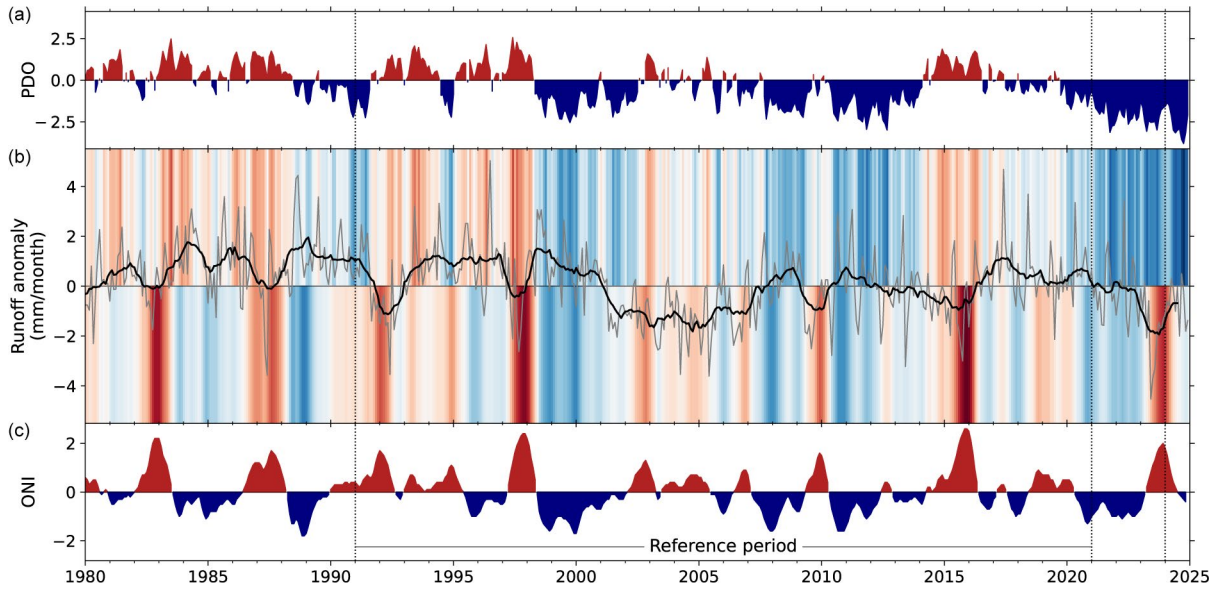

Fig. 2.40. Interannual variability of global runoff (b) and its connections with the (a) Pacific Decadal Oscillation (PDO) and (c) Oceanic Niño index (ONI). In panel (b), the gray line represents the monthly time series of anomalies compared with the base period 1991–2020, the black line represents the 12-month moving average, and the shading indicates the phase of the two indices (PDO in the upper part and ONI in the lower part).

Unauthenticated | Downloaded 11/21/25 11:34 AM UTC

southeastern Europe (Toreti et al. 2024b), Southeast Asia, and parts of Siberia. Conversely, Central America, Central and Northern Europe, the Indian subcontinent, the Pacific coast of Asia, and insular Southeast Asia experienced wetter-than-usual conditions.

A similar pattern was observed in freshwater discharge into the oceans, which remained below normal overall, though with notable regional variations (Fig. 2.41; Plate 2.1s). Discharge

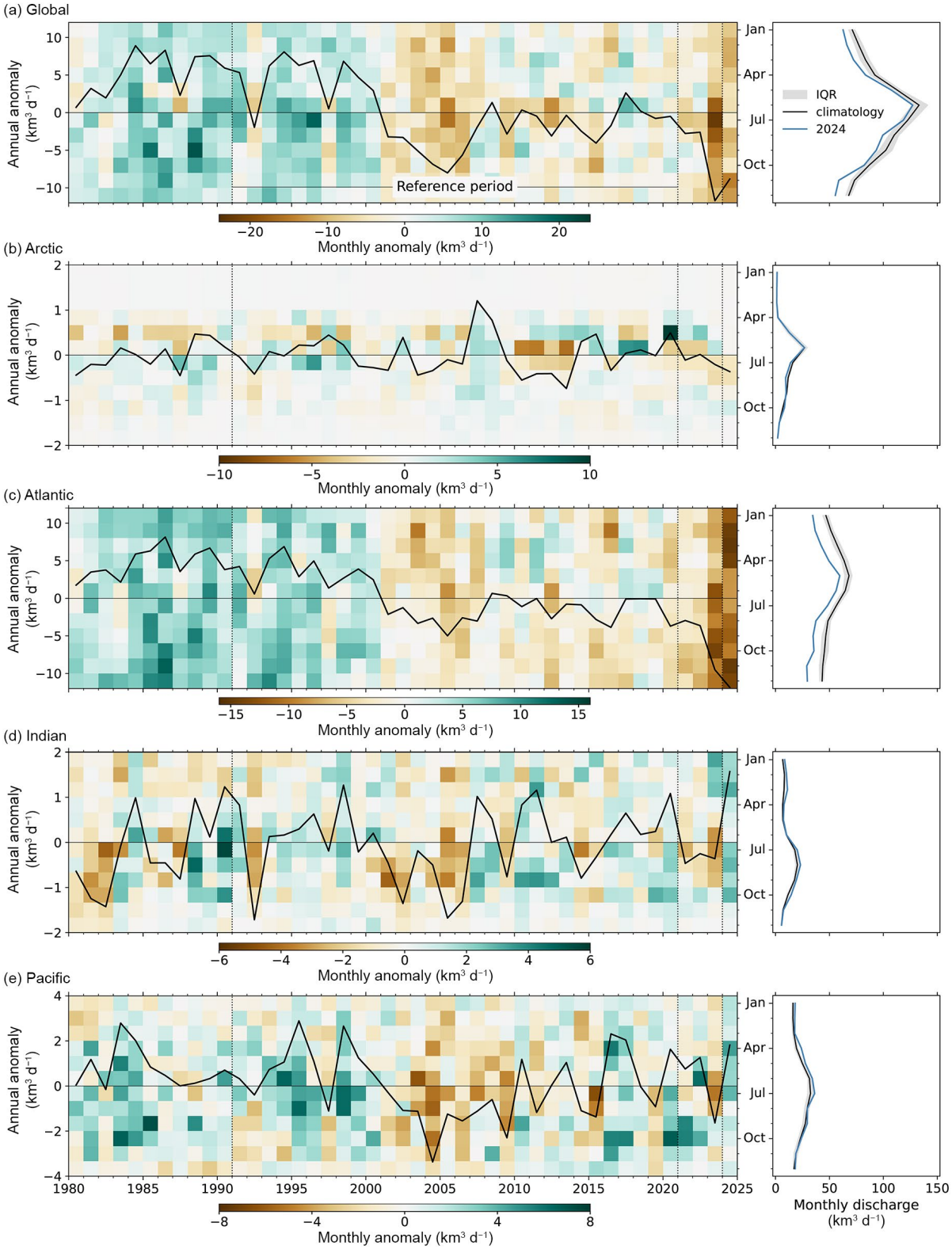

Fig. 2.41. Interannual variability and seasonality of freshwater discharge to the (a) global, (b) Arctic, (c) Atlantic, (d) Indian, and (e) Pacific Ocean basins (km³ day⁻¹). In the left panels, the black line represents the annual discharge anomaly, and the background heat map shows the monthly anomalies with respect to the reference seasonality in the base period 1991–2020. The right panels exhibit the seasonality, where the black line represents the climatological mean, the gray shading indicates the interquartile range in the climatology, and the blue line shows the seasonal variation in 2024.

Unauthenticated | Downloaded 11/21/25 11:34 AM UTC

into the Arctic Ocean was slightly below normal, particularly in summer. The Mackenzie and Nelson Rivers (North America) and the Lena River (Asia) experienced low discharge, whereas the Ob River (Asia) exhibited above-normal discharge (see section 5h for more details). The Atlantic basin faced severe drought conditions, receiving the lowest discharge in the series. Below-normal discharge persisted throughout the year, intensifying during the beginning of 2024 when El Niño was present. Major rivers, including the Amazon, Paraná, and Mississippi (America) as well as the Congo and Nile (Africa) had below-normal discharge. Exceptions to this pattern were the flooding that affected Rio Grande Do Sul (Brazil) in late April (see Sidebar 7.1; Dijk et al. 2025) and the Congo basin in January (WMO 2025b), the latter of which was the worst in six decades. Unlike the Atlantic basin, the Indian Ocean experienced its highest discharge from rivers in the time series, with above-average discharge spanning both wet seasons, while values remained normal during dry seasons. Severe flooding impacted Bangladesh in August (Dijk et al. 2025). The Pacific Ocean also received above-normal discharge, with the largest positive anomalies occurring between April and July.

The river discharge and runoff data used in this analysis are derived from the historical simulation of the Global Flood Awareness System version 4 (GloFASv4) of the Copernicus Emergency Management Service (Joint Research Centre - European Commission 2025). GloFASv4 employs the LISFLOOD-OS hydrological model (Burek et al. 2013), incorporating surface fields that represent land characteristics (Choulga et al. 2024) and parameters calibrated against discharge records from nearly 2000 stations, or regionalized where necessary. The historical simulation spans from 1979 to the present, utilizing a 0.05-degree grid and a daily temporal resolution. ERA5 (Hersbach et al. 2020) serves as the meteorological forcing input.

10. GROUNDWATER AND TERRESTRIAL WATER STORAGE

—M. Rodell and D. N. Wiese

In addition to the continued diminishment of polar ice sheets and glaciers, five regions around the world experienced major (>15 cm) changes in terrestrial water storage (TWS) from 2023 to 2024 (Plate 2.1t). By far the largest of these changes resulted from drought that encompassed most of Brazil and its neighbors to the north. For the equatorial portion of this region, it was a continuation of drought from 2023 (see Plate 2.1u), dropping TWS to record lows. A second major TWS change was a wet event that straddled Uruguay, northwestern Argentina, and southern Brazil, a reversal from the prior year (see section 7d). Changes in the rest of South America were small, though eastern Brazil remained wetter than normal. In contrast, TWS changes in North America were relatively unsubstantial, with some recovery from drought in the central plains of the United States and eastern Mexico, and continued TWS declines in north-central Canada and in the southwestern United States and northern Mexico, with record-low TWS and subsequent wildfires in some parts of these regions.

Remarkably large changes occurred in two regions of Africa. Zambia was at the center of a widespread TWS decline, extending a drought that has been its worst in at least two decades, while Tanzania, already experiencing pluvial conditions in prior years, accumulated even more TWS. Except for the Zambian drought region and another region in western equatorial Africa, a majority of sub-Saharan Africa gained water as the most intense (in terms of extent, duration, and TWS anomalies) wet event in the 23-year TWS record continued (Rodell and Li 2023), associated with unusually heavy rainfall. This led to all-time high TWS and flooding in several African drainage basins including those of the Niger, Congo, Nile, and Senegal Rivers, as well as Lake Chad and eastern lake basins.

The fifth region to experience a major change in TWS was the northern half of Australia's Northern Territory, which was pounded by rain from tropical cyclones in February and March (see section 4g7 for details), continuing northern Australia's wetting trend from the previous year. Much of Australia gained water, except for small declines along the northwestern and southeastern coasts. TWS remained elevated in much of New South Wales and Victoria.

Despite high temperatures, rainfall alleviated drought conditions in western Europe and even caused flooding in southern Spain; however, drought worsened in the Balkan Peninsula. A large area of western Russia and Kazakhstan experienced wetter-than-normal conditions

Unauthenticated | Downloaded 11/21/25 11:34 AM UTC

in 2024 as did parts of Southeast Asia, excluding southern India and Cambodia. TWS changes were mixed in the rest of Asia, with TWS remaining depleted in the Arabian Peninsula, the Middle East, and eastward into south central Asia, due to a combination of drought and overexploitation of water resources (Rodell et al. 2018).

Figures 2.42 and 2.43 display deseasonalized time series of monthly zonal-mean and global-mean TWS anomalies. Gaps indicate intervals when satellite observations were unavailable. We excluded regions from the averages where TWS declines are dominated by ice sheet and glacier ablation: Antarctica, Greenland, the Gulf Coast of Alaska, polar islands, High Mountain Asia, alpine western Canada, and the southern Andes. A 20°-wide zone of drying in the northern midlatitudes remained stable in 2024. Except for the northern portion, a 23°-wide equatorial zone of wetting diminished as the massive drought in South America counteracted the pluvial in Africa. South of that zone, TWS declines in South America and southern Africa overpowered the increase in northern Australia. A gradual decline in the boreal latitudes reflects ongoing drought in Canada and lingering depressed levels of TWS in much of northern Eurasia. Consistent with the end of El Niño, global-mean non-ice TWS (Fig. 2.43) recovered somewhat in 2024 from a near-record low a few months prior, but it remained in a lower range that was established after an abrupt decline during 2014–16 (Rodell et al. 2024).

TWS anomalies are derived from Gravity Recovery and Climate Experiment (GRACE) and GRACE Follow-On (GRACE-FO) satellite observations of Earth's time-varying gravity field (Tapley et al. 2004; Landerer et al. 2020). Uncertainty in these estimates is about 1 cm–2 cm equivalent height of water over a 500,000 km^2 region at midlatitudes (Wiese et al. 2016). Satellite observations are used because in situ measurements of groundwater, soil moisture, surface waters, snow, and ice (the components of TWS) do not provide the spatial density and vertical completeness required to monitor TWS at continental scales. On multi-year timescales, groundwater is typically the primary contributor of variations in TWS, except in the humid tropics and cold regions where surface water and ice/snow, respectively, are dominant (Getirana et al. 2017).

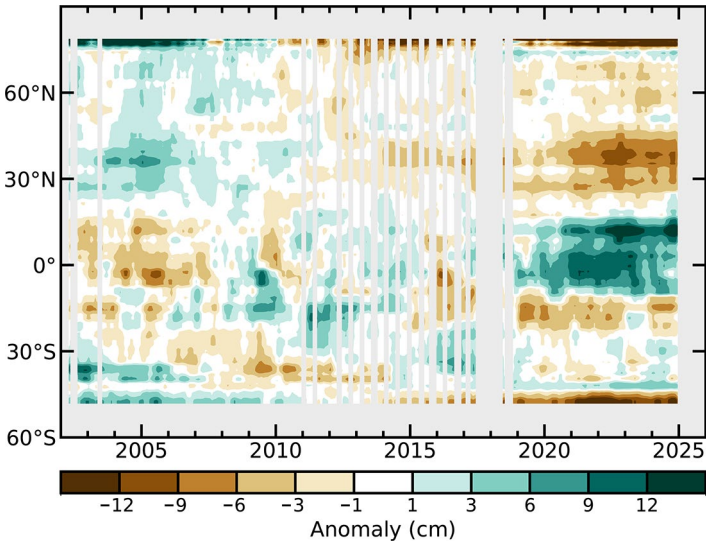

Fig. 2.42. Zonal means of monthly terrestrial water storage anomalies—excluding those in Antarctica, Greenland, the Gulf Coast of Alaska, polar islands, High Mountain Asia, alpine western Canada, and the southern Andes—in cm equivalent height of water, based on gravity observations from the Gravity Recovery and Climate Experiment (GRACE) and GRACE Follow-On (GRACE-FO). The anomalies are relative to a 2002–20 base period.

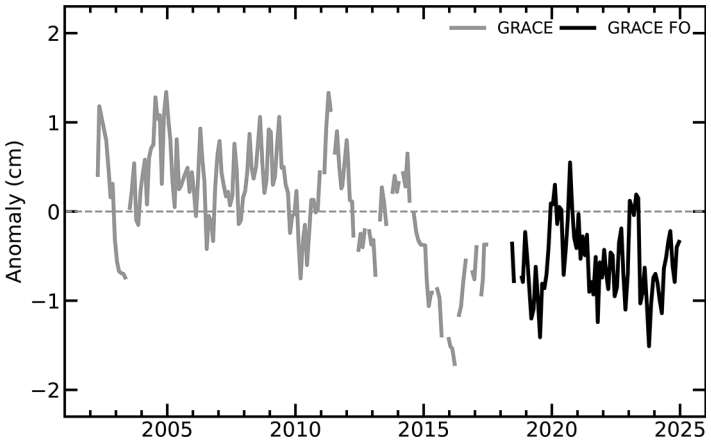

Fig. 2.43. Global average terrestrial water storage anomalies from Gravity Recovery and Climate Experiment (GRACE; gray) and GRACE Follow-On (GRACE-FO; black)—excluding those in Antarctica, Greenland, the gulf coast of Alaska, polar islands, High Mountain Asia, alpine western Canada, and the southern Andes—in cm equivalent height of water, relative to a 2002–20 base period.

Unauthenticated | Downloaded 11/21/25 11:34 AM UTC

11. SOIL MOISTURE

—J. Lems, W. Preimesberger, A. Gruber, D. D. Kovács, S. Hahn, M. Formanek, B. L. Harris, N. Rodriguez-Fernandez, T. Frederikse, R. Kidd, R. A. M. de Jeu, and W. A. Dorigo

Soil moisture is a crucial factor in land–atmosphere interactions, influencing surface air temperature, precipitation generation, and extreme weather events, including heatwaves and wildfires (Seneviratne et al. 2010).

In 2024, global soil moisture conditions were wetter than the 1991–2020 average (Fig. 2.44), with notable regional contrasts (Plate 2.1v). America, southern Africa, northern Europe, and Asia experienced drier-than-average conditions, while eastern South America, East Africa (including the Sahel), India, East Asia, and northern Australia saw above-average soil moisture levels. The Northern Hemisphere experienced wetter-than-normal conditions, while the Southern Hemisphere remained drier than average (Fig. 2.44). This contrast closely resembled that of 2023 (Hirschi 2024); however, the Northern Hemisphere saw a notable increase in soil moisture compared to the previous year. Consistent with the trend of the past five years, the most pronounced wet anomalies in the Northern Hemisphere were concentrated between the equator and 30°N (Fig. 2.45).

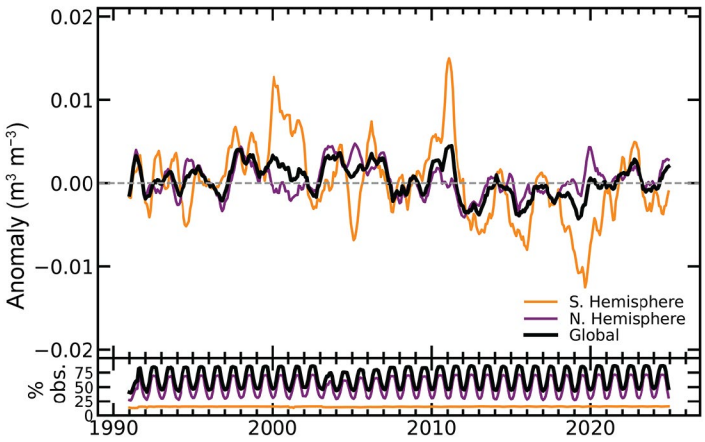

Fig. 2.44. (top) Time series of global (black), Northern Hemisphere (purple), and Southern Hemisphere (orange) monthly surface soil moisture anomalies (m³ m⁻³) for the period 1991–2024 (1991–2020 base period), and (bottom) the valid observations as a percentage (%) of total global land surface. Data are masked where no retrieval is possible or where the quality is not assured and flagged, for example due to dense vegetation, frozen soil, permanent ice cover, or radio frequency interference. (Source: Copernicus Climate Change Service [C3S] Soil Moisture.)

A strong El Niño in the first quarter of the year contributed to drier and warmer conditions in North America, Southeast Asia, Australia, and southern Africa (Song 2018; Hoell et al. 2017; Figs. 2.32, 2.46). In April, the El Niño transitioned to a neutral phase, which aligned with a return to normal soil moisture conditions in the Southern Hemisphere towards the end of 2024 (Fig. 2.44).

Wetter-than-normal conditions were present throughout most of the year in northern Australia, with wet anomalies that were particularly widespread in March (Fig. 2.46). Similarly, strong wet anomalies were also observed in India, starting in May and lasting through to the end of the year. In August and September, anomalously high soil moisture in Afghanistan and Pakistan was associated with heavy rain and flash floods. Also, parts of East Asia experienced noticeable wetter-than-normal conditions in 2024, similar to the last couple of years.

The Sahel experienced prolonged wet anomalies from August to November, with soil moisture amounts twice as high as normal in some areas. Meanwhile, northern and southern Africa faced extreme drought conditions, particularly southern Africa, which remained dry even after El Niño subsided.

Widespread drier-than-normal soil moisture conditions persisted across North and South America throughout 2024, with the

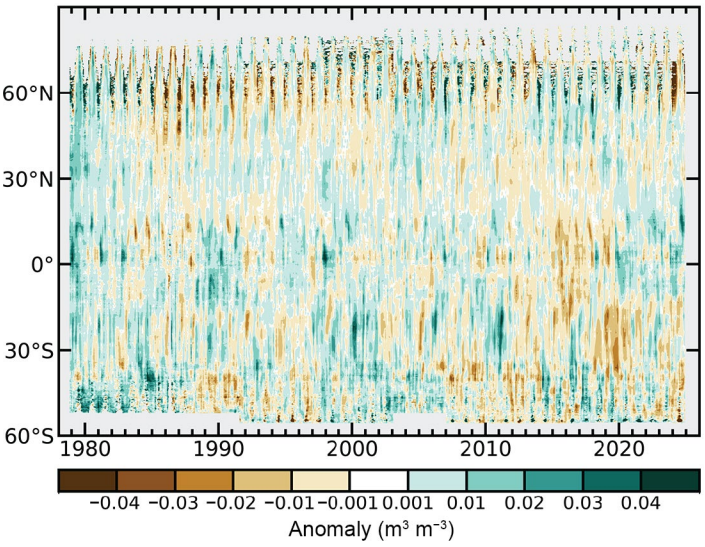

Fig. 2.45. Time–latitude diagram of monthly surface soil moisture anomalies (m³ m⁻³; 1991–2020 base period). Data are masked where no retrieval is possible or where the quality is not assured and flagged, for example due to dense vegetation, frozen soil, permanent ice cover, or radio frequency interference. (Source: Copernicus Climate Change Service [C3S] Soil Moisture).

Unauthenticated | Downloaded 11/21/25 11:34 AM UTC

continent experiencing the most significant negative soil moisture anomaly globally. Following a record-breaking warm and dry October (NCEI 2024), the drought footprint reached a nationwide record in the United States (Fig. 2.46), with 47% of the nation under moderate to extreme drought (section 2d12). September was exceptionally dry in inland South America and in Eastern Europe, primarily affecting Ukraine. Generally, Europe exhibited a distinct east–west contrast, with Western Europe experiencing a wetter-than-average summer, while Eastern and Southern Europe remained dry for most of the year.

Soil moisture was observed by microwave satellite remote sensing of the upper few centimeters of the soil layer, as provided by the COMBINED product of the Copernicus Climate Change Service (C3S) version 202312 (Dorigo et al. 2025). C3S combines multi-sensor data in the 1978–2024 period through statistical merging (Gruber et al. 2017, 2019). Wet and dry anomalies here refer to the deviation from the 1991–2020 average. Note that changes in spatiotemporal coverage (both between seasons and periods, e.g., resulting from the inclusion of additional sensors) can introduce uncertainties in the domain-averaged soil moisture time series (e.g., Bessenbacher et al. 2023).

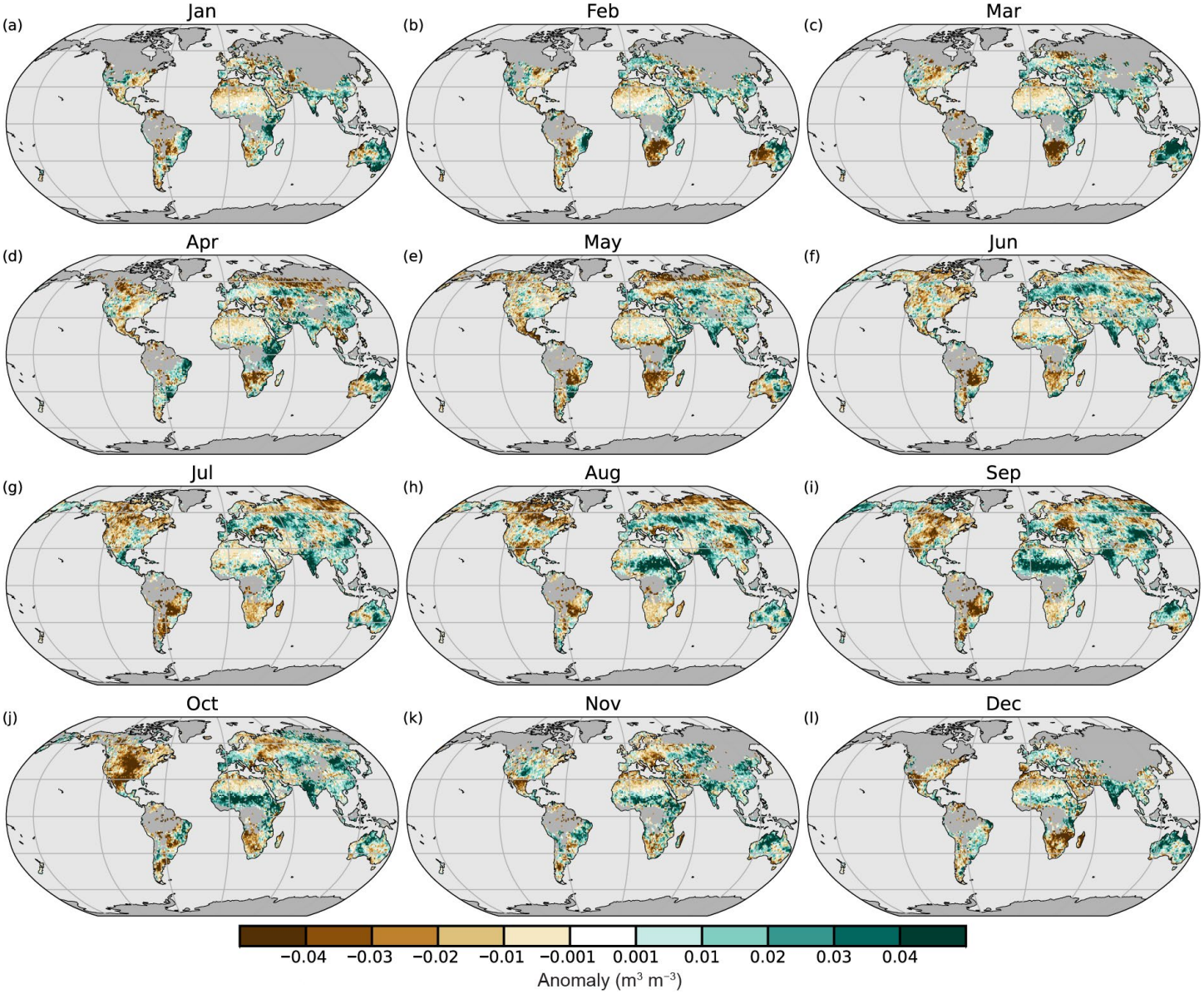

Fig. 2.46. Monthly average soil moisture anomalies for 2024 ($m^3\ m^{-3}$; 1991–2020 average). Data are masked where no retrieval is possible or where the quality is not assured and flagged, for example due to dense vegetation, frozen soil, permanent ice cover, or radio frequency interference. (Source: Copernicus Climate Change Service [C3S] Soil Moisture.)

Unauthenticated | Downloaded 11/21/25 11:34 AM UTC

12. MONITORING DROUGHT USING THE SELF-CALIBRATING PALMER DROUGHT SEVERITY INDEX

—J. Barichivich, T. J. Osborn, I. Harris, A. Gollop, G. van der Schrier, and P. D. Jones

The self-calibrating Palmer Drought Severity Index (scPDSI) for 1950–2024 indicates a decline in global drought severity and extent in 2024, following the record-high peak in late 2023 (Barichivich et al. 2024; Fig. 2.47). Extreme drought (scPDSI ≤–4) affected around 5% of the global land throughout 2024, down from over 7% in July–August 2023. Severe and extreme drought combined (scPDSI ≤–3) stabilized near 12% of the global land area after reaching a record 17% in July 2023. Similarly, moderate or worse drought (scPDSI ≤–2) affected about 23% of global land in 2024 compared to 28% in mid-2023. Most of this decline occurred in regions where drought conditions of 2023 transitioned to normal or wetter conditions, particularly in the La Plata Basin, much of non-Mediterranean Europe, and the midlatitudes of Central Asia (Fig. 2.48). Meanwhile, severe drought persisted in southwestern and northern North America, parts of tropical South America, the Mediterranean and northwest Africa, southern Africa, parts of the Middle East, southern Australia, and Mongolia (Plate 2.1w).

In Canada, 2024 ranked as the driest year on the nationally averaged yearly scPDSI for the 1950–2024 period. In the United States, severe-to-extreme drought conditions persisted through much of Arizona and New Mexico. Mexico and most countries across Central and South America experienced a mix of moderate drought and normal conditions (Plate 2.1w). On a country-averaged basis, 2024 was the third-driest year in both Peru and Brazil, with vast areas of the Amazon basin enduring extreme drought. By mid-October, the Rio Negro at Manaus, a major tributary of the Amazon River, recorded its lowest water levels since records began in 1902 (updated from Barichivich et al. 2018). In contrast, Chile experienced a moisture recovery in 2024 following a prolonged megadrought (Garreaud et al. 2025). In terms of average drought severity, 2024 ranked as the 18th-driest year since 1950, following the driest years on record in 2021 and 2022.

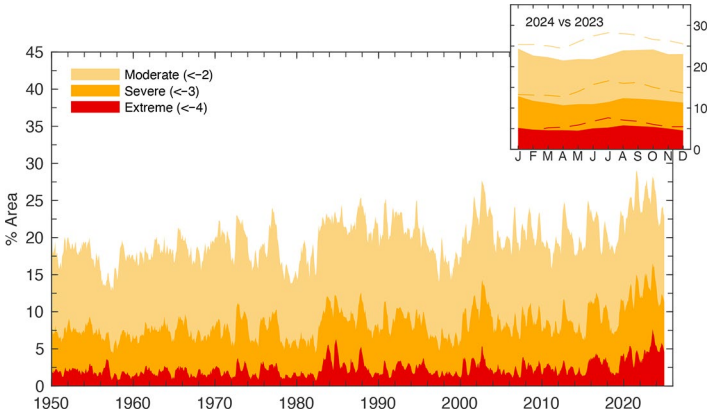

Fig. 2.47. Percentage of global land area (excluding ice sheets and deserts) with self-calibrating Palmer Drought Severity Index (scPDSI) indicating moderate (<–2), severe (<–3), and extreme (<–4) drought for each month of 1950–2024. Inset: each month of 2024 (shading) compared with 2023 (dashed lines).

Northwest Africa experienced record or near-record drought levels (Plate 2.1w), with 2024 being the driest year in the Canary Islands and Morocco, second driest in Algeria, and third driest in Tunisia. In southeastern Europe, it was the driest year in Greece and third driest in Bulgaria and Romania. In Italy, 2024 was ranked sixth driest for country-average drought severity, with the top six drought years all occurring in the last eight years.

Although uncertain due to sparser observations, moisture patterns in tropical Africa did not change much in 2024 with respect to 2023 (Fig. 2.48). Southern Africa experienced a continuation of drought conditions seen since 2018, and its severity continued mostly as moderate (Plate 2.1w). In Australia, the moisture pattern in 2024 also remained similar to that in 2023, with the coastal parts of the

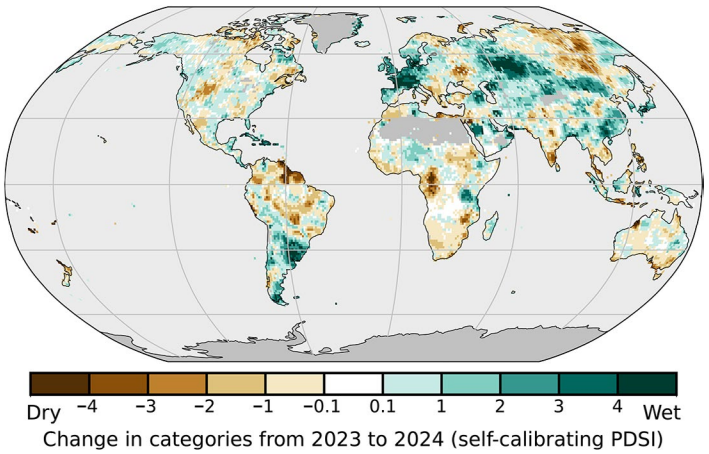

Fig. 2.48. Change in drought categories from 2023 to 2024 (mean self-calibrating Palmer Drought Severity Index [scPDSI] for 2024 minus mean scPDSI for 2023). Increases in drought severity are indicated by negative values (brown), and decreases by positive values (green). No calculation is made where a drought index is meaningless (gray areas: ice sheets or deserts with approximately zero mean precipitation).

Unauthenticated | Downloaded 11/21/25 11:34 AM UTC

country continuing under moderate drought (Plate 2.1w). Wet conditions seen through most of India and Southeast Asia since 2022 continued during 2024. Most of the previous severe-to-extreme drought conditions through China and Kazakhstan shifted to normal or wet conditions, but Mongolia saw continued drought.

Hydrological drought results from a period of abnormally low precipitation, sometimes exacerbated by a concurrent increase in evapotranspiration (ET). Its occurrence can be apparent in reduced river discharge (section 2d9), groundwater storage, (section 2d10), and/or soil moisture (section 2d11), depending on season and duration of the event. Here, the scPDSI (Wells et al. 2004; van der Schrier et al. 2013) is presented, using global precipitation and Penman–Monteith Potential ET from the Climatic Research Unit terrestrial series (CRU TS 4.09) dataset (Harris et al. 2020). A simple water balance at the core of the scPDSI estimates actual evapotranspiration, soil moisture content, and runoff based on the input precipitation and potential loss of moisture to the atmosphere. Estimated soil moisture categories are calibrated over the complete 1901–2024 period to ensure that "extreme" droughts and pluvials (wet periods) relate to events that do not occur more frequently than in approximately 2% of the months. This calibration affects direct comparison with other hydrological cycle variables in Plate 2.1w that use a different baseline period. All country rankings mentioned above are based on the ranking of spatial averages of annual scPDSI for each country for the 1950–2024 period; pre-1950 data are not used for rankings because observational coverage is poor in some countries.

13. LAND EVAPORATION

—D. G. Miralles, O. M. Baez-Villanueva, O. Bonte, E. Tronquo, S. Haghdoost, and H. E. Beck

A clear understanding of the spatial and temporal dynamics of terrestrial evaporation is fundamental for evaluating the impacts of natural and anthropogenic forcing on hydrological systems, since evaporation serves as a direct nexus between the energy and water balances. The global-mean land evaporation in 2024 aligned well with the multidecadal trend of approximately +0.4 mm year^{-1} (Fig. 2.49), a trend that has been attributed to an increase in atmospheric evaporative demand with global warming (Brutsaert 2017) and global greening (Yang et al. 2023). Despite 2024 being overall an El Niño year, which usually implies negative global evaporation anomalies due to the proliferation of drought conditions in the Southern Hemisphere (Martens et al. 2018; Miralles et al. 2014), it was also the warmest year on record (section 2b1). The latter explains the high mean evaporation in the Northern Hemisphere and the subsequent positive global anomaly, which is not an isolated event but contributes to the long-term increase witnessed since the early 1980s (Fig. 2.49).

The latitudinal anomaly profiles in Fig. 2.50 reveal the overall positive anomalies in Northern Hemisphere regions, which are consistent with warm temperatures in Europe, Asia, and North

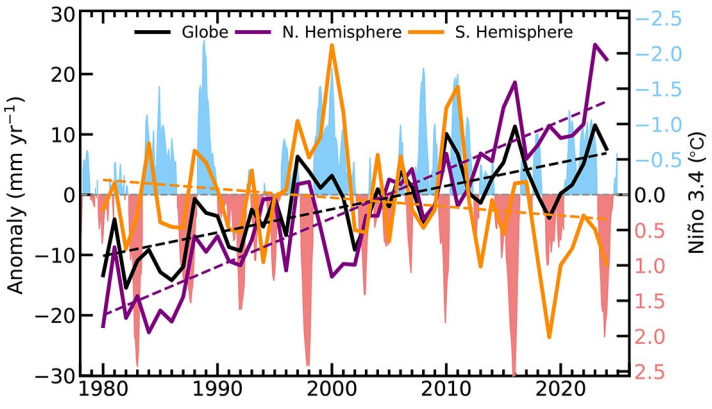

Fig. 2.49. Land evaporation anomaly (mm yr^{-1}; 1991–2020 base period) for the Northern Hemisphere, Southern Hemisphere, and the entire globe (purple, orange, and black solid lines, respectively). Linear trends in evaporation (dashed lines) and the Niño-3.4 index (right axis, shaded area) are also shown. (Source: Global Land Evaporation Amsterdam Model version 4 [GLEAM4] and NOAA Physical Sciences Laboratory [PSL].)

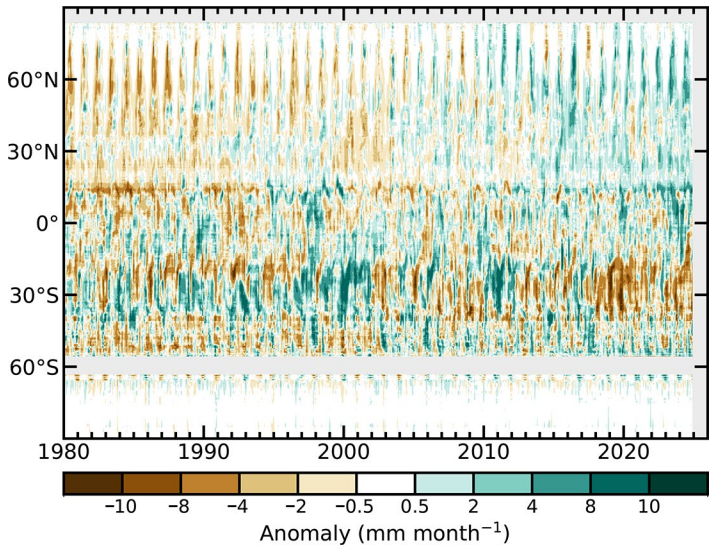

Fig. 2.50. Zonal mean terrestrial evaporation anomalies (mm month^{-1}; relative to 1991–2020). (Source: Global Land Evaporation Amsterdam Model version 4 [GLEAM4].)

Unauthenticated | Downloaded 11/21/25 11:34 AM UTC

America (section 2b1). The largest negative anomalies occurred in the latitudinal band from 0° to 30°S, and they reflect the extraordinary drought conditions experienced in South America and southern Africa in 2024 (sections 2d11, 2d12). Drought conditions tend to be associated with high atmospheric water demand, which initially enhances evaporation and accelerates soil desiccation. However, as soil moisture decreases, evaporation rates decline, leading to negative evaporation anomalies in later stages of the drought event (Miralles et al. 2019). This pattern is reflected in the positive evaporation anomalies at those latitudes during the first half of 2024, which then transitioned into negative anomalies in the second half (Fig. 2.50).

In terms of global patterns, there was a mix of positive and negative evaporation anomalies across different regions in 2024, reflecting a complex interplay of meteorological variables and land surface processes (Plate 2.1x). As expected during El Niño years, lower-than-usual evaporation occurred as a result of soil moisture limitations in southern Africa and most of South America; as mentioned above, those soil moisture limitations were caused by persistent drought events (Marengo et al. 2024). On the other hand, the lower-than-usual evaporation in western North America is less typical of El Niño conditions, and was also triggered by precipitation scarcity (section 2d5). Most of the world was, however, dominated by positive evaporation anomalies, as expected given the high temperatures in 2024 (Plate 2.1x). Major tropical forested regions experienced higher evaporation than normal, as the high atmospheric demand for water increased transpiration despite the negative anomalies in precipitation leading to lower-than-usual interception loss (i.e., water evaporating directly from wet canopies during and after precipitation events).

The evaporation estimates used in this analysis were obtained from the Global Land Evaporation Amsterdam Model version 4 (GLEAM4; Miralles et al. 2025), which integrates satellite observations and reanalysis data. GLEAM4 separately estimates the main components of terrestrial evaporation, including soil evaporation, transpiration, interception loss, and sublimation, and its estimates are routinely validated against in situ measurements from eddy-covariance flux towers and other ground-based observations. Despite recent advancements, uncertainties remain high, particularly in regions with sparse observational data. Ongoing efforts aim to refine different evaporation components by leveraging new satellite missions and improved reanalysis products. Future developments are expected to leverage emerging technologies from thermal missions—such as Ecosystem Spaceborne Thermal Radiometer Experiment on Space Station (ECOSTRESS; Fisher et al. 2020) and Thermal Infrared Imaging Satellite for High-resolution Natural Resource Assessment (TRISHNA; Lagouarde et al. 2018), along with hyper-resolution optical remote sensing from CubeSats (McCabe et al. 2017)—to improve global evaporation monitoring and understanding of its response to climate change.

Unauthenticated | Downloaded 11/21/25 11:34 AM UTC

e. Atmospheric circulation

1. MEAN SEA LEVEL PRESSURE AND RELATED MODES OF VARIABILITY

—D. Fereday, D. Campos, and G. Macara

Mean sea level pressure (MSLP) variability is characterized by large-scale modes that drive weather and climate anomalies and extremes. These modes include the Arctic Oscillation, the North Atlantic Oscillation (NAO), and the Pacific–North American (PNA) pattern in the Northern Hemisphere (NH) as well as the Southern Annular Mode (SAM; also known as the Antarctic Oscillation) in the Southern Hemisphere (SH; Kaplan 2011). Because of its direct tropical impact and important extratropical teleconnections to both hemispheres (Capotondi et al. 2015; Yeh et al. 2018), the El Niño–Southern Oscillation (ENSO) is one of the most significant global climate drivers (see section 4b for details).

In the NH, the NAO index fluctuated through the winter into early spring (December–March), remaining overall fairly neutral (Figs. 2.51a,e). An important driver of winter circulation variability in the NH is the stratospheric polar vortex. The vortex was unusually variable in winter 2023/24, with two major sudden stratospheric warmings (SSWs) occurring in January and March (Fig. 2.51e). Such events tend to favor a negative NAO (Baldwin and Dunkerton 2001), leaving northern Europe colder and drier, and southern Europe milder and wetter. However, this does not always occur (Kodera et al. 2016), and neither SSW in 2024 produced a strong negative NAO response (Lee at al. 2025). Nevertheless, the NH temperature anomalies for January–March 2024 resembled those seen in other El Niño winters that experienced an SSW (Ciasto and Butler 2024), with northeast North America having been warmer and southwest North America and northern Eurasia having been cooler. In NH spring, low-pressure anomalies over western Europe (Fig. 2.51b) were consistent with increased precipitation (see section 7f2). In NH summer, MSLP anomalies in North America remained weak (Fig. 2.51c). The summer NAO, an important driver of summer European climate (Folland et al. 2009), was also near-neutral. In December 2024, the PNA was positive, as was the winter NAO, consistent with warmer conditions in the eastern United States and drier conditions in the western United States (see section 7b2).

The Southern Oscillation Index (SOI), calculated by the MSLP difference between Tahiti and Darwin, highlights the atmospheric component of ENSO (Allan et al. 1996; Kaplan 2011). During 2024, the SOI transitioned slowly from negative to positive values through the year, associated with the decay of El Niño and neutral conditions in the second half of the year that gave way to La Niña-like conditions in the tropical Pacific Ocean by the end of 2024 (see section 4b for details). During the austral winter, with neutral SOI conditions, a pattern similar to the Pacific–South American (PSA) pattern (O'Kane and Franzke 2025) developed in the South Pacific, allowing the presence of an area of above-normal MSLP centered over the Bellingshausen Sea (Fig. 2.52c). This atmospheric blocking pattern was associated with wetter-than-normal conditions in south-central Chile during the winter (e.g., Rutllant and Fuenzalida 1991; Campos and Rondanelli 2023; see also Fig. 2.46; see section 7d3) despite the

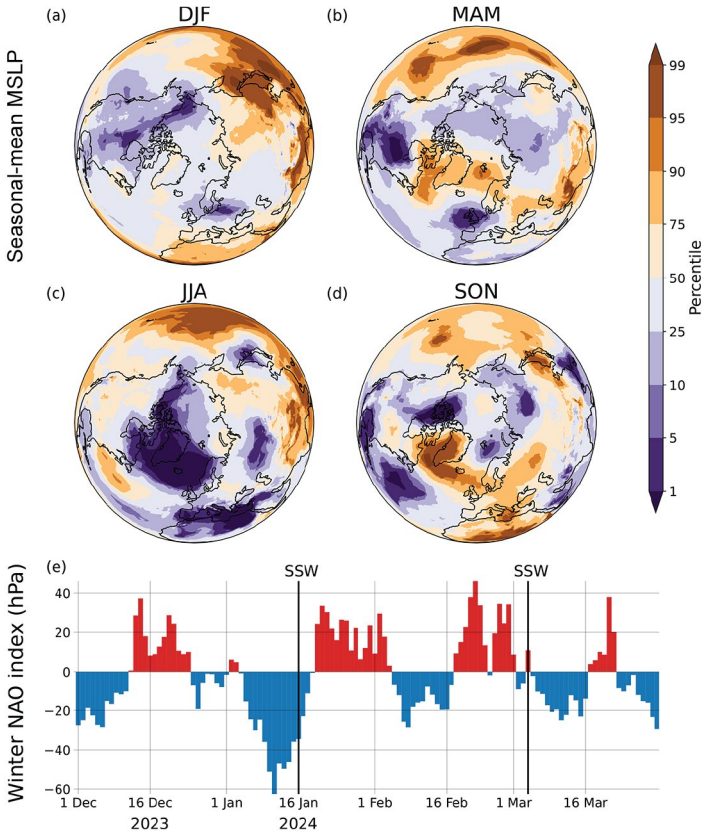

Fig. 2.51. Northern Hemisphere mean sea level pressure (MSLP) for 2024. Panels (a)–(d): seasonal mean MSLP for Dec 2023 to Nov 2024. Fields are anomalies with respect to a 1991–2020 climatology, expressed as percentiles. (Source: ERA5.) Panel (e): daily North Atlantic Oscillation (NAO) index for Dec 2023 to Mar 2024 defined as Azores minus Iceland MSLP. Black lines show the dates of the two major sudden stratospheric warmings. (Source: National Centers for Environmental Prediction reanalysis version 1 [NCEPv1].)

Unauthenticated | Downloaded 11/21/25 11:34 AM UTC

midterm megadrought (Garreaud et al. 2020). MSLP was also above-normal over and to the east of New Zealand during austral winter, associated with drier-than-normal conditions over the country during June and July and the country's third-warmest winter on record.

The annual MSLP anomalies in the SH (Plate 2.1y) resemble the positive phase of the SAM, which is the leading mode of extratropical variability in the SH (Fogt and Marshall 2020), explaining up to 34% of the variance of the extratropical atmospheric circulation. Two prominent centers of positive anomalies were observed in the extratropics: one in the southern Pacific Ocean and one in the southern Indian Ocean. At a seasonal scale, positive SAM conditions prevailed during the first months of the year where El Niño conditions were present (74% of the days between January and April; Figs. 2.52a,e). In the austral autumn, MSLP was higher than normal south of Australia, with below-average rainfall across southern parts of the country. In contrast, significant flooding affected large parts of central and northern parts of Australia, associated mostly with a monsoon trough (see section 4f) and Severe Tropical Cyclone Megan in March (see section 4g7). More frequent southwesterly winds than normal contributed to New Zealand observing its coolest autumn since 2012. During the austral winter (June–August), a period of nearly 45 consecutive days with the SAM in the negative phase was registered around August (Fig. 2.52e), associated with the positioning of the blocking high in the Bellingshausen Sea and an increase of the subtropical jet stream. From September to December, the SAM was variable, spending approximately half of the time in each phase (Fig. 2.52e).

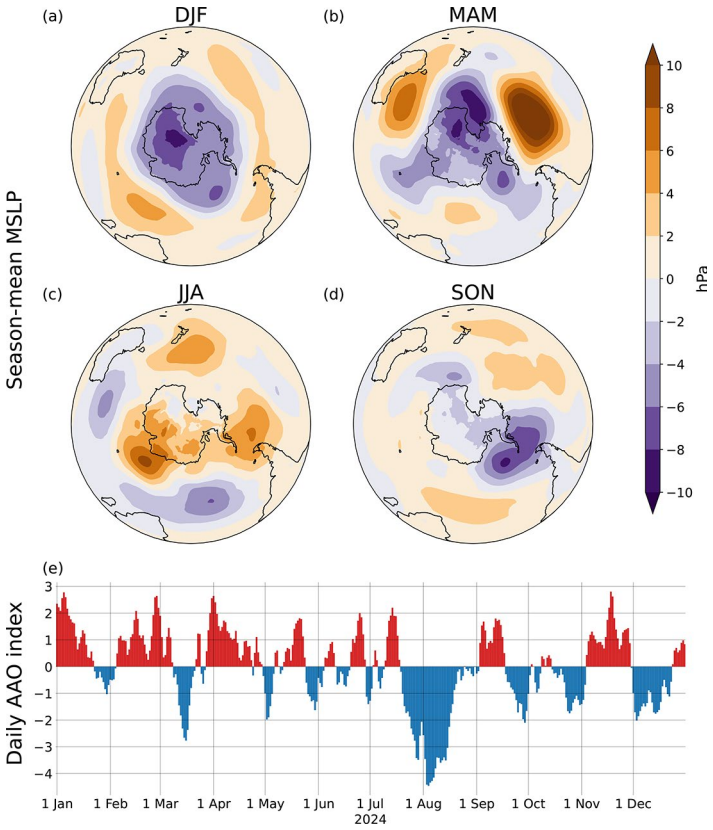

Fig. 2.52. Southern Hemisphere mean sea level pressure (MSLP) for 2023/24. Panels (a)–(d): seasonal-mean MSLP for Dec 2023 to Nov 2024. Fields are anomalies with respect to a 1991–2020 climatology. (Source: ERA5.) Panel (e): daily Antarctic Oscillation (AAO) index for Jan–Dec 2024. (Source: NOAA National Center for Environmental Prediction).

2. LAND AND OCEAN SURFACE WINDS

—C. Azorin-Molina, R. J. H. Dunn, L. Ricciardulli, T. R. McVicar, J. P. Nicolas, C. A. Mears, Z. Zeng, and M. G. Bosilovich

Northern Hemisphere land surface wind speeds at ~10 m above ground in 2024 were generally lower with respect to the 1991–2020 climatology (Plate 2.1z), with an anomaly (−0.034 m s^{-1}) similar to that reported for 2023 (Azorin-Molina et al. 2024; Table 2.9). The most notable spatial feature in the wind speed anomalies is an interhemispheric asymmetry, characterized by negative values in all northern regions (except for Central Asia) and positive values in South America. The "reversal" observed around the 2010s (Zeng et al. 2019), following decades of "stilling" (McVicar et al. 2012), is weakening as shown in Fig. 2.53a. In recent years, weak variations have been observed in the frequency of moderate (>3 m s^{-1}, Fig. 2.53c) and strong (>10 m s^{-1}, Fig. 2.53d) winds, although a declining trend persists for both categories over the period 1973–2024.

Land surface winds are assessed by comparing observations with reanalyses: 1) the Met Office Hadley Centre Integrated Surface Dataset 3 (HadISD3) observational dataset (1973–2024; Dunn et al. 2012, 2016; Dunn 2019); 2) the Global Historical Climatology Network hourly (GHCNh) observational dataset (1974–2023; Menne et al. 2025); 3) ERA5 (1979–2024; Hersbach et al. 2020; Bell et al. 2021); and 4) MERRA-2 (1980–2024; Gelaro et al. 2017). Atmospheric reanalyses can generally reproduce the climatology of station-based wind observations; however, they tend to underestimate the magnitude of observed anomalies and fail to accurately capture the multidecadal variability, even though their performance has consistently improved since the

Unauthenticated | Downloaded 11/21/25 11:34 AM UTC

mid-1990s (Fig. 2.53b; e.g., Torralba et al. 2017; Wohland et al. 2019).

Over the period 1979–2024, terrestrial wind speed declined (–0.052 m s^{-1} $decade^{-1}$) across all regions in the NH (Table 2.9), with the strongest decline observed in North America (–0.069 m s^{-1} $decade^{-1}$) and the weakest in East Asia (–0.027 m s^{-1} $decade^{-1}$). The interhemispheric asymmetry in the long-term changes of wind speeds persists (Zha et al. 2021): despite limited SH land observations, positive trends are reported in South America (+0.054 m s^{-1} $decade^{-1}$). This dipole in trend direction between hemispheres is partly captured by ERA5 (Fig. 2.54a).

In 2024, globally averaged ocean wind speed anomalies (relative to the 1991–2020 base period) were opposite in sign compared to land surfaces, with slightly positive values for radiometers (Remote Sensing Systems [RSS], +0.051 m s^{-1}) and close to zero for scatterometers (Advanced Scatterometer [ASCAT], –0.003 m s^{-1}) and reanalysis (ERA5, +0.006 m s^{-1}); see Fig. 2.55. Satellite wind datasets from RSS include the merged radiometers (Special Sensor Microwave/Imager [SSM/I] series, Special Sensor Microwave Imager/Sounder [SSMIS] series, Advanced Microwave Scanning Radiometer 2 [AMSR2] and AMSR for the Earth Observing System [AMSR-E], Tropical Rainfall Measuring Mission Microwave Imager [TMI], WindSat, and Global Precipitation Measurement Microwave Imager [GMI]), and the Quick Scatterometer (QuickSCAT) and ASCAT scatterometers (Wentz 1997, 2015; Wentz et al. 2007, 2024;

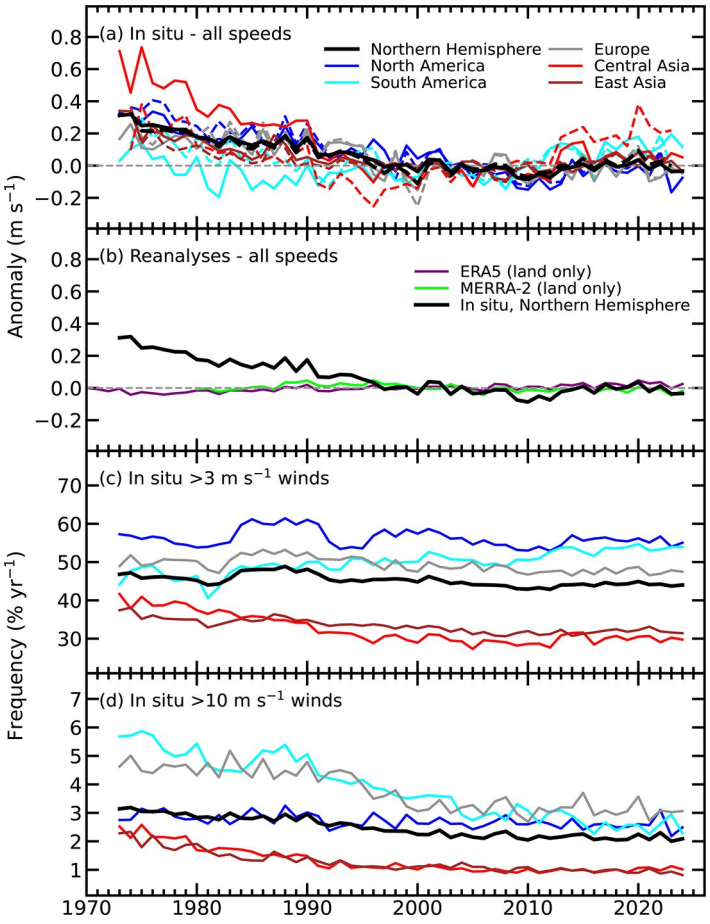

Fig. 2.53. Land surface Northern Hemisphere (20°N–70°N) and regional surface wind speed anomaly time series (m s^{-1}; 1991–2020 reference period). Panel (a) shows the Met Office Hadley Centre Integrated Surface Dataset 3 (HadISD3) observational dataset (1973–2024) in solid lines and Global Historical Climatology Network hourly (GHCNh; 1974–2023) in dashed lines, and (b) ERA5 (1970–2024) and MERRA-2 (1980–2024). The lower panels show HadISD3 occurrence frequencies (% yr^{-1}) for wind speeds (c) >3 m s^{-1} and (d) >10 m s^{-1}, with the same legend as in (a).

Table 2.9. Northern Hemisphere (20°N–70°N) and regional statistics for land surface wind speed (m s^{-1}) using the observational HadISD3 dataset for 1979–2024.

Region	Mean Wind Speed 1991–2020 (m s^{-1})	Wind Speed Anomaly 2024 (m s^{-1})	Wind Speed Trend 1979–2024 (m s^{-1} $decade^{-1}$)	Confidence Interval 5% (m s^{-1} $decade^{-1}$)	Confidence Interval 95% (m s^{-1} $decade^{-1}$)	Number of Stations
Northern Hemisphere	3.297	–0.034	–0.052	–0.066	–0.040	2811
North America	3.645	–0.075	–0.069	–0.084	–0.052	845
Europe	3.640	–0.048	–0.049	–0.067	–0.035	866
Central Asia	2.741	+0.052	–0.065	–0.098	–0.039	303
East Asia	2.720	–0.036	–0.027	–0.041	–0.014	538
South America	3.451	+0.116	+0.054	+0.039	+0.072	101

Unauthenticated | Downloaded 11/21/25 11:34 AM UTC

Ricciardulli and Wentz 2015; Ricciardulli and Manaster 2021). The ocean wind anomaly map for 2024 (Plate 2.1z) shows notable regional features, including: 1) a large negative anomaly in the tropical Atlantic, similar to 2023 but slightly reduced in both extent and magnitude; 2) a positive anomaly in the tropical Pacific, indicating the transition from El Niño to La Niña-like conditions; 3) slightly negative anomalies over the Indian Ocean; and 4) a dominance of moderate positive anomalies over the Southern Ocean, Greenland Sea, and North Pacific Ocean. The comparison between the RSS ASCAT anomaly time series and maps and ERA5 shows they are consistent both temporally and spatially. In the long term (1988–2024), ocean winds exhibit slightly positive trends (Fig. 2.55) for both RSS (+0.030 m s^{-1} $decade^{-1}$) and ERA5 (+0.030 m s^{-1} $decade^{-1}$) averaged over 60°S–60°N, and display similar spatial patterns (Fig. 2.54a) as those shown for the anomalies. Spatially, the trend map reveals a positive trend in the central Pacific and Southern Ocean, consistently observed in many of the past years.

The causes behind the opposite land (negative) and ocean (positive) anomalies are not yet attributable (see discussion in McVicar et al. 2012, for example). Long-term trends and multidecadal variability (stilling versus reversal) of land and ocean surface winds have primarily been attributed to decadal ocean–atmosphere oscillations (Zeng et al. 2019). Anthropogenic global warming is also driving the opposite trends between the Northern (negative) and Southern (positive) Hemisphere (Zha et al. 2021) due to changes in the pressure gradient (Zhang et al. 2021). Changes in land cover (Minola et al. 2022), data encoding issues (Dunn et al. 2022a), and biases in anemometer readings (Azorin-Molina et al. 2023; Liu et al. 2024) are likely secondary drivers of the observed trends and variability.

3. UPPER-AIR WINDS

—L. Haimberger, M. Mayer, C. T. Sabeerali, P. Rohini, O. P. Sreejith, and V. Schenzinger

Global atmospheric circulation patterns from the surface to stratospheric levels can be strongly impacted by oceanic temperatures and ENSO state. During October–December (OND; Plate 2.1aa) in 2024, a weakly negative Indian Ocean dipole (IOD) and La Niña conditions were indicated by the positive–negative 850-hPa zonal wind dipole over the equatorial

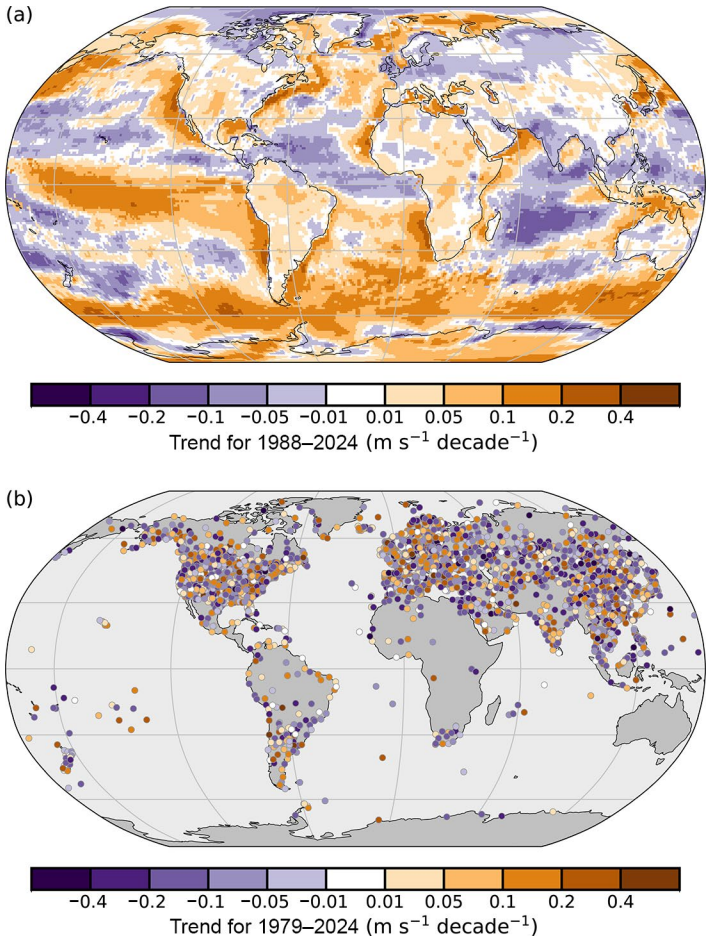

Fig. 2.54. Wind speed trends (m s^{-1} $decade^{-1}$) from the (a) ERA5 output over land/ice and Remote Sensing System (RSS) satellite radiometers (Special Sensor Microwave/Imager [SSM/I], Special Sensor Microwave Imager/Sounder [SSMIS], Tropical Rainfall Measuring Mission Microwave Imager [TMI], AMSR2 [Advanced Microwave Scanning Radiometer 2], ASMR-E [Advanced Microwave Scanning Radiometer for the Earth Observing System], WindSat, and Global Precipitation Measurement Microwave Imager [GMI]) over ocean for 1988–2024 (shaded areas), and (b) the observational Met Office Hadley Centre Integrated Surface Dataset 3 [HadISD3] dataset over land (circles) for 1979–2024.

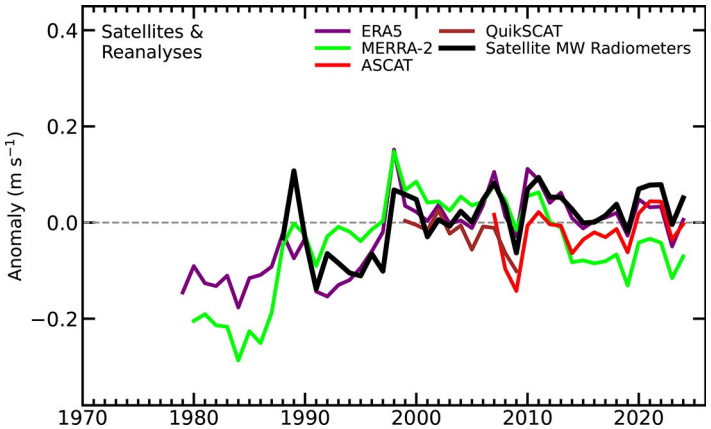

Fig. 2.55. Annual global anomalies of global mean wind speed (m s^{-1}; 1991–2020 base period) over the ocean from merged satellite radiometers, the Quick Scatterometer (QuickSCAT) and Advanced Scatterometer (ASCAT), and ERA5 and MERRA-2 reanalyses.

Unauthenticated | Downloaded 11/21/25 11:34 AM UTC

Indian and western Pacific Ocean basins, feeding the convective maximum over the Indonesian region with moisture. However, eastward wind anomalies covered the Niño-3.4 region of the eastern Pacific, along with westward wind anomalies near the South American coast, converging on positive sea surface temperature (SST) anomalies in the far eastern Pacific.

The year 2024 as a whole was relatively normal; the global wind anomaly was slightly positive (Fig. 2.53a). Trends for the period 1991–2024 were negative, with MERRA-2 having been the only outlier. In the Southern Ocean, the Antarctic Oscillation (AAO) anomaly turned from positive to moderately negative in the second half of 2024, leaving the significantly positive trends of the past three decades practically unchanged also for 1991–2024 (from 0.21 [MERRA, JRA55] to 0.23 [JRA-3Q] and 0.32 [ERA5] m s^{-1} $decade^{-1}$, not shown).

The imprint of ENSO in eastward wind anomalies of the Niño-3.4 region (5°S–5°N, 170°W–120°W), where El Niño events lead to significant reduction of the predominant easterlies (e.g., Trenberth 1997), is considered. Since the 1982/83 El Niño, the eastward anomalies appear to have weakened, even during strong El Niño events, in terms of temperature. This has led to a significant negative trend of ~0.4±0.2 m s^{-1} $decade^{-1}$ (across reanalyses) over the period 1991–2024 (Fig. 2.56). The 2023/24 El Niño, which coincided with a negative Pacific Decadal Oscillation (PDO) index, had a relatively weak westerly wind anomaly despite simultaneous global record temperatures. Generally, the westerly wind anomaly maxima appear stronger if the PDO and ENSO are in phase, in accord with Yoon and Yeh (2010).

Looking further back, it is noteworthy that the apparent "quiet" period from the strong 1940–42 El Niño until 1982, in terms of Niño-3.4 westerly wind anomalies, was associated with a mostly negative PDO. This is considered a robust result in terms of data quality, at least at the 850-hPa level, since there are enough surface wind data assimilated, and there are also long radiosonde station records nearby (e.g., Marshall Islands back to 1948).

Figure 2.57b depicts anomalies in pressure vertical velocity and zonal/vertical velocities averaged over the region spanning from 10°S to 10°N for the OND season. Although the conventional Oceanic Niño Index (ONI) indicated neutral ENSO conditions until November 2024 (see section 4b), other indices, such as the relative ONI (L'Heureux et al. 2024) and the Multivariate ENSO Index (https://psl.noaa.gov/enso/mei/), signaled La Niña conditions beginning in mid-2024. Indeed, the 2024 OND season displayed a pronounced descending motion over the central/eastern Pacific, similar to a classical La Niña pattern (see Fig. 2.49 in Mayer et al. 2023). At the same time, a strong ascending motion was observed over the Indo-Pacific Warm Pool, while descending motion prevailed over the tropical western Indian Ocean.

Anomalies of upper-tropospheric circulation in boreal autumn 2024, as reflected by 200-hPa velocity potential and divergent wind anomalies (Fig. 2.57a), were also consistent with La Niña conditions. Anomalously strong divergence prevailed in the Indo-Pacific Warm Pool, indicating enhanced convection, while anomalously strong convergence was seen in the central to eastern tropical Pacific, indicating anomalously strong sinking. Anomalous upper-air divergence extending well into the eastern Indian Ocean was consistent with a weakly positive IOD. The magnitude of 200-hPa divergent wind anomalies over the equatorial Pacific was weaker than during the protracted La Niña of 2020–22, consistent with the only

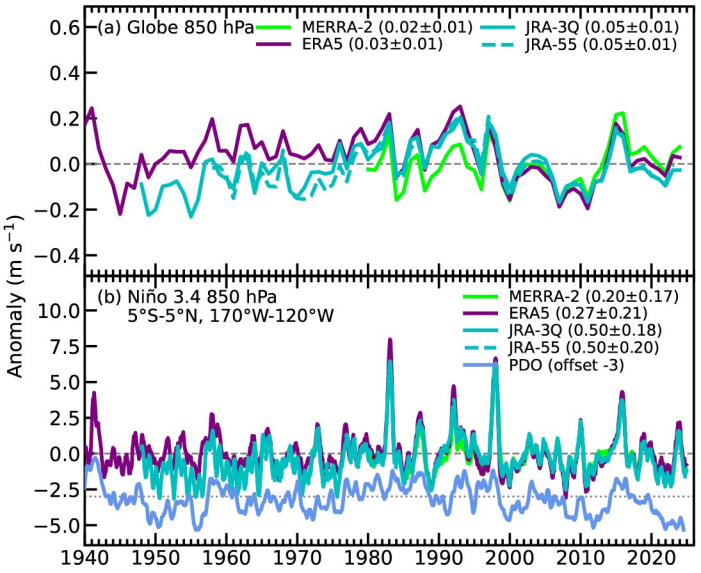

Fig. 2.56. Eastward wind speed anomalies (m s^{-1}; 1991–2020 climatology) averaged (a) globally and (b) over the Nino-3.4 region (5°S–5°N, 170°W–120°W), as depicted from two fourth-generation (MERRA-2 [Gelaro et al. 2017] and JRA-55 [Kobayashi et al. 2015]) and two fifth-generation (the Japanese Reanalysis for Three Quarters of a Century [JRA-3Q; Kosaka et al. 2024] and ERA5 [Hersbach et al. 2020] reanalyses). The Pacific Decadal Oscillation (PDO) index from the NOAA Physical Sciences Laboratory (PSL) Ensemble SST product is shown in panel (b) with the zero shifted for better visibility.

Unauthenticated | Downloaded 11/21/25 11:34 AM UTC

weak negative SST anomalies in OND 2024. The enhanced upper-tropospheric divergence in the Caribbean and central North Atlantic was consistent with the active 2024 hurricane season from mid-September to mid-November (see section 4g2 for details). The weak anomalous convergence over the east central tropical Pacific region was in line with the below-average Pacific hurricane activity (see section 4g3).

The quasi-biennial oscillation in 2024 was near-normal. The stratospheric zonal-mean zonal wind was dominated by a westerly shear zone, which descended from the 12-hPa level down to 80 hPa at about 1.37±0.87 km month^{-1}, which is faster than average, but not unusual. The maximum easterly amplitude occurred in February at 20hPa (–31.6 m s^{-1}) and the maximum westerly amplitude at 40 hPa in October (13.8 m s^{-1}). This amplitude is on the weaker end for a westerly shear zone, but still not an outlier in the historical record. The new easterly formed in October and started descending from the 10-hPa level.

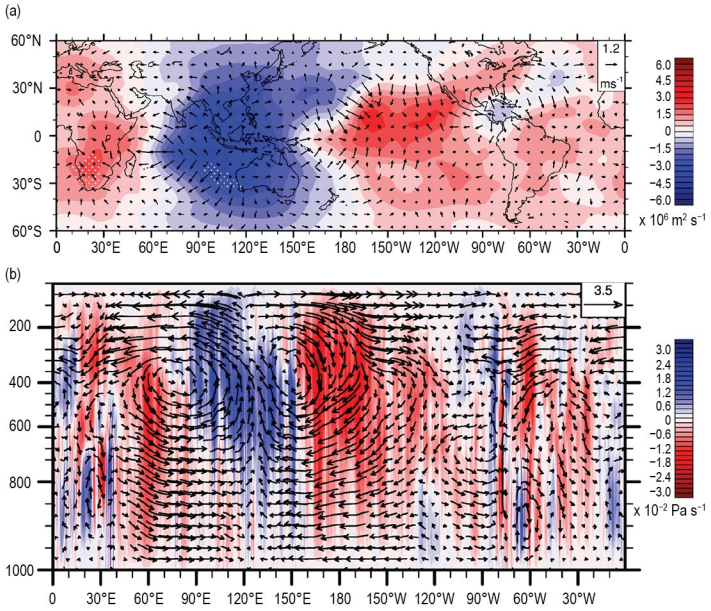

Fig. 2.57. (a) 200-hPa (colors) velocity potential (× 10^6 m^2 s^{-1}) and (arrows) divergent wind anomalies (m s^{-1}) with respect to the 1991–2020 climatology for Oct–Dec 2024; stippling indicates regions with anomalies exceeding 1.65 standard deviations of the seasonal anomalies. Based on ERA5 data. (b) Anomalies of pressure vertical velocity (shaded; units: × 10^{-2} Pa s^{-1}) and u/w anomalies (arrows) averaged over the region 10°S–10°N (zonal [divergent + rotational] wind anomaly [u] unit: m s^{-1}, pressure vertical velocity anomaly [w] unit: × 10^{-2} Pa s^{-1}).

4. NOVEL LIGHTNING FLASH DENSITIES FROM SPACE

—M. Füllekrug, E. Williams, C. Price, S. Goodman, R. Holzworth, S.-E. Enno, and B. Viticchie

The European Organisation for the Exploitation of Meteorological Satellites (EUMETSAT) recently launched the Lightning Imager (LI) onboard the Meteosat Third Generation (MTG) geostationary satellite in support of climate monitoring and lightning warning alerts as a proxy measure for high-impact weather. MTG-LI started to deliver publicly available lightning flash occurrence times and locations on 4 July 2024, 1500 UTC (EUMETSAT 2024). The optical emissions from lightning flashes are recorded with four cameras with slightly overlapping field of views which cover Europe, Africa, the Middle East, the eastern part of South America, and a large part of the Atlantic Ocean (EUMETSAT 2023). South America is also covered by the Geostationary Lightning Mapper (GLM) on the Geostationary Operational Environmental Satellite 16 (GOES-16) (Rudlosky and Virts 2021). The field of view of MGT-LI extends from 80°S to 80°N latitude to cover part of the Antarctic and Arctic, where lightning occurrence may increase as a result of fast rising near-surface temperatures (Holzworth et al. 2021). The lightning flash densities were accumulated in a map with a spatial resolution of 0.1° × 0.1° from July 2024 to January 2025 (Fig. 2.58). These lightning flash densities are largest ~177 fl km^{-2} yr^{-1} along the western side of the Virunga Mountains as part of the Albertine

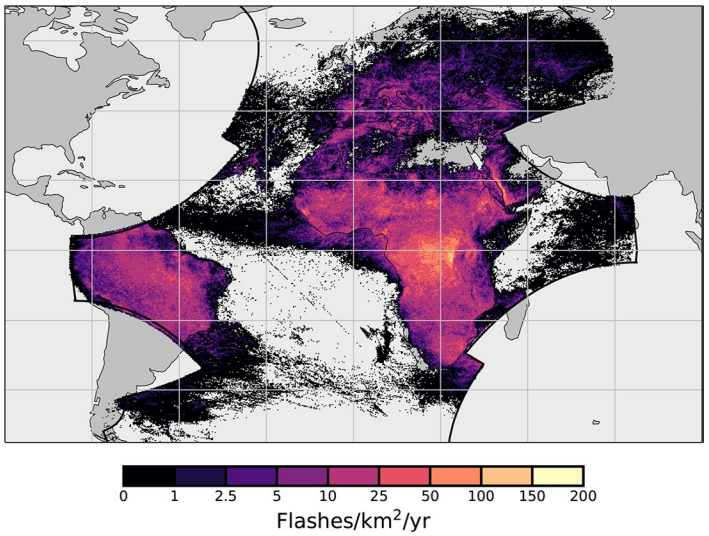

Fig. 2.58. Lightning flash densities (fl km^2 yr^{-1}) calculated from the European Organisation for the Exploitation of Meteorological Satellites' (EUMETSAT) Lightning Imager (LI) on the Meteosat Third Generation (MTG) geostationary satellite from Jul 2024 to Jan 2025. The largest lightning flash densities, ~177 fl km^2 yr^{-1}, are found west of the Virunga Mountains and Lake Kivu along the border between East and Central Africa. Many lightning flashes are detected over the Atlantic and Indian Oceans as part of thunderstorm systems driven by the trade winds.

Unauthenticated | Downloaded 11/21/25 11:34 AM UTC

Rift and Lake Kivu in Africa, where Rwanda, the Democratic Republic of Congo, and Uganda meet. Although lightning is mainly a continental phenomenon (Füllekrug et al. 2022), relatively large flash densities were observed over the Atlantic and Indian Oceans. These lightning flash densities follow the outflow of thunderstorms from the continents, for example westerlies at midlatitudes and easterlies at low latitudes. It is thought that many of the optical pulses recorded by MTG-LI are caused by in-cloud (IC) lightning flashes, which are more common than cloud-to-ground (CG) lightning flashes (Rakov and Uman 2003).

The lightning flash densities over the oceans and the continents have different seasonal variability. Figure 2.59 shows the differences between lightning flash densities during July and December 2024. Over the continents, the lightning flash densities migrate seasonally following the solar insolation, which increases surface temperature and thereby facilitates the development of deep convection. Over the oceans, the lightning flash densities are larger in December compared to July. Four key areas can be distinguished: 1) the Mediterranean Sea, the relative warmth of which interacts with cold European air to enhance instability and deep convection during the winter months, and where numerous particularly intense lightning discharges commonly known as superbolts occur (Holzworth et al. 2019); 2) the Cape Verde Islands, possibly linked to the Atlantic winter storm tracks; 3) the Mid-Atlantic off the coast of western Africa linked to the Intertropical Convergence Zone (ITCZ); and 4) the southern Atlantic off the coast of southern Brazil, due to cooler continental air in winter (July) moving out over the warm Brazil and South Atlantic currents. It is thought that the increase of lightning flash densities over the oceans are caused by the larger heat storing capacity of the oceans when compared to the continents during the winter months, and that warmer ocean currents might assist the initiation of deep convection (Virts et al. 2015; Füllekrug et al. 2002). In this context, it is interesting to note that Lake Victoria (Africa) exhibits a different diurnal cycle when compared to the land around it (Virts and Goodman 2020). It is expected that such regional and seasonal climatological differences will become more evident when MTG-LI lightning flashes accumulate over time, allowing for more detailed analyses with particular emphasis on annual anomalies. Thunderstorms over Lake Victoria are an important area of study because of the risks to local fishers (Thiery et al. 2016; Roberts et al. 2022). Another interesting area of research with EUMETSAT's novel lightning flash densities is the propagation of atmospheric instabilities associated with thunderstorms and lightning across the Atlantic, which have the potential to develop into hurricanes in the Caribbean and the southeastern United States (Price et al. 2009).

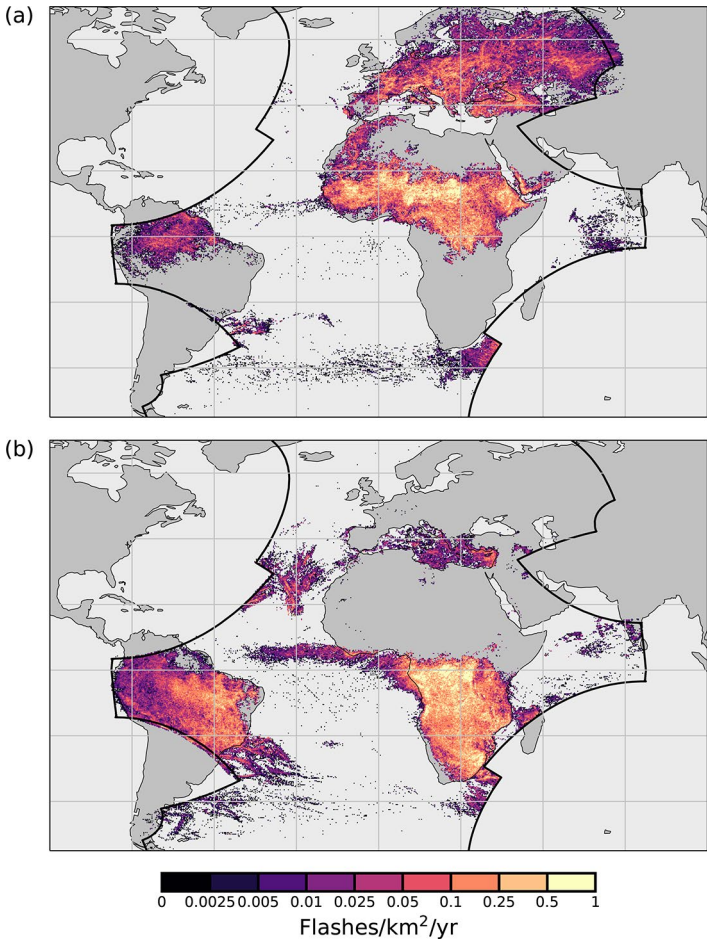

Fig. 2.59. Lightning flash densities (fl km^2 yr^{-1}) for (a) Jul 2024 and (b) Dec 2024.

Unauthenticated | Downloaded 11/21/25 11:34 AM UTC

f. Earth radiation budget

1. EARTH RADIATION BUDGET AT TOP-OF-ATMOSPHERE

—T. Wong, P. W. Stackhouse Jr., P. Sawaengphokhai, J. Garg, and N. G. Loeb

The Earth radiation budget (ERB) at top-of-atmosphere (TOA) is defined by the exchange of incoming total solar irradiance (TSI) and outgoing radiation from Earth given by the sum of reflected shortwave (RSW) and outgoing longwave radiation (OLR). This balance is vital in understanding Earth's climate system and global temperature variations. Over the past two decades, the climate system has amassed a large net positive imbalance, representing a sizeable surplus of energy to the Earth–atmosphere system (Loeb et al. 2021, 2022; von Schuckmann et al. 2023). This net positive imbalance continued in 2024 with a global annual mean of +0.85 W m^{-2} despite the transition from El Niño to La Niña-like conditions.

An analysis of the Clouds and the Earth's Radiant Energy System (CERES) TOA ERB measurements (Table 2.10) shows that the global annual-mean OLR increased by 0.35 W m^{-2} relative to 2023, and RSW by 0.65 W m^{-2}, while the corresponding TSI component remained unchanged in 2024 relative to 2023 (rounded to the nearest 0.05 W m^{-2}). As a consequence of the increase in both OLR and RSW, the global annual-mean net radiation decreased by 1.00 W m^{-2}. Figure 2.60 shows regional annual-mean difference maps in OLR and RSW between 2024 and 2023. The largest reductions in OLR and increases in RSW, indicative of the increases in deep convection, are observed over the tropical Indian Ocean, Australia, the region just east and southeast of

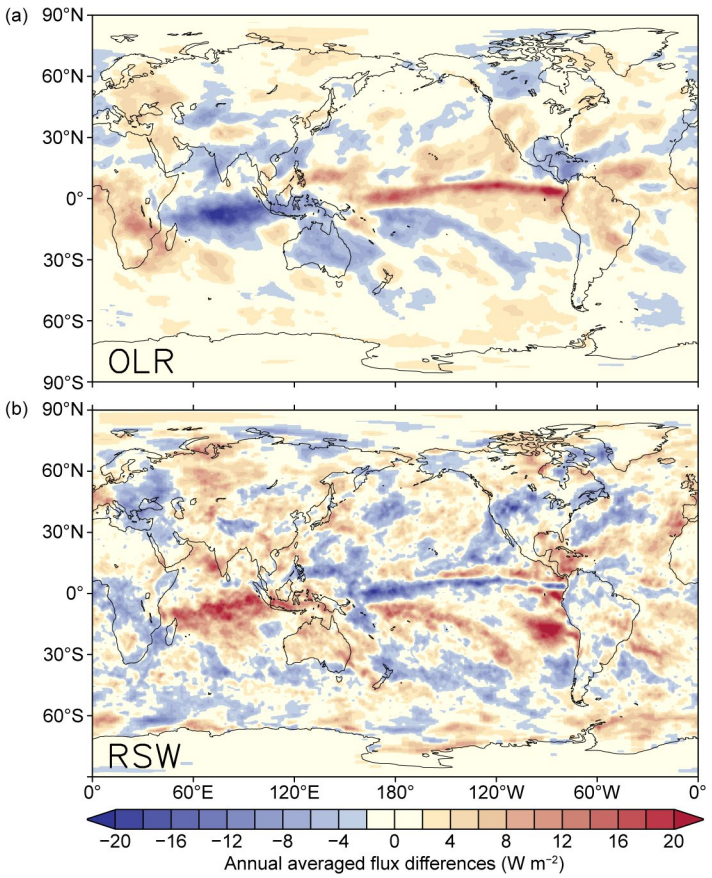

Fig. 2.60. Annual average top-of-atmosphere flux differences (W m^{-2}) between 2024 and 2023 for (a) outgoing longwave radiation (OLR) and (b) reflected shortwave radiation (RSW). The annual mean maps for 2024 were derived after adjusting Dec 2024 Fast Longwave and Shortwave Radiative Fluxes (FLASHFlux) version 4C data using the difference between Clouds and the Earth's Radiant Energy System (CERES) EBAF Ed4.2.1 and CERES FLASHFlux version 4C data in 2023.

Table 2.10. Global annual mean top-of-atmosphere (TOA) radiative flux changes between 2023 and 2024, the 2024 global annual mean radiative flux anomalies relative to their corresponding 2001–23 mean climatological values, the mean 2001–23 climatological values, and the 2-sigma interannual variabilities of the 2001–23 global annual mean fluxes (all units in W m^{-2}) for the outgoing longwave radiation (OLR), total solar irradiance (TSI), reflected shortwave (RSW), absorbed solar radiation (ASR, determined from TSI–RSW), and total net fluxes (Net). All flux values have been rounded to the nearest 0.05 W m^{-2} and only balance to that level of significance.

Global	One Year Change (2024 minus 2023) (W m^{-2})	2024 Anomaly (Relative to 2001–23) (W m^{-2})	Climatological Mean (2001–23) (W m^{-2})	Interannual Variability (2001–23) (W m^{-2})
OLR	+0.35	+1.15	240.40	±0.70
TSI	+0.00	+0.25	340.20	±0.20
RSW	+0.65	–0.85	98.90	±1.20
ASR	–0.65	+1.10	241.30	±1.25
Net	–1.00	–0.05	0.90	±0.95

Unauthenticated | Downloaded 11/21/25 11:34 AM UTC

the Australian continent, and the South Pacific Convergence Zone. The largest increases in OLR and decreases in RSW are observed to cover the entire extent of the equatorial Pacific Ocean. There is also an area of increased RSW off the west coast of South America that does not have a corresponding OLR decrease; this may be due to a thickening of stratocumulus clouds there. These large regional changes represent the response of the climate system as it transitioned from El Niño into La Niña-like conditions. Additional studies are required to understand fully the effects of this El Niño–Southern Oscillation (ENSO) transition as well as other climate drivers on the observed regional changes in the Earth radiation budget during the past year. While the 2024 global annual-mean anomalies, relative to their 2001–23 climatology, for TSI, RSW, and net anomalies (Table 2.10) were near or within their corresponding 2-sigma interannual variability, the 2024 OLR anomaly continued to be outside the range of natural variability observed during the past two decades. This large 2024 OLR anomaly illustrates that the Earth climate system continues to labor excessively to remove the large surplus of energy currently stored within its system.

The global monthly-mean TOA OLR anomaly varied between +0.80 W m^{-2} and +1.55 W m^{-2} in 2024 (Fig. 2.61). This variability is consistent with NOAA's High-resolution Infrared Radiation Sounder (HIRS; Lee and NOAA CDR Program 2018) and NASA's Atmospheric Infrared Sounder (AIRS; Susskind et al. 2012) OLR datasets (not shown). The 2024 global annual-mean TOA OLR anomaly was +1.15 W m^{-2}. The global monthly-mean TOA absorbed solar radiation (ASR, determined from TSI minus RSW) anomaly also remained positive between +0.55 W m^{-2} and +1.65 W m^{-2} in 2024. The 2024 global annual-mean TOA ASR anomaly was +1.10 W m^{-2}. The global monthly-mean TOA total net anomaly, which is calculated from ASR anomaly minus OLR anomaly, varied between –1.00 and +0.35 W m^{-2} in 2024. The global annual-mean TOA total net anomaly for 2024 was –0.05 W m^{-2}. Further analyses are needed to understand the significance and impacts of these observed global changes.

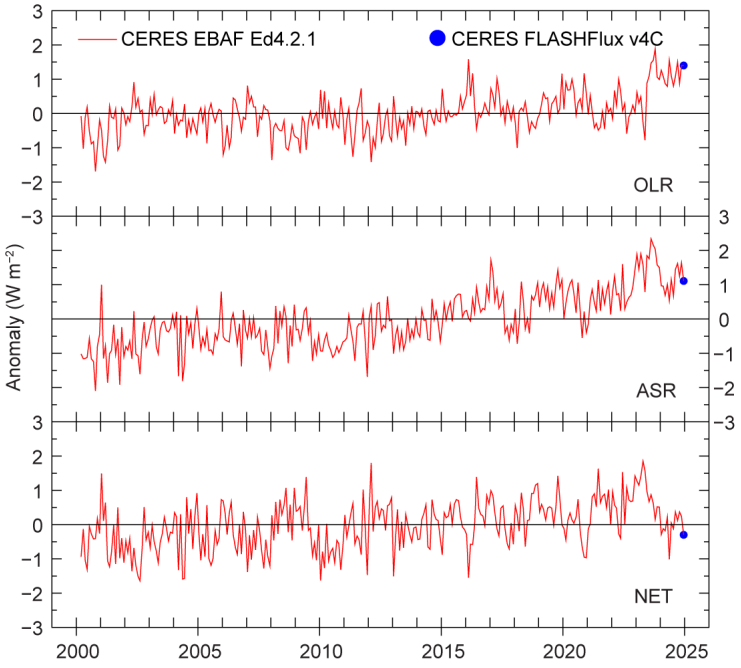

Fig. 2.61. Time series of global monthly mean deseasonalized anomalies (W m^{-2}) of top-of-atmosphere Earth radiation budget for outgoing longwave radiation (OLR; top), absorbed solar radiation (ASR, determined from total solar irradiance [TSI] minus reflected shortwave [RSW]; middle), and total net (TSI–RSW–OLR; bottom) from Mar 2000 to Dec 2024. Anomalies are relative to their calendar month climatology (2001–23). The time series show the Clouds and the Earth's Radiant Energy (CERES) EBAF Ed4.2.1 1-Deg data (Mar 2000–Nov 2024) in solid red line and the CERES Fast Longwave and Shortwave Radiative Fluxes (FLASHFlux) version 4C data (Dec 2024) in solid blue dot; see text for merging procedure (Sources: https://ceres-tool.larc.nasa.gov/ord-tool/jsp/EBAFTOA421Selection.jsp; https://ceres-tool.larc.nasa.gov/ord-tool/jsp/FLASH_TISASelection.jsp).

The TSI data are from a "Community-Consensus TSI Composite" using the methodology defined by Dudok de Wit et al. (2017). The TOA RSW and TOA OLR data are from two different CERES datasets. The data for March 2000–November 2024 are based on the CERES Energy Balanced and Filled (EBAF) Ed4.2.1 product (Loeb et al. 2009, 2012, 2018), which were constructed with measurements from the CERES instruments (Wielicki et al. 1996, 1998) aboard *Terra*, *Aqua*, and NOAA-20 spacecraft. The data for December 2024 are from the CERES Fast Longwave and Shortwave Radiative Fluxes (FLASHFlux) version 4C product (Kratz et al. 2014), which were created using CERES measurements from *Terra* and NOAA-20 spacecraft. The FLASHFlux to EBAF data normalization procedure (Stackhouse et al. 2016) results in 2-sigma monthly uncertainties of ±0.40 W m^{-2}, ±0.00 W m^{-2}, ±0.45 W m^{-2}, and ±0.50 W m^{-2} for the OLR, TSI, RSW, and total net radiation, respectively (rounded to the nearest 0.05 W m^{-2}).

Unauthenticated | Downloaded 11/21/25 11:34 AM UTC

2. MAUNA LOA APPARENT TRANSMISSION RECORD UPDATE FOR 2024

—J. A. Augustine, L. Soldo, K. O. Lantz, A. Baron, K. Smith, E. Asher, and J.-P. Vernier

Since 2018, the Northern Hemisphere (NH) lower stratosphere (LS) has been continuously infused with aerosols from a series of volcanic eruptions (e.g., Raikoke, Ulawun, La Soufriere, Hunga) and wildfire events (e.g., Pacific Northwest; Boone et al. 2020). These perturbations are evident from both a composite, multi-platform analysis from the Global Space-based Stratospheric Aerosol Climatology (GloSSAC; Thomason et al. 2018; Kovilakam et al. 2020) and from aerosol extinction time series imagery from the Stratospheric Aerosol and Gas Experiment (SAGE-III) limb sounder on board the International Space Station (ISS). Although the Hunga eruption occurred in the Southern Hemisphere (20.54°S), its stratospheric plume extended to the latitude of the Mauna Loa Observatory (MLO, 19.536°N, 155.576°W, elevation 3397 m a.s.l.) on the Big Island of Hawaii (Augustine et al. 2024). These events have kept the apparent atmospheric transmission at MLO near or below 0.93 since 2018.

Broadband pyrheliometer measurements of the direct solar beam at MLO have been used to derive atmospheric transmission since 1958 (Ellis and Pueschel 1971). The high altitude and pristine environment there makes transmission a fitting proxy of the extent and variability of stratospheric aerosols. Bodhaine et al. (1981) demonstrated that the principal tropospheric influence on the transmission is the perennial passage of dust from springtime storms in Asia. The complete time series (Fig. 2.62) begins with a very clean period, until the Agung eruption in 1963. That period serves as a baseline-level clean stratosphere, as there were no impactful volcanic events from the mid-1930s to 1963 (Ammann et al. 2003; Sato et al. 1993). Since Agung, a series of eruptions have kept the transmission generally lower than pre-1963 baseline levels.

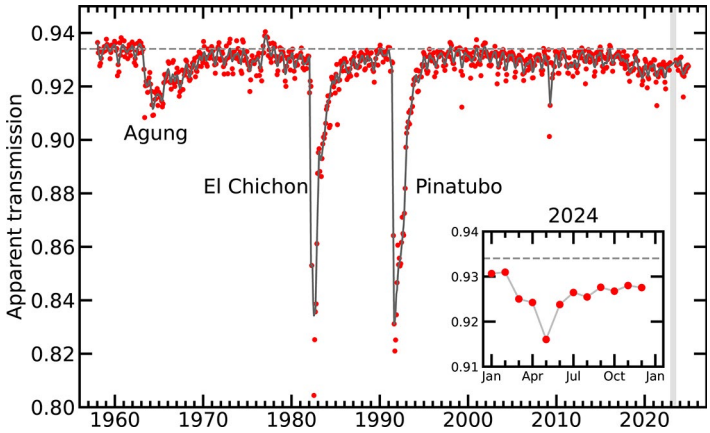

Fig. 2.62. Apparent transmission at Mauna Loa, Hawaii, from 1958 through 2024. Red dots are monthly averages of morning transmission and the black curve is a locally weighted scatterplot smoothing (LOWESS) fit with a six-month smoother applied. Inset shows new data for 2024. Horizontal dashed lines represent the average transmission of the clean period before the eruption of Agung (Ammann et al. 2003; Sato et al. 1993). The shaded area represents the period from Dec 2022 through Jun 2023 when the station was down due to the eruption of Mauna Loa in late Nov 2022.

The extended transmission reduction from 2018 through 2024 is evident in Fig. 2.62. New data for 2024, shown in the inset of Fig. 2.62, have an annual mean of 0.926±0.00387. The year began with a relatively high transmission of ~0.93 in January and February as the LS was recovering from the Hunga eruption. Reduction of the transmission in March and April was probably caused by dust because, after a lull in 2023, several strong spring storms in the desert regions of northwest China and Mongolia brought dust to Japan and Korea and then to Mauna Loa. The latter is supported by the aerosol optical depth (AOD) product from NASA's Moderate Resolution Imaging Spectroradiometer (https://earthobservatory.nasa.gov/global-maps/MODAL2_M_AER_OD). It shows relatively high AOD over Hawaii from March through May, followed by dramatic clearing in June as easterly tropospheric winds became more persistent. The sharp minimum in May was likely due to both Asian dust and stratospheric plumes from explosive eruptions of Ruang in Indonesia on 16 and 29 April 2024, which sent eruptive plumes 21,000 m and 19,000 m above mean sea level, well into the LS. Other NH explosive eruptions in 2024, e.g., Kanlaon in the Philippines, did not penetrate the tropopause. An aerosol layer in the LS centered at ~5°S is apparent in a latitudinal cross section of the aerosol extinction coefficient from SAGE for August 2024 (https://sage.nasa.gov/2024/09/sage-iii-iss-science-highlight/). Residual Hunga aerosol was supplemented in the tropics by Ruang and now extends beyond 30°N, overlying MLO.

Unauthenticated | Downloaded 11/21/25 11:34 AM UTC

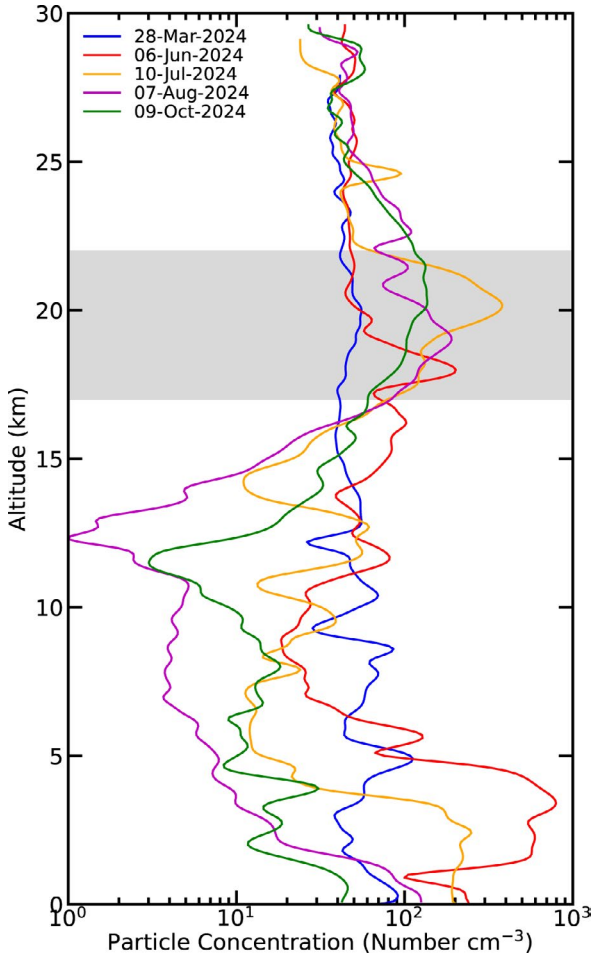

Fig. 2.63. Particle number concentration profiles at standard temperature and pressure (STP; number STP cm^{-3}) from the Portable Optical Particle Spectrometer (POPS) aboard the NOAA Global Monitoring Laboratory balloon platform launched from Hilo, Hawaii, ~60 km east of Mauna Loa. The shaded area highlights lower-stratosphere (LS) aerosol signals in Jun, Jul, Aug, and Oct 2024 that arose from the Ruang eruptions in Apr 2024.

Trajectories from the Hybrid Single-Particle Lagrangian Integrated Trajectory model (HYSPLIT; Stein et al. 2015) reveal that the stratospheric plume from Ruang reached the longitude of MLO around 14 May. NOAA balloon sondes (Todt et al. 2023; Asher et al. 2024) from Hilo, Hawaii, ~60 km east of MLO, on 6 June, 10 July, 7 August, and 9 October carrying the Portable Optical Particle Spectrometer (POPS; Gao et al. 2016) confirm the presence of the Ruang signal between 17,000 m and 22,000 m a.s.l. (Fig. 2.63). That signal was also sampled by a NASA balloon at Baura, Brazil, on 1 June 2024 (https://science.larc.nasa.gov/balneo/). The highest aerosol number concentrations were observed in June (200 Number cm^{-3}) and July (300 Number cm^{-3}), with back trajectories indicating that LS signals at Hilo were from Ruang. Slowly increasing transmission after July that is apparent in the inset of Fig. 2.62, along with the sequence of sondes in Fig. 2.63, reflect a diminishing Ruang signal to the end of the year.

Major wildfire activity in 2024 occurred in South and Central America and Canada from July through September (section 2h3). However, trajectory and the Copernicus Atmosphere Monitoring Service's (CAMS) analyses (https://atmosphere.copernicus.eu/south-america-sees-historic-emissions-during-2024-wildfire-season) suggest that smoke from those fires had little to no presence over Hawaii.

Unauthenticated | Downloaded 11/21/25 11:34 AM UTC

g. Atmospheric composition

1. LONG-LIVED GREENHOUSE GASES

—X. Lan, B. D. Hall, G. Dutton, and I. Vimont

In 2024, the atmospheric burdens of the three most important long-lived greenhouse gases (LLGHGs), carbon dioxide (CO_2), methane (CH_4), and nitrous oxide (N_2O), showed no sign of slowing in their increases. The globally averaged CO_2 level at Earth's surface in 2024—as derived from remote marine boundary layer measurements made by NOAA's Global Monitoring Laboratory—reached 422.8±0.1 ppm (parts per million by moles in dry air; Fig. 2.64a; Table 2.11; uncertainties are reported as one sigma in this section), a 52% increase from the pre-industrial level of ~278 ppm (Etheridge et al. 1996). Globally averaged CH_4 and N_2O levels reached 1930.0±0.6 ppb (parts per billion by moles in dry air) and 337.7±0.1 ppb in 2024, which are 165% and 25% increases from pre-industrial levels, respectively. Yet again, these three LLGHGs are setting record highs.

Carbon dioxide is the most important and abundant anthropogenic greenhouse gas (GHG). Annual growth in global-mean CO_2 has risen from 0.6±0.1 ppm yr^{-1} in the early 1960s to an average of 2.4 ppm yr^{-1} during 2011–20 (Lan et al. 2025a). The increase in CO_2 by 3.4 ppm from 2023 to 2024 tied with that of 2015/16 as the highest on record since systematic measurements started in the 1960s. The main driver of increasing atmospheric CO_2 is fossil fuel (FF) burning; overall emissions, including cement production, increased from 3.0±0.2 Pg C yr^{-1} in the 1960s to 9.7±0.5 Pg C yr^{-1} in the past decade (2014–23; Friedlingstein et al. 2025). Emissions in 2024 are estimated at 10.2±0.5 Pg C yr^{-1} (Friedlingstein et al. 2025). Together with the measured atmospheric increase, it is estimated that about 45% of the FF-emitted CO_2 since 1958 has remained in the atmosphere, with the remaining portion entering the oceans and terrestrial biosphere (Friedlingstein et al. 2025). While increasing emissions of CO_2 from FF combustion are roughly monotonic, the CO_2 growth rate varies from year to year (standard deviation = 0.4 ppm in 2015–24) with variability mostly driven by terrestrial biosphere exchange of CO_2. The El Niño–Southern Oscillation (ENSO) changes regional temperature and precipitation patterns and influences photosynthetic CO_2 uptake, respiratory release, and fires. It is the main driver of CO_2 interannual variability (Betts et al. 2016; Liu et al. 2017). The record-high CO_2 increase in 2024 was likely driven by the record-high global temperature and large fire carbon emissions during the year.

Atmospheric CH_4 is the second most important LLGHG, and in 2024 its globally averaged abundance at Earth's surface reached 1930.0±0.6 ppb (Lan et al. 2025b),

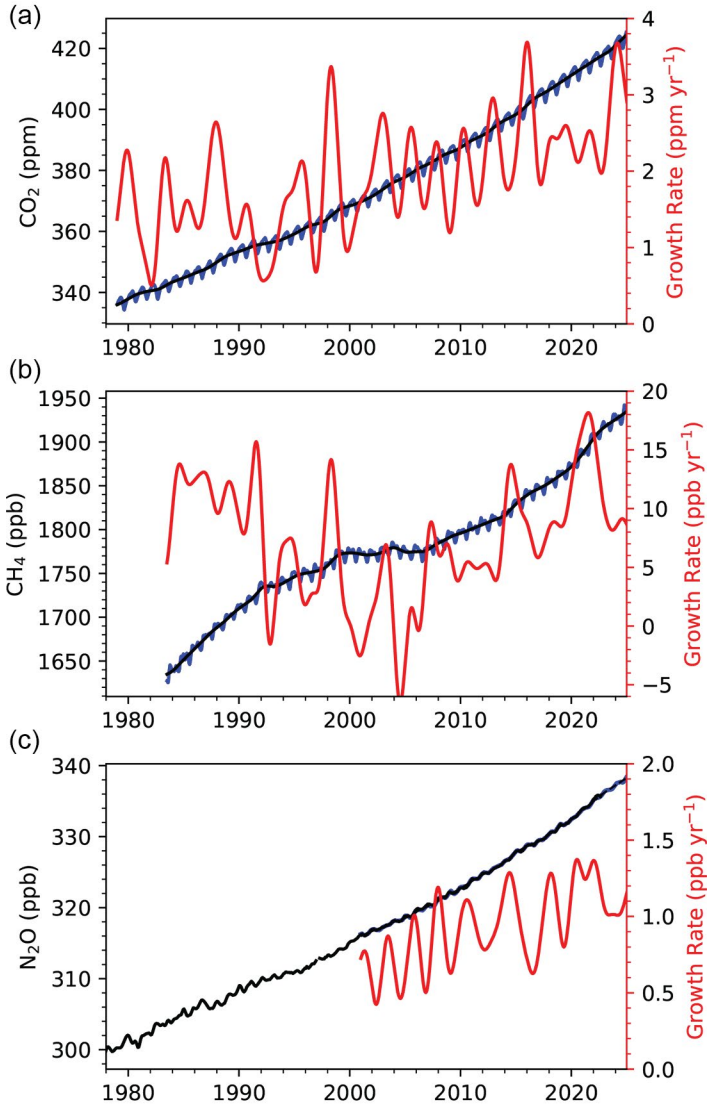

Fig. 2.64. Global mean dry-air remote surface mole fractions (approximately weekly data in blue and deseasonalized trend in black; left axis) and instantaneous growth rates (red, right axis) calculated as time derivatives of deseasonalized trend curves of (a) carbon dioxide (CO_2), (b) methane (CH_4), and (c) nitrous oxide (N_2O) derived from marine boundary layer measurements from the NOAA Global Greenhouse Gases Reference Network. See Dlugokencky et al. (1994) for methods. N_2O data prior to 2000 are insufficient and noisy, and therefore hinder the calculation of a growth rate.

Unauthenticated | Downloaded 11/21/25 11:34 AM UTC

about 2.65 times its pre-industrial level of 729±9 ppb (Mitchell et al. 2013). Global CH_4 increased by an average rate of 11.5±1.4 ppb yr^{-1} between 1984 and 1991, followed by a smaller increase of 5.4±1.8 ppb yr^{-1} between 1992 and 1998, and a further reduced rate near zero (0.7±3.0 ppb yr^{-1}) between 1999 and 2006. Atmospheric CH_4 growth restarted in 2007 and has accelerated since 2014, and further accelerated in 2020–24 with an average rate of increase of 12.6±2.0 ppb yr^{-1} (Fig. 2.64b). Atmospheric CH_4 increased by 8.4±0.4 ppb from 2023 to 2024.

Atmospheric CH_4 is emitted by anthropogenic sources such as fossil fuel exploitation, livestock, waste and landfills, and rice cultivation areas, as well as natural sources such as wetlands and shallow lakes. The ongoing reduction in atmospheric $\delta^{13}C$-CH_4 since 2008 (Michel et al. 2024) indicates increased emissions from microbial sources (Basu et al. 2022), including emissions from livestock as well as natural wetlands and lakes, which have more negative $\delta^{13}C$-CH_4 signatures. Small increases in FF emissions may also play a role in the post-2006 global CH_4 increase (Oh et al. 2023; Lan et al. 2019, 2021; Basu et al. 2022). The contribution of the hydroxyl radical, the main sink for CH_4, is still uncertain, but is less likely to be a major contributor (Morgenstern et al. 2025; Zhao et al. 2019; Lan et al. 2021). Recent studies suggest a dominant role of increased tropical wetland emissions in the post-2020 CH_4 surge (Lin et al. 2024; L. Feng et al. 2022; Peng et al. 2022). Sustained increases in wetland CH_4 emissions may be an indication of an emerging carbon climate feedback (Nisbet et al. 2023; Zhang et al. 2023).

Nitrous oxide (N_2O) is a potent greenhouse gas with an atmospheric lifetime of 120 years (Tian et al. 2024). It is produced by microbes that rely on nitrogen from natural and agricultural soils, animal manure, and the oceans (Davidson 2009). Increased agricultural emissions related to fertilizer usage are the major source of its long-term increase (Tian et al. 2023). The average global atmospheric abundance of N_2O in 2024 was 337.7±0.1 ppb, a 25% increase over its pre-industrial level of 270 ppb (Rubino et al. 2019). Recent growth reached an average rate of 1.3±0.1 ppb yr^{-1} from 2020 to 2022 (Fig. 2.64c), larger than the average rate between 2010 and 2019 (1.0±0.2 ppb yr^{-1}), strongly suggesting increased emissions (Tian et al. 2023). Atmospheric N_2O increased by 1.0±0.1 ppb from 2023 to 2024.

The impacts of LLGHGs on global climate can be estimated using the effective radiative forcing (ERF) of LLGHGs, the change of radiative energy caused by added LLGHGs to the atmosphere, following the approach used in the Intergovernmental Panel on Climate Change's Sixth Assessment Report (Forster et al. 2021). Increased atmospheric abundances of LLGHGs are largely responsible for increasing global temperature (Forster et al. 2023; IPCC 2013). Since the industrial era (1750), increasing atmospheric CO_2 has accounted for 64% of the increase in ERF by LLGHGs, reaching 2.33 W m^{-2} in 2024 (Fig. 2.65). The increase in CH_4 contributed a 0.57 W m^{-2} increase in ERF between 1750 and 2024 while the CH_4-related production of tropospheric ozone and stratospheric water vapor also contributes to ~0.30 W m^{-2} indirect radiative forcing (Myhre et al. 2014). The increase in atmospheric N_2O abundance contributed to a 0.23 W m^{-2} increase in ERF between 1750 and 2024.

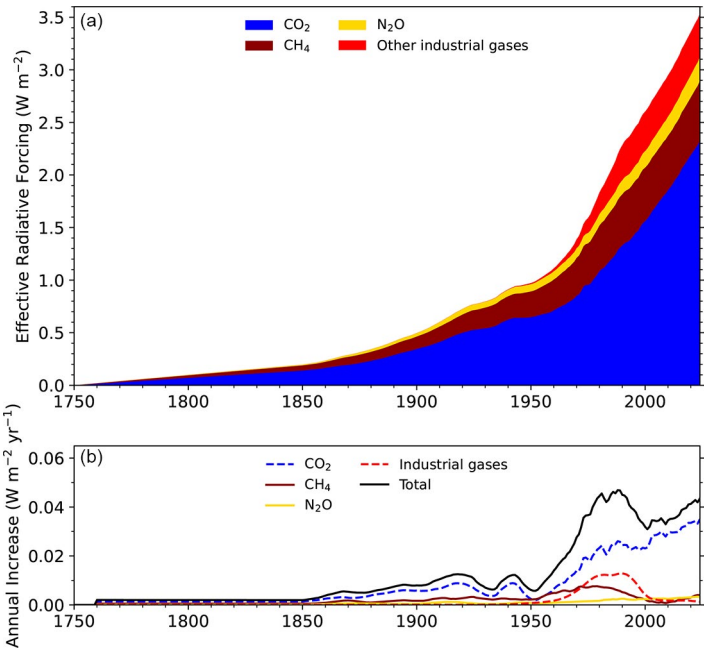

Fig. 2.65. (a) Effective radiative forcing (W m^{-2}) due to long-lived greenhouse gases (LLGHGs; see Table 2.11 for details on industrial gases). (b) Annual increase in effective radiative forcing (W m^{-2} yr^{-1}) smoothed by a 10-year running average.

Unauthenticated | Downloaded 11/21/25 11:34 AM UTC

Table 2.11. Summary table of long-lived greenhouse gases for 2024 (CO_2 mixing ratios are in ppm, N_2O and CH_4 in ppb, and all others in ppt).

Compound Class	Industrial Designation or Common Name	Chemical Formula	ERF[a]	Effective Rad. Efficiency (W m^{-2} ppb^{-1})[b]	Effective Rad. Forcing[a] (ERF or SARF) (W m^{-2})	Mean Surface Mole Fraction, 2024 [Change from Prior Year][c]	Lifetime (yrs)[b]
Acidic Oxide	Carbon Dioxide	CO_2	Y	1.33×10^{-5}	2.33	422.8 [3.4]	
Alkane	Methane	CH_4	Y	3.89×10^{-4}	0.57	1930.0 [8.4]	9.1
Nitride	Nitrous Oxide	N_2O	Y	3.20×10^{-3}	0.23	337.7 [1.0]	109
Chlorofluorocarbons	CFC-11	CCl_3F	N(Y)[e]	0.30	0.057 (0.063)	214.5 [–2.7][d]	52
Chlorofluorocarbons	CFC-12	CCl_2F_2	N(Y)[e]	0.36	0.156 (0.172)	481.5 [–3.9][d]	102
Chlorofluorocarbons	CFC-113	CCl_2FCClF_2	N	0.30	0.020	66.6 [–0.6][d,f]	93
Hydrochlorofluorocarbons	HCFC-22	$CHClF_2$	N	0.21	0.052	245.3 [–2.2]	11.6
Hydrochlorofluorocarbons	HCFC-141b	CH_3CCl_2F	N	0.16	0.004	24.4 [–0.1]	8.8
Hydrochlorofluorocarbons	HCFC-142b	CH_3CClF_2	N	0.19	0.004	20.7 [–0.3]	17.1
Hydrofluorocarbons	HFC-134a	CH_2FCF_3	N	0.17	0.022	134.7 [5.2]	13.5
Hydrofluorocarbons	HFC-152a	CH_3CHF_2	N	0.10	<0.001	7.73 [0.38]	1.5
Hydrofluorocarbons	HFC-143a	CH_3CF_3	N	0.17	0.005	32.4 [1.7]	52
Hydrofluorocarbons	HFC-125	CHF_2CF_3	N	0.23	0.01	47.5 [4.0]	31
Hydrofluorocarbons	HFC-32	CH_2F_2	N	0.11	0.003	38.2 [4.4]	5.3
Hydrofluorocarbons	HFC-23	CHF_3	N	0.19	0.007	37.8 [1.0]	228
Hydrofluorocarbons	HFC-365mfc	$CH_3CF_2CH_2CF_3$	N	0.24	<0.001	1.03 [0.04]	8.9
Hydrofluorocarbons	HFC-227ea	CF_3CHFCF_3	N	0.27	<0.001	2.39 [0.19]	36
Chlorocarbons	Methyl Chloroform	CH_3CCl_3	N	0.07	<0.001	0.87 [–0.11]	5
Chlorocarbons	Carbon Tetrachloride	CCl_4	N	0.17	0.012	73.0 [–0.8][d]	30
Chlorocarbons	Methyl Chloride	CH_3Cl	N	0.005	<0.001	550 [5]	0.9
Bromocarbons	Methyl Bromide	CH_3Br	N	0.004	<0.001	6.52 [0.08]	0.8
Bromocarbons	Halon 1211	$CBrClF_2$	N	0.31	0.001	2.75 [–0.09]	16
Bromocarbons	Halon 1301	$CBrF_3$	N	0.31	0.001	3.3 [0]	72
Bromocarbons	Halon 2402	$CBrF_2CBrF_2$	N	0.33	<0.001	0.390 [–0.005]	28
Fully Fluorinated Species	Sulfur Hexafluoride	SF_6	N	0.57	0.007	11.8 [0.4]	850–1280
Fully Fluorinated Species	PFC-14	CF_4	N	0.1	0.005	90.4 [1.0]	~50,000
Fully Fluorinated Species	PFC-116	C_2F_6	N	0.26	0.001	5.33 [0.09]	~10,000
Fully Fluorinated Species	PFC-218	C_3F_8	N	0.28	<0.001	0.78 [0.02]	~2600
Fully Fluorinated Species	PFC-318	c-C_4F_8	N	0.33	<0.001	2.18 [0.08]	~3200

[a] Effective Radiative Forcing (ERF) calculated by multiplying the stratospheric-temperature-adjusted radiative efficiency (SARF) by the global mole fraction (in ppb) and then applying a tropospheric adjustment factor for the species indicated based on recommended values from chapters 6 and 7 in the Intergovernmental Panel on Climate Change Sixth Assessment Report Working Group I (IPCC AR6 WGI) Report. The Radiative Forcing column is either ERF (where indicated) or SARF. The adjustments to the SARF are CO_2: 5%±5%, CH_4: –14%±15%, N_2O: 7%±13%–16%

[b] Effective radiative efficiencies and lifetimes were taken from Appendix A in WMO (2022) and Hodnebrog et al. (2020a), except CH_4 which is from Prather et al. (2012). For CO_2, numerous removal processes complicate the derivation of a global lifetime. AGGI = Annual Greenhouse Gas Index. For radiative forcing, see https://www.esrl.noaa.gov/gmd/aggi/aggi.html

[c] Mole fractions are global, annual, midyear surface means determined from the NOAA Cooperative Global Air Sampling Network (Hofmann et al. 2006), except for PFC-14, PFC-116, PFC-218, PFC-318, and HFC-23, which were measured by the Advanced Global Atmospheric Gases Experiment (AGAGE; Mühle et al. 2010; Miller et al. 2010). Changes indicated in brackets are the differences between the 2024 and 2023 means. All values are preliminary and subject to minor updates.

[d] Global mean estimates derived from multiple NOAA measurement programs ("Combined Dataset").

[e] ERF-calculated values for CFC-11 and CFC-12 are highly uncertain but recommended by the IPCC AR6 WGI Report. Thus, they are included in parentheses here as the lower confidence value. The adjustment to the SARF for these values is 12%±13% (Hodnebrog et al. (2020b).

[f] Measurements of CFC-113 are known to be a combination of CFC-113 and CFC-113a, with CFC-113a contributing approximately 0.3 ppt to the 2024 reported abundance of CFC-113.

Unauthenticated | Downloaded 11/21/25 11:34 AM UTC

2. OZONE-DEPLETING GASES

—I. J. Vimont, B. D. Hall, S. A. Montzka, G. Dutton, J. Mühle, M. Crotwell, K. Petersen, S. Clingan, and D. Nance

Since 1987, the Montreal Protocol (Montreal Protocol 1989) and its Amendments (The Protocol; https://ozone.unep.org/treaties/montreal-protocol) have regulated the production and consumption of ozone-depleting substances (ODSs) and their replacement chemicals. Controlled chemicals include chlorofluorocarbons, hydrochlorofluorocarbons, and hydrofluorocarbons, (CFCs, HCFCs, and HFCs, respectively), as well as halons and methyl bromide. While The Protocol was initially enacted to limit damage to the stratospheric ozone layer by limiting ODS production for dispersive uses, these controls have also limited the impact of these gases on Earth's radiation budget. Through the 2016 Kigali Amendment, The Protocol also limits production and consumption of some HFCs that do not destroy stratospheric ozone, but like the CFCs and HCFCs they replace, are strong greenhouse gases.

Emissions of a chemical do not necessarily cease once production has been phased out for dispersive uses, nor are emissions the only factor controlling the atmospheric abundance of a trace gas species. Reservoirs that exist, e.g., in equipment and insulating foams (known as "banks") can continue to emit controlled chemicals for years after the final phase-out of production has occurred. The observed atmospheric trends of ODSs and their replacements (Fig. 2.66) result from the combination of emissions and the rate at which compounds degrade via loss processes such as photolysis. As an example, CFC-11 and CFC-12 production for dispersive use was scheduled to be globally phased out in 2010, but they have long atmospheric lifetimes and remain present in large banks that continue to emit both compounds. CFC-12, the most abundant CFC, declined by 4 ppt in 2024 to 481.4 ppt (Table 2.11). Conversely, methyl chloroform (CH_3CCl_3) has relatively small banks and a short lifetime and, having been phased out in 2015, has declined in the atmosphere to 0.87 ppt, 99% lower than its peak abundance.

While the transition from CFCs to HCFCs resulted in an increase in the atmospheric abundance of several HCFCs during the 1990s and 2000s, the mole fractions of the three most abundant HCFCs (HCFC-22, HCFC-141b, and HCFC-142b) have started to decline (Fig. 2.66; Table 2.11). For example, HCFC-22 declined by 2.2 ppt in 2024 to 245.3 ppt. The combined radiative forcing from these three HCFCs peaked in 2021 and is now declining (Western et al. 2024). In contrast, mole fractions of several HFCs, used as replacements for HCFCs, have increased substantially since their introduction in the mid-1990s, in particular HFC-134a, HFC-32, and HFC-23. There is substantial interest in HFC-23 because it is a potent greenhouse gas and is emitted primarily as a by-product of HCFC-22 production (UNEP 2024). The production of chlorinated and fluorinated compounds such as HFCs and some plastics can also result in emissions of ODSs. Recent increases in abundances and emissions of CFC-13, CFC-112a, CFC-113a, CFC-114a, and CFC-115 (not shown), chemicals controlled by the Montreal Protocol, have been identified and could be related to uses and processes not controlled by the Montreal Protocol (Western et al. 2023). Of these, CFC-115 is the most abundant at ~8.8 ppt.

While global measurements of ODSs mainly represent the composition of the planetary boundary layer close to Earth's surface,

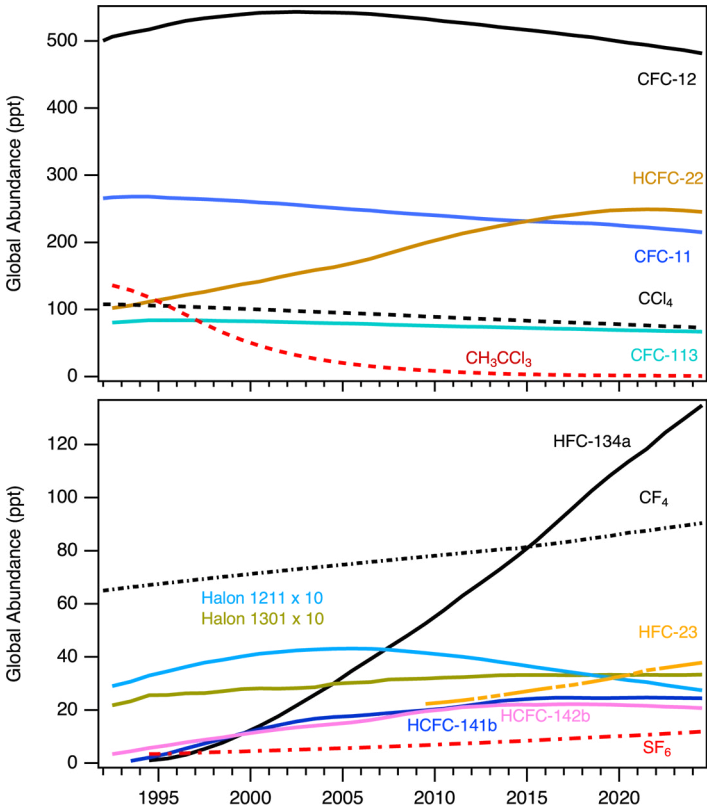

Fig. 2.66. Global mean abundances (mole fractions) at Earth's surface (ppt = pmol mol^{-1} in dry air) for several halogenated gases, many of which deplete stratospheric ozone. See Table 2.11 for the 2024 global mean mole fractions of these and other gases.

Unauthenticated | Downloaded 11/21/25 11:34 AM UTC

destruction of the ozone layer is dependent on the amount of reactive halogen in the stratosphere. In order to track progress towards the ozone layer's recovery, equivalent effective stratospheric chlorine (EESC) is used as a measure of the reactive halogen loading in the stratosphere based on globally distributed surface measurements, atmospheric transport, and chemical reactivity (Daniel et al. 1995; Newman et al. 2007). While EESC provides a measure of reactive stratospheric halogen, it is also useful to scale the EESC to provide context relative to stratospheric ozone recovery. The Ozone Depleting Gas Index (ODGI) assesses the EESC relative to 1980, where an ODGI of 0 represents the EESC level in 1980, and an ODGI of 100 represents peak EESC, which occurred in 1996/97 at midlatitudes and in 2001/02 over Antarctica. The EESC and, therefore, also the ODGI, are reported for the midlatitudes and the Antarctic in order to capture the range of ozone layer recovery timescales due to differences in transport and chemical degradation processes in the stratosphere. At the beginning of 2024, reactive halogen in the Antarctic (represented by air with a mean transit time from the surface of 5.5 years) had decreased 28% from the peak relative to the 1980 benchmark. Likewise, reactive halogen in the midlatitude region (represented by air with a mean transit time from the surface of three years) declined by 55% (Fig. 2.67; https://gml.noaa.gov/odgi/).

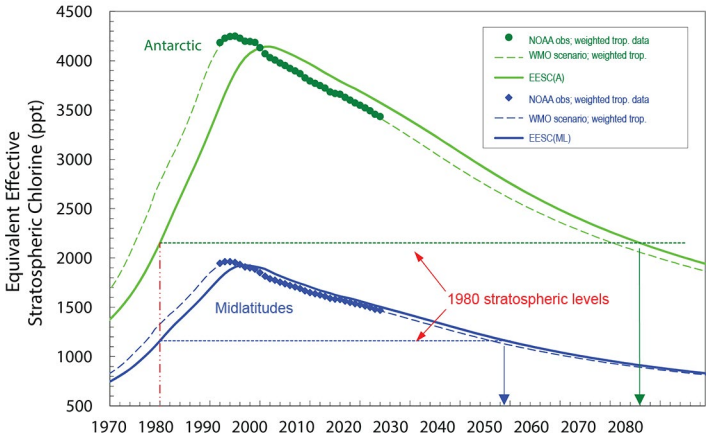

Fig. 2.67. Equivalent effective stratospheric chlorine (EESC) calculated for air representative of the Antarctic (green) and midlatitude (blue) stratosphere (EESC[A] and EESC[ML], respectively). Dashed lines represent tropospheric measurement-derived scenarios, based on past measurements and, for the future, full adherence to all controls from The Protocol based on the World Meteorological Organization (WMO)/United Nations Environment Programme 2018 Ozone Assessment. Solid blue and green arrows indicate currently predicted dates for the return of EESC to 1980s levels in midlatitudes (year 2048) and over the Antarctic (year 2076), respectively. Solid lines depict inferred stratospheric changes based on the measured tropospheric curves.

3. TROPOSPHERIC AEROSOLS

—S. Rémy, N. Bellouin, M. Parrington, M. Ades, M. Alexe, A. Benedetti, O. Boucher, E. di Tomaso, and Z. Kipling

Atmospheric aerosols play an important role in the climate system by scattering and absorbing radiation, and by affecting the life cycle, optical properties, and precipitation activity of clouds (IPCC AR6, chapter 6; Szopa et al. 2021). Aerosols in the boundary layer also represent a serious public health issue in many countries and are thus subject to monitoring and forecasting as part of air quality policies.

The Copernicus Atmosphere Monitoring Service (CAMS; https://atmosphere.copernicus.eu) runs near-real-time (NRT) global analyses and forecasts of aerosols and trace gases. CAMS also produces a reanalysis of global aerosols and trace gases that covers the years between 2003 and 2024 (CAMSRA; Inness et al. 2019) by combining state-of-the-art numerical modeling and aerosol remote sensing retrievals from the Moderate Resolution Imaging Spectroradiometer (MODIS) onboard the *Terra* and *Aqua* satellites (Levy et al. 2013) and the Advanced Along Track Scanning Radiometer (AATSR) onboard the Envisat satellite (Popp et al. 2016). This section uses data exclusively from the CAMS reanalysis, focusing on aerosol optical depth at 550 nm in the middle of the visible light spectrum (AOD550), as well as surface particulate matter (PM2.5) concentrations. AOD550 is a vertically integrated quantity while PM2.5 is a surface parameter.

AOD550 and PM2.5 absolute values in 2024 (Plates 2.1ab, ac, respectively) show maxima from pollution over the industrial regions of India and China, as well as from dust over the Sahara and the Middle East. High values in 2024 also arose from seasonal vegetation fires in equatorial Africa and the southern Amazon Basin, and occasionally from extreme fires, most notably across large parts of Canada and eastern Siberia. A strong seasonality appears in AOD550, driven mainly by dust episodes between March and July in the Sahara, Middle East, and Taklimakan/Gobi

Unauthenticated | Downloaded 11/21/25 11:34 AM UTC

regions, as well as seasonal biomass burning emissions in tropical regions of Africa, South America, and Indonesia (Fig. 2.68c). Globally averaged AOD550 in 2024 was the highest since 2019, driven by higher-than-usual fire activity over large parts of North and South America as well as equatorial Africa.

The AOD550 anomalies (Plate 2.1ab) are dominated by the large fire events over western Brazil, Canada, equatorial Africa, and eastern Siberia. The PM2.5 anomalies mostly match those in AOD, except for the PM2.5 anomalies caused by large fires, which caused elevated aerosol plumes with a clear AOD signature, but without a PM2.5 one. Over parts of South America, a series of recent years with positive anomalies led to a positive trend of AOD since 2012. Dust storm activity was higher than usual over the western Sahara (with the signal mostly in PM2.5) and the southern Arabian Peninsula, and lower than usual over the eastern Sahara. The negative anomalies of AOD and PM2.5 over East Asia, the eastern United States, and Europe can be explained by ongoing decreasing long-term trends in these regions. Conversely, the positive anomalies over India and Iran are associated with increasing long-term trends over these regions. The exceptional nature of the fires in the summer of 2024 in South America, Canada, and equatorial Africa is highlighted by Plate 2.1ad, which shows the number of extreme AOD days in 2024 as compared to the climatological distribution of daily AOD over the 2003–24 period. Interestingly, for the South American fires, the highest number of extreme AOD days is found over the Pacific and Atlantic Oceans from transported plumes of smoke originating from Bolivia and southern Brazil. Fires also caused a significant number over parts of Siberia, while the high values over India are mostly from anthropogenic sources.

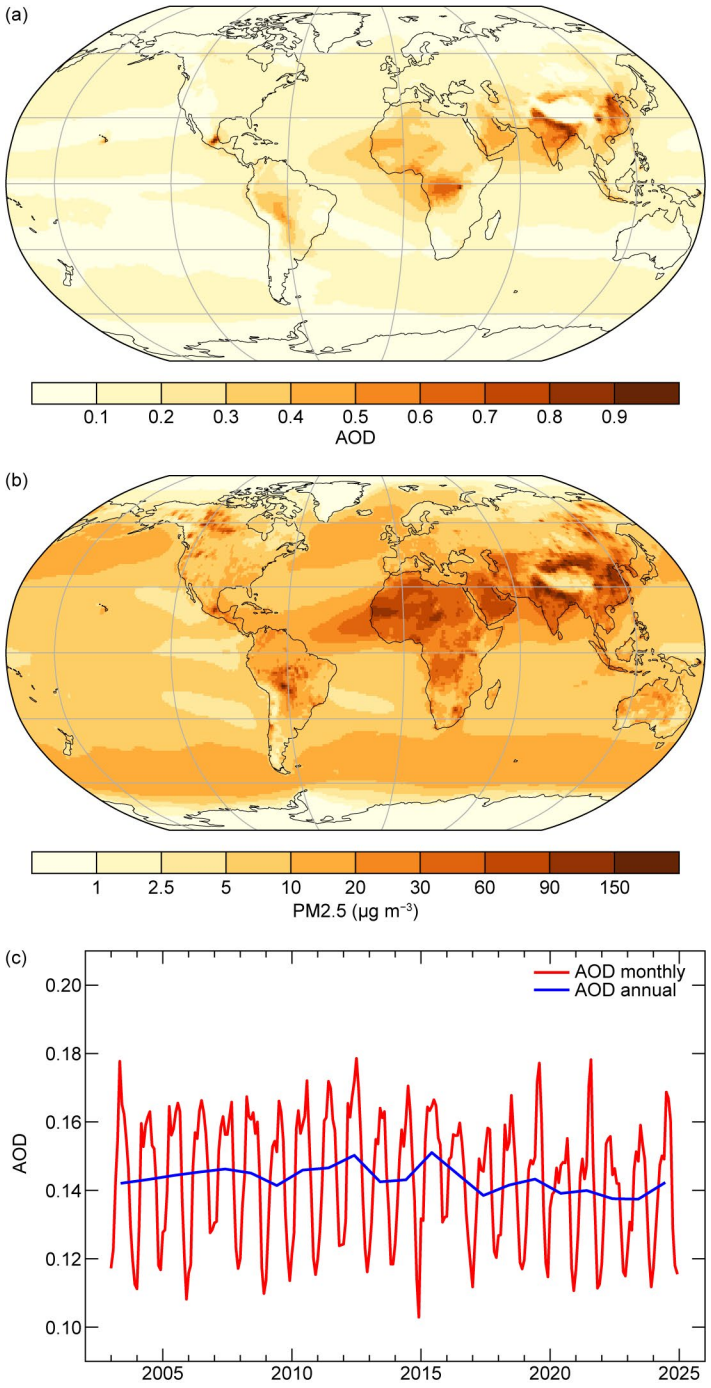

Fig. 2.68. (a) Global aerosol optical depth (AOD) at 550 nm in 2024. (b) Global surface particulate matter (PM2.5) concentrations (μg m^{-3}) in 2024. (c) Global average of total AOD at 550 nm averaged over monthly (red) and annual (blue) periods for the period 2003–24.

The AOD550 nm and PM2.5 2003–24 trends (Fig. 2.69a,b) are generally collocated, although discrepancies can occur, particularly in regions mainly affected by fires and dust transport. Between 2003 and 2024, there is a significant negative trend in both quantities over most of the United States, Europe, East Asia, and most of the eastern Sahara. The first three can be attributed to a decrease in anthropogenic emissions while the last is caused mainly by a decrease of desert dust emissions. Positive trends in AOD are noted over parts of Siberia, driven by biomass burning events, as well as over India and Iran, driven by an increase in anthropogenic emissions (Satheesh et al. 2017). Interestingly, the positive trend in AOD over Iran and the Indian subcontinent is not matched by a corresponding positive trend in PM2.5. This means that in the CAMS reanalysis, the increasing trend in aerosol burden over these areas is simulated aloft and not at surface, which could be an artefact, or because of elevated aerosol plumes such as those from desert dust or fire events.

Unauthenticated | Downloaded 11/21/25 11:34 AM UTC

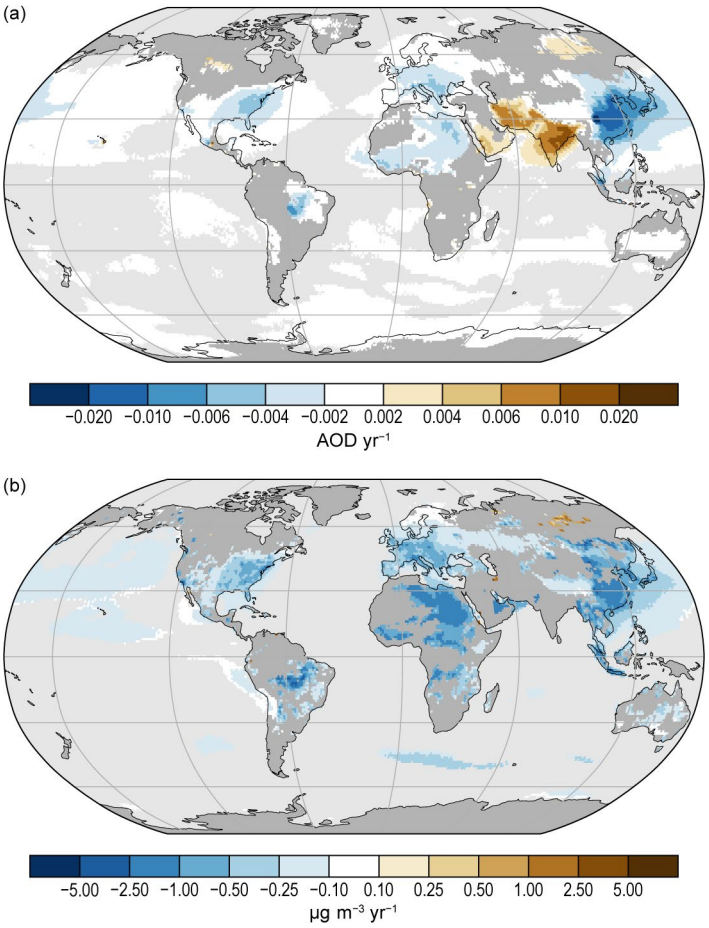

Fig. 2.69. (a),(b) linear trends of total aerosol optical depth (AOD yr^{-1}) and particulate matter (PM2.5), respectively, (μg m^{-3} yr^{-1}) for the period 2003–24. Only trends that are statistically significant (95% confidence level) are shown. Regions with decreasing trends include the eastern United States, most of Europe, and parts of Brazil and China, as well as the Korean peninsula and Japan.

Tarasick et al. 2019; Gulev et al. 2021; Chang et al. 2024). On the global scale, the tropospheric ozone burden (TOB) increased from the mid-1990s to 2019, based on a range of in situ and satellite observations. Last year's *State of the Climate* report (Cooper et al. 2024a) reported an apparent leveling-off of ozone for the period 2020–23, mainly at northern midlatitudes, likely initiated by the economic downturn associated with the Coronavirus disease 2019 (COVID-19) pandemic. However, the updated tropospheric ozone product from the Aura Ozone Monitoring Instrument (OMI) and the Microwave Limb Sounder (MLS) satellite instruments (based on the new OMI Collection 4 total ozone) does not support a sustained leveling-off of ozone on the global scale (Fig. 2.70a), and the long-term trend for the period 2004–24 is positive. Notably, 2024 experienced the highest TOB since the OMI/MLS record began in 2004.

Anthropogenic AOD and radiative forcing resulting from aerosol–radiation interactions (RFari) and aerosol–cloud interactions (RFaci) are shown in Appendix Fig. A2.12 for 2024 and the period 2003–24. They are estimated using the methods described in Bellouin et al. (2020). There was a small increase in anthropogenic AOD again this year, but aerosol radiative forcing has remained fairly flat recently.

4. TROPOSPHERIC OZONE

—O. R. Cooper, J. R. Ziemke, K.-L. Chang, and P. Effertz

Tropospheric ozone contributes to almost all of ozone's effective radiative forcing (tropospheric and stratospheric), estimated to be 0.51 (0.25–0.76) W m^{-2} for the period 1750–2023 (Forster et al. 2024). A short-lived climate forcer, its lifetime is on the order of three to four weeks (Archibald et al. 2020) and, therefore, its global distribution is highly variable and difficult to quantify (Gaudel et al. 2018;

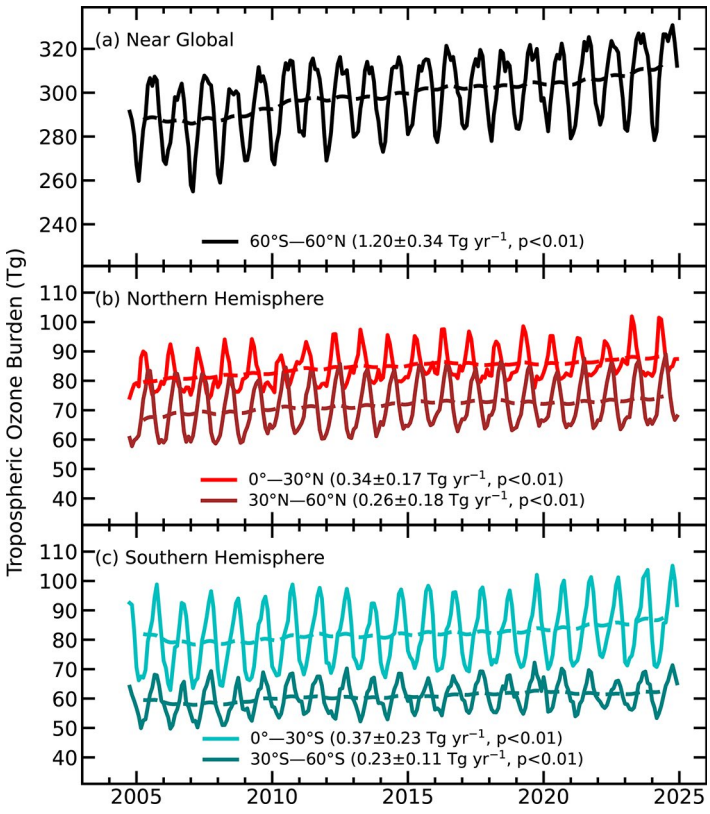

Fig. 2.70. Monthly averages (solid lines) and 12-month running means (dashed lines) of Ozone Monitoring Instrument (OMI)/Microwave Limb Sounder (MLS) tropospheric ozone burdens (Tg) from Oct 2004 through Dec 2024 for (a) near global (60°S–60°N; black), (b) the Northern Hemisphere tropics (0°–30°N; red) and midlatitudes (30°N–60°N; dark red), and (c) the Southern Hemisphere tropics (0°–30°S; blue) and midlatitudes (30°S–60°S; green). Slopes of linear fits to the data are presented with their 95%-confidence-level uncertainties.

Unauthenticated | Downloaded 11/21/25 11:34 AM UTC

Averaged over the entire year of 2024, and relative to 2005–23, positive ozone anomalies were widespread across the Northern Hemisphere (NH), with the largest anomalies found above central Asia, the tropical North Atlantic, the eastern North Pacific, and western North America (Plate 2.1ae). Anomalies in the Southern Hemisphere (SH) were generally positive across the tropics and across much of the midlatitudes, with weaker positive anomalies across southern Australia and the central South Pacific Ocean.

Over the full 20-year record, global (60°S–60°N) TOB increased at the average rate of 1.20±0.34 Tg yr^{-1}, equal to a total increase of ~8% (Fig. 2.70). Regarding the impact of COVID-19, the updated OMI/MLS product shows a brief leveling-off of ozone from 2019 to 2020 and into 2021, similar to other satellite products (Ziemke et al. 2022); however, by the end of 2021, ozone began to increase again through 2024. Regionally, the strongest trends (2004–24) have occurred above central and southern Asia and also across western North America and central South America (Fig. 2.71). Strong ozone decreases were not observed above any region of the globe.

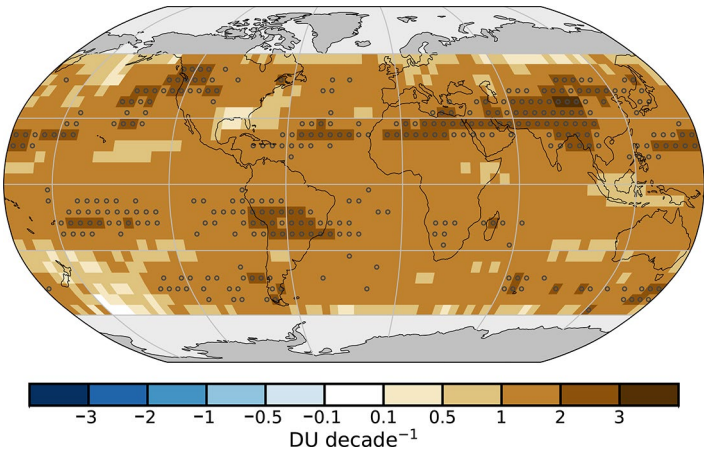

Fig. 2.71. Linear trends in Ozone Monitoring Instrument (OMI)/Microwave Limb Sounder (MLS) tropospheric column ozone (DU decade^{-1}) on a 5° × 5° grid from Oct 2004 through Dec 2024. Circles denote trends with p-values <0.05. Trends were calculated using a multivariate linear regression model (e.g., Randel and Cobb 1994 and references therein) that included a seasonal cycle fit and the Niño-3.4 index as an El Niño–Southern Oscillation proxy; trend uncertainties included autoregressive adjustment via Weatherhead et al. (1998).

Ozone trends at the surface are often decoupled from the trends in the free troposphere (Gulev et al. 2021; Chang et al. 2023), and the availability of long-term surface ozone records is too limited spatially to produce a globally representative surface ozone product (Sofen et al. 2016). However, global chemistry climate models can estimate surface ozone trends, and their output can be evaluated against reliable observations. Ozone trends from six surface sites are reported here, all located in remote environments and suitable for evaluating coarse resolution global models. These records are now 25 to 50 years in length (Fig. 2.72; Table 2.12). In the Arctic, Barrow Atmospheric Observatory (at sea level) reported a weak positive trend of 0.45±0.30 ppbv decade^{-1}, while the high-elevation site of Summit, Greenland, showed decreasing ozone since 2000 (–1.89±0.85 ppbv decade^{-1}). In the remote North Atlantic Ocean, Tudor Hill, Bermuda (sea level),

Table 2.12. Ozone trends at the six baseline monitoring sites shown in Fig. 2.72. Trends are estimated by the generalized least-squares method, based on monthly anomalies referenced to the monthly 2000–20 base period (Chang et al. 2021), and reported with 95% confidence intervals and *p*-values. The trends at the Mauna Loa Observatory (MLO) were adjusted to account for interannual meteorological variability following the methods of Chang et al. (2024), spanning the period 1974–2024.

Site Name — Latitude, Longitude, Elevation	Years With Data	Trend, ppbv decade^{-1}	*p*-value
Summit, Greenland — 72.6°N, 38.5°W, 3238 m	2000–present	–1.89±0.85	p<0.01
Barrow Atmospheric Observatory, Alaska — 71.3°N, 156.6°W, 11 m	1973–present	0.45±0.30	p<0.01
Tudor Hill, Bermuda — 32.3°N, 64.9°W, 30 m	1988–98, 2003–present	–0.65±1.04	p=0.21
Mauna Loa Observatory (MLO), Hawaii — 19.5°N, 155.6°W, 3397 m	1973–present	1.21±0.30	p<0.01
Arrival Heights, Antarctica — 77.8°S, 166.8°W, 50 m	1996–present	–0.04±0.52	p=0.88
South Pole, Antarctica — 90.0°S, 59.0°E, 2840 m	1975–present	0.35±0.33	p=0.03

Unauthenticated | Downloaded 11/21/25 11:34 AM UTC

reported high interannual variability and a weak negative trend (−0.65±1.04 ppbv decade^{-1}), while Mauna Loa (3400 m a.s.l.) in the tropical North Pacific Ocean showed a clear ozone increase since 1973 (1.21±0.30 ppbv decade^{-1}). The Antarctic site of Arrival Heights showed no trend since 1996, while ozone has increased slightly at South Pole (0.35±0.33 ppbv decade^{-1}).

The combined OMI/MLS satellite product (Ziemke et al. 2019) has been reported by the *State of the Climate* reports since 2012, covering most of the globe (60°S–60°N). The product now provides a continuous record of TOB spanning a full 20 years (2004–24). This edition of the *State of the Climate* report uses the latest version of the product, based on the new OMI Collection 4 L1b retrievals (Kleipool et al. 2022), which correct for instrument drift through the end of 2024. The vertical resolution of OMI/MLS monthly tropospheric column ozone is ~3 km near the tropopause with a regional precision (standard deviation) of ~2 Dobson units (DU; ~7%) in all latitude bands; trend uncertainties are about 0.5 DU decade^{-1} (1.5% decade^{-1}).

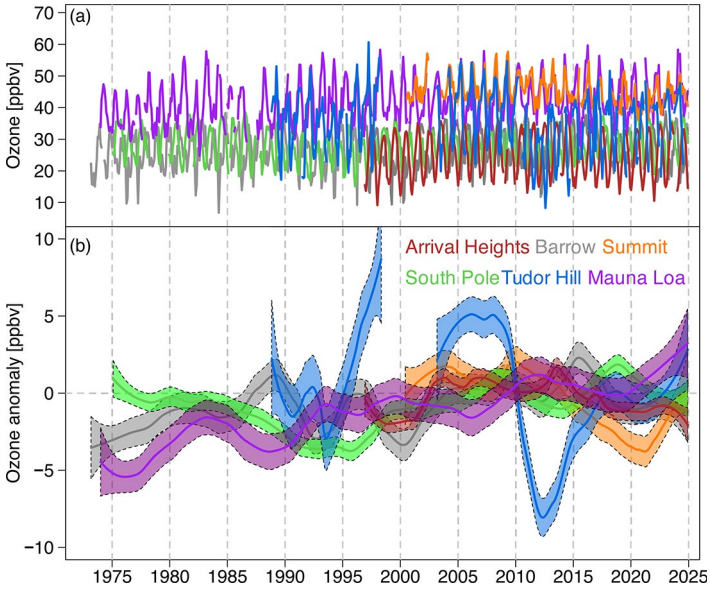

Fig. 2.72. (a) Monthly mean surface ozone (ppbv) at Barrow Observatory, Alaska (gray), Summit, Greenland (orange), Tudor Hill, Bermuda (blue), Mauna Loa, Hawaii (purple), Arrival Heights, Antarctica (red), and the South Pole (green). Monthly means are produced for months with at least 50% data availability using observations from all 24 hours of the day. The locations of each site are listed in Table 2.12. (b) The same time series after conversion to monthly anomalies referenced to the monthly climatological values over 2000–20 and smoothed using locally weighted scatterplot smoothing (LOWESS) regression (Chang et al. 2021).

5. STRATOSPHERIC AEROSOLS

—S. Khaykin, G. Taha, T. Sakai, I. Morino, and B. Liley

Stratospheric aerosols play a large role in the chemical and radiative balance of the atmosphere (Kremser et al. 2016). Explosive volcanic eruptions may directly inject sulfur dioxide (SO_2) and ash into the stratosphere, leading to significant perturbations of stratospheric aerosol burden at hemispheric and global scales that can last from several months to several years. Another important emerging source of particulate matter in the stratosphere is injection of smoke from wildfires via associated pyrocumulonimbus (pyroCb)—the fire-generated storms that can overshoot the tropopause (Peterson et al. 2021).

Despite the continued decay of the stratospheric aerosol perturbation produced by the eruption of the Hunga submarine volcano in January 2022, the stratospheric aerosol optical depth (sAOD) remained elevated above the background level in 2024 (Fig. 2.73a). Due to its extreme explosiveness, the Hunga eruption produced aerosol layers throughout the stratosphere (Taha et al. 2022) and resulted in the largest perturbation of the global sAOD in the last three decades (Khaykin et al. 2022). Augmenting the Hunga perturbation were additional lower stratospheric injections (up to 20 km–21 km) from two consecutive eruptions of the Ruang volcano in North Sulawesi, Indonesia, on 18 and 29 April 2024 (Dodangodage et al. 2025). Extrapolation of the stable decay of the Hunga southern hemispheric sAOD during early 2024 leads to an inference of the total lifetime of the Hunga-induced stratospheric aerosol load of 2.5 years, spanning from mid-January 2022 to mid-July 2024.

The eruption of Ruang ended the era of Hunga-induced sAOD perturbation. The Ruang aerosols spread throughout the tropics in less than two months and were transported farther into the southern extratropics during the austral winter (Fig. 2.73a). Figures 2.73b–e display quarterly zonal-mean extinction ratio (ER, aerosol-to-molecular extinction ratio) from the Ozone Mapping and Profiler Suite Limb Profiler (OMPS-LP) observations, summarizing the stratospheric aerosol latitude–altitude distribution during 2024. During the first three months of 2024, the Hunga aerosols were still present in the tropical mid-stratosphere (21 km–29 km) and the southern extratropical lower stratosphere (Fig. 2.73b). During the three months following the

Unauthenticated | Downloaded 11/21/25 11:34 AM UTC

Ruang eruption, the Ruang aerosols were observed at 18 km–23 km together with a possible contribution from remnants of Hunga above that layer (Fig. 2.73c). During July–September 2024, the Ruang layer intensified, and the isentropic transport of its aerosols to the southern extratropical lowermost stratosphere can be seen (Fig. 2.73d). Further transport of Ruang aerosols towards the southern high latitudes and their upwelling in the tropics to altitudes of 19 km–24 km in October–December, as well as a modest transport into the northern extratropics during this period, can be inferred from Fig. 2.73e.

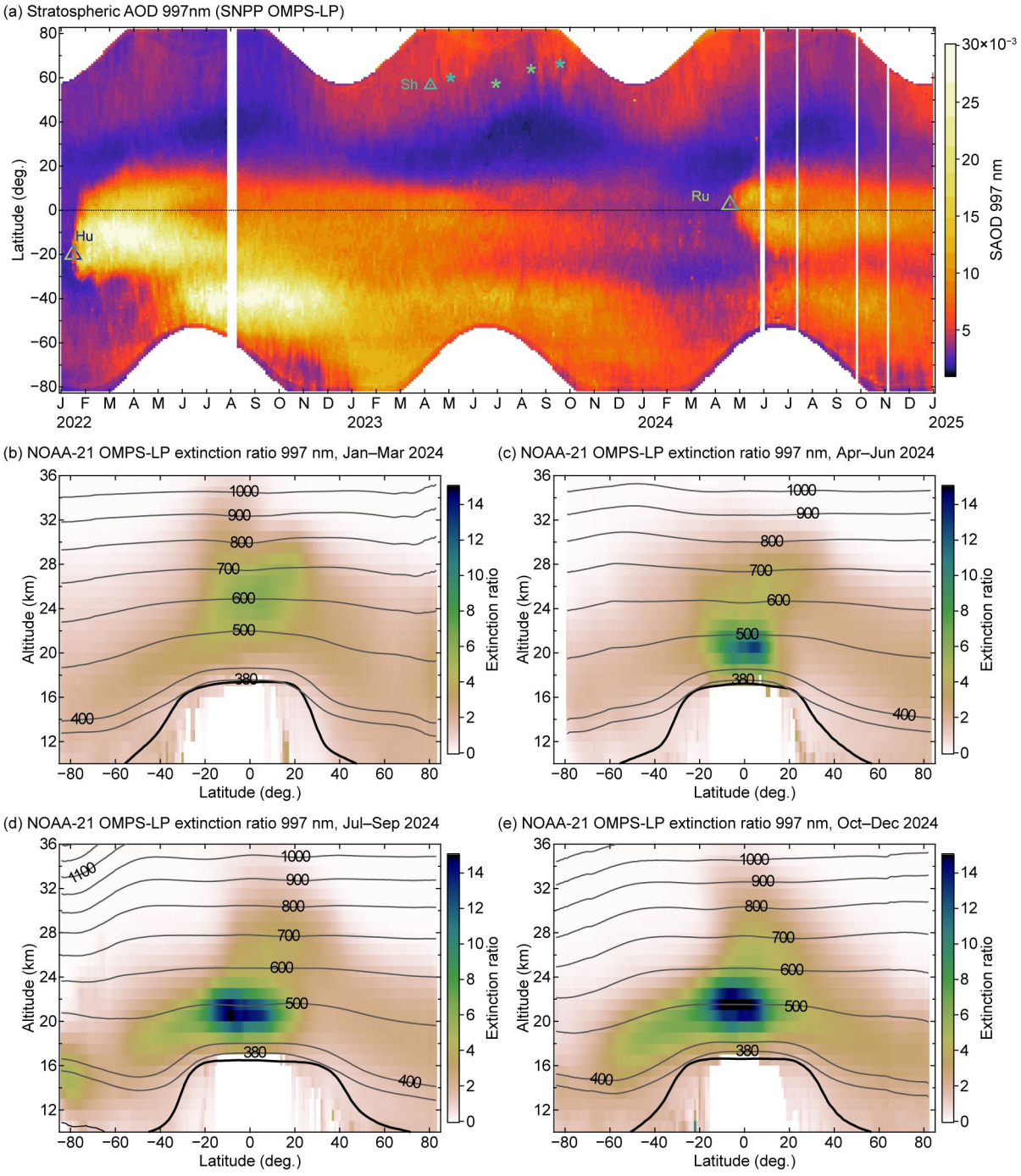

Fig. 2.73. Global evolution of the stratospheric aerosol from the Suomi National Polar-orbiting Partnership (SNPP) and NOAA-21 Ozone Mapping and Profiler Suite–Limb Profile (OMPS-LP) observations at 997 nm during 2022–24. (a) zonal-mean stratospheric aerosol optical depth (sAOD). The triangles indicate the eruptions of Hunga (Hu), Shiveluch (Sh), and Ruang (Ru) volcanoes, whereas the stars indicate the wildfire events with measurable stratospheric impact in Canada and Russia during summer 2023. (b)–(e) NOAA-21 OMPS-LP three-month zonal mean latitude–altitude section of the aerosol-to-molecular extinction ratio (ER) during 2024. The thick black line is the tropopause altitude, and the thin black lines are the potential temperature levels in Kelvin (K).

Unauthenticated | Downloaded 11/21/25 11:34 AM UTC

Figure 2.74 shows three decades of sAOD observations by ground-based Network for the Detection for Stratospheric Change (NDACC) lidars at Observatoire de Haute Provence (OHP; 43.9°N) and Lauder observatory (45°S) together with the corresponding zonally averaged satellite data from the International Space Station's (ISS) Stratospheric Aerosol and Gas Experiment III (SAGE III) instrument and the Global Space-based Stratospheric Aerosol Climatology (GloSSAC). These stations, located nearly antipodally on the globe, respectively represent the northern and southern extratropics. The OHP time series (Fig. 2.74a) during the twenty-first century is largely modulated by several moderate volcanic eruptions as well as by the extreme Pacific Northwest Event (PNE) wildfire outbreak in August 2017 (Khaykin et al. 2018; Peterson et al. 2018). The largest impact on the NH sAOD was caused by the Raikoke eruption in June 2019. Since that time, the OHP sAOD remained elevated, owing to contributions of boreal wildfires and the transport of Hunga aerosols (Khaykin et al. 2024). In late 2024, a subtle increase in sAOD was most likely related to the transport of Ruang aerosol into northern midlatitudes.

In the southern midlatitude stratosphere (Fig. 2.74b), the most significant sAOD perturbations were caused by the 2019/20 Australian New Year (ANY) wildfire super outbreak (Khaykin et al. 2020; Peterson et al. 2021) and the eruption of the Hunga submarine volcano in January 2022. The massive transport of Ruang sulfates into the southern extratropics is reflected in the SH extratropical sAOD enhancement peaking in October 2024 (Fig. 2.74b).

Unlike 2023, which had multiple pyrocumulonimbus clouds in the NH that reached the lowermost stratosphere (Zhang et al. 2024), there were no significant stratospheric intrusions of the smoke during 2024, and most of the aerosol seen in the NH stratosphere originated from the Hunga and Ruang eruptions.

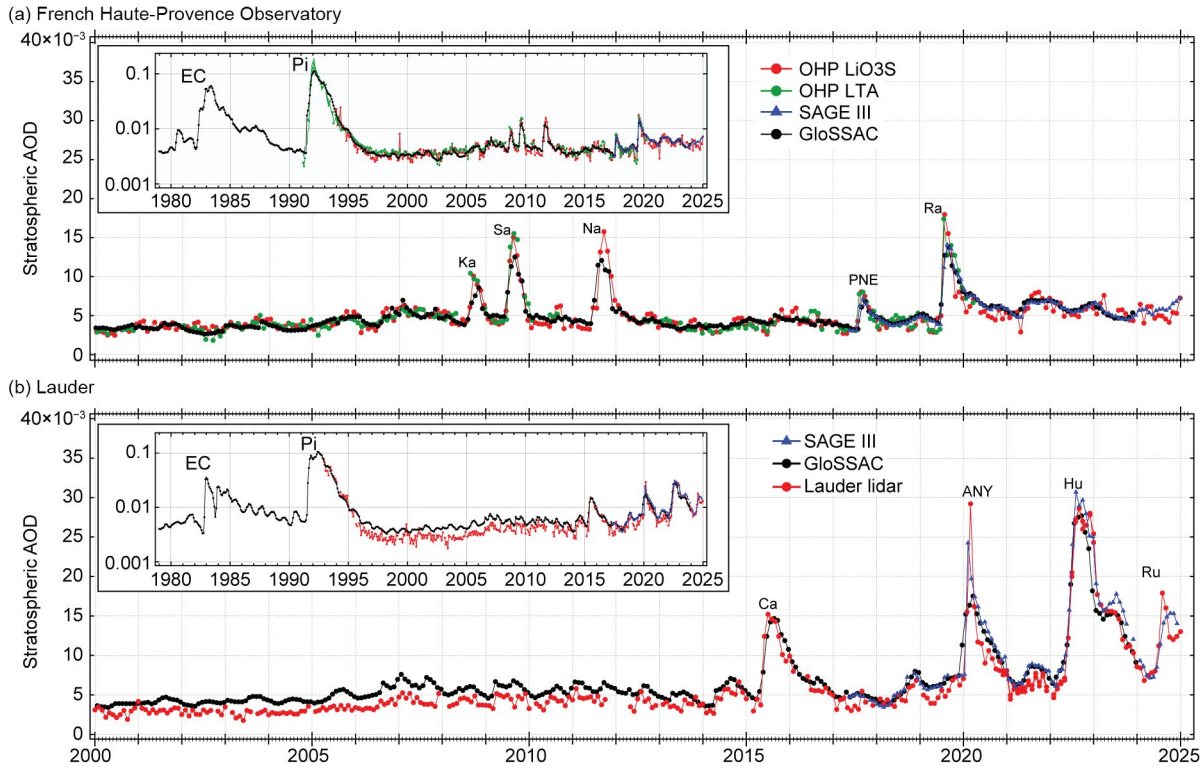

Fig. 2.74. Time series of monthly mean aerosol optical depth at 532 nm of the stratospheric overworld (380 K; 33 km) from ground-based lidars at (a) French Haute-Provence Observatory (OHP, 43.9°N, 5.7°E, Stratospheric Ozone Lidar at OHP [LiO3S] and the Lidar Temperature Aerosol [LTA] instruments) and (b) New Zealand's Lauder station (45°S, 179°E, Lauder aerosol lidar) and the corresponding monthly/zonal-mean values from satellite observations within 40°N–50°N and 50°S–40°S latitude bands from the ISS's Stratospheric Aerosol and Gas Experiment III (SAGE III) instrument and Global Space-based Stratospheric Aerosol Climatology (GloSSAC) merged satellite record. The embedded panels display the log-scaled time series from the beginning of the GloSSAC record. The literal notations indicate the most significant volcanic eruptions: El Chichón (EC), Pinatubo (Pi), Kasatochi (Ka), Sarychev (Sa), Nabro (Na), Raikoke (Ra), Calbuco (Ca), Hunga (Hu), Ruang (Ru); and wildfire events: Pacific Northwest Event (PNE, British Columbia, Canada) and Australian New Year (ANY) super outbreak.

Unauthenticated | Downloaded 11/21/25 11:34 AM UTC

6. STRATOSPHERIC OZONE

—M. Weber, W. Steinbrecht, C. Arosio, R. van der A, S. M. Frith, J. Anderson, L. M. Ciasto, M. Coldewey-Egbers, S. Davis, D. Degenstein, V. E. Fioletov, L. Froidevaux, J. de Laat, D. Loyola, A. Rozanov, V. Sofieva, K. Tourpali, R. Wang, T. Warnock, and J. D. Wild

About 90% of total column ozone resides in the stratosphere; only 10% resides in the troposphere. In 2024, total column ozone was well above the average of 1998–2008 over most of the globe except for two narrow zonal bands in the tropics and a patch over Antarctica (Plate 2.1af). In the NH, anomalies reached values of +60 DU or more in some regions, for example the Canadian Arctic. The time series in Fig. 2.75b show that the 2024 annual zonal mean at northern midlatitudes (35°N–60°N) was close to the high values observed during the 1960s. In March 2024, Arctic (60°N–90°N) total column ozone reached 475 DU, the highest value seen since 1979 (Fig. 2.75e). The variation in annual-mean total column ozone in the extratropics is largely driven by variations in the stratospheric circulation in winter/early spring. During boreal winter/spring 2024, the Brewer–Dobson (BD) circulation, which transports ozone from the tropical source region to middle and high latitudes, was particularly strong (Newman et al. 2024). Combined with the lower stratospheric quasi-biennial oscillation (QBO) in its easterly phase and the strong El Niño conditions in the first half of 2024, total column ozone was reduced in the tropics and strongly enhanced in the extratropics (Figs. 2.75a,b,d; Plate 2.1af; Baldwin et al. 2001; Oman et al. 2013; Butchart 2014; Domeisen et al. 2019).

In the SH midlatitudes and in October in the Antarctic (Fig. 2.75d,e), the last two years were closer to the high end of the range of interannual variability, ending the series of years of low total column ozone from 2020 to 2022, caused by Australian wildfires (Solomon et al. 2023) and a series of volcanic eruptions, including Hunga (Santee et al. 2023; Fleming et al. 2024).

Generally, observed total column ozone values in recent years have tended to be at the low end of projections from chemistry climate models (CCMs; see Figs. 2.75a–d), based on current scenarios for ODSs and GHGs. Overall, the data show the slow path of ozone recovery due to the ODS phase-out by the Montreal Protocol and its Amendments (WMO 2022).

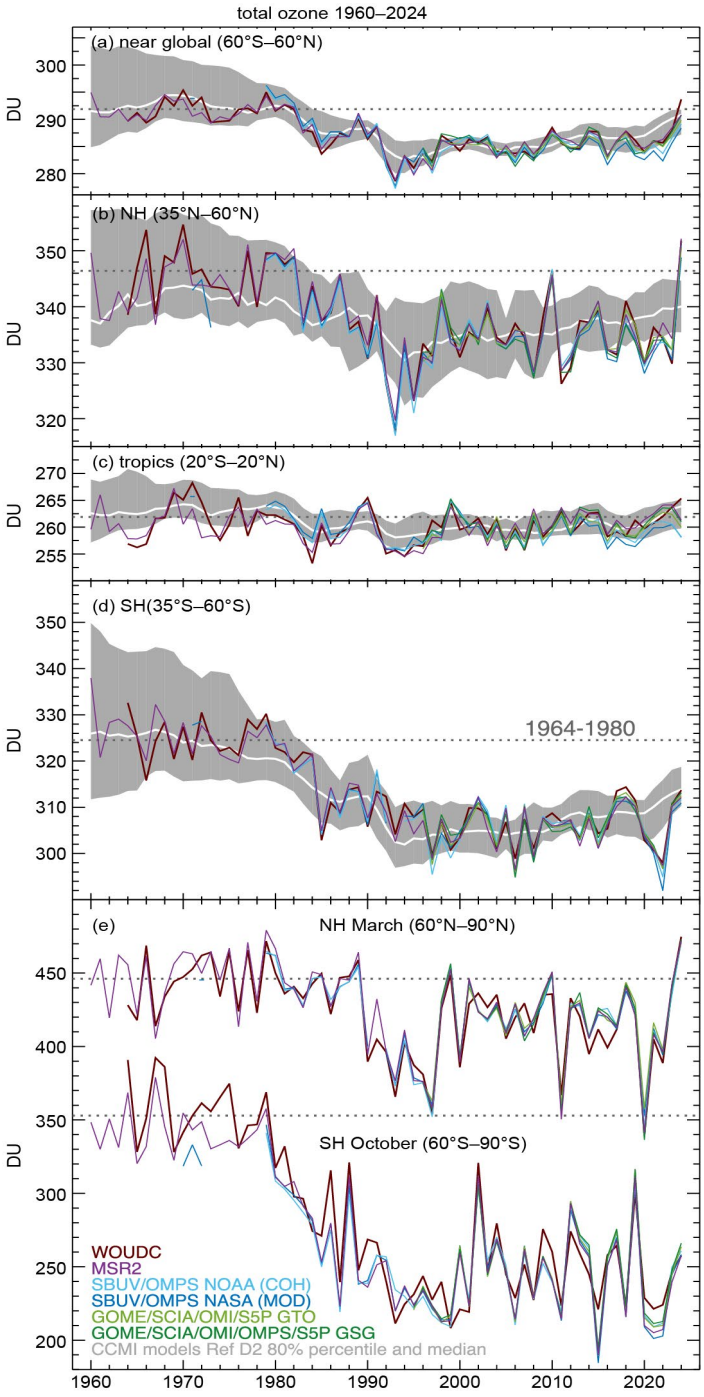

Fig. 2.75. Time series of annual mean total column ozone (DU) in (a)–(d) four zonal bands, and (e) polar (60°–90°) total column ozone in Mar (Northern Hemisphere; NH) and Oct (Southern Hemisphere; SH), the months when polar ozone losses usually are largest. Values are plotted at the tick mark start of each year. The dotted gray lines in each panel show the average ozone level for 1964–1980 calculated from the World Ozone and Ultraviolet Radiation Data Centre's (WOUDC) data. Most of the observational data for 2024 are preliminary. The thick white lines in (a)–(d) show the median from Chemistry-Climate Model Initiative (CCMI)-2022 ref D2 model runs (Plummer et al. 2021). The model data have been smoothed using a three-point triangle function. The gray-shaded areas provide the 80th percentile range. All datasets have been bias-corrected by subtracting individual data averages and adding the multi-instrument mean from the reference period 1998–2008.

Unauthenticated | Downloaded 11/21/25 11:34 AM UTC

Figure 2.76 shows the evolution of ozone profiles at two stratospheric levels and for three latitude bands. The 2-hPa level (or 42-km altitude) represents the upper stratosphere (Figs. 2.76a–c), and the 50-hPa level (or 22-km altitude) the lower stratosphere (Figs. 2.76d–f). Ozone in the upper stratosphere is controlled to a large degree by photochemistry. The year 2024 continued the slow upper-stratospheric ozone increase due to declining ODSs and cooling of the upper stratosphere, as predicted by models (e.g., WMO 2022), although observed values in recent years have tended to be at the lower end of expectations from CCM simulations (gray-shaded region in Figs. 2.76a–c).

Ozone in the lower stratosphere (Figs. 2.76d–f) is controlled to a large degree by transport variations and is the main contributor to the already discussed total column ozone variations. Consistent with the strong El Niño and the easterly shear phase of the QBO in the lower stratosphere from January to April, ozone values were very low in the tropical band in 2024 (Fig. 2.76e; see also the El Niño years 1998 and 2016). In the Northern Hemisphere extratropical band in 2024 (Fig. 2.76d), ozone at 50 hPa was near the high end of recent values for almost all individual datasets. However, the enhancement was not as large as that seen for total column ozone in Fig. 2.75b, because a large fraction of the total column enhancement in 2024 came from levels lower than 50 hPa. In the SH (Fig. 2.76f) in 2024, ozone at 50 hPa from the zonal-mean satellite datasets again approached the range predicted by CCMs, ending the low excursions from 2020 to 2022 due to the Australian wildfires and recent volcanic eruptions, events which were not considered in the CCM projections.

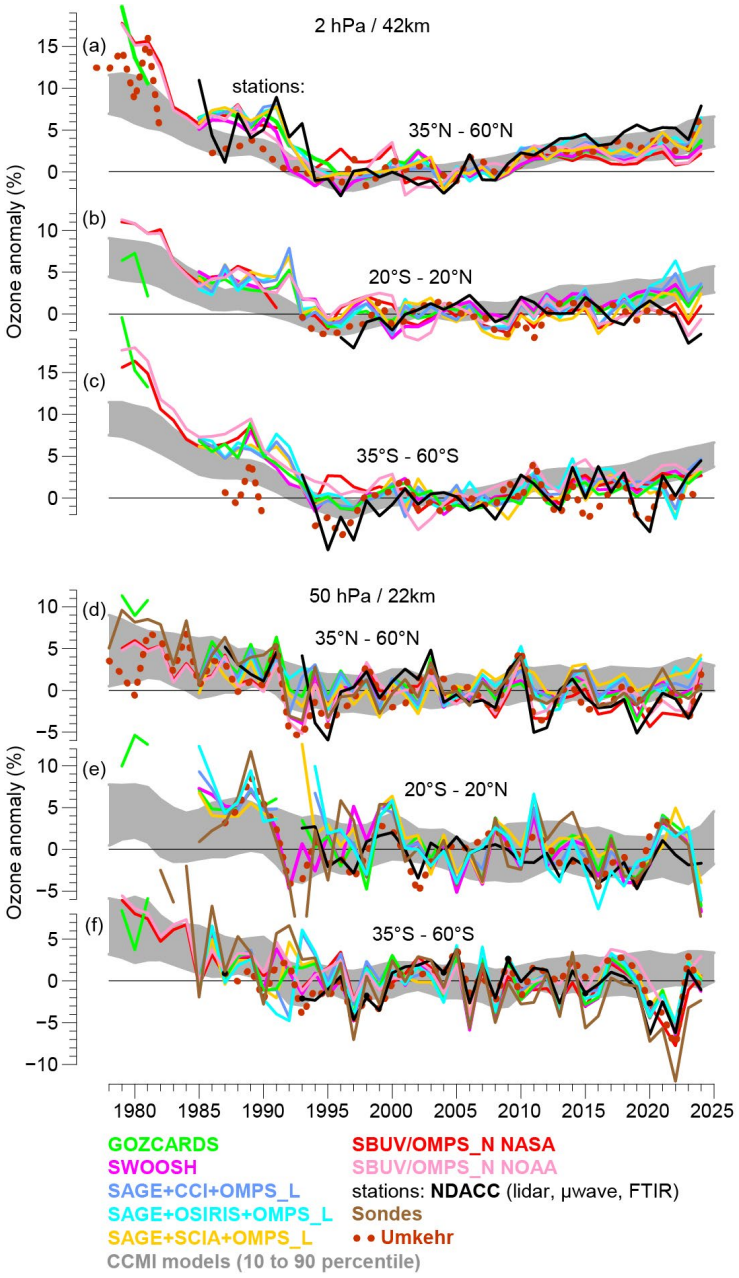

Fig. 2.76. Annual mean anomalies of ozone in the (a)–(c) upper stratosphere near 42-km altitude or 2-hPa pressure, and in the (d)–(f) lower stratosphere near 22 km or 50 hPa for three zonal bands: (a),(d) 35°N–60°N, (b),(e) 20°S–20°N (tropics), and (c),(f) 35°S–60°S, respectively. Anomalies are referenced to the 1998–2008 baseline. Annual means are plotted at the tick marks of the start of each year. Colored lines are long-term records obtained by merging different limb (Global Ozone Chemistry and Related Trace Gas Data Records for the Stratosphere [GOZCARDS], Stratospheric Water and Ozone Satellite Homogenized [SWOOSH], Stratospheric Aerosol and Gas Experiment [SAGE]+Climate Change Initiative [CCI]+Ozone Mapping and Profiler Suite Limb Profiler [OMPS-LP], SAGE+Scanning Imaging Absorption Spectrometer for Atmospheric Chartography [SCIAMACHY]+OMPS-LP, SAGE+Optical Spectrograph and InfraRed Imaging System [OSIRIS]+OMPS-LP) and nadir-viewing (Solar Backscatter Ultraviolet Radiometer [SBUV], OMPS Nadir Profile [OMPS-NP]) satellite instruments. The nadir-viewing instruments have a much coarser altitude resolution than the limb-viewing instruments. This can cause differences in some years, especially at 50 hPa. Red dots are results from ground-based Umkehr data (Petropavlovskikh et al. 2025). The black line is from merging ground-based ozone records at seven Network for the Detection of Atmospheric Composition Change (NDACC) stations employing differential absorption lidars and microwave radiometers. See Steinbrecht et al. (2017), WMO (2022), and Arosio et al. (2019) for details on the various datasets. Gray shaded area shows the range of chemistry-climate model simulations from the Chemistry-Climate Model Initiative (CCMI)-1 refC2 (SPARC/IO3C/GAW 2019). Ozone data for 2024 are not yet complete for all instruments and are still preliminary.

Unauthenticated | Downloaded 11/21/25 11:34 AM UTC

7. STRATOSPHERIC WATER VAPOR

—S. M. Davis, K. H. Rosenlof, E. A. Asher, H. Vömel, and R. M. Stauffer

In 2024, stratospheric water vapor (WV) continued to be strongly influenced by the January 2022 eruption of the Hunga volcano (20.5°S, 175.4°W), which injected 150 Tg of WV into the stratosphere (~10% of the entire stratospheric burden; Millán et al. 2022; Vömel et al. 2022). In addition to the ongoing influence from the Hunga eruption, deseasonalized tropical lower-stratospheric WV anomalies (using a climatological base period of 2004–21) started the year positive following record-high values in 2023 (Davis et al. 2024), but then became negative for much of the year before returning to positive in November and December 2024 (Figs. 2.77a,c, 2.78, 2.79). Overall, 2024 continued the positive WV anomalies observed in the last five years in the global stratosphere (Konopka et al. 2022; Zolghadrshojaee et al. 2024) with some notable variability that was likely due to natural fluctuations.

Zonal-mean WV provided by satellite measurements (Fig. 2.77) shows that the lingering positive anomalies from Hunga were evident in the tropical upper stratosphere (above 10 hPa) in 2024 (Fig. 2.77a). In the tropics (Figs. 2.77a, 2.78), the positive anomaly decreased as the year progressed, with a return to near-normal values around July, likely driven by upward vertical transport of drier air that entered the stratosphere more recently and was not impacted by the Hunga eruption. At the start of 2024, the lingering effects of the Hunga WV perturbation were evident in the middle stratosphere (e.g., 26 hPa, Fig. 2.77b; see also Fig. 2.78) at extratropical latitudes in both hemispheres. Positive WV anomalies, including some record values (see hatched regions, Fig. 2.78), were also present in the lower stratosphere throughout 2024. Attribution of these extratropical lower-stratosphere anomalies is subject to ongoing research, but they are plausibly explained as some combination of poleward transport of the positive tropical lowermost stratosphere anomalies from the end of 2023 (Figs. 2.77a,c) as well as downward transport of Hunga-impacted air from above.

Even though the mid- and upper-stratospheric WV anomalies were still dramatically perturbed by Hunga in 2024, tropical lower-stratospheric WV anomalies (i.e., at pressures greater than ~30 hPa) followed a more typical progression influenced by other factors. Anomalies in this region are expected to be primarily caused by anomalies in tropical tropopause temperatures, which control freeze-drying of air ascending into the stratosphere (Mote et al. 1996). Indeed, lower-stratospheric satellite WV anomalies are highly correlated with tropical (15°S–15°N) cold-point tropopause (CPT) temperature anomalies (Figs. 2.79b,c). While 2022 and 2023 had the first- and second-warmest MERRA-2 tropical CPT temperatures on record (the annual-mean anomaly was +0.76 K in 2022 and +0.73 K in 2023), 2024 was cooler than average (–0.23 K), ranking 39th out of 45 years (since 1980, based on the MERRA-2 reanalysis). Accordingly, while 2023 and 2022 ranked as the first- and

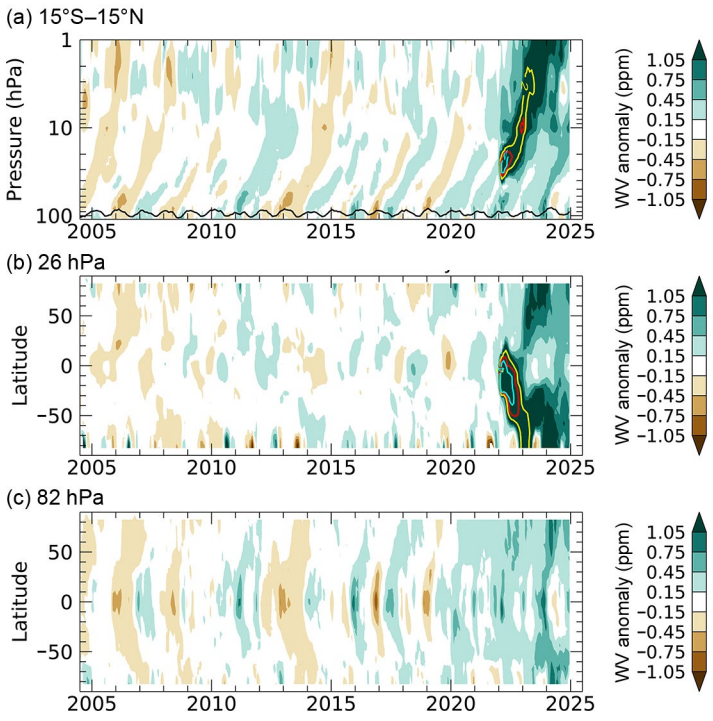

Fig. 2.77. (a) Pressure–time contour of tropical (15°S–15°N) lower-stratospheric water vapor (WV) anomalies, with the +2-, +3-, and +4-ppm values shown as yellow, red, and cyan contour lines, respectively. The black line shows the MERRA-2 tropical cold point pressure. (b),(c) Latitude–time contour of WV anomalies at (b) 26 hPa (middle stratosphere) and (c) 82 hPa (lower stratosphere), respectively. All panels are based on merged satellite data from the Stratospheric Water and Ozone Satellite Homogenized version 2.7 (SWOOSH v2.7) dataset (a combination of Aura Microwave Limb Sounder (MLS), Atmospheric Chemistry Experiment—Fourier Transform Spectrometer (ACE-FTS), and Stratospheric Aerosol and Gas Experiment III (SAGE III)/ISS WV data, Davis et al. 2016). Anomalies are differences from the mean 2004–21 water vapor mixing ratios (ppm) for each month. Tick marks denote the beginning of each year.

Unauthenticated | Downloaded 11/21/25 11:34 AM UTC

second-most positive annual-mean tropical (15°S–15°N) WV anomalies at 82 hPa (+0.39 ppm in 2023 and +0.27 ppm in 2022; parts per million, i.e., μmol mol^{-1}) based on the Stratospheric Water and OzOne Satellite Homogenized (SWOOSH) combined WV record (Davis et al. 2016), 2024 was near the median (10th out of the 20 years since 2005 with sufficient satellite sampling of the tropics) with an anomaly of +0.07 ppm. As is typical, the tropical lower-stratosphere WV anomalies propagate both upward and to higher latitudes, becoming evident at other frost-point measurement stations with a lag of several months at subtropical and midlatitude stations (Hurst et al. 2011).

Two important drivers of interannual variations in CPT temperatures and stratospheric WV concentrations entering the stratosphere are the ENSO and the QBO in equatorial stratospheric winds. Strong El Niño conditions were present at the beginning of 2024 through January–March, followed by a transition to ENSO-neutral conditions by April–June, and then La Niña-like conditions from September through the end of the year (see section 4f). During boreal winter, both La Niña and strong El Niño conditions are associated with a wetter tropical lowermost stratosphere (e.g., Garfinkel et al. 2021), which seems consistent with conditions at the beginning and end of 2024. However, also during the first half of 2024, there was easterly QBO shear between the 50-hPa and 70-hPa levels (section 2e3), which is consistent with stronger upwelling and cold CPT temperatures (e.g., Fig. 2.79c). This behavior is consistent with the anomalously dry

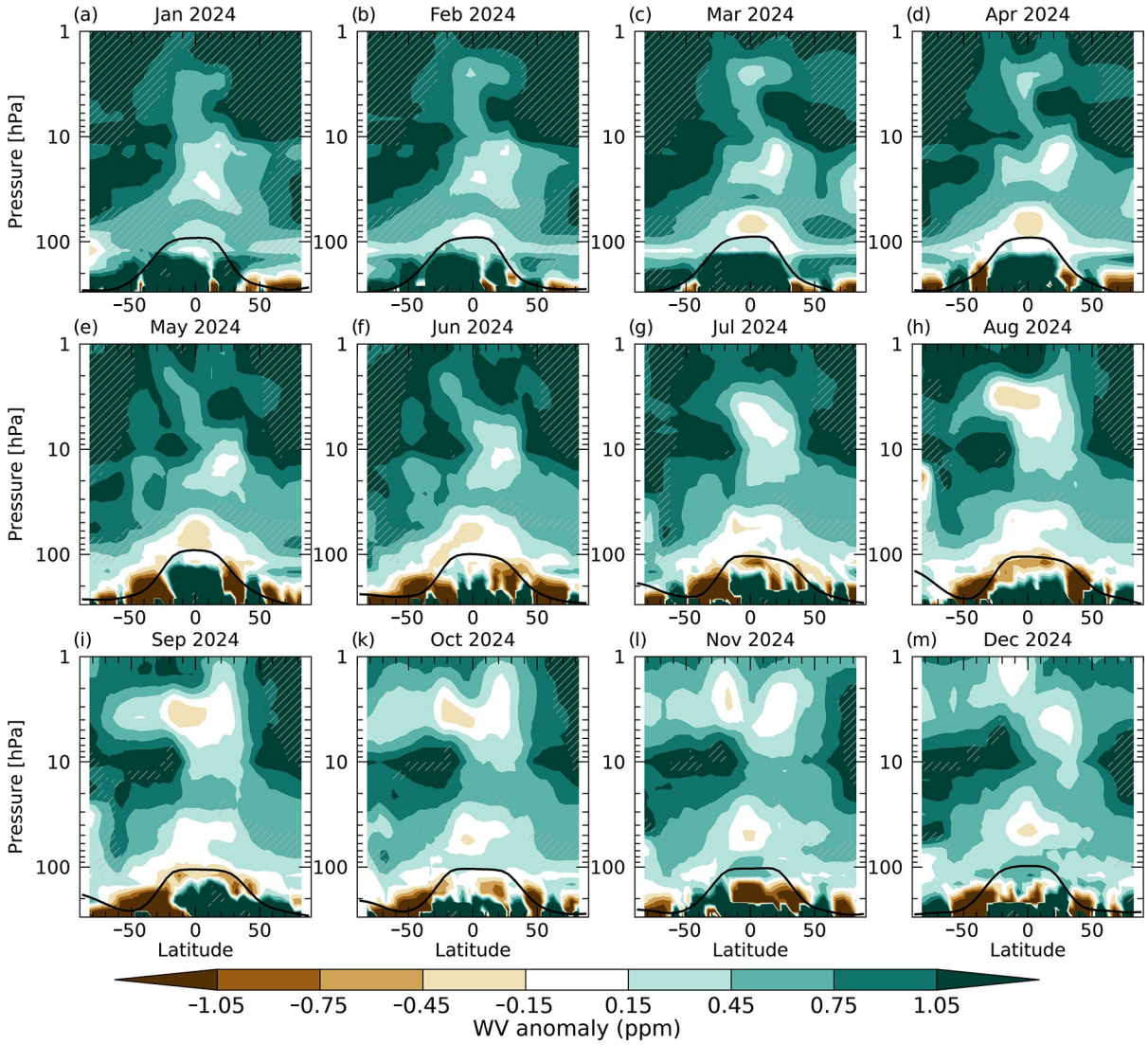

Fig. 2.78. Latitude–pressure cross-sections of zonally averaged water vapor (WV) anomalies (ppm; 2004–21 base period). Hatching shows where the zonal-mean WV was at record values for the given month. Black lines show the monthly mean tropopause pressure from the MERRA-2 reanalysis.

Unauthenticated | Downloaded 11/21/25 11:34 AM UTC

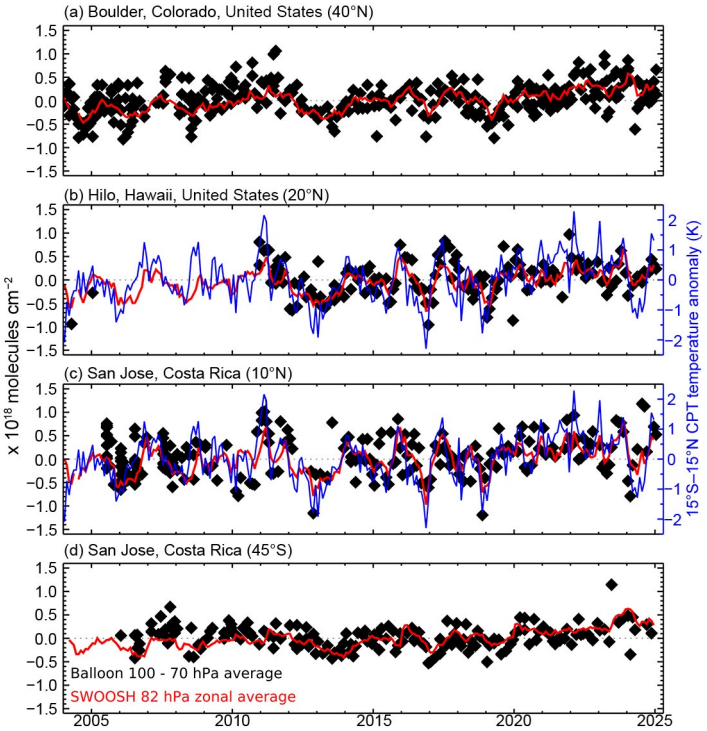

Fig. 2.79. Lower-stratospheric water vapor (WV) anomalies over four balloon-borne frost point (FP) hygrometer stations. Each panel shows the lower-stratospheric anomalies (relative to each station) of individual FP soundings (black diamonds) and of monthly zonal averages from Stratospheric Water and Ozone Satellite Homogenized (SWOOSH) data at 82 hPa in the 5° latitude band containing the FP station (red lines). High-resolution FP vertical profile data were averaged between 70 hPa and 100 hPa for comparison with the SWOOSH 82 hPa level. Anomalies for SWOOSH and FP data are calculated relative to the 2004–21 period for all sites except Hilo (2011–21). Tropical cold-point tropopause temperature anomalies based on the MERRA-2 reanalysis ([b],[c], blue lines) are generally well correlated with the tropical lower-stratospheric WV anomalies.

conditions in the tropical lower stratosphere during the middle of the year (Figs. 2.77a,c, 2.78c–f). After June, the 70-hPa–50-hPa wind shear then reversed to westerly for the remainder of the year, which is consistent with the anomalously wet conditions in the tropical lowermost stratosphere at the end of 2024.

8. CARBON MONOXIDE

—J. Flemming and A. Inness

The global burden of carbon monoxide (CO) in 2024 was the second highest since 2003, mainly because of exceptionally high emissions from wildfires in South America (Fig. 2.80). The emitted CO was transported in the adjacent outflow regions over the Pacific and Atlantic Oceans, leading to positive CO anomalies throughout the SH midlatitudes and tropics (Plate 2.1ag).

CO is emitted into the atmosphere by anthropogenic combustion processes, such as road transport and energy generation, as well as from wildfires. Similar in size to, or even larger than these emissions, is the chemical production of CO in the atmosphere from formaldehyde as part of the oxidation chains of methane, isoprene, and other volatile organic trace gases. Oxidation of CO by reaction with the hydroxyl radical (OH) is the main loss process for CO, resulting in an atmospheric lifetime of 1–2 months. The presence of CO contributes to the production of tropospheric ozone, a relatively short-lived species among radiatively important molecules that affect the climate.

According to the CAMS (https://atmosphere.copernicus.eu/) reanalysis of atmospheric composition, produced by the European Center for Medium-Range Weather Forecasts (ECMWF) and detailed in Inness et al. (2019), the global CO burden decreased between 2003 and 2014 because of decreased anthropogenic emissions in most parts of the world, along with a strong decrease in fire activities in South America. In recent years, positive global and regional CO anomalies occurred because of regionally intensified wildfires related to exceptional meteorological conditions, such as the intensive peat fires in Indonesia in 2015—which caused the highest global CO burden since 2003 (Fig. 2.80)—and the exceptional wildfires in South America in 2024. The latter led to the highest CO burden over the continent in the CAMS reanalysis record (Fig. 2.81). The increased fire intensity in South America was caused by anomalous dry and hot conditions, which started in mid-2023 (de Laat et al. 2025). While fires in the Amazon

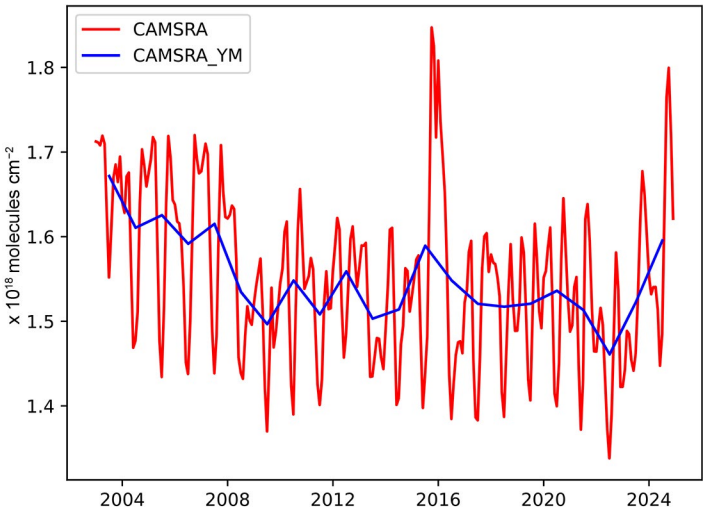

Fig. 2.80. Global monthly-mean (red) and yearly-mean (YM; blue) of the total-column carbon monoxide from the Copernicus Atmosphere Monitoring Service (CAMS) reanalysis for the period 2003–24.

Unauthenticated | Downloaded 11/21/25 11:34 AM UTC

region of Brazil and Bolivia in August–September 2024 were the main cause of the increased CO burden, fires in other regions contributed as well: Venezuela experienced strong fires in January–March, and the Pantanal wetlands in Brazil, the world's largest tropical wetland area, suffered from intensive peat fires in May.

As in previous years, boreal wildfires over Canada and Eastern Siberia in summer led to regional positive CO anomalies against the background of decreasing CO burden in the NH. Less-intensive fire activity over many parts of central and southern Africa contributed to a localized negative CO anomaly in 2024. India is a region where anthropogenic sources, including the burning of agricultural waste in winter, continued to increase the regional CO burden.

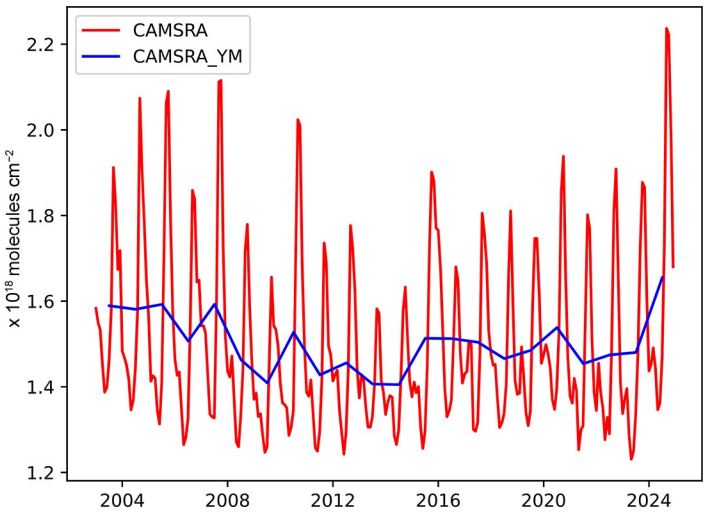

Fig. 2.81. Monthly-mean (red) and yearly-mean (YM; blue) of the total column carbon monoxide from the Copernicus Atmosphere Monitoring Service (CAMS) reanalysis over South America (70°S–10°N, 83°W–30°W) for the period 2003–24.

CAMS has produced a retrospective analysis of CO, aerosols, and ozone since 2003 by assimilating satellite retrievals of atmospheric composition with the ECMWF model (Inness et al. 2019). This CAMS reanalysis assimilated global thermal infrared total column CO retrievals (V6 from 2003 to 2016; NRT V7 from January 2017 to June 2019; NRT V8 from July 2019 to present) of the Measurement of Pollution in the Troposphere (MOPITT) satellite instrument (Deeter et al. 2014, 2017, 2019), excluding observations poleward of 65°N/S, using the ECWMF four-dimensional variational assimilation (4D-VAR) data assimilation system. The anthropogenic emissions were taken from the Monitoring Atmospheric Composition and Climate and CityZen (MACCity) inventory (Granier et al. 2011) that accounts for projected emission trends according to the emission scenario Representation Concentration Pathways (RCP) 8.5 scenario, but COVID-19-related emissions modifications were not applied. Biomass burning emissions were taken from the Global Fire Assimilation System (GFASv1.2; Kaiser et al. 2012; section 2h3) that is based on MODIS fire radiative power retrievals (Giglio et al. 2016). Monthly-mean biogenic emissions simulated by the Model of Emissions of Gases and Aerosols from Nature (MEGAN) 2.1 following Sindelarova et al. (2014) were used for the period 2003–17, and after 2017 a monthly climatology derived from the 2003–17 data was applied.

Unauthenticated | Downloaded 11/21/25 11:34 AM UTC

Sidebar 2.2: Operational satellite instruments monitor a range of indirect short-lived climate forcers

—O. R. COOPER, E. PENNINGTON, J. WORDEN, K. BOWMAN, S. KONDRAGUNTA, Z. WEI, AND K. YANG

Earth's effective radiative forcing (ERF) due to total anthropogenic activities since 1750 is 2.79 (1.78 to 3.61) W m^{-2}, which is a balance between the warming effect of greenhouse gases and the cooling effect of aerosols and land use change (surface albedo changes and effects of irrigation; Forster et al. 2024). Long-lived greenhouse gases (LLGHGs: carbon dioxide [CO_2], nitrous oxide [N_2O], and halogenated greenhouse gases) accumulate in the atmosphere on decadal to centennial time scales, while short-lived climate forcers (SLCFs) have lifetimes ranging from a few hours to about two decades. SLCFs that exert a climate effect through their radiative forcing are known as direct SLCFs (e.g., ozone, methane, primary and secondary aerosols), while indirect SLCFs are precursors of other direct climate forcers (IPCC 2021). For example, carbon monoxide (CO) and nitrogen oxides (NO_x = NO+NO_2) are ozone precursors, while ammonia (NH_3) is a precursor of secondary aerosols (e.g., ammonium nitrate).

In terms of SLCFs, previous editions of the *State of the Climate* report have focused on methane, tropospheric and stratospheric ozone (direct SLCFs; sections 2g1, 2g4, 2g6), and carbon monoxide (indirect SLCF; section 2g8). The *State of the Climate* also provides updates on aerosols (sections 2g3, 2g5), but no distinction is made between primary aerosols (direct SLCFs) and secondary aerosols (indirect SLCFs). Advances in satellite instrumentation and retrieval algorithms now allow for operational monitoring of several indirect SLCFs; here, three operational satellite products that can improve understanding of the regional and global scale production of tropospheric ozone and secondary aerosols are described.

Tropospheric column nitrogen dioxide (NO_2): NO_2 is an indirect SLCF that reacts with CO, methane, and volatile organic compounds (VOCs) in the presence of sunlight to produce ozone, which is both a SLCF and an air pollutant detrimental to human health and vegetation (Monks et al. 2015). Over the past two decades, several satellite instruments have monitored changes in tropospheric column NO_2, allowing scientists to identify regions where ozone production is increasing or decreasing (Duncan et al. 2016; He et al. 2024). The Ozone Mapping and Profiler Suite (OMPS) instrument is currently monitoring NO_2 on three NOAA operational polar-orbiting satellites (Suomi National Polar-orbiting Partnership [SNPP] since 2012, NOAA-20 since 2018, and NOAA-21 since 2023; Huang et al. 2022). Figure SB2.4a presents annual average tropospheric column NO_2 for the most recent five years (2020–24), showing well-known hotspots associated with fossil fuel combustion across North America, Europe, the Middle East, South Asia, East Asia, and southern Africa. A region of frequent biomass burning is also visible above south-central Africa. Figure SB2.4b presents the 2020–24 period as anomalies with respect to 2012–19. Previously documented NO_2 decreases have persisted across Mexico City (Mexico), South Africa, the northeastern United States, western Europe, and especially across East Asia (Duncan et al. 2016; Elshorbany et al. 2024). Notable increases are found above western Texas, eastern Europe, Iraq, Iran, and eastern India (Gyawali 2023; Elshorbany et al. 2024).

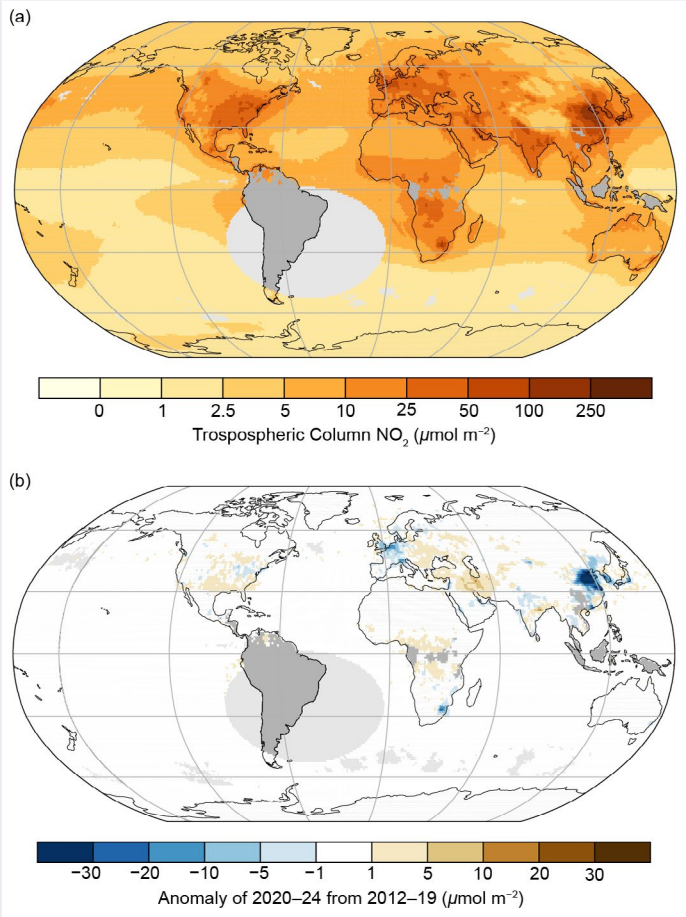

Fig. SB2.4. (a) Ozone Mapping and Profiler Suite (OMPS) tropospheric-column nitrogen dioxide (NO_2), 2020–24; (b) Anomalies of OMPS tropospheric column NO_2 for the period 2020–24, with reference to 2012–19. Units are µmol m^{-2}. Gray areas indicate regions with low data availability, and portions of South America and the South Atlantic are omitted due to instrument interference caused by the South Atlantic Anomaly (Finlay et al. 2020).

Ammonia (NH_3): Ammonia is produced from agricultural practices (Behera et al. 2013), fossil fuel combustion, and wildfires (Lindaas et al. 2021). When this indirect SLCF combines with nitric acid (HNO_3; an oxidation product of NO_2) it forms

Unauthenticated | Downloaded 11/21/25 11:34 AM UTC

ammonium nitrate (NH_4NO_3), a secondary aerosol and SLCF, which reflects sunlight (Nowak et al. 2012). The Cross-Track Infrared Sounder (CrIS) flies on the same NOAA operational satellites as the OMPS instrument, and provides midday retrievals of column ammonia, with a peak sensitivity of around 700 hPa (Bowman 2021a). Figure SB2.5a presents average CrIS ammonia for the year 2024, revealing three major hotspots. The enhancements above northeastern China and the Indo-Gangetic Plain are associated with anthropogenic activity and are similar to previous years (2020–23, not shown). In contrast, the enhancement above central South America is produced by wildfires and is elevated compared to previous years. Peak ammonia concentrations occurred in September (Fig. SB2.5b) during a period of record-breaking wildfires across Bolivia (CAMS 2024; sections 2g8, 2h3). The ammonia plume was prevented from spreading westward by the Andes Mountains and instead advected eastward across the South Atlantic Ocean.

Peroxyacetyl nitrate (PAN): Acyl peroxynitrates (PANs) are a class of thermally unstable reservoir species for nitrogen oxides, commonly produced by wildfires and fossil fuel combustion (Juncosa Calahorrano et al. 2021). CrIS detects PANs with highest sensitivity in the mid-troposphere (450 hPa; Bowman 2021b), with peroxyacetyl nitrate (PAN) being the most abundant species (Payne et al. 2022). PAN is stable at low temperatures and can therefore transport NO_x over long distances, especially in the free troposphere. When PAN descends to warmer layers of the atmosphere, its thermal decomposition releases NO_x, which is then available for ozone production (Fischer et al. 2014). CrIS detected enhanced PANs above North America during summer 2023, produced by the record-breaking Canadian wildfire season (Cooper et al. 2024b). Canada experienced its second strongest wildfire season in 2024 (CAMS 2024; section 2h3), and the CrIS PANs product shows strong enhancements above Canada and the central United States during July 2024 (Fig. SB2.6a), similar to the enhancements above the downwind region of the North Atlantic Ocean and to the enhancements above East Asia that are attributed to anthropogenic activity. By September, the PANs hotspots had shifted to the biomass burning regions of South America and southern Africa, with plumes of PANs extending from both regions into the South Atlantic Ocean (Fig. SB2.6b).

These examples demonstrate the unique capability of satellites to monitor indirect SLCFs on a global scale. The benefits of this knowledge go beyond the simple understanding of trace gas distributions, because the chemistry and transport connections between these trace gases amplify their impact on climate and air quality (Szopa et al. 2021). For example,

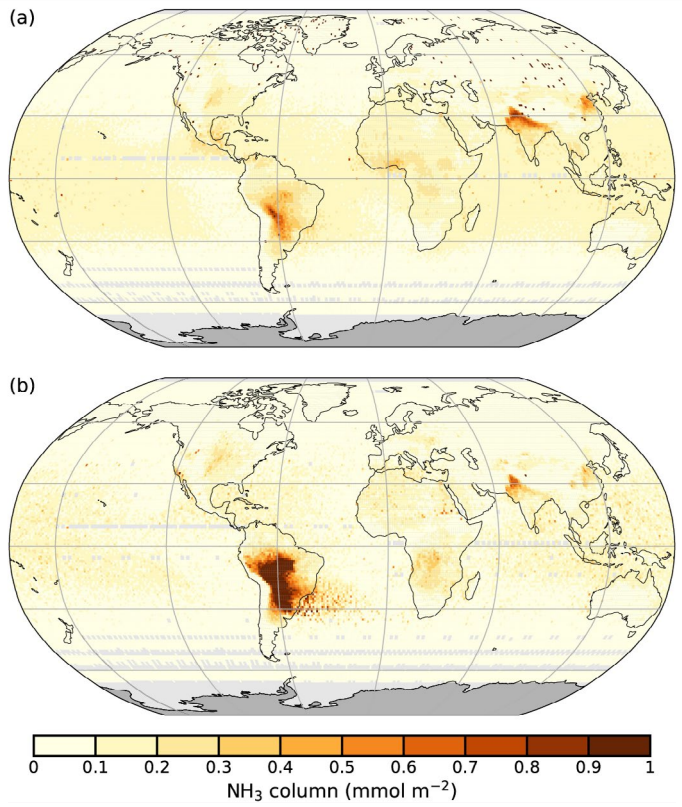

Fig. SB2.5. (a) Cross-Track Infrared Sounder (CrIS) ammonia (NH_3) averaged over the entire year of 2024; (b) CrIS NH_3 averaged over Sep 2024. Units are m mol m^{-2}. Both images show NH_3 for the total atmospheric column.

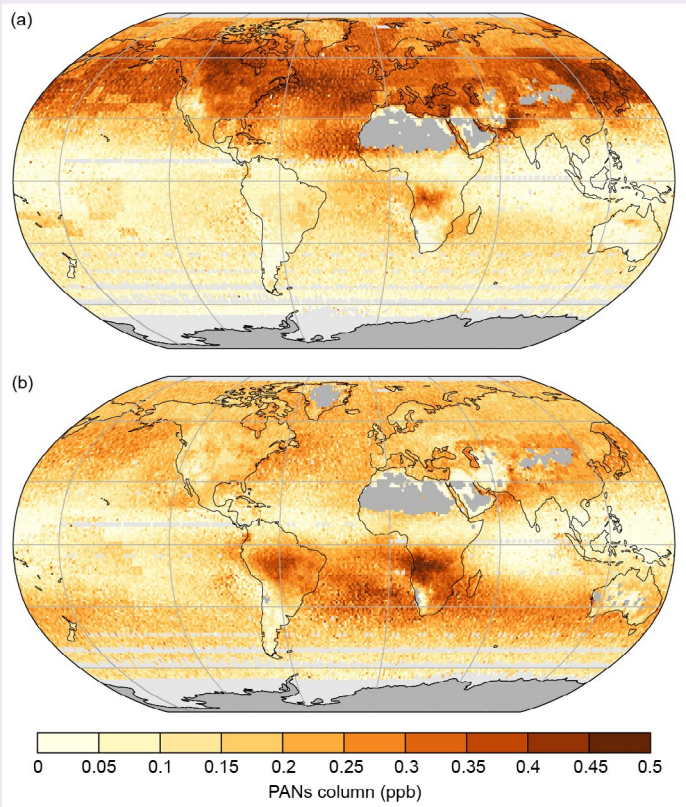

Fig. SB2.6. (a) Cross-Track Infrared Sounder (CrIS) acyl peroxynitrates (PANs) averaged over Jul 2024; (b) CrIS PANs averaged over Sep 2024. Units are ppb. Both images show PANs between 825 hPa and 215 hPa.

Unauthenticated | Downloaded 11/21/25 11:34 AM UTC

NO_2, NH_3, and PAN are all produced by biomass burning, and wildfires (many of which are ignited by humans) are becoming more intense due to climate change (Byrne et al. 2024). The connections of these indirect SLCFs with respect to ERF are as follows: NO_2 is a precursor of PAN, which then transports NO_x downwind where it can produce ozone far from its origin (potential ERF increase); the ozone produced from NO_2 subsequently impacts methane (direct SLCF) by reducing its lifetime (potential ERF decrease); NH_3 and NO_2 generated by fires can produce secondary aerosols (potential ERF decrease).

With existing and expanded data assimilation methods, satellite retrievals of indirect SLCFs can be assimilated into global atmospheric chemistry models, such as the Unified Forecast System (UFS; Jacobs 2021), Goddard Earth Observing System Composition Forecast Modeling System (GEOS-CF; Keller et al. 2021), or the Copernicus Atmosphere Monitoring Service (CAMS) European Centre for Medium-Range Weather Forecasts (ECMWF) reanalysis of atmospheric composition (Innes et al. 2019), to quantify their impact on air quality and Earth's radiation budget.

Unauthenticated | Downloaded 11/21/25 11:34 AM UTC

h. Land surface properties

1. TERRESTRIAL SURFACE ALBEDO DYNAMICS

—F. Cappucci, R. Urraca, and N. Gobron

The terrestrial surface albedo is a key variable controlling the amount of radiative energy absorbed by Earth's surface. Defined as the nondimensional ratio of reflected solar radiation to incident irradiance, the terrestrial surface albedo is influenced by a range of factors. An increase in vegetation density causes a "darkening" effect (negative anomalies) in the visible spectrum (0.3 μm–0.7 μm), as vegetation absorbs more radiation, while near-infrared (0.7 μm–5.0 μm) albedo increases slightly, due to healthy vegetation's higher reflectivity. In contrast, desertification or snow-covered surfaces result in a greater shortwave (0.3 μm–5.0 μm) albedo.

The 2024 anomaly (2003–20 reference period) of white sky albedo in visible spectrum (Plate 2.1ah, Fig. 2.82a) continued the darkening trend of Earth's surface as already seen in previous years (Cappucci et al. 2024; Duveiller and Gobron 2023).

The decrease in shortwave (Plate 2.1aj) white sky surface albedo over Canada was driven by the exceptional heatwaves that affected the region during the first half of 2024, which contributed to early snowmelt and large-scale wildfires. The decline in the shortwave albedo over central Europe, Scandinavia, and Greenland's coastline is also linked to the loss of snow and ice in all these areas (section 2c5).

The albedo brightening (positive anomaly) in the visible spectrum (Plate 2.1ah) over South America, (mainly Brazil, Bolivia, and Paraguay) and over southern Africa (including Zambia, Zimbabwe, Namibia, and Botswana) can be attributed to vegetation decline resulting from prolonged drought during the second and third quarters of the year, often associated with high temperatures (sections 2b1, 2d12). Surface darkening in the visible spectrum over northeastern Brazil and the Horn of Africa was characteristic of El Niño and the Indian Ocean dipole, respectively, where abundant precipitation occurring during the first half of the year contributed to healthier vegetation. A decrease in visible surface albedo, accompanied by an increase in near-infrared spectrum (Plate 2.1ai), was recorded in central and eastern Europe, eastern China, Japan, northern Australia, and sub-Saharan northeast Africa, characteristic of an increase in vegetation activity driven by the above-average precipitation that occurred over these areas during the first half of the year (section 2d6).

The patterns of the zonally averaged albedo anomalies in the shortwave (Fig. 2.83c) during 2024 exhibit a large decline in albedo at high latitudes (above 60°N), most evident in spring driven by early snowmelt, a tendency already consolidated since early in the century (Young 2023). The increased vegetation density over China and India has resulted in lowering the visible albedo (persistent negative anomalies) and increasing the near-infrared albedo (positive anomalies), which is clear between 10°N and 30°N for 2023 and 2024 (Figs. 2.83a,b, respectively). Over the southern tropical zone, surface visible brightening is evident during the second and third quarters of 2024, and is associated with a decline in vegetation health, particularly over South America and southern Africa. Between 30°S and 40°S, a persistent

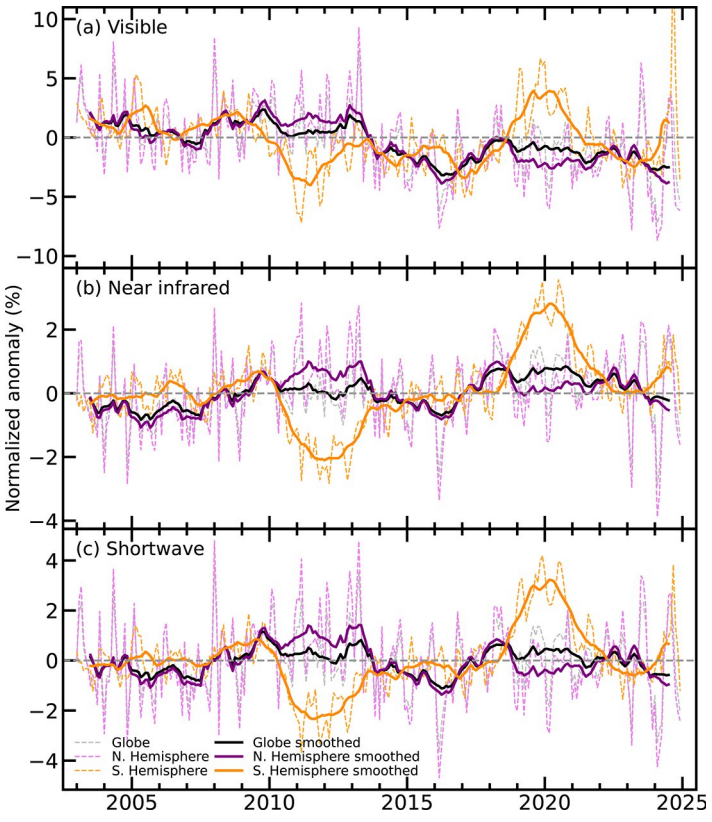

Fig. 2.82. Global (black lines), Northern Hemisphere (purple), and Southern Hemisphere (orange) land surface (a) visible, (b) near-infrared, and (c) shortwave broadband albedo anomalies (%; 2003–20 reference period) for the period 2003–24. Dotted lines denote monthly values; solid lines indicate the 12-month running averaged mean.

Unauthenticated | Downloaded 11/21/25 11:34 AM UTC

surface darkening trend in both visible and near-infrared domains, which had already started in 2022, is also evident in 2024.

The globally smoothed average anomaly (solid black line) enables the detection of long-term patterns of darkening or brightening in the terrestrial surface albedo over time. Although its amplitude shows minimal variability during the 2003–24 period, with fluctuations within ±3% in the visible domain and ±2% in the near-infrared and shortwave domains (Fig. 2.82), notable trends emerge.

A positive plateau in global shortwave albedo from 2018 to 2020 was followed by consecutive drops from 2021, with a persistent decline emerging in mid-2023 and consolidating through 2024 (Fig. 2.82c). Furthermore, 2024 saw the third-darkest (negative) shortwave anomalies since 2003 both globally (−0.58%) and in the Northern Hemisphere (NH; −0.96%). The acceleration of albedo decline in 2023/24 coincides with the record-positive anomalies in absorbed solar radiation (ASR), especially in 2023 (Fig. 2.61; section 2f1), as well as global surface temperature during these years. Surface albedo anomalies have a weak contribution to ASR on a global scale due to cloud masking, which attenuates surface albedo effect on ASR by a factor of about three. However, the decline in albedo caused by snow and ice loss above 55°N and ice loss above 55°S dominates polar ASR anomalies, contributing around +0.03°C of the +0.22°C ASR-driven warming in 2023 (Goessling et al. 2025).

This analysis is based on satellite products derived from the Moderate Resolution Imaging Spectroradiometer (MODIS) instrument on board the *Aqua* and *Terra* satellite platforms to generate a long-term record from 2002 to 2022 (Schaaf et al. 2002). The 2023 and 2024 data are derived from the Visible Infrared Imaging Radiometer Suite (VIIRS) on board the Suomi NPP satellite. Although the similarity in spectral band configuration makes VIIRS the optimal continuation of the MODIS archive (Liu et al. 2017), a small difference between VIIRS and MODIS surface albedo was noted, with VIIRS data being bias-corrected accordingly.

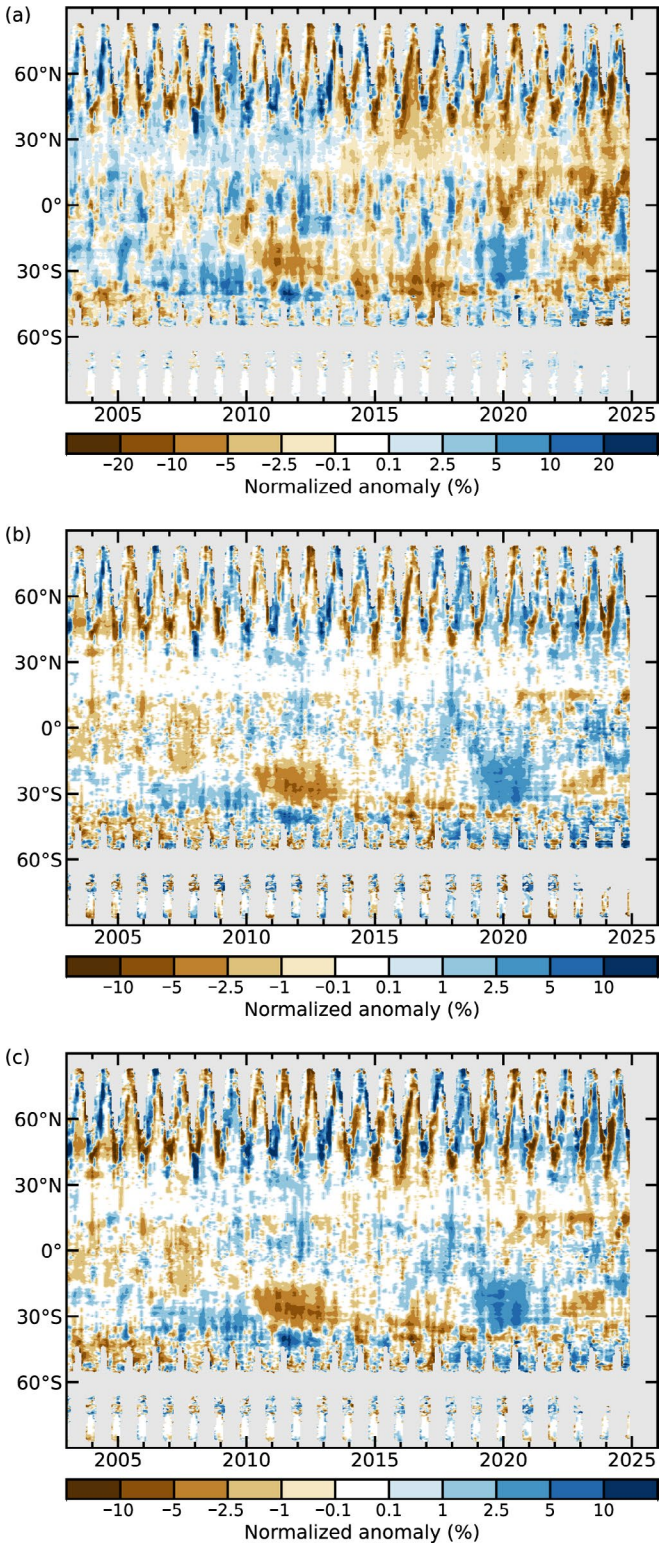

Fig. 2.83. Zonally averaged white-sky (a) visible, (b) near-infrared, and (c) shortwave broadband land surface albedo anomalies (%) for the period 2003–24 using a 2003–20 reference period.

2. TERRESTRIAL VEGETATION DYNAMICS

—N. Gobron and F. Cappucci

The fraction of absorbed photosynthetically active radiation (FAPAR) measures the amount of radiation absorbed by plant canopies. FAPAR is a key indicator of vegetation density, health, and productivity, and plays a crucial role in evaluating how effectively plants absorb carbon dioxide from the atmosphere. According to the FAPAR record in 2024, extreme deviations from

Unauthenticated | Downloaded 11/21/25 11:34 AM UTC

the 1998–2020 average (above 0.04 and below −0.04) accounted for 13% of land areas, with 11% showing an increase in productivity and 2% showing a decrease.

As illustrated in Plate 2.1ak, Earth's surfaces continued their greening trend in 2024 due to both higher temperatures (section 2b1) as well as plentiful rainfall (section 2d5). This is especially noticeable over continental Europe, excluding Bulgaria and Ukraine. The North American Arctic experienced an exceptional level of tundra greenness, with northern Alaska and central and eastern Canada all showing significantly above-average levels of greenness (Frost et al. 2024). In contrast, northeastern Siberia was again suffering from highly active wildfires. Northeastern Brazil vegetation recovered from 2023, particularly during the first half of the year. Positive anomaly patterns were seen in eastern Africa—including Kenya, Somalia, and Ethiopia—where, remarkably, overall green conditions were present due to extreme rainfall at the end of 2023; however, vegetated productivity declined in the second half of the year, especially in Somalia due to below-average rainfall between October and December. Northern and eastern Australia reported greener annual conditions, building on the higher-than-normal levels seen during the first six months of the year.

In Canada, forests in Quebec still bear the scars of fires in 2023, as evidenced by negative annual anomalies indicating that the area has not yet fully recovered. Additionally, there were persistent and large-scale fires that affected British Columbia and Alberta in July 2024 (section 2h3), and the number of wildfires increased in the Northwest Territories through August following heatwaves across the region.

The prolonged spring heatwaves that affected Central America contributed to vegetation decline in Chihuahua (Mexico) and Yucatan (Guatemala), and set records in high temperature and drought. Conversely, the state of Nuevo León (Mexico) experienced a significant increase in photosynthetic activity due to recovery of vegetation surfaces from last year.

Several regions in South America, including the Amazon and other areas of Brazil and Bolivia, experienced an extended period of drought, characterized by low rainfall and high temperatures. This led to severe summer wildfires affecting the forests. While the Sahel received excess rainfall (section 2d5), several countries in southern Africa, including Namibia, Botswana, Nigeria, Zambia, and Mozambique, experienced severe rainfall deficits and record-high temperatures. India and Pakistan, along with China, still exhibited a strong annual greenness due to agricultural intensification (Park et al. 2023) despite occasional heatwaves and floods.

The monthly anomalies of longitude-averaged FAPAR from 1998 to 2024 (compared to the 1998–2020 base period, Fig. 2.84) reveal that all latitudes between 2002 and 2013, particularly in the Southern Hemisphere (SH), experienced significant vegetation decline (values below −0.04). This was followed by an increasing greenness of surfaces in both hemispheres thereafter. Furthermore, during 2024, positive values were observed at almost all latitudes, with exceptionally high values (exceeding +0.04) noted around 50°N at the start of the year and shifting to around 10°N in the latter part of the year.

Figure 2.85 shows the global and hemispheric results, with the SH showing greater seasonal variability than the NH. FAPAR monthly anomalies over the SH were positive before 2002, in 2011, and after 2014, except for 2019. There were strong positive peaks (above +0.01) during the summers of 2000, 2017, and 2023, corresponding to fewer extreme events such as fire or drought, compared to the negative peaks (below −0.01) in 2008/09. A severe drought that affected a significant portion of South America and southern Africa led to an extreme negative deviation of −0.015 in October 2024. The NH was positive in 1998 but negative from 1999 to 2013 and positive thereafter, reaching a peak

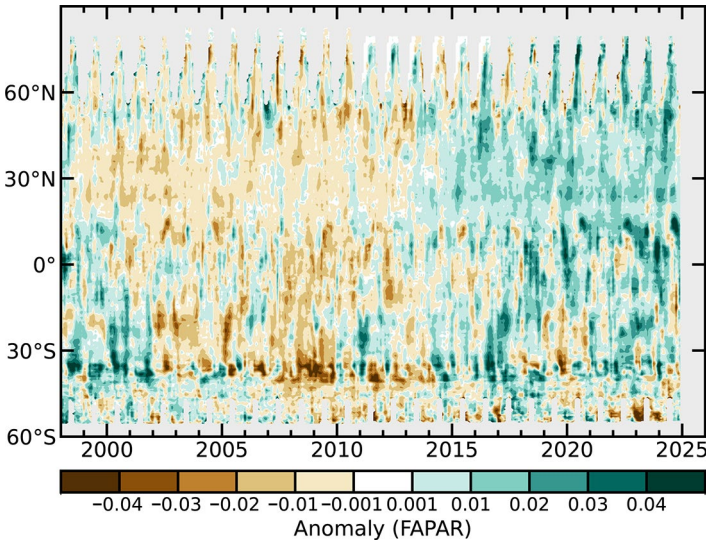

Fig. 2.84. Zonally averaged fraction of absorbed photosynthetically active radiation (FAPAR) anomalies for the period 1998–2024 (1998–2020 base period).

Unauthenticated | Downloaded 11/21/25 11:34 AM UTC

(above 0.014) in spring 2024. This greening trend is directly linked to the increase of land surface temperatures but also to the carbon dioxide fertilization effect (Zhu et al. 2016).

FAPAR, an essential climate variable (GCOS 2022), was estimated using optical space sensors. The 2024 analysis combines 27 years of global products from four optical sensors: the Sea-Viewing Wide Field-of-View Sensor (SeaWiFS; 1998–2002); Envisat/ Medium Resolution Imaging Spectrometer (MERIS; 2003–10), *Terra-Aqua*/MODIS (2011–16), and EU Copernicus Sentinel-3/Ocean and Land Colour Instrument (OLCI; 2017–24; Gobron et al. 2010, 2022; Pinty et al. 2011).

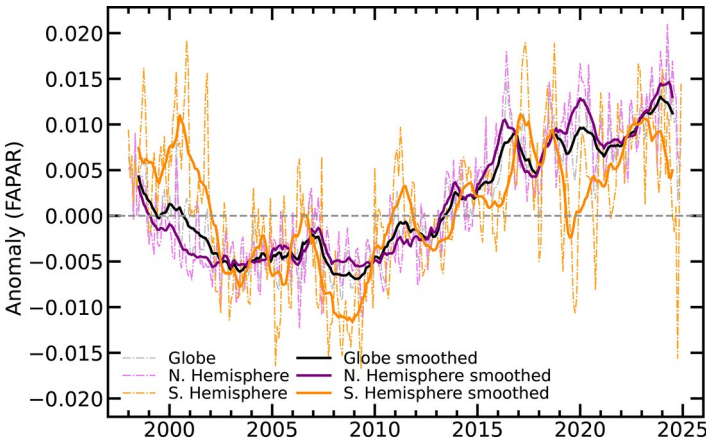

Fig. 2.85. Global (black line), Northern Hemisphere (purple), and Southern Hemisphere (orange) fraction of absorbed photosynthetically active radiation (FAPAR) anomalies for 1998–2024 (1998–2020 base period). Dotted lines denote each monthly period; solid lines indicate the six-month running averaged mean.

Uncertainties of the four datasets were derived through error propagation techniques and comparisons against multiple proxies using ground-based measurements (Bai et al. 2022) and radiative transfer simulations, all of which provide an estimate of the uncertainties and biases. This long-term FAPAR dataset has an estimated average uncertainty of approximately 5% to 10%.

3. BIOMASS BURNING

—J. W. Kaiser, M. Parrington, and D. Armenteras

Two distinct trends in global biomass burning were identified over the last decade, both of which persisted into 2024. Many savanna regions, which are responsible for most global fire emissions, have experienced a decline related to agricultural expansion. In contrast, many forested, wetland, and boreal regions have witnessed an increase in both the duration and intensity of wildfire episodes (see Plate 2.1al). This is attributable to climate change, which has led to increased drought periods and, consequently, heightened flammability of the landscape (e.g., Xing and Wang 2023 for the Arctic). The magnitude of biomass burning, denoted as "fire activity" or "wildfires", is here described as the quantity of carbon that is consumed by fire and released into the atmosphere. Of this, 80% to 95% is emitted as carbon dioxide (CO_2), with the remainder being oxidized to CO_2 in the atmosphere or released as particulate matter. In a stable ecosystem, the bulk of this CO_2 is typically assimilated through vegetation re-growth. However, it is estimated that 20% currently contributes to the long-term buildup of atmospheric CO_2 (Zheng et al. 2023).

Global annual total estimated fire emissions were below the 2003–20 average in 2024 by approximately 7%, but were still the second highest since 2016 (after 2023), according to the Copernicus Atmosphere Monitoring Service's (CAMS) Global Fire Assimilation System version 1.4 (GFASv1.4; Fig. 2.86; Table 2.13). The global total was affected by anomalously large-scale wildfires that burned persistently in forests across South and North America at different points throughout the year (Figs. 2.87, 2.88). In the latter, Canada again experienced an extreme year with fire activity above any year between 2003 and 2022, with the annual total having been second only to the record fires of 2023 (Fig. 2.88). The western United States experienced its seventh-highest annual total fire emissions since 2003 with a +22% anomaly. The year 2024 also saw an increase in

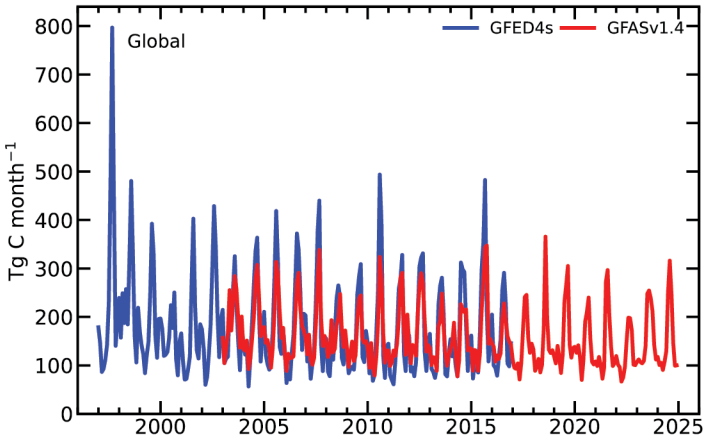

Fig. 2.86. Global monthly carbon consumption (Tg C month^{-1}) in biomass burning.

Unauthenticated | Downloaded 11/21/25 11:34 AM UTC

Table 2.13. Annual continental-scale biomass burning budgets in terms of carbon emission (Tg C yr^{-1}) from the Copernicus Atmosphere Monitoring Service Global Fire Assimilation System version 1.4 (CAMS-GFASv1.4).

Name of Region	Location	Biomass Burning 2003–20 Mean value (Range)	Biomass Burning 2024 Value	Biomass Burning 2024 Anomaly (%)
Global	–	1954 (1669–2293)	1812	–142 (–7%)
North America	30°N–75°N, 190°E–330°E	86 (58–114)	148	+62 (+71%)
Central America	13°N–30°N, 190°E–330°E	43 (29–62)	46	+3 (+7%)
South America	13°N–60°S, 190°E–330°E	352 (225–526)	486	+134 (+38%)
Europe and Mediterranean	30°N–75°N, 330°E–60°E	30 (16–58)	22	–8 (–28%)
N. Hem. Africa	0°–30°N, 330°E–60°E	394 (314–457)	305	–89 (–23%)
S. Hem. Africa	0°–35°S, 330°E–60°E	482 (429–544)	446	–36 (–7%)
Northern Asia	30°N–75°N, 60°E–190°E	185 (97–425)	156	–29 (–16%)
South-East Asia	10°N–30°N, 60°E–190°E	116 (80–153)	86	–31 (–26%)
Tropical Asia	10°N–10°S, 60°E–190°E	149 (24–448)	24	–125 (–84%)
Australia	10°S–50°S, 60°E–190°E	117 (49–221)	94	–22 (–19%)
Canada	47°N–75°N, 219°E–310°E	46 (10–80)	111	+65 (+141%)
Arctic	67°N–90°N, 0°–360°	7 (1–35)	16	+8 (+117%)

wildfire emissions from boreal Eurasia, following persistent wildfires in the Sakha Republic and Amur Oblast in the east of Russia. The first contributed to the third strongest wildfires in the Arctic after 2019/20 (Fig. 2.88). Overall, however, North Asia experienced a negative anomaly of –16%.

South America experienced its highest fire activity since 2007, but approximately equal with 2010, at 38% above the 2003–20 mean (Fig. 2.88). The spring seasonal fires in the northern tropics of South America led to Venezuela, Guyana, Suriname, and Brazil's Roraima state all experiencing their highest annual total emissions. In central regions, Bolivia, the Pantanal wetlands, and some parts of the Brazilian Amazon experienced historic fires with the highest emissions of the past two decades, largely driven by drought conditions (section 2d11). Bolivia experienced its highest fire activity since at least 2003, with each month during January to November exceeding its 2003–20 monthly mean. Fires in Pantanal burned 1.2 million hectares between January and August, 14% of which were on either indigenous lands or protected natural areas including the Pantanal wetlands (Alencar et al. 2024). In Brazil, Amazon fire emissions peaked higher than any year since 2010, with emissions in the states of Mato Grosso and Pará well above average, as El Niño-driven drought (see section 7d; Marengo et al. 2024)

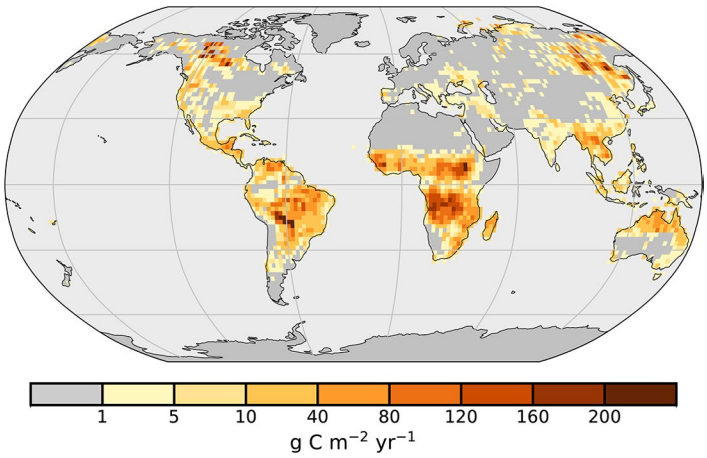

Fig. 2.87. Global map of fire activity in 2024 in terms of carbon consumption (g C m^{-2} yr^{-1}). (Source: Copernicus Atmosphere Monitoring Service Global Fire Assimilation System version 1.4 [CAMS-GFASv1.4.])

Unauthenticated | Downloaded 11/21/25 11:34 AM UTC

significantly increased fire risk despite reduced deforestation. Earlier seasonal drying also heightened flammability, leading to widespread fire outbreaks (Feron et al. 2024).

African fire carbon emissions accounted for roughly half of the total global emissions during the 2000s, but their contribution shrunk to ~40% during recent years (Fig. 2.87; Plate 2.1al). The decrease in savanna regions persisted in 2024 over Northern Hemisphere Africa with emissions 23% below the 2003–20 average, the fourth successive year with lower fire activity than any years in the record prior to 2019. Southern Hemisphere Africa also contributed to the trend despite increased fire activity in several regions, including the central African tropical forest. Fire activity in southeast and tropical Asia generally continued reducing trends. In the latter—including Indonesia—El Niño-induced drought combined with land-clearing fires on palm, pulp, and rice plantations have led to extreme fires in the past. However, the fire activity of 2024 was lower than during any year from 2003 to 2016 (Fig. 2.88) despite the El Niño conditions at the beginning of the year. Increased wildfire emissions occurred in tropical regions of Australia between September and November, related to warmer and drier conditions (Plate 2.1al).

GFAS is operated by CAMS and produces global fire emission estimates (Kaiser et al. 2012) in near-real-time based on the MODIS Fire Radiative Power products (Giglio et al. 2016). A combination of near-real-time and consistently reprocessed products are used here, with input from MODIS Collection 6 for the entire period of 2003–24. The biases with respect to Collection 5 and between satellites have been corrected, and a more extensive spurious signal mask has been applied. Archived MODIS input is used for 1 January 2003 to 18 December 2016 and August 2024, and near-real-time (NRT) input is used otherwise. The replacement for August 2024 is necessary due to corrupt NRT input, and uses an updated land cover map. The time series in Fig. 2.86 also places GFAS in the context of the Global Fire Emissions Database version 4.1 (GFED4s), which is primarily based on burnt area observation and dates back to 1997 (van der Werf et al. 2017).

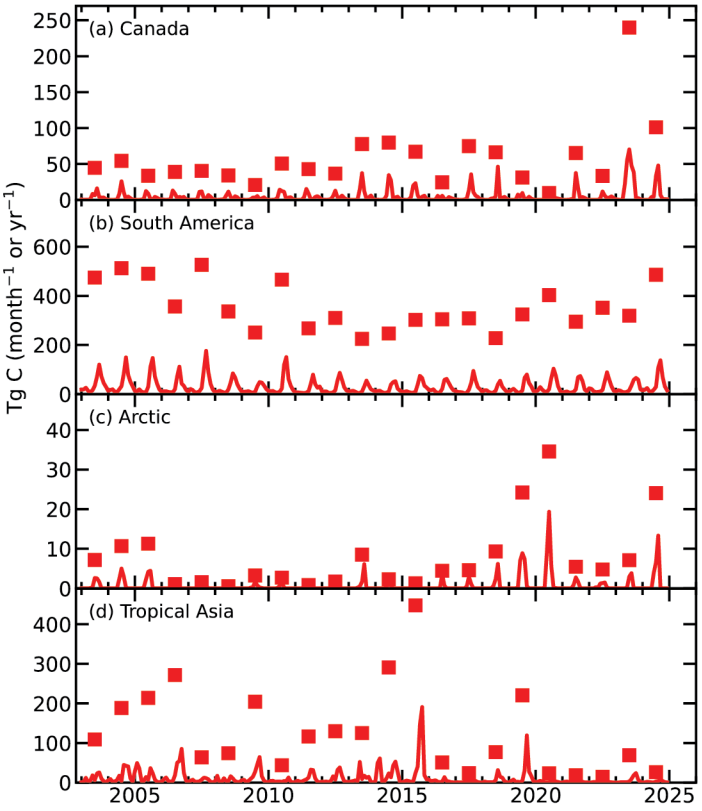

Fig. 2.88. Regional time series of monthly (lines in Tg C month^{-1}) and annual (symbols in Tg C yr^{-1}) biomass burning activity in (a) Canada, (b) South America, (c) the Arctic, and (d) tropical Asia.

4. PHENOLOGY

—D. L. Hemming, O. Anneville, Y. Aono, T. Crimmins, N. Estrella, R. Holliday, S.-I. Matsuzaki, A. Menzel, I. Mrekaj, J. O'Keefe, A. D. Richardson, J. Rozkošný, T. Rutishauser, R. Shinohara, S. J. Thackeray, A. J. H. van Vliet, and J. Garforth

Vegetation phenology, "the rhythm of the seasons", is strongly influenced by climate variations and can modify climate through land–atmosphere exchanges of energy, moisture, and carbon (Hassan et al. 2024).

PhenoCam (https://phenocam.nau.edu/) is a network of over 900 automated digital cameras monitoring phenological changes in a wide range of ecosystems around the world (Richardson 2019; Seyednasrollah et al. 2019). The highest-density and longest-running PhenoCam sites (there are over 75 with more than 10 years of observations) are in the United States. Indicators of 'start of season' (SOS_{PC}) and 'end of season' (EOS_{PC}) were estimated from PhenoCam data (Table 2.14) and ground observation of red oak (*Quercus rubra*; SOS_{GO}, EOS_{GO}) in Harvard Forest, a deciduous forest in Massachusetts in the United States (Richardson and O'Keefe 2009; O'Keefe and VanScoy 2024), and from red oak observations across the northeastern United States

Unauthenticated | Downloaded 11/21/25 11:34 AM UTC

contributed to *Nature's Notebook* (SOS_{NN}, EOS_{NN}), the USA National Phenology Network (USA NPN) phenology monitoring platform (Rosemartin et al. 2014; Crimmins et al. 2022). Interannual variations in the start and end of season dates at Harvard Forest are broadly consistent with larger-scale data from USA NPN's *Nature's Notebook* program (Figs. 2.89a,b; Table 2.15). In 2024, SOS_{PC}, SOS_{GO}, and SOS_{NN} were three, six, and four days later, respectively, than in 2023, while EOS_{PC}, EOS_{GO}, and EOS_{NN} were seven, four, and four days earlier. SOS_{PC} (EOS_{PC}) was two days earlier (one day earlier) than the 2011–20 baseline mean, resulting in a growing season length of 168 days: 10 days shorter than in 2023, and one day longer than the baseline.

The USA NPN's extended Spring Index (SI-x), a model that reflects the onset of spring-season biological activity (Schwartz et al. 2013; Crimmins et al. 2017), estimated widespread later "first leaf" in 2024 across the eastern and southern United States and earlier first leaf across the western and central United States compared with 2023. In contrast, compared with the baseline (2011–20 mean), first leaf in 2024 was early across most of the eastern United States, and late across the west (Figs. 2.89a,b). Consistent with the SOS_{PC} and SOS_{GO} observations at Harvard Forest, first leaf was later (by three days) in 2024 than in 2023 and earlier (by one day) in 2024 compared to the baseline. Likewise, first leaf and SOS_{PC} observations from a selection of nine other sites across the USA showed consistent patterns (see Fig. 2.89 for details).

Start- and end-of-season indicators for native oak trees (*Quercus robur* and/or *Quercus petraea*) at European sites in Germany (D), the Netherlands (NL), Slovakia (SK), and the

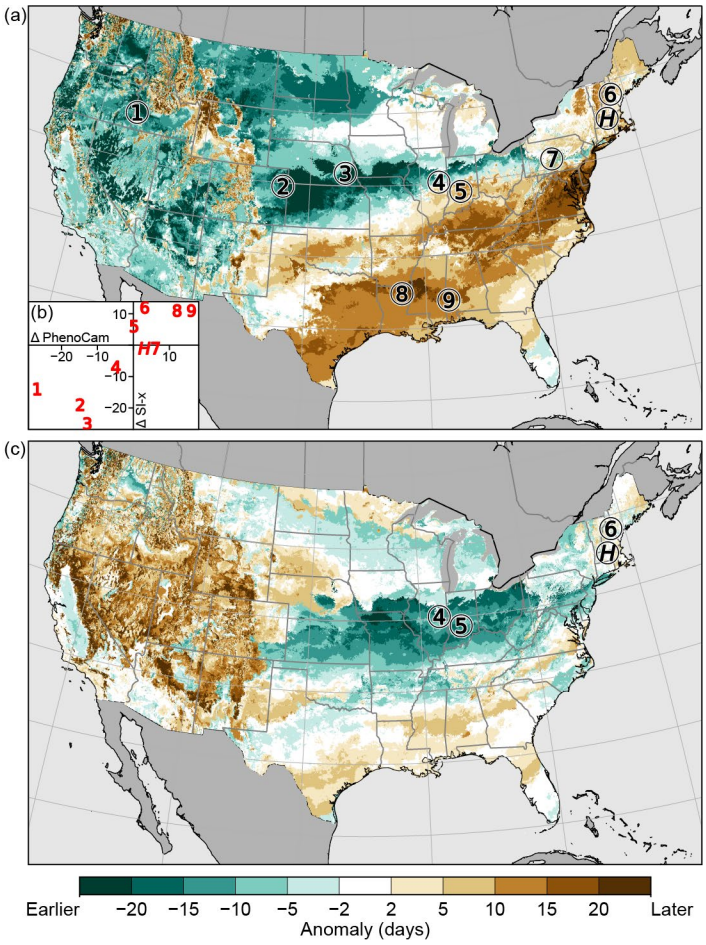

Fig. 2.89. 2024 "first leaf" date anomalies across the United States relative to (a) 2023 and (c) the 2011–20 baseline, estimated using the USA National Phenological Network (USA NPN) extended Spring Index (SI-x) model (Source: USA NPN data—https://www.usanpn.org/data). Negative (green) values show earlier first-leaf estimates in 2024 and positive (brown) are later. First-leaf SI-x anomalies are generally consistent with start of season PhenoCam (SOS_{PC}) anomalies at the 10 selected sites highlighted on map (a), see Table 2.14 for details. The scatter plot (b, inset in [a]) shows PhenoCam date anomalies on the x axis, and first-leaf SI-x date anomalies on the y axis (Deming regression, y = 1.02±0.04 x – 0.29±0.49, r^2 = 0.69). Map (c) shows the four sites from (a) for which the data record is long enough to calculate the 2011–20 baseline.

Table 2.14. PhenoCam sites across USA used in this assessment.

PhenoCam Site Name (#)	Location	Ecosystem Type
ARS Great Basin (1)	Reynolds Creek, Idaho	Shrub Community
NEON Site – D10 Central Plains (2)	Arikaree River, Colorado	Grass Community
Nine Mile Prairie, University of Nebraska (3)	Lancaster County, Nebraska	Grass Community
University of Illinois Energy Farm (4)	Urbana, Illinois	Restored Prairie Community
Morgan Monroe State Forest (5)	Indiana	Deciduous Forest
Bartlett Experimental Forest (6)	New Hampshire	Deciduous Forest
Susquehanna Shale Hills Critical Zone Observatory (7)	Pennsylvania	Deciduous Forest
Russell Sage State Wildlife Management Area (8)	Louisiana	Deciduous Forest
NEON Site – D08 Ozarks Complex (9)	Lenoir Landing, Alabama	Deciduous Forest
Harvard Forest (H)	Petersham, Massachusetts	Deciduous Forest

Unauthenticated | Downloaded 11/21/25 11:34 AM UTC

United Kingdom (UK) are represented by observations of first leaf (SOS) and leaf fall or "bare tree" (EOS; Table 2.15; Figs. 2.90c,d). They have been shown to be strongly influenced by spring and autumn/winter temperatures across Europe (Menzel et al. 2020). Compared to the baseline (2000–20 mean), SOS dates in D, NL, SK, and UK were all earlier by 11, 13, 12, and 8 days, respectively, while EOS dates were mostly later by 2, 5, 3, and 0 days (Table 2.15). Spring temperatures in D, NL, UK, and SK were much warmer (record high in SK; see section 7f) than average, resulting in very early 2024 SOS in D and SK, and the earliest SOS on record in NL and UK. Above-average temperatures in autumn/winter combined with ample precipitation across most of Europe resulted in generally later-than-average EOS dates. In some locations of SK, where extreme summer drought occurred (see section 7f), very early yellowing and leaf fall was observed at the end of August. With the warmer autumn/winter and consequently later EOS dates, the growing season length in 2024 was significantly longer than the baseline.

In Kyoto, Japan, the full bloom date (FBD) for native cherry tree (*Prunus jamasakura*) in 2024 was two days earlier than the baseline (2000–20 mean; Table 2.15; Fig. 2.90e), but 10 days later than the record set in 2023. Annual FBDs have been recorded since 812 AD (Aono and Kazui 2008), and for the Arashiyama district of Kyoto, they are recorded in newspapers and on web sites from daily observations at train stations by railway passengers.

Monitoring data on lake water concentrations of the photosynthetic pigment chlorophyll-*a* were available to estimate spring phytoplankton phenology in 10 Northern Hemisphere lakes (Fig. 2.91). The seasonal timing was estimated for 'start of season' (SOS_L; Park et al. 2016), 'day of maximum concentration' (DOM_L), and 'center of gravity' (COG_L), which is an estimate of the mid-point of the plankton bloom (Edwards and Richardson 2004). The lake basins showed great interannual variation and mixed phenological behavior in 2024 relative to 2000–20. The SOS_L and COG_L occurred earlier than the baseline median for most of the lakes—8 and 7 of 10, respectively—whereas no consistent pattern was observed for DOM_L (5 earlier and 5 later than the baseline median).

Table 2.15. Day of year (doy) and date of start of season (SOS), end of season (EOS) and full bloom date (FBD; cherry tree observations only) for land phenology records in USA (Harvard: PhenoCam, red oak, and USA National Phenology Network [USA-NPN] mean covering northeastern USA), Europe oak records (Germany, Netherlands, Slovakia, and United Kingdom), and Japan (native cherry tree observations in Japan). The baseline period is 2000–20 for all records except PhenoCam and USA-NPN, which have baseline periods of 2011–20. Growing season length for 2024 and the baseline mean are calculated as EOS minus SOS or FBD as appropriate for the record. Negative/positive values represent earlier/later dates for 2024 relative to the baseline.

Location / Record	SOS/FBD **2024** (doy, date)	SOS/FBD **Baseline** (doy, date)	SOS/FBD **Difference 2024 – Baseline** (days)	EOS **2024** (doy, date)	EOS **Baseline** (doy, date)	EOS **Difference 2024 – Baseline** (days)	Growing Season **EOS – SOS 2024** (days)	Growing Season **EOS – SOS Baseline Mean** (days)
Harvard PhenoCam	125 4 May	127 6 May	–2	293 19 Oct	294 20 Oct	–1	168	167
Harvard Red oak	128 7 May	128 7 May	0	295 21 Oct	293 19 Oct	+2	167	164
USA-NPN	120 29 Apr	126 5 May	–6	268 24 Sep	276 2 Oct	–8	148	150
Germany	107 17 Apr	118 28 Apr	–11	312 8 Nov	310 6 Nov	+2	205	192
Netherlands	97 6 Apr	110 20 Apr	–13	336 1 Dec	331 27 Nov	+5	239	221
Slovakia	104 14 Apr	116 26 Apr	–12	294 20 Oct	291 17 Oct	+3	190	175
UK	106 15 Apr	114 23 Apr	–8	334 29 Nov	334 29 Nov	0	228	221
Japan	95 4 Apr	97 6 Apr	–2	-	-	-	-	-

Unauthenticated | Downloaded 11/21/25 11:34 AM UTC

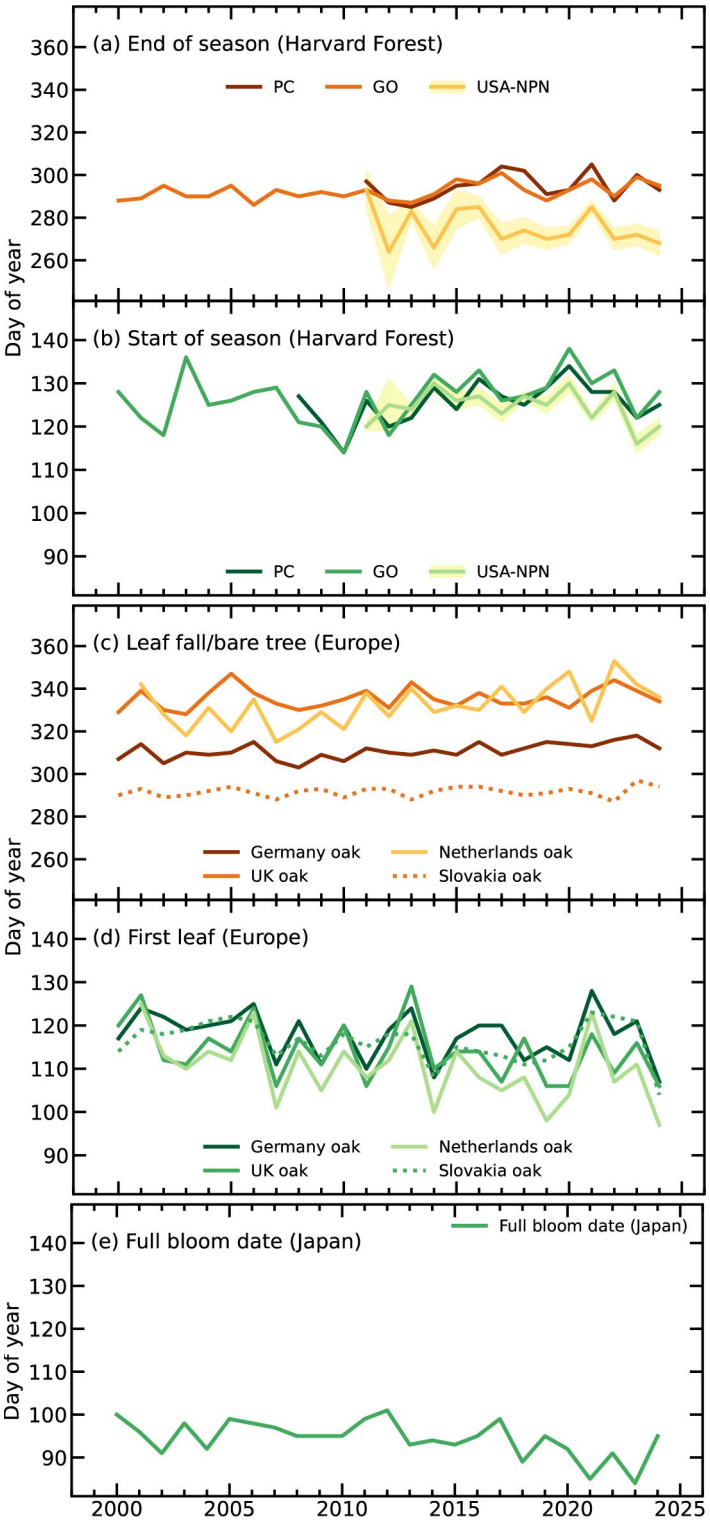

Fig. 2.90. Day of year of spring (green shades) and autumn (orange and yellow) vegetation phenology indicators for (a),(b) Harvard Forest, Massachusetts, derived from PhenoCam (PC), ground observations (GO) of red oak (*Quercus rubra*), and the USA National Phenology Network (USA NPN) regional-scale means of red oak observations (calculated across the northeastern states of Pennsylvania, New Jersey, New York, Connecticut, Rhode Island, Massachusetts, Vermont, New Hampshire, and Maine, with ±1 std. error shaded); (c),(d) Germany, United Kingdom, Netherlands, and Slovakia mean of native oak observations (*Quercus robur* or *Quercus petraea*), and (e) full bloom date observations of native cherry trees (*Prunus jamasakura*) in Kyoto (Arashiyama district), Japan.

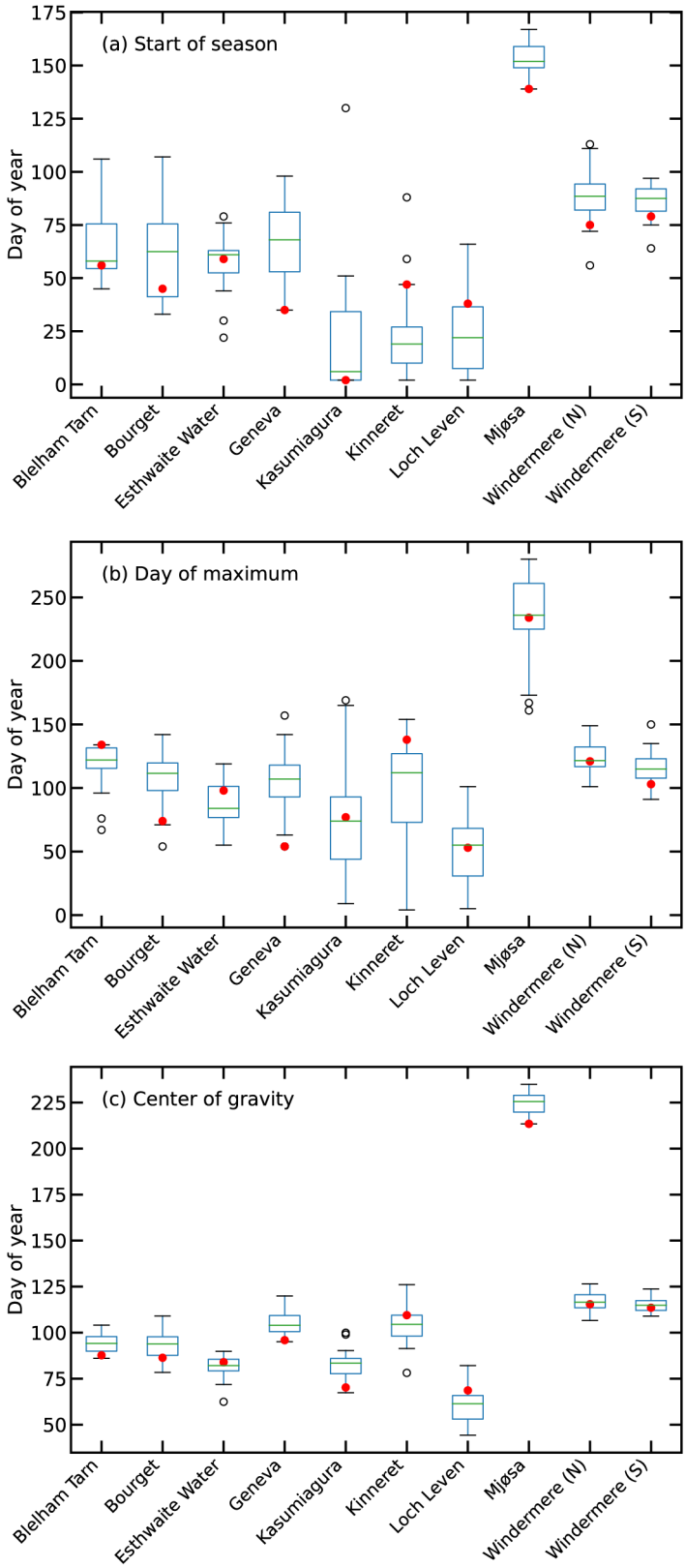

Fig. 2.91. Phenological metrics based on lake chlorophyll-*a* concentrations as a proxy of phytoplankton biomass: (a) start of season, (b) day of maximum, and (c) center of gravity. Boxplots show variation during the 2000–20 baseline period, and red dots show 2024 values. The 10 lakes are in the Northern Hemisphere (Blelham Tarn in the United Kingdom, Bourget in France, Esthwaite Water in the United Kingdom, Geneva in France/Switzerland, Kasumigaura in Japan, Kinneret in Israel, Loch Leven in the United Kingdom, Mjøsa in Norway, and north and south basins of Windermere in the United Kingdom).

Unauthenticated | Downloaded 11/21/25 11:34 AM UTC

5. VEGETATION OPTICAL DEPTH

—R. M. Zotta, W. Preimesberger, R. De Jeu, T. Frederikse, and W. Dorigo

Vegetation optical depth (VOD) is a radiative transfer model parameter derived from space-borne passive microwave sensors that indicates the attenuation of Earth's emitted or reflected radiation by vegetation. It serves as an indicator of vegetation water content (VWC) and vegetation density. VOD has proven valuable in many applications, including vegetation condition monitoring (Moesinger et al. 2022; Vreugdenhil et al. 2022). Positive VOD anomalies indicate above-average vegetation development, while negative anomalies indicate stressed or underdeveloped vegetation with lower VWC compared to normal conditions, either due to stressed vegetation, overall lower biomass, or both.

In 2024, the overall VOD anomaly in the NH was similar to that observed in 2023 (Zotta et al. 2023; Fig. 2.92). In contrast, in the SH, where vegetation development is influenced by variations in the El Niño–Southern Oscillation (ENSO; Miralles et al. 2014; Martens et al. 2017), overall VOD was lower than in 2023 (Figs. 2.92, 2.93). Here, negative anomalies prevailed, especially in the first quarter of the year (Appendix Fig. A2.13), during the strong El Niño event.

Widespread positive anomalies (Plate 2.1am), which intensified relative to 2023 (Appendix Fig. A2.14), were observed in large regions across Australia and parts of eastern Africa. In Australia, these patterns were likely driven by above-average rainfall (section 7h4) boosting vegetation growth. Substantial positive anomaly patterns were observed during the first half of 2024 across large parts of Kenya, Somalia, Ethiopia, and South Sudan (Appendix Fig. A2.13), likely a consequence of two consecutive seasons of wetter-than-normal conditions facilitating vegetation recovery after an extended drought period (WFP 2024). Additionally, notable positive VOD anomaly patterns emerged in the Sahel starting in September, likely driven by substantial rainfall (section 7e5) that boosted vegetation activity. At the monthly time scale (Appendix Fig. A2.13), striking positive patterns were observed in North America across portions of the Plains and Midwest, where exceptionally warm temperatures led to favorable winter crop conditions (USDA and USDC 2024) in the year's first quarter. Strong positive VOD anomaly patterns also emerged in Spain in October, likely due to record rainfall amounts (section 7f4).

Large-scale negative anomaly patterns in VOD were identified across multiple regions, including extended areas in Africa, Mexico, Central and South America, and Eastern Europe (Plate 2.1am). During the first quarter of 2024, lower-than-usual VOD continued to be evident in southern

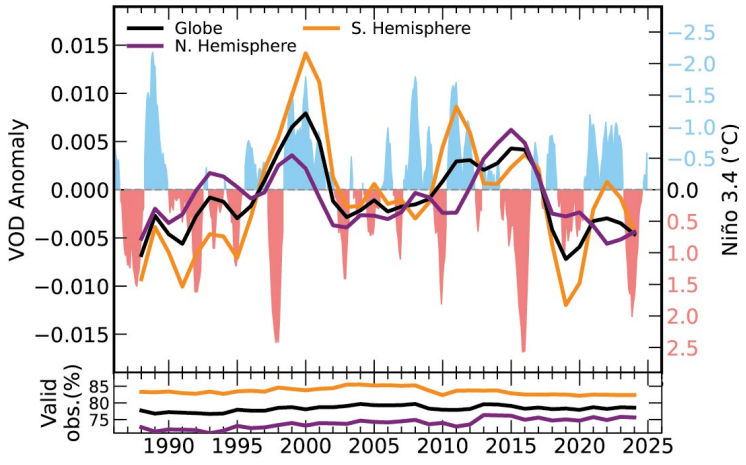

Fig. 2.92. Yearly vegetation optical depth (VOD) anomaly averages computed from the 1991–2020 climatology and yearly Niño-3.4 index. The Niño-3.4 index tracks the state of the El Nino–Southern Oscillation (ENSO). A negative Niño-3.4 index corresponds to a negative ENSO phase. (Source: VOD Climate Archive version 2 [VODCA v2]; NOAA Physical Sciences Laboratory [https://psl.noaa.gov/data/timeseries/month/DS/Nino34/].)

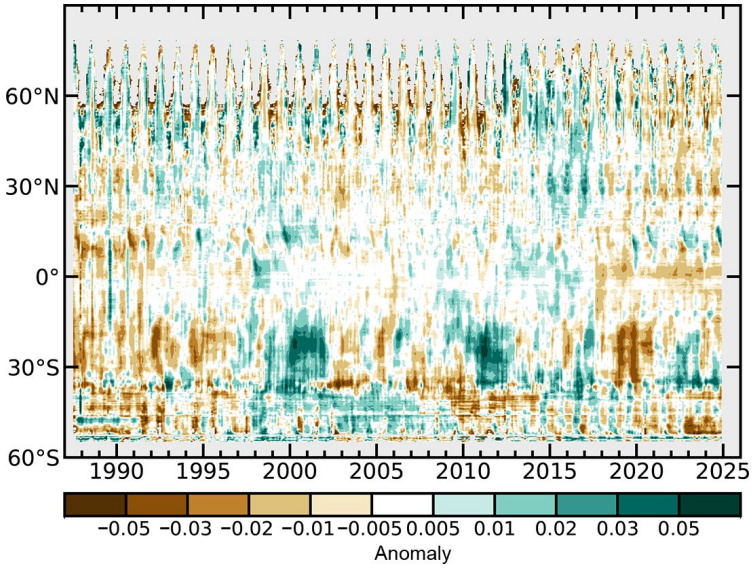

Fig. 2.93. Time–latitude diagram of monthly vegetation optical depth (VOD) anomalies (1991–2020 base period). Data are masked where no retrieval is possible or where the quality of the retrieval is not assured and flagged due to frozen soil, radio frequency interference, etc. (Source: VOD Climate Archive version 2 [VODCA v2].)

Unauthenticated | Downloaded 11/21/25 11:34 AM UTC

Africa (Appendix Fig. A2.13), where ENSO is a significant factor in agricultural productivity (UNOCHA 2024). Specifically, negative VOD anomalies in February and March were recorded in Namibia, Botswana, Zimbabwe, Zambia, and Angola. These regions experienced their driest conditions in decades (Van Dijk et al. 2025), which deteriorated the vegetation (UNOCHA 2024). In Zambia, severe drought and high temperatures devastated agricultural production (Van Dijk et al. 2025). In the Americas, Mexico experienced a prolonged dry spell which, combined with intense heatwaves (section 7b3), severely impacted crop growth (Climate.gov 2024). The reduction in VOD observed in the Pantanal region in Brazil is likely a result of extreme drought (NASA 2024). Persistent drought conditions significantly affected vegetation condition across West, Central, and North Africa during the first half of the year, contributing to the observed negative VOD anomalies (Appendix Fig. A2.13; Toreti et al. 2024a). Similarly, declines in VOD in Romania, Ukraine, and southern Russia are likely attributable to extended drought conditions that adversely affected local vegetation (Toreti et al. 2024b).

Long-term patterns associated with land-use changes persisted in 2024 (Plate 2.1am; Zotta et al. 2023). Regions including northern Mongolia, Bolivia, Paraguay, and Brazil experienced below-average VOD due to deforestation and land degradation (Song et al. 2018). Conversely, intensified agricultural practices in India and reforestation efforts in northeastern China contributed to above-average VOD (Song et al. 2018).

The VOD data originate from the VOD Climate Archive version 2 (VODCA v2, Zotta et al. 2024a,b). VODCA combines VOD observations derived with the Land Parameter Retrieval Model (Meesters et al. 2005; van der Schalie et al. 2017) from various space-borne radiometers—including the Special Sensor Microwave/Imager (SSM/I), Tropical Rainfall Measuring Mission (TRMM), WindSat, Advanced Microwave Scanning Radiometer for the Earth Observing System (AMSR-E), and Advanced Microwave Scanning Radiometer 2 (AMSR2)—into a long-term, harmonized dataset. Here, VODCA CXKu, which integrates C-, X-, and Ku-band observations and provides daily data at 0.25° spatial resolution, was used.

Unauthenticated | Downloaded 11/21/25 11:34 AM UTC

Acknowledgments

a Introduction

R.J.H.D., J.B., and K.M.W. were supported by the Met Office Hadley Centre Climate Programme funded by the U.K. Department for Science, Innovation and Technology (DSIT). G.A.M. is supported by NOAA. The editors thank Emily Carlisle, John Kennedy, David Parker, Jessica Poulton, Nick Rayner, Ruben Urraca, and the five anonymous reviewers for their insight, thoughts, and suggestions while reviewing this chapter. We also thank Fumi Sezaki and Ayaka Bunno (Japanese Meteorological Association [JMA]), Julien Nicolas (European Centre for Medium-Range Weather Forecasts [ECMWF]), and Mike Bosilovich (NASA) for their help in providing the reanalysis data used in this chapter. Many of the figures in this chapter were produced with the help of the Matplotlib version 3.7.2 (Hunter et al. 2007), Iris version 3.7.0 (Hattersley et al. 2023), and Cartopy version 0.21.1 (Elson et al. 2022) packages.

b2 Lake Surface Temperatures

Lake surface water temperatures from satellite data have been generated within the Climate Change Initiative Lakes project funded by the European Space Agency (ESA) (4000125030/18/I-NB) with adaptation funded by the E.U. Copernicus Climate Change Service (C3S) programme and extensions by the U.K. Earth Observation Climate Information Service (EOCIS) project (NE/X019071/1). Part of the in situ data used for the validation of the satellite data and for this report have kindly been made publicly available by the Fisheries and Oceans Canada (FOC), the National Data Buoy Center from NOAA, the Hungarian Meteorological Office, the Upper Great Lakes Observing System (UGLOS), and the North Temperate Lakes Long-Term Ecological Research (NTL-LTER). The authors gratefully acknowledge the late Alon Rimmer for always supplying data for Lake Kinneret.

b3 Night Marine Air Temperatures

R.C. and E. K. were supported by the Natural Environmental Research Council (NERC) through National Capability funding (AtlantiS: NE/Y005589/1). R. J. was supported by funding from the U.S. Department of Energy (DOE) (DE-SC0023332).

b4 Surface Temperature Extremes

R.J.H.D. was supported by the Met Office Hadley Centre Climate Programme funded by DSIT.

b5 Tropospheric Temperature

Work performed by Stephen Po-Chedley at Lawrence Livermore National Laboratory (LLNL) was supported by the Regional and Global Model Analysis Program (RGMA) of the Office of Science at the DOE and performed under the auspices of the DOE under Contract DE- AC52-07NA27344. Work performed by Cheng-Zhi Zou was supported by NOAA/Office of Low Earth Orbit (LEO) Proving Ground and Risk Reduction (PGRR) Program.

b7 Equivalent Temperature

Paul Stoy was supported by the U.S. National Science Foundation (NSF) (Hydrological Sciences award 2422397). Tom Matthews and Tom Wood were supported by a U.K. Research and Innovation Future Leaders Fellowship (grant MR/X03450X/1).

c1 Permafrost Temperatures and Active-Layer Thickness

Research on James Ross Island was supported by the Czech Antarctic Research Programme and the Czech Science Foundation project (GM22-28659M). The Circumpolar Active Layer Monitoring (CALM) program is funded by the NSF Project 1836377. The Svalbard permafrost data is part of the Svalbard Integrated Earth Observing System (SIOS). The Swiss Permafrost Monitoring Network (PERMOS) is financially supported by MeteoSwiss (in the framework of Global Climate Observing System [GCOS] Switzerland), the Federal Office for the Environment, and the Swiss Academy of Sciences, and acknowledges the contribution of its partner

Unauthenticated | Downloaded 11/21/25 11:34 AM UTC

institutions. The French Network PermaFRANCE is financially supported by the Grenoble Observatory for Sciences of the Universe and the French Research Infrastructure Critical Zone Observatories: Research and Application (OZCAR). The Chinese Permafrost Monitoring Network is financially supported by the Chinese National Science Foundation (41931180) and Cryosphere Research Station on Qinghai–Xizang Plateau, Chinese Academy of Sciences (CAS).

c2 Rock Glacier Velocity

Rock glacier monitoring at Hinteres Langtalkar and Dösen rock glaciers (AT) is supported by the Hohe Tauern National Park Carinthia through its long-term permafrost monitoring program. Laurichard (FR) survey is supported by "Observation and Experimentation System for Environmental Research" (SOERE/All'envi-OZCAR Research Infrastructure) and the PermaFrance observatory "Monitoring the mountain permafrost in the French Alps" as well as French National Research Agency in the framework of the Investments for the Future programs: Risk@UGA (ANR-15-IDEX-02) and LabEx OSUG@2020 (ANR10 LABX56). The Ecrins National Park has been supporting field surveys since the early 2000s. PERMOS is financially supported by MeteoSwiss in the framework of GCOS Switzerland, the Federal Office for the Environment, and the Swiss Academy of Sciences. PERMOS acknowledges the important contribution of the partner institutions and principal investigators. The time series for Central Asian rock glaciers was compiled within the ESA Permafrost Climate Change Initiative (Permafrost_CCI) project (4000123681/18/I-NB). The time series for the Dry Andes was supported by the Center for Advanced Studies in Arid Zones (CEAZA) and the Leading House for the Latin American Region (University of St. Gallen), grant number MOB1829.

c3 Alpine Glaciers

The World Glacier Monitoring Service mass balance dataset is the primary data used in the section.

c4 Lake Ice Cover

We thank Al and Sue Stangel, Alexander Mills, Ann LaLiberte, Beth Kohlman, B.J. Bauer, Bob Katzenberger, Bonny Pederson, Brendan Wiltse, Brian D. Neill, Brian Vlach, John Barten, Rick Brascke, Calvin Maurer, Carl C. Nelson, Carol Wendorf, Cheryl and Dorothy Zingler, Clare and Dan Shirley, Craig Hillman, Dale Robertson, Dan Brumm, Daniel L. Anderson, Dave and Lynda J. Urshan, David Kahan, Don Pierson, Don McClanathan, Donald and Mureil Fornasiere, Doug Fitzgerald, Douglas Pierzina, Dr. Neal D. Mundahl, Duane Williams and Edie Evarts, Duncan A. Brown, Earl Cook, Fred Buckley, Gary Teigen, Gay Alberts Ruby, Gene Cooper, George Grevich, Greg Sass, Holly Waterfield, Huaxia Yao, James and Sharon Fenner, James W. Danielson, Jan Henning L'Abée-Lund, Jeff Goelzer, Jeffrey G. Lowe, Jerry Evans, Jerry Sondreal, Jim and Judy Daugherty, Joe Jenkins, Joel Rasmussen, John and Catherine Bart, John Maier, Jonathan Ross, Dan Drumm, Martin Kainz, Joy Krubsack, Kay and Rich Rezanka, Kay Olson, Kay Wepfer, Kay Wepfer, Ken Blumenfeld, Larry and Marlene Lotto, Larry Peterson, Lars Rudstam, Lolita Olson, Lowell Dague, Marge Kellor, Mark Biller, Mark Holland, Mark J. and Rosie Peters, Mary Jane Dillingham, Mary Lou Fry, Randell Fry, Merja Pulkkanen, Michael Allen, Michael Bradley, Michael Kolecheck, Michael Traufler, Mickey and Dennis Chick, Mike, Jeff, and Thomm Backus, Molly Hibbard, Morris and Doris Whiting, Mr. and Mrs. Jay R. Mackie, Mr. and Mrs. William Bergersen, Mrs. Gale Wheeler, Mrs. Kathy Elhard, Mrs. Margery Armstrong, Myron Hagelstrom, Nancy Putnam, Nancy Steenport, Patricia Bebak, Patrick Collins, Paulette Janssen, Pete Boulay, Peter Bearup, Rachel Dahlke, Raymond (Joe) Jenkins, Richard L. Tamke, Rock Anderson, Ron Pabich, Ronald Jones, Ross Swain, Sally Ketchen, Sandra Anderson, Scott Schoepp, Sogee Spinner, Sharon Natzel, Shin-Ichiro Matsuzaki, Susan Reineking, Susan Verhaalen, Tana McNutt, Theodore (Ted) Peters, Thomas Sommerfeldt, Tom Stangl, Travis Campbell, Virgil Luehrs, Walt and Nancy Quillinan, Walter R. Brown, Water Dahlke III, William and Brenda Jones, and William Hanson for their dedication and efforts to collect and share in situ ice phenological records with us. A part of this research was enabled by an intern, Jessica Ollinik, from the Canadian Institute of Ecology and Evolution's Living Data Project, which is funded by the Government of Canada through a Natural Sciences and Engineering Research Council of Canada (NSERC) Collaborative Research and Training Experience (CREATE) grant.

Unauthenticated | Downloaded 11/21/25 11:34 AM UTC

c5 Northern Hemisphere Continental Snow Cover Extent

This work is funded in part by NOAA's Climate Data Record (CDR) Program at the National Centers for Environmental Information.

d1 Surface Humidity

Kate Willett was supported by the Met Office Hadley Centre Climate Programme funded by DSIT.

d2 Humid-Heat extremes

Kate Willett was supported by the U.K.–China Research & Innovation Partnership Fund through the Met Office Climate Science for Service Partnership (CSSP) China under the International Science Partnerships Fund (ISPF). Kate Willett was also supported by the Met Office Hadley Centre Climate Programme funded by DSIT.

Cassandra Rogers was supported by the Australian Climate Service.

Thank you to Mitchell Black and Ulrike Bende-Michl from the Bureau of Meteorology for providing initial reviews of this section.

d6 Precipitation Extremes

The National Center for Atmospheric Research is sponsored by the National Science Foundation under Cooperative Agreement No. 1852977. Stephen Blenkinsop was supported by the UK NERC funded grant no. NE/Y503241/1.

d7 Cloudiness

Clouds and the Earth's Radiant Energy System (CERES) Energy Balanced and Filled (EBAF) data were obtained from the NASA Langley Research Center CERES ordering tool at https://ceres.larc.nasa.gov/data/.

d9 River Discharge

The Global Flood Awareness System (GloFAS) is part of the Copernicus Emergency Management Service, which is funded by the European Union Space Program.

d10 Groundwater and Terrestrial Water Storage

This work was supported by NASA's Gravity Recovery and Climate Experiment Follow-On (GRACE-FO) Science Team.

d11 Soil Moisture

This study uses satellite soil moisture observations from the C3S's Climate Data Store (CDS; 2025): Soil moisture gridded data from 1978 to present. Accessed on 11 February 2025, 10.24381/cds.d7782f18

d12 Monitoring Drought using the Self-Calibrating Palmer Drought Severity Index

Jonathan Barichivich was supported by the European Research Council (ERC) under the Horizon Europe research and innovation programme (ERC-starting grant CATES, grant agreement No. 101043214). Tim Osborn received funding from the U.K. NERC (NE/S015582/1). Ian Harris and Amee Gollop received funding from U.K. National Centre for Atmospheric Science (NCAS). The research presented in the drought section was carried out on the High-Performance Computing Cluster supported by the Research and Specialist Computing Support service at the University of East Anglia.

d13 Land Evaporation

D.G.M. acknowledges support from the European Research Council (ERC) under grant agreement no. 101088405 (HEAT). H.E.B. is supported by the King Abdullah University of Science and Technology (KAUST).

e1 Mean Sea Level Pressure and Related Modes of Variability

David Fereday was supported by the Met Office Hadley Centre Climate Programme funded by DSIT.

Unauthenticated | Downloaded 11/21/25 11:34 AM UTC

e2 Surface Winds

C.A.M. was supported by the Spanish National Research Council (CSIC), University of Valencia (UV), Generalitat Valenciana (GVA) and funded by PROMETEO Grant CIPROM/2023/38, International Global Change Laboratory (LINCGLOBAL)-CSIC ref. LINCG24042, and the Interdisciplinary Thematic Platform for Climate and Climate Services (PTI-CLIMA). R.J.H.D. was supported by the Met Office Hadley Centre Climate Programme funded by DSIT. L.R. was supported by NASA Ocean Vector Wind Science Team grant 80NSSC23K0984. Z.Z. was supported by the National Natural Science Foundation of China grant 42071022.

e4 Lightning

The work of M.F. was sponsored by the Royal Society (U.K.) grant NMG/R1/180252 and NERC (U.K.) under grants NE/L012669/1 and NE/H024921/1.

E.W. is supported for studies on global circuit response to climate change from the Physical and Dynamic Meteorology Program at the NSF on grant no. 6942679.

C.P. was supported in his lightning research by the Israel Science Foundation (ISF) grant 2701/17, and the Ministry of Energy grant no. 220-17-002. S.G. was supported by NASA Grant 80NSSC21K0923 and NASA Contract 80GSFC20C044. The authors wish to thank Peter Thorne at Maynooth University in Ireland and at the ECMWF for suggesting and initiating this work and for recommending that lightning be made an essential climate variable. The Meteosat Third Generation Lightning Imager (MTG-LI) data used to generate the Figures are available from https://user.eumetsat.int/resources/user-guides/mtg-data-access-guide.

f1 Earth Radiation Budget at Top-of-Atmosphere

This research has been supported by the NASA CERES project. The resources of the NASA Langley Atmospheric Sciences Data Center are utilized to process the instantaneous Single Scanner Footprint (SSF) data used as input to EBAF Ed4.2.1 and processes the Fast Longwave and Shortwave Radiative Fluxes (FLASHFlux) Time Interpolated and Spatially Averaged (TISA) version 4C. We further acknowledge the efforts of Walt Miller and Pam Mlynczak of the CERES team, who monitor CERES data production and produce the FLASHFlux TISA version 4C monthly averaged data products, respectively.

f2 Mauna Loa Clear-Sky Atmospheric Solar Transmission

Key balloon data from Hilo used in this 2024 update of the Mauna Loa apparent atmospheric transmission would not have been possible without the generous cooperation afforded by Global Monitoring Laboratory (GML) staff, Matthew Martinsen, Darryl Kuniyuki, and David Nardini, at the Mauna Loa Observatory.

g1 Long-Lived Greenhouse Gases

This research was supported in part by NOAA cooperative agreement NA22OAR4320151, for the Cooperative Institute for Earth System Research and Data Science (CIESRDS).

g2 Ozone-Depleting Gases

This research was supported in part by NOAA cooperative agreement NA22OAR4320151, for the Cooperative Institute for Earth System Research and Data Science (CIESRDS).

g3 Tropospheric Aerosols

This research has been supported by the Copernicus Atmospheric Monitoring Service (CAMS) program managed by ECMWF (Framework Agreement ECMWF/Copernicus/2021/CAMS2_35_HYGEOS) on behalf of the European Commission. A large number of observational datasets are used in the CAMS reanalysis; the authors would like to thank all the actors that created and made public the remote sensing products assimilated in the CAMS Reanalysis: NASA, NOAA, the European Organisation for the Exploitation of Meteorological Satellites (EUMETSAT), and the ESA.

Unauthenticated | Downloaded 11/21/25 11:34 AM UTC

g4 Tropospheric Ozone

The NOAA Proving Ground and Risk Reduction (PGRR) Program supported the contributions by O. R. Cooper and K.-L. Chang. K.-L. Chang was also supported by NOAA cooperative agreement NA22OAR4320151. P. Effertz was supported by NOAA cooperative agreement NA22OAR4320151. Funding for J. Ziemke for this research was provided in part by NASA NNH14ZDA001N-DSCOVR, NASA Suomi National Polar-orbiting Partnership (SNPP) and Joint Polar Satellite System (JPSS) Satellites Standard Products for Earth System Data Records, and Code 614 programmatic support for long-term ozone trends.

g5 Stratospheric Aerosols

Lidar observations at the Haute-Provence Observatory (OHP) are funded by the French National Centre for Scientific Research/National Institute of Sciences of the Universe (CNRS/INSU) and the National Centre for Space Studies (CNES). S. Khaykin's work is supported by National Agency for Research (ANR) PyroStrat 21-CE01- 335 0007-01 project. We thank Christine David, Alain Hauchecorne, Julien Jumelet, Philippe Keckhut (Laboratory for Atmospheres, Observations, and Space [LATMOS]) and the lidar station operators for their contributions to long-term monitoring of stratospheric aerosol at OHP. Lidar observation at Lauder are funded in part by the Greenhouse gases Observing SATellite (GOSAT) project. We thank Richard Querel (National Institute of Water and Atmospheric Research [NIWA]), Osamu Uchino, Tomohiro Nagai (Meteorological Research Institute [MRI]) and Yushitaka Jin (MRI) for their contributions to long-term monitoring of stratospheric aerosol at Lauder. G. Taha's work is supported by the NASA Earth Science Division grant 80NSSC23K1037.

g6 Stratospheric Ozone

Carlo Arosio, Melanie Coldewey-Egbers, Diego Loyola, Viktoria Sofieva, Alexei Rozanov, and Mark Weber are grateful to the E.U. C3S, C3S2_312a_Lot2 Ozone, and to the ESA's Climate Change Initiative Ozone (CCI+) projects for supporting the generation and extension of the Global Ozone Monitoring Experiment-type Total Ozone Essential Climate Variable (GTO-ECV) total ozone and Stratospheric Aerosol and Gas Experiment (SAGE) CCI Ozone Mapping and Profiler Suite (OMPS) data records. Carlo Arosio, Viktoria Sofieva, Kleareti Tourpali, Alexei Rozanov, and Mark Weber are grateful for the support of the ESA project Ozone Recovery from Merged Observational Data and Model Analysis (OREGANO). The OSIRIS Team is grateful for the support of the Canadian Space Agency since 1993. The NASA Long Term Measurement of Ozone program WBS 479717 supports Stacey M. Frith. Lucien Froidevaux's contribution, with the assistance of Ryan Fuller, was performed at the California Institute of Technology's Jet Propulsion Laboratory (JPL), under contract with NASA. Jeannette Wild was supported by NOAA grant NA19NES4320002 (Cooperative Institute for Satellite Earth System Studies [CISESS]) at the University of Maryland's Earth System Science Interdisciplinary Center (ESSIC). Melanie Coldewey-Egbers and Diego Loyola acknowledge the partial support by the German Aerospace Center (DLR) projects "Methods for analyzing and assessing changes in the atmosphere and the climate system" (MABAK) and INPULS.

g7 Stratospheric Water Vapor

We would like to acknowledge assistance with water vapor sonde launches from NOAA GML staff in Boulder, Colorado, and Hilo, Hawaii, and international collaborators in San Jose, Costa Rica, and Lauder, New Zealand. This research was supported by the NASA Upper Atmosphere Composition Observations (UACO) program.

g8 Carbon Monoxide

CAMS is funded by the E.U.

h2 Terrestrial Vegetation Dynamics

The authors thank the providers of the remote sensing dataset needed to perform this analysis and the Joint Research Centre's (JRC) Big Data Analytics Platform (BDAP) (https://doi.org/10.5281/zenodo.10214201).

Unauthenticated | Downloaded 11/21/25 11:34 AM UTC

h4 Phenology

Deborah Hemming and Rebecca Holliday acknowledge support from the Met Office Hadley Centre Climate Programme funded by DSIT. Andrew Richardson acknowledges support from the NSF LTER (award 1832210); John O'Keefe and Greta VanScoy also acknowledge support from the NSF through the LTER (award 1832210) program. Nature's Calendar (Woodland Trust) in the U.K. thanks all its volunteer recorders and support from players of People's Postcode Lottery. Theresa Crimmins and the USA National Phenology Network (NPN) acknowledge support from the NSF through the Division of Biological Infrastructure (award 2404760), the U.S. Fish and Wildlife Service (agreements F16AC01075 and F19AC00168), and the U.S. Geological Survey (G14AC00405 and G18AC00135). The USA NPN thanks the many participants contributing phenology observations to Nature's Notebook. De Natuurkalender (Nature's Calendar) program in the Netherlands thanks all the volunteers and school children in the Global Learning and Observations to Benefit the Environment (GLOBE) program for their many observations. The Slovak Hydrometeorological Institute thanks all its volunteer observers for participating in the phenological observation program. Orlane Anneville acknowledges support from the National Institute of Agricultural Research (INRAE). Stephen Thackeray thanks Werner Eckert, Heidrun Feuchtmayr, Alba Alemany, Shin-Ichiro Matsuzaki, Ryuichiro Shinohara, Jan-Erik Thrane, Linda May, and all field and lab workers associated with the provision of the lake chlorophyll-*a* data. We acknowledge funding from Vassdragsforbundet for Mjøsa med tilløpselver (https://www.vassdragsforbundet.no/om-oss/). Windermere, Blelham Tarn, Esthwaite Water, and Loch Leven monitoring were supported by NERC award numbers NE/R016429/1 and NE/Y006208/1 as part of the U.K. Status, Change and Projections of the Environment (UK-SCAPE) and U.K. Challenges Programmes delivering National Capability. Data for Lakes Geneva and Bourget were contributed by the Observatory on LAkes (OLA), © Observation and Experimentation System for Environmental Research (SOERE) OLA-IS, AnaEE-France, INRAE of Thonon-les-Bains, International Commission for the Protection of the Waters of Lake Geneva (CIPEL), Intercommunity Committee for the Sanitation of Lake Bourget (CISALB).

h5 Vegetation Optical Depth

R. M. Zotta and W. Dorigo acknowledge the TU Wien Wissenschaftspreis 2015, a personal grant awarded to W. Dorigo. We also acknowledge support from the ESA CCI and the C3S.

Sidebar 2.1 Super Extreme Land Surface Temperature Hotspots

This study has been funded through the ESA within the framework of the Land Surface Temperature project under the CCI (LST_cci), contract number 4000123553/18/I-NB, and was supported by NERC [NERC grant reference number NE/X019071/1, "U.K. EO Climate Information Service"] and the U.K.–China Research & Innovation Partnership Fund through the Met Office Climate Science for Service Partnership (CSSP) China under the International Science Partnerships Fund (ISPF). The authors are grateful to the ESA for creating the CCI program, which has strengthened the consistency of the many research communities related to developing, processing, qualifying, and using satellite CDRs.

Unauthenticated | Downloaded 11/21/25 11:34 AM UTC

Appendix 1: Acronyms

4D-VAR	four-dimensional variational assimilation
AAO	Antarctic Oscillation
AATSR	Advanced Along-Track Scanning Radiometer
ACE-FTS	Atmospheric Chemistry Experiment—Fourier Transform Spectrometer
AIRS	Atmospheric Infrared Sounder
ALT	active-layer thickness
AMSR2	Advanced Microwave Scanning Radiometer 2
AMSR-E	Advanced Microwave Scanning Radiometer for the Earth Observing System
ANR	National Agency for Research
ANT_EAST	East Antarctic
ANT_PEN	Antarctic Peninsula
ANT_SVL	Antarctic: southern Victoria Land
ANY	Australian New Year
AOD	aerosol optical depth
AOD550	aerosol optical depth at 550 nm
ASCAT	Advanced Scatterometer
ASR	absorbed solar radiation
AT	Austria
BAR_WS	Barents Sea region—West Siberia
BCS	Beaufort Chukchi Sea—Arctic Alaska and Mackenzie Delta region
BD	Brewer–Dobson
BDAP	Big Data Analytics Platform
C3S	Copernicus Climate Change Service
Ca	Calbuco
CALM	Circumpolar Active Layer Monitoring
CAMS	Copernicus Atmosphere Monitoring Service
CAMSRA	Copernicus Atmosphere Monitoring Service reanalysis
CAN	Canada
CAS	Chinese Academy of Sciences
CCI+	Climate Change Initiative Ozone
CCM	chemistry climate model
CCMI	Chemistry-Climate Model Initiative
CDR	Climate Data Record
CEAZA	Center for Advanced Studies in Arid Zones
CENT_SIB	Central Siberia
CERES	Clouds and the Earth's Radiant Energy System
CFC	chlorofluorocarbon
CG	cloud-to-ground
CH	Switzerland
CH_3CCl_3	methyl chloroform
CH_4	methane
CI	confidence interval
CIESRDS	Cooperative Institute for Earth System Research and Data Science
CIPEL	International Commission for the Protection of the Waters of Lake Geneva
CISALB	Intercommunity Committee for the Sanitation of Lake Bourget
CISESS	Cooperative Institute for Satellite Earth System Studies
CLASSnmat	Climate Linked Atlantic Sector Science Night Marine Air Temperature
CNES	National Centre for Space Studies
CNRS	French National Centre for Scientific Research

Unauthenticated | Downloaded 11/21/25 11:34 AM UTC

CO	carbon monoxide
CO_2	carbon dioxide
COGL	center of gravity
COSMIC	Constellation Observing System for Meteorology, Ionosphere, and Climate
COVID-19	Coronavirus disease 2019
C_p	specific heat capacity of air
CPT	cold-point tropopause
CREATE	Collaborative Research and Training Experience
CrIS	Cross-Track Infrared Sounder
CRU TS	Climatic Research Unit terrestrial series
CRUTEM5	Climatic Research Unit temperature version 5
CSIC	Spanish National Research Council
CSSP	Climate Science for Service Partnership
D	Germany
DE	Germany
DLR	German Aerospace Center
DOE	U.S. Department of Energy
DOML	day of maximum concentration
DU	Dobson unit
EAST_SIB	East Siberia
EBAF	Energy Balanced and Filled
EC	El Chichón
ECMWF	European Center for Medium-Range Weather Forecasts
ECOSTRESS	Ecosystem Spaceborne Thermal Radiometer Experiment on Space Station
EESC	equivalent effective stratospheric chlorine
EESC[A]	equivalent effective stratospheric chlorine calculated for air representative of the Antarctic
EESC[ML]	equivalent effective stratospheric chlorine calculated for air representative of the midlatitude stratosphere
ENSO	El Niño–Southern Oscillation
EOCIS	Earth Observation Climate Information Service
EOS	end of season
ER	extinction ratio
ERB	Earth radiation budget
ERC	European Research Council
ERF	effective radiative forcing
ESA	European Space Agency
ESSIC	Earth System Science Interdisciplinary Center
ET	evapotranspiration
EUMETSAT	European Organisation for the Exploitation of Meteorological Satellites
EUR	Europe
FAPAR	fraction of absorbed photosynthetically active radiation
FBD	full bloom date
FF	fossil fuel
FLASHFlux	Fast Longwave and Shortwave Radiative Fluxes
FOC	Fisheries and Oceans Canada
FP	frost point
FR	France
GCOS	Global Climate Observing System
GEOS-CF	Goddard Earth Observing System Composition Forecast Modeling System
GFAS	Global Fire Assimilation System
GFED4S	Global Fire Emissions Database version 4.1

Unauthenticated | Downloaded 11/21/25 11:34 AM UTC

GHCN	Global Historical Climatology Network
GHCNDEX	Global Historical Climatology Network Daily Extremes
GHCNh	Global Historical Climatology Network hourly
GHG	greenhouse gas
GISS	Goddard Institute for Space Studies
GISTEMP	Goddard Institute for Space Studies Surface Temperature Analysis
GLEAM4	Global Land Evaporation Amsterdam Model version 4
GLM	Geostationary Lightning Mapper
GLOBE	Global Learning and Observations to Benefit the Environment
GloFASv4	Global Flood Awareness System version 4
GloSSAC	Global Space-based Stratospheric Aerosol Climatology
GMI	Global Precipitation Measurement Microwave Imager
GMST	global mean surface temperature
GNSS	Global Navigation Satellite System
GNSS-RO	Global Navigation Satellite System Radio Occultation
GO	ground observation
GOES	Geostationary Operational Environmental Satellite
GOSAT	Greenhouse gases Observing SATellite
GOZCARDS	Global Ozone Chemistry and Related Trace Gas Data records for the Stratosphere
GPCC	Global Precipitation Climatology Centre
GPCP	Global Precipitation Climatology Project
GRACE	Gravity Recovery and Climate Experiment
GRACE-FO	Gravity Recovery and Climate Experiment Follow-On
GREALM	Global Reservoirs and Lakes Monitor
GSL	Global Snow Lab
Gt	gigaton
GTO-ECV	Global Ozone Monitoring Experiment-type Total Ozone Essential Climate Variable
GVA	Generalitat Valenciana
HadCRUT5	Met Office Hadley Centre/Climatic Research Unit Temperature version 5
HadEX3	Met Office Hadley Centre Extremes Dataset version 3
HadISD3	Met Office Hadley Centre Integrated Surface Dataset 3
HadISDH	Met Office Hadley Centre Integrated Surface Dataset of Humidity
HadISDH.blend	Met Office Hadley Centre Integrated Surface Dataset of Humidity over Land and Ocean
HadISDH.extremes	Met Office Hadley Centre Integrated Surface Dataset of Humidity Extremes
HadISDH.land	Met Office Hadley Centre Integrated Surface Dataset of Humidity over Land
HadISDH.marine	Met Office Hadley Centre Integrated Surface Dataset of Humidity over Ocean
HadSST4	Met Office Hadley Centre Sea Surface Temperature Dataset version 4
HCFC	hydrochlorofluorocarbon
HFC	hydrofluorocarbon
HIRS	High-resolution Infrared Radiation Sounder
HNO_3	nitric acid
Hu	Hunga
HYSPLIT	Hybrid Single-Particle Lagrangian Integrated Trajectory
IAK_CMV	Interior Alaska and central Mackenzie Valley, Northwest Territories
IC	in-cloud
ICESat-2	Ice, Cloud, and land Elevation Satellite 2
INRAE	National Institute of Agricultural Research
INSU	National Institute of Sciences of the Universe
IOD	Indian Ocean dipole
IR	infrared
ISF	Israel Science Foundation
ISPF	International Science Partnerships Fund

Unauthenticated | Downloaded 11/21/25 11:34 AM UTC

ISS	International Space Station
IT	Italy
ITCZ	Intertropical Convergence Zone
JMA	Japanese Meteorological Agency
JPSS	Joint Polar Satellite System
JRA-3Q	Japanese Reanalysis for Three Quarters of a Century
JRA-55	Japanese 55-year Reanalysis
JRC	Joint Research Centre
K	Kelvin
Ka	Kasatochi
KAUST	King Abdullah University of Science and Technology
KOMPSAT-5	Korea Multi-Purpose Satellite-5
L	latent heat of vaporization
LATMOS	Laboratory for Atmospheres, Observations, and Space
LEO	Office of Low Earth Orbit
LI	Lightning Imager
LINCGLOBAL	International Global Change Laboratory
LiO3s	Stratospheric Ozone Lidar at Haute-Provence Observatory
LLGHG	long-lived greenhouse gases
LLNL	Lawrence Livermore National Laboratory
LOWESS	locally weighted scatterplot smoothing
LS	lower stratosphere
LST	land surface temperature
LST_cci	Climate Change Initiative for Land Surface Temperature
LSWT	lake surface water temperature
LTA	Lidar Temperature Aerosol
LTT	lower-tropospheric temperature
LWCRE	longwave cloud radiative effect
MABAK	Methods for analyzing and assessing changes in the atmosphere and the climate system
MACCity	Monitoring Atmospheric Composition and Climate and CityZen
MCM	million cubic meters
MEGAN	Model of Emissions of Gases and Aerosols from Nature
MERIS	Medium Resolution Imaging Spectrometer
MetOp	Meteorological Operational satellite
MLO	Mauna Loa Observatory
MLS	Microwave Limb Sounder
MNT_FRA	French Alps
MNT_IT	Italian Alps
MNT_NOR	Norwegian mountains
MNT_QTP	Qinghai–Tibet Plateau
MNT_SWI	Swiss Alps
MODIS	Moderate Resolution Imaging Spectroradiometer
MOPITT	Measurement of Pollution in the Troposphere
MRI	Meteorological Research Institute
MSLP	mean sea-level pressure
MSU	Microwave Sounding Unit
MSWEP	Multi-Source Weighted-Ensemble Precipitation
MTG	Meteosat Third Generation
MWR	Microwave Radiometer
N_2O	nitrous oxide
Na	Nabro
NA	North America

Unauthenticated | Downloaded 11/21/25 11:34 AM UTC

NAO	North Atlantic Oscillation
NCAS	National Centre for Atmospheric Science
NCEP	National Centers for Environmental Prediction
NDACC	Network for the Detection for Stratospheric Change
NERC	Natural Environmental Research Council
NH	Northern Hemisphere
NH_3	ammonia
NH_4NO_3	ammonium nitrate
NIWA	National Institute of Water and Atmospheric Research
NL	The Netherlands
NMAT	night marine air temperature
NO	Norway
NO_2	nitrogen dioxide
NOAAGlobalTemp	NOAA Merged Land Ocean Global Surface Temperature Analysis
NOx	nitrogen oxides
NRT	near-real-time
NSERC	Natural Sciences and Engineering Research Council of Canada
NSF	National Science Foundation
NTL-LTER	North Temperate Lakes Long-Term Ecological Research
ODGI	Ozone Depleting Gas Index
ODS	ozone-depleting substance
OH	hydroxyl radical
OHP	Haute-Provence Observatory
OLA	Observatory of alpine LAkes
OLCI	Ocean and Land Colour Instrument
OLR	outgoing longwave radiation
OLS	ordinary least-squares
OMI	Ozone Monitoring Instrument
OMPS	Ozone Mapping and Profiler Suite
OMPS-LP	Ozone Mapping and Profiler Suite Limb Profiler
OMPS-NP	Ozone Mapping and Profiler Suite Nadir Profile
ONI	Oceanic Niño Index
OSIRIS-REx	Origins, Spectral Interpretation, Resource Identification, and Security—Regolith Explorer
OZCAR	Critical Zone Observatories: Research and Application
PAN	Peroxyacetyl nitrate
PANs	Acyl peroxynitrates
PC	PhenoCam
PDO	Pacific Decadal Oscillation
Permafrost_CCI	Permafrost Climate Change Initiative
PERMOS	Swiss Permafrost Monitoring Network
PGRR	Proving Ground and Risk Reduction
Pi	Pinatubo
PM2.5	particulate matter
PNA	Pacific–North American
PNE	Pacific Northwest Event
POPS	Portable Optical Particle Spectrometer
PSA	Pacific–South American
PTI-CLIMA	Interdisciplinary Thematic Platform for Climate and Climate Services
pyroCb	pyrocumulonimbus
q	specific humidity
QBO	quasi-biennial oscillation
QTP	Qinghai–Tibet Plateau

Unauthenticated | Downloaded 11/21/25 11:34 AM UTC

QuickSCAT	Quick Scatterometer
Ra	Raikoke
RATPAC	Radiosonde Atmospheric Temperature Products for Assessing Climate
RCP	Representation Concentration Pathways
RFaci	aerosol–cloud interactions
RFari	aerosol–radiation interactions
RGMA	Regional and Global Model Analysis Program
RGV	rock glacier velocity
RH	relative humidity
RSS	Remote Sensing Systems
RSW	reflected shortwave
Ru	Ruang
Rx1day	one-day maxima
Rx5day	accumulated five-day maxima
Sa	Sarychev
SAGE III	Stratospheric Aerosol and Gas Experiment III
SAM	Southern Annular Mode
sAOD	stratospheric aerosol optical depth
SAT	surface high temperature
SBUV	Solar Backscatter Ultraviolet Radiometer
SCE	snow cover extent
SCIAMACHY	Scanning Imaging Absorption Spectrometer for Atmospheric Chartography
scPDSI	self-calibrating Palmer Drought Severity Index
SeaWiFS	Sea-Viewing Wide Field-of-View Sensor
SEH	super extreme hotspot
Sh	Shiveluch
SH	Southern Hemisphere
SIOS	Svalbard Integrated Earth Observing System
SI-x	Spring Index
SJ	Svalbard
SK	Slovakia
SLCF	short-lived climate forcer
SLSTR/A	Sea and Land Surface Temperature Radiometer onboard the Sentinel-3A platform
SLSTR/B	Sea and Land Surface Temperature Radiometer onboard the Sentinel-3B platform
SNPP	Suomi National Polar-orbiting Partnership
SO_2	sulfur dioxide
SOERE	Observation and Experimentation System for Environmental Research
SOI	Southern Oscillation Index
SOS	start of season
SSF	Single Scanner Footprint
SSM/I	Special Sensor Microwave/Imager
SSMIS	Special Sensor Microwave Imager/Sounder
SST	sea surface temperature
SSU	Stratospheric Sounding Unit
SSW	sudden stratospheric warming
STP	standard temperature and pressure
SW	shortwave
SWCRE	shortwave cloud radiative effect
SWOOSH	Stratospheric Water and OzOne Satellite Homogenized
SWOT	Surface Water and Ocean Topography
T	dry-bulb air temperature
T12	water vapor channel

Unauthenticated | Downloaded 11/21/25 11:34 AM UTC

T2	upper-tropospheric temperature
T2m	near-surface air temperature at ~1.5 m^{-2} m above the surface
TCWV	total column water vapor
TDX	TerraSAR-X add-on for Digital Elevation Measurement
Teq	equivalent temperature
TISA	Time Interpolated and Spatially Averaged
TLS	Lower-stratosphere temperatures
TMI	Tropical Rainfall Measuring Mission Microwave Imager
TOA	top-of-atmosphere
TOB	tropospheric ozone burden
Tq	latent temperature
TRISHNA	Thermal Infrared Imaging Satellite for High-resolution Natural Resource Assessment
TRMM	Tropical Rainfall Measuring Mission
TROPOMI	Tropospheric Monitoring Instrument
TSI	total solar irradiance
TSX	TerraSAR-X
TTT	tropical tropospheric temperatures
T_w	wet-bulb temperature
T_wN	minimum humid-heat intensity
TWS	terrestrial water storage
T_wX	humid-heat intensity
TXx	highest annual maximum temperature
U.K.	United Kingdom
U.S.	United States
UACO	Upper Atmosphere Composition Observations
UAHNMAT	University of Alabama in Huntsville Night Marine Air Temperature
UFS	Unified Forecast System
UGLOS	Upper Great Lakes Observing System
UK-SCAPE	United Kingdom Status, Change and Projections of the Environment
UNIS	University Centre in Svalbard
USA NPN	USA National Phenology Network
UT	upper troposphere
UTH	upper tropospheric humidity
UV	University of Valencia
VIIRS	Visible Infrared Imaging Radiometer Suite
VOC	volatile organic compound
VOD	vegetation optical depth
VODCA	Vegetation Optical Depth Climate Archive
VWC	vegetation water content
w.e.	water equivalent
WGMS	World Glacier Monitoring Service
WMO	World Meteorological Organization
WOUDC	World Ozone and Ultraviolet Radiation Data Centre
WV	water vapor
YM	yearly mean

Unauthenticated | Downloaded 11/21/25 11:34 AM UTC

Appendix 2: Datasets and sources

Section 2b Temperature

Sub-section	General Variable or Phenomenon	Specific Dataset or Variable	Source
2b1	Temperature, [Near] Surface	Berkeley Earth	https://berkeleyearth.org/data/
2b1, 2b4, 2b7	Temperature, [Near] Surface	ERA5	https://www.ecmwf.int/en/forecasts/dataset/ecmwf-reanalysis-v5
2b1	Temperature, [Near] Surface	HadCRUT5	https://www.metoffice.gov.uk/hadobs/hadcrut5/
2b1	Temperature, [Near] Surface	Climatic Research Unit Temperature Version 5 (CRUTEM5)	https://www.metoffice.gov.uk/hadobs/crutem5/
2b1, 2b3	Temperature, [Near] Surface	Met Office Hadley Centre Sea Surface Temperature Dataset (HadSST) Version 4	https://www.metoffice.gov.uk/hadobs/hadsst4/
2b1, 2b4, 2b7	Temperature, [Near] Surface	Japanese Reanalysis for Three Quarters of a Century (JRA-3Q)	https://search.diasjp.net/en/dataset/JRA3Q
2b1, 2b2	Temperature, [Near] Surface	NASA/Goddard Institute for Space Studies (GISS) Global Temperature Version 4	https://data.giss.nasa.gov/gistemp/
2b1	Temperature, [Near] Surface	NOAA/NCEI NOAAGlobalTemp	https://www.ncei.noaa.gov/products/land-based-station/noaa-global-temp
2b2	Lake Temperature	Full Lake Surface Temperature Water Dataset	https://cds.climate.copernicus.eu/datasets/satellite-lake-water-temperature
2b2	Lake Temperature	National Buoy Data Center Great Lakes Buoys	https://www.ndbc.noaa.gov/mobile/region.php?reg=great_lakes
2b2	Lake Temperature	Balaton Lakes	https://odp.met.hu/climate/observations_hungary/hourly/historical/
2b2	Lake Temperature	Canadian Lakes	https://www.meds-sdmm.dfo-mpo.gc.ca/isdm-gdsi/waves-vagues/data-donnees/index-eng.asp
2b2	Lake Temperature	Biel and Thun Lakes (Switzerland); Biwa and Mikata Lakes (Japan)	https://portal.gemstat.org/applications/public.html?publicuser=PublicUser
2b2	Lake Temperature	Trout Lake	https://portal.edirepository.org/nis/metadataviewer?packageid=knb-lter-ntl.116.10
2b2	Lake Temperature	European Space Agency (ESA) Climate Change Initiative (CCI) LAKES Lake Surface Water Temperature (LSWT) Version 2.0.2	https://catalogue.ceda.ac.uk/uuid/a07deacaffb8453e93d57ee214676304

Unauthenticated | Downloaded 11/21/25 11:34 AM UTC

Sub-section	General Variable or Phenomenon	Specific Dataset or Variable	Source
2b3	Nighttime Marine Air Temperature	Climate Linked Atlantic Sector Science Night Marine Air Temperature (CLASSnmat)	https://catalogue.ceda.ac.uk/uuid/5bbf48b128bd488dbb10a56111feb36a
2b3	Nighttime Marine Air Temperature	University of Alabama in Huntsville Night Marine Air Temperature (UAHNMAT) Version 1	https://www.nsstc.uah.edu/climate/; https://doi.org/10.1002/joc.6354
2b4	Temperature, [Near] Surface	MERRA-2	https://gmao.gsfc.nasa.gov/gmao-products/merra-2/
2b4	Temperature, [Near] Surface	Global Historical Climatology Network Daily Extremes (GHCNDEX)	https://www.climdex.org/
2b5	Temperature, Upper Atmosphere	ERA5	https://www.ecmwf.int/en/forecasts/dataset/ecmwf-reanalysis-v5
2b5	Temperature, Upper Atmosphere	MERRA-2	https://gmao.gsfc.nasa.gov/gmao-products/merra-2/
2b5	Temperature, Upper Atmosphere	JRA-3Q	https://search.diasjp.net/en/dataset/JRA3Q
2b5	Temperature, Upper Atmosphere	NOAA National Environmental Satellite, Data, and Information Service (NESDIS) Center for Satellite Applications and Research (STAR) Microwave Sounding Unit (MSU) Version 5	https://www.star.nesdis.noaa.gov/data/mscat/MSU_AMSU_v5.0/Monthly_Atmospheric_Layer_Mean_Temperature/
2b5	Temperature, Upper Atmosphere	Radiosone Observation Correction Using Reanalyses (RAOBCORE) Radiosonde Innovation Composite Homogenization (RICH) Version 1.9	https://webdata.wolke.img.univie.ac.at/haimberger/v1.9/
2b5	Temperature, Upper Atmosphere	Radiosonde Atmospheric Temperature Products for Assessing Climate (RATPAC) A2	https://www.ncei.noaa.gov/products/weather-balloon/radiosonde-atmospheric-temperature-products
2b5	Temperature, Upper Atmosphere	Remote Sensing Systems (RSS) Version 4.0	https://www.remss.com/measurements/upper-air-temperature/
2b5	Temperature, Upper Atmosphere	University of Alabama in Huntsville (UAH) Microwave Sounding Unit (MSU) Version 6.1	https://www.nsstc.uah.edu/data/msu/v6.1/
2b5	Sea Surface Temperature	Niño 3.4 Index	https://psl.noaa.gov/data/timeseries/month/DS/Nino34_CPC/

Unauthenticated | Downloaded 11/21/25 11:34 AM UTC

Sub-section	General Variable or Phenomenon	Specific Dataset or Variable	Source
2b6	Temperature, Upper Atmosphere	Aura Microwave Limb Sounder (MLS)	https://discnrt1.gesdisc.eosdis.nasa.gov/data/Aura_MLS_NRT/ML2T_NRT.005/
2b7	Equivalent Temperature, [Near] Surface	Met Office Hadley Centre International Surface Dataset of Humidity Over Land (HadISDH.land).4.6.1.2024f	https://www.metoffice.gov.uk/hadobs/hadisdh/
2b7	Equivalent Temperature, [Near] Surface	ERA5	https://www.ecmwf.int/en/forecasts/dataset/ecmwf-reanalysis-v5

Section 2c Cryosphere

Sub-section	General Variable or Phenomenon	Specific Dataset or Variable	Source
2c1	Permafrost	Global Terrestrial Network for Permafrost (GTN-P)	http://gtnpdatabase.org/
2c1	Permafrost	GTN-P Global Mean Annual Ground Temperature Data for Permafrost	https://doi.org/10.1594/PANGAEA.884711
2c1	Permafrost	Permafrost Temperature at Chinese Qinghai–Tibet Plateau (QTP) Sites	https://nsidc.org/data/GGD700/versions/1
2c1	Permafrost	Permafrost Temperature in European Mountains	https://zenodo.org/records/13628540
2c1	Permafrost	Permafrost Temperature at French Sites	https://permafrance.osug.fr
2c1	Permafrost	Permafrost Temperature at Norwegian Sites	https://cryo.met.no/
2c1, 2c2	Permafrost	Permafrost Temperature at Swiss Sites (Swiss Permafrost Monitoring Network [PERMOS])	https://www.permos.ch; https://www.permos.ch/doi/permos-dataset-2022-1
2c1	Active Layer Depth	Circumpolar Active Layer Monitoring (CALM)	https://www.gwu.edu/~calm/
2c2	Rock Glacier Velocity	Regional Rock Glacier Velocity	Available from authors upon request. Austria: V. Kaufmann and A. Kellerer-Pirklbauer, Central Asia: A. Kääb, Dry Andes: S. Vivero, France: X. Bodin, D. Cusicanqui and E. Thibert, Switzerland: R. Delaloye, J. Noetzli and C. Pellet
2c3	Glacier Mass, Area or Volume	World Glacier Monitoring Service	https://dx.doi.org/10.5904/wgms-fog-2022-09

Unauthenticated | Downloaded 11/21/25 11:34 AM UTC

Sub-section	General Variable or Phenomenon	Specific Dataset or Variable	Source
2c4	Lake Ice	ERA5	https://www.ecmwf.int/en/forecasts/dataset/ecmwf-reanalysis-v5
2c4	Lake Ice	Lake Ice Clearance and Formation Data for Green Lakes Valley, 1968—Ongoing. Version 6. Environmental Data Initiative	https://doi.org/10.6073/pasta/e89a9a6984ebbcdbbc85c16d65298dd2
2c4	Lake Ice	Global Lake and River Ice Phenology Database, Version 1	https://doi.org/10.7265/N5W66HP8
2c4	Lake Ice	Mountain Lake Biology, Chemistry, Physics, and Climate Data Since 1959 at Castle Lake Version 1. Environmental Data Initiative	https://doi.org/10.6073/pasta/a8e3b81cfe5864731b29ad42506c65d7
2c4	Lake Ice	Great Lakes Annual Maximum Ice Cover (%)	https://www.glerl.noaa.gov/data/ice/
2c4	Lake Ice	Great Lakes Ice	https://www.glerl.noaa.gov/data/ice
2c4	Lake Ice	Geographic Variation and Temporal Trends in Ice Phenology in Norwegian Lakes During a Century, Dryad	https://datadryad.org/stash/dataset/doi:10.5061/dryad.bk3j9kd9x
2c4	Lake Ice	Lake Surface Water Temperature and Ice Cover in Subalpine Lake Lunz, Austria	https://doi.org/10.1080/20442041.2017.1294332
2c4	Temperature, [Near] Surface	NASA/Goddard Institute for Space Studies (GISS) Global Temperature	https://data.giss.nasa.gov/gistemp/
2c5	Snow Properties	Northern Hemisphere (NH) Snow Cover Extent (SCE) Version 1	https://doi.org/10.7289/V5N014G9; https://www.snowcover.org

Unauthenticated | Downloaded 11/21/25 11:34 AM UTC

Section 2d Hydrological cycle			
Sub-section	**General Variable or Phenomenon**	**Specific Dataset or Variable**	**Source**
2d1	Humidity, [Near] Surface	ERA5	https://www.ecmwf.int/en/forecasts/dataset/ecmwf-reanalysis-v5
2d1, 2d2	Humidity, [Near] Surface	Met Office Hadley Centre Integrated Surface Dataset of Humidity over Land (HadISDH.land.4.6.1.2024f), Met Office HadISDH over Ocean (HadISDH.marine.1.6.1.2024), Met Office HadISDH over Land and Ocean (HadISDH.blend.1.5.1.2024f), Met Office HadISDH of Humidity Extremes (HadISDH.extremes.1.2.0.2024f)	https://www.metoffice.gov.uk/hadobs/hadisdh
2d1	Humidity, [Near] Surface	Japanese Reanalysis for Three Quarters of a Century (JRA-3Q)	https://jra.kishou.go.jp/JRA-3Q/index_en.html
2d1	Humidity, [Near] Surface	MERRA-2	https://disc.gsfc.nasa.gov/datasets/M2T1NXSLV_5.12.4/summary
2d3	Water Vapor, Total Column	Constellation Observing System for Meteorology, Ionosphere and Climate (COSMIC)	https://cdaac-www.cosmic.ucar.edu/
2d3	Water Vapor, Total Column	ERA5	https://www.ecmwf.int/en/forecasts/dataset/ecmwf-reanalysis-v5
2d3	Water Vapor, Total Column	Global Navigation Satellite System (GNSS) Ground-Based Total Column Water Vapor	https://doi.org/10.25326/68
2d3	Water Vapor, Total Column	JRA-3Q	https://jra.kishou.go.jp/JRA-3Q/index_en.html
2d3	Water Vapor, Total Column	MERRA-2	https://gmao.gsfc.nasa.gov/gmao-products/merra-2/
2d3	Water Vapor, Total Column	Special Sensor Microwave Imager (SSM/I)–Advanced Microwave Scanning Radiometer for Earth Observing System (AMSR-E) Ocean Total Column Water Vapor	https://www.remss.com
2d4	Humidity, Upper Atmosphere	Upper-Troposphere Humidity (UTH)	Available on request to Brian Soden (bsoden@miami.edu)
2d4	Humidity, Upper Atmosphere	ERA5	https://www.ecmwf.int/en/forecasts/dataset/ecmwf-reanalysis-v5
2d4	Humidity, Upper Atmosphere	High Resolution Infrared Sounder (HIRS)	https://www.ncei.noaa.gov/products/climate-data-records/hirs-ch12-brightness-temperature

Unauthenticated | Downloaded 11/21/25 11:34 AM UTC

Sub-section	General Variable or Phenomenon	Specific Dataset or Variable	Source
2d4	Temperature, Upper Atmosphere	NOAA National Environmental Satellite, Data, and Information Service (NESDIS) Center for Satellite Applications and Research (STAR) Microwave Sounding Unit (MSU) Version 5	https://www.star.nesdis.noaa.gov/pub/smcd/emb/mscat/data/MSU_AMSU_v5.0/Monthly_Atmospheric_Layer_Mean_Temperature/
2d5, 2d6	Precipitation	Global Precipitation Climatology Centre (GPCC)	https://www.dwd.de/EN/ourservices/gpcc/gpcc.html
2d5	Precipitation	GPCPv2.3	https://www.ncei.noaa.gov/products/global-precipitation-climatology-project; https://rda.ucar.edu/datasets/d728008/dataaccess/
2d6	Precipitation	Multi-Source Weighted-Ensemble Precipitation (MSWEP)	https://www.gloh2o.org/mswep/
2d6	Precipitation	Met Office Hadley Centre Dataset of Extreme Indices (HadEX3) Version 3	https://www.metoffice.gov.uk/hadobs/hadex3/
2d6	Precipitation	ERA5	https://cds.climate.copernicus.eu/datasets/reanalysis-era5-single-levels
2d6	Precipitation	Global Historical Climatology Network Daily Extremes (GHCNDEX)	https://www.climdex.org
2d6	Precipitation	MERRA-2	https://gmao.gsfc.nasa.gov/gmao-products/merra-2/ https://disc.gsfc.nasa.gov/datasets/M2SMNXEDI_2/summary
2d7	Cloud properties	PATMOS-xv6.0	https://www.ncei.noaa.gov/products/climate-data-records/avhrr-hirs-cloud-properties-patmos
2d7	Cloud Properties	Clouds and the Earth's Radiant Energy System Energy Balance and Filled (CERES EBAF) Version 4.2	https://ceres.larc.nasa.gov/data/
2d8	Lake Water Storage and Level	'GloLakes' Lake and Reservoir Storage	https://doi.org/10.5194/essd-16-201-2024
2d8	Lake Water Storage and Level	Global Lakes and Reservoir Monitor (GREALM) Lake Level	https://ipad.fas.usda.gov/cropexplorer/global_reservoir/
2d9	River Discharge	Global Flood Awareness System Version (GloFAS) 4	https://ewds.climate.copernicus.eu/datasets/cems-glofas-historical; https://data.jrc.ec.europa.eu/dataset/68050d73-9c06-499c-a441-dc5053cb0c86
2d9	River Discharge	ERA5	https://cds.climate.copernicus.eu/datasets/reanalysis-era5-single-levels
2d10	Groundwater and Terrestrial Water Storage	Gravity Recovery and Climate Experiment (GRACE)/GRACE Follow-On (GRACE-FO)	https://podaac.jpl.nasa.gov/dataset/TELLUS_GRAC-GRFO_MASCON_CRI_GRID_RL06.3_V4

Unauthenticated | Downloaded 11/21/25 11:34 AM UTC

Sub-section	General Variable or Phenomenon	Specific Dataset or Variable	Source
2d11	Soil Moisture	Copernicus Climate Change Service (C3S) Version 202012 product based on the ESA Climate Change Initiative for Soil Moisture (ESA CCI SM) Version 05.2 Merging Algorithm	https://cds.climate.copernicus.eu/datasets/satellite-soil-moisture
2d12	Drought	Climatic Research Unit Gridded Time Series (CRU TS) 4.09	https://crudata.uea.ac.uk/cru/data/drought/
2d13	Land Evaporation	Global Land Evaporation Amsterdam Model (GLEAM)	https://www.gleam.eu/
2d13	Modes of Variability	Niño 3.4 index	https://psl.noaa.gov/data/timeseries/month/DS/Nino34

Section 2e Atmospheric circulation

Sub-section	General Variable or Phenomenon	Specific Dataset or Variable	Source
2e1, 2e3	Modes of Variability	Antarctic Oscillation (AAO)/Southern Annular Mode (SAM)	https://ftp.cpc.ncep.noaa.gov/cwlinks/norm.daily.aao.index.b790101.current.ascii
2e1	Pressure, Sea Level or Near-Surface	ERA5	https://www.ecmwf.int/en/forecasts/dataset/ecmwf-reanalysis-v5
2e2	Wind, [Near] Surface	ERA5	https://www.ecmwf.int/en/forecasts/dataset/ecmwf-reanalysis-v5
2e2	Wind, [Near] Surface	Met Office Hadley Centre Integrated Surface Dataset (HadISD) Version v3.4.1.2024f	https://hadleyserver.metoffice.gov.uk/hadisd/v341_2024f/index.html
2e2	Wind, [Near] Surface	Global Historical Climate Network hourly (GHCNh)	https://www.ncei.noaa.gov/products/global-historical-climatology-network-hourly
2e2	Wind, [Near] Surface	MERRA-2	https://gmao.gsfc.nasa.gov/gmao-products/merra-2/
2e2	Wind, [Near] Surface	Remote Sensing System (RSS) Merged 1-Degree Monthly Radiometer Winds	https://www.remss.com/measurements/wind/
2e2	Wind, [Near] Surface	Remote Sensing System (RSS) Advanced Scatterometer (ASCAT)	https://www.remss.com/missions/ascat/
2e2	Wind, [Near] Surface	Remote Sensing System (RSS) QuickScat4	https://www.remss.com/missions/qscat/

Unauthenticated | Downloaded 11/21/25 11:34 AM UTC

Sub-section	General Variable or Phenomenon	Specific Dataset or Variable	Source
2e3	Modes of Variability	Pacific Decadal Oscillation	https://psl.noaa.gov/data/timeseries/month/data/pdo.timeseries.sstens.data
2e3	Wind, [Upper Atmosphere]	Quasi-biennial Oscillation (QBO)	https://www.atmohub.kit.edu/data/singapore2023.dat
2e3	Wind, [Upper Atmosphere]	ERA5 Hourly Data on Pressure Levels from 1940 to Present. Copernicus Climate Change Service (C3S) Climate Data Store (CDS)	https://cds.climate.copernicus.eu/datasets/reanalysis-era5-single-levels
2e3	Wind, [Upper Atmosphere]	MERRA-2	https://gmao.gsfc.nasa.gov/gmao-products/merra-2/
2e3	Wind, [Upper Atmosphere]	Japanese 55-Year Reanalysis (JRA-55) Atmospheric Reanalysis	https://jra.kishou.go.jp/JRA-55/index_en.html
2e3	Wind, [Upper Atmosphere]	Japanese Reanalysis for Three-Quarters of a Century (JRA-3Q)	https://jra.kishou.go.jp/JRA-3Q/index_en.html
2e4	Lightning	European Organisation for the Exploitation of Meteorological Satellites (EUMETSAT)	https://www.eumetsat.int/features/animations-europes-first-lightning-imager; https://user.eumetsat.int/news-events/news/mtg-lightning-imager-li-level-2-data-available

Section 2f Earth's radiation budget

Sub-section	General Variable or Phenomenon	Specific Dataset or Variable	Source
2f1	TOA Earth Radiation Budget	Clouds and the Earth's Radiant Energy System (CERES) Energy Balanced and Filled (EBAF) Version 4.2.1	https://ceres-tool.larc.nasa.gov/ord-tool/jsp/EBAFTOA421Selection.jsp
2f1	TOA Earth Radiation Budget	CERES Fast Longwave And Shortwave Radiative Fluxes (FLASHflux) Version 4C	https://ceres-tool.larc.nasa.gov/ord-tool/jsp/FLASH_TISASelection.jsp
2f1	TOA Earth Radiation Budget	Community-Consensus Total Solar Irradiance (TSI) Composit	https://spot.colorado.edu/~koppg/TSI/TSI_Composite-SIST.txt
2f2	Solar Transmission, Apparent	Mauna Loa Observatory	https://www.esrl.noaa.gov/gmd/webdata/grad/mloapt/mauna_loa_transmission.dat
2f2	Aerosol Optical Depth	NASA's Moderate Resolution Imaging Spectroradiometer (MODIS)	https://earthobservatory.nasa.gov/global-maps/MODAL2_M_AER_OD

Unauthenticated | Downloaded 11/21/25 11:34 AM UTC

Sub-section	General Variable or Phenomenon	Specific Dataset or Variable	Source
2f2	Aerosol Optical Depth	Copernicus Atmosphere Monitoring Service (CAMS)	https://atmosphere.copernicus.eu/south-america-sees-historic-emissions-during-2024-wildfire-season
2f2	Aerosol Extinction Coefficient	Stratospheric Aerosol and Gas Experiment (SAGE) Limb Sounder	https://sage.nasa.gov/2024/09/sage-iii-iss-science-highlight/
2f2	Stratospheric Aerosol Loadings	Balloon Network for Stratospheric Aerosol Observations (BalNeO)	https://science.larc.nasa.gov/balneo/
2f2	Stratospheric Aerosol Loadings	Balloon Baseline Stratospheric Aerosol Profiles (B2SAP)	https://csl.noaa.gov/projects/b2sap/pops.php?loc=HIH

Section 2g Atmospheric composition

Sub-section	General Variable or Phenomenon	Specific Dataset or Variable	Source
2g1	Trace Gases	Atmospheric Gas Trends	https://gml.noaa.gov/ccgg/trends/
2g1	Trace Gases	Global Greenhouse Gas Reference Network	https://gml.noaa.gov/ccgg/about.html
2g1	Trace Gases	Atmospheric Greenhouse Gas Index (AGGI)	https://gml.noaa.gov/ccgg/trends/
2g2	Trace Gases	Halocarbons and Other Atmospheric Trace Species	https://gml.noaa.gov/hats/data.html
2g2	Trace Gases	Ozone-Depleting Gas Index (ODGI)	https://gml.noaa.gov/odgi/
2g3	Aerosols	Copernicus Atmosphere Monitoring Service Reanalysis (CAMSRA)	https://www.ecmwf.int/en/research/climate-reanalysis/cams-reanalysis
2g4	Ozone, Surface	NOAA Global Monitoring Laboratory	https://gml.noaa.gov/aftp/data/ozwv/SurfaceOzone/
2g4	Ozone, Tropospheric	Ozone Monitoring Instrument (OMI)/ Microwave Limb Sounder (MLS)	https://acdb-ext.gsfc.nasa.gov/Data_services/cloud_slice/; https://avdc.gsfc.nasa.gov/
2g5	Stratospheric Aerosols	Haute-Provence Observatory (OHP) Lidar Temperature Aerosol (LTA) Lidar	https://www-air.larc.nasa.gov/missions/ndacc/data.html?station=haute.provence/ames/lidar/
2g5	Stratospheric Aerosols	Stratospheric Ozone Lidar at Haute-Provence Observatory (LiO3S)	https://www-air.larc.nasa.gov/missions/ndacc/data.html?station=haute.provence/ames/lidar/

Unauthenticated | Downloaded 11/21/25 11:34 AM UTC

Sub-section	General Variable or Phenomenon	Specific Dataset or Variable	Source
2g5	Stratospheric Aerosols	Lauder Aerosol Lidar	https://www-air.larc.nasa.gov/missions/ndacc/data.html?station=lauder/ames/lidar/
2g5	Stratospheric Aerosols	Stratospheric Aerosol and Gas Experiment III (SAGE III) Version 5.3	https://asdc.larc.nasa.gov/project/SAGE%20III-ISS/g3bssp_53
2g5	Stratospheric Aerosols	Global Space-based Stratospheric Aerosol Climatology (GloSSAC) Version 2	https://asdc.larc.nasa.gov/project/GloSSAC
2g5	Stratospheric Aerosols	Ozone Mapping and Profiler Suite Limb Profiler (OMPS-LP) Version 2.1	https://disc.gsfc.nasa.gov/datasets/OMPS_NPP_LP_L2_AER_DAILY_2/summary
2g6	Ozone, Total Column and Stratospheric	Global Ozone Monitoring Experiment (GOME)/ Scanning Imaging Absorption Spectrometer for Atmospheric Cartography (SCIAMACHY)/GOME2 (GSG) Merged Total Ozone	https://www.iup.uni-bremen.de/UVSAT/data/wfdoas/
2g6	Ozone, Total Column and Stratospheric	GOME/SCIAMACHY/GOME2 (GTO) Merged Total Ozone	https://atmos.eoc.dlr.de/app/products/gto-ecv
2g6	Ozone, Total Column and Stratospheric	Global Ozone Chemistry and Related Trace Gas Data Records (GOZCARDS) Ozone Profiles	https://disc.gsfc.nasa.gov/datasets/GozMmlpO3_1/summary
2g6	Ozone, Total Column and Stratospheric	Multi Sensor Reanalysis (MSR-2) of Total Ozone	https://www.temis.nl/protocols/O3global.html
2g6	Ozone, Total Column and Stratospheric	NASA Backscatter Ultraviolet Radiometer (BUV)/Solar Backscatter Ultraviolet Radiometer (SBUV)/Ozone Mapping and Profiler Suite (OMPS) Version 8.7 (MOD) Merged Ozone	https://acd-ext.gsfc.nasa.gov/Data_services/merged/
2g6	Ozone, Total Column and Stratospheric	NOAA SBUV V8.6 OMPS V4r1 Cohesive Dataset (COH)	https://ftp.cpc.ncep.noaa.gov/SBUV_CDR/
2g6	Ozone, Total Column and Stratospheric	Network for the Detection of Atmospheric Composition Change (NDACC) Lidar, Microwave, and Fourier Transform Infrared Spectroscopy (FTIR)	https://www-air.larc.nasa.gov/missions/ndacc
2g6	Ozone, Total Column and Stratospheric	Chemistry-Climate Model Initiative (CCMI)-2022 Model Runs	https://blogs.reading.ac.uk/ccmi/ccmi-2022/

Unauthenticated | Downloaded 11/21/25 11:34 AM UTC

Sub-section	General Variable or Phenomenon	Specific Dataset or Variable	Source
2g6	Ozone, Total Column and Stratospheric	SAGE-Climate Change Initiative (CCI)-OMPS	https://climate.esa.int/en/projects/ozone/data
2g6	Ozone, Total Column and Stratospheric	SAGE/Origins, Spectral Interpretation, Resource Identification, and Security (OSIRIS)	https://doi.org/10.5194/amt-11-489-2018 https://research-groups.usask.ca/osiris/
2g6	Ozone, Total Column and Stratospheric	SAGE-SCIA-OMPS	https://doi.org/10.5194/amt-2018-275 https://www.iup.uni-bremen.de/DataRequest/
2g6	Ozone, Total Column and Stratospheric	Stratospheric Water and Ozone Satellite Homogenized (SWOOSH)	https://csl.noaa.gov/groups/csl8/swoosh/
2g6	Ozone, Total Column and Stratospheric	World Ozone and Ultraviolet Radiation Data Centre (WOUDC) Ground-Based Ozone	https://woudc.org/data/dataset_info.php?id=totalozone
2g7	Stratospheric Water Vapor	The Aura Microwave Limb Sounder Version 5.0 Data, as Merged Into SWOOSH	https://csl.noaa.gov/groups/csl8/swoosh/
2g7	Tropopause Temperature	MERRA-2	https://gmao.gsfc.nasa.gov/gmao-products/merra-2/
2g7	Stratospheric Water Vapor	NOAA Frostpoint Hygrometer (FPH)	https://gml.noaa.gov/aftp/data/ozwv/WaterVapor/
2g7	Stratospheric Water Vapor	Cryogenic Frostpoint Hygrometer (CFH)	https://ndacc.org
2g8	Trace Gases	Copernicus Atmosphere Monitoring Service Reanalysis (CAMSRA) for Carbon Monoxide	https://ads.atmosphere.copernicus.eu/datasets/cams-global-radiative-forcing-auxilliary-variables?tab=overview

Section 2h Land surface properties

Sub-section	General Variable or Phenomenon	Specific Dataset or Variable	Source
2h1	Albedo	Moderate Resolution Imaging Spectroradiometer (MODIS)/Terra+Aqua Bidirectional Reflectance Distribution Function (BDRF)/Albedo Albedo Daily L3 Global 0.05 Deg Climate Modeling Grid (CMG) Version 061	https://www.earthdata.nasa.gov/centers/lp-daac
2h1	Albedo	VIIRS VNP43C3 Collection 1.0	https://www.earthdata.nasa.gov/centers/lp-daac

Unauthenticated | Downloaded 11/21/25 11:34 AM UTC

Sub-section	General Variable or Phenomenon	Specific Dataset or Variable	Source
2h2	Fraction of Absorbed Photosynthetically Active Radiation (FAPAR)	Joint Research Centre (JRC) Two-Stream Inversion Package (TIP) MODIS	https://fapar.jrc.ec.europa.eu
2h2	FAPAR	Medium Resolution Imaging Spectrometer (MERIS)	https://fapar.jrc.ec.europa.eu
2h2	FAPAR	Sea-Viewing Wide Field-of-View Sensor (SeaWIFS) FAPAR	https://fapar.jrc.ec.europa.eu/
2h2	FAPAR	Ocean and Land Colour Instrument (OLCI)	https://dataspace.copernicus.eu/
2h3	Biomass, Greenness or Burning	Global Fire Assimilation System Version (GFAS) 1.2	https://ads.atmosphere.copernicus.eu/cdsapp#!/dataset/cams-global-fire-emissions-gfas v1.4 available upon request
2h3	Biomass, Greenness or Burning	Global Fire Emissions Database	https://www.globalfiredata.org/data.html
2h4	Phenology	MODIS Normalized Difference Vegetative Index (NDVI)	https://modis.gsfc.nasa.gov/data/dataprod/mod13.php
2h4	Temperature [Near] Surface	MERRIS-2 Monthly Temperature	https://goldsmr4.gesdisc.eosdis.nasa.gov/data/MERRA2_MONTHLY/M2TMNXLND.5.12.4/
2h4	Phenology	USA-National Phenology Network (NPN) Phenology Data	https://www.usanpn.org/data/observational
2h4	Phenology	USA-National Phenology Network (NPN) Spring Index Raster Data Products	https://data.usanpn.org/geoserver-request-builder/
2h4	Phenology	German Oak Phenology Data	https://opendata.dwd.de/
2h4	Phenology	Harvard Forest	https://harvardforest1.fas.harvard.edu/exist/apps/datasets/showData.html?id=hf003
2h4	Phenology	Natures Calendar	https://naturescalendar.woodlandtrust.org.uk/
2h4	Phenology	PhenoCam	https://phenocam.sr.unh.edu
2h4	Phenology	UK Cumbrian Lakes Data	https://catalogue.ceh.ac.uk/documents/bf30d6aa-345a-4771-8417-ffbcf8c08c28/
2h4	Phenology	UK Loch Leven	https://catalogue.ceh.ac.uk/documents/ac973b0d-2c99-4e00-8931-22aa0881006d
2h4	Phenology	Dutch Oak Phenology Data	https://www.natuurkalender.nl/
2h4	Phenology	Lakes Geneva and Bourget Data	https://si-ola.inrae.fr/si_lacs/login.jsf

Unauthenticated | Downloaded 11/21/25 11:34 AM UTC

Sub-section	General Variable or Phenomenon	Specific Dataset or Variable	Source
2h5	Vegetation Optical Depth	Global Long-term Microwave Vegetation Optical Depth Climate Archive Version 2 (VODCAv2)	https://researchdata.tuwien.ac.at/records/t74ty-tcx62
2h5	Modes of Variability	Niño 3.4 Index	https://psl.noaa.gov/data/timeseries/month/DS/Nino34

Sidebar 2.1 Super extreme land surface temperature hotspots

Sub-section	General Variable or Phenomenon	Specific Dataset or Variable	Source
SB2.1	Temperature [Near] Surface	Climatic Research Unit Temperature Version 5 (CRUTEM5)	https://www.metoffice.gov.uk/hadobs/crutem5/
SB2.1	Temperature [Near] Surface	Centre for Environmental Data Analysis (CEDA) Archive, European Space Agency (ESA) Land Surface Temperature Climate Change Initiative (LST_cci)—Sea and Land Surface Temperature Radiometer Onboard the Sentinel-3B Platform (SLSTR-B)	https://catalogue.ceda.ac.uk/uuid/5f66a881adf846bfaad58b0e6068f0ea/
SB2.1	Temperature [Near] Surface	CEDA Archive, Earth Observation Climate Information Service (EOCIS)—SLSTR-B	https://catalogue.ceda.ac.uk/uuid/fc0bc3d5887d441296091a8025f8f45d/

Sidebar 2.2 Short-lived greenhouse gases

Sub-section	General Variable or Phenomenon	Specific Dataset or Variable	Source
SB2.2	Trace Gases [NH3]	Cross-track Infrared Sounder (CrIS) Column NH3	https://doi.org/10.5067/7I3KMUCCJNEN
SB2.2	Trace Gases [PAN]	CrIS Partial Column Acyl Peroxynitrates (PANs) Data	https://doi.org/10.5067/W0W6L8M6J85X
SB2.2	Total Column Ozone	Ozone Mapping and Profiler Suite (OMPS) Satellite Instrument Data	https://www.ncei.noaa.gov/metadata/geoportal/rest/metadata/item/gov.noaa.ncdc%3AC01464/html

Unauthenticated | Downloaded 11/21/25 11:34 AM UTC

Appendix 3: Supplemental materials

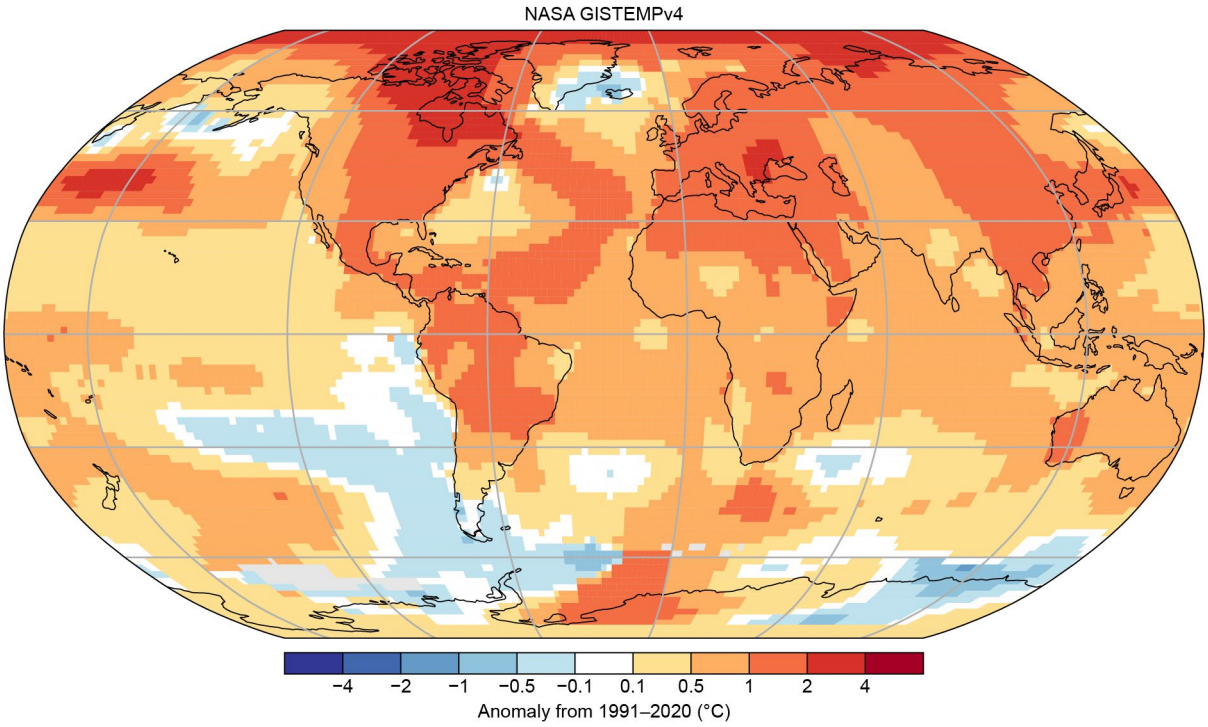

Fig. A2.1. Global surface temperature anomalies (°C). (Source: NASA Goddard Institute for Space Studies Surface Temperature Analysis version 4 [GISTEMPv4].)

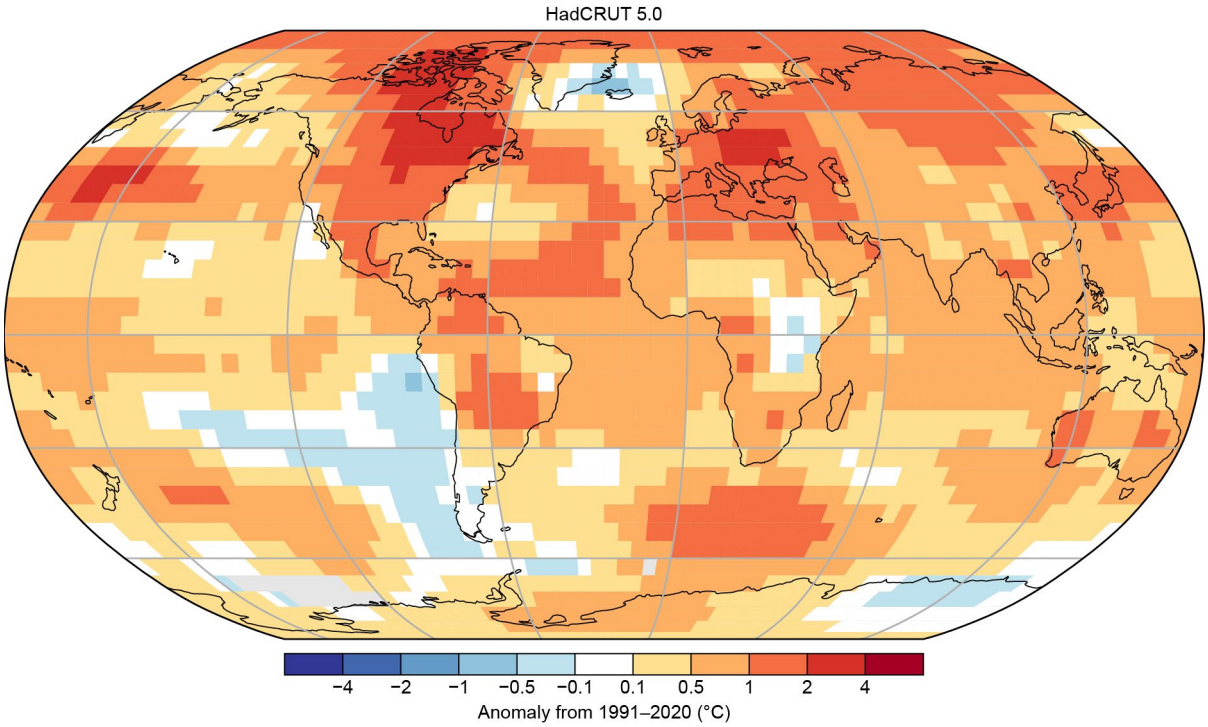

Fig. A2.2. Global surface temperature anomalies (°C). (Source: HadCRUTS.)

Unauthenticated | Downloaded 11/21/25 11:34 AM UTC

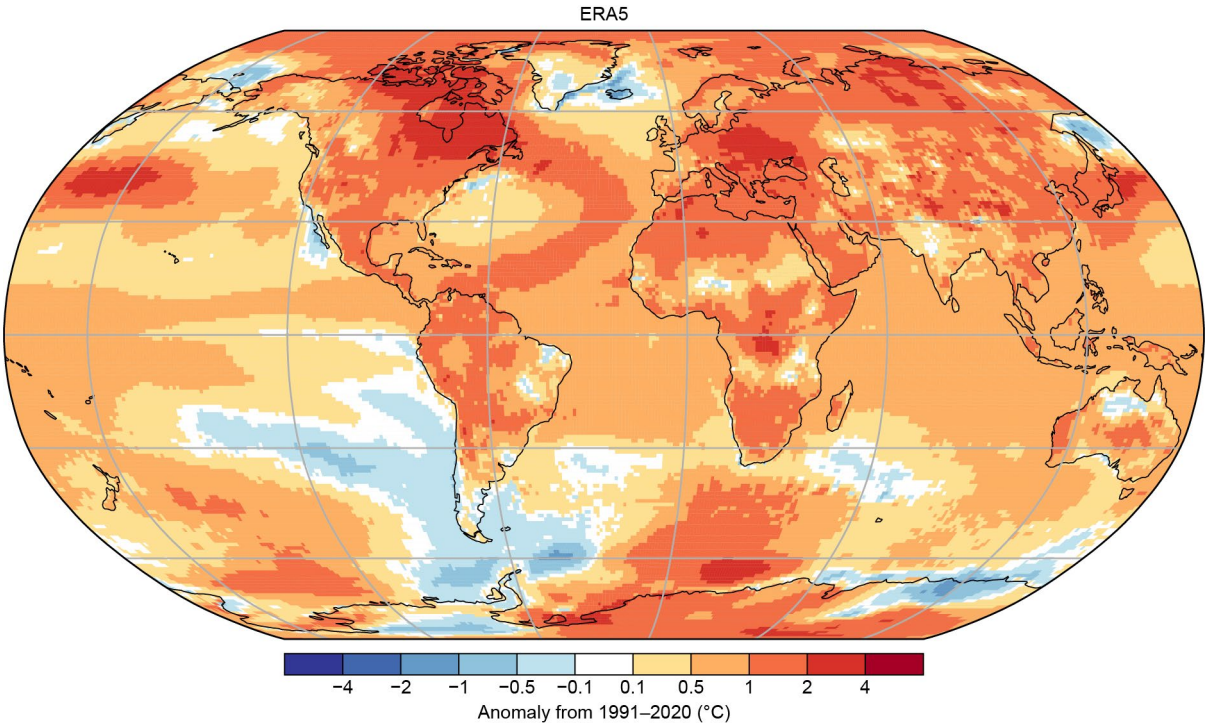

Fig. A2.3. Global surface temperature anomalies (°C). (Source: ERA5.)

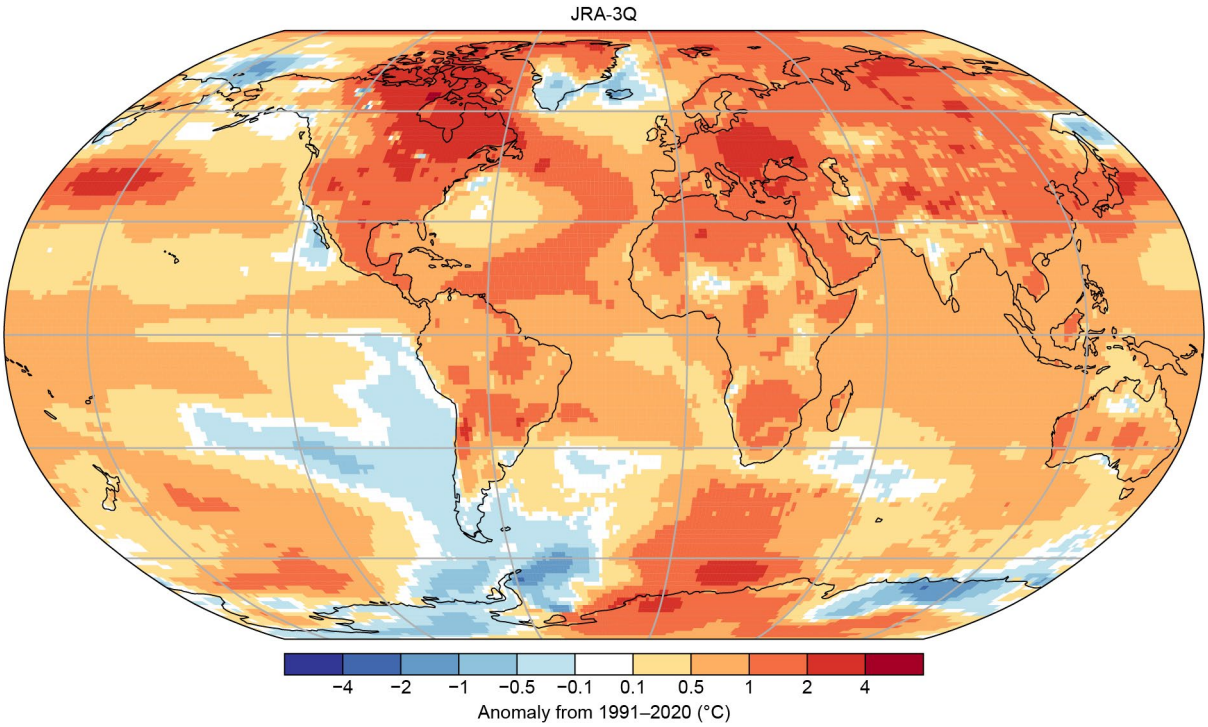

Fig. A2.4. Global surface temperature anomalies (°C). (Source: Japanese Reanalysis for Three Quarters of a Century [JRA-3Q].)

Unauthenticated | Downloaded 11/21/25 11:34 AM UTC

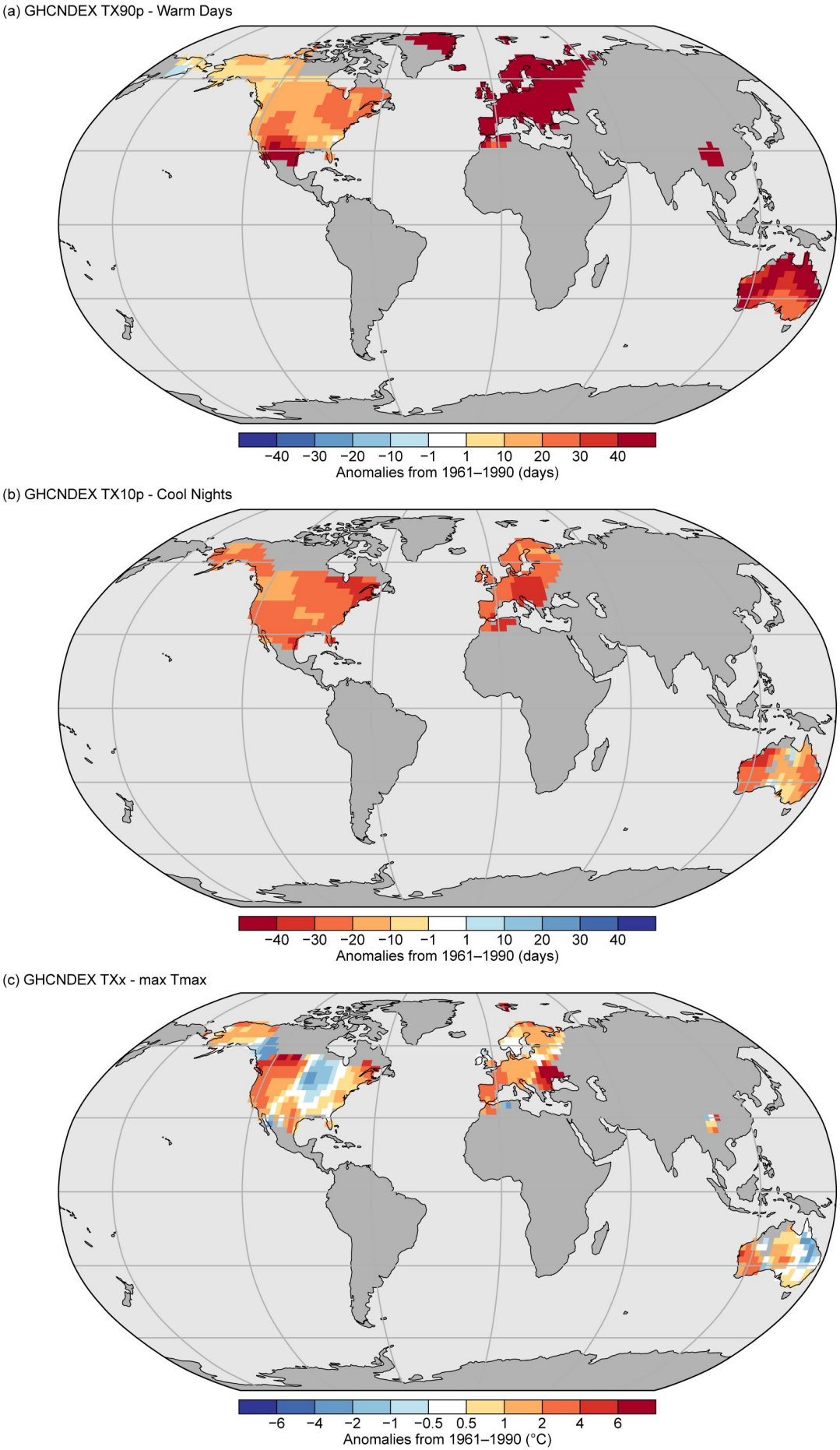

Fig. A2.5. Global Historical Climatology Network Daily Extremes (GHCNDEX) (a) warm day threshold exceedance (TX90p), (b) cool night threshold exceedance (TN10p), and (c) annual highest daily maximum temperature (TXx).

Unauthenticated | Downloaded 11/21/25 11:34 AM UTC

Table A2.1. Ten highest annual global equivalent temperature anomalies (Teq) and their constituent parts (air temperature [Ta]; latent temperature [Tq]) in °C (1991–2020 base period) since 1979 for ERA5.

Rank	Ta Year	Ta (°C)	Tq Year	Tq (°C)	Teq (Year)	Teq (°C)
1	2024	0.72	2024	0.85	2024	1.57
2	2023	0.60	2023	0.59	2023	1.19
3	2016	0.44	2016	0.50	2016	0.94
4	2020	0.43	2019	0.44	2019	0.84
5	2019	0.40	2020	0.38	2020	0.82
6	2017	0.34	2017	0.33	2017	0.68
7	2022	0.30	1998	0.27	2015	0.53
8	2021	0.27	2015	0.27	2018	0.52
9	2018	0.26	2018	0.25	2021	0.41
10	2015	0.26	2010	0.15	2022	0.40

Table A2.2. Ten highest annual global equivalent temperature anomalies (Teq) and their constituent parts (air temperature [Ta]; latent temperature [Tq]) in °C (1991–2020 base period) since 1979 for the Japanese Reanalysis for Three Quarters of a Century (JRA-3Q).

Rank	Ta Year	Ta (°C)	Tq Year	Tq (°C)	Teq (Year)	Teq (°C)
1	2024	0.67	2024	0.98	2024	1.65
2	2023	0.57	2023	0.74	2023	1.30
3	2016	0.42	2016	0.45	2016	0.86
4	2020	0.38	2020	0.41	2020	0.79
5	2019	0.36	1998	0.33	2019	0.68
6	2017	0.30	2019	0.32	2017	0.52
7	2015	0.25	2015	0.24	2015	0.49
8	2022	0.24	2017	0.23	2022	0.44
9	2018	0.22	2022	0.21	2021	0.38
10	2021	0.19	2021	0.19	1998	0.36

Table A2.3. Top ten ranked global equivalent temperature anomalies (Teq) and their constituent parts (air temperature [Ta]; latent temperature [Tq]) in °C (1991–2020 base period) since 1979 for the Met Office Hadley Centre Integrated Surface Dataset of Humidity (HadISDH; land-only).

Rank	Ta Year	Ta (°C)	Tq Year	Tq (°C)	Teq (Year)	Teq (°C)
1	2024	0.96	2024	1.13	2024	2.04
2	2023	0.74	2023	0.74	2023	1.49
3	2020	0.58	2016	0.61	2016	1.14
4	2016	0.55	1998	0.58	2020	1.03
5	2019	0.44	2020	0.46	1998	0.72
6	2015	0.42	2010	0.35	2017	0.67
7	2017	0.39	2022	0.31	2019	0.64
8	2021	0.37	2017	0.29	2021	0.63
9	2022	0.33	2021	0.27	2022	0.62
10	2018	0.24	2019	0.21	2015	0.60

Unauthenticated | Downloaded 11/21/25 11:34 AM UTC

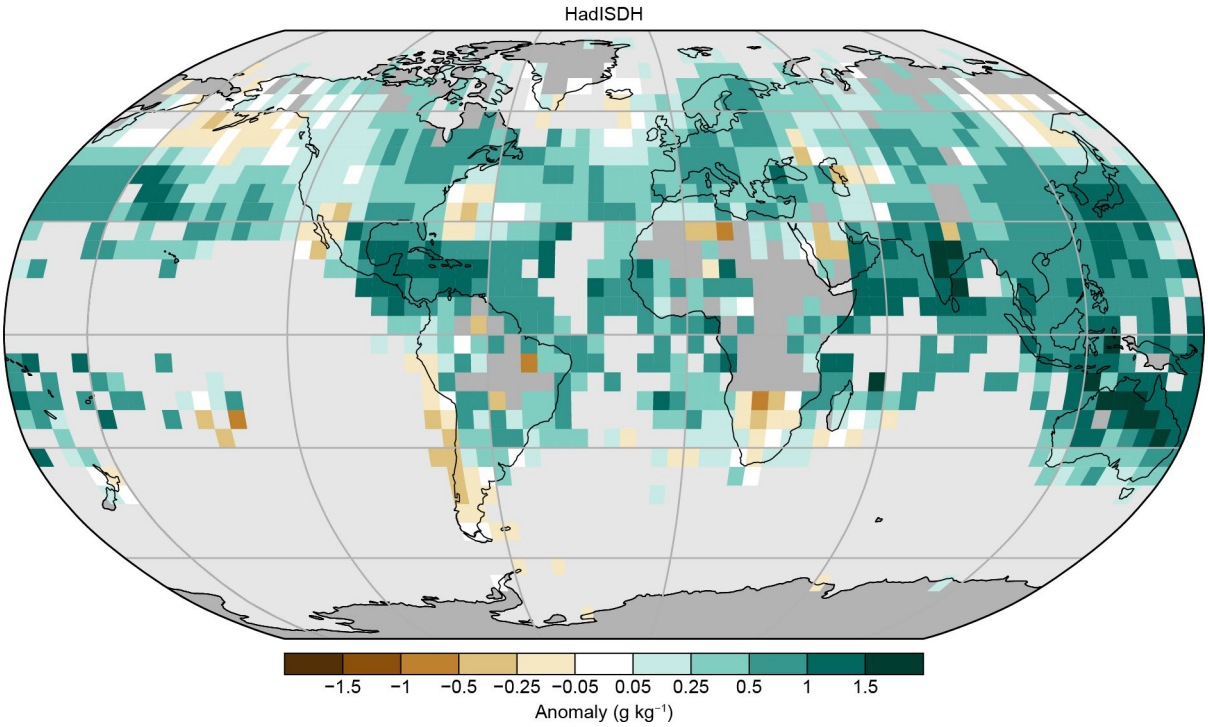

Fig. A2.6. Surface specific humidity anomaly (g kg^{-1}) relative to 1991–2020 from Met Office Hadley Centre Integrated Surface Dataset of Humidity Blend (HadISDH.blend.1.5.1.2024f).

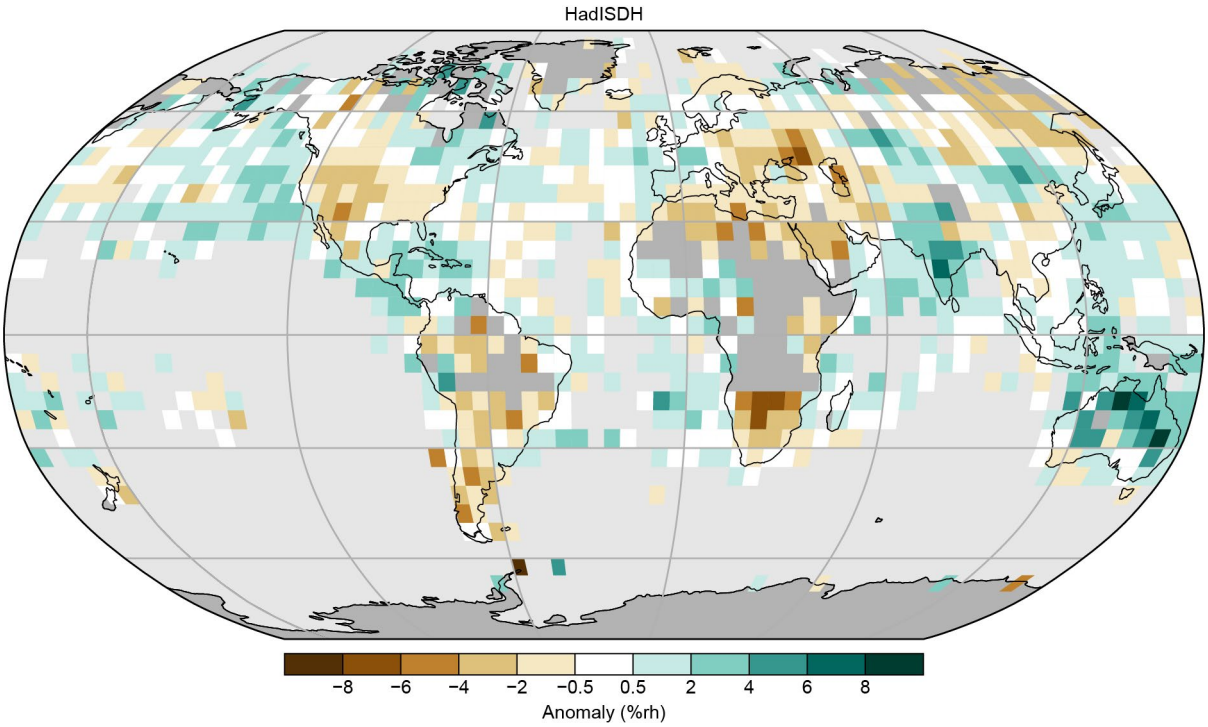

Fig. A2.7. Surface relative humidity anomaly (%rh) relative to 1991–2020 from Met Office Hadley Centre Integrated Surface Dataset of Humidity over Land and Ocean (HadISDH.blend.1.5.1.2024f).

Unauthenticated | Downloaded 11/21/25 11:34 AM UTC

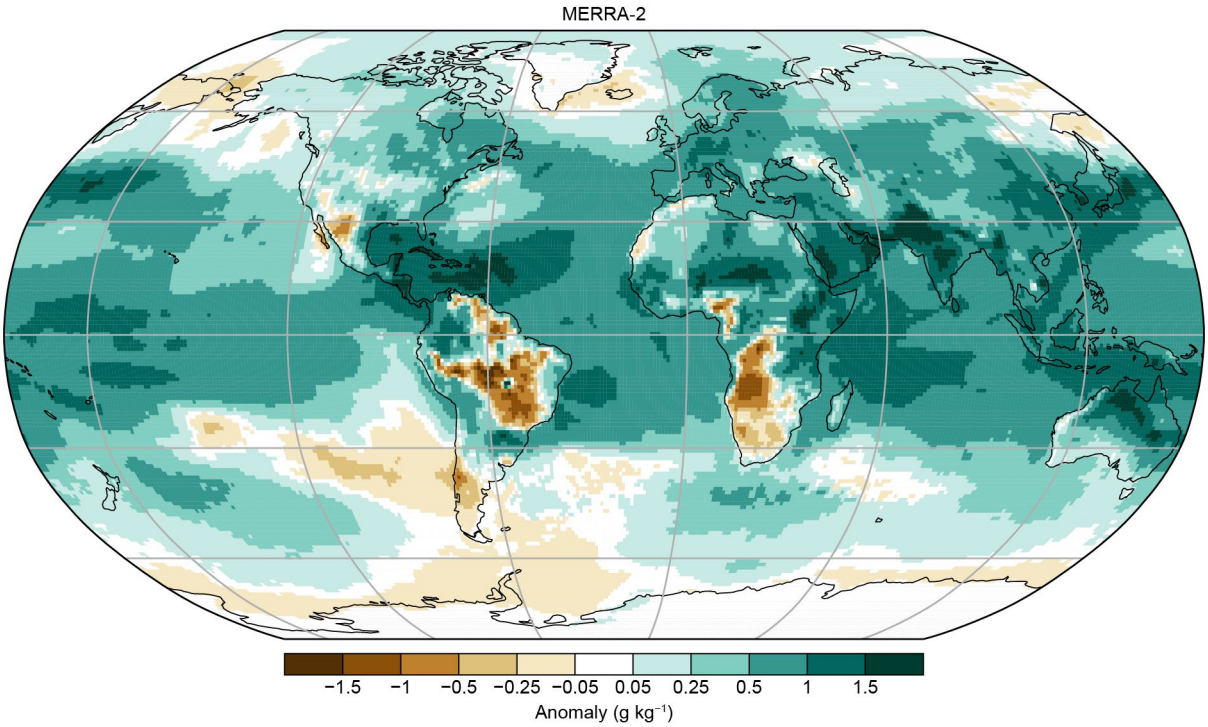

Fig. A2.8. Surface specific humidity anomaly (g kg^{-1}) relative to 1991–2020 from MERRA-2.

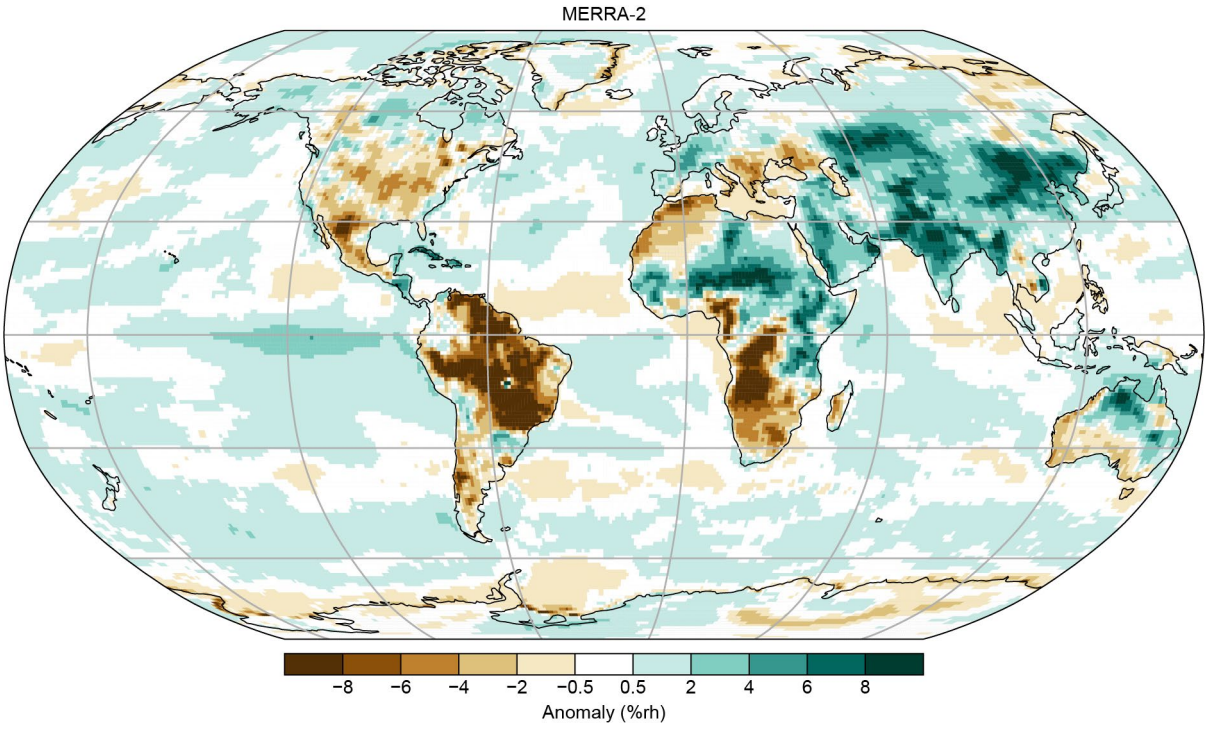

Fig. A2.9. Surface relative humidity anomaly (%rh) relative to 1991–2020 from MERRA-2.

Unauthenticated | Downloaded 11/21/25 11:34 AM UTC

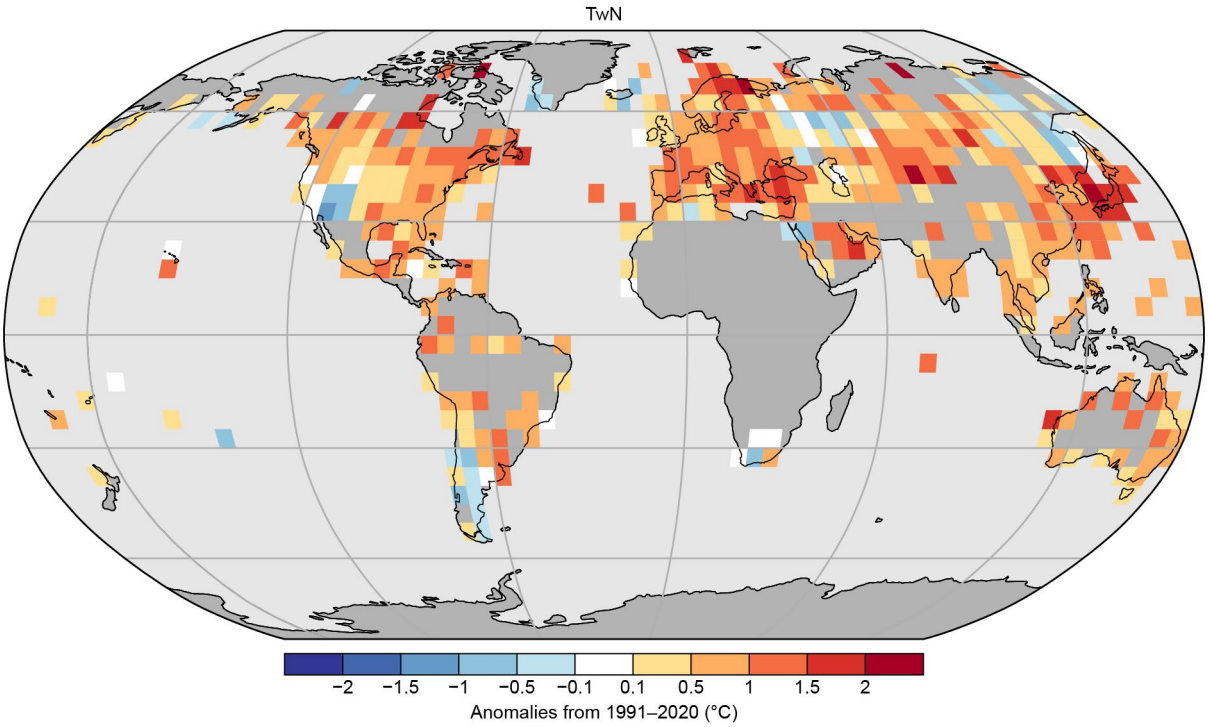

Fig. A2.10. 2024 minimum humid-heat intensity as measured by the annual median of the global median monthly minimum of the daily minimum wet-bulb temperature (T_wN; °C) from the Met Office Hadley Centre Integrated Surface Dataset of Humidity Extremes (HadISDH.extremes). Gray gridboxes (over land) represent regions with insufficient data.

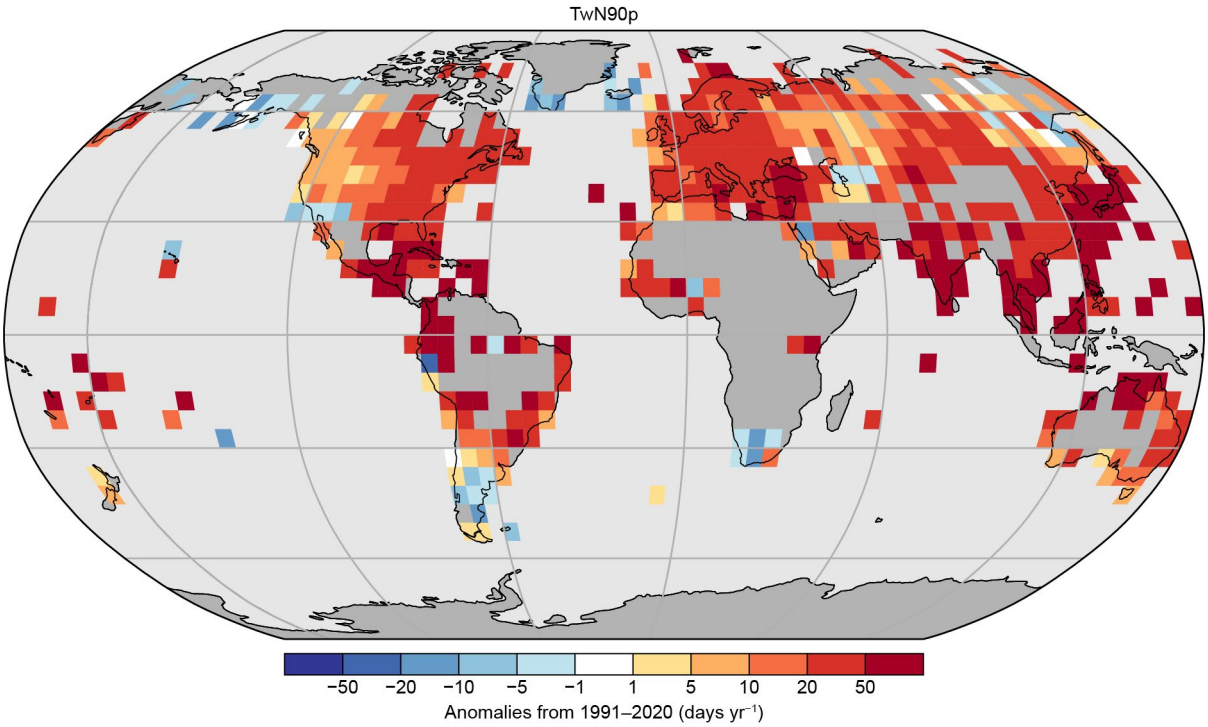

Fig. A2.11. 2024 high daily minimum humid-heat frequency anomalies as measured by the number of days where the daily minimum wet-bulb temperature exceeds the local daily 90th percentile (T_wN90p; days yr^{-1}; calculated over the 1991–2020 period) from the Met Office Hadley Centre Integrated Surface Dataset of Humidity Extremes (HadISDH.extremes). Gray gridboxes (over land) represent regions with insufficient data.

Unauthenticated | Downloaded 11/21/25 11:34 AM UTC

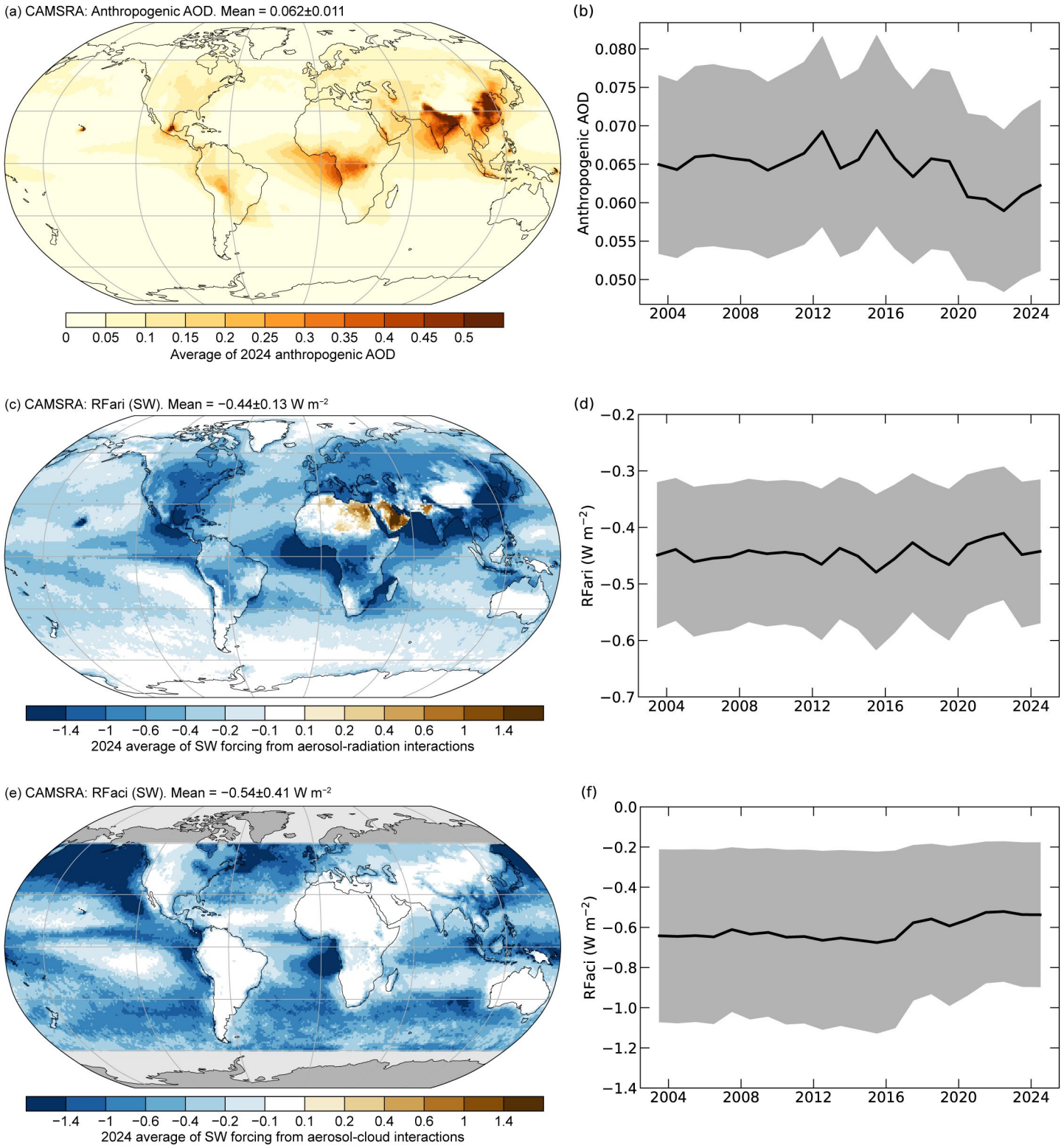

Fig. A2.12. Copernicus Atmosphere Monitoring Service reanalysis (CAMSRA) (a) 2024 average of anthropogenic aerosol optical depth (AOD); (b) global annual average of anthropogenic AOD from 2003 to 2024. Radiative forcing in the shortwave (SW) spectrum due to (c),(d) aerosol-radiation (RFari) and (e),(f) aerosol-cloud interactions (RFaci). The left column shows the distributions for the year 2024. The right column shows the time series of global averages for the period 2003–24, with the mean ±1-σ uncertainties of these estimates shown in gray.

Unauthenticated | Downloaded 11/21/25 11:34 AM UTC

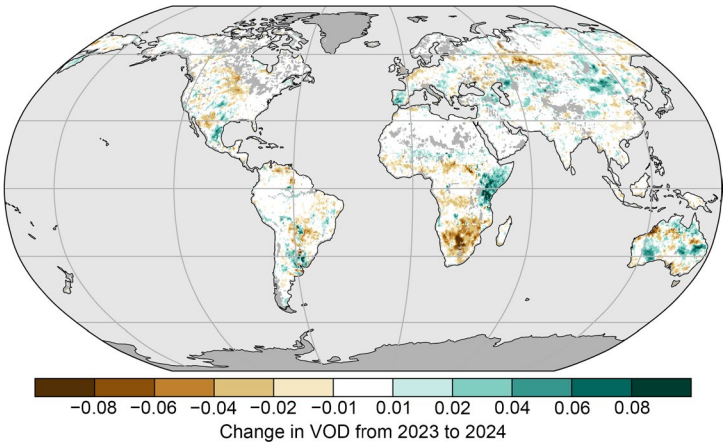

Fig. A2.13. The difference in average CXKu vegetation optical depth (VOD) between the years 2023 and 2024. Brown (green) colors indicate areas where VOD in 2024 were lower (higher) than in 2023. (Source: Vegetation Optical Depth Climate Archive version 2 [VODCAv2]).

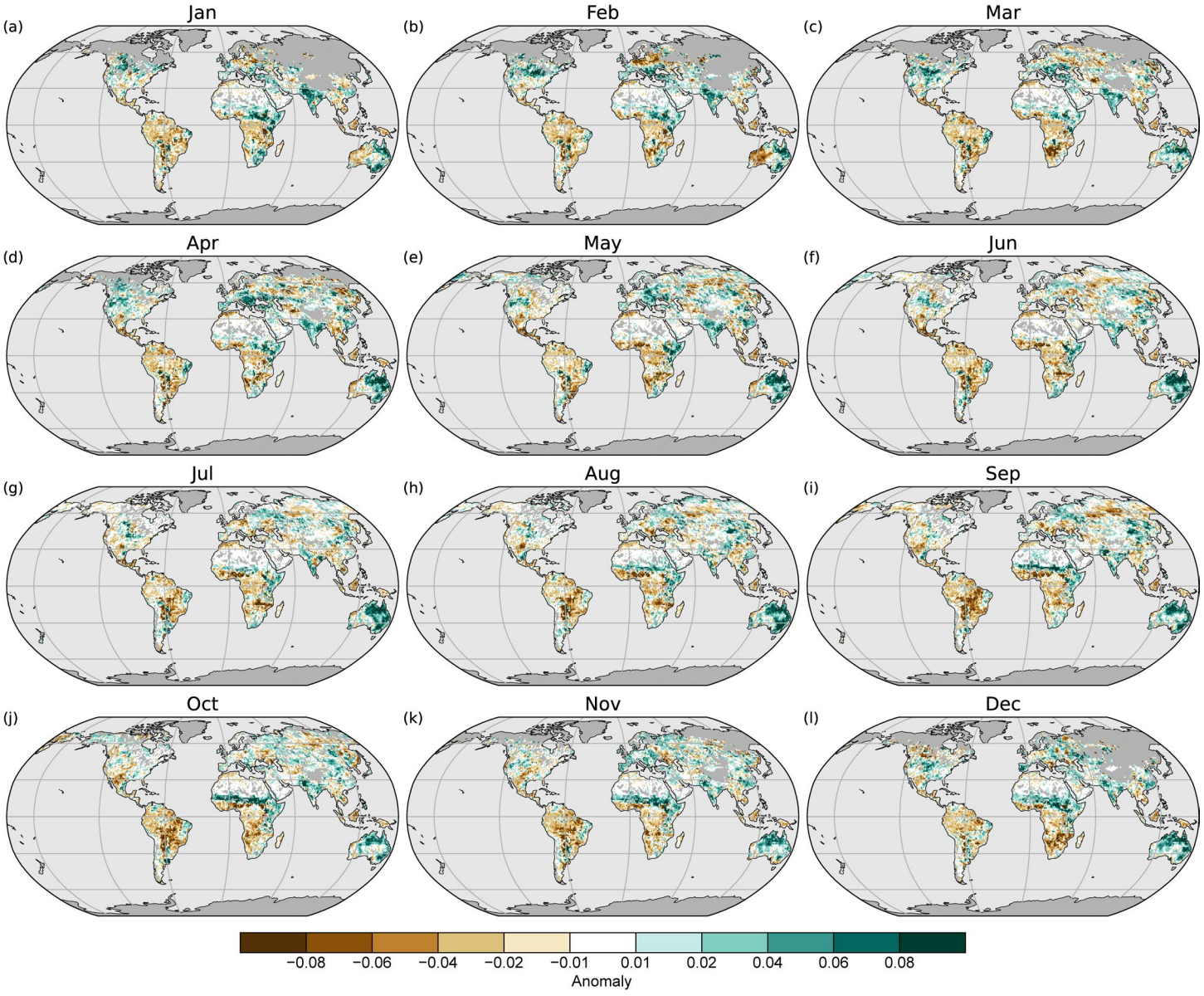

Fig. A2.14. Vegetation Optical Depth Climate Archive (VODCA) monthly CXKu vegetation optical depth (VOD) anomalies in 2024 (1991–20 base period). VOD cannot be retrieved over frozen or snow-covered areas, which is why they are masked out in winter.

Unauthenticated | Downloaded 11/21/25 11:34 AM UTC

References

Alencar, A., and Coauthors, 2024: Fogo no Brasil em 2024: O retrato fundiário da área queimada nos biomas. Tech. Note IPAM (Amazon Environmental Research Institute), Map-Biomas Network, 21 pp., https://ipam.org.br/wp-content/uploads/2024/10/NT_Fogo_Fundiario_ENG_v01.pdf.

Allan, R. J., J. A. Lindesay, and D. E. Parker, 1996: *El Niño Southern Oscillation and Climatic Variability*. CSIRO Publishing, 405 pp.

Ammann, C. M., G. A. Meehl, W. M. Washington, and C. S. Zender, 2003: A monthly and latitudinally varying volcanic forcing dataset in simulations of 20th century climate. *Geophys. Res. Lett.*, **30**, 1657, https://doi.org/10.1029/2003GL016875.

Aono, Y., and K. Kazui, 2008: Phenological data series of cherry tree flowering in Kyoto, Japan, and its application to reconstruction of springtime temperatures since the 9th century. *Int. J. Climatol.*, **28**, 905–914, https://doi.org/10.1002/joc.1594.

Archibald, A. T., and Coauthors, 2020: Tropospheric ozone assessment report. *Elementa*, **8**, 034, https://doi.org/10.1525/elementa.2020.034.

Arguez, A., and Coauthors, 2020: Should we expect each year in the next decade (2019–28) to be ranked among the top 10 warmest years globally? *Bull. Amer. Meteor. Soc.*, **101**, E655–E663, https://doi.org/10.1175/BAMS-D-19-0215.1.

Arosio, C., A. Rozanov, E. Malinina, M. Weber, and J. P. Burrows, 2019: Merging of ozone profiles from SCIAMACHY, OMPS and SAGE II observations to study stratospheric ozone changes. *Atmos. Meas. Tech.*, **12**, 2423–2444, https://doi.org/10.5194/amt-12-2423-2019.

Asher, E., and Coauthors, 2024: Balloon baseline stratospheric aerosol profiles (B^2SAP)—Perturbations in the Southern Hemisphere, 2019–2022. *J. Geophys. Res. Atmos.*, **129**, e2024JD041581, https://doi.org/10.1029/2024JD041581.

Augustine, J. A., K. O. Lantz, J.-P. Vernier, and L. Soldo, 2024: Mauna Loa apparent transmission record update for 2023 [in "State of the Climate in 2023"]. *Bull. Amer. Meteor. Soc.*, **105** (8), S1–S484, https://doi.org/10.1175/2024BAMSStateoftheClimate.1.

Azisov, E., M. Hoelzle, S. Vorogushyn, T. Saks, R. Usubaliev, M. Esenaman Uulu, and M. Barandun, 2022: Reconstructed centennial mass balance change for Golubin glacier, northern Tien Shan. *Atmosphere*, **13**, 954, https://doi.org/10.3390/atmos13060954.

Azorin-Molina, C., and Coauthors, 2023: Biases in wind speed measurements due to anemometer changes. *Atmos. Res.*, **289**, 106771, https://doi.org/10.1016/j.atmosres.2023.106771.

—— , R. J. H. Dunn, L. Ricciardulli, C. A. Mears, J. P. Nicolas, T. R. McVicar, Z. Zeng, and M. G. Bosilovich, 2024: Land and ocean surface winds [in "State of the Climate in 2023"]. *Bull. Amer. Meteor. Soc.*, **105** (8), S76–S79, https://doi.org/10.1175/BAMS-D-24-0116.1.

Bai, G., and Coauthors, 2022: GBOV (Ground-Based Observation for Validation): A copernicus service for validation of land products. *IGARSS 2022 – 2022 IEEE Int. Geoscience and Remote Sensing Symp.*, Kuala Lumpur, Malaysia, Institute of Electrical and Electronics Engineers, 4304–4307, https://doi.org/10.1109/IGARSS46834.2022.9883162.

Bai, X., J. Wang, C. Sellinger, A. Clites, and R. Assel, 2012: Interannual variability of Great Lakes ice cover and its relationship to NAO and ENSO. *J. Geophys. Res.*, **117**, C03002, https://doi.org/10.1029/2010JC006932.

Baldwin, M. P., and T. J. Dunkerton, 2001: Stratospheric harbingers of anomalous weather regimes. *Science*, **294**, 581–584, https://doi.org/10.1126/science.1063315.

—— , and Coauthors, 2001: The quasi-biennial oscillation. *Rev. Geophys.*, **39**, 179–299, https://doi.org/10.1029/1999RG000073.

Barichivich, J., E. Gloor, P. Peylin, R. J. Brienen, J. Schöngart, J. C. Espinoza, and K. C. Pattnayak, 2018: Recent intensification of Amazon flooding extremes driven by strengthened Walker circulation. *Sci. Adv.*, **4**, eaat8785, https://doi.org/10.1126/sciadv.aat8785.

—— , T. J. Osborn, I. Harris, G. van der Schrier, and P. D. Jones, 2024: Monitoring global drought using the self-calibrating palmer drought severity index [in "State of the Climate in 2023"]. *Bull. Amer. Meteor. Soc.*, **105** (8), S70–S71, https://doi.org/10.1175/2024BAMSStateoftheClimate.1.

Basu, S., and Coauthors, 2022: Estimating emissions of methane consistent with atmospheric measurements of methane and δ^{13}C of methane. *Atmos. Chem. Phys.*, **22**, 15 351–15 377, https://doi.org/10.5194/acp-22-15351-2022.

Beck, H. E., E. F. Wood, M. Pan, C. K. Fisher, D. G. Miralles, A. I. J. M. Van Dijk, T. R. McVicar, and R. F. Adler, 2019: MSWEP V2 global 3-hourly 0.1° precipitation: Methodology and quantitative assessment. *Bull. Amer. Meteor. Soc.*, **100**, 473–500, https://doi.org/10.1175/BAMS-D-17-0138.1.

Becker, A., P. Finger, A. Meyer-Christoffer, B. Rudolf, K. Schamm, U. Schneider, and M. A. Ziese, 2013: A description of the global land-surface precipitation data products of the Global Precipitation Climatology Centre with sample applications including centennial (trend) analysis from 1901–present. *Earth Syst. Sci. Data*, **5**, 71–99, https://doi.org/10.5194/essd-5-71-2013.

Behera, S. N., M. Sharma, V. P. Aneja, and R. Balasubramanian, 2013: Ammonia in the atmosphere: A review on emission sources, atmospheric chemistry and deposition on terrestrial bodies. *Environ. Sci. Pollut. Res.*, **20**, 8092–8131, https://doi.org/10.1007/s11356-013-2051-9.

Bell, B., and Coauthors, 2021: The ERA5 global reanalysis: Preliminary extension to 1950. *Quart. J. Roy. Meteor. Soc.*, **147**, 4186–4227, https://doi.org/10.1002/qj.4174.

Bellouin, N., and Coauthors, 2020: Radiative forcing of climate change from the Copernicus reanalysis of atmospheric composition. *Earth Syst. Sci. Data*, **12**, 1649–1677, https://doi.org/10.5194/essd-12-1649-2020.

Bessenbacher, V., D. L. Schumacher, M. Hirschi, S. I. Seneviratne, and L. Gudmundsson, 2023: Gap-filled multivariate observations of global land–climate interactions. *J. Geophys. Res. Atmos.*, **128**, e2023JD039099, https://doi.org/10.1029/2023JD039099.

Betts, R. A., C. D. Jones, J. R. Knight, R. F. Keeling, and J. J. Kennedy, 2016: El Niño and a record CO_2 rise. *Nat. Climate Change*, **6**, 806–810, https://doi.org/10.1038/nclimate3063.

Birkett, C., C. Reynolds, B. Beckley, and B. Doorn, 2011: From research to operations: The USDA global reservoir and lake monitor. Coastal Altimetry, S. Vignudelli et al., Eds., Springer, 19–50.

Bock, O., 2025: Global GNSS integrated water vapour data, 19942024. AERIS, accessed 15 July 2025, https://doi.org/10.25326/68.

—— , C. Mears, S. P. Ho, and S. Xi, 2024: Total column water vapor [in "State of the Climate in 2023"]. *Bull. Amer. Meteor. Soc.*, **105** (8), S57–S59, https://doi.org/10.1175/BAMS-D-24-0116.1.

Unauthenticated | Downloaded 11/21/25 11:34 AM UTC

Bodhaine, B. A., B. G. Mendonca, J. M. Harris, and J. M. Miller, 1981: Seasonal variations in aerosols and atmospheric transmission at Mauna Loa observatory. *J. Geophys. Res.*, **86**, 7395–7398, https://doi.org/10.1029/JC086iC08p07395.

Boone, C. D., P. F. Bernath, and M. D. Fromm, 2020: Pyrocumulonimbus stratospheric plume injections measured by the ACE-FTS. *Geophys. Res. Lett.*, **47**, e2020GL088442, https://doi.org/10.1029/2020GL088442.

Bowman, K. W., 2021a: TROPESS CrIS-JPSS1 L2 ammonia for forward stream, standard product V1. GES DISC, accessed 31 January 2025, https://doi.org/10.5067/7I3KMUCCJNEN.

——, 2021b: TROPESS CrIS-JPSS1 L2 peroxyacetyl nitrate for forward stream, standard product V. GES DISC, accessed 31 January 2025, https://doi.org/10.5067/W0W6L8M6J85X.

Brohan, P., J. J. Kennedy, I. Harris, S. F. Tett, and P. D. Jones, 2006: Uncertainty estimates in regional and global observed temperature changes: A new data set from 1850. *J. Geophys. Res.*, **111**, D12106, https://doi.org/10.1029/2005JD006548.

Brutsaert, W., 2017: Global land surface evaporation trend during the past half century: Corroboration by Clausius-Clapeyron scaling. *Adv. Water Resour.*, **106**, 3–5, https://doi.org/10.1016/j.advwatres.2016.08.014.

Burek, P., J. van der Knijff, and A. de Roo, 2013: LISFLOOD, distributed water balance and flood simulation model – Revised user manual 2013. Publications Office, 139 pp., https://doi.org/10.2788/24719.

Butchart, N., 2014: The Brewer-Dobson circulation. *Rev. Geophys.*, **52**, 157–184, https://doi.org/10.1002/2013RG000448.

Byrne, B., and Coauthors, 2024: Carbon emissions from the 2023 Canadian wildfires. *Nature*, **633**, 835–839, https://doi.org/10.1038/s41586-024-07878-z.

Caine, T. N. (Nel), J. F. Morse, and Niwot Ridge LTER, 2024: Lake ice clearance and formation data for Green Lakes Valley, 1968—Ongoing. Environmental Data Initiative, https://doi.org/10.6073/PASTA/947534B780396B2E79D2206C98640262.

Campos, D., and R. Rondanelli, 2023: ENSO-related precipitation variability in Central Chile: The role of large scale moisture transport. *J. Geophys. Res. Atmos.*, **128**, e2023JD038671, https://doi.org/10.1029/2023JD038671.

CAMS, 2024: CAMS Global wildfires review 2024: A harsh year for the Americas. https://atmosphere.copernicus.eu/cams-global-wildfires-review-2024-harsh-year-americas.

Capotondi, A., and Coauthors, 2015: Understanding ENSO diversity. *Bull. Amer. Meteor. Soc.*, **96**, 921–938, https://doi.org/10.1175/BAMS-D-13-00117.1.

Cappucci, F., N. Gobron, and G. Duveiller, 2024: Land surface properties: Terrestrial surface albedo dynamics [in "State of the Climate in 2023"]. *Bull. Amer. Meteor. Soc.*, **105** (8), S12–S155, https://doi.org/10.1175/BAMS-D-24-0116.1.

Carrea, L., O. Embury, and C. J. Merchant, 2015: Datasets related to in-land water for limnology and remote sensing applications: Distance-to-land, distance-to-water, water-body identifier and lake-Centre co-ordinates. *Geosci. Data J.*, **2**, 83–97, https://doi.org/10.1002/gdj3.32.

——, and Coauthors, 2019: Lake surface temperature [in "State of the Climate in 2018"]. *Bull. Amer. Meteor. Soc.*, **100** (8), S13–S14, https://doi.org/10.1175/2019BAMSStateoftheClimate.1.

——, and Coauthors, 2020: Lake surface temperature [in "State of the Climate in 2019"]. *Bull. Amer. Meteor. Soc.*, **101** (8), S26–S28, https://doi.org/10.1175/BAMS-D-20-0104.1.

——, and Coauthors, 2021: Lake surface water temperature [in "State of the Climate in 2020"]. *Bull. Amer. Meteor. Soc.*, **102** (8), S28–S31, https://doi.org/10.1175/BAMS-D-21-0098.1.

——, and Coauthors, 2022a: Lake surface water temperature [in "State of the Climate in 2021"]. *Bull. Amer. Meteor. Soc.*, **103** (8), S28–S30, https://doi.org/10.1175/BAMS-D-22-0092.1.

——, and Coauthors, 2022b: ESA Lakes climate change initiative (Lakes_cci): Lake products, version 2.0.2. NERC EDS Centre for Environmental Data Analysis, accessed 6 July 2022, https://doi.org/10.5285/a07deacaffb8453e93d57ee214676304.

——, and Coauthors, 2023a: Satellite-derived multivariate worldwide lake physical variable timeseries for climate studies. *Sci. Data*, **10**, 30, https://doi.org/10.1038/s41597-022-01889-z.

——, and Coauthors, 2023b: Lake surface temperature [in "State of the Climate in 2022"]. *Bull. Amer. Meteor. Soc.*, **104** (9), S1–S516, https://doi.org/10.1175/2023BAMSStateoftheClimate.1.

——, and Coauthors, 2024: Lake surface temperature [in "State of the Climate in 2023"]. *Bull. Amer. Meteor. Soc.*, **105** (8), S1–S484, https://doi.org/10.1175/2024BAMSStateoftheClimate.1.

Cassidy, E., 2024: Typhoons line up in the western Pacific. NASA Earth Observatory, https://earthobservatory.nasa.gov/images/153575/typhoons-line-up-in-the-western-pacific.

Cattiaux, J., A. Ribes, and E. Cariou, 2024: How extreme were daily global temperatures in 2023 and early 2024? *Geophys. Res. Lett.*, **51**, e2024GL110531, https://doi.org/10.1029/2024GL110531.

Chandra, S., E. K. Suenaga, F. Scordo, and T. A. Daniel, 2023: Mountain Lake Chemistry and physics profile data since 2015 at Castle Lake. Environmental Data Initiative, accessed 5 February 2025, https://doi.org/10.6073/PASTA/72811937CB436A198EC9B10483EDC2A4.

Chang, K. L., M. G. Schultz, X. Lan, A. McClure-Begley, I. Petropavlovskikh, X. Xu, and J. R. Ziemke, 2021: Trend detection of atmospheric time series: Incorporating appropriate uncertainty estimates and handling extreme events. *Elementa*, **9**, 00035, https://doi.org/10.1525/elementa.2021.00035.

——, and Coauthors, 2023: Diverging ozone trends above western North America: Boundary layer decreases versus free tropospheric increases. *J. Geophys. Res. Atmos.*, **128**, e2022JD038090, https://doi.org/10.1029/2022JD038090.

——, O. R. Cooper, A. Gaudel, I. Petropavlovskikh, P. Effertz, G. Morris, and B. C. McDonald, 2024: Technical note: Challenges in detecting free tropospheric ozone trends in a sparsely sampled environment. *Atmos. Chem. Phys.*, **24**, 6197–6218, https://doi.org/10.5194/acp-24-6197-2024.

Cheng, L., and Coauthors, 2025: Record high temperatures in the ocean in 2024. *Adv. Atmos. Sci.*, **42**, 1092–1109, https://doi.org/10.1007/s00376-025-4541-3.

Choulga, M., F. Moschini, C. Mazzetti, S. Grimaldi, J. Disperati, H. Beck, P. Salamon, and C. Prudhomme, 2024: Technical note: Surface fields for global environmental modelling. *Hydrol. Earth Syst. Sci.*, **28**, 2991–3036, https://doi.org/10.5194/hess-28-2991-2024.

Christy, J. R., 2017: Lower and mid-tropospheric temperature [in "State of the Climate in 2016"]. *Bull. Amer. Meteor. Soc.*, **98** (8), S16–S17, https://doi.org/10.1175/2017BAMSStateoftheClimate.1.

Unauthenticated | Downloaded 11/21/25 11:34 AM UTC

Chung, E., B. Soden, and V. O. John, 2013: Intercalibrating microwave satellite observations for monitoring long-term variations in upper- and midtropospheric water vapor. *J. Atmos. Oceanic Technol.*, **30**, 2303–2319, https://doi.org/10.1175/JTECH-D-13-00001.1.

—— , —— , B. J. Sohn, and L. Shi, 2014: Upper-tropospheric moistening in response to anthropogenic warming. *Proc. Natl. Acad. Sci. USA*, **111** (32) 11636-11641, https://doi.org/10.1073/pnas.1409659111.

—— , —— , X. Huang, L. Shi, and V. O. John, 2016: An assessment of the consistency between satellite measurements of upper tropospheric water vapor. *J. Geophys. Res. Atmos.*, **121**, 2874–2887, https://doi.org/10.1002/2015JD024496.

Ciasto, L., and A. Butler, 2024: And that's a wrap on this season's stratospheric polar vortex. NOAA, https://www.climate.gov/news-features/blogs/polar-vortex/and-thats-wrap-seasons-stratospheric-polar-vortex.

Cicoira, A., J. Beutel, J. Faillettaz, and A. Vieli, 2019: Water controls the seasonal rhythm of rock glacier flow. *Earth Planet. Sci. Lett.*, **528**, 115844, https://doi.org/10.1016/j.epsl.2019.115844.

Climate.gov, 2024: Multi-year drought and heat waves across Mexico. NOAA, accessed 1 February 2025, https://www.climate.gov/news-features/event-tracker/multi-year-drought-and-heat-waves-across-mexico-2024.

Cooper, O. R., J. R. Ziemke, and K.-L. Chang, 2024a: Tropospheric ozone [in "State of the Climate in 2023"]. *Bull. Amer. Meteor. Soc.*, **105** (8), S94–S96, https://doi.org/10.1175/BAMS-D-24-0116.1.

—— , and Coauthors, 2024b: Early season 2023 wildfires generated record-breaking surface ozone anomalies across the U.S. Upper Midwest. *Geophys. Res. Lett.*, **51**, e2024GL111481, https://doi.org/10.1029/2024GL111481.

Cornes, R. C., and R. Junod, 2024: Night marine air temperature [in "State of the Climate in 2023"]. *Bull. Amer. Meteor. Soc.*, **105** (8), S35–S37, https://doi.org/10.1175/2024BAMSStateoftheClimate.1.

—— , E. C. Kent, D. I. Berry, and J. J. Kennedy, 2020: CLASSnmat: A global night marine air temperature data set, 1880–2019. *Geosci. Data J.*, **7**, 170–184, https://doi.org/10.1002/gdj3.100.

—— , T. Cropper, R. Junod, and E. C. Kent, 2023: Night marine air temperature [in "State of the Climate in 2022"]. *Bull. Amer. Meteor. Soc.*, **104** (9), S31–S32, https://doi.org/10.1175/2023BAMSStateoftheClimate.1.

Crimmins, T. M., R. L. Marsh, J. Switzer, M. A. Crimmins, K. L. Gerst, A. H. Rosemartin, and J. F. Weltzin, 2017: USA National Phenology Network gridded products documentation. USGS Open-File Rep. 2017-1003, 34 pp., https://doi.org/10.3133/ofr20171003.

—— , E. G. Denny, E. E. Posthumus, A. H. Rosemartin, R. Croll, M. Montano, and H. Panci, 2022: Science and management advancements made possible by the USA National Phenology Network's nature's notebook platform. *BioScience*, **72**, 908–920, https://doi.org/10.1093/biosci/biac061.

Cusicanqui, D., P. Lacroix, X. Bodin, B. A. Robson, A. Kääb, and S. MacDonell, 2024: Detection and reconstruction of rock glaciers kinematic over 24 years (2000-2024) from Landsat imagery. EGUsphere, https://doi.org/10.5194/egusphere-2024-2393.

Daniel, J. S., S. Solomon, and D. L. Albritton, 1995: On the evaluation of halocarbon radiative forcing and global warming potentials. *J. Geophys. Res.*, **100**, 1271–1285, https://doi.org/10.1029/94JD02516.

Davidson, E. A., 2009: The contribution of manure and fertilizer nitrogen to atmospheric nitrous oxide since 1860. *Nat. Geosci.*, **2**, 659–662, https://doi.org/10.1038/ngeo608.

Davies, B., and Coauthors, 2024: Accelerating glacier volume loss on Juneau icefield driven by hypsometry and melt-accelerating feedbacks. *Nat. Commun.*, **15**, 5099, https://doi.org/10.1038/s41467-024-49269-y.

Davis, S. M., and Coauthors, 2016: The Stratospheric Water and Ozone Satellite Homogenized (SWOOSH) database: A long-term database for climate studies. *Earth Syst. Sci. Data*, **8**, 461–490, https://doi.org/10.5194/essd-8-461-2016.

—— , K. Rosenlof, E. Asher, H. Vömel, R. Stauffer, and D. Hurst, 2024: Stratospheric water vapor [in "State of the Climate in 2023"]. *Bull. Amer. Meteor. Soc.*, **105** (8), S101–S103, https://doi.org/10.1175/BAMS-D-24-0116.1.

Deeter, M. N., and Coauthors, 2014: The MOPITT version 6 product: Algorithm enhancements and validation. *Atmos. Meas. Tech.*, **7**, 3623–3632, https://doi.org/10.5194/amt-7-3623-2014.

—— , D. P. Edwards, G. L. Francis, J. C. Gille, S. Martínez-Alonso, H. M. Worden, and C. Sweeney, 2017: A climate-scale satellite record for carbon monoxide: The MOPITT version 7 product. *Atmos. Meas. Tech.*, **10**, 2533–2555, https://doi.org/10.5194/amt-10-2533-2017.

—— , and Coauthors, 2019: Radiance-based retrieval bias mitigation for the MOPITT instrument: The version 8 product. *Atmos. Meas. Tech.*, **12**, 4561–4580, https://doi.org/10.5194/amt-12-4561-2019.

de Laat, A. T. J., N. Andela, M. Forkel, V. Huijnen, D. Kinalzcyzk, and D. van Wees, 2025: Sentinel-5p reveals unexplained large wildfire carbon emissions in the Amazon in 2024. ESS Open Archive, https://doi.org/10.22541/essoar.173869416.69575859/v1.

de Pablo, M. A., M. Ramos, G. Vieira, A. Molina, R. Ramos, C. N. Maior, M. Prieto, and J. Ruiz-Fernández, 2024: Interannual variability of ground surface thermal regimes in Livingston and deception islands, Antarctica (2007–2021). Land Degrad. *Dev.*, **35**, 378–393, https://doi.org/10.1002/ldr.4922.

Dijk, V., and Coauthors, 2025: Global Water Monitor 2024 summary report. Global Water Monitor Consortium, 57 pp., https://www.globalwater.online/globalwater/report/#gallery.

Dlugokencky, E. J., L. P. Steele, P. M. Lang, and K. A. Masarie, 1994: The growth rate and distribution of atmospheric methane. *J. Geophys. Res.*, **99**, 17021–17043, https://doi.org/10.1029/94JD01245.

Dodangodage, R., P. F. Bernath, M. Wyatt, and C. Boone, 2025: Atmospheric chemistry experiment (ACE) satellite observations of aerosols and SO_2 emissions from the 2024 Ruang volcanic eruption. *J. Quant. Spectrosc. Radiat. Transfer*, **333**, 109333, https://doi.org/10.1016/j.jqsrt.2024.109333.

Domeisen, D. I. V., C. I. Garfinkel, and A. H. Butler, 2019: The teleconnection of El Niño Southern Oscillation to the stratosphere. *Rev. Geophys.*, **57**, 5–47, https://doi.org/10.1029/2018RG000596.

Donat, M. G., L. V. Alexander, H. Yang, I. Durre, R. Vose, and J. Caesar, 2013: Global Land-Based datasets for monitoring climatic extremes. *Bull. Amer. Meteor. Soc.*, **94**, 997–1006, https://doi.org/10.1175/BAMS-D-12-00109.1.

Dorigo, W., W. Preimesberger, C. Reimer, R. Van der Schalie, A. Pasik, R. De Jeu, and C. Paulik, 2025: Soil moisture gridded data from 1978 to present, v202312.0.0. Copernicus Climate Change Service (C3S) Climate Data Store (CDS), accessed 10 February 2025, https://doi.org/10.24381/cds.d7782f18.

Unauthenticated | Downloaded 11/21/25 11:34 AM UTC

Dudok de Wit, T., G. Kopp, C. Fröhlich, and M. Schöll, 2017: Methodology to create a new total solar irradiance record: Making a composite out of multiple data records. *Geophys. Res. Lett.*, **44**, 1196–1203, https://doi.org/10.1002/2016GL071866.

Duncan, B. N., L. N. Lamsal, A. M. Thompson, Y. Yoshida, Z. Lu, D. G. Streets, M. M. Hurwitz, and K. E. Pickering, 2016: A space-based, high-resolution view of notable changes in urban NO_x pollution around the world (2005–2014). J. Geophys. *Res. Atmos.*, **121**, 976–996, https://doi.org/10.1002/2015JD024121.

Dunn, R. J., 2019: HadISD version 3: Monthly updates. Hadley Centre Tech. Note 103, 10 pp., https://www.metoffice.gov.uk/research/library-and-archive/publications/science/climate-science-technical-notes.

——, K. M. Willett, P. W. Thorne, E. V. Woolley, I. Durre, A. Dai, D. E. Parker, and R. S. Vose, 2012: HadISD: A quality-controlled global synoptic report database for selected variables at long-term stations from 1973–2011. *Climate Past*, **8**, 1649–1679, https://doi.org/10.5194/cp-8-1649-2012.

——, ——, D. E. Parker, and L. Mitchell, 2016: Expanding HadISD: Quality-controlled, sub-daily station data from 1931. *Geosci. Instrum. Method Data Syst.*, **5**, 473–491, https://doi.org/10.5194/gi-5-473-2016.

——, C. Azorin-Molina, M. J. Menne, Z. Zeng, N. W. Casey, and C. Shen, 2022a: Reduction in reversal of global stilling arising from correction to encoding of calm periods. *Environ. Res. Commun.*, **4**, 061003, https://doi.org/10.1088/2515-7620/ac770a.

——, M. G. Donat, and L. V. Alexander, 2022b: Comparing extremes indices in recent observational and reanalysis products. *Front. Climate*, **4**, 989505, https://doi.org/10.3389/fclim.2022.989505.

Dunn, R. J. H., and C. P. Morice, 2022: On the effect of reference periods on trends in percentile-based extreme temperature indices. *Environ. Res. Lett.*, **17**, 034026, https://doi.org/10.1088/1748-9326/ac52c8.

——, and Coauthors, 2020: Development of an updated global land in situ–based data set of temperature and precipitation extremes: HadEX3. *J. Geophys. Res. Atmos.*, **125**, e2019JD032263, https://doi.org/10.1029/2019JD032263.

——, M. G. Donat, R. W. Schlegel, and M. G. Bosilovich, 2024a: Surface temperature extremes [in "State of the Climate in 2023"]. *Bull. Amer. Meteor. Soc.*, **105** (8), S37–S39, https://doi.org/10.1175/BAMS-D-24-0116.1.

——, and Coauthors, 2024b: Observed global changes in sector-relevant climate extremes indices—An extension to HadEX3. *Earth Space Sci.*, **11**, e2023EA003279, https://doi.org/10.1029/2023EA003279.

Duveiller, G., and N. Gobron, 2023: Land surface properties: Terrestrial surface albedo dynamics [in "State of the Climate in 2022"]. *Bull. Amer. Meteor. Soc.*, **104** (9), S102–S103, https://doi.org/10.1175/BAMS-D-23-0090.1.

DW, 2024: Pakistan: Lahore records heaviest rainfall in years. Accessed 13 February 2025, https://www.dw.com/en/pakistan-lahore-records-heaviest-rainfall-in-years/a-69829897.

ECMWF, 2025: Global Climate Highlights 2024. Climate Copernicus, accessed 13 February 2025, https://climate.copernicus.eu/global-climate-highlights-2024.

Edwards, M., and A. Richardson, 2004: Impact of climate change on marine pelagic phenology and trophic mismatch. *Nature*, **430**, 881–884, https://doi.org/10.1038/nature02808.

Ellis, H. T., and R. F. Pueschel, 1971: Solar radiation: Absence of air pollution trends at Mauna Loa. *Science*, **172**, 845–846, https://doi.org/10.1126/science.172.3985.845.

Elshorbany, Y., and Coauthors, 2024: Tropospheric ozone precursors: Global and regional distributions, trends, and variability. *Atmos. Chem. Phys.*, **24**, 12 225–12 257, https://doi.org/10.5194/acp-24-12225-2024.

Elson, P., and Coauthors, 2022: SciTools/cartopy: v0.21.1 (v0.21.1). Zenodo, https://doi.org/10.5281/zenodo.7430317.

Estilow, T. W., A. H. Young, and D. A. Robinson, 2015: A long-term Northern Hemisphere snow cover extent data record for climate studies and monitoring. *Earth Syst. Sci. Data*, **7**, 137–142, https://doi.org/10.5194/essd-7-137-2015.

Etheridge, D. M., L. P. Steele, R. L. Langenfelds, R. J. Francey, J. M. Barnola, and V. I. Morgan, 1996: Natural and anthropogenic changes in atmospheric CO_2 over the last 1000 years from air in Antarctic ice and firn. *J. Geophys. Res.*, **101**, 4115–4128, https://doi.org/10.1029/95JD03410.

Etzelmüller, B., and Coauthors, 2020: Twenty years of European Mountain permafrost dynamics—The PACE legacy. *Environ. Res. Lett.*, **15**, 104070, https://doi.org/10.1088/1748-9326/abae9d.

——, K. Isaksen, J. Czekirda, S. Westermann, C. Hilbich, and C. Hauck, 2023: Rapid warming and degradation of Mountain permafrost in Norway and Iceland. *Cryosphere*, **17**, 5477–5497, https://doi.org/10.5194/tc-17-5477-2023.

EUMETSAT, 2023: Animations from Europe's first lightning imager. https://www.eumetsat.int/features/animations-europes-first-lightning-imager.

——, 2024: MTG lightning imager data available. https://user.eumetsat.int/news-events/news/mtg-lightning-imager-li-level-2-data-available.

Feng, L., P. I. Palmer, S. Zhu, R. J. Parker, and Y. Liu, 2022: Tropical methane emissions explain large fraction of recent changes in global atmospheric methane growth rate. *Nat. Commun.*, **13**, 1378, https://doi.org/10.1038/s41467-022-28989-z.

Feng, Y., and Coauthors, 2022: Decadal lake volume changes (2003–2020) and driving forces at a global scale. *Remote Sens.*, **14**, 1032, https://doi.org/10.3390/rs14041032.

Feron, S., and Coauthors, 2024: South America is becoming warmer, drier, and more flammable. *Commun. Earth Environ.*, **5**, 501, https://doi.org/10.1038/s43247-024-01654-7.

Finlay, C. C., C. Kloss, N. Olsen, M. D. Hammer, L. Tøffner-Clausen, A. Grayver, and A. Kuvshinov, 2020: The CHAOS-7 geomagnetic field model and observed changes in the South Atlantic anomaly. *Earth Planets Space*, **72**, 156, https://doi.org/10.1186/s40623-020-01252-9.

Fischer, E. V., and Coauthors, 2014: Atmospheric peroxyacetyl nitrate (PAN): A global budget and source attribution. *Atmos. Chem. Phys.*, **14**, 2679–2698, https://doi.org/10.5194/acp-14-2679-2014.

Fisher, J. B., and Coauthors, 2020: ECOSTRESS: NASA's next generation mission to measure evapotranspiration from the international space station. *Water Resour. Res.*, **56**, e2019WR026058, https://doi.org/10.1029/2019WR026058.

Fleming, E. L., P. A. Newman, Q. Liang, and L. D. Oman, 2024: Stratospheric temperature and ozone impacts of the hunga Tonga-hunga Ha'apai water vapor injection. *J. Geophys. Res. Atmos.*, **129**, e2023JD039298, https://doi.org/10.1029/2023JD039298.

Fogt, R. L., and G. J. Marshall, 2020: The Southern annular mode: Variability, trends, and climate impacts across the Southern Hemisphere. *Wiley Interdiscip. Rev.: Climate Change*, **11**, e652, https://doi.org/10.1002/wcc.652.

Unauthenticated | Downloaded 11/21/25 11:34 AM UTC

Folland, C. K., J. Knight, H. W. Linderholm, D. Fereday, S. Ineson, and J. W. Hurrell, 2009: The summer North Atlantic oscillation: Past, present, and future. *J. Climate*, **22**, 1082–1103, https://doi.org/10.1175/2008JCLI2459.1.

Forster, P., and Coauthors, 2021: The Earth's energy budget, climate feedbacks, and climate sensitivity. *Climate Change 2021: The Physical Science Basis*, V. Masson-Delmotte et al., Eds., Cambridge University Press, 923–1054, https://doi.org/10.1017/9781009157896.009.

Forster, P. M., and Coauthors, 2023: Indicators of global climate change 2022: Annual update of large-scale indicators of the state of the climate system and human influence. *Earth Syst. Sci. Data*, **15**, 2295–2327, https://doi.org/10.5194/essd-15-2295-2023.

—— ., and Coauthors, 2024: Indicators of global climate change 2023: Annual update of key indicators of the state of the climate system and human influence. *Earth Syst. Sci. Data*, **16**, 2625–2658, https://doi.org/10.5194/essd-16-2625-2024.

Foster, M. J., C. Phillips, A. K. Heidinger, E. E. Borbas, Y. Li, W. P. Menzel, A. Walther, and E. Weisz, 2023: PATMOS-x version 6.0: 40 years of merged AVHRR and HIRS global cloud data. *J. Climate*, **36**, 1143–1160, https://doi.org/10.1175/JCLI-D-22-0147.1.

Free, M., D. J. Seidel, J. K. Angel, J. Lanzante, I. Durre, and T. C. Peterson, 2005: Radiosonde atmospheric temperature products for assessing climate (RATPAC): A new data set of large-area anomaly time series. *J. Geophys. Res.*, **110**, D22101, https://doi.org/10.1029/2005JD006169.

Friedlingstein, P., and Coauthors, 2025: Global Carbon Budget 2024. *Earth Syst. Sci. Data*, **17**, 965–1039, https://doi.org/10.5194/essd-17-965-2025.

Frost, G. V., and Coauthors, 2024: NOAA Arctic Report Card 2024: Tundra greenness. NOAA Tech. Rep. OAR ARC 24-09, 9 pp., https://doi.org/10.25923/5t2g-fm41.

Füllekrug, M., E. Williams, and C. Price, 2002: Intense oceanic lightning. *Ann. Geophys.*, **20**, 133–137, https://doi.org/10.5194/angeo-20-133-2002.

——, ——, ——, S. Goodman, R. Holzworth, K. Virts, and D. Buechler, 2022: Sidebar 2.1: Lightning [in "State of the Climate in 2021"]. *Bull. Amer. Meteor. Soc.*, **103** (8), S79, https://doi.org/10.1175/2022BAMSStateoftheClimate.1.

Gao, R. S., and Coauthors, 2016: A light-weight, high-sensitivity particle spectrometer for $PM_{2.5}$ aerosol measurements. *Aerosol Sci. Technol.*, **50**, 88–99, https://doi.org/10.1080/02786826.2015.1131809.

Garfinkel, C. I., and Coauthors, 2021: Influence of the El Niño–Southern Oscillation on entry stratospheric water vapor in coupled chemistry–ocean CCMI and CMIP6 models. *Atmos. Chem. Phys.*, **21**, 3725–3740, https://doi.org/10.5194/acp-21-3725-2021.

Garreaud, R., and Coauthors, 2025: Hyperdroughts in central Chile: Drivers, impacts and projections. EGUsphere, https://doi.org/10.5194/egusphere-2025-517.

Garreaud, R. D., J. P. Boisier, R. Rondanelli, A. Montecinos, H. H. Sepúlveda, and D. Veloso-Aguila, 2020: The central Chile mega drought (2010–2018): A climate dynamics perspective. *Int. J. Climatol.*, **40**, 421–439, https://doi.org/10.1002/joc.6219.

Gaudel, A., and Coauthors, 2018: Tropospheric ozone assessment report: Present-day distribution and trends of tropospheric ozone relevant to climate and global atmospheric chemistry model evaluation. *Elementa*, **6**, 39, https://doi.org/10.1525/elementa.291.

GCOS, 2022: The 2022 Global Climate Observing System (GCOS) implementation plan. WMO GCOS-244, 98 pp., https://gcos.wmo.int/en/publications/gcos-implementation-plan2022.

Gelaro, R., and Coauthors, 2017: The Modern-Era Retrospective Analysis for Research and Applications, version 2 (MERRA-2). J. Climate, **30**, 5419–5454, https://doi.org/10.1175/JCLI-D-16-0758.1.

Getirana, A., S. Kumar, M. Girotto, and M. Rodell, 2017: Rivers and floodplains as key components of global terrestrial water storage variability. *Geophys. Res. Lett.*, **44**, 10 359–10 310, https://doi.org/10.1002/2017GL074684.

Gettelman, A., and Coauthors, 2024: Has reducing ship emissions brought forward global warming? *Geophys. Res. Lett.*, **51**, e2024GL109077, https://doi.org/10.1029/2024GL109077.

Ghent, D. J., J. S. Anand, K. Veal, and J. J. Remedios, 2024: The operational and climate land surface temperature products from the sea and land surface temperature radiometers on Sentinel-3A and 3B. Remote Sens., **16**, 3403, https://doi.org/10.3390/rs16183403.

Giglio, L., W. Schroeder, and C. O. Justice, 2016: The Collection 6 MODIS active fire detection algorithm and fire products. *Remote Sens. Environ.*, **178**, 31–41, https://doi.org/10.1016/j.rse.2016.02.054.

GISTEMP Team, 2025: GISS Surface Temperature Analysis (GISTEMP), version 4. NASA Goddard Institute for Space Studies, accessed 20 January 2025, https://data.giss.nasa.gov/gistemp/.

Gobron, N., B. Belward, P. Pinty, and W. Knorr, 2010: Monitoring biosphere vegetation 1998–2009. *Geophys. Res. Lett.*, **37**, L15402, https://doi.org/10.1029/2010GL043870.

—— , and Coauthors, 2022: Evaluation of Sentinel-3A and Sentinel-3B ocean land colour instrument green instantaneous fraction of absorbed photosynthetically active radiation. *Remote Sens. Environ.*, **270**, 112850, https://doi.org/10.1016/j.rse.2021.112850.

Goessling, H. F., T. Rackow, and T. Jung, 2025: Recent global temperature surge intensified by record-low planetary albedo. *Science*, **387**, 68–73, https://doi.org/10.1126/science.adq7280.

Good, E. J., 2016: An in situ–based analysis of the relationship between land surface "skin" and screen-level air temperatures. *J. Geophys. Res. Atmos.*, **121**, 8801–8819, https://doi.org/10.1002/2016JD025318.

—— , D. J. Ghent, C. E. Bulgin, and J. J. Remedios, 2017: A spatio-temporal analysis of the relationship between near-surface air temperature and satellite land surface temperatures using 17 years of data from the ATSR series. *J. Geophys. Res. Atmos.*, **122**, 9185–9210, https://doi.org/10.1002/2017JD026880.

—— , F. M. Aldred, D. J. Ghent, K. L. Veal, and C. Jimenez, 2022: An analysis of the stability and trends in the LST_cci land surface temperature datasets over Europe. *Earth Space Sci.*, **9**, e2022EA002317, https://doi.org/10.1029/2022EA002317.

Granier, C., and Coauthors, 2011: Evolution of anthropogenic and biomass burning emissions of air pollutants at global and regional scales during the 1980–2010 period. *Climatic Change*, **109**, 163–190, https://doi.org/10.1007/s10584-011-0154-1.

Gruber, A., W. A. Dorigo, W. Crow, and W. Wagner, 2017: Triple Collocation-Based merging of satellite soil moisture retrievals. *IEEE Trans. Geosci. Remote Sens.*, **55**, 6780–6792, https://doi.org/10.1109/TGRS.2017.2734070.

—— , T. Scanlon, R. van der Schalie, W. Wagner, and W. Dorigo, 2019: Evolution of the ESA CCI soil moisture climate data records and their underlying merging methodology. *Earth Syst. Sci. Data*, **11**, 717–739, https://doi.org/10.5194/essd-11-717-2019.

Unauthenticated | Downloaded 11/21/25 11:34 AM UTC

Gulev, S. K., and Coauthors, 2021: Changing state of the climate system. Climate Change 2021: The Physical Science Basis, V. Masson-Delmotte et al., Eds., Cambridge University Press, 287–422, https://doi.org/10.1017/9781009157896.004.

Gyawali, M. S., and Coauthors, 2023: Tracking NO_2 pollution changes over Texas: Synthesis of in situ and satellite observations. *J. Geophys. Res. Atmos.*, **128**, e2022JD037473, https://doi.org/10.1029/2022JD037473.

Haimberger, L., C. Tavolato, and S. Sperka, 2012: Homogenization of the global radiosonde temperature dataset through combined comparison with reanalysis background series and neighboring stations. *J. Climate*, **25**, 8108–8131, https://doi.org/10.1175/JCLI-D-11-00668.1.

Han, Y., Q. Lin, S. Huang, C. Du, J. Shen, and K. Zhang, 2024: Human impacts dominate global loss of lake ecosystem resilience. *Geophys. Res. Lett.*, **51**, e2024GL109298, https://doi.org/10.1029/2024GL109298.

Hansen, J., R. Ruedy, M. Sato, and K. Lo, 2010: Global surface temperature change. *Rev. Geophys.*, **48**, RG4004, https://doi.org/10.1029/2010RG000345.

Harris, I., T. J. Osborn, P. D. Jones, and D. H. Lister, 2020: Version 4 of the CRU TS monthly high-resolution gridded multivariate climate dataset. *Sci. Data*, **7**, 109, https://doi.org/10.1038/s41597-020-0453-3.

Hassan, T., R. Gulzar, M. Hamid, R. Ahmad, S. A. Waza, and A. A. Khuroo, 2024: Plant phenology shifts under climate warming: A systematic review of recent scientific literature. *Environ. Monit. Assess.*, **196**, 36, https://doi.org/10.1007/s10661-023-12190-w

Hattersley, R., and Coauthors, 2023: SciTools/iris: v3.7.0 (v3.7.0). Zenodo, https://doi.org/10.5281/zenodo.8305232.

He, J., and Coauthors, 2024: COVID-19 perturbation on US air quality and human health impact assessment. *PNAS Nexus*, **3**, pgad483, https://doi.org/10.1093/pnasnexus/pgad483.

Hersbach, H., and Coauthors, 2020: The ERA5 global reanalysis. *Quart. J. Roy. Meteor. Soc.*, **146**, 1999–2049, https://doi.org/10.1002/qj.3803.

Hirschi, M., and Coauthors, 2024: Soil moisture [in "State of the Climate in 2023"]. *Bull. Amer. Meteor. Soc.*, **105** (8), Si–S484, https://doi.org/10.1175/2024BAMSStateoftheClimate.1.

Ho, S.-P., and Coauthors, 2020: The COSMIC/FORMOSAT-3 radio occultation mission after 12 years: Accomplishments, remaining challenges, and potential impacts of COSMIC-2. *Bul. Amer. Meteor. Sci.*, **101**, E1107–E1136, https://doi.org/10.1175/BAMS-D-18-0290.1.

Hodnebrog, Ø., and Coauthors, 2020a: Updated global warming potentials and radiative efficiencies of halocarbons and other weak atmospheric absorbers. *Rev. Geophys.*, **58**, e2019RG000691, https://doi.org/10.1029/2019RG000691.

——, and Coauthors, 2020b: The effect of rapid adjustments to halocarbons and N_2O on radiative forcing. *npj Climate Atmos. Sci.*, **3**, 43, https://doi.org/10.1038/s41612-020-00150-x.

Hoell, A., C. Funk, J. Zinke, and L. Harrison, 2017: Modulation of the southern Africa precipitation response to the El Niño Southern Oscillation by the subtropical Indian Ocean dipole. *Climate Dyn.*, **48**, 2529–2540, https://doi.org/10.1007/s00382-016-3220-6.

Hofmann, D. J., J. H. Butler, E. J. Dlugokencky, J. W. Elkins, K. Masarie, S. A. Montzka, and P. Tans, 2006: The role of carbon dioxide in climate forcing from 1979 to 2004: Introduction of the annual greenhouse gas index. *Tellus*, **58B**, 614–619, https://doi.org/10.1111/j.1600-0889.2006.00201.x.

Holzworth, R. H., M. P. McCarthy, J. B. Brundell, A. R. Jacobson, and C. J. Rodger, 2019: Global distribution of superbolts. *J. Geophys. Res. Atmos.*, **124**, 9996–10 005, https://doi.org/10.1029/2019JD030975.

——, J. B. Brundell, M. P. McCarthy, A. R. Jacobson, C. J. Rodger, and T. S. Anderson, 2021: Lightning in the Arctic. *Geophys. Res. Lett.*, **48**, e2020GL091366, https://doi.org/10.1029/2020GL091366.

Hou, J., A. I. J. M. Van Dijk, L. J. Renzullo, and P. R. Larraondo, 2024: GloLakes: Water storage dynamics for 27 000 Lakes globally from 1984 to present derived from satellite altimetry and optical imaging. *Earth Syst. Sci. Data*, **16**, 201–218, https://doi.org/10.5194/essd-16-201-2024.

Hrbáček, F., and Coauthors, 2023: Active layer and permafrost thermal regimes in the ice-free areas of Antarctica. *Earth-Sci. Rev.*, **242**, 104458, https://doi.org/10.1016/j.earscirev.2023.104458.

Hu, G., and Coauthors, 2024: Spatiotemporal characteristics and variability in the thermal state of permafrost on the Qinghai–Tibet Plateau. *Permafrost Periglacial Processes*, **35**, 143–156, https://doi.org/10.1002/ppp.2219.

Hu, Y., and Coauthors, 2025: Rock glacier velocity: An essential climate variable quantity for permafrost. *Rev. Geophys.*, **63**, e2024RG000847, https://doi.org/10.1029/2024RG000847.

Huang, X., K. Yang, S. Kondragunta, Z. Wei, L. Valin, J. Szykman, and M. Goldberg, 2022: NO_2 retrievals from NOAA-20 OMPS: Algorithm, evaluation, and observations of drastic changes during COVID-19. *Atmos. Environ.*, **290**, 119367, https://doi.org/10.1016/j.atmosenv.2022.119367.

Huffman, G. J., R. Adler, A. Behrangi, D. Bolvin, E. Nelkin, G. Gu, and M. Ehsani, 2023: The new version 3.2 Global Precipitation Climatology Project (GPCP) Monthly and Daily precipitation products. *J. Climate*, **36**, 7635–7655, https://doi.org/10.1175/JCLI-D-23-0123.1.

Hunter, J. D., 2007: Matplotlib: A 2D graphics environment. *Comput. Sci. Eng.*, **9**, 90–95, https://doi.org/10.1109/MCSE.2007.55.

Hurst, D. F., S. J. Oltmans, H. Vömel, K. H. Rosenlof, S. M. Davis, E. A. Ray, E. G. Hall, and A. F. Jordan, 2011: Stratospheric water vapor trends over boulder, Colorado: Analysis of the 30 year boulder record. *J. Geophys. Res.*, **116**, D02306, https://doi.org/10.1029/2010JD015065.

Ingram, W., 2010: A very simple model for the water vapour feedback on climate change. *Quart. J. Roy. Meteor. Soc.*, **136**, 30–40, https://doi.org/10.1002/qj.546.

Inness, A., and Coauthors, 2019: The CAMS reanalysis of atmospheric composition. *Atmos. Chem. Phys.*, **19**, 3515–3556, https://doi.org/10.5194/acp-19-3515-2019.

IPCC, 2013: *Climate Change 2013: The Physical Science Basis.* T. F. Stocker et al., Eds., Cambridge University Press, 1535 pp.

——, 2021: Annex VII: Glossary. *Climate Change 2021: The Physical Science Basis*, V. Masson-Delmotte et al., Eds., Cambridge University Press, 2215–2256, https://doi.org/10.1017/9781009157896.022.

Isaksen, K., and Coauthors, 2022: Exceptional warming over the Barents area. *Sci. Rep.*, **12**, 9371, https://doi.org/10.1038/s41598-022-13568-5.

Jacobs, N. A., 2021: Open innovation and the case for community model development. *Bull. Amer. Meteor. Soc.*, **102**, E2002–E2011, https://doi.org/10.1175/BAMS-D-21-0030.1.

Unauthenticated | Downloaded 11/21/25 11:34 AM UTC

Jasinski, M. F., and Coauthors, 2023: ATLAS/ICESat-2 L3A along track inland surface water data, version 6. NASA National Snow and Ice Data Center Distributed Active Archive Center, accessed 31 December 2024, https://doi.org/10.5067/ATLAS/ATL13.006.

John, V. O., L. Shi, E.-S. Chung, R. P. Allan, S. A. Buehler, and B. J. Soden, 2024: Upper tropospheric humidity [in "State of the Climate in 2023"]. *Bull. Amer. Meteor. Soc.*, **105** (8), S59–60, https://doi.org/10.1175/2024BAMSStateoftheClimate.1.

Joint Research Centre–European Commission, 2025: Global flood awareness system. Accessed 12 February 2025, https://global-flood.emergency.copernicus.eu/.

Juncosa Calahorrano, J. F., V. H. Payne, S. Kulawik, B. Ford, F. Flocke, T. Campos, and E. V. Fischer, 2021: Evolution of acyl peroxynitrates (PANs) in wildfire smoke plumes detected by the cross-track infrared sounder (CrIS) over the western U.S. during summer 2018. *Geophys. Res. Lett.*, **48**, e2021GL093405, https://doi.org/10.1029/2021GL093405.

Junod, R. A., and J. R. Christy, 2020: A new compilation of globally gridded night-time marine air temperatures: The UAHNMATv1 dataset. *Int. J. Climatol.*, **40**, 2609–2623, https://doi.org/10.1002/joc.6354.

Kääb, A., and J. Røste, 2024: Rock glaciers across the United States predominantly accelerate coincident with rise in air temperatures. *Nat. Commun.*, **15**, 7581, https://doi.org/10.1038/s41467-024-52093-z.

——, T. Strozzi, T. Bolch, R. Caduff, H. Trefall, M. Stoffel, and A. Kokarev, 2021: Inventory and changes of rock glacier creep speeds in Ile Alatau and Kungöy Ala-Too, Northern Tien Shan, since the 1950s. *Cryosphere*, **15**, 927–949, https://doi.org/10.5194/tc-15-927-2021.

Kainz, M. J., R., Ptacnik, S., Rasconi, and H. H. Hager, 2017: Irregular changes in lake surface water temperature and ice cover in subalpine Lake Lunz, Austria. *Inland Waters*, **7**, 27–33, https://doi.org/10.1080/20442041.2017.1294332.

Kaiser, J. W., and Coauthors, 2012: Biomass burning emissions estimated with a global fire assimilation system based on observed fire radiative power. *Biogeosciences*, **9**, 527–554, https://doi.org/10.5194/bg-9-527-2012.

Kamal, M., T. I. Sanjid, A. Rony, and F. Piya, 2024: The August 2024 Bangladesh flood: Examining meteorological triggers, forecasting limitations, and Cross-Border water dynamics. ESS Open Archive, https://doi.org/10.22541/essoar.173257596.62658483/v1.

Kaplan, A., 2011: Patterns and indices of climate variability [in "State of the Climate in 2010"]. *Bull. Amer. Meteor. Soc.*, **92** (6), S20–S25, https://doi.org/10.1175/1520-0477-92.6.S1.

Keller, C. A., and Coauthors, 2021: Description of the NASA GEOS composition forecast modeling system GEOS-CF v1.0. *J. Adv. Model. Earth Syst.*, **13**, e2020MS002413, https://doi.org/10.1029/2020MS002413.

Kellerer-Pirklbauer, A., and Coauthors, 2024: Acceleration and interannual variability of creep rates in Mountain permafrost landforms (rock glacier velocities) in the European Alps over the time period 1995–2022 based on geodetic surveys: Climatic factors versus site-specific effects. *Environ. Res. Lett.*, **19**, 034022, https://doi.org/10.1088/1748-9326/ad25a4.

Kennedy, J. J., N. A. Rayner, C. P. Atkinson, and R. E. Killick, 2019: An ensemble data set of sea surface temperature change from 1850: The Met Office Hadley Centre HadSST.4.0.0.0 data set. *J. Geophys. Res. Atmos.*, **124**, 7719–7763, https://doi.org/10.1029/2018JD029867.

Khaykin, S., and Coauthors, 2020: The 2019/20 Australian wildfires generated a persistent smoke-charged vortex rising up to 35 km altitude. *Commun. Earth Environ.*, **1**, 22, https://doi.org/10.1038/s43247-020-00022-5.

——, and Coauthors, 2022: Global perturbation of stratospheric water and aerosol burden by Hunga eruption. *Commun. Earth Environ.*, **3**, 316, https://doi.org/10.1038/s43247-022-00652-x.

——, and Coauthors, 2024: Stratospheric aerosols [in "State of the Climate in 2023"]. *Bull. Amer. Meteor. Soc.*, **105** (8), S96–S98, https://doi.org/10.1175/BAMS-D-24-0116.1.

Khaykin, S. M., S. Godin-Beekmann, A. Hauchecorne, J. Pelon, F. Ravetta, and P. Keckhut, 2018: Stratospheric smoke with unprecedentedly high backscatter observed by lidars above Southern France. *Geophys. Res. Lett.*, **45**, 1639–1646, https://doi.org/10.1002/2017GL076763.

Kleipool, Q., and Coauthors, 2022: Ozone Monitoring Instrument (OMI) collection 4: Establishing a 17-year-long series of detrended level-1b data. *Atmos. Meas. Tech.*, **15**, 3527–3553, https://doi.org/10.5194/amt-15-3527-2022.

Kobayashi, S., and Coauthors, 2015: The JRA-55 reanalysis: General specifications and basic characteristics. *J. Meteor. Soc. Japan*, **93**, 5–48, https://doi.org/10.2151/jmsj.2015-001.

Kodera, K., H. Mukougawa, P. Maury, M. Ueda, and C. Claud, 2016: Absorbing and reflecting sudden stratospheric warming events and their relationship with tropospheric circulation. *J. Geophys. Res. Atmos.*, **121**, 80–94, https://doi.org/10.1002/2015JD023359.

Konopka, P., M. Tao, F. Ploeger, D. F. Hurst, M. L. Santee, J. S. Wright, and M. Riese, 2022: Stratospheric moistening after 2000. *Geophys. Res. Lett.*, **49**, e2021GL097609, https://doi.org/10.1029/2021GL097609.

Kosaka, Y., and Coauthors, 2024: The JRA-3Q reanalysis. *J. Meteor. Soc. Japan*, **102**, 49–109, https://doi.org/10.2151/jmsj.2024-004.

Kothari, R., 2024: Cleanup begins in Valencia after Spain's worst floods in history claim over 200 lives. The Watchers, https://watchers.news/2024/11/01/valencia-cleanup-spain-worst-flood-record-october-2024/.

Kovilakam, M., L. W. Thomason, N. Ernest, L. Rieger, A. Bourassa, and L. Millán, 2020: The global space-based stratospheric aerosol climatology (version 2.0): 1979–2018. *Earth Syst. Sci. Data*, **12**, 2607–2634, https://doi.org/10.5194/essd-12-2607-2020.

Kraemer, B. M., A. Seimon, R. Adrian, and P. B. McIntyre, 2020: Worldwide lake level trends and responses to background climate variation. *Hydrol. Earth Syst. Sci.*, **24**, 2593–2608, https://doi.org/10.5194/hess-24-2593-2020.

Kratz, D. P., P. W. Stackhouse Jr., S. K. Gupta, A. C. Wilber, P. Sawaengphokhai, and G. R. McGarragh, 2014: The fast longwave and shortwave flux (FLASHFlux) data product: Single-Scanner footprint fluxes. *J. Appl. Meteor. Climatol.*, **53**, 1059–1079, https://doi.org/10.1175/JAMC-D-13-061.1.

Kremser, S., and Coauthors, 2016: Stratospheric aerosol-observations, processes, and impact on climate. *Rev. Geophys.*, **54**, 278–335, https://doi.org/10.1002/2015RG000511.

Lagouarde, J.-P., and Coauthors, 2018: The Indian-French TRISHNA Mission: Earth Observation in the thermal infrared with high spatio-temporal resolution. *IGARSS 2018 – 2018 IEEE Int. Geoscience and Remote Sensing Symp.*, Valencia, Spain, Institute of Electrical and Electronics Engineers, 4078–4081, https://doi.org/10.1109/IGARSS.2018.8518720.

Unauthenticated | Downloaded 11/21/25 11:34 AM UTC

Lambiel, C., and R. Delaloye, 2004: Contribution of real-time kinematic GPS in the study of creeping Mountain permafrost: Examples from the western Swiss Alps. *Permafrost Periglacial Processes*, **15**, 229–241, https://doi.org/10.1002/ppp.496.

Lan, X., and Coauthors, 2019: Long-term measurements show little evidence for large increases in total U.S. methane emissions over the past decade. *Geophys. Res. Lett.*, **46**, 4991–4999, https://doi.org/10.1029/2018GL081731.

——, and Coauthors, 2021: Improved constraints on global methane emissions and sinks using $\delta^{13}C\text{-}CH_4$. *Global Biogeochem. Cycles*, **35**, e2021GB007000, https://doi.org/10.1029/2021GB007000.

——, P. Tans, and K. W. Thoning, 2025a: Trends in globally-averaged CO_2 determined from NOAA global monitoring laboratory measurements, version 2025-05. Accessed 1 June 2025, https://doi.org/10.15138/9N0H-ZH07.

——, K. W. Thoning, and E. J. Dlugokencky, 2025b: Trends in globally-averaged CH_4, N_2O, and SF_6 determined from NOAA global monitoring laboratory measurements, version 2025-05. Accessed 1 June 2025, https://doi.org/10.15138/P8XG-AA10.

Landerer, F. W., and Coauthors, 2020: Extending the global mass change data record: GRACE follow-on instrument and science data performance. *Geophys. Res. Lett.*, **47**, e2020GL088306, https://doi.org/10.1029/2020GL088306.

Lavers, D. A., A. Simmons, F. Vamborg, and M. J. Rodwell, 2022: An evaluation of ERA5 precipitation for climate monitoring. *Quart. J. Roy. Meteor. Soc.*, **148**, 3152–3165, https://doi.org/10.1002/qj.4351.

Lee, H.-T., and NOAA CDR Program, 2018: NOAA Climate Data Record (CDR) of Monthly Outgoing Longwave Radiation (OLR), version 2.7. NOAA National Centers for Environmental Information, accessed 5 January 2023, https://doi.org/10.7289/V5W37TKD.

Lee, S. H., A. H. Butler, and G. L. Manney, 2025: Two major sudden stratospheric warmings during winter 2023/2024. *Weather*, **80**, 45–53, https://doi.org/10.1002/wea.7656.

Lehner, B., and Coauthors, 2011: High-resolution mapping of the world's reservoirs and dams for sustainable river-flow management. *Front. Ecol. Environ.*, **9**, 494–502, https://doi.org/10.1890/100125.

Lenssen, N. J. L., G. A. Schmidt, J. E. Hansen, M. J. Menne, A. Persin, R. Ruedy, and D. Zyss, 2019: Improvements in the GISTEMP uncertainty model. *J. Geophys. Res. Atmos.*, **124**, 6307–6326, https://doi.org/10.1029/2018JD029522.

Levene, H., 1960: Robust tests for equality of variances. *Contributions to Probability and Statistics: Essays in Honor of Harold Hotelling*, Ingram Olkin, Harold Hotelling et al., Eds., Stanford University Press, 278–292.

Levy, R. C., S. Mattoo, L. A. Munchak, L. A. Remer, A. M. Sayer, F. Patadia, and N. C. Hsu, 2013: The Collection 6 MODIS aerosol products over land and ocean. *Atmos. Meas. Tech.*, **6**, 2989–3034, https://doi.org/10.5194/amt-6-2989-2013.

L'Heureux, M. L., D. S. Harnos, E. Becker, B. Brettschneider, M. Chen, N. C. Johnson, A. Kumar, and M. K. Tippett, 2024: How well do seasonal climate anomalies match expected El Niño–Southern Oscillation (ENSO) impacts? *Bull. Amer. Meteor. Soc.*, **105**, E1542–E1551, https://doi.org/10.1175/BAMS-D-23-0252.1.

Lin, X., and Coauthors, 2024: Recent methane surges reveal heightened emissions from tropical inundated areas. *Nat. Commun.*, **15**, 10894, https://doi.org/10.1038/s41467-024-55266-y.

Lindaas, J., and Coauthors, 2021: Emissions of reactive nitrogen from western U.S. wildfires during summer 2018. *J. Geophys. Res. Atmos.*, **126**, e2020JD032657, https://doi.org/10.1029/2020JD032657.

Liu, J., and Coauthors, 2017: Contrasting carbon cycle responses of the tropical continents to the 2015–2016 El Niño. *Science*, **358**, eaam5690, https://doi.org/10.1126/science.aam5690.

Liu, R., X. Zhang, W. Wang, Y. Wang, H. Liu, M. Ma, and G. Tang, 2024: Global-scale ERA5 product precipitation and temperature evaluation. *Ecol. Indic.*, **166**, 112481, https://doi.org/10.1016/j.ecolind.2024.112481.

Liu, Y., and Coauthors, 2017: Evaluation of the VIIRS BRDF, albedo and NBAR products suite and an assessment of continuity with the long term MODIS record. *Remote Sens. Environ.*, **201**, 256–274, https://doi.org/10.1016/j.rse.2017.09.020.

——, L. Zhou, Y. Qin, C. Azorin-Molina, C. Shen, R. Xu, and Z. Zeng, 2024: Impacts of anemometer changes, site relocations and processing methods on wind speed trends in China. *Atmos. Meas. Tech.*, **17**, 1123–1131, https://doi.org/10.5194/amt-17-1123-2024.

Loeb, N. G., B. A. Wielicki, D. R. Doelling, G. L. Smith, D. F. Keyes, S. Kato, N. Manalo-Smith, and T. Wong, 2009: Toward optimal closure of the earth's top-of-atmosphere radiation budget. *J. Climate*, **22**, 748–766, https://doi.org/10.1175/2008JCLI2637.1.

——, S. Kato, W. Su, T. Wong, F. G. Rose, D. R. Doelling, J. R. Norris, and X. Huang, 2012: Advances in understanding top-of-atmosphere radiation variability from satellite observations. *Surv. Geophys.*, **33**, 359–385, https://doi.org/10.1007/s10712-012-9175-1.

——, and Coauthors, 2018: Clouds and the Earth's Radiant Energy System (CERES) Energy Balanced and Filled (EBAF) Top-of-Atmosphere (TOA) edition-4.0 data product. *J. Climate*, **31**, 895–918, https://doi.org/10.1175/JCLI-D-17-0208.1.

——, G. C. Johnson, T. J. Thorsen, J. M. Lyman, F. G. Rose, and S. Kato, 2021: Satellite and ocean data reveal marked increase in earth's heating rate. *Geophys. Res. Lett.*, **48**, e2021GL093047, https://doi.org/10.1029/2021GL093047.

——, and Coauthors, 2022: Evaluating twenty-year trends in earth's energy flows from observations and reanalyses. *J. Geophys. Res. Atmos.*, **127**, e2022JD036686, https://doi.org/10.1029/2022JD036686.

MacCallum, S. N., and C. J. Merchant, 2012: Surface water temperature observations of large Lakes by optimal estimation. *Can. J. Remote Sens.*, **38**, 25–45, https://doi.org/10.5589/m12-010.

Maciel, D. A., Lousada, F. Fassoni-Andrade, A. Pacheco Quevedo, R. Barbosa, C. C. F. Paule-Bonnet, and E. M. L. D. M. Novo, 2024: Sentinel-1 data reveals unprecedented reduction of open water extent due to 2023-2024 drought in the central Amazon basin. *Environ. Res. Lett.*, **19**, 124034, https://doi.org/10.1088/1748-9326/ad8a71.

Magnin, F., L. Ravanel, X. Bodin, P. Deline, E. Malet, J. Krysiecki, and P. Schoeneich, 2023: Main results of permafrost monitoring in the French Alps through the PermaFrance network over the period 2010–2022. *Permafrost Periglacial Processes*, **35**, 3–23, https://doi.org/10.1002/ppp.2209.

Magnusson, L., and Coauthors, 2025: Severe rain in central Europe from Storm Boris. ECMWF, accessed 29 May 2025, https://www.ecmwf.int/en/newsletter/182/news/severe-rain-central-europe-storm-boris.

Marengo, J., and Coauthors, 2024: The drought of Amazonia in 2023-2024. *Amer. J. Climate Change*, **13**, 567–597, https://doi.org/10.4236/ajcc.2024.133026.

Unauthenticated | Downloaded 11/21/25 11:34 AM UTC

Martens, B., and Coauthors, 2017: GLEAM v3: Satellite-based land evaporation and root-zone soil moisture. *Geosci. Model Dev.*, **10**, 1903–1925, https://doi.org/10.5194/gmd-10-1903-2017.

—— , W. Waegeman, W. A. Dorigo, N. E. C. Verhoest, and D. G. Miralles, 2018: Terrestrial evaporation response to modes of climate variability. *npj Climate Atmos. Sci.*, **1**, 43, https://doi.org/10.1038/s41612-018-0053-5.

Matthews, T., M. Byrne, R. Horton, C. Murphy, R. Pielke Sr., C. Raymond, P. Thorne, and R. L. Wilby, 2022: Latent heat must be visible in climate communications. *Wiley Interdiscip. Rev.: Climate Change*, **13**, e779, https://doi.org/10.1002/wcc.779.

—— , —— , P. C. Stoy, and K. M. Willett, 2024: Sidebar 2.2: Near-surface equivalent temperature as a key climate change metric [in "State of the Climate in 2023"]. *Bull. Amer. Meteor. Soc.*, **105** (8), S30–S32, https://doi.org/10.1175/2024BAMS-StateoftheClimate.1.

—— , C. Raymond, J. Foster, J. W. Baldwin, C. Ivanovich, Q. Kong, P. Kinney, and R. M. Horton, 2025: Mortality impacts of the most extreme heat events. *Nat. Rev. Earth Environ.*, **6**, 193–210, https://doi.org/10.1038/s43017-024-00635-w.

Mayer, M., L. Haimberger, C. T. Sabeerali, V. Schenzinger, D. E. Surendran, and O. P. Sreejith, 2023: Upper air winds [in "State of the Climate in 2022"]. *Bull. Amer. Meteor. Soc.*, **104** (9), S74–S76, https://doi.org/10.1175/BAMS-D-23-0090.1.

McCabe, M. F., B. Aragon, R. Houborg, and J. Mascaro, 2017: CubeSats in hydrology: Ultrahigh-resolution insights into vegetation dynamics and terrestrial evaporation. *Water Resour. Res.*, **53**, 10 017–10 024, https://doi.org/10.1002/2017WR022240.

McCarthy, M. P., and R. Toumi, 2004: Observed interannual variability of tropical troposphere relative humidity. *J. Climate*, **17**, 3181–3191, https://doi.org/10.1175/1520-0442(2004)017<3181:OIVOTT>2.0.CO;2.

McVicar, T. R., and Coauthors, 2012: Global review and synthesis of trends in observed terrestrial near-surface wind speeds: Implications for evaporation. J. Hydrol., 416–417, 182–205, https://doi.org/10.1016/j.jhydrol.2011.10.024.

Mears, C. A., and F. J. Wentz, 2016: Sensitivity of satellite-derived tropospheric temperature trends to the diurnal cycle adjustment. *J. Climate*, **29**, 3629–3646, https://doi.org/10.1175/JCLI-D-15-0744.1.

—— , A. D. Smith, K. L. Ricciardulli, J. Wang, H. Huelsing, and F. J. Wentz, 2018: Construction and uncertainty estimation of a satellite-derived total precipitable water data record over the world's oceans. *Earth Space Sci.*, **5**, 197–210, https://doi.org/10.1002/2018EA000363.

—— , J. P. Nicolas, O. Bock, S. P. Ho, and X. Zhou, 2023: Total column water vapor [in "State of the Climate in 2022"]. *Bull. Amer. Meteor. Soc.*, **104** (9), S54–S55, https://doi.org/10.1175/BAMS-D-23-0090.1.

Meesters, A. G., R. A. M. De Jeu, and M. Owe, 2005: Analytical derivation of the vegetation optical depth from the microwave polarization difference index. *IEEE Geosci. Remote Sens. Lett.*, **2**, 121–123, https://doi.org/10.1109/LGRS.2005.843983.

Menne, M. J., and Coauthors, 2025: The Global Historical Climatology Network hourly (GHCNh) dataset. *29th Conf. of Applied Climatology*, New Orleans, LA, Amer. Meteor. Soc., 9.1, https://ams.confex.com/ams/105ANNUAL/meetingapp.cgi/Paper/446924.

Menzel, A., Y. Yuan, M. Matiu, T. Sparks, H. Scheifinger, R. Gehrig, and N. Estrella, 2020: Climate change fingerprints in recent European plant phenology. *Global Change Biol.*, **26**, 2599–2612, https://doi.org/10.1111/gcb.15000.

Messager, M. L., B. Lehner, G. Grill, I. Nedeva, and O. Schmitt, 2016: Estimating the volume and age of water stored in global Lakes using a geo-statistical approach. *Nat. Commun.*, **7**, 13603, https://doi.org/10.1038/ncomms13603.

MeteoSwiss, 2025: Klimabulletin Jahr 2024. 14 pp.

Michel, S. E., and Coauthors, 2024: Rapid shift in methane carbon isotopes suggests microbial emissions drove record high atmospheric methane growth in 2020-2022. *Proc. Natl. Acad. Sci. USA*, **121**, e2411212121, https://doi.org/10.1073/pnas.2411212121.

Mildrexler, D. J., M. Zhao, and S. W. Running, 2006: Where are the hottest spots on earth? *EoS, Trans. Amer. Geophys. Union*, **87**, 461–467, https://doi.org/10.1029/2006EO430002.

Millán, L., and Coauthors, 2022: The Hunga Tonga-Hunga Ha'apai hydration of the stratosphere. *Geophys. Res. Lett.*, **49**, e2022GL099381, https://doi.org/10.1029/2022GL099381.

Miller, B. R., and Coauthors, 2010: HFC-23 (CHF_3) emission trend response to HCFC-22 ($CHClF_2$) production and recent HFC-23 emission abatement measures. *Atmos. Chem. Phys.*, **10**, 7875–7890, https://doi.org/10.5194/acp-10-7875-2010.

Minola, L., H. Reese, H. W. Lai, C. Azorin-Molina, J. A. Guijarro, S. W. Son, and D. Chen, 2022: Wind stilling–reversal across Sweden: The impact of land-use and large-scale atmospheric circulation changes. *Int. J. Climatol.*, **42**, 1049–1071, https://doi.org/10.1002/joc.7289.

Miralles, D. G., and Coauthors, 2014: El Niño–La Niña cycle and recent trends in continental evaporation. *Nat. Climate Change*, **4**, 122–126, https://doi.org/10.1038/nclimate2068.

—— , P. Gentine, S. I. Seneviratne, and A. J. Teuling, 2019: Land-atmospheric feedbacks during droughts and heatwaves: State of the science and current challenges. *Ann. N. Y. Acad. Sci.*, **1436**, 19–35, https://doi.org/10.1111/nyas.13912.

—— , and Coauthors, 2025: GLEAM4: Global land evaporation and soil moisture dataset at 0.1 resolution from 1980 to near present. *Sci. Data*, **12**, 416, https://doi.org/10.1038/s41597-025-04610-y.

Mitchell, L., E. Brook, J. E. Lee, C. Buizert, and T. Sowers, 2013: Constraints on the late Holocene anthropogenic contribution to the atmospheric methane budget. *Science*, **342**, 964–966, https://doi.org/10.1126/science.1238920.

Moesinger, L., R.-M. Zotta, R. van Der Schalie, T. Scanlon, R. de Jeu, and W. Dorigo, 2022: Monitoring vegetation condition using microwave remote sensing: The standardized vegetation optical depth index (SVODI). *Biogeosciences*, **19**, 5107–5123, https://doi.org/10.5194/bg-19-5107-2022.

Mollaret, C., C. Hilbich, C. Pellet, A. Flores-Orozco, R. Delaloye, and C. Hauck, 2019: Mountain permafrost degradation documented through a network of permanent electrical resistivity tomography sites. *Cryosphere*, **13**, 2557–2578, https://doi.org/10.5194/tc-13-2557-2019.

Monks, P. S., and Coauthors, 2015: Tropospheric ozone and its precursors from the urban to the global scale from air quality to short-lived climate forcer. *Atmos. Chem. Phys.*, **15**, 8889–8973, https://doi.org/10.5194/acp-15-8889-2015.

Montreal Protocol, 1989: Montreal Protocol on substances that deplete the ozone layer. Final act 1987. *J. Environ. Law*, **1**, 128–136, https://doi.org/10.1093/jel/1.1.128.

Morán-Tejeda, E., J. L. Ceballos, K. Peña, J. Lorenzo-Lacruz, and J. I. López-Moreno, 2018: Recent evolution and associated hydrological dynamics of a vanishing tropical Andean glacier: Glaciar de Conejeras, Colombia. *Hydrol. Earth Syst. Sci.*, **22**, 5445–5461, https://doi.org/10.5194/hess-22-5445-2018.

Unauthenticated | Downloaded 11/21/25 11:34 AM UTC

Morgenstern, O., and Coauthors, 2025: Radiocarbon monoxide indicates increasing atmospheric oxidizing capacity. *Nat. Commun.*, **16**, 249, https://doi.org/10.1038/s41467-024-55603-1.

Morice, C. P., and Coauthors, 2021: An updated assessment of near-surface temperature change from 1850: The HadCRUT5 data set. *J. Geophys. Res. Atmos.*, **126**, e2019JD032361, https://doi.org/10.1029/2019JD032361.

Mote, P. W., and Coauthors, 1996: An atmospheric tape recorder: The imprint of tropical tropopause temperatures on stratospheric water vapor. *J. Geophys. Res.*, **101**, 3989–4006, https://doi.org/10.1029/95JD03422.

Mühle, J., and Coauthors, 2010: Perfluorocarbons in the global atmosphere: Tetrafluoromethane, hexafluoroethane, and octafluoropropane. *Atmos. Chem. Phys.*, **10**, 5145–5164, https://doi.org/10.5194/acp-10-5145-2010.

Myhre, G., D. Shindell, and J. Pongratz, 2014: Anthropogenic and natural radiative forcing. *Climate Change 2013: The Physical Science Basis*, T. F. Stocker et al., Eds., Cambridge University Press, 659–740.

NASA, 2024: NASA, NOAA: Sun reaches maximum phase in 11-year solar cycle. Accessed 28 February 2025, https://science.nasa.gov/science-research/heliophysics/nasa-noaa-sun-reaches-maximum-phase-in-11-year-solar-cycle/.

NASA Earth Observatory, 2024: Intense, widespread drought grips South America. Accessed 10 February 2025, https://earthobservatory.nasa.gov/images/153447/intense-widespread-drought-grips-south-america.

Newman, P. A., J. S. Daniel, D. W. Waugh, and E. R. Nash, 2007: A new formulation of equivalent effective stratospheric chlorine (EESC). *Atmos. Chem. Phys.*, **7**, 4537–4552, https://doi.org/10.5194/acp-7-4537-2007.

—— , L. R. Lait, N. A. Kramarova, L. Coy, S. M. Frith, L. D. Oman, and S. S. Dhomse, 2024: Record high March 2024 Arctic total column ozone. *Geophys. Res. Lett.*, **51**, e2024GL110924, https://doi.org/10.1029/2024GL110924.

Nisbet, E. G., and Coauthors, 2023: Atmospheric methane: Comparison between methane's record in 2006–2022 and during glacial terminations. *Global Biogeochem. Cycles*, **37**, e2023GB007875, https://doi.org/10.1029/2023GB007875.

NOAA, 2024: Great Lakes ice coverage reaches historic low. https://research.noaa.gov/great-lakes-ice-coverage-reaches-historic-low/.

—— , 2025: Great Lakes ice cover database 1973-2024. GLERL, accessed 2 June 2025, https://www.glerl.noaa.gov/data/ice/#historical.

NOAA/NCEI, 2024: Monthly Global Climate Report for November 2024. https://www.ncei.noaa.gov/access/monitoring/monthly-report/global/202411#precip.

—— , 2025a: Global Climate Report Annual 2024. https://www.ncei.noaa.gov/access/monitoring/monthly-report/global/202413.

—— , 2025b: Monthly Drought Report for Annual 2024. Accessed 11 February 2025, https://www.ncei.noaa.gov/access/monitoring/monthly-report/drought/202413.

Noetzli, J., and Coauthors, 2024a: Enhanced warming of European Mountain permafrost in the early 21st century. *Nat. Commun.*, **15**, 10508, https://doi.org/10.1038/s41467-024-54831-9.

Nowak, J. B., and Coauthors, 2012: Ammonia sources in the California South Coast air basin and their impact on ammonium nitrate formation. *Geophys. Res. Lett.*, **39**, L07804, https://doi.org/10.1029/2012GL051197.

O'Gorman, P. A., and C. J. Muller, 2010: How closely do changes in surface and column water vapor follow Clausius–Clapeyron scaling in climate change simulations? *Environ. Res. Lett.*, **5**, 025207, https://doi.org/10.1088/1748-9326/5/2/025207.

Oh, Y., and Coauthors, 2023: CarbonTracker CH_4 2023. Accessed 1 June 2025, https://doi.org/10.25925/40jt-qd67.

Okamoto-Mizuno, K., K. Mizuno, S. Michie, A. Maeda, and S. Iizuka, 1999: Effects of humid heat exposure on human sleep stages and body temperature. *Sleep*, **22**, 767–773, https://doi.org/10.1093/sleep/22.6.767.

O'Kane, T. J., and C. L. Franzke, 2025: Pacific–South American pattern. *Atmospheric Oscillations*, Elsevier, 171–181, https://doi.org/10.1016/B978-0-443-15638-0.00008-3.

O'Keefe, J., and G. VanScoy, 2024: Phenology of woody species at Harvard Forest since 1990. Harvard Forest Data Archive: HF003, accessed 1 February 2025, https://harvardforest1.fas.harvard.edu/exist/apps/datasets/showData.html?id=HF003.

Oman, L. D., A. R. Douglass, J. R. Ziemke, J. M. Rodriguez, D. W. Waugh, and J. E. Nielsen, 2013: The ozone response to ENSO in aura satellite measurements and a chemistry–climate simulation. *J. Geophys. Res. Atmos.*, **118**, 965–976, https://doi.org/10.1029/2012JD018546.

O'Neill, H. B., S. L. Smith, C. R. Burn, C. Duchesne, and Y. Zhang, 2023: Widespread permafrost degradation and thaw subsidence in northwest Canada. *J. Geophys. Res. Earth Surf.*, **128**, e2023JF007262, https://doi.org/10.1029/2023JF007262.

Osborn, T. J., P. D. Jones, D. H. Lister, C. P. Morice, I. R. Simpson, J. P. Winn, E. Hogan, and I. C. Harris, 2021: Land surface air temperature variations across the globe updated to 2019: The CRUTEM5 data set. *J. Geophys. Res. Atmos.*, **126**, e2019JD032352, https://doi.org/10.1029/2019JD032352.

Pakistan Meteorological Department, 2025: State of Pakistan Climate 2024. Climate Data Processing Center, 23 pp., https://cdpc.pmd.gov.pk/Pakistan_Climate_2024.pdf.

Pandey, K., and R. Sengupta, 2024: Climate India 2024: An assessment of extreme weather events. Center for Science and Environment Down to Earth Rep., 60 pp., https://www.cseindia.org/climate-india-2024-an-assessment-of-extreme-weather-events-12460.

Park, T., and Coauthors, 2016: Changes in growing season duration and productivity of Northern vegetation inferred from long-term remote sensing data. *Environ. Res. Lett.*, **11**, 084001, https://doi.org/10.1088/1748-9326/11/8/084001.

—— , M. K. Gumma, W. Wang, P. Panjala, S. K. Dubey, and R. R. Nemani, 2023: Greening of human-dominated ecosystems in India. *Commun. Earth Environ.*, **4**, 419, https://doi.org/10.1038/s43247-023-01078-9.

Payne, V. H., and Coauthors, 2022: Satellite measurements of peroxyacetyl nitrate from the Cross-Track infrared sounder: Comparison with ATom aircraft measurements. *Atmos. Meas. Tech.*, **15**, 3497–3511, https://doi.org/10.5194/amt-15-3497-2022.

Pellet, C., and Coauthors, 2024: Rock glacier velocity [in "State of Climate 2023"]. *Bull. Amer. Meteor. Soc.*, **105** (8), 44–46, https://doi.org/10.1175/BAMS-D-24-0116.1.

Pelto, M., 2024: Alpine Glaciers [in "State of the Climate in 2023"]. *Bull. Amer. Meteor. Soc.*, **105** (8), S46–S47, https://doi.org/10.1175/BAMS-D-24-0116.1.

Pelto, M. S., and J. Pelto, 2025: The loss of ice worm glacier, North Cascade range, Washington USA. Water, **17**, 432, https://doi.org/10.3390/w17030432.

Peng, S., and Coauthors, 2022: Wetland emission and atmospheric sink changes explain methane growth in 2020. *Nature*, **612**, 477–482, https://doi.org/10.1038/s41586-022-05447-w.

Unauthenticated | Downloaded 11/21/25 11:34 AM UTC

PERMOS, 2024: *Swiss Permafrost Bulletin 2023* (Annual Report of the Swiss Permafrost Monitoring Network PERMOS No. 5). Swiss Permafrost Monitoring Network PERMOS, 25 pp., https://doi.org/10.13093/permos-bull-2024.

—— , 2025: *Swiss Permafrost Bulletin 2024* (Annual Report of the Swiss Permafrost Monitoring Network PERMOS No. 6). Swiss Permafrost Monitoring Network PERMOS, https://doi.org/10.13093/permos-bull-2025.

Peterson, D. A., J. Campbell, E. Hyer, M. Fromm, G. Kablick, J. Cossuth, and M. DeLand, 2018: Wildfire-driven thunderstorms cause a volcano-like stratospheric injection of smoke. *npj Climate Atmos. Sci.*, **1**, 30, https://doi.org/10.1038/s41612-018-0039-3.

—— , and Coauthors, 2021: Australia's Black Summer pyrocumulonimbus super outbreak reveals potential for increasingly extreme stratospheric smoke events. *npj Climate Atmos. Sci.*, **4**, 38, https://doi.org/10.1038/s41612-021-00192-9.

Peterson, T. C., K. M. Willett, and P. W. Thorne, 2011: Observed changes in surface atmospheric energy over land. *Geophys. Res. Lett.*, **38**, L16707, https://doi.org/10.1029/2011GL048442.

Petropavlovskikh, I., and Coauthors, 2025: Ozone trends in homogenized Umkehr, ozonesonde, and COH overpass records. *Atmos. Chem. Phys.*, **25**, 2895–2936, https://doi.org/10.5194/acp-25-2895-2025.

Phillips, C., and M. Foster, 2024: Cloudiness [in "State of the Climate in 2023"]. *Bull. Amer. Meteor. Soc.*, **105** (8), S63–S65, https://doi.org/10.1175/BAMS-D-24-0116.1.

Pi, X., and Coauthors, 2022: Mapping global lake dynamics reveals the emerging roles of small Lakes. *Nat. Commun.*, **13**, 5777, https://doi.org/10.1038/s41467-022-33239-3.

Pinto, I., and Coauthors, 2024: Conflict, poverty and water management issues exposing vulnerable communities in Africa to extreme floods that are now common events because of climate change. Imperial College London, 33 pp., https://spiral.imperial.ac.uk/server/api/core/bitstreams/a494f174-d954-4905-9569-0039d372762c/content.

Pinty, B., and Coauthors, 2011: Exploiting the MODIS albedos with the Two-stream Inversion Package (JRC-TIP): 2. Fractions of transmitted and absorbed fluxes in the vegetation and soil layers. *J. Geophys. Res.*, **116**, D09106, https://doi.org/10.1029/2010JD015373.

Plummer, D., and Coauthors, 2021: CCMI-2022: A new set of Chemistry-Climate Model Initiative (CCMI) community simulations to update the assessment of models and support upcoming ozone assessment activities. *SPARC Newsletter*, No. 57, 22–30, https://www.sparc-climate.org/wp-content/uploads/sites/5/2021/07/ SPARCnewsletter_Jul2021_web.pdf.

Po-Chedley, S., J. R. Christy, L. Haimberger, and C. A. Mears, 2021: Tropospheric temperature [in "State of the Climate in 2020"]. *Bull. Amer. Meteor. Soc.*, **102** (8), S34–S37, https://doi.org/10.1175/BAMS-D-21-0098.1.

—— , —— , —— , —— , and C.-Z. Zou, 2024: Tropospheric temperature [in "State of the Climate in 2023"]. *Bull. Amer. Meteor. Soc.*, **105** (8), S39–S41, https://doi.org/10.1175/BAMS-D-24-0116.1.

Pogliotti, P., E. Cremonese, and U. Morra di Cella, 2023: Warming permafrost in the western Alps: A further evidence of elevation dependent warming? *J. Alp. Res.*, **111** (2), https://doi.org/10.4000/rga.11784.

Popp, T., and Coauthors, 2016: Development, production and evaluation of aerosol climate data records from European satellite observations (Aerosol_cci). Remote Sens., **8**, 421, https://doi.org/10.3390/rs8050421.

Prather, M. J., C. D. Holmes, and J. Hsu, 2012: Reactive greenhouse gas scenarios: Systematic exploration of uncertainties and the role of atmospheric chemistry. *Geophys. Res. Lett.*, **39**, L09803, https://doi.org/10.1029/2012GL051440.

Price, C., M. Asfur, and Y. Yair, 2009: Maximum hurricane intensity preceded by increase in lightning frequency. *Nat. Geosci.*, **2**, 329–332, https://doi.org/10.1038/ngeo477.

Pucik, T., 2024: Meteorological analysis of extreme flash flood situation in the Valencia region. European Severe Storms Laboratory, accessed 29 May 2025, https://www.essl.org/cms/meteorological-analysis-of-extreme-flash-flood-situation-in-the-valencia-region/.

Raghuraman, S. P., B. Soden, A. Clement, G. Vecchi, S. Menemenlis, and W. Yang, 2024: The 2023 global warming spike was driven by the El Niño–Southern Oscillation. *Atmos. Chem. Phys.*, **24**, 11 275–11 283, https://doi.org/10.5194/acp-24-11275-2024.

Rakov, V. A., and M. A. Uman, 2003: *Lightning Physics and Effects.* Cambridge University Press, 687 pp., https://doi.org/10.1017/CBO9781107340886.

Randel, W. J., and J. B. Cobb, 1994: Coherent variations of monthly mean total ozone and lower stratospheric temperature. *J. Geophys. Res.*, **99**, 5433–5447, https://doi.org/10.1029/93JD03454.

—— , X. Wang, J. Starr, R. R. Garcia, and D. Kinnison, 2024: Long-term temperature impacts of the Hunga volcanic eruption in the stratosphere and above. *Geophys. Res. Lett.*, **51**, e2024GL111500, https://doi.org/10.1029/2024GL111500.

RGIK, 2023a: Guidelines for inventorying rock glaciers: Baseline and practical concepts (version 1.0). IPA Action Group Rock Glacier Inventories and Kinematics, 26 pp., https://doi.org/10.51363/unifr.srr.2023.002.

—— , 2023b: Rock glacier velocity as an associated parameter of ECV permafrost: Baseline concepts (version 3.2). IPA Action Group Rock Glacier Inventories and Kinematics, 13 pp.

Ricciardulli, L., and F. J. Wentz, 2015: A scatterometer geophysical model function for climate-quality winds: QuikSCAT Ku-2011. *J. Atmos. Oceanic Technol.*, **32**, 1829–1846, https://doi.org/10.1175/JTECH-D-15-0008.1.

—— , and A. Manaster, 2021: Intercalibration of ASCAT scatterometer winds from MetOp-A, -B, and -C, for a stable climate data record. *Remote Sens.*, **13**, 3678, https://doi.org/10.3390/rs13183678.

Richardson, A. D., 2019: Tracking seasonal rhythms of plants in diverse ecosystems with digital camera imagery. *New Phytol.*, **222**, 1742–1750, https://doi.org/10.1111/nph.15591.

—— , and J. O'Keefe, 2009: Phenological differences between understory and overstory. *Phenology of Ecosystem Processes*, A. Noormets, Ed., Springer, 87–117.

Roberts, R., and Coauthors, 2022: Taking the HIGHWAY to save lives on Lake Victoria. *Bull. Amer. Meteor. Soc.*, **103**, E485–E510, https://doi.org/10.1175/BAMS-D-20-0290.1.

Rodell, M., and B. Li, 2023: Changing intensity of hydroclimatic extreme events revealed by GRACE and GRACE-FO. Nat. *Water*, **1**, 241–248, https://doi.org/10.1038/s44221-023-00040-5.

—— , J. S. Famiglietti, D. N. Wiese, J. T. Reager, H. K. Beaudoing, F. W. Landerer, and M. H. Lo, 2018: Emerging trends in global freshwater availability. *Nature*, **557**, 651–659, https://doi.org/10.1038/s41586-018-0123-1.

—— , and Coauthors, 2024: An abrupt decline in global terrestrial water storage and its relationship with sea level change. *Surv. Geophys.*, **45**, 1875–1902, https://doi.org/10.1007/s10712-024-09860-w.

Unauthenticated | Downloaded 11/21/25 11:34 AM UTC

Rohde, R. A., and Z. Hausfather, 2020: The Berkeley Earth land/ocean temperature record. *Earth Syst. Sci. Data*, **12**, 3469–3479, https://doi.org/10.5194/essd-12-3469-2020.

Rosemartin, A. H., and Coauthors, 2014: Organizing phenological data resources to inform natural resource conservation. *Biol. Conserv.*, **173**, 90–97, https://doi.org/10.1016/j.biocon.2013.07.003.

Rubino, M., and Coauthors, 2019: Revised records of atmospheric trace gases CO_2, CH_4, N_2O, and $\delta^{13}C$-CO_2 over the last 2000 years from Law Dome, Antarctica. *Earth Syst. Sci. Data*, **11**, 473–492, https://doi.org/10.5194/essd-11-473-2019.

Rudlosky, S. D., and K. S. Virts, 2021: Dual geostationary lightning mapper observations. *Mon. Wea. Rev.*, **149**, 979–998, https://doi.org/10.1175/MWR-D-20-0242.1.

Rutllant, J. A., and H. Fuenzalida, 1991: Synoptic aspects of the central Chile rainfall variability associated with the Southern Oscillation. *Int. J. Climatol.*, **11**, 63–76, https://doi.org/10.1002/joc.3370110105.

Santee, M. L., and Coauthors, 2023: Strong evidence of heterogeneous processing on stratospheric sulfate aerosol in the extrapolar Southern Hemisphere following the 2022 Hunga Tonga-Hunga Ha'apai eruption. *J. Geophys. Res. Atmos.*, **128**, e2023JD039169, https://doi.org/10.1029/2023JD039169.

Santer, B. D., and Coauthors, 2008: Consistency of modelled and observed temperature trends in the tropical troposphere. *Int. J. Climatol.*, **28**, 1703–1722, https://doi.org/10.1002/joc.1756.

Satheesh, S. K., and Coauthors, 2017: Variability of atmospheric aerosols over India. Observed Climate Variability and Change over the Indian Region, Springer, 221–248, https://doi.org/10.1007/978-981-10-2531-0_13.

Sato, M., J. E. Hansen, M. P. McCormick, and J. B. Pollack, 1993: Stratospheric aerosol optical depths, 1850–1990. *J. Geophys. Res.*, **98**, 22 987–22 994, https://doi.org/10.1029/93JD02553.

Schaaf, C. B., and Coauthors, 2002: First operational BRDF, albedo nadir reflectance products from MODIS. Remote Sens. *Environ.*, **83**, 135–148, https://doi.org/10.1016/S0034-4257(02)00091-3.

Schwartz, M. D., T. R. Ault, and J. L. Betancourt, 2013: Spring onset variations and trends in the continental United States: Past and regional assessment using temperature-based indices. *Int. J. Climatol.*, **33**, 2917–2922, https://doi.org/10.1002/joc.3625.

Sen, P. K., 1968: Estimates of the regression coefficient based on Kendall's tau. *J. Amer. Stat. Assoc.*, **63**, 1379–1389, https://doi.org/10.1080/01621459.1968.10480934.

Seneviratne, S. I., T. Corti, E. L. Davin, M. Hirschi, E. B. Jaeger, I. Lehner, B. Orlowsky, and A. J. Teuling, 2010: Investigating soil moisture–climate interactions in a changing climate: A review. *Earth-Sci. Rev.*, **99**, 125–161, https://doi.org/10.1016/j.earscirev.2010.02.004.

Seyednasrollah, B., A. M. Young, K. Hufkens, T. Milliman, M. A. Friedl, S. Frolking, and A. D. Richardson, 2019: Publisher correction: Tracking vegetation phenology across diverse biomes using version 2.0 of the PhenoCam dataset. *Sci. Data*, **6**, 261, https://doi.org/10.1038/s41597-019-0270-8.

Shao, X., S.-P. Ho, X. Jing, X. Zhou, Y. Chen, T.-C. Liu, B. Zhang, and J. Dong, 2023: Characterizing the tropospheric water vapor spatial variation and trend using 2007–2018 COSMIC radio occultation and ECMWF reanalysis data. *Atmos. Chem. Phys.*, **23**, 14 187–14 218, https://doi.org/10.5194/acp-23-14187-2023.

Sharma, S., and Coauthors, 2021: Loss of ice cover, shifting phenology, and more extreme events in Northern Hemisphere lakes. *J. Geophys. Res. Biogeosci.*, **126**, e2021JG006348, https://doi.org/10.1029/2021JG006348.

——, and Coauthors, 2022: Author correction: Long-term ice phenology records spanning up to 578 years for 78 lakes around the Northern Hemisphere. *Sci. Data*, **9**, 419, https://doi.org/10.1038/s41597-022-01531-y.

Shi, L., and J. J. Bates, 2011: Three decades of intersatellite-calibrated High-Resolution Infrared Radiation Sounder upper tropospheric water vapor. *J. Geophys. Res.*, **116**, D04108, https://doi.org/10.1029/2010JD014847.

Simmons, A. J., 2022: Trends in the tropospheric general circulation from 1979 to 2022. *Wea. Climate Dyn.*, **3**, 777–809, https://doi.org/10.5194/wcd-3-777-2022.

Simpson, I. R., K. A. McKinnon, D. Kennedy, D. M. Lawrence, F. Lehner, and R. Seager, 2024: Observed humidity trends in dry regions contradict climate models. *Proc. Natl. Acad. Sci. USA*, **121**, e2302480120, https://doi.org/10.1073/pnas.2302480120.

Sindelarova, K., and Coauthors, 2014: Global data set of biogenic VOC emissions calculated by the MEGAN model over the last 30 years. *Atmos. Chem. Phys.*, **14**, 9317–9341, https://doi.org/10.5194/acp-14-9317-2014.

Smith, S. L., H. B. O'Neill, K. Isaksen, J. Noetzli, and V. E. Romanovsky, 2022: The changing thermal state of permafrost. *Nat. Rev. Earth Environ.*, **3**, 10–23, https://doi.org/10.1038/s43017-021-00240-1.

——, V. E. Romanovsky, K. Isaksen, K. E. Nyland, N. I. Shiklomanov, D. A. Streletskiy, and H. H. Christiansen, 2024: Permafrost [in "State of the Climate in 2023"]. *Bull. Amer. Meteor. Soc.*, **105** (8), 314–317, https://doi.org/10.1175/BAMS-D-24-0116.1.

Soci, C., and Coauthors, 2024: The ERA5 global reanalysis from 1940 to 2022. *Quart. J. Roy. Meteor. Soc.*, **150**, 4014–4048, https://doi.org/10.1002/qj.4803.

Sofen, E. D., D. Bowdalo, and M. J. Evans, 2016: How to most effectively expand the global surface ozone observing network. *Atmos. Chem. Phys.*, **16**, 1445–1457, https://doi.org/10.5194/acp-16-1445-2016.

Solomon, S., K. Stone, P. Yu, D. M. Murphy, D. Kinnison, A. R. Ravishankara, and P. Wang, 2023: Chlorine activation and enhanced ozone depletion induced by wildfire aerosol. *Nature*, **615**, 259–264, https://doi.org/10.1038/s41586-022-05683-0.

Song, F., G. J. Zhang, V. Ramanathan, and L. R. Leung, 2022: Trends in surface equivalent potential temperature: A more comprehensive metric for global warming and weather extremes. *Proc. Natl. Acad. Sci. USA*, **119**, e2117832119, https://doi.org/10.1073/pnas.2117832119.

Song, X.-P., M. C. Hansen, S. V. Stehman, P. V. Potapov, A. Tyukavina, E. F. Vermote, and J. R. Townshend, 2018: Global land change from 1982 to 2016. *Nature*, **560**, 639–643, https://doi.org/10.1038/s41586-018-0411-9.

Sorg, A., A. Kääb, A. Roesch, C. Bigler, and M. Stoffel, 2015: Contrasting responses of central Asian rock glaciers to global warming. *Sci. Rep.*, **5**, 8228, https://doi.org/10.1038/srep08228.

South African Weather Service, 2024: Cape Town's record-breaking July 2024 rainfall. Document Reference: CS-CMS-LETT-003, accessed 12 August 2024, https://www.suidkaapforum.com/News/Article/National-News/cape-town-s-record-breaking-july-2024-rainfall-202408120436.

SPARC/IO3C/GAW, 2019: SPARC/IO3C/GAW report on long-term ozone trends and uncertainties in the stratosphere. I. Petropavlovskikh et al., Eds., SPARC Rep. 9, WCRP-17/2018, GAW Rep. 241, 102 pp., https://doi.org/10.17874/f899e57a20b.

Unauthenticated | Downloaded 11/21/25 11:34 AM UTC

Spencer, R. W., J. R. Christy, and W. D. Braswell, 2017: UAH version 6 global satellite temperature products: Methodology and results. *Asia-Pac. J. Atmos. Sci.*, **53**, 121–130, https://doi.org/10.1007/s13143-017-0010-y.

Stackhouse, P. W., T. Wong, D. P. Kratz, P. Sawaengphokhai, A. C. Wiber, S. K. Gupta, and N. G. Loeb, 2016: Earth radiation budget at top-of-atmosphere [in "State of the Climate in 2015"]. *Bull. Amer. Meteor. Soc.*, **97** (8), S41–S43, https://doi.org/10.1175/2017BAMSStateoftheClimate.1.

Staub, B., C. Lambiel, and R. Delaloye, 2016: Rock glacier creep as a thermally-driven phenomenon: A decade of inter-annual observation from the Swiss Alps. *XI Int. Conf. on Permafrost*, Potsdam, Germany, Alfred Wegener Institute Helmholtz Center for Polar and Marine Research, 96–97, https://doi.org/10.2312/GFZ.LIS.2016.001.

Stein, A. F., R. R. Draxler, G. D. Rolph, B. J. B. Stunder, M. D. Cohen, and F. Ngan, 2015: NOAA's HYSPLIT atmospheric transport and dispersion modeling system. *Bull. Amer. Meteor. Soc.*, **96**, 2059–2077, https://doi.org/10.1175/BAMS-D-14-00110.1.

Steinbrecht, W., and Coauthors, 2017: An update on ozone profile trends for the period 2000 to 2016. *Atmos. Chem. Phys.*, **17**, 10 675–10 690, https://doi.org/10.5194/acp-17-10675-2017.

Steiner, A. K., and Coauthors, 2020: Observed temperature changes in the troposphere and stratosphere from 1979 to 2018. *J. Climate*, **33**, 8165–8194, https://doi.org/10.1175/JCLI-D-19-0998.1.

Stocker, M., F. Ladstädter, and A. K. Steiner, 2021: Observing the climate impact of large wildfires on stratospheric temperature. *Sci. Rep.*, **11**, 22994, https://doi.org/10.1038/s41598-021-02335-7.

—— , A. K. Steiner, F. Ladstädter, U. Foelsche, and W. J. Randel, 2024: Observed impacts of the Hunga Tonga eruption on stratospheric temperature. *EGU General Assembly 2024*, Vienna, Austria, EGU, EGU24-11683, https://doi.org/10.5194/egusphere-egu24-11683.

Stoy, P. C., J. Roh, and G. T. Bromley, 2022: It's the heat and the humidity: The complementary roles of temperature and specific humidity to recent changes in the energy content of the near-surface atmosphere. *Geophys. Res. Lett.*, **49**, e2021GL096628, https://doi.org/10.1029/2021GL096628.

Streletskiy, D. A., and Coauthors, 2025: Thawing permafrost is subsiding in the Northern Hemisphere—Review and perspectives. *Environ. Res. Lett.*, **20**, 013006, https://doi.org/10.1088/1748-9326/ada2ff.

Susskind, J., G. Molnar, L. Iredell, and N. G. Loeb, 2012: Interannual variability of outgoing longwave radiation as observed by AIRS and CERES. *J. Geophys. Res.*, **117**, D23107, https://doi.org/10.1029/2012JD017997.

Szopa, S., and Coauthors, 2021: Short-lived climate forcers. *Climate Change 2021: The Physical Science Basis*, V. Masson-Delmotte et al., Eds., Cambridge University Press, 817–922, https://doi.org/10.1017/9781009157896.008.

Taha, G., R. Loughman, P. R. Colarco, T. Zhu, L. W. Thomason, and G. Jaross, 2022: Tracking the 2022 Hunga Tonga-Hunga Ha'apai aerosol cloud in the upper and Middle stratosphere using space-based observations. *Geophys. Res. Lett.*, **49**, e2022GL100091, https://doi.org/10.1029/2022GL100091.

Tandon, A., 2024: Record-breaking Philippines typhoon season was 'supercharged' by climate change. Carbon Brief, https://www.carbonbrief.org/record-breaking-philippines-typhoon-season-was-supercharged-by-climate-change/.

Tapley, B. D., S. Bettadpur, J. C. Ries, P. F. Thompson, and M. M. Watkins, 2004: GRACE measurements of mass variability in the Earth system. *Science*, **305**, 503–505, https://doi.org/10.1126/science.1099192.

Tarasick, D. W., and Coauthors, 2019: Tropospheric ozone assessment report: Tropospheric ozone from 1877 to 2016, observed levels, trends and uncertainties. *Elementa*, **7**, 39, https://doi.org/10.1525/elementa.376.

The GlaMBIE Team, 2025: Community estimate of global glacier mass changes from 2000 to 2023. *Nature*, **639**, 382–388, https://doi.org/10.1038/s41586-024-08545-z.

Thibert, E., and X. Bodin, 2022: Changes in surface velocities over four decades on the Laurichard rock glacier (French Alps). Permafrost Periglacial Processes, **33**, 323–335, https://doi.org/10.1002/ppp.2159.

Thiery, W., E. Davin, S. Seneviratne, K. Bedka, S. Lhermitte, and N. van Lipzig, 2016: Hazardous thunderstorm intensification over Lake Victoria. *Nat. Commun.*, **7**, 12786, https://doi.org/10.1038/ncomms12786.

Thomason, L. W., and Coauthors, 2018: A global space-based stratospheric aerosol climatology: 1979–2016. *Earth Syst. Sci. Data*, **10**, 469–492, https://doi.org/10.5194/essd-10-469-2018.

Tian, H., and Coauthors, 2024: Global nitrous oxide budget 1980–2020. *Earth Syst. Sci. Data*, **16**, 2543–2604, https://doi.org/10.5194/essd-16-2543-2024.

Todt, M. A., E. Asher, E. Hall, P. Cullis, A. Jordan, K. Xiong, D. F. Hurst, and T. Thornberry, 2023: Baseline balloon stratospheric aerosol profiles (B2SAP)—Systematic measurements of aerosol number density and size. *J. Geophys. Res. Atmos.*, **128**, e2022JD038041, https://doi.org/10.1029/2022JD038041.

Toreti, A., and Coauthors, 2024a: Global drought overview September 2024 – GDO analytical report. Publications Office of the European Union Rep. JRC139423, 36 pp., https://data.europa.eu/doi/10.2760/7511271.

—— , and Coauthors, 2024b: Drought in Europe - July 2024: GDO analytical report. 24 pp., https://doi.org/10.2760/420832.

—— , and Coauthors, 2024c: Drought in the Amazon and the La Plata basins - December 2024: GDO analytical report. 30 pp., https://doi.org/10.2760/9524487.

Torralba, V., F. J. Doblas-Reyes, and N. Gonzalez-Reviriegol, 2017: Uncertainty in recent near-surface wind speed trends: A global reanalysis intercomparison. *Environ. Res. Lett.*, **12**, 114019, https://doi.org/10.1088/1748-9326/aa8a58.

Trenberth, K. E., 1997: The definition of El Niño. *Bull. Amer. Meteor. Soc.*, **78**, 2771–2777, https://doi.org/10.1175/1520-0477(1997)078<2771:TDOENO>2.0.CO;2.

—— , and J. T. Fasullo, 2013: Regional energy and water cycles: Transports from ocean to land. *J. Climate*, **26**, 7837–7851, https://doi.org/10.1175/JCLI-D-13-00008.1.

UNEP, 2024: Report of the Scientific Assessment Panel in response to Decision XXXV/7: Emissions of HFC-23. 35 pp., https://ozone.unep.org/system/files/documents/SAP_Report_on_HFC23_September2024.pdf.

United Nations, 2016: Paris Agreement to the United Nations Framework Convention on Climate Change, Dec. *12*, **2015**, T.I.A.S. No. 16-1104. 54 pp., https://unfccc.int/sites/default/files/resource/parisagreement_publication.pdf.

UNOCHA, 2024: Southern Africa: El Niño regional humanitarian overview. OCHA, https://www.unocha.org/publications/report/mozambique/southern-africa-el-nino-regional-humanitarian-overview-september-2024.

Unauthenticated | Downloaded 11/21/25 11:34 AM UTC

USDA and USDC, 2024: *Weekly Weather and Crop Bulletin*. Vol. 111, No. 11, 28 pp., https://downloads.usda.library.cornell.edu/usda-esmis/files/cj82k728n/m326np628/pk02f026h/wwcb1124.pdf.

van der Schalie, R., and Coauthors, 2017: The merging of radiative transfer based surface soil moisture data from SMOS and AMSR-E. Remote Sens. *Environ.*, **189**, 180–193, https://doi.org/10.1016/j.rse.2016.11.026.

van der Schrier, G., J. Barichivich, K. R. Briffa, and P. D. Jones, 2013: A scPDSI-based global dataset of dry and wet spells for 1901–2009. *J. Geophys. Res. Atmos.*, **118**, 4025–4048, https://doi.org/10.1002/jgrd.50355.

van der Werf, G. R., and Coauthors, 2017: Global fire emissions estimates during 1997–2016. *Earth Syst. Sci. Data*, **9**, 697–720, https://doi.org/10.5194/essd-9-697-2017.

Van Dijk, A. I. J. M., and Coauthors, 2025: Global Water Monitor 2024, Summary Report. Global Water Monitor Consortium, 58 pp., https://www.globalwater.online/globalwater/report/.

Virts, K. S., and S. J. Goodman, 2020: Prolific lightning and thunderstorm initiation over the Lake Victoria basin in East Africa. *Mon. Wea. Rev.*, **148**, 1971–1985, https://doi.org/10.1175/MWR-D-19-0260.1.

——, J. M. Wallace, M. L. Hutchins, and R. H. Holzworth, 2015: Diurnal and seasonal lightning variability over the Gulf Stream and the Gulf of Mexico. *J. Atmos. Sci.*, **72**, 2657–2665, https://doi.org/10.1175/JAS-D-14-0233.1.

Vivero, S., X. Bodin, D. Farías-Barahona, S. MacDonell, N. Schaffer, B. A. Robson, and C. Lambiel, 2021: Combination of aerial, satellite, and UAV photogrammetry for quantifying rock glacier kinematics in the Dry Andes of Chile (30°S) since the 1950s. *Front. Remote Sens.*, **2**, 784015, https://doi.org/10.3389/frsen.2021.784015.

Vömel, H., S. Evan, and M. Tully, 2022: Water vapor injection into the stratosphere by Hunga Tonga-Hunga Ha'apai. *Science*, **377**, 1444–1447, https://doi.org/10.1126/science.abq2299.

von Schuckmann, K., and Coauthors, 2023: Heat stored in the earth system 1960–2020: Where does the energy go? *Earth Syst. Sci. Data*, **15**, 1675–1709, https://doi.org/10.5194/essd-15-1675-2023.

Vose, R. S., and Coauthors, 2021: Implementing full spatial coverage in NOAA's global temperature analysis. *Geophys. Res. Lett.*, **48**, e2020GL090873, https://doi.org/10.1029/2020GL090873.

Vreugdenhil, M., and Coauthors, 2022: Microwave remote sensing for agricultural drought monitoring: Recent developments and challenges. *Front. Water*, **4**, 1045451, https://doi.org/10.3389/frwa.2022.1045451.

Wang, L., and Coauthors, 2023: Quantification of water released by thawing permafrost in the source region of the Yangtze River on the Tibetan Plateau by InSAR monitoring. *Water Resour. Res.*, **59**, e2023WR034451, https://doi.org/10.1029/2023WR034451.

Weatherhead, E. C., and Coauthors, 1998: Factors affecting the detection of trends: Statistical considerations and applications to environmental data. *J. Geophys. Res.*, **103**, 17 149–17 161, https://doi.org/10.1029/98JD00995.

Wells, N., S. Goddard, and M. J. Hayes, 2004: A self-calibrating palmer drought severity index. *J. Climate*, **17**, 2335–2351, https://doi.org/10.1175/1520-0442(2004)017<2335:ASPDSI>2.0.CO;2.

Wentz, F. J., 1997: A well-calibrated ocean algorithm for special sensor microwave/imager. *J. Geophys. Res.*, **102**, 8703–8718, https://doi.org/10.1029/96JC01751.

——, 2015: A 17-yr climate record of environmental parameters derived from the Tropical Rainfall Measuring Mission (TRMM) microwave imager. *J. Climate*, **28**, 6882–6902, https://doi.org/10.1175/JCLI-D-15-0155.1.

——, L. Ricciardulli, K. Hilburn, and C. Mears, 2007: How much more rain will global warming bring? *Science*, **317**, 233–235, https://doi.org/10.1126/science.1140746.

Wentz, K., T. Meissner, F. Wentz, and A. Manaster, 2024: Absolute intercalibration of spaceborne microwave radiometers. *J. Atmos. Oceanic Technol.*, **41**, 1121–1138, https://doi.org/10.1175/JTECH-D-24-0024.1.

Western, L. M., and Coauthors, 2023: Author correction: Global increase of ozone-depleting chlorofluorocarbons from 2010 to 2020. *Nat. Geosci.*, **16**, 546, https://doi.org/10.1038/s41561-023-01205-3.

——, and Coauthors, 2024: A decrease in radiative forcing and equivalent effective chlorine from hydrochlorofluorocarbons. *Nat. Climate Change*, **14**, 805–807, https://doi.org/10.1038/s41558-024-02038-7.

Weyhenmeyer, G. A., and Coauthors, 2024: Global lake health in the anthropocene: Societal implications and treatment strategies. *Earth's Future*, **12**, e2023EF004387, https://doi.org/10.1029/2023EF004387.

WFP, 2024: Eastern Africa Seasonal Monitor: Severe flooding across equatorial areas, April–May 2024. ReliefWeb, 15 pp., https://reliefweb.int/report/kenya/eastern-africa-seasonal-monitor-severe-flooding-across-equatorial-areas-april-may-2024.

WGMS, 2023: Global Glacier Change Bulletin. No. 5 (2020–2021), ISC(WDS)/IUGG(IACS)/UNEP/UNESCO/WMO, World Glacier Monitoring Service, 148 pp., https://doi.org/10.5904/wgms-fog-2023-09.

Wielicki, B. A., B. R. Barkstrom, E. F. Harrison, R. B. Lee, I. I. I. G. L. Smith, and J. E. Cooper, 1996: Clouds and the Earth's Radiant Energy System (CERES): An Earth observing system experiment. *Bull. Amer. Meteor. Soc.*, **77**, 853–868, https://doi.org/10.1175/1520-0477(1996)077<0853:CATERE>2.0.CO;2.

——, and Coauthors, 1998: Clouds and the Earth's Radiant Energy System (CERES): Algorithm overview. *IEEE Trans. Geosci. Remote Sens.*, **36**, 1127–1141, https://doi.org/10.1109/36.701020.

Wiese, D. N., F. W. Landerer, and M. M. Watkins, 2016: Quantifying and reducing leakage errors in the JPL RL05M GRACE Mascon solution. *Water Resour. Res.*, **52**, 7490–7502, https://doi.org/10.1002/2016WR019344.

Willett, K. M., 2023a: HadISDH.extremes Part I: A gridded wet bulb temperature extremes index product for climate monitoring. *Adv. Atmos. Sci.*, **40**, 1952–1967, https://doi.org/10.1007/s00376-023-2347-8.

——, 2023b: HadISDH.extremes Part II: Exploring humid heat extremes using wet bulb temperature indices. *Adv. Atmos. Sci.*, **40**, 1968–1985, https://doi.org/10.1007/s00376-023-2348-7.

——, 2023c: Sidebar 2.1: Assessing humid heat extremes over land [in "State of the Climate in 2022"]. *Bull. Amer. Meteor. Soc.*, **104** (9), S51–S53, https://doi.org/10.1175/BAMS-D-23-0090.1.

——, C. N. Williams Jr., R. J. H. Dunn, P. W. Thorne, S. Bell, M. de Podesta, P. D. Jones, and D. E. Parker, 2013: HadISDH: An updateable land surface specific humidity product for climate monitoring. *Climate Past*, **9**, 657–677, https://doi.org/10.5194/cp-9-657-2013.

——, R. J. H. Dunn, P. W. Thorne, S. Bell, M. de Podesta, D. E. Parker, P. D. Jones, and C. N. Williams Jr., 2014: HadISDH land surface multi-variable humidity and temperature record for climate monitoring. *Climate Past*, **10**, 1983–2006, https://doi.org/10.5194/cp-10-1983-2014.

Unauthenticated | Downloaded 11/21/25 11:34 AM UTC

—— , —— , J. Kennedy, and D. Berry, 2020: Development of the HadISDH.marine humidity climate monitoring dataset. *Earth Syst. Sci. Data*, **12**, 2853–2880, https://doi.org/10.5194/essd-12-2853-2020.

—— , R. M. Horton, Y. T. E. Lo, C. Raymond, and C. D. W. Rogers, 2024: Humid-heat extremes over land [in "State of the Climate in 2023"]. *Bull. Amer. Meteor. Soc.*, **105** (8), S55–S56, https://doi.org/10.1175/2024BAMSStateoftheClimate.1.

WMO, 2022: Scientific Assessment of Ozone Depletion: 2022. WMO Ozone Research and Monitoring GAW Rep. 278, 520 pp., https://ozone.unep.org/sites/default/files/2023-02/Scientific-Assessment-of-Ozone-Depletion-2022.pdf.

—— , 2024: State of the Climate 2024. Update for COP29. WMO, 12 pp., https://library.wmo.int/idurl/4/69075.

—— , 2025a: State of the Global Climate 2024. WMO-1368, 42 pp., https://library.wmo.int/records/item/69455-state-of-the-global-climate-2024.

—— , 2025b: State of the Climate 2024. Significant Weather & Climate Events. https://wmo.int/sites/default/files/2025-03/State%20of%20the%20Global%20Climate%202024_Extremes%20Supplement.pdf

Wohland, J., N.-E. Omrani, D. Witthaut, and N.-S. Keenlyside, 2019: Inconsistent wind speed trends in current twentieth century reanalyses. *J. Geophys. Res. Atmos.*, **124**, 1931–1940, https://doi.org/10.1029/2018JD030083.

Woolway, R. I., and C. J. Merchant, 2018: Intralake heterogeneity of thermal responses to climate change: A study of large Northern Hemisphere lakes. *J. Geophys. Res. Atmos.*, **123**, 3087–3098, https://doi.org/10.1002/2017JD027661.

—— , and Coauthors, 2017: Lake surface temperature [in "State of the Climate in 2016"]. *Bull. Amer. Meteor. Soc.*, **98** (8), S13–S14, https://doi.org/10.1175/2017BAMSStateoftheClimate.1.

—— , and Coauthors, 2018: Lake surface temperature [in "State of the Climate in 2017"]. *Bull. Amer. Meteor. Soc.*, **99** (8), S13–S15, https://doi.org/10.1175/2018BAMSStateoftheClimate.1.

WWA, 2024a: Climate change increased Typhoon Gaemi's wind speeds and rainfall, with devastating impacts across the western Pacific region. WWA, 58 pp., https://www.worldweatherattribution.org/climate-change-increased-typhoon-gaemis-wind-speeds-and-rainfall/.

—— , 2024b: Rapid urbanisation and climate change key drivers of dramatic flood impacts in Nepal. WWA, 30 pp., https://www.worldweatherattribution.org/rapid-urbanisation-and-climate-change-key-drivers-of-dramatic-flood-impacts-in-nepal/.

Xing, J. W., and M. M. Wang, 2023: Trend and drivers of satellite-detected burned area changes across Arctic region since the 21st century. J. Geophys. Res. Atmos., 128, https://doi.org/10.1029/2023JD038946.

Xu, H., L. Zhang, Z. Jin, A. Wang, Z. Liu, and F. Wang, 2025: Physiological strain under different wet bulb temperatures during daylong humid heat exposure in young men. *Build. Environ.*, **274**, 112783, https://doi.org/10.1016/j.buildenv.2025.112783.

Xu, N., H. Lu, W. Li, and P. Gong, 2024: Natural Lakes dominate global water storage variability. *Sci. Bull.*, **69**, 1016–1019, https://doi.org/10.1016/j.scib.2024.02.023.

Yang, Y., and Coauthors, 2023: Evapotranspiration on a greening earth. *Nat. Rev. Earth Environ.*, **4**, 626–641, https://doi.org/10.1038/s43017-023-00464-3.

Yao, F., B. Livneh, B. Rajagopalan, J. Wang, J.-F. Crétaux, Y. Wada, and M. Berge-Nguyen, 2023: Satellites reveal widespread decline in global lake water storage. *Science*, **380**, 743–749, https://doi.org/10.1126/science.abo2812.

Yeh, S., and Coauthors, 2018: ENSO atmospheric teleconnections and their response to greenhouse gas forcing. *Rev. Geophys.*, **56**, 185–206, https://doi.org/10.1002/2017RG000568.

Yoon, J., and S.-W. Yeh, 2010: Influence of the Pacific decadal oscillation on the relationship between El Niño and the northeast Asian summer monsoon. *J. Climate*, **23**, 4525–4537, https://doi.org/10.1175/2010JCLI3352.1.

Yosef, Y., E. Aguilar, and P. Alpert, 2021: Is it possible to fit extreme climate change indices together seamlessly in the era of accelerated warming? *Int. J. Climatol.*, **41**, E952–E963, https://doi.org/10.1002/joc.6740.

Young, S. S., 2023: Global and regional snow cover decline: 2000–2022. *Climate*, **11**, 162, https://doi.org/10.3390/cli11080162.

Yu, P., and Coauthors, 2021: Persistent stratospheric warming due to 2019–2020 Australian wildfire smoke. *Geophys. Res. Lett.*, **48**, e2021GL092609, https://doi.org/10.1029/2021GL092609.

Zeng, Z., and Coauthors, 2019: A reversal in global terrestrial stilling and its implications for wind energy production. *Nat. Climate Change*, **9**, 979–985, https://doi.org/10.1038/s41558-019-0622-6.

Zha, J., and Coauthors, 2021: Projected changes in global terrestrial near-surface wind speed in 1.5°C–4.0°C global warming levels. *Environ. Res. Lett.*, **16**, 114016, https://doi.org/10.1088/1748-9326/ac2fdd.

Zhang, G. F., and Coauthors, 2021: Uneven warming likely contributed to declining near-surface wind speeds in northern China between 1961 and 2016. *J. Geophys. Res. Atmos.*, **126**, e2020JD033637, https://doi.org/10.1029/2020JD033637.

Zhang, S., S. Solomon, C. D. Boone, and G. Taha,2024: Investigating the vertical extent of the 2023 summer Canadian wildfire impacts with satellite observations. *Atmos. Chem. Phys.*, **24**, 11 727–11 736, https://doi.org/10.5194/acp-24-11727-2024.

Zhang, W., and Coauthors, 2025: A year marked by extreme precipitation and floods: Weather and climate extremes in 2024. *Adv. Atmos. Sci.*, **42**, 1045–1063, https://doi.org/10.1007/s00376-025-4540-4.

Zhang, X., L. Alexander, G. C. Hegerl, P. Jones, A. K. Tank, T. C. Peterson, B. Trewin, and F. W. Zwiers, 2011: Indices for monitoring changes in extremes based on daily temperature and precipitation data. *Wiley Interdiscip. Rev.: Climate Change*, **2**, 851–870, https://doi.org/10.1002/wcc.147.

Zhang, Z., B. Poulter, A. F. Feldman, Q. Ying, P. Ciais, S. Peng, and X. Li, 2023: Recent intensification of wetland methane feedback. *Nat. Climate Change*, **13**, 430–433, https://doi.org/10.1038/s41558-023-01629-0.

Zhao, L., and Coauthors, 2024: Investigation, monitoring, and simulation of permafrost on the Qinghai–Tibet Plateau: A review. *Permafrost Periglacial Processes*, **35**, 412–422, https://doi.org/10.1002/ppp.2227.

Zhao, Y., and Coauthors, 2019: Inter-model comparison of global hydroxyl radical (OH) distributions and their impact on atmospheric methane over the 2000–2016 period. *Atmos. Chem. Phys.*, **19**, 13 701–13 723, https://doi.org/10.5194/acp-19-13701-2019.

Zhao, Y., H. Norouzi, M. Azarderakhsh, and A. AghaKouchak, 2021: Global patterns of hottest, coldest, and extreme diurnal variability on earth. *Bull. Amer. Meteor. Soc.*, **102**, E1672–E1681, https://doi.org/10.1175/BAMS-D-20-0325.1.

Zheng, B., and Coauthors, 2023: Record-high CO_2 emissions from boreal fires in 2021. *Science*, **379**, 912–917, https://doi.org/10.1126/science.ade0805.

Unauthenticated | Downloaded 11/21/25 11:34 AM UTC

Zhou, X., and Coauthors, 2024: Antarctic vortex dehydration in 2023 as a substantial removal pathway for Hunga Tonga-Hunga Ha'apai water vapor. *Geophys. Res. Lett.*, **51**, e2023GL107630, https://doi.org/10.1029/2023GL107630.

Zhu, Z., and Coauthors, 2016: Greening of the Earth and its drivers. *Nat. Climate Change*, **6**, 791–795, https://doi.org/10.1038/nclimate3004.

Ziemke, J. R., and Coauthors, 2019: Trends in global tropospheric ozone inferred from a composite record of TOMS/OMI/MLS/OMPS satellite measurements and the MERRA-2 GMI simulation. *Atmos. Chem. Phys.*, **19**, 3257–3269, https://doi.org/10.5194/acp-19-3257-2019.

——, and Coauthors, 2022: NASA satellite measurements show global-scale reductions in free tropospheric ozone in 2020 and again in 2021 during COVID-19. *Geophys. Res. Lett.*, **49**, e2022GL098712, https://doi.org/10.1029/2022GL098712.

Ziese, M., A. Rauthe-Schöch, S. Hänsel, P. Finger, E. Rustemeier, and U. Schneider, 2022: GPCC full data daily version 2022 at 1.0°: Daily Land-Surface precipitation from Rain-Gauges built on GTS-based and historic data: Globally gridded daily totals (version 2022, p. approx. 25 MB per gzip file) [NetCDF]. GPCC, https://doi.org/10.5676/DWD_GPCC/FD_D_V2022_100.

Zolghadrshojaee, M., S. Tegtmeier, S. M. Davis, and R. Pilch Kedzierski, 2024: Variability and long-term changes in tropical cold-point temperature and water vapor. *Atmos. Chem. Phys.*, **24**, 7405–7419, https://doi.org/10.5194/acp-24-7405-2024.

Zotta, R. M., R. van der Schalie, W. Preimesberger, R. De Jeu, and W. Dorigo, 2023: Vegetation optical depth [in "State of the Climate in 2023"]. *Bull. Amer. Meteor. Soc.*, **105** (8), S113–S114, https://doi.org/10.1175/BAMS-D-24-0116.1.

——, L. Moesinger, R. van der Schalie, M. Vreugdenhil, W. Preimesberger, T. Frederikse, R. De Jeu, and W. Dorigo, 2024a: VODCA v2: Multi-sensor, multi-frequency vegetation optical depth data for long-term canopy dynamics and biomass monitoring (1.0.0). TU Wien, accessed 16 January 2025, https://doi.org/10.48436/t74ty-tcx62.

——, ——, ——, ——, ——r, ——, ——, and ——, 2024b: VODCA v2: Multi-sensor, multi-frequency vegetation optical depth data for long-term canopy dynamics and biomass monitoring. *Earth Syst. Sci. Data*, **16**, 4573–4617, https://doi.org/10.5194/essd-16-4573-2024.

Zou, C.-Z., H. Xu, X. Hao, and Q. Liu, 2023: Mid-tropospheric layer temperature record derived from satellite microwave observations with backward merging approach. *J. Geophys. Res. Atmos.*, **128**, e2022JD037472, https://doi.org/10.1029/2022JD037472.

Zou, D., and Coauthors, 2024: Estimation of permafrost ground ice to 10-m depth on the Qinghai–Tibet Plateau. *Permafrost Periglacial Processes*, **35**, 423–434, https://doi.org/10.1002/ppp.2226]

Unauthenticated | Downloaded 11/21/25 11:34 AM UTC

STATE OF THE CLIMATE IN 2024

GLOBAL OCEANS

G. C. Johnson and R. Lumpkin, Eds.

Special Online Supplement to the *Bulletin of the American Meteorological Society* Vol. 106, No. 8, August, 2025

https://doi.org/10.1175/BAMS-D-25-0074.1

Corresponding author: Gregory C. Johnson / gcj3@uw.edu

©2025 American Meteorological Society
For information regarding reuse of this content and general copyright information, consult the AMS Copyright Policy.

Unauthenticated | Downloaded 11/21/25 11:34 AM UTC

STATE OF THE CLIMATE IN 2024
Global Oceans

Editors

Jessica Blunden
James Reagan

Chapter Editors

Anthony Arguez
Josh Blannin
Peter Bissolli
Kyle R. Clem
Howard J. Diamond
Matthew L. Druckenmiller
Robert J. H. Dunn
Catherine Ganter
Nadine Gobron
Gregory C. Johnson
Rick Lumpkin
Rodney Martinez
Ademe Mekonnen
Twila A. Moon
Gary A. Morris
Marilyn N. Raphael
Carl J. Schreck III
Laura Stevens
Richard L. Thoman
Kate M. Willett
Zhiwei Zhu

Technical Editor

Lukas Noguchi

BAMS Special Editor for Climate

Timothy DelSole

American Meteorological Society

Unauthenticated | Downloaded 11/21/25 11:34 AM UTC

Cover Credit:
NEMO float after deployment in sea ice from the German icebreaker Polarstern Bremerhaven. Photo courtesy of the Argo Program (https://argo.ucsd.edu)

How to cite this document:
Global Oceans is one chapter from the *State of the Climate in 2024* annual report and is available from https://doi.org/10.1175/BAMS-D-25-0074.1. Compiled by NOAA's National Centers for Environmental Information, *State of the Climate in 2024* is based on contributions from scientists from around the world. It provides a detailed update on global climate indicators, notable weather events, and other data collected by environmental monitoring stations and instruments located on land, water, ice, and in space. The full report is available from https://doi.org/10.1175/2025BAMSStateoftheClimate.1.

Citing the complete report:
Blunden, J. and J. Reagan, Eds., 2025: "State of the Climate in 2024". Bull. Amer. Meteor. Soc., 106 (8), Si–S513 https://doi.org/10.1175/2025BAMSStateoftheClimate.1.

Citing this chapter:
Johnson, G. C. and R. L. Lumpkin, Eds., 2025: Global Oceans [in "State of the Climate in 2024"]. Bull. Amer. Meteor. Soc., 106 (8), S173–S232, https://doi.org/10.1175/BAMS-D-25-0074.1.

Citing a section (example):
Lumpkin, R., M. Le Hénaff, F. P. Tuchen, and R. C. Perez, 2025: Surface currents [in "State of the Climate in 2024"]. Bull. Amer. Meteor. Soc., 106 (8), S204–S207, https://doi.org/10.1175/BAMS-D-25-0074.1.

Unauthenticated | Downloaded 11/21/25 11:34 AM UTC

Editor and Author Affiliations (alphabetical by name)

Beckley, Brian, KBR, Inc., Greenbelt, Maryland; NASA Goddard Space Flight Center, Greenbelt, Maryland

Bellas-Manley, Ashley, Colorado Center for Astrodynamics Research, Cooperative Institute for Research in Environmental Sciences, University of Colorado Boulder, Boulder, Colorado

Carter, Brendan R., Cooperative Institute for Climate, Ocean, and Ecosystem Studies, University of Washington, Seattle, Washington; NOAA/OAR Pacific Marine Environmental Laboratory, Seattle, Washington

Cetinić, Ivona, NASA Goddard Space Flight Center, Greenbelt, Maryland; Universities Space Research Association, Columbia, Maryland

Chambers, Don P., College of Marine Science, University of South Florida, St. Petersburg, Florida

Chan, Duo, School of Ocean and Earth Science, University of Southampton, Southampton, United Kingdom

Cheng, Lijing, International Center for Climate and Environment Sciences, Institute of Atmospheric Physics, Chinese Academy of Sciences, Beijing, China

Dong, Shenfu, NOAA/OAR Atlantic Oceanographic and Meteorological Laboratory, Miami, Florida

Feely, Richard A., NOAA/OAR Pacific Marine Environmental Laboratory, Seattle, Washington

Franz, Bryan A., NASA Goddard Space Flight Center, Greenbelt, Maryland

Gao, Meng, NASA Goddard Space Flight Center, Greenbelt, Maryland; Science Systems and Applications, Inc., Lanham, Maryland

Garg, Jay, ADNET Systems, Inc., Hampton, Virginia

Giglio, Donata, Department of Atmospheric and Oceanic Sciences, University of Colorado Boulder, Boulder, Colorado

Graham, Garrett, North Carolina Institute for Climate Studies, North Carolina State University, Asheville, North Carolina

Hamlington, Benjamin D., Center for Coastal Physical Oceanography, Old Dominion University, Norfolk, Virginia

Hobbs, Will, Australian Antarctic Program Partnership, Institute for Marine and Antarctic Studies, University of Tasmania, Hobart, Tasmania; Australian Research Council Centre of Excellence for Climate Extremes, University of Tasmania, Hobart, Tasmania

Hu, Zeng-Zhen, NOAA/NWS National Centers for Environmental Prediction Climate Prediction Center, College Park, Maryland

Huang, Boyin, NOAA/NESDIS National Centers for Environmental Information, Asheville, North Carolina

Jersild, Annika, Earth System Science Interdisciplinary Center/Cooperative Institute for Satellite Earth System Studies, University of Maryland, College Park, Maryland

Jevrejeva, Svetlana, National Oceanography Centre, Liverpool, United Kingdom

Johns, William E., Rosenstiel School of Marine and Atmospheric Science, University of Miami, Miami, Florida

Johnson, Gregory C., School of Oceanography, University of Washington, Seattle, Washington ; NOAA/OAR Pacific Marine Environmental Laboratory, Seattle, Washington (retired)

Killick, Rachel. E., Met Office Hadley Center, Exeter, United Kingdom

Kuusela, Mikael, Department of Statistics and Data Science, Carnegie Mellon University, Pittsburg, Pennsylvania

Lamont, Tarron, Department of Forestry, Fisheries and the Environment, Cape Town, South Africa

Landerer, F. W., Jet Propulsion Laboratory, California Institute of Technology, Pasadena, California

Landschützer, Peter, Flanders Marine Institute, InnovOcean Campus, Ostend, Belgium

Le Hénaff, Matthieu, NOAA/OAR Atlantic Oceanographic and Meteorological Laboratory, Miami, Florida

Leuliette, Eric, NOAA/NWS NCWCP Laboratory for Satellite Altimetry, College Park, Maryland

Locarnini, Ricardo, NOAA/NESDIS National Centers for Environmental Information, Silver Spring, Maryland

Lumpkin, Rick, NOAA/OAR Atlantic Oceanographic and Meteorological Laboratory, Miami, Florida

Lyman, John M., Cooperative Institute for Marine and Atmospheric Research, University of Hawai'i, Honolulu, Hawai'i; NOAA/OAR Pacific Marine Environmental Laboratory, Seattle, Washington

Merrifield, Mark A., Integrative Oceanography Division, Scripps Institution of Oceanography, La Jolla, California

Mishonov, Alexey, Earth System Science Interdisciplinary Center/Cooperative Institute for Satellite Earth System Studies, University of Maryland, College Park, Maryland; NOAA/NESDIS National Centers for Environmental Information, Silver Spring, Maryland

Mitchum, Gary T., College of Marine Science, University of South Florida, St. Petersburg, Florida

Moat, Ben I., National Oceanography Centre, Southampton, United Kingdom

Nerem, R. Steven, Colorado Center for Astrodynamics Research, Cooperative Institute for Research in Environmental Sciences, University of Colorado Boulder, Boulder, Colorado

Oe, Mitsuho, Japan Meteorological Agency, Tokyo, Japan

Perez, Renellys C., NOAA/OAR Atlantic Oceanographic and Meteorological Laboratory, Miami, Florida

Reagan, James, NOAA/NESDIS National Centers for Environmental Information, Silver Spring, Maryland

Schlegal, Robert W., Laboratoire d'Océanographie de Villefranche, Sorbonne Université, Villefranche-sur-mer, France

Schmid, Claudia, NOAA/OAR Atlantic Oceanographic and Meteorological Laboratory, Miami, Florida

Smeed, David A., National Oceanography Centre, Southampton, United Kingdom

Smith, Ryan H., NOAA/OAR Atlantic Oceanographic and Meteorological Laboratory, Miami, Florida

Speich, Sabrina, Laboratoire de Météorologie Dynamique, Institut Pierre-Simon Laplace, ENS-PSL, Paris, France

Stackhouse, Jr., Paul W., NASA Langley Research Center, Hampton, Virginia

Sukianto, Thea, Department of Statistics and Data Science, Carnegie Mellon University, Pittsburg, Pennsylvania

Sweet, William, NOAA/NOS Center for Operational Oceanographic Products and Services, Silver Spring, Maryland

Thompson, Philip R., Cooperative Institute for Marine and Atmospheric Research, University of Hawai'i, Honolulu, Hawai'i

Triñanes, Joaquin A., Laboratory of Systems, Technological Research Institute, Universidad de Santiago de Compostela, Campus Universitario Sur, Santiago de Compostela, Spain; Cooperative Institute for Marine and Atmospheric Studies, Rosenstiel School of Marine and Atmospheric Science, University of Miami, Miami, Florida; NOAA/OAR Atlantic Oceanographic and Meteorological Laboratory, Miami, Florida

Tuchen, Franz Philip, Cooperative Institute for Marine and Atmospheric Studies, University of Miami, Miami, Florida; NOAA/OAR Atlantic Oceanographic and Meteorological Laboratory, Miami, Florida

Volkov, Denis L., Cooperative Institute for Marine and Atmospheric Studies, University of Miami, Miami, Florida; NOAA/OAR Atlantic Oceanographic and Meteorological Laboratory, Miami, Florida

Wanninkhof, Rik, NOAA/OAR Atlantic Oceanographic and Meteorological Laboratory, Miami, Florida

Weller, Robert A., Department of Physical Oceanography, Woods Hole Oceanographic Institution, Woods Hole, Massachusetts

Westberry, Toby K., Oregon State University, Corvallis, Oregon

Widlansky, Matthew J., Cooperative Institute for Marine and Atmospheric Research, University of Hawai'i, Honolulu, Hawai'i

Unauthenticated | Downloaded 11/21/25 11:34 AM UTC

Editor and Author Affiliations (continued)

Willis, Joshua K., Jet Propulsion Laboratory, California Institute of Technology, Pasadena, California

Yin, Xungang, NOAA/NESDIS National Centers for Environmental Information, Asheville, North Carolina

Yu, Lisan, Department of Physical Oceanography, Woods Hole Oceanographic Institution, Woods Hole, Massachusetts

Zhang, Huai-Min, NOAA/NESDIS National Centers for Environmental Information, Asheville, North Carolina

Editorial and Production Team

Allen, Jessicca, Graphics Support, Cooperative Institute for Satellite Earth System Studies, North Carolina State University, Asheville, North Carolina

Camper, Amy V., Graphics Support, Innovative Consulting and Management Services, LLC, NOAA/NESDIS National Centers for Environmental Information, Asheville, North Carolina

Carroll, Lauren, Content Team Lead, Communications and Outreach, NOAA/NESDIS National Centers for Environmental Information, Asheville, North Carolina

Haley, Bridgette O., Graphics Support, NOAA/NESDIS National Centers for Environmental Information, Asheville, North Carolina

Love-Brotak, S. Elizabeth, Lead Graphics Production, NOAA/NESDIS National Centers for Environmental Information, Asheville, North Carolina

Ohlmann, Laura, Technical Editor, Innovative Consulting and Management Services, LLC, NOAA/NESDIS National Centers for Environmental Information, Asheville, North Carolina

Noguchi, Lukas, Technical Editor, Innovative Consulting and Management Services, LLC, NOAA/NESDIS National Centers for Environmental Information, Asheville, North Carolina

Riddle, Deborah B., Graphics Support, NOAA/NESDIS National Centers for Environmental Information, Asheville, North Carolina

Veasey, Sara W., Visual Communications Team Lead, Communications and Outreach, NOAA/NESDIS National Centers for Environmental Information, Asheville, North Carolina

Unauthenticated | Downloaded 11/21/25 11:34 AM UTC

3. Table of Contents

Unauthenticated | Downloaded 11/21/25 11:34 AM UTC

3. GLOBAL OCEANS

G. C. Johnson and R. Lumpkin, Eds.

a. Overview

—G. C. Johnson and R. Lumpkin

El Niño ebbed in early 2024, reaching neutral status in May and crossing the threshold into La Niña conditions in December. The global average annual sea surface temperature was 0.06°C above the previous record set in 2023. Marine heatwaves in 2024 were, as in 2023, more widespread, long-lived, and severe than in previous years. From 2023 to 2024, ocean heat content from 0 dbar to 2000 dbar increased at a rate equivalent to ~1.5 W m^{-2} of heat applied over the ocean surface, and global sea level increased by 4.6 (±1.4) mm, both reaching record-high levels in 2024. Maps of air–sea flux data estimate that the oceans absorbed carbon at a rate of ~2.7 Pg C yr^{-1} in 2024, which was below the 2014–23 average of ~3.7 Pg C yr^{-1}.

In the Pacific Ocean, given the shift from a strong El Niño to weak La Niña conditions, surface currents across the equatorial Pacific in 2024 were strongly anomalously westward, and sea surface temperatures, sea surface salinities, 0 m–2000 m ocean heat content, and sea level all decreased sharply in the eastern equatorial Pacific from 2023 to 2024. Fluxes of carbon dioxide from ocean to atmosphere were anomalously lower than average during 2024 off Peru and out to about 140°W, likely owing to the El Niño in the first few months of the year. As in 2023, chlorophyll-*a* anomalies in 2024 were low in a wedge in the central and eastern equatorial Pacific, but high just outside that wedge. The Pacific Decadal Oscillation has been in a negative phase since 2020, with sea surface temperature, ocean heat content, and sea surface height values in the center of the North Pacific basin all higher than average, along with relatively lower values around the edges in 2024. A persistent 2020–24 poleward shift in the Kuroshio extension also continued to be evident east of Japan in both ocean heat content and zonal surface current anomalies.

In the Indian Ocean, sea surface temperature, ocean heat content, and sea level were all above average in 2024 across much of the basin, except for a large patch of below-average ocean heat content along 20°S–30°S. Surface currents near the equator were anomalously eastward. Surface salinities were primarily strongly anomalously fresh north of about 12°S in 2024, consistent with anomalously high freshwater input (precipitation minus evaporation) from the atmosphere to the ocean in the region. Chlorophyll-*a* anomalies were quite negative offshore of Somalia and Oman, as well as northeast of Madagascar, but generally positive in the rest of the basin. There was also a prominent ridge of high sea level and ocean heat content extending eastward from Africa just north of Madagascar, which was associated with anomalous westward surface currents on its northern flank.

In the Atlantic, sea surface temperature, ocean heat content, and sea level were all well above average across much of the basin in 2024, with some below-average values of ocean heat content in a patch extending from east of Cape Cod to about 55°N, 25°W. A band of anomalously eastward surface current and above-average ocean heat content directly north of a band of anomalously westward surface current along the Gulf Stream extension west of 70°W is consistent with an anomalous northward shift of the axis of this current in 2024. Sea surface salinity was anomalously high in much of the basin but anomalously low around the Intertropical Convergence Zone and in the Labrador Sea. Updates of time series of the Atlantic meridional overturning circulation at two latitudes revealed little evidence of a trend over the past few decades.

Arctic and Southern Ocean conditions for 2024 are discussed in detail in Chapter 5 and Chapter 6, respectively.

Unauthenticated | Downloaded 11/21/25 11:34 AM UTC

b. Sea surface temperatures

— X. Yin, R. W. Schlegel, B. Huang, D. Chan, G. Graham, Z.-Z. Hu, and H.-M. Zhang

1. INTRODUCTION

The state of sea surface temperatures (SSTs) in the global ocean is described and analyzed using four gridded SST datasets: the Daily OISST (DOISSTv2.1; Huang et al. 2021), ERSSTv5 (Huang et al. 2017), the Hadley Centre Sea Surface Temperature Dataset version 4 (HadSST.4.0.1.0; Kennedy et al. 2019), and Dynamically Consistent ENsemble of Temperature (DCENTv1.0; Chan et al. 2024). DOISSTv2.1 is blended from in situ observations and satellite measurements, covering the period from 1981 to present. It is a high-resolution SST product providing daily mean SSTs, analyzed on 0.25-degree latitude–longitude grids. The latter three products are in situ observation-based SST products, containing monthly mean SST data covering the period from preindustrial times (1854 for ERSSTv5, 1850 for HadSST.4.0.1.0 and DCENTv1.0) to present. The spatial resolution is 2-degree latitude-longitude for ERSSTv5 and 5-degree latitude-longitude for HadSST.4.0.1.0 and DCENTv1.0. SST anomalies (SSTAs) are calculated relative to a 1991–2020 baseline climatology.

A marine heatwave (MHW) is defined as five or more consecutive days of SST above the 90th-percentile daily climatology (Hobday et al. 2016). MHWs are categorized as moderate when the greatest temperature anomaly during the event is less than double the difference between the 90th percentile and the seasonal climatology. When this value is more than double, triple, or quadruple the difference, the MHW is categorized as strong, severe, or extreme, respectively (Hobday et al. 2018). The direct inverse is used to detect and categorize marine cold spells (MCSs; i.e., days below the 10th percentile). MHWs and MCSs are assessed here using the DOISSTv2.1. The baseline period used to detect events in this report is 1991–2020, matching the current advice from the World Meteorological Organization (WMO) for defining climate normals. This year's report is the first to shift to the new baseline for MHWs and MCSs. All previous reports used the 1982–2011 baseline. This means that the values for MHWs will appear lower in this report than in previous years, even though, in absolute terms, the ocean continues to warm.

2. SEA SURFACE TEMPERATURES IN 2024

Record-breaking ocean temperatures in 2023 (Huang et al. 2024; Hu et al. 2024; Jiang et al. 2025) persisted into 2024. Based on DOISSTv2.1, daily global mean SSTs were at record-high levels from the beginning of 2024 until late June. Although the all-time daily record set in 2023 was not surpassed, global mean daily SSTs in 2024 were extraordinary as they significantly ($p < 0.05$) deviated from the normal SSTs throughout the year. In DOISSTv2.1, 2024 was the only year in which all daily global mean SSTs fell outside—and, in fact, above—the two standard deviations (2-SD) of the 1991–2020 SST climate normals (Yin et al. 2024), indicating that the global ocean was abnormally warm in 2024. Here, the standard deviation for each calendar day is computed based on the global mean SSTs in the same day of years during the current climate normal period of 1991–2020.

In terms of annual average global mean SST, the global ocean in 2024 was the warmest in the 171-year record of ERSSTv5. This is the second year in a row that the global ocean set a record for the warmest year. The annual average global mean SSTA in 2024 was +0.47±0.01°C, exceeding that in 2023, now the second warmest year, +0.41±0.01°C on record, by a large margin. In ERSSTv5, the warmest 10 years for the global ocean were all from the last decade, with SSTAs ranging from +0.14±0.01°C to +0.47±0.01°C. Here, the uncertainties, reported as 95% confidence intervals and expressed as ± values, were estimated by the Student's t-test using a 500-member ERSSTv5 ensemble with randomly drawn parameter values within reasonable ranges during ERSSTv5 reconstructions (Huang et al. 2015, 2020).

In 2024, annual average SSTAs were well above (>+0.2°C) the 1991–2020 climatology in most of the global ocean (Fig. 3.1a). The majority of the Indian Ocean, Atlantic Ocean, and midlatitude central-western Pacific Ocean in both hemispheres had SSTAs above +0.5°C. The 2024 ocean warming was particularly pronounced in the midlatitude North Pacific, where SSTAs mostly exceeded +2°C in a zone stretching from Japan eastward across the dateline, and in the North Atlantic, where a horseshoe-shaped SST pattern with SSTAs above +1°C emerged across the

Unauthenticated | Downloaded 11/21/25 11:34 AM UTC

entire basin. Meanwhile, regions including the Okhotsk Sea, Bering Sea, Greenland Sea, southeastern Pacific, and the central-eastern Pacific between 40°S and 20°S were seen with SSTAs below (<0.2°C) the climatology. The two polar oceans—the Arctic Ocean and the Southern Ocean—were comparable to their climatologies, primarily due to extensive seasonal ice coverage.

The annual average SST difference between 2023 and 2024 (2024 minus 2023) reveals that 2023 to 2024 warming was dominant in the Southern Hemisphere (Fig. 3.1b). Across the Indo-Pacific Ocean and the tropical South Atlantic Ocean, the SST difference was mostly positive and exceeded 0.5°C over the eastern Indian Ocean. In the midlatitude Southern Hemisphere, approximately south of 30°S, three warming centers and three cooling centers were almost evenly distributed in an alternating pattern. The warm center over the southeastern Pacific and the Southern Ocean along 120°W was the most pronounced warming region globally, with SSTs increasing by more than 1°C in a large area. The strong cooling along the central-eastern equatorial Pacific and the southeast tropical Pacific reflects the El Niño–Southern Oscillation phase transition from the 2023/24 El Niño event (Tan et al. 2024) to the late 2024 La Niña conditions.

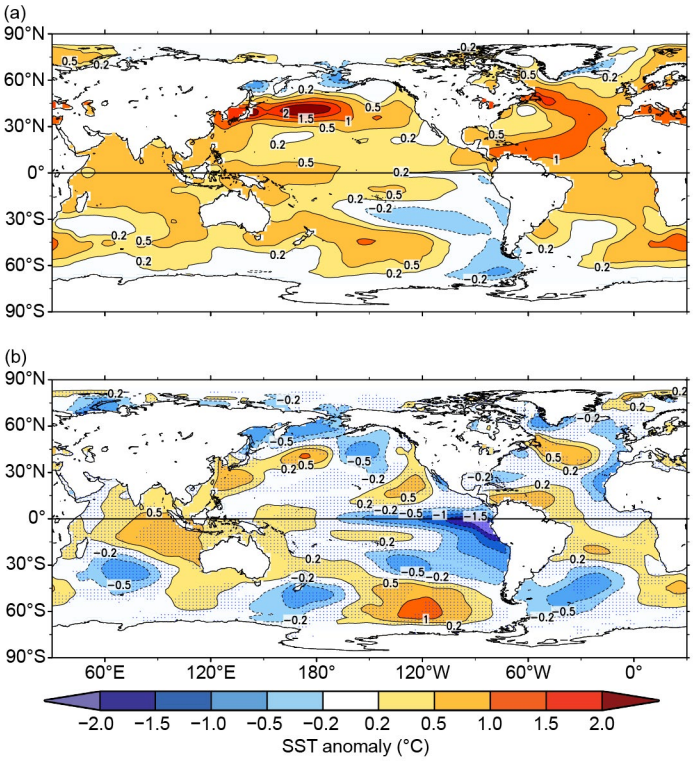

Fig. 3.1. Annual average (a) sea surface temperature anomalies (SSTAs; °C) in 2024 relative to 1991–2020 climatology and (b) differences of annual mean SSTAs from the previous year (2024 minus 2023; °C). The stippled areas in panel (b) indicate that the 2024-minus-2023 SSTA difference is significant at 95% confidence. (Source: ERSSTv5.)

Seasonal average SSTAs (Fig. 3.2) provide further insights into the temporal evolution of SSTs in 2024. Consistent with the annual result (Fig. 3.1a), positive SSTAs were dominant globally in all seasons. From boreal winter (December 2023–February 2024, Fig. 3.2a) throughout boreal autumn (September–November 2024, Fig. 3.2d), SST patterns exhibited steady and progressive changes over time in two regions: In the central-eastern equatorial Pacific, a typical El Niño SST pattern was evident during the winter season (Fig. 3.2a; Tan et al. 2024), as indicated by SSTAs above +0.5°C. However, the El Niño SST pattern began to diminish in the spring (Fig. 3.2b) and eventually transitioned to a weak La Niña SST pattern during the summer and autumn seasons (Figs. 3.2c,d). In the midlatitude central-western Pacific, the area with SSTAs over +1°C was first seen approximately west of 160°W between 30°N and 45°N in the winter (Fig. 3.2a). In the following three seasons (Figs. 3.2b–d), the area gradually expanded, particularly northward, with central SSTA contours increasing from 1.5°C to 2°C.

The tropical Atlantic Ocean was warmer than normal by more than 1°C across most of the western portion in the winter (Fig. 3.2a), and this warm area expanded to the west coasts in the spring (Fig. 3.2b). This pattern disappeared over the next two seasons (Figs. 3.2c,d); instead, a horseshoe-shaped SST pattern that was visible on the annual map (Fig. 3.1a) appeared and peaked during the summer (Fig. 3.2c).

Except for an area south of Madagascar during the first three seasons, the Indian Ocean was warmer than normal in all seasons. During the winter (Fig. 3.2a), a large band area with SSTAs exceeding +1°C extended from the Arabian Sea to Madagascar and then turned toward the southwest of Australia. However, similar to the El Niño pattern, this pattern vanished in the subsequent seasons.

Unauthenticated | Downloaded 11/21/25 11:34 AM UTC

In the Arctic, coastal SSTAs were negative during the winter and spring (Figs. 3.2a,b) in all seas except the Barents Sea in the winter and became positive during the summer and autumn (Figs. 3.2c d), except in the Chukchi Sea in the summer.

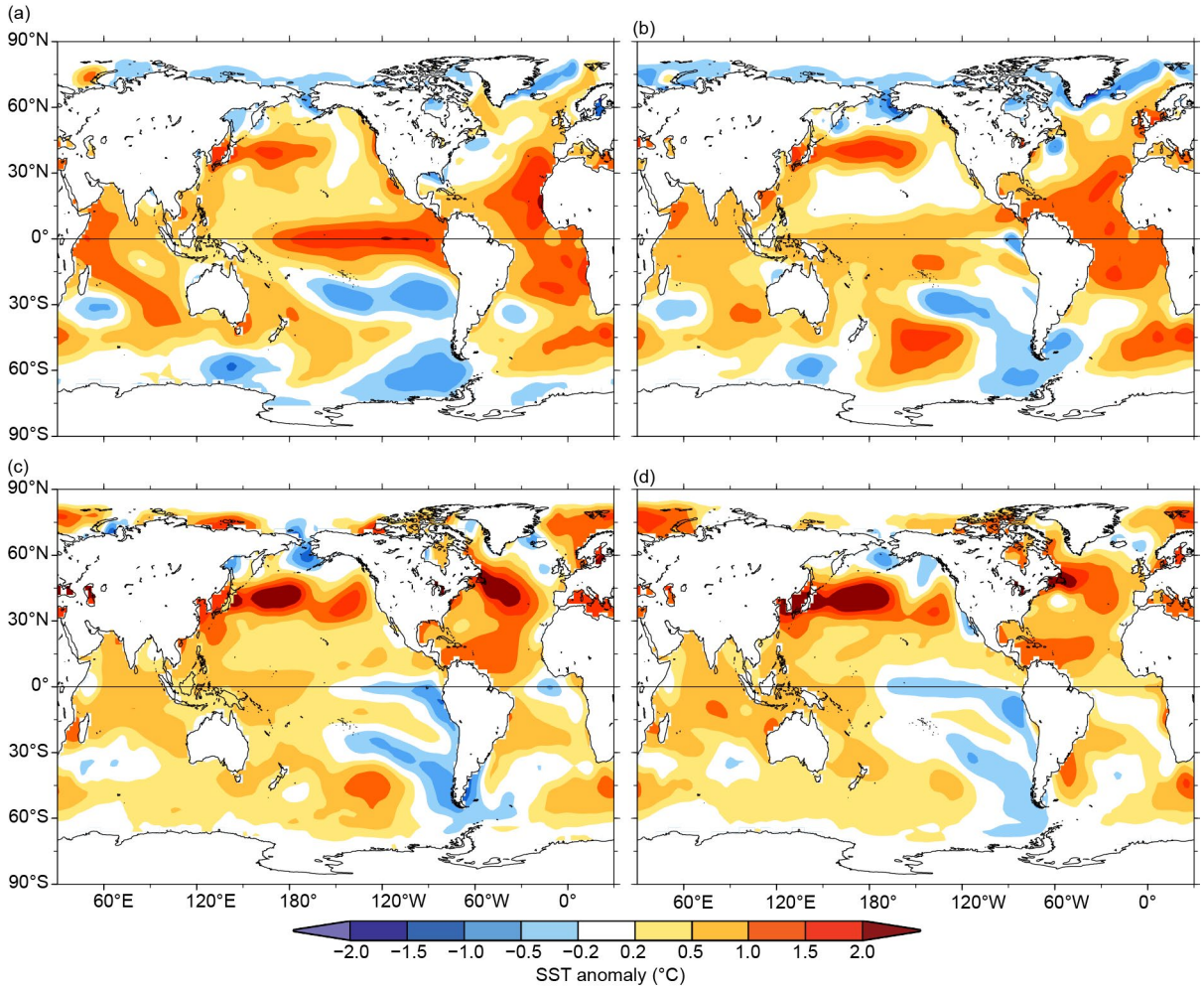

Fig. 3.2. Seasonal average sea surface temperature anomalies (SSTAs; °C; 1991–2020 base period) for (a) Dec 2023–Feb 2024, (b) Mar–May 2024, (c) Jun–Aug 2024, and (d) Sep–Nov 2024. (Source: ERSSTv5.)

3. MARINE HEATWAVES AND COLD SPELLS

In 2024, 91% of the global ocean experienced at least one marine heatwave (Fig. 3.3b) and 26% experienced at least one marine cold spell (Fig. 3.3d). The most common MHW category (Hobday et al. 2018) in 2024 was Category 2 (Strong, 46%), with the coverage of Category 3 (Severe) events reaching 8%. Category 1 (Moderate) MCSs have remained the most common (16%) cool events in all years since 1987. The ocean experienced a global average of 100 MHW days (nine MCS days) in 2024. This is far greater than the 2016 MHW record of 58 days (MCS record of 55 days in 1982; Figs. 3.3a,c). This equates to a daily average MHW coverage of 27% (2% MCS; Figs. 3.3a,c).

The year 2024 started off where 2023 ended: hot, with most of the Atlantic Ocean, the majority of all oceans within ±20° of the equator, and large patches of the Southern Ocean south of Africa and Australia in a MHW state (see Fig. 3.2 for seasonal SST anomalies). The MHW north of the equator in the Atlantic was a continuation of the basin-scale event that started in January 2023 and has continued nearly unabated for two years through to the end of 2024. It seems only a matter of time before this event gains a unique name for itself as "The Blob" did in the northeast Pacific.

Similar in size to this North Atlantic event was another event, loosely connected just to the south of the equator. Another holdover from 2023, the basin-scale event picked up steam going into March, but finally dissipated in June, just as a MHW larger than Western Europe began to develop in the North Atlantic. While this event persisted nearly to the end of the year, it broke up twice, potentially signifying different key drivers of the anomalous heat. From August to late

Unauthenticated | Downloaded 11/21/25 11:34 AM UTC

November, the Barents and Kara Seas experienced what has become a perennially recurring Category 4 MHW. The Gulf of Aden, and much of the surrounding waters, experienced a noteworthy MHW in February, while the Mediterranean Sea had exceptionally intense regional MHWs from July to September.

Notable MCSs within ±60° of the equator have nearly vanished since the late 1990s, with 2024 being no exception. Some high-category events took place throughout the year, though almost all were either an expression of seasonal changes in the ice edge of the polar regions or particularly pronounced anti-cyclonic eddies within the western boundary currents. That being said, the Russian coastline of the Barents Sea exhibited intense cooling from May to June, with the Kara Sea experiencing a widespread Category 4 MCS from June to July.

4. SEA SURFACE TEMPERATURE TRENDS

Time series of annual mean SSTAs from three analyses spatially averaged on global and basin scales (Fig. 3.4) differ from region to region but generally agree for a given region among the analyses and generally increase over the lengths of the records. Linear trends in ERSSTv5 for the regions shown in Fig. 3.4 were computed for the two periods of 1950–2024 and 2000–24 (Table 3.1). For comparison, trends of global mean SSTA are also

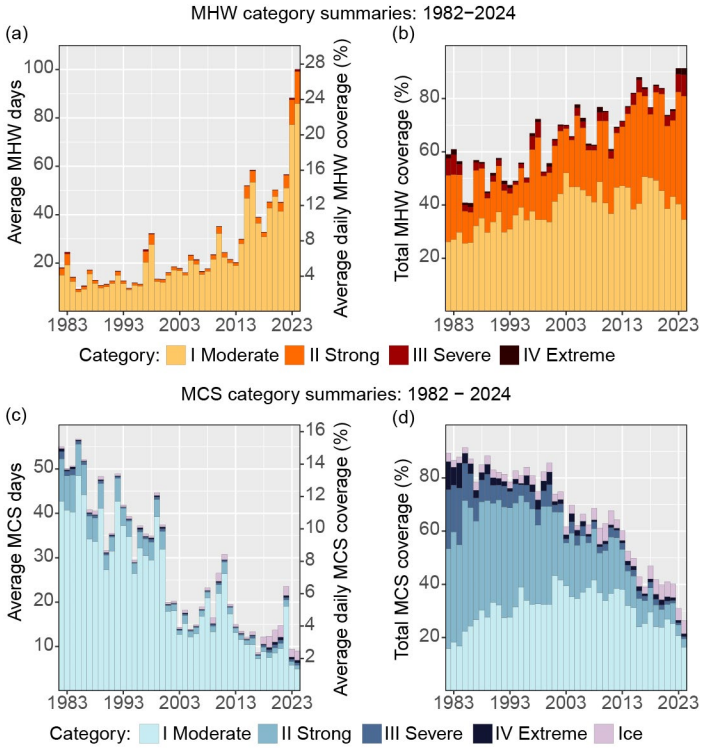

Fig. 3.3. Annual global (a),(b) marine heatwave (MHW) and (c),(d) marine cold spell (MCS) occurrences based on the 1991–2020 base period. (a) Average count of MHW days experienced over the surface of the ocean each year (left y-axis), also expressed as the percent of the surface of the ocean experiencing a MHW on any given day (right y-axis) of that year; (b) total percent of the surface area of the ocean that experienced a MHW at some point during the year; (c) same as (a) but for MCS; and (d) same as (b) but for MCS. Values shown are for the highest category of MHW/MCS experienced at any point. (Source: Daily OISST [DOISSTv2.1.])

Table 3.1. Linear trends (°C decade^{-1}) of global and regional mean annual sea surface temperature anomalies (SSTAs) from ERSSTv5, the Hadley Centre Sea Surface Temperature Dataset version 4 (HadSST4.0.1.0), the Dynamically Consistent ENsemble of Temperature (DCENTv1.0), and the Daily OISST (DOISSTv2.1). The uncertainties at a 95% confidence level, expressed as ± values, are estimated by accounting for the effective sampling number quantified by lag–1 autocorrelation on the degrees of freedom of annual mean SSTAs.

Product	Region	1950–2024	2000–24
DCENTv1.0	Global	0.13±0.01	0.19±0.06
HadSST.4.0.1.0	Global	0.12±0.02	0.21±0.07
DOISSTv2.1	Global	N/A	0.22±0.06
ERSSTv5	Global	0.11±0.01	0.18±0.06
ERSSTv5	Tropical Pacific (30°S–30°N)	0.10±0.03	0.15±0.14
ERSSTv5	North Pacific (30°N–60°N)	0.11±0.04	0.44±0.12
ERSSTv5	Tropical Indian (30°S–30°N)	0.14±0.02	0.19±0.08
ERSSTv5	North Atlantic (30°N–60°N)	0.12±0.03	0.25±0.10
ERSSTv5	Tropical Atlantic (30°S–30°N)	0.12±0.02	0.22±0.10
ERSSTv5	Southern Ocean (30°S–60°S)	0.10±0.01	0.15±0.05

Unauthenticated | Downloaded 11/21/25 11:34 AM UTC

assessed from DOISSTv2.1 (2000–24 only), HadSST.4.0.1.0, and DCENTv1.0. For each region, the trend of 2000–24 is greater than that of 1950–2024, indicating an accelerated ocean warming in the last few decades, particularly since the 1980s in most regions, as is apparent in Fig. 3.4.

For the global ocean, trends in ERSSTv5 during 1950–2024 and 2000–24 are 0.11±0.01°C decade^{-1} and 0.18±0.06°C decade^{-1}, respectively. At regional scales, between 1950–2024 and

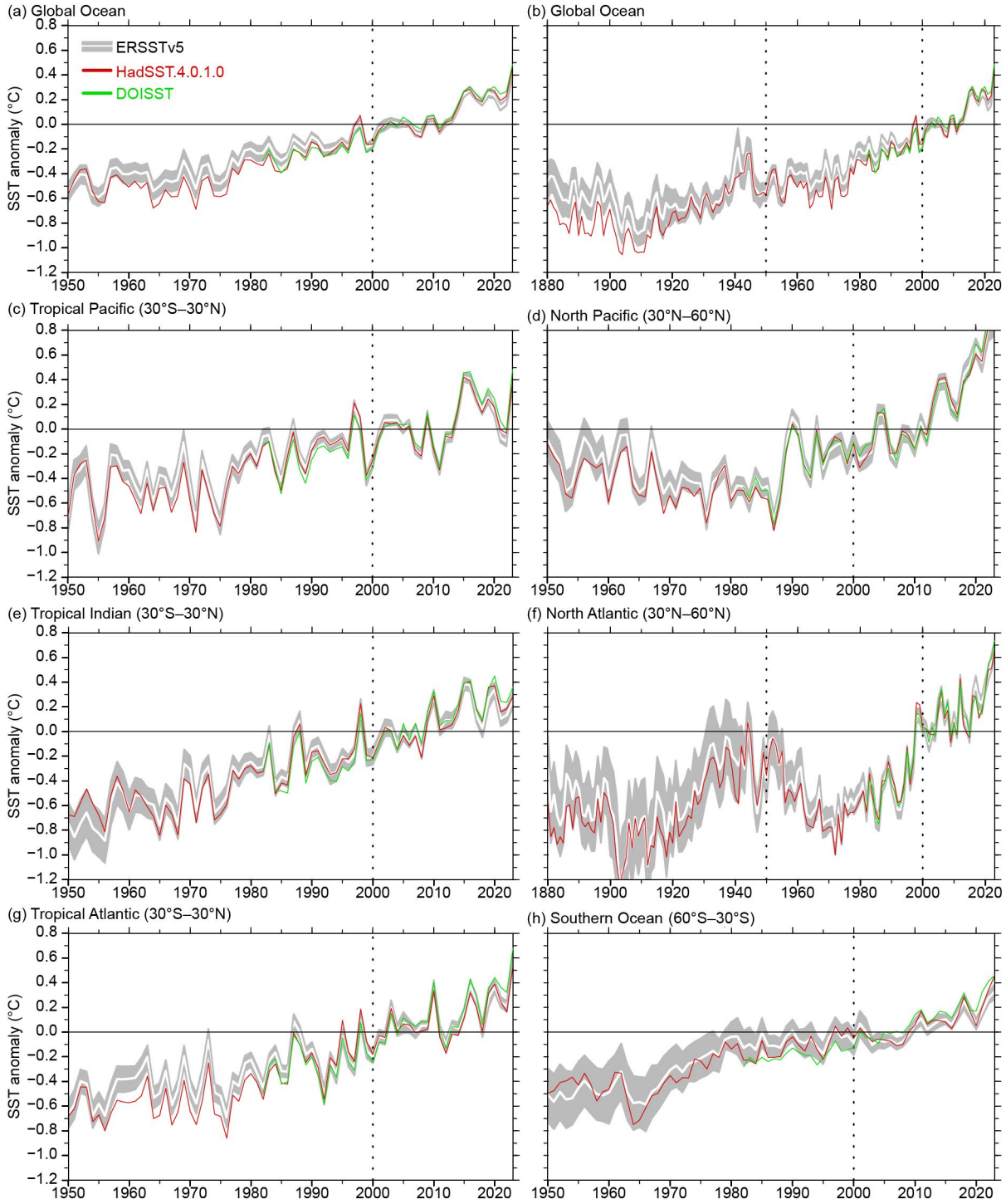

Fig. 3.4. Regional mean annual average sea surface temperature anomalies (SSTAs; °C) of ERSSTv5 (solid white), Hadley Centre Sea Surface Temperature dataset (HadSST.4.0.1.0; solid red), and Daily OISST (DOISSTv2.1; solid green) for the period 1950–2024 except for (b) and (f). (a) global ocean; (b) global ocean for 1880–2024; (c) tropical Pacific; (d) North Pacific; (e) tropical Indian; (f) North Atlantic for 1880–2024; (g) tropical Atlantic; and (h) Southern Ocean. Shadings provide the two-standard-deviation envelopes derived from a 500-member ensemble analysis based on ERSSTv5 and centered on the SSTAs of ERSSTv5. The starting years of the two periods for trend assessment, 1950 and 2000, are indicated by vertical dotted black lines.

Unauthenticated | Downloaded 11/21/25 11:34 AM UTC

2000–24, the warming rate difference is the highest for the North Pacific, from 0.11±0.04°C decade^{-1} to 0.44±0.12°C decade^{-1}, followed by the North Atlantic, from 0.12±0.03°C decade^{-1} to 0.25±0.10°C decade^{-1}. During the longer term since 1950, trends among different regions are comparable, ranging from 0.10°C decade^{-1} to 0.14°C decade^{-1} with the highest trends in the tropical Indian Ocean. During the shorter term since 2000, trends among different regions are widely spread, ranging from 0.15°C decade^{-1} to 0.44°C decade^{-1} with the highest trends observed in the North Pacific, suggesting an acceleration of the warming (Hu et al. 2024). Global trends calculated from different SST products, ranging from 0.11°C decade^{-1} to 0.13°C decade^{-1} over 1950–2024 and from 0.18°C decade^{-1} to 0.22°C decade^{-1} over 2000–24, are statistically indistinguishable with uncertainties considered (Table 3.1).

Departures of both DOISSTv2.1 and HadSST.4.0.1.0 from ERSSTv5 (Fig. 3.4) generally fall within the 2-SD envelope (gray shading), which was derived from a 500-member ensemble analysis of ERSSTv5 and centered on the SSTA of ERSSTv5 (Huang et al. 2020). An exception is the global mean SSTAs before the 1910s, when uncertainties in ERSSTv5 are large, and the HadSST.4.0.1.0 falls outside the 2-SD range of ERSSTv5. This is because in situ observations were scarce at the time, and different data reconstruction algorithms based on limited observations led to higher uncertainties in SST reconstructions. The SSTAs in the North Atlantic exhibit interdecadal variations in the long term since 1880 (Fig. 3.3f). This may be primarily associated with the Atlantic Multidecadal Variability (Schlesinger and Ramankutty 1994).

Unauthenticated | Downloaded 11/21/25 11:34 AM UTC

c. Ocean temperature and heat content anomalies

—G. C. Johnson, J. M. Lyman, L. Cheng, D. Giglio, R. E. Killick, M. Kuusela, R. Locarnini, A. Mishonov, M. Oe, J. Reagan, and T. Sukianto

The oceans are central to the transport of heat in Earth's ocean–atmosphere system (e.g., Donohoe et al. 2024). They have also absorbed ~89% of the excess heat energy entering Earth at the top of the atmosphere from 1971 to 2020 (e.g., von Schuckmann et al. 2023). Since this warming is greatest at the surface, it has increased the strength and duration of marine heatwaves (MHWs; e.g., Oliver et al. 2021) and the stratification of the upper ocean (e.g., Li et al. 2020), impacting biogeochemical cycles, ocean circulation, and ecosystems. This warming is linked to increased energy that fuels tropical cyclones (e.g., Walsh et al. 2016), sea level rise (section 3f), the melting of sea ice, ice shelves, marine terminating glaciers and ice sheets (von Schuckmann et al. 2023), and coral bleaching (e.g., Hughes et al. 2017). Here, we discuss ocean temperature and heat content anomalies for 2024 relative to 2023 as well as to a 1993–2022 climatology. We focus primarily on the upper 2 km, where temperature profiles collected by the Argo array, which first reached sparse near-global coverage around 2005, have greatly improved ocean sampling and the ability to map subsurface ocean temperature fields.

Weekly maps of ocean heat content anomaly (OHCA) relative to a 1993–2022 baseline mean (this particular 30-year time period is used because 1993 is the first full year that satellite sea surface height measurements used in this section were collected) as well as temperature for 58 pressure layers from 0 dbar to 2000 dbar were generated using Random Forest regression following Lyman and Johnson (2023) with V2.2 improvements as described at https://www.pmel.noaa.gov/rfrom/. In situ ocean temperature profiles, including Argo data downloaded from an Argo Global Data Assembly Centre in January 2025 (http://doi.org/10.17882/42182#98916), were used for training data for these maps, and prediction variables included satellite sea surface height and temperature, location, and time. In situ global estimates of OHCA for three depth layers (0 m–700 m, 700 m–2000 m, and 2000 m–6000 m) from six different research groups are also discussed. These same Argo data are used along with shipboard Conductivity-Temperature-Depth (CTD) data downloaded from the World Ocean Database (Mishonov et al. 2024; https://www.ncei.noaa.gov/access/world-ocean-database-select/dbsearch.html) in January 2025 to update a 2000-dbar–6000-dbar multidecadal estimate of deep and abyssal ocean temperature trends (Johnson and Purkey 2024).

El Niño conditions ebbed in early 2024, reached the neutral threshold in May 2024, and crossed the threshold to La Niña conditions in December 2024. Hence, the 2024-minus-2023 difference of 0-m–2000-m OHCA (Fig. 3.5b) shows a decrease across the entire equatorial Pacific—albeit stronger in the east than the west—with ocean heat content anomalies for 2024 (Fig. 3.5a) that are negative across the equatorial Pacific. Ridges of high values in 2024-minus-2023 differences are found close to the coast of the Americas at higher latitudes and farther west at lower latitudes, with troughs of low values just to the west of the high value ridges, and are likely owed to the Rossby Wave signatures of the recent El Niño and preceding La Niñas propagating in succession from the eastern boundary westward. As in 2022 and 2023, the centers of the North and South Pacific continued to be anomalously warm in 2024, with colder conditions around the edges (Fig. 3.5a), consistent with a continued negative Pacific Decadal Oscillation index in the Northern Hemisphere (section 3b). However, the centers of these basins did cool slightly from 2023 to 2024 (Fig. 3.5b), consistent with a weakening of the negative Pacific Decadal Oscillation index. As in 2022 and 2023, cold anomalies just south of the Kuroshio Extension and warm anomalies within that current in 2024 are associated with a long-lasting northward shift of that current (see Fig. 3.19a). Pacific marginal seas mostly cooled from 2023 to 2024, leaving them warm but closer to climatological means in 2024 than in 2023.

In the Indian Ocean, the 2024-minus-2023 difference of OHCA (Fig. 3.5b) mostly increased, with a decrease from west of Australia that ends just east of Madagascar. The 2024 OHCA anomalies (Fig. 3.5a) were mostly positive, with regions of somewhat negative values found from west of Australia to just east of Madagascar.

The 2024-minus-2023 difference of OHCA (Fig. 3.5b) in the Atlantic Ocean was weakly positive in most of the tropics and the northern North Atlantic, with cooling in the western subtropical North Atlantic, the Caribbean Sea, and the higher-latitude South Atlantic. Cooling on the north

Unauthenticated | Downloaded 11/21/25 11:34 AM UTC

side of the Gulf Stream extension east of about 70°W continued from 2023 to 2024 (it was also present from 2022 to 2023), suggesting a continued southward shift in the axis of that current in the region (Figs. 3.19a,b). Much of the Atlantic Ocean exhibited OHCA well above the 1993–2022 average (Fig. 3.5a), as it has in recent years. In addition to the cool region on the northern edge of the Gulf Stream extension east of about 70°W already noted, the cooler-than-average conditions were found southeast of Greenland, where they have persisted for several years.

As expected, the large-scale statistically significant regional patterns in the 1993–2024 local linear trends of 0-m–2000-m OHCA (Fig. 3.5c) are similar to those from 1993–2023 (Johnson et al. 2024) and earlier *State of the Climate* reports for 0 m–700 m.

Near-global average seasonal temperature anomalies in the upper 2000 dbar of the ocean since 1993 (Fig. 3.6) show signatures of El Niño and La Niña events (Fig. 3.6a) and a surface-intensified warming trend over the 32-year time period (Fig. 3.6b). Boreal winter 2023/24 shows a typical El Niño signature, with a near-surface warm anomaly and a relatively cool (compared to surrounding years) subsurface anomaly centered at about 200 dbar. Other El Niño winters prominent in this record are 1997/98, 2010/11, and 2015/16. La Niña winters, which show the opposite pattern, include 1998–2001, 2007/08, and 2020–23. While near-surface warm anomalies in 2024 slowly reduced over the year as El Niño

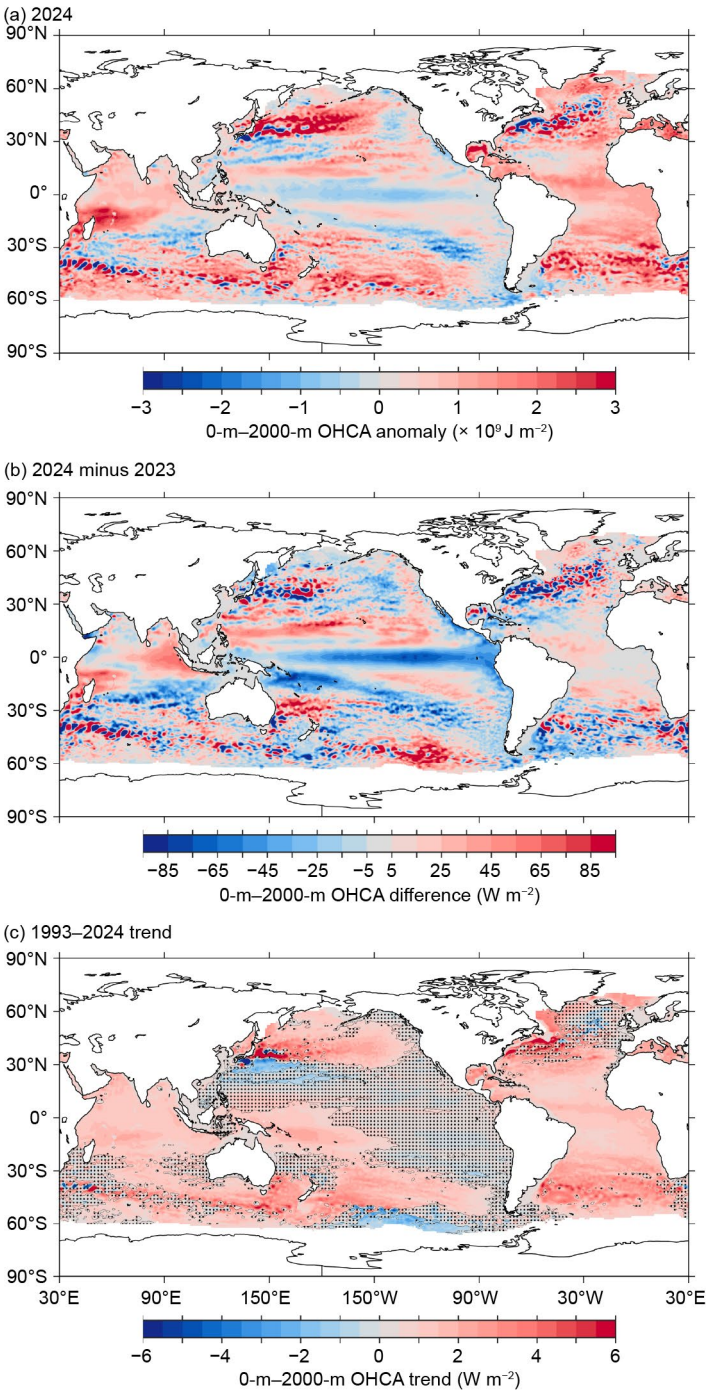

Fig. 3.5. (a) Random Forest Regression Ocean Maps (RFROM) v2 estimate of 0-m–2000-m ocean heat content anomaly (OHCA; × 10⁹ J m⁻²) for 2024 analyzed following Lyman and Johnson (2023) with v2.2 improvements as in https://www.pmel.noaa.gov/rfrom/. Values are displayed relative to a 1993–2022 baseline. (b) 2024-minus-2023 of 0-m–2000-m OHCA expressed as a local surface heat flux equivalent (W m⁻²). For (a) and (b) comparisons, note that 95 W m⁻² applied over one year results in a 3 × 10⁹ J m⁻² change of OHCA. (c) Linear trend for 1993–2024 0-m–2000-m annual OHCA (W m⁻²). Areas with statistically insignificant trends at 5%–95% confidence (taking into account the decorrelation time scale of the residuals when estimating effective degrees of freedom) are stippled.

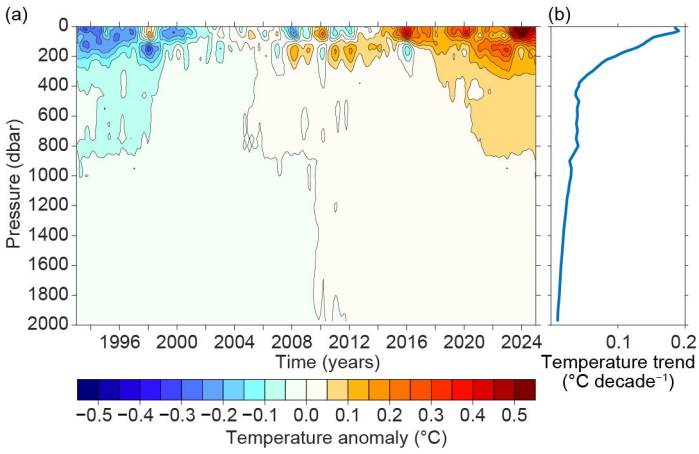

Fig. 3.6. (a) Near-global (66.5°S–81.5°N, but excluding seasonally ice-covered regions within that latitude range) average monthly ocean temperature anomalies (°C; from Random Forest Regression Ocean Maps [RFROM] v2.2, Lyman and Johnson [2023]) relative to 1993–2022 average monthly values, smoothed with a five-month Hanning filter and contoured at 0.05°C intervals (see color bar) vs. pressure and time. (b) Linear trend of temperature anomalies over the period 2004–24 in (a) plotted vs. pressure in °C decade⁻¹ (blue line) with 5%–95% confidence intervals (light blue shading).

Unauthenticated | Downloaded 11/21/25 11:34 AM UTC

faded and eventually transitioned to weak La Niña conditions, the near-surface ocean remained record warm during the first half of the year and was second warmest behind 2023 in the second half of the year. Near 200 dbar, conditions were cooler in 2024 than during the previous few years when La Niña dominated but were still warmer than the 30-year (1993–2022) average. The 1993–2024 length warming trend (Fig. 3.6b) is strongest near the surface (0.19°C decade^{-1} at 30 dbar), diminishing steadily with increasing pressure to reach 0.04°C decade^{-1} by 400 dbar, remaining relatively constant until 800 dbar, and then steadily diminishing again with increasing pressure to about 0.01°C decade^{-1} at around 2000 dbar.

Globally integrated annually averaged OHCA estimates from 0 m–700 m and 700 m–2000 m from six research groups are presented (Fig. 3.7). As noted in previous reports, year-round, near-global sampling in both of those layers commenced around 2005 from Argo, making estimates relatively certain after that date. Deep expendable bathythermographs sampling to 700 m were deployed extensively over much of the globe (with the notable exception of the high southern latitudes) starting in the early 1990s (Lyman and Johnson 2014), hence the upper layer results may be fairly robust back to 1993. Results for the 700-m–2000-m layer, which is quite sparsely sampled prior to about 2005, should be interpreted with caution in earlier years.

The various estimates of annual globally integrated 0-m–700-m OHCA (Fig. 3.7a) consistently show large increases since 1993, with all six analyses reporting 2024 as a record high. The 700-m–2000-m OHCA annual analyses (Fig. 3.7b) show a smaller, but still distinct long-term warming trend, and again all six analyses report 2024 as a record high in that deeper layer. The water column from 0 m to 700 m gained 13±7 ZJ and from 700 m to 2000 m gained 3.9±1.5 ZJ (means and standard deviations given) from 2023 to 2024. Causes of differences among estimates are discussed in Johnson et al. (2015, 2024).

The estimated linear rates of heat gain for each of the five global integral estimates of 0-m–700-m OHCA that extended from 1993 through 2024 (Fig. 3.7a) range from 0.39±0.06 W m^{-2} to 0.46±0.07 W m^{-2}. These estimates are applied over the surface area of Earth (Table 3.2) rather than the surface area of the ocean, to relate directly to the top-of-the-atmosphere energy imbalance (e.g., Loeb et al. 2021; section 2f1). For average ocean

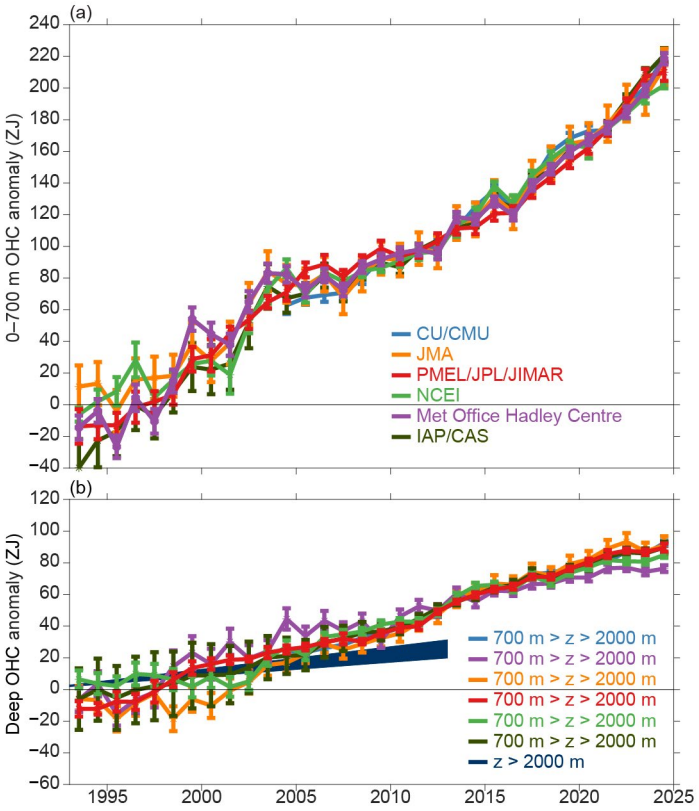

Fig. 3.7. (a) Annual average global integrals of in situ estimates of upper (0-m–700-m) ocean heat content anomaly (OHCA; ZJ; 1 ZJ = 10^{21} J) for the period 1993–2024 with standard errors of the mean. The Meteorological Research Institute (MRI)/Japan Meteorological Agency (JMA) estimate is an update of Ishii et al. (2017). The Pacific Marine Environmental Laboratory (PMEL)/Jet Propulsion Laboratory (JPL)/Cooperative Institute for Marine and Atmospheric Research (CIMAR) estimate is from Random Forest Regression Ocean Maps (RFROM) v2.2 after Lyman and Johnson (2023). The Met Office Hadley Centre estimate is computed from gridded monthly temperature anomalies following Palmer et al. (2007) and Good et al. (2013). Both the PMEL and Met Office estimates use Cheng et al. (2014) eXpendable BathyThermograph (XBT) corrections and Gouretski and Cheng (2020) mechanical bathythermograph corrections (MBT) corrections. The NCEI estimate follows Levitus et al. (2012). The Institute of Atmospheric Physics (IAP)/Chinese Academy of Sciences (CAS) estimate was reported in Cheng et al. (2025). The University of Colorado (CU)/Carnegie Mellon University (CMU) estimate is detailed in Giglio et al. (2025). See Johnson et al. (2015, 2024) for details on uncertainties, methods, and datasets. For comparison, all estimates have been individually offset (vertically on the plot), first to their individual 2005–22 means (the best sampled time period) and then to their collective 1993 mean. (b) Annual average global integrals of in situ estimates of intermediate (700-m–2000-m) OHCA for 1993–2024 (ZJ) with standard errors of the mean and a long-term trend with one-standard-error uncertainty shown from January 1988 to October 2014 for deep and abyssal (2000 dbar–6000 dbar) OHCA following Johnson and Purkey (2024) but updated as detailed in the text.

Unauthenticated | Downloaded 11/21/25 11:34 AM UTC

air–sea heat fluxes, estimates should be multiplied by 1.41. Linear trends from the 700-m–2000-m layer over the same time period range from 0.17±0.03 W m^{-2} to 0.24±0.04 W m^{-2}. Trends from all five groups in both layers agree within 5%–95% uncertainties. Using shipboard and Deep Argo CTD data collected from 1968 through 2024 to update the estimate of Johnson and Purkey (2024) for 2000 dbar–6000 dbar, the linear trend is 0.070±0.016 W m^{-2} from January 1988 to October 2014 (these dates are global volume average times of first and last sampling used in the local trend calculations), consistent with previously reported decadal deep and abyssal warming trends (e.g., Purkey and Johnson 2010), although with smaller uncertainties owing to the use of more data than in previous estimates. Summing the three layers (despite their different time periods as given above), the full-depth ocean heat gain rate applied to Earth's entire surface ranges from 0.66 W m^{-2} to 0.74 W m^{-2}.

Table 3.2. Trends of ocean heat content increase (in W m^{-2} applied over the 5.1 × 10^{14} m^2 surface area of Earth) from six different research groups over three depth ranges (see Fig. 3.7 for details). For the upper (0-m–700-m) and intermediate (700-m–2000-m) depth ranges, estimates cover 1993–2023, with 5%–95% uncertainties based on the residuals taking their temporal correlation into account when estimating degrees of freedom (Von Storch and Zwiers 1999). The 2000-m–6000-m depth range estimate, an update of Johnson and Purkey (2024), uses data from 1970 to 2024, having a global average start and end date of Jan 1988 to Oct 2014, again with 5%–95% uncertainty.

Research Group	0 m–700 m Global Ocean Heat Content Trends (W m^{-2})	700 m–2000 m Global Ocean Heat Content Trends (W m^{-2})	2000 m–6000 m Global Ocean Heat Content Trends (W m^{-2})
MRI/JMA	0.39±0.06	0.24±0.03	—
PMEL/JPL/JIMAR	0.42±0.09	0.21±0.02	—
NCEI	0.40±0.04	0.19±0.04	—
Met Office Hadley Centre	0.42±0.07	0.18±0.03	—
IAP/CAS	0.46±0.07	0.21±0.02	—
Johnson and Purkey	—	—	0.07±0.02

Unauthenticated | Downloaded 11/21/25 11:34 AM UTC

d. Salinity

—G. C. Johnson, J. Reagan, J. M. Lyman, R. Locarnini, and C. Schmid

1. INTRODUCTION

As noted in previous reports, ocean density is determined by salinity, temperature, and pressure of seawater. The vertical density structure sets the ocean stratification and impacts its interaction with the atmosphere. Horizontal density gradients are directly related to vertical ocean current shear through the thermal wind relation. In high latitudes, salinity variation plays an important role in setting ocean density. Various factors, including advection, precipitation and evaporation, river run-off, ice melt, and ice freezing (Ren et al. 2011; Yu 2011) contribute to salinity variations that impact crucial ocean–atmosphere exchanges of heat and dissolved gases, influencing phenomena like marine heatwaves and deep or bottom water formation, as well as nutrient and oxygen exchange between the surface mixed layer and denser waters below. Ocean salinity is a predictor for tropical cyclone intensity (Balaguru et al. 2012), seasonal precipitation forecasting (Li et al. 2016), and air–sea carbon dioxide (CO_2) flux (Landschützer et al. 2013).

The sea surface salinity (SSS) analysis relies on Argo data downloaded in January 2025, with annual anomaly maps relative to a seasonal climatology generated following Johnson and Lyman (2012) as well as monthly maps of bulk (as opposed to skin) SSS data from the Blended Analysis of Surface Salinity (BASS; Xie et al. 2014). BASS blends in situ SSS data with data from the *Aquarius* (Le Vine et al. 2014; mission ended in June 2015), Soil Moisture and Ocean Salinity (SMOS; Font et al. 2013), and the Soil Moisture Active Passive (SMAP; Fore et al. 2016) satellite missions. Despite the larger uncertainties of satellite data relative to Argo data, their higher spatial and temporal sampling allow higher spatial and temporal resolution maps than are possible using in situ data alone at present. To investigate interannual changes of subsurface salinity, all available salinity profile data are quality controlled following Mishonov et al. (2024) and then used to derive 1° monthly mean gridded salinity anomalies relative to a long-term monthly mean for the years 1955–2022 from World Ocean Atlas 2023 (WOA 2023; J. Reagan et al. 2024) at standard depths from the surface to 2000 m. Note that all salinity values used in this section are reported as observed, on the dimensionless Practical Salinity Scale-78 (PSS-78; Fofonoff and Lewis 1979).

In recent years, the largest source of salinity profiles is the profiling floats of the Argo program (Riser et al. 2016). These data are a mix of real-time (preliminary) and delayed-mode (scientific quality controlled) observations. Hence, the estimates presented here may be subject to instrument biases such as a positive salinity drift identified in a subset of Argo Conductivity-Temperature-Depth and will change after all data are subjected to scientific quality control.

2. SEA SURFACE SALINITY

—G. C. Johnson and J. M. Lyman

As noted in previous reports (e.g., Johnson et al. 2020), since salinity has no direct feedback to the atmosphere, unlike sea surface temperature (SST) anomalies, which are often damped by heat exchange with the atmosphere, large-scale SSS anomalies can be quite persistent. Generally, regions dominated by evaporation, such as the subtropics, exhibit higher salinity values, while areas where precipitation prevails, like the Intertropical Convergence Zone (ITCZ) and high latitudes, have fresher water (e.g., Wüst 1936; Schmitt 1995).

In the tropical Pacific, the ITCZ became fresher from 2023 to 2024 (Fig. 3.8b). The northern edge of the South Pacific Convergence Zone freshened and the southern side got saltier, suggesting a northward shift of that zone. The western equatorial Pacific also became saltier, suggesting a westward contraction of the fresh pool there with the transition from El Niño to La Niña over the year. There was also a large freshening in the climatologically fresh area west of Central America. As in 2022 and 2023, in the North Pacific, the center of the basin was mostly anomalously salty in 2024, and the periphery was generally anomalously fresh (Fig. 3.8a). Much of the South Pacific was anomalously salty in 2024.

In the Atlantic, SSS increased from 2023 to 2024 in the region of the ITCZ and the eastern equatorial area as well as in the Caribbean Sea and the Gulf of America/Gulf of Mexico (Fig. 3.8b). The center of the subtropics in both hemispheres was generally anomalously salty in 2024

Unauthenticated | Downloaded 11/21/25 11:34 AM UTC

(Fig. 3.8a), as it had been in 2022 and 2023 and other recent years. The ITCZ remained anomalously fresh in 2024, although somewhat less so than in 2023.

The equatorial Indian Ocean freshened south of the equator from 2023 to 2024, as did the western Arabian Gulf, whereas in the eastern Arabian basin and south of about 10°S (especially just west of Australia) the basin mostly became saltier (Fig. 3.8b). These changes resulted in an anomalously fresh region across much of the Indian Ocean north of about 10°S in 2024 (Fig. 3.8a), with weakly anomalously salty conditions south of about 10°S in that basin.

Sea surface salinity trends from 2005 to 2024 are mostly statistically insignificant, but, as in 2023 (Fig. 3.8c), there is statistically significant freshening in the eastern third of the Pacific ITCZ, the Gulf of Alaska, northeastern portions of the North Atlantic Ocean, the Greenland–Iceland–Norwegian Seas, the western Bay of Bengal, and the Gulf of Guinea. These are all climatologically fresh areas where precipitation is strong. There are also statistically significant freshening trends in the eastern Gulf of Arabia and northeast of Hawai'i, which are not climatologically fresh. Salty trends are evident in portions of the subtropics in all the ocean basins, which are climatologically salty and subject to strong evaporation, as well as the western Pacific sector of the Southern Ocean and west of Chile, which are neither. This overall "salty gets saltier and fresh gets fresher" trend, which has been evident to varying degrees and discussed in *State of the Climate* reports since 2006, is expected on a warming Earth: As the atmosphere warms, it can hold more moisture, enabling an increased hydrological cycle over the ocean (Held and Soden 2006; Durack and Wijffels 2010; Durack et al. 2012, Skliris et al. 2014).

In 2024, the seasonal BASS SSS anomalies (Fig. 3.9) show the progression of many of the features observed in the annual anomaly map using Argo data alone (Fig. 3.8a) but with higher spatial and temporal resolution, albeit likely with less accuracy. The Pacific ITCZ had the strongest fresh anomalies in the first two seasons of 2024, whereas the western equatorial Pacific became saltier in the last two seasons. In the Atlantic, the fresh anomalies in the Gulf of Guinea and the ITCZ weakened as the year progressed but, in contrast, the anomalies in the Amazon/Orinoco River plume region

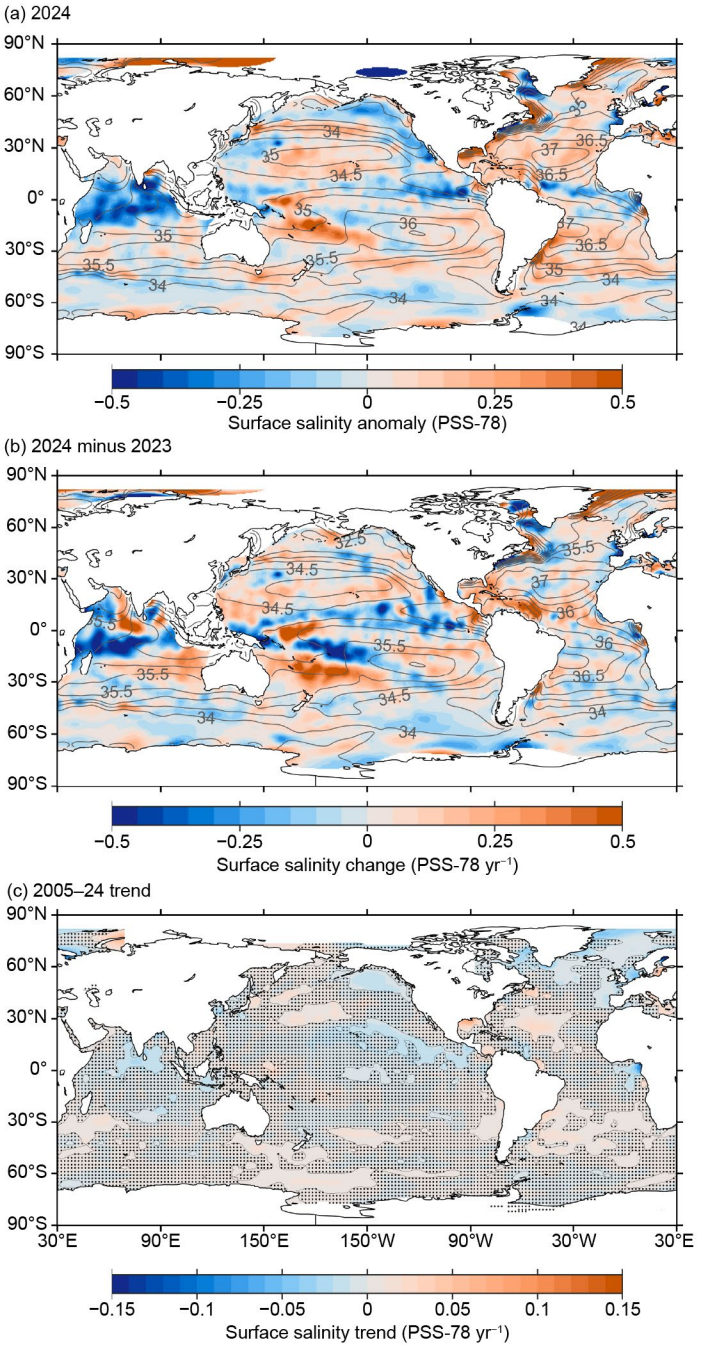

Fig. 3.8. (a) Map of the 2024 annual surface salinity anomaly (colors, Practical Salinity Scale-78 [PSS-78]) with respect to monthly climatological 1955–2022 salinity fields from World Ocean Atlas 2023 (WOA 2023; yearly average; gray contours at 0.5 intervals, PSS-78). (b) Difference of 2024 and 2023 surface salinity maps (colors, PSS-78 yr^{-1}). White ocean areas are too data-poor (retaining <80% of a large-scale signal) to map. (c) Map of local linear trends estimated from annual surface salinity anomalies for the period 2005–24 (colors, PSS-78 yr^{-1}). Areas with statistically insignificant trends at 5%–95% confidence (taking into account the decorrelation time scale of the residuals when estimating effective degrees of freedom) are stippled. All maps are made using Argo data.

Unauthenticated | Downloaded 11/21/25 11:34 AM UTC

started out salty and became fresher. In the Indian Ocean, the fresh basin-wide anomaly along the equator and in the Bay of Bengal in December 2023–February 2024 persisted in March–May 2024 and then weakened somewhat in the equatorial region while remaining strong in the northern Bay of Bengal even into September–November 2024.

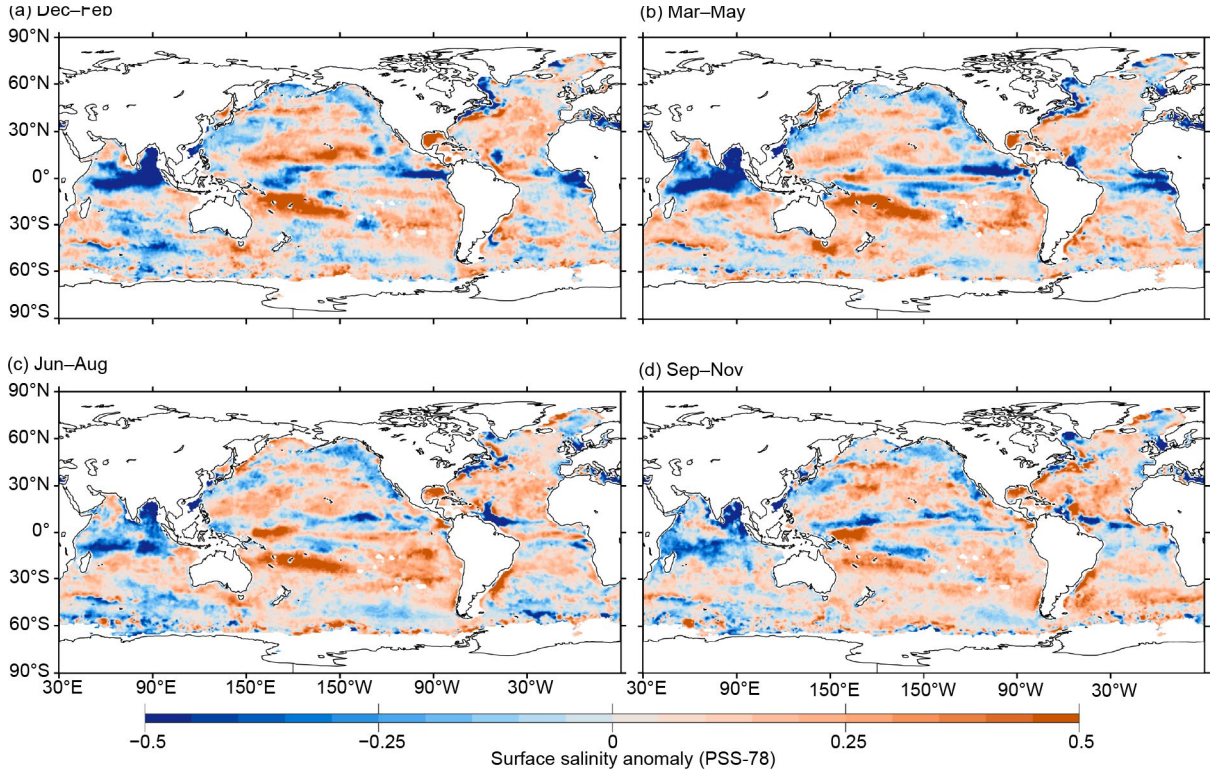

Fig. 3.9. Seasonal maps of sea surface salinity anomalies (colors) from monthly blended maps of satellite and in situ salinity data (Blended Analysis of Surface Salinity [BASS]; Xie et al. 2014) relative to monthly climatological 1955–2022 salinity fields from World Ocean Atlas 2023 (WOA 2023) for (a) Dec 2023–Feb 2024, (b) Mar–May 2024, (c) Jun–Aug 2024, and (d) Sep–Nov 2024.

3. SUBSURFACE SALINITY

—J. Reagan, R. Locarnini, and C. Schmid

Salinity changes at the surface of the ocean can be propagated to depth primarily through two pathways: subduction and convection. Subduction occurs in areas where isopycnals outcrop (intersect the surface) and are followed by downward movement of water along sloped isopycnal (constant density) surfaces. Convection is the movement of water from the surface to deeper depths through vertical mixing and penetrates deepest at high latitudes during winter. The propagation of salinity anomalies into the ocean's interior can impact ocean dynamics through changes in seawater density and is therefore an important variable to monitor.

The pattern of basin-average Atlantic salinity anomalies (Fig. 3.10a) in 2024 is similar to that of 2020 (J. R. Reagan et al. 2024), with salty anomalies (>0.06) near the surface weakening to ~0.01 between 500-m and 600-m depth. Positive salinity anomalies are dominant from 0-m–800-m depth from mid-2017 through 2024. Basin-average changes from 2023 to 2024 (Fig. 3.10b) reveal large salinification near the surface (max of 0.03 at 30 m), with a sharp drop to near 0 at 150-m depth, and slightly positive salinity anomalies (~0.003) from 200 m to 400 m with slight freshening (~−0.001) below 600 m. The causes of the salinity changes from 2023 to 2024 are clearer in the change in zonally averaged salinity between 2023 and 2024 (Fig. 3.10c). Large changes (>0.15) in the upper 30 m near 10°N with changes of >0.06 surrounding this area from 0 m–75 m and 5°N–25°N are primarily responsible for the near-surface salinification. Additional salinification occurred in the South Atlantic subtropical underwater subduction zone near ~20°S (0 m–250 m) and in the North Atlantic from 50 m to 250 m poleward of 50°N (Fig. 3.10c).

Basin average Pacific salinity anomalies (Fig. 3.10d) for 2024 continued a pattern that started in mid-2022 (J. Reagan et al. 2024). Since 2022, there has been movement toward salinification in

Unauthenticated | Downloaded 11/21/25 11:34 AM UTC

the upper 100 m and freshening from 125 m to 600 m in the Pacific. This pattern is clearer in the Pacific basin average difference between 2023 and 2024 (Fig. 3.10c). Salinification of ~0.018 in the upper 30 m transitioned to freshening from 125 m to 600 m with a max freshening of ~−0.01 at 200 m. The 0-m–100-m salinification between 2023 and 2024 can be attributed to large (>0.06) positive zonally averaged salinity changes at the 25°S and 25°N subduction zones (Fig. 3.10f), with the 25°S subduction zone changes as large as 0.12 in the upper 50 m. The deeper changes are primarily due to weak freshening (>−0.03) in much of the South Pacific at depths greater than 150 m, with stronger freshening (<−0.03) between 10°S–20°S and 150 m–350 m. There was also a pocket of strong freshening (<−0.09) centered at 100 m and 5°N.

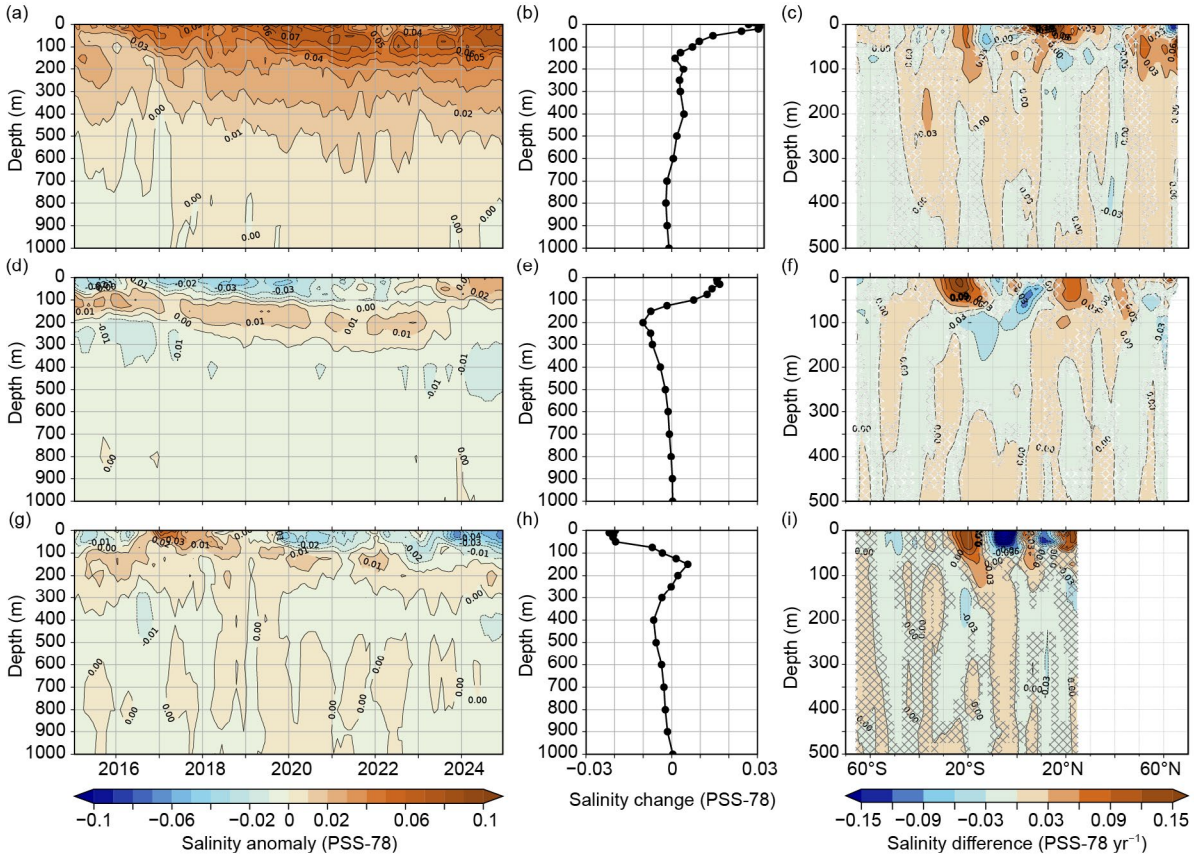

Fig. 3.10. Average monthly salinity anomalies (Practical Salinity Scale-78 [PSS-78]) vs. depth for the (a) Atlantic, (d) Pacific, and (g) Indian basins. Change in salinity from 2023 to 2024 vs. depth for the (b) Atlantic, (e) Pacific, and (h) Indian basins. Change in the zonal-average salinity from 2023 to 2024 vs. latitude and depth in the (c) Atlantic, (f) Pacific, and (i) Indian Ocean basins with areas of statistically insignificant change, defined as <±1 std. dev. and calculated from all year-to-year changes between 2005 and 2024, are stippled in gray. Data are smoothed using a three-month running mean. Anomalies are relative to the long-term (1955–2022) World Ocean Atlas (WOA) 2023 monthly salinity climatology (J. R. Reagan et al. 2024).

The basin average Indian Ocean salinity anomalies in 2024 continued the same pattern of salinity anomalies that has been evident since 2020 (brief disruption in late 2021/early 2022) with freshening near the surface, salinification below, and weak ± anomalies below 400 m (Fig. 3.10g). While the pattern in 2024 is similar to that of the previous five years, there were some notable changes between 2023 and 2024 (Fig. 3.10h). Strong freshening (~−0.02) in the upper 50 m transitioned abruptly to weak salinification (~0.005) at 150 m and then quickly changed back to weak freshening (max ~−0.008 at 400 m) from 300 m to 900 m. The negative change in salinity between 2023 and 2024 near the surface is due to large freshening (<−0.06) from 0 m to 100 m between 0° and 10°S, with values <−0.24 near the surface at 5°S. Similar to both the Atlantic and Pacific, there was salinification in the subduction zone at 20°S (from 0 m to 250 m, maximum of ~0.12 at 50 m) and additional salinification in the upper 100 m at 8°N and 22°N, but these positive changes do not negate the aforementioned near-surface freshening.

Unauthenticated | Downloaded 11/21/25 11:34 AM UTC

The 2005–24 zonally averaged salinity trends from 0 m to 1000 m resemble what has been documented in prior *State of the Climate* reports (e.g., J. Reagan et al. 2022, 2023, 2024; Fig. 3.11), and they continue to follow the "wet gets wetter and dry gets drier" paradigm introduced in the previous subsection. Atlantic zonally averaged significant salinity changes from 2023 to 2024 (Fig. 3.10c) mostly act to reinforce, or at least not counter, the zonally averaged significant salinity trends, with the exception being the 2023 to 2024 salinification in the North Atlantic from 50 m to 500 m between 50°N and 65°N where there has been a dominant freshening trend from 2005 to 2024 (Fig. 3.11a). The zonally averaged significant salinity changes from 2023 to 2024 in the Pacific (Fig. 3.10f) were mostly located in regions of insignificant zonally averaged salinity trends (Fig. 3.11b), but salinity decreased between 2023 and 2024 in the region centered at 15°S and 200 m where significant positive salinity trends were observed. The largest counter to the 2005–24 significant salinity trends occurred in the Indian Ocean, where there was an increase in zonally averaged salinity during 2023–24 from 0° to 10°N and from 0 m to 50 m (Fig. 3.10i); this opposed the significant freshening trend that has been evident over the past 20-year time period (Fig. 3.11c).

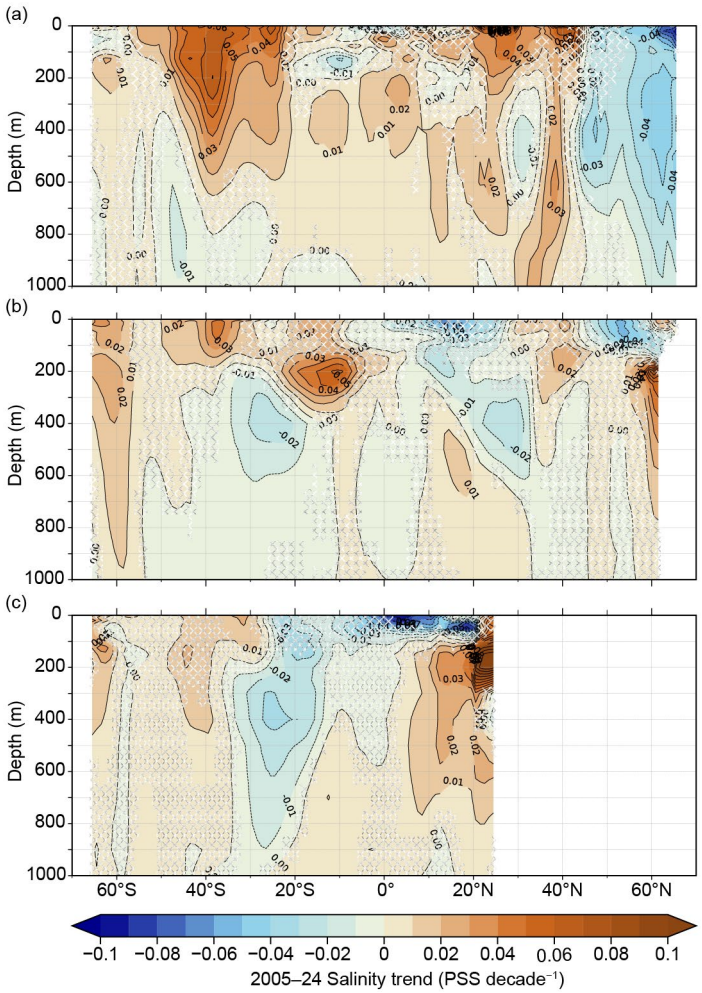

Fig. 3.11. Linear trend of zonally averaged salinity (Practical Salinity Scale-78 [PSS-78] decade^{-1}) for the period 2005–24 vs. latitude and depth for the (a) Atlantic, (b) Pacific, and (c) Indian Ocean computed using least squares regression. Areas stippled in gray are not significant at the 95% confidence interval.

Unauthenticated | Downloaded 11/21/25 11:34 AM UTC

e. Global ocean heat, freshwater, and momentum fluxes

—L. Yu, P. W. Stackhouse, J. Garg, and R. A. Weller

The ocean and the atmosphere interact through the exchange of heat, freshwater, and momentum across their interface. These air–sea fluxes are key to maintaining the global climate system's equilibrium in response to incoming solar radiation. The ocean absorbs the majority of shortwave radiation reaching Earth's surface and redistributes this energy to the atmosphere through longwave radiation, evaporation (latent heat flux), and conduction (sensible heat flux). Any remaining heat is stored in the ocean and transported by ocean processes that are predominantly driven by wind stress. Evaporation not only mediates heat but also moisture transfer, the latter of which, together with precipitation, determines the surface freshwater flux across the open ocean. Changes in these air–sea fluxes act as pivotal drivers for changes in ocean circulation, thereby affecting the global distribution of heat and salt from the tropics to the poles.

Here, we present the surface heat flux, freshwater flux, and wind stress in 2024 and their changes from 2023. The net surface heat flux (Q_{net}) comprises four components: shortwave (SW), longwave (LW), latent heat (LH), and sensible heat (SH). We calculate the net surface freshwater flux into the ocean, excluding inputs from rivers and glaciers, as the difference between precipitation (P) and evaporation (E), referred to as the $P–E$ flux. Data from multiple research groups are synthesized to produce global maps of Q_{net}, $P–E$, and wind stress (Figs. 3.12–3.14) and provide a long-term view over time (Fig. 3.15). Annual anomalies are relative to a 2001–15 climatology for all analyses in this section, since 2001 is the starting year for the Q_{net} estimates used here.

SW and LW in 2023 and 2024 were sourced from the Fast Longwave And Shortwave Radiative Fluxes (FLASHFlux) version 4A product (Stackhouse et al. 2006), which have been radiometrically scaled to the SW and LW products from the Clouds and the Earth's Radiant Energy System (CERES) EBAF Edition 4.2 (Loeb et al. 2018; Kato et al. 2018). P was derived from the GPCP version 2.3 products (Adler et al. 2018). Estimates for LH, SH, E, and wind stress were produced by the second generation of the OAFlux2 (Yu and Well 2007; Yu 2019), computed from satellite retrievals and the bulk parameterization COARE version 3.6 (Fairall et al. 2003). The Q_{net} time series begins in 2001, aligning with the availability of CERES EBAF 4.2 products, while the $P–E$ and wind stress time series extend back 37 years, starting in 1988.

1. SURFACE HEAT FLUXES

The 2024 Q_{net} anomaly pattern (Fig. 3.12a) shows predominantly positive anomalies (indicating downward heat input and ocean surface warming) across tropical oceans between 30°S and 30°N. In contrast, negative Q_{net} anomalies (indicating upward heat release and surface cooling) were observed at higher latitudes, poleward of ±30° latitude. This suggests that tropical oceans were the primary heat gain regions in 2024, with substantial positive Q_{net} anomalies (~10 W m^{-2}) over the tropical Indian Ocean, equatorial Pacific and Atlantic, and the western tropical Atlantic. Meanwhile, heat loss at higher latitudes is most pronounced in the central Pacific between 30°N and 50°N, where sea surface temperature (SST) anomalies of ~1°C (Fig. 3.1) persisted throughout the year, reflecting the prolonged negative phase of the Pacific Decadal Oscillation (PDO).

The 2024-minus-2023 Q_{net} difference pattern generally differs from the 2024 anomaly pattern, with the most noticeable deviations in equatorial regions. Compared to 2023, Q_{net} anomalies in 2024 were positive in the equatorial cold tongues, strongest in the Pacific (~25 W m^{-2}) and slightly weaker in the Atlantic (~10 W m^{-2}). This difference pattern is primarily driven by surface turbulent heat flux (LH+SH; Fig.3.12d) pattern, with a smaller contribution from net downward surface radiation (SW+LW; Fig. 3.12c). In the equatorial Pacific, the Q_{net} increase corresponds to 2024 SST anomalies. The transition from El Niño in 2023 to neutral conditions in early 2024 and later to La Niña conditions strengthened the cold tongue, leading to a cooler sea surface that suppressed LH+SH. As a result, less heat was lost from the sea surface, contributing to positive Q_{net} anomalies. For the SW+LW difference pattern, organized positive anomalies (~5 W m^{-2} to 10 W m^{-2}) are evident along the Intertropical Convergence Zone (ITCZ) and South Pacific Convergence Zone (SPCZ) in the Pacific, while negative anomalies of similar magnitude dominate the tropical Indian Ocean. Elsewhere, the SW+LW difference anomalies remain generally weak.

The midlatitude North Pacific in 2024 was characterized by large negative Q_{net} anomalies (~20 W m^{-2}) that extended along the Kuroshio Extension and its recirculation gyre between

Unauthenticated | Downloaded 11/21/25 11:34 AM UTC

20°N and 40°N, surrounded by positive Q_{net} anomalies to its east. This pattern reflects the prolonged influence of the negative PDO phase, with SST anomalies of +1°C (see Fig. 3.1) persisting throughout 2024. Meanwhile, the midlatitude North Atlantic between 30°N and 50°N experienced the opposite trend, with positive anomalies near the Gulf Stream extension surrounded by weak negative Q_{net} anomalies to the east. These patterns of Q_{net} anomalies were primarily driven by surface turbulent heat fluxes in response to contrasting changes in surface winds across these two basins (Fig. 3.14b). Stronger winds over the broad North Pacific enhanced turbulent heat loss, resulting in negative Q_{net} anomalies, whereas weaker winds over the North Atlantic reduced turbulent heat loss, increasing ocean heat gain (negative anomalies).

The South Pacific in 2024 tended to gain more heat (positive Q_{net} difference anomalies), particularly between 40°S and 15°S, perhaps related to the northward shift of the SPCZ visible in salinity changes (see Fig. 3.8b). Net downward radiation (SW+LW) increased slightly (~5 W m^{-2}), while turbulent heat loss (LH+SH) decreased substantially (>10 W m^{-2}). In contrast, the South Indian Ocean tended to lose more heat (negative Q_{net} difference anomalies) due to reduced downward radiative fluxes and increased turbulent heat loss. Changes in the South Atlantic were generally mild.

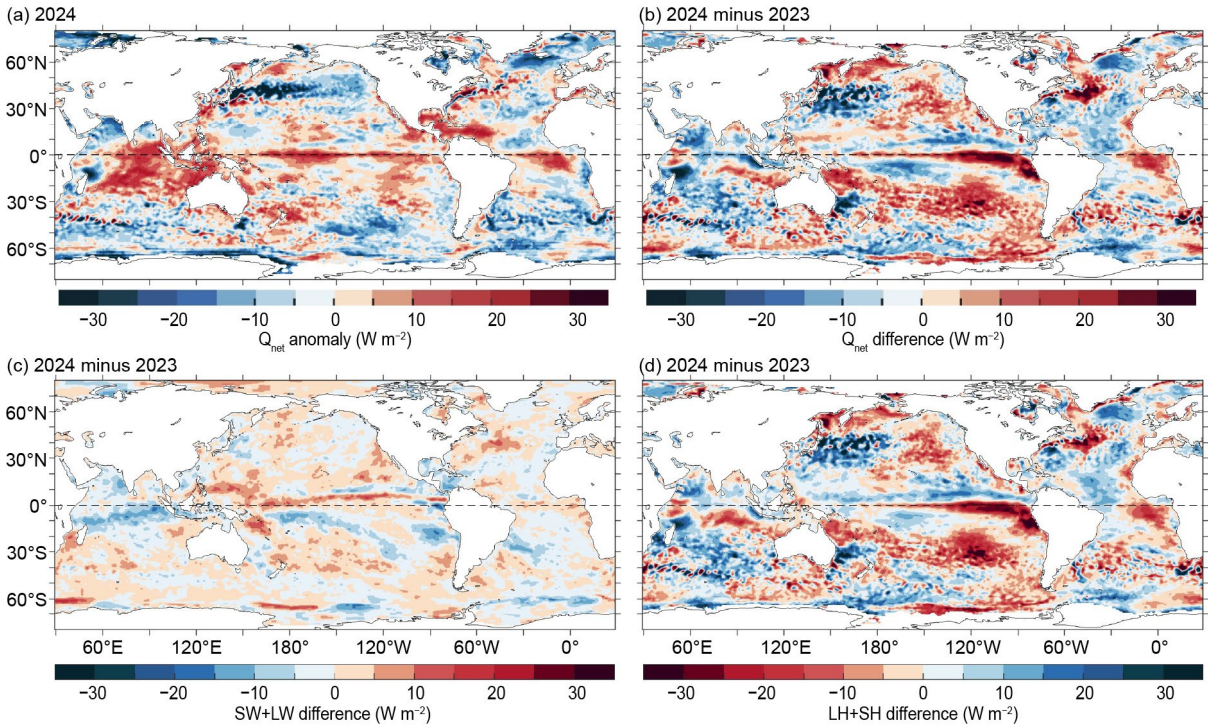

Fig. 3.12. (a) Surface heat flux (Q_{net}) anomalies (W m^{-2}) for 2024 relative to the 2001–15 climatology. Positive values denote ocean heat gain. (b) 2024-minus-2023 difference for (b) 2024-minus-2023 difference for (b) Q_{net}, (c) net surface radiation shortwave (SW) + longwave (LW), and (d) turbulent heat fluxes latent heat (LH) + sensible heat (SH), respectively. Positive tendencies denote more ocean heat gain in 2024 than in 2023. LH+SH are from the Woods Hole Oceanographic Institution (WHOI) OAFlux2, and SW+LW from Fast Longwave And SHortwave Radiative Fluxes (FLASHFlux). Net radiative fluxes are defined as the difference between the incoming and outgoing radiation (positive indicates radiative flux into the ocean).

2. SURFACE FRESHWATER FLUXES

The 2024 *P*–*E* anomalies (Fig. 3.13a) indicate a slight freshwater gain (positive anomalies) in the tropical oceans, while the extratropical oceans experienced freshwater loss (negative anomalies), particularly in the South Indian and Pacific Oceans between 60°S and 30°S, and in the North Pacific between 10°N and 50°N. Freshwater loss was most pronounced in the midlatitude central Pacific (>20 cm per year), associated with the prolonged negative PDO phase. Conversely, freshwater gain was most substantial in the western tropical Pacific and the tropical Indian Ocean, coinciding with the widespread warming in these regions (see Fig. 3.1).

Unauthenticated | Downloaded 11/21/25 11:34 AM UTC

The pattern of the 2024-minus-2023 differences in *P*–*E* (Fig. 3.13b) is distinct, primarily reflecting tropical changes associated with interannual ENSO variability. Pacific ITCZ rainfall decreased by more than 60 cm in 2024 compared to 2023, concurrent with the ENSO phase transition, while rainfall in the tropical Indian Ocean increased by over 40 cm. Rainfall also increased in the central Pacific, east of the SPCZ. These prominent *P*–*E* features were primarily driven by changes in precipitation (Fig. 3.13d).

The 2024-minus-2023 differences in evaporation (Fig. 3.13c) show a moderate increase (~10 cm yr^{-1}) along the Pacific ITCZ, contrasted by a substantial decrease (~25 cm yr^{-1}) in the eastern equatorial Pacific cold tongue. Evaporation also increased in the midlatitude North Pacific where large SST anomalies persisted throughout 2024, associated with the negative PDO phase. Elsewhere, changes in *P*–*E* were relatively minor.

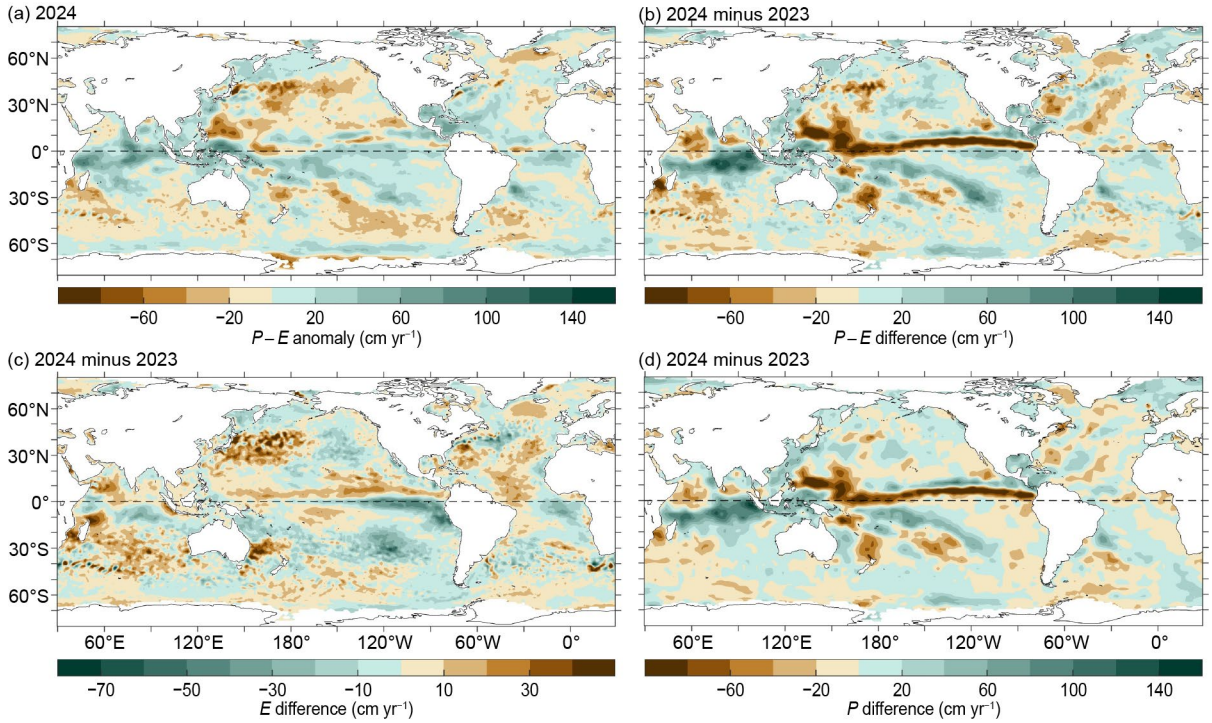

Fig. 3.13. (a) Surface freshwater precipitation (*P*)–evaporation (*E*) flux anomalies (cm yr^{-1}) for 2024 relative to the 2001–15 climatology. Positive values denote ocean freshwater gain. 2024-minus-2023 differences for (b) *P*–*E*, (c) *E*, and (d) *P*. Positive values denote ocean freshwater gain. *P* is from the GPCP version 2.3 product, and *E* is from the Woods Hole Oceanographic Institution (WHOI) OAFlux2.

3. WIND STRESS

In 2024, the tropical basins were predominantly characterized by weak negative wind stress anomalies, with considerable magnitude in the tropical North Atlantic, eastern Pacific basin, and eastern tropical Indian Ocean (Fig. 3.14a). This pattern suggests that northeast trade winds slightly strengthened in the tropical North Pacific but weakened in the tropical Atlantic. In mid- to high latitudes, wind anomalies were more pronounced. Over the Antarctic Circumpolar Current (ACC) region (40°S–60°S), Southern Hemisphere westerlies weakened substantially, with anomalies falling below −0.04 N m^{-2}. Meanwhile, midlatitude westerlies in the North Atlantic also weakened by more than 0.04 N m^{-2}, whereas those in the central North Pacific slightly strengthened (~0.02 N m^{-2}). The 2024-minus-2023 differences (Fig. 3.14b) show a distinct anomaly pattern: slightly stronger trade winds in the tropical North Pacific and a general weakening of westerlies across the Southern Ocean and the North Atlantic.

Wind patterns exhibit substantial spatial variability, leading to divergence and convergence in Ekman transport. These variations generate vertical velocity, known as Ekman pumping, which is characterized by downwelling (negative) and upwelling (positive) velocities, represented by W_{EK} at the base of the Ekman layer. The computation of W_{EK} follows the equation: $W_{EK} = 1/\rho\nabla\times(\tau/f)$, where ρ is the water density and f the Coriolis parameter.

Unauthenticated | Downloaded 11/21/25 11:34 AM UTC

The 2024 W_{EK} anomalies showed distinct positive anomalies in a narrow off-equatorial band of the eastern Pacific and pronounced negative anomalies in a similar narrow off-equatorial band in the Indian Ocean, both exceeding 16 cm day^{-1} (Fig. 3.14c). These patterns suggest a weakening of the regional climatological conditions.

The 2024-minus-2023 W_{EK} difference map (Fig. 3.14d) deviates from the 2024 mean anomaly pattern, reflecting wind pattern changes associated with the transition from El Niño in 2023 to ENSO neutral in early 2024 and then weak La Niña conditions by late 2024. Downwelling (negative) anomalies enhanced in the near-equatorial Pacific and Atlantic, while upwelling (positive) anomalies strengthened in the near-equatorial Indian Ocean. Outside of the equatorial zones, W_{EK} anomalies with substantial magnitudes were observed at higher latitudes, particularly in the Indo-Pacific sector of the ACC regions and the subpolar North Atlantic.

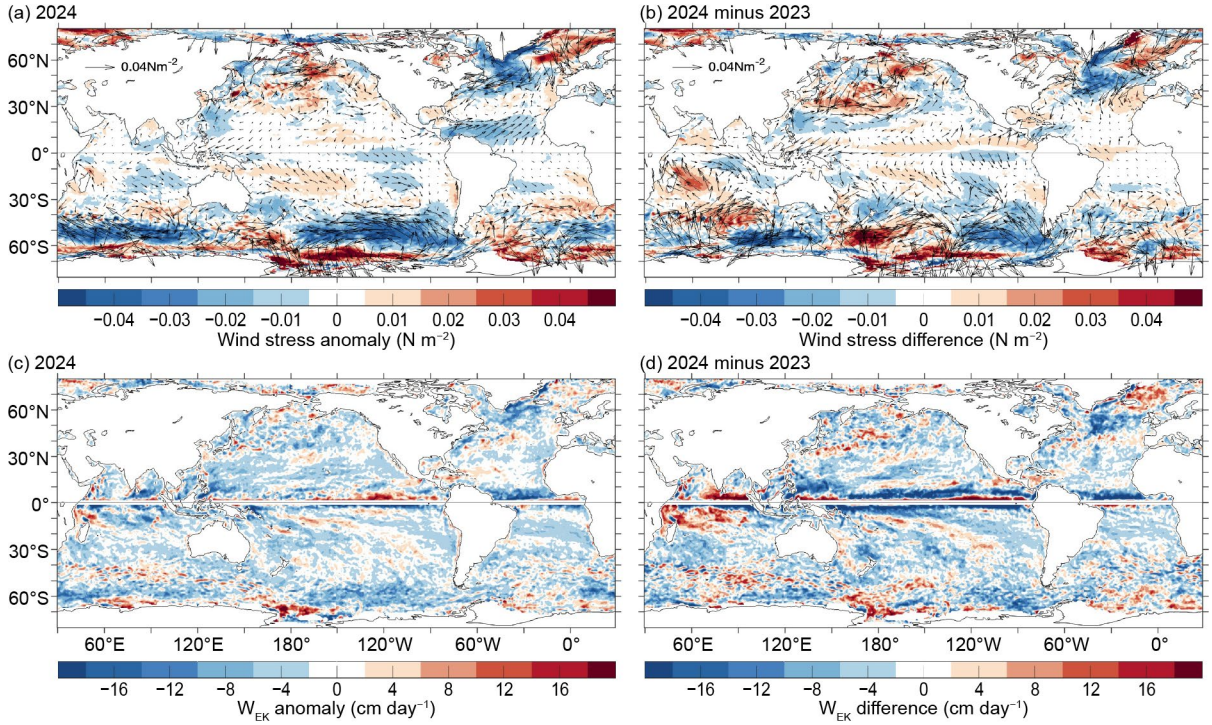

Fig. 3.14. (a) Wind stress magnitude (shaded) and vector anomalies (N m^{-2}) for 2024 relative to a 2001–15 climatology. (b) 2024-minus-2023 differences in wind stress. (c) Ekman vertical velocity (W_{EK}; cm day^{-1}) anomalies for 2024 relative to a 2001–15 climatology. Positive values denote upwelling and negative values denote downwelling. (d) 2024-minus-2023 differences of W_{EK}. Wind stress and W_{EK} fields are from the Woods Hole Oceanographic Institution (WHOI) OAFlux2.

4. LONG-TERM PERSPECTIVE

A long-term perspective on ocean surface forcing changes in 2024 is presented using a three-decade annual-mean time series of Q_{net}, $P-E$, and wind stress averaged over global ice-free oceans (Figs. 3.15a–c). Q_{net} anomalies are referenced to the 2001–15 mean, where positive anomalies indicate increased net downward heat flux into the ocean, contributing to ocean surface warming. The $P-E$ and wind stress time series span 37 years, starting in 1988, and are also referenced to the 2001–15 mean for consistency. Positive anomalies in $P-E$ denote increased freshwater flux into the ocean, leading to sea surface freshening. Similarly, positive anomalies in wind stress denote increased wind stress magnitude. Error bars in the time series represent one standard deviation of year-to-year variability.

Annual means of Q_{net}, $P-E$, and wind stress serve as indicators of the heat, freshwater, and momentum balance at the ocean surface. Q_{net} remained relatively stable from 2001 to 2010 but showed an upward trend thereafter. Between 2011 and 2016, Q_{net} increased by approximately 3±0.9 W m^{-2}, rising from ~–1±1 W m^{-2} during the 2011 La Niña to a peak of ~+2±1 W m^{-2} during the strong 2015/16 El Niño. This increase in Q_{net} coincided with a 0.35°C increase in global-mean SST (see Fig. 3.3). Subsequently, Q_{net} decreased during the 2017/18 La Niña and continued its decline

Unauthenticated | Downloaded 11/21/25 11:34 AM UTC

throughout the 2020–23 triple-dip La Niña. In 2024, Q_{net} was slightly higher by 0.4±0.9 W m^{-2}.

The *P*–*E* time series shows distinct decadal variability. A notable downward trend occurred in the 1990s, followed by a relatively stable period in the 2000s, and substantial interannual fluctuations in the 2010s. After peaking in 2015/16, *P*–*E* decreased by approximately 4±2 cm yr^{-1}, reaching a low point in 2021 before gradually recovering. In 2024, *P*–*E* increased by 0.8±2 cm yr^{-1} compared to 2023, approaching the climatological mean.

The wind stress time series has remained relatively stable over the past two decades following a notable regime shift around 1999. From 2000 onward, the trend has been steady, with minor interannual fluctuations. A slight reduction occurred in 2009 followed by a small increase in 2021. In 2024, the wind stress level was similar to 2023, remaining slightly weaker than the climatological mean.

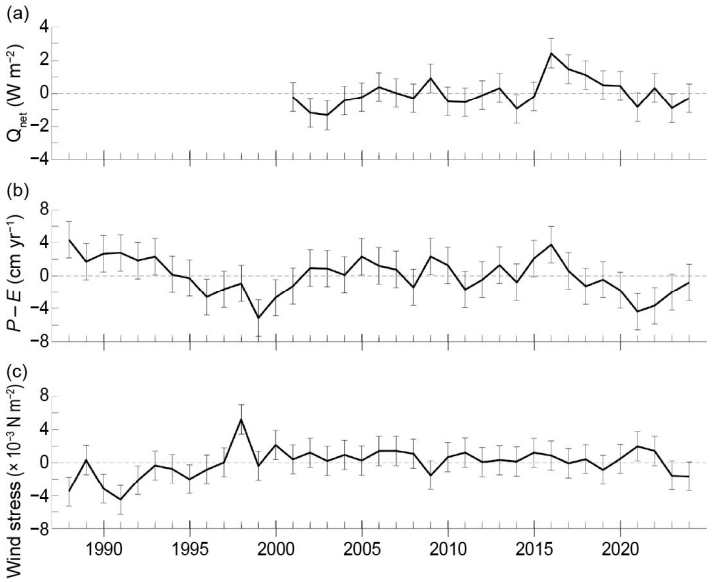

Fig. 3.15. Annual mean time series of global ocean surface (a) net surface heat flux (Q_{net}; W m^{-2}) from a combination of Clouds and the Earth's Radiant Energy System (CERES) EBAF4.2 short wave (SW) + long wave (LW) and the Woods Hole Oceanographic Institution (WHOI) OAFlux2 latent heat (LH) + sensitive heat (SH). The 2024 Q_{net} is based on FLASHFlux SW+LW as adjusted to EBAF and OAFlux2 LH+SH. (b) Net freshwater flux anomaly (*P*–*E*; cm yr^{-1}) from a combination of GPCP *P* and OAFlux2 *E*. (c) Wind stress magnitude anomalies (N m^{-2}) from WHOI OAFlux2. Error bars denote one standard deviation of annual-mean variability.

Unauthenticated | Downloaded 11/21/25 11:34 AM UTC

f. Sea level variability and change

—P. R. Thompson, M. J. Widlansky, B. Beckley, A. Bellas-Manley, D. P. Chambers, B. D. Hamlington, S. Jevrejeva, F. W. Landerer, E. Leuliette, M. A. Merrifield, G. T. Mitchum, R. S. Nerem, and W. Sweet

Annual average global mean sea level (GMSL) from satellite altimetry (1993–present; Beckley et al. 2024) reached a new high in 2024, rising to 105.8 mm above the 1993 mean (Fig. 3.16a). This marks the 13th consecutive year (and 29th out of the last 31) that GMSL increased relative to the previous year, reflecting unprecedented subsurface ocean temperatures during 2024 (section 3c; Cheng et al. 2025) and the combined effects of ongoing trend and acceleration in GMSL. The average linear trend over the entire altimetry era is 3.3±0.4 mm yr^{-1} (Fig. 3.16a) when corrected for glacial isostatic adjustment (GIA; −0.25±0.1 mm yr^{-1}; Tamisea and Mitrovica 2011; Caron and Ivins 2020), while acceleration in GMSL, at 0.078±0.025 mm yr^{-2}, has doubled the decadal rate of GMSL rise during the altimetry era (Hamlington et al. 2024). A quadratic fit with corrections for the eruption of Mount Pinatubo (Fasullo et al. 2016) yields a climate-driven linear trend of 3.1±0.4 mm yr^{-1} and acceleration of 0.092±0.025 mm yr^{-2} (updated from Nerem et al. 2018).

The thermosteric (i.e., ocean warming) contribution to GMSL change was 1.5±0.3 mm yr^{-1} during 2005–24 (Fig. 3.16a), which primarily reflects warming of the upper 2000 m of the ocean as measured by Argo profiling floats and analyzed by Scripps Institution of Oceanography (SIO; Roemmich and Gilson 2009). The deep ocean below 2000 m contributes less than 10% of the thermosteric trend based on measurements made by deep Argo floats and ship-based observations (Johnson and Purkey 2024). Mass concentration anomalies from GRACE and GRACE Follow-On (GRACE-FO) missions produced by the NASA Jet Propulsion Laboratory (JPL; Wiese et al. 2022) show the average mass contribution to GMSL rise during the 2005–24 period was 2.1±0.4 mm yr^{-1} when corrected for GIA –1.0±0.3 mm yr^{-1}; Caron and Ivins 2020; Fig. 3.16a). The trend in the sum of thermosteric and mass contributions, 3.5±0.5 mm yr^{-1}, agrees with the GMSL trend of 3.8±0.4 mm yr^{-1} measured by altimetry since 2005 (Leuliette and Willis 2011; Chambers et al. 2017).

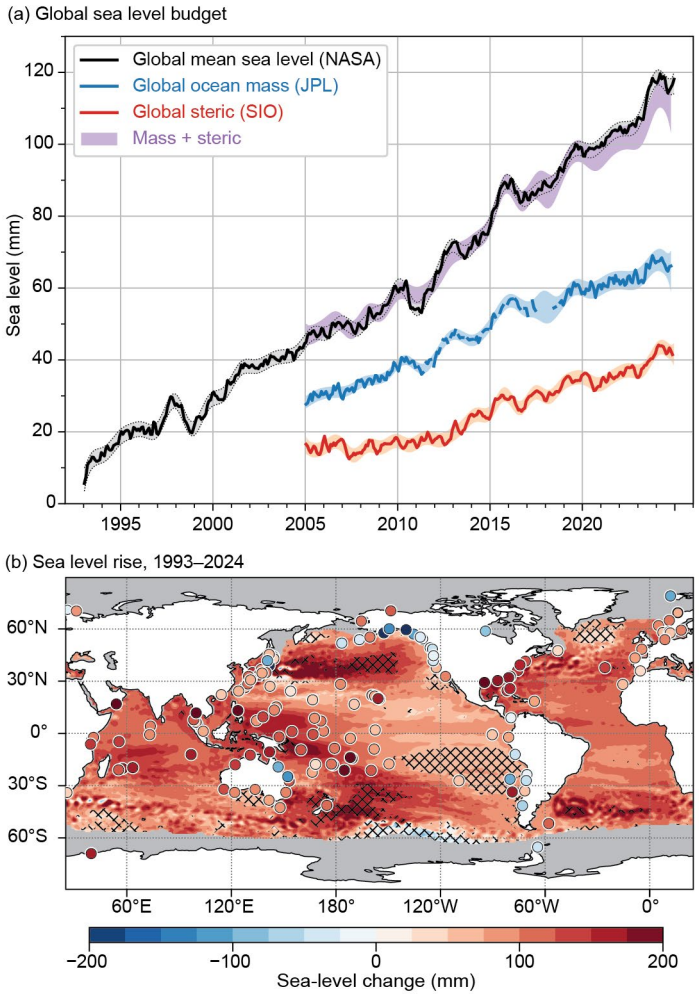

Fig. 3.16. (a) Global mean sea level (GMSL) observed by satellite altimeters (1993–2024) produced with support from the NASA Sea Level Change and Ocean Surface Topography Science Teams (black). Monthly global ocean mass (2005–24) from GRACE and GRACE-Follow-On (GRACE-FO) calculated from mass concentrations produced by NASA Jet Propulsion Laboratory (JPL; blue). GRACE and GRACE-FO data within 300 km of land were excluded. Monthly global mean thermosteric sea level (2005–24) from Scripps Institute of Oceanography (SIO) for depths above 2000 m and long-term trends from Johnson and Purkey (2024; JP24) for depths below 2000 m (red). Shading around the GMSL, mass, and thermosteric series represents a 95% confidence range for annual and longer variations, including glacial isostatic adjustment (GIA) uncertainty for the GMSL and mass time series. The confidence ranges for mass and thermosteric are used to produce a 95% confidence range for the sum of the contributions to GMSL (purple). (b) Total local sea level change during 1993–2024 as measured by satellite altimetry (contours) and tide gauges (circles). Hatching indicates local changes that differ from the change in GMSL by more than one standard deviation. The trend map was generated using gridded delayed-mode and near-real-time altimetry data produced by the Copernicus Climate Change Service and obtained from the Copernicus Marine Service. Tide-gauge observations were obtained from the University of Hawai'i Sea Level Center Fast Delivery database.

Unauthenticated | Downloaded 11/21/25 11:34 AM UTC

Spatial structure in sea level trends (Fig. 3.16b) has become increasingly uniform as the altimetry record has lengthened and the impact of transient fluctuations on regional sea level trends has lessened. Presently, only a small fraction of the global ocean has experienced sea level trends that differ from the GMSL trend by more than one standard deviation (hatched areas, Fig. 3.16b). However, sea level changes relative to land (i.e., the quantity measured by tide gauges; circles, Fig. 3.16b), which is most relevant for societal impacts, can differ substantially from satellite-derived changes in tectonically active regions (e.g., Japan) and areas strongly affected by vertical land movement such as glacial isostatic adjustment (e.g., Alaska; Fig. 3.16b).

Monthly GMSL anomalies peaked during March 2024 as the strong El Niño conditions that persisted through the 2023/24 boreal winter were ending (see section 4b for details), which impacted GMSL via global patterns of oceanic heat content and precipitation (Nerem et al. 1999; Hamlington et al. 2020). The return to El Niño–Southern Oscillation (ENSO)-neutral conditions by mid-year, followed by development of La Niña-like conditions late in the year, caused GMSL anomalies to fall during the second half of 2024. Despite decreasing seasonal anomalies, annually averaged GMSL increased by 4.6±1.4 mm from 2023 to 2024. This annual change is approximately half of the change from 2022 to 2023 but is still an above-average annual increase for the altimetry record. The sum of annual increases in the global mean steric contribution, 4.16±0.66 mm, and global mean mass contribution, 1.78±0.90 mm, slightly exceeds the observed annual increase in GMSL reported above, although the sum of the contributions is within the standard error of the expected total.

Local sea level anomalies averaged during 2024 were well above the 1993–2022 baseline (a 30-year period that starts with the first full year that satellite sea level maps are available) over most regions of the global ocean (Fig. 3.17a), except for near-normal conditions across much of the equatorial Pacific and parts of the tropical South Pacific. In these latter two regions, there were annual decreases in sea level from 2023 to 2024 (Fig. 3.17b). Year-over-year decreases of 5 cm to 10 cm in these regions, which also extended along the coasts of Central and South America, resulted from the change in ENSO conditions described above (see section 4b for details).

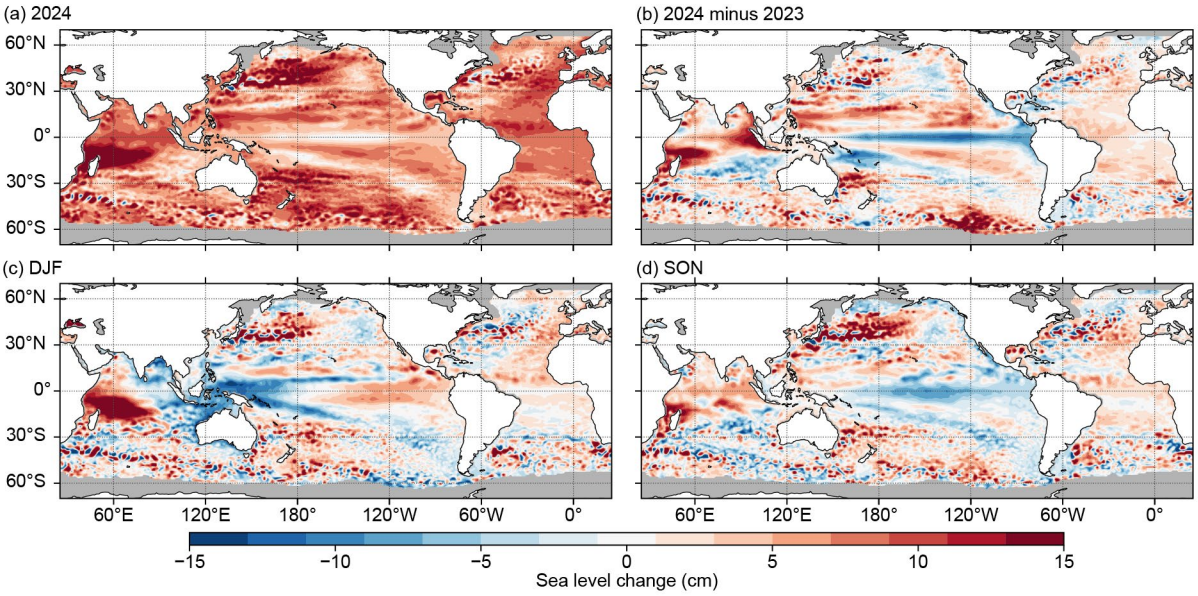

Fig. 3.17. (a) Annual average sea level anomaly during 2024 relative to average sea level at each location during 1993–2022. (b) Average 2024-minus-2023 sea level anomaly. (c) Average sea level anomaly during Dec–Feb (DJF) 2024 relative to the 1993–2022 DJF average. (d) Same as (c), but for Sep–Nov (SON). Units are given in cm. Global mean sea level was subtracted from panels (c),(d) to emphasize regional, non-secular change. These maps were generated using gridded delayed-mode and near-real-time altimetry data produced by the Copernicus Climate Change Service and obtained from the Copernicus Marine Service.

Unauthenticated | Downloaded 11/21/25 11:34 AM UTC

In contrast, sea levels increased year-over-year in most of the tropical North Pacific, a feature commonly observed following the termination of El Niño that is associated with high sea levels around Hawai'i (e.g., Long et al. 2020). In the tropical South Pacific, year-over-year changes were predominantly positive east of the dateline, while the southwestern Pacific experienced decreasing sea levels, a pattern that has been linked to post-El Niño conditions and, in some cases, associated with exposed island reefs during especially low tides (e.g., Widlansky et al. 2014).

Large annual anomalies and positive year-over-year changes in the Indian Ocean reflect changes in the state of the Indian Ocean dipole (IOD). The IOD began 2024 in an extreme positive phase, which is associated with above-normal sea levels in the western Indian Ocean (Kumar et al. 2020), before transitioning to neutral by boreal summer. Sea levels in the Atlantic Ocean were mostly higher in 2024 compared to the previous year (Fig. 3.17b), consistent with long-term trends. One exception was the northwestern Caribbean and the U.S. East Coast, where year-over-year changes were negative. Despite this localized interannual decline, sea level anomalies in 2024 remained well above normal relative to the 1993–2022 baseline (Fig. 3.17a). Characteristics of oceanic eddies remained evident in the mid- and higher latitudes, both in year-over-year changes (Fig. 3.17b) and in the seasonal anomalies (Figs. 3.17c,d).

Seasonal sea level anomalies after removing the long-term trend (Figs. 3.17c,d) indicate the transition from an El Niño-associated sea level pattern (high in the east, low in the west) in early 2024 (December 2023–February 2024) to a more La Niña-like configuration (lower sea levels in most of the equatorial Pacific) by late 2024 (September–November). In the northwestern Pacific as well as around the Maritime Continent and into the Indonesian Throughflow region, sea level anomalies increased during 2024, ending the year with near-climatological values. In the tropical Indian Ocean, 2024 began with sea levels (December 2023–February 2024) that were well above normal—exceeding 15 cm in the southwestern basin—while below-normal sea levels were observed in the eastern region. After removing the long-term trend, negative anomalies extended poleward to include the Bay of Bengal and the western coast of Australia. By September–November 2024, these anomalies moderated, with sea levels in the Bay of Bengal and near Australia becoming positive. However, well-above-normal sea levels persisted in the western Indian Ocean, particularly near Africa and Madagascar, consistent with positive ocean heat content anomalies in the region (see Fig. 3.5a).

Ongoing trends, year-to-year variability, and seasonal changes in sea level impact coastal communities by increasing the magnitude and frequency of positive sea level extremes that contribute to flooding and erosion (e.g., Wahl et al. 2014; Kendon et al. 2024; Li et al. 2022). Minor impacts tend to emerge when local water levels exceed the 99th percentile of the observed daily maxima (Sweet et al. 2014). Using 1993–2022 as the epoch for calculating percentiles (consistent with the altimetry baseline), daily sea level maxima that exceed the 99th percentile—hereafter referred to as extreme sea level events—occurred more frequently in recent years compared to previous decades (Sweet et al. 2024). Tide-gauge records with at least 80% completeness during 1993–2024 and 80% completeness during both 2023 and 2024 were analyzed. Across the 110 records that met these criteria, the median number of extreme sea level events per year and location increased from one during the 1993–97 pentad to five during the 2020–24 pentad. The 90th percentile of events per year and location increased from 6 during 1993–97 to 17 during 2020–24.

Thirty-four of the 110 locations experienced more than 10 extreme sea level events during 2024 (Fig. 3.18a). These locations were distributed around the global ocean and were concentrated in areas where sea level trends and/or annual sea level anomalies were largest (Figs. 3.17a, 3.18b). The greatest number of extreme events occurred in Hawai'i, where two locations experienced more than 30 events due to the combination of interannual increases in sea level (Figs. 3.17a,b) and local mesoscale variability. The elevated numbers of events along the North Atlantic western boundary current system reflect a continuation of extremely high sea levels from the previous year (Fig. 3.18c), which reflects ongoing ocean warming of the region (Fig. 3.5c;

Unauthenticated | Downloaded 11/21/25 11:34 AM UTC

Volkov et al. 2023) and trends in the amplitude of the seasonal cycle (Barroso et al. 2024; Yang and Chen 2025). Elevated numbers of extreme sea level events elsewhere in the Indian Ocean, western Pacific at midlatitudes, and eastern North Atlantic (Fig. 3.18 a) are generally consistent with the positive sea level anomalies in these regions (Fig. 3.17).

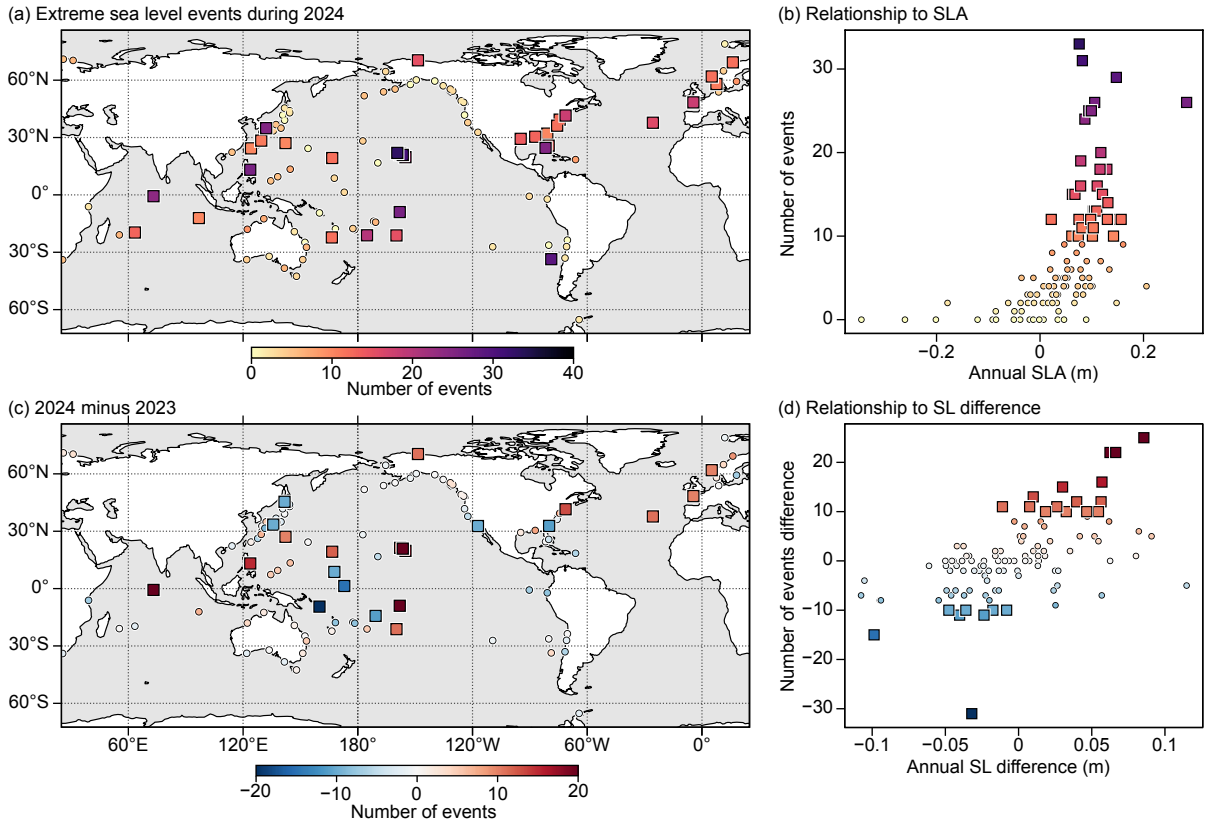

Fig. 3.18. (a) Number of extreme sea level events from tide gauges during 2024. (b) Counts in (a) as a function of annual sea level anomaly during 2024. Square markers in (a) and (b) highlight locations with more than 10 extreme events. (c) Change in number of extreme sea level events from 2023 to 2024. (d) Counts in (c) as a function of the change in annual sea level from 2023 to 2024. Square markers in (c) and (d) highlight locations where the magnitudes of changes in counts of extreme events were greater than 10. Counts of extreme sea level events were calculated from hourly tide gauge observations obtained from the University of Hawai'i Sea Level Center Fast Delivery database.

Unauthenticated | Downloaded 11/21/25 11:34 AM UTC

g. Surface currents

—R. Lumpkin, M. Le Hénaff, F. P. Tuchen, and R. C. Perez

This section describes variations of ocean surface currents, transports, and associated features, such as rings. Here, geostrophic and total surface currents are obtained from in situ and satellite observations. See Lumpkin et al. (2012) for details of these calculations. Zonal geostrophic current anomalies are calculated with respect to a 1993–2023 climatology (with 1993 being the first full year that satellite sea level data are available) and are discussed below for individual ocean basins.

In terms of ocean surface current retrieval methodologies, 2024 saw the continued development of Artificial Intelligence-based approaches that could be leveraged for future reports. The approaches developed by Fablet et al. (2024), Martin et al. (2024), and Kugusheva et al. (2024) all combine low-resolution altimetry sea surface height observations with higher-resolution sea surface temperature (SST), and, in the case of Kugusheva et al. (2024), chlorophyll-*a* satellite measurements. These approaches are all based on deep learning and neural networks, and they provide surface current estimates that are more accurate (Kugusheva et al. 2024), with higher resolution (Martin et al. 2024), and with a better estimation of the ageostrophic component of the current (Fablet et al. 2024). These approaches are promising for the retrieval of surface current estimates of high quality, and therefore have the potential for increased value in their applications.

In 2024, near-surface in situ measurements (12-m depth or shallower) were available from 10 mooring sites in the tropical Atlantic, 3 sites along the equator in the tropical Pacific, and 3 sites in the Indian Ocean, as part of the Global Tropical Moored Buoy Array (GTMBA, e.g., McPhaden et al. 2023). As part of the Tropical Atmosphere Ocean (TAO) recapitalization efforts, it is expected that the number of tropical Pacific moorings with near-surface current information will increase substantially in 2025/26.

1. PACIFIC OCEAN

In 2024, zonal geostrophic currents in the equatorial Pacific (Fig. 3.19a) exhibited annual mean westward (negative) current anomalies exceeding –10 cm s^{-1} between 2°S and 3°N across the basin, with the strongest anomalies of –23 cm s^{-1} along the equator at 160°E–165°E. Because these westward anomalies are a reversal of the El Niño-associated eastward anomalies of 2023 (Lumpkin et al. 2024), the 2024-minus-2023 difference map (Fig. 3.19b) reached westward values of –30 cm s^{-1}, covering nearly the entire equatorial waveguide in the Pacific basin.

Zonal current anomalies in December 2023–February 2024 (Fig. 3.20a) indicated an intensification and southward shift of the North Equatorial Countercurrent (NECC), with eastward anomalies of 16 cm s^{-1} at 6°N (south of the climatological core of the NECC) and westward anomalies of –10 cm s^{-1} at 9°N. Anomalies near the equator were close to zero during this season. In contrast, dramatic westward anomalies exceeding –10 cm s^{-1}, with an equatorial peak of –25 cm s^{-1}, dominated the central Pacific in March–May 2024 (Fig. 3.20b) concurrent with the relaxation from strong

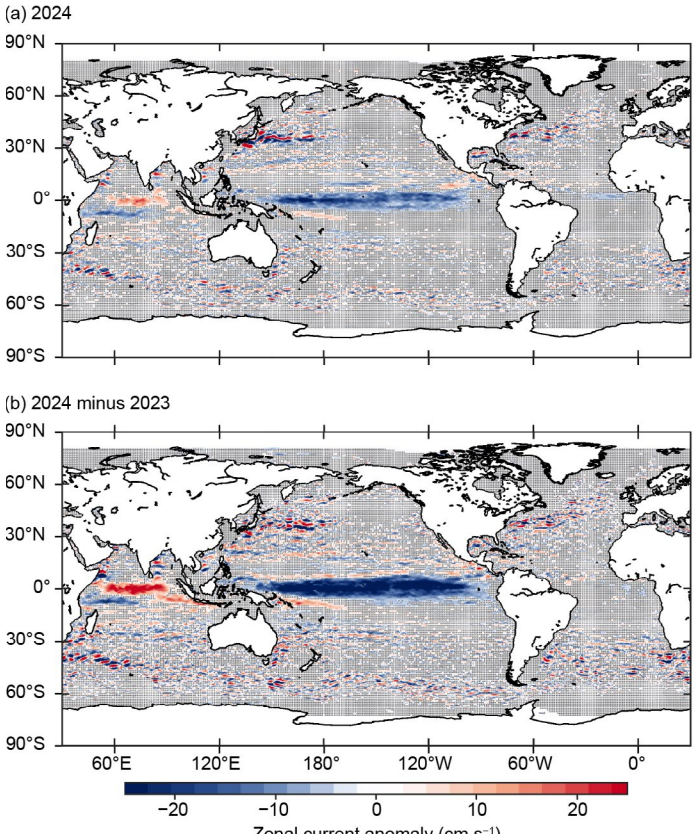

Fig. 3.19. Annually averaged geostrophic zonal current anomalies (cm s^{-1}) with respect to the seasonal climatology for (a) 2024 and (b) 2024 minus 2023. Values are only shown where they are significantly different from zero.

Unauthenticated | Downloaded 11/21/25 11:34 AM UTC

El Niño SST conditions in December 2023–February 2024 to El Niño–Southern Oscillation (ENSO)-neutral conditions in April–June (see section 4b). These anomalies weakened significantly in June–August (Fig. 3.20c) and September–November (Fig. 3.20d) but were still present through the end of the year.

In 2020–24, the annual-average latitude of the Kuroshio Extension in the region 141°E–153°E, 32°N–38°N was shifted north of its long-term (1993–2024) location of 35.4°N to a maximum of 36.8°N in 2021 and to 36.1°N in 2024. This can be seen as alternating eastward/westward current anomalies in Fig. 3.19a that persisted through the year (Fig. 3.20) and also in a band of increased ocean heat content anomaly (Fig. 3.5a). This 2020–24 northward shift of the Kuroshio Extension corresponded with a multi-year increase in averaged eddy kinetic energy. This pattern is associated with a meander of the Kuroshio Current off the southern coast of Japan (Qiu et al. 2020) seen in the 2024 altimetry data that has persisted since 2017 (Qiu and Chen 2021) and was noted in last year's *State of the Climate in 2023* report.

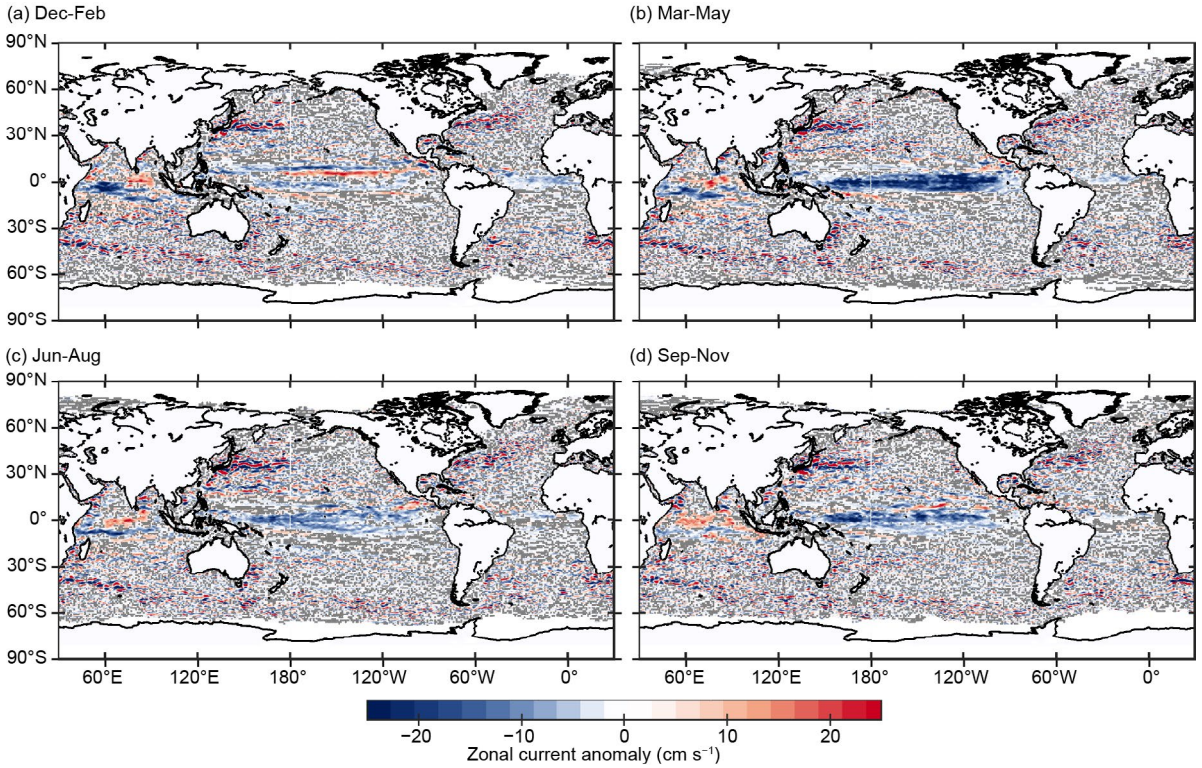

Fig. 3.20. Seasonally averaged zonal geostrophic anomalies (cm s^{-1}) with respect to seasonal climatology for (a) Dec 2023–Feb 2024, (b) Mar–May 2024, (c) Jun–Aug 2024, and (d) Sep–Nov 2024. Values are only shown where they are significantly different from zero.

In a recent study by Tuchen et al. (2024), a long-term increase of the near-surface total (geostrophic plus wind-driven) zonal currents in the tropical Pacific as well as poleward transport was shown based on a synthesis product of surface drifter data, reanalysis winds, and satellite altimetry (Fig. 3.21). Between 1993 and 2022, the westward surface currents near the equator increased by ~20%, while the eastward NECC increased in strength by ~30%. At the same time, the divergent poleward flow north and south of the equator in the central Pacific increased by ~60% and 20%, respectively. These multi-decadal trends are attributed to increased easterlies and cross-equatorial winds, likely due to natural modes of variability. As a consequence of accelerating zonal currents, tropical instability waves (TIWs) in the Pacific Ocean have significantly intensified over the same time period (Wang et al. 2024). This is due to increased meridional shear of zonal velocity in the central equatorial Pacific, causing intensified barotropic energy

Unauthenticated | Downloaded 11/21/25 11:34 AM UTC

conversion from the mean flow into higher-frequency fluctuations like TIWs. Continued monitoring of surface and subsurface currents through drifters, moorings, and repeat shipboard observations will be necessary to distinguish between internal and external variability.

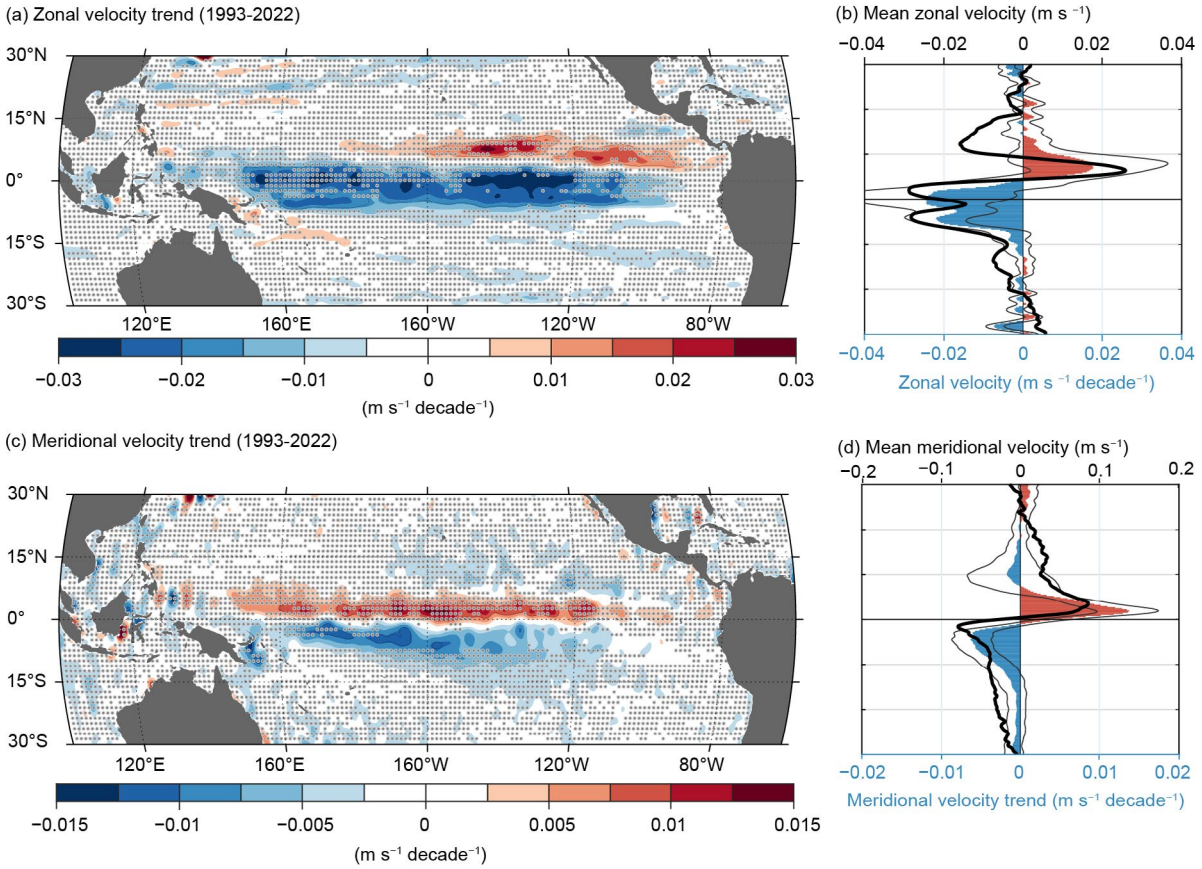

Fig. 3.21. (a) Surface zonal total velocity trend (m s^{-1} decade^{-1}) between 1993 and 2022 in the tropical Pacific. Regions where trends are not significantly different from zero at 97.5% confidence are stippled. (b) Zonally averaged (100°W–170°W) mean surface zonal velocity (black line) and surface zonal velocity trend (colored bars) as functions of latitude. Thin black lines indicate the 2.5%– 97.5% confidence intervals on the trend. (c) and (d) Same as (a) and (b) but for total meridional velocity.

2. INDIAN OCEAN

Annually-averaged geostrophic zonal current anomalies in the Indian Ocean (Fig. 3.19a) exhibited 10 cm s^{-1} to 14 cm s^{-1} eastward anomalies at 2°S–1°N and –5 cm s^{-1} to –8 cm s^{-1} westward anomalies between 6°S and 10°S. Because the equatorial currents were anomalously westward in 2023, the 2024-minus-2023 difference map (Fig. 3.19b) has strong eastward differences exceeding 20 cm s^{-1} on the equator. These eastward anomalies were not present in December 2023–February 2024 (Fig. 3.20a). They developed in March–May (Fig. 3.20b), strengthened in June–August (Fig. 3.20c), and persisted through September–November (Fig. 3.20d). Unlike in 2022/23, there was no evidence of a southward shift in the Somali Current extension.

3. ATLANTIC OCEAN

Annual mean geostrophic zonal current anomalies in the tropical Atlantic Ocean in 2024 did not exceed ±5 cm s^{-1} (Fig. 3.19a). Because a similar situation was observed in 2023, the 2024-minus-2023 difference map (Fig. 3.19b) is not remarkable. Westward –5 cm s^{-1} to –7 cm s^{-1} anomalies between 1°S and 3°N in the eastern half of the basin in December 2023–February 2024 (Fig. 3.20a) disappeared by March–May (Fig. 3.20b), and no significant anomalies reappeared in June–November (Figs. 3.20c,d). In 2024, the equatorial Atlantic experienced a series

Unauthenticated | Downloaded 11/21/25 11:34 AM UTC

of pronounced equatorial wave propagation events that had an impact on surface zonal velocities near the equator. According to operational reanalysis data from the European Centre for Medium-Range Weather Forecasts' Ocean ReAnalysis System 5 (ORAS5), surface zonal velocity anomalies reached values of +40 cm s^{-1} in March, causing a reversal of the surface currents that usually flow from east to west in this region and season. This situation led to a reduction in upper-ocean current shear between the surface current and the subsurface Equatorial Undercurrent. Likely, the late phase of the 2023/24 El Niño event caused westerly wind anomalies in the western equatorial Atlantic through an atmospheric teleconnection that excited equatorial waves in early 2024.

In the subtropical North Atlantic, a band of strong positive and negative anomalies of magnitude 15 cm s^{-1} to 20 cm s^{-1} east of Cape Hatteras (Fig. 3.19a) and west of 70°W indicated that the Stream extension in that region was shifted anomalously northward in 2024 compared to the long-term mean.

Unauthenticated | Downloaded 11/21/25 11:34 AM UTC

h. Meridional overturning circulation and heat transport in the Atlantic Ocean

—D. L. Volkov, J. K. Willis, W. Hobbs, D. A. Smeed, W. E. Johns, B. I. Moat, R. C. Perez, S. Dong, R. H. Smith, S. Speich, and T. Lamont

The observing network for the meridional overturning circulation (MOC) volume transport and the associated meridional heat transport (MHT) in the Atlantic Ocean consists of several trans-basin moored arrays and synthetic estimates based on the combination of satellite and in situ data (Fig. 3.22; Frajka-Williams et al. 2019). Here, moving from north to south, we present the updated Atlantic MOC/MHT time series for: 1) the synthetic estimates at 41°N based on satellite altimetry and Argo data (Willis and Hobbs 2025), 2) the moored RAPID–Meridional Overturning Circulation and Heat-flux Array–Western Boundary Time Series (henceforth RAPID) array at ~26.5°N (Moat et al. 2024), 3) the moored South Atlantic MOC Basin-wide Array (SAMBA) at ~34.5°S (Meinen et al. 2013, 2018), and 4) the synthetic estimates at ~34.5°S based on satellite altimetry, expendable bathythermograph, and Argo data (Dong et al. 2021). Only the synthetic estimates are updated through 2024. The estimates from the moored arrays are updated through 2022 for RAPID and through 2023 for SAMBA (MOC only). The updates for the Overturning in the Subpolar North Atlantic Program (OSNAP) trans-basin array and for the Meridional Overturning Variability Experiment (MOVE) array in western tropical North Atlantic at ~16°N are pending. Highlights here include a major revision of the Florida Current (FC) transport estimates that significantly amended the MOC/MHT at ~26.5°N (Volkov et al. 2024a) and the continued increase in the MOC/MHT at 41°N first documented in the previous year's report (Volkov et al. 2024b).

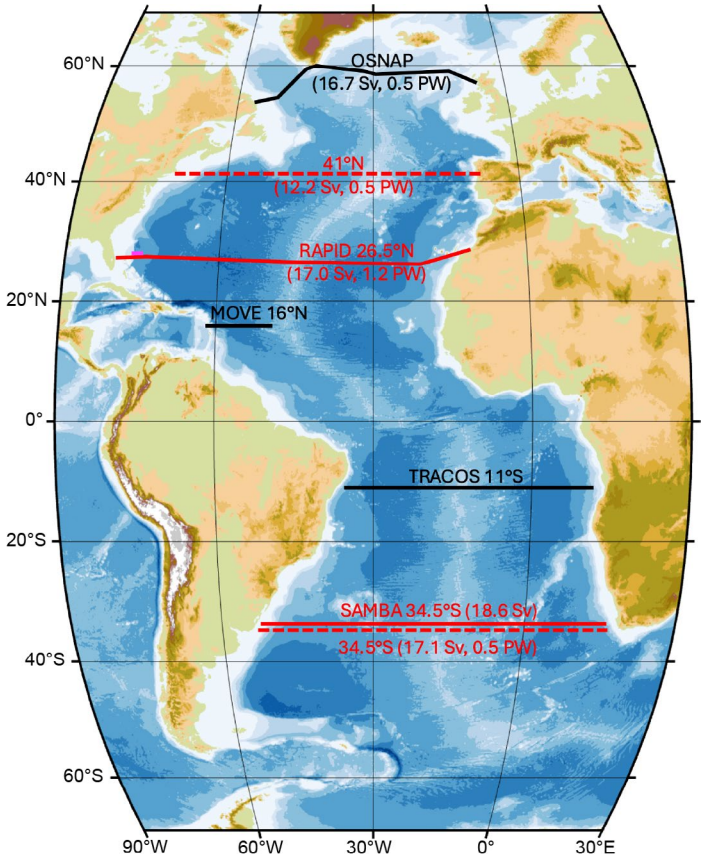

Fig. 3.22. The Atlantic meridional overturning circulation (MOC) observing network: moored arrays (solid red and black lines) and sections across which the MOC and meridional heat transport (MHT) are estimated by synthesizing in situ measurements (Argo, eXpendable BathyThermograph [XBT]) with satellite altimetry data (dashed red lines). The red lines show the sections that have updates covered in this report, while the black lines show the sections for which updates are pending. The record mean MOC and MHT values are shown in parentheses.

The synthetic MOC/MHT time series at 41°N were reproduced from Willis (2010) and Hobbs and Willis (2012) and extended to December 2024 (Fig. 3.23a; Willis and Hobbs 2025). Each individual estimate represents a three-month average with an uncertainty of ±2.3 Sverdrup (Sv) for the MOC and ±0.23 petaWatt (PW) for the MHT. The record-length time-mean MOC and MHT are 12.2 Sv and 0.46 PW, respectively. The MOC transport at 41°N was 16.2 Sv in 2024, 15.1 Sv in 2023, 12.8 Sv in 2022, and 11.2 Sv in 2021, with only the 2023 and 2024 means being statistically different from the time-mean given the uncertainty (Fig. 3.23a). The MHT was 0.74 PW in 2024 and 0.66 PW in 2023, both of which are significantly greater than the time-mean and the MHT of 0.54 PW in 2022. As quality control of Argo and altimeter data are ongoing, improvements in the estimate over the past few years are common. The improvements implemented since the *State of the Climate in 2023* report (Volkov et al. 2024b) resulted in a small decrease in the MOC transport of 0.1 Sv to 0.6 Sv in the 2021 through 2023 values, relative to last year's report. While this change is smaller than the year-to-year uncertainty in the estimate at 41°N, it is worth noting that the recent high values of the MOC in 2023 and 2024 persisted and remained unusually high, relative to the mean and variability in the Atlantic MOC volume and heat transports of the previous 20 years.

Unauthenticated | Downloaded 11/21/25 11:34 AM UTC

The RAPID moored array at ~26.5°N is the oldest trans-basin MOC observing array, marking 20 years of operation in April 2024. At this latitude, most of the northward volume transport in the upper limb of the MOC and in the horizontal gyre circulation is carried by the FC. The FC volume transport has been estimated from motion-induced voltages measured on submarine cables nearly continuously since 1982 (Baringer and Larsen 2001; Meinen et al. 2010). Thus, the 40+ years record of the FC transport can serve as an index of the MOC's strength in the subtropical North Atlantic. A small negative trend in the FC transport of about −0.3 Sv decade^{-1} was reported earlier (e.g., Baringer et al. 2015; Volkov et al. 2021). A major revision of the cable record was performed last year, showing that the negative trend was largely spurious, and that the FC had remained remarkably stable with a mean transport of about 32 Sv (Volkov et al. 2024a). After applying a correction for the secular change in geomagnetic field to the cable record, the negative trend was reduced to −0.1±0.2 Sv decade^{-1}, which is statistically insignificant. Because the FC transport is an integral component of the MOC/MHT estimate at ~26.5°N, the revision of the former led to a revision of the latter; both were made publicly available in September 2024 (Volkov et al. 2024a; Moat et al. 2024).

The corrected FC transport increased the record mean MOC value from 16.8 Sv to 17 Sv. This increase is smaller than the ±0.9 Sv uncertainty of annual transport estimates (McCarthy et al. 2015). Most importantly, the correction reduced the negative trend that was present in the 2004–22 MOC record from –1.3±0.7 Sv decade^{-1} to −0.8±0.7 Sv decade^{-1}. The MOC time series at ~26.5°N exhibits a decadal-scale variability, with a decline in 2004–09, an increase in 2009–18, and a decline since then (Fig. 3.23b; e.g., Moat et al. 2020; Smeed et al. 2018). In 2021 and 2022, the MOC was 15.9 Sv and 15.2 Sv, respectively, which is significantly smaller than the time-mean. The latter value was the second-lowest MOC on record, behind 2009. The MOC and MHT at ~26.5°N are highly correlated (r=0.95), suggesting that most of the poleward heat transport is carried by the overturning circulation. The time-mean MHT is 1.21 PW with a monthly standard deviation of 0.25 PW. In 2022, the MHT was 1.11 PW, which is less than the 1.18 PW in 2021 and the time-mean of 1.21 PW. However, this MHT decrease is barely significant. In recent years, the ratio of MHT to MOC has become higher due to the increasing temperature in the Florida Straits (Johns et al. 2023). Therefore, the decrease of MHT in 2022 was not as profound as the corresponding decrease of MOC.

The MOC/MHT time series at 41°N and ~26.5°N are somewhat coherent, with a correlation of 0.5, which is statistically significant at a 95% confidence level. At both latitudes, the MOC/MHT was high during 2004–08 but dropped to a record-low value in 2009. However, the following increase of MOC/MHT in 2010–18 was stronger at ~26.5°N than at 41°N (Fig. 3.23). This led to heat convergence and associated sea level rise in the subtropical gyre of the North Atlantic, which also translated to accelerated sea level rise and significantly increased flood risk along the southeast U.S. coast, including the Gulf of America/Gulf of Mexico (Domingues et al. 2018; Volkov et al. 2019, 2023). MOC/MHT divergence between ~26.5°N and 41°N in 2021/22 was due to the opposing MOC/MHT tendencies at the two latitudes (Fig. 3.23). As soon as the RAPID dataset is updated, it will be possible to see whether this divergence continued through 2023/24 and how it impacted the regional heat content and sea level. The dependence of coastal sea level on MOC-related gyre-scale processes

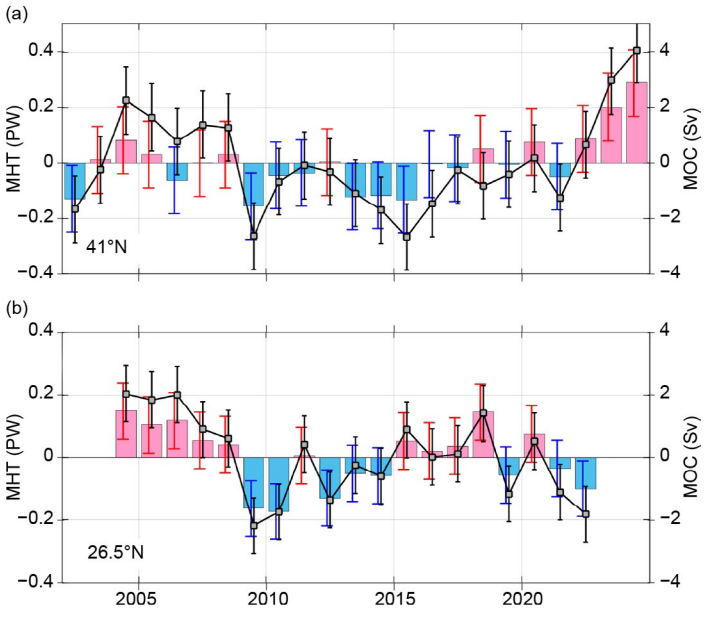

Fig. 3.23. Annual mean anomalies of meridional overturning circulation (MOC; Sverdrup [Sv]) transport (black curve) and meridional heat transport (MHT; petaWatt [PW]; pink and blue bars) relative to the respective record-length time-mean values at (a) 41°N and (b) ~26.5°N. Error bars show uncertainties for annual mean values.

Unauthenticated | Downloaded 11/21/25 11:34 AM UTC

is one among many examples of why the continued monitoring of MOC/MHT at ~26.5°N and 41°N is important. Because regional ocean heat content and sea level are proportional to the time-integral of MHT divergence, the observed time series of MOC/MHT provides one to three years of advance predictability for sea level.

Preliminary estimates of the MOC transport at ~34.5°S have been updated from March 2009 to December 2022 using data from SAMBA's two most inshore moorings (Fig. 3.24a). The mean MOC volume transport from the SAMBA array is 18.6 Sv with a decreasing trend of −0.56±0.32 Sv yr^{-1}. While statistically significant, the trend is largely controlled by the high annual mean values at the start of the record (25.7 Sv in 2009 and 18.9 Sv in 2010) and the low annual mean values at the end of the record from 2020 to 2022 (between 9.8 Sv and 18.4 Sv). These outlier years appear to be driven primarily by density differences, rather than by pressure differences or wind forcing, and are not evident in the synthetic time series. The mean synthetic MOC and MHT estimates at ~34.5°S are 17.1 Sv and 0.48 PW, respectively. In 2023/24, the synthetic MOC and MHT are not significantly different from record mean values considering the uncertainties (Fig. 3.24b). No long-term trend was found for the synthetic MOC, but the synthetic MHT experienced an increasing trend of 0.02±0.01 PW $decade^{-1}$ due to strong warming in the upper ocean. While SAMBA and the synthetic estimates agree well on seasonal timescales, the differences in the amplitude of their annual mean fluctuations are profound, with the SAMBA MOC being an order of magnitude more variable (Fig. 3.24). While the ground truth is unknown, it is necessary to determine the reasons for these differences, which probably arise from different instrumentation, sampling characteristics, and methodologies used.

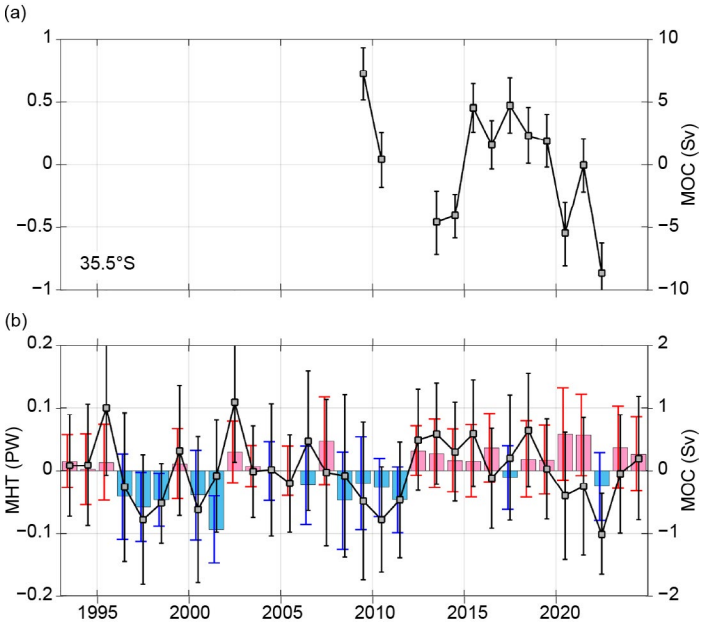

Fig. 3.24. Annual mean anomalies of meridional overturning circulation (MOC) transport (Sverdrup [Sv]; black curves) and meridional heat transport (MHT; PW; pink and blue bars) relative to the respective record-length time-mean values for (a) the South Atlantic MOC Basin-wide Array (SAMBA) and (b) synthetic estimates at 34.5°S. No MHT updates are available for the SAMBA. Error bars show uncertainties of the annual mean values.

The observational MOC/MHT estimates serve as important indicators of climate variability. The updated estimates in the North Atlantic reveal MOC/MHT divergence between 26.5°N and 41°N in the most recent years, which is part of the interannual-to-interdecadal variability that dominates the yearly time series. In the South Atlantic, it is still necessary to reconcile the MOC transports obtained from the moored SAMBA array and from the synthetic estimates at 34.5°S. Overall, the existing MOC/MHT estimates are still short compared to the climate time scales. They are just starting to showcase the decadal-scale changes. Sustained observations are therefore necessary to fully resolve inter-decadal variability and to detect a possible MOC decline projected by climate models and proxy-based reconstructions.

Unauthenticated | Downloaded 11/21/25 11:34 AM UTC

i. Global ocean phytoplankton

—B. A. Franz, I. Cetinić, M. Gao, and T. K. Westberry

Marine phytoplankton play a crucial role in global ecosystems, contributing about 50% of Earth's total net primary production. They meet the energy demands of oceanic food webs and provide a key mechanism for carbon sequestration, transporting carbon to the deep ocean (Field et al. 1998; Siegel et al. 2023). Diversity, abundance, and distribution of phytoplankton are influenced by both biotic factors—such as grazing by zooplankton and viruses—and abiotic factors like the availability of nutrients and light. These, in turn, depend on physical conditions like ocean temperature, stratification, and circulation (e.g., Behrenfeld et al. 2006). Observations from spaceborne ocean color sensors offer a global view of phytoplankton dynamics, tracking spatial and temporal variations by measuring near-surface concentrations of chlorophyll-*a* (Chl*a*; mg m^{-3}) and phytoplankton carbon (C_{phy}; mg m^{-3}). While Chl*a* levels reflect both phytoplankton biomass and physiological state, C_{phy} quantifies phytoplankton carbon biomass. Although Chl*a* and C_{phy} often covary, differences in their distribution can reveal shifts in the physiological or compositional makeup of phytoplankton communities (Dierssen 2010; Geider et al. 1997; Cetinić et al. 2012; Siegel et al. 2013; Westberry et al. 2016).

In this report, we evaluate the global distribution of phytoplankton over the one-year period from October 2023 through September 2024 (the analysis year, which is necessarily different from other sections owing to time required to finalize instrument calibrations and gather data from ancillary sources) using remotely sensed Chl*a* and C_{phy} measurements from a continuous 27-year record (1997–2024) that combines observations of the Sea-Viewing Wide Field-of-View Sensor (SeaWiFS; 1997–2010), Moderate Resolution Imaging Spectroradiometer on *Aqua* (MODIS-A, 2002–present), and Visible Infrared Imaging Radiometer Suite on NOAA-20 (VIIRS-N20, 2017–present). The MODIS-A daytime sea surface temperature (SST; °C) is also assessed over a consistent time period to provide context on the physical state of the oceans. The ocean color data from VIIRS-N20, MODIS-A, and SeaWiFS correspond to NASA processing version R2022. The Chl*a* product was derived using the Ocean Color Index algorithm of Hu et al. (2012), but with updated algorithm coefficients (Hu et al. 2019; O'Reilly and Werdell 2019; Werdell et al. 2023). C_{phy} was derived from the particle backscattering coefficient (b_{bp}) at 443 nm (Generalized Inherent Optical Properties algorithm; Werdell et al. 2013; McKinna et al. 2016, 2024) and a linear relationship between b_{bp} and C_{phy} (Graff et al. 2015). In merging the time series of SeaWiFS and MODIS-A, differences between the sensors were assessed over the overlapping period from 2003 through 2008, and mean bias corrections (−0.0021 mg m^{-3} in Chl*a*, −6.7e-5 m^{-1} in b_{bp} , or −0.78 mg m^{-3} of C_{phy}) were derived and applied to the SeaWiFS time series. Similarly, the overlap period of 2018 to 2020 was used to assess the differences between MODIS-A and VIIRS-N20, and bias corrections (−0.0021 mg m^{-3} in Chl*a*, −3.1e-4 m^{-1} in b_{bp} , or −3.6 mg m^{-3} of C_{phy}) were applied to the VIIRS-N20 timeseries. The bias corrections between the VIIRS-N20 and MODIS-A b_{bp} time series are relatively large, due to residual sensor radiometric calibration errors and sensitivity of the b_{bp} retrievals to spectral sampling differences between the sensors (i.e., Werdell and McKinna 2019). Efforts are underway at NASA to reduce this retrieval bias, but additional caution is warranted here in the interpretation of C_{phy} anomalies from VIIRS-N20 relative to the climatological record that is dominated by MODIS-A. However, the VIIRS-N20 instrument is temporally stable (Twetd et al. 2022) and thus provides the primary reference to assess changes over the current analysis year.

Changes in the global distribution of phytoplankton were assessed by subtracting monthly climatological means for MODIS-A Chl*a* and C_{phy} (October 2002–September 2023) from the VIIRS-N20 bias-adjusted monthly mean values for the 2024 analysis year. These monthly anomalies were then averaged to produce the global Chl*a* and C_{phy} annual mean anomaly maps (Figs. 3.25a,b). Similar calculations were performed on MODIS-A SST data to produce an equivalent SST annual mean anomaly for the same time period and climatological reference period (Fig. 3.25c). The permanently stratified ocean (PSO), which is used for the analyses depicted in Figs. 3.26 and 3.27, is defined as the region spanning the tropical and subtropical oceans where annual average SST is greater than 15°C (black lines near 40°N and 40°S in Fig. 3.25).

Unauthenticated | Downloaded 11/21/25 11:34 AM UTC

There, surface mixed layers are typically low in nutrients and shallower than the nutricline (Behrenfeld et al. 2006).

For the 2024 analysis year, the distribution of SST anomalies (Fig. 3.25c) is consistent with initially strong but declining El Niño conditions, including a pronounced tongue of anomalously warm waters extending across the equatorial Pacific with anomalously cool waters north and south of the feature. A similar but inverse feature is evident in the Chl*a* anomalies, with concentrations depressed (<20%) within the warm tongue and strongly elevated (>40%) in the adjacent cooler waters (Fig. 3.25a). Negative SST anomalies within the PSO are typically associated with deeper surface mixed layers (Deser et al. 2010), which reduces phytoplankton light exposure rates leading to higher cellular Chl*a* and a decoupling between Chl*a* and C_{phy} variability (Behrenfeld et al. 2016). While C_{phy} and Chl*a* anomalies appear to covary in the equatorial Pacific and the Indian Ocean south of the equator, C_{phy} is depressed where Chl*a* is elevated in the North and South Atlantic, consistent with observations in 2023 (Franz et al. 2024a). Similar decoupling between Chl*a* and C_{phy} is also observed in the Arabian Sea (Chl*a* depressed with C_{phy} elevated) and in the Indian Ocean east of Madagascar (Chl*a* elevated with C_{phy} depressed). Patches of depressed Chl*a* are visible throughout the subpolar and polar regions outside of the PSO (Fig. 3.25a), and the C_{phy} anomalies are generally elevated (Fig. 3.25b). Observed heterogeneity in biomass indicators outside of the PSO are a result of the ephemeral nature of phytoplankton blooms in these waters as well as poor spatial and temporal sampling due to clouds and low-light conditions that limit interpretation of interannual variability in higher latitude regions.

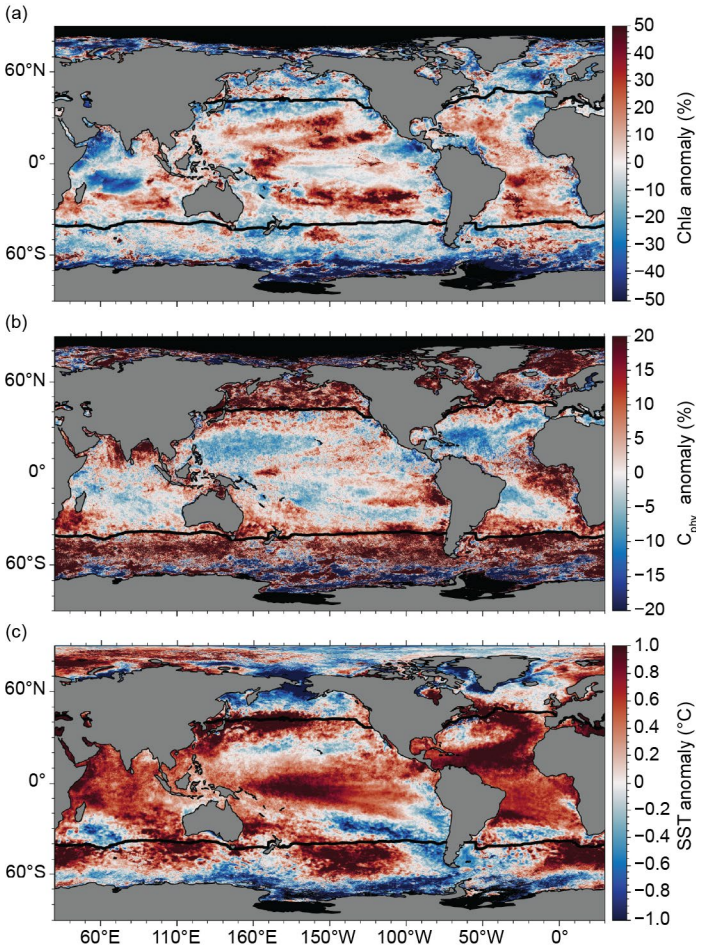

Fig. 3.25. Spatial distribution of average monthly (a) VIIRS on NOAA-20 (VIIRS-N20) chlorophyll-*a* (Chl*a*) anomalies (%), (b) VIIRS-N20 phytoplankton carbon (C_{phy}) anomalies (%), and (c) Moderate Resolution Imaging Spectroradiometer on *Aqua* (MODIS-A) sea surface temperature (SST) anomalies (°C) for Oct 2023–Sep 2024, where monthly differences were derived relative to the MODIS-A climatological record (Oct 2002–Sep 2023). Chl*a* and C_{phy} are stated as % difference from climatology, while SST is shown as an absolute difference. Also shown in each panel is the location of the mean 15°C SST isotherm (black lines) delineating the permanently stratified ocean. Differences in the SST anomalies here versus in Fig. 3.1 are owing to differences in analysis years, climatological periods, smoothing, and data sources.

Annual variability of Chl*a* and C_{phy} within the PSO typically exhibits two distinct peaks (Figs. 3.26a,b), reflecting the springtime increases of biomass in the Northern (Figs. 3.26c,d) and Southern Hemispheres (SH; Figs. 3.26g,h). The timing of peaks in C_{phy} lags two to three months behind those of Chl*a*, reflecting a reduction in phytoplankton chlorophyll-to-carbon ratios as the seasonal bloom progresses (e.g., Westberry et al. 2016) and the tight coupling between phytoplankton biomass and its losses (e.g., grazing). The timing of seasonal peaks and troughs observed in the 2024 analysis year are consistent with the monthly climatologies. The SH PSO anomalies for C_{phy} (Fig. 3.26h) were modestly low in the first half of the analysis year (October–March). A similar but stronger pattern was observed in 2023 (Franz et al. 2024a) and was traced to error in the measurements due to continuing influence of stratospheric aerosols from the 2022 Hunga eruptions (Franz et al. 2024b). Low Chl*a* and C_{phy} in the equatorial region

Unauthenticated | Downloaded 11/21/25 11:34 AM UTC

over the first half of the year is consistent with an expected response to the prevailing El Niño conditions over that time period, which leads to reduced upwelling and vertical transport of nutrients and thus reduced phytoplankton abundance and productivity (Behrenfeld et al. 2001; Chavez et al. 2011).

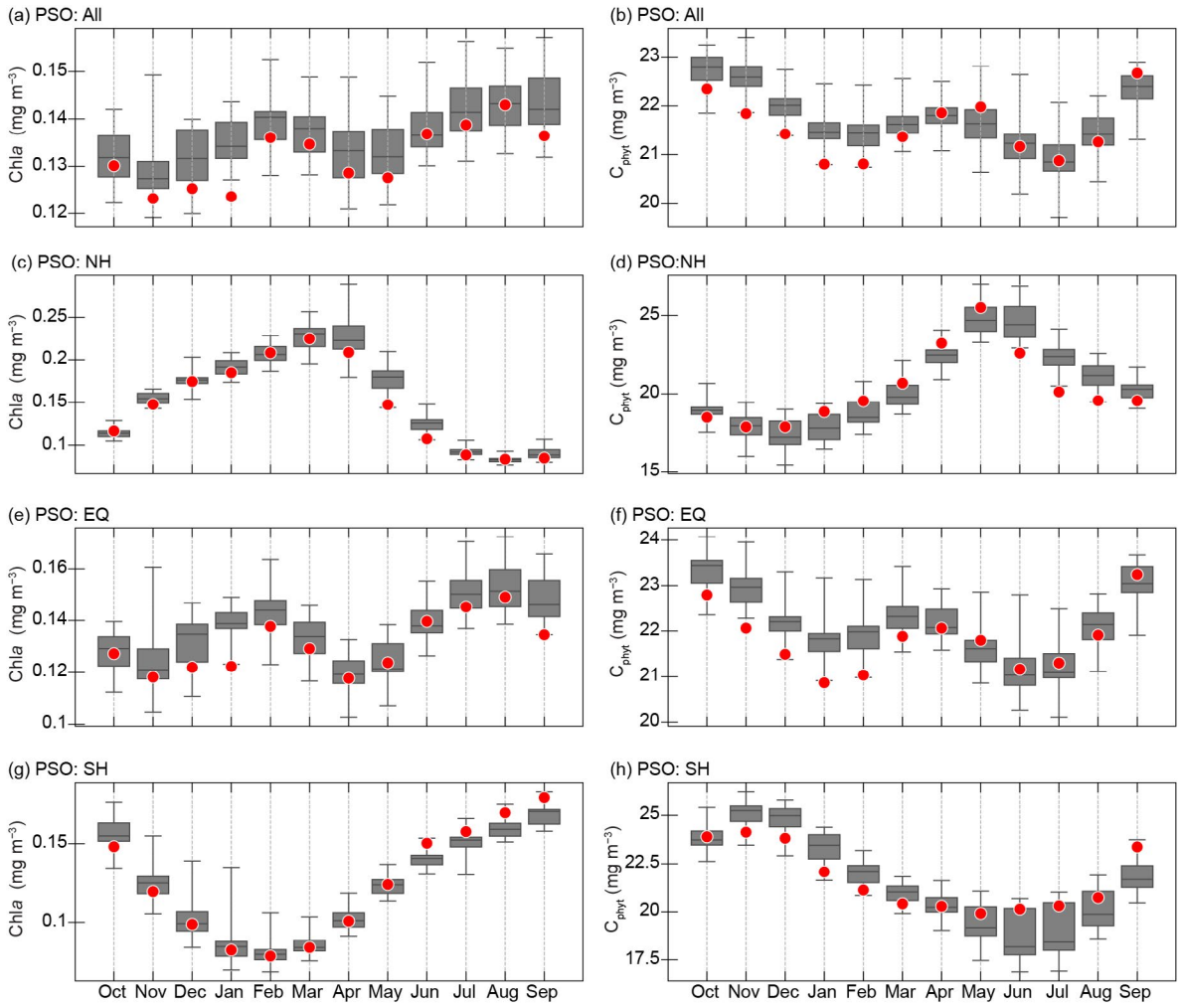

Fig. 3.26. Distribution of Oct 2023–Sep 2024 monthly means (red circles) for (a) VIIRS on NOAA-20 (VIIRS-N20) chlorophyll-*a* (Chl*a*) and (b) VIIRS-N20 phytoplankton carbon (C_{phy}) for the permanently stratified ocean (PSO) region (see Fig. 3.25), superimposed on the climatological values as derived from the combined time series of the Sea-Viewing Wide Field-of-View Sensor (SeaWiFS), Moderate Resolution Imaging Spectroradiometer on *Aqua* (MODIS-A), and Visible Infrared Imaging Radiometer Suite on NOAA-20 (VIIRS-N20) over the period of Oct 1998–Sep 2023. Gray boxes show the interquartile range of the climatology, with a black line for the median value and whiskers extending to minimum and maximum values. Subsequent panels show latitudinally segregated subsets of the PSO for the (c),(d) Northern Hemisphere above tropics (NH), (e),(f) tropical ±23.5° latitudes (EQ), and (g),(h) Southern Hemisphere below tropics (SH). Units for (a), (c), (e), and (g) are Chl*a* (mg m^{-3}) and (b), (d), (f), and (h) are C_{phy} (mg m^{-3}).

Over the 27-year time series of spatially averaged monthly mean Chl*a* within the PSO, concentrations vary by 5.7% (0.008 mg m^{-3}, standard deviation) around a long-term average of 0.136 mg m^{-3} (Fig. 3.27a). C_{phy} over the same 27-year period varies by 3.2% (0.69 mg m^{-3}) around an average of 21.8 mg m^{-3} (Fig. 3.27c). Chl*a* monthly anomalies within the PSO (Fig. 3.27b) vary by 4.5% (0.006 mg m^{-3}) over the multi-mission time series, with the largest deviations generally associated with El Niño-Southern Oscillation (ENSO) events (r = −0.39), as demonstrated by the correspondence of Chl*a* anomaly variations with the Multivariate ENSO Index (MEI; Wolter and Timlin 1998; presented in the inverse to illustrate the covariation). C_{phy} anomalies (Fig. 3.27d), which vary by 2.0% (0.43 mg m^{-3}), are less correlated with the MEI (r = −0.28) due to the inherent lag between environmental change, phytoplankton growth, and biomass accumulation. The mean anomalies in 2024 for Chl*a* and C_{phy} within the PSO indicate modestly depressed concentrations in the early part of the analysis year—consistent with El Niño conditions that limited

Unauthenticated | Downloaded 11/21/25 11:34 AM UTC

phytoplankton production—with concentrations returning to a nominal state following relaxation of El Niño forcings.

Through continuous ocean color monitoring, we can track changes in the global distribution of phytoplankton, which are crucial for driving biogeochemical processes, influencing the oceans' role in the global carbon cycle, and exerting control over marine ecosystems, food webs, and fisheries. Small fluctuations in Chl*a* and C_{phy} help with differentiating between climate-driven changes in phytoplankton biomass and shifts in their physiology and community dynamics. The recently launched Plankton, Aerosol, Cloud, ocean Ecosystem (PACE) mission, which is equipped with the first global hyperspectral instrument for ocean color measurement, is expected to improve the identification of phytoplankton absorption features (Werdell et al. 2019). This instrument will also help separate these features from non-algal optical signals (e.g., Pahlevan et al. 2021; Siegel et al. 2005), enabling more accurate assessments of phytoplankton species and community composition changes (e.g., Cetinić et al. 2024). These advancements will result in enhanced capacity to understand the impacts of climate forces on global phytoplankton communities.

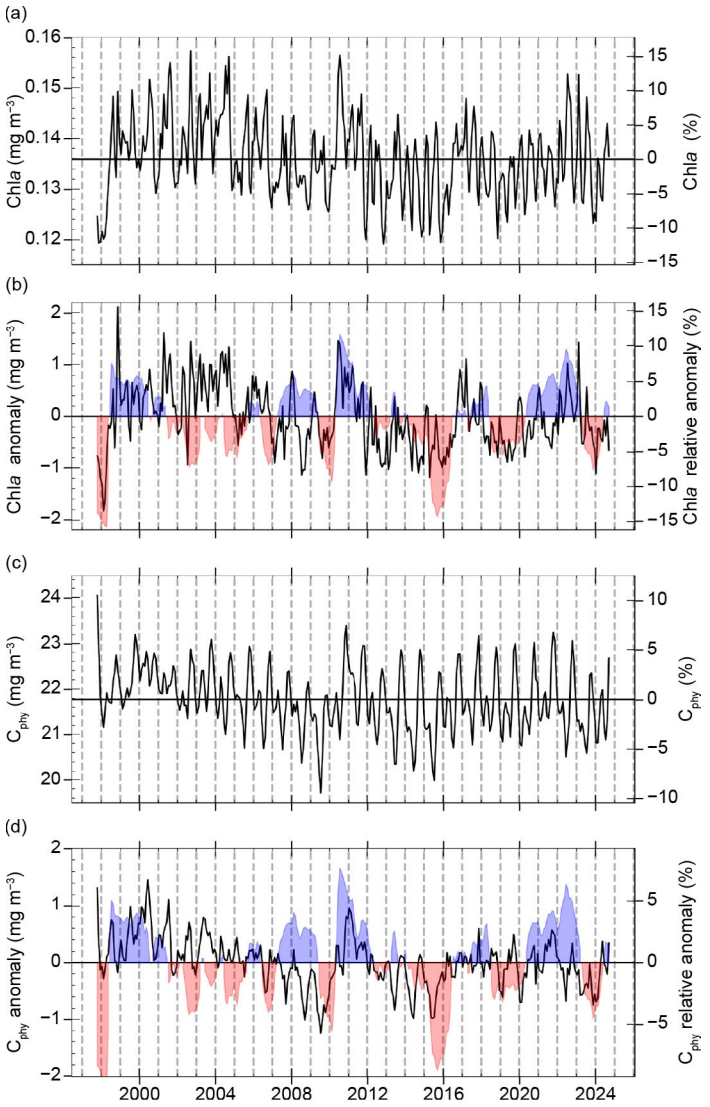

Fig. 3.27. Twenty-seven-year, multi-mission record of chlorophyll-*a* (Chl*a*; mg m^{-3}) and phytoplankton carbon (C_{phy}; mg m^{-3}) averaged over the permanently stratified ocean (PSO; Oct 1997–Sep 2024). (a) Monthly Chl*a*, with the horizontal line indicating the multi-mission mean Chl*a* concentration for the entire PSO region. (b) Monthly Chl*a* anomalies after subtraction of the multi-mission climatological mean (Fig. 3.26a). (c) Monthly C_{phy}, with the horizontal line indicating the multi-mission mean C_{phy} concentration for the entire PSO region. (d) Monthly C_{phy} anomalies after subtraction of the multi-mission climatological mean (Fig. 3.26b). Shaded blue and red colors show the Multivariate El Niño–Southern Oscillation Index, inverted and scaled to match the range of the Chl*a* and C_{phy} anomalies, where blue indicates La Niña and red indicate El Niño conditions.

Unauthenticated | Downloaded 11/21/25 11:34 AM UTC

j. Global ocean carbon cycle

—A. Jersild, R. Wanninkhof, J. A. Triñanes, P. Landschützer, R. A. Feely, and B. R. Carter

1. INTRODUCTION

The oceans play a major role in the global carbon cycle by taking up a substantial fraction of the excess carbon dioxide that humans release into the atmosphere. As a consequence of humankind's collective carbon dioxide (CO_2) release into the atmosphere, referred to as anthropogenic CO_2 (C_{ant}) emissions, the atmospheric CO_2 concentration has risen from pre-industrial levels of about 278 ppm (parts per million) to 422.5 ppm in 2024 (see section 2g1 for details). Marine C_{ant} is the primary cause of anthropogenic ocean acidification. Over the last decade, the global ocean has continued to take up C_{ant}, and therefore is a major mediator of global climate change. Of the 10.8±0.9 Pg C yr^{-1} C_{ant} released during the period 2014–23, 2.9±0.4 Pg C yr^{-1} (27%) accumulated in the ocean, 3.2±0.9 Pg C yr^{-1} (30%) accumulated on land, and 5.2±0.02 Pg C yr^{-1} (48%) remained in the atmosphere, with an imbalance of −0.4 Pg C yr^{-1} (−4%; see Table 7 in Friedlingstein et al. 2025). This decadal C_{ant} uptake estimate by the ocean is a consensus view from a combination of measured ocean decadal CO_2 inventory changes, global ocean biogeochemical models, and global air–sea CO_2 flux estimates based on surface ocean fugacity of CO_2 (fCO_{2w})[1] measurements.

The ocean interior is more challenging to observe than the surface ocean, leading to reduced temporal and spatial coverage relative to surface ocean fCO_2. Machine-learning gap filling techniques are employed to provide increased resolution of interior C_{ant} estimates. An example includes Carter et al. (2024), which overall agrees with estimates given by Friedlingstein et al. (2025), but suggests lower seasonal and interannual variability in the interior. Results demonstrate that the changes in the total carbon ocean inventory ($C_{inventory}$) can be primarily attributable to air–sea CO_2 flux and riverine inorganic carbon inputs. These estimates, however, are derived from expected patterns based on measurements that predate 2024.

2. AIR–SEA CARBON DIOXIDE FLUXES

Ocean uptake of CO_2 is estimated from the net air–sea CO_2 flux derived from a bulk flux formula determined from the product of the difference of air and surface seawater fCO_2 (ΔfCO_2) and gas transfer coefficients. Gas transfer is parameterized with wind, described in Wanninkhof (2014). This calculation provides a net flux estimate. Here, 0.65 Pg C yr^{-1} is applied as the river adjustment (Regnier et al. 2022) as recommended in the Global Carbon Budget 2024. The data sources for fCO_{2w} are annual updates of observations from the Surface Ocean CO_2 Atlas (SOCAT) composed of moorings, autonomous surface vehicles, and ship-based observations (Bakker et al. 2016), with SOCAT v2024 containing 38.6 million data points from 1957 through 2023 (Bakker et al. 2024). The increased observations and improved mapping techniques, including machine learning methods summarized in Rödenbeck et al. (2015), provide annual global fCO_{2w} fields on a 1° latitude × 1° longitude grid at monthly time scales. For this report, we use the self-organizing maps feed-forward neural network (SOM-FNN) approach of Landschützer et al. (2013, 2014), using SOCATv2024 for training. The monthly 2024 fCO_{2w} maps use as predictor variables: sea surface temperature (SST; Rayner et al. 2003); chlorophyll-*a* (Globcolour; Maritorena et al. 2010); mixed-layer depth (de Boyer Montégut et al. 2004 merged with Schmidtko et al. 2013), and salinity (Good et al. 2013). For atmospheric CO_2, the zonally resolved NOAA marine boundary layer atmospheric CO_2 product is used (Lan et al. 2023). The gas transfer coefficients are determined using ERA5 winds (Hersbach et al. 2018). The air–sea CO_2 flux maps for 2024 do not include fCO_{2w} observations for 2024 that have a year's latency but rather are created by extrapolation using the predictor variables. The uptake of the fCO_2-based models such as the Flanders Marine Institute (VLIZ) SOM-FNN used here is larger than the model-based estimates, with differences in uptake of ≈0.3 Pg C in 2023. This difference has decreased in recent years and is within the uncertainty of the approaches.

The VLIZ SOM-FNN results (Fig. 3.28) show a steady ocean CO_2 sink (S_{ocean}) from 1982 to 1998, followed by a period of decreasing uptake from 1998 to 2002. There is a strong increase in the ocean sink from 2002 onward that continues through 2016, after which the global uptake

[1] The fugacity is the partial pressure of CO_2 (pCO_2) corrected for non-ideality. They are numerically similar for surface waters with $fCO_2 \approx 0.994\ pCO_2$.

Unauthenticated | Downloaded 11/21/25 11:34 AM UTC

decreases substantially until 2024. The C_{ant} flux of 2.7 Pg C yr^{-1} for 2024 (green line in Fig. 3.28) shows a ≈1 Pg C decrease in uptake below the 2014–23 average of 3.7±0.31 Pg C yr^{-1}. The amplitude of seasonal variability is ≈2.3 Pg C with a minimum uptake in June–September.

Sea surface temperature anomalies can manifest themselves in differing ways on fCO_{2w}. Positive SST anomalies will decrease solubility and thereby increase fCO_{2w}. However, in regions with high fCO_{2w} due to upwelling, warmer SSTs will lower fCO_{2w} as a result of decreased upwelling of cold, CO_2-rich water.

The annual average flux map for 2024 (Fig. 3.29a) shows the characteristic pattern of high effluxes (ocean-to-air CO_2 fluxes) in tropical, coastal upwelling, and open ocean upwelling regions. Coastal upwelling regions include those in the Arabian Sea and off the west coasts of North and South America, along with West Africa. The western Bering Sea was a strong CO_2 source in 2024, a clear juxtaposition to the strong sink in the surrounding regions. This regional source is hypothesized to result from a local outcropping of shallow isopycnals with high CO_2 values; however, this has not been independently verified. Cumulatively, the regions of effluxes are substantial CO_2 sources to the atmosphere (≈1 Pg C). The primary CO_2 uptake regions are in the subtropical and subpolar regions. The largest sinks are poleward of the sub-tropical fronts. In the Southern Ocean, the area near the polar front (~60°S) was a weak to moderate sink in 2024, with a source closer to the Antarctic coast along the lower latitudes Southern Ocean. This source was not apparent in the previous iteration (see Fig, 3.28a in last year's report) but rather than a physical phenomenon, is attributed to new observations in the region and changes in the source of predictor variables used in the approach.

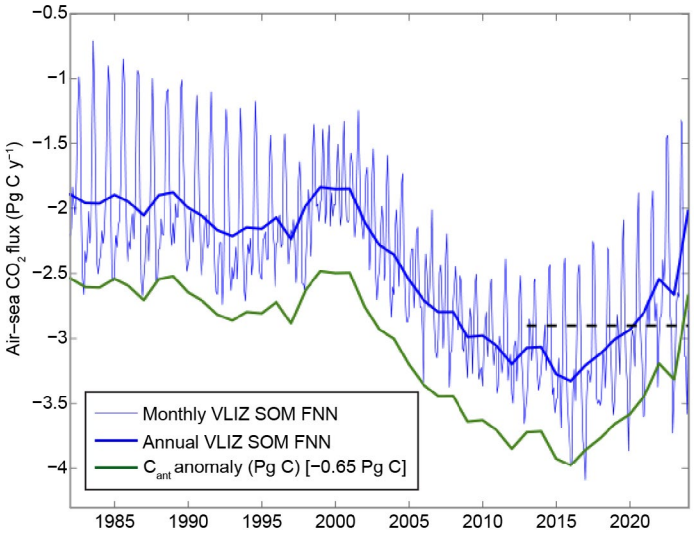

Fig. 3.28. Global annual (thick blue line) and monthly (thin blue line) net air–sea carbon dioxide (CO_2) fluxes (Pg C yr^{-1}) for the period 1982–2024 using the Flanders Marine Institute (VLIZ) self-organizing maps feed-forward neural network (SOM-FFN) output. The annual anthropogenic CO_2 (C_{ant}) air–sea flux (solid green line) includes the riverine adjustment of –0.65 Pg C. Black dashed line is the 2014–23 mean C_{ant} flux based on models and data-based products (Friedlingstein et al. 2025). Negative values indicate CO_2 uptake by the ocean.

In the Northern Hemisphere, the entire North Atlantic is a large sink, while in the North Pacific the sink region is punctuated by a substantial source of CO_2 in the western subpolar North Pacific and the central Bering Sea. The Northern Hemisphere sinks are in part due to the position of the western boundary currents, whose cooling waters when transported poleward cause an increase in solubility and contribute to CO_2 uptake at high latitudes. The Gulf Stream/North Atlantic Drift in the Atlantic extends farther north than the Kuroshio in the Pacific, extending the region of a strong sink in the North Atlantic poleward.

The ocean carbon uptake anomalies (Fig. 3.29c) in 2024 relative to the 1990–2020 average, adjusted for the 20-year trend, show the effect of the El Niño condition in the second half of 2023 lasting through spring 2024, with reduced upwelling and lower effluxes of CO_2 in the eastern equatorial Pacific (EEP). The Southern Ocean shows overall reduced uptake (~60°S–45°S) when compared to the 20-year trend, although the larger region is still overall an ocean sink. This reduction in uptake, which is nearly 50% smaller than previous estimates, is likely due to a combination of temporal variation, methodological improvements, and data sparsity in the region (Hauck et al. 2023).

The spatial differences in CO_2 fluxes between 2024 and 2023 (Fig. 3.29b) show predominant orange shaded regions depicting more efflux, or less influx, leading to a substantially smaller CO_2 uptake by the ocean in 2024 (Fig. 3.28). The eastern and central equatorial Pacific shows regions of more outgassing right along the equator in 2024 compared to 2023 and more uptake,

Unauthenticated | Downloaded 11/21/25 11:34 AM UTC

or less outgassing, immediately to the north. The increased efflux along the equator reflects the residual impacts of the El Niño that lingered into early 2024, leading to a reduced uptake in the EEP. The regions of increased effluxes or decreased influxes in the Northern Hemisphere correspond with the positive SST anomalies in the boreal summer, which often correspond with regions with marine heatwaves. The strong source in the western subpolar North Pacific and Bering Sea (Fig 3.29a) shows up as a positive anomaly compared to the long-term average, similar to the anomaly observed in 2023.

3. OCEAN INTERIOR INVENTORY ESTIMATES

The ocean inventory of dissolved inorganic carbon (DIC) varies over time due to surface CO_2 fluxes, interior ocean cycling of organic matter, riverine inputs, and sedimentary exchanges. While this variability can be monitored directly using ship-based measurements, the ocean interior is more challenging to observe than the surface ocean. There is, therefore, less spatial and temporal coverage of these measurements than surface ocean fCO_2 observations. For this reason, interior ocean DIC observations are primarily used in decadal retrospective analyses that quantify the accumulation of C_{ant} throughout the ocean.

As with surface ocean fCO_2 observations, machine learning gap-filling techniques are now being used to map the available measurements onto data products that have better spatial and temporal resolution (Keppler et al. 2023). Here (Fig. 3.30) we use the Empirical Seawater Property Estimation Routines (ESPERs: Carter et al. 2021) to project DIC onto the temperature and salinity climatology of Roemmich and Gilson (2009), which is supplemented for deep and high-latitude regions using the static climatology from Lauvset et al. (2016). Recent methods for estimating the time-varying C_{ant} in the ocean interior (Carter et al. 2024) allow the $C_{inventory}$ estimates and their year-to-year increases (attributable primarily to S_{ocean}) to be separated into natural variations (ΔC_{nat}) and anthropogenic accumulation (ΔC_{ant}).

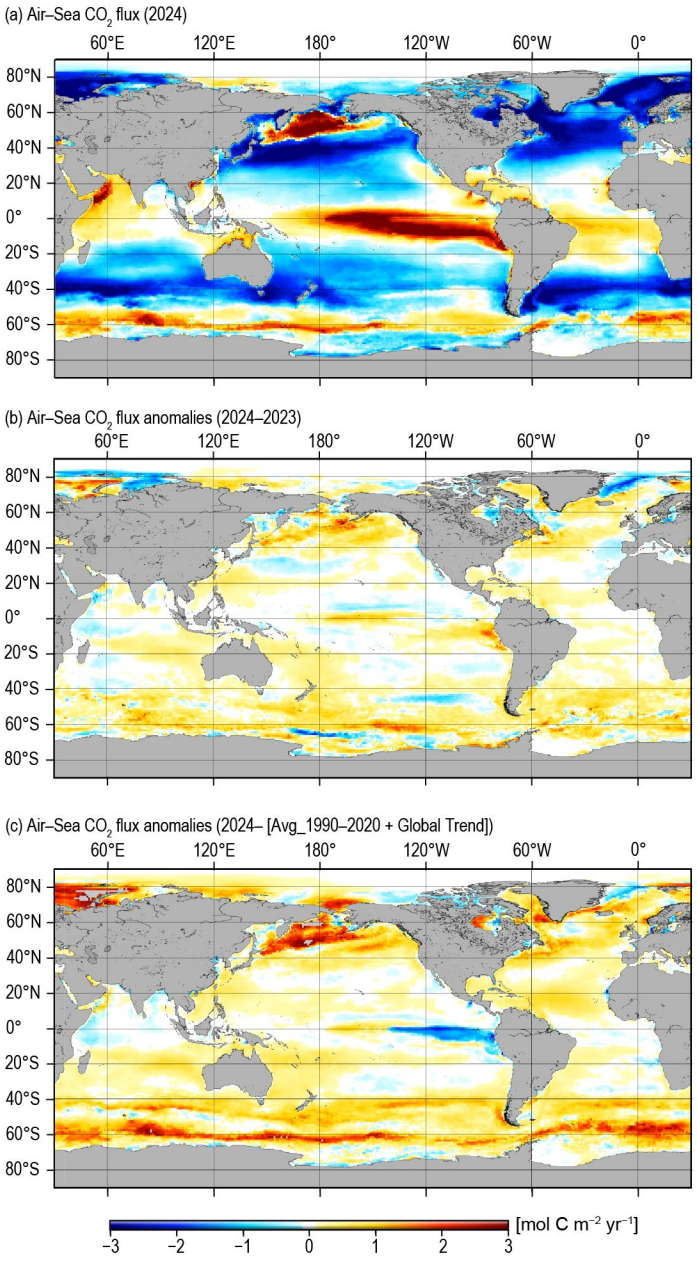

Fig. 3.29. Global map of (a) net air–sea carbon dioxide (CO_2) fluxes for 2024, (b) net air–sea CO_2 flux anomalies for 2024 minus 2023, and (c) net air–sea CO_2 flux anomalies for 2024 relative to 1990–2020 average values, adjusted for the 20-year trend using the Flanders Marine Institute (VLIZ) self-organizing maps feed-forward neural network (SOM-FNN) approach. Units are all mol C m^2 yr^{-1}. Ocean CO_2 uptake regions are shown in blue. For reference, a global ocean CO_2 uptake of 2.8 Pg C yr^{-1} equals a flux density of –0.65 mol C m^2 yr^{-1}.

These ocean inventory change estimates show substantial seasonal variability attributable to C_{nat} (Fig. 3.30a). There is a maximum in the rate of estimated $C_{inventory}$ accumulation each austral winter when the larger ocean areas of the Southern Hemisphere are cooling, followed by warming and release of CO_2 to the atmosphere in the austral summer. Substantial interannual variability in the $C_{inventory}$ can still be seen when the changes are averaged over annual cycles (Fig. 3.30b). This variability is also attributable to C_{nat} variability. The C_{ant} changes are relatively steady from year to year, and the variations generally oppose the much larger variations in the C_{nat}. This

Unauthenticated | Downloaded 11/21/25 11:34 AM UTC

anticorrelation results when increases in ocean overturning generate anomalous loss of deep carbon accumulated from organic matter respiration and anomalous uptake of C_{ant} with ventilation of older waters (DeVries et al. 2017).

The changes in the $C_{inventory}$ are primarily attributable to the air–sea CO_2 flux and riverine inorganic carbon inputs, allowing a comparison to be made between the black bars in Fig. 3.30b and the green line in Fig. 3.28. These methods suggest several differences: the mean inventory uptake estimate is lower over the 2014–23 period at a rate of 2.9 Pg C yr^{-1} compared to the 3.7 (±0.31) Pg C yr^{-1} estimate from air–sea fluxes. The seasonal and interannual variability in the estimates is also notably greater in the inventory estimates, yet the inventory estimates do not show the recent (post-2016) relaxation of ocean CO_2 uptake. There is also an indication that there was an anomalously low $C_{inventory}$ increase in 2023 of 0.8 Pg C yr^{-1}, consistent with strong upwelling from the persistent La Niña that concluded in that year, whereas 2024 shows an increase of 3.9 Pg C that is similar to the estimated 2024 C_{ant} accumulation of 3.7 Pg C.

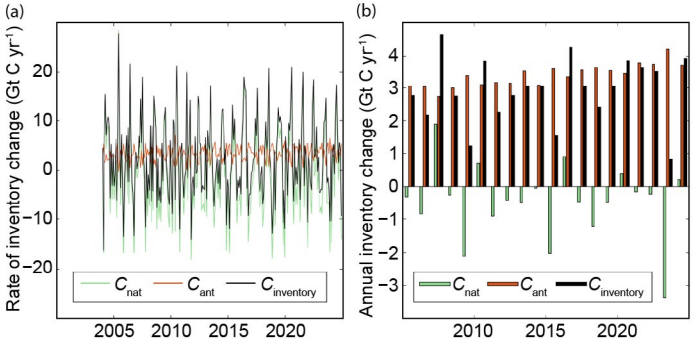

Fig. 3.30. Time series of the rate of inventory change in the total dissolved inorganic carbon ocean inventory ($C_{inventory}$), the change attributable to anthropogenic carbon accumulation (ΔC_{ant}), and the residual between these values attributed to natural processes (C_{nat}). Units are Gt C yr^{-1}.

Ocean interior inventory mapping can take advantage of regular updates to the underlying climatologies to provide timely and detailed information about ocean carbon inventory variations. However, as of yet, these estimates solely provide projections of expected patterns based on DIC measurements that predate 2024 and rely on the Argo-array-dominated temperature and salinity patterns from 2024 to generate the estimates for the most recent years. Furthermore, the methodological uncertainties for this approach have yet to be quantified.

Unauthenticated | Downloaded 11/21/25 11:34 AM UTC

Acknowledgments

Sandra Bigley provided invaluable assistance in assembling the sections of this chapter and copyediting.

Unauthenticated | Downloaded 11/21/25 11:34 AM UTC

Appendix 1: Acronyms

ACC	Antarctic Circumpolar Current
BASS	Blended Analysis of Surface Salinity
b_{bp}	particle backscattering coefficient
C_{ant}	anthropogenic CO_2
CAS	Chinese Academy of Sciences
Chl*a*	chlorophyll-*a*
$C_{inventory}$	changes in the total ocean inventory
C_{nat}	natural variations of CO_2
CO_2	carbon dioxide
C_{phy}	phytoplankton carbon
CTD	Conductivity-Temperature-Depth
DCENT	Dynamically Consistent ENsemble of Temperature
DIC	dissolved inorganic carbon
DOISST	Daily OISST
E	Evaporation
EEP	eastern equatorial Pacific
ENSO	El Niño–Southern Oscillation
ESPERs	Empirical Seawater Property Estimation Routines
FC	Florida Current
fCO_{2w}	surface ocean fugacity of CO_2
FLASHFlux	Fast Longwave And Shortwave Radiative Fluxes
GIA	glacial isostatic adjustment
GMSL	global mean sea level
GRACE	Gravity Recovery and Climate Experiment
GRACE-FO	GRACE Follow-On
GTMBA	Global Tropical Moored Buoy Array
HadSST	Hadley Centre Sea Surface Temperature
IAP	Institute of Atmospheric Physics
IOD	Indian Ocean dipole
ITCZ	Intertropical Convergence Zone
JP24	Johnson and Purkey 2024
JPL	Jet Propulsion Laboratory
LH	latent heat flux
LW	longwave radiation
MBT	mechanical bathythermograph
MCS	marine cold spell
MEI	Multivariate ENSO Index
MHT	meridional heat transport
MHW	marine heatwave
MOC	meridional overturning circulation
MODIS-A	Moderate Resolution Imaging Spectroradiometer on *Aqua*
MOVE	Meridional Overturning Variability Experiment
NECC	North Equatorial Countercurrent
NH	Northern Hemisphere
OHCA	ocean heat content anomaly
ORAS5	Ocean ReAnalysis System 5
OSNAP	Overturning in the Subpolar North Atlantic Program
P	precipitation
PACE	Plankton, Aerosol, Cloud, ocean Ecosystem

Unauthenticated | Downloaded 11/21/25 11:34 AM UTC

$_pCO_2$	partial pressure of CO_2
PDO	Pacific Decadal Oscillation
PMEL	Pacific Marine Environmental Laboratory
PSO	permanently stratified ocean
PSS-78	Practical Salinity Scale-78
Q_{net}	net surface heat flux
RFROM	Random Forest Regression Ocean Maps
SAMBA	South Atlantic MOC Basin-wide Array
SH	sensible heat
SH	Southern Hemisphere
SIO	Scripps Institution of Oceanography
SMAP	Soil Moisture Active Passive
SMOS	Soil Moisture and Ocean Salinity
SOCAT	Surface Ocean CO_2 Atlas
S_{ocean}	steady ocean CO_2 sink
SOM-FNN	self-organizing maps feed-forward neural network
SPCZ	South Pacific Convergence Zone
SSS	sea surface salinity
SST	sea surface temperature
SSTA	sea surface temperature anomaly
SW	shortwave radiation
TAO	Tropical Atmosphere Ocean
TIW	tropical instability waves
VIIRS-N20	Visible Infrared Imaging Radiometer Suite on NOAA-20
VLIZ	Flanders Marine Institute
W_{EK}	Ekman vertical velocity
WMO	World Meteorological Organization
WOA 2023	World Ocean Atlas 2023
XBT	Expendable Bathythermograph
ΔfCO_2	fCO_2 difference
ΔC_{ant}	anthropogenic accumulation
ΔC_{nat}	natural variations

Unauthenticated | Downloaded 11/21/25 11:34 AM UTC

Appendix 2: Datasets and sources

Section 3b Sea surface temperature

Sub-section	General Variable or Phenomenon	Specific Dataset or Variable	Source
3b	Sea Surface Temperature	ERSSTv5	https://doi.org/10.7289/V5T72FNM
3b	Sea Surface Temperature	Hadley Centre Sea Surface Temperature Dataset (HadSST) Version 4	https://www.metoffice.gov.uk/hadobs/hadsst4/
3b	Sea Surface Temperature	NOAA Daily Optimum Interpolated Temperature (DOISST) Version 2.1	https://doi.org/10.25921/RE9P-PT57
3b	Sea Surface Temperature	Dynamically Consistent ENsemble of Temperature (DCENT) Version 1.0	https://www.ospo.noaa.gov/products/ocean/sst/contour/

Section 3c Ocean heat content

Sub-section	General Variable or Phenomenon	Specific Dataset or Variable	Source
3c	Ocean Heat Content	Random Forest Regression Ocean Maps (RFROM) Version 2	https://www.pmel.noaa.gov/rfrom/
3c	Ocean Heat Content	Argo	http://doi.org/10.17882/42182#98916
3c	Ocean Heat Content	Argo Monthly Climatology	https://sio-argo.ucsd.edu/RG_Climatology.html
3c	Ocean Heat Content	CLIVAR and Carbon Hydrographic Data Office	https://cchdo.ucsd.edu/
3c	Ocean Heat Content	University of Colorado/ Carnegie Mellon University (CU/CMU)	https://zenodo.org/records/10645137
3c	Ocean Heat Content	Institute of Atmospheric Physics (IAP)/Chinese Academy of Sciences (CAS)	http://www.ocean.iap.ac.cn/pages/dataService/dataService.html
3c	Ocean Heat Content	Meteorological Research Institute (MRI)/Japan Meteorological Agency (JMA)	https://www.data.jma.go.jp/kaiyou/english/ohc/ohc_global_en.html
3c	Ocean Heat Content	NCEI	https://www.ncei.noaa.gov/access/global-ocean-heat-content/

Unauthenticated | Downloaded 11/21/25 11:34 AM UTC

Sub-section	General Variable or Phenomenon	Specific Dataset or Variable	Source
3c	Ocean Heat Content	Pacific Marine Environmental Laboratory (PMEL)/Jet Propulsion Laboratory (JPL)/ Cooperative Institute for Marine and Atmospheric Research (CIMAR)	https://www.pmel.noaa.gov/rfrom/
3c	Ocean Heat Content	UK Met Office EN4.2.2	https://www.metoffice.gov.uk/hadobs/en4/download-en4-2-2.html

Section 3d Salinity

Sub-section	General Variable or Phenomenon	Specific Dataset or Variable	Source
3d2	Ocean Salinity	Aquarius Version 3.0	http://podaac.jpl.nasa.gov/aquarius
3d2	Ocean Salinity	Argo	https://usgodae.org/argo/argo.html
3d2	Ocean Salinity	Blended Analysis for Surface Salinity	ftp://ftp.cpc.ncep.noaa.gov/precip/BASS
3d2	Ocean Salinity	Soil Moisture Active Passive (SMAP)	https://podaac.jpl.nasa.gov/SMAP
3d2	Ocean Salinity	Soil Moisture Ocean Salinity (SMOS)	https://earth.esa.int/eogateway/missions/smos
3d2	Ocean Salinity	World Ocean Atlas 2023	https://www.ncei.noaa.gov/products/world-ocean-atlas
3d3	Ocean Salinity	NCEI Salinity Anomaly	https://www.ncei.noaa.gov/access/global-ocean-heat-content/

Section 3e Global ocean heat, freshwater, and momentum flux

Sub-section	General Variable or Phenomenon	Specific Dataset or Variable	Source
3e1	Air–Sea Fluxes (Shortwave/Longwave Radiation)	Clouds and the Earth's Radiant Energy System (CERES) Energy Balanced and Filled (EBAF) Version 4.2	https://asdc.larc.nasa.gov/project/CERES/CERES_EBAF_Edition4.2
3e1	Air–Sea Fluxes (Shortwave/Longwave Radiation)	CERES FlashFlux	https://cmr.earthdata.nasa.gov/search/concepts/C1719147151-LARC_ASDC.html
3e1	Air–Sea Fluxes (Latent Heat/Sensible Heat)	Objectively Analyzed Air–Sea Heat Fluxes (OAFlux2)	https://oaflux.whoi.edu/

Unauthenticated | Downloaded 11/21/25 11:34 AM UTC

Sub-section	General Variable or Phenomenon	Specific Dataset or Variable	Source
3e2	Evaporation	OAFLux2	https://oaflux.whoi.edu/
3e2	Precipitation	GPCPv2.3	https://psl.noaa.gov/data/gridded/data.gpcp.html
3e3	Wind Stress	OAFlux2	https://oaflux.whoi.edu/

Section 3f Sea Level variability and change

Sub-section	General Variable or Phenomenon	Specific Dataset or Variable	Source
3f	Ocean Heat Content	Argo Monthly Climatology	https://sio-argo.ucsd.edu/RG_Climatology.html
3f	Ocean Mass	Gravity Recovery and Climate Experiment (GRACE)/Grace Follow-On (GRACE-FO)	https://grace.jpl.nasa.gov/data/get-data
3f	Sea Level / Sea Surface Height	Argo	https://usgodae.org/argo/argo.html
3f	Sea Level / Sea Surface Height	NASA Making Earth Science Data Records for Use in Research Environments (MEaSURES)	https://podaac.jpl.nasa.gov/dataset/SEA_SURFACE_HEIGHT_ALT_GRIDS_L4_2SATS_5DAY_6THDEG_V_JPL2205
3f	Sea Level / Sea Surface Height	NASA Sea Level Change and Ocean Surface Topography Program	https://sealevel.nasa.gov/data_tools/16/
3f	Sea Level / Sea Surface Height	Copernicus Climate Change Service (C3S) Altimetry Data	https://climate.copernicus.eu/sea-level
3f	Sea Level / Sea Surface Height	Tide Gauge	http://uhslc.soest.Hawai'i.edu/

Section 3g Surface currents

Sub-section	General Variable or Phenomenon	Specific Dataset or Variable	Source
3g	Ocean Currents	Global Tropical Moored Buoy Array (GTMBA)	https://www.pmel.noaa.gov/gtmba/
3g3	Ocean Currents	Atlantic Ocean Monitoring	https://www.aoml.noaa.gov/phod/altimetry/cvar/
3g	Surface Velocity	Drifter/Altimetry/Wind Synthesis Product	https://www.aoml.noaa.gov/ftp/pub/phod/lumpkin/decomp/

Unauthenticated | Downloaded 11/21/25 11:34 AM UTC

Section 3h Meridional overturning circulation and heat transport in the Atlantic Ocean

Sub-section	General Variable or Phenomenon	Specific Dataset or Variable	Source
3h	Ocean Currents	Atlantic Ship of Opportunity Expendable Bathythermograph (XBT)	https://www.aoml.noaa.gov/phod/goos/xbt_network/
3h	Ocean Currents	Argo	https://usgodae.org/argo/argo.html
3h	Ocean Currents	Florida Current Transport	https://www.aoml.noaa.gov/phod/floridacurrent/data_access.php
3h	Ocean Currents	Global Temperature and Salinity Profile Program (GTSPP)	https://www.ncei.noaa.gov/products/global-temperature-and-salinity-profile-programme
3h	Ocean Currents	Meridional Overturning Variability Experiment (MOVE) array	https://mooring.ucsd.edu/move/
3h	Ocean Currents	Overturning in the Subpolar North Atlantic Program (OSNAP)	https://www.o-snap.org/
3h	Ocean Currents	RAPID–Meridional Overturning Circulation and Heat-flux Array–Western Boundary Time Series (RAPID)	https://rapid.ac.uk/rapidmoc/
3h	Ocean Currents	South Atlantic MOC Basin-wide Array (SAMBA)	https://www.aoml.noaa.gov/phod/research/moc/samoc/sam/

Section 3i Global ocean phytoplankton

Sub-section	General Variable or Phenomenon	Specific Dataset or Variable	Source
3i	Daytime Sea Surface Temperature	Moderate Resolution Imaging Spectroradiometer on *Aqua* (MODIS-A) Version R2022.0	https://oceancolor.gsfc.nasa.gov/data/reprocessing/r2022/aqua/
3i	Phytoplankton Chlorophyll Particle Backscattering Coefficient	MODIS-A	https://modis.gsfc.nasa.gov/data/dataprod/chlor_a.php
3i	Phytoplankton Chlorophyll Particle Backscattering Coefficient	Sea-viewing Wide Field-of-view Sensor (SeaWiFS) Version R2022.0	https://oceancolor.gsfc.nasa.gov/data/reprocessing/r2022/seawifs/
3i	Phytoplankton Chlorophyll Particle Backscattering Coefficient	Visible Infrared Imaging Radiometer Suite (VIIRS)-NOAA20 Version R2022.0	https://data.nasa.gov/dataset/noaa-20-viirs-global-mapped-chlorophyll-chl-nrt-data-version-r2022-0

Unauthenticated | Downloaded 11/21/25 11:34 AM UTC

Section 3j Global ocean carbon cycle			
Sub-section	**General Variable or Phenomenon**	**Specific Dataset or Variable**	**Source**
3j2	Atmospheric Carbon Dioxide	NOAA Greenhouse Gas Marine Boundary Layer Reference	https://gml.noaa.gov/ccgg/mbl/mbl.html
3j2	Chlorophyll	GlobColour	https://www.globcolour.info/
3j2	Mixed Layer Depth	de Boyer Montegut (2004; 2023 update); Monthly Isopycnal & Mixed-layer Ocean Climatology (MMOC)	https://www.seanoe.org/data/00806/91774/; https://www.pmel.noaa.gov/mimoc/
3j2	Ocean Carbon	Surface Ocean CO_2 Atlas (SOCAT) Version 2024	https://socat.info/index.php/data-access/
3j2	Ocean Salinity	Hadley Center EN4	https://www.metoffice.gov.uk/hadobs/en4/
3j3	Ocean Salinity	Argo Monthly Climatology	https://sio-argo.ucsd.edu/RG_Climatology.html
3j3	Ocean Temperature	Argo Monthly Climatology	https://sio-argo.ucsd.edu/RG_Climatology.html
3j2	Sea Surface Temperature	NOAA OISST Version 2.1	https://www.ncei.noaa.gov/products/optimum-interpolation-sst
3j2	Winds [Near] Surface	ERA5	https://www.ecmwf.int/en/forecasts/dataset/ecmwf-reanalysis-v5

Unauthenticated | Downloaded 11/21/25 11:34 AM UTC

References

Adler, R. F., and Coauthors, 2018: The Global Precipitation Climatology Project (GPCP) monthly analysis (new version 2.3) and a review of 2017 global precipitation. *Atmosphere*, **9**, 138, https://doi.org/10.3390/atmos9040138.

Bakker, D. C. E., and Coauthors, 2016: A multi-decade record of high-quality fCO_2 data in version 3 of the Surface Ocean CO_2 Atlas (SOCAT). *Earth Syst. Sci. Data*, **8**, 383–413, https://doi.org/10.5194/essd-8-383-2016.

—— , and Coauthors, 2024: Surface Ocean CO_2 Atlas Database Version 2024 (SOCATv2024) (NCEI Accession 0293257), NOAA National Centers for Environmental Information [data set], https://doi.org/10.25921/9wpn-th28.

Balaguru, K., P. Chang, R. Saravanan, L. R. Leung, Z. Xu, M. Li, and J. S. Hsieh, 2012: Ocean barrier layers' effect on tropical cyclone intensification. *Proc. Natl. Acad. Sci. USA*, **109**, 14343–14347, https://doi.org/10.1073/pnas.1201364109.

Baringer, M. O., and J. C. Larsen, 2001: Sixteen years of Florida Current transport at 27°N. Geophys. *Res. Lett.*, **28**, 3179–3182, https://doi.org/10.1029/2001GL013246.

—— , and Coauthors, 2015: Meridional overturning circulation observations in the North Atlantic Ocean [in "State of the Climate in 2014"]. *Bull. Amer. Meteor. Soc.*, **96**, S78–S80, https://doi.org/10.1175/2015BAMSStateoftheClimate.1.

Barroso, A., T. Wahl, S. Li, A. Enriquez, J. Morim, S. Dangendorf, C. Piecuch, and P. Thompson, 2024: Observed spatiotemporal variability in the annual sea level cycle along the global coast. *J. Geophys. Res. Oceans*, **129**, e2023JC020300, https://doi.org/10.1029/2023JC020300.

Beckley, B., and Coauthors, 2024: Global mean sea level trend from integrated multi-mission ocean altimeters TOPEX/Poseidon, Jason-1, OSTM/Jason-2, Jason-3, and Sentinel-6 version 5.2. PO.DAAC, accessed 5 February 2025, https://doi.org/10.5067/GMSLM-TJ152.

Behrenfeld, M. J., and Coauthors, 2001: Biospheric primary production during an ENSO transition. *Science*, **291**, 2594–2597, https://doi.org/10.1126/science.1055071.

—— , and Coauthors, 2006: Climate-driven trends in contemporary ocean productivity. *Nature*, **444**, 752–755, https://doi.org/10.1038/nature05317.

—— , and Coauthors, 2016: Revaluating ocean warming impacts on global phytoplankton. *Nat. Climate Change*, **6**, 323–330, https://doi.org/10.1038/nclimate2838.

Caron, L., and E. R. Ivins, 2020: A baseline Antarctic GIA correction for space gravimetry. *Earth Planet. Sci. Lett.*, **531**, 115957, https://doi.org/10.1016/j.epsl.2019.115957.

Carter, B. R., and Coauthors, 2021: New and updated global empirical seawater property estimation routines. *Limnol. Oceanogr. Methods*, **19**, 785–809, https://doi.org/10.1002/lom3.10461.

—— , J. Schwinger, R. Sonnerup, A. J. Fassbender, J. D. Sharp, and L. M. Dias, 2025: Tracer-based Rapid Anthropogenic Carbon Estimation (TRACE). *Earth Syst. Sci. Data*, https://doi.org/10.5194/essd-2024-560, in press.

Cetinić, I., M. J. Perry, N. T. Briggs, E. Kallin, E. A. D'Asaro, and C. M. Lee, 2012: Particulate organic carbon and inherent optical properties during 2008 North Atlantic Bloom Experiment. *J. Geophys. Res.*, **117**, C06028, https://doi.org/10.1029/2011JC007771.

—— , and Coauthors, 2024: Phytoplankton composition from sPACE: Requirements, opportunities, and challenges. *Remote Sens. Environ.*, **302**, 113964, https://doi.org/10.1016/j.rse.2023.113964.

Chambers, D. P., A. Cazenave, N. Champollion, H. Dieng, W. Llovel, R. Forsberg, K. von Schuckmann, and Y. Wada, 2017: Evaluation of the global mean sea level budget between 1993 and 2014. *Surv. Geophys.*, **38**, 309–327, https://doi.org/10.1007/s10712-016-9381-3.

Chan, D., G. Gebbie, P. Huybers, and E. C. Kent, 2024: A Dynamically Consistent ENsemble of Temperature at the Earth surface since 1850 from the DCENT dataset. *Sci. Data*, **11**, 953, https://doi.org/10.1038/s41597-024-03742-x.

Chavez, F. P., M. Messié, and J. T. Pennington, 2011: Marine primary production in relation to climate variability and change. *Ann. Rev. Mar. Sci.*, **3**, 227–260, https://doi.org/10.1146/annurev.marine.010908.163917.

Cheng, L., J. Zhu, R. Cowley, T. Boyer, and S. Wijffels, 2014: Time, probe type, and temperature variable bias corrections to historical expendable bathythermograph observations. *J. Atmos. Oceanic Technol.*, **31**, 1793–1825, https://doi.org/10.1175/JTECH-D-13-00197.1.

—— , and Coauthors, 2025: Record high temperatures in the ocean in 2024. *Adv. Atmos. Sci.*, **42**, 1092–1109, https://doi.org/10.1007/s00376-025-4541-3.

de Boyer Montégut, C., G. Madec, A. S. Fischer, A. Lazar, and D. Ludicone, 2004: Mixed layer depth over the global ocean: An examination of profile data and a profile-based climatology. *J. Geophys. Res.*, **109**, C12003, https://doi.org/10.1029/2004JC002378.

Deser, C., M. A. Alexander, S. P. Xie, and A. S. Phillips, 2010: Sea surface temperature variability: Patterns and mechanisms. *Ann. Rev. Mar. Sci.*, **2**, 115–143, https://doi.org/10.1146/annurev-marine-120408-151453.

DeVries, T., M. Holzer, and F. Primeau, 2017: Recent increase in oceanic carbon uptake driven by weaker upper-ocean overturning. *Nature*, **542**, 215–218, https://doi.org/10.1038/nature21068.

Dierssen, H. M., 2010: Perspectives on empirical approaches for ocean color remote sensing of chlorophyll in a changing climate. *Proc. Natl. Acad. Sci. USA*, **107**, 17073–17078, https://doi.org/10.1073/pnas.0913800107.

Domingues, R., G. Goni, M. Baringer, and D. L. Volkov, 2018: What caused the accelerated sea level changes along the United States East Coast during 2010–2015? *Geophys. Res. Lett.*, **45**, 13367–13376, https://doi.org/10.1029/2018GL081183.

Dong, S., G. Goni, R. Domingues, F. Bringas, M. Goes, J. Christophersen, and M. Baringer, 2021: Synergy of in situ and satellite ocean observations in determining meridional heat transport in the Atlantic Ocean. *J. Geophys. Res. Oceans*, **126**, e2020JC017073, https://doi.org/10.1029/2020JC017073.

Donohoe, A., R. Fajber, T. Cox, K. C. Armour, D. S. Battisti, and G. H. Roe, 2024: Model biases in the atmosphere–ocean partitioning of poleward heat transport are persistent across three CMIP generations. *Geophys. Res. Lett.*, **51**, e2023GL106639, https://doi.org/10.1029/2023GL106639.

Durack, P. J., and S. E. Wijffels, 2010: Fifty-year trends in global ocean salinities and their relationship to broad-scale warming. *J. Climate*, **23**, 4342–4362, https://doi.org/10.1175/2010JCLI3377.1.

—— , —— , and R. J. Matear, 2012: Ocean salinities reveal strong global water cycle intensification during 1950 to 2000. *Science*, **336**, 455–458, https://doi.org/10.1126/science.1212222.

Unauthenticated | Downloaded 11/21/25 11:34 AM UTC

Fablet, R., B. Chapron, J. Le Sommer, and F. Sévellec, 2024: Inversion of sea surface currents from satellite-derived SST-SSH synergies with 4DVarNets. *J. Adv. Model. Earth Syst.*, **16**, e2023MS003609, https://doi.org/10.1029/2023MS003609.

Fairall, C. W., E. F. Bradley, J. E. Hare, A. A. Grachev, and J. B. Edson, 2003: Bulk parameterization of air–sea fluxes: Updates and verification for the COARE algorithm. *J. Climate*, **16**, 571–591, https://doi.org/10.1175/1520-0442(2003)016<0571:BPOAS-F>2.0.CO;2.

Fasullo, J., R. Nerem, and B. Hamlington, 2016: Is the detection of accelerated sea level rise imminent?. *Sci. Rep.*, **6**, 31245, https://doi.org/10.1038/srep31245.

Field, C. B., M. J. Behrenfeld, J. T. Randerson, and P. Falkowski, 1998: Primary production of the biosphere: Integrating terrestrial and oceanic components. *Science*, **281**, 237–240, https://doi.org/10.1126/science.281.5374.237.

Fofonoff, N. P., and E. L. Lewis, 1979: A practical salinity scale. *J. Oceanogr. Soc. Japan*, **35**, 63–64, https://doi.org/10.1007/BF02108283.

Font, J., and Coauthors, 2013: SMOS first data analysis for sea surface salinity determination. *Int. J. Remote Sens.*, **34**, 3654–3670, https://doi.org/10.1080/01431161.2012.716541.

Fore, A. G., S. H. Yueh, W. Q. Tang, B. W. Stiles, and A. K. Hayashi, 2016: Combined active/passive retrievals of ocean vector wind and sea surface salinity with SMAP. *IEEE Trans. Geosci. Remote Sens.*, **54**, 7396–7404, https://doi.org/10.1109/TGRS.2016.2601486.

Frajka-Williams, E., and Coauthors, 2019: Atlantic meridional overturning circulation: Observed transport and variability. *Front. Mar. Sci.*, **6**, 260, https://doi.org/10.3389/fmars.2019.00260.

Franz, B. A., I. Cetinic, M. Gao, A. Siegel, and T. K. Westberry, 2024a: Global ocean phytoplankton [in "State of the Climate in 2023"]. *Bull. Amer. Meteor. Soc.*, **105**, S194–S197, https://doi.org/10.1175/BAMS-D-24-0100.1

—— , —— , A. Ibrahim, and A. M. Sayer, 2024b: Anomalous trends in global ocean carbon concentrations following the 2022 eruptions of Hunga Tonga-Hunga Ha'apa. *Commun. Earth Environ.*, **5**, 247, https://doi.org/10.1038/s43247-024-01421-8.

Friedlingstein, P., and Coauthors, 2025: Global carbon budget 2024. *Earth Syst. Sci. Data*, **17**, 965–1039, https://doi.org/10.5194/essd-17-965-2025.

Geider, R. J., H. L. MacIntyre, and T. M. Kana, 1997: Dynamic model of phytoplankton growth and acclimation: Responses of the balanced growth rate and the chlorophyll *a*: Carbon ratio to light, nutrient-limitation and temperature. *Mar. Ecol. Prog. Ser.*, **148**, 187–200, https://doi.org/10.3354/meps148187.

Giglio, D., T. Sukianto, and M. Kuusela, 2025: Global ocean heat content anomalies and ocean heat uptake based on mapping Argo data using local Gaussian processes (4.0.0). Zenodo, accessed 22 January 2025, https://doi.org/10.5281/zenodo.14720478.

Good, S. A., M. J. Martin, and N. A. Rayner, 2013: EN4: Quality controlled ocean temperature and salinity profiles and monthly objective analyses with uncertainty estimates. *J. Geophys. Res. Oceans*, **118**, 6704–6716, https://doi.org/10.1002/2013JC009067.

Gouretski, V., and L. Cheng, 2020: Correction for systematic errors in the global dataset of temperature profiles from mechanical bathythermographs. *J. Atmos. Oceanic Technol.*, **37**, 841–855, https://doi.org/10.1175/JTECH-D-19-0205.1.

Graff, J. R., T. K. Westberry, A. J. Milligan, M. B. Brown, G. Dall'Olmo, V. V Dongen-Vogels, K. M. Reifel, and M. J. Behrenfeld, 2015: Analytical phytoplankton carbon measurements spanning diverse ecosystems. *Deep-Sea Res. I*, **102**, 16–25, https://doi.org/10.1016/j.dsr.2015.04.006.

Hamlington, B. D., C. G. Piecuch, J. T. Reager, H. Chandanpurkar, T. Frederikse, R. S. Nerem, J. T. Fasullo, and S.-H. Cheon, 2020: Origin of interannual variability in global mean sea level. *Proc. Natl. Acad. Sci. USA*, **117**, 13983–13990, https://doi.org/10.1073/pnas.1922190117.

—— ., and Coauthors, 2024: The rate of global sea level rise doubled during the past three decades. *Commun. Earth Environ.*, **5**, 601, https://doi.org/10.1038/s43247-024-01761-5.

Hauck, J., and Coauthors, 2023: The Southern Ocean carbon cycle 1985–2018: Mean, seasonal cycle, trends, and storage. *Global Biogeochem. Cycles*, **37**, e2023GB007848, https://doi.org/10.1029/2023GB007848.

Held, I. M., and B. J. Soden, 2006: Robust responses of the hydrological cycle to global warming. *J. Climate*, **19**, 5686–5699, https://doi.org/10.1175/JCLI3990.1.

Hersbach, H., and Coauthors, 2018: ERA5 hourly data on single levels from 1959 to present. Copernicus Climate Change Service (C3S) Climate Data Store (CDS), accessed 2 January 2024, https://doi.org/10.24381/cds.adbb2d47.

Hobbs, W. R., and J. K. Willis, 2012: Midlatitude North Atlantic heat transport: A time series based on satellite and drifter data. *J. Geophys. Res.*, **117**, C01008, https://doi.org/10.1029/2011JC007039.

Hobday, A. J., and Coauthors, 2016: A hierarchical approach to defining marine heatwaves. *Prog. Oceanogr.*, **141**, 227–238, https://doi.org/10.1016/j.pocean.2015.12.014.

—— , and Coauthors, 2018: Categorizing and naming marine heatwaves. *Oceanography*, **31** (2), 162–173, https://doi.org/10.5670/oceanog.2018.205.

Hu, C., Z. Lee, and B. A. Franz, 2012: Chlorophyll *a* algorithms for oligotrophic oceans: A novel approach based on three-band reflectance difference. *J. Geophys. Res.*, **117**, C01011, https://doi.org/10.1029/2011JC007395.

—— , L. Feng, Z. Lee, B. A. Franz, S. W. Bailey, P. J. Werdell, and C. W. Proctor, 2019: Improving satellite global chlorophyll *a* data products through algorithm refinement and data recovery. *J. Geophys. Res. Oceans*, **124**, 1524–1543, https://doi.org/10.1029/2019JC014941.

Hu, Z.-Z., M. J. McPhaden, B. Huang, J. Zhu, and Y. Liu, 2024: Accelerated warming in the North Pacific since 2013. *Nat. Climate Change*, **14**, 929–931, https://doi.org/10.1038/s41558-024-02088-x.

Huang, B., and Coauthors, 2015: Extended Reconstructed Sea Surface Temperature version 4 (ERSST.v4). Part I: Upgrades and intercomparisons. *J. Climate*, **28**, 911–930, https://doi.org/10.1175/JCLI-D-14-00006.1.

—— , and Coauthors, 2017: Extended Reconstructed Sea Surface Temperature, version 5 (ERSSTv5): Upgrades, validations, and intercomparisons. *J. Climate*, **30**, 8179–8205, https://doi.org/10.1175/JCLI-D-16-0836.1.

—— , and Coauthors, 2020: Uncertainty estimates for sea surface temperature and land surface air temperature in NOAAGlobalTemp version 5. *J. Climate*, **33**, 1351–1379, https://doi.org/10.1175/JCLI-D-19-0395.1.

Unauthenticated | Downloaded 11/21/25 11:34 AM UTC

—— , C. Liu, V. Banzon, E. Freeman, G. Graham, B. Hankins, T. Smith, and H.-M. Zhang, 2021: Improvements of the Daily Optimum Interpolation Sea Surface Temperature (DOISST) version 2.1. *J. Climate*, **34**, 2923–2939, https://doi.org/10.1175/JCLI-D-20-0166.1.

—— , X. Yin, J. A. Carton, L. Chen, G. Graham, P. Hogan, T. Smith, and H.-M. Zhang, 2024: Record high sea surface temperatures in 2023. *Geophys. Res. Lett.*, **51**, e2024GL108369, https://doi.org/10.1029/2024GL108369.

Hughes, T. P., and Coauthors, 2017: Global warming and recurrent mass bleaching of corals. *Nature*, **543**, 373–377, https://doi.org/10.1038/nature21707.

Ishii, M., Y. Fukuda, S. Hirahara, S. Yasui, T. Suzuki, and K. Sato, 2017: Accuracy of global upper ocean heat content estimation expected from present observational data sets. *SOLA*, **13**, 163–167, https://doi.org/10.2151/sola.2017-030.

Jiang, N., C. Zhu, Z.-Z. Hu, M. J. McPhaden, T. Lian, C. Zhou, W. Qian, and D. Chen, 2025: El Niño and sea surface temperature pattern effects lead to historically high global mean surface temperatures in 2023. *Geophys. Res. Lett.*, **52**, e2024GL113733, https://doi.org/10.1029/2024GL113733.

Johns, W. E., S. Elipot, D. A. Smeed, B. Moat, B. King, D. L. Volkov, and R. H. Smith, 2023: Towards two decades of Atlantic Ocean mass and heat transports at 26.5°N. *Philos. Trans. Roy. Soc.*, **A381**, 20220188, https://doi.org/10.1098/rsta.2022.0188.

Johnson, G. C., and J. M. Lyman, 2012: Sea surface salinity [in "State of the Climate in 2011"]. *Bull. Amer. Meteor. Soc.*, **93** (7), S68–S69, S72, https://doi.org/10.1175/2012BAMSStateoftheClimate.1.

—— , and S. G. Purkey, 2024: Refined estimates of global ocean deep and abyssal decadal warming trends. *Geophys. Res. Lett.*, **51**, e2024GL111229, https://doi.org/10.1029/2024GL111229.

—— , J. M. Lyman, J. K. Willis, T. Boyer, J. Antonov, S. A. Good, C. M. Domingues, and N. Bindoff, 2014: Ocean heat content [in "State of the Climate in 2013"]. *Bull. Amer. Meteor. Soc.*, **95** (7), S54–S57, https://doi.org/10.1175/2014BAMSStateoftheClimate.1.

—— , and Coauthors, 2024: Ocean heat content [in "State of the Climate in 2023"]. *Bull. Amer. Meteor. Soc.*, **105** (8), S167–S172, https://doi.org/10.1175/BAMS-D-24-0100.1.

—— , J. Reagan, J. M. Lyman, T. Boyer, C. Schmid, and R. Locarnini, 2020: Salinity [in "State of the Climate in 2019"]. *Bull. Amer. Meteor. Soc.*, **101** (8), S129–S183, https://doi.org/10.1175/BAMS-D-20-0105.1.

—— , and Coauthors, 2024: Ocean heat content [in "State of the Climate in 2023"]. *Bull. Amer. Meteor. Soc.*, **105** (8), S169–S172, https://doi.org/10.1175/BAMS-D-24-0100.1.

Kato, S., and Coauthors, 2018: Surface irradiances of edition 4.0 Clouds and the Earth's Radiant Energy System (CERES) Energy Balanced and Filled (EBAF) data product. *J. Climate*, **31**, 4501–4527, https://doi.org/10.1175/JCLI-D-17-0523.1.

Kendon, M., and Coauthors, 2024: State of the UK climate 2023. *Int. J. Climatol.*, **44** (S1), 1–117, https://doi.org/10.1002/joc.8553.

Kennedy, J. J., N. A. Rayner, C. P. Atkinson, and R. E. Killick, 2019: An ensemble data set of sea surface temperature change from 1850: The Met Office Hadley Centre HadSST.4.0.0.0 data set. *J. Geophys. Res. Atmos.*, **124**, 7719–7763, https://doi.org/10.1029/2018JD029867.

Keppler, L., P. Landschützer, S. K. Lauvset, and N. Gruber, 2023: Recent trends and variability in the oceanic storage of dissolved inorganic carbon. *Global Biogeochem. Cycles*, **37**, e2022GB007677, https://doi.org/10.1029/2022GB007677.

Kugusheva, A., H. Bull, E. Moschos, A. Ioannou, B. Le Vu, and A. Stegner, 2024: Ocean satellite data fusion for high-resolution surface current maps. *Remote Sens.*, **16**, 1182, https://doi.org/10.3390/rs16071182.

Kumar, P., B. Hamlington, S.-H. Cheon, W. Han, and P. Thompson, 2020: 20th century multivariate Indian Ocean regional sea level reconstruction. *J. Geophys. Res. Oceans*, **125**, e2020JC016270, https://doi.org/10.1029/2020JC016270.

Lan, X., P. Tans, and K. Thoning, 2023: NOAA greenhouse gas marine boundary layer reference: CO_2. NOAA Global Monitoring Laboratory, accessed 15 January 2025, https://doi.org/10.15138/DVNP-F961.

Landschützer, P., N. Gruber, D. C. E. Bakker, U. Schuster, S. Nakaoka, M. R. Payne, T. P. Sasse, and J. Zeng, 2013: A neural network-based estimate of the seasonal to inter-annual variability of the Atlantic Ocean carbon sink. *Biogeosciences*, **10**, 7793–7815, https://doi.org/10.5194/bg-10-7793-2013.

—— , —— , —— , and —— , 2014: Recent variability of the global ocean carbon sink. *Global Biogeochem. Cycles*, **28**, 927–949, https://doi.org/10.1002/2014GB004853.

Lauvset, S. K., and Coauthors, 2016: A new global interior ocean mapped climatology: The 1° × 1° GLODAP version 2. *Earth Syst. Sci. Data*, **8**, 325–340, https://doi.org/10.5194/essd-8-325-2016.

Leuliette, E. W., and J. K. Willis, 2011: Balancing the sea level budget. *Oceanography*, **24** (2), 122–129, https://doi.org/10.5670/oceanog.2011.32.

Le Vine, D. M., E. P. Dinnat, G. S. E. Lagerloef, P. de Matthaeis, S. Abraham, C. Utku, and H. Kao, 2014: Aquarius: Status and recent results. *Radio Sci.*, **49**, 709–720, https://doi.org/10.1002/2014RS005505.

Levitus, S., and Coauthors, 2012: World ocean heat content and thermosteric sea level change (0–2000 m), 1955. *Geophys. Res. Lett.*, **39**, L10603, https://doi.org/10.1029/2012GL051106.

Li, G., L. Cheng, J. Zhu, K. Trenberth, M. Mann, and J. Abraham, 2020: Increasing ocean stratification over the past half-century. *Nat. Climate Change*, **10**, 1116–1123, https://doi.org/10.1038/s41558-020-00918-2.

Li, L., R. W. Schmitt, C. C. Ummenhofer, and K. B. Karnauskas, 2016: North Atlantic salinity as a predictor of Sahel rainfall. *Sci. Adv.*, **2**, e1501588, https://doi.org/10.1126/sciadv.1501588.

Li, S., T. Wahl, A. Barroso, S. Coats, S. Dangendorf, C. Piecuch, Q. Sun, P. Thompson, and L. Liu, 2022: Contributions of different sea-level processes to high-tide flooding along the U.S. Coastline. *J. Geophys. Res. Oceans*, **127**, e2021JC018276, https://doi.org/10.1029/2021JC018276.

Loeb, N. G., and Coauthors, 2018: Clouds and the Earth's Radiant Energy System (CERES) Energy Balanced and Filled (EBAF) Top-of-Atmosphere (TOA) edition-4.0 data product. *J. Climate*, **31**, 895–918, https://doi.org/10.1175/JCLI-D-17-0208.1.

—— , G. C. Johnson, T. J. Thorsen, J. M. Lyman, F. G. Rose, and S. Kato, 2021: Satellite and ocean data reveal marked increase in Earth's heating rate. *Geophys. Res. Lett.*, **48**, e2021GL093047, https://doi.org/10.1029/2021GL093047.

Long, X., M. J. Widlansky, F. Schloesser, P. R. Thompson, H. Annamalai, M. A. Merrifield, and H. Yoon, 2020: Higher Sea Levels at Hawaii Caused by Strong El Niño and Weak Trade Winds. *J. Climate*, **33**, 3037–3059, https://doi.org/10.1175/JCLI-D-19-0221.1.

Unauthenticated | Downloaded 11/21/25 11:34 AM UTC

Lumpkin, R., G. Goni, and K. Dohan, 2012: Surface currents [in "State of the Climate in 2011"]. *Bull. Amer. Meteor. Soc.*, **93** (7), S75–S78, https://doi.org/10.1175/2012BAMSStateoftheClimate.1.

—— , F. Bringas, and R. Perez, 2024: Surface currents [in "State of the Climate in 2023"]. *Bull. Amer. Meteor. Soc.*, **105** (8), S23–S27, https://doi.org/10.1175/BAMS-D-24-0100.1.

Lyman, J. M., and G. C. Johnson, 2014: Estimating global ocean heat content changes in the upper 1800 m since 1950 and the influence of climatology choice. *J. Climate*, **27**, 1946–1958, https://doi.org/10.1175/JCLI-D-12-00752.1.

—— , and G. C. Johnson, 2023: Global high-resolution random forest regression maps of ocean heat content anomalies using in situ and satellite data. *J. Atmos. Oceanic Technol.*, **40**, 575–586, https://doi.org/10.1175/JTECH-D-22-0058.1.

Maritorena, S., O. H. Fanton d'Andon, A. Mangin, and D. A. Siegel, 2010: Merged satellite ocean color data products using a bio-optical model: Characteristics, benefits and issues. *Remote Sens. Environ.*, **114**, 1791–1804, https://doi.org/10.1016/j.rse.2010.04.002.

Martin, S. A., G. E. Manucharyan, and P. Klein, 2024: Deep learning improves global satellite observations of ocean eddy dynamics. *Geophys. Res. Lett.*, **51**, e2024GL110059, https://doi.org/10.1029/2024GL110059.

McCarthy, G. D., and Coauthors, 2015: Measuring the Atlantic meridional overturning circulation at 26°N. *Prog. Oceanogr.*, **130**, 91–111, https://doi.org/10.1016/j.pocean.2014.10.006.

McKinna, L. I. W, P. J. Werdell, and B. A. Franz, 2016: An update on NASA's generalized inherent optical properties algorithm framework. *Proc. Ocean Optics XXIII*, Victoria, B.C., Canada, The Oceanography Society.

—— , I. Cetinic, and J. Werdell, 2024: The status of NASA IOP data products for the PACE era. *Ocean Sciences Meeting 2024*, New Orleans, LA, Amer. Geophys. Union, OT24F-156.

McPhaden, M. J., K. J. Connell, G. R. Foltz, R. C. Perez, and K. Grissom, 2023: Tropical ocean observations for weather and climate: A decadal overview of the Global Tropical Moored Buoy Array. *Oceanography*, **36** (2–3), 32–43, https://doi.org/10.5670/oceanog.2023.211.

Meinen, C. S., M. O. Baringer, and R. F. Garcia, 2010: Florida Current transport variability: An analysis of annual and longer-period signals. *Deep-Sea Res. I*, **57**, 835–846, https://doi.org/10.1016/j.dsr.2010.04.001.

—— , and Coauthors, 2013: Temporal variability of the meridional overturning circulation at 34.5°S: Results from two pilot boundary arrays in the South Atlantic. *J. Geophys. Res. Oceans*, **118**, 6461–6478, https://doi.org/10.1002/2013JC009228.

—— , and Coauthors, 2018: Meridional overturning circulation transport variability at 34.5°S during 2009–2017: Baroclinic and barotropic flows and the dueling influence of the boundaries. *Geophys. Res. Lett.*, **45**, 4180–4188, https://doi.org/10.1029/2018GL077408.

Mishonov, A. V., and Coauthors, 2024: World Ocean Database 2023. NOAA Atlas NESDIS 97, 206 pp., https://doi.org/10.25923/z885-h264.

Moat, B. I., and Coauthors, 2020: Pending recovery in the strength of the meridional overturning circulation at 26°N. *Ocean Sci.*, **16**, 863–874, https://doi.org/10.5194/os-16-863-2020.

—— , and Coauthors, 2024: Atlantic meridional overturning circulation observed by the RAPID-MOCHA-WBTS (RAPID-Meridional Overturning Circulation and Heatflux Array-Western Boundary Time Series) array at 26N from 2004 to 2023 (v2023.1). British Oceanographic Data Centre, Natural Environment Research Council, accessed 17 January 2025, https://doi.org/10.5285/223b34a3-2dc5-c945-e063-7086abc0f274.

Nerem, R. S., D. P. Chambers, E. W. Leuliette, G. T. Mitchum, and B. S. Giese, 1999: Variations in global mean sea level associated with the 1997–1998 ENSO event: Implications for measuring long term sea level change. *Geophys. Res. Lett.*, **26**, 3005–3008, https://doi.org/10.1029/1999GL002311.

—— , B. D. Beckley, J. T. Fasullo, B. D. Hamlington, D. Masters, and G. T. Mitchum, 2018: Climate-change-driven accelerated sea-level rise detected in the altimeter era. *Proc. Natl. Acad. Sci. USA*, **115**, 2022–2025, https://doi.org/10.1073/pnas.1717312115.

Oliver, E. C. J., J. A. Benthuysen, S. Darmaraki, M. G. Donat, A. J. Hobday, N. J. Holbrook, R. W. Schlegel, and A. Sen Gupta, 2021: Marine heatwaves. *Ann. Rev. Mar. Sci.*, **13**, 313–342, https://doi.org/10.1146/annurev-marine-032720-095144.

O'Reilly, J. E., and P. J. Werdell, 2019: Chlorophyll algorithms for ocean color sensors - OC4, OC5 & OC6. *Remote Sens. Environ.*, **229**, 32–47, https://doi.org/10.1016/j.rse.2019.04.021.

Pahlevan, N., B. Smith, C. Binding, D. Gurlin, L. Li, M. Bresciani, and C. Giardino, 2021: Hyperspectral retrievals of phytoplankton absorption and chlorophyll-*a* in inland and nearshore coastal waters. *Remote Sens. Environ.*, **253**, 112200, https://doi.org/10.1016/j.rse.2020.112200.

Palmer, M. D., K. Haines, S. F. B. Tett, and T. J. Ansell, 2007: Isolating the signal of ocean global warming. *Geophys. Res. Lett.*, **34**, L23610, https://doi.org/10.1029/2007GL031712.

Purkey, S. G., and G. C. Johnson, 2010: Warming of global abyssal and deep Southern Ocean waters between the 1990s and 2000s: Contributions to global heat and sea level rise budgets. *J. Climate*, **23**, 6336–6351, https://doi.org/10.1175/2010JCLI3682.1.

Qiu, B., and S. Chen, 2021: Revisit of the occurrence of the Kuroshio large meander south of Japan. *J. Phys. Oceanogr.*, **51**, 3679–3694, https://doi.org/10.1175/JPO-D-21-0167.1.

—— , —— , N. Schneider, E. Oka, and S. Sugimoto, 2020: On the reset of the wind-forced decadal Kuroshio extension variability in late 2017. *J. Climate*, **33**, 10813–10828, https://doi.org/10.1175/JCLI-D-20-0237.1.

Rayner, N. A., D. E. Parker, E. B. Horton, C. K. Folland, L. V. Alexander, D. P. Rowell, E. C. Kent, and A. Kaplan, 2003: Global analyses of sea surface temperature, sea ice, and night marine air temperature since the late nineteenth century. *J. Geophys. Res.*, **108**, 4407, https://doi.org/10.1029/2002JD002670.

Reagan, J., T. Boyer, C. Schmid, and R. Locarnini, 2022: State of the Climate in 2021. *Bull. Amer. Meteor. Soc.*, **103** (8), S1–S465, https://doi.org/10.1175/2022BAMSStateoftheClimate.1.

—— , —— , —— , and —— , 2023: Subsurface salinity [in "State of the Climate in 2022"]. *Bull. Amer. Meteor. Soc.*, **104** (9), S165–S167, https://doi.org/10.1175/BAMS-D-23-0076.2.

—— , —— , —— , and —— , 2024: Subsurface salinity [in "State of the Climate in 2023"]. *Bull. Amer. Meteor. Soc.*, **105** (8), S175–S187, https://doi.org/10.1175/BAMS-D-24-0100.1.

Reagan, J. R., and Coauthors, 2024: Salinity. Vol. 2, World Ocean Atlas 2023, NOAA Atlas NESDIS 90, 52 pp., https://doi.org/10.25923/70qt-9574.

Unauthenticated | Downloaded 11/21/25 11:34 AM UTC

Regnier, P., L. Resplandy, R. G. Najjar, and P. Ciais, 2022: The land-to-ocean loops of the global carbon cycle. *Nature*, **603**, 401–410, https://doi.org/10.1038/s41586-021-04339-9.

Ren, L., K. Speer, and E. P. Chassignet, 2011: The mixed layer salinity budget and sea ice in the Southern Ocean. *J. Geophys. Res.*, **116**, C08031, https://doi.org/10.1029/2010JC006634.

Riser, S. C., and Coauthors, 2016: Fifteen years of ocean observations with the global Argo array. *Nat. Climate Change*, **6**, 145–153, https://doi.org/10.1038/nclimate2872.

Rödenbeck, C., and Coauthors, 2015: Data-based estimates of the ocean carbon sink variability – First results of the Surface Ocean pCO_2 Mapping intercomparison (SOCOM). Biogeosciences, **12**, 7251–7278, https://doi.org/10.5194/bg-12-7251-2015.

Roemmich, D., and J. Gilson, 2009: The 2004–2008 mean and annual cycle of temperature, salinity, and steric height in the global ocean from the Argo Program. *Prog. Oceanogr.*, **82**, 81–100, https://doi.org/10.1016/j.pocean.2009.03.004.

Schlesinger, M. E., and N. Ramankutty, 1994: An oscillation in the global climate system of period 65–70 years. *Nature*, **367**, 723–726, https://doi.org/10.1038/367723a0.

Schmidtko, S., G. C. Johnson, and J. M. Lyman, 2013: MIMOC: A global monthly isopycnal upper-ocean climatology with mixed layers. *J. Geophys. Res. Oceans*, **118**, 1658–1672, https://doi.org/10.1002/jgrc.20122.

Schmitt, R. W., 1995: The ocean component of the global water cycle. *Rev. Geophys.*, **33**, 1395–1409, https://doi.org/10.1029/95RG00184.

Siegel, D. A., S. Maritorena, N. B. Nelson, M. J. Behrenfeld, and C. R. McClain, 2005: Colored dissolved organic matter and its influence on the satellite-based characterization of the ocean biosphere. *Geophys. Res. Lett.*, **32**, L20605, https://doi.org/10.1029/2005GL024310.

—— , and Coauthors, 2013: Regional to global assessments of phytoplankton dynamics from the SeaWiFS mission. *Remote Sens. Environ.*, **135**, 77–91, https://doi.org/10.1016/j.rse.2013.03.025.

—— , T. DeVries, I. Cetinić, and K. M. Bisson, 2023: Quantifying the ocean's biological pump and its carbon cycle impacts on global scales. *Ann. Rev. Mar. Sci.*, **15**, 329–356, https://doi.org/10.1146/annurev-marine-040722-115226.

Skliris, N., R. Marsh, S. A. Josey, S. A. Good, C. Liu, and R. P. Allan, 2014: Salinity changes in the World Ocean since 1950 in relation to changing surface freshwater fluxes. *Climate Dyn.*, **43**, 709–736, https://doi.org/10.1007/s00382-014-2131-7.

Smeed, D. A., and Coauthors, 2018: The North Atlantic Ocean is in a state of reduced overturning. *Geophys. Res. Lett.*, **45**, 1527–1533, https://doi.org/10.1002/2017GL076350.

Stackhouse, P. W., D. P. Kratz, G. R. McGarragh, S. K. Gupta, and E. B. Geier, 2006: Fast Longwave and Shortwave Radiative Flux (FLASHFlux) products from CERES and MODIS measurements. *Proc. 12th Conf. on Atmospheric Radiation*, Amer. Meteor. Soc., P1.10, https://ams.confex.com/ams/pdfpapers/113479.pdf.

Sweet, W. V., J. Park, J. J. Marra, C. Zervas, and S. Gill, 2014: Sea level rise and nuisance flood frequency changes around the United States. NOAA Tech. Rep. NOS CO-OPS 073, 66 pp.

Sweet, W. V., A. S. Genz, M. Menendez, J. J. Marra, and J. Obeysekera, 2024: Implications of variability and trends in coastal extreme water levels. *Geophys. Res. Lett.*, **51**, e2024GL108864, https://doi.org/10.1029/2024GL108864.

Tamisiea, M. E., and J. X. Mitrovica, 2011: The moving boundaries of sea level change: Understanding the origins of geographic variability. *Oceanography*, **24** (2), 24–39, https://doi.org/10.5670/oceanog.2011.25.

Tan, W., Z.-Z. Hu, M. J. McPhaden, C. Zhu, X. Li, and Y. Liu, 2024: On the divergent evolution of ENSO after the coastal El Niños in 2017 and 2023. *Geophys. Res. Lett.*, **51**, e2024GL108198, https://doi.org/10.1029/2024GL108198.

Tuchen, F. P., R. C. Perez, G. R. Foltz, M. J. McPhaden, and R. Lumpkin, 2024: Strengthening of the equatorial Pacific upper-ocean circulation over the past three decades. *J. Geophys. Res. Oceans*, **129**, e2024JC021343, https://doi.org/10.1029/2024JC021343.

Twedt, K., N. Lei, X. Xiong, A. Angal, S. Li, T. Chang, and J. Sun, 2022: On-orbit calibration and performance of NOAA-20 VIIRS reflective solar bands. *IEEE Trans. Geosci. Remote Sens.*, **60**, 1–13, https://doi.org/10.1109/TGRS.2021.3108970.

Volkov, D. L., S.-K. Lee, R. Domingues, H. Zhang, and M. Goes, 2019: Interannual sea level variability along the southeastern seaboard of the United States in relation to the gyre-scale heat divergence in the North Atlantic. *Geophys. Res. Lett.*, **46**, 7481–7490, https://doi.org/10.1029/2019GL083596.

—— , and Coauthors, 2021: Meridional overturning circulation and heat transport in the Atlantic Ocean [in "State of the Climate in 2020"]. *Bull. Amer. Meteor. Soc.*, **102**, S176–S179, https://doi.org/10.1175/BAMS-D-21-0083.1.

—— , K. Zhang, W. E. Johns, J. K. Willis, W. Hobbs, M. Goes, H. Zhang, and D. Menemenlis, 2023: Atlantic meridional overturning circulation increases flood risk along the United States southeast coast. *Nat. Commun.*, **14**, 5095, https://doi.org/10.1038/s41467-023-40848-z.

—— , R. H. Smith, R. F. Garcia, D. A. Smeed, B. I. Moat, W. E. Johns, and M. O. Baringer, 2024a: Florida Current transport observations reveal four decades of steady state. *Nat. Commun.*, **15**, 7780, https://doi.org/10.1038/s41467-024-51879-5.

—— , and Coauthors, 2024b: Meridional overturning circulation and heat transport in the Atlantic Ocean [in "State of the Climate in 2023"]. *Bull. Amer. Meteor. Soc.*, **105** (8), S191–S193, https://doi.org/10.1175/BAMS-D-24-0100.1.

von Schuckmann, K., and Coauthors, 2023: Heat stored in the Earth system 1960–2020: Where does the energy go? *Earth Syst. Sci. Data*, **15**, 1675–1709, https://doi.org/10.5194/essd-15-1675-2023.

Von Storch, H., and F. W. Zwiers, 1999: *Statistical Analysis in Climate Research*. Cambridge University Press, 484 pp.

Wahl, T., F. M. Calafat, and M. E. Luther, 2014: Rapid changes in the seasonal sea level cycle along the US Gulf coast from the late 20th century. *Geophys. Res. Lett.*, **41**, 491–498, https://doi.org/10.1002/2013GL058777.

Walsh, K. J. E., and Coauthors, 2016: Tropical cyclones and climate change. *Wiley Interdiscip. Rev.: Climate Change*, **7**, 65–89, https://doi.org/10.1002/wcc.371.

Wang, M., S.-P. Xie, H. Sasaki, M. Nonaka, and Y. Du, 2024: Intensification of Pacific tropical instability waves over the recent three decades. *Nat. Climate Change*, **14**, 163–170, https://doi.org/10.1038/s41558-023-01915-x.

Wanninkhof, R., 2014: Relationship between wind speed and gas exchange over the ocean revisited. *Limnol. Oceanogr. Methods*, **12**, 351–362, https://doi.org/10.4319/lom.2014.12.351.

Werdell, P. J., and L. I. McKinna, 2019: Sensitivity of inherent optical properties from ocean reflectance inversion models to satellite instrument wavelength suites. *Front. Earth Sci.*, **7**, 54, https://doi.org/10.3389/feart.2019.00054.

—— , and Coauthors, 2013: Generalized ocean color inversion model for retrieving marine inherent optical properties. *Appl. Opt.*, **52**, 2019–2037, https://doi.org/10.1364/AO.52.002019.

Unauthenticated | Downloaded 11/21/25 11:34 AM UTC

—— , and Coauthors, 2019: The Plankton, aerosol, cloud, ocean ecosystem mission: Status, science, advances. *Bull. Amer. Meteor. Soc.*, **100**, 1775–1794, https://doi.org/10.1175/BAMS-D-18-0056.1.

—— , J. O'Reilly, C. Hu, L. Feng, Z. Lee, B. Franz, S. Bailey, and C. Proctor, 2023: Chlorophyll *a*. NASA Algorithm Publication Tool, v1.1, accessed 22 January 2025, https://doi.org/10.5067/JCQB8QALDOYD.

Westberry, T. K., P. Schultz, M. J. Behrenfeld, J. P. Dunne, M. R. Hiscock, S. Maritorena, J. L. Sarmiento, and D. A. Siegel, 2016: Annual cycles of phytoplankton biomass in the subarctic Atlantic and Pacific Ocean. *Global Biogeochem. Cycles*, **30**, 175–190, https://doi.org/10.1002/2015GB005276.

Widlansky, M. J., A. Timmermann, S. McGregor, M. F. Stuecker, and W. Cai, 2014: An interhemispheric tropical sea level seesaw due to El Niño Taimasa. *J. Climate*, **27**, 1070–1081, https://doi.org/10.1175/JCLI-D-13-00276.1.

Wiese, D. N., D.-N. Yuan, C. Boening, F. W. Landerer, and M. M. Watkins, 2022: JPL GRACE and GRACE-FO Mascon ocean, ice, and hydrology equivalent HDR water height RL06.1M CRI filtered version 3.0. PO.DAAC, accessed 13 February 2024, https://doi.org/10.5067/TEMSC-3MJ62.

Willis, J., and W. Hobbs, 2025: Atlantic meridional overturning circulation near 41N from altimetry and argo observations (2025_01). Zenodo, accessed 18 January 2025, https://doi.org/10.5281/zenodo.14681441.

—— , 2010: Can in situ floats and satellite altimeters detect long-term changes in Atlantic Ocean overturning? *Geophys. Res. Lett.*, **37**, L06602, https://doi.org/10.1029/2010GL042372.

Wolter, K., and M. S. Timlin, 1998: Measuring the strength of ENSO events: How does 1997/98 rank? *Weather*, **53**, 315–324, https://doi.org/10.1002/j.1477-8696.1998.tb06408.x.

Wüst, G., 1936: Oberflächensalzgehalt, Verdunstung und Niederschlag auf dem Weltmeere. Länderkundliche Forschung: Festschrift zur Vollendung des sechzigsten Lebensjahres Norbert Krebs, J. Engelhorns Nachfahren, 347–359.

Xie, P., and Coauthors, 2014: An in situ—satellite blended analysis of global sea surface salinity. *J. Geophys. Res. Oceans*, **119**, 6140–6160, https://doi.org/10.1002/2014JC010046.

Yang, J., and K. Chen, 2025: Profound changes in the seasonal cycle of sea level along the United States mid-Atlantic coast. *Geophys. Res. Lett.*, **52**, e2024GL112273, https://doi.org/10.1029/2024GL112273.

Yin, X., B. Huang, J. A. Carton, L. Chen, G. Graham, C. Liu, T. Smith, and H.-M. Zhang, 2024: The 1991–2020 sea surface temperature normals. *Int. J. Climatol.*, **44**, 668–685, https://doi.org/10.1002/joc.8350.

Yu, L., 2011: A global relationship between the ocean water cycle and near-surface salinity. *J. Geophys. Res.*, **116**, C10025, https://doi.org/10.1029/2010JC006937.

—— , 2019: Global air-sea fluxes of heat, fresh water, and momentum: Energy budget closure and unanswered questions. *Ann. Rev. Mar. Sci.*, **11**, 227–248, https://doi.org/10.1146/annurev-marine-010816-060704.

—— , and R. A. Weller, 2007: Objectively analyzed air–sea heat fluxes for the global ice-free oceans (1981–2005). *Bull. Amer. Meteor. Soc.*, **88**, 527–540, https://doi.org/10.1175/BAMS-88-4-527]

Unauthenticated | Downloaded 11/21/25 11:34 AM UTC

STATE OF THE CLIMATE IN 2024

THE TROPICS

H. J. Diamond and C. J. Schreck, Eds.

Special Online Supplement to the *Bulletin of the American Meteorological Society* Vol. 106, No. 8, August, 2025

https://doi.org/10.1175/BAMS-D-25-0086.1

Corresponding author: Howard J. Diamond / howard.diamond@noaa.gov

©2025 American Meteorological Society
For information regarding reuse of this content and general copyright information, consult the AMS Copyright Policy.

Unauthenticated | Downloaded 11/21/25 11:34 AM UTC

STATE OF THE CLIMATE IN 2024
The Tropics

Editors

Jessica Blunden
James Reagan

Chapter Editors

Anthony Arguez
Josh Blannin
Peter Bissolli
Kyle R. Clem
Howard J. Diamond
Matthew L. Druckenmiller
Robert J. H. Dunn
Catherine Ganter
Nadine Gobron
Gregory C. Johnson
Rick Lumpkin
Rodney Martinez
Ademe Mekonnen
Twila A. Moon
Gary A. Morris
Marilyn N. Raphael
Carl J. Schreck III
Laura Stevens
Richard L. Thoman
Kate M. Willett
Zhiwei Zhu

Technical Editor

Lukas Noguchi

BAMS Special Editor for Climate

Timothy DelSole

American Meteorological Society

Unauthenticated | Downloaded 11/21/25 11:34 AM UTC

Cover Credit:
Historic flooding in the River Arts District of Asheville, North Carolina, caused by Hurricane Helene. Photograph courtesy of Stephan Pruitt/Fiasco Media. http://www.fiasco-media.com/

How to cite this document:
The Tropics is one chapter from the *State of the Climate in 2024* annual report and is available from https://doi.org/10.1175/BAMS-D-25-0086.1. Compiled by NOAA's National Centers for Environmental Information, *State of the Climate in 2024* is based on contributions from scientists from around the world. It provides a detailed update on global climate indicators, notable weather events, and other data collected by environmental monitoring stations and instruments located on land, water, ice, and in space. The full report is available from https://doi.org/10.1175/2025BAMSStateoftheClimate.1.

Citing the complete report:
Blunden, J. and J. Reagan, Eds., 2025: "State of the Climate in 2024". Bull. Amer. Meteor. Soc., 106 (8), Si–S513 https://doi.org/10.1175/2025BAMSStateoftheClimate.1.

Citing this chapter:
Diamond, H. J. and C. J. Schreck, Eds., 2025: The Tropics [in "State of the Climate in 2024"]. Bull. Amer. Meteor. Soc., 106 (8), S233–S299, https://doi.org/10.1175/BAMS-D-25-0086.1.

Citing a section (example):
Schreck, C., 2025: Hurricane Helene: Inside western North Carolina's historic flood [in "State of the Climate in 2024"]. Bull. Amer. Meteor. Soc., 106 (8), S284–S286, https://doi.org/10.1175/BAMS-D-25-0086.1.

Unauthenticated | Downloaded 11/21/25 11:34 AM UTC

Editor and Author Affiliations (alphabetical by name)

Allgood, Adam, NOAA/NWS National Centers for Environmental Prediction Climate Prediction Center, College Park, Maryland

Becker, Emily J., Rosenstiel School of Marine, Atmospheric, and Earth Science, University of Miami, Miami, Florida

Blake, Eric S., NOAA/NWS National Hurricane Center, Miami, Florida

Camargo, Suzana J., Lamont-Doherty Earth Observatory, Columbia University, Palisades, New York; Columbia Climate School, Columbia University, New York, New York

Chen, Lin, Institute for Climate and Application Research (ICAR)/KLME/ILCEC/CIC-FEMD, Nanjing University of Information Science and Technology, Nanjing, China

Coelho, Caio A.S., Centro de Previsão do Tempo e Estudos Climáticos/National Institute for Space Research, Center for Weather Forecasts and Climate Studies, Cachoeira Paulista, Brazil

Diamond, Howard J., NOAA/OAR Air Resources Laboratory, College Park, Maryland

Fauchereau, Nicolas, National Institute of Water and Atmospheric Research, Ltd., Auckland, New Zealand

Fogarty, Chris, Canadian Hurricane Centre, Dartmouth, Canada

Goldenberg, Stanley B., NOAA/OAR Atlantic Oceanographic and Meteorological Laboratory, Miami, Florida

Harnos, Daniel S., NOAA/NWS National Centers for Environmental Prediction Climate Prediction Center, College Park, Maryland

He, Qiong, Earth System Modeling Center, Nanjing University of Information Science and Technology, Nanjing, China

Hu, Zeng-Zhen, NOAA/NWS National Centers for Environmental Prediction Climate Prediction Center, College Park, Maryland

Klotzbach, Philip J., Department of Atmospheric Science, Colorado State University, Fort Collins, Colorado

Kumar, Arun, NOAA/NWS National Centers for Environmental Prediction Climate Prediction Center, College Park, Maryland

Landsea, Chris W., NOAA/NWS National Hurricane Center, Miami, Florida

L'Heureux, Michelle, NOAA/NWS National Centers for Environmental Prediction Climate Prediction Center, College Park, Maryland

Lin, I-I., National Taiwan University, Taipei, Taiwan

Long, Lindsey N., NOAA/NWS National Centers for Environmental Prediction Climate Prediction Center, College Park, Maryland

Lorrey, Andrew M., National Institute of Water and Atmospheric Research, Ltd., Auckland, New Zealand

Lopez, Hosmay, NOAA/OAR Atlantic Oceanographic and Meteorological Laboratory, Miami, Florida

Luo, Jing-Jia, Institute for Climate and Application Research, Nanjing University of Information Science and Technology, Nanjing, China

Magee, Andrew D., School of Environmental and Life Sciences, University of Newcastle, Callaghan, New South Wales, Australia

Pasch, Richard J., NOAA/NWS National Hurricane Center, Miami, Florida

Pezza, Alexandre B., Greater Wellington Regional Council, Wellington, New Zealand

Rosencrans, Matthew, NOAA/NWS National Centers for Environmental Prediction Climate Prediction Center, College Park, Maryland

Schreck, Carl J., Cooperative Institute for Satellite Earth System Studies, North Carolina Institute for Climate Studies, North Carolina State University, Asheville, North Carolina

Trewin, Blair C., Bureau of Meteorology, Melbourne, Australia

Trinanes, Joaquin A., Laboratory of Systems, Technological Research Institute, Universidad de Santiago de Compostela, Campus Universitario Sur, Santiago de Compostela, Spain; Cooperative Institute for Marine and Atmospheric Studies, Rosenstiel School of Marine and Atmospheric Science, University of Miami, Miami, Florida; NOAA/OAR Atlantic Oceanographic and Meteorological Laboratory, Miami, Florida

Truchelut, Ryan E., WeatherTiger, Tallahassee, Florida

Uehling, John, Cooperative Institute Satellite Earth System Studies, North Carolina Institute for Climate Studies, North Carolina State University, Asheville, North Carolina

Wang, Bin, School of Ocean and Earth Science and Technology, Department of Meteorology, University of Hawaii at Manoa, Honolulu, Hawaii; International Pacific Research Center, Honolulu, Hawaii

Wang, Hui, NOAA/NWS National Centers for Environmental Prediction Climate Prediction Center, College Park, Maryland

Wood, Kimberly M., Department of Hydrology and Atmospheric Sciences, University of Arizona, Tucson, Arizona

Editorial and Production Team

Allen, Jessicca, Graphics Support, Cooperative Institute for Satellite Earth System Studies, North Carolina State University, Asheville, North Carolina

Camper, Amy V., Graphics Support, Innovative Consulting and Management Services, LLC, NOAA/NESDIS National Centers for Environmental Information, Asheville, North Carolina

Carroll, Lauren, Content Team Lead, Communications and Outreach, NOAA/NESDIS National Centers for Environmental Information, Asheville, North Carolina

Haley, Bridgette O., Graphics Support, NOAA/NESDIS National Centers for Environmental Information, Asheville, North Carolina

Love-Brotak, S. Elizabeth, Lead Graphics Production, NOAA/NESDIS National Centers for Environmental Information, Asheville, North Carolina

Ohlmann, Laura, Technical Editor, Innovative Consulting and Management Services, LLC, NOAA/NESDIS National Centers for Environmental Information, Asheville, North Carolina

Noguchi, Lukas, Technical Editor, Innovative Consulting and Management Services, LLC, NOAA/NESDIS National Centers for Environmental Information, Asheville, North Carolina

Riddle, Deborah B., Graphics Support, NOAA/NESDIS National Centers for Environmental Information, Asheville, North Carolina

Veasey, Sara W., Visual Communications Team Lead, Communications and Outreach, NOAA/NESDIS National Centers for Environmental Information, Asheville, North Carolina

Unauthenticated | Downloaded 11/21/25 11:34 AM UTC

4. Table of Contents

Unauthenticated | Downloaded 11/21/25 11:34 AM UTC

4. THE TROPICS

H. J. Diamond and C. J. Schreck, Eds.

a. Overview

—H. J. Diamond and C. J. Schreck

In 2024, the Oceanic Niño Index (ONI; Fig. 4.1) transitioned from El Niño during the early part of the year to a neutral phase of the El Niño–Southern Oscillation (ENSO) during the Northern Hemisphere spring of 2024. El Niño developed in boreal spring 2023, strengthened steadily through the summer and autumn, and then peaked in November 2023–January 2024. In April–June (AMJ) 2024, El Niño transitioned to ENSO-neutral, where it continued through October–December 2024. For the global tropics (defined here as 20°S–20°N), the NOAA Merged Land Ocean Global Surface Temperature Analysis (NOAA GlobalTemp; Vose et al. 2021) indicates that the combined average land and ocean surface temperature was 1.20°C above the 1991–2020 average, making 2024 the warmest year for the tropics in the 175-year data record. The seven warmest years in the tropics since 1850 have all occurred from 2015 onward. Data from the Global Precipitation Climatology Project indicate a mean annual total precipitation value of 1377 mm across the tropics over land. This is 50 mm below the 1991–2020 average and was the eighth lowest for the 1979–2024 period of record.

Globally, 82 named tropical cyclones (TCs; ≥34 kt or ≥17 m s^{-1}) were observed during the 2024 Northern Hemisphere season (January–December 2024) and the 2023/24 Southern Hemisphere season (July 2023–June 2024; see Table 4.2), as documented by the National Hurricane Center and the Joint Typhoon Warning Center in the International Best Track Archive for Climate Stewardship Version 4.1 (Knapp et al. 2010). Overall, this number was below the 1991–2020 global average of 87 TCs and was equal to the 82 TCs reported during the 2023 season (Diamond and Schreck 2024). The record for most named storms in a single TC season is 104 in 1992, and the fewest since 1980 is 67 in 1985.

Of the 82 named storms, 43 reached hurricane strength (one-minute maximum sustained winds ≥64 kt), and 23 reached major hurricane strength (one-minute maximum winds ≥96 kt; equivalent to Category 3+ on the Saffir–Simpson Hurricane Wind Scale [SSHWS]). Both of these counts were below their 1991–2020 averages. The accumulated cyclone energy (ACE; an integrated metric of the strength, frequency, and duration of tropical storms and hurricanes; Bell et al. 2000) rebounded from the lowest on record in 2022 (since reliable data began in 1981) to above-normal levels in 2023, but then for 2024 was again below normal. Of the seven TC basins, only the North Atlantic and South Indian had above-normal numbers of named storms in 2024 in contrast to zero basins in 2022 and four in 2023, and no basins in 2024 were above average for ACE relative to their 1991–2020 climatology. Note that the North Atlantic has a longer period of reliable records than other basins, and it was above normal relative to 1951–2020. Globally, four storms reached Category 5 intensity on the SSHWS (one-minute maximum sustained winds ≥137 kt) during 2024, compared with only three in 2022 and seven in 2023. Three basins had at least one Category 5 storm: the North Atlantic, the Eastern North Pacific, and the Western North Pacific.

The 2024 Atlantic hurricane season produced 18 named storms; of the 11 of these that became hurricanes, 5 became major hurricanes thereafter. The 18 named storms during 2024 was the ninth-highest number since 1851. The 2024 Atlantic hurricane season was classified by NOAA as an extremely active season based on above-normal ACE relative to 1951–2020. Eight of the last nine

Unauthenticated | Downloaded 11/21/25 11:34 AM UTC

Atlantic hurricane seasons (2016–2021, 2023, and 2024) have been classified as above normal, with 2022 classified as a near-normal season. NOAA uses 1951–2020 terciles of ACE to delineate below-normal, normal, and above-normal seasons. The year 2024's ACE of 162×10^4 kt^2 places it in the upper tercile and is greater than the ACE value in the North Atlantic in 2023 of 146×10^4 kt^2. Two storms of particular note in 2024 were Hurricanes Helene and Milton in the North Atlantic. Both of these systems were extreme events that shattered records, and both are highlighted in the two sidebars of this chapter.

Unauthenticated | Downloaded 11/21/25 11:34 AM UTC

b. ENSO and the tropical Pacific

—A. Kumar, Z-Z. Hu, M. L'Heureux, and E. Becker

The El Niño–Southern Oscillation (ENSO) is an ocean and atmosphere-coupled climate phenomenon across the tropical Pacific Ocean; its warm and cold phases are called El Niño and La Niña, respectively. NOAA's Climate Prediction Center (CPC) classifies and assesses the strength and duration of El Niño and La Niña events using the Oceanic Niño Index (ONI; shown for mid-2023 through 2024 in Fig. 4.1). The ONI is the three-month (seasonal) running average of sea surface temperature (SST) anomalies in the Niño-3.4 region (5°S–5°N, 170°W–120°W), currently calculated as the departure from the 1991–2020 base period mean. El Niño is classified when the ONI is at or greater than +0.5°C for at least five consecutive, overlapping seasons, while La Niña is classified when the ONI is at or less than −0.5°C for at least five consecutive, overlapping seasons.

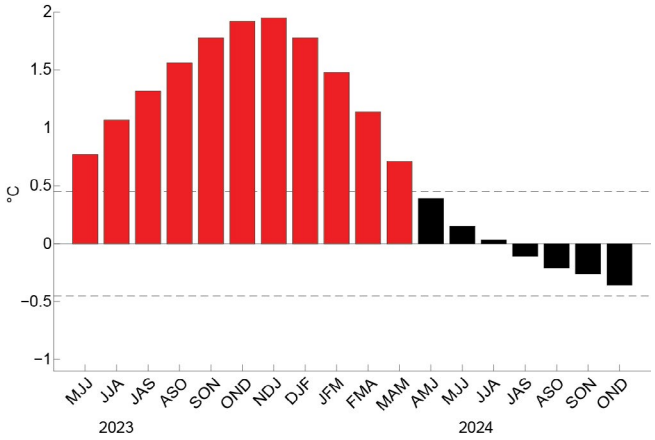

Fig. 4.1. Time series of the Oceanic Niño Index (ONI; °C) from mid-2023 through 2024. Overlapping three-month seasons are labeled on the x-axis, with initials indicating the first letter of each month in the season. Red bars indicate positive values that are higher than 0.5°C (El Niño). Black bars indicate values between −0.5°C and 0.5°C (neutral El Niño–Southern Oscillation). ONI values are derived from the ERSSTv5 dataset and are based on departures from the 1991–2020 period monthly means (Huang et al. 2017).

The time series of the ONI (Fig. 4.1) shows a transition from 2023's El Niño to ENSO-neutral in 2024. El Niño developed in boreal spring 2023, strengthened steadily through the summer and autumn, and then peaked in November 2023–January 2024. In April–June (AMJ) 2024, El Niño transitioned to ENSO-neutral where it continued through October–December 2024.

1. OCEANIC CONDITIONS

Figure 4.2 displays the SST (left column) and SST anomalies (right column) during December–February (DJF) 2023/24 through September–November (SON) 2024. During DJF,

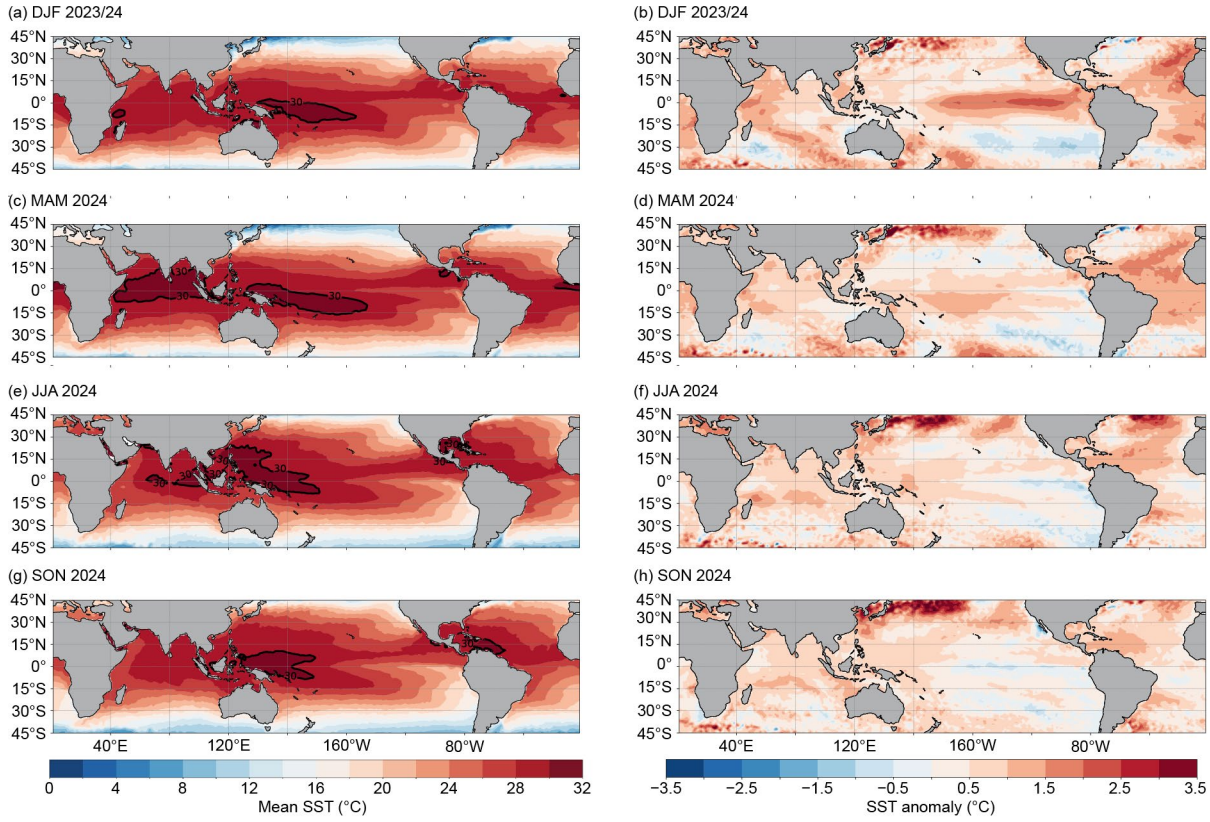

Fig. 4.2. Mean sea surface temperatures (SST; left) and SST anomalies (right) for (a),(b) Dec–Feb (DJF) 2023/24, (c),(d) Mar–May (MAM) 2024, (e),(f) Jun–Aug (JJA) 2024, and (g),(h) Sep–Nov (SON) 2024. The bold contour for SST is 30°C. Anomalies are departures from the 1991–2020 seasonal adjusted OISSTv2.1 climatology (Huang et al. 2021).

Unauthenticated | Downloaded 11/21/25 11:34 AM UTC

above-average SSTs on the equator, reflecting El Niño, were strongest east of the dateline, maximizing around +2.0°C, with positive anomalies extending eastward to the coastal regions of South America (Fig. 4.2b). The warm SST anomalies declined by March–May (MAM) 2024, when the highest SST anomalies were around +1.0°C and extended slightly south of the equator and in the vicinity of the dateline. By June–August (JJA), above-average SSTs in the central and eastern equatorial Pacific declined further while, over a narrow equatorial region in the eastern Pacific, weak below-average SSTs emerged. In SON 2024, below-average SSTs extended westward to the dateline. The variations in the equatorial Pacific SST anomalies were embedded within above-average SSTs throughout most of the global oceans. Further, during JJA and SON, an enhanced east-to-west SST gradient in the equatorial Pacific, with warm (cold) anomalies in the western (central and eastern) Pacific, accentuated La Niña-like atmospheric conditions, which will be discussed in the next subsection.

The weakening of El Niño in early 2024 was also reflected in the evolution of sub-surface temperature anomalies (Fig. 4.3). In DJF 2023/24, the sub-surface temperatures in the eastern Pacific were above average and were confined near the surface. These near-surface warm temperature anomalies extended to the dateline, while below-average sub-surface temperatures were evident in the western Pacific and at depth in the central Pacific. In MAM 2024, below-average temperatures became established along the thermocline in the eastern Pacific and extended westward to the dateline. The switch from above- to below-average subsurface temperatures was consistent with the transition away from El Niño. Between MAM and SON 2024, the amplitude and the vertical structure of the below-average subsurface temperatures did not undergo appreciable changes. Compared to the ENSO-neutral SST anomalies across the equatorial Pacific Ocean, the subsurface ocean anomalies were more reflective of La Niña conditions during 2024.

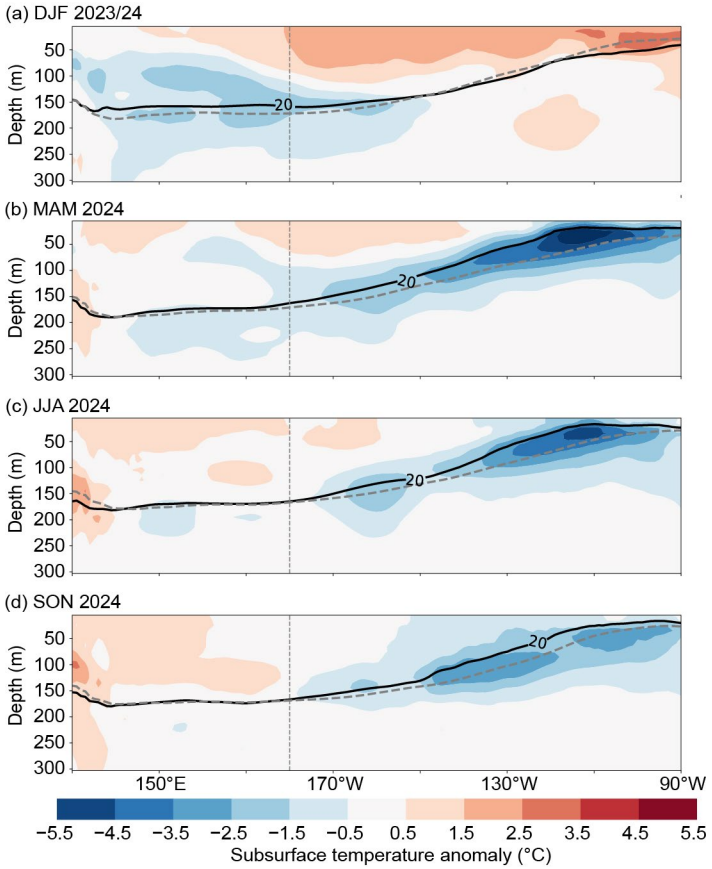

Fig. 4.3. Equatorial depth–longitude section of Pacific Ocean temperature anomalies (°C) averaged between 5°S and 5°N during (a) Dec–Feb (DJF) 2023/24, (b) Mar–May (MAM) 2024, (c) Jun–Aug (JJA) 2024, and (d) Sep–Nov (SON) 2024. The 20°C isotherm (thick black solid line) approximates the center of the oceanic thermocline. The gray, dashed line shows the 1991–2020 climatology of the 20°C isotherm. The data are derived from a reanalysis system that assimilates oceanic observations into an oceanic general circulation model (Behringer 2007). Anomalies are departures from the 1991–2020 period monthly means.

2. ATMOSPHERIC CIRCULATION

DJF 2023/24 featured large-scale tropical atmospheric circulation anomalies that were broadly consistent with El Niño. Typically, during El Niño, convection/rainfall is enhanced (negative outgoing longwave radiation [OLR], green shading) near the dateline and central tropical Pacific and is suppressed (positive OLR, brown shading) over the Maritime Continent (Fig. 4.4a). This anomalous rainfall pattern mostly dissipated by MAM 2024 as ENSO-neutral conditions returned to the tropical Pacific (Fig. 4.4b), and the continuation of these conditions in JJA 2024 was associated with weak convective anomalies over the tropical Pacific (Fig. 4.4c). By SON 2024,

Unauthenticated | Downloaded 11/21/25 11:34 AM UTC

below-average rainfall anomalies near the dateline reflected weak La Niña-like conditions, with anomalies almost opposite of those observed during DJF 2023/24 (Fig. 4.4a). A La Niña-like rainfall pattern was observed in SON despite ONI values that classified conditions as ENSO-neutral. This rainfall pattern was likely tied to above-average SSTs in the western Pacific and slightly below-average SSTs in the eastern Pacific.

Like convection, the low- and upper-level wind anomalies were indicative of a transition from El Niño in DJF 2023/24 to ENSO-neutral in MAM 2024. In the equatorial central and eastern Pacific Ocean, the tropical low-level 850-hPa trade winds were anomalously westerly in DJF 2023/24 (Fig. 4.5a). In MAM, a lack of a coherent anomalous wind pattern reflected ENSO-neutral SST conditions (Fig. 4.5b). In JJA 2024, low-level easterly wind anomalies emerged near 130°W and in the far western Pacific (Fig. 4.5c). This pattern continued through SON (Fig. 4.5d).

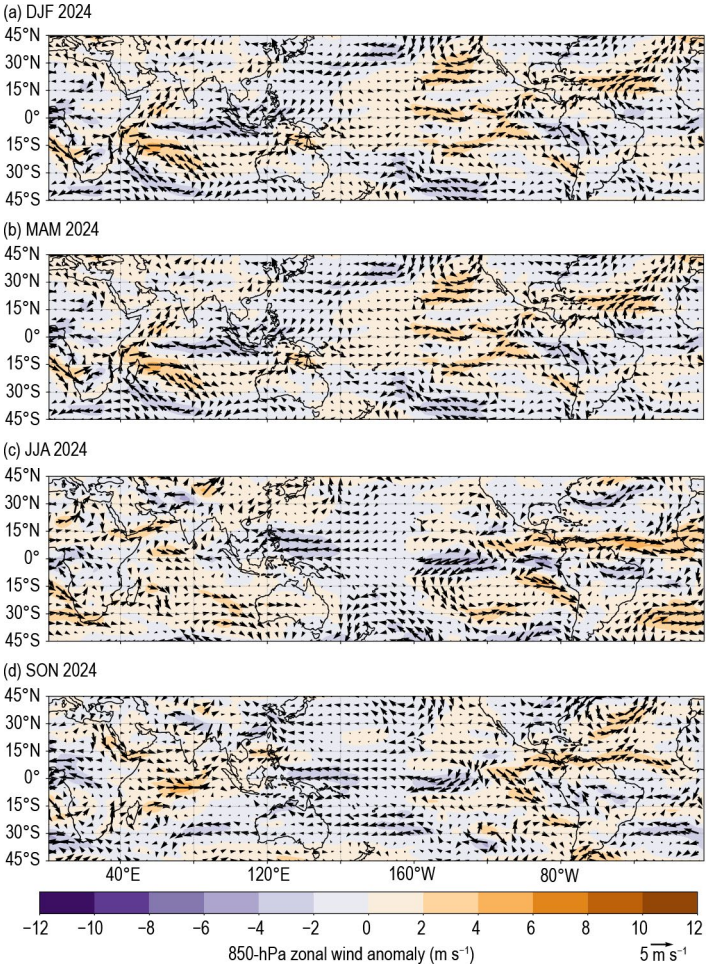

Fig. 4.5. Anomalous 850-hPa wind vectors (m s^{-1}, arrows) and zonal wind speed (m s^{-1}, shading) during (a) Dec–Feb (DJF) 2023/24, (b) Mar–May (MAM) 2024, (c) Jun–Aug (JJA) 2024, and (d) Sep–Nov (SON) 2024. The reference wind vector is located at the bottom right. Anomalies are departures from the 1991–2020 period monthly means. Data are from the National Centers for Environmental Prediction (NCEP) National Center for Atmospheric Research (NCAR) reanalysis (Kalnay et al. 1996).

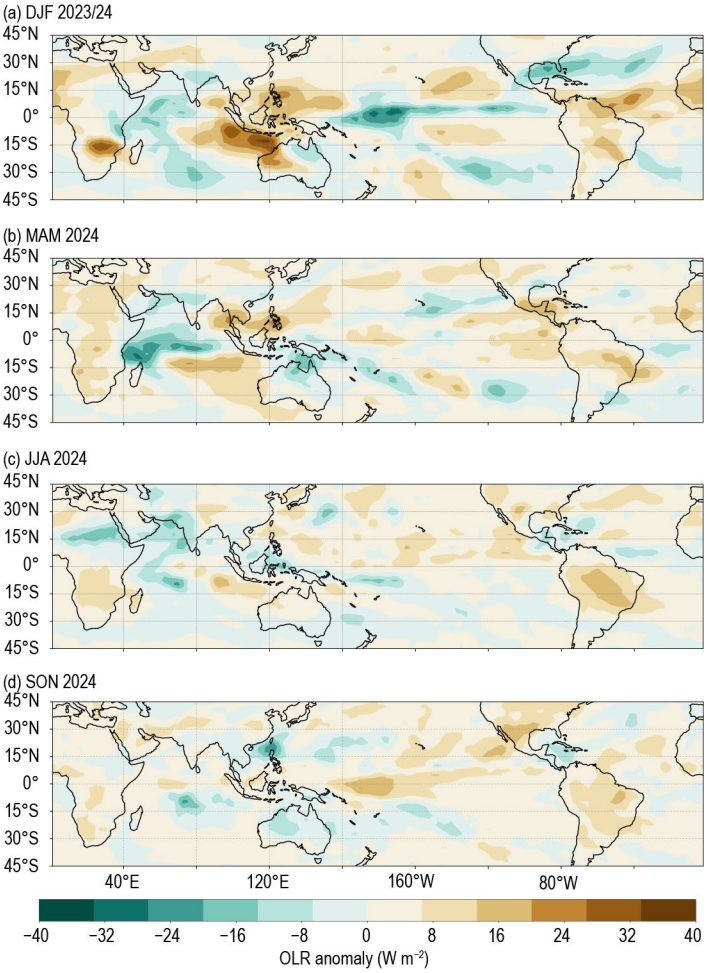

Fig. 4.4. Outgoing longwave radiation (OLR) anomalies (W m^{-2}) during (a) Dec–Feb (DJF) 2023/24, (b) Mar–May (MAM) 2024, (c) Jun–Aug (JJA) 2024, and (d) Sep–Nov (SON) 2024. Anomalies are departures from the 1991–2020 period monthly means. Data are from Guo et al. (2024).

Reflecting El Niño, upper-level (200-hPa) easterly wind anomalies were observed over the equatorial eastern Pacific Ocean during DJF 2023/24 (Fig. 4.6a). In MAM 2024, with the emergence of ENSO-neutral conditions, upper-level winds returned to their climatological conditions (Fig. 4.6b). During JJA and SON 2024, westerly wind anomalies emerged near the equator in the eastern Pacific, near 110°W, and in the far western Pacific. While the anomalies in rainfall and winds were weak overall during SON 2024, there were hints of a La Niña-like atmospheric pattern. However, the collective oceanic and atmospheric system

Unauthenticated | Downloaded 11/21/25 11:34 AM UTC

still reflected ENSO-neutral, because the SST anomalies were not strong enough to reach La Niña thresholds in SON.

3. GLOBAL PRECIPITATION

ENSO-driven teleconnections can affect precipitation anomalies globally (Bjerknes 1969; Ropelewski and Halpert 1989). While a rigorous attribution is beyond the scope of this chapter, some precipitation anomalies that resemble the expected ENSO teleconnection impacts can be identified. Of note are SON 2024 rainfall anomalies that were drier than average over the southern United States and northeast region of South America and were reminiscent of teleconnections associated with La Niña. Even though the SON 2024 ONI value categorized this season as ENSO-neutral, the enhancement in the east-to-west equatorial SST gradient and La Niña-like below-average rainfall anomalies near the dateline may be a contributing factor to this pattern.

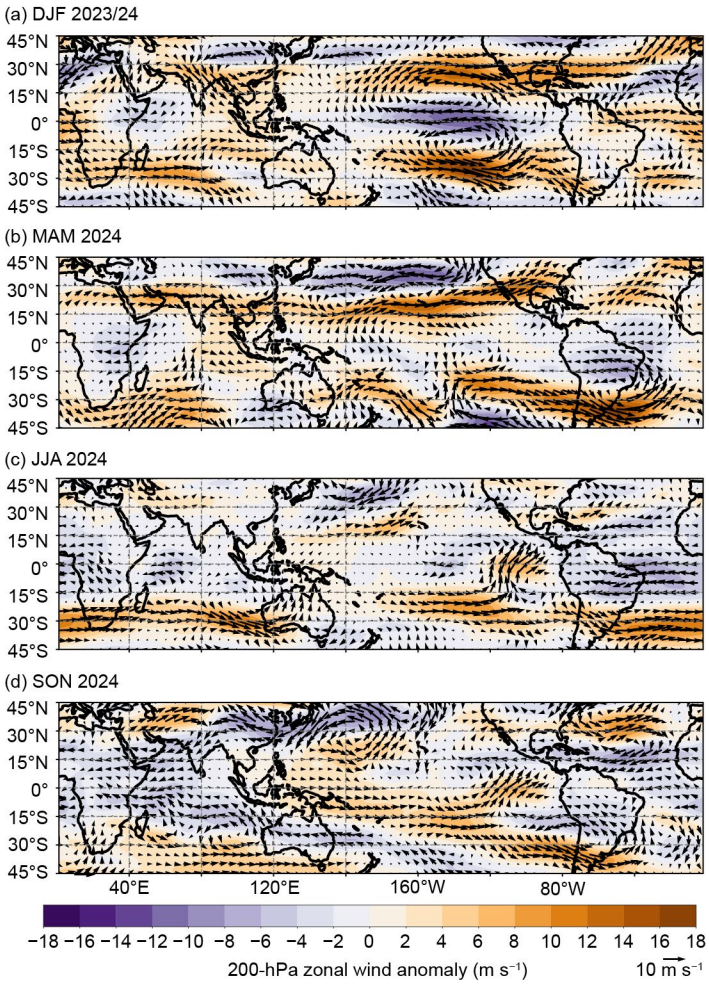

Fig. 4.6. Anomalous 200-hPa wind vectors and zonal wind speed (shading) during (a) Dec–Feb (DJF) 2023/24, (b) Mar–May (MAM) 2024, (c) Jun–Aug (JJA) 2024, and (d) Sep–Nov (SON) 2024. The reference wind vector is located at the bottom left. Anomalies (m s^{-1}) are departures from the 1991–2020 period monthly means. Data are from the National Centers for Environmental Prediction (NCEP) National Center for Atmospheric Research (NCAR) reanalysis (Kalnay et al. 1996).

Unauthenticated | Downloaded 11/21/25 11:34 AM UTC

c. Tropical intraseasonal activity

—A. Allgood and C. J. Schreck

Organized tropical intraseasonal activity is modulated by several different modes of coherent atmospheric variability, most notably the Madden–Julian Oscillation (MJO; Madden and Julian 1971, 1972, 1994; Zhang 2005). The MJO is characterized by eastward-propagating envelopes of large-scale anomalous enhanced and suppressed convection that typically circumnavigate the globe in a 30-day to 60-day period. MJO-related convective anomalies are similar in spatial extent to those generated by the atmospheric response to the El Niño–Southern Oscillation (ENSO), but the latter signal remains largely stationary and lasts for several months. MJO convective anomalies can influence the low-frequency base state of the tropics, including modulation of ENSO events (Moore and Kleeman 1999). Other impactful modes of variability include convectively coupled atmospheric waves, such as Kelvin waves, which exhibit a faster phase speed than the MJO, as well as westward-propagating equatorial Rossby waves (Wheeler and Kiladis 1999; Kiladis et al. 2009). These waves are typically narrower (zonally) than the MJO and may not couple as well to the broader convective regime. The MJO can be identified through time–longitude analyses of various atmospheric fields, including anomalous 200-hPa velocity potential (Fig. 4.7b), anomalous zonal winds at 200-hPa and 850-hPa (Fig. 4.8a), and anomalous outgoing longwave radiation (Fig. 4.7a). Another diagnostic tool frequently used to identify MJO activity is the Wheeler and Hendon (2004) Real-time Multivariate MJO (RMM) index. In RMM plots, robust atmospheric anomalies on a spatial scale resembling the MJO appear as a signal outside of the unit circle (Fig. 4.9). Eastward propagation is represented by counterclockwise looping of the index about the origin.

Periods of robust MJO activity at the end of 2023 and the beginning of 2024 may have helped begin a period of weakening El Niño conditions, with strong upwelling of colder waters from oceanic Kelvin wave activity instigated from MJO-associated trade wind surges (Fig. 4.8a; dashed contours). The MJO was active during January and early February, with the enhanced convective

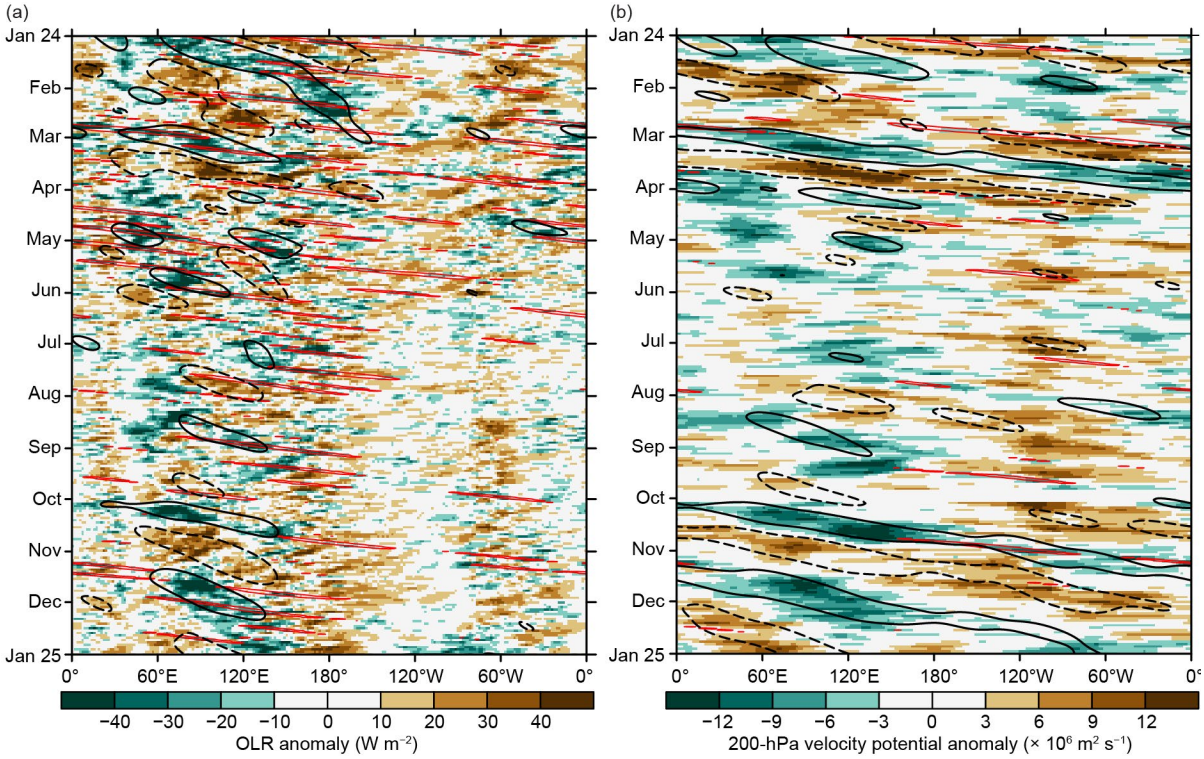

Fig. 4.7. Time–longitude section of (a) High Resolution Infrared Radiation Sounder (HIRS) outgoing longwave radiation (OLR; Schreck et al. 2018) anomalies (W m^{-2}) on the left and (b) 200-hPa velocity potential anomalies (× 10^6 m^2 s^{-1}) from the Climate Forecast System Reanalysis (Saha et al. 2014) on the right. Both variables are averaged over 10°S–10°N. Time increases downward on this graph, beginning with Jan 2024 at the top and ending with Jan 2025 at the bottom. Negative anomalies indicate enhanced convection, and positive anomalies indicate suppressed convection. Contours identify anomalies filtered for the Madden–Julian Oscillation (black) and atmospheric Kelvin waves (red). Contours are drawn at ±12 W m^{-2} and ±4 × 10^6 m^2 s^{-1} with the enhanced (suppressed) convective phase of these phenomena indicated by solid (dashed) contours. Anomalies are departures from the 1991–2020 base period daily means.

Unauthenticated | Downloaded 11/21/25 11:34 AM UTC

phase propagating from the Indian Ocean across the Pacific. In late February, the RMM-based MJO index entered the unit circle (Fig. 4.9a), which typically indicates weakening. This apparent weakening may have been partly due to the low-frequency base state having begun its evolution away from robust El Niño conditions as the convective signals and wind signals both remained strong (Figs. 4.7, 4.8). The RMM index re-amplified in March as the signal returned to the Indian Ocean, almost completing a high-amplitude circumnavigation of the globe during the month, indicating the increasing prevalence of the intraseasonal signal in contrast to the ENSO base state. The trade wind surge associated with this MJO activity further weakened the El Niño conditions.

As the warm ENSO state continued to weaken during boreal spring, the MJO also exhibited a less coherent signal. The RMM index remained inside the unit circle throughout most of April–June, with occasional increases in amplitude over the Indian Ocean or Maritime Continent (Fig. 4.9b). Eastward propagating signals remained apparent, particularly in the upper-level velocity potential anomaly field during April (Fig. 4.7). The RMM index completed several tight counterclockwise circuits displaced towards the bottom right of the RMM diagram. Objective filtering shows a prevalence of atmospheric Kelvin wave activity (Fig. 4.7, red contours) during this time, some of which coupled well with convection, resulting in an eastward-propagating intraseasonal signal that was faster than the canonical MJO phase speed. The displacement with respect to the origin of the RMM diagram was likely due to the evolving base state.

The ENSO base state transitioned to neutral during May, with SSTs remaining near or slightly above average while there were below-average water temperatures in the upper ocean (Fig. 4.8b). The MJO remained incoherent during June, with a more chaotic state dominating the global tropics during this period. Atmospheric Kelvin wave activity continued to provide eastward propagating bursts of convection, one of which may have contributed to the formation of Hurricane Beryl over the central tropical Atlantic in late June. During July, a stronger convectively coupled Kelvin wave crossed the Pacific, and a slower MJO signal evolved from this activity towards the end of the month. A more coherent MJO evolution was observed during August, with

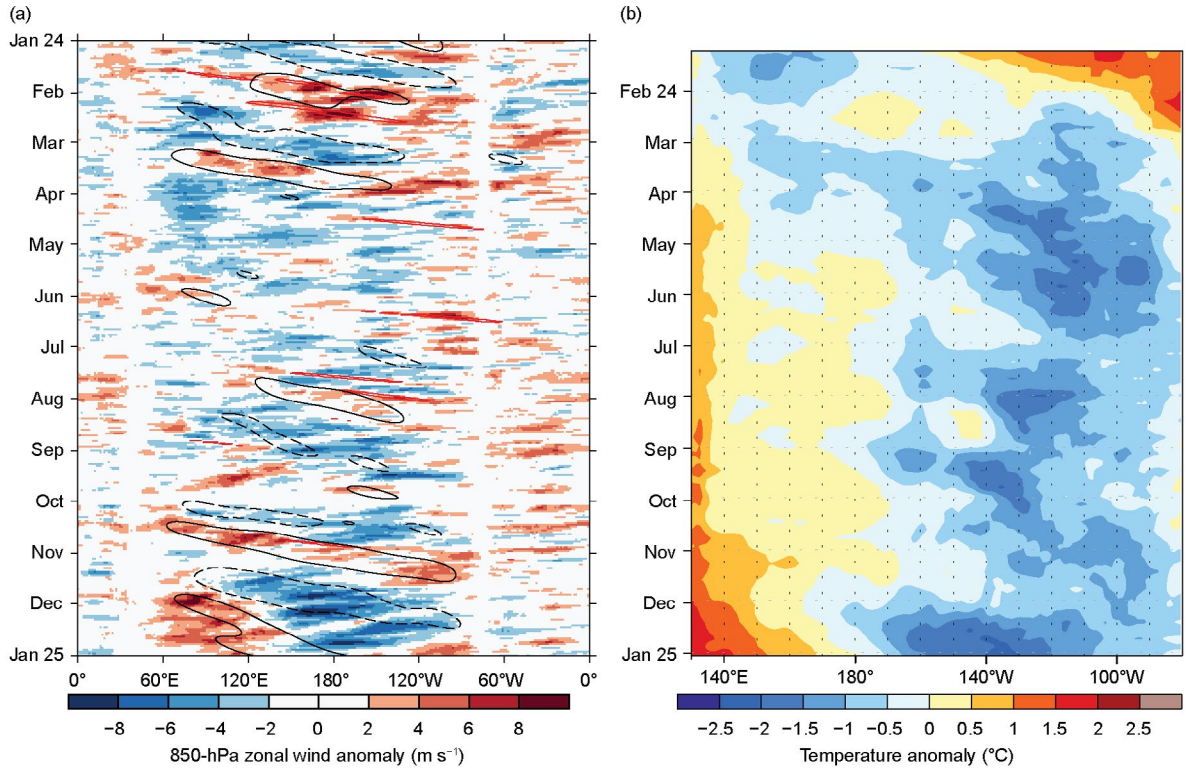

Fig. 4.8. (a) Time–longitude section for 2024 of anomalous 850-hPa zonal wind anomaly (m s^{-1}) averaged over 10°S–10°N. Contours identify anomalies filtered for the Madden–Julian Oscillation (black). (b) Time–longitude section for 2024 of the anomalous equatorial Pacific Ocean heat content, calculated as the mean temperature anomaly (°C) between 0-m and 300-m depth. Yellow/red (blue) shading indicates above- (below-) average heat content. Anomalies are departures from the 1991–2020 base period pentad means. Data in (b) are derived from an analysis system that assimilates oceanic observations into an oceanic general circulation model (Behringer et al. 1998).

Unauthenticated | Downloaded 11/21/25 11:34 AM UTC

the signal crossing the Indian Ocean and Maritime Continent. Enhanced trade winds over the Pacific associated with this MJO activity helped cool equatorial SSTs, though La Niña conditions did not develop. Robust MJO activity continued during September, with the enhanced convective phase crossing the Maritime Continent and Pacific. Enhanced convection over the Pacific tends to generate anomalous westerlies aloft over the Western Hemisphere, and this signal may have contributed to an overall lack of tropical cyclone activity across the Atlantic main development region during the peak of the Atlantic hurricane season. When the MJO entered the Western Hemisphere in late September, the Atlantic season became more active.

The last three months of 2024 were notable for consistently coherent and robust MJO activity, with well-defined propagation of the RMM index and clear, continuous tracking on the objective filtering of the upper-level velocity potential field. During October, the enhanced convective phase moved from the Western Hemisphere to the Indian Ocean, picking up amplitude as it crossed the Maritime Continent and Pacific. Despite cooling SSTs across the equatorial central Pacific, the MJO contributed to a temporary breakdown in the trade wind regime, which may have helped delay the onset of La Niña conditions. The signal continued its eastward progression during November, crossing the Western Hemisphere and Indian Ocean before returning to the Maritime Continent. This placement of the MJO envelopes, which promoted reduced shear across the Atlantic, may have contributed to the development of four late-season tropical cyclones in the Atlantic basin, a continuation of October hyperactivity. During December, the MJO signal slowed significantly as it crossed the Maritime Continent and western Pacific. This intraseasonal signal contributed to an unusually late development of a negative Indian Ocean dipole structure across the Indian Ocean. A trade wind surge was also observed across the Pacific basin during this period, though it began to weaken at the end of the year as the MJO began crossing the Pacific.

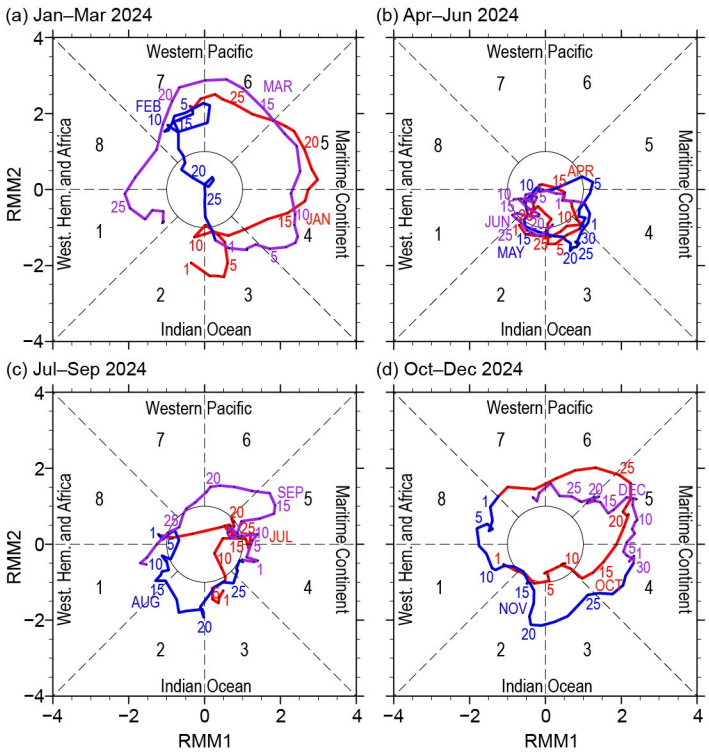

Fig. 4.9. Wheeler and Hendon (2004) Real-time Multivariate Madden–Julian Oscillation (RMM) index for (a) Jan–Mar, (b) Apr–Jun, (c) Jul–Sep, and (d) Oct–Dec 2024. Each point represents the Madden–Julian Oscillation (MJO) amplitude and location on a given day, and the connecting lines illustrate its propagation. Amplitude is indicated by distance from the origin, with points inside the circle representing weak or no MJO. The eight phases around the origin identify the region experiencing enhanced convection, and counterclockwise movement is consistent with eastward propagation.

Unauthenticated | Downloaded 11/21/25 11:34 AM UTC

d. Intertropical convergence zones

1. PACIFIC

—N. Fauchereau

Tropical Pacific rainfall patterns are dominated by two convergence zones: the Intertropical Convergence Zone (ITCZ; Schneider et al. 2014) north of the equator and the South Pacific Convergence Zone (SPCZ; Vincent 1994) in the southwest Pacific. The position and intensity of these convergence zones throughout the year are highly sensitive to sea surface temperature (SST) anomalies, and therefore the state of the El Niño–Southern Oscillation (ENSO) phenomenon (Trenberth 1984).

At the beginning of 2024, the tropical Pacific was in an El Niño state, with positive SST anomalies straddling the central and eastern equatorial Pacific and SST anomalies in the Niño-3.4 region reaching +1.5°C in January–March. Rainfall anomalies in the first quarter of 2024 largely reflected canonical ENSO conditions as far as the ITCZ was concerned, with an ITCZ shifted south of its climatological position over the January–March 2024 period (Fig. 4.10). However, the signal within the SPCZ was less clear overall. While the SPCZ during El Niño events tends to be shifted north and east of its climatological position, leading to drier conditions than normal in the southwest Pacific (e.g., from Vanuatu to Tonga), large positive anomalies affected parts of the same region during the first three months of 2024.

Figure 4.10 summarizes the behavior for both convergence zones during 2024 using rainfall from the Multi-Source Weighted-Ensemble Precipitation (MSWEP) 2.8.0 dataset (Beck et al. 2019). Rainfall transects over 20°S to 30°N are presented for each quarter of the year, averaged across successive 30-degree longitude bands, starting in the western Pacific at 150°E–180°E. The 2024 seasonal variation is compared against the longer-term 1991–2020 climatology.

The transects for October–December 2024 (Fig. 4.10d) for the central Pacific (180°E to 150°W, especially 150°E to the dateline) show that the SPCZ was shifted south and west of its

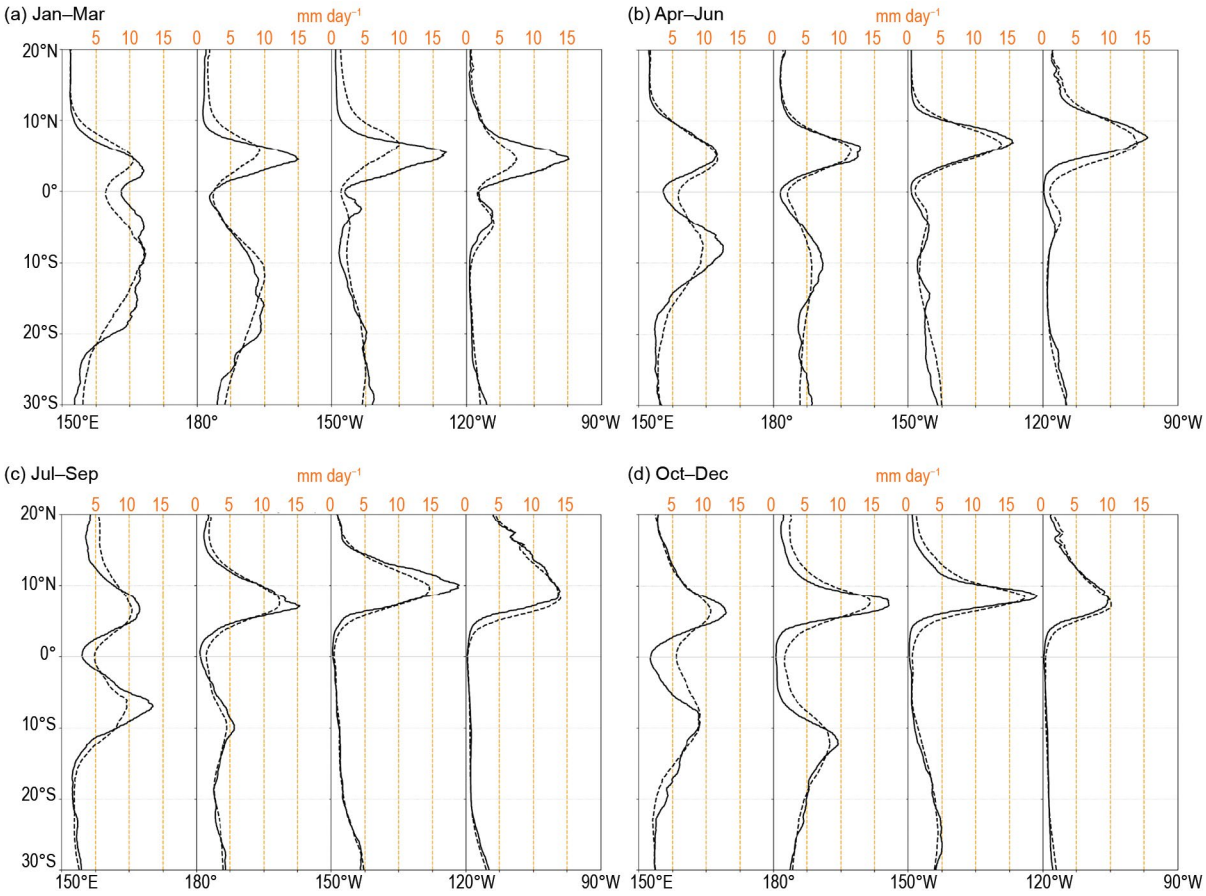

Fig. 4.10. Rainfall rate (mm day⁻¹) for (a) Jan–Mar, (b) Apr–Jun, (c) Jul–Sep, and (d) Oct–Dec 2024. The separate panels for each quarter show the 2024 rainfall cross-section between 30°S and 20°N (solid line) and the 1991–2020 climatology (dotted line), separately for four 30° sectors from 150°E–180° to 120°W–90°W. (Source: Multi-Source Weighted-Ensemble Precipitation [MSWEP] v2.8.0.)

Unauthenticated | Downloaded 11/21/25 11:34 AM UTC

climatological position, while rainfall rates within the ITCZ were reduced compared to climatology, a signature consistent with typical seasonal anomalies recorded during La Niña.

The precipitation anomaly patterns that emerged at the end of 2024 in the tropical Pacific (Fig. 4.11a, October–December anomalies) largely resembled the typical La Niña response recorded during this season (Fig. 4.11b). In the western part of the Pacific south of the equator, the main signal was enhanced precipitation (suppressed precipitation) south (north) of a line extending approximately diagonally from Papua New Guinea in the western Pacific to south of the islands of French Polynesia in the eastern Pacific. This can be readily interpreted as an SPCZ shifted southwest of its climatological position, a typical La Niña signal. Similarly, anomalies recorded along and north of the equator indicated an ITCZ shifted north of its climatological position, consistent with the canonical La Niña pattern shown in Fig. 4.11b.

Figure 4.12 shows a more detailed comparison of the western Pacific (150°E–180°E) rainfall transect during October–December 2024, when La Niña-like conditions started to emerge more clearly in the central and western Pacific. During this three-month period the recorded rainfall (black line) closely corresponded to the rainfall rates recorded on average for all La Niña years (thick blue line).

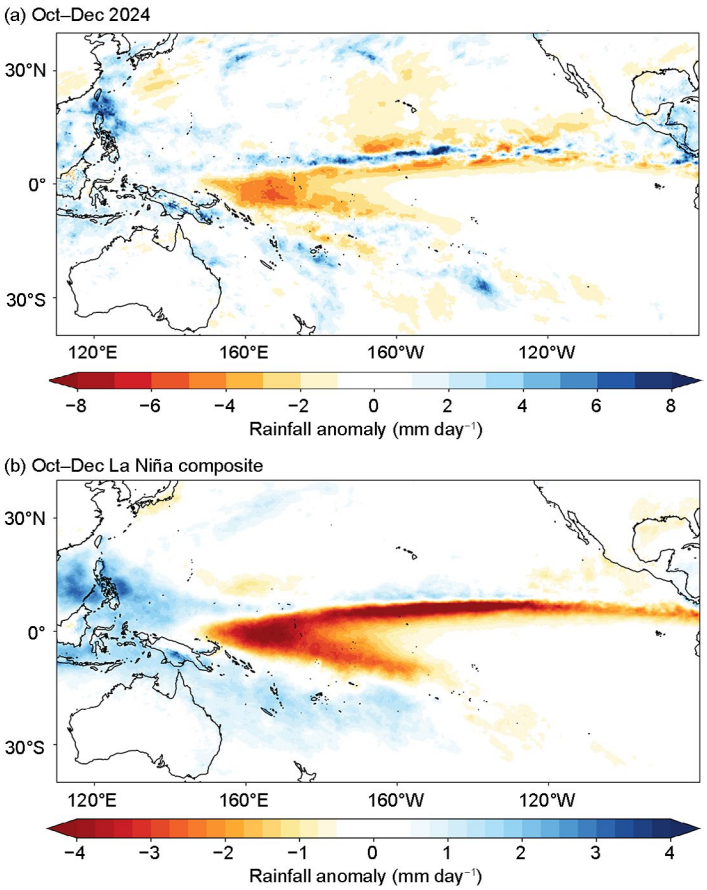

Fig. 4.11. (a) Rainfall anomalies (mm day^{-1}) for Oct–Dec 2024. The anomalies are calculated with respect to the 1991–2020 climatology. (b) Composite rainfall anomalies (mm day^{-1}) for Oct–Dec during La Niña phases (Oceanic Niño Index values <–0.5°C, period 1979–2023). (Source: Multi-Source Weighted-Ensemble Precipitation [MSWEP] v2.8.0.)

2. ATLANTIC

—A. B. Pezza and C. A. S. Coelho

The Atlantic ITCZ is a well-organized convective band that oscillates between approximately 5°N–12°N during July–November and 5°S–5°N during January–May (Waliser and Gautier 1993; Nobre and Shukla 1996). Equatorial atmospheric Kelvin waves can modulate ITCZ intraseasonal variability (Guo et al. 2014). ENSO and the Southern Annular Mode (SAM) can also influence the ITCZ on interannual time scales (Münnich and Neelin 2005). The SAM, also known as the Antarctic Oscillation, describes the north–south movement of the westerly wind belt that circles Antarctica. A positive SAM event reflects a contraction of the westerly wind belt away from the equator, with stronger subtropical ridges and less precipitation in the midlatitudes (Ding et al. 2012; Liu et al. 2021; Moreno et al. 2018).

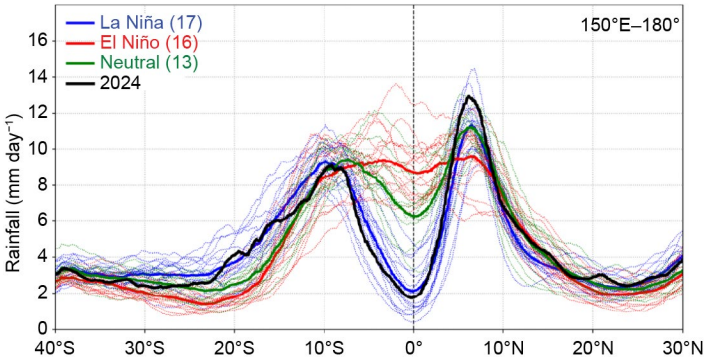

Fig 4.12. Rainfall rate (mm day^{-1}) for Oct–Dec for each year from 1979 to 2024, averaged over the longitude sector 150°E–180°. The cross-sections are color-coded according to NOAA's Oceanic Niño Index (with a threshold of ±0.5°C), except 2024, which is shown in black. Dotted lines are individual years, and solid lines the average over all years in each El Niño–Southern Oscillation phase. The inset legend indicates how many years went into each composite sample. (Source: Multi-Source Weighted-Ensemble Precipitation [MSWEP] v2.8.0.)

The South Atlantic responded to the strong El Niño's transition to a borderline La Niña development by the end of 2024. The Atlantic had widespread, dramatically above-normal SSTs

Unauthenticated | Downloaded 11/21/25 11:34 AM UTC

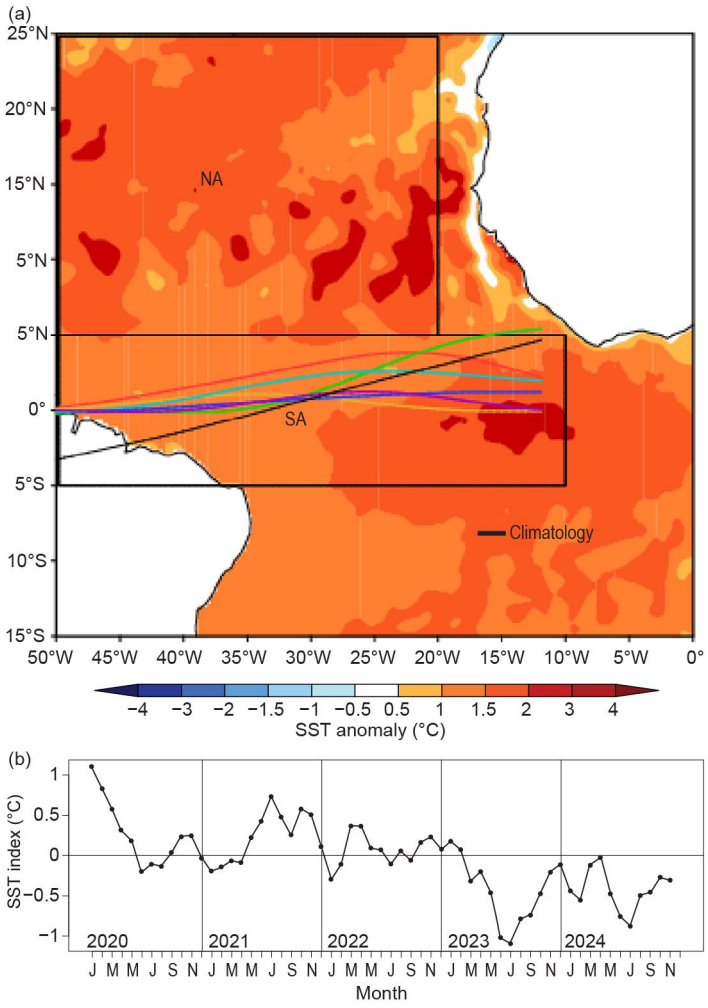

developing around the equator in the first half of 2024 (Fig. 4.13a). However, this signal mostly amplified the longer-term background with a proportionally similar SST gradient to what was observed in 2023. As a result, the ITCZ remained north of its climatological position for most of the year, and the South Atlantic index remained negative, similar to what occurred in 2023 (Figs. 4.13a,b).

Despite the ITCZ displacement, positive rainfall anomalies in the South Atlantic encircled most of the northeastern coast of Brazil during the rainy season, responding to the widespread warm waters across low latitudes (Fig. 4.14a). Importantly, this anomalous oceanic convection south of the equator occurred despite the unfavorable meridional water temperature gradient. As expected, the sea level pressure anomalies over the South Atlantic semi-permanent anticyclone region responded to the intense convective activity over the waters to the north, with negative anomalies centered around 20°S, 25°W. Additionally, the signature of a well-developed South Atlantic Convergence Zone is also seen between 30°W and 40°W (Fig. 4.14b), bringing some limited relief to a drought-stricken South American continent north of 25°S.

Fig. 4.13. (a) Atlantic Intertropical Convergence Zone (ITCZ) position inferred from outgoing longwave radiation (Liebmann and Smith 1996) during Mar 2024. The colored thin lines indicate the approximate position for the six pentads of the month. The thick black line indicates the Atlantic ITCZ climatological position for Mar. The sea surface temperature (SST) anomalies (°C) for Mar 2024 calculated with respect to the 1982–2020 climatology are shaded. The two boxes indicate the areas used for the calculation of the Atlantic index in panel (b), which shows the monthly OISST (Huang et al. 2021) anomaly time series averaged over the South Atlantic (SA) sector (SA region: 5°S–5°N, 10°W–50°W) minus the SST anomaly time series averaged over the North Atlantic (NA) sector (NA region: 5°N–25°N, 20°W–50°W) for the period 2020–24, forming the Atlantic index. The positive phase of the index indicates favorable conditions for enhanced Atlantic ITCZ activity south of the equator.

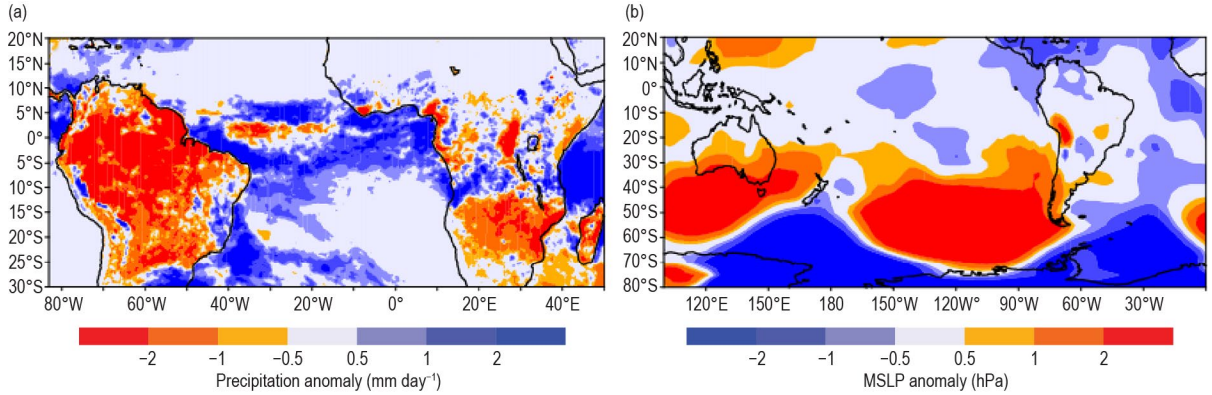

Fig. 4.14. Jan–May 2024 (a) precipitation anomalies (mm day^{-1}) over the Atlantic sector and (b) South American and high-latitude mean sea level pressure (MSLP; hPa) anomalies (Kalnay et al. 1996). Precipitation anomalies are calculated with respect to the 1998–2023 climatology and are derived from the Climate Prediction Center Morphing technique (CMORPH; Joyce et al. 2004). MSLP anomalies are calculated with respect to the 1991–2020 climatology and are derived from the National Centers for Environmental Prediction (NCEP) National Center for Atmospheric Research (NCAR) reanalysis (Kalnay et al. 1996).

Unauthenticated | Downloaded 11/21/25 11:34 AM UTC

e. Global monsoon summary

—B. Wang and Q. He

The global monsoon is the predominant mode causing annual variations in global precipitation and the tropical circulation (Wang and Ding 2008). Figure 4.15 presents the monsoon domain (purple lines) defined by rainfall characteristics (rainy summer versus dry winter; Wang 1994) rather than the traditional definition using wind (Ramage 1971). The Northern Hemisphere (NH) monsoon includes five regional monsoons: northern Africa, India, East Asia, the western North Pacific, and North America. The Southern Hemisphere (SH) monsoon consists of three monsoons: southern Africa, Australia, and South America.

Here, the precipitation and low-level circulation anomalies in the 2024 "monsoon year" are first described, with focus on the SH summer (November 2023–April 2024) and NH summer (May–October 2024) monsoons. Quantitative measures of the regional and global monsoon anomalies are presented thereafter using monsoon precipitation and circulation indices.

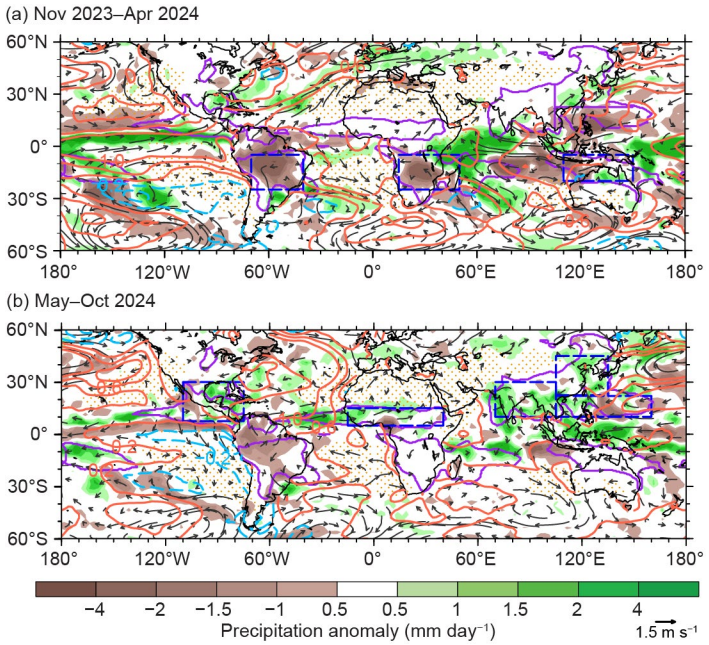

Fig. 4.15. Summer mean precipitation anomalies (mm day^{-1}) and 850-hPa wind anomalies (m s^{-1}) for (a) the Southern Hemisphere (SH) summer monsoon season: Nov 2023–Apr 2024 and (b) the Northern Hemisphere (NH) summer monsoon season: May–Oct 2024. The anomalies are departures from the 1991–2020 climatology. Purple lines outline the global monsoon precipitation domain. The orange (cyan) contours denote positive (negative) sea surface temperature anomalies with a contour interval of 0.4°C. The blue rectangular boxes denote the regions where the regional monsoon precipitation indices are measured. The dotted area represents the dry region with a local summer precipitation rate below 1 mm day^{-1}. Two criteria define the monsoon domains: 1) the annual precipitation range (summer-minus-winter mean) exceeds 300 mm, and 2) the summer precipitation is >55% of the total annual precipitation amount, where the summer here means May–Sep for the NH and Nov–Mar for the SH (Wang and Ding 2008). (Source: GPCP; Huffman et al. 2009.)

1. PRECIPITATION AND CIRCULATION ANOMALIES

During SH summer, the mature El Niño weakened the Walker circulation, leading to increased rainfall over the equatorial Pacific from 150°E to 80°W and suppressed rainfall from the western Maritime Continent to the eastern equatorial Indian Ocean (65°E–120°E) and South American monsoon region (Fig. 4.15a). All three subtropical highs over the SH ocean basins were weakened, resulting in a weak SH summer monsoon and suppressed monsoon rainfall.

During the 2024 NH summer monsoon season (May–October), the Niño-3.4 sea surface temperature (SST) anomaly decreased from +0.3°C in May to −0.3°C in October. During the decay of El Niño, cooling occurred in the eastern equatorial Pacific, suppressing rainfall along the equator and over South America and increasing precipitation over the Maritime Continent (Fig. 4.15b). The increased rainfall anomaly over the Maritime Continent excites an atmospheric Rossby wave under the effect of easterly vertical shear associated with the Asian monsoon (Wang and Xie 1996), enhancing Indian summer monsoon rainfall. The enhanced Indian and Maritime Continent precipitation further enhanced the western Pacific subtropical high so that East Asian monsoon rainfall also increased (Fig. 4.15b). At the same time, suppressed South American precipitation heating induced equatorial westerlies over the equatorial Atlantic that converged into western Africa, increasing rainfall over the northern African monsoon region.

2. REGIONAL MONSOON PRECIPITATION AND CIRCULATION

Regional monsoon precipitation and circulation indices are used to measure the integrated regional monsoon intensity. The regional monsoon precipitation indices are defined by the anomalous precipitation rate (mm day^{-1}) averaged over each of the blue rectangular box regions

Unauthenticated | Downloaded 11/21/25 11:34 AM UTC

shown in Fig. 4.15. The precipitation averaged in each blue box can serve well as a representation of the precipitation averaged over the corresponding actual regional monsoon domain (Yim et al. 2014). The definitions of the circulation indices for each monsoon region are presented in Table 4.1. These circulation indices are generally defined by the meridional shear of the zonal winds at 850 hPa, which measures the intensity (relative vorticity) of the monsoon troughs, except for those of the northern African and East Asian monsoons. The northern African monsoon circulation index is defined by the westerly monsoon strength, reflecting the south–north thermal contrast across the northern African monsoon region. The East Asian summer monsoon circulation index is determined by the meridional wind strength, reflecting the east–west thermal contrast between the Asian continent and the western North Pacific.

Table 4.1 shows that the precipitation and circulation indices are well correlated for most regional monsoons, with the monthly mean correlation coefficients ranging from 0.7 to 0.88, except for the southern African monsoon. Thus, the regional precipitation and circulation indices generally provide consistent measurements of the strength of each regional monsoon system. In addition, the circulation indices represent the land monsoon precipitation in each monsoon region well, with correlation coefficients between 0.70 and 0.79, except in the Indian and southern African land monsoon regions where the leading modes of the precipitation anomalies in these regions show a dipolar pattern (Yim et al. 2014).

Figure 4.16 shows areal-averaged monsoon precipitation and circulation intensities for each regional monsoon. During austral summer (November 2023 to April 2024), the Australian summer monsoon precipitation and circulation were normal (Fig. 4.16g). Increased rainfall in northern Australia was offset by decreased rainfall over Indonesia (Fig. 4.15a). However, the South American summer monsoon rainfall was extremely deficient (3 standard deviations below

Table 4.1. Definition of the regional summer monsoon circulation indices and their correlation coefficients with the corresponding regional summer monsoon precipitation indices for the period 1979/80–2023/24. The precipitation indices are defined by the areal mean precipitation anomalies over the blue box regions shown in Fig. 4.15. R (r) represents the correlation coefficient between the total (land) monsoon precipitation and the corresponding circulation index. The correlation coefficients were computed using monthly time series (180 summer months; Jun–Sep in the Northern Hemisphere [1980–2024] and Dec–Mar in the Southern Hemisphere [1979/80–2023/24]). All R (r) values have significance at the 99% confidence level.

Regional monsoon	Definition of the circulation index	R (r)
Indian (ISM)	U850 (5°N–15°N, 40°E–80°E) minus U850 (25°N–30°N, 60°E–90°E)	0.71 (0.58)
Western North Pacific (WNPSM)	U850 (5°N–15°N, 100°E–130°E) minus U850 (20°N–35°N, 110°E–140°E)	0.87 (0.71)
East Asian (EASM)	V850 (20°N–35°N, 120°E–140°E) plus V850 (10°N–25°N, 105°E–115°E)	0.72 (0.72)
North American (NASM)	U850 (5°N–15°N, 130°W–100°W) minus U850 (20°N–30°N, 110°W–80°W)	0.85 (0.79)
Northern African (NAFSM)	U850 (0°–10°N, 40°W–10°E)	0.70 (0.70)
South American (SASM)	U850 (20°S–5°S, 70°W–40°W) minus U850 (35°S–20°S, 70°W–40°W)	0.78 (0.78)
Southern African (SAFSM)	U850 (12°S–2°S, 10°W–30°E) minus U850 (30°S–10°S, 40°E–60°E)	0.58 (0.47)
Australian (AUSSM)	U850 (15°S–0°, 90°E–130°E) minus U850 (30°S–20°S, 100°E–140°E)	0.88 (0.79)

Unauthenticated | Downloaded 11/21/25 11:34 AM UTC

average), while the circulation index was somewhat weaker than normal (0.5 standard deviations below average; Fig 4.16h). Similarly, the southern African summer monsoon precipitation was deficient (1.5 standard deviations below average), and the circulation intensity was moderately below average (0.6 standard deviations; Fig 4.16f). The previous two years of land surface conditions, which were caused by severed drought, may have amplified the deficient rainfall when the monsoon circulation is weaker than normal. Even a weak circulation anomaly could result in severe drought due to the dry land surface feedback.

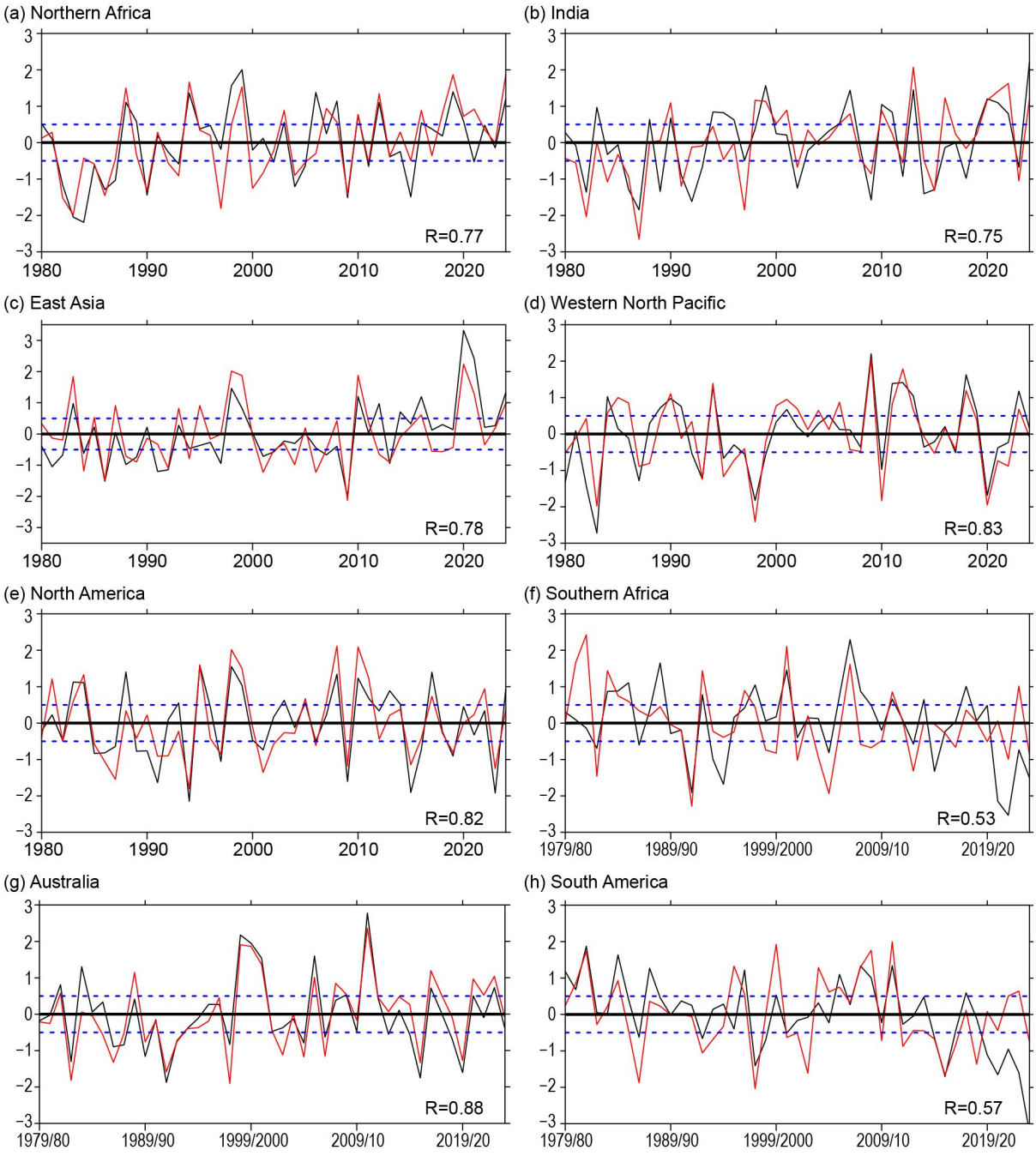

Fig. 4.16. (a)–(h) Temporal variations of summer monsoon precipitation (black lines) and low-level circulation (red lines) indices for eight regional monsoons. The precipitation indices represent the anomalous precipitation rate averaged over the blue rectangular box regions shown in Fig. 4.15. The corresponding circulation indices are defined in Table 4.1. All indices were normalized by their corresponding standard deviation (ordinate) derived for the period of 1979/80–2023/24. Numbers in the bottom right of each panel denote the correlation coefficient between the seasonal mean precipitation and circulation indices (sample size: 45). Dashed lines indicate ±0.5 std. dev. The summer monsoon seasons are May–Oct for the Northern Hemisphere and Nov–Apr for the Southern Hemisphere. (Data source: GPCP for precipitation; ERA5 [Hersbach et al. 2020] for circulation.)

Unauthenticated | Downloaded 11/21/25 11:34 AM UTC

During boreal summer from May to October 2024, the northern African, Indian, and East Asian monsoon precipitation and circulation indices were all positive, exceeding 1 standard deviation (Figs. 4.16a–c), contributing to the increased NH land monsoon rainfall (Fig. 4.17a). The western North Pacific and North American monsoon circulation and rainfall indices were near average (Figs. 4.16d,e). The NH regional monsoon responses were similar to past observed La Niña events.

3. NORTHERN AND SOUTHERN HEMISPHERE LAND MONSOON PRECIPITATION

Since monsoon rainfall over land has more important socioeconomic impacts than oceanic monsoon rainfall, land monsoon rainfall (LMR) in the SH (November 2023–April 2024) and NH (May–October 2024) summers was examined. The mean precipitation rate (mm day^{-1}) averaged over land areas in the NH and SH monsoon domains was used to measure the NH and SH LMR intensity, respectively.

Year-to-year variations in the NH and SH LMR are dominated by the El Niño–Southern Oscillation (ENSO; Wang et al. 2012; Fig. 4.17). Both the NH and SH summer LMR are significantly anti-correlated with the simultaneous Niño-3.4 index. The NH LMR has a simultaneous correlation of −0.73 from 1980 to 2024 (Fig. 4.17a). The SH LMR is also negatively correlated with the Niño-3.4 index (r = 0.75) during 1979/80–2019/20. However, the negative correlation was reversed during the three-year La Niña from 2020/21 to 2022/23 (Wang and He 2024), and the correlation coefficient for the entire period of 1979/80–2023/24 dropped to −0.58 (Fig. 4.17b). During the 2023/24 season, the ENSO and SH LMR resumed their canonical negative correlation.

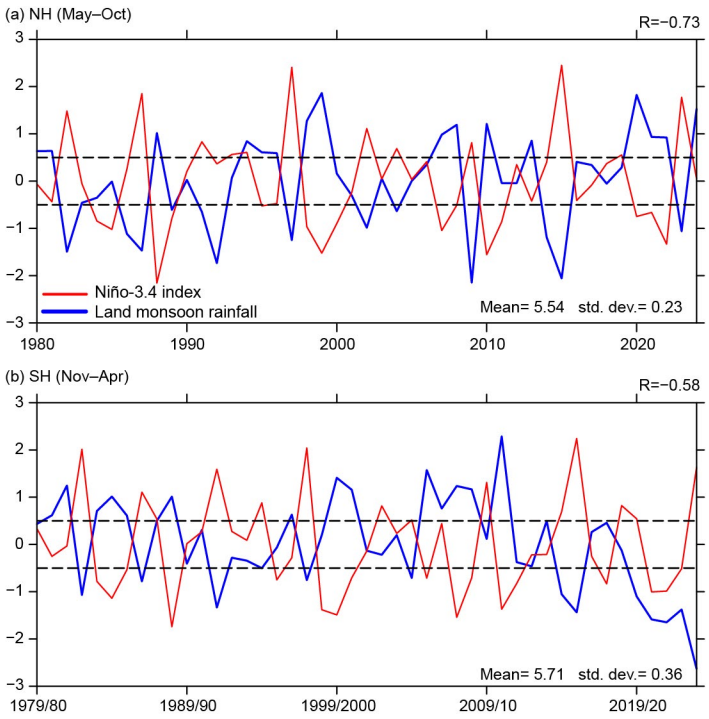

Fig. 4.17. Anticorrelation between the El Niño–Southern Oscillation and the Northern Hemisphere (NH) and Southern Hemisphere (SH) land monsoon rainfall. (a) NH summer (May–Oct) land monsoon precipitation anomaly (blue) normalized by its standard deviation (std. dev.). The climatological mean NH summer land monsoon precipitation (mean) and std. dev. are shown in the lower right panel (mm day^{-1}). Numbers in the top right of each panel denote the correlation coefficient (R) between the seasonal mean precipitation anomaly and the simultaneous Niño-3.4 index (red). Dashed lines indicate ±0.5. (b) As in (a) except for the SH summer (Nov–Apr). The land monsoon precipitation excludes monsoon rainfall from the oceanic monsoon domain. (Source: GPCP for precipitation; HadISST and ERSSTv5 for SST.)

From November 2023 to April 2024, the tropical Pacific SSTs rebounded from the previous 2020–22 triple La Niña with a strong El Niño. Notably, during the 2023/24 season, the SH LMR reached a historical minimum with an anomaly of –2.5 standard deviations (Fig. 4.17b). This low record was primarily caused by severe dry conditions over the South American and southern African monsoon regions (Figs. 4.15a, 4.16f,h). The SH land monsoon regions experienced severe dry conditions for four consecutive years, beginning in 2019/20. The reasons behind the continuing drought conditions require further exploration.

During the NH summer 2024, corresponding to the rapid decay of El Niño and transition towards La Niña conditions, the NH LMR increased by 1.5 standard deviations (i.e., about 0.35 mm day^{-1}) in the NH land monsoon regions (Fig. 4.17a). The increased NH LMR under neutral ENSO conditions is not consistent with the historically observed negative El Niño–NH LMR relationship, though the direction of change from 2023 to 2004 is.

4. SUMMARY

From November 2023 to April 2024, the South American and southern African land monsoon regions experienced severe deficient rainfall (Figs. 4.16f,h), consistent with the influence of a

Unauthenticated | Downloaded 11/21/25 11:34 AM UTC

strong El Niño. From May to October 2024, the Asian and northern African land monsoon rainfall was well above average despite neutral ENSO conditions (Figs. 4.15b, 4.16a–c). The total SH land monsoon rainfall reached a historical minimum with an anomaly of –2.5 standard deviations (Fig. 4.17b) despite normal Australian monsoon rainfall. The drought in South America and southern Africa compounded the drought conditions that were already present from the prior three years of deficient monsoon rainfall. The negative correlation between ENSO and SH land monsoon rainfall broke down during the previous three-year La Niña period. The nonstationary ENSO–monsoon relationship may arise from the impacts of diverse ENSO evolution and anomalous surface conditions from other oceans and the middle and high latitudes.

Unauthenticated | Downloaded 11/21/25 11:34 AM UTC

f. Indian Ocean dipole

—L. Chen and J-J. Luo

The Indian Ocean dipole (IOD) is a significant mode of interannual climate variability in the tropical Indian Ocean (IO), characterized by a zonal dipole of sea surface temperature (SST) anomalies in the equatorial IO (Saji et al. 1999; Luo et al. 2010, 2012). The IOD can arise from tropical El Niño–Southern Oscillation forcing and/or local air–sea interaction processes in the tropical IO (Luo et al. 2007, 2010). Typically, the IOD begins to form during the boreal summer, reaches its peak in boreal autumn, and dissipates rapidly in boreal winter. A negative IOD (nIOD) event usually features warm SST anomalies in the eastern IO and weak cold SST anomalies in the western IO, and vice versa for a positive event. The IOD exhibits nonlinear behavior, for instance, the intensity of a nIOD event is generally weaker than that of a positive IOD event, which is due to the asymmetric ocean–atmosphere coupling between the two phases of the IOD (Luo et al. 2007; Hong et al. 2008).

In 2024, the tropical Indian Ocean experienced a weak nIOD event, characterized by significant warm SST anomalies in the eastern pole (Fig. 4.18a). According to the OISST dataset, the IOD index for this nIOD event reached –0.64°C in October–November, with a magnitude of +0.74°C in its eastern pole (Figs. 4.18a,b). Concurrently, the Pacific Ocean was experiencing a transition from an El Niño that peaked during the 2023/24 winter to La Niña-like conditions late in 2024 (Fig. 4.18c). Following the strong 2023/24 El Niño, the tropical Indian Ocean was marked by a warm Indian Ocean basin mode throughout 2024 (Fig. 4.18c). During the 2023/24 winter, easterly wind anomalies were prevalent along the equatorial Indian Ocean (Fig. 4.18b), partly due to the anomalous Walker circulation associated with the concurrent El Niño (Figs. 4.18c, 4.20).

The decay rate of the warm SST anomalies associated with the 2023/24 El Niño to the subsequently cold SST anomalies in the eastern and central tropical Pacific was slower than normal (Figs. 4.18c, 4.19), giving rise to a borderline weak La Niña event by the end of 2024 (Fig. 4.18c). This slow decay pace may have contributed to the prolonged easterly wind anomalies along the central equatorial IO until September 2024. Anomalous cold SSTs emerged in the central eastern Pacific in August 2024 (Fig. 4.18c) and then continued to slowly increase in magnitude in boreal autumn (Fig. 4.19). In accordance with the onset of La Niña-like conditions, a reversal in surface zonal wind anomalies occurred in the equatorial Indian Ocean during boreal autumn 2024 (Figs. 4.18b, 4.20d). Specifically, low-level westerly wind anomalies emerged in tandem with the zonal dipole of SST anomalies. This signified the full establishment of an nIOD event in boreal autumn 2024.

Despite the modest amplitude of the nIOD event in 2024, positive air–sea feedback processes among the anomalous SSTs, low-level

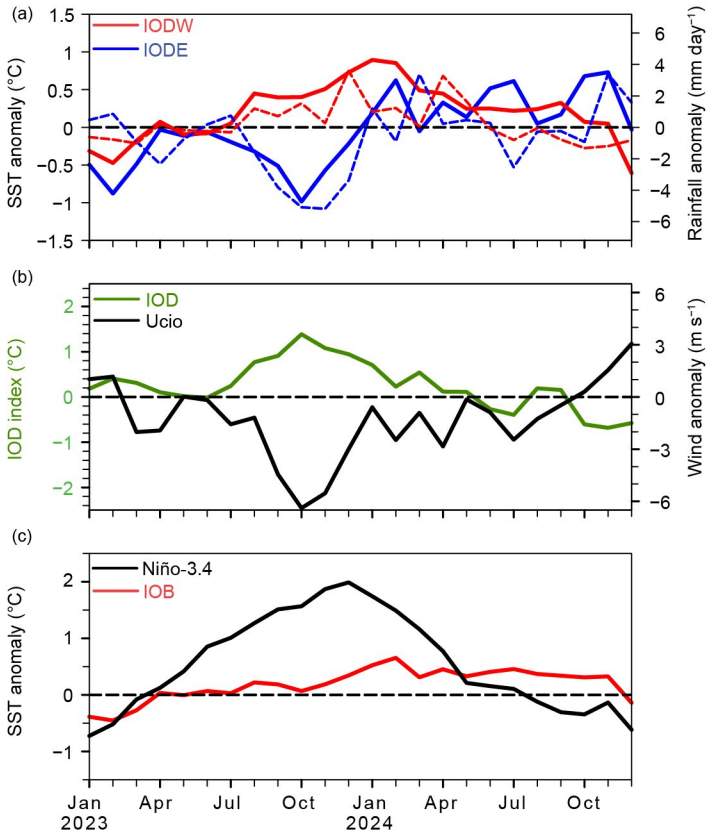

Fig. 4.18. (a) Monthly anomalies of sea surface temperature (SST; °C; solid lines) and precipitation (mm day^{-1}; dashed lines) in the eastern part of the Indian Ocean dipole (IODE; 10°S–0°, 90°E–110°E; blue lines) and the western part of the IOD (IODW; 10°S–10°N, 50°E–70°E; red lines). (b) As in (a), but for the IOD index (measured by the SST difference between IODW and IODE; green line) and surface zonal wind anomaly (m s^{-1}) in the central equatorial IO (Ucio; 5°S–5°N, 70°E–90°E; black line). (c) As in (a), but for the SST anomalies in the Niño-3.4 region (5°S–5°N, 170°W–120°W; black line) and the tropical IO (Indian Ocean basin [IOB]; 20°S–10°N, 40°E–120°E; red line). The climatology is established using the 1982–2024 base period as a reference. Anomalies are calculated by subtracting the climatological annual cycle and detrending the data. (Sources: NOAA OISST [Reynolds et al. 2002]; monthly CMAP precipitation analysis [available at https://psl.noaa.gov/data/gridded/data.cmap.html]; and JRA-55 atmospheric reanalysis [Ebita et al. 2011].)

Unauthenticated | Downloaded 11/21/25 11:34 AM UTC

winds, and precipitation fields occurred in boreal autumn. In response to the zonal contrast of SST anomalies associated with the nIOD in SON (Fig. 4.19d), a dipole structure of precipitation anomalies formed along the equatorial Indian Ocean, with wet conditions in the eastern pole and dry conditions in the western pole (Figs. 4.18a, 4.20d). This precipitation anomaly dipole helped reinforce low-level westerly wind anomalies (Figs. 4.18b, 4.20d), which in turn intensified the nIOD-related SST anomaly.

From the perspective of the tropical Indo-Pacific Ocean sector, the remote impacts of tropical Pacific conditions on the development of the IOD were evident. The slow transition from El Niño to La Niña in 2024 (Fig. 4.18c) resulted in persistent surface easterly wind anomalies along the equatorial IO until September. Following the emergence of cold SST anomalies in the central eastern equatorial Pacific in August, surface zonal wind anomalies in the equatorial IO began to change from easterly to westerly. Due to positive air–sea interactions, an nIOD event with a warm wet east pole and a cold dry west pole occurred in boreal autumn 2024.

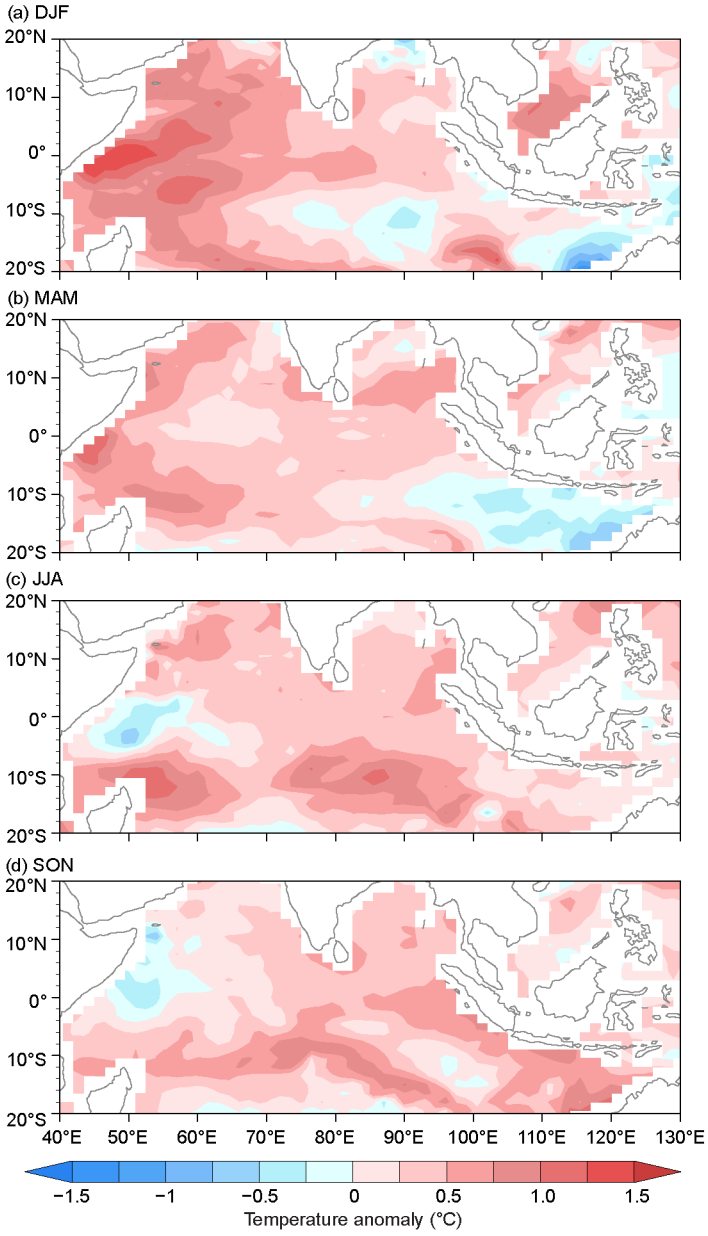

Fig. 4.19. Sea surface temperature (SST) anomalies (°C, colored scale) during (a) Dec 2023–Feb 2024, (b) Mar–May 2024, (c) Jun–Aug 2024, and (d) Sep–Nov 2024. The climatology is established using the 1982–2024 base period as a reference. Anomalies are calculated by subtracting the climatological annual cycle and detrending the data. (Sources: NOAA OISST [Reynolds et al. 2002].)

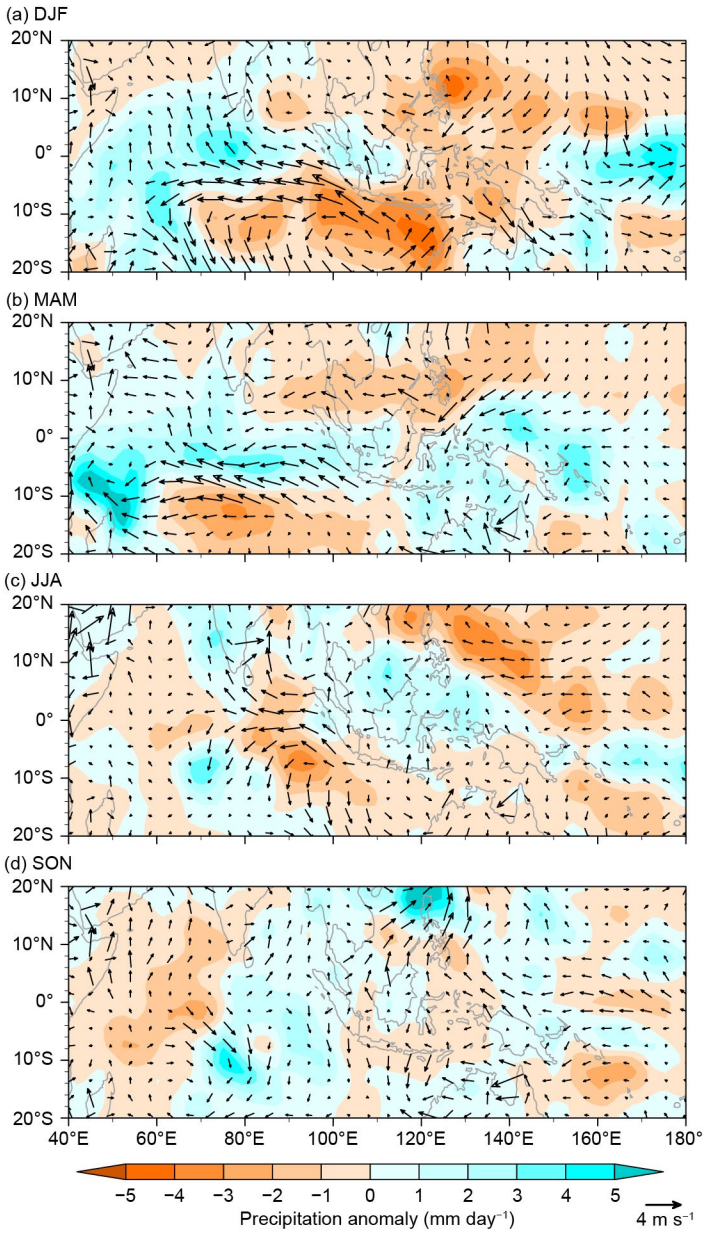

Fig. 4.20. Precipitation (mm day^{-1}) and surface wind (m s^{-1}) anomalies during (a) Dec 2023–Feb 2024, (b) Mar–May 2024, (c) Jun–Aug 2024, and (d) Sep–Nov 2024. (Sources: monthly GPCP precipitation analysis [available at https://www.nccs.nasa.gov/services/data-collections/atmosphere-based-products/gpcp] and ERA5 atmospheric reanalysis [Hersbach et al. 2020].)

Unauthenticated | Downloaded 11/21/25 11:34 AM UTC

In summary, a weak nIOD event occurred in autumn 2024, with the IOD index attaining a value of −0.64°C during October–November. The evolution of this weak nIOD was influenced by both local air–sea interactions within the Indian Ocean and remote forcing from the Pacific Ocean. The development of this nIOD event was accompanied by a transition from El Niño to La Niña, which exhibited a slower-than-normal decaying pace, partly contributing to a delayed onset of the nIOD in the Indian Ocean. During the development of this nIOD in boreal autumn, local air–sea interactions played a role. The Indian Ocean displayed classic nIOD characteristics, including a zonal dipole of SST anomalies and precipitation anomalies, as well as low-level westerly wind anomalies.

Unauthenticated | Downloaded 11/21/25 11:34 AM UTC

g. Tropical cyclones

1. OVERVIEW

—H. J. Diamond and C. J. Schreck

The IBTrACS dataset comprises historical tropical cyclone (TC) best-track data from numerous sources around the globe, including all of the World Meteorological Organization (WMO) Regional Specialized Meteorological Centers (RSMCs; Knapp et al. 2010). This dataset represents the most complete compilation of global TC data. From these data, 1991–2020 climatological values of TC activity for each basin using statistics from both the WMO RSMCs and the Joint Typhoon Warning Center (JTWC) are calculated following Schreck et al. (2014). These values are referenced in each subsection. Tallying the global TC numbers is challenging and involves more than simply adding up basin totals, as some storms cross TC basin boundaries, some TC basins overlap, and multiple agencies track and categorize them. The Northern Hemisphere (NH) basins are typically measured from January to December, while Southern Hemisphere (SH) basins are typically measured from July to June. Global values here are the sum of NH for 2024 and SH for 2023/24. Unless otherwise noted, the statistics are based on preliminary data from NOAA's National Hurricane Center (NHC) and the JTWC. However, differences between the JTWC and the WMO RSMCs or other local agencies will be noted as appropriate.

Based on preliminary data from the NHC and the JTWC as archived in IBTrACS (Fig. 4.21), the combined 2024 season had 82 named storms (sustained wind speeds ≥34 kt or 17 m s^{-1}), which is 15 fewer than two seasons ago in 2022 (Diamond and Schreck 2022), but the same number as in 2023 (Diamond and Schreck 2023). The total of the past two seasons was below the 1991–2020 average of 87. In 2024, there were 43 hurricanes/typhoons/cyclones (HTCs; sustained wind speeds ≥64 kt or 33 m s^{-1}), 23 of which reached major HTC status (sustained wind speeds ≥96 kt or 49 m s^{-1}), which was nearly double the number of major HTCs from 2022 but seven less than that of 2023. The accumulated cyclone energy (ACE) for the season was 613 × 10^4 kt^2, which was 29.2% less than 2023 (Diamond and Schreck 2024).

In sections 4g2–4g8, 2023/24 SH and 2024 NH seasonal TC activities are described and compared to the historical record for each of the seven WMO-defined TC basins. For simplicity, all counts are broken down by the U.S. Saffir–Simpson Hurricane Wind Scale (SSHWS). The overall picture of global TCs during 2024 is shown in Fig. 4.21, and counts by category and intensity are documented in Table 4.2.

The central and eastern North Pacific basins each had below-normal ACE relative to 1991–2020. Table 4.2 uses this climatological period to classify seasons for consistency among basins. However, NOAA uses the terciles from 1951 to 2020 to classify North Atlantic ACE, owing to the longer record of data there. The 2024 seasonal ACE value was 167% of the 1951–2020 median (which is 96.7).

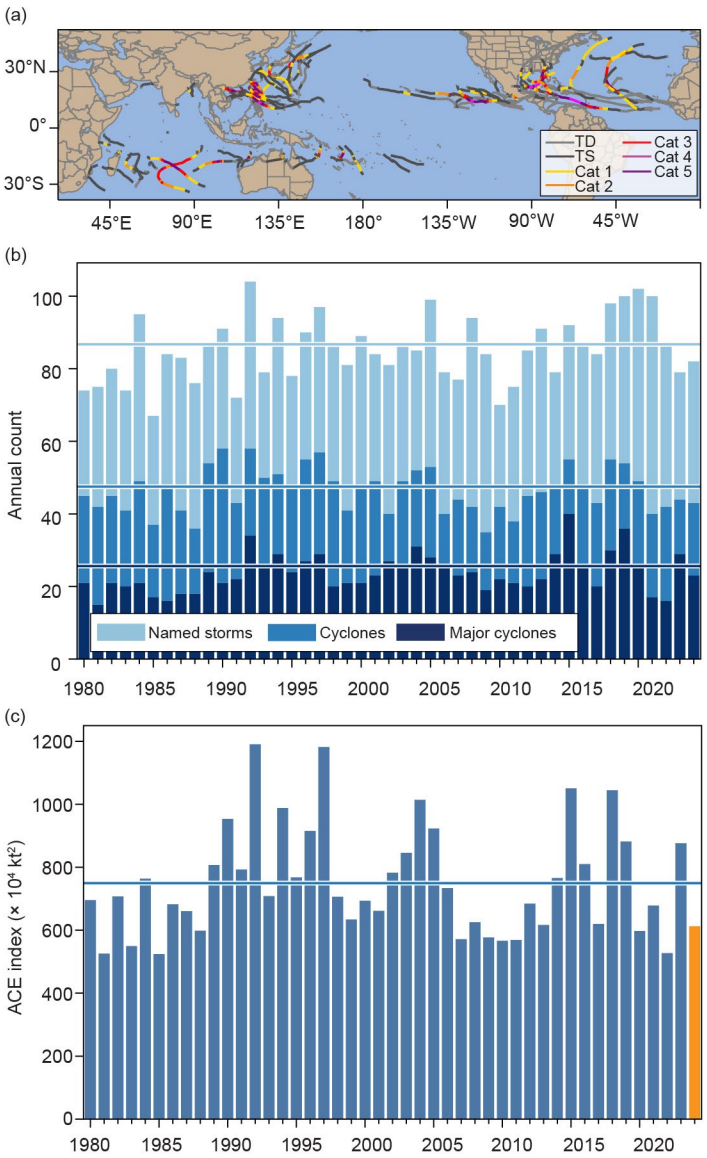

Fig. 4.21. (a) Global summary of tropical cyclone (TC) tracks for the 2024 season; (b) global TC counts; and (c) global accumulated cyclone energy (ACE) values (× 10^4 kt^2). Horizontal lines in (b) and (c) are the 1991–2020 normal values.

Unauthenticated | Downloaded 11/21/25 11:34 AM UTC

This value is above NOAA's threshold for an above-normal season (126.1, or 130% of the median) and meets the definition of a hyperactive season (ACE above 159.6, or 165%).

The North Atlantic season was one of the most unusual in history. It began with a record-breaking start with Hurricane Beryl in June, which was the earliest Category 5 storm on record as it made its way across the Caribbean, eventually making landfall along the Texas coast as a Category 1 hurricane. However, there was a lull in the season from mid-August until late September, which was remarkable given that the pre-seasonal outlooks called for an extremely active season. In late September, activity ramped back up significantly in the western Gulf of America/Gulf of Mexico with Hurricanes Helene and Milton. The storm caused widespread damage in Florida and throughout the southeastern United States. Helene brought destruction far inland from Georgia to the mountains of western North Carolina, including Asheville, North Carolina, where the editorial staff and many scientists involved with this report live and work. Hurricane Milton caused significant damage across a sizable swath of Florida before exiting into the Atlantic. Two sidebar articles detail these storms, including one by the co-editor of this chapter, who was a first-hand witness to the ravages of Hurricane Helene.

Table 4.2. Global counts of tropical cyclone (TC), hurricane/typhoon/cyclone (HTC), major HTC, and Category 5 storm activity by basin for 2024. "+" denotes top tercile; "++" is top 10%; "–" is bottom tercile; "––" is bottom 10% (all relative to 1991–2020). (Note that some inconsistencies between Table 4.2 and the text of the various basin write-ups in section 4g exist and are unavoidable, as tallying global TC numbers is challenging and involves more than simply adding up basin totals; this is because some storms cross TC basin boundaries, some TC basins overlap, and multiple agencies are involved in tracking and categorizing TCs.)

Basin	TCs	HTCs	Major HTCs	Cat 5	ACE ($\times 10^4$ kt^2)
North Atlantic	18 +	11 +	5 +	2 ++	162
Eastern N. Pacific	13 –	5 –	3	1 +	83 –
Western N. Pacific	23 –	15	9	1 –	204 –
North Indian	4 –	1	0	0	7 –
South Indian	13 +	5	2 –	0	71 –
Australian	9 –	6 +	3 +	0	64
Southwest Pacific	6	2	1	0	22 –
Global	82 –	43	23 +	4 +	613 –

2. ATLANTIC BASIN

—M. Rosencrans, E. S. Blake, C. W. Landsea, H. Wang, S. B. Goldenberg, R. J. Pasch, D. S. Harnos, H. Lopez, and L. N. Long

(i) 2024 seasonal activity

The 2024 Atlantic hurricane season produced 18 named storms; of the 11 of these that became hurricanes, 5 became major hurricanes thereafter. (Fig. 4.22a). The HURDAT2 (Landsea and Franklin 2013) 1991–2020 seasonal averages (included in IBTrACS) are 14.4 named storms, 7.2 hurricanes, and 3.2 major hurricanes. The total of 18 named storms during 2024 was the ninth

Unauthenticated | Downloaded 11/21/25 11:34 AM UTC

highest in the HURDAT2 database since 1851. The 2024 Atlantic hurricane season was classified by NOAA as an extremely active ("hyperactive") season. Eight of the last nine Atlantic hurricane seasons (2016–2021, 2023, and 2024) have been classified as either above normal or hyperactive, with 2022 classified as a near-normal season.

Three of the 18 named storms during 2024 were short-lived (<2 days), a relatively low proportion of the total count. There has been a large artificial increase (approximately five per year) in these "shorties" since 2000 (Landsea et al. 2010). These increased counts primarily reflect new observational capabilities, such as scatterometers, Advanced Microwave Sounding Units, and the Advanced Dvorak Technique, and have no association with any known climate variability (Villarini et al. 2011).

The 2024 seasonal ACE value was 167% of the 1951–2020 median (which is 96.7; Fig. 4.22b). This value falls above NOAA's threshold for an above-normal season (126.1, or 130% of median) and for a hyperactive season (ACE above 159.6, or 165%). Since the current Atlantic high-activity era began in 1995 (Goldenberg et al. 2001; Bell et al. 2019, 2020; Lopez et al. 2024), there have been 21 above-normal seasons, with 11 being hyperactive. By comparison, the preceding 24-year low-activity era of 1971–94 had only two above-normal seasons, and none were hyperactive. The 2024 season was only the third hyperactive year since the hyperactive 2010 season.

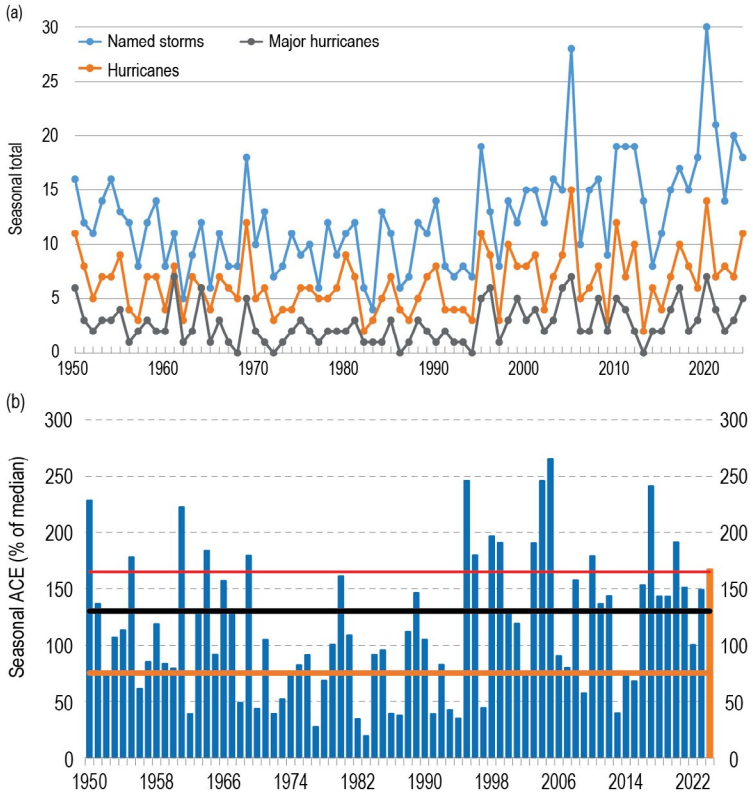

Fig. 4.22. Seasonal Atlantic hurricane activity during the period 1950–2024. (a) Numbers of named storms (blue), hurricanes (orange), and major hurricanes (gray). (b) The accumulated cyclone energy (ACE) index expressed as percent of the 1951–2020 median value. ACE is calculated by summing the squares of the six-hourly maximum sustained surface wind speed (kt) for all periods while the storm is at least of tropical storm strength. The black (orange) line represents NOAA's threshold for an above-normal (below-normal) season and the red line is NOAA's threshold for a hyperactive season (https://www.cpc.ncep.noaa.gov/products/outlooks/Background.html). Note that there is a low bias in activity during the 1950s to the early 1970s due to the lack of (or lower quality) satellite imagery and a technique (Dvorak) to interpret tropical cyclone intensity for systems over the open ocean. (Source: HURDAT2 [Landsea and Franklin 2013].)

(ii) Storm formation times, regions, and landfalls

TC activity was robust but highly variable during the core months of the season (August–October [ASO; Fig. 4.23a]), with no activity outside of the defined North Atlantic hurricane season (1 June–30 November). During the Atlantic hurricane season, at least one named storm developed every month, including six named storm formations during September. Activity for the calendar year started on 19 June with the development of Tropical Storm Alberto. Named storm formations were above normal in June, near-normal in July, and slightly below-normal for August. September started slowly, but finished with above-normal activity, while October had nearly double its climatological activity with three named storms (including one hurricane and one major hurricane). Three named storms developed in November, including a rare November major hurricane.

Of the 18 named storms in 2024, 56% (10 of 18) formed in the main development region (MDR; Fig. 4.23b). The MDR spans the tropical Atlantic Ocean and Caribbean Sea between 9.5°N and 21.5°N (Goldenberg and Shapiro 1996; Goldenberg et al. 2001). Since 1950, approximately 42% of named storms form in the MDR in any given year, and 18% form in the Gulf of America/Gulf of Mexico. The associated MDR-related ACE value (ACE from named storms that developed in the MDR) was 166% of the median annual MDR ACE. With three tropical storm and two hurricane

Unauthenticated | Downloaded 11/21/25 11:34 AM UTC

formations, ACE from named storms that formed in the Gulf of America/Gulf of Mexico was 33.2×10^4 kt^2 compared to the 1950–2023 median of 4.7×10^4 kt^2. Gulf of America/Gulf of Mexico ACE represented about a normal fraction of the overall tropical activity, contributing 21% of the total annual ACE.

Named storms and their tracks largely fell into two clusters: one across the Caribbean and Gulf of America/Gulf of Mexico, and another farther east, near ~50°W (Fig. 4.23c). The cluster of activity over the Gulf of America/Gulf of Mexico resulted in five landfalling hurricanes in the contiguous United States. Many of those systems had prior landfalls in countries and territories across the Caribbean and Central America. Hurricane Beryl had devastating impacts along much of its path in the Caribbean and Texas, where it came ashore with winds of 80 kt (41 m s^{-1}). Hurricane Beryl became the earliest Category 5 storm on record for the North Atlantic basin when the storm reached a peak intensity of 145 kt on 2 July (Beven et al. 2024).

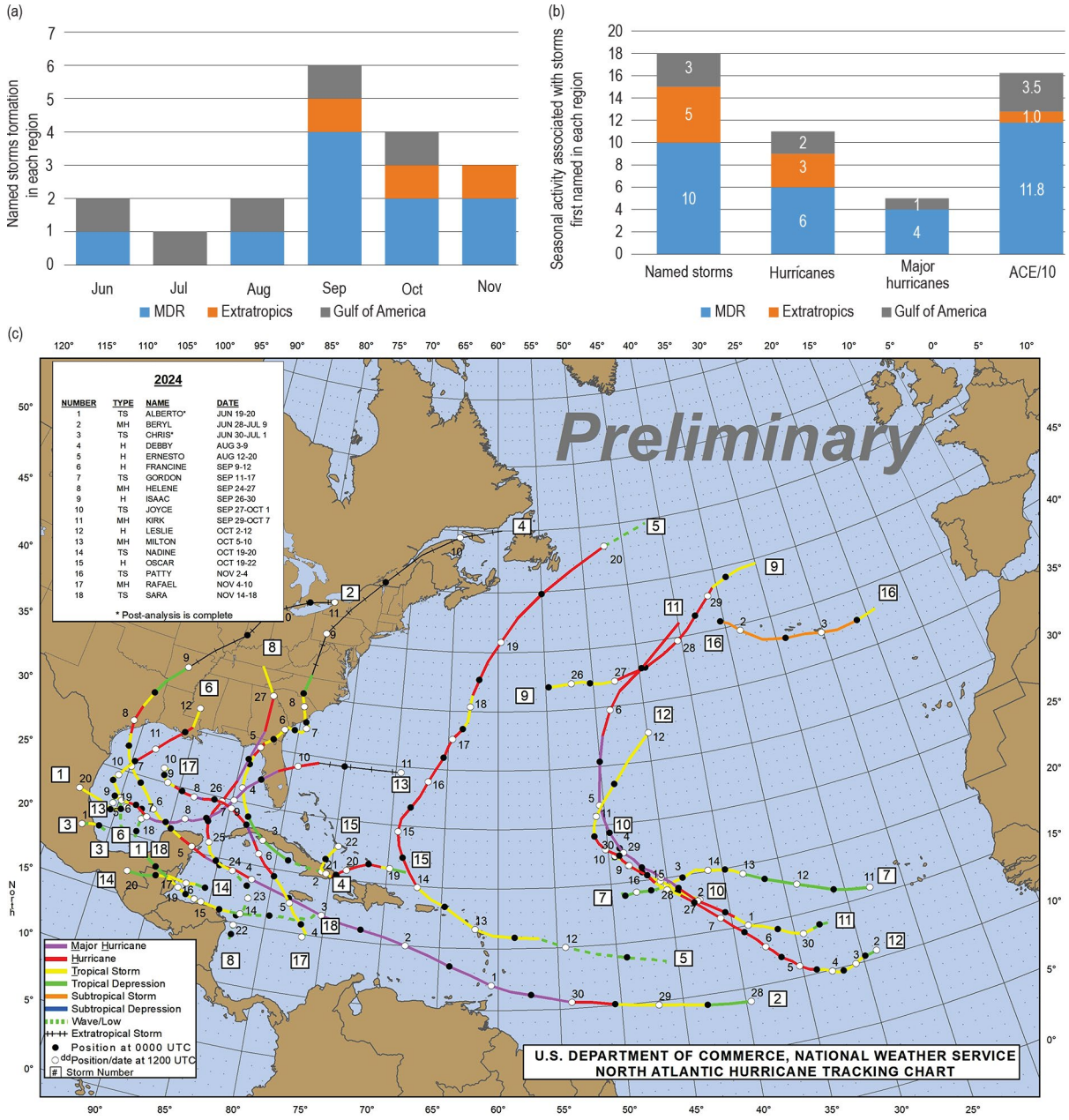

Fig. 4.23. Atlantic tropical cyclone (TC) activity in 2024. (a) Named storm counts for the month and region where the storm was first named and (b) total seasonal counts for the three storm classifications and accumulated cyclone energy (ACE) for each region where the storm was first named. ACE reflects the entire storm ACE and is attributed to the region in which the storm was first named. (c) 2024 Atlantic basin storm tracks. The "extratropics" includes all regions except for the main development region and the Gulf of America/Gulf of Mexico. (Source: HURDAT2; Landsea and Franklin [2013].)

Unauthenticated | Downloaded 11/21/25 11:34 AM UTC

Hurricanes Helene (see Sidebar 4.1), Milton (see Sidebar 4.2), Debby, and Francine also made landfall along the Gulf Coast, each bringing significant impacts to coastal and inland areas. There were no hurricane landfalls along the U.S. East Coast, which typically has a higher risk during an active season. Only two storms impacted the East Coast, with Milton exiting Florida's east coast as a Category 1 hurricane and Debby making a second landfall in South Carolina as a subtropical storm.

(iii) Sea surface temperatures

Sea surface temperatures (SSTs) were exceptionally high throughout the MDR (Fig. 4.24a), with an ASO area-averaged SST anomaly of +0.96°C (Fig. 4.24b), the second-highest value since at least 1950 (behind 2023 at +1.16°C). The MDR SST anomalies during 2023 and 2024 were twice that of the next closest anomaly (+0.45°C) which occurred during 2010. The area-averaged SST anomaly in the MDR was 0.55°C higher than the average of the remainder of the global tropics (Fig. 4.24c), the same as 2023. The warm MDR signal combined with the above-normal SSTs farther north in the extratropical Atlantic is typical of the warm phase of the Atlantic Multidecadal Oscillation (Enfield and Mestas-Nuñez 1999; Bell and Chelliah 2006) and is a ubiquitous characteristic of Atlantic high-activity eras such as 1950–69 and 1995–present (Goldenberg et al. 2001; Vecchi and Soden 2007; Bell et al. 2018).

In the Atlantic extratropics, the largest ASO SST anomalies (exceeding +1.5°C) occupied portions of the central North Atlantic (Fig. 4.24a). The area-averaged SST anomaly in the North Atlantic (red box, Fig. 4.24a) was +0.73°C, reflecting a continuation of exceptional warmth that began in 2012. A small area near the coast of Africa exhibited near- or slightly below-normal SSTs (Fig. 4.24a), potentially related to factors contributing to a lull in activity during early September.

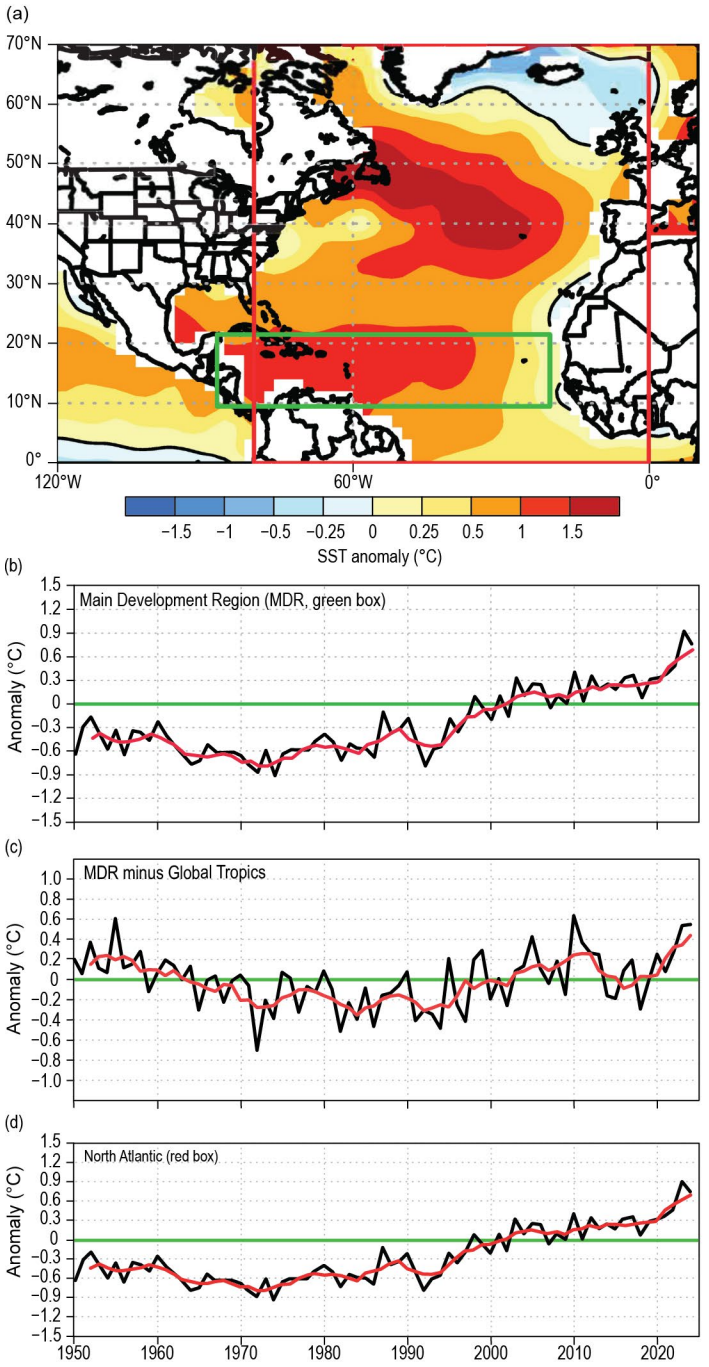

Fig. 4.24. (a) Aug–Oct 2024 sea surface temperature (SST) anomalies (°C). (b)–(d) Time series of Aug–Oct area-averaged SST anomalies (black) and five-point running mean of the time series (red): (b) in the main development region (MDR; green box in [a] spanning 9.5°N–21.5°N and 87.5°W–20°W), (c) difference between the MDR and the global tropics (20°S–20°N), and (d) in the North Atlantic (red box in [a] spanning 0°–70°N and 80°W–0°). Anomalies are departures from the 1991–2020 period means. (Source: ERSSTv5 [Huang et al. 2017].)

El Niño–Southern Oscillation (ENSO)-neutral conditions prevailed throughout the North Atlantic hurricane season, based on the Oceanic Niño Index (ONI) values, which ranged from 0.0°C in June–August (JJA) to −0.3°C in September–November (SON). To account for the global tropical average SSTs during those periods, the relative ONI (L'Heureux et al. 2024) had values of −0.51°C for JJA and −0.82°C for SON, with a value of −0.76°C for ASO. The latter metric indicates La Niña conditions, which may also help explain the late-season activity and anomalously low wind shear.

Unauthenticated | Downloaded 11/21/25 11:34 AM UTC

(iv) Atmospheric conditions

Climatologically, the ASO peak in Atlantic hurricane activity largely reflects the June–September peak in the West African monsoon. The interrelated circulation features of an enhanced monsoon act to further increase hurricane activity, while those of an anomalously weak monsoon act to suppress it (Gray 1990; Hastenrath 1990; Landsea et al. 1992; Bell and Chelliah 2006; Bell et al. 2018, 2020). The association on multidecadal time scales between the Atlantic Multidecadal Oscillation or Atlantic Multidecadal Variability (AMV) and Atlantic hurricane activity in part exists because of their common relationship to the West African monsoon (Bell and Chelliah 2006).

The West African monsoon was well above average as a whole, with a northward displacement of the core of highest precipitation during ASO, as indicated by the negative outgoing longwave radiation (OLR) anomalies reaching to north of 20°N, outside the typical monsoon region (red box, Fig. 4.25a). East of 10°E, cloudiness was dramatically enhanced (Fig. 4.25a). The OLR time series shows that an enhanced monsoon has largely prevailed throughout the current Atlantic high-activity era and warm AMV of 1995–present (Fig. 4.25b), with a 2024 value of 240.5 W m^{-2}. This value would be even lower were it not for the northward displacement outside the averaging area. By contrast, a much weaker monsoon with OLR values well above 240 W m^{-2} in the Sahel region was typical of the low-activity era and cool AMV period of the 1980s and early 1990s. Precipitation across the Sahel was well above normal (NOAA 2024), further indicating an extremely strong West African monsoon.

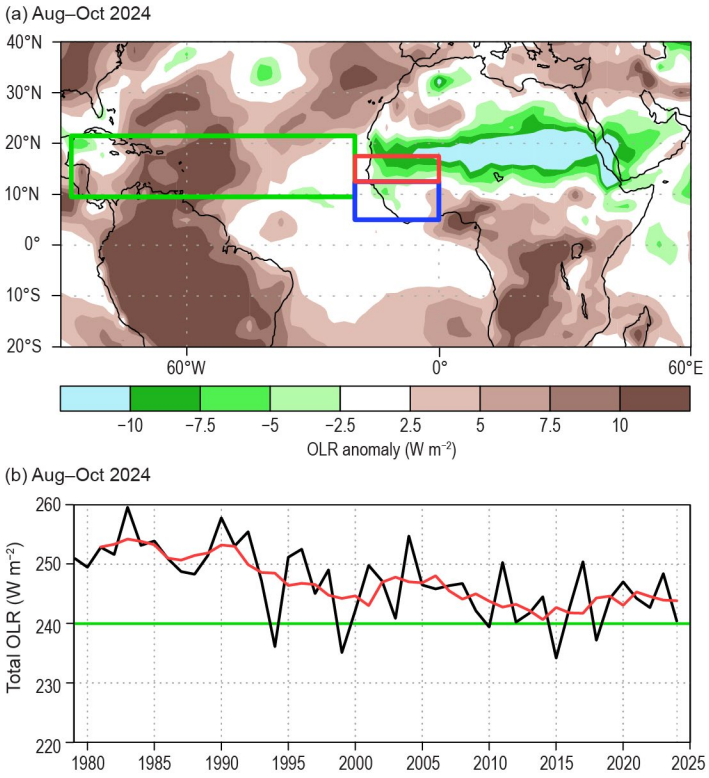

Fig. 4.25. (a) Aug–Oct 2024 anomalous outgoing longwave radiation (OLR; W m^{-2}), with negative (positive) values indicating enhanced (suppressed) convection. The green box denotes the Atlantic main development region. Anomalies are departures from the 1991–2020 means. (b) Time series of Aug–Oct total OLR (W m^{-2}; black), five-point running mean of the time series (red) averaged over the African Sahel region (red box in [a] spanning 12.5°N–17.5°N and 20°W–0°). The green line represents the threshold for deep convection (240 W m^{-2}). (Source: [Liebmann and Smith 1996] for OLR.)

Despite a robust and locally record-setting monsoon, the 200-hPa velocity potential anomalies (not shown) do not indicate enhanced divergence aloft. Streamflow anomalies at 200-hPa indicate anti-cyclonic flow over the Bahamas. Analysis of ASO 700-hPa–225-hPa layer average winds (Fig. 4.26a) also show the presence of an anomalous ridge, potentially contributing to the lack of storms developing near the Greater Antilles and the lack of a cluster of storm tracks through that region.

The 2024 ASO 200-hPa–to–850-hPa vertical wind shear was below average for much of the MDR and slightly above average for the Gulf of America/Gulf of Mexico (Fig. 4.26b). The area-averaged magnitude of the vertical wind shear for the entire MDR was 5.1 m s^{-1} (Fig. 4.26c) and for the Gulf of America/Gulf of Mexico was 10.8 m s^{-1} (Fig. 4.26d). The 200-hPa–850-hPa vertical wind shear over the MDR was the lowest on record since 1950, while over the Gulf of America/Gulf of Mexico the value was above the upper threshold of 10 m s^{-1} considered conducive to hurricane formation on monthly time scales (Bell et al. 2017). Note that the MDR shows strong multidecadal variability in vertical wind shear, which is correlated with multidecadal fluctuations in TC activity, whereas there is no such variability in the Gulf of America/Gulf of Mexico (Figs. 4.26c,d; Goldenberg et al. 2001). The vertical wind shear was highly variable during the season. Beryl developed in a pocket of low wind shear during July, which was followed by

Unauthenticated | Downloaded 11/21/25 11:34 AM UTC

increased vertical wind shear across the Caribbean during September, only to return to record-low levels during October and November. Hurricanes Francine and Milton also developed and intensified in small pockets of low wind shear above areas of very warm SSTs.

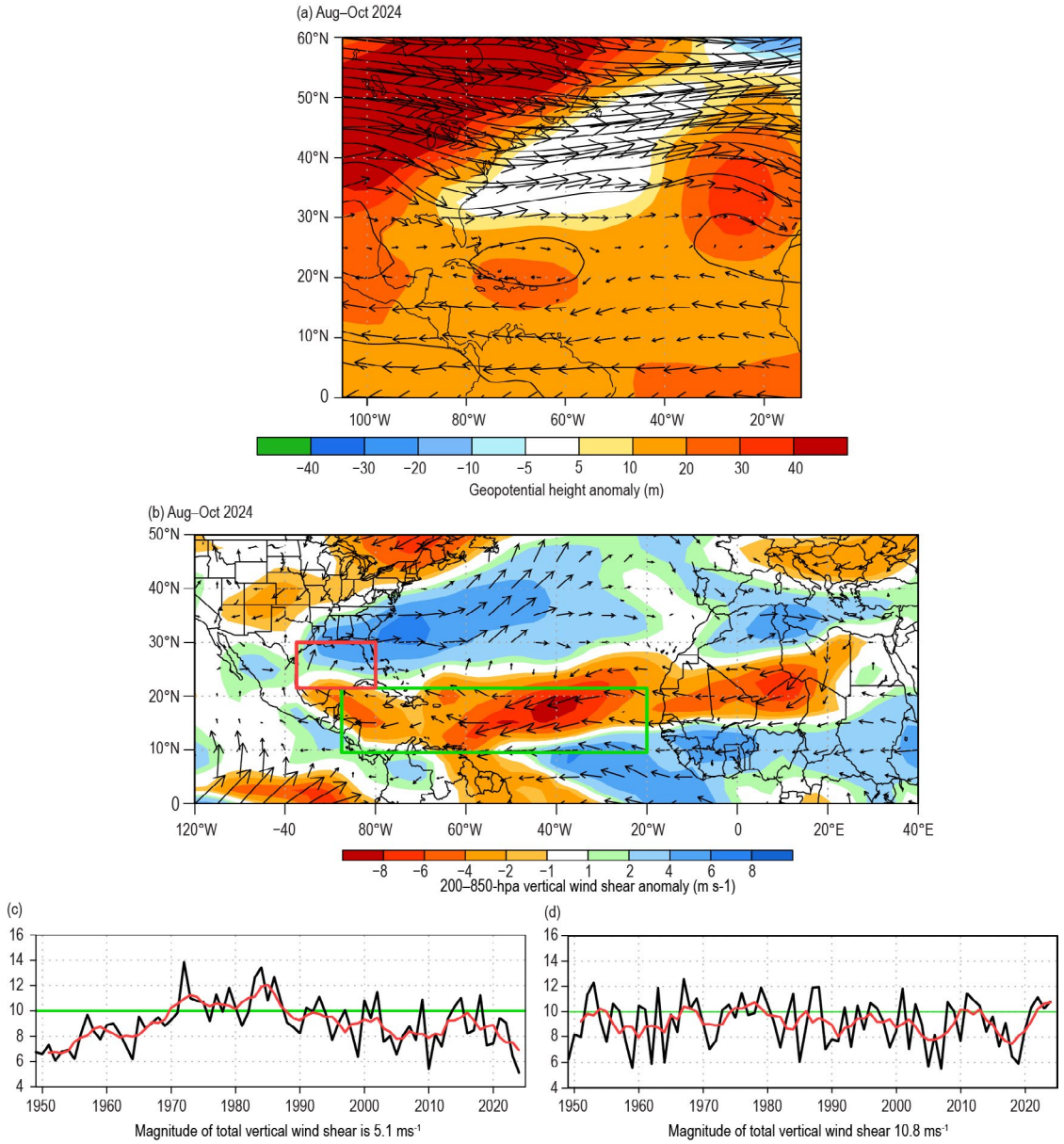

Fig. 4.26. (a) Aug–Oct 500-hPa geopotential heights (contours, interval is 30 gpm) and anomalies (shaded) with 700-hPa–225-hPa layer mean winds (m s^{-1}, vector); (b) Aug–Oct (ASO) magnitude of the 200-hPa–850-hPa vertical wind shear (m s^{-1}): 2024 anomalous magnitude and vector, and (c),(d) time series of ASO vertical shear magnitude (black) and five-point running mean of the time series (red) averaged over (c) the main development region (MDR; spanning 10°N–21.5°N and 85°W–20°W; green box) and (d) the western Gulf of America/Gulf of Mexico (spanning 21.5°N–30°N and 97.5°W–80°W; red box). Anomalies are departures from the 1991–2020 means. (Source: National Centers for Environmental Prediction [NCEP] National Center for Atmospheric Research [NCAR] reanalysis [Kalnay et al. 1996].)

(v) Unique aspects of the 2024 Atlantic hurricane season

A defining feature of the 2024 North Atlantic hurricane season was the distinct alternating periods of activity and inactivity, with record activity in early July, an active November, and a distinct mid-season minimum. Hurricane Beryl developed at the end of June over extremely warm SSTs and in an area with low vertical wind shear (Fig. 4.27a), setting a record for the strongest hurricane ever at the start of the season. Beryl contributed the largest amount of ACE for any named storm of 2024. After Beryl, Hurricanes Debby and Ernesto developed in early and mid-August, respectively. From 20 August to 9 September, there was no activity in the Atlantic,

Unauthenticated | Downloaded 11/21/25 11:34 AM UTC

which climatologically is one of the busiest periods for Atlantic hurricane activity. The Atlantic season peaks on average on 10 September (Landsea and Franklin 2013). The lull relaxed somewhat with Hurricane Francine (9–12 September) and Tropical Storm Gordon (11–17 September), but the activity was still below normal for the peak of the season. This lull was followed by continuous activity from 24 September to 12 October, with activity after 24 September (including four major hurricanes, of which two reached Category 4 and one reached Category 5 strength; Fig. 4.23a)—the highest amount of activity for that period on record, according to the HURDAT2 dataset. Additionally, activity into November was well above the climatological normals. The 200-hPa–850-hPa vertical wind shear was record low during each of those months, most likely contributing to an active latter portion of the season.

There are many climate forcings that may have contributed to the lull in activity from the latter half of August through the first part of September, which included the climatological peak of the season. One potential contributing factor was the extreme nature of the West African monsoon, which resulted in African easterly waves being either weak or moving off the west coast of Africa too far to the north and over cooler waters (Fig. 4.25a). Additionally, the 300-hPa temperatures were well above normal (Fig. 4.27b), a frequent occurrence with El Niño that persists for several months after the El Niño weakens (Hogikyan et al. 2022). The 300-hPa temperatures over the Atlantic had been above normal since the second half of 2023, likely driven by a strong El Niño. The increased atmospheric temperatures resulted in increased vertical stability and may have also mitigated the impacts of the anomalously warm SSTs resulting in the unusual lull in activity.

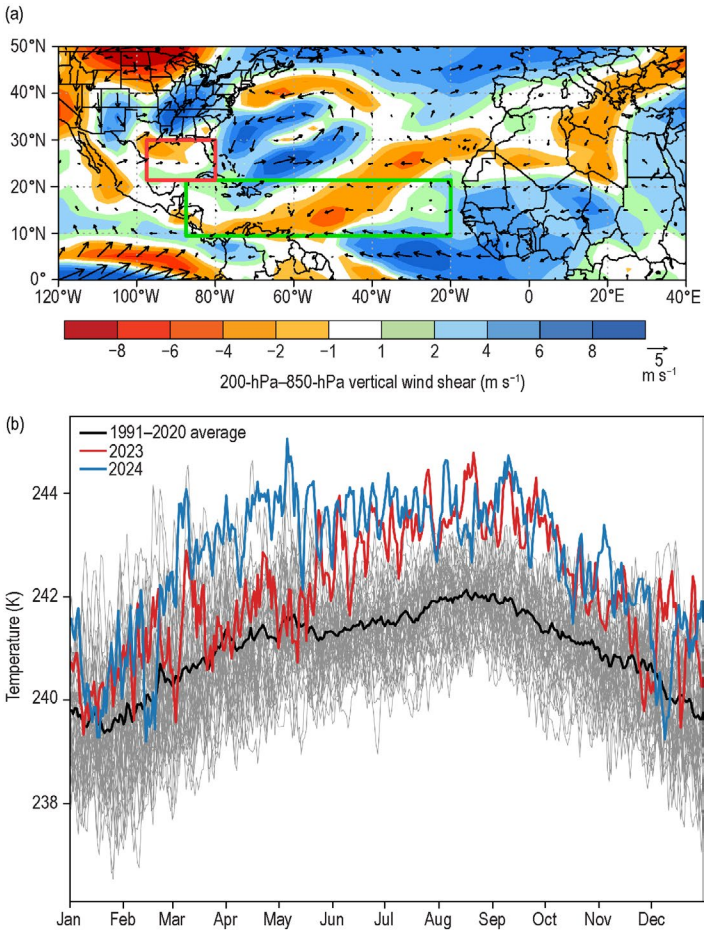

Fig. 4.27. (a) Jul 2024 anomalous magnitude and vector of the 200-hPa–850-hPa vertical wind shear (m s⁻¹). (b) Daily 300-hPa temperatures (K) for over the tropical Atlantic (10°N–20°N, 60°W–20°W). The thick black line depicts the 1991–2020 long-term average. Thin gray lines correspond with individual years from 1982 through 2022. The year 2023 is plotted in red, and 2024 is plotted in blue. Anomalies are departures from the 1991–2020 means. (Source: National Centers for Environmental Prediction [NCEP] National Center for Atmospheric Research [NCAR] reanalysis [Kalnay et al. 1996].)

3. EASTERN NORTH PACIFIC AND CENTRAL NORTH PACIFIC BASINS

—K. M. Wood and C. J. Schreck

(i) Seasonal activity

Numbers reported in this section are combined from the two agencies responsible for issuing advisories and warnings in the eastern North Pacific (ENP) basin: NOAA's National Hurricane Center in Miami, Florida (spanning the Pacific Coast of North America to 140°W), and NOAA's Central Pacific Hurricane Center in Honolulu, Hawaii (spanning 140°W and the dateline, the Central North Pacific [CNP]).

A total of 13 named storms formed within the combined ENP/CNP basin in 2024; 5 of these became hurricanes, of which 3 became major hurricanes thereafter (Fig. 4.28a). All three categories were below normal compared with the 1991–2020 averages of 16.9 named storms, 8.8 hurricanes, and 4.6 major hurricanes. All TCs occurred between the official ENP hurricane season start date of 15 May 2024 and end date of 30 November 2024. The first named storm of the season, Tropical Storm Aletta, marked the latest first formation on record (4 July), breaking the

Unauthenticated | Downloaded 11/21/25 11:34 AM UTC

previous record held by Tropical Storm Agatha in 2016 (2 July). The final named storm, Tropical Storm Lane, weakened to a tropical depression on 3 November. One named storm developed within the CNP (Hurricane Hone) and one ENP TC crossed 140°W (Hurricane Gilma); 2 active TCs in this region is below the 1991–2020 average of 3.4 for the CNP.

The 2024 seasonal ACE index was 82.5×10^4 kt^2, or 62% of the 1991–2020 mean of 132.8×10^4 kt^2 (Fig. 4.28b; Bell et al. 2000), a below-normal value that was approximately half of the activity produced in 2023 (Wood and Schreck 2024). The three TCs that achieved major hurricane intensity, or a maximum sustained wind speed of greater than 96 kt (49 m s^{-1}), produced 66% of the season's ACE (Gilma, John, Kristy). After a late start with the formation of Aletta, TC activity was sporadic throughout the season (Fig. 4.28c). Early August produced one hurricane (Carlotta) and three tropical storms (Daniel, Emilia, Fabio) that overlapped in time, leading to higher daily ACE values. Later in August, Hurricane Gilma lasted over a week and reached Category 4 intensity on the SSHWS. In September, Hurricane John underwent rapid intensification prior to making landfall in Mexico. Finally, in late October, Hurricane Kristy peaked with an intensity of 140 kt (72 m s^{-1}), making it a Category 5 hurricane. On a monthly basis, July ACE comprised 2.2% of the season's total (average is 21.5%), August ACE was 61.5% (average is 29.5%), September ACE was 9.5% (average is 23.8%), and October ACE was 26.1% (average is 12.7%).

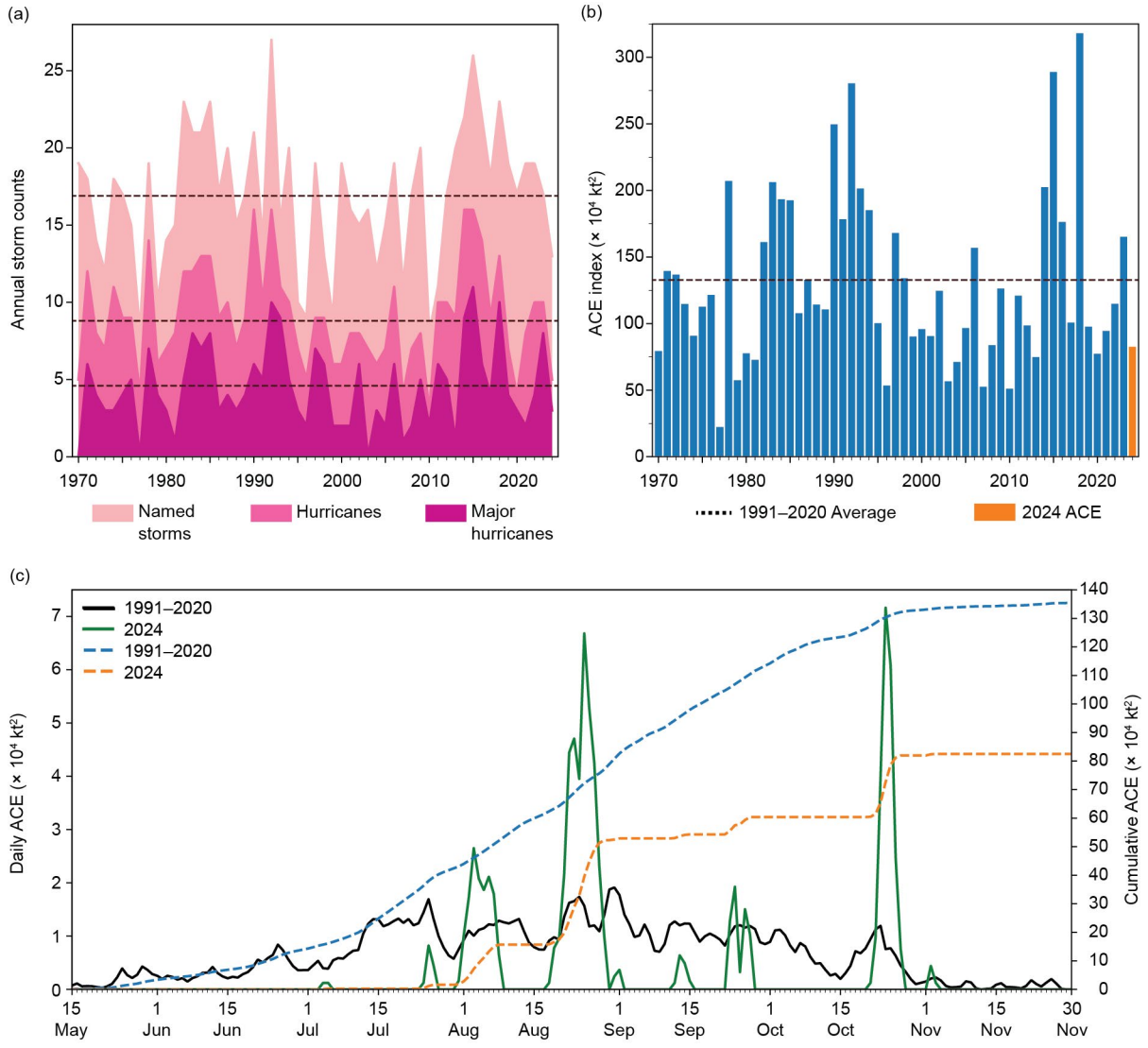

Fig. 4.28. (a) Annual eastern North Pacific and central North Pacific storm counts by category during the period 1970–2024, with the 1991–2020 average by category denoted by dashed lines. (b) Annual accumulated cyclone energy (ACE; × 10⁴ kt²) during 1970–2024, with 2024 highlighted in orange and the 1991–2020 average denoted by the dashed line. (c) Daily ACE for the 1991–2020 average (solid black) and during 2024 (solid green); accumulated daily ACE for the 1991–2020 average (dashed blue) and during 2024 (dashed orange).

Unauthenticated | Downloaded 11/21/25 11:34 AM UTC

(ii) Environmental influences on the 2024 season

Although negative SST anomalies related to a developing La Niña event characterized the equatorial eastern Pacific during the 2024 ENP hurricane season, near- or above-average SST anomalies dominated much of the North Pacific, including along the tracks of the TCs that developed (Fig. 4.29a). Wind shear was also near or below normal in the region where most TCs formed (Fig. 4.29c). However, above-normal OLR persisted across the basin (Fig. 4.29b), indicating suppressed convection and associated sinking air that likely contributed to the below-average activity in the ENP during 2024. The low-level easterly anomalies (Fig. 4.29d) were consistent with La Niña and likely suppressed TC activity by reducing the background cyclonic vorticity and the growth of easterly waves over the eastern Pacific (Maloney and Hartmann 2001; Aiyyer and Molinari 2008).

The formation and lifecycle of ENP TCs can be influenced by intraseasonal tropical variability such as the Madden–Julian Oscillation (MJO) and convectively-coupled equatorial Kelvin waves (e.g., Maloney and Hartmann 2001; Aiyyer and Molinari 2008; Schreck and Molinari 2011; Ventrice et al. 2012a,b; Schreck 2015, 2016). A strong MJO signal was present in late May and early June but did not result in ENP TC activity; instead, short-lived Aletta appeared to develop during the suppressed phase of the MJO, an event potentially related to the passage of an easterly wave (Fig. 4.30). Kristy was the only TC that appeared to form during an active MJO phase in 2024. Instead, easterly waves (red contours) at times coinciding with Kelvin waves appeared to contribute to the formation of many ENP TCs.

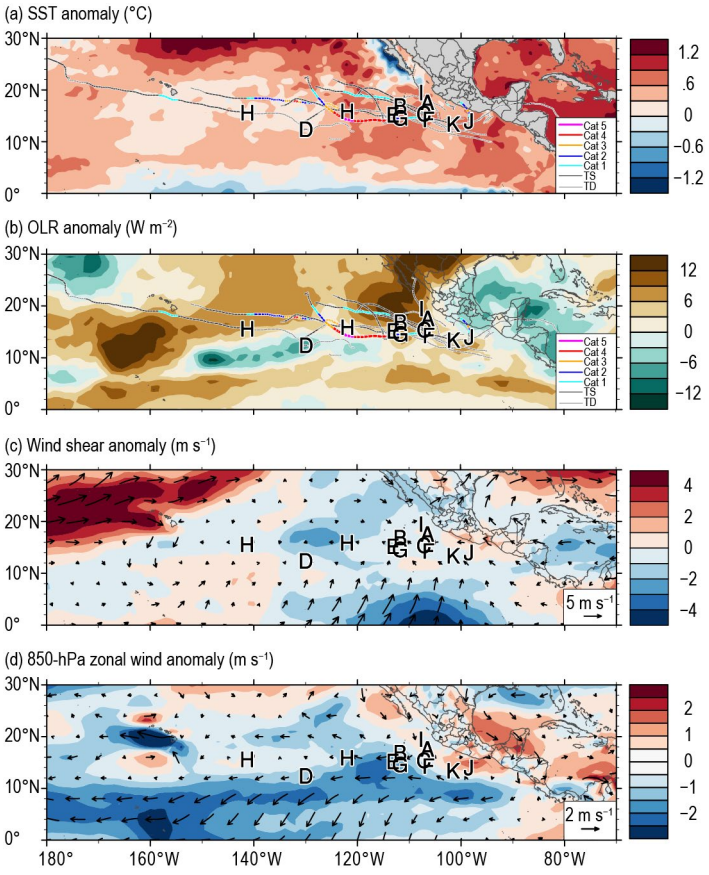

Fig. 4.29. 1 Jul–31 Oct 2024 anomaly maps of (a) sea surface temperature (SST; ºC; Banzon and Reynolds 2013), (b) outgoing longwave radiation (OLR; W m^{-2}; Schreck et al. 2018), (c) 200-hPa–850-hPa vertical wind shear (m s^{-1}) vector (arrows) and scalar (shading) anomalies, and (d) 850-hPa wind (m s^{-1}, arrows) and zonal wind (shading) anomalies. Anomalies are relative to the annual cycle from 1991–2020. Letters denote where each TC attained tropical storm intensity. Wind data are obtained from CFSR (Saha et al. 2014).

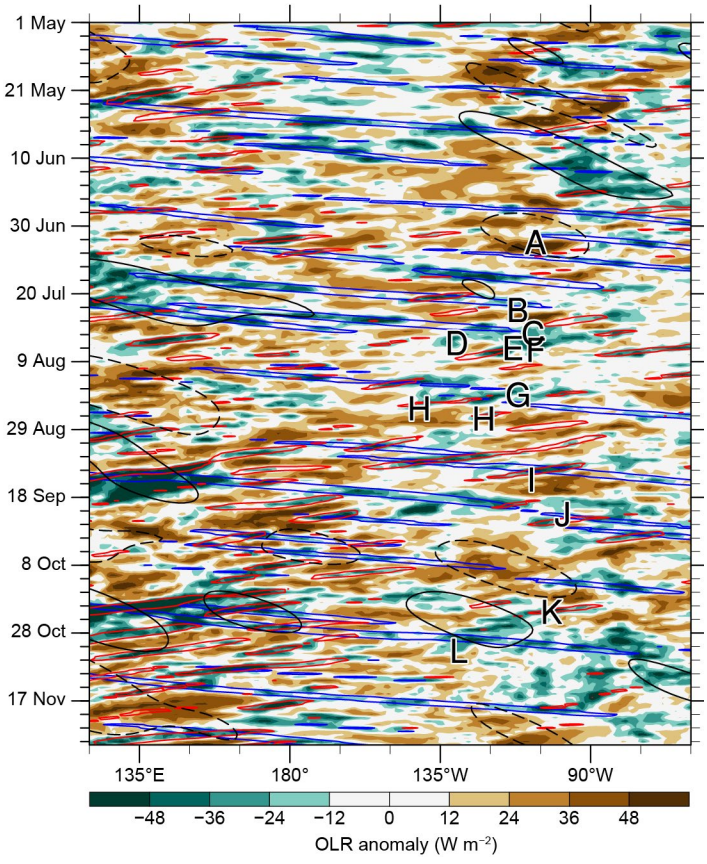

Fig. 4.30. Longitude–time Hovmöller diagram of 5°N–15°N average outgoing longwave radiation (W m^{-2}; Schreck et al. 2018). Unfiltered anomalies from a daily climatology are shaded. Negative anomalies (green) indicate enhanced convection. Anomalies filtered for Kelvin waves are contoured in blue at –12 W m^{-2}, easterly wave-filtered anomalies in red at –18 W m^{-2}, and Madden–Julian Oscillation-filtered anomalies in black at ±12 W m^{-2} (dashed for positive, solid for negative). Letters denote the longitude and time when each tropical cyclone first attained tropical storm intensity.

Unauthenticated | Downloaded 11/21/25 11:34 AM UTC

(iii) Notable ENP TCs and impacts in 2024

Although September produced less than 10% of the season's activity by ACE, both landfalling (or near-landfalling in the case of Ileana) TCs occurred during this month: Tropical Storm Ileana and Hurricane John. This frequency is about the same as the long-term average for Mexico, which is 1.8 TCs per year (Raga et al. 2013). The 2024 season breaks the three-year streak of above-average landfalling TC activity that occurred during 2021–23 (Wood and Schreck 2022, 2023, 2024).

Note that post-season analysis revealed that Ileana's center remained over water in the Gulf of California; while the storm did not technically make landfall, it produced gusts in excess of 40 kt (20.5 m s^{-1}) and up to 240 mm of rain—conditions that resulted in flooding, mudslides, and power outages (Berg 2024). Conversely, John rapidly intensified by an estimated 45 kt (23 m s^{-1}) in 12 hours from strong-tropical-storm to Category 3-hurricane strength before making landfall in the Mexican state of Guerrero. Heavy rain of at least 500 mm, with some estimates exceeding 950 mm, alongside strong winds produced widespread damage estimated around $2.45 billion (U.S. dollars; Gallagher Re 2025) and at least 29 deaths. Notably, John impacted a similar region to that of Category 5 Hurricane Otis in 2023, less than one year after the latter hit (Wood and Schreck 2024; Klotzbach et al. 2024) and caused damages of up to $16 billion (U.S. dollars; Reinhart and Reinhart 2024); the damage caused by Otis exacerbated John's effects on landscapes and infrastructure. In addition to the landfalling TCs, Tropical Storm Eleven-E produced heavy rainfall in southern Mexico, the remnants of Gilma affected Hawaii, and Hurricane Hone produced heavy rainfall on the Big Island of Hawaii while passing to its south.

As is becoming typical in the ENP, all three major hurricanes in 2024 exceeded the rapid intensification threshold of at least 30 kt (15.4 m s^{-1}) in 24 hours. Hurricanes John and Kristy reached a peak 24-hour intensification change of 65 kt (33 m s^{-1}). Hurricane Gilma was not as explosive, but did intensify by 40 kt (20.5 m s^{-1}) in 24 hours. The two major hurricanes that did not make landfall (Gilma and Kristy) also underwent at least one rapid weakening period while over open ocean (≤–30 kt or –15.4 m s^{-1} in 24 hours; Wood and Ritchie 2015), with a peak decrease of –50 kt for Gilma and –45 kt for Kristy.

4. WESTERN NORTH PACIFIC BASIN

—S. J. Camargo

(i) Overview

There were 23 tropical cyclones in the western North Pacific in 2024 (bottom quartile <23), continuing the trend of a below-normal number of systems in the basin since 2020. Figure 4.31 compares the activity for 2024 as identified by both the Joint Typhoon Warning Center (JTWC) and the Japan Meteorological Agency (JMA) with their climatologies for 1991–2020. Fifteen of the 23 storms reached typhoon intensity (median: 16), but only one reached super typhoon status (≥130 kt; bottom quartile <3). There were a large number of typhoons (eight) that were close to the super typhoon threshold, reaching Category 4 on the SSHWS. Overall, 65% of the tropical storms intensified into typhoons (median: 64%), while only 7% of the typhoons reached super typhoon status (bottom quartile <17%). There were also five tropical depressions in the basin. Furthermore, Hurricane Hone, which formed in the eastern North Pacific and reached maximum intensity in the central North Pacific, briefly crossed into the western North Pacific (WNP) as a tropical depression. Figure 4.31a shows the number of tropical storms and typhoons identified by the JTWC for the period 1945–2024.

There were 26 TCs recorded by JMA (median: 25.5), including 10 tropical storms (TSs; top quartile >8), three severe tropical storms (bottom quartile: <4), and 13 typhoons (median: 13.5), with 50% of the storms reaching typhoon intensity (median: 55%). As in previous years, there were differences between the JTWC and JMA storm counts, intensities and categories. Maliski, Wukong, Soulik, and Pabuk were considered tropical depressions by the JTWC and tropical storms by the JMA; Tropical Storms Prapiroon and Trami and Typhoon Maria were labeled severe tropical storms by the JMA, and Pulasan was considered to be a typhoon by the JTWC and a tropical storm by the JMA. The number of all TCs (1951–1976) and tropical storms, severe tropical storms, and typhoons (1977–2024) according to the JMA are shown in Fig. 4.31b. The Philippine

Unauthenticated | Downloaded 11/21/25 11:34 AM UTC

Atmospheric, Geophysical and Astronomical Services Administration (PAGASA) named 17 TCs that entered its area of responsibility, including Tropical Depression Querubin (17–19 December), which was not numbered or named by either the JMA or the JTWC.

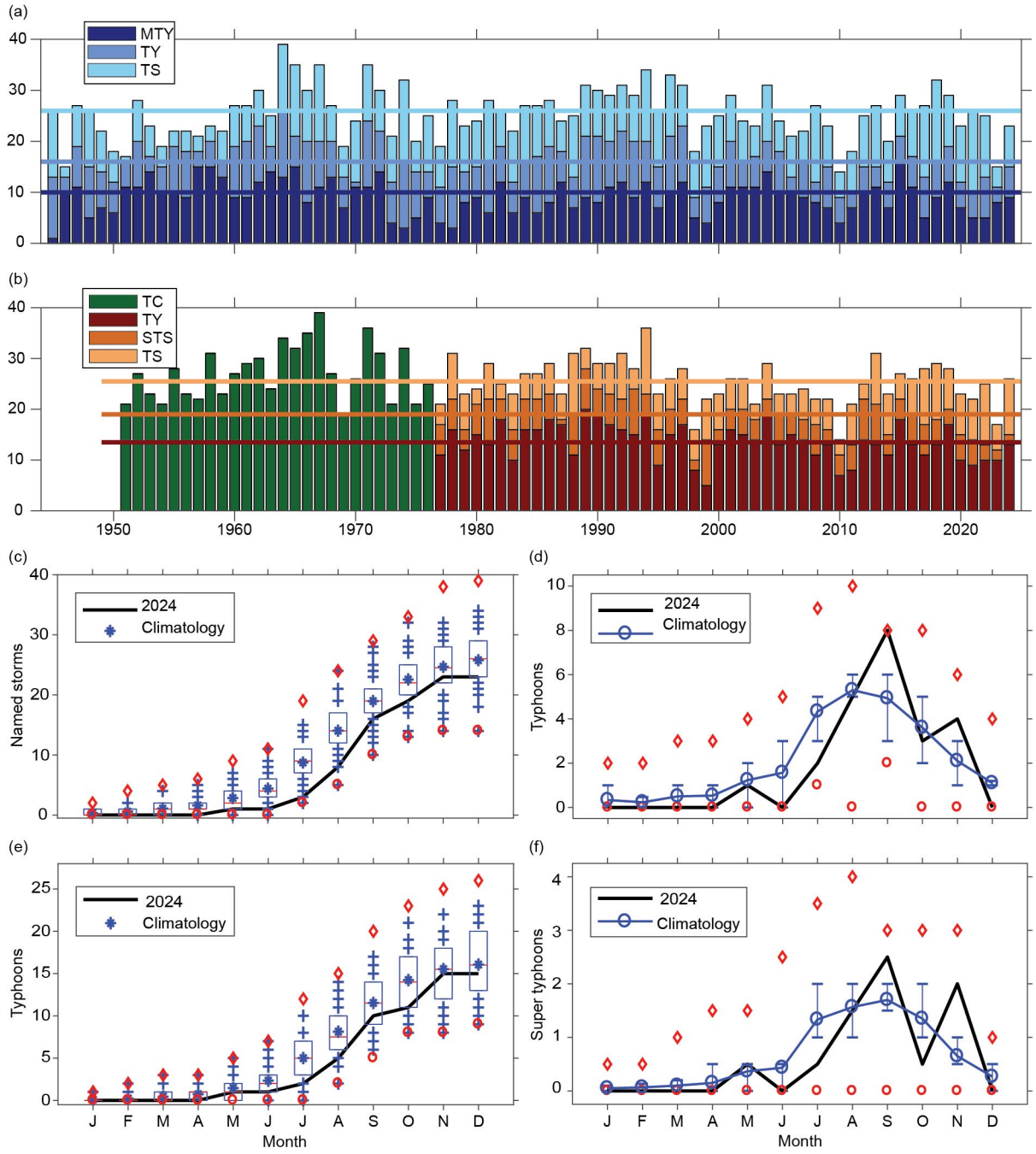

Fig. 4.31. (a) Number of tropical storms (TS), typhoons (TY), and major typhoons (MTY ≥96 kt) per year in the western North Pacific (WNP) for the period 1945–2024 based on the Joint Typhoon Warning Center (JTWC). (b) Number of tropical cyclones (TCs; all storms that reach TS intensity or higher) from 1951 to 1976; number of TS, severe tropical storms (STS) and TY from 1977 to 2024 based on the Japan Meteorological Agency (JMA). (c) Cumulative number of tropical cyclones with TS intensity or higher (named storms) per month in the WNP in 2024 (black line), and climatology (1991–2020) as box plots (interquartile range: box, median: red line, mean: blue asterisk, values in the top or bottom quartile: blue crosses, high [low] records in the 1945–2023 period: red diamonds [circles]). (e) As in (c) but for the number of typhoons. (d),(f) Number of tropical cyclones and typhoons per month in 2024 (black line) and the climatological mean (blue line); the red diamonds and circles denote the maximum and minimum monthly historical records, and the blue error bars show the climatological interquartile range for each month (in the case of no error bars, the upper and/or lower percentiles coincide with the median). (Sources: 1945–2023 JTWC best-track dataset, 2024 JTWC preliminary operational track data for panels [a], [c], [d], [e], and [f]. 1951–2024 Regional Specialized Meteorological Center–Tokyo, JMA best-track dataset for panel [b].)

Unauthenticated | Downloaded 11/21/25 11:34 AM UTC

(ii) Seasonal activity

Similar to 2023, the 2024 typhoon season had a late start. The first storm of the season to develop was Typhoon Ewiniar in late May (24–31 May), followed by Tropical Depression Maliski (31 May–1 June). No storms occurred in June. Therefore, the early season (January–June) had a total of two TCs (bottom quartile <3) with only one reaching typhoon intensity (bottom quartile <1). This was the 15th year in the historical record (1945–2024) with no TC activity in the month of June. The cumulative monthly number of TCs and typhoons for 2024 are shown in Figs. 4.31c,e, respectively, with the number of TCs and typhoons per month displayed in Figs. 4.31d,f. In Figs. 4.31c–f, the 2024 values are compared with the respective climatological values as well as the historical maxima and minima.

One tropical depression and three tropical storms were active in July, including Category 4 Typhoon Gaemi (19–25 July), marking another low-activity month (bottom quartile: TCs <3, typhoons <2). In August, the seasonal activity was close to normal, with the occurrence of one tropical depression (Wukong; 13–15 August) and five TCs (median: 5) including three typhoons (median: 3). The most active month of the 2024 season was September with a total of nine storms forming in the basin, including Tropical Depression Soulik (18–19 September) and eight TCs (top quartile >6). Additionally, Hurricane Hone, which formed in the eastern North Pacific and reached maximum intensity in the central North Pacific, crossed into the western North Pacific as a tropical depression in early September. Of the eight TCs, three were tropical storms and five were typhoons (top quartile >4), including Typhoons Yagi and Krathon that reached Category 4 intensity. Three TCs (median: 3) were present in October, including one typhoon (bottom quartile <2), Kong-Rey, that also reached Category 4 intensity. The peak typhoon season (July–October) was close to normal, with a total of 18 TCs (median: 18), including 10 typhoons (median: 11.5), though none reached super typhoon status (bottom quartile <2).

November was active, with the presence of four typhoons (top quartile >2). Typhoons Yinxing and Usagi reached Category 4 intensity, and Man-Yi reached Category 5 intensity, making it the only super typhoon in the 2024 season. The season ended with Tropical Depression Pabuk (22–26 December). The late typhoon season (November and December) was therefore active, with four TCs (top quartile >4) reaching typhoon intensity (top quartile >2), one of which became a super typhoon (top quartile >1).

In summary, while the total number of TCs in 2024 (23) was below normal—with low-level activity in the early season and close-to-normal activity in the peak season—the high level of activity during September and November led to a total of major typhoons (9) that was only slightly below normal (median: 10). Of note is that all of the major typhoons reached either Category 4 (eight) or 5 (one) intensity.

The total ACE in 2024 (Fig. 4.32a) was below normal, at 92% of the value of the bottom quartile threshold, despite the occurrence of eight major typhoons. The ACE in 2024 was the 15th lowest of the 80 years in the historical record. Typically, low ACE values are associated with La Niña events (Camargo and Sobel

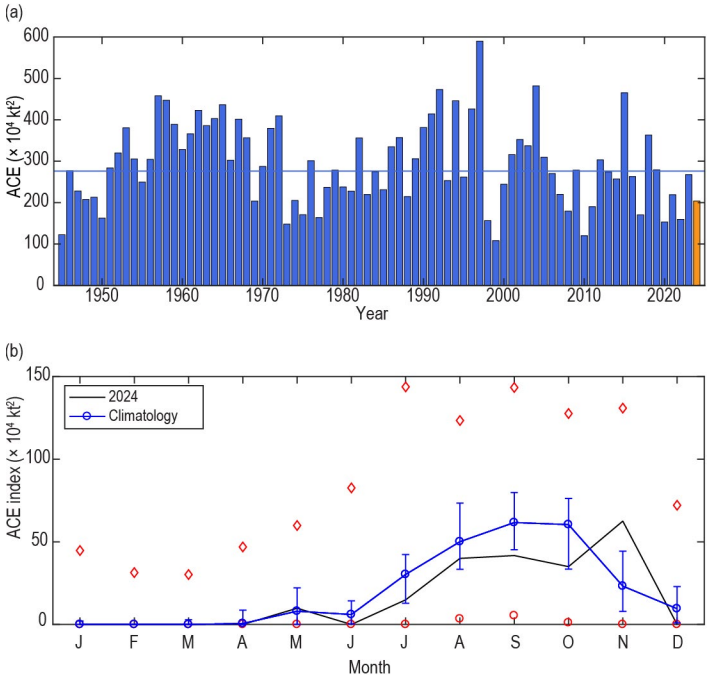

Fig. 4.32. (a) Accumulated cyclone energy (ACE; × 10⁴ kt²) per year in the western North Pacific for the period 1945–2024. The solid blue line indicates the median for the climatology (1991–2020). (b) ACE per month in 2024 (black line) and the median during 1991–2020 (blue line); the blue error bars indicate the climatological interquartile range. In the case of no error bars, the upper and/or lower percentiles coincide with the median. The red diamonds and circles denote the maximum and minimum values per month during the 1945–2023 period. (Source: 1945–2023 Joint Typhoon Warning Center [JTWC] best-track dataset, 2024 JTWC preliminary operational track data.)

Unauthenticated | Downloaded 11/21/25 11:34 AM UTC

2005), and the tropical atmospheric circulation could be described as La Niña-like starting in September 2024. ACE was zero in the months of January to April, June, and December. ACE was in the bottom quartile in September and below normal for July, August, and October (Fig. 4.32b). ACE was close to its median value in May and in the top quartile in November. The November ACE was the 10th highest in the historical record. ACE was in the bottom quartile in the early and peak seasons but in the top quartile in the late season, due to the high ACE value in November associated with the presence of two Category 4 typhoons (Yinxing and Usagi) and one Super Typhoon (Man-Yi). Climatologically, November represents 9.1% of the total seasonal ACE, but it was 30.7% in 2024. Only November 1954 had a higher contribution to the total seasonal ACE (42.8%).

In 2024, five typhoons had ACE values in the top quartile of ACE for individual storms' climatological distribution: Shanshan, Krathon, Man-Yi, Yagi, and Yinxing (listed from low to high ACE values). These five typhoons combined contributed 51% of the total seasonal ACE, with Yinxing contributing the most at 12%.

During La Niña events, typically the mean typhoon genesis location is shifted to the northwest part of the WNP basin (Chia and Ropelewski 2002; Camargo and Sobel 2005; Camargo et al. 2007a) and is associated with short tracks, weak storms, and low ACE values. The mean genesis position in 2024 was 18.3°N, 134.1°E, northwest of the climatological mean of 13.3°N, 140.5°E, with standard deviations of 1.9° and 7.7°, respectively. These values exclude Hurricane/Tropical Depression Hone, which formed in the eastern North Pacific. The mean genesis position in 2024 (see July–October [JASO] 2024 storms' genesis and track locations in Figs. 4.33a,b), displayed the typical northwest shift of La Niña events in the 1950–2023 period (mean La Niña genesis position of 14.8°N, 136.1°E), even though La Niña conditions only officially emerged during November–January 2024/25, according to NOAA's Climate Prediction Center (https://origin.cpc.ncep.noaa.gov/products/analysis_monitoring/ensostuff/ONI_v5.php). Similarly, the mean track position in 2024 (21.5°N, 132.0°E) was northwest of the mean climatological track position (17.8°N, 135.9°E, with standard deviations of 1.6° and 5.2°, respectively).

There were 82.75 days with active TCs in 2024 (bottom quartile <86 days). Of these, 40.75 days had typhoons (bottom quartile <42.75 days) and 18 days had major typhoons (Categories 3–5; median: 23 days). Overall, 38.9% of the active days had typhoons, which is slightly above the median of 36.6%. The median lifetime of TCs in 2024 was 6.25 days (bottom quartile <7 days), while that of typhoons was 6.5 days (bottom quartile <7.75 days); in other words, many short-lived storms occurred in 2024. Typhoon Shanshan had the longest lifetime (11.25 days), followed by Typhoon Man-Yi (10.75 days) and Typhoon Yinxin (9.25 days). Only Typhoons Shanshan and Man-Yi were in the top quartile of the lifetime climatological distribution (>10 days). During 11–13 November, there were four storms simultaneously active in the WNP: Typhoons Yinxin, Toraji, Man-Yi, and Usagi, the most in 2024 (historical record is six simultaneously active TCs, which occurred in August 1996).

(iii) Environmental conditions

The 2023/24 strong El Niño event weakened through March–May 2024, with ENSO-neutral conditions until the end of 2024, when La Niña conditions developed. Nevertheless, the tropical atmospheric circulation had La Niña characteristics starting in September. Figure 4.33 shows the environmental conditions and tracks during the peak typhoon season (JASO) in 2024. The SST anomalies (Fig. 4.33a) were slightly above normal in most of the tropics and strongly positive near the coast of Asia near Japan and Korea and in a zonal band centered around 40°N extending eastward. The typhoon tracks were concentrated near Asia, with multiple tracks during the JASO period passing between the northern Philippines and Taiwan, as well as affecting the region with high SSTs close to Japan and Korea.

The genesis potential index (Fig. 4.33b; Emanuel and Nolan 2004; Camargo et al. 2007b) expresses the enhanced or reduced probability of TC formation through a nonlinear empirical combination of environmental factors known to affect TC genesis. There was a region of positive genesis potential anomalies in the western part of the basin, with a maximum between the Philippines and Taiwan, extending to 30°N, with weaker anomalies west of Japan. The typhoon genesis locations occurred at or close to the positive anomalies in the region.

Unauthenticated | Downloaded 11/21/25 11:34 AM UTC

The potential intensity anomalies (Fig. 4.33c; Emanuel 1988) are similar to the SST pattern, with positive anomalies in a zonal band near 30°N–40°N around Korea and Japan extending towards the central Pacific. The relative humidity anomalies were dry in the eastern part of the basin with positive anomalies near the Philippines, Taiwan, and east of Japan. The monsoon trough, which is defined by 850-hPa zonal winds anomalies (Fig. 4.33e), tends to be restricted to the western part of the basin during La Niña events. This was the case in 2024, with the edge of the monsoon trough close to the Philippines. These environmental conditions help explain the low level of activity in JASO 2024, as only a small area in the western North Pacific had environmental conditions conducive for genesis formation. This region of high SSTs, potential intensity, and mid-level relative humidity during the peak typhoon season helped explain the shift of the genesis and tracks northward and towards the Asian continent, as well as the high number of typhoons affecting the Philippines. An active MJO over the region contributed to the high level of TC activity in September and November. A few recent papers related the decrease in TC activity in the WNP in the last few years to decadal variability (e.g., Zhao et al. 2018, 2020; Chan and Liu 2022).

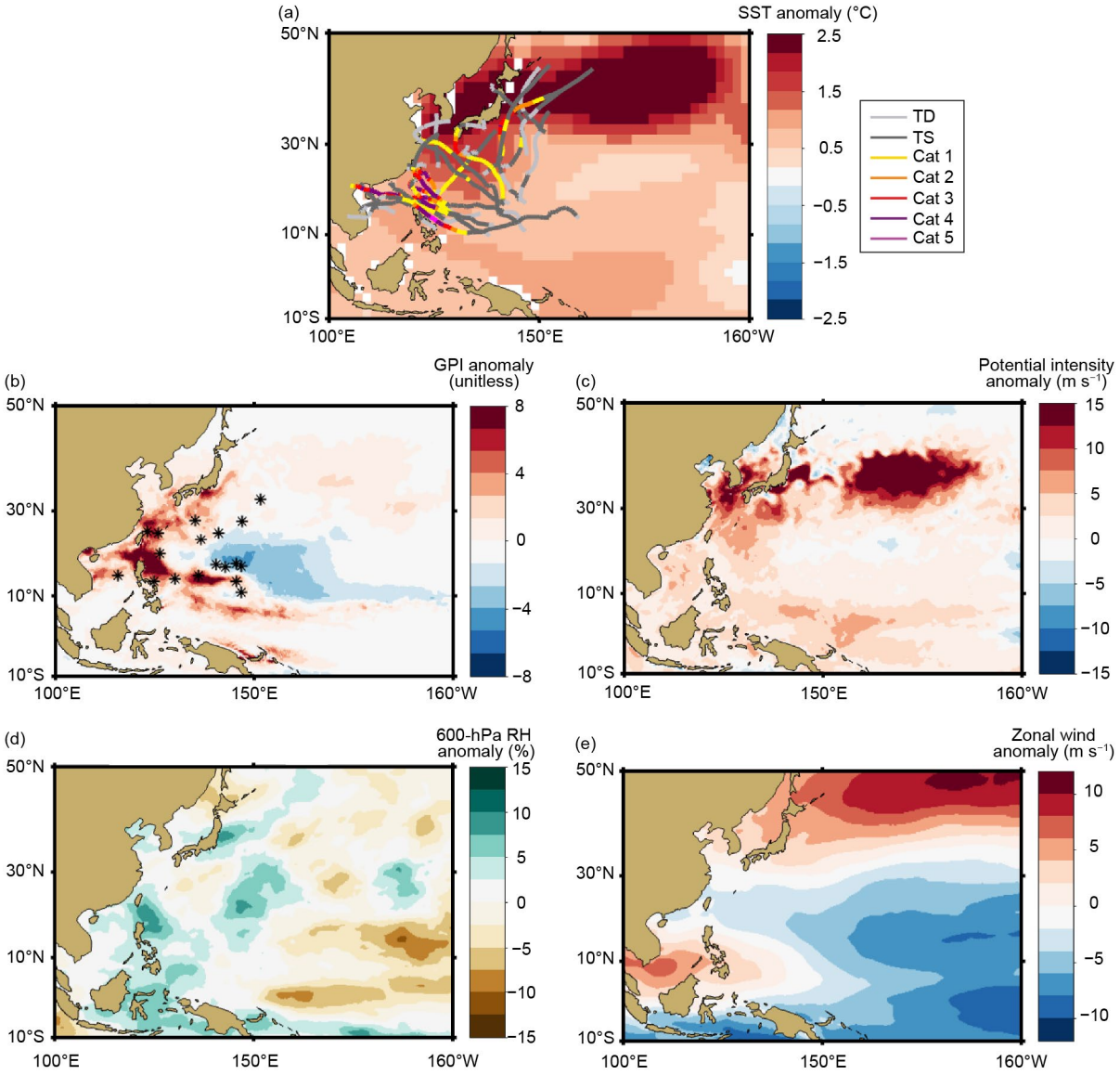

Fig. 4.33. Jul–Oct (JASO) 2024: (a) Sea surface temperature (SST) anomalies (°C) and the tracks of JASO 2024 storms (including tropical depressions [TD], tropical storms [TS], and typhoon-strength storms [Cat]), with colors denoting their intensity, (b) genesis potential index anomalies and first position of JASO 2024 storms marked with an asterisk, (c) potential intensity anomalies (m s^{-1}), (d) 600-hPa relative humidity anomalies (%), and (e) 850-hPa zonal wind anomalies (m s^{-1}). (Data sources: SST: ERSSTv5 [Huang et al. 2017]; other environmental fields: ERA5 reanalysis [Hersbach et al. 2020]; tracks and first position: Joint Typhoon Warning Center preliminary operational track data.)

Unauthenticated | Downloaded 11/21/25 11:34 AM UTC

(iv) Impacts

Nineteen storms (including tropical depressions) made landfall in the western North Pacific (median: 17.5, climatology 1951–2000). Four of these storms made landfall as tropical depressions (median: 3), five as tropical storms (median: 7), four as typhoons (median: 4), and six as major typhoons (Category 3 or higher, top quartile >6). Here, landfalls are defined as instances when the center of a storm that is over the ocean moves over land. The observed TC tracks were interpolated into 15-minute intervals. A high-resolution land mask was used to determine the occurrence of landfall. In cases of multiple landfalls, only the highest-intensity landfall event for each storm was considered.

The Philippines was affected by six storms between late October and mid-November. First, Tropical Storm Trami caused flooding and landslides, and was then followed by Category 4 Typhoons Kong-Rey and Yingxing, Typhoon Toraji, Super Typhoon Man-Yi, and Category 4 Typhoon Usagi, which collectively affected more than 13 million people and caused a total of 160 reported deaths, 135 injuries, and 21 missing persons, according to Relief Web. The most intense storm to make landfall in the northern Philippines, Super Typhoon Man-Yi, killed 14 people and left two missing in the Philippines, according to their National Disaster Risk Reduction Management Council. These successive typhoons brought heavy precipitation, floods, landslides, and storm surge to the Philippines. The impacts required substantial governmental and international assistance to the country. By late January 2025, 12,700 people were still displaced, with 39,800 houses totally destroyed and 373,000 partially damaged.

5. NORTH INDIAN OCEAN BASIN

—J. Uehling and C. J. Schreck

(i) Seasonal activity

The North Indian Ocean (NIO) TC season typically occurs between April and December and sees two peaks of activity, May–June and October–December, due to the presence of the monsoon trough over tropical waters of the NIO during these periods. TC genesis typically occurs in the Arabian Sea and the Bay of Bengal between 8°N and 15°N. On average, the Bay of Bengal experiences four times more TCs than the Arabian Sea (Dube et al. 1997).

The 2024 NIO TC season had four named storms according to JTWC, which was below the IBTrACS–JTWC 1991–2020 climatology of 5.4. One storm formed in the Arabian Sea and three formed in the Bay of Bengal. One storm reached cyclone strength and none reached major cyclone strength. These values were below the climatological average of 2.1 cyclones and 1.1 major cyclones (Fig. 4.34). The 2024 seasonal ACE index (January–December) of 7.4 × 10^4 kt^2 was less than a third of the 1991–2020 mean of 24.6 × 10^4 kt^2.

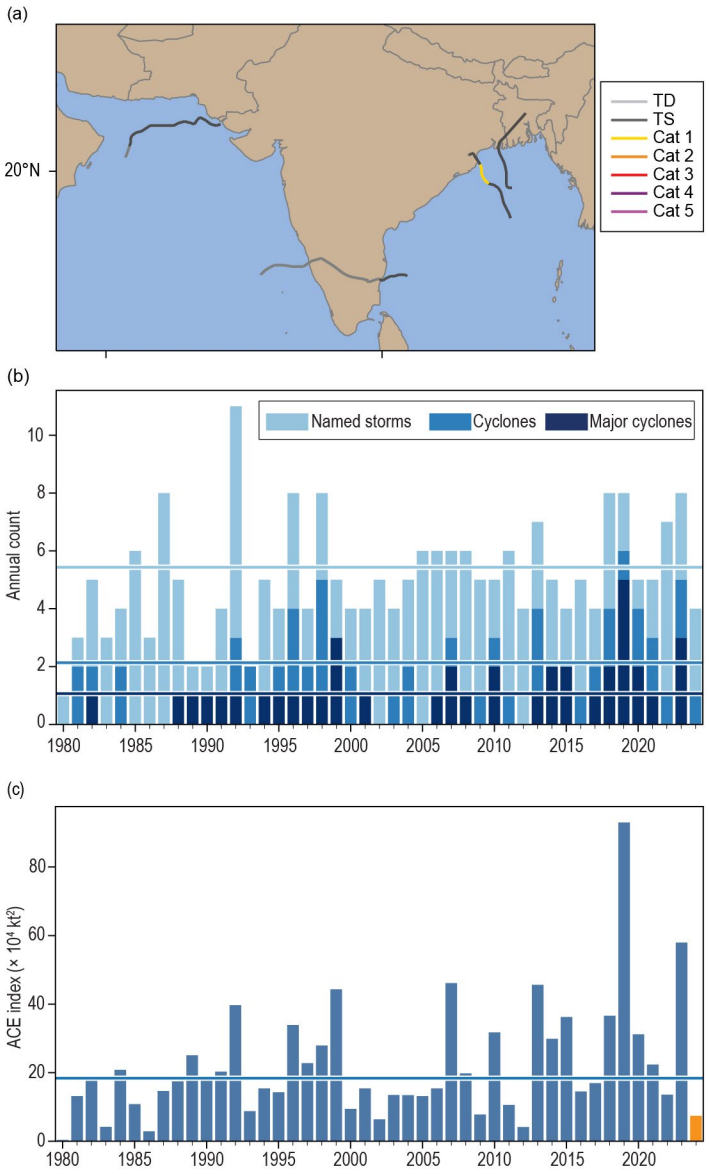

Fig. 4.34. (a) North Indian Ocean (NIO) tropical cyclone tracks in 2024. (b),(c) Annual tropical cyclone statistics in the NIO basin for the period 1980–2024: (b) number of named storms, cyclones, and major cyclones, and (c) accumulated cyclone energy (ACE; × 10^4 kt^2). Horizontal lines, representing the 1991–2020 climatology, are included in both (b) and (c).

Unauthenticated | Downloaded 11/21/25 11:34 AM UTC

The most active part of the 2024 North Indian cyclone season was during the post-monsoon period from October to December. SSTs were particularly warm, and convection was enhanced across the Bay of Bengal during this period (Figs. 4.35a,b). Due in large part to the anomalously high SSTs and convection, both tropical cyclones that occurred during the second half of the year (Severe Cyclonic Storm Dana and Cyclonic Storm Fengal) formed in the Bay of Bengal. During the post-monsoon period, wind shear across the Bay of Bengal was anomalously light, which likely facilitated the strengthening of Dana into the season's only tropical cyclone-strength system (Fig. 4.35c). Additionally, low-level anomalous easterlies were observed across the Bay of Bengal (Fig. 4.35d). The conditions for tropical cyclones overall were favorable, with light shear and warm SSTs in the Bay of Bengal, which explains the activity there during the second half of the year. Conditions were generally less favorable in the Arabian Sea, where lower SSTs and less convective activity inhibited the formation of tropical cyclones despite the light vertical wind shear.

(ii) Individual tropical cyclones and impacts

The North Indian Ocean cyclone season began on 25 May with the formation of Cyclonic Storm Remal. Remal peaked as a strong tropical storm and made landfall near the border between India and Bangladesh. Remal brought strong winds and heavy rainfall to the region, resulting in significant damage and numerous fatalities, according to the Associated Press. After a lull in activity, the second storm of the season, Cyclonic Storm Asna, formed in late August. Asna originated from a low-pressure area over India but strengthened into a moderate-strength tropical storm over the Arabian Sea before dissipating without further impacting land. The precursor to Asna caused flooding damage across parts of India.

In late October, Severe Cyclonic Storm Dana became the only cyclone strength storm of the season. Dana peaked as a Category 1-equivalent TC with maximum sustained winds of 65 kt (33 m s^{-1}) and a minimum central pressure of 985 hPa. Dana made landfall as a severe cyclonic storm in India, bringing gusty winds and

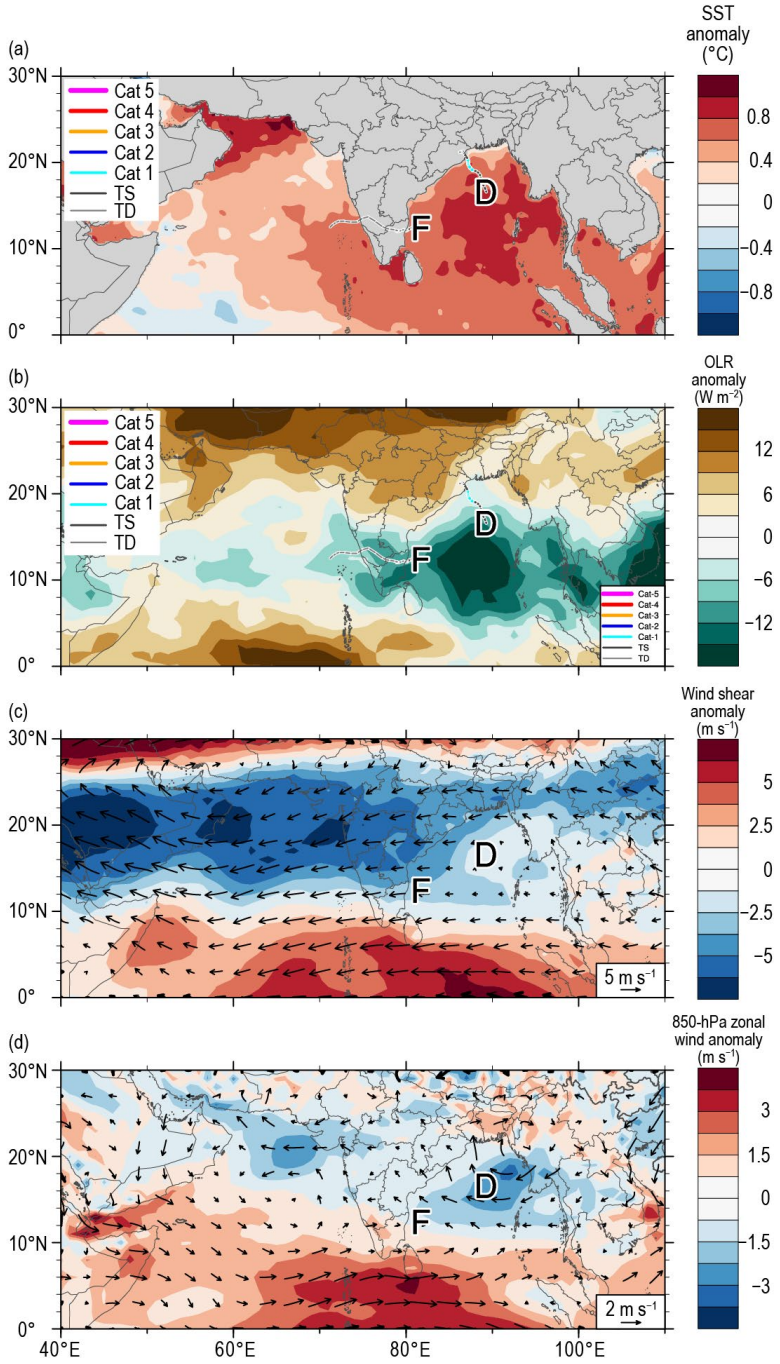

Fig. 4.35. Oct–Dec 2024 North Indian Ocean (NIO) anomaly maps of (a) sea surface temperature (SST; °C; Banzon and Reynolds 2013), (b) outgoing longwave radiation (OLR; W m^{-2}; Schreck et al. 2018), (c) 200-hPa–850-hPa vertical wind shear (m s^{-1}) vector (arrows) and scalar anomalies (shading), and (d) 850-hPa winds (m s^{-1}, arrows) and zonal wind anomalies (shading). Anomalies are relative to the annual cycle for 1991–2020. Letter symbols denote where each NIO tropical cyclone attained its initial tropical storm intensity. (Source: Wind data from CFSR [Saha et al. 2014].)

Unauthenticated | Downloaded 11/21/25 11:34 AM UTC

heavy rainfall. The storm resulted in millions of dollars in damages and several fatalities due to the high winds, heavy rainfall, and storm surge, according to The Economic Times. The final storm of the year was Cyclonic Storm Fengal, which peaked with maximum sustained winds of 52 kt (27 m s^{-1}) and a minimum central pressure of 987 hPa. Fengal made landfall in southern India and resulted in numerous fatalities and some significant damage, according to The Weather Channel.

Overall, the 2024 North Indian Cyclone seasonal activity was below average, with fewer-than-average named storms, only one cyclone-strength storm, and no major-tropical-cyclone-strength storms. This resulted in a much below-average ACE of just 7.4 × 10^4 kt^2. The strongest storm of the year by wind speed was Severe Cyclonic Storm Dana (65 kt); however, the strongest storm of the year by minimum central pressure was Cyclonic Storm Remal at 978 hPa.

6. SOUTH INDIAN OCEAN BASIN

—A. D. Magee and C. J. Schreck

(i) Seasonal activity

The South Indian Ocean (SIO) TC basin extends south of the equator and from the East African coastline to 90°E. While TC activity can occur year-round, the peak season is typically between November and April when the Intertropical Convergence Zone is situated in the Southern Hemisphere. The 2023/24 season includes TCs that occurred from July 2023 to June 2024. Landfalling TCs typically impact Madagascar, Mozambique, and the Mascarene Islands, including Mauritius and La Réunion; however, impacts can be felt in other locations within the region. Above-normal storm activity was observed in the SIO basin during the 2023/24 season, with 13 named storms, according to the JTWC, compared to the IBTrACS–JTWC 1991–2020 mean of 10.4 (Fig. 4.36). There were five cyclones, two of which were major cyclones, representing below-normal activity compared to a 1991–2020 mean of 6.0 and 3.5, respectively. Compared to the previous three seasons, the 2023/24 TC season was less destructive and deadly.

The 2023/24 seasonal ACE index was 70.7 × 10^4 kt^2, which is below the 1991–2020 climatology of 94.3 × 10^4 kt^2. Cyclone-favorable conditions, including

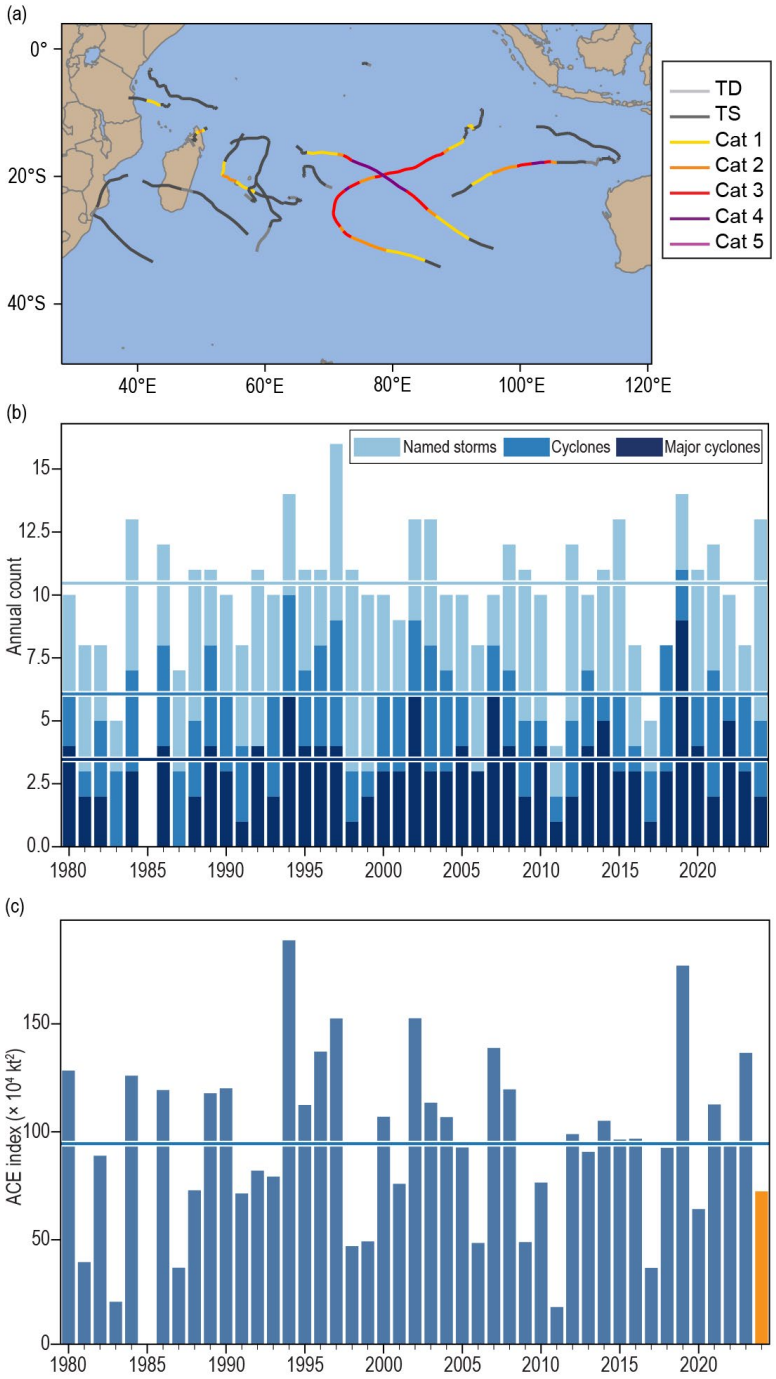

Fig. 4.36. (a) South Indian Ocean (SIO) tropical cyclone tracks in 2024. (b),(c) Annual tropical cyclone statistics in the SIO basin for the period 1980–2024: (b) number of named storms, cyclones, and major cyclones, and (c) accumulated cyclone energy (ACE; × 10^4 kt^2). Horizontal lines, representing the 1991–2020 climatology, are included in both (b) and (c).

Unauthenticated | Downloaded 11/21/25 11:34 AM UTC

anomalously high SSTs, were present to the north of Madagascar extending towards the southeast beyond 20°S (Fig. 4.37a); negative OLR anomalies towards the east of Madagascar (Fig. 4.37b) and favorable wind shear anomalies (north of 20°S) persisted across much of the basin between January and March 2024 (Fig 4.37c).

(ii) Noteworthy TCs and impacts

TC Alvaro formed in the Mozambique Channel on 30 December 2023 and was the first named storm of the 2023/24 SIO cyclone season. The system intensified into a moderate tropical storm and continued to strengthen despite vertical wind shear. On 1 January 2024, TC Alvaro reached its peak intensity of 60 kt (31 m s^{-1}) and a minimum central pressure of 989 hPa. On the same day, the system made landfall in Madagascar's Morombe District as a severe tropical storm, with sustained winds of 54 kt (28 m s^{-1}). The cyclone caused significant damage, resulting in 19 fatalities and affecting nearly 33,000 people, with over 17,000 displaced. After crossing Madagascar, Alvaro re-entered the Indian Ocean and briefly re-intensified but was hindered by strong wind shear, which caused its transition into a post-tropical depression by 3 January.

TC Belal formed on 11 January in the monsoon trough north-northeast of Madagascar, intensifying rapidly under favorable conditions, including high sea surface temperatures and strong outflow. It reached its peak intensity on 14 January with maximum sustained winds of 89 kt (45 m s^{-1}) and a minimum central pressure of 968 hPa, developing a well-defined eye before succumbing to wind shear and dry air, eventually weakening into a remnant low on 18 January. The storm significantly impacted Réunion, where escalating cyclone alerts were issued as its eyewall approached, resulting in four fatalities, power outages for 150,000 people, and water access disruptions for 37,000 residents. Fatalities were also reported on Mauritius.

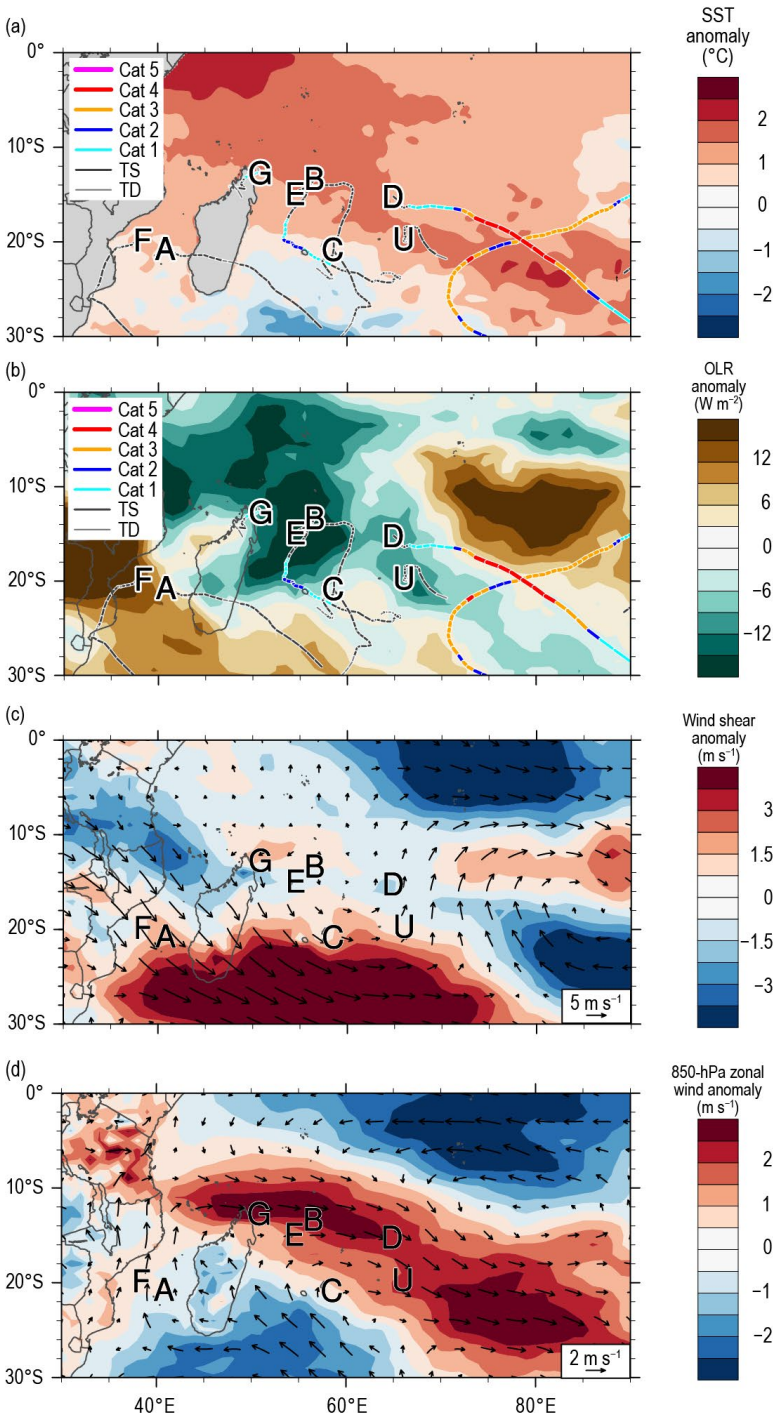

Fig. 4.37. January–March 2024 Southern Indian Ocean (SIO) anomaly maps of: (a) sea surface temperature (SST; °C; Banzon and Reynolds 2013), (b) outgoing longwave radiation (OLR; W m^{-2}; Schreck et al. 2018), (c) 200-hPa–850-hPa vertical wind shear (m s^{-1}) vector (arrows) and scalar anomalies (shading), and (d) 850-hPa winds (m s^{-1}, arrows) and zonal wind anomalies (shading). Anomalies are relative to the annual cycle for 1991–2020. Letter symbols denote where each SIO tropical cyclone attained its initial tropical storm intensity (Source: Wind data from CFSR [Saha et al. 2014]).

Unauthenticated | Downloaded 11/21/25 11:34 AM UTC

Severe TC Anggrek was the first severe TC of the season that exhibited multiple cycles of strengthening and weakening over two weeks near the Cocos (Keeling) Islands. Initially forming as a tropical low on 12 January near the boundary of the Australian and Tropical Cyclone Warning Centre Jakarta areas of responsibility, Anggrek became a named TC on 15 January as it reached Category 1 intensity. The system tracked southeast before shifting westward and weakened due to less favorable sea surface temperatures. The system later intensified under improved conditions and entered into the basin on 25 January. Anggrek reached its peak intensity with sustained maximum winds of 115 kt (59 m s^{-1}) on 28 January and a minimum central pressure of 944 hPa on 29 January—making it a Category 4 system on the SSHWS—as it moved southwestward, steered by a ridge to the east. Strong wind shear caused the cyclone to weaken, with its eye gradually disappearing by 30 January.

Severe TC Djoungou formed northeast of the Mascarene Islands and was first noted by Météo France on 8 February 2024 under favorable conditions of high sea surface temperatures and low wind shear. Gradually organizing, it was classified as a tropical disturbance on 15 February and quickly intensified over the following days, developing a banding eye feature. Named Djoungou by the Mauritius Meteorological Service, it reached severe tropical storm status later on 16 February and underwent rapid intensification, achieving Category 4-equivalent SSHWS intensity with maximum sustained winds of 119 kt (61 m s^{-1}) and a central pressure of 942 hPa on 18 February. The cyclone's structure deteriorated soon after as it encountered increasing wind shear, weakening the cyclone into a post-tropical depression after crossing into the Australian basin on 19 February.

TC Gamane formed on 25 March, north-northeast of Toamasina, Madagascar, and rapidly intensified under favorable conditions, reaching peak intensity on 27 March as a Category 2-equivalent cyclone (SSHWS) with maximum sustained winds of 89 kt (46 m s^{-1}) and a minimum central pressure of 970 hPa. It made landfall near Vohémar the same day, bringing heavy rainfall and flooding before weakening over Madagascar's mountainous terrain and weakening into a disturbance by 28 March. The cyclone caused 19 fatalities, three missing persons, displaced over 2500 people, and affected at least 90,000 residents; the Sambava District in northern Madagascar received 300 mm of rain in 24 hours. Damage to roads slowed relief efforts, and the storm caused an estimated $77 million (U.S. dollars) in losses, severely impacting the Sava, Analanjirofo, and Diana regions of Madagascar.

TC Hidaya formed near the Seychelles on 30 April, intensifying into a Category 1 cyclone on 3 May, with maximum sustained winds of 80 kt (41 m s^{-1}) and a minimum central pressure of 974 hPa, before weakening and making landfall near Kilindoni, Tanzania, as a tropical storm later that day. Hidaya was a rare occurrence in recorded history, being one of only a few cyclones to make landfall in Tanzania, alongside a cyclone in 1872, an unnamed system in 1952, and Tropical Depression Atang in 2002. It was also the most intense cyclone ever recorded in this portion of the Indian Ocean. The storm struck after weeks of severe flooding, compounding impacts with five fatalities and widespread destruction of infrastructure. Over 1500 houses were damaged or destroyed, ferry services between Zanzibar and Dar es Salaam were suspended, and parts of the Lindi-Dar es Salaam highway were washed out. Power outages and fallen trees added to the disruption, with total damages in Tanzania estimated around $184 million (U.S. dollars).

7. AUSTRALIAN BASIN

—B. C. Trewin

(i) Seasonal activity

The 2023/24 TC season was slightly below average in the broader Australian basin (areas south of the equator and between 90°E and 160°E, which includes the Australian, Papua New Guinea, and Indonesian areas of responsibility). The season produced 8 TCs, below the 1991–2020 average of 9.5, consistent with the El Niño conditions that prevailed in late 2023 and early 2024. The 1991–2020 IBTrACS seasonal averages for the basin are 10.2 named storms, 5 TCs, and 2.5 major TCs, which compares with the 2023/24 IBTrACS-based counts of 9, 6, and 3, respectively (Fig. 4.38).

Unauthenticated | Downloaded 11/21/25 11:34 AM UTC

There were three TCs (Anggrek, Neville, and Olga) in the western sector of the broader Australian region during 2023/24, two in the northern sector (Lincoln and Megan), and three in the eastern sector (Jasper, Kirrily, and Paul). Four TCs made landfall on mainland Australia (Jasper, Kirrily, Lincoln, and Megan). Two of the eight TCs (Jasper and Olga) reached Australian Category 5 intensity within the Australian basin.

(ii) Landfalling and other significant TCs

There were four landfalls in mainland Australia during the season at tropical cyclone intensity: two on the east coast of Queensland (TCs Jasper and Kirrily) and two on the Gulf of Carpentaria coast of the Northern Territory (TCs Lincoln and Megan). There were no landfalls at tropical cyclone intensity on the west coast in 2023/24, although parts of Western Australia were impacted by remnant tropical lows from cyclones that had made landfall elsewhere.

TC Jasper was the first major landfall of the season. It formed south of the Solomon Islands on 5 December and intensified steadily as it tracked south, reaching Australian Category 5 intensity on 8 December and reaching its peak intensity with maximum sustained 10-minute winds of 115 kt (59 m s^{-1}) near 14°S, 157°E. Jasper then turned west towards the Queensland coast and weakened to Australian Category 1 south of Willis Island before intensifying slightly to Australian Category 2 prior to its landfall near Wujal, south of Cooktown, on 13 December. This is the earliest in the season that a system has made landfall at cyclone intensity on the east coast in the satellite era. TC Jasper weakened quickly to a tropical low after landfall but remained slow-moving over the Cape York Peninsula for several days.

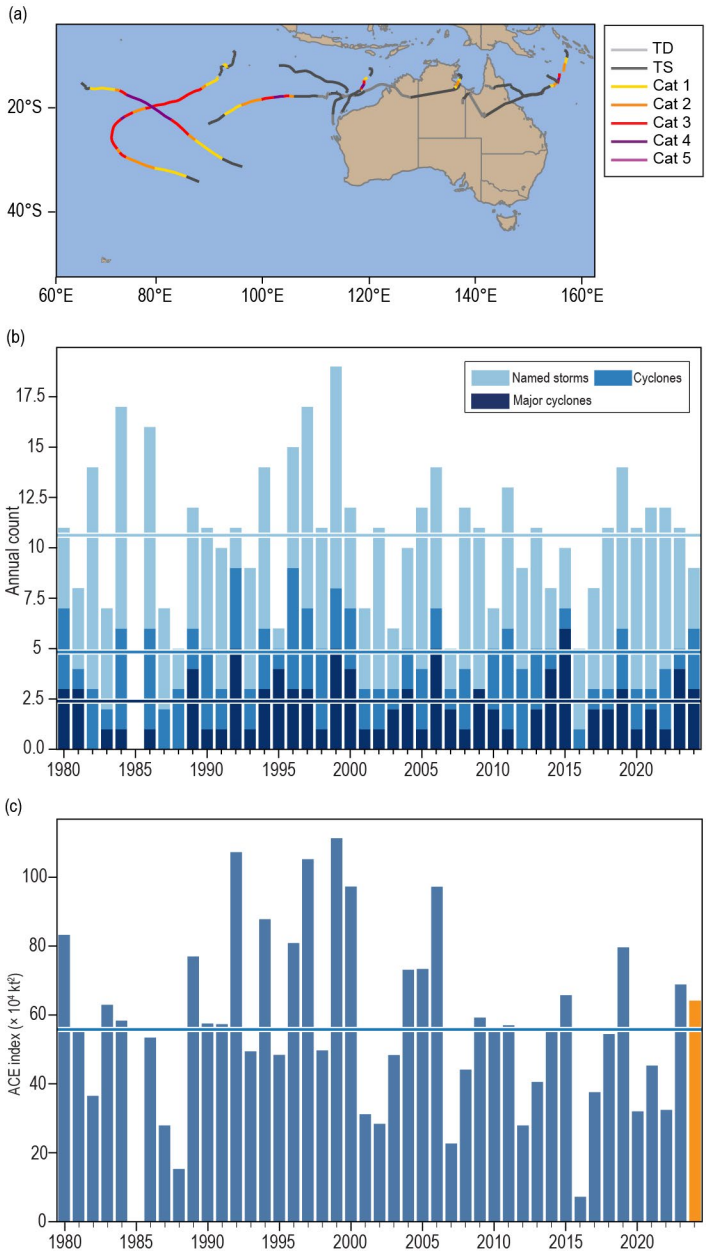

Fig. 4.38. (a) Australian tropical cyclone tracks in 2024. (b),(c) Annual tropical cyclone statistics for the Australian basin for the period 1980–2024: (b) number of named storms, cyclones, and major cyclones, and (c) accumulated cyclone energy (ACE; × 10^4 kt^2). Horizontal lines, representing the 1991–2020 climatology, are included in both (b) and (c).

TC Jasper's main impacts arose from exceptional and persistent rainfall at and after landfall, with five-day rainfall totals exceeding 1000 mm in many locations. It was especially wet on 18 December due to the convergence of northeasterly flow near the coast as a surface trough extended east from the remnants of Jasper. Cape Tribulation received 861.2 mm on that day, the highest December daily total ever observed at a Bureau of Meteorology (BoM) gauge in Australia and the third highest in any month. Whyanbeel Valley, near Daintree, received 2085.8 mm during 14–19 December. There was major flooding along the Barron and Daintree Rivers and many smaller streams, with the Barron River at Myola reaching its highest level in over 100 years, leading to some property inundation and widespread road damage.

The second east coast landfall of the season was TC Kirrily, which made landfall as a Category 1 system at Rollingstone, near Townsville in Queensland, on 25 January, having peaked offshore at Category 3 intensity with 10-minute mean winds of 64 kt (33 m s^{-1}) at Flinders Reef. TC Kirrily's

Unauthenticated | Downloaded 11/21/25 11:34 AM UTC

main impacts were from flooding in western Queensland as the remnant low moved through the region over the following week, briefly emerging over the southern Gulf of Carpentaria on 1–2 February before moving south again. Westmoreland Station, south of the Gulf near the Queensland–Northern Territory border, received 332.0 mm of rain on 2 February, a February record for the area.

TCs Lincoln and Megan both made landfall on the same part of the Gulf of Carpentaria coast, east of Port McArthur in the Northern Territory. Lincoln was briefly a Category 1 storm before its landfall on 16 February but then had a long track as a tropical low, moving west across the Northern Territory and northern Western Australia, emerging off the west coast and then tracking southwest parallel to it before its final landfall north of Carnarvon on 24 February. TC Megan formed east of Groote Eylandt, in the western Gulf of Carpentaria, on 16 March and intensified as it moved south-southwest towards the coast, reaching its peak intensity as a Category 4 system with maximum 10-minute mean winds 89 kt (46 m s^{-1}) and a minimum central pressure of 950 hPa overnight on 17–18 March, before making landfall as a Category 3 system on the 18th.

TC Megan had substantial impacts on Groote Eylandt, including significant damage to a wharf when a bulk carrier was pushed against it, badly disrupting mineral exports. Very heavy rain also fell both on Groote Eylandt and the mainland, with two-day totals of 680.4 mm at Groote Eylandt Airport on 16–17 March and 370.6 mm at Borroloola on 18–19 March. The McArthur River reached a record flood height at Borroloola on 22 March, and much of the community was evacuated, although building inundation was ultimately limited. Lincoln and Megan both also brought heavy rain to central and northwestern parts of the Northern Territory, with numerous daily totals exceeding 100 mm. This exacerbated seasonal flooding in the region, resulting in significant inundation in a number of Indigenous communities. Much of the region had its wettest January–March on record, with Victoria River Downs having already exceeded its record annual rainfall by the end of March.

Of those TCs that did not make landfall, the most intense were Olga in April and Neville in March. Olga peaked at Australian Category 5 strength with maximum 10-minute mean winds of 111 kt (57 m s^{-1}) near 16°S, 119°E on 8 April, while Neville peaked at Australian Category 4 status with maximum 10-minute mean winds of 99 kt (51 m s^{-1}) near 18°S, 103°E on 22 March. Both remained well off the Western Australian coast as cyclones, although Neville's precursor low had some impacts on the Cocos (Keeling) Islands, and Olga resulted in disruption to offshore oil and gas facilities.

8. SOUTHWEST PACIFIC BASIN

—A. D. Magee and A. M. Lorrey

(i) Seasonal activity

The 2023/24 southwest Pacific TC season officially began in November 2023 and ended in April 2024. The data for the season was gathered from the Fiji Meteorological Service, Australia's BoM to Bureau of Meteorology (BoM), and New Zealand MetService, Ltd. The southwest Pacific basin (SWP), as defined by Diamond et al. (2012) as 135°E–120°W, experienced a total of nine named TCs, including five severe storms. In comparison to the 1991–2020 seasonal average of 9.8 named TCs, including 4.3 severe storms, as reported by the Southwest Pacific Enhanced Archive for Tropical Cyclones (SPEArTC), the 2023/24 southwest Pacific TC season was considered to be near-normal.

Figure 4.39 illustrates the TC activity in the basin, which spans the area 160°E–120°W to avoid overlap with the Australian basin and double counting of storms. Four of the nine named TCs in the southwest Pacific were in the Australian basin and are shown in Fig. 4.38 instead. It is important to note that the climatological definition of the southwest Pacific basin (Diamond et al. 2012) is used for this seasonal description and does not align with the World Meteorological Organization-designated boundaries for the Regional Specialized Meteorological Center or TC Warning Center areas of responsibility. The below section describes events that both formed and passed into the southwest Pacific basin (135°E–120°W) and uses the Australian TC Intensity Scale.

Unauthenticated | Downloaded 11/21/25 11:34 AM UTC

(ii) Storm tracks, landfalls, and impacts

Severe TC Lola was the strongest storm of 2023/24 and also the strongest off-season storm on record in the basin (followed by Severe TC Xavier in October 2006). It formed on 19 October northeast of Honiara in the Solomon Islands. Favorable conditions for cyclone development, including warm sea surface temperatures (30°C–31°C), low vertical wind shear, and strong upper-level outflow, contributed to its rapid intensification. The system moved southwest before consolidating into a tropical depression on 21 October. It intensified rapidly into an Australian Category 5 severe TC on 24 October when sustained winds of 115 kt (59 m s^{-1}) and a minimum central pressure of 930 hPa occurred. Severe TC Lola tracked south under the influence of an upper-level ridge, making landfall in Vanuatu near Sowan on 25 October as a weakening system. In Vanuatu, TC Lola caused extensive damage, compounding the devastation from TCs Judy and Kevin that occurred in March 2023, from which the country was still recovering. Lola directly impacted 10,000 households, destroying homes, critical infrastructure, and crops across the Malampa and Shefa provinces. Schools, health centers, and communications infrastructure sustained heavy damage, while agricultural losses, particularly in subsistence farming and cash crops, devastated livelihoods. In the Solomon Islands, the island of Tikopia experienced severe impacts, including widespread damage to homes and essential facilities. New Zealand, Australia, and France mobilized humanitarian aid to support recovery efforts. Overall, Severe TC Lola caused at least four fatalities and an estimated $360 million (U.S. dollars) in damage.

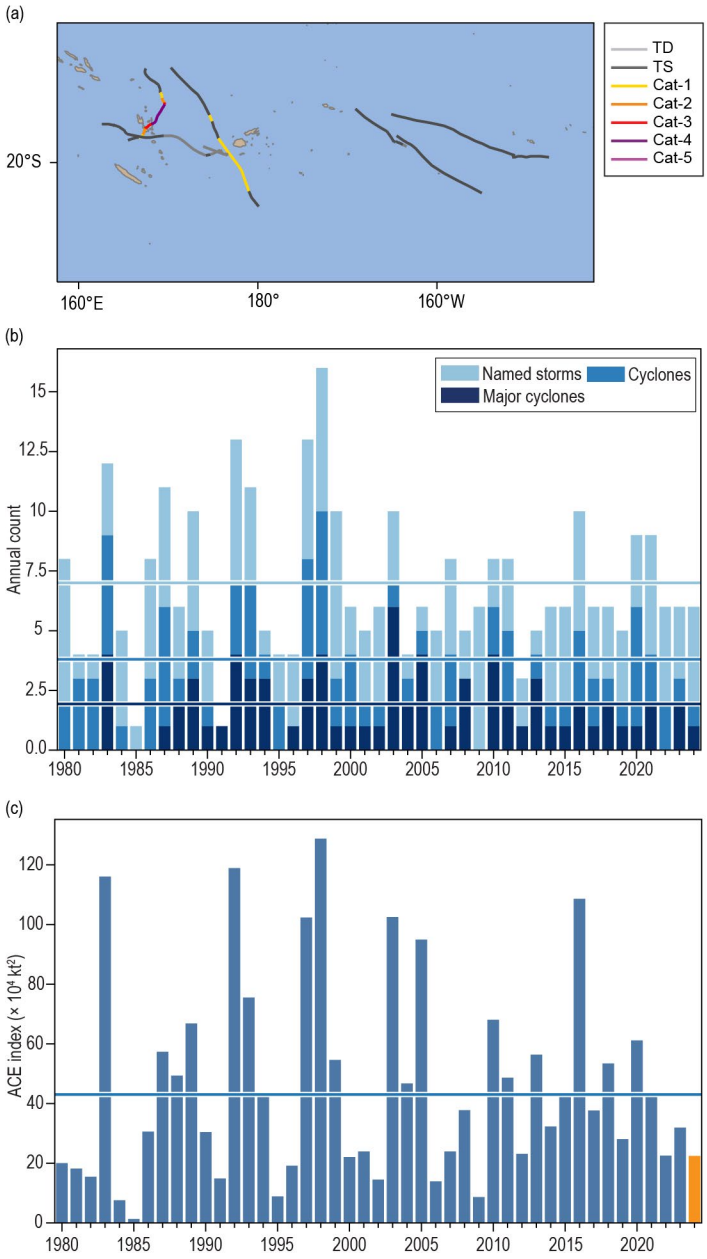

Fig. 4.39. (a) Southwest Pacific tropical cyclone tracks in 2024. (b),(c) Annual tropical cyclone statistics for the southwest Pacific basin for the period 1980–2024: (b) number of named storms, cyclones, and major cyclones, and (c) accumulated cyclone energy (ACE; × 10^4 kt^2). Horizontal lines, representing the 1991–2020 climatology, are included in both (b) and (c).

Severe TC Mal began as a low-pressure system located to the north of the Solomon Islands on 10 November 2023, moved east, and subsequently strengthened into a tropical depression on 11–12 November as it moved toward Fiji. While initially disorganized, this low-pressure system further organized into an Australian Category 1 TC on 13 November when it was named TC Mal by the Fiji Meteorological Service. Severe TC Mal reached peak intensity as an Australian Category 3 system, with peak sustained winds of 74 kt (38 m s^{-1}) and minimum central pressure of 977 hPa on 13 November. Passage of this storm to the southwest of Fiji caused trees to become uprooted due to high winds, and there were power outages in several parts of the country along with heavy rainfall. On 15 November, Severe TC Mal moved southeast and began deteriorating under the influence of high wind shear.

Severe TC Jasper was the third system of the 2023/24 southwest Pacific TC season, directly following Severe TC Mal (an Australian Category 3 TC), and marked the first named storm and severe TC of the 2023/24 Australian region's TC season (see section 4g7 for more details). TC Jasper was first noted as an area of low pressure in the South Pacific Ocean and was initially

Unauthenticated | Downloaded 11/21/25 11:34 AM UTC

slow to develop as it tracked southwestward through Fiji's area of responsibility. The system gradually consolidated as it approached the Australian region, prompting the BoM to upgrade it to an Australian Category 1 TC and name it Jasper. The storm rapidly intensified, reaching Australian Category 5 severe TC status on 7 December, with peak sustained winds of 115 kt (59 m s^{-1}) and a minimum central pressure of 926 hPa. Jasper soon encountered increasing wind shear, causing it to weaken as it approached northern Queensland. However, it re-intensified and made landfall as an Australian Category 2 TC near Wujal on 13 December. The TC brought heavy rainfall, peaking at 2252 mm at Bairds near the Daintree River (for the seven days to 9am local time on 19 December), leading to significant flooding. Severe TC Jasper was recorded as the wettest TC in Australian history, surpassing TC Peter of 1979. One person died, another went missing, and the Insurance Council of Australia estimated damages at $1 billion Australian dollars ($670 million U.S. dollars).

Severe TC Kirrily originated from a tropical low in the Coral Sea on 12 January. Favorable conditions, including warm sea surface temperatures and low wind shear, allowed the system to intensify, and it was named Kirrily as it became the fourth named storm of the 2023/24 southwest Pacific TC season. Kirrily peaked as an Australian Category 3 TC on 25 January, with sustained winds of 65 kt (33 m s^{-1}) and a minimum central pressure of 973 hPa, before making landfall northwest of Townsville, Australia. It weakened rapidly after landfall, tracking northwest along the coast, eventually becoming a tropical low the same day. The remnants of Kirrily moved inland toward Queensland, producing heavy rainfall and some thunderstorms, but the storm caused minimal damage near its landfall location, with minor roof damage and fallen trees reported. While significant flooding was avoided, severe thunderstorms in southeast Queensland led to further impacts, with total losses estimated at $120 million (U.S. dollars).

Five additional TCs formed or entered the SWP basin during the 2023/24 TC season, and it is notable that there was enhanced TC activity to the east of the dateline. As such, many of these named storm systems tracked over remote areas of ocean. In February 2024, three systems developed: TC Nat (peak intensity of 50 kt [26 m s^{-1}], 985 hPa; Australian Category 2), TC Osai (peak intensity of 45 kt [23 m s^{-1}], 990 hPa; Australian Category 1), and TC Lincoln (peak intensity of 45 kt [23 m s^{-1}], 990 hPa; Australian Category 1). In March, Severe TC Megan reached peak intensity as an Australian Category 4 system, with sustained winds of 90 kt (46 m s^{-1}) and a minimum central pressure of 950 hPa. The season concluded with TC Paul, a small and short-lived Australian Category 2 TC, which reached a peak intensity with winds of 50 kt (26 m s^{-1}) and had a minimum central pressure of 994 hPa.

Unauthenticated | Downloaded 11/21/25 11:34 AM UTC

h. Tropical cyclone heat potential

—J. Trinanes and I-I. Lin

Tropical cyclone heat potential (TCHP) is an indicator of the amount of heat stored in the upper ocean that can potentially promote tropical cyclone (TC) intensification because, in addition to sea surface temperatures (SST), subsurface thermal structure is important for TC genesis and development (Shay et al. 2000; Goni and Trinanes 2003; Lin et al. 2008; Kang et al. 2024; Gao et al. 2025). TCHP is the ocean heat content calculated by integrating the ocean temperature between SST and the 26°C isotherm (D26), which has been reported as a useful predictor for TC intensification (Leipper and Volgenau 1972; Mainelli et al. 2008; Dare and McBride 2011; Knaff et al. 2018). TCs traveling over regions of high TCHP conditions experience higher enthalpy fluxes from the ocean into the atmosphere, favoring intensification and leading to reduced SST cooling (e.g., Lin et al. 2013). Areas in the ocean with TCHP values above 50 kJ cm^{-2} have been statistically linked to TC intensification, including rapid intensification. Rapid intensification is typically defined to be when maximum sustained wind speed increases by at least 30 kt in a 24-hour period and generally occurs in situations in which atmospheric and oceanic conditions are favorable (e.g., Shay et al. 2000; Mainelli et al. 2008; Lin et al. 2020; Knaff et al. 2018, 2020). In addition to upper ocean heat content, upper ocean salinity conditions may also modulate TC intensification as storms traveling over areas of fresh water-induced barrier layers may receive increased air–sea heat fluxes caused by reduced upper ocean mixing and cooling (e.g., Balaguru et al. 2012; Domingues et al. 2015).

In this section we present an assessment and analysis of the upper-ocean heat content conditions during 2024 based on estimates of two parameters: 1) TCHP (e.g., Goni et al. 2009, 2017) global anomalies with respect to their long-term mean (1993–2022) and 2) TCHP anomaly value differences in 2024 compared to conditions observed in 2023. TCHP anomalies during 2024 (Fig. 4.40a) were computed for June–November in the Northern Hemisphere and November 2023–April 2024 in the Southern Hemisphere. The seven regions where TCs are known to form, travel, and weaken/intensify are highlighted in Fig. 4.40. In all these regions, TCHP values exhibit large temporal and spatial variability due to mesoscale features (e.g., surface currents and associated eddies and rings), and short- to long-term modes of climate variability (e.g., the North Atlantic Oscillation, the El Niño–Southern Oscillation [ENSO], the Pacific Decadal Oscillation). The differences in TCHP anomalies between 2024 and 2023 presented in Fig. 4.41 are computed for the primary months of TC activity in each hemisphere as described above.

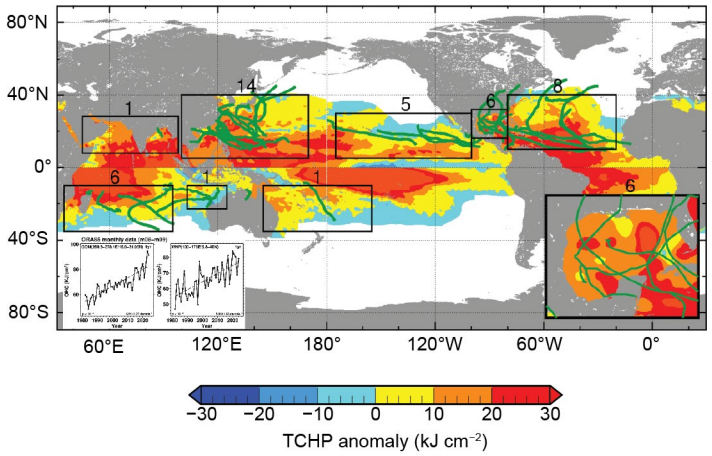

Fig. 4.40. Global anomalies of tropical cyclone heat potential (TCHP; kJ cm^{-2}) during 2024 computed as described in the text. The numbered boxes indicate the seven regions where tropical cyclones (TC) occur: from left to right: southwest Indian, North Indian, northwest Pacific, southeast Indian, South Pacific, northeast Pacific, and North Atlantic (shown as Gulf of America/Gulf of Mexico and tropical Atlantic separately). The green lines indicate the trajectories of all TCs reaching at least Category 1 (1-minute average wind ≥64 kts) and above during Nov 2023–Apr 2024 in the Southern Hemisphere and Jun–Nov 2024 in the Northern Hemisphere, while purple lines indicate Category 1 TCs that occurred outside these periods. The numbers above each box correspond to the number of Category 1 and above cyclones that traveled within each box. The Gulf of America/Gulf of Mexico conditions are shown in the inset in the lower right corner. The two boxes at the bottom left show 40-year ocean heat content (OHC) trends in the northwest Pacific and the Gulf of America/Gulf of Mexico, calculated from the European Centre for Medium-Range Weather Forecasts' Ocean Reanalysis System 4 (ORAS4) data.

TCHP anomalies during 2024 exhibited above-average values in all TC regions, and basins with positive anomaly reaching 30 kJ cm^{-2}, showing favorable ocean conditions for TCs, though the increase in the southwest Pacific and northeast Pacific was less pronounced (Fig. 4.40a). Because 2023 was dominated by El Niño, while 2024 saw a transition from El Niño early on to La Niña-like conditions by the end of the year (section 4.1), the TCHP difference between 2023 and 2024 is positive over the western North Pacific (~20 kJ cm^{-2}) while the eastern North Pacific TCHP

Unauthenticated | Downloaded 11/21/25 11:34 AM UTC

difference between 2023 and 2024 is negative (Fig. 4.41). This is understandable given that during the 2023 El Niño event, eastern North Pacific SSTs were much higher when compared to a year that shifted toward La Niña conditions (i.e., 2024). Pronounced TCHP positive differences in 2024 (as compared to 2023) were also observed in the southwestern Indian Ocean. In addition to the 2024 comparison with respect to the climatology in Fig. 4.40a and interannual differences with 2023 in Fig. 4.41, long-term ocean heat content (OHC) trends over major TC basins were calculated using 43 years of ocean reanalysis data from the European Centre for Medium-Range Weather Forecasts' Ocean Reanalysis System 4 (ORAS4) data. As given in the examples below (Figs. 4.40b,c), both the northwest Pacific Ocean and the Gulf of America/Gulf of Mexico exhibit robust increases in OHC of ~5 KJ cm^{-2} $decade^{-1}$ to 6 KJ cm^{-2} $decade^{-1}$. This long-term increase indicates an overall tendency for OHC to be more favorable for TC development and intensification.

In terms of individual storms, Hurricane Milton (October 2024) was the most intense TC globally. The storm rapidly intensified to Category 5 intensity over the southern part of the Gulf of America/Gulf of Mexico, where the water was relatively shallow. Over this shallower water region, the OHC computation from satellite altimetry can have more uncertainty, as the entire water column temperature can be above 26°C. As indicated by Price (2009) and Pun et al. (2019), since the entire (shallow) water column over this shallow region is warm, the TC-induced ocean cooling effect can be greatly inhibited, allowing for a high sea–air heat flux favoring intensification. Hurricane Helene traveled in a south-to-north trajectory across the Gulf of America/Gulf of Mexico and rapidly intensified to a Category 4 hurricane (on the SSHWS) before making landfall in Florida. As in Fig. 4.40, the OHC in the Gulf of America/Gulf of Mexico was anomalously positive. Helene's translation speed was fast during its rapid intensification period (~11 m s^{-1}). This fast translation speed can also effectively reduce the TC-induced ocean cooling effect to favor sea–air heat fluxes, since the faster the translation speed, the smaller the cooling effect (Price 1981; Chang et al. 2020). Furthermore, both Hurricanes Milton and Helene occurred during a marine heatwave (Choi et al. 2024).

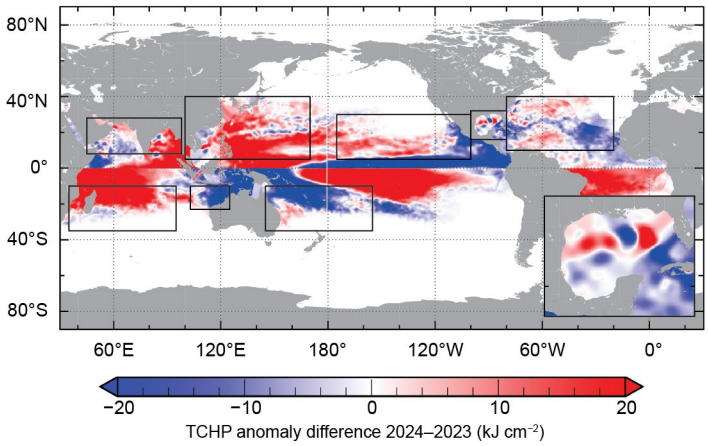

Fig. 4.41. Tropical cyclone heat potential (TCHP) anomaly difference between the 2024 and 2023 tropical cyclone seasons (kJ cm^{-2}; Jun–Nov in the Northern Hemisphere and Nov–Apr in the Southern Hemisphere). The Gulf of America/Gulf of Mexico conditions are shown in the inset in the lower right corner.

Another TC that notably intensified over extremely high OHC was Cyclone Chido over the southwestern Indian Ocean. In December 2024, Chido rapidly intensified to Category 4 and made landfall in southeast Africa with a confirmed death toll of ~170. Finally, over the western North Pacific, Super Typhoon Yagi intensified to Category 4 over OHC of 80 kJ cm^{-2}–90 kJ cm^{-2} over the South China Sea. It was one of the most damaging TCs to both China and Vietnam in recent years, with a death toll exceeding 800.

In summary, increased ocean heat content, along with warm SSTs, favor TC development given similar atmospheric dynamic conditions such as vertical wind shear. From a TC-ocean perspective, the TC-induced cooling effect is inhibited when OHC is high (e.g., Shay et al. 2000; Rogers 2017; Lin et al. 2021). From an interannual perspective, 2024 was primarily an ENSO-neutral year for the Northern Hemisphere TC season, as compared to 2023 when El Niño conditions predominated during the Northern Hemisphere TC season. On longer time scales, OHC in the western north Pacific and Gulf of America/Gulf of Mexico has increased from 5 kJ cm^{-2} $decade^{-1}$ to 6 kJ cm^{-2} $decade^{-1}$ over the past four decades.

Unauthenticated | Downloaded 11/21/25 11:34 AM UTC

Sidebar 4.1: Hurricane Helene: Inside western North Carolina's historic flood

—C. SCHRECK

Overview

Hurricane Helene made landfall on 26 September in the Big Bend region of Florida as a Category 4 hurricane—the strongest storm to make landfall in the Big Bend on record. Damaging storm surge extended southward from the Big Bend to Fort Myers. Despite the strong winds and storm surge, Helene is perhaps most infamous for the inland flooding associated with its torrential rainfall. Over 200 deaths have been attributed to Helene, which is second only to Hurricane Katrina (2005) for the most deaths in the contiguous United States since 1970. Nearly half of those deaths (105) occurred in western North Carolina (WNC), which experienced historic flooding. The region experienced a predecessor rain event (PRE; Galarneau et al. 2010; Moore et al. 2013) followed by the remnant eyewall from Helene. The combined three-day rainfall totals exceeded the 1000-year recurrence interval (NOAA Atlas 14; Bonin et al. 2006) and broke records throughout WNC. This sidebar provides an overview of Hurricane Helene and its impacts with a focus on rainfall observations from the Community Collaborative Rain, Hail and Snow Network (CoCoRaHS) volunteer network (Reges et al. 2016), including those taken by author Schreck, NC-BC-161, about 10 km north of Asheville, North Carolina.

Subseasonal to seasonal setup

The 2024 Atlantic hurricane season was widely expected to be hyperactive due to the confluence of near-record warm SSTs in the Atlantic and cool El Niño–Southern Oscillation (ENSO) neutral/weak La Niña. However, activity was eerily quiet before Helene. The typical peak of the season, 20 August–23 September, was the quietest since 1994 in terms of accumulated cyclone energy.

In mid-September, the lull was extended in part by the enhanced phase of the Madden–Julian Oscillation (MJO) over the western Pacific, which is typically less favorable for Atlantic activity. By the end of the month, however, the MJO was over the Western Hemisphere with associated equatorial westerlies enhancing the Central American Gyre—a broad and seasonal area of low pressure that occurs over the eastern Pacific Ocean and western Caribbean Sea. Helene emerged as a large system from the east side of this gyre and marked the beginning of an active end to the hurricane season.

A ridge over the central United States suppressed precipitation over WNC during late summer. The CoCoRaHS station, NC-BC-161, received 87 mm of rainfall from 3 August to 23 September, which is less than half of the climatological amount for that period. As a result of dry conditions across the region, portions of WNC were in moderate-to-severe drought prior to Helene's deluge.

Predecessor rainfall event

While Hurricane Helene was developing in the western Caribbean, a cold front was moving southeastward from the Northern Plains across the United States. This front and its associated precipitation reached WNC on the afternoon of 25 September, while Helene was first reaching hurricane strength tracking northward through the Yucatan Strait. Despite being more than 1500 km away, Helene's broad circulation was already spreading moist tropical air northward towards the front. The result was a Predecessor Rain Event (PRE)—an extreme precipitation event that occurs when the moisture associated with a tropical cyclone meets a frontal boundary far in advance of the storm itself (Galarneau et al. 2010; Moore et al. 2012). The flooding associated with PREs can be particularly devastating because they occur so far ahead of the storm itself. The PRE exacerbated the flooding impact from the hurricane.

In the case of Hurricane Helene, the ascent associated with the frontal boundary was further enhanced by the upslope flow of low-level southwesterlies impinging on the escarpment of the Southern Appalachian Mountains. During the storm's first 18 hours (1700 UTC 25 September to 1100 UTC 26 September), most CoCoRaHS stations in the French Broad River Valley, which includes Asheville, recorded 125 mm to 200 mm of rainfall, including 166 mm at author Schreck's station, NC-BC-161 (Fig. SB4.1a). These rainfall rates equate to a 100-year to 1000-year recurrence interval according to Atlas 14, and they accounted for at least half of the total rainfall at many stations in the French Broad River Valley over the entire three-day event (Fig. SB4.1d). At the end of this 18-hour verification period, Helene was still located >1000 km to the southwest of Asheville.

Primary Storm

On 26 September, Helene rapidly intensified to a Category 4 hurricane as it traversed record warm SSTs in the Gulf of America/Gulf of Mexico. However, the rainfall associated with the PRE decreased during this period. Helene made landfall in Florida around 0300 UTC on 27 September with maximum winds of 120 kt (62 m s^{-1}). The outer rainbands arrived in WNC around the same time. The 24-hour period ending 1100 UTC 27 September (Fig. SB4.1b) included the latter stages of the PRE and the outer bands. Rainfall in the French Broad River Valley was generally 75 mm–150 mm with 250 mm–330 mm along the escarpment to the east.

The upper-level trough associated with the cold front was then centered near northern Mississippi. The trough steered Helene rapidly northward through Georgia and upstate South Carolina and then northwestward through WNC. The

Unauthenticated | Downloaded 11/21/25 11:34 AM UTC

remnant eyewall passed through Asheville around 1300 UTC 27 September with gusts of 50 kt–60 kt in the valleys and higher winds along the ridges. Unfortunately, the days of heavy rain had loosened the roots of many trees, millions of which toppled and led to widespread disruptions of cellular service and power for days after the storm. Windfallen trees severed power lines and fiber optic internet cables. At its peak, over 700,000 customers were without power. Phone and internet service was virtually non-existent in the days following the storm (Jones 2024), which further hampered recovery efforts.

The rainfall ended over most of the region around 1700 UTC 27 September. The 28 September CoCoRaHS observations (Fig. SB4.1c) were dominated by the core of the Helene, with most of the daily precipitation occurring in less than six hours. The French Broad River Valley received 25 mm–75 mm, but an additional 150 mm–200 mm fell along the escarpment.

Impacts and recovery

The combined rainfall from the PRE, the rainbands, and the inner core led to totals of around 250 mm–350 mm for the French Broad River Valley and 450 mm–600 mm along the escarpment (Fig. SB4.1d). The complex topography of the Southern Appalachians enhanced the rainfall through orographic lift and funneled that rainfall downslope into the river valleys. In much of the region, the only land flat enough for development is along those rivers. Towns including Erwin in Tennessee and Marshall, Barnardsville, Burnsville, and Chimney Rock in North Carolina were among those that were devastated when the mountains channeled the flood waters, washing away large parts of the infrastructure.

The valleys and rivers are broader near Swannanoa and Asheville, North Carolina, but numerous flooded tributaries converged into the Swannanoa and French Broad Rivers. Prior

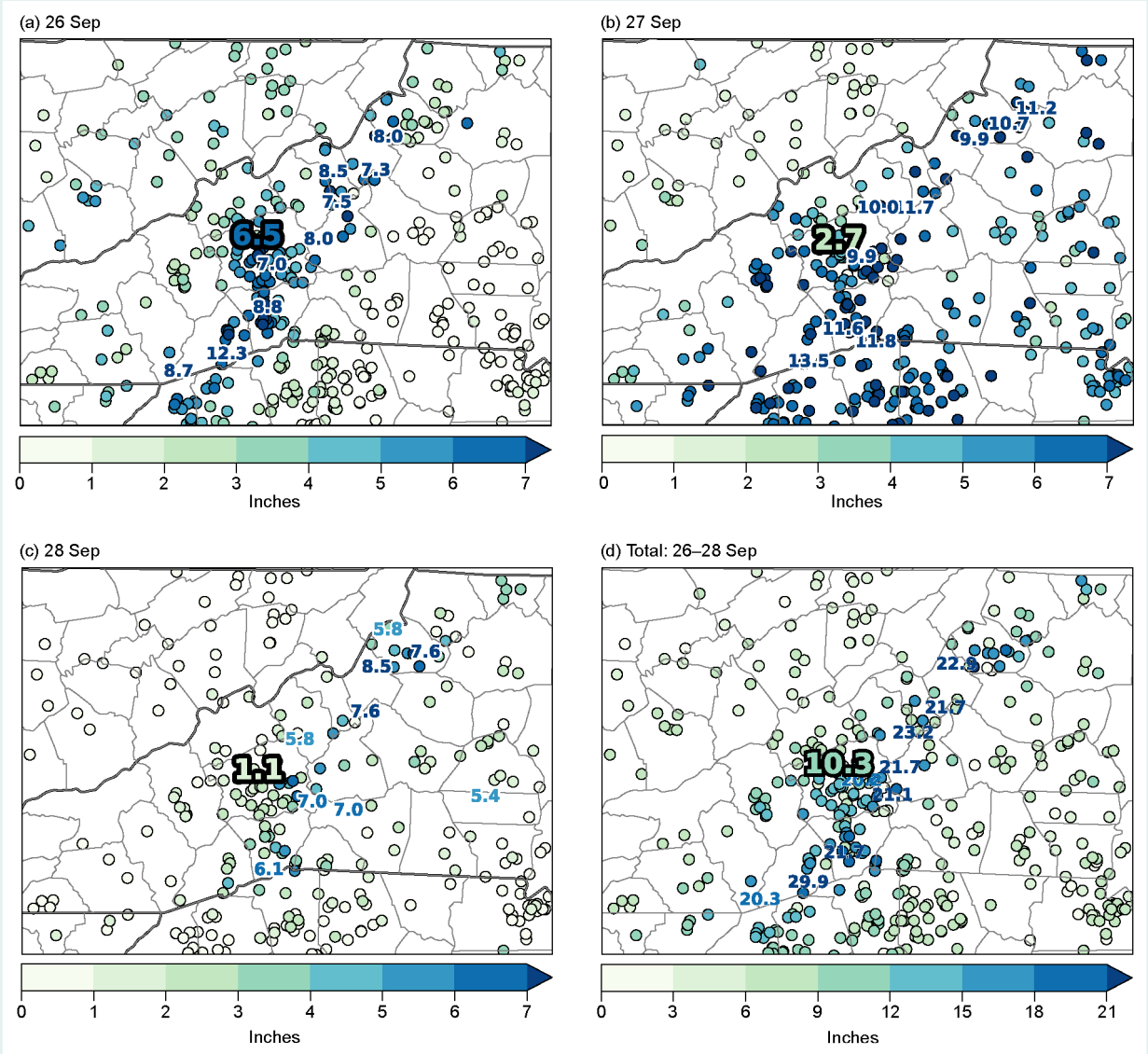

Fig. SB4.1. Community Collaborative Rain, Hail and Snow Network (CoCoRaHS; Reges et al. 2016) daily observations for 26–28 Sep 2024, and the three-day storm total (inches). Author Schreck's station, NC-BC-161, is highlighted by the large bolded number in each panel.

Unauthenticated | Downloaded 11/21/25 11:34 AM UTC

to Helene, the floods of record for the region occurred in July 1916 and September 2004. In both cases, the floods were caused by a pair of remnant hurricanes passing through the region about 10 days apart—two unnamed storms in 1916 and Hurricanes Frances and Ivan in 2004. The French Broad and Swannanoa Rivers exceeded their major flood stages in both events and caused hundreds of millions of today's equivalent dollars' worth of damage. Unknown dozens died in 1916, and 11 perished in the 2004 flood. One of the communications challenges from Helene was that a single tropical cyclone—with its associated PRE—would exceed both of these historical floods.

Fig. SB4.2 shows a hydrograph from the French Broad River at Fletcher, North Carolina (29 km south of Asheville). The river gradually rose throughout the PRE event. It reached its moderate flood stage—and the 2004 highwater mark—around 1200 UTC 27 September as the inner core approached. Even though the rainfall amounts with the core of the storm were lower than previous days (Fig. SB4.1c), the river rose rapidly during this time and topped the 1916 flood by nearly 0.5 m.

The floods wreaked havoc on the infrastructure across the region. The initial recovery was slowed by closures of Interstates 26 and 40 going in and out of Asheville due to flooding, landslides, downed trees, or washed-out roads and bridges. The floodwaters also washed out a 1-m water main that connected the city of Asheville with its primary reservoir. It took nearly three weeks to restore water pressure to the system (Boyle 2024a). The loss of water briefly shut down the data center for NOAA's National Centers for Environmental Information, which relies on city water to cool its computers. The floods also washed significant amounts of clay into the reservoir, preventing the city from being able to treat the water. More than 100,000 people were left without potable water for 53 days until the system could be fully pressurized, treated, flushed, and tested (Boyle 2024b). Recovery from the storm is expected to take years.

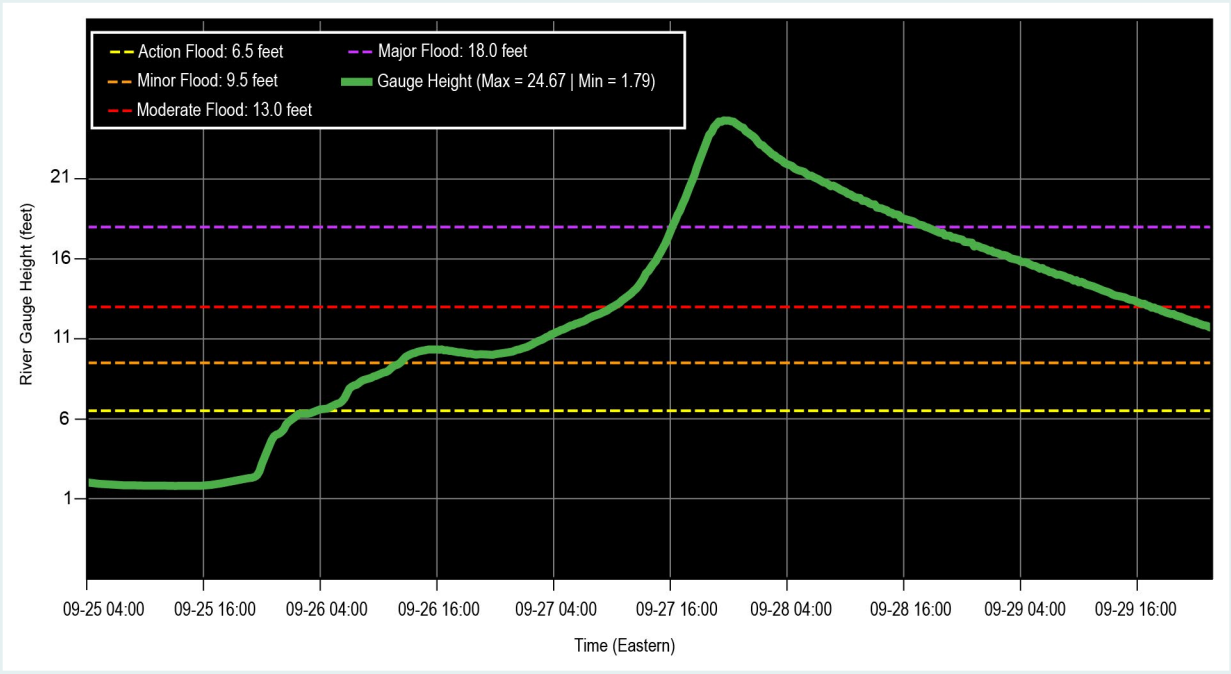

Fig. SB4.2. Hydrograph of the French Broad River gauge in Asheville, North Carolina, prior to, during, and following the passage of Hurricane Helene.

Unauthenticated | Downloaded 11/21/25 11:34 AM UTC

Sidebar 4.2: Hurricane Milton: A record-setting hurricane with major Florida impacts

—P. KLOTZBACH, C. FOGARTY, AND R. TRUCHELUT

Hurricane Milton was the strongest October hurricane on record in the Gulf of America/Gulf of Mexico (hereafter referred to as Gulf), achieving a maximum intensity of 155 kt (80 m s^{-1}) and a minimum central pressure of 895 hPa on 7 October. Milton weakened considerably before landfall but still was a major Category 3 hurricane with maximum sustained winds of 100 kt (51 m s^{-1}) when it made landfall near Siesta Key, Florida, early on 10 October. The storm caused significant surge, freshwater flooding, and wind damage along the west coast of Florida, while an outbreak of destructive tornadoes occurred in east-central and southeastern Florida. In addition, Milton's severe wind and storm surge impacts on Florida's Gulf Coast compounded existing damage caused by Hurricane Helene, with just 12 days separating Helene and Milton's landfalls in Florida.

This sidebar focuses on the meteorological history of Milton, highlighting several records that Milton set during its northeastward track across the Gulf. North Atlantic (hereafter Atlantic) hurricane records from 1851 to 2023 are taken from the National Hurricane Center's hurricane database (HURDAT2; Landsea and Franklin 2013). Milton's observed values were predominately from the National Hurricane Center's operational b-decks, from which tropical cyclone numerical model guidance was initialized in real time every six hours. All times are listed in hours Coordinated Universal Time (UTC).

Milton developed into a tropical depression from an area of low pressure in the Bay of Campeche on 5 October at 1200 UTC and intensified to a 35 kt (18 m s^{-1}) tropical storm six hours later. Over the next 48 hours, the system underwent explosive intensification to a Category 5 hurricane with maximum sustained winds of 150 kt (77 m s^{-1}) in an environment of anomalously warm sea surface temperatures in the range of 29°C–30°C, as well as low vertical wind shear (<10 kt; 5 m s^{-1}) as it tracked northeastward across the Gulf. Later on 7 October, Milton achieved its peak intensity of 155 kt (80 m s^{-1}) and 895 hPa (Fig. SB4.3). Milton's high-end rapid intensification was extremely unusual for a system tracking northeastward in the Atlantic.

Milton underwent an eyewall replacement cycle and temporarily weakened before re-strengthening to a Category 5 hurricane later on 8 October. The next day, an upper-level trough to Milton's northwest began to impinge on the system, imparting strong northwesterly wind shear (>30 kt; >15 m s^{-1}) over the system. The shear caused the storm to weaken rapidly, with its maximum sustained winds decreasing by 35 kt (from 135 kt [69 m s^{-1}] to 100 kt [51 m s^{-1}]) and its central pressure rising from 919 hPa to 958 hPa in the ~12 hours prior to landfall. Following landfall, Milton continued to weaken as it tracked northeast across the Florida Peninsula. Interaction with the trough to Milton's northwest also hastened Milton's transition to an extratropical cyclone later on 10 October, shortly after it emerged from the east coast of Florida into the southwest Atlantic.

Hurricane Milton set several records as it traversed northeastward across the Gulf. As noted earlier, Milton's peak intensity of 155 kt (80 m s^{-1}) was the strongest on record for an October hurricane in the Gulf, and its minimum central pressure of 895 hPa was the lowest on record for an October hurricane in the Gulf and for any Atlantic hurricane since Wilma in 2005. Its peak 24-hr intensification rate of 80 kt (41 m s^{-1}) and 48-hr intensification rate of 115 kt (59 m s^{-1}) are also the recorded maxima for any Gulf hurricane. Only two named storms on record (Wilma in 2005 and Felix in 2007) have intensified more rapidly in a 24-hr period, while Milton is tied with Felix and trails only Wilma (120 kt) for the most intensification by an Atlantic named storm in a 48-hour period. Milton was a Category 5 hurricane for slightly longer than one day. This places it just behind Camille in 1969 and Allen in 1980 for the longest amount of time on record that a system has spent at Category 5 intensity in the Gulf.

Hurricane Milton caused significant wind, flooding, and storm surge impacts for areas along the west coast of Florida that had experienced considerable impacts from Hurricane Helene less than two weeks earlier. Milton's interaction with an upper-level trough hastened its extratropical transition and

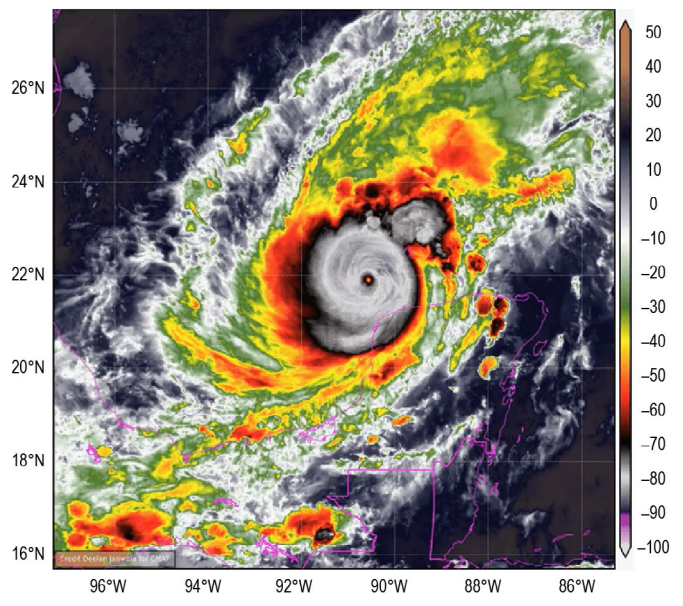

Fig. SB4.3. Geostationary Operational Environmental Satellites (GOES)-16 infrared satellite image of Hurricane Milton near the time of its peak intensity at 2357 UTC on 7 Oct 2024. (Image credit: NOAA via https://cyclonicwx.com/.)

Unauthenticated | Downloaded 11/21/25 11:34 AM UTC

then shifted its maximum precipitation to the left side of the storm track (Atallah et al. 2007). Milton brought over 450 mm of rainfall to the Albert Whitted Airport in Saint Petersburg, Florida. The storm also brought a substantial storm surge of 2 m–3 m to the south of where it made landfall, with a peak storm surge of ~3 m in southern Sarasota County. Peak wind gusts over land of ~85 kt (44 m s^{-1}) were recorded at numerous stations between St. Petersburg and Sarasota.

Milton was also notable for the severity and destructiveness of a tornado outbreak that spawned 46 tornadoes in Florida. Three of these tornadoes were classified as EF-3; by comparison, only five hurricane-spawned tornadoes for the entire continental United States from 1995 to 2023 were classified as EF-3, based on data from NOAA's Storm Prediction Center. This strong tornado outbreak was likely driven by the two following factors: First, strong upper-level westerly winds combined with low-level southeasterly winds advecting a deep tropical air mass over the Florida peninsula to produce pronounced horizontal wind shear. Second, eastern Florida (where the strongest tornadoes occurred) received considerable sunshine in the morning prior to Milton's landfall, allowing for significant atmospheric instability to be present prior to the outer rain bands coming onshore. This combination of instability and strong shear created an extremely conducive environment for the tornado outbreak (Fig. SB4.4).

As noted earlier, Hurricane Milton's impacts exacerbated pre-existing damage from Hurricane Helene, with recovery efforts from Helene such as debris removal along the west-central Florida coast not having been completed prior to Milton. The fewer than 12 days separating Helene and Milton is the shortest time on record between Florida major hurricane landfalls. According to the latest estimates from NOAA's National Centers for Environmental Information, Milton was responsible for 15 direct fatalities and $34.3 billion (U.S. dollars) in damage. It was the last of five hurricanes (including Beryl, Debby, Francine, and Helene) that buffeted the southern United States during the extremely active 2024 Atlantic hurricane season.

Fig. SB4.4. Damage to a home in Wellington, Florida, from a tornado estimated at EF-3 intensity. (Image credit: Palm Beach Post.)

Unauthenticated | Downloaded 11/21/25 11:34 AM UTC

Appendix 1: Acronyms

ACE	accumulated cyclone energy
AMV	Atlantic Multidecadal Variability
AUSSM	Australian summer monsoon
BoM	Bureau of Meteorology
Cat	category
CMORPH	Climate Prediction Center Morphing technique
CNP	Central North Pacific
CoCoRaHS	Community Collaborative Rain, Hail and Snow Network
CPC	Climate Prediction Center
D26	26°C isotherm
EASM	East Asian summer monsoon
ENP	eastern North Pacific
ENSO	El Niño–Southern Oscillation
HTCs	hurricanes/typhoons/cyclones
IO	Indian Ocean
IOB	Indian Ocean basin
IOD	Indian Ocean dipole
IODE	eastern part of the Indian Ocean dipole
IODW	western part of the Indian Ocean dipole
ISM	Indian summer monsoon
ITCZ	Intertropical Convergence Zone
JMA	Japan Meteorological Agency
JTWC	Joint Typhoon Warning Center
LMR	land monsoon rainfall
MDR	main development region
MJO	Madden–Julian Oscillation
MSLP	mean sea level pressure
MSWEP	Multi-Source Weighted-Ensemble Precipitation
MTY	major typhoon
NAFSM	North African summer monsoon
NASM	North American summer monsoon
NCAR	National Centers for Atmospheric Research
NCEP	National Centers for Environmental Prediction
NH	Northern Hemisphere
NHC	National Hurricane Center
NIO	North Indian Ocean
nIOD	negative Indian Ocean dipole
NOAA GlobalTemp	NOAA Merged Land Ocean Global Surface Temperature Analysis
OHC	ocean heat content
OLR	outgoing longwave radiation
ONI	Oceanic Niño Index
ORAS4	Ocean Reanalysis System 4
PAGASA	Philippine Atmospheric, Geophysical and Astronomical Services Administration
PRE	predecessor rain event
RMM	Real-time Multivariate Madden–Julian Oscillation
RSMC	Regional Specialized Meteorological Center
SAFSM	South African summer monsoon
SAM	Southern Annular Mode
SASM	South American summer monsoon

Unauthenticated | Downloaded 11/21/25 11:34 AM UTC

SH	Southern Hemisphere
SIO	South Indian Ocean
SPCZ	South Pacific Convergence Zone
SPEArTC	Southwest Pacific Enhanced Archive for Tropical Cyclones
SSHWS	Saffir–Simpson Hurricane Wind Scale
SST	sea surface temperature
STS	severe tropical storm
SWP	southwest Pacific basin
TC	tropical cyclone
TCHP	tropical cyclone heat potential
TD	tropical depression
TS	tropical storm
TY	typhoon
WMO	World Meteorological Organization
WNC	western North Carolina
WNP	western North Pacific
WNPSM	western North Pacific summer monsoon

Unauthenticated | Downloaded 11/21/25 11:34 AM UTC

Appendix 2: Datasets and sources

Section 4b ENSO and the tropical Pacific

Sub-section	General Variable or Phenomenon	Specific Dataset or Variable	Source
4b2	Outgoing Longwave Radiation	National Centers for Environmental Prediction (NCEP) Climate Prediction Center (CPC) Outgoing Longwave Radiation (OLR) (Liebmann and Smith, 1996)	https://www.cpc.ncep.noaa.gov/products/global_precip/html/wpage.olr.html
4b	Sea Surface Temperature	ERSSTv5	https://doi.org/10.7289/V5T72FNM
4b1	Sea Surface Temperature	OISSTv2.1	https://www.ncei.noaa.gov/products/optimum-interpolation-sst
4b1	Subsurface Ocean Temperature	Global Ocean Data Assimilation System (GODAS, Behringer 2007)	https://www.cpc.ncep.noaa.gov/products/GODAS/
4b2	Wind Vectors/Wind Speed	NCEP National Center for Atmospheric Research Reanalysis 1	https://psl.noaa.gov/data/gridded/data.ncep.reanalysis.html

Section 4c Tropical intraseasonal activity

Sub-section	General Variable or Phenomenon	Specific Dataset or Variable	Source
4c	Outgoing Longwave Radiation (OLR)	High Resolution Infrared Radiation Sounder (HIRS) OLR (Schreck et al. 2018)	https://www.ncei.noaa.gov/access/metadata/landing-page/bin/iso?id=gov.noaa.ncdc:C00875
4c	Subsurface Ocean Heat Content	Global Ocean Data Assimilation System (GODAS, Behringer et al. 1998)	https://www.cpc.ncep.noaa.gov/products/GODAS/
4c	Wind Velocity Potential Anomalies	Climate Forecast System Reanalysis (CFSR)	https://climatedataguide.ucar.edu/climate-data/climate-forecast-system-reanalysis-cfsr

Section 4d Intertropical convergence zones

Sub-section	General Variable or Phenomenon	Specific Dataset or Variable	Source
4d1	Precipitation	Multisource Weighted Ensemble Precipitation (MSWEP Version 2.8.0)	https://www.gloh2o.org/mswep/
4d2	Precipitation	Climate Prediction Center Morphing Technique (CMORPH)	https://www.ncei.noaa.gov/products/climate-data-records/precipitation-cmorph

Unauthenticated | Downloaded 11/21/25 11:34 AM UTC

Sub-section	General Variable or Phenomenon	Specific Dataset or Variable	Source
4d2	Outgoing Longwave Radiation (OLR)	National Centers for Environmental Prediction (NCEP) Climate Prediction Center (CPC) OLR (Liebmann and Smith, 1996)	https://www.cpc.ncep.noaa.gov/products/global_precip/html/wpage.olr.html
4d2	Sea Level Pressure	NCEP National Center for Atmospheric Research (NCAR) Reanalysis 1	https://psl.noaa.gov/data/gridded/data.ncep.reanalysis.html
4d2	Sea Surface Temperature	OISSTv2.1	https://www.ncei.noaa.gov/products/optimum-interpolation-sst

Section 4e Global monsoon summary

Sub-section	General Variable or Phenomenon	Specific Dataset or Variable	Source
4e	Precipitation	GPCP	https://www.ncei.noaa.gov/products/climate-data-records/precipitation-gpcp-monthly
4e	Sea Surface Temperature	ERSSTv5	https://doi.org/10.7289/V5T72FNM
4e	Sea Surface Temperature	HadISST	https://www.metoffice.gov.uk/hadobs/hadisst/
4e	Wind, [Near] Surface	ERA5	https://www.ecmwf.int/en/forecasts/dataset/ecmwf-reanalysis-v5
4e	Wind, Upper Atmosphere	ERA5	https://www.ecmwf.int/en/forecasts/dataset/ecmwf-reanalysis-v5

Section 4f Indian Ocean dipole

Sub-section	General Variable or Phenomenon	Specific Dataset or Variable	Source
4f	Precipitation	Climate Prediction Center Merged Analysis of Precipitation (CMAP)	https://www.cpc.ncep.noaa.gov/products/global_precip/html/wpage.cmap.html
4f	Sea Surface Temperature	OISSTv2	https://www.ncei.noaa.gov/products/optimum-interpolation-sst
4f	Wind, [Near] Surface	JRA-55 Atmospheric Reanalysis	http://jra.kishou.go.jp/JRA-55/index_en.html
4f	Wind, [Near] Surface	ERA5	https://www.ecmwf.int/en/forecasts/dataset/ecmwf-reanalysis-v5

Unauthenticated | Downloaded 11/21/25 11:34 AM UTC

Section 4g Tropical cyclones

Sub-section	General Variable or Phenomenon	Specific Dataset or Variable	Source
4g2	Outgoing Longwave Radiation	National Centers for Environmental Prediction (NCEP) Climate Prediction Center (CPC) Outgoing Longwave Radiation (OLR) (Liebmann and Smith, 1996)	https://www.cpc.ncep.noaa.gov/products/global_precip/html/wpage.olr.html
4g3, 4g5	Outgoing Longwave Radiation	High Resolution Infrared Radiation Sounder (HIRS) OLR (Schreck et al. 2018)	https://www.ncei.noaa.gov/access/metadata/landing-page/bin/iso?id=gov.noaa.ncdc:C00875
4g3, 4g5, 4g6	Sea Surface Temperature	NOAA OISST v2	https://www.ncei.noaa.gov/products/optimum-interpolation-sst
4g4	Sea Surface Temperature	ERSSTv5	https://doi.org/10.7289/V5T72FNM
4g1, 4g2, 4g3, 4g5, 4g6, 4g7	Tropical Cyclone Data	International Best Track Archive for Climate Stewardship (IBTrACS)	https://www.ncei.noaa.gov/products/international-best-track-archive
4g2	Tropical Cyclone Data	HURDAT2	www.aoml.noaa.gov/hrd/hurdat/Data_Storm.html
4g4	Tropical Cyclone Data	Regional Specialized Meteorological Center (RSMC) Tokyo, Japanese Meteorological Agency (JMA) Best-Track Database	www.jma.go.jp/jma/jma-eng/jma-center/rsmc-hp-pub-eg/besttrack.html
4g4	Tropical Cyclone Data	Joint Typhoon Warning Center (JTWC) Best-Track Database	https://www.metoc.navy.mil/jtwc/jtwc.html?best-tracks
4g8	Tropical Cyclone Data	Southwest Pacific Enhanced Archive of Tropical Cyclones (SPEArTC)	https://apdrc.soest.hawaii.edu/projects/speartc/
4g2	Wind, [Near] Surface	NCEP National Center for Atmospheric Research (NCAR) Reanalysis 1	https://psl.noaa.gov/data/gridded/data.ncep.reanalysis.html
4g4	Wind, [Near] Surface	ERA5	https://www.ecmwf.int/en/forecasts/dataset/ecmwf-reanalysis-v5
4g3, 4g5, 4g6	Wind, [Near] Surface	Climate Forecast System Reanalysis (CFSR)	https://climatedataguide.ucar.edu/climate-data/climate-forecast-system-reanalysis-cfsr

Unauthenticated | Downloaded 11/21/25 11:34 AM UTC

Section 4h Tropical cyclone heat potential			
Sub-section	**General Variable or Phenomenon**	**Specific Dataset or Variable**	**Source**
4h	Ocean Heat Content	ECMWF Ocean Reanalysis System 4 (ORAS4)	https://www.ecmwf.int/en/forecasts/dataset/ocean-reanalysis-system-4

Sidebar 4.1 Hurricane Helene: Inside Western North Carolina's Historic Flood			
Sub-section	**General Variable or Phenomenon**	**Specific Dataset or Variable**	**Source**
SB4.1	Precipitation	Community Collaborative Rain, Hail and Snow Network (CoCoRaHS) Volunteer Network	https://www.cocorahs.org/
SB4.1	Precipitation Frequency Data	NOAA Atlas 14	https://hdsc.nws.noaa.gov/pfds/

Sidebar 4.2 Hurricane Milton: A record-setting gulf major hurricane with major Florida impacts			
Sub-section	**General Variable or Phenomenon**	**Specific Dataset or Variable**	**Source**
SB4.2	Tropical Cyclone Data	HURDAT2	www.aoml.noaa.gov/hrd/hurdat/Data_Storm.html

Unauthenticated | Downloaded 11/21/25 11:34 AM UTC

References

Aiyyer, A., and J. Molinari, 2008: MJO and tropical cyclogenesis in the Gulf of Mexico and eastern Pacific: Case study and idealized numerical modeling. *J. Atmos. Sci.*, **65**, 2691–2704, https://doi.org/10.1175/2007JAS2348.1.

Atallah, E., L. F. Bosart, and A. R. Aiyyer, 2007: Precipitation distribution associated with landfalling tropical cyclones over the eastern United States. *Mon. Wea. Rev.*, **135**, 2185–2206, https://doi.org/10.1175/MWR3382.1.

Balaguru, K., P. Chang, R. Saravanan, L. R. Leung, Z. Xu, M. Li, and J. S. Hsieh, 2012: Ocean barrier layers' effect on tropical cyclone intensification. *Proc. Natl. Acad. Sci. USA*, **109**, 14343–14347, https://doi.org/10.1073/pnas.1201364109.

Banzon, V. F., and R. W. Reynolds, 2013: Use of WindSat to extend a microwave-based daily optimum interpolation sea surface temperature time series. *J. Climate*, **26**, 2557–2562, https://doi.org/10.1175/JCLI-D-12-00628.1.

Beck, H. E., E. F. Wood, M. Pan, C. K. Fisher, D. G. Miralles, A. I. J. M. van Dijk, T. R. McVicar, and R. F. Adler, 2019: MSWEP V2 global 3-hourly 0.1° precipitation: Methodology and quantitative assessment. *Bull. Amer. Meteor. Soc.*, **100**, 473–500, https://doi.org/10.1175/BAMS-D-17-0138.1.

Behringer, D. W., 2007: The Global Ocean Data Assimilation System (GODAS) at NCEP. Preprints, *11th Symp. on Integrated Observing and Assimilation Systems for Atmosphere, Oceans, and Land Surface (IOAS-AOLS)*, San Antonio, TX, Amer. Meteor. Soc., 3.3, https://ams.confex.com/ams/87ANNUAL/techprogram/paper_119541.htm.

——, M. Ji, and A. Leetmaa, 1998: An improved coupled model for ENSO prediction and implications for ocean initialization. Part I: The ocean data assimilation system. *Mon. Wea. Rev.*, **126**, 1013–1021, https://doi.org/10.1175/1520-0493(1998)126<1013:AICMFE>2.0.CO;2.

Bell, G. D., and M. Chelliah, 2006: Leading tropical modes associated with interannual and multidecadal fluctuations in North Atlantic hurricane activity. *J. Climate*, **19**, 590–612, https://doi.org/10.1175/JCLI3659.1.

——, and Coauthors, 2000: Climate Assessment for 1999. *Bull. Amer. Meteor. Soc.*, **81** (6), S1–S50, https://doi.org/10.1175/1520-0477(2000)81[s1:CAF]2.0.CO;2.

——, S. Goldenberg, C. Landsea, E. Blake, R. Pasch, M. Chelliah, and K. Mo, 2004: Atlantic hurricane season [in "State of the Climate in 2003"]. *Bull. Amer. Meteor. Soc.*, **85** (6), S20–S24, https://doi.org/10.1175/1520-0477-85.6s.S1.

——, E. Blake, C. Landsea, K. Mo, R. Pasch, M. Chelliah, and S. Goldenberg, 2006: Atlantic basin [in "State of the Climate in 2005"]. *Bull. Amer. Meteor. Soc.*, **87** (6), S33–S37, https://doi.org/10.1175/1520-0477-87.6.S1.

——, ——, T. B. Kimberlain, C. W. Landsea, J. Schemm, R. J. Pasch, and S. B. Goldenberg, 2011: Atlantic basin [in "State of the Climate in 2010"]. *Bull. Amer. Meteor. Soc.*, **92** (6), S115–S121, https://doi.org/10.1175/1520-0477-92.6.S1.

——, ——, C. W. Landsea, C. Wang, J. Schemm, T. Kimberlain, R. J. Pasch, and S. B. Goldenberg, 2017: Atlantic basin [in "State of the Climate in 2016"]. *Bull. Amer. Meteor. Soc.*, **98** (8), S108–S112, https://doi.org/10.1175/2017BAMSStateoftheClimate.1

——, ——, ——, S. B. Goldenberg, and R. J. Pasch, 2018: Atlantic basin [in "State of the Climate in 2017"]. *Bull. Amer. Meteor. Soc.*, **99** (8), S114–S118, https://doi.org/10.1175/2018BAMSStateoftheClimate.1.

——, ——, ——, H. Wang, S. B. Goldenberg, and R. J. Pasch 2019a: Atlantic basin [in "State of the Climate in 2018"]. *Bull. Amer. Meteor. Soc.*, **100** (9), S113–S119, https://doi.org/10.1175/2019BAMSStateoftheClimate.1.

——, ——, ——, M. Rosencrans, H. Wang, S. B. Goldenberg, and R. J. Pasch, 2020: Atlantic basin [in "State of the Climate in 2019"]. *Bull. Amer. Meteor. Soc.*, **101** (7), S204–S212, https://doi.org/10.1175/BAMS-D-20-0077.1.

Berg, R., 2024: Tropical cyclone report: Tropical storm max (EP162023), 8–10 October 2023. NHC Tech. Rep., 20 pp., https://www.nhc.noaa.gov/data/tcr/EP162023_Max.pdf.

Beven J. L. II, C. Fritz, and L. Alaka, 2024: Tropical cyclone report: Hurricane Beryl (AL022024), 8–10 October 2023. NHC Tech. Rep., 76 pp., https://www.nhc.noaa.gov/data/tcr/AL022024_Beryl.pdf.

Bjerknes, J., 1969: Atmospheric teleconnections from the equatorial Pacific. *Mon. Wea. Rev.*, **97**, 163–172, https://doi.org/10.1175/1520-0493(1969)097<0163:ATFTEP>2.3.CO;2.

Bonnin, G. M., D. Martin, B. Lin, T. Parzybok, M. Yekta, and D. Riley, 2006: Delaware, District of Columbia, Illinois, Indiana, Kentucky, Maryland, New Jersey, North Carolina, Ohio, Pennsylvania, South Carolina, Tennessee, Virginia, West Virginia. Precipitation-Frequency Atlas of the United States, Vol. 2,Version 3.0, NOAA Atlas 14, 301 pp., https://repository.library.noaa.gov/view/noaa/22610.

Boyle, J., 2024a: Asheville potable water is back, city boil water notice lifted. Asheville Watchdog, accessed 17 December 2024, https://avlwatchdog.org/asheville-potable-water-is-back-city-boil-water-notice-lifted/.

——, 2024b: Water back to majority of Asheville customers, but higher elevations still waiting. Asheville Watchdog, accessed 17 December 2024, https://avlwatchdog.org/water-back-to-majority-of-asheville-customers-but-higher-elevations-still-waiting/.

Camargo, S. J., and A. H. Sobel, 2005: Western North Pacific tropical cyclone intensity and ENSO. *J. Climate*, **18**, 2996–3006, https://doi.org/10.1175/JCLI3457.1.

——, A. W. Robertson, S. J. Gaffney, P. Smyth, and M. Ghil, 2007a: Cluster analysis of typhoon tracks. Part II: Large-scale circulation and ENSO. *J. Climate*, **20**, 3654–3676, https://doi.org/10.1175/JCLI4203.1.

——, K. A. Emanuel, and A. H. Sobel, 2007b: Use of a genesis potential index to diagnose ENSO effects on tropical cyclone genesis. *J. Climate*, **20**, 4819–4834, https://doi.org/10.1175/JCLI4282.1.

Chan, J. C. L., and K. S. Liu, 2002: Recent decrease in the difference in tropical cyclone occurrence between the Atlantic and the western North Pacific. *Adv. Atmos. Sci.*, **39**, 1387–1397, https://doi.org/10.1007/s00376-022-1309-x.

Chang, Y.-T., I.-I. Lin, H.-C. Huang, Y.-C. Liao, and C.-C. Lien, 2020: The Association of Typhoon Intensity Increase with Translation Speed Increase in the South China Sea. *Sustainability*, **12**, 939, https://doi.org/10.3390/su12030939.

Chia, H. H., and C. F. Ropelewski, 2002: The interannual variability in the genesis location of tropical cyclones in the northwest Pacific. *J. Climate*, **15**, 2934–2944, https://doi.org/10.1175/1520-0442(2002)015<2934:TIVITG>2.0.CO;2.

Choi, H.-Y., M.-S. Park, H.-S. Kim, and S. Lee, 2024: Marine heatwave events strengthen the intensity of tropical cyclones. *Commun. Earth Environ.*, **5**, 1–8, https://doi.org/10.1038/s43247-024-01239-4.

Unauthenticated | Downloaded 11/21/25 11:34 AM UTC

Dare, R. A., and J. L. McBride, 2011: Sea surface temperature response to tropical cyclones. *Mon. Wea. Rev.*, **139**, 3798–3808, https://doi.org/10.1175/MWR-D-10-05019.1.

Diamond, H. J., and C. J. Schreck III, Eds., 2022: The tropics [in "State of the Climate in 2021"]. *Bull. Amer. Meteor. Soc.*, **103** (8), S193–S256, https://doi.org/10.1175/BAMS-D-22-0069.1.

—— , and —— , Eds., 2023: The tropics [in "State of the Climate in 2022"]. *Bull. Amer. Meteor. Soc.*, **104** (8), S207–S270, https://doi.org/10.1175/BAMS-D-23-0078.1.

—— , and —— , Eds., 2024: The tropics [in "State of the Climate in 2023"]. *Bull. Amer. Meteor. Soc.*, **105** (8), S214–S276, https://doi.org/10.1175/BAMS-D-24-0098.1.

—— , A. M. Lorrey, K. R. Knapp, and D. H. Levinson, 2012: Development of an enhanced tropical cyclone tracks database for the southwest Pacific from 1840 to 2010. *Int. J. Climatol.*, **32**, 2240–2250, https://doi.org/10.1002/joc.2412.

Ding, Q., E. J. Steig, D. S. Battisti, and J. M. Wallace, 2012: Influence of the tropics on the Southern Annular Mode. *J. Climate*, **25**, 6330–6348, https://doi.org/10.1175/JCLI-D-11-00523.1.

Domingues, R., and Coauthors, 2015: Upper ocean response to Hurricane Gonzalo (2014): Salinity effects revealed by targeted and sustained underwater glider observations. *Geophys. Res. Lett.*, **42**, 7131–7138, https://doi.org/10.1002/2015GL065378.

Dube, S. K., D. Rao, P. C. Sinha, T. S. Murty, and N. Bahuluyan, 1997: Storm surge in the Bay of Bengal and Arabian Sea: The problem and its prediction. *Mausam*, **48**, 283–304, https://doi.org/10.54302/mausam.v48i2.4012.

Ebita, A., and Coauthors, 2011: The Japanese 55-year Reanalysis "JRA-55": An interim report. *SOLA*, **7**, 149–152, https://doi.org/10.2151/sola.2011-038.

Emanuel, K. A., 1988: The maximum intensity of hurricanes. *J. Atmos. Sci.*, **45**, 1143–1155, https://doi.org/10.1175/1520-0469(1988)045<1143:TMIOH>2.0.CO;2.

—— , and D. S. Nolan, 2004: Tropical cyclone activity and the global climate system. *Proc. 26th Conf. on Hurricanes and Tropical Meteorology*, Miami, FL, Amer. Meteor. Soc., 10A.2, https://ams.confex.com/ams/26HURR/techprogram/paper_75463.htm.

Enfield, D. B., and A. M. Mestas-Nuñez, 1999: Multiscale variabilities in global sea surface temperatures and their relationships with tropospheric climate patterns. *J. Climate*, **12**, 2719–2733, https://doi.org/10.1175/1520-0442(1999)012<2719:MVIGSS>2.0.CO;2.

Galarneau, T. J., L. F. Bosart, and R. S. Schumacher, 2010: Predecessor rain events ahead of tropical cyclones. *Mon. Wea. Rev.*, **138**, 3272–3297, https://doi.org/10.1175/2010MWR3243.1.

Gallagher Re, 2025: Gallagher Re natural catastrophe and climate report 2024. Data, insights, and perspectives. Accessed 27 January 2025, https://www.ajg.com/gallagherre/news-and-insights/gallagherre-natural-catastrophe-and-climate-report-2024/.

Gao, C., L. Zhou, I.-I. Lin, C. Wang, S. Guan, F.-F. Jin, and R. Murtugudde, 2025: Crucial role of subsurface ocean variability in tropical cyclone genesis. *Nat. Commun.*, **16**, 1–10, https://doi.org/10.1038/s41467-025-56433-5.

Goldenberg, S. B., and L. J. Shapiro, 1996: Physical mechanisms for the association of El Niño and West African rainfall with Atlantic major hurricane activity. *J. Climate*, **9**, 1169–1187, https://doi.org/10.1175/1520-0442(1996)009<1169:PMFTAO>2.0.CO;2.

—— , C. W. Landsea, A. M. Mestas-Nuñez, and W. M. Gray, 2001: The recent increase in Atlantic hurricane activity: Causes and implications. *Science*, **293**, 474–479, https://doi.org/10.1126/science.1060040.

Goni, G. J., and J. A. Trinanes, 2003: Ocean thermal structure monitoring could aid in the intensity forecast of tropical cyclones. *Eos, Trans. Amer. Geophys. Union*, **84**, 573–578, https://doi.org/10.1029/2003EO510001.

—— , and Coauthors, 2009: Applications of satellite-derived ocean measurements to tropical cyclone intensity forecasting. *Oceanography*, **22** (3), 190–197, https://doi.org/10.5670/oceanog.2009.78.

—— , and Coauthors, 2017: Autonomous and Lagrangian ocean observations for Atlantic tropical cyclone studies and forecasts. *Oceanography*, **30** (2), 92–103, https://doi.org/10.5670/oceanog.2017.227.

Gray, W. M., 1990: Strong association between West African rainfall and U.S. landfall of intense hurricanes. *Science*, **249**, 1251–1256, https://doi.org/10.1126/science.249.4974.1251.

Guo, Y., X. Jiang, and D. E. Waliser, 2014: Modulation of the convectively coupled Kelvin waves over South America and the tropical Atlantic Ocean in association with the Madden–Julian oscillation. *J. Atmos. Sci.*, **71**, 1371–1388, https://doi.org/10.1175/JAS-D-13-0215.1.

—— , S. Wu, H.-T. Lee, and P. Xie, 2024: CPC new OLR data set. *26th Conf. on Satellite Meteorology, Oceanography, and Climatology*, Baltimore, MD, Amer. Meteor. Soc., 8.5, https://ams.confex.com/ams/104ANNUAL/webprogram/Paper435981.html.

Hastenrath, S., 1990: Decadal-scale changes of the circulation in the tropical Atlantic sector associated with Sahel drought. *Int. J. Climatol.*, **10**, 459–472, https://doi.org/10.1002/joc.3370100504.

Hersbach, H., and Coauthors, 2020: The ERA5 global reanalysis. *Quart. J. Roy. Meteor. Soc.*, **146**, 1999–2049, https://doi.org/10.1002/qj.3803.

Hogikyan, A., L. Resplandy, and S. Fueglistaler, 2022: Cause of the Intense Tropics-Wide Tropospheric Warming in Response to El Niño. *J. Climate*, **35**, 2933–2944, https://doi.org/10.1175/JCLI-D-21-0728.1.

Hong, C.-C., T. Li, and J.-J. Luo, 2008: Asymmetry of the Indian Ocean dipole. Part II: Model diagnosis. *J. Climate*, **21**, 4849–4858, https://doi.org/10.1175/2008JCLI2223.1.

Huang, B., and Coauthors, 2017: Extended Reconstructed Sea Surface Temperature, version 5 (ERSSTv5): Upgrades, validations, and intercomparisons. *J. Climate*, **30**, 8179–8205, https://doi.org/10.1175/JCLI-D-16-0836.1.

—— , C. Liu, V. Banzon, E. Freeman, G. Graham, B. Hankins, T. Smith, and H.-M. Zhang, 2021: Improvements of the Daily Optimum Interpolation Sea Surface Temperature (DOISST) version 2.1. *J. Climate*, **34**, 2923–2939, https://doi.org/10.1175/JCLI-D-20-0166.1.

Huffman, G. J., R. F. Adler, D. T. Bolvin, and G. Gu, 2009: Improving the global precipitation record: GPCP version 2.1. *Geophys. Res. Lett.*, **36**, L17808, https://doi.org/10.1029/2009GL040000.

Jones, A. R., 2024: Buncombe's blackout: Severed fiber lines made it impossible to call, text or use data on phones. Asheville Watchdog, accessed 17 December 2024, https://avlwatchdog.org/buncombes-blackout-severed-fiber-lines-made-it-impossible-to-call-text-or-use-data-on-phones/.

Unauthenticated | Downloaded 11/21/25 11:34 AM UTC

Joyce, R. J., J. E. Janowiak, P. A. Arkin, and P. Xie, 2004: CMORPH: A method that produces global precipitation estimates from passive microwave and infrared data at high spatial and temporal resolution. *J. Hydrometeor.*, **5**, 487–503, https://doi.org/10.1175/1525-7541(2004)005<0487:CAMTPG>2.0.CO;2.

Kalnay, E., and Coauthors, 1996: The NCEP/NCAR 40-Year Reanalysis Project. *Bull. Amer. Meteor. Soc.*, **77**, 437–471, https://doi.org/10.1175/1520-0477(1996)077<0437:TNYRP>2.0.CO;2.

Kang, S. K., and Coauthors, 2024: Anomalously large latent heat fluxes in low to moderate wind conditions within the eddy-rich zone of the Northwestern Pacific. *Front. Mar. Sci.*, **11**, https://doi.org/10.3389/fmars.2024.1298641.

Kiladis, G. N., M. C. Wheeler, P. T. Haertel, K. H. Straub, and P. E. Roundy, 2009: Convectively coupled equatorial waves. *Rev. Geophys.*, **47**, RG2003, https://doi.org/10.1029/2008RG000266.

Klotzbach, P., C. Fogarty, and R. Truchelut, 2024: Hurricane Otis: The strongest landfalling hurricane on record for the west coast of Mexico [in "State of the Climate in 2023"]. *Bull. Amer. Meteor. Soc.*, **105** (8), S264–S265, https://doi.org/10.1175/BAMS-D-24-0098.1.

Knaff, J. A., C. R. Sampson, and K. D. Musgrave, 2018: An operational rapid intensification prediction aid for the western North Pacific. *Wea. Forecasting*, **33**, 799–811, https://doi.org/10.1175/WAF-D-18-0012.1.

—— , —— , and B. R. Strahl, 2020: A tropical cyclone rapid intensification prediction aid for the Joint Typhoon Warning Center's areas of responsibility. *Wea. Forecasting*, **35**, 1173–1185, https://doi.org/10.1175/WAF-D-19-0228.1.

Knapp, K. R., M. C. Kruk, D. H. Levinson, H. J. Diamond, and C. J. Neumann, 2010: The International Best Track Archive for Climate Stewardship (IBTrACS): Unifying tropical cyclone data. *Bull. Amer. Meteor. Soc.*, **91**, 363–376, https://doi.org/10.1175/2009BAMS2755.1.

—— , J. A. Knaff, C. R. Sampson, G. M. Riggio, and A. D. Schnapp, 2013: A pressure-based analysis of the historical western North Pacific tropical cyclone intensity record. *Mon. Wea. Rev.*, **141**, 2611–2631, https://doi.org/10.1175/MWR-D-12-00323.1.

Landsea, C. W., and J. L. Franklin, 2013: Atlantic hurricane database uncertainty and presentation of a new database format. *Mon. Wea. Rev.*, **141**, 3576–3592, https://doi.org/10.1175/MWR-D-12-00254.1.

—— , W. M. Gray, P. W. Mielke, and K. J. Berry, 1992: Long-term variations of western Sahelian monsoon rainfall and intense U.S. landfalling hurricanes. *J. Climate*, **5**, 1528–1534, https://doi.org/10.1175/1520-0442(1992)005<1528:LTVOWS>2.0.CO;2.

—— , G. A. Vecchi, L. Bengtsson, and T. R. Knutson, 2010: Impact of duration thresholds on Atlantic tropical cyclone counts. *J. Climate*, **23**, 2508–2519, https://doi.org/10.1175/2009JCLI3034.1.

Leipper, D. F., and D. Volgenau, 1972: Hurricane heat potential of the Gulf of Mexico. *J. Phys. Oceanogr.*, **2**, 218–224, https://doi.org/10.1175/1520-0485(1972)002<0218:HHPOTG>2.0.CO;2.

L'Heureux, M. L., and Coauthors, 2024: A relative sea surface temperature index for classifying ENSO events in a changing climate. *J. Climate*, **37**, 1197–1211, https://doi.org/10.1175/JCLI-D-23-0406.1.

Liebmann, B., and C. A. Smith, 1996: Description of a complete (interpolated) outgoing longwave radiation dataset. *Bull. Amer. Meteor. Soc.*, **77**, 1275–1277, https://doi.org/10.1175/1520-0477-77.6.1274.

Lin, I.-I., C.-C. Wu, I.-F. Pun, and D.-S. Ko, 2008: Upper-Ocean Thermal Structure and the Western North Pacific Category 5 Typhoons. Part I: Ocean Features and the Category 5 Typhoons' Intensification. *Mon. Wea. Rev.*, **136**, 3288–3306, https://doi.org/10.1175/2008MWR2277.1.

—— , and Coauthors, 2013: An ocean coupling potential intensity index for tropical cyclones. *Geophys. Res. Lett.*, **40**, 1878–1882, https://doi.org/10.1002/grl.50091.

—— , and Coauthors, 2020: ENSO and tropical cyclones. *El Niño Southern Oscillation in a Changing Climate, Geophys. Monogr.*, Vol. 253, Amer. Geophys. Union, 377–408, https://doi.org/10.1002/9781119548164.ch17.

Liu, T., J. Li, C. Sun, T. Lian, and Y. Zhang, 2021: Impact of the April–May SAM on central Pacific Ocean sea temperature over the following three seasons. *Climate Dyn.*, **57**, 775–786, https://doi.org/10.1007/s00382-021-05738-4.

Lopez, H., S.-K. Lee, R. West, D. Kim, G. R. Foltz, G. J. Alaka, and H. Murakami, 2024: Projected increase in the frequency of extremely active Atlantic hurricane seasons. *Sci. Adv.*, **10**, eadq7856H, https://doi.org/10.1126/sciadv.adq7856.

Luo, J.-J., S. Masson, S. Behera, and T. Yamagata, 2007: Experimental forecasts of the Indian Ocean dipole using a coupled OAGCM. *J. Climate*, **20**, 2178–2190, https://doi.org/10.1175/JCLI4132.1.

—— , R. Zhang, S. K. Behera, Y. Masumoto, F.-F. Jin, R. Lukas, and T. Yamagata, 2010: Interaction between El Niño and extreme Indian Ocean dipole. *J. Climate*, **23**, 726–742, https://doi.org/10.1175/2009JCLI3104.1.

—— , W. Sasaki, and Y. Masumoto, 2012: Indian Ocean warming modulates Pacific climate change. *Proc. Natl. Acad. Sci. USA*, **109**, 18 701–18 706, https://doi.org/10.1073/pnas.1210239109.

Madden, R., and P. Julian, 1971: Detection of a 40–50 day oscillation in the zonal wind in the tropical Pacific. *J. Atmos. Sci.*, **28**, 702–708, https://doi.org/10.1175/1520-0469(1971)028<0702:DOADOI>2.0.CO;2.

—— , and —— , 1972: Description of global-scale circulation cells in the tropics with a 40–50 day period. *J. Atmos. Sci.*, **29**, 1109–1123, https://doi.org/10.1175/1520-0469(1972)029<1109:DOGSCC>2.0.CO;2.

—— , and —— , 1994: Observations of the 40–50-day tropical oscillation—A review. *Mon. Wea. Rev.*, **122**, 814–837, https://doi.org/10.1175/1520-0493(1994)122<0814:OOTDTO>2.0.CO;2.

Mainelli, M., M. DeMaria, L. Shay, and G. Goni, 2008: Application of oceanic heat content estimation to operational forecasting of recent Atlantic category 5 hurricanes. *Wea. Forecasting*, **23**, 3–16, https://doi.org/10.1175/2007WAF2006111.1.

Maloney, E. D., and D. L. Hartmann, 2001: The Madden–Julian oscillation, barotropic dynamics, and North Pacific tropical cyclone formation. Part I: Observations. *J. Atmos. Sci.*, **58**, 2545–2558, https://doi.org/10.1175/1520-0469(2001)058<2545:TMJOBD>2.0.CO;2.

Moore, A. M., and R. Kleeman, 1999: Stochastic forcing of ENSO by the intraseasonal oscillation. *J. Climate*, **12**, 1199–1220, https://doi.org/10.1175/1520-0442(1999)012<1199:SFOEBT>2.0.CO;2.

Moore, B. J., L. F. Bosart, D. Keyser, and M. L. Jurewicz, 2013: Synoptic-scale environments of predecessor rain events occurring east of the Rocky Mountains in association with Atlantic basin tropical cyclones. *Mon. Wea. Rev.*, **141**, 1022–1047, https://doi.org/10.1175/MWR-D-12-00178.1.

Unauthenticated | Downloaded 11/21/25 11:34 AM UTC

Moreno, P. I., and Coauthors, 2018: Onset and evolution of Southern Annular Mode-like changes at centennial timescale. *Sci. Rep.*, **8**, 3458, https://doi.org/10.1038/s41598-018-21836-6.

Münnich, M., and J. D. Neelin, 2005: Seasonal influence of ENSO on the Atlantic ITCZ and equatorial South America. *Geophys. Res. Lett.*, **32**, L21709, https://doi.org/10.1029/2005GL023900.

NOAA, 2024: Climate Diagnostics Bulletin, September 2023. 87 pp., https://www.cpc.ncep.noaa.gov/products/CDB/CDB_Archive_pdf/PDF/CDB.sep2023_color.pdf.

Nobre, P., and J. Shukla, 1996: Variations of sea surface temperature, wind stress, and rainfall over the tropical Atlantic and South America. *J. Climate*, **9**, 2464–2479, https://doi.org/10.1175/1520-0442(1996)009<2464:VOSSTW>2.0.CO;2.

Price, J. F., 1981: Upper Ocean Response to a Hurricane. *J. Phys. Oceanogr.*, **11**, 153–175, https://doi.org/10.1175/1520-0485(1981)011<0153:UORTAH>2.0.CO;2.

—— , 2009: Metrics of hurricane-ocean interaction: vertically-integrated or vertically-averaged ocean temperature? *Ocean Sci.*, **5**, 351–368, https://doi.org/10.5194/os-5-351-2009.

Pun, I.-F., and Coauthors, 2019: Rapid Intensification of Typhoon Hato (2017) over Shallow Water. *Sustainability*, **11**, 3709, https://doi.org/10.3390/su11133709.

Raga, G. B., B. Bracamontes-Ceballos, L. Farfán, and R. Romero-Centeno, 2013: Landfalling tropical cyclones on the Pacific coast of Mexico: 1850–2010. *Atmósfera*, **26**, 209–220, https://doi.org/10.1016/S0187-6236(13)71072-5.

Ramage, C. S., 1971: *Monsoon Meteorology*. Academic Press, 296 pp.

Reges, H. W., N. Doesken, J. Turner, N. Newman, A. Bergantino, and Z. Schwalbe, 2016: CoCoRaHS: The evolution and accomplishments of a volunteer rain gauge network. *Bull. Amer. Meteor. Soc.*, **97**, 1831–1846, https://doi.org/10.1175/BAMS-D-14-00213.1.

Reinhart, B. J., and A. Reinhart, 2024: Tropical Cyclone Report: Hurricane Otis (EP182023), 22–25 October 2023. NHC Tech. Rep., 39 pp., https://www.nhc.noaa.gov/data/tcr/EP182023_Otis.pdf.

Reynolds, R. W., N. A. Rayner, T. M. Smith, D. C. Stokes, and W. Wang, 2002: An improved in situ and satellite SST analysis for climate. *J. Climate*, **15**, 1609–1625, https://doi.org/10.1175/1520-0442(2002)015<1609:AIISAS>2.0.CO;2.

Rogers, R. F., and Coauthors, 2017: Rewriting the Tropical Record Books: The Extraordinary Intensification of Hurricane Patricia (2015). *Bull. Amer. Meteor. Soc.*, **98**, 2091–2112, https://doi.org/10.1175/BAMS-D-16-0039.1.

Ropelewski, C. F., and M. S. Halpert, 1989: Precipitation patterns associated with the high index phase of the Southern Oscillation. *J. Climate*, **2**, 268–284, https://doi.org/10.1175/1520-0442(1989)002<0268:PPAWTH>2.0.CO;2.

Saha, S., and Coauthors, 2014: The NCEP Climate Forecast System version 2. *J. Climate*, **27**, 2185–2208, https://doi.org/10.1175/JCLI-D-12-00823.1.

Saji, N. H., B. N. Goswami, P. N. Vinayachandran, and T. Yamagata, 1999: A dipole mode in the tropical Indian Ocean. *Nature*, **401**, 360–363, https://doi.org/10.1038/43854.

Schneider, T., T. Bischoff, and G. H. Haug, 2014: Migrations and dynamics of the Intertropical Convergence Zone. *Nature*, **513**, 45–53, https://doi.org/10.1038/nature13636.

Schreck, C. J., 2015: Kelvin waves and tropical cyclogenesis: A global survey. *Mon. Wea. Rev.*, **143**, 3996–4011, https://doi.org/10.1175/MWR-D-15-0111.1.

—— , 2016: Convectively coupled Kelvin waves and tropical cyclogenesis in a semi-Lagrangian framework. *Mon. Wea. Rev.*, **144**, 4131–4139, https://doi.org/10.1175/MWR-D-16-0237.1.

—— , and J. Molinari, 2011: Tropical cyclogenesis associated with Kelvin waves and the Madden–Julian Oscillation. *Mon. Wea. Rev.*, **139**, 2723–2734, https://doi.org/10.1175/MWR-D-10-05060.1.

—— , K. R. Knapp, and J. P. Kossin, 2014: The impact of best track discrepancies on global tropical cyclone climatologies using IBTrACS. *Mon. Wea. Rev.*, **142**, 3881–3899, https://doi.org/10.1175/MWR-D-14-00021.1.

—— , H.-T. Lee, and K. R. Knapp, 2018: HIRS outgoing longwave radiation—Daily climate data record: Application toward identifying tropical subseasonal variability. *Remote Sens.*, **10**, 1325, https://doi.org/10.3390/rs10091325.

Shay, L. K., G. J. Goni, and P. G. Black, 2000: Effects of a warm oceanic feature on Hurricane Opal. *Mon. Wea. Rev.*, **128**, 1366–1383, https://doi.org/10.1175/1520-0493(2000)128<1366:EOAWOF>2.0.CO;2.

Trenberth, K. E., 1984: Signal versus noise in the Southern Oscillation. *Mon. Wea. Rev.*, **112**, 326–332, https://doi.org/10.1175/1520-0493(1984)112<0326:SVNITS>2.0.CO;2.

Vecchi, G. A., and B. J. Soden, 2007: Effect of remote sea surface temperature change on tropical cyclone potential intensity. *Science*, **450**, 1066–1070, https://doi.org/10.1038/nature06423.

Ventrice, M. J., C. D. Thorncroft, and M. A. Janiga, 2012a: Atlantic tropical cyclogenesis: A three-way interaction between an African easterly wave, diurnally varying convection, and a convectively coupled atmospheric Kelvin wave. *Mon. Wea. Rev.*, **140**, 1108–1124, https://doi.org/10.1175/MWR-D-11-00122.1.

—— , —— , and C. J. Schreck, 2012b: Impacts of convectively coupled Kelvin waves on environmental conditions for Atlantic tropical cyclogenesis. *Mon. Wea. Rev.*, **140**, 2198–2214, https://doi.org/10.1175/MWR-D-11-00305.1.

Villarini, G., G. A. Vecchi, T. R. Knutson, and J. A. Smith, 2011: Is the recorded increase in short-duration North Atlantic tropical storms spurious? *J. Geophys. Res.*, **116**, D10114, https://doi.org/10.1029/2010JD015493.

Vincent, D. G., 1994: The South Pacific Convergence Zone (SPCZ): A review. *Mon. Wea. Rev.*, **122**, 1949–1970, https://doi.org/10.1175/1520-0493(1994)122<1949:TSPCZA>2.0.CO;2.

Vose, R. S., and Coauthors, 2021: Implementing full spatial coverage in NOAA's global temperature analysis. *Geophys. Res. Lett.*, **48**, e2020GL090873, https://doi.org/10.1029/2020GL090873.

Waliser, D. E., and C. Gautier, 1993: A satellite-derived climatology of the ITCZ. *J. Climate*, **6**, 2162–2174, https://doi.org/10.1175/1520-0442(1993)006<2162:ASDCOT>2.0.CO;2.

Wang, B., 1994: Climatic regimes of tropical convection and rainfall. *J. Climate*, **7**, 1109–1118, https://doi.org/10.1175/1520-0442(1994)007<1109:CROTCA>2.0.CO;2.

—— , and Z. Xie, 1996: Low-frequency equatorial waves in vertically sheared zonal flow. Part I: Stable waves. *J. Atmos. Sci.*, **53**, 449–467, https://doi.org/10.1175/1520-0469(1996)053<0449:LFEWIV>2.0.CO;2.

—— , and Q. Ding, 2008: Global monsoon: Dominant mode of annual variation in the tropics. *Dyn. Atmos. Ocean*, **44**, 165–183, https://doi.org/10.1016/j.dynatmoce.2007.05.002.

—— , and Q. He, 2024: Global monsoon summary [in "State of the Climate in 2023"]. *Bull. Amer. Meteor. Soc.*, **105** (8), S245–S248, https://doi.org/10.1175/BAMS-D-24-0098.1.

Unauthenticated | Downloaded 11/21/25 11:34 AM UTC

—— , J. Liu, H. J. Kim, P. J. Webster, and S. Y. Yim, 2012: Recent change of the global monsoon precipitation (1979–2008). *Climate Dyn.*, **39**, 1123–1135, https://doi.org/10.1007/s00382-011-1266-z.

Wheeler, M., and G. N. Kiladis, 1999: Convectively coupled equatorial waves: Analysis of clouds and temperature in the wavenumber–frequency domain. *J. Atmos. Sci.*, **56**, 374–399, https://doi.org/10.1175/1520-0469(1999)056<0374:CCEWAO>2.0.CO;2.

—— , and H. H. Hendon, 2004: An all-season real-time multivariate MJO index: Development of an index for monitoring and prediction. *Mon. Wea. Rev.*, **132**, 1917–1932, https://doi.org/10.1175/1520-0493(2004)132<1917:AARMMI>2.0.CO;2.

Wood, K. M., and E. A. Ritchie, 2015: A definition for rapid weakening in the North Atlantic and eastern North Pacific. *Geophys. Res. Lett.*, **42**, 10 091–10 097, https://doi.org/10.1002/2015GL066697.

—— , and C. J. Schreck, 2020: Eastern North Pacific and central North Pacific basins [in "State of the Climate in 2019"]. *Bull. Amer. Meteor. Soc.*, **101** (8), S212–S214, https://doi.org/10.1175/BAMS-D-20-0077.1.

—— , and —— , 2023: Eastern North Pacific and central North Pacific basins [in "State of the Climate in 2022"]. *Bull. Amer. Meteor. Soc.*, **104** (8), S239–S243, https://doi.org/10.1175/BAMS-D-23-0078.1.

—— , and —— , 2024: Eastern North Pacific and central North Pacific basins [in "State of the Climate in 2023"]. *Bull. Amer. Meteor. Soc.*, **105** (8), S245–S248, https://doi.org/10.1175/BAMS-D-24-0098.1.

Yim, S. Y., B. Wang, J. Liu, and Z. W. Wu, 2014: A comparison of regional monsoon variability using monsoon indices. *Climate Dyn.*, **43**, 1423–1437, https://doi.org/10.1007/s00382-013-1956-9.

Zhang, C., 2005: Madden–Julian Oscillation. *Rev. Geophys.*, **43**, RG2003, https://doi.org/10.1029/2004RG000158.

Zhao, J. W., R. F. Zhan, Y. Q. Wang, and H. M. Xu, 2018: Contribution of the Interdecadal Pacific oscillation to the recent abrupt decrease in tropical cyclone genesis frequency over the western North Pacific since 1998. *J. Climate*, **31**, 8211–8224, https://doi.org/10.1175/JCLI-D-18-0202.1.

Unauthenticated | Downloaded 11/21/25 11:34 AM UTC

STATE OF THE CLIMATE IN 2024

THE ARCTIC

R. L. Thoman, T. A. Moon, and M. L. Druckenmiller, Eds.

Special Online Supplement to the *Bulletin of the American Meteorological Society* Vol. 106, No. 8, August, 2025

https://doi.org/10.1175/BAMS-D-25-0104.1

Corresponding author: Richard L. Thoman / rthoman@alaska.edu

©2025 American Meteorological Society
For information regarding reuse of this content and general copyright information, consult the AMS Copyright Policy.

Unauthenticated | Downloaded 11/21/25 11:34 AM UTC

STATE OF THE CLIMATE IN 2024

The Arctic

Editors

Jessica Blunden
James Reagan

Chapter Editors

Anthony Arguez
Josh Blannin
Peter Bissolli
Kyle R. Clem
Howard J. Diamond
Matthew L. Druckenmiller
Robert J. H. Dunn
Catherine Ganter
Nadine Gobron
Gregory C. Johnson
Rick Lumpkin
Rodney Martinez
Ademe Mekonnen
Twila A. Moon
Gary A. Morris
Marilyn N. Raphael
Carl J. Schreck III
Laura Stevens
Richard L. Thoman
Kate M. Willett
Zhiwei Zhu

Technical Editor

Lukas Noguchi

BAMS Special Editor for Climate

Timothy DelSole

American Meteorological Society

Unauthenticated | Downloaded 11/21/25 11:34 AM UTC

Cover Credit:
Mulgrove Hills tundra landscape of shrubs, rock, and snow in the Alaskan Arctic.
Photo credit: J. J. Frost

How to cite this document:
The Arctic is one chapter from the *State of the Climate in 2024* annual report and is available from https://doi.org/10.1175/BAMS-D-25-0104.1. Compiled by NOAA's National Centers for Environmental Information, *State of the Climate in 2024* is based on contributions from scientists from around the world. It provides a detailed update on global climate indicators, notable weather events, and other data collected by environmental monitoring stations and instruments located on land, water, ice, and in space. The full report is available from https://doi.org/10.1175/2025BAMSStateoftheClimate.1.

Citing the complete report:
Blunden, J. and J. Reagan, Eds., 2025: "State of the Climate in 2024". Bull. Amer. Meteor. Soc., 106 (8), Si–S513 https://doi.org/10.1175/2025BAMSStateoftheClimate.1.

Citing this chapter:
Thoman, R. L., T. A. Moon, and M. L. Druckenmiller, Eds.,
2025: The Arctic [in "State of the Climate in 2024"]. Bull. Amer. Meteor. Soc., 106 (8), S300–S356, https://doi.org/10.1175/BAMS-D-25-0104.1.

Citing a section (example):
Smith, S. L., V. E. Romanovsky, K. Isaksen, K. E. Nyland, N. I. Shiklomanov, D. A. Streletskiy, and H. H. Christiansen, 2025: Permafrost [in "State of the Climate in 2024"]. Bull. Amer. Meteor. Soc., 106 (8), S338–S341, https://doi.org/10.1175/BAMS-D-25-0104.1.

Unauthenticated | Downloaded 11/21/25 11:34 AM UTC

Editor and Author Affiliations (alphabetical by name)

Askjaer, Thomas G., Danish Meteorological Institute, Copenhagen, Denmark

Ballinger, Thomas J., International Arctic Research Center, University of Alaska Fairbanks, Fairbanks, Alaska

Bhatt, Uma S., Geophysical Institute, University of Alaska Fairbanks, Fairbanks, Alaska

Berner, Logan T., School of Informatics, Computing, and Cyber Systems, Northern Arizona University, Flagstaff, Arizona

Bernhard, Germar H., Biospherical Instruments Inc., San Diego, California

Bigalke, Siiri, Department of Geography, Portland State University, Portland, Oregon

Bjerke, Jarle W., Norwegian Institute for Nature Research, Trondheim, Norway; FRAM – High North Research Centre for Climate and the Environment, Tromsø, Norway

Bliss, Angela, NASA Goddard Space Flight Center, Greenbelt, Maryland

Box, Jason E., Geological Survey of Denmark and Greenland (GEUS), Copenhagen, Denmark

Brady, Mike, Climate Research Division, Environment and Climate Change Canada, Toronto, Canada

Brettschneider, Brian, NOAA/NWS Alaska Region, Anchorage, Alaska

Butler, Amy H., Chemical Sciences Laboratory, Boulder, Colorado

Christiansen, Hanne H., Arctic Geophysics Department, University Centre in Svalbard, Longyearbyen, Norway

Crawford, Alex, Department of Environment and Geography, University of Manitoba, Winnipeg, Canada

Decharme, Bertrand, Centre National de Recherches Météorologiques, Météo-France/CNRS, Toulouse, France

Derksen, Chris, Climate Research Division, Environment and Climate Change Canada, Toronto, Canada

Divine, Dmitry, Norwegian Polar Institute, Fram Centre, Tromsø, Norway

Druckenmiller, Matthew L., National Snow and Ice Data Center, Cooperative Institute for Research in Environmental Sciences, University of Colorado, Boulder, Colorado

Elias Chereque, Alesksandra, Department of Physics, University of Toronto, Toronto, Canada

Epstein, Howard E., Department of Environmental Sciences, University of Virginia, Charlottesville, Virginia

Farrell, Sinead, Department of Geographical Sciences, University of Maryland, College Park, Maryland

Fausto, Robert S., Geological Survey of Denmark and Greenland (GEUS), Copenhagen, Denmark

Fettweis, Xavier, SPHERES Research Unit, University of Liège, Liège, Belgium

Fioletov, Vitali E., Environment and Climate Change Canada, Toronto, Canada

Forbes, Bruce C., Arctic Centre, University of Lapland, Rovaniemi, Finland

Frost, Gerald V. (JJ), Alaska Biological Research, Inc., Fairbanks, Alaska

Gerland, Sebastian, Norwegian Polar Institute, Fram Centre, Tromsø, Norway

Grooß, Jens-Uwe, Forschungszentrum Jülich (ICE-4), Jülich, Germany

Hanna, Edward, Department of Geography and Lincoln Climate Research Group, Lincoln, United Kingdom

Hendricks, Stefan, Alfred Wegener Institute, Helmholtz Centre for Polar and Marine Research, Bremerhaven, Germany

Howell, Stephen, Climate Research Division, Environment and Climate Change Canada, Toronto, Canada

Ialongo, Iolanda, Finnish Meteorological Institute, Helsinki, Finland

Isaksen, Ketil, Norwegian Meteorological Institute, Oslo, Norway

Jia, Gensuo, Institute of Atmospheric Physics, Chinese Academy of Sciences, Beijing, China

Johnsen, Bjørn, Norwegian Radiation and Nuclear Safety Authority, Østerås, Norway

Kaleschke, Lars, Alfred Wegener Institute, Helmholtz Centre for Polar and Marine Research, Bremerhaven, Germany

Kim, Seong-Joong, Korea Polar Research Institute, Incheon, South Korea

Labe, Zachary M., Geophysical Fluid Dynamics Laboratory, Princeton, New Jersey

Lader, Rick, International Arctic Research Center, University of Alaska Fairbanks, Fairbanks, Alaska

Lakkala, Kaisa, Finnish Meteorological Institute, Sodankylä, Finland

Lara, Mark J., Department of Plant Biology, University of Illinois, Urbana, Illinois; Department of Geography, University of Illinois, Urbana, Illinois

Lee, Simon H., School of Earth and Environmental Sciences, University of St Andrews, St Andrews, United Kingdom

Loomis, Bryant D., NASA Goddard Space Flight Center, Greenbelt, Maryland

Luojus, Kari, Arctic Research Centre, Finnish Meteorological Institute, Helsinki, Finland

Macander, Matthew J., Alaska Biological Research, Inc., Fairbanks, Alaska

Magnússon, Rúna Í., Plant Ecology and Nature Conservation Group, Wageningen University & Research, Wageningen, Netherlands

Mankoff, Ken D., Business Integra, New York, New York; NASA Goddard Institute for Space Studies, New York, New York

McClelland, James W., Marine Biological Laboratory, Woods Hole, Massachusetts

Medley, Brooke, Cryospheric Sciences Laboratory, NASA Goddard Space Flight Center, Greenbelt, Maryland

Meier, Walter N., National Snow and Ice Data Center, Cooperative Institute for Research in Environment Sciences, University of Colorado, Boulder, Colorado

Montesano, Paul M., NASA Goddard Space Flight Center, Greenbelt, Maryland

Moon, Twila A., National Snow and Ice Data Center, Cooperative Institute for Research in Environmental Sciences, University of Colorado, Boulder, Colorado

Mote, Thomas L., University of Georgia, Athens, Georgia

Motrøen Gjelten, Herdis, Norwegian Meteorological Institute, Oslo, Norway

Mudryk, Lawrence, Climate Research Division, Environment and Climate Change Canada, Toronto, Canada

Müller, Rolf, Forschungszentrum Jülich (IEK-7), Jülich, Germany

Neigh, Christopher S. R., NASA Goddard Space Flight Center, Greenbelt, Maryland

Nyland, Kelsey E., George Washington University, Washington, DC

Overland, James E., NOAA/OAR Pacific Marine Environmental Laboratory, Seattle, Washington

Perovich, Donald K., Dartmouth College, Hanover, New Hampshire

Petty, Alek, NASA Goddard Space Flight Center, Greenbelt, Maryland

Phoenix, Gareth K., School of Biosciences, University of Sheffield, Sheffield, United Kingdom

Poinar, Kristin, University at Buffalo, Buffalo, New York

Ricker, Robert, NORCE Norwegian Research Centre, Tromsø, Norway

Romanovsky, Vladimir E., Geophysical Institute, University of Alaska Fairbanks, Fairbanks, Alaska

Scheller, Johan H., Department of Ecoscience, Arctic Research Centre Aarhus University, Roskilde, Denmark

Serreze, Mark C., National Snow and Ice Data Center, Cooperative Institute for Research in Environmental Sciences, University of Colorado, Boulder, Colorado

Shiklomanov, Alexander I., University of New Hampshire, Durham, New Hampshire; Arctic and Antarctic Research Institute, St. Petersburg, Russia

Shiklomanov, Nikolay I., George Washington University, Washington, DC

Smith, Benjamin E., Polar Science Center, Applied Physics Laboratory, University of Washington, Seattle, Washington

Smith, Sharon L., Geological Survey of Canada, Natural Resources Canada, Ottawa, Canada

Spencer, Robert G. M., Florida State University, Tallahassee, Florida

Streletskiy, Dmitry A., George Washington University, Washington, DC

Suslova, Anya, Woodwell Climate Research Center, Falmouth, Massachusetts

Svendby, Tove, The Climate and Environmental Research Institute NILU, Kjeller, Norway

Tank, Suzanne E., University of Alberta, Edmonton, Canada

Unauthenticated | Downloaded 11/21/25 11:34 AM UTC

Editor and Author Affiliations (continued)

Tian-Kunze, Xiangshan, Alfred Wegener Institute, Helmholtz Centre for Polar and Marine Research, Bremerhaven, Germany

Tedesco, Marco, Lamont-Doherty Earth Observatory, Columbia University, Palisades, New York

Timmermans, Mary-Louise, Yale University, New Haven, Connecticut

Thoman, Richard L., International Arctic Research Center, University of Alaska Fairbanks, Fairbanks, Alaska

Tømmervik, Hans, Norwegian Institute for Nature Research, Trondheim, Norway; FRAM – High North Research Centre for Climate and the Environment, Tromsø, Norway

Tretiakov, Mikhail, Arctic and Antarctic Research Institute, St. Petersburg, Russia

Waigl, Christine F., Geophysical Institute, University of Alaska Fairbanks, Fairbanks, Alaska

Walker, Donald (Skip) A., Institute of Arctic Biology, University of Alaska Fairbanks, Fairbanks, Alaska

Walsh, John E., International Arctic Research Center, University of Alaska Fairbanks, Fairbanks, Alaska

Wang, Muyin, NOAA/OAR Pacific Marine Environmental Laboratory, Seattle, Washington; Cooperative Institute for Climate, Ocean, and Ecosystem Studies, University of Washington, Seattle, Washington

Webster, Melinda, Polar Science Center, Applied Physics Laboratory, University of Washington, Seattle, Washington

Yang, Dedi, Environmental Sciences Division, Oak Ridge National Laboratory, Oak Ridge, Tennessee

Zolkos, Scott, Woodwell Climate Research Center, Falmouth, Massachusetts

Editorial and Production Team

Allen, Jessicca, Graphics Support, Cooperative Institute for Satellite Earth System Studies, North Carolina State University, Asheville, North Carolina

Camper, Amy V., Graphics Support, Innovative Consulting and Management Services, LLC, NOAA/NESDIS National Centers for Environmental Information, Asheville, North Carolina

Carroll, Lauren, Content Team Lead, Communications and Outreach, NOAA/NESDIS National Centers for Environmental Information, Asheville, North Carolina

Haley, Bridgette O., Graphics Support, NOAA/NESDIS National Centers for Environmental Information, Asheville, North Carolina

Love-Brotak, S. Elizabeth, Lead Graphics Production, NOAA/NESDIS National Centers for Environmental Information, Asheville, North Carolina

Ohlmann, Laura, Technical Editor, Innovative Consulting and Management Services, LLC, NOAA/NESDIS National Centers for Environmental Information, Asheville, North Carolina

Noguchi, Lukas, Technical Editor, Innovative Consulting and Management Services, LLC, NOAA/NESDIS National Centers for Environmental Information, Asheville, North Carolina

Riddle, Deborah B., Graphics Support, NOAA/NESDIS National Centers for Environmental Information, Asheville, North Carolina

Veasey, Sara W., Visual Communications Team Lead, Communications and Outreach, NOAA/NESDIS National Centers for Environmental Information, Asheville, North Carolina

Unauthenticated | Downloaded 11/21/25 11:34 AM UTC

5. Table of Contents

Unauthenticated | Downloaded 11/21/25 11:34 AM UTC

5. THE ARCTIC

R. L. Thoman, T. A. Moon, and M. L. Druckenmiller, Eds.

a. Overview

—R. L. Thoman, T. A. Moon, and M. L. Druckenmiller

The Arctic environment in 2024 continued on a trajectory that has put it in a state far different from that of the twentieth century. Ongoing accumulation of greenhouse gases in the atmosphere continues to quickly warm the Arctic, resulting in rapid changes in the cryosphere that are driving cascading impacts to climate, ecological, and societal systems.

Many weather- and climate-related impacts in the Arctic are the result of compounding change, such as increased riverbank erosion, which is proximately due to increased river discharge from higher seasonal precipitation, yet is also exacerbated by thawing permafrost. However, even individual storms occur within very different ocean and ice conditions than were typically present in the late twentieth century. As a result, the impacts, including high winds, excessive precipitation, and coastal inundation, may be quite different nowadays, as exemplified by the October 2024 storm in northwest Alaska that produced severe coastal flooding in several communities. To share some of these impacts with a wider audience, select extreme weather impacts around the greater Arctic have been highlighted through the inclusion of sidebars in recent *State of the Climate* Arctic chapters (e.g., Benestad et al. 2023; Thoman et al. 2024).

Average surface air temperatures for the Arctic overall (poleward of 60°N) for 2024 averaged 1.27°C above the 1991–2020 baseline average, the second-highest annual temperature since records began in 1900. For the 11th consecutive year, the Arctic annual temperature anomaly was larger than the global average anomaly. Seasonally, summer (July–September) 2024 ranked as the third-highest average temperature, and autumn (October–December) 2024 saw its highest average temperature on record. At the subseasonal scale, an intense August heatwave brought all-time record high temperatures to parts of the northwest North American Arctic. Closely but not completely tied to spring and summer air temperature trends, productivity of tundra and boreal forest vegetation has dramatically increased in recent decades. Overall "tundra greenness" was the fifth highest since 1982. However, local to regional "browning" (reduced vegetation productivity) shows that disturbance factors besides temperatures, such as wildfire, can be important.

Sea ice is one of the most iconic features of the Arctic environment and plays an important role in regulating global climate, regional ecosystems, and economic activities. Sea ice extent typically reaches the annual maximum in March, and in 2024 the maximum was near the 1991–2020 average overall, but somewhat below average in the Barents Sea and Gulf of St. Lawrence. The annual minimum sea ice extent occurs in September, and in 2024 the September monthly average was the sixth lowest in the 46-year satellite record. The Northern Sea Route along the north Russia coast opened later than the past 20 years' average due to persistent ice in the southwest Chukchi Sea. The Northwest Passage's southern route through northwest Canada opened again this year and, quite unusually, the deepwater northern route was also almost entirely ice free at the end of September.

Decreasing sea ice extent during the late spring and summer months exposes larger areas of ocean to direct warming during the time of year of high incoming solar radiation. Poleward of 65°N, open ocean surface temperatures typically peak in August. In 2024, late summer sea surface temperature anomalies showed significant regional variability, with the waters in the Barents and Kara Seas 2°C–4°C warmer than normal. In sharp regional contrast, Chukchi Sea sea surface temperatures were the lowest in more than 40 years, while just to the east, sea surface temperatures in the southern Beaufort Sea were significantly above the 1991–2020 average.

Unauthenticated | Downloaded 11/21/25 11:34 AM UTC

Like sea ice, permafrost (soils or other earth materials that have remained frozen for at least two years) is an important feature of Arctic environments that occurs widely on land and throughout some submarine continental shelf areas that were exposed land during the last Ice Age (about 15,000 years ago). Unlike many parts of the Arctic environmental system, permafrost temperatures and the summer surface thaw zone cannot be monitored from space-borne instruments and depend on in situ measurements. While long-term observations are not available over most of the Asian Arctic, observations elsewhere show multi-decade warming of deeper permafrost continuing across the Arctic, with some sites in North America and Svalbard having seen their highest temperatures on record in 2024. Overall, colder permafrost is warming more rapidly; areas where permafrost temperatures are close to freezing have slower rates of warming as ice changes phase to liquid water.

Precipitation monitoring in the Arctic has historically been limited due to the lack of in situ measurements over the Arctic Ocean, a sparse land station network, and significant problems with solid precipitation undercatch because of the inherent difficulties in capturing solid precipitation in strong wind environments. Recent advances in reanalyses that combine observations and computer simulations now allow for more robust regional-scale precipitation analysis and historical comparisons. In 2024, Arctic-wide annual precipitation was the third highest on record, and summer (July through September) precipitation was the highest since 1950. Rivers serve as regional integrators of precipitation. Arctic river discharge overall for both 2023 and 2024 was close to the 1991–2020 average, albeit with significant differences across basins. For example, in North America, Mackenzie River discharge was well below average in both years, but Yukon River discharge was above average in both years; most basins in Eurasia saw above-normal discharge in 2024 but below-average discharge in 2023.

In much of the Arctic, snow is the dominant form of precipitation for most of the year, and the presence or absence of snow cover is a critical factor in many climate and environmental processes. During the 2023/24 snow season, there were marked regional and continental scale differences in snow cover duration. The snow cover duration varied from the shortest to date in the twenty-first century over parts of Canada to at or near the longest in this century in parts of the Nordic and Asian Arctic.

Melt and discharge from the Greenland Ice Sheet play important roles in modulating North Atlantic weather and climate. In 2024, the total amount of ice decreased, as it has every year since the late 1990s, but the loss was 50%–80% less than the 2002–23 annual average. This was the result of an unusual but persistent weather pattern that inhibited the development and persistence of warm air masses over Greenland during the summer. Ongoing monitoring of the Greenland Ice Sheet, which holds enough water to raise global sea levels by more than seven meters if entirely melted, is critical for understanding drivers of melt and ice sheet dynamics.

The Arctic stratosphere experienced two major sudden warming events early in 2024 that resulted in enhanced ozone transport into the region from lower latitudes. As a result, surface ultraviolet radiation was reduced in parts of the Asian Arctic in spring and the central Arctic and North America in summer.

Special Notes: The 1991–2020 baseline is used in this chapter except where data availability requires use of a different baseline. This chapter includes a focus on Arctic river discharge (section 5h), which alternates yearly with a section on glaciers and ice caps outside of Greenland.

Unauthenticated | Downloaded 11/21/25 11:34 AM UTC

b. Atmosphere

—A. H. Butler, S. H. Lee, G. H. Bernhard, V. E. Fioletov, J-U. Grooß, I. Ialongo, B. Johnsen, K. Lakkala, R. Müller, and T. Svendby

The dynamics and chemistry of the Arctic atmosphere are affected by both strong year-to-year internal variability and long-term changes forced by greenhouse gases, ozone-depleting substances, and aerosols. The atmosphere is also closely coupled to Arctic sea ice and snow cover; positive feedbacks with sea ice loss have amplified long-term polar atmospheric warming (Dai et al. 2019; He et al. 2024).

In 2024, the most notable features of the atmospheric circulation were: 1) an unusually disturbed Arctic stratospheric polar vortex, with two reversals of the zonal winds at 60°N and 10 hPa (known as major sudden stratospheric warmings [SSWs]; Baldwin et al. 2021); 2) persistently high total column ozone corresponding to substantial reductions in surface ultraviolet (UV) radiation from spring through summer; 3) a monthly record-high positive Arctic Oscillation in August, corresponding to low sea level pressure anomalies over the Arctic, despite strong blocking high pressure aloft; and 4) persistent blocking high pressure over the Hudson Bay that lasted throughout summer and autumn.

1. THE ARCTIC STRATOSPHERE IN 2024

The Arctic stratosphere experienced two SSWs: one on 16 January and another on 4 March 2024 (Qian et al. 2024; Lee et al. 2025). The occurrence of two SSWs in a single winter is relatively unusual, occurring only about once every decade (Lee et al. 2025). These events are evident in Fig. 5.1a that shows a metric of large-scale circulation, the polar cap (60°N–90°N) averaged geopotential height (PCH), which is the altitude of a given atmospheric pressure. In general, when the PCH is anomalously positive, the polar circulation is predominantly anti-cyclonic, and the polar air is warmer (and vice versa when the PCH is anomalously negative). Near the surface, the PCH is negatively correlated with the Arctic Oscillation, the dominant pattern of Northern Hemisphere climate variability that describes a fluctuation in atmospheric mass between the pole and the midlatitudes (Thompson and Wallace 2000). The PCH indicates when the polar

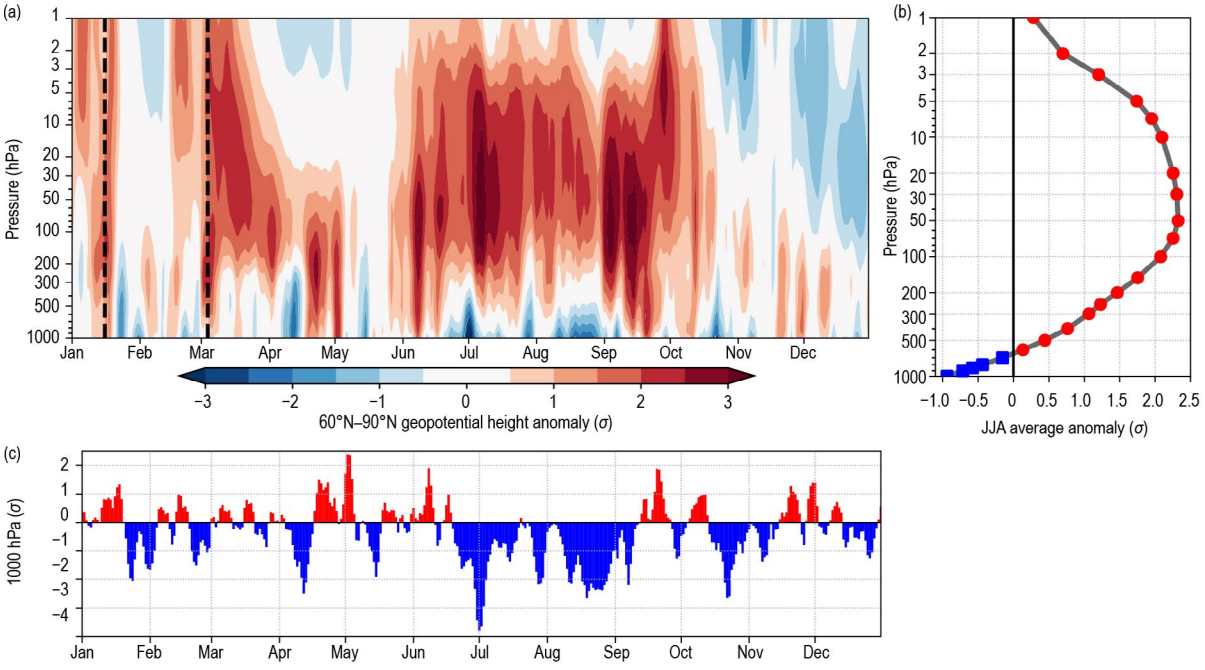

Fig. 5.1. (a) Vertical profile of daily standardized Arctic polar cap (60°N–90°N) geopotential height (PCH) anomalies during 2024. Anomalies are shown with respect to a 30-day centered running mean 1991–2020 climatology and standardized at each pressure level by the standard deviation of each calendar day during 1991–2020 (smoothed with a 30-day running mean). Standardizing makes vertical coupling easier to visualize, given the large differences in magnitude of the raw geopotential height values from the surface to 1 hPa. Dashed vertical lines show the dates of the two 2024 sudden stratospheric warmings. (b) The Jul–Sep average of standardized PCH anomalies. The near-surface PCH anomalies were negative (blue), while upper atmosphere anomalies were positive (red). (c) 1000-hPa standardized PCH anomalies (closely correlated to the Arctic Oscillation, multiplied by –1) for 1 Jan–31 Dec 2024. (Data source: Once-daily 0000 UTC ERA5 at 1° horizontal resolution [Hersbach et al. 2020].)

Unauthenticated | Downloaded 11/21/25 11:34 AM UTC

atmosphere is vertically coupled (i.e., has the same-signed anomalies from the surface to the upper stratosphere).

The two SSWs had limited surface climate impacts via dynamical downward coupling (Lee et al. 2025) but resulted in significant stratospheric ozone transport from the tropics to the Arctic and record-high total column ozone over the polar cap in March (Newman et al. 2024; Fig. 5.2a, Fig 5.4b). After the stratospheric polar vortex dissipated in the spring, this anomalous ozone then persisted in the Arctic throughout summer and into autumn, contributing to new monthly high total column ozone records in May, June, July, and October (Figs. 5.2b, 5.4b). Spatially, 2024 Arctic total column ozone anomalies from the Ozone Monitoring Instrument (OMI; 2005–24) showed large and significant enhancements, especially over Asia in March and the central Arctic/North Atlantic in July (Figs. 5.2a,b). These regions of enhanced ozone corresponded to regions with the strongest surface UV radiation reductions (up to 20%) in those months (Figs. 5.2c,d). Negative UV anomalies calculated from ground-based measurements for some stations were up to 13% larger in magnitude than those from satellite data (OMI instrument; Figs. 5.2c,d). Differences between ground- and satellite-based measurements of UV radiation at the surface are caused by variability within the satellite footprint and by the albedo climatology used in satellite retrievals, which do not always match the actual albedo (Bernhard et al. 2015).

Summer temperatures in the Arctic lowermost stratosphere (~150 hPa) set monthly record highs (Figs. 5.1a, 5.4a). This warmth in the free atmosphere may be in part related to localized absorption of sunlight by the persistent anomalously high ozone that was transported downward from the mid-to-upper stratosphere (e.g., Williams et al. 2024; Fig. 5.4b).

The stratospheric polar vortex reformed at its usual time in late August but stayed anomalously weak until mid-October, and then finally strengthened by December (Fig. 5.1a, blue shading at 10 hPa).

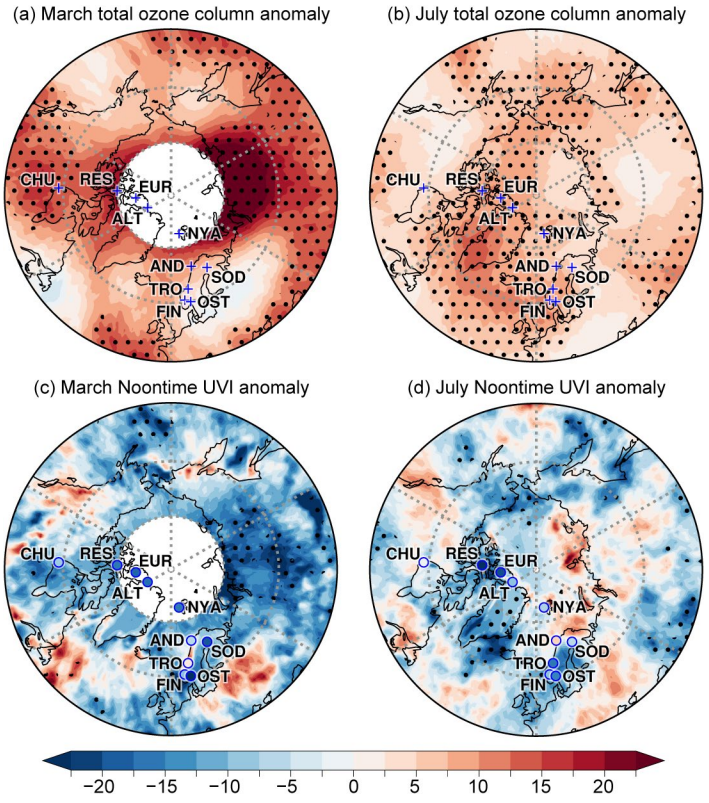

Base	Mar Noontime UVI (satellite)	Mar Noontime UVI (ground-based)	Jul Noontime UVI (satellite)	Jul Noontime UVI (ground-based)
ALT	N/A	−17%	−3%	−9%
EUR	N/A	−18%	−12%	−20%
NYA	N/A	−16%	0%	−7%
RES	N/A	−16%	−15%	−28%
AND	−8%	−6%	−1%	5%
SOD	−10%	−19%	−2%	−6%
TRO	8%	2%	−11%	−16%
FIN	−3%	−9%	−13%	−9%
OST	−19%	−29%	−16%	−15%
CHU	−16%	−8%	−3%	−1%

Fig. 5.2. Monthly mean anomaly maps of (a),(b) total ozone column (%) and (c),(d) noontime ultraviolet index (UVI; %) for Mar (a),(c) and Jul (b),(d) 2024 relative to 2005–23 means. Stippling indicates pixels where anomalies exceed 2 std. dev. Maps are based on the Ozone Monitoring Instrument (OMI) Level-2 Total Column Ozone version 3 (OMTO3) total ozone product (Bhartia and Wellemeyer 2002), which is derived from measurements of the OMI. (c),(d) also compares UVI anomalies from OMI [%] from OMI satellite with ground-based measurements at nine locations (shaded marker). Site acronyms of ground stations are ALT: Alert (83°N); EUR: Eureka (80°N); NYA: Ny-Ålesund (79°N); RES: Resolute (75°N); AND: Andøya (69°N); SOD: Sodankylä (67°N); TRO: Trondheim (63°N); FIN: Finse (61°N); OST: Østerås (60°N); and CHU: Churchill (59°N). White areas centered at the North Pole (and values of N/A in the table) indicate latitudes where OMI data are not available because of polar darkness in March.

2. THE ARCTIC TROPOSPHERE IN 2024

Winter (January–March; JFM) and spring (April–June; AMJ) were generally characterized by statistically insignificant seasonally-averaged 500-hPa geopotential height anomalies across the Arctic (Figs. 5.3a,b). However, anomalous high pressure (or "blocking") over the Hudson Bay persisted throughout 2024, exceeding +2 std. dev. in summer (July–September; JAS) and autumn

Unauthenticated | Downloaded 11/21/25 11:34 AM UTC

(October–December; OND). This persistent blocking was associated with predominantly northerly upper-tropospheric winds over the Baffin Bay, and may have contributed to less Greenland Ice Sheet melt (see section 5g and Sidebar 5.3).

In addition, summer was marked by strong blocking over the Barents–Kara Seas region, coincident with record-warm August sea surface temperatures over the Barents Sea (section 5e) and anomalously low geopotential heights over the Arctic Ocean and near Iceland (Fig. 5.3c). Despite the overall positive PCH anomalies in the mid- to upper troposphere (Figs. 5.1b,c), the near-surface was characterized by strongly negative PCH anomalies

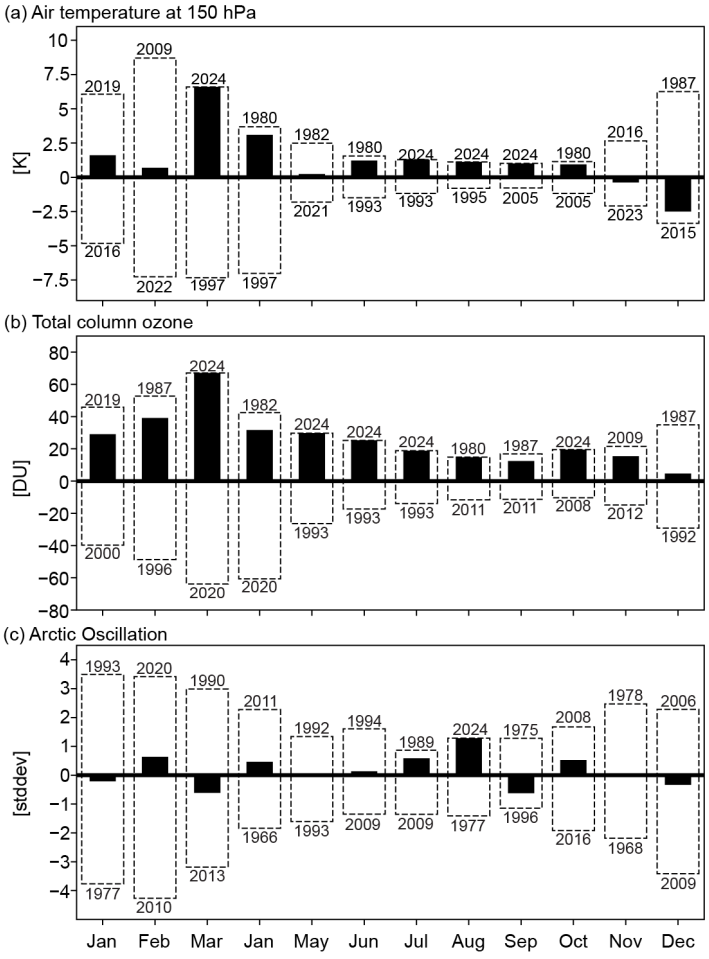

Fig. 5.4. (a) Polar cap averaged temperature anomalies at 150 hPa (~13.5 km) for each month of 2024 (black bars), compared to the previous monthly record (maximum and minimum) values over the period 1958–2024 (dashed bars). The year of the maximum/minimum monthly record is provided. Data are from ERA5 (Hersbach et al. 2020). (b) Same as (a) but for polar cap averaged total column ozone anomalies over the period 1980–2024. Data are from MERRA-2 reanalysis (Gelaro et al. 2017). (c) Same as (a) but for the Arctic Oscillation (AO) over the period 1958–2024. The AO index is from NOAA's Climate Prediction Center. All anomalies are calculated relative to the 1991–2020 climatology. Figure adapted from L'Heureux et al. (2010).

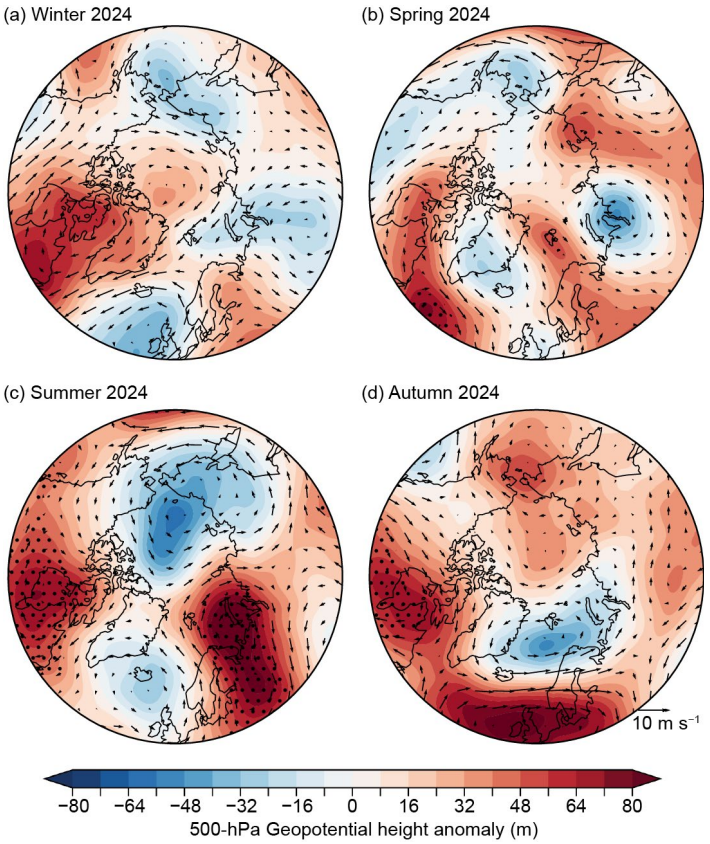

Fig. 5.3. 50-hPa geopotential height (m; shading) and 200-hPa wind (m s^{-1}; vectors) anomalies for (a) winter, (b) spring, (c) summer, and (d) autumn. Anomalies are calculated relative to the 1991–2020 climatology. Stippling indicates that the anomaly exceeds ±2 standard deviations of the 1991–2020 climate. (Data source: ERA5 [Hersbach et al. 2020].)

(Figs. 5.1b,c) and anomalously low sea level pressure (section 5c), corresponding to a record-positive (since 1958) Arctic Oscillation for the month of August (Fig 5.4c). In other words, the lowermost Arctic atmosphere was at odds with the circulation above it through most of summer (Fig. 5.1b). A positive Arctic Oscillation pattern typically corresponds to anomalously cool temperatures over the central Arctic, the Bering Strait, and Baffin Bay, but anomalous warmth over northernmost Eurasia, Scandinavia, and North America south of the Hudson Bay (e.g., Park and Ahn 2016). This roughly corresponds to regional surface air temperature (SAT) variations seen during summer 2024 (section 5c).

Autumn saw developing moderate high pressure over the North Atlantic, with anomalously strong upper-level westerly wind flow from southern Greenland to southern Scandinavia and continued strong blocking over the Hudson Bay (Fig. 5.3d).

Unauthenticated | Downloaded 11/21/25 11:34 AM UTC

c. Surface air temperature

—T. J. Ballinger, A. Crawford, M. C. Serreze, S. Bigalke, J. E. Walsh, B. Brettschneider, R. L. Thoman, U. S. Bhatt, E. Hanna, H. Motrøen Gjelten, S-J. Kim, J. E. Overland, and M. Wang

1. OVERVIEW

Widespread warming surface (i.e., two-meter) air and upper ocean temperatures (section 5e) characterize the changing Arctic (60°N–90°N) environment. Northern high-latitude surface air temperature changes continue to exceed global (90°S–90°N) scale changes, a phenomenon termed Arctic Amplification. After accounting for natural variability, studies have estimated that the Arctic is warming approximately three times faster than the global mean based on observational data and climate model simulations since 1980 (Sweeney et al. 2023; Zhou et al. 2024). Pervasive warming and an enhanced hydrological cycle, associated with increased precipitation (section 5d), represent key controls of Arctic environmental changes (Box et al. 2019). Daily maximum temperature extremes are both increasing and occurring more often (Polyakov et al. 2024), resulting in a surge of unprecedented extreme Arctic weather events in the last three years (Overland 2024). In this section, we place 2024 Arctic air temperatures in historical perspective and discuss notable seasonal anomaly patterns that occurred during 2024. Annual air temperatures follow the calendar year, while seasons are defined as winter (January–March), spring (April–June), summer (July–September), and autumn (October–December).

2. HISTORICAL CONTEXT TO 2024 ANNUAL AND SEASONAL TEMPERATURES

Annual Arctic and global surface air temperature anomalies from NASA's GISTEMP version 4 dataset are shown in Fig. 5.5a. During 2024, the Arctic had its second-warmest year over the period since 1900, with temperature anomalies 1.27°C above the 1991–2020 mean. This dataset indicates that 2024 was the warmest year on record globally since at least 1900; however, the relative magnitude of Arctic temperature anomalies continues to be larger. This is evidenced by air temperature warming of 2.26°C in the Arctic versus 1.26°C globally during the past 125 years (Fig. 5.5a). The year 2024 also marks the 11th consecutive year in which Arctic regional temperature departures exceeded those of Earth as a whole. Another noticeable feature of this dataset is that this past decade (2015–24) has been the Arctic's warmest, and has been characterized by several new annual and seasonal temperature records.

Arctic temperature anomalies were also comparatively higher than the global average in each season of 2024 (Figs. 5.5b–d). This is striking given that seasonal global temperature records were also set during winter and spring 2024. Seasonal temperature departures in 2024 from the 1991–2020 means were some of the highest in the Arctic since 1900, with winter at 1.14°C (sixth warmest), spring at 0.82°C (sixth warmest), and summer at 0.83°C (third warmest). Most notably, Autumn 2024 observed its highest temperatures on record at 2.28°C above the 1991–2020 mean, roughly 0.25°C higher than the next warmest autumn in 2020.

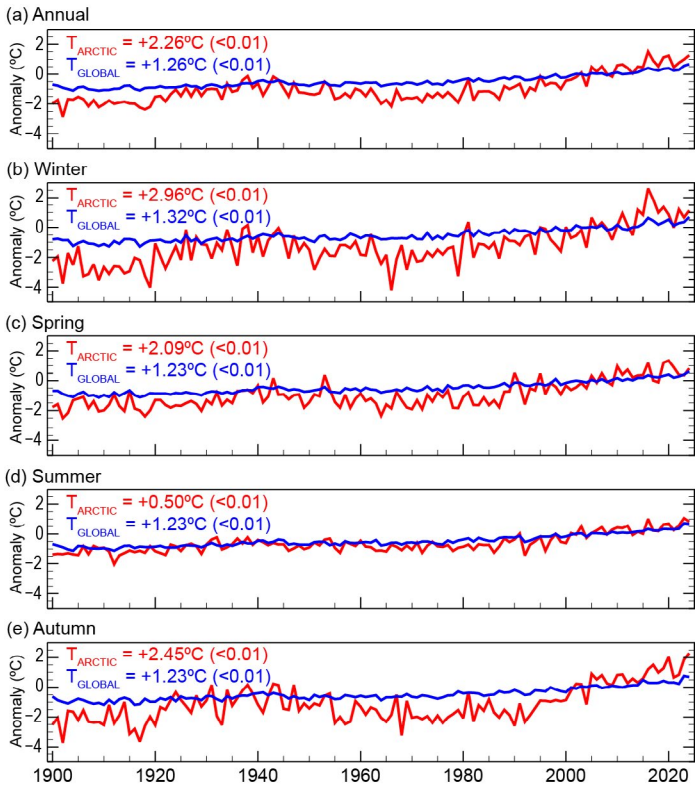

Fig. 5.5. Time series of (a) annual, (b) winter, (c) spring, (d) summer, and (e) autumn surface air temperature anomalies (°C) for 1900–2024 relative to the 1991–2020 mean and averaged across Arctic (60°N–90°N; red) and Global (90°S–90°N; blue) land and ocean areas. Annual time series in (a) reflect the Jan–Dec average. The total arctic (T_{ARCTIC}) and total global (T_{GLOBAL}) air temperature change during the full period of record, defined as the linear least-squares regression trend multiplied by the 125-year period, is shown in each panel along with the respective statistical significance (p-value) of the trends. (Data source: NASA GISTEMPv4 data obtained from the NASA Goddard Institute for Space Studies.)

Unauthenticated | Downloaded 11/21/25 11:34 AM UTC

The annual and seasonal air temperature anomalies display Arctic Amplification signatures (Fig. 5.5). A multitude of mechanisms and feedbacks drive Arctic Amplification at different times of the year. Meridional atmospheric circulation patterns can enhance heat and moisture transport into the Arctic and lead to more year-round warm extremes, whereas albedo feedbacks involving the amount, quality, and duration of snow and ice cover are constrained by sunlight that is prevalent in the warm season and absent at the highest northern latitudes during winter months (Cohen et al. 2020). During autumn and winter, when Arctic Amplification is strongest (Figs. 5.5b,e), the accumulation of heat in the Arctic Ocean is released to the overlying atmosphere, driving higher air temperatures (Taylor et al. 2022). Patterns of seasonal air temperature anomalies align with some of these processes that influence Arctic Amplification.

3. SEASONAL AIR TEMPERATURE ANOMALY PATTERNS IN 2024

Seasonal air temperature anomaly patterns from ERA5 reanalysis are shown in Fig. 5.6. Stippled areas indicate record seasonal warmth since 1950. Winter 2024 saw positive anomalies over the central Arctic Ocean (+3°C to +4°C) with smaller magnitude anomalies generally found over Arctic lands (Fig. 5.6a). Exceptions include the North Slope of Alaska, northern Baffin Island, northern Quebec, and Severnaya Zemlya, where the largest wintertime positive anomalies (+5°C to +6°C) were found. The latter two areas were associated with negative pressure anomalies to the west (Fig. 5.7a) that enhanced southerly winds and warm air advection. The largest cold anomalies were located over the Kamchatka Peninsula, including the Sea of Okhotsk, and the North Sea and Norwegian Sea of the Atlantic Arctic.

Similar to the preceding winter, spring 2024 featured positive anomalies of +2°C to +4°C over northern Canada and eastern Siberia (Fig. 5.5b). Record warmth is found within these areas, including over the eastern half of Hudson Bay, which also experienced record-early

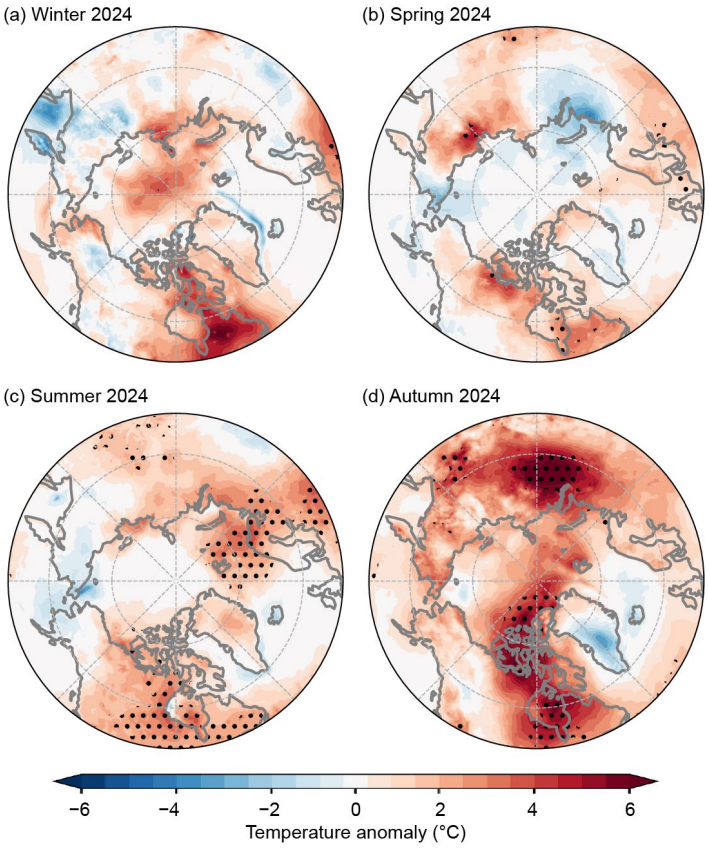

Fig. 5.6. Seasonal surface air temperature anomalies (°C) in 2024 for (a) winter, (b) spring, (c) summer, and (d) autumn. Temperature anomalies are shown relative to their 1991–2020 means. Stippled areas indicate record-high seasonal temperatures since 1950. (Data source: ERA5 air temperature data obtained from the Copernicus Climate Change Service.)

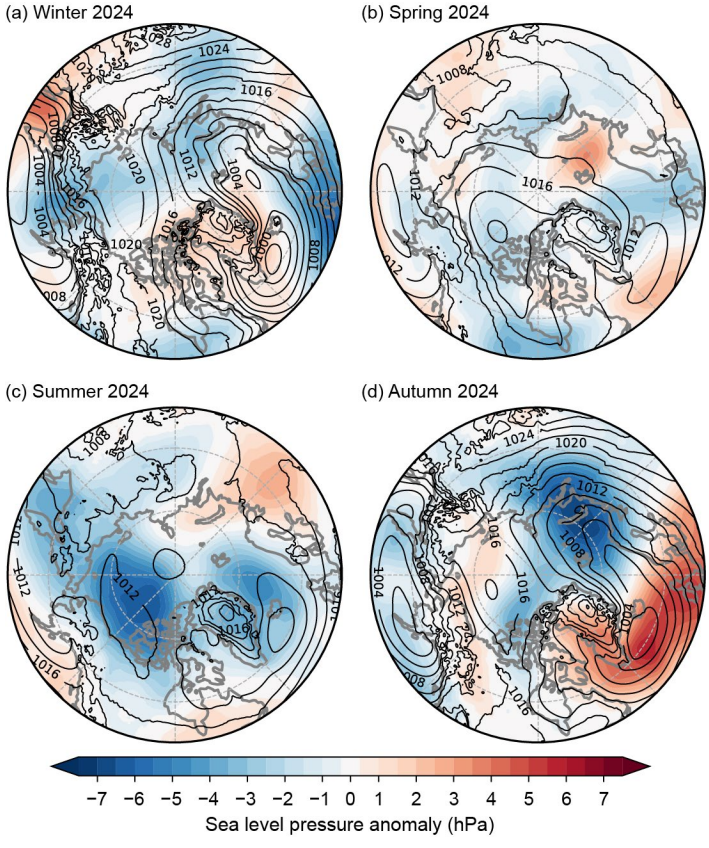

Fig. 5.7. Seasonal sea level pressure (SLP) anomalies (shading) and absolute values (isobars; both in hPa) in 2024 for (a) winter, (b) spring, (c) summer, and (d) autumn. SLP anomalies are shown relative to their 1991–2020 means. (Data source: ERA5 SLP data obtained from the Copernicus Climate Change Service.)

Unauthenticated | Downloaded 11/21/25 11:34 AM UTC

sea ice retreat. Small negative temperature anomalies extended offshore from the northeastern and northwestern Russian coastlines. However, unlike winter 2024, air temperatures over the Arctic Ocean during spring were average to slightly below average, linked to a relatively weak sea-level pressure (SLP) anomaly pattern over the region (Fig. 5.6b).

Continued warmth across portions of northern Canada and northern Eurasia characterized summer 2024. Record-high air temperatures since 1950 were found in Nunavut, northern portions of Manitoba, Ontario, and Quebec, and across much of southern Hudson Bay where seasonal departures were 2°C–3°C above the 1991–2020 mean (Fig. 5.6c). Areas with record temperature anomalies were also found in the eastern Arctic, extending from northern Scandinavia and across the Norwegian Sea and Barents Sea to the northern Svalbard coast. A few areas, including the western Chukchi Sea, central Bering Sea, and adjacent lands, were marked by negative temperature anomalies associated with an extensive area of lower-than-normal SLP across the western Arctic (Fig. 5.7c).

As mentioned in the previous section, a warm summer was followed by a record-warm autumn in 2024. Except for southern Greenland, Iceland, and the Chukchi Sea, most of the Arctic saw positive air temperature anomalies (Fig. 5.6d). Record spring and summer warmth continued into autumn for northern Ontario and Quebec, as well as Hudson Bay, where the record-early sea ice retreat resulted in exceptional ocean heat uptake throughout summer. This spatial pattern of warm extremes extended northward across the Canadian Archipelago and Lincoln Sea (6°C above normal). A record anomaly temperature pattern of similar magnitude was also found east of the Ural Mountains in northwestern Russia, which was supported by anomalous low pressure, suggestive of an active storm track and warm air masses frequently traversing the region (Fig. 5.7d).

Unauthenticated | Downloaded 11/21/25 11:34 AM UTC

Sidebar 5.1: **North American August heat**

—R. LADER AND R. L. THOMAN

Record Heat

A major heat event impacted northwest North America in early August 2024 from northeast Alaska (AK) across northern Yukon Territory (YT) and into the western Northwest Territories (NT). This same region also experienced above-normal temperatures in summer 2023 and, for parts of northwest Canada, this was the second consecutive summer with record-high temperatures. The August heat event was driven by larger-scale meridional winds enhanced through adiabatic warming during multiple mountain range crossings.

All-time record and August record-high temperatures are listed in Table SB5.1 for climate stations with at least 40 years of observations. The all-time records are particularly notable in the high latitudes because of rapidly declining solar radiation at this time of year. Maximum hourly near-surface air temperatures for the week of 4–10 August from ERA5 (Hersbach et al. 2020) indicate a broad area of temperatures of 33.0°C or higher along the Mackenzie River in NT (Fig. SB5.1a).

In addition to record maximum temperatures, this event led to extreme high minimum temperatures and precipitation patterns that exhibited clear topographical influences. An all-time record-high daily minimum temperature of 21.7°C was recorded at Delta Junction, AK (64°00′N, 145°43′W, 389 m a.s.l.) on 6 August. The highest daily minimum near-surface air temperatures from ERA5 show areas in excess of 18.0°C in interior Alaska and along the Beaufort Sea coast in Canada (Fig. SB5.1b). For reference, the average daily minimum temperature at Inuvik, NT, for this time of year is around 7°C. Total accumulated precipitation during this event was low, particularly in the Yukon Flats region of AK, and across north-central NT where less than 5 mm fell (Fig. SB5.1c). The influence of terrain height is evident as the southern coastal mountains of AK, which were inundated with over 50 mm of precipitation, effectively blocked moisture from advecting farther inland (Fig. SB5.1d). Moreover, downsloping air flow from the Alaska Range likely contributed to the local temperature maxima seen in interior Alaska, and similarly, the Yukon Ranges in NT.

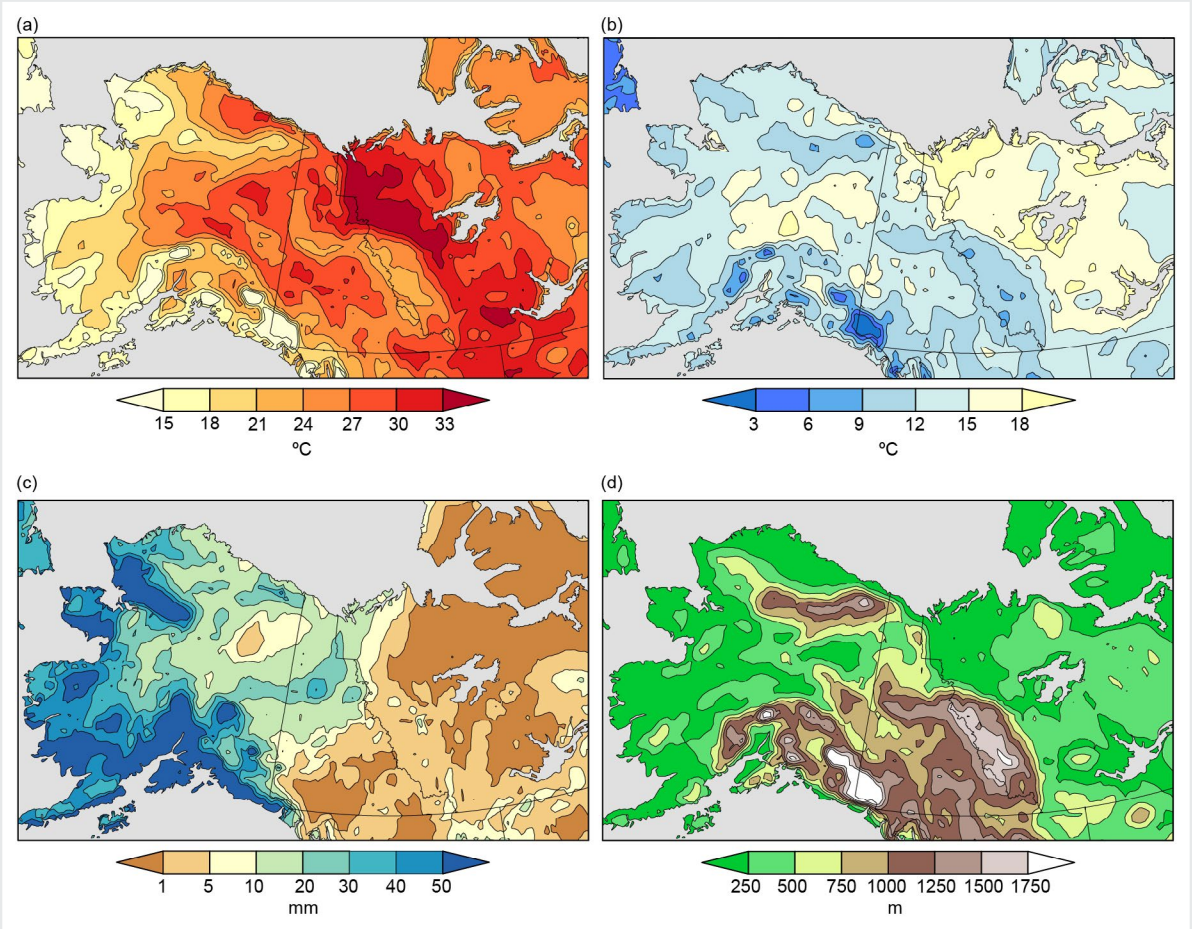

Fig. SB5.1. (a) Maximum hourly near-surface air temperature (°C), (b) maximum daily minimum near-surface air temperature (°C), and (c) total precipitation (mm) for 4–10 August 2024. Terrain height (m) is shown in (d). (Data source: ERA5.)

Unauthenticated | Downloaded 11/21/25 11:34 AM UTC

Large-Scale Anomalies

A mid-tropospheric ridge developed across eastern AK and YT at the beginning of the heat event, before strengthening and propagating to the east over central NT. The 500-hPa height anomalies from the National Centers for Environmental Prediction (NCEP)/National Center for Atmospheric Research (NCAR) Reanalysis version 1 (R1; Kalnay et al. 1996) exceeded 160 m over northern YT on 5 August, with low pressure farther west near the Gulf of Anadyr (Fig. SB5.2a). By 7 August, the gradient between these two features had increased as the area of low pressure moved into the Bering Sea, and the high pressure ridge strengthened across western NT. Anomalous 500-hPa heights in excess of 200 m extended from the Mackenzie River eastward (Fig. SB5.2b). By 9 August, the gradient had weakened, and the low pressure in the Bering Sea began influencing all of AK with negative 500-hPa height anomalies extending eastward. The highest departures from normal, still in excess of 200 m, covered much of the central and eastern NT (Fig. SB5.2c).

The influence of the mid-tropospheric height pattern was reflected in the near-surface air temperatures. As the 500-hPa ridge developed on 5 August, temperature anomalies of +4°C to +6°C were seen over the North Slope of AK and across the Mackenzie Delta (Fig. SB5.2d). Notably, negative air temperature anomalies were shown over south-coastal Alaska as southerly flow advected moist, cool air inland. By 7 August, the magnitude of this heat event was apparent relative to the circumpolar region, with temperature anomalies in excess of +10°C across a broad swath of far northwestern North America (Fig. SB5.2e). Negative temperature anomalies remained in southern Alaska, while downsloping winds warmed and dried the air farther north. By 9 August, the heat event reached its peak across NT, while negative temperature anomalies were seen across AK as low pressure from the west and a weakening pressure gradient no longer supported extreme heat (Fig. SB5.2f).

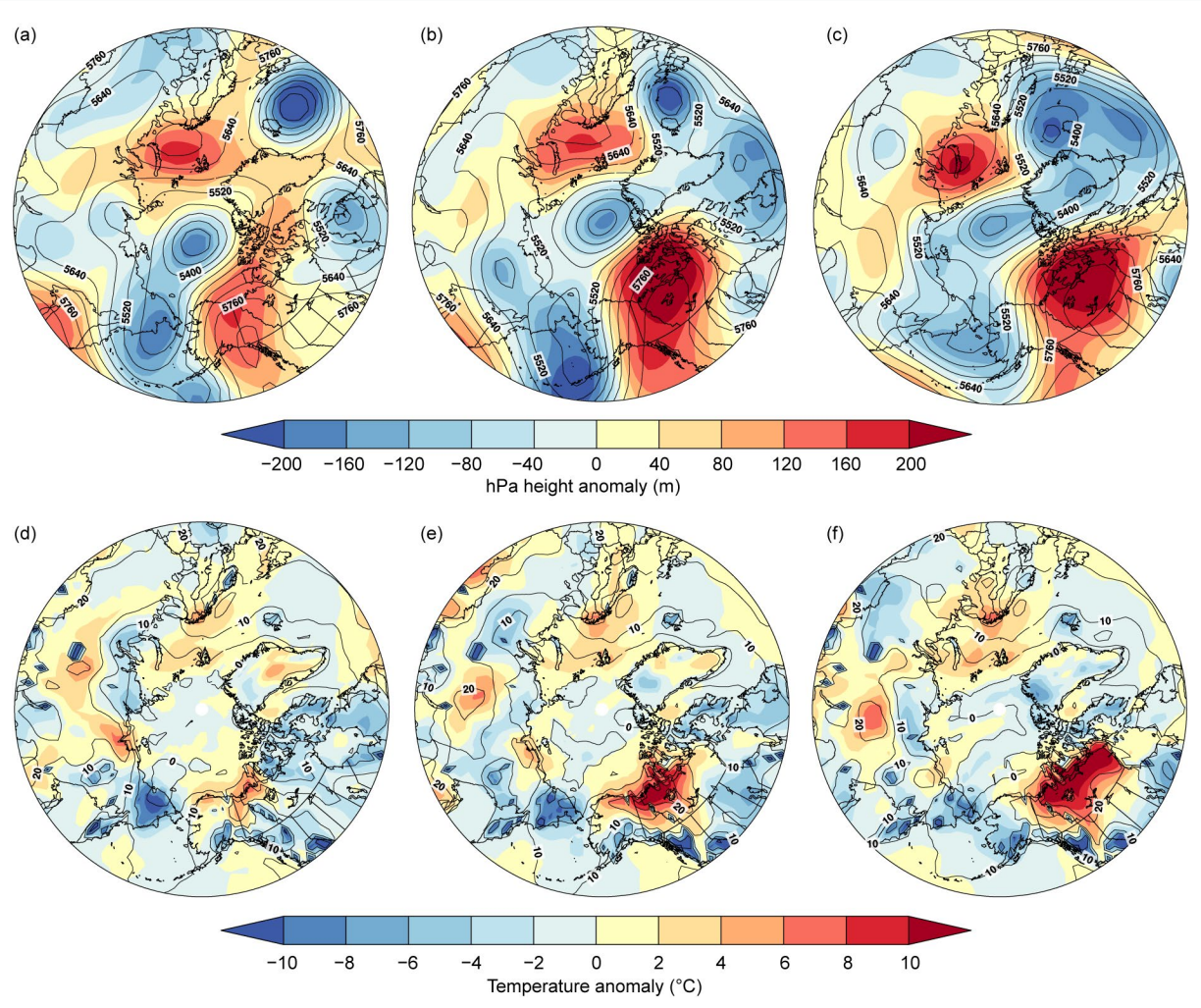

Fig. SB5.2. 500-hPa heights (contours) and anomalies (shading) on (a) 5 Aug, (b) 7 Aug, and (c) 9 Aug (m) and near-surface air temperatures (contours) and anomalies (shading) on (d) 5 Aug, (e) 7 Aug, and (f) 9 Aug (°C) during the 2024 heat event. Anomalies are relative to the 1991–2020 base period. (Data source: National Centers for Environmental Prediction (NCEP)/National Center for Atmospheric Research (NCAR) Reanalysis 1)

Unauthenticated | Downloaded 11/21/25 11:34 AM UTC

Discussion

The 2024 August heat marks another record-setting event to impact high-latitude North America in recent years. In 2023, Canada observed its warmest summer and autumn seasons on record, and both YT and NT recorded their warmest annual temperatures (Cheng et al. 2024). Some of the new 2024 records listed in Table SB5.1 broke records set in 2023. The hot, dry conditions supported wildfire activity across NT, where an additional 585,000 hectares burned during 1–11 August, contributing to NT's third-highest annual area burned on record; YT, which was not as hot and received more precipitation, saw minimal increases in wildfire activity (<10,000 hectares of new area burned; CIFFC 2025). This follows a record-breaking wildfire year across Canada in 2023 when approximately 15 million hectares burned, leading to community evacuations and health impacts from smoke inhalation (Jain et al. 2024). Wildfire is also increasing across permafrost regions. In 2024, permafrost temperatures across Alaska were the second highest of record, and 335 Tg of direct fire carbon emissions were observed throughout the pan-Arctic (Natali et al. 2024). These events show how compounding hazards (AghaKouchak et al. 2020) such as heat and wildfire are leading to greater impacts.

Methods and Data

Station observations are available for AK from the NOAA Applied Climate Information System online tool (https://xmacis.rcc-acis.org), and from Environment and Climate Change Canada for YT and NT (https://climate.weather.gc.ca). ERA5 data are provided by the Copernicus Climate Change Service Climate Data Store (https://doi.org/10.24381/cds.adbb2d47). NCEP/NCAR Reanalysis 1 data are provided by the NOAA Physical Sciences Laboratory (https://psl.noaa.gov). Canada wildfire information is available from the Canadian Interagency Forest Fire Centre (https://ciffc.net/).

Table SB5.1. Locations setting monthly or annual record-high temperatures during August 2024. Data sources given in the Methods and Data section.

Annual Record Temperatures

Location	Latitude	Longitude	Elevation (m)	Maximum Temperature (°C)	Date of Maximum
Deadhorse, Alaska (AK)	70°12′N	148°28′W	17	31.7	6 Aug
Kuparuk, AK	70°20′N	149°37′W	20	31.1	6 Aug
Fort McPherson, Northwest Territories (NT)	67°24′N	134°51′W	35	35.1	8 Aug
Inuvik, NT	68°19′N	133°31′W	103	34.8	7 Aug
Paulatuk, NT	69°21′N	124°04′W	6	31.0	8 Aug

August Record Temperatures

Location	Latitude	Longitude	Elevation (m)	Maximum Temperature (°C)	Date of Maximum
Tuktoyaktuk, NT	69°26′N	133°01′W	5	29.9	7 Aug
Fort Good Hope, NT	66°14′N	128°38′W	82	37.0	9 Aug
Norman Wells, NT	65°17′N	126°45′W	94	36.8	9 Aug

Unauthenticated | Downloaded 11/21/25 11:34 AM UTC

d. Precipitation

—M. C. Serreze, S. Bigalke, R. Lader, A. Crawford, and T. J. Ballinger

1. INTRODUCTION

Obtaining accurate measurements of Arctic precipitation to assess anomalies and change is challenged by the sparse observation network—notably over the Arctic Ocean—and observation errors due to factors such as gauge undercatch of solid precipitation (Serreze et al. 2003). Studies of Arctic precipitation have increasingly relied on output from atmospheric reanalysis projects, the most recent of these being ERA5 (Hersbach et al. 2020), which performs slightly better than other reanalyses at matching observed precipitation (Barrett et al. 2020; Loeb et al. 2022). In this section, ERA5 is used along with the gauge-based GPCC version 2022 dataset (land-only measurements; Becker et al. 2013; Schneider et al. 2022) to assess 2024 precipitation anomalies and trends. The Arctic is taken as the region poleward of 60°N. Winter, spring, summer, and autumn are defined as January–March, April–June, July–September, and October–December. A key finding is that, for the Arctic as a whole, annual precipitation based on ERA5 for 2024 was the third highest of the 1950–2024 record, consistent with the observed pattern that Arctic precipitation is increasing.

2. SUMMARY

Pan-Arctic annual precipitation for 2024 was 105% of the 1991–2020 average based on ERA5. Percent anomalies by season were 102% for winter, 101% for spring, 108% for summer, and 109% for autumn. Expressed as ranks, pan-Arctic annual precipitation for 2024 from ERA5 was the third highest over the 1950–2024 record. Corresponding ranks for winter, spring, summer, and autumn and are 17th, 20th, 1st, and 4th, respectively.

3. REGIONAL ANOMALIES

Figure 5.8 shows seasonal precipitation totals derived from ERA5 during 2024, expressed as anomalies with respect to 1991–2020 means. Prominent features of 2024 were: 1) strong negative anomalies in winter over the Alaskan Panhandle; 2) generally small anomalies during spring that were positive over the Barents Sea and part of Canada and mostly negative over Eurasia; 3) summer dryness over large parts of the Eurasian and North American continents but with wet conditions over central and northern Alaska and Scandinavia; and 4) wet conditions in autumn over the Barents Sea and coastal Norway and negative anomalies off the southeast coast of Greenland.

Precipitation along the Alaskan Panhandle is strongly driven by orographic uplift. Especially dry winter conditions here point to few cases of upslope winds. While negative summer anomalies dominated northern Canada, those over northern Eurasia were primarily found over the western side of the continent. Nevertheless, averaged over the Arctic region as a whole, summer precipitation ended up as the wettest in the record (see discussion below), in considerable part because of the positive anomalies over Alaska, the Barents Sea region, and the Canadian Arctic

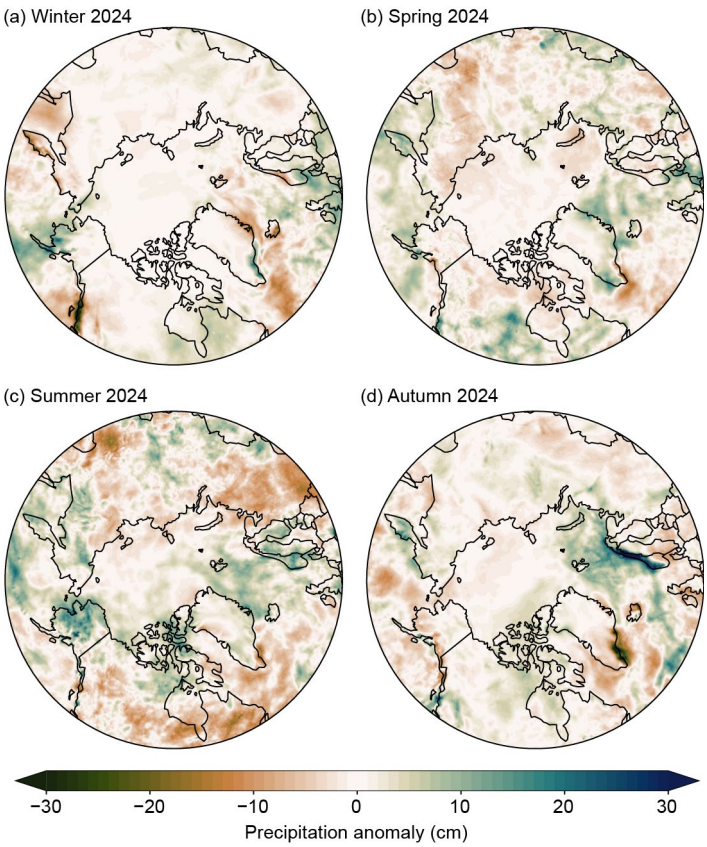

Fig. 5.8. Seasonal precipitation anomalies (1991–2020 baseline) for 2024 for (a) winter, (b) spring, (c) summer, and (d) autumn. Green shades denote above-normal precipitation; brown shades denote below-normal precipitation. (Data source: ERA5.)

Unauthenticated | Downloaded 11/21/25 11:34 AM UTC

Archipelago. According to ERA5, some of the high summer precipitation over Alaska was associated with convective activity (thunderstorms). Based on analysis of the cyclone detection and tracking algorithm developed by Crawford and Serreze (2016) and applied to ERA5 sea level pressure data, strong positive anomalies in the Barents Sea in autumn relate to an uptick in extratropical cyclone activity (15.3% more frequent than the 1991–2020 mean). The coast of Norway is another region where orographic uplift is important; the strongly positive autumn anomalies there point to strong moist upslope winds associated with a series of especially strong storms (averaging 14.0% stronger than the 1991–2020 mean based on the cyclone algorithm). The southeast coast of Greenland is known for exceptionally high precipitation due to orographic uplift, yet the negative anomalies here point to fewer upslope events in 2024. Anomalies from the Barents Sea, Norway, and Greenland were all connected to a general northeast shift in storm tracks.

4. HEAVY PRECIPITATION EVENTS

For any given year, there is a statistical expectation of regionally heavy precipitation events that can approach or exceed previous records, even in a stable climate. Figure 5.9 plots heavy precipitation events in 2024 by season in terms of ranks of the maximum five-day precipitation events (Rx5) in each season (relative to the 1950–2024 period). Generally, heavy precipitation events are scattered across the Arctic. A notable feature is the band of heavy events in winter stretching from south of the Aleutians northward across western Alaska into the East Siberian Sea, which is aligned with warmer-than-average conditions (section 5c; Fig. 5.9a). There were also some heavy events over the Canadian Arctic Archipelago and Lincoln Sea in summer.

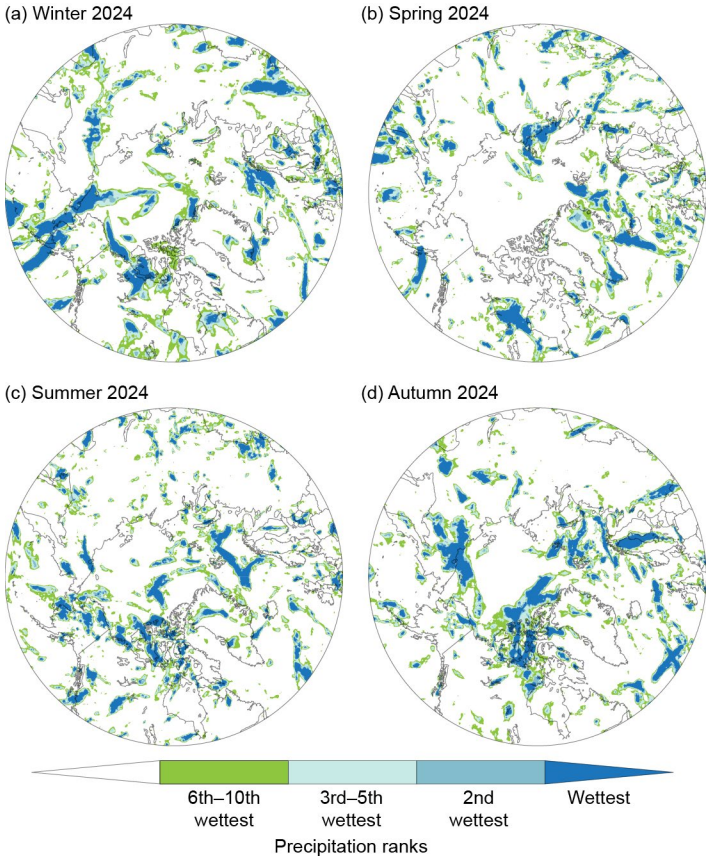

Fig. 5.9. Ranks of maximum five-day precipitation for 2024 for (a) winter, (b) spring, (c) summer, and (d) autumn. (Data source: ERA5, 1950–present.)

5. HISTORICAL PERSPECTIVE

Climate models project increased Arctic precipitation and more frequent heavy precipitation events as the climate warms, as well as an increase in the proportion of precipitation falling as rain. There is observational evidence of a transition to liquid precipitation in the warmer parts of the Arctic (Box et al. 2021), although the coldest areas are expected to see snowfall increases through the twenty-first century (McCrystall et al. 2021; Bigalke and Walsh 2022). Past studies have revealed large spatial variability in trends (Yu and Zhong 2021). However, as discussed in the arctic precipitation section of the 2023 *BAMS State of the Climate* report (Serreze et al. 2024) and presented here with updates, pan-Arctic precipitation assessed since 1950 now has detectable upward trends in all seasons, as well as in the annual mean.

In Fig. 5.10, the Arctic precipitation time series from ERA5 (as a percentage of 1991–2020 averages for the region poleward of 60°N) is plotted along with the corresponding time series from the station-based GPCC dataset for the period 1950–2024. The GPCC dataset is for land only, while ERA5 covers ocean areas as well as land. While the percent anomaly time series are generally similar, there are substantial differences for individual years due to the absence of coverage over the Arctic Ocean in GPCC and inherent uncertainties in each data source. Nevertheless, the time

Unauthenticated | Downloaded 11/21/25 11:34 AM UTC

series agree with respect to a positive annual trend and record-high precipitation for summer 2024.

Based on ERA5, the trend in annual mean precipitation stands at +0.68 cm decade^{-1}, or a 14.1% percent change since 1950. Corresponding seasonal changes are +0.23 cm decade^{-1} for winter, +0.09 cm decade^{-1} for spring, +0.13 cm decade^{-1} for summer, and +0.23 cm decade^{-1} for autumn.

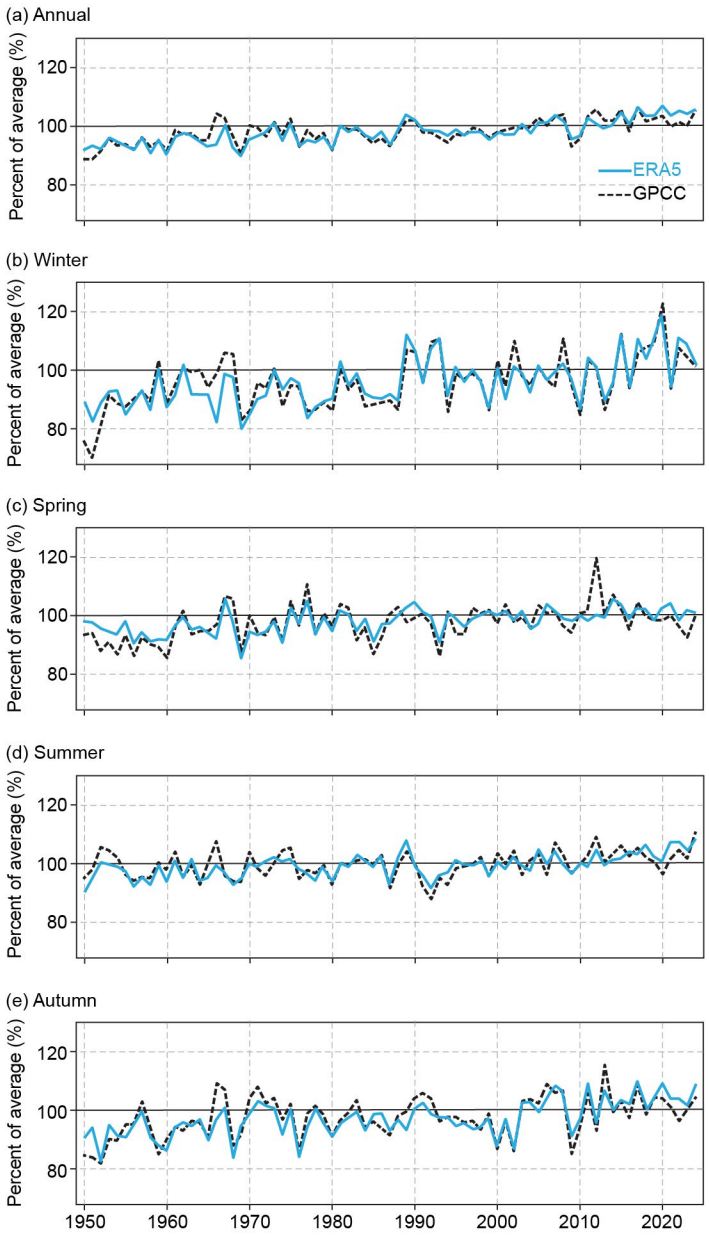

Fig. 5.10. Time series of Arctic (60°N–90°N) precipitation from 1950 through 2024 expressed as a percentage of the 1991–2020 average (shown by the horizontal black lines at 100%). Results are from ERA5 (blue lines) and GPCC 1.0° data (black lines). GPCC values are for land only; ERA5 values are for land plus ocean.

Unauthenticated | Downloaded 11/21/25 11:34 AM UTC

e. Sea surface temperature

—M.-L. Timmermans and Z. Labe

Arctic Ocean sea surface temperatures (SSTs) in the summer are primarily influenced by the amount of incoming solar radiation absorbed by the sea surface and by the flow of warm waters into the Arctic from the North Atlantic and North Pacific Oceans. Solar warming of the Arctic Ocean surface is influenced by the sea ice distribution (with greater warming occurring in ice-free regions), cloud cover, and upper-ocean stratification. Inflows of relatively warm Arctic river waters can provide an additional heat source in coastal regions.

Arctic SST is an essential indicator of the strength of the ice–albedo feedback cycle in any given summer sea ice melt season. As the brighter sea ice cover decreases, more incoming solar radiation is absorbed by the darker ocean surface and, in turn, the warmer ocean melts more sea ice. Marine ecosystems are also influenced by SSTs, which affect the timing and development of primary production cycles, available habitat, and other factors, such as the occurrence of harmful algal blooms. In addition, higher SSTs are associated with delayed autumn sea ice freeze-up and increased ocean heat storage throughout the year.

The SST data presented here are from the 0.25° × 0.25° NOAA OISST version 2.1 product (Reynolds et al. 2002, 2007; Huang et al. 2021). The period of our analysis spans June 1982 through September 2024, with 1991–2020 used as the climatological reference period. Here, we focus most closely on August 2024 mean SSTs in context with the climatological record. August mean SSTs provide the most appropriate representation of Arctic Ocean summer SSTs because sea ice extent is near a seasonal low at this time of year, and there is not yet the influence of surface cooling and subsequent sea ice growth that typically takes place in the latter half of September (Timmermans and Labe 2024).

August 2024 mean SSTs were as high as ~12°C in the southern Barents Sea and reached values as high as ~7°C in other Arctic basin marginal regions (Figs. 5.11a,b). August 2024 mean SSTs were anomalously high compared to the 1991–2020 August mean (around 1°C–4°C higher) in the Barents, Kara, Laptev and southern Beaufort Seas, and anomalously low (around 0.5°C–4.0°C below the 1991–2020 mean; Fig. 5.11c) in the East Siberian, Chukchi, and northern Beaufort Seas. The cold SSTs in the Arctic Pacific sector also extended through the Bering Sea (Fig. 5.12). The general pattern of August 2024 SSTs is consistent with regional patterns of anomalously warm and cold surface-air temperatures in summer 2024 (section 5c). Regional SST variations differ significantly from year to year. For example, there were considerably higher SSTs in the northern Barents Sea in August 2024 compared to August 2023, with differences of up to 2°C, and mostly lower 2024 SSTs in the Kara and southern Beaufort Seas (Fig. 5.11d).

Below-normal August 2024 SSTs in the Chukchi Sea were also observed in June, July, and September, as well as in the eastern sector of the Bering Sea (Fig. 5.12). This is consistent

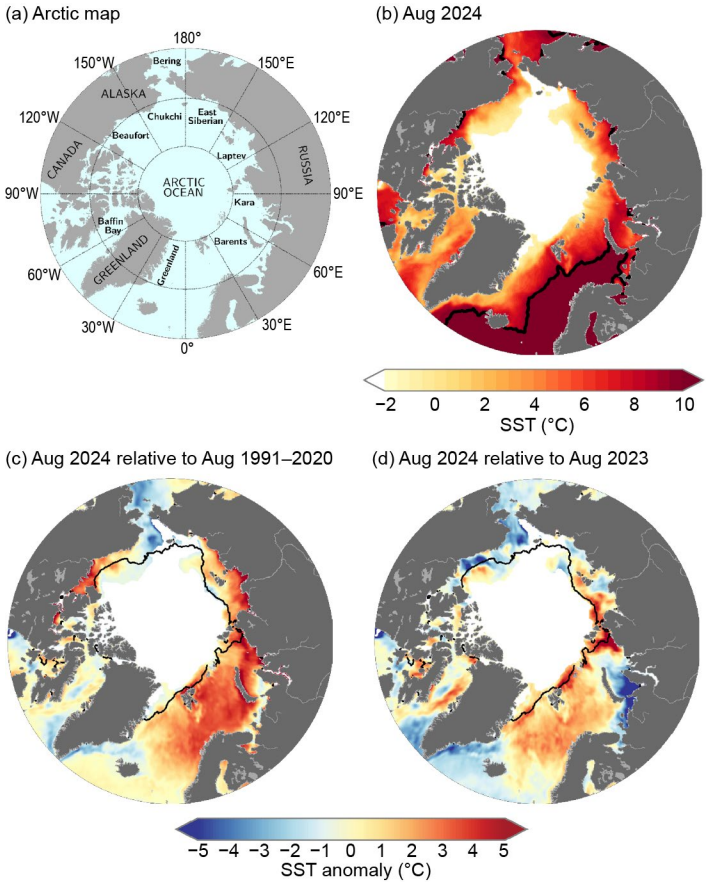

Fig. 5.11. (a) Arctic Ocean map showing relevant marginal sea locations and geographic features. (b) Mean sea surface temperature (SST; °C) in Aug 2024. Black contours indicate the 10°C-SST isotherm. (c) SST anomalies (°C) in Aug 2024 relative to the Aug 1991–2020 mean. (d) Difference between Aug 2024 SSTs and Aug 2023 SSTs (negative values indicate where 2024 was cooler). White shading in all panels is the Aug 2024 mean sea ice extent. Black lines in (c) and (d) indicate the Aug 1991–2020 median ice edge. Sea ice concentration data are the NOAA National Snow and Ice Data Center Climate Data Record of Passive Microwave Sea Ice Concentration, version 2 and version 4 (Peng et al. 2013; Meier et al. 2021a,b).

Unauthenticated | Downloaded 11/21/25 11:34 AM UTC

with relatively cold spring and summer 2024 surface air temperatures in the region (section 5c) and persistent areas of above-normal sea ice extent (Fig. 5.11c). Above-normal August 2024 SSTs in the Kara and Laptev Seas were also observed in July (Figs. 5.12b,c) as sea ice began to retreat from those regions, suggesting that the ice–albedo feedback was playing a role in ice retreat and SST warming. The transition from below-normal to above-normal August SSTs from June to August in the Barents Sea corresponded with the transition from anomalously cool surface air temperatures in spring to warm ones in summer (section 5c). A similar spatial pattern of SST anomalies persisted from August through the end of the melt season in September (Fig. 5.12d), although with generally reduced warm anomalies in the marginal seas, signifying cooling in the latter half of September.

The Arctic Ocean has experienced mean August SST warming trends from 1982 to 2024, with statistically significant (at the 95% confidence interval) linear warming trends in almost all regions (Fig. 5.13). Mean August SSTs for the entire region of the Arctic Ocean north of 65°N exhibit a linear warming trend of 0.03±0.01°C yr^{-1} (Fig. 5.14a). For context, both the North Pacific and North Atlantic (between 50°N and 65°N) show linear warming trends over this same period of 0.04±0.01°C yr^{-1}.

Regionally, the Kara and Laptev Seas show the strongest warming trends in the Arctic Ocean, with August SST linear trends in these seas of around 0.12°C yr^{-1} (Fig. 5.13). This is consistent with trends to earlier melt onset in these regions (section 5f). Statistically significant linear trends in August SST are also observed in the Barents Sea (0.06±0.02°C yr^{-1}), where August 2024 mean SSTs were the highest on record (Fig. 5.14b). On the other hand, there is no statistically significant trend in August SSTs in the Beaufort and Chukchi Seas (Figs. 5.14c,d), although the southernmost

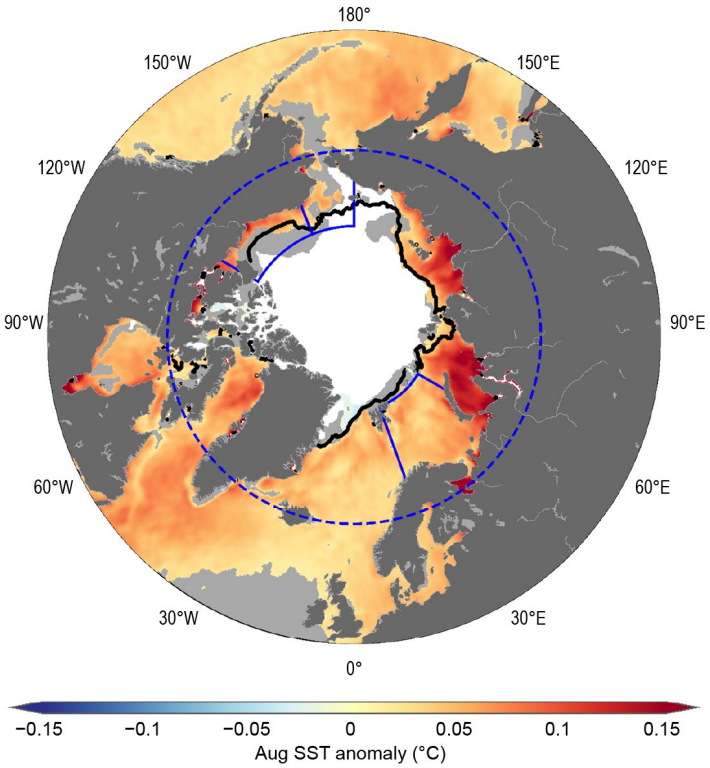

Fig. 5.13. Linear sea surface temperature (SST) trend (°C yr^{-1}) for Aug of each year from 1982 through 2024. The trend is only shown for values that are statistically significant at the 95% confidence interval; the region is shaded light gray otherwise. White shading is the Aug 2024 mean sea ice extent, and the black line indicates the Aug 1991–2020 median ice edge. The dashed blue circle marks 65°N (the Arctic Ocean region), and solid blue line boundaries delineate the Barents, Beaufort, and Chukchi Seas.

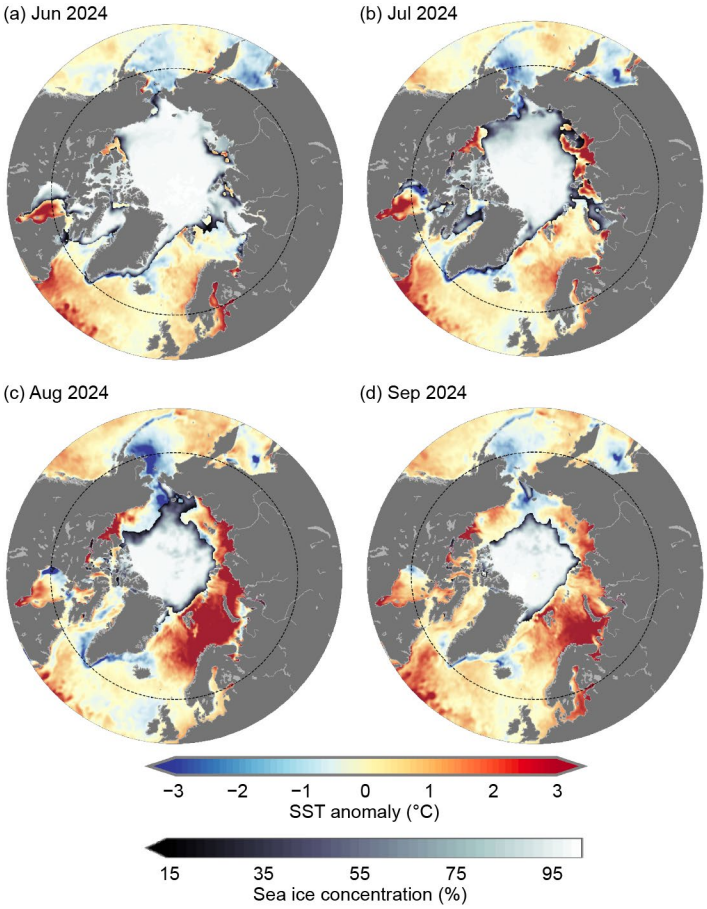

Fig. 5.12. Sea surface temperature (SST) anomalies (°C) for (a) Jun 2024, (b) Jul 2024, (c) Aug 2024, and (d) Sep 2024 relative to the 1991–2020 mean for the respective months. The mean sea ice concentration for the corresponding month is also shown. While sea ice extent is lowest in Sep, SSTs cool in the latter part of the month. The dashed circle indicates the latitudinal bound of the maps in Fig. 5.11. See Fig. 5.11 caption for sea ice dataset information.

Unauthenticated | Downloaded 11/21/25 11:34 AM UTC

portion of the Beaufort Sea does show a statistically significant warming trend (Fig. 5.13). The Beaufort Sea shows considerable interannual variability in mean August SST values (Fig. 5.14c), while Chukchi Sea trends are notably influenced by anomalously cool SSTs in the region in recent years with record-low August 2024 mean SSTs (Fig. 5.14d).

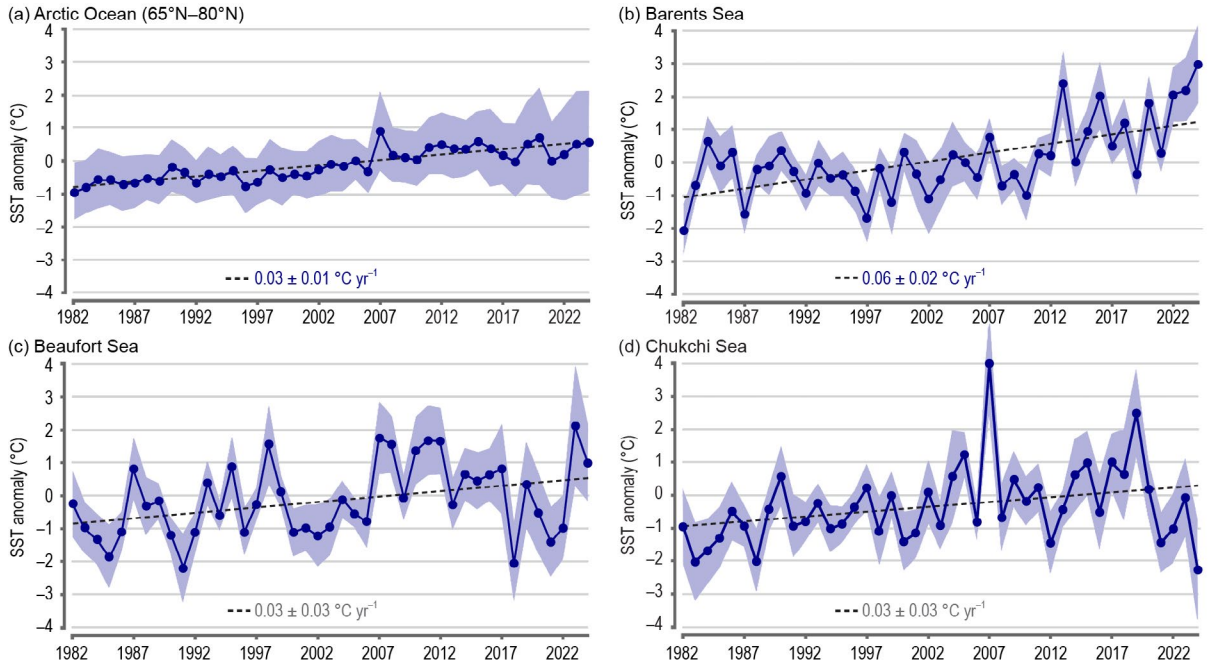

Fig. 5.14. Area-averaged SST anomalies (°C) for Aug of each year (1982–2024) relative to the 1991–2020 Aug mean for (a) the Arctic Ocean (65°N–80°N; indicated by the dashed blue circle in Fig. 5.13), (b) the Barents Sea, (c) the Beaufort Sea, and (d) the Chukchi Sea regions shown by blue boundaries in Fig. 5.13. The dotted lines show the linear SST anomaly trends over 1982–2024, and numbers in the legends indicate the trends in °C yr^{-1} (with 95% confidence intervals; trends that are not statistically significant are labeled in gray). Blue shading indicates ±1 standard deviation of the regional mean SST anomaly fields.

Unauthenticated | Downloaded 11/21/25 11:34 AM UTC

f. Sea ice

—W. N. Meier, A. Petty, S. Hendricks, D. Perovich, S. Farrell, M. Webster, D. Divine, S. Gerland, L. Kaleschke, R. Ricker, X. Tian-Kunze, and A. Bliss

Sea ice is the frozen interface between the ocean and atmosphere in the Arctic. It limits ocean–atmosphere exchanges of energy and moisture and plays a critical role in Arctic ecosystems and Earth's climate. The presence of sea ice affects human activities in the Arctic, including Indigenous hunting and transportation as well as marine navigation. Arctic September sea ice extent has declined 46% over 1979–2024, and 2024 sea ice conditions continued to illustrate the profound and ongoing changes in the region.

1. SEA ICE EXTENT

Arctic sea ice extent (defined as the total area covered by at least 15% ice concentration) in 2024 was generally on par with extents of the last 15 years, but much lower than those of all earlier decades within the observational record. For comparisons in this section, a climatological period of 1991–2020 is used. Extent during winter (January–March) 2024 was higher than in 2023 and fell within the lowest 10% of the climatological range. Extent values are from the National Snow and Ice Data Center's Sea Ice Index (Fetterer et al. 2017), one of several extent products (Ivanova et al. 2014; Lavergne et al. 2019) derived from satellite-borne passive microwave sensors operating since 1979. Extent was lower than average in the Barents Sea, Bering Sea, and the Gulf of St. Lawrence.

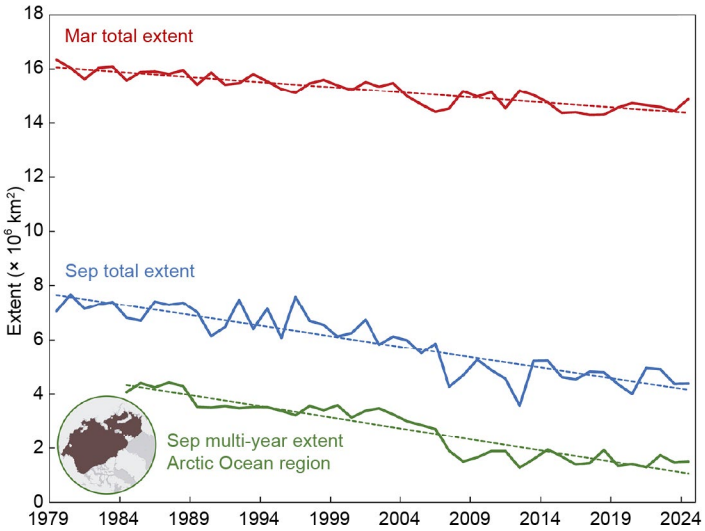

Fig. 5.15. Mar (red) and Sep (blue) total extent for 1979–2024; multi-year Sep extent (green) for 1984–2024 and linear trend lines (dashed lines). The Arctic Ocean region map is inset in the bottom left.

By March, the month with the most extensive coverage, the total sea ice extent of 14.87×10^6 km^2 was 0.16×10^6 km^2 (1.1%) lower than average and the 15th lowest March extent in the 46-year record. The March 2024 pan-Arctic extent continued the statistically significant downward trend of –2.5% decade^{-1} over the 1979–2024 record (Fig. 5.15). On a regional basis, March 2024 was characterized by near-average extent across most of the Arctic, with slightly lower-than-average extent in the Barents Sea and Gulf of St. Lawrence (Fig. 5.16a).

After March, the seasonal retreat of sea ice began. The 2024 and 2023 extents were similar during the spring and summer melt seasons (April–September), with extents at or just below the interdecile range during spring before dropping well below the lower interdecile after June. A notable feature of spring 2024 was a very early opening of the eastern Hudson Bay, resulting in record-low extent in the region from mid-May through June.

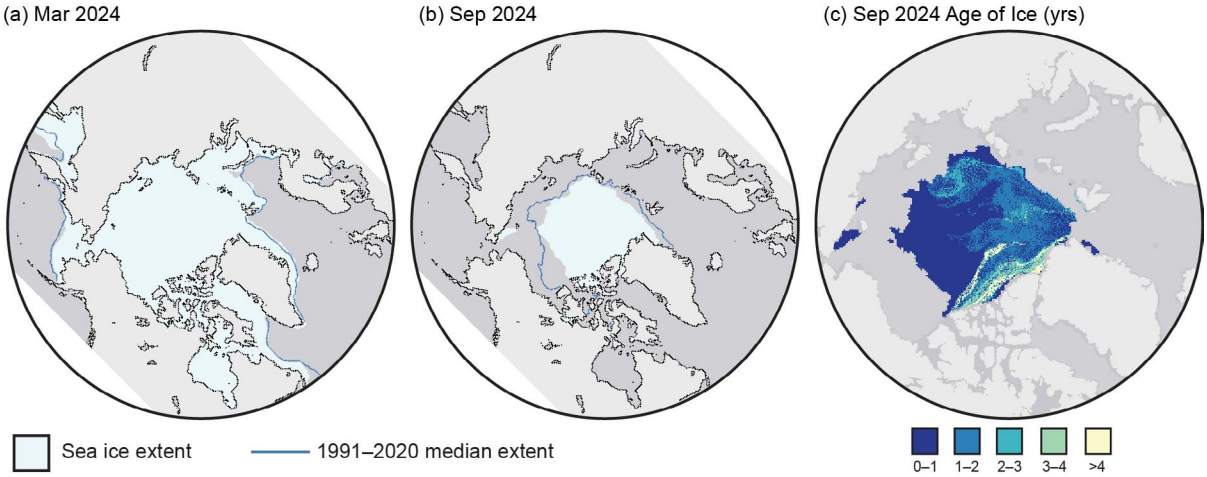

Fig. 5.16. Monthly average sea ice extent (light blue) for (a) Mar 2024 and (b) Sep 2024; the median extent for 1991–2020 is shown by the dark blue contour. (c) Sep 2024 sea ice age extent.

Unauthenticated | Downloaded 11/21/25 11:34 AM UTC

The Northern Sea Route along the northern Russian coast was relatively slow to open, with sea ice extending southward to the coast in the East Siberian Sea until late August. Afterward, an ice-free passage did open up, but a large remnant of ice between Wrangel Island and mainland Siberia survived through the melt season. The northern Northwest Passage route through the Canadian Archipelago reached a record-low sea ice extent in early October, briefly becoming virtually ice-free (Sidebar 5.2).

September, the month of the annual minimum sea ice extent, was characterized by below-average coverage in the Pacific sector with open water extending far northward from the coast in the Beaufort, Chukchi, and Siberian Seas (Fig. 5.16b). The September 2024 sea ice extent of 4.38×10^6 km^2 was 1.20×10^6 km^2 (21.6%) lower than the 1991–2020 average and the sixth-lowest September extent on record. The September trend from 1979 through 2024 is –13.9% decade^{-1}, and like all other months, is statistically significant. The 18 lowest September extents in the satellite record have all occurred in the last 18 years (2007–24). The 2024 freeze-up period (October–December) was slower than that of 2023 with much lower-than-average extent, particularly in Hudson Bay.

2. SEA ICE AGE, THICKNESS, AND VOLUME

Sea ice age is a rough proxy for thickness as multiyear ice (ice that survives at least one summer melt season) grows thicker over successive winters. Multiyear ice age based on Tschudi et al. (2019a,b) is presented here for the period 1984–2024 (Fig. 5.15). One week before the 2024 annual minimum extent, when the age values of the remaining sea ice are incremented by one year, the amount of multiyear ice remaining in the Arctic continued to be far lower than during the 1980s and 1990s (Fig. 5.16). Since 2012, the Arctic has been nearly devoid of the oldest ice (>4 years old); this continued in 2024 (Fig. 5.16c), with an end-of-summer old ice extent of 118,000 km^2 compared to ~1.5×10^6 km^2 in the 1980s. In the 41 years since ice-age records began in 1984, the Arctic has changed from a region dominated by multiyear sea ice to one where first-year sea ice prevails. A younger ice cover implies a thinner, less voluminous ice pack that is more sensitive to atmospheric and oceanic changes.

Sea ice drifts with winds and ocean currents while growing and melting thermodynamically. Ice divergence creates leads where, in freezing conditions, new ice forms while ice convergence leads to dynamic thickening. Sea ice thickness provides a record of the cumulative effect of dynamic and thermodynamic processes and thus is an important indicator of overall ice conditions. The European Space Administration's (ESA) CryoSat-2/Soil Moisture Ocean Salinity (SMOS) satellites have provided a record of seasonal (October–April) ice thickness and volume (Ricker et al. 2017; ESA 2023) since the 2010/11 winter. Since 2018, the NASA ICESat-2 satellite has also provided thickness estimates (Petty et al. 2020, 2023a,b). Some differences between these two products are seen in the monthly average winter Arctic thickness (Fig. 5.17a), but both products show monthly thicknesses from the 2023/24 winter similar to the mean of this short overlapping period (2018 onwards, see Fig. 5.17a). April

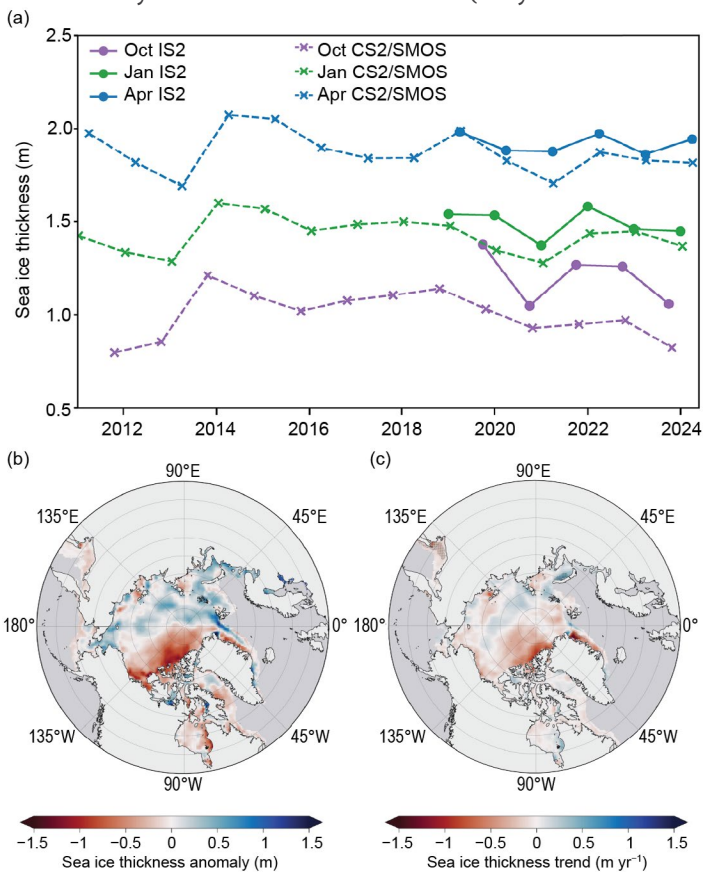

Fig. 5.17. (a) 2011–24 Oct (purple), Jan (green), and Apr (blue) monthly average sea ice thickness (m), calculated over an inner Arctic Ocean domain, same as the Arctic Ocean region in Fig. 5.14, from ICESat-2 (circles) and CryoSat-2/Soil Moisture Ocean Salinity (SMOS; crosses). (b) Apr 2024 sea ice thickness anomaly (m) map from CryoSat-2/SMOS (relative to the 2011–23 average); (c) CryoSat-2/SMOS Mar thickness trend map over the period 2011–24.

Unauthenticated | Downloaded 11/21/25 11:34 AM UTC

2024 thickness (Fig. 5.17b) from CryoSat-2/SMOS relative to the 2011–23 April mean shows that the Eurasian sector of the Arctic Ocean had relatively thicker sea ice than the 2011–23 mean. Sea ice was thinner than average in much of the North American sector, particularly in the Beaufort Sea and north of Greenland, as well as in the Canadian Archipelago. There is no significant trend in overall sea ice thickness since 2011 (Fig. 5.17a), which is consistent with the lack of a trend in multiyear ice extent during the same time period. However, there is substantial regional variability in the trends (Fig. 5.17c); thinning sea ice across much of the Eurasian side of the Arctic, particularly the Kara Sea, contrasts with thickening ice across the North American side, particularly north of the Canadian Archipelago and the East Greenland Sea. Sea ice thickness from CryoSat-2/SMOS integrated with ice concentration to provide winter volume estimates for 2011–24 also shows no substantial trend over the relatively short 14-year time series.

Unauthenticated | Downloaded 11/21/25 11:34 AM UTC

Sidebar 5.2: **Record-low sea ice conditions in the Northwest Passage in 2024**

—S. HOWELL AND M. BRADY

The Northwest Passage through the Canadian Arctic Archipelago (CAA) provides a shorter transit connecting the Atlantic and Pacific Oceans compared to the Northern Sea Route, Panama Canal, Suez Canal, or transiting around Cape Horn. The Northwest Passage has two primary routes: a preferred, shorter deepwater northern route directly through the Parry Channel, and a shallow-water southern route south of Victoria Island. The Northwest Passage was discovered by Sir Robert McClure in the 1850s, but ever-present sea ice has always prevented practical navigation. The recent loss of sea ice from climate change has challenged this notion.

Based on the 1991–2020 mean, sea ice area in the northern route of the Northwest Passage decreases gradually during the spring and summer months of May–September to about 73×10^3 km^2, then increases in mid-September with the onset of freeze-up (Fig. SB5.3). In 2024, sea ice area gradually declined below the 1991–2020 mean until August. It then declined rapidly until the end of September, reaching the lowest observed sea ice area since 1968 at 4×10^3 km^2 (Fig. SB5.3). The 2024 low eclipsed the previous record-low ice area of 9×10^3 km^2 set in September 2011 (Fig. SB5.3). Remarkably, there was virtually no sea ice present in and to the south of the Parry Channel at the end of September 2024 (Fig. SB5.4).

Low ice years within the Northwest Passage routes are driven by rapid sea ice melt associated with anomalously warm air temperatures, together with an atmospheric circulation pattern that prevents sea ice from being exported southward from higher-latitude regions (Howell et al. 2009, 2013). Air temperatures over the CAA were anomalously high during

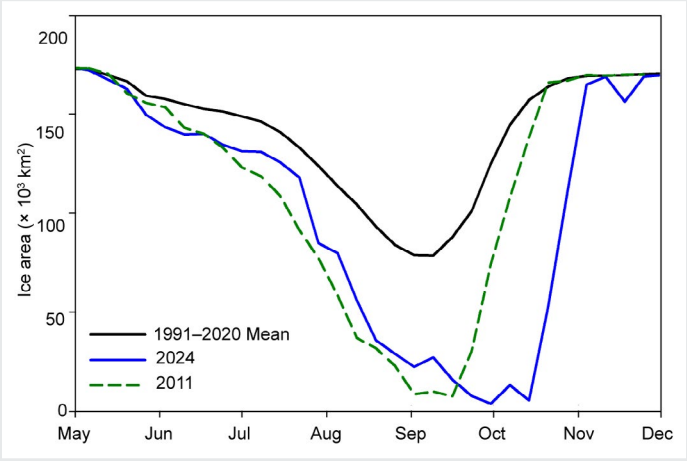

Fig. SB5.3. Time series of total sea ice area (× 10³ km²) within the Northwest Passage northern route for 2024 (solid blue line), 2011 (dashed green line), and the 1991–2020 mean (solid black line). (Data source: Canadian Ice Service.)

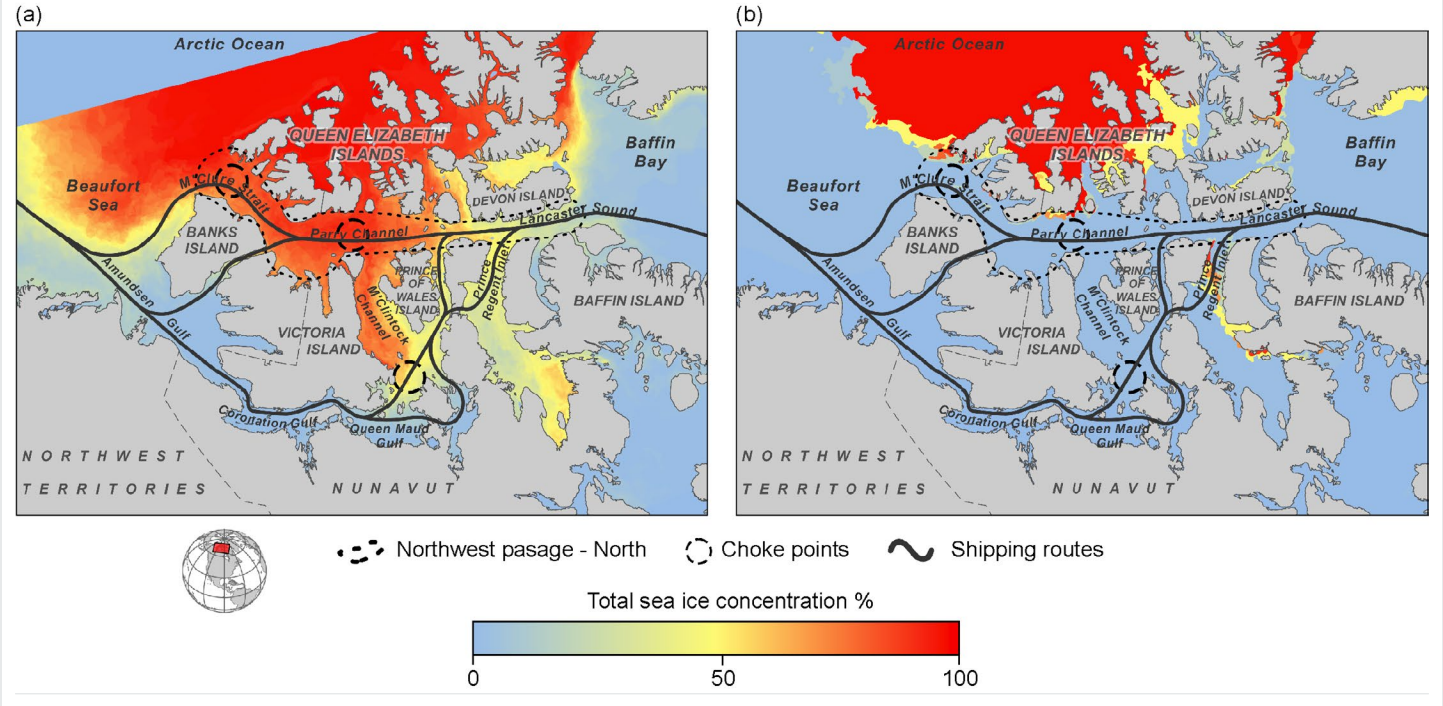

Fig. SB5.4. Spatial distribution of sea ice concentration (%) in the Canadian Arctic on 30 Sep for (a) the 1991–2020 mean and (b) 2024. (Data source: Canadian Ice Service.)

Unauthenticated | Downloaded 11/21/25 11:34 AM UTC

summer 2024 (see section 5c) and only ~2×10^3 km^2 of sea ice was exported southward from the Queen Elizabeth Islands into the northern route of the Northwest Passage during the melt season compared to a longer-term average of 27×10^3 km^2 (Howell et al. 2024). In addition, at the start of the 2024 melt season, the Northwest Passage northern route only contained about 10% multi-year ice, with the remaining 90% being made up of seasonal first-year ice. For the 1991–2020 mean, the Northwest Passage northern route contained 36% multi-year ice and 64% seasonal first-year ice. Since 2007, low-ice years in the Northwest Passage routes have been a more common occurrence as a result of less multi-year ice, which is thicker and more resilient to melt (Howell et al. 2023; see section 5f).

Although sea ice conditions in the Northwest Passage have been low since 2007, it is important to note that the process of Arctic Ocean sea ice export that transports thick multi-year ice southward from higher-latitude regions into the channels of the Northwest Passage still continues to operate (Howell et al. 2023). Specifically, the southward advection of Arctic Ocean sea ice creates or sustains "choke points", which are regions that almost always contain thick multi-year ice. These choke points are the most hazardous to maritime navigation and create barriers to a complete transit of the Northwest Passage (Fig. SB5.4). It has long been known that because of this process of sea ice transport, climate warming may not ease navigation conditions in the Northwest Passage (Melling 2002). Climate models have difficulty resolving the processes that create choke points within narrow Northwest Passage channels and may present a false sense of optimism regarding the feasibility of future navigation (Mudryk et al. 2021).

When warming does clear the Northwest Passage of sea ice, this is only temporary as sea ice returns most rapidly to the choke point regions, resulting in only a moderate increase in the shipping season. Cook et al. (2024) demonstrated that even during the recent low ice period from 2007 to 2021, the Northwest Passage shipping season length was reduced in several choke point regions. Sea ice is able to return to the choke points because it is sourced from the reservoir of the Arctic's oldest and thickest ice situated north of the CAA. As long as this multi-year sea ice reservoir remains and acts as an ice source for the choke points, climate change is unlikely to result in sustained shipping season increases in many Northwest Passage regions. The reservoir of multi-year ice to the north of the CAA is expected to persist even when the Arctic Ocean is classified as sea ice-free during the summer months (Sigmond et al. 2018; Notz and SIMIP Community 2020; Jahn et al. 2024; Fol et al. 2025). Overall, consistent lengthening of the shipping season along the entirety of all Northwest Passage routes as a result of climate change will be highly variable, and assumptions that less sea ice will enable safe transit should be avoided.

Unauthenticated | Downloaded 11/21/25 11:34 AM UTC

g. Greenland Ice Sheet

—K. Poinar, J. E. Box, T. L. Mote, X. Fettweis, B. D. Loomis, B. E. Smith, B. C. Medley, K. D. Mankoff, T. G. Askjaer, J. H. Scheller, R. S. Fausto, and M. Tedesco

The Greenland Ice Sheet loses mass when the sum of surface melt, surface water vapor flux, submarine melt, and discharge of solid ice exceeds the accumulated snowfall and rainfall. Net mass loss has occurred annually since the 1990s (Mouginot et al. 2019; Mankoff et al. 2021). Three independent estimates of the mass balance of the ice sheet over the 2024 mass balance year (1 September 2023 to 31 August 2024) are presented: input–output-derived mass balance of –76±48 Gt, gravity-derived mass balance of –55±35 Gt, and elevation-derived mass balance of –98±63 Gt. These three independent values agree within measurement uncertainties. All three measurements indicate that the Greenland Ice Sheet lost mass; however, the loss was 50%–80% less than the 2002–23 annual average.

Surface mass balance (SMB) comprises mass input from net snow accumulation and rainfall, and mass loss from melt, sublimation, and evaporation. These quantities are influenced by turbulent heat and water vapor energy fluxes, snow cover, and albedo, for which we summarize observations over the 2024 mass balance year.

Meteorological data from land-based weather stations (operated by the Danish Meteorological Institute) and on-ice weather stations operated by the Programme for Monitoring of the Greenland Ice Sheet (PROMICE; Fausto et al. 2021) across Greenland indicate that air temperatures were near the 1991–2020 average. During autumn (September–November 2023) and winter (December–February 2023/24), temperatures were above average. Spring (March–May 2024) temperatures were average, with above-average temperatures only in the far west and north. Summer (June–August 2024) temperatures were slightly above the 1999–2020 average at stations in the north and northeast, while Summit Station (+1.9°C anomaly) had its fourth-highest temperature on record (Fig. 5.18; section 5c). Summer temperatures were as much as 2.6°C below average in the south and west (Fig. 5.18), consistent with results from the Copernicus Arctic Regional Reanalysis (CARRA; Schyberg 2020; not shown). Thus, in situ data and CARRA suggest that the ERA5 summer 2024 anomaly is too positive for the west and south (Fig. 5.6c). Snow accumulation on the ice sheet (Vandecrux et al. 2023) during September 2023 through June 2024 was slightly below the 1991–2020 average in the north and northeast and substantially above average in the south and west (Fig. 5.18). The results from

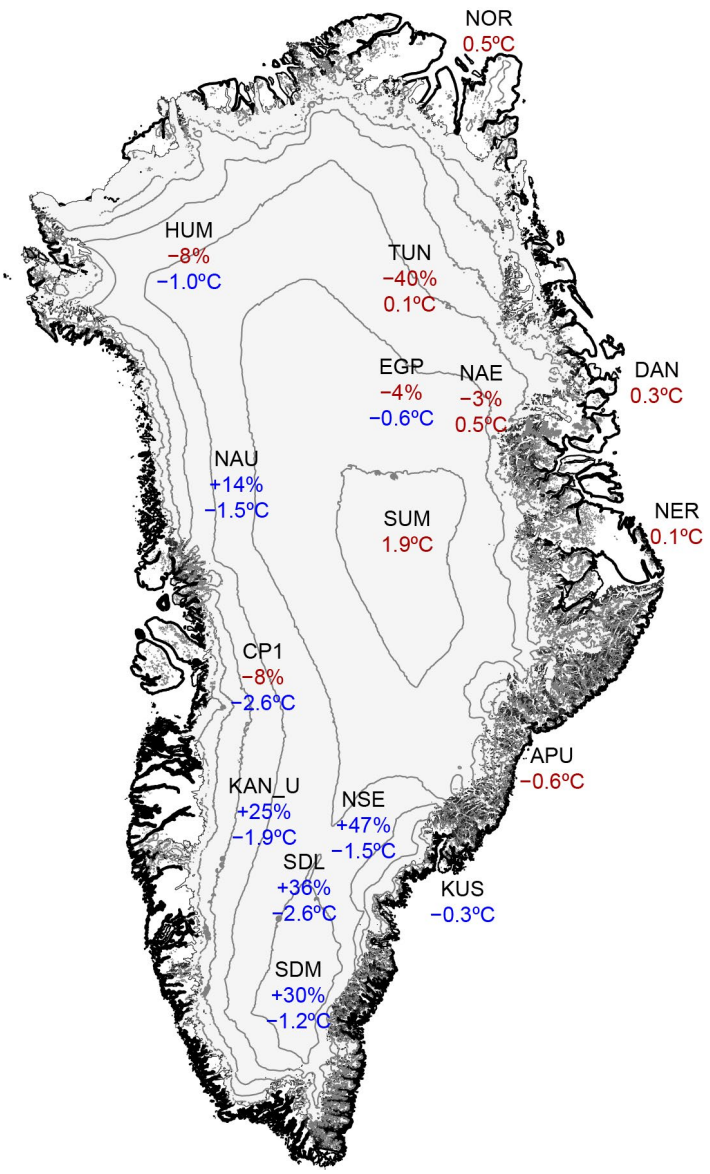

Fig. 5.18. Snowfall accumulation anomalies observed at 10 on-ice Programme for Monitoring of the Greenland Ice Sheet (PROMICE)/Greenland Climate Network (GC-Net) automated weather stations from Sep 2023 through Jun 2024 compared to 1991–2020 (top number, %) and near-surface air temperature anomalies from Jun through Aug 2024 compared to 1999–2020 (bottom number, °C). Summit Station (SUM) and Danish Meteorological Institute stations along the coast show air temperature anomalies compared to 1991–2020. Contours illustrate elevation above sea level. Red text indicates a warm temperature anomaly or a negative accumulation anomaly, while blue text indicates a cold temperature anomaly or a positive accumulation anomaly.

Unauthenticated | Downloaded 11/21/25 11:34 AM UTC

ERA5 (Fig. 5.8) are integrated over three-month seasons while the in situ data are integrated over the hydrological season from end-of-summer 2023 to end-of-summer 2024. The in situ data both for air temperature and snowfall have added credibility in their spatial coherence of the anomalies.

The average albedo during the melt season across the Greenland Ice Sheet was recorded by Sentinel-3 (Wehrlé et al. 2021) and found to be higher (brighter) than average (Fig. 5.19a). This was largely because of anomalously low air temperatures and excess snow cover, especially across the western ice sheet. Snow cover on the ice sheet in May and June slowed the onset of melt (Fig. 5.19b), especially in the west, where surface melt extent remained largely below the 1991–2020 mean all summer. This resulted in a below-average number of melt days observed across much of the western ice sheet (Fig. 5.19c; Sidebar 5.2). Across the eastern ice sheet, however, the melt season saw above-average duration.

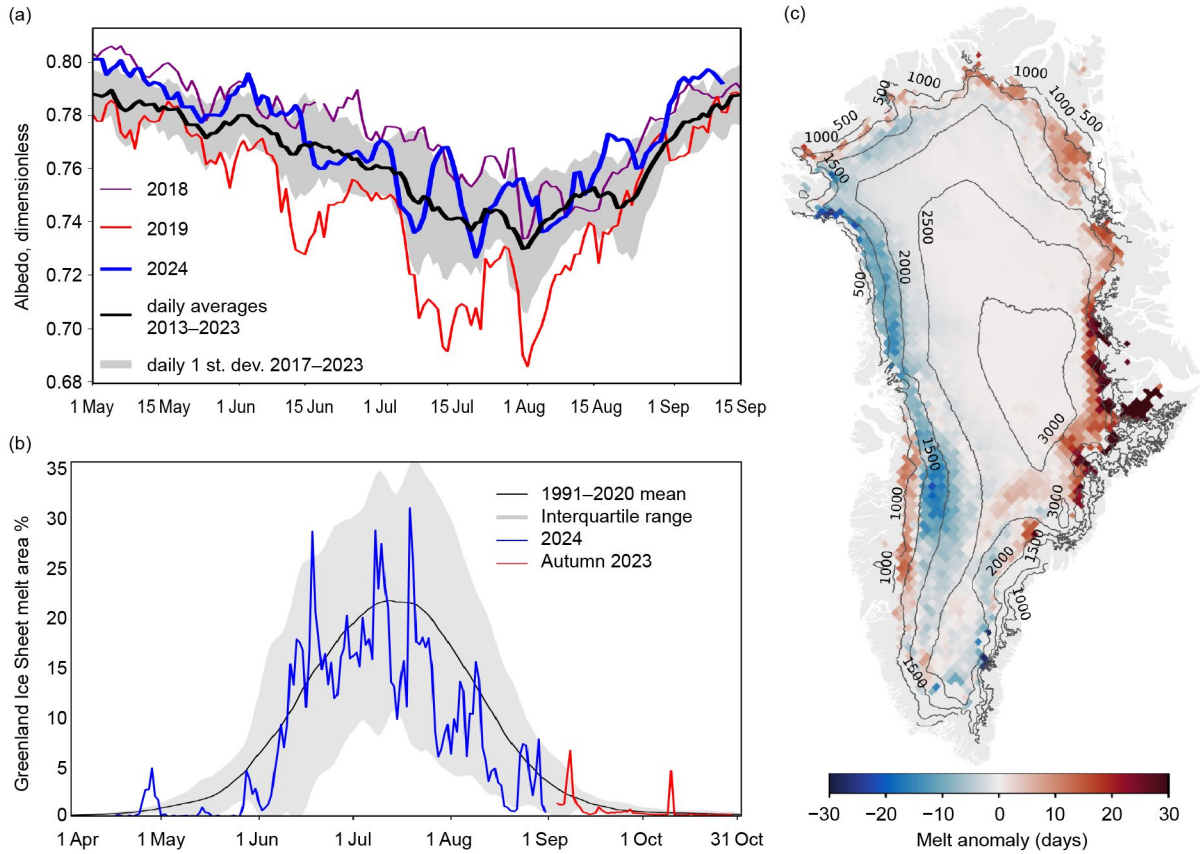

Fig. 5.19. (a) Greenland daily snow and ice albedo from Sentinel-3 for the 2024 melt season, alongside the 2017–23 average and recent bright-albedo (2018) and dark-albedo (2019) years. (b) Surface melt extent as a percentage (%) of ice sheet area during autumn 2023 (red) and spring/summer 2024 (blue), derived from passive microwave satellite observations (Mote 2007). (c) Number of surface melt days from 1 Apr to 31 Aug 2024, expressed as an anomaly with respect to 1991–2020, also derived from passive microwave.

The Modèle Atmosphérique Régionale version 3.14.1 regional climate model (MAR; Fettweis et al. 2020) forced by ERA5 (Hersbach et al. 2020) provides SMB values at 5-km horizontal resolution. The ice-sheet-wide total SMB over the 2024 mass balance year was 433±39 Gt, which is 17% above the 1991–2020 mean of 372±124 Gt yr^{-1}. This above-average SMB resulted from precipitation that was 7% higher than the 1991–2020 mean (6% higher snowfall, 21% higher rainfall), as well as runoff that was 5% lower. These anomalies do not exceed the 1991–2020 standard deviation and are thus statistically insignificant.

Tidewater glaciers contribute to ice mass loss by discharging icebergs into the ocean and through submarine melt. PROMICE estimates the sum of iceberg discharge and submarine melt from mass flow rate measurements collected near, but not precisely at, glacier calving fronts (Mankoff et al. 2020). Because the calving undergoes short-term advance and retreat, this is an

Unauthenticated | Downloaded 11/21/25 11:34 AM UTC

approximation of terminus mass loss. For the 2024 mass balance year, estimated terminus mass loss was 488±46 Gt. This is 7% above the 1991–2020 mean and continues a period of increased loss that began in 2005 and peaked over 2020/21.

The terminus mass loss (488±46 Gt output) and basal melt (23±6 Gt output, Karlsson et al. 2021) is subtracted from the net SMB (431±39 Gt input) to obtain an input–output mass balance of –76±48 Gt over the 2024 mass balance year (Fig. 5.20). This is just 51% of the average input–output-derived annual mass loss over 1991–2020 of –156±80 Gt.

The Gravity Recovery and Climate Experiment (GRACE; 2002–17) and GRACE Follow-On (GRACE-FO; 2018–present) satellite missions measure gravity anomalies to observe changes in total ice mass (Tapley et al. 2019). We follow Colgan et al. (2015) to eliminate peripheral non-ice-sheet ice from these observations, yielding –55±35 Gt over the 2024 mass balance year (Fig. 5.20). This is just 21% of the average annual loss of –266±16 Gt over the 2002–23 GRACE/GRACE-FO record.

ICESat-2 measures ice sheet surface height. Changes in this value reflect changes in ice mass and firn air content; thus, model-based estimates of the latter (Gardner et al. 2023; Medley et al. 2022) were subtracted from ICESat-2 observations (Smith et al. 2023) to report mass change. We quantify uncertainty from the difference between models and from uncertainties in the height measurement and the air content. ICESat-2-derived mass change over the 2024 mass balance year was –98±56 Gt (Fig. 5.20).

The ICESat-2, GRACE-FO, and input–output mass balances agree within 43 Gt (56%) and give an average 2024 mass balance across all three methods of –77±50 Gt. This below-average ice loss occurred due to above-average precipitation, below-average melt, and despite glacier flow rates that were higher than the 1991–2020 average.

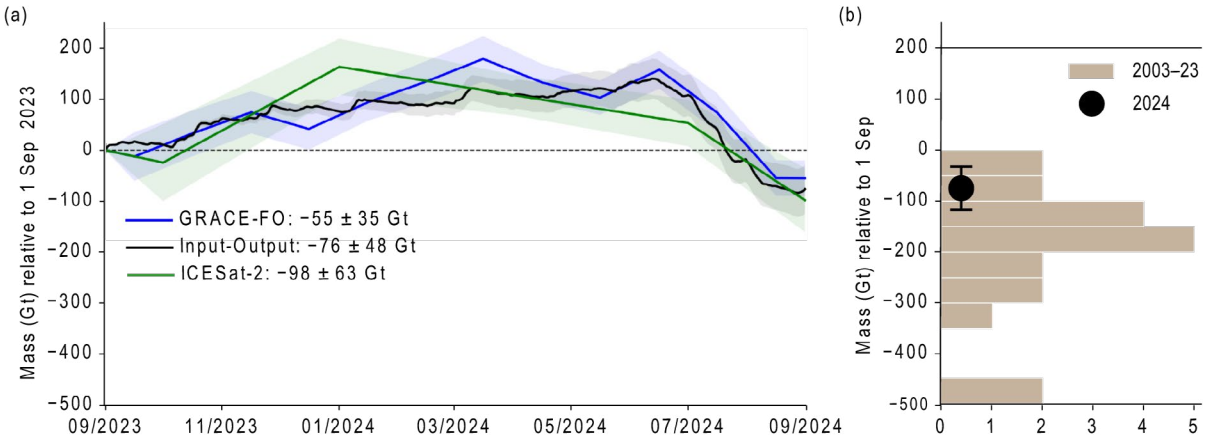

Fig. 5.20. (a) Observed mass balance (Gt) of the Greenland Ice Sheet over the 2024 mass balance year from the Gravity Recovery and Climate Experiment Follow-On (GRACE-FO), ICESat-2, and input–output, with uncertainties shaded. (b) Histogram of annual mass balance in years from 2003 to 2023, with full mass balance year observations by more than one method, shown as the average of the methods; and the multi-method averaged 2024 mass balance of –77±50 Gt.

Unauthenticated | Downloaded 11/21/25 11:34 AM UTC

Sidebar 5.3: **Why Greenland Ice Sheet melt was so low in 2024**

—J. BOX

Greenland Ice Sheet mass loss was muted in summer 2024 by the combined effect of anomalously north polar air influx and snowfall. The summer 2024 Greenland low melt anomaly was part of an Arctic-wide extreme in atmospheric circulation characterized by an extremely positive Arctic Oscillation Index (AOI). When the AOI is in its positive phase, a ring of strong winds circulating around the North Pole acts to confine colder air across the Arctic. This atmospheric state shielded Greenland from warm south air. The downstream air–sea exchange over near-record-warm North Atlantic sea surface temperatures (Timmermans and Labe 2024; see section 3b) instead entered the Barents Sea, producing record-high air temperatures and glacial melt on Svalbard to the east of Greenland (Arctic Council 2024; NASA 2024).

Here, additional details are provided on this low mass loss year for Greenland. Ice sheet automatic weather station data (Fausto et al. 2021; Vandecrux et al. 2023) recorded below-average June–August near-surface air temperatures and above-average snow accumulation (see section 5g, Fig. 5.18). A survey of Greenland and Arctic atmospheric circulation explains the situation. The June–August Greenland Blocking Index (GBI), which is useful in indicating south-to-north atmospheric heat and moisture transport for Greenland, (Hanna et al. 2016), ranked 2024 as the eighth lowest since 1961 (z-score of –1.1), consistent with projections for the GBI to have a negative tendency under anthropogenic climate change (Delhasse et al. 2021). Atmospheric circulation during July, and even more so in August (Fig. SB5.5), drew cold polar air down the western ice sheet where melting is normally concentrated. The typical southern summer warm air masses were deflected away from Greenland, as indicated by the second-highest AOI (z-score of +1.95) since 1961 (Fig. SB5.6). When the AOI is in its positive phase, a ring of strong winds circulating around the North Pole reduces north–south air exchanges between the polar region and the midlatitudes. The AOI was especially positive in August and moderately positive in July, but essentially neutral in June. The reduced summer temperatures over Greenland as compared with northern Canada (see section 5c, Fig. 5.6c) may have also been influenced by additional northerly advection due to the strong blocking high pressure over Canada (see section 5b, Fig. 5.3c).

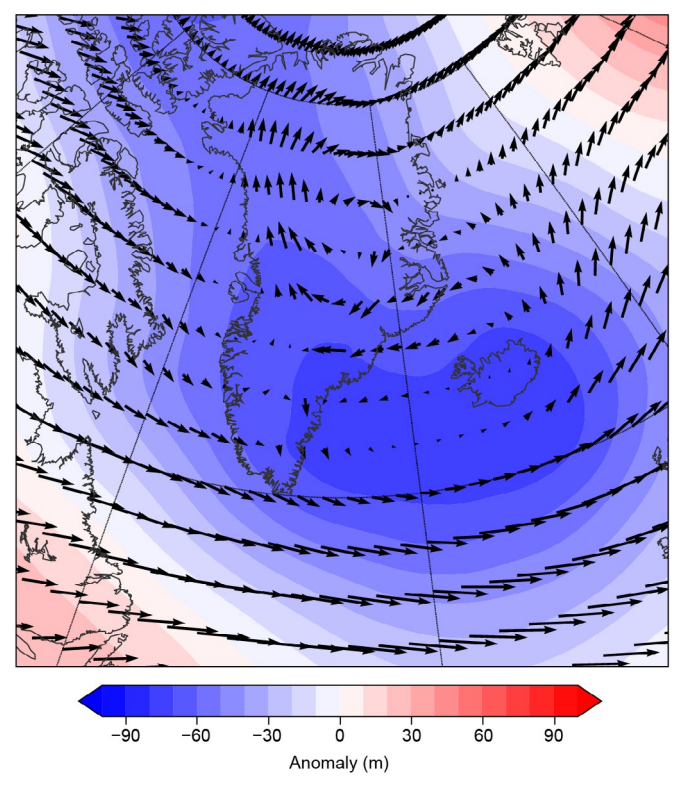

Fig. SB5.5. Jul–Aug 2024 ERA5 (Hersbach et al. 2020) wind vectors (arrows, m s^{-1}) at 700 hPa and geopotential height anomalies (m) at that level, approximately 3000 m above sea level, indicate the prevailing pattern during mid-to-late melt season. The 2024 season was marked by suppressed melt that resulted from cold polar air flowing southward along the western ice sheet where most surface melting typically occurs.

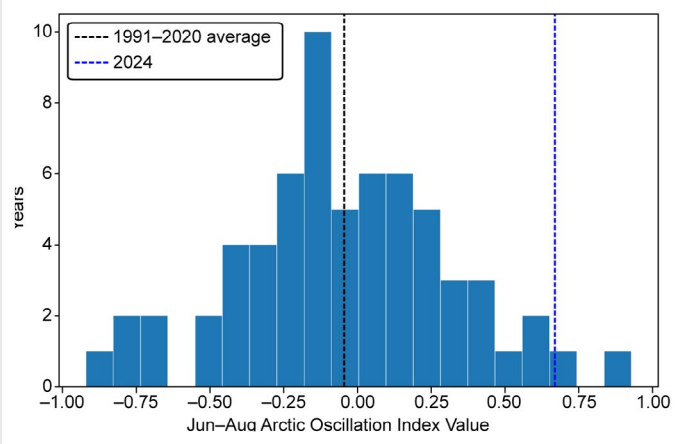

Fig. SB5.6. A highly anomalous summer 2024 Arctic Oscillation Index (AOI) relative to historical conditions since 1961 and the 1991–2020 average. Vertical lines indicate the June –August (JJA) 1991–2020 average (black) and the JJA 2024 AOI (blue). The bars indicate the number of years since 1961 within AOI intervals of 0.0924. The Arctic Oscillation is a weather pattern that involves the shifting of air pressure between the Arctic and midlatitudes (NCEP 2025; Zhou et al. 2001). The AOI is obtained from the 2024 pattern relative to the leading mode of empirical orthogonal function (EOF) analysis of monthly mean 1000-mb heights during the 1979–2000 period.

Unauthenticated | Downloaded 11/21/25 11:34 AM UTC

h. Arctic river discharge

—J. W. McClelland, A. I. Shiklomanov, A. Suslova, M. Tretiakov, R. G. M. Spence, S. E. Tank, and S. Zolkos

The Arctic Ocean accounts for approximately 1% of the global ocean's volume, yet receives more than 10% of global river discharge (McClelland et al. 2012). Consequently, effects of river inputs on ocean processes are more pronounced in the Arctic, and changes in river inputs have greater potential to impact physics, chemistry, and biology than in other oceans. Because rivers naturally integrate the processes that are occurring throughout their watersheds, trends in the discharge and chemistry of Arctic rivers can also be indicative of widespread changes in precipitation, permafrost thaw, and other anthropogenic impacts on land (Holmes et al. 2013; Tank et al. 2023).

Multiple studies over the past 20 years have demonstrated that discharge from Arctic rivers is increasing. Evidence first emerged from long-term Russian datasets (Peterson et al. 2002) and more recently from shorter U.S. and Canadian datasets (Durocher et al. 2019). While uncertainty remains around drivers of this trend, it is consistent with intensification of the Arctic hydrologic cycle (Rawlins et al. 2010). Warming is driving increased atmospheric moisture transport into the Arctic, resulting in greater precipitation (section 5d). This is particularly evident during colder months of the year. For example, snowfall has increased during autumn and early winter in western Siberia (Wegmann et al. 2015) and in the Canadian Arctic (Kopec et al. 2016; Yu and Zhong 2021). Evaporation is also increasing with warming, but the river discharge trend aligns with an overall increase in net precipitation.

River discharge was last included in the 2022 *State of the Climate* report, so discharge data for 2023 and 2024 are presented here. Data analysis and presentation focus on eight rivers that collectively drain much of the pan-Arctic watershed (Fig. 5.21). Six of these rivers are in Eurasia and two are in North America. Discharge measurements for the Eurasian rivers were initiated during different years, with discharge being tracked on all six by 1936. Discharge measurements did not begin until 1973 for the Mackenzie River and 1976 for the Yukon River in North America. Years are presented as "water years", 1 October–30 September, a common practice in hydrology to align runoff and associated precipitation within the same year. Thus, water year 2024 covers the period 1 October 2023 through 30 September 2024. The data used in this analysis are freely available through the Arctic Great Rivers Observatory (arcticgreatrivers.org).

Combined annual discharge for the eight rivers was 2387 km^3 for 2023 and 2447 km^3 for 2024 (Table 5.1). These values were similar to

Fig. 5.21. Watersheds of the eight largest Arctic rivers included in this analysis. Collectively, these rivers drain approximately 70% of the 16.8 million km² pan-Arctic watershed (indicated by the red boundary line). The red dots show the location of the discharge monitoring stations.

Table 5.1. Annual discharge (km³) for the eight largest Arctic rivers. Results are shown for 2023 and 2024 along with mean values for the 1991–2020 reference period. Values for years 2024 and 2023 are provisional data and are subject to modification until official data are published.

Water Year	Yukon	Mackenzie	S. Dvina	Pechora	Ob'	Yenisey	Lena	Kolyma	Total
2024	242	192	102	118	471	743	491	88	2447
2023	273	233	70	84	337	731	578	80	2387
1991–2020	215	297	108	119	424	618	582	80	2442

Unauthenticated | Downloaded 11/21/25 11:34 AM UTC

average discharge for the 1991–2020 reference period, differing by less than 3% from the reference average for both years. There were, however, notable departures from reference averages for some individual rivers. For example, Yenisey discharge was much higher (+18% in 2023, +20% in 2024) and Mackenzie discharge was much lower (–22% in 2023, –35% in 2024) than the reference during both years. The Yenisey values continued a pattern of higher-than-reference discharge that was highlighted in the 2022 *State of the Climate* report, but these values should be viewed with caution as data accuracy for the Yenisey has declined significantly since 2003 due to a lack of direct discharge measurements for rating curve updates (Tretiyakov et al. 2022). In contrast with the Yenisey, discharge values for the Mackenzie swung from remarkable highs in the 2022 report to record lows in this report. The low Mackenzie discharge values during 2023, and even more so during 2024, were driven by extreme drought conditions in southerly portions of the watershed (Government of Northwest Territories 2025; section 5d).

Average monthly discharge values for the Eurasian rivers during 2023 and 2024 were similar to average reference values throughout the year (Fig. 5.22a). The North American rivers, on the other hand, showed substantial departures from reference averages during some months (Fig. 5.22b). Average discharge for the North American rivers was particularly low during May, June, and July 2024. This effect was driven by very low discharge in the Mackenzie River. Discharge was also below average in the Mackenzie during all other months of 2024, but these lows were opposed by above-average discharge in the Yukon. Monthly discharge values were lower in the Mackenzie and higher in the Yukon (relative to reference) during 2023 as well, but the Mackenzie lows were less extreme during 2023 than during 2024 for most months. Exceptions were July, August, and September, when discharge in the Mackenzie was far below average during both years.

The 89-year time series available for the Eurasian Arctic rivers demonstrates a continuing, and perhaps accelerating, increase in their combined discharge (Fig. 5.23a). There is a positive linear trend across the entire time series showing that average annual discharge of Eurasian Arctic rivers is increasing by 2.5 km^3 per year. When data are considered from 1976 through 2024 (the period of record for North American rivers), the average annual increase in discharge for Eurasian Arctic rivers is 3.9 km^3 per year. For the North American Arctic rivers, the average discharge increase over the 1976–2024 timeframe is 1.1 km^3 per year (Fig. 5.23b). These observations show that, although river discharge varies widely over interannual to decadal timeframes, longer-term increases in river discharge are a pan-Arctic phenomenon. Evidence of increasing Arctic river discharge is strongest for Eurasian rivers where datasets are longest, but the signal of change in North American rivers is becoming increasingly robust as discharge measurements

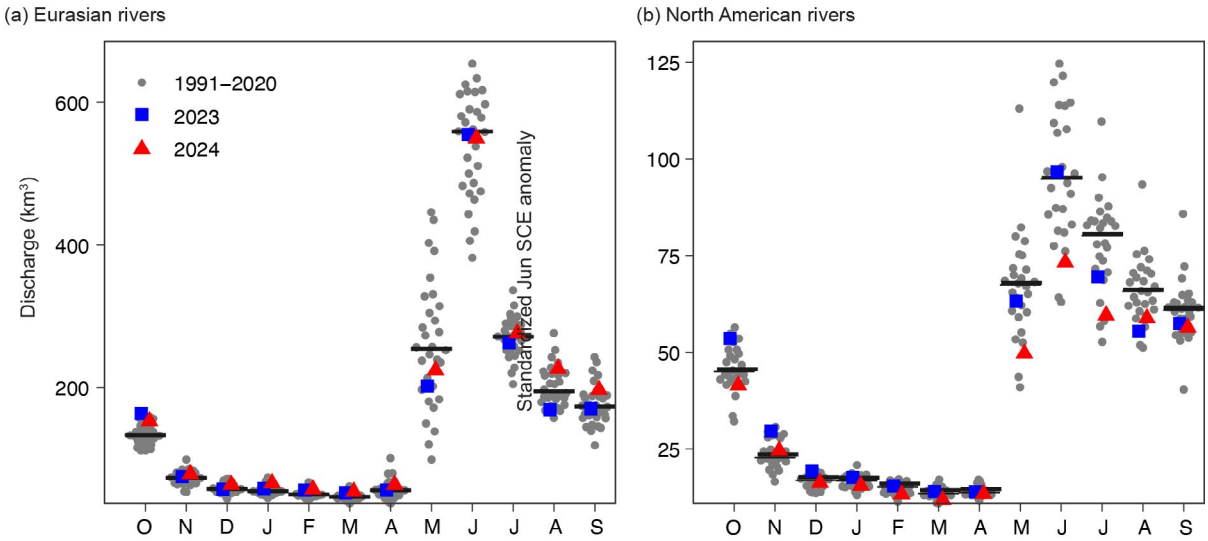

Fig. 5.22. Monthly discharge (km^3) in (a) Eurasian and (b) North American rivers for 2023 and 2024 compared to monthly discharge throughout the 1991–2020 reference period. Gray dots mark the combined monthly discharge of contributing rivers during individual years, and black bars mark the average monthly discharge of combined rivers over the reference period. Note the different magnitudes of discharge between the Eurasian and North American rivers (see y-axes).

Unauthenticated | Downloaded 11/21/25 11:34 AM UTC

continue and the overall observational period becomes longer.

The timing of the spring freshet, when discharge rapidly shifts from low to high flow conditions, is also changing across the pan-Arctic domain (Fig. 5.23c). The spring freshet is starting earlier in Eurasia and North America, showing a linear change of approximately nine days over the 1976–2024 timeframe. This seasonal shift is associated with earlier snowmelt in the Arctic (Derksen and Mudryk 2023; section 5g), which is driven by warming air temperatures as well as more frequent rain-on-snow events during the spring (Shrestha et al. 2021; Dou et al. 2021).

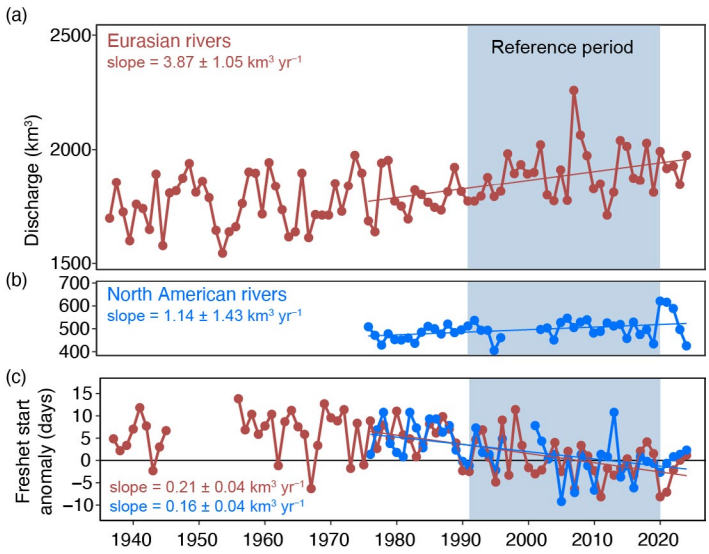

Fig. 5.23. Long-term trends in annual discharge (km³) for (a) Eurasian (dark red) and (b) North American (blue) Arctic rivers, and (c) freshet start day anomalies relative to the 1991–2020 reference period average for both. Freshet start day anomalies were calculated for individual rivers and then averaged by continent. Time series gaps reflect insufficient monthly (North American river discharge) and daily (Eurasian river freshet start day anomalies) data for calculations during some timeframes. Reported slopes are for 1976–2024 ($p<0.05$ in all cases).

Unauthenticated | Downloaded 11/21/25 11:34 AM UTC

i. Terrestrial snow cover

—L. Mudryk, A. Elias Chereque, C. Derksen, K. Luojus, and B. Decharme

Many components of the Arctic land surface are directly influenced by snow cover, including the surface energy budget, permafrost, terrestrial and freshwater ecosystems, and the ground thermal regime, with implications for the carbon cycle (Brown et al. 2017; Meredith et al. 2019; and references therein). Even following the snow cover season, the influence of spring snowmelt timing persists through impacts on river discharge timing and magnitude, surface water, soil moisture, vegetation phenology, and fire risk (Meredith et al. 2019).

Snow cover extent (SCE) anomalies during 1967 to 2024 are illustrated for both the North American and Eurasian sectors of the Arctic in Fig. 5.24 (relative to the 1991–2020 baseline; data from the NOAA snow chart climate data record; Robinson et al. 2012). In May 2024, Eurasian Arctic SCE was slightly above normal (20th-lowest May value in the 58-year record), related to cold spring conditions over northern Europe and western Russia (section 5c, Fig. 5.6b); however, by June, Eurasian SCE had dropped below normal (14th-lowest June value in the 58-year record). North American Arctic SCE during 2024 was below normal throughout May and June (SCE values for each month ranked seventh lowest in the 58-year record). See section 2c5 for more details.

Snow cover duration (SCD) anomalies for the 2023/24 snow season (difference from the average number of days with snow cover) are shown in Fig. 5.25 (data from the NOAA daily Interactive Multisensor Snow and Ice Mapping System [IMS] snow cover product; U.S. National Ice Center 2008). SCD anomalies are computed separately for each half of the snow season: the "onset period" of August 2023 to January 2024 (relative to a 25-year baseline starting in August 1998; Fig. 5.25a), and the "melt period" of February 2024 to July 2024 (relative to a 25-year baseline starting in February 1999; Fig. 5.25b). During the 2023/24 snow season in Eurasia, broad portions of the continent experienced either early snow onset (northern Europe and parts of eastern Siberia) or delayed snow melt (western Russia and easternmost Siberia). This combination of early onset and delayed melt led to one of the longer snow seasons of the past 26 years across the majority of the Eurasian Arctic (rank of season length shown in Fig. 5.25c). For North America,

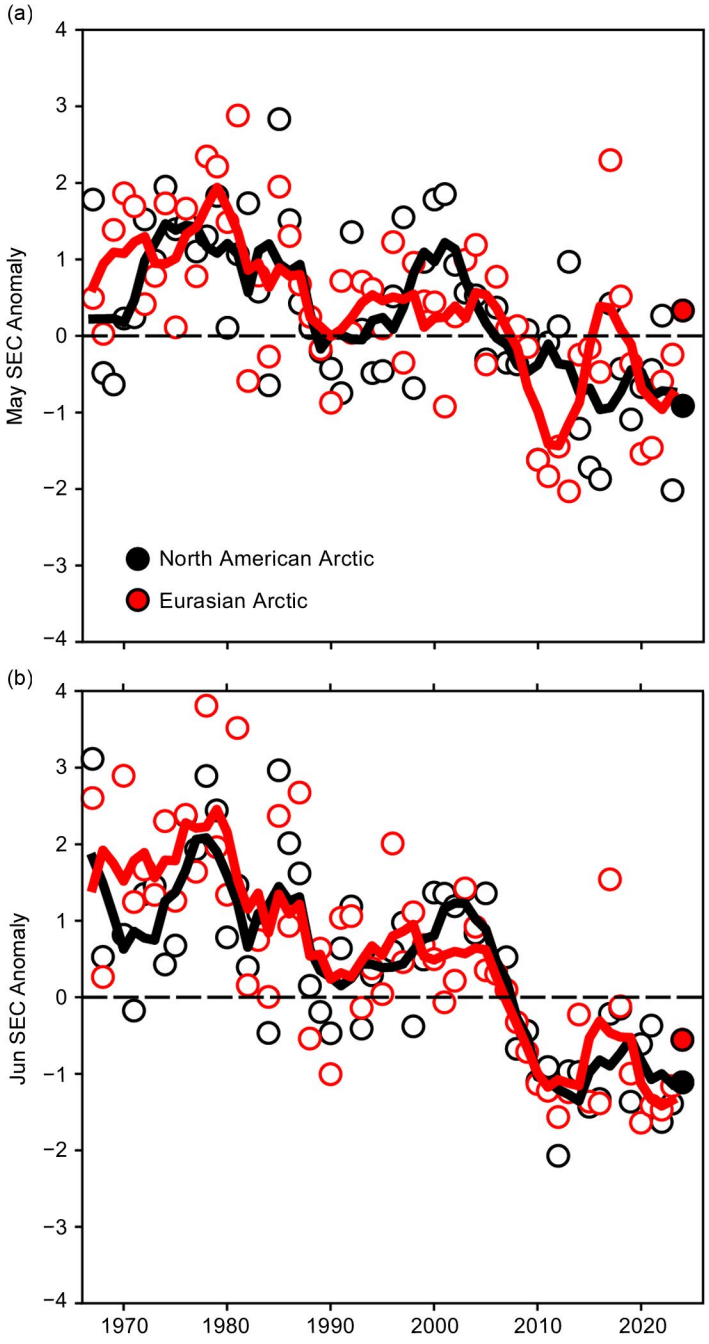

Fig. 5.24. Monthly snow cover extent (SCE) anomalies for Arctic terrestrial land areas (poleward of 60°N) for (a) May and (b) Jun from 1967 to 2024. Anomalies are relative to the average for 1991–2020 and standardized (each observation differenced from the mean and divided by the standard deviation, and thus unitless). Solid black and red lines depict five-year running means for North America and Eurasia, respectively. Filled circles highlight 2024 anomalies. (Data source: Robinson et al. [2012].)

Unauthenticated | Downloaded 11/21/25 11:34 AM UTC

a combination of late onset and early spring melt resulted in one of the shortest snow seasons of the last 26 years across portions of northern Canada (Fig. 5.25c).

Finally, snow water equivalent (SWE), a measure of water contained within the snowpack, is used to characterize Arctic snow accumulation over the 2023/24 season. Maps of SWE anomalies are shown in Fig. 5.26 (anomaly shown for each month is the average of four products relative to their respective 1991–2020 baselines: Snow Climate Change Initiative [CCI; Luojus et al. 2022], MERRA-2 [GMAO 2015], ERA5-Land [Muñoz Sabater 2019], and Crocus-ERA5 [Decharme et al. 2024]). Four datasets are considered because averaging multiple SWE products has been shown to be more accurate than individual datasets when validated with in situ observations (Mortimer et al. 2020). In April 2024, the majority of Arctic land areas on both continents had positive SWE anomalies, indicating higher-than-normal snowfall accumulations since the preceding autumn (April is the approximate month that total snow mass across the terrestrial pan-Arctic region peaks, before increasing May and June temperatures lead to melt). Strong reductions in the relative amount of SWE occurred over the North American Arctic during May, while over Eurasia large regions of above-normal SWE still existed. By June, the amount and extent of Eurasian snow cover was also greatly reduced, consistent with the anomalies in Fig. 5.24b. However, SWE anomalies between the Ob and Yenisei Rivers and at the far eastern tip of the continent were still

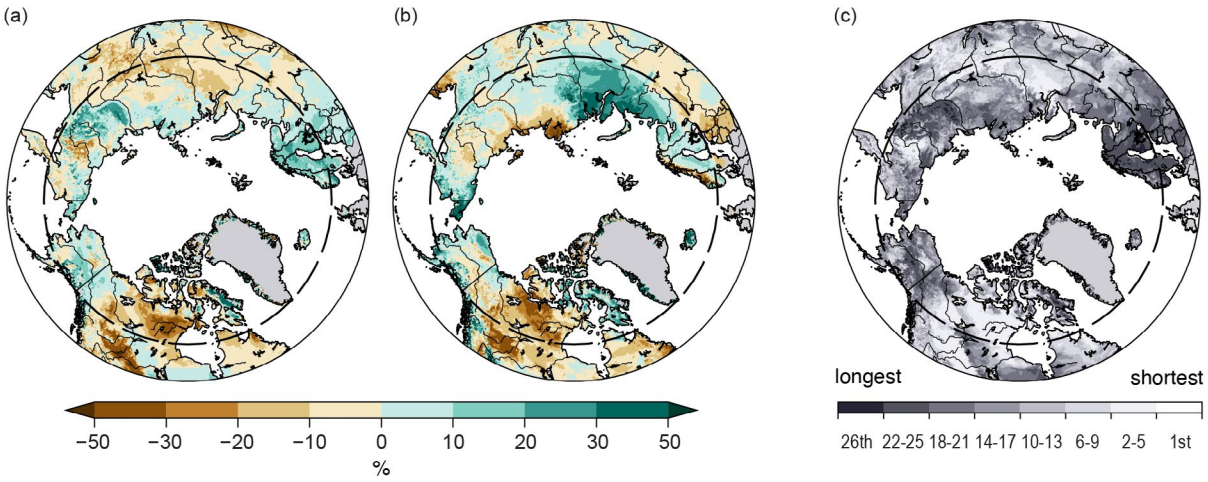

Fig. 5.25. Snow cover duration (SCD) anomalies (% difference relative to climatological number of snow-free days for the 1998/99–2022/23 baseline) for the 2023/24 snow year: (a) snow onset period (Aug 2023–Jan 2024) and (b) snow melt period (Feb–Jul 2024). (c) Rank of the 2023/24 snow season length within the past 26 years of observation. Brown (green) indicates more (fewer) snow-free days than average. Latitude 60°N is marked by the gray dashed circle. (Data source: U.S. National Ice Center [2008].)

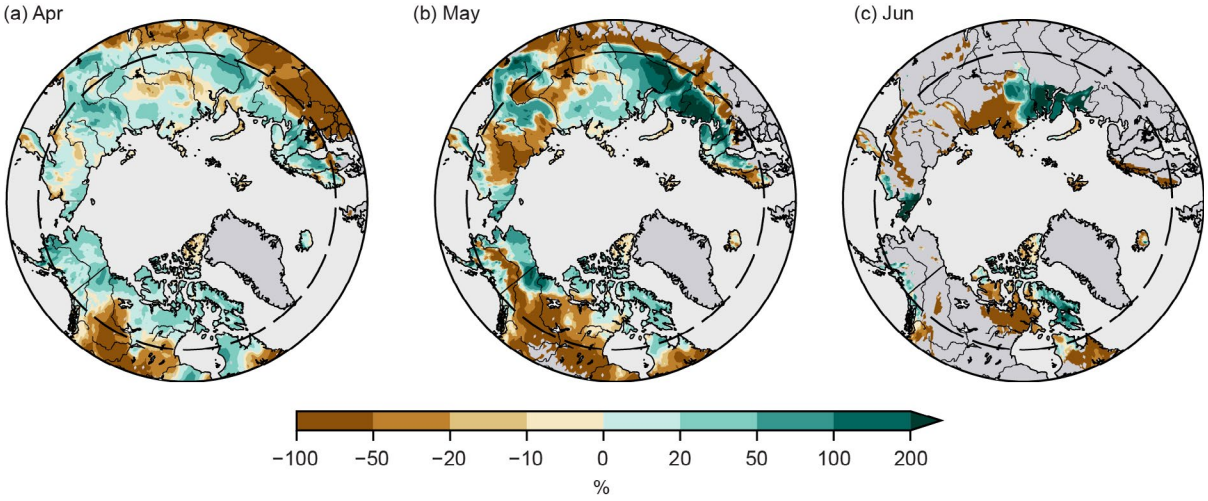

Fig. 5.26. Snow water equivalent (SWE) anomalies (% difference from the 1991–2020 baseline) in 2024 for (a) Apr, (b) May, and (c) Jun. Brown (green) indicates lower (higher) snow amounts than average. Latitude 60°N is marked by the gray dashed circle. (Data source: selection of four SWE products from Snow Climate Change Initiative [CCI; Luojus et al. 2022]; MERRA-2 [GMAO 2015]; ERA5-Land [Muñoz Sabater 2019]; and Crocus [Decharme et al. 2024].)

Unauthenticated | Downloaded 11/21/25 11:34 AM UTC

above normal, consistent with the longer-than-normal melt season observed in those regions (Fig 5.25b). Over North America, most of the Canadian Arctic Archipelago had below-normal SWE during June except for Baffin Island.

In summary, snow accumulation during the 2023/24 winter was above average across both continents; however, the duration of the snow season contrasted strongly between them. Over much of northern Canada, warm spring temperatures resulted in a shorter-than-normal snow season, consistent with or even shorter than what has typically been observed over the last 15 years (Fig. 5.25c). Over broad portions of Eurasia and Alaska, early snow onset and above-normal SWE during most of May resulted in a longer-than-normal snow season (Fig. 5.25c) and higher-than-average May SCE (Fig 5.24a). However, by June, Eurasian SCE was back down to values consistent with those seen over the past 15 years.

Unauthenticated | Downloaded 11/21/25 11:34 AM UTC

j. Permafrost

—S. L. Smith, V. E. Romanovsky, K. Isaksen, K. E. Nyland, N. I. Shiklomanov, D. A. Streletskiy, and H. H. Christiansen

Permafrost refers to earth materials (e.g., bedrock, mineral soil, organic matter) that remain at or below 0°C for at least two consecutive years, although most permafrost has existed for centuries to many millennia. Extensive regions of high-latitude landscapes are underlain by permafrost. The active layer, which thaws and refreezes annually, overlies the permafrost. Warming of permafrost (especially if ice-rich), active-layer thickening, and ground ice melt cause changes in surface topography, hydrology, and landscape stability, with implications for Arctic infrastructure, ecosystem integrity, and human livelihoods (Smith et al. 2022; Hjort et al. 2022; Wolken et al. 2021). Changes in permafrost conditions also affect the rate of release of greenhouse gases into the atmosphere, potentially accelerating global warming (Miner et al. 2022; Schuur et al. 2022).

Permafrost conditions respond to shifts in the surface energy balance through interrelated changes in ground temperature and active-layer thickness (ALT). Ground temperatures fluctuate seasonally near the surface, while below the depth of seasonal temperature variation, they reflect longer-term climate. Long-term changes in permafrost temperatures are driven by changes in air temperature but also reflect local variability due to influences such as snow cover, vegetation characteristics, and soil moisture (Romanovsky et al. 2017; Smith et al. 2022). Monitoring sites across the Arctic (Fig. 5.27) have been recording ground temperature in the upper 30 m for up to five decades, providing critical data on changes in permafrost conditions. Observed changes in ALT are more reflective of shorter-term (year-to-year) fluctuations in climate and are especially sensitive to changes in summer air temperature and precipitation.

Since the 1980s, permafrost temperatures have continued to increase on a decadal time scale across the Arctic. Greater increases are generally observed in colder permafrost (temperature <–2°C) at higher latitudes (Smith et al. 2022, 2024a), partly due to greater increases in air temperature (Figs. 5.27, 5.28). Over the last 30 years, positive ALT trends (Fig. 5.29) are evident from all permafrost regions examined, but trends are more muted for the Alaskan North Slope, northwestern Canada, and East Siberia (Smith et al. 2024a).

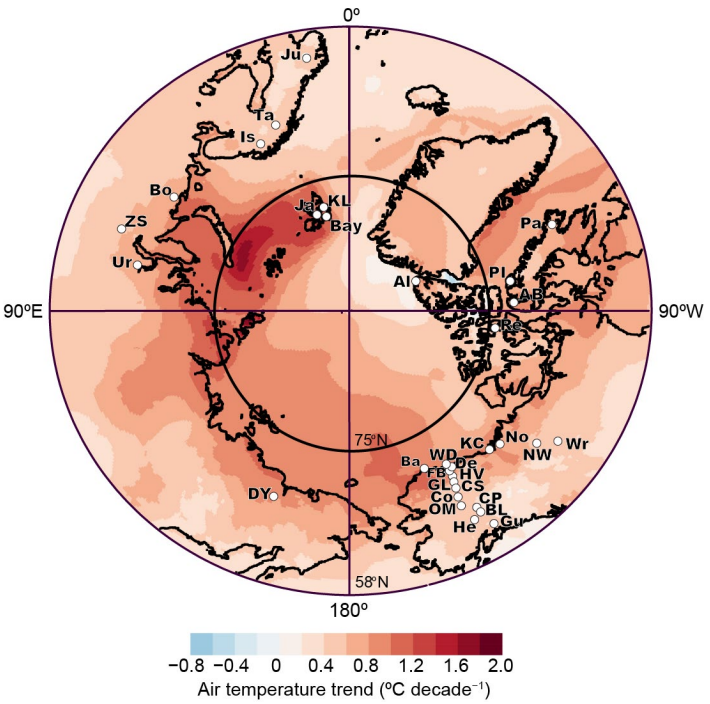

Fig. 5.27. Locations of the permafrost temperature monitoring sites (for which data are shown in Fig. 5.28), superimposed on annual average surface air temperature trends (°C decade^{-1}) during 1981–2024 from ERA5 (Hersbach et al. 2020; data available at https://cds.climate.copernicus.eu), which largely covers the period of record for permafrost monitoring. See Table 5.2 for site names. Information about these sites is available at http://gtnpdatabase.org/ and https://permafrost.gi.alaska.edu/sites_map.

1. PERMAFROST TEMPERATURE

Permafrost temperatures in 2024 were the highest on record at 8 of the 25 reporting sites; all of the record sites were in North America except for one on Svalbard (Table 5.2). Temperatures were higher in 2024 compared to 2023 at 13 of 21 North American sites (Figs. 5.28a,b). In the Beaufort–Chukchi region, permafrost temperatures in 2024 were the same or up to 0.2°C higher than those in 2023 at seven of eight sites (Fig. 5.28a). The higher temperatures reflect the increase in air temperatures that occurred in 2023 following a period of cooling that started in 2019/20. For discontinuous permafrost in Alaska and northwestern Canada, the 2024 permafrost temperatures were higher than those in 2023 at 5 of the 10 of sites, three of which reported record-high temperatures (Fig. 5.28b). Record-high temperatures were also observed at all three

Unauthenticated | Downloaded 11/21/25 11:34 AM UTC

sites reporting in the eastern and high Canadian Arctic (Fig. 5.28c). The high Arctic cold permafrost of Svalbard was warmer in 2024 at the two sites reporting compared to 2023 (Fig. 5.28d). In warmer permafrost at one of two other reporting Nordic sites, temperatures in 2024 were higher than in 2023 (Fig. 5.28d; Table 5.2).

Throughout the Arctic, warming of permafrost with temperatures near 0°C (temperatures >–2°C) is slower (generally <0.3°C decade^{-1}) than colder permafrost sites due to latent heat effects related to melting ground ice. At cold continuous permafrost sites in the Beaufort–Chukchi region, permafrost temperatures have increased by 0.4°C decade^{-1} to 0.8°C decade^{-1} with similar increases (0.3°C decade^{-1} to 0.8°C decade^{-1}) for the three sites reporting in 2024 in the eastern and high Canadian Arctic (Figs. 5.28a,c; Table 5.2). Permafrost in Svalbard has warmed by up to 0.7°C decade^{-1} (Fig. 5.28d; Table 5.2), and significant permafrost warming has been detected down to 100-m depth (Isaksen et al. 2022). In the discontinuous permafrost regions of Scandinavia (Juvvasshøe and Iskoras), warming is continuing at rates of about 0.1°C decade^{-1} to 0.2°C decade^{-1}, with thawing occurring at Iskoras (Fig. 5.28d; Isaksen et al. 2022). Similar rates (Figs. 5.28b,d) are observed in the warm permafrost of northwestern North America (e.g., Smith et al. 2024b).

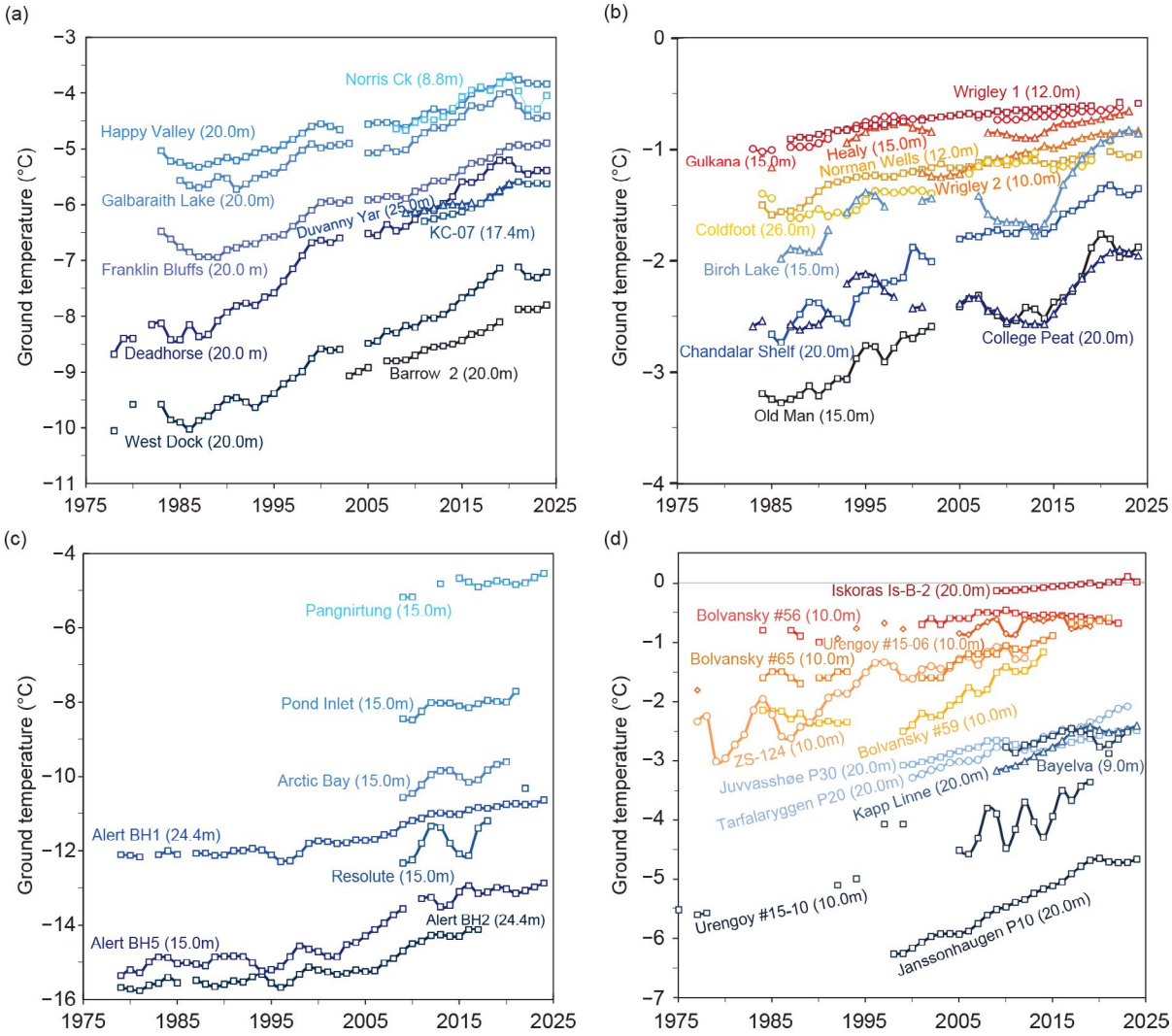

Fig. 5.28. Time series of mean annual ground temperature (°C) at depths of 9 m–26 m below the surface at selected measurement sites that fall roughly into Adaptation Actions for a Changing Arctic priority regions (see Romanovsky et al. 2017): (a) cold continuous permafrost of northwestern North America and northeastern East Siberia (Beaufort–Chukchi region); (b) discontinuous permafrost in Alaska and northwestern Canada; (c) cold continuous permafrost of eastern and high Arctic Canada (Baffin Davis Strait); and (d) continuous to discontinuous permafrost in Scandinavia, Svalbard, and Russia/Siberia (Barents region). Temperatures are measured at or near the depth of zero annual amplitude, where the seasonal ground temperature variations are less than 0.1°C. Note differences in y-axis value ranges. Borehole locations are shown in Fig. 5.27 (data are updated from Smith et al. 2024a).

Unauthenticated | Downloaded 11/21/25 11:34 AM UTC

Table 5.2. Rate of change in mean annual ground temperature (°C decade^{-1}) for permafrost monitoring sites shown in Fig. 5.28. The periods of record are shown in parentheses below the rates of change. For sites where measurements began prior to 2000, the rate of change for the entire available record and the period after 2000 are provided. Stations with record-high 2024 temperatures are indicated with a thermometer icon (🌡) and are underlined. Asterisks denote sites not reporting in 2024. Regions correspond to those shown in Fig. 5.28.

Region	Site	Entire Record	Since 2000
Northeast Siberia *(Beaufort–Chukchi Region)*	Duvany Yar (DY)*	NA	+0.4 (2009–20)
Alaskan Arctic plain *(Beaufort–Chukchi Region)*	West Dock (WD), Deadhorse (De), Franklin Bluffs (FB) 🌡, Barrow (Ba) 🌡	+0.5 to +0.8 (1978–2024)	+0.5 to +0.7 (2000–24)
Northern foothills of the Brooks Range, Alaska *(Beaufort–Chukchi Region)*	Happy Valley (HV), Galbraith Lake (GL)	+0.4 (1983–2024)	+0.4 (2000–24)
Northern Mackenzie Valley *(Beaufort–Chukchi Region)*	Norris Ck (No)*, KC-07 (KC)	NA	+0.4 to +0.6 (2008–24)
Southern foothills of the Brooks Range, Alaska *(Discontinuous Permafrost: Alaska and Northwestern Canada)*	Coldfoot (Co) 🌡, Chandalar Shelf (CS), Old Man (OM)	+0.2 to +0.4 (1983–2024)	+0.2 to +0.3 (2000–24)
Interior Alaska *(Discontinuous Permafrost: Alaska and Northwestern Canada)*	College Peat (CP), Birch Lake (BL), Gulkana (Gu)*, Healy (He)*	+0.1 to +0.3 (1983–2024)	<+0.05 to +0.4 (2000–24)
Central Mackenzie Valley *(Discontinuous Permafrost: Alaska and Northwestern Canada)*	Norman Wells (NW), Wrigley (Wr1, Wr2 🌡)	+0.1 (1984–2024)	+0.1 to +0.2 (2000–24)
Baffin Island *(Baffin Davis Strait Region)*	Pangnirtung (Pa) 🌡, Pond Inlet (PI)*	NA	+0.3 (2009–24)
High Canadian Arctic *(Baffin Davis Strait Region)*	Resolute (Re)*	NA	+1.1 (2009–22)
High Canadian Arctic *(Baffin Davis Strait Region)*	Alert (Al) @ 15 m 🌡, Alert (Al) @ 24 m 🌡	+0.6, +0.4 (1979–2024)	+0.8, +0.6 (2000–24)
Northwest Siberia *(Barents Region)*	Urengoy 15-06* and 15-08* (Ur)	+0.2 to +0.5 (1974–2021)	+0.1 to +0.8 (2005–21)
Russian European North *(Barents Region)*	Bolvansky 56* and 65* (Bo)	+0.1 to +0.3 (1984–2022)	0 to +0.5 (2001–22)
Svalbard *(Barents Region)*	Janssonhaugen (Ja), Bayelva (Bay)*, Kapp Linne 1 (KL) 🌡	+0.7 (1998–2024)	+0.1 to +0.7 (2000–24)
Northern Scandinavia *(Barents Region)*	Tarfalarggen (Ta)*, Iskoras Is-B-2 (Is) 🌡	NA	+0.1 to +0.5 (2000–24)
Southern Norway *(Barents Region)*	Juvvasshøe (Ju)	+0.2 (1999–2024)	+0.2 (2000–24)

Unauthenticated | Downloaded 11/21/25 11:34 AM UTC

2. ACTIVE-LAYER THICKNESS

Active-layer thickness is measured either directly using thaw tubes or inferred from the end-of-season thaw depth measurements by mechanical probing or from the maximum seasonal depth of the 0°C isotherm interpolated from borehole temperature records. The ALT trends shown in Fig. 5.29 are based primarily on spatially distributed mechanical probing across representative landscapes to determine the depth to the top of permafrost.

The highest long-term (1999–2024) rates of ALT increases of 0.4 m decade^{-1} and 0.2 m decade^{-1} are observed in the Alaskan Interior and West Siberia, respectively, with 2024 ALT values well above the 2009–18 mean for both regions. A record-high 2024 ALT anomaly was observed on Svalbard in response to exceptionally high summer air temperatures, especially in August.

Sites on the North Slope of Alaska, Greenland, northwestern Canada (2023 data), and East Siberia (2023 data) indicate no significant ALT changes over the last five years. This can be partially attributed to climatic influences, such as a lack of recent pronounced summer warming in northern Alaska and the Russian European North (Kaverin et al. 2021; Nyland et al. 2021). However, thaw propagation into ice-rich ground layers can cause surface subsidence that is not accounted for in thaw depth measurements, as manual probing obscures the relation between atmospheric climate and permafrost thaw. Widespread subsidence has been documented across northwestern Canada (O'Neill et al. 2023) and reported from a few sites in Alaska (Nyland et al. 2021), suggesting the underestimation of ice-rich permafrost thaw inferred from ALT records. Presently, the absence of standardized, long-term observations of ground surface displacement precludes the analysis of subsidence contribution to permafrost thaw at a broad geographic scale (Streletskiy et al. 2025).

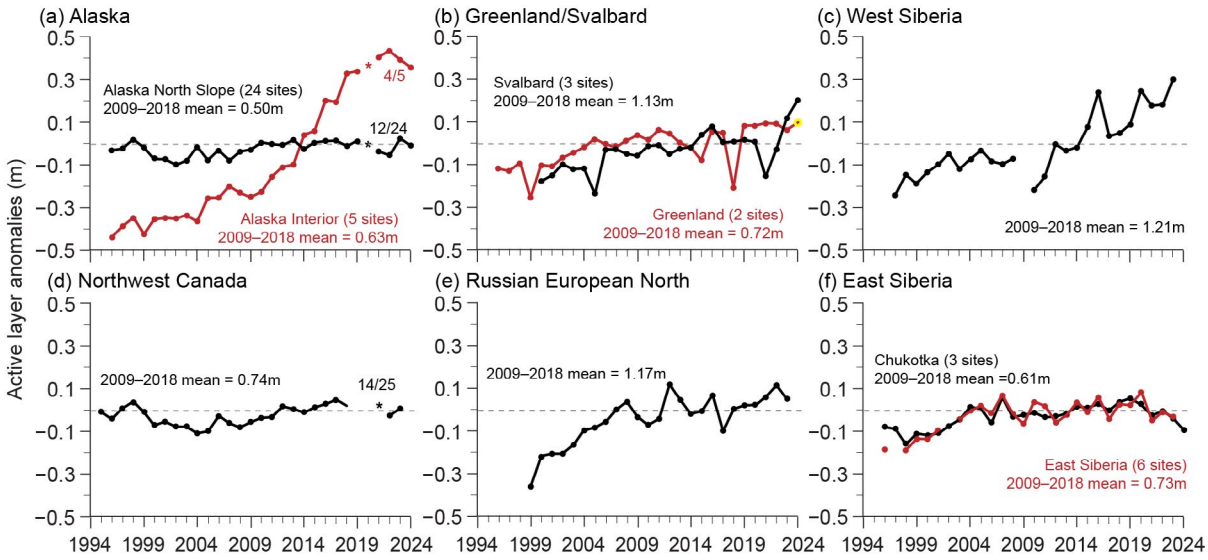

Fig. 5.29. Average annual active-layer thickness (ALT) anomalies (m), relative to the 2009–18 mean, for six Arctic regions observed by the Circumpolar Active Layer Monitoring program. Positive and negative anomalies indicate thicker or thinner ALT than the 10-year reference, respectively. Numbers of sites vary by region because only sites with >20 years of continuous thaw depth observations from the end of the thaw season are included. Asterisks represent atypical observations, for example, due to pandemic-related restrictions (fraction of sites for these years are provided on graph). Canadian ALT is derived from thaw tubes that record the maximum thaw depth over the previous year. Since Canadian sites were not visited in 2020 and 2021, the maximum thaw depth recorded during the 2022 visit could have occurred during any summer between 2019 and 2021, although the data point is plotted in 2021. Site-specific data and metadata are available at https://www2.gwu.edu/~calm/.

Unauthenticated | Downloaded 11/21/25 11:34 AM UTC

k. Tundra greenness

—G. V. Frost, M. J. Macander, U. S. Bhatt, L. T. Berner, J. W. Bjerke, H. E. Epstein, B. C. Forbes, G. Jia, M. J. Lara, P. M. Montesano, R. Í. Magnússon, C. S. R. Neigh, G. K. Phoenix, H. Tømmervik, C. Waigl, D. A. Walker, and D. Yang

The Arctic tundra biome occupies Earth's northernmost lands, collectively encompassing a 5.1 million km^2 region bounded by the Arctic Ocean to the north and the boreal forest biome to the south (Raynolds et al. 2019). While Arctic tundra ecosystems are treeless and lack the vertical structure of forests, they are heterogeneous across spatial scales, ranging from broad latitudinal climate gradients to landscape-scale variations in soil, hydrological, and permafrost conditions (Fig. 5.30). During past millennia, Arctic ecosystems have accumulated large amounts of carbon, as a large proportion of the carbon fixed by living plants became preserved in permafrost (Schuur et al. 2022; See et al. 2024). In recent decades, the Arctic has warmed dramatically, far exceeding the global rate of warming (section 5c) and placing the circumpolar region at the forefront of global climate and environmental change. Today, the circumpolar region lies at the crossroads of multiple feedback mechanisms that connect the living Arctic with a warming climate, declining near-shore sea ice extent, changes in seasonal snow cover, and thawing permafrost soils that contain large amounts of carbon (section 5f). Some of the most compelling evidence of broad scale changes in this remote region come from long-term satellite observations that began in 1982. By the late 1990s, Earth-observing satellites began to detect a sharp increase in the productivity of tundra vegetation, a phenomenon known today as "the greening of the Arctic."

Fig. 5.30. Arctic tundra landscapes exhibit a variety of striking geomorphic landforms and vegetation patterns that arise from permafrost processes, such as (a) solifluction on hillslopes and (b) ice-wedge development in polygonal ground (both Seward Peninsula, Alaska). Many of these features are sensitive to climate warming; (c) thawing of ice-rich permafrost can lead to surface subsidence (thermokarst) and changes in soil moisture, as seen in polygonal ground in Svalbard. (d) Changes in the amount and persistence of seasonal snow can also affect the productivity and phenology of tundra vegetation.

Global vegetation has been continuously monitored from space since late 1981 by a series of satellites equipped with the Advanced Very High-Resolution Radiometer (AVHRR), providing a record that has entered its 44th year. Beginning in 2000, the circumpolar AVHRR record has been complemented by newer sensors that provide surface reflectance products with improved calibration and higher spatial resolution, including the Moderate Resolution Imaging Spectroradiometer (MODIS) and a constellation of several Landsat satellites. While both AVHRR and MODIS are nearing the end of service, continuity of these records will be maintained by Landsat and the Visible Infrared Imaging Radiometer Suite (VIIRS) sensor, first launched in 2011 (Román et al. 2024). All of these spaceborne sensors monitor global vegetation greenness using the Normalized Difference Vegetation Index (NDVI), a spectral metric that exploits the unique way in which green vegetation absorbs and reflects visible and infrared light, respectively. Here, the ongoing phenomenon of Arctic greening based on the legacy AVHRR, MODIS, and Landsat datasets is reported upon.

The long-term AVHRR NDVI dataset is the Global Inventory Modeling and Mapping Studies third generation version 1.2 dataset (GIMMS-3g+) with a spatial resolution of about 8 km (Pinzon et al. 2023). For MODIS, trends were computed by combining 16-day NDVI products from the *Terra* (MOD13A1, version 6.1) and *Aqua* (MYD13A1, version 6.1) satellites (Didan 2021a,b), referred to as MODIS MCD13A1, at a much higher spatial resolution of 500 m. Landsat provides tundra greenness data at a much higher spatial resolution of 30 m; a time series of greenness from Landsat Collection 2 (Crawford et al. 2023) was computed using the methods of Berner et al. (2023). All data were masked to the extent of the Circumpolar Arctic Vegetation Map (Raynolds

Unauthenticated | Downloaded 11/21/25 11:34 AM UTC

et al. 2019) and exclude permanent ice and water. For all records, the annual maximum NDVI (MaxNDVI), the peak greenness value observed in midsummer (late July or early August in most of the Arctic), is summarized.

In 2024, the circumpolar average MaxNDVI value from GIMMS-3g+ was the fifth highest in the 43 years of record for that sensor, but nonetheless represented a 2.6% decline compared to 2023 (Fig. 5.31). The MODIS-observed circumpolar average MaxNDVI value in 2024 was the second highest in the 25-year record for that sensor, continuing a sequence of record or near-record values that began in 2020. Based on the MODIS record, tundra greenness reached a new record-high value in the North American Arctic, and was much higher than normal in northern Alaska, central and eastern Canada, and Greenland (Fig. 5.32). Localized areas of lower-than-normal greenness in Canada's Northwest Territories were likely the result of intense wildfire activity in 2023 and 2024. The Eurasian Arctic, however, featured a mixture of positive and negative departures

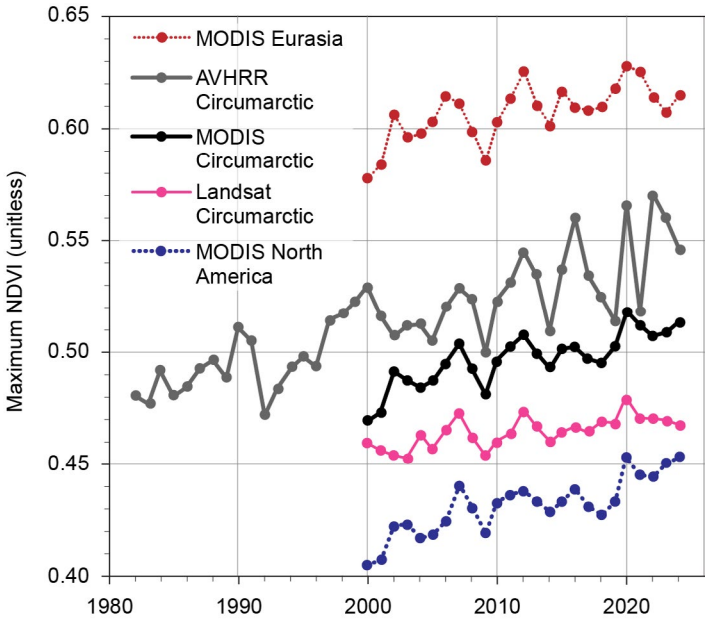

Fig. 5.31. Time series of circumpolar mean Maximum Normalized Difference Vegetation Index (MaxNDVI) from Advanced Very High-Resolution Radiometer (AVHRR) Global Inventory Modeling and Mapping Studies third generation (GIMMS-3g+; 1982–2024; gray), Moderate Resolution Imaging Spectroradiometer (MODIS) MCD13A1 (2000–2024; black), and Landsat Collection 2 (2000–23; pink). The MODIS record is further divided by continent for Arctic Eurasia (red) and North America (blue).

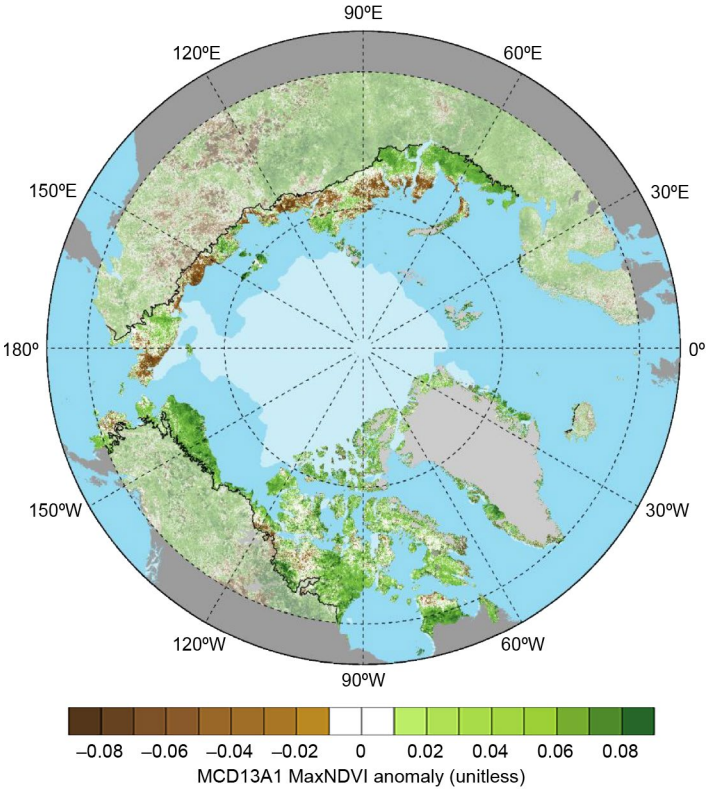

Fig. 5.32. Circumpolar Maximum Normalized Difference Vegetation Index (MaxNDVI) anomalies for the 2024 growing season relative to mean values (2000–24) for Arctic tundra (solid colors) and boreal forest (muted colors) north of 60° latitude from the Moderate Resolution Imaging Spectroradiometer (MODIS) MCD13A1 dataset. The circumpolar tree line is indicated by the black lines, and the 2024 minimum sea ice extent is indicated by light shading.

from normal, a pattern that was also evident in summer 2023. Interestingly, while some of the Eurasian regions with below-normal MaxNDVI also experienced cooler-than-normal summer temperatures (e.g., the easternmost Chukchi Peninsula), others experienced very warm conditions (e.g., north-central Siberia), complicating the degree to which greening can be attributed simply to warmer summer temperatures (section 5c). Negative anomalies in northeastern Siberia could partly reflect the highly active fire season in that region. Nonetheless, the long-term trend in both AVHRR- and MODIS-observed tundra greenness is strongly positive (greening) for most of the circumpolar region (Fig. 5.33). Trends in Landsat-observed MaxNDVI are relatively subdued, but like the other legacy records, recent MaxNDVI values have exceeded the long-term average following the record-high value observed in 2020.

Earth-observing satellites provide foundational datasets for monitoring Arctic environmental change, and help to overcome the long-standing access barriers posed by the region's remoteness, as well as new ones arising from the Russian invasion of Ukraine (López-Blanco et al. 2024) and uncertainties in

Unauthenticated | Downloaded 11/21/25 11:34 AM UTC

long-standing funding and logistical support for Arctic research in the United States. Nonetheless, field studies provide crucial information needed to connect spaceborne observations with patterns of change (or stability) on the ground. Increases in the abundance, distribution, and height of Arctic shrubs are a major driver of Arctic greening and have important impacts on biodiversity, surface energy balance, permafrost temperatures, and biogeochemical cycling, particularly in the Low Arctic (Mekonnen et al. 2021). However, while changes to the Arctic climate have generally favored greening, ecological disturbances, extreme events, and other causes of browning are also increasing in frequency (Parmentier et al. 2024; Phoenix et al. 2025). For example, greening trends in many parts of the Arctic have been partially offset by increasing wildfires during the past two decades, especially during 2019–21 (Zhu et al. 2024). Understanding the regional variability of complex Arctic greening trends and attributing its drivers continues to be a subject of multidisciplinary scientific research.

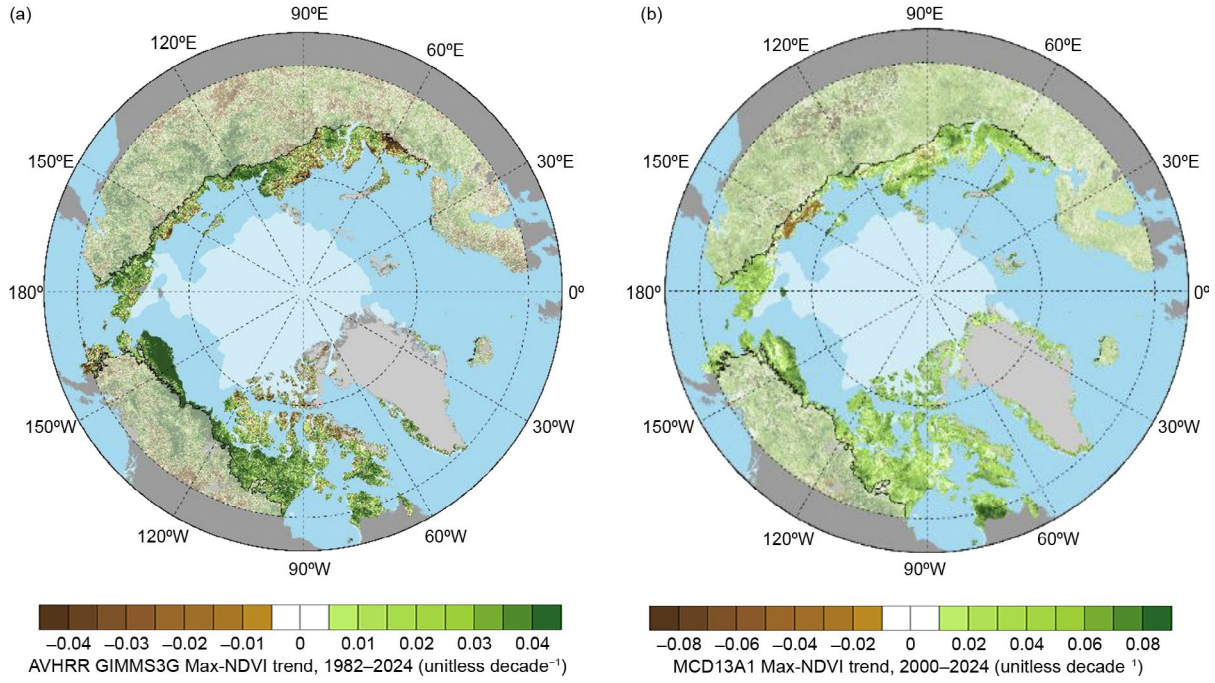

Fig. 5.33. Magnitude of the Maximum Normalized Difference Vegetation Index (MaxNDVI) trend calculated as the change decade^{-1} via ordinary least-squares regression for Arctic tundra (solid colors) and boreal forest (muted colors) north of 60° latitude during (a) 1982–2024 based on the Advanced Very High-Resolution Radiometer (AVHRR) Global Inventory Modeling and Mapping Studies third generation (GIMMS-3g+) dataset, and (b) 2000–24 based on the Moderate Resolution Imaging Spectroradiometer (MODIS) MCD13A1 dataset. The circumpolar tree line is indicated by black lines, and the 2024 minimum sea ice extent is indicated by light shading in each panel.

Unauthenticated | Downloaded 11/21/25 11:34 AM UTC

Acknowledgments

a. Overview

The authors and chapter editors appreciate support provided by NOAA's Global Ocean Monitoring and Observing Arctic Research Program, including content editing funded through the Cooperative Institute for Earth System Research and Data Science (CIESRDS) via NOAA Cooperative Agreement NA22OAR4320151 (M. Druckenmiller and T. Moon) and by the Cooperative Institute for Climate, Ocean, and Ecosystem Studies (CICOES) under NOAA Cooperative Agreement NA20OAR4320271 (R. Thoman).

b. Atmosphere

The authors thank the Academy of Finland for supporting ultraviolet measurements through the FARPOCC, SAARA, and CHAMPS (grant no. 329225) projects.

e. Sea surface temperature

M.-L. Timmermans acknowledges support from the National Science Foundation (NSF) Office of Polar Programs and the Office of Naval Research. Z.M. Labe acknowledges support from NOAA and its Geophysical Fluid Dynamics Laboratory (GFDL).

h. Arctic river discharge

James McClelland and coauthors acknowledge NSF support for the Arctic Great Rivers Observatory (NSF 1913888, 1914081, 1914215, 1913962, 2230812). Discharge data for the Mackenzie River are courtesy of Environment and Climate Change Canada.

Unauthenticated | Downloaded 11/21/25 11:34 AM UTC

Appendix 1: Acronyms

ALT	active-layer thickness
AO	Arctic Oscillation
AOI	Arctic Oscillation Index
AVHRR	Advanced Very High-Resolution Radiometer
CAA	Canadian Arctic Archipelago
CARRA	Copernicus Arctic Regional Reanalysis
CCI	Climate Change Initiative
EOF	empirical orthogonal function
ESA	European Space Administration
GBI	Greenland Blocking Index
GC-Net	Greenland Climate Network
GIMMS-3g+	Global Inventory Modeling and Mapping Studies third generation
GRACE	Gravity Recovery and Climate Experiment
GRACE-FO	Gravity Recovery and Climate Experiment Follow-On
IMS	Interactive Multisensor Snow and Ice Mapping System
MAR	Modèle Atmosphérique Régionale
MaxNDVI	Maximum Normalized Difference Vegetation Index
MODIS	Moderate Resolution Imaging Spectroradiometer
NDVI	Normalized Difference Vegetation Index
OMI	Ozone Monitoring Instrument
OMTO3	Ozone Monitoring Instrument Level-2 Total Column Ozone version 3
PCH	polar cap averaged geopotential height
PROMICE	Programme for Monitoring of the Greenland Ice Sheet
SAT	surface air temperature
SCD	snow cover duration
SCE	snow cover extent
SLP	sea level pressure
SMB	surface mass balance
SMOS	Soil Moisture Ocean Salinity
SST	sea surface temperature
SSW	sudden stratospheric warming
SWE	snow water equivalent
T_{ARCTIC}	total arctic
T_{GLOBAL}	total global
UV	ultraviolet
VIIRS	Visible Infrared Imaging Radiometer Suite

Unauthenticated | Downloaded 11/21/25 11:34 AM UTC

Appendix 2: Datasets and sources

Section 5b Atmosphere

Sub-section	General Variable or Phenomenon	Specific Dataset or Variable	Source
5b, 5b1, 5b2	Geopotential Height	ERA5	https://www.ecmwf.int/en/forecasts/dataset/ecmwf-reanalysis-v5
5b2	Ozone, Total Column and Stratospheric	Aura Ozone Monitoring Instrument (OMI)/ Microwave Limb Sounder (MLS)	https://disc.gsfc.nasa.gov/datasets/ML2O3_004/summary
5b2	Ozone, Total Column and Stratospheric	OMI/Aura Level-2 Total Column Ozone (OMTO3) Version 3	https://disc.gsfc.nasa.gov/datasets/OMTO3_003/summary

Section 5c Surface air temperature

Sub-section	General Variable or Phenomenon	Specific Dataset or Variable	Source
5c3	Pressure, Sea Level or Near-Surface	ERA5	https://www.ecmwf.int/en/forecasts/dataset/ecmwf-reanalysis-v5
5c2	Temperature, [Near] Surface	NASA GISTEMPv4	https://data.giss.nasa.gov/gistemp/
5c3	Temperature, [Near] Surface	ERA5	https://www.ecmwf.int/en/forecasts/dataset/ecmwf-reanalysis-v5

Section 5d Precipitation

Sub-section	General Variable or Phenomenon	Specific Dataset or Variable	Source
5d	Precipitation	ERA5	https://www.ecmwf.int/en/forecasts/dataset/ecmwf-reanalysis-v5
5d4	Precipitation	GPCC	https://opendata.dwd.de/climate_environment/GPCC/html/download_gate.html

Section 5e Sea surface temperature

Sub-section	General Variable or Phenomenon	Specific Dataset or Variable	Source
5e	Sea Surface Temperature	OISSTv2.1	https://www.ncei.noaa.gov/products/optimum-interpolation-sst

Unauthenticated | Downloaded 11/21/25 11:34 AM UTC

Section 5f Sea ice

Sub-section	General Variable or Phenomenon	Specific Dataset or Variable	Source
5f1	Sea Ice Extent	National Snow and Ice Data Center (NSIDC) Sea Ice Extent	https://nsidc.org/data/g02135
5f2	Sea Ice Thickness	European Space Agency (ESA) Cryosat-2/ Soil Moisture and Ocean Salinity (SMOS)	https://earth.esa.int/eogateway/catalog/smos-cryosat-l4-sea-ice-thickness
5f2	Sea Ice Thickness	NASA Ice, Cloud, and land Elevation Satellite 2 (ICESat-2)	https://icesat-2.gsfc.nasa.gov/icesat-2-data

Section 5g Greenland Ice Sheet

Sub-section	General Variable or Phenomenon	Specific Dataset or Variable	Source
5g	Air Temperature	Danish Meteorological Institute (DMI)/ Programme for Monitoring the Greenland Ice Sheet (PROMICE) Weather	https://eng.geus.dk/products-services-facilities/data-and-maps/glaciological-data-from-greenland-promice
5g	Glacier Ablation	PROMICE Glacier Front Line (Greenland)	https://doi.org/10.22008/promice/data/calving_front_lines
5g	Glacier Mass, Area or Volume	Gravity Recovery and Climate Experiment (GRACE) /GRACE Follow-On (GRACE-FO)	https://grace.jpl.nasa.gov/data/get-data/
5g	Ice Sheet Albedo	Sentinel-3 Snow and Ice Products (SICE)	https://eo4society.esa.int/projects/pre-operational-sentinel-3-snow-and-ice-products-sice/
5g	Ice Sheet Discharge	Ice Discharge (Greenland)	https://doi.org/10.22008/promice/data/ice_discharge/d/v02
5g	Ice Sheet Melt	Special Sensor Microwave Imager/Sounder (SSMIS)	https://nsidc.org/data/nsidc-0001
5g	Ice Sheet Surface-Height	Ice, Cloud, and land Elevation Satellite 2 (ICESat-2)	https://icesat-2.gsfc.nasa.gov/icesat-2-data
5g	Air Temperature	Copernicus Climate Change Service (C3S) Arctic Regional Reanalysis	https://cds.climate.copernicus.eu/datasets/reanalysis-carra-single-levels?tab=overview

Unauthenticated | Downloaded 11/21/25 11:34 AM UTC

Section 5h Arctic river discharge			
Sub-section	**General Variable or Phenomenon**	**Specific Dataset or Variable**	**Source**
5h	River Discharge	Arctic Great Rivers Observatory	https//:arcticgreatrivers.org/

Section 5i Terrestrial snow cover			
Sub-section	**General Variable or Phenomenon**	**Specific Dataset or Variable**	**Source**
5i	Snow Properties	Crocus Snowpack Model	http://www.umr-cnrm.fr/spip.php?article265
5i	Snow Properties	ERA5	https://www.ecmwf.int/en/forecasts/dataset/ecmwf-reanalysis-v5
5i	Snow Properties	MERRA-2	http://gmao.gsfc.nasa.gov/reanalysis/MERRA-2/
5i	Snow Properties	European Space Agency Snow CCI SWE	https://snow-cci.enveo.at/
5i	Snow Properties	NOAA Interactive Multi-sensor Snow and Ice Mapping System (Snow Cover Duration)	https://usicecenter.gov/Products/ImsHome
5i	Snow Properties	NOAA Snow Chart Climate Data Record	https://www.ncei.noaa.gov/products/climate-data-records/snow-cover-extent

Section 5j Permafrost			
Sub-section	**General Variable or Phenomenon**	**Specific Dataset or Variable**	**Source**
5i1	Permafrost	Global Terrestrial Network for Permafrost (GTN-P)	http://gtnpdatabase.org/
5i1	Permafrost	Permafrost Temperature	http://permafrost.gi.alaska.edu/sites_map
5i1	Temperature, [Near] Surface	ERA5	https://www.ecmwf.int/en/forecasts/dataset/ecmwf-reanalysis-v5
5i2	Permafrost	Circumpolar Active Layer Monitoring Program (CALM) Active-Layer Thickness	https://www2.gwu.edu/~calm/

Unauthenticated | Downloaded 11/21/25 11:34 AM UTC

Section 5k Tundra greenness

Sub-section	General Variable or Phenomenon	Specific Dataset or Variable	Source
5k	Vegetative Index	Global Inventory Modeling and Mapping Studies third generation (GIMMS-3g+) Version 1	https://daac.ornl.gov/VEGETATION/guides/Global_Veg_Greenness_GIMMS_3G.html
5k	Vegetative Index	MODIS MCD13A1 and MYD13A1 Normalized Difference Vegetative Index (NDVI)	https://lpdaac.usgs.gov/products/mod13a1v006/
5k	Vegetative Index	Landsat Collection 2 Normalized Difference Vegetative Index (NDVI)	https://www.usgs.gov/landsat-missions/landsat-collection-2

Sidebar 5.1: North American August heat

Sub-section	General Variable or Phenomenon	Specific Dataset or Variable	Source
SB5.1	Geopotential Height	National Centers for Environmental Prediction (NCEP)/National Center for Atmospheric Research (NCAR) Reanalysis 1	https://psl.noaa.gov/data/gridded/data.ncep.reanalysis.html
SB5.1	Temperature, [Near] Surface	ERA5	https://www.ecmwf.int/en/forecasts/dataset/ecmwf-reanalysis-v5
SB5.1	Temperature, [Near] Surface	NOAA Applied Climate Information System Online Tool	https://xmacis.rcc-acis.org
SB5.1	Temperature, [Near] Surface	Environment and Climate Change Canada	https://climate.weather.gc.ca
SB5.1	Temperature, [Near] Surface	NCEP/NCAR Reanalysis 1	https://psl.noaa.gov/data/gridded/data.ncep.reanalysis.html
SB5.1	Wildfire Properties	Canadian Interagency Forest Fire Centre	https://ciffc.net/

Sidebar 5.2: Record-low sea ice conditions in the Northwest Passage in 2024

Sub-section	General Variable or Phenomenon	Specific Dataset or Variable	Source
SB5.2	Sea Ice Area	Canadian Ice Service	https://www.canada.ca/en/environment-climate-change/services/ice-forecasts-observations/latest-conditions/archive-overview.html

Unauthenticated | Downloaded 11/21/25 11:34 AM UTC

Sidebar 5.3: Why Greenland Ice Sheet melt was so low in 2024

Sub-section	General Variable or Phenomenon	Specific Dataset orVariable	Source
SB5.3	Geopotential Height	ERA5	https://www.ecmwf.int/en/forecasts/dataset/ecmwf-reanalysis-v5
SB5.3	Teleconnections	Arctic Oscillation Index	https://www.cpc.ncep.noaa.gov/products/precip/CWlink/daily_ao_index/ao.shtml
SB5.3	Winds, Upper Air	ERA5	https://www.ecmwf.int/en/forecasts/dataset/ecmwf-reanalysis-v5

Unauthenticated | Downloaded 11/21/25 11:34 AM UTC

References

AghaKouchak, A., and Coauthors, 2020: Climate extremes and compound hazards in a warming world. *Annu. Rev. Earth Planet. Sci.*, **48**, 519–548, https://doi.org/10.1146/annurev-earth-071719-055228.

Arctic Council, 2024: An archipelago in transformation: Climate scientist Ketil Isaksen on record-breaking changes on Svalbard. Arctic Council, accessed 13 February 2025, https://arctic-council.org/news/an-archipelago-in-transformation-climate-scientist-ketil-isaksen-on-record-breaking-changes-on-svalbard/.

Baldwin, M. P., and Coauthors, 2021: Sudden stratospheric warmings. *Rev. Geophys.*, **59**, e2020RG000708, https://doi.org/10.1029/2020RG000708.

Barrett, A. P., J. C. Stroeve, and M. C. Serreze, 2020: Arctic Ocean precipitation from atmospheric reanalyses and comparisons with North Pole drifting stations. *J. Geophys. Res. Oceans*, **125**, e2019JC015415, https://doi.org/10.1029/2019JC015415.

Becker, A., P. Finger, A. Meyer-Christoffer, B. Rudolf, K. Schamm, U. Schneider, and M. Ziese, 2013: A description of the global land-surface precipitation data products of the Global Precipitation Climatology Centre with sample applications including centennial (trend) analysis from 1901–present. *Earth Syst. Sci. Data*, **5**, 71–99, https://doi.org/10.5194/essd-5-71-2013.

Benestad, R., and Coauthors, 2023: Extreme weather and climate events in 2022 [in "State of the Climate in 2022"]. *Bull. Amer. Meteor. Soc.*, **104** (8), S15–S17, https://doi.org/10.1175/BAMS-D-23-0079.1.

Berner, L. T., J. J. Assmann, S. Normand, and S. J. Goetz, 2023: 'LandsatTS': an R package to facilitate retrieval, cleaning, cross-calibration, and phenological modeling of Landsat time series data. *Ecography*, **2023**, e06768, https://doi.org/10.1111/ecog.06768.

Bernhard, G., and Coauthors, 2015: Comparison of OMI UV observations with ground-based measurements at high northern latitudes. *Atmos. Chem. Phys.*, **15**, 7391–7412, https://doi.org/10.5194/acp-15-7391-2015.

Bhartia, P. K., and C. W. Wellemeyer, 2002: TOMS-V8 total O3 algorithm. OMI Algorithm Theoretical Basis Document Volume II. NASA Goddard Space Flight Center Tech. Doc. ATBD-OMI-02, 91 pp., https://eospso.gsfc.nasa.gov/sites/default/files/atbd/ATBD-OMI-02.pdf.

Bigalke, S., and J. E. Walsh, 2022: Future changes of snow in Alaska and the Arctic under stabilized global warming scenarios. *Atmosphere*, **13**, 541, https://doi.org/10.3390/atmos13040541.

Box, J. E., and Coauthors, 2019: Key indicators of Arctic climate change: 1971–2017. *Environ. Res. Lett.*, **14**, 045010, https://doi.org/10.1088/1748-9326/aafc1b.

—— , and Coauthors, 2021: Recent developments in Arctic climate observation indicators. AMAP Arctic Climate Change Update 2021: Key Trends and Impacts, Arctic Monitoring and Assessment Programme, 7–29, https://www.amap.no/documents/doc/amap-arctic-climate-change-update-2021-key-trends-and-impacts/3594.

Brown, R., and Coauthors, 2017: Arctic terrestrial snow cover. Snow, Water, Ice and Permafrost in the Arctic (SWIPA) 2017, Arctic Monitoring and Assessment Programme (AMAP), 25–64, https://www.amap.no/documents/doc/snow-water-ice-and-permafrost-in-the-arctic-swipa-2017/1610.

Cheng, V. Y. S., F. Wu, M. Beauchemin, and L. Chisholm, 2024: Canada [in "State of the Climate in 2023"]. *Bull. Amer. Meteor. Soc.*, **105** (8), S380–S382, https://doi.org/10.1175/2024BAMSStateoftheClimate_Chapter7.1.

CIFFC, 2025: Canadian Interagency Forest Fire Centre. Accessed 5 February 2025, https://ciffc.net/.

Cohen, J., and Coauthors, 2020: Divergent consensuses on Arctic amplification influence on midlatitude severe winter weather. *Nat. Climate Change*, **10**, 20–29, https://doi.org/10.1038/s41558-019-0662-y.

Colgan, W., and Coauthors, 2015: Hybrid glacier Inventory, Gravimetry and Altimetry (HIGA) mass balance product for Greenland and the Canadian Arctic. *Remote Sens. Environ.*, **168**, 24–39, https://doi.org/10.1016/j.rse.2015.06.016.

Cook, A. J., J. Dawson, S. E. L. Howell, J. E. Holloway, and M. Brady, 2024: Sea ice choke points reduce the length of the shipping season in the Northwest Passage. *Commun. Earth Environ.*, **5**, 362, https://doi.org/10.1038/s43247-024-01477-6.

Crawford, A. D., and M. C. Serreze, 2016: Does the summer Arctic frontal zone influence Arctic Ocean cyclone activity? *J. Climate*, **29**, 4977–4993, https://doi.org/10.1175/JCLI-D-15-0755.1.

Crawford, C. J., and Coauthors, 2023: The 50-year Landsat collection 2 archive. *Sci. Remote Sens.*, **8**, 100103, https://doi.org/10.1016/j.srs.2023.100103.

Dai, A., D. Luo, M. Song, and J. Liu, 2019: Arctic amplification is caused by sea-ice loss under increasing CO_2. *Nat. Commun.*, **10**, 121, https://doi.org/10.1038/s41467-018-07954-9.

Decharme, B., A. Barbu, and S. R. Buarque, 2024: Crocus-ERA5 daily snow product over the Northern Hemisphere at 0.25° resolution, 2023v2. Zenodo, accessed 3 September 2024, https://doi.org/10.5281/zenodo.14513248.

Delhasse, A., E. Hanna, C. Kittel, and X. Fettweis, 2021: Brief communication: CMIP6 does not suggest any atmospheric blocking increase in summer over Greenland by 2100. *Int. J. Climatol.*, **41**, 2589–2596, https://doi.org/10.1002/joc.6977.

Derksen, C., and L. Mudryk, 2023: Assessment of Arctic seasonal snow cover rates of change. *Cryosphere*, **17**, 1431–1443, https://doi.org/10.5194/tc-17-1431-2023.

Didan, K., 2021a: MODIS/Terra vegetation indices 16-day L3 global 500m SIN grid V061. Accessed 19 May 2025, https://doi.org/10.5067/MODIS/MOD13A1.061.

—— , 2021b: MODIS/Aqua vegetation indices 16-day L3 global 500m SIN grid V061. Accessed 19 May 2025, https://doi.org/10.5067/MODIS/MYD13A1.061.

Dou, T., and Coauthors, 2021: Trends and spatial variation in rain-on-snow events over the Arctic Ocean during the early melt season. *Cryosphere*, **15**, 883–895, https://doi.org/10.5194/tc-15-883-2021.

Durocher, M., A. I. Requena, D. H. Burn, and J. Pellerin, 2019: Analysis of trends in annual streamflow to the Arctic Ocean. *Hydrol. Processes*, **33**, 1143–1151, https://doi.org/10.1002/hyp.13392.

ESA, 2023: European Space Agency SMOS-CryoSat L4 sea ice thickness, version 206. Accessed 1 September 2024, https://doi.org/10.57780/sm1-4f787c3.

Fausto, R. S., and Coauthors, 2021: Programme for Monitoring of the Greenland Ice Sheet (PROMICE) automatic weather station data. *Earth Syst. Sci. Data*, **13**, 3819–3845, https://doi.org/10.5194/essd-13-3819-2021.

Fetterer, F., K. Knowles, W. N. Meier, M. Savoie, and A. K. Windnagel, 2017: Sea Ice Index, version 3 (updated daily). National Snow and Ice Data Center, accessed 4 October 2024, https://doi.org/10.7265/N5K072F8.

Unauthenticated | Downloaded 11/21/25 11:34 AM UTC

Fettweis, X., and Coauthors, 2020: GrSMBMIP: Intercomparison of the modelled 1980–2012 surface mass balance over the Greenland Ice Sheet. *Cryosphere*, **14**, 3935–3958, https://doi.org/10.5194/tc-14-3935-2020.

Fol, M., B. Tremblay, S., Pfirman, R. Newton, S. Howell, and J.-F. Lemieux, 2025: Revisiting the Last Ice Area projections from a high-resolution Global Earth System Model. *Commun. Earth Environ.*, **6**, 46, https://doi.org/10.1038/s43247-025-02034-5

Gardner, A. S., N.-J. Schlegel, and E. Larour, 2023: Glacier Energy and Mass Balance (GEMB): A model of firn processes for cryosphere research. *Geosci. Model Dev.*, **16**, 2277–2302, https://doi.org/10.5194/gmd-16-2277-2023.

Gelaro, R., and Coauthors, 2017: The Modern-Era Retrospective Analysis for Research and Applications, version 2 (MERRA-2). *J. Climate*, **30**, 5419–5454, https://doi.org/10.1175/JCLI-D-16-0758.1.

GMAO, 2015: MERRA-2tavg1_2d_lnd_Nx:2d, 1-hourly, time-averaged, single-level, assimilation, land surface diagnostics V5.12.4. Goddard Earth Sciences Data and Information Services Center, accessed 3 August 2024, https://doi.org/10.5067/RKPHT8KC1Y1T.

Government of Northwest Territories, 2025: *NWT Water Monitoring Bulletin*—June 9, 2025. Tech. Data, 31 pp., https://www.gov.nt.ca/ecc/en/newsroom/nwt-water-monitoring-bulletin-january-17-2025.

Hanna, E., T. E. Cropper, R. J. Hall, and J. Cappelen, 2016: Greenland Blocking Index 1851–2015: A regional climate change signal. *Int. J. Climatol.*, **36**, 4847–4861, https://doi.org/10.1002/joc.4673.

He, S., H. Drange, T. Furevik, H. Wang, K. Fan, L. S. Graff, and Y. J. Orsolini, 2024: Relative impacts of sea ice loss and atmospheric internal variability on the winter Arctic to East Asian surface air temperature based on large-ensemble simulations with NorESM2. *Adv. Atmos. Sci.*, **41**, 1511–1526, https://doi.org/10.1007/s00376-023-3006-9.

Hersbach, H., and Coauthors, 2020: The ERA5 global reanalysis. *Quart. J. Roy. Meteor. Soc.*, **146**, 1999–2049, https://doi.org/10.1002/qj.3803.

Hjort, J., D. Streletskiy, G. Doré, Q. Wu, K. Bjella, and M. Luoto, 2022: Impacts of permafrost degradation on infrastructure. *Nat. Rev. Earth Environ.*, **3**, 24–38, https://doi.org/10.1038/s43017-021-00247-8.

Holmes, R. M., and Coauthors, 2013: Climate change impacts on the hydrology and biogeochemistry of Arctic rivers. *Climactic Change and Global Warming of Inland Waters: Impacts and Mitigation for Ecosystems and Societies*, C. R. Goldman, M. Kumagai, and R. D. Robarts, Eds., Wiley, 3–26.

Howell, S. E. L., C. R. Duguay, and T. Markus, 2009: Sea ice conditions and melt season duration variability within the Canadian Arctic Archipelago: 1979–2008. *Geophys. Res. Lett.*, **36**, L10502, https://doi.org/10.1029/2009GL037681.

—— , T. Wohlleben, A. Komarov, L. Pizzolato, and C. Derksen, 2013: Recent extreme light sea ice years in the Canadian Arctic Archipelago: 2011 and 2012 eclipse 1998 and 2007. *Cryosphere*, **7**, 1753–1768, https://doi.org/10.5194/tc-7-1753-2013.

—— ., D. G. Babb, J. C. Landy, and M. Brady, 2023: Multi-year sea ice conditions in the Northwest Passage: 1968–2020. *Atmos.–Ocean*, **61**, 202–216, https://doi.org/10.1080/07055900.2022.2136061.

—— , —— , —— , I. A. Glissenaar, K. McNeil, B. Montpetit, and M. Brady, 2024: Sea ice transport and replenishment across and within the Canadian Arctic Archipelago, 2016–2022. *Cryosphere*, **18**, 2321–2333, https://doi.org/10.5194/tc-18-2321-2024.

Huang, B., C. Liu, V. Banzon, E. Freeman, G. Graham, B. Hankins, T. Smith, and H. Zhang, 2021: Improvements of the Daily Optimum Interpolation Sea Surface Temperature (DOISST) version 2.1. *J. Climate*, **34**, 2923–2939, https://doi.org/10.1175/JCLI-D-20-0166.1.

Isaksen, K., J. Lutz, A. M. Sorensen, O. Godoy, L. Ferrighi, S. Eastwood, and S. Aaboe, 2022: Advances in operational permafrost monitoring on Svalbard and in Norway. *Environ. Res. Lett.*, **17**, 095012, https://doi.org/10.1088/1748-9326/ac8e1c.

Ivanova, N., O. M. Johannessen, L. T. Pedersen, and R. T. Tonboe, 2014: Retrieval of Arctic sea ice parameters by satellite passive microwave sensors: A comparison of eleven sea ice concentration algorithms. *IEEE Trans. Geosci. Remote Sens.*, **52**, 7233–7246, https://doi.org/10.1109/TGRS.2014.2310136.

Jahn, A., M. M. Holland, and J. E. Kay, 2024: Projections of an ice-free Arctic Ocean. *Nat. Rev. Earth Environ.*, **5**, 164–176, https://doi.org/10.1038/s43017-023-00515-9.

Jain, P., and Coauthors, 2024: Drivers and impacts of the record-breaking 2023 wildfire season in Canada. *Nat. Commun.*, **15**, 6764, https://doi.org/10.1038/s41467-024-51154-7.

Kalnay, E., and Coauthors, 1996: The NCEP/NCAR 40-Year Reanalysis Project. *Bull. Amer. Meteor. Soc.*, **77**, 437–471, https://doi.org/10.1175/1520-0477(1996)077<0437:TNYRP>2.0.CO;2.

Karlsson, N. B., and Coauthors, 2021: A first constraint on basal melt-water production of the Greenland ice sheet. *Nat Commun.*, **12**, 3461, https://doi.org/10.1038/s41467-021-23739-z.

Kaverin, D., and Coauthors, 2021: Long-term active layer monitoring at CALM sites in the Russian European North. *Polar Geogr.*, **44**, 203–216, https://doi.org/10.1080/1088937X.2021.1981476.

Kopec, B., X. Feng, F. A. Michel, and E. Posmentier, 2016: Influence of sea ice on Arctic precipitation. *Proc. Natl. Acad. Sci. USA*, **113**, 46–51, https://doi.org/10.1073/pnas.1504633113.

Lavergne, T. and Coauthors, 2019: Version 2 of the EUMETSAT OSI SAF and ESA CCI sea-ice concentration climate data records, *Cryosphere*, **13**, 49–78, https://doi.org/10.5194/tc-13-49-2019.

Lee, S. H., A. H. Butler, and G. L. Manney, 2025: Two major sudden stratospheric warmings during winter 2023/2024. *Weather*, **80**, 45–53, https://doi.org/10.1002/wea.7656.

L'Heureux, M., A. H. Butler, B. Jha, A. Kumar, and W. Wang, 2010: Unusual extremes in the negative phase of the Arctic Oscillation during 2009. *Geophys. Res. Lett.*, **37**, L10704, https://doi.org/10.1029/2010GL043338.

Loeb, N. A., A. Crawford, J. C. Stroeve, and J. Hanesiak, 2022: Extreme precipitation in the eastern Canadian Arctic and Greenland: An evaluation of atmospheric reanalyses. *Front. Environ. Sci.*, **10**, 866929, https://doi.org/10.3389/fenvs.2022.866929.

López-Blanco, E., and Coauthors, 2024: Towards an increasingly biased view on Arctic change. *Nat. Clim. Chang.*, **14**, 152–155, https://doi.org/10.1038/s41558-023-01903-1.

Unauthenticated | Downloaded 11/21/25 11:34 AM UTC

Luojus, K., and Coauthors, 2022: ESA Snow Climate Change Initiative (Snow_cci): Snow Water Equivalent (SWE) level 3C daily global climate research data package (CRDP) (1979–2020), version 2.0. NERC EDS Centre for Environmental Data Analysis, accessed 3 September 2024, https://doi.org/10.5285/4647cc9ad3c044439d6c643208d3c494.

Mankoff, K. D., A. Solgaard, W. Colgan, A. P. Ahlstrøm, S. A. Khan, and R. S. Fausto, 2020: Greenland Ice Sheet solid ice discharge from 1986 through March 2020. *Earth Syst. Sci. Data*, **12**, 1367–1383, https://doi.org/10.5194/essd-12-1367-2020.

——, and Coauthors, 2021: Greenland Ice Sheet mass balance from 1840 through next week. *Earth Syst. Sci. Data*, **13**, 5001–5025, https://doi.org/10.5194/essd-13-5001-2021.

McClelland, J. W., R. M. Holmes, K. H. Dunton, and R. Macdonald, 2012: The Arctic Ocean estuary. *Estuaries Coasts*, **35**, 353–368, https://doi.org/10.1007/s12237-010-9357-3.

McCrystall, M., J. Stroeve, M. C. Serreze, B. C. Forbes, and J. Screen, 2021: New climate models reveal faster and larger increases in Arctic precipitation than previously projected. *Nat. Commun.*, **12**, 6765, https://doi.org/10.1038/s41467-021-27031-y.

Medley, B., T. A. Neumann, H. J. Zwally, B. E. Smith, and C. M. Stevens, 2022: Simulations of firn processes over the Greenland and Antarctic ice sheets: 1980–2021. *Cryosphere*, **16**, 3971–4011, https://doi.org/10.5194/tc-16-3971-2022.

Meier, W. N., F. Fetterer, A. K. Windnagel, and J. S. Stewart, 2021a: NOAA/NSIDC climate data record of passive microwave sea ice concentration, version 4. [1982-2021]. National Snow and Ice Data Center, accessed 2 February 2025, https://doi.org/10.7265/efmz-2t65.

——, ——, ——, and ——, 2021b: Near-real-time NOAA/NSIDC climate data record of passive microwave sea ice concentration, version 2 [1982–2021]. Accessed 2 February 2025, https://doi.org/10.7265/tgam-yv28.

Mekonnen, Z. A., and Coauthors, 2021: Arctic tundra shrubification: A review of mechanisms and impacts on ecosystem carbon balance. *Environ. Res. Lett.*, **16**, 053001, https://doi.org/10.1088/1748-9326/abf28b.

Melling, H., 2002: Sea ice of the northern Canadian Arctic Archipelago. *J. Geophys. Res.*, **107**, 3181, https://doi.org/10.1029/2001JC001102.

Meredith, M., and Coauthors, 2019: Polar regions. The Ocean and Cryosphere in a Changing Climate, H.-O. Pörtner et al., Eds., Cambridge University Press, 203–320, https://doi.org/10.1017/9781009157964.005.

Miner, K. R., and Coauthors, 2022: Permafrost carbon emissions in a changing Arctic. *Nat. Rev. Earth Environ.*, **3**, 55–67, https://doi.org/10.1038/s43017-021-00230-3.

Mortimer, C., L. Mudryk, C. Derksen, K. Luojus, R. Brown, R. Kelly, and M. Tedesco, 2020: Evaluation of long-term Northern Hemisphere snow water equivalent products. *Cryosphere*, **14**, 1579–1594, https://doi.org/10.5194/tc-14-1579-2020.

Mote, T., 2007: Greenland surface melt trends 1973–2007: Evidence of a large increase in 2007. *Geophys. Res. Lett.*, **34**, L22507, https://doi.org/10.1029/2007GL031976.

Mouginot, J., and Coauthors, 2019: Forty-six years of Greenland Ice Sheet mass balance from 1972 to 2018. *Proc. Natl. Acad. Sci. USA*, **116**, 9239–9244, https://doi.org/10.1073/pnas.1904242116.

Mudryk, L. R., J. Dawson, S. E. L. Howell, C. Derksen, T. A. Zagon, and M. Brady, 2021: Impact of 1, 2 and 4°C of global warming on ship navigation in the Canadian Arctic. *Nat. Climate Change*, **11**, 673–679, https://doi.org/10.1038/s41558-021-01087-6.

Muñoz Sabater, J., 2019: ERA5-Land hourly data from 1950 to present. Copernicus Climate Change Service (C3S) Climate Data Store (CDS), accessed 3 September 2024, https://doi.org/10.24381/cds.e2161bac.

NASA, 2024: Svalbard melts. Accessed 13 February 2024, https://earthobservatory.nasa.gov/images/153189/svalbard-melts.

Natali, S. M., and Coauthors, 2024: Arctic terrestrial carbon cycling. Arctic Report Card 2024, T. A. Moon, M. L. Druckenmiller, and R. L. Thoman, Eds., NOAA Tech. Rep. OAR ARC 24-11, 8 pp., https://doi.org/10.25923/0GPP-MN10.

NCEP, 2025: Arctic Oscillation Index. Accessed 13 February 2025, https://www.cpc.ncep.noaa.gov/products/precip/CWlink/daily_ao_index/ao.shtml.

Newman, P. A., L. R. Lait, N. A. Kramarova, L. Coy, S. M. Frith, L. D. Oman, and S. S. Dhomse, 2024: Record high March 2024 Arctic total column ozone. *Geophys. Res. Lett.*, **51**, e2024GL110924, https://doi.org/10.1029/2024GL110924.

Notz, D., and SIMIP Community, 2020: Arctic sea ice in CMIP6. *Geophys. Res. Lett.*, **47**, e2019GL086749, https://doi.org/10.1029/2019GL086749.

Nyland, K. E., N. I. Shiklomanov, D. A. Streletskiy, F. E. Nelson, A. E. Klene, and A. L. Kholodov, 2021: Long-term Circumpolar Active Layer Monitoring (CALM) program observations in Northern Alaskan tundra. *Polar Geogr.*, **44**, 167–185, https://doi.org/10.1080/1088937X.2021.1988000.

O'Neill, H. B., S. L. Smith, C. R. Burn, C. Duchesne, and Y. Zhang, 2023: Widespread permafrost degradation and thaw subsidence in northwest Canada. *J. Geophys. Res. Earth Surf.*, **128**, e2023JF007262, https://doi.org/10.1029/2023JF007262.

Overland, J. E., 2024: Emergence of Arctic extremes. *Climate*, **12**, 109, https://doi.org/10.3390/cli12080109.

Park, H. J., and J. B. Ahn, 2016: Combined effect of the Arctic Oscillation and the western Pacific pattern on East Asia winter temperature. *Climate Dyn.*, **46**, 3205–3221, https://doi.org/10.1007/s00382-015-2763-2.

Parmentier, F.-J. W., and Coauthors, 2024: Rapid ice-wedge collapse and permafrost carbon loss triggered by increased snow depth and surface runoff. *Geophys. Res. Let.*, **51**, e2023GL108020, https://doi.org/10.1029/2023GL108020.

Peng, G., W. N. Meier, D. J. Scott, and M. H. Savoie, 2013: A long-term and reproducible passive microwave sea ice concentration data record for climate studies and monitoring. *Earth Syst. Sci. Data*, **5**, 311–318, https://doi.org/10.5194/essd-5-311-2013.

Peterson, B. J., R. M. Holmes, J. W. McClelland, C. J. Vörösmarty, R. B. Lammers, A. I. Shiklomanov, I. A. Shiklomanov, and S. Rahmstorf, 2002: Increasing river discharge to the Arctic Ocean. *Science*, **298**, 2171–2173, https://doi.org/10.1126/science.1077445.

Petty, A. A., N. T. Kurtz, R. Kwok, T. Markus, and T. A. Neumann, 2020: Winter Arctic sea ice thickness from ICESat-2 freeboards. *J. Geophys. Res. Oceans*, **125**, e2019JC015764, https://doi.org/10.1029/2019JC015764.

——, N. Keeney, A. Cabaj, P. Kushner, and M. Bagnardi, 2023a: Winter Arctic sea ice thickness from ICESat-2: Upgrades to freeboard and snow loading estimates and an assessment of the first three winters of data collection. *Cryosphere*, **17**, 127–156, https://doi.org/10.5194/tc-17-127-2023.

——, N. Kurtz, R. Kwok, T. Markus, T. A. Neumann, and N. Keeney, 2023b: ICESat-2 L4 monthly gridded sea ice thickness, version 3. NASA National Snow and Ice Data Center Distributed Active Archive Center, accessed 1 September 2024, https://doi.org/10.5067/ZCSU8Y5U1BQW.

Unauthenticated | Downloaded 11/21/25 11:34 AM UTC

Phoenix, G. K., and Coauthors, 2025: Browning events in Arctic ecosystems: Diverse causes with common consequences. *PLOS Climate*, **4**, e0000570, https://doi.org/10.1371/journal.pclm.0000570.

Pinzon, J. E., C. J. Tucker, U. S. Bhatt, G. V. Frost, and M. J. Macander, 2023: Global Vegetation Greenness (NDVI) from AVHRR GIMMS-3G+, 1981-2022. Accessed 19 May 2025, https://doi.org/10.3334/ORNLDAAC/2187.

Polyakov, I. V., T. J. Ballinger, R. Lader, and X. Zhang, 2024: Modulated trends in Arctic surface air temperature extremes as a fingerprint of climate change. *J. Climate*, **37**, 2381–2404, https://doi.org/10.1175/JCLI-D-23-0266.1.

Qian, L., J. Rao, R. Ren, C. Shi, and S. Liu, 2024: Enhanced stratosphere-troposphere and tropics-Arctic couplings in the 2023/24 winter. *Commun. Earth Environ.*, **5**, 631, https://doi.org/10.1038/s43247-024-01812-x.

Rawlins, M. A., and Coauthors, 2010: Analysis of the arctic system freshwater cycle intensification: Observations and expectations. *J. Climate*, **23**, 5715–5737, https://doi.org/10.1175/2010JCLI3421.1.

Raynolds, M. K., and Coauthors, 2019: A raster version of the Circumpolar Arctic Vegetation Map (CAVM). Remote Sens. *Environ.*, **232**, 111297, https://doi.org/10.1016/j.rse.2019.111297.

Reynolds, R. W., N. A. Rayner, T. M. Smith, D. C. Stokes, and W. Wang, 2002: An improved in situ and satellite SST analysis for climate. *J. Climate*, **15**, 1609–1625, https://doi.org/10.1175/1520-0442(2002)015<1609:AIISAS>2.0.CO;2.

—— , T. M. Smith, C. Liu, D. B. Chelton, K. S. Casey, and M. G. Schlax, 2007: Daily high-resolution-blended analyses for sea surface temperature. *J. Climate*, **20**, 5473–5496, https://doi.org/10.1175/2007JCLI1824.1.

Ricker, R., S. Hendricks, L. Kaleschke, X. Tian-Kunze, J. King, and C. Haas, 2017: A weekly Arctic sea-ice thickness data record from merged CryoSat-2 and SMOS satellite data. *Cryosphere*, **11**, 1607–1623, https://doi.org/10.5194/tc-11-1607-2017.

Robinson, D. A., T. W. Estilow, and NOAA CDR Program, 2012: NOAA Climate Data Record (CDR) of Northern Hemisphere (NH) Snow Cover Extent (SCE), version 1. NOAA National Centers for Environmental Information, accessed 3 September 2024, https://doi.org/10.7289/V5N014G9.

Román, M. O., and Coauthors, 2024: Continuity between NASA MODIS Collection 6.1 and VIIRS Collection 2 land products. *Remote Sens. Environ.*, **302**, 113963, https://doi.org/10.1016/j.rse.2023.113963.

Romanovsky, V., and Coauthors, 2017: Changing permafrost and its impacts. Snow, Water, Ice and Permafrost in the Arctic (SWIPA) 2017, Arctic Monitoring and Assessment Program (AMAP), 65–102, https://www.amap.no/documents/doc/snow-water-ice-and-permafrost-in-the-arctic-swipa-2017/1610.

Schneider, U., P. Finger, E. Rustemeier, M. Ziese, and S. Hänsel, 2022: Global precipitation analysis products of the GPCC. 17 pp., https://opendata.dwd.de/climate_environment/GPCC/PDF/GPCC_intro_products_v2022.pdf.

Schuur, E. A. G., and Coauthors, 2022: Permafrost and climate change: Carbon cycle feedbacks from the warming Arctic. *Annu. Rev. Environ. Resour.*, **47**, 343–371, https://doi.org/10.1146/annurev-environ-012220-011847.

Schyberg H., and Coauthors, 2020: Arctic regional reanalysis on single levels from 1991 to present. Copernicus Climate Change Service (C3S) Climate Data Store (CDS), accessed 26 March 2025, https://doi.org/10.24381/cds.713858f6

See, C. R., and Coauthors, 2024: Decadal increases in carbon uptake offset by respiratory losses across northern permafrost ecosystems. *Nat. Clim. Chang.*, **14**, 853–862, https://doi.org/10.1038/s41558-024-02057-4.

Serreze, M. C., M. P. Clark, and D. H. Bromwich, 2003: Monitoring precipitation over the Arctic terrestrial drainage system: Data requirements, shortcomings, and applications of atmospheric reanalysis. *J. Hydrometeor.*, **4**, 387–407, https://doi.org/10.1175/1525-7541(2003)4<387:MPOTAT>2.0.CO;2.

—— , S. Bigalke, R. Lader, T. J. Ballinger, and J. E. Walsh, 2024: Precipitation [in "State of the Climate in 2023"]. *Bull. Amer. Meteor. Soc.*, **105** (8), S295–S297, https://doi.org/10.1175/BAMS-D-24-0101.1.

Shrestha, R. R., K. E. Bennett, D. L. Peters, and D. Yang, 2021: Hydrologic extremes in Arctic rivers and regions: Historical variability and future perspectives. *Arctic Hydrology, Permafrost and Ecosystems*, D. Yang and D. L. Kane, Eds., Springer Nature Switzerland, 187–218, https://doi.org/10.1007/978-3-030-50930-9_7.

Sigmond, M., J. C. Fyfe, and N. C. Swart, 2018: Ice-free Arctic projections under the Paris Agreement. *Nat. Climate Change*, **8**, 404–408, https://doi.org/10.1038/s41558-018-0124-y.

Smith, B., and Coauthors, 2023: ATLAS/ICESat-2 L3B gridded Antarctic and Arctic land ice height change, version 3. NASA National Snow and Ice Data Center Distributed Active Archive Center, accessed 7 February 2025, https://doi.org/10.5067/ATLAS/ATL15.003.

Smith, S. L., H. B. O'Neill, K. Isaksen, J. Noetzli, and V. E. Romanovsky, 2022: The changing thermal state of permafrost. *Nat. Rev. Earth Environ.*, **3**, 10–23, https://doi.org/10.1038/s43017-021-00240-1.

—— , V. E. Romanovsky, K. Isaksen, K. Nyland, N. I. Shiklomanov, D. A. Streletskiy, and H. H. Christiansen, 2024a: Permafrost [in "State of the Climate in 2023"]. *Bull. Amer. Meteor. Soc.*, **105** (8), S314–S317, https://doi.org/10.1175/BAMS-D-24-0101.1.

—— , C. Duchesne, and H. B. O'Neill, 2024b: Long-term permafrost monitoring in Northern Canada—What have we learned? 12th Int. Conf. on Permafrost, Whitehorse, YT, Canada, International Permafrost Association, 398–404, https://doi.org/10.52381/ICOP2024.84.1.

Streletskiy, D. A., and Coauthors, 2025: Thawing permafrost is subsiding in the Northern Hemisphere—Review and perspectives. *Environ. Res. Lett.*, **20**, 013006, https://doi.org/10.1088/1748-9326/ada2ff.

Sweeney, A. J., Q. Fu, S. Po-Chedley, H. Wang, and M. Wang, 2023: Internal variability increased Arctic amplification during 1980–2022. *Geophys. Res. Lett.*, **50**, e2023GL106060, https://doi.org/10.1029/2023GL106060.

Tank, S. E., and Coauthors, 2023: Recent trends in the chemistry of major northern rivers signal widespread Arctic change. *Nat. Geosci.*, **16**, 789–796, https://doi.org/10.1038/s41561-023-01247-7.

Tapley, B. D., and Coauthors, 2019: Contributions of GRACE to understanding climate change. *Nat. Climate Change*, **5**, 358–369, https://doi.org/10.1038/s41558-019-0456-2.

Taylor, P. C., and Coauthors, 2022: Process drivers, inter-model spread, and the path forward: A review of amplified Arctic warming. *Front. Earth Sci.*, **9**, 758361, https://doi.org/10.3389/feart.2021.758361.

Thoman, R. L., M. Brubaker, M. Heata, and J. Jeuring, 2024: Summer 2023 weather and climate impacts [in "State of the Climate in 2023"]. *Bull. Amer. Meteor. Soc.*, **105** (8), S293–S294, https://doi.org/10.1175/BAMS-D-24-0101.1.

Unauthenticated | Downloaded 11/21/25 11:34 AM UTC

Thompson, D. W. J., and J. M. Wallace, 2000: Annular modes in the extratropical circulation. Part I: Month-to-month variability. *J. Climate*, **13**, 1000–1016, https://doi.org/10.1175/1520-0442(2000)013<1000:AMITEC>2.0.CO;2.

Timmermans, M.-L., and Z. M. Labe, 2024: Sea surface temperature. Arctic Report Card 2024, T. A. Moon, M. L. Druckenmiller, and R. L. Thoman, Eds., NOAA Tech. Rep. OAR ARC 24-07, 7 pp., https://doi.org/10.25923/9z96-aq19.

Tretiyakov, M. V., O. V. Muzhdaba, A. A. Piskun, and R. A. Terekhova, 2022: The state of the Roshydromet Hydrological Observation Network in the mouth areas of RFAZ. *Water Resour.*, **49**, 796–807, https://doi.org/10.1134/S0097807822050153.

Tschudi, M., W. N. Meier, J. S. Stewart, C. Fowler, and J. Maslanik, 2019a: EASE-grid sea ice age, version 4. NASA National Snow and Ice Data Center Distributed Active Archive Center, accessed 4 October 2024, https://doi.org/10.5067/UTAV7490FEPB.

——, ——, and ——, 2019b: Quicklook Arctic weekly EASE-grid sea ice age, version 1. NASA National Snow and Ice Data Center Distributed Active Archive Center, accessed 4 October 2024, https://doi.org/10.5067/2XXGZY3DUGNQ.

U.S. National Ice Center, 2008: IMS daily Northern Hemisphere snow and ice analysis at 1 km, 4 km, and 24 km resolutions, version 1. National Snow and Ice Data Center, accessed 3 August 2024, https://doi.org/10.7265/N52R3PMC.

Vandecrux, B., and Coauthors, 2023: The historical Greenland Climate Network (GC-Net) curated and augmented level-1 dataset. *Earth Syst. Sci. Data*, **15**, 5467–5489, https://doi.org/10.5194/essd-15-5467-2023.

Wegmann, M., and Coauthors, 2015: Arctic moisture source for Eurasian snow cover variations in autumn. *Environ. Res. Lett.*, **10**, 054015, https://doi.org/10.1088/1748-9326/10/5/054015.

Wehrlé, A., J. E. Box, A. M. Anesio, and R. S. Fausto, 2021: Greenland bare-ice albedo from PROMICE automatic weather station measurements and Sentinel-3 satellite observations. *GEUS Bull.*, **47**, 5284, https://doi.org/10.34194/geusb.v47.5284.

Williams, R. S., M. I. Hegglin, P. Jöckel, H. Garny, and K. P. Shine, 2024: Air quality and radiative impacts of downward-propagating sudden stratospheric warmings (SSWs). *Atmos. Chem. Phys.*, **24**, 1389–1413, https://doi.org/10.5194/acp-24-1389-2024.

Wolken, G. J., and Coauthors, 2021: Glacier and permafrost hazards. Arctic Report Card 2021, T. A. Moon, M. L. Druckenmiller, and R. L. Thoman, Eds., NOAA Tech. Rep. OAR ARC 21-13, 93–101, https://doi.org/10.25923/v40r-0956.

Yang, X., and Coauthors, 2020: C3S Arctic regional reanalysis—Full system documentation. Copernicus Climate Change Service (C3S), accessed 26 Mar 2025, https://datastore.copernicus-climate.eu/documents/reanalysis-carra/CARRAFullSystemDocumentationFinal.pdf.

Yu, L., and S. Zhong, 2021: Trends in Arctic seasonal and extreme precipitation in recent decades. *Theor. Appl. Climatol.*, **145**, 1541–1559, https://doi.org/10.1007/s00704-021-03717-7.

Zhou, S., A. J. Miller, J. Wang, and J. K. Angell, 2001: Trends of NAO and AO and their associations with stratospheric processes. *Geophys. Res. Lett.*, **28**, 4107–4110, https://doi.org/10.1029/2001GL013660.

Zhou, W., L. R. Leung, and J. Lu, 2024: Steady threefold Arctic amplification of externally forced warming masked by natural variability. *Nat. Geosci.*, **17**, 508–515, https://doi.org/10.1038/s41561-024-01441-1.

Zhu, X., G. Jia, and X. Xu, 2024: Wildfire emissions offset more permafrost ecosystem carbon sink in the 21st century. *Earth's Future*, **12**, e2024EF005098, https://doi.org/10.1029/2024EF005098.

Unauthenticated | Downloaded 11/21/25 11:34 AM UTC

STATE OF THE CLIMATE IN 2024

ANTARCTICA AND THE SOUTHERN OCEAN

M. N. Raphael and K. R. Clem, Eds.

Special Online Supplement to the *Bulletin of the American Meteorological Society* Vol. 106, No. 8, August, 2025

https://doi.org/10.1175/BAMS-D-25-0087.1

Corresponding author: Marilyn N. Raphael / raphael@geog.ucla.edu

©2025 American Meteorological Society
For information regarding reuse of this content and general copyright information, consult the AMS Copyright Policy.

Unauthenticated | Downloaded 11/21/25 11:34 AM UTC

STATE OF THE CLIMATE IN 2024
Antarctica and the Southern Ocean

Editors

Jessica Blunden
James Reagan

Chapter Editors

Anthony Arguez
Josh Blannin
Peter Bissolli
Kyle R. Clem
Howard J. Diamond
Matthew L. Druckenmiller
Robert J. H. Dunn
Catherine Ganter
Nadine Gobron
Gregory C. Johnson
Rick Lumpkin
Rodney Martinez
Ademe Mekonnen
Twila A. Moon
Gary A. Morris
Marilyn N. Raphael
Carl J. Schreck III
Laura Stevens
Richard L. Thoman
Kate M. Willett
Zhiwei Zhu

Technical Editor

Lukas Noguchi

BAMS Special Editor for Climate

Timothy DelSole

American Meteorological Society

Unauthenticated | Downloaded 11/21/25 11:34 AM UTC

Cover Credit:
Dr. Naomi Ochwat of the University of Colorado (right, blue jacket) and Ms. Liliana Margonari of the University of Buenos Aires (left, orange jacket) on a rock ledge overlooking Crane Glacier in the Antarctic Peninsula on 26 February 2024. The field work was supported by NASA grant 80NSSC22K0386. The team was supported by Argentina's Direction National Antarctica. Photo credit: Dr. Ted Scambos, University of Colorado Boulder

How to cite this document:
Antarctica and the Southern Ocean is one chapter from the *State of the Climate in 2024* annual report and is available from https://doi.org/10.1175/BAMS-D-25-0087.1. Compiled by NOAA's National Centers for Environmental Information, *State of the Climate in 2024* is based on contributions from scientists from around the world. It provides a detailed update on global climate indicators, notable weather events, and other data collected by environmental monitoring stations and instruments located on land, water, ice, and in space. The full report is available from https://doi.org/10.1175/2025BAMSStateoftheClimate.1.

Citing the complete report:
Blunden, J. and J. Reagan, Eds., 2025: "State of the Climate in 2024". Bull. Amer. Meteor. Soc., 106 (8), Si–S513 https://doi.org/10.1175/2025BAMSStateoftheClimate.1.

Citing this chapter:
Raphael, M. N. and K. R. Clem, Eds., 2025: Antarctica and the Southern Ocean [in "State of the Climate in 2024"]. Bull. Amer. Meteor. Soc., 106 (8), S357–S400, https://doi.org/10.1175/BAMS-D-25-0087.1.

Citing a section (example):
MacFerrin, M., T. Mote, A. F. Banwell, and T. Scambos, 2025: Ice sheet seasonal melt extent and duration [in "State of the Climate in 2024"]. Bull. Amer. Meteor. Soc., 106 (8), S372–S374, https://doi.org/10.1175/BAMS-D-25-0087.1.

Unauthenticated | Downloaded 11/21/25 11:34 AM UTC

Editor and Author Affiliations (alphabetical by name)

Adjou, Mohamed, ISEN Engineering School, LaBISEN, Knowledge Learning and Information Modeling (KLaIM), Brest, France; University of Brest, Institut Universitaire Européen de la Mer (IUEM) UAR3113, Plouzané, France

Adusumilli, Susheel, Scripps Institution of Oceanography, University of California, San Diego, La Jolla, California

Amory, Charles, Université Grenoble Alpes, Institut des Géosciences de l'Environnement, IRD, CNRS, Grenoble INP, Grenoble, France

Bahrami, Mahsa, Department of Geography, Pennsylvania State University, State College, Pennsylvania

Baiman, Rebecca, Department of Atmospheric and Oceanic Sciences, University of Colorado Boulder, Boulder, Colorado

Banwell, Alison F., Earth Science and Observation Center, Cooperative Institute for Research in Environmental Sciences (ESOC/CIRES), University of Colorado Boulder, Boulder, Colorado

Barreira, Sandra, Argentine Naval Hydrographic Service, Buenos Aires, Argentina

Beadling, Rebecca L., Department of Earth and Environmental Science, Temple University, Philadelphia, Pennsylvania

Clem, Kyle R., School of Geography, Environment and Earth Sciences, Victoria University of Wellington, Wellington, New Zealand

Colwell, Steve, British Antarctic Survey, Cambridge, United Kingdom

Coy, Lawrence, Science Systems and Applications, Inc., Lanham, Maryland; NASA Goddard Space Flight Center, Greenbelt, Maryland

Datta, Rajashree T., Department of Civil Engineering and Geosciences, TU Delft, The Netherlands

De Laat, Jos, Royal Netherlands Meteorological Institute (KNMI), DeBilt, The Netherlands

du Plessis, Marcel, Department of Marine Sciences, University of Gothenburg, Sweden

Fogt, Ryan L., Department of Geography, Ohio University, Athens, Ohio

Fricker, Helen A., Scripps Institution of Oceanography, University of California, San Diego, La Jolla, California

Hancock, Alyce M., Southern Ocean Observing System (SOOS), Institute for Marine and Antarctic Studies (IMAS), University of Tasmania, Hobart, Australia

Johnson, Bryan, NOAA/OAR Earth System Research Laboratory, Global Monitoring Division, Boulder, Colorado; University of Colorado Boulder, Boulder, Colorado

Josey, Simon A., National Oceanography Centre, Southampton, United Kingdom

Keller, Linda M., Antarctic Meteorological Research and Data Center, Space Science and Engineering Center, University of Wisconsin-Madison, Madison, Wisconsin

Kittel, Christoph, Department of Geography, University of Liège, Liège, Belgium; Physical Geography Research Group, Department of Geography, Vrije Universiteit Brussel, Brussels, Belgium

Kramarova, Natalya A., NASA Goddard Space Flight Center, Greenbelt, Maryland

Lait, Leslie R., NASA Ames Research Center, Moffett Field, California

Lazzara, Matthew A., Department of Physical Sciences, School of Arts and Sciences, Madison Area Technical College; Antarctic Meteorological Research and Data Center, Space Science and Engineering Center, University of Wisconsin-Madison, Madison, Wisconsin

Lieser, Jan L., Bureau of Meteorology, Hobart, Australia; Institute for Marine and Antarctic Studies (IMAS), University of Tasmania, Hobart, Australia

MacFerrin, Michael, Earth Science and Observation Center, Cooperative Institute for Research in Environmental Sciences (ESOC/CIRES), University of Colorado Boulder, Boulder, Colorado

MacLennan, Michelle L., British Antarctic Survey, Cambridge, United Kingdom

Massom, Robert A., Australian Antarctic Division, Australian Antarctic Program Partnership (AAPP) and Australian Centre for Excellence in Antarctic Science (ACEAS), Hobart, Australia

Mikolajczyk, David E., Antarctic Meteorological Research and Data Center, Space Science and Engineering Center, University of Wisconsin-Madison, Madison, Wisconsin

Milward, James, Department of Earth and Environmental Science, Temple University, Philadelphia, Pennsylvania

Mote, Thomas L., Department of Geography, University of Georgia, Athens, Georgia

Newman, Paul A., NASA Goddard Space Flight Center, Greenbelt, Maryland

Norton, Taylor, Antarctic Meteorological Research and Data Center, Space Science and Engineering Center, University of Wisconsin-Madison, Madison, Wisconsin

Petropavlovskikh, Irina, NOAA/OAR Earth System Research Laboratory, Global Monitoring Division, Boulder, Colorado; University of Colorado Boulder, Boulder, Colorado

Pezzi, Luciano P., Laboratory of Ocean and Atmosphere Studies (LOA), Earth Observation and Geoinformatics Division (DIOTG), National Institute for Space Research (INPE), São José dos Campos, Brazil

Raphael, Marilyn N., Department of Geography, University of California, Los Angeles, Los Angeles, California

Reid, Phillip, Bureau of Meteorology, Hobart, Australia; Australian Antarctic Program Partnership (AAPP), Hobart, Tasmania, Australia

Ryan-Keogh, Thomas J., Southern Ocean Carbon-Climate Observatory, Council for Scientific and Industrial Research (CSIR), Cape Town, South Africa

Santee, Michelle L., NASA Jet Propulsion Laboratory, Pasadena, California

Scambos, Theodore, Earth Science and Observation Center, Cooperative Institute for Research in Environmental Sciences (ESOC/CIRES), University of Colorado Boulder, Boulder, Colorado

Schulz, Cristina, Department of Marine and Environmental Sciences, Northeastern University, Boston, Massachussetts

Shi, Jia-Rui, Courant Institute of Mathematical Sciences, New York University, New York City, New York

Souza, Everaldo, Federal University of Pará (UFPA), Belém, Brazil

Stammerjohn, Sharon, Institute of Arctic and Alpine Research, University of Colorado Boulder, Boulder, Colorado

Thomalla, Sandy, Southern Ocean Carbon-Climate Observatory, Council for Scientific and Industrial Research (CSIR), Cape Town, South Africa; Marine and Antarctic Research Centre for Innovation and Sustainability, Department of Oceanography, University of Cape Town, Cape Town, South Africa

Trusel, Luke, Department of Geography, Pennsylvania State University, State College, Pennsylvania

Wille, Jonathan D., Institute for Atmospheric and Climate Science, ETH Zürich, Zürich, Switzerland; Institut des Géosciences de l'Environnement, IRD, CNRS, Grenoble INP, Saint Martin d'Hères, France

Unauthenticated | Downloaded 11/21/25 11:34 AM UTC

Editorial and Production Team

Allen, Jessicca, Graphics Support, Cooperative Institute for Satellite Earth System Studies, North Carolina State University, Asheville, North Carolina

Camper, Amy V., Graphics Support, Innovative Consulting and Management Services, LLC, NOAA/NESDIS National Centers for Environmental Information, Asheville, North Carolina

Carroll, Lauren, Content Team Lead, Communications and Outreach, NOAA/NESDIS National Centers for Environmental Information, Asheville, North Carolina

Haley, Bridgette O., Graphics Support, NOAA/NESDIS National Centers for Environmental Information, Asheville, North Carolina

Love-Brotak, S. Elizabeth, Lead Graphics Production, NOAA/NESDIS National Centers for Environmental Information, Asheville, North Carolina

Ohlmann, Laura, Technical Editor, Innovative Consulting and Management Services, LLC, NOAA/NESDIS National Centers for Environmental Information, Asheville, North Carolina

Noguchi, Lukas, Technical Editor, Innovative Consulting and Management Services, LLC, NOAA/NESDIS National Centers for Environmental Information, Asheville, North Carolina

Riddle, Deborah B., Graphics Support, NOAA/NESDIS National Centers for Environmental Information, Asheville, North Carolina

Veasey, Sara W., Visual Communications Team Lead, Communications and Outreach, NOAA/NESDIS National Centers for Environmental Information, Asheville, North Carolina

Unauthenticated | Downloaded 11/21/25 11:34 AM UTC

6. Table of Contents

Unauthenticated | Downloaded 11/21/25 11:34 AM UTC

6. ANTARCTICA AND THE SOUTHERN OCEAN

M. N. Raphael and K. R. Clem, Eds.

a. Overview

—M. N. Raphael and K. R. Clem

In 2024, atmospheric conditions over Antarctica exhibited significant anomalies, and were marked by major surface and stratospheric warming and pressure fluctuations. The first half of the year (January–June) featured persistent below-normal surface pressure over the continent, a distinct zonal wavenumber-3 pattern with three deep atmospheric troughs extending over the Weddell Sea, Prydz Bay, and Ross Ice Shelf, and a positive phase of the Southern Annular Mode, with strong circumpolar westerlies. Surface pressure anomalies in February and April were particularly pronounced, with multiple stations recording record-low pressures.

Strong stratospheric warming occurred in July followed by extreme surface warming in August. The surface warming was likely intensified by a compound event: 1) a strong ridge of surface high pressure along coastal East Antarctica advected warm maritime air into the continental interior, and 2) a significant positive geopotential height and temperature anomaly in the stratosphere propagated downward to the surface. As a result, multiple monthly records for high temperatures and pressure were set in August.

The Antarctic Ice Sheet's surface mass balance (SMB) in 2024 was shaped by contrasting periods of high snowfall and regional drought. The most significant anomaly occurred in May, when extreme snowfall led to record-high SMB gains across much of East and West Antarctica. Enhanced meridional moisture transport and atmospheric river events—which funneled moisture from the South Pacific and Atlantic Oceans toward the continent—supported/generated this extreme snowfall. In contrast, September emerged as the driest September on record, with a severe shortage of snowfall over the ice sheet. This was linked to an anomalously deep and eastward-shifted Amundsen Sea Low, which suppressed precipitation and led to below-average SMB across West Antarctica.

There was continued ice sheet mass loss in the Amundsen Sea sector of West Antarctica, where observations show that thinning has persisted since 1992. Additional losses were observed in the Antarctic Peninsula, particularly near the Larsen C Ice Shelf and Bellingshausen Sea. However, some regions of East Antarctica, notably Dronning Maud Land and Totten Glacier, exhibited localized mass gains due to increased snowfall.

A net Antarctic mass loss of 125 Gt occurred between January and November 2024, exceeding the long-term annual average of 100 Gt per year. Although this loss was not as extreme as in some previous years, it underscored the continued trend of mass decline, particularly in West Antarctica and the Antarctic Peninsula.

Antarctic sea ice remained anomalously low in 2024, with record- or near-record-low extents observed for much of the year. The annual daily minimum sea ice extent was recorded on 18 February at 1.97 million km^2, the third lowest on record. The seasonal cycle was again disrupted, with delayed autumn–winter expansion and an early spring–summer retreat. By late 2024, sea ice conditions began to recover slightly, with overall sea ice extent approaching near-average values in November and December. However, this temporary return to average conditions did not offset the negative trend observed since 2016.

Regionally, the eastern Weddell Sea experienced particularly severe low sea ice coverage, likely due to warmer sea surface temperatures and weakened stratification in the upper ocean. This reduction in sea ice caused increased exposure of coastal regions to oceanic and atmospheric variability. In contrast, the western Weddell Sea and some parts of the Ross and Amundsen Seas

Unauthenticated | Downloaded 11/21/25 11:34 AM UTC

saw temporary sea ice expansion driven by localized cold air outbreaks and persistent southerly winds.

Across the Southern Ocean, sea surface temperatures increased markedly, with positive anomalies persisting through 2024. This continued the positive trend observed since 2005. The western Pacific region showed the greatest increases, especially from February to July. In concert with the sea surface temperatures, ocean heat content also increased to levels higher than previously experienced. The region of greatest increase in sea surface temperatures coincided with the regions of below-average sea ice extent. Chlorophyll, an important marker of ocean biogeochemistry, was at elevated levels during December and January (2023/24), most notably in the Atlantic.

The 2024 Antarctic ozone hole appeared approximately a week later than average on 25 August and was among the least severe ozone holes recorded over the past three decades. It ranked 26th in size, with an average area of 19.6 million km^2 from 7 September to 13 October. The daily minimum ozone concentration was slightly higher than the 1992–2023 mean, and the ozone hole reached its maximum extent later than usual, peaking at 22.4 million km^2 on 28 September. The delayed start to the ozone hole development was due to strong planetary wave activity during mid-May to mid-August, which led to a significant warming of the Antarctic stratosphere in late July to early August and transported ozone into the Antarctic stratosphere, increasing concentrations at a time when they would normally be decreasing. Additionally, average stratospheric temperatures in September and decreased levels of chlorine and bromine in the Antarctic polar vortex led to a 2024 ozone hole that was not as deep nor as extensive as those observed in the early 2000s. The 2024 ozone hole broke up on 21 December, two weeks later than average.

More details on Antarctica's climate, weather, ice, ocean, and ozone are presented below for 2024. Unless otherwise stated, the 2024 anomalies and standard deviations are all based on the 1991–2020 climatology. Note that some sections use different climatology periods due to data availability, while others use non-traditional seasons centered around specific phenomena of interest, such as surface melt (October to April) and the Southern Ocean chlorophyll season (June to July); these details are stated at the beginning of each section. Common geographic regions and place names referenced throughout the chapter are shown in Fig. 6.1.

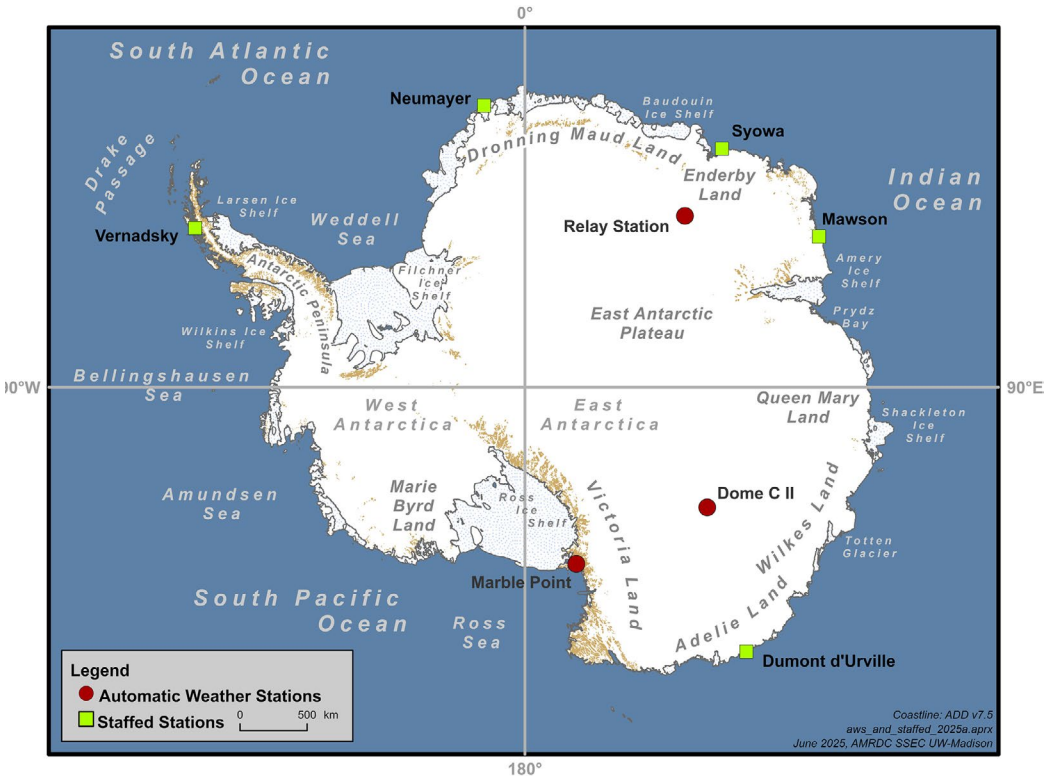

Fig. 6.1. Map of the Antarctic, showing stations, geographic regions, and prominent features discussed in this chapter. Figure courtesy of Samuel Batzli, University of Wisconsin-Madison.

Unauthenticated | Downloaded 11/21/25 11:34 AM UTC

b. Atmospheric circulation and surface observations

—K. R. Clem, T. Norton, D. Mikolajczyk, L. M. Keller, M. A. Lazzara, S. Colwell, S. Barreira, and R. L. Fogt

The Antarctic atmosphere in 2024 was largely characterized by month-to-month variability. The main atmospheric event of the year was a major surface and stratospheric warming during July and August. The surface warming began over the eastern Weddell Sea and Dronning Maud Land in July, triggered by the development of a strong high-pressure system in the southeast Atlantic. August saw the greatest number of new pressure and temperature records during the event as high pressure in the South Atlantic built poleward into East Antarctica, and widespread positive pressure anomalies developed over the remainder of the continent with a likely connection to downward-propagating positive geopotential height anomalies from the stratosphere. For the rest of the year, pressure and temperature were variable from month to month. One notable event occurred in September when a deep cyclone developed over the Antarctic Peninsula, resulting in record-low monthly mean pressure at all long-term staffed weather stations in the region (dating back to 1950). This pattern continued to direct warm northerly airflow over the eastern Weddell Sea and Dronning Maud Land into spring—a persistent feature seen there since March 2023—contributing to more declines and record-low sea ice extents over the eastern Weddell Sea (section 6f), and continued increases in surface mass balance (SMB) over Dronning Maud Land (section 6c).

To investigate these features from 2024 in detail, we employ ERA5 (Hersbach et al. 2020), staffed weather station data from the READER archive (Turner et al. 2004) and automatic weather station (AWS) data from the Antarctic Meteorological Research and Data Center (AMRDC) data repository (AMRDC 2022). First, surface temperature and pressure anomalies from ERA5 were grouped and averaged over four periods of relatively persistent features: January–June, July–August, September–October, and November–December (Fig. 6.2). Figure 6.3 shows the vertical structure of the monthly geopotential height (Fig. 6.3a) and temperature (Fig. 6.3b) anomalies averaged over the polar cap (60°S–90°S) and the monthly circumpolar zonal wind anomalies (Fig. 6.3c) averaged over 50°S–70°S. Observed monthly temperature and pressure anomalies for select staffed and automated weather stations are shown in Fig. 6.4; see Fig. 6.1 for station locations and geographical references made in this section and throughout the

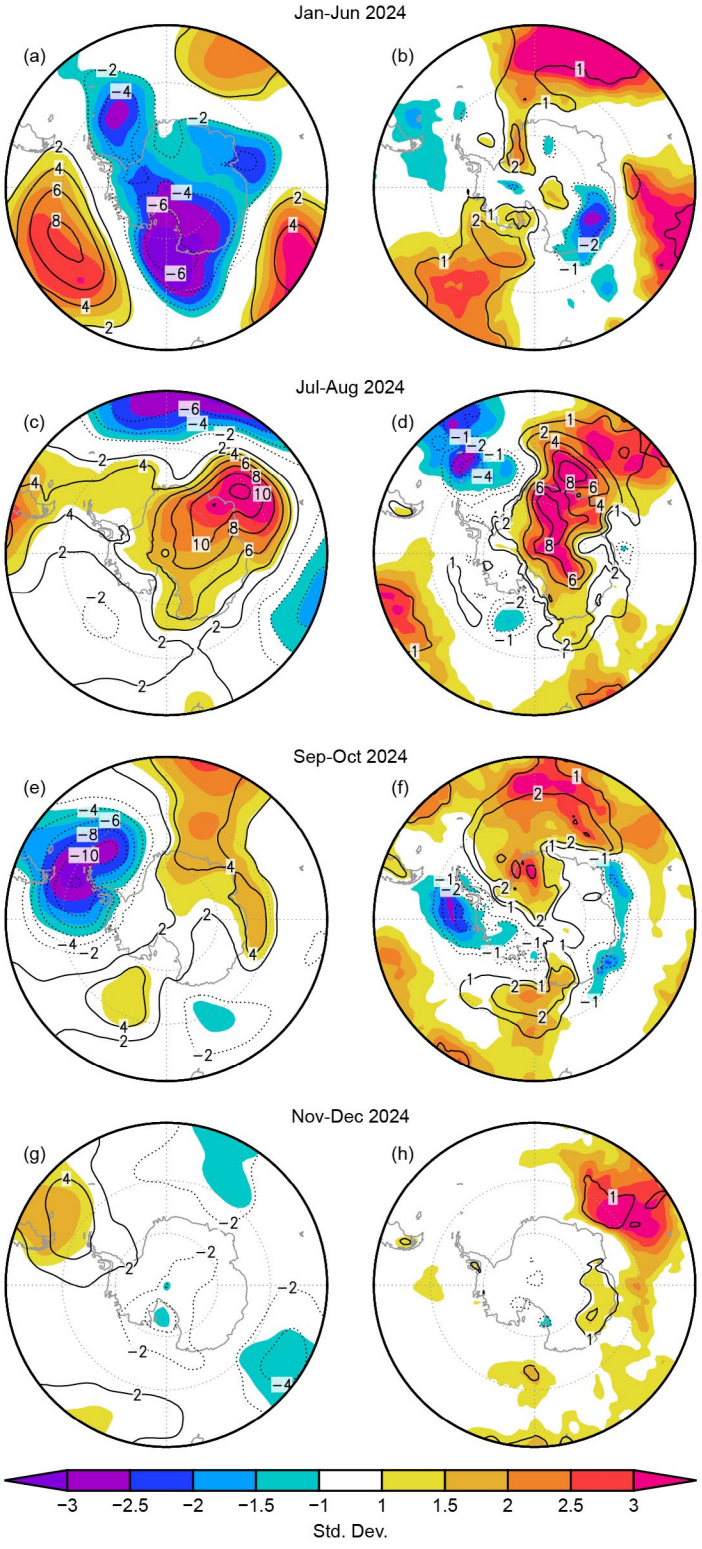

Fig. 6.2. (left) Surface pressure (hPa) and (right) 2-m temperature anomalies (°C) relative to 1991–2020 for (a),(b) Jan–Jun 2024; (c),(d) Jul–Aug 2024; (e),(f) Sep–Oct 2024, and (g),(h) Nov–Dec 2024. Contour interval is 2 for both fields with an additional ±1°C contour added for 2-m temperature; zero contours are omitted. Shading shows the std. dev. of the anomalies. (Source: ERA5)

Unauthenticated | Downloaded 11/21/25 11:34 AM UTC

chapter. All anomalies and standard deviations presented are based on the 1991–2020 climatology.

The first half of the year (January–June) was characterized by below-normal surface pressure over the continent (Fig. 6.2a) accompanied by three deep troughs extending offshore over the Weddell Sea, Prydz Bay, and Ross Ice Shelf/Ross Sea. The three troughs were each flanked by strong high-pressure anomalies (each 2–3 std. dev. above average) along 50°S–60°S—one in the central South Pacific, one south of Africa, and one south of Australia—producing a distinct zonal wavenumber-3 pattern and a positive phase of the Southern Annular Mode (SAM); the SAM index was positive in all six months (Fig. 6.3). Within this period were two months of more pronounced negative pressure anomalies over the polar cap (region south of 60°S) in February and April (as illustrated by the geopotential height anomalies in Fig. 6.3a), with April also seeing a significant strengthening of the circumpolar westerlies to more than 2 std. dev. above average (Fig. 6.3c). Record-low monthly mean pressures were recorded at various stations, including Neumayer in February (since 1981; not shown), and in April at Dumont d'Urville (Fig. 6.4d), Marble Point AWS (Fig. 6.4e), Ferrell AWS (since 1985; not shown), and Gill AWS (since 1981; not shown). In June, McMurdo recorded its lowest monthly pressure on record (since 1956; not shown).

Surface temperature anomalies during January–June reflect the wave-3 structure, with three main regions of above-average temperatures on the eastern sides of the troughs, and below-average temperatures on the western sides. Western Dronning Maud Land and western Marie Byrd Land experienced the most pronounced warming, while below-average temperatures were noted over Adélie Land. Two new temperature records were set: Neumayer recorded its warmest February on record (since 1981), and Dome C II AWS recorded its coldest April on record (since 1980; neither shown). The regionally varying temperature anomalies largely cancel out when averaged over the polar cap (Fig. 6.3b), except in February and March, which stood out with above-average temperatures over the continent.

July and August were marked by two major events: a strong stratospheric warming event in July (section 6h) and a major surface warming event in August (Fig. 6.3b), both of which produced monthly anomalies well over 3 std. dev. above the months' respective climatologies. The dominant surface circulation feature was a strong ridge of high pressure centered along the East Antarctic coast between 40°E and 60°E (Fig. 6.2c). Warm maritime air from the South Atlantic flowed onshore across Dronning Maud Land and Prydz Bay, penetrating deep into the continental interior and reaching the high plateau and Adélie Land (Fig. 6.2d). The ridge was most pronounced

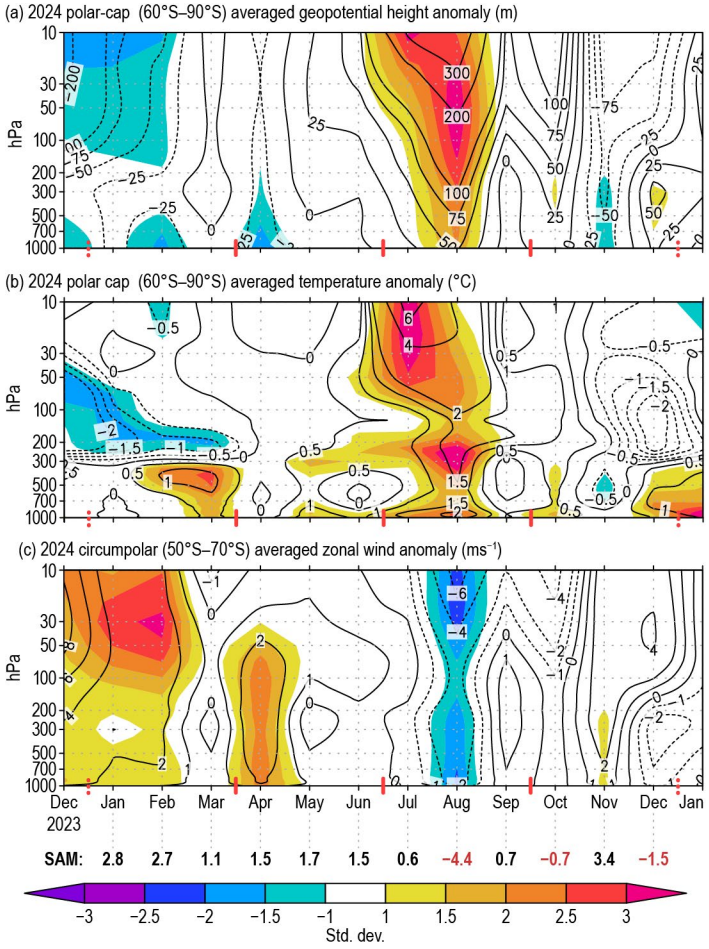

Fig. 6.3. Area-averaged (weighted by cosine of latitude) monthly anomalies over the southern polar region in 2024 relative to 1991–2020: (a) polar cap (60°S–90°S) averaged geopotential height anomalies (m; contour interval is 25 m up to ±100 m and 100 m after ±100 m); (b) polar cap averaged temperature anomalies (°C; contour interval is 0.5°C up to ±2°C and 2°C after ±2°C); (c) circumpolar (50°S–70°S) averaged zonal wind anomalies (m s^{-1}; contour interval is 2 m s^{-1} with an additional contour at ±1 m s^{-1}). Shading depicts standardized monthly anomalies as indicated by the color bar at bottom. Red vertical bars indicate the four climate periods used for compositing in Fig. 6.3; the dashed lines near Dec 2023 and Dec 2024 indicate circulation anomalies wrapping around the calendar year. Values from the Marshall (2003) Southern Annular Mode (SAM) index are shown below (c) in black (positive values) and red (negative values). (Source: ERA5)

Unauthenticated | Downloaded 11/21/25 11:34 AM UTC

along the coast in July, confining the warming to Dronning Maud Land but, in August, it extended poleward into East Antarctica (Fig. 6.2d), compounded by the downward propagation of positive geopotential height anomalies from the stratospheric warming (Fig. 6.3a). Notably, the SAM index reached its lowest August value since 1963, which was the second-lowest August value on record (since 1957).

Numerous monthly mean records were set in July and August. Syowa recorded its highest pressure on record in July (Fig. 6.4b) when the ridge was centered along the coast. In August, record-high pressures were reported in nearly every region of Antarctica, including Relay Station AWS on the plateau (Fig. 6.4f), Marble Point AWS on the Ross Ice Shelf (Fig. 6.4e), and Bellingshausen on the Antarctic Peninsula (not shown). There were also record-high temperatures throughout much of East Antarctica in August, with Relay Station AWS, Syowa, Mawson, and Davis all recording their warmest August on record (Fig. 6.4; Davis not shown). While weather observations are sparse over the ice sheet interior, ERA5 estimates a broad area of temperatures 6°C–10°C above average across much of the interior for the two-month period (Fig. 6.2d), consistent with available observations (Fig. 6.4). Also noteworthy was Dome C II AWS, which recorded its windiest August on record (since 1980; not shown).

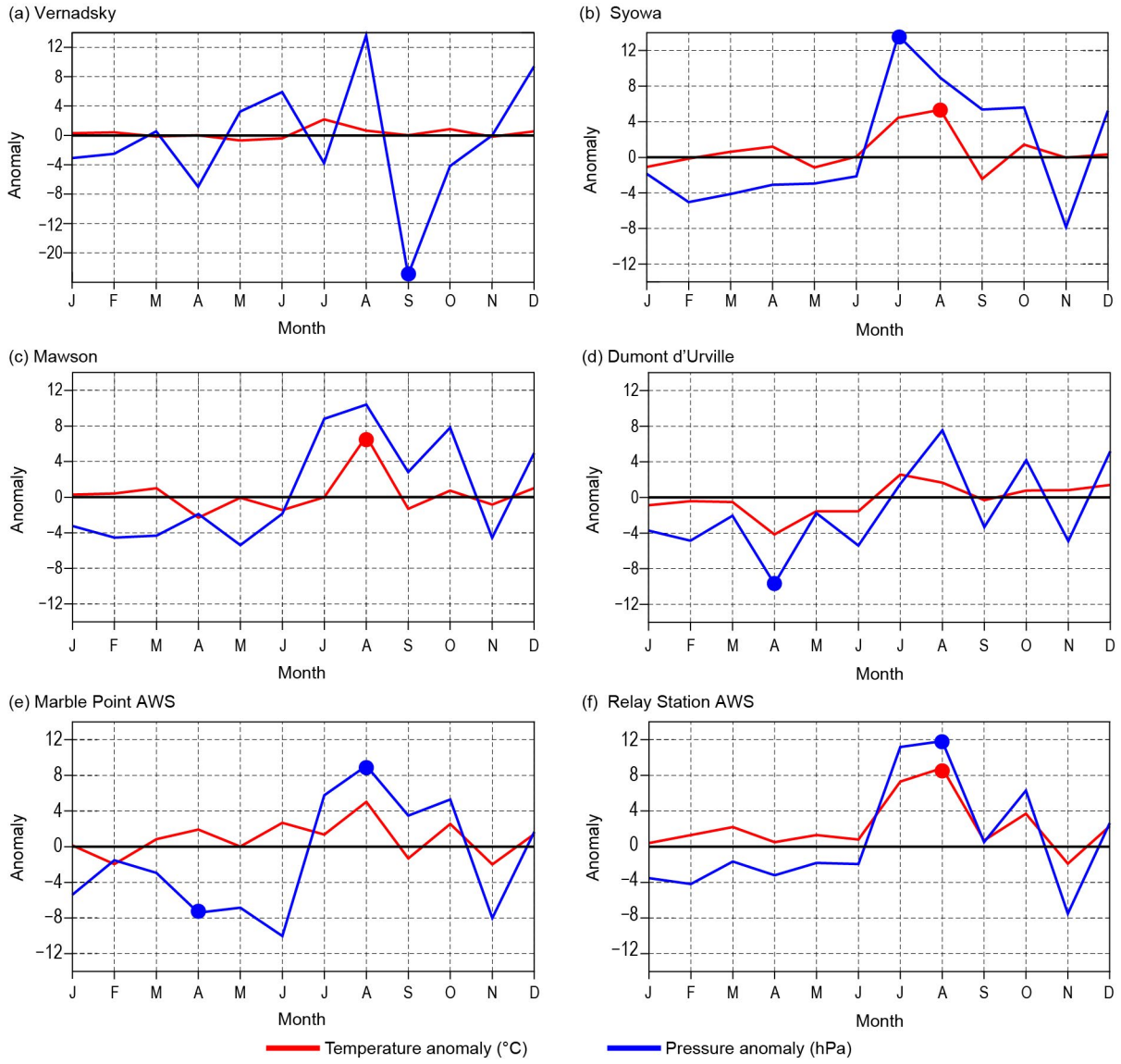

Fig. 6.4. Observed monthly Antarctic surface air temperature and station pressure anomalies during 2024 from six representative stations (four staffed [a]–[d], and two automatic [e],[f]). Anomalies for temperature (°C) are shown in red and mean sea level pressure/surface pressure (hPa) are shown in blue. Filled circles denote monthly mean records set in 2024. The station records start in 1950 for Vernadsky, 1957 for Syowa, 1954 for Mawson, 1956 for Dumont d'Urville, 1980 for Marble Point automatic weather station (AWS), and 1995 for Relay Station AWS. See Fig. 6.1 for station locations. Note the y-axis in (a) extends from +14 to –20, while all other panels range from ±14.

Unauthenticated | Downloaded 11/21/25 11:34 AM UTC

Pressure and temperature largely returned to average values during September and October (Figs. 6.2e,f, 6.3a,b), except for a regionally significant low-pressure system that developed over the Antarctic Peninsula in September, with Vernadsky recording pressure 20 hPa below average. Vernadsky (Fig. 6.4a), Rothera, Bellingshausen, Esperanza, and Marambio all recorded their lowest September pressure on record. Above-average surface pressure persisted over the southeast Atlantic Ocean and coastal East Antarctica. The low–high pressure couplet resulted in continued warm northerly flow and above-average temperatures over the eastern Weddell Sea and Dronning Maud Land, contributing to record-low sea ice extents in the eastern Weddell Sea during the winter of 2024 (section 6f). The cyclone also suppressed precipitation across West Antarctica, contributing to record-low SMB over the grounded ice sheet in September (section 6c).

The year concluded with a moderate (1.5 std. dev.) negative pressure anomaly over the polar cap in November followed by generally above-average pressure in December (Fig. 6.3a). November featured a pronounced positive phase of the SAM (highest SAM index value of the year: +3.4) with intensified circumpolar westerlies and below-average temperatures over the polar cap (Figs. 6.3b,c). The Ross Ice Shelf region saw record-low November pressures at Ferrell AWS and Gill AWS (not shown). December was relatively calm (not shown), with generally above-average temperatures and near-average pressure, except for a strong ridge of high pressure (>2 std. dev.) over the Antarctic Peninsula and Weddell Sea, which led to anomalously warm conditions in West Antarctica.

Unauthenticated | Downloaded 11/21/25 11:34 AM UTC

c. Ice sheet surface mass balance

—L. Trusel, M. Maclennan, R. Baiman, M. Bahrami, C. Kittel, R. Tri Datta, and C. Amory

Surface mass balance (SMB) represents the net effect of all processes that add or remove mass from the surface of an ice sheet. For the Antarctic Ice Sheet (AIS), snowfall is the primary SMB contributor, delivering ~2300 Gt annually (van Wessem et al. 2018; Agosta et al. 2019; Mottram et al. 2021). Sublimation represents the largest negative term in the AIS SMB, given that most surface melt refreezes within the firn (Mottram et al. 2021). Strong SMB gradients exist spatially (Fig. 6.5a), with high relief coastal areas receiving >500 mm water equivalent (w.e.) yr^{-1} compared to <50 mm w.e. yr^{-1} across the high-elevation plateau of East Antarctica. Strong seasonal variability likewise exists, with the largest mass gains occurring in austral autumn (March–May) and the least in austral summer (December–February; Fig. 6.6a). Although only SMB on grounded ice directly affects sea level, SMB on floating ice shelves is critical for maintaining firn layer health and ice shelf stability (The Firn Symposium Team 2024). Typically, high-magnitude extreme precipitation events (EPEs) delivered by atmospheric rivers (ARs) drive AIS SMB gains (Turner et al. 2019; Wille et al. 2021; Maclennan et al. 2022), while reduced AR activity can lead to anomalously low snowfall and a more negative mass balance (Davison et al. 2023). Sea ice can also play an influential role in SMB by modulating the amount and extent of moisture transport over the ice sheet (Wang et al. 2020; Trusel et al. 2023; Hanna et al. 2024; Kolbe et al. 2025).

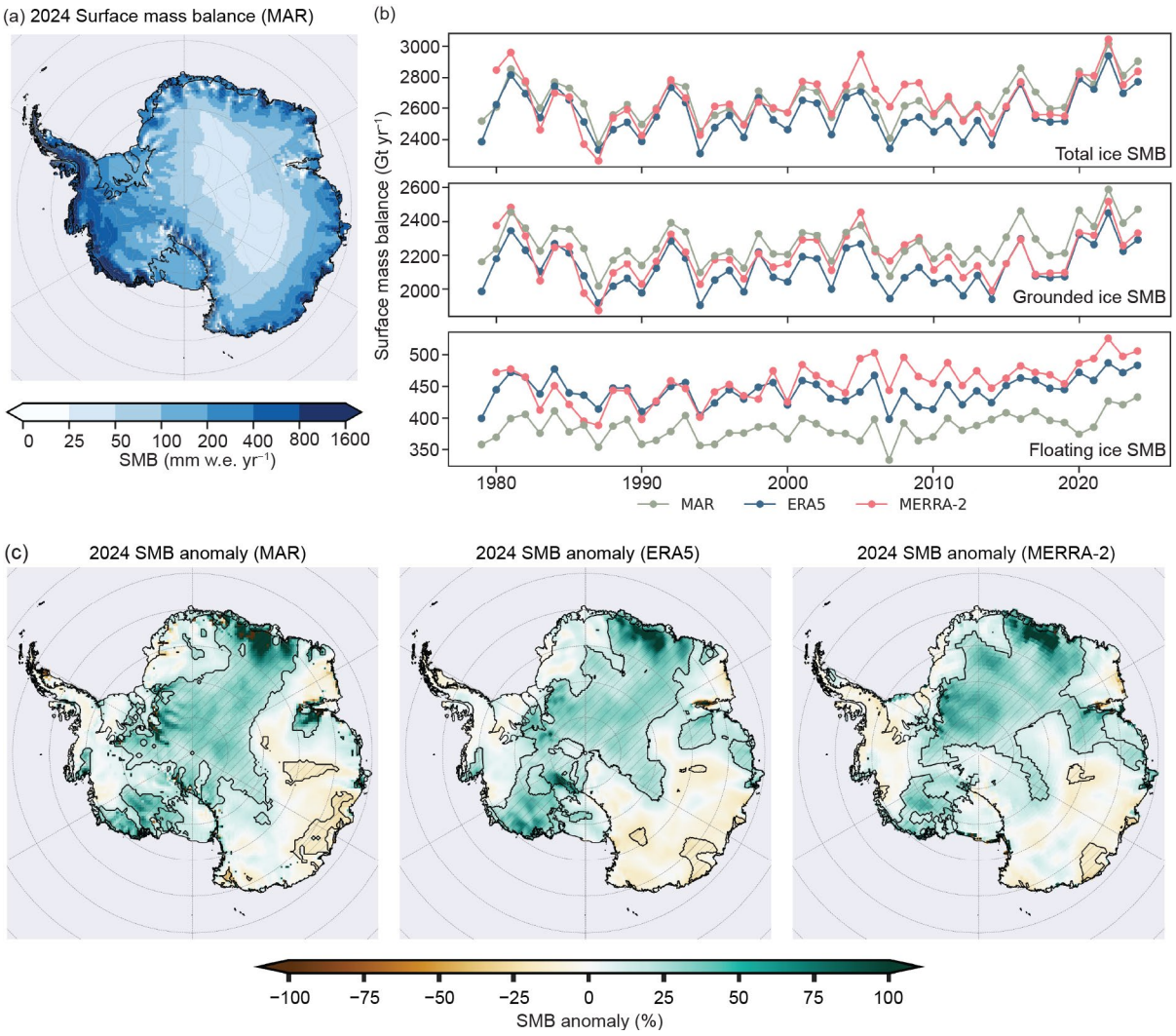

Fig. 6.5. (a) Model for Surface Mass Balance of the Arctic Ice Sheets (MAR) 2024 surface mass balance (SMB; mm water equivalent [w.e.] yr^{-1}). (b) Time series of SMB in Gt (10^{12} kg) yr^{-1} over the full ice sheet and its grounded and floating portions. (c) Annual MAR, ERA5, and MERRA-2 SMB anomalies for 2024 relative to the 1991–2020 mean (%). The 2024 SMB anomalies are higher than the 1991–2020 standard deviation of the respective datasets in the hatched areas outlined in black.

Unauthenticated | Downloaded 11/21/25 11:34 AM UTC

Here, we estimate the 2024 SMB as total precipitation minus evaporation and sublimation (P–E) using ERA5 (Hersbach et al. 2020) and MERRA-2 (Gelaro et al. 2017) reanalyses, following recent studies (e.g., Medley and Thomas 2019; Lenaerts et al. 2019). Though important biases remain, particularly regarding ice sheet–cloud–radiation feedbacks and precipitation,

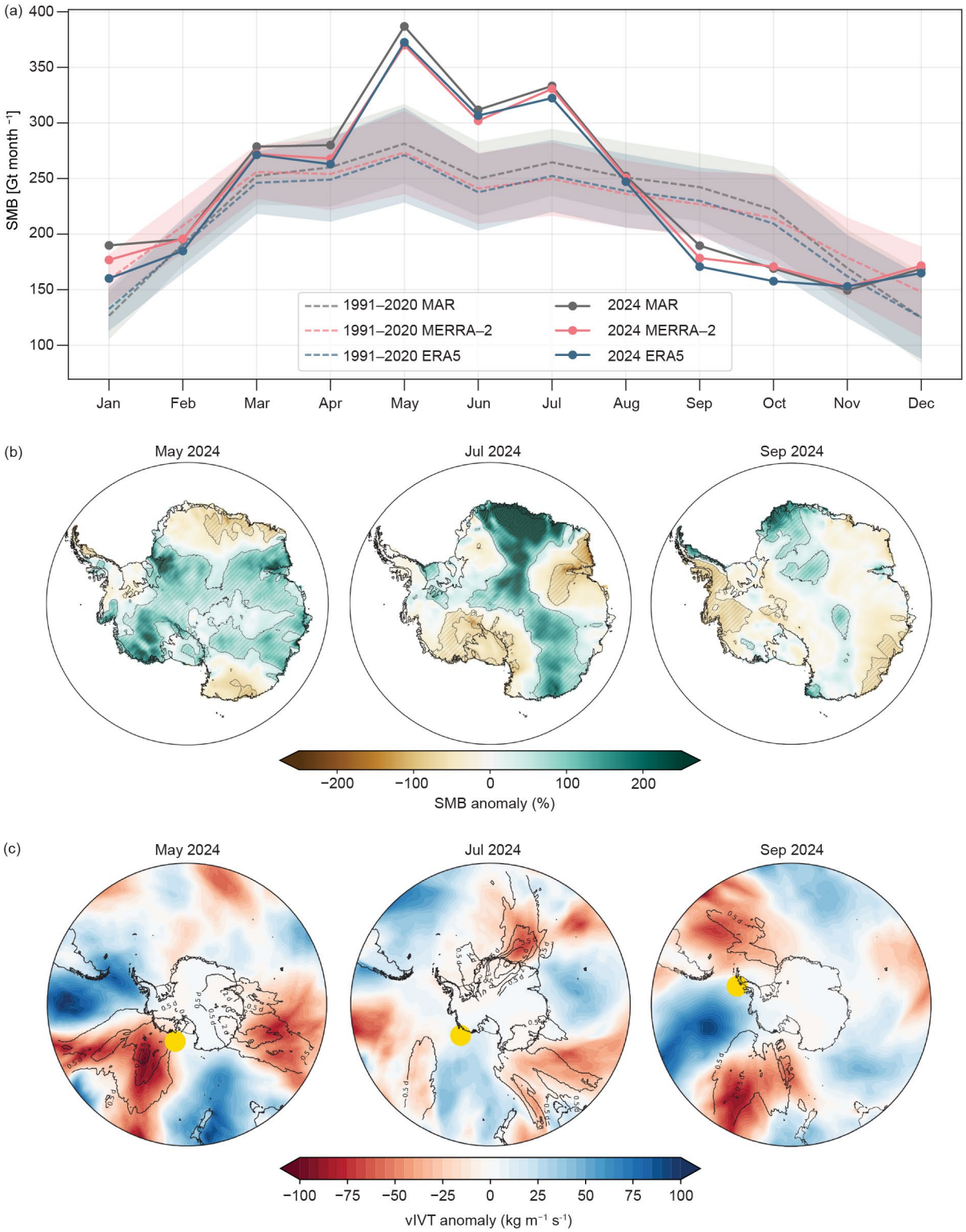

Fig. 6.6. (a) Monthly cycle of (grounded and floating) Antarctic Ice Sheet surface mass balance (SMB) in Gt month^{-1} for MERRA-2 (pink), ERA5 (blue), and the Model for Surface Mass Balance of the Arctic Ice Sheets (MAR; gray). The 2024 values are shown with a solid line and the 1991–2020 average is shown in a dotted line; 1 std. dev. is shaded. (b) Monthly SMB anomalies (ERA5), with hatched regions indicating anomalies exceeding 1 std. dev. relative to the 1991–2020 average. (c) Anomalies in ERA5 meridional integrated vapor transport (vIVT) with negative values (reds) indicating enhanced moisture transport toward Antarctica, contours representing the number of days featuring atmospheric rivers detected in MERRA-2, and yellow dot representing the monthly mean Amundsen Sea Low center following Hosking et al. (2014).

Unauthenticated | Downloaded 11/21/25 11:34 AM UTC

evaluations of both reanalyses indicate that they reliably represent recent Antarctic climate (Gossart et al. 2019; Medley and Thomas 2019; Wang et al. 2016). SMB was also assessed using the polar-oriented regional climate model Model for Surface Mass Balance of the Arctic Ice Sheets (MAR) forced by ERA5, which explicitly represents ice sheet SMB processes, including firn evolution and meltwater runoff (Kittel et al. 2021). ERA5 offers the highest resolution (0.25°), followed by MAR (35 km) and MERRA-2 (0.625° × 0.5°). While ERA5 and MAR extend back to 1979, MERRA-2 begins in 1980. To ensure spatial consistency, each dataset was bilinearly regridded to the ERA5 grid before masking with grounded and floating ice extents from the Antarctic Digital Database (Gerrish et al. 2023). Annual and monthly anomalies in SMB and vector-invariant water transport (vIVT) are compared to 1991–2020 climatologies and we detect ARs in MERRA-2 using an approach adapted from Wille et al. (2021).

In 2024, the grounded AIS SMB equaled 2291 Gt (ERA5), 2333 Gt (MERRA-2), and 2472 Gt (MAR), representing anomalies of 1.2 to 1.7 std. devs. above the 1991–2020 climatological means (ERA5: 2104±109 Gt yr^{-1}; MERRA-2: 2186±106 Gt yr^{-1}; MAR: 2254±97 Gt yr^{-1}). These results were the second highest on record in MAR (behind only 2022), fifth highest in ERA5, and sixth in MERRA-2. Considering floating ice shelves alone, 2024 ranked as the highest on record in MAR and second highest in ERA5 and MERRA-2. Despite elevated SMB in 2024 and other recent years, no significant trend ($p \leq 0.01$) was detected for total or grounded SMB, although significant positive trends exist across the AIS's floating ice shelves in MAR (0.6 Gt yr^{-1}) and MERRA-2 (1.5 Gt yr^{-1}).

Examination of SMB across months further highlights the exceptional conditions in 2024. May emerged as the most anomalous month of the year (Fig. 6.6a) and ranked among the snowiest on record over the full ice sheet (first, second, and third in MAR, MERRA-2, and ERA5, respectively). Heavy gains in May more than offset the largely typical low SMB observed from January through April, yielding the highest cumulative SMB on record from May to August according to ERA5, before below-average precipitation during September–November ultimately reduced the cumulative SMB anomaly. The positive SMB anomalies in May were widespread, with much of East and West Antarctica experiencing significant mass gains (Fig. 6.6b). This pattern aligned with positive anomalies in southward vIVT and AR activity that funneled moisture from lower latitudes into the Ross–Amundsen and Wilkes Land sectors (Fig. 6.6c). Moreover, moisture transport toward West Antarctica passed over regions exhibiting sea surface temperature anomalies exceeding 2°C in the South Pacific Ocean (section 6g) and reduced sea ice in the Ross–Amundsen Sea (not shown; section 6f), conditions that likely contributed to enhanced SMB. The widespread but generally low-magnitude, positive SMB anomalies of May contrast to the high localized SMB conditions in July, when particularly strong SMB increases in Dronning Maud Land were driven by focused ARs (Fig. 6.6) on the western side of a strong ridge of high pressure (section 6c).

In contrast, September was the driest on record over the grounded ice sheet in all datasets assessed, driven by an acute shortfall of precipitation across West Antarctica (Fig. 6.6b). Typically, 6.5±0.8 Gt day^{-1} of snowfall occurs in September according to MERRA-2 climatology, yet 2024 averaged only 4.9 Gt day^{-1}, largely due to an absence of EPEs. Normally, days in the top 15% of snowfall contribute 78±41 Gt (38% of total September snowfall), but no days in September 2024 featured snowfall in the top 15% of daily precipitation. Antarctic EPEs are often associated with elevated vIVT anomalies and ARs (Turner et al. 2019; Wille et al. 2021; Maclennan et al. 2022), however, in September 2024, few ARs with high vIVT reached the continent and instead were concentrated equatorward over the Amundsen Sea (Fig. 6.6c). A likely driver of this lack of snowfall and landfalling ARs was the extreme eastward position of the Amundsen Sea Low (see Fig. 6.2e)—farther east than any September since 1959 according to the approach of Hosking et al. (2016)—which acted to suppress moisture transport toward West Antarctica and contributed to the extreme low SMB.

Unauthenticated | Downloaded 11/21/25 11:34 AM UTC

d. Ice sheet seasonal melt extent and duration

—M. MacFerrin, T. Mote, A. F. Banwell, and T. Scambos

Surface melt on the Antarctic Ice Sheet (AIS) occurs primarily on the low-elevation coastal margins, especially on the Antarctic Peninsula and on the ice shelves surrounding the continent. It plays a small role in the total mass balance of the AIS relative to far larger contributions from snow accumulation, glacier calving, and basal melting. However, surface melting is a key measure of ice sheet and ice shelf stability. As meltwater percolates and re-freezes, it increases the density of the underlying firn, and if melt volume is sufficient, the accumulated meltwater can induce ice shelf break up (Banwell et al. 2013) and glacier acceleration through hydrofracture (Scambos et al. 2014). This section focuses on the melt season spanning 1 October 2023 through 30 April 2024. The 2024/25 Antarctic melt season will be discussed in next year's report.

Daily surface melt is mapped using satellite-derived passive-microwave brightness temperatures. The source data are distributed as daily composited polar stereographic brightness temperatures by the National Snow and Ice Data Center (NSIDC; products NSIDC-0001, Meier et al. 2019 and NSIDC-0007, Gloerson 2006) spanning 1979 through the present day. Daily passive microwave brightness temperatures using the 37-GHz horizontal polarization as well as the 37- and 19-GHz vertical polarization channels have been acquired by the Scanning Multichannel Microwave Radiometer (SMMR), Special Sensor Microwave Imager (SSM/I), and Special Sensor Microwave Imager Sounder (SSMIS) sensors aboard the NOAA Nimbus-7 and Defense Meteorological Satellite Program (DMSP) F8, F11, F13, F17, and F18 satellites. The austral melt season is defined here as 1 October through 30 April. Although small brief melt events can be measured along Antarctica's coastal margins throughout the year and even during the austral winter, the vast majority of melt happens during these seven months, with most melt typically occurring in December and January. An ice extent mask of 25-km grid cells for the AIS was developed from the Quantarctica v3.0 Detailed Basemap dataset (Norwegian Polar Institute 2018). All 25-km cells that contain ≥50% land ice or ice shelf are included. We divide the AIS into seven melt extent and climate regions by clustering glaciological drainage basins (based on The IMBIE Team 2019; Fig. 6.7b). Melt is determined by 37-GHz horizontally polarized brightness

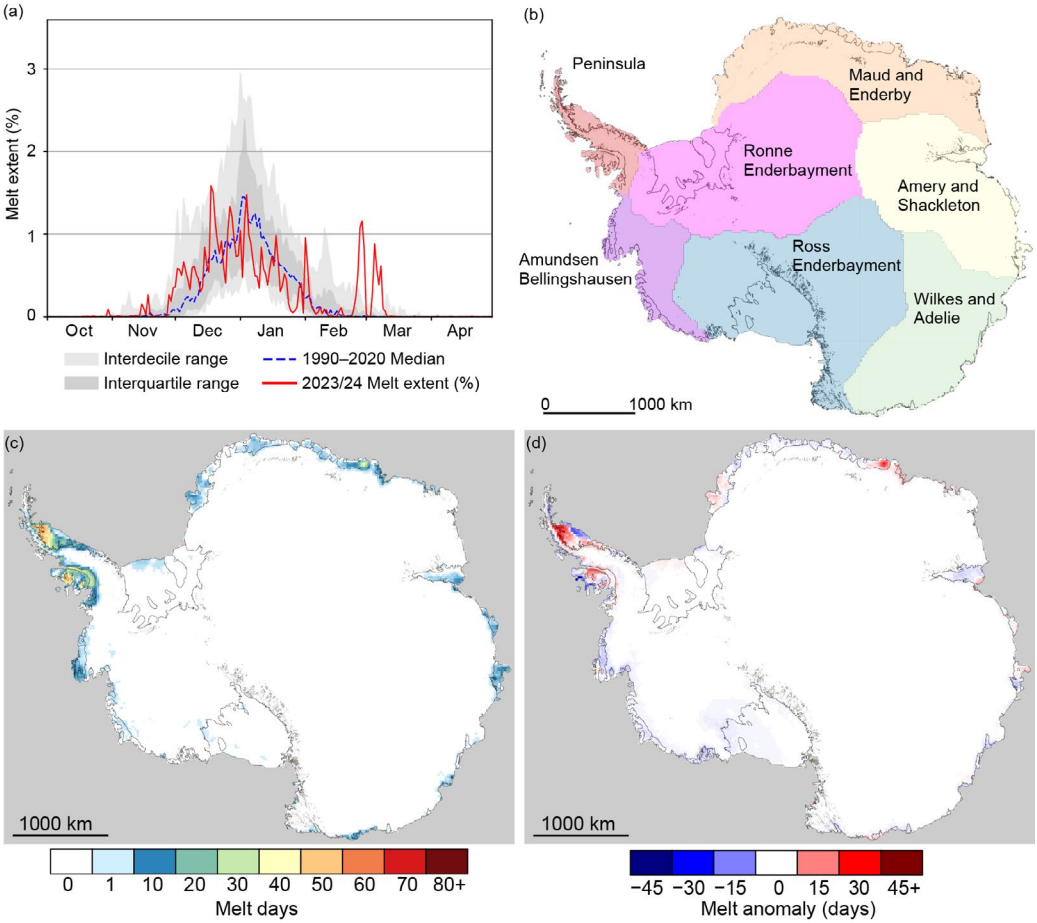

Fig. 6.7. (a) Daily surface melt extent (%; from National Snow and Ice Data Center [NSIDC]-0001, 0007) across the Antarctic Ice Sheet for the 2023/24 melt season, with 1990–2020 median values in blue and interdecile and interquartile ranges shaded in gray. (b) Reference map of Antarctic melt analysis regions, including the two shown in Fig. 6.8. (c) Map of the sum of melt days across the Antarctic Ice Sheet. (d) Map of the anomaly of the sum of melt days compared to mean values from the 1990–2020 reference period.

Unauthenticated | Downloaded 11/21/25 11:34 AM UTC

temperatures that exceed a dynamically established threshold each season from a simple microwave emission model that would be expected in the presence of liquid water in near-surface layers of ice and snowpack. The method used here was first developed to track the Greenland Ice Sheet's surface melt (Mote and Anderson 1995; Mote 2007, 2014). Large seasonal fluctuations in passive microwave emissions from some areas of dry polar firn in Antarctica can create false positive melt indications in an unmodified version of the Greenland algorithm. This was mitigated by filtering areas that only marginally exceed the melt threshold (<10K) in the 37-GHz horizontal polarization in regions with a negative 18/19-GHz minus 37-GHz frequency gradient in the vertical polarization, which has been used in previous season reports of Antarctic melt (MacFerrin et al. 2021, 2022, 2023).

According to passive-microwave satellite observations, the 2023/24 melt season recorded an overall below-average cumulative melt index (days · area) of 6.90 million km^2-days; this was about 8.6% below the median melt index of 7.55 million km^2-days during the 1990–2020 baseline period (Fig. 6.7). However, the 2023/24 melt season was punctuated by substantial spatial and temporal positive and negative anomalies in individual regions.

The Antarctic Peninsula (Figs. 6.8a,c) saw an annual melt index of 4.72 million km^2-days, 10.2% above the baseline mean value of 4.28 million km^2-days. Melt in the Peninsula was strongly affected by significant melting in late December and early January, followed by two widespread melt events in late February and early March that resulted in the northern Larsen C Ice Shelf having up to 30 days more melt than the baseline 1990–2020 median. Those late-season melt periods (28–29 February and 4–8 March 2024) broke previous daily records for areal melt extents

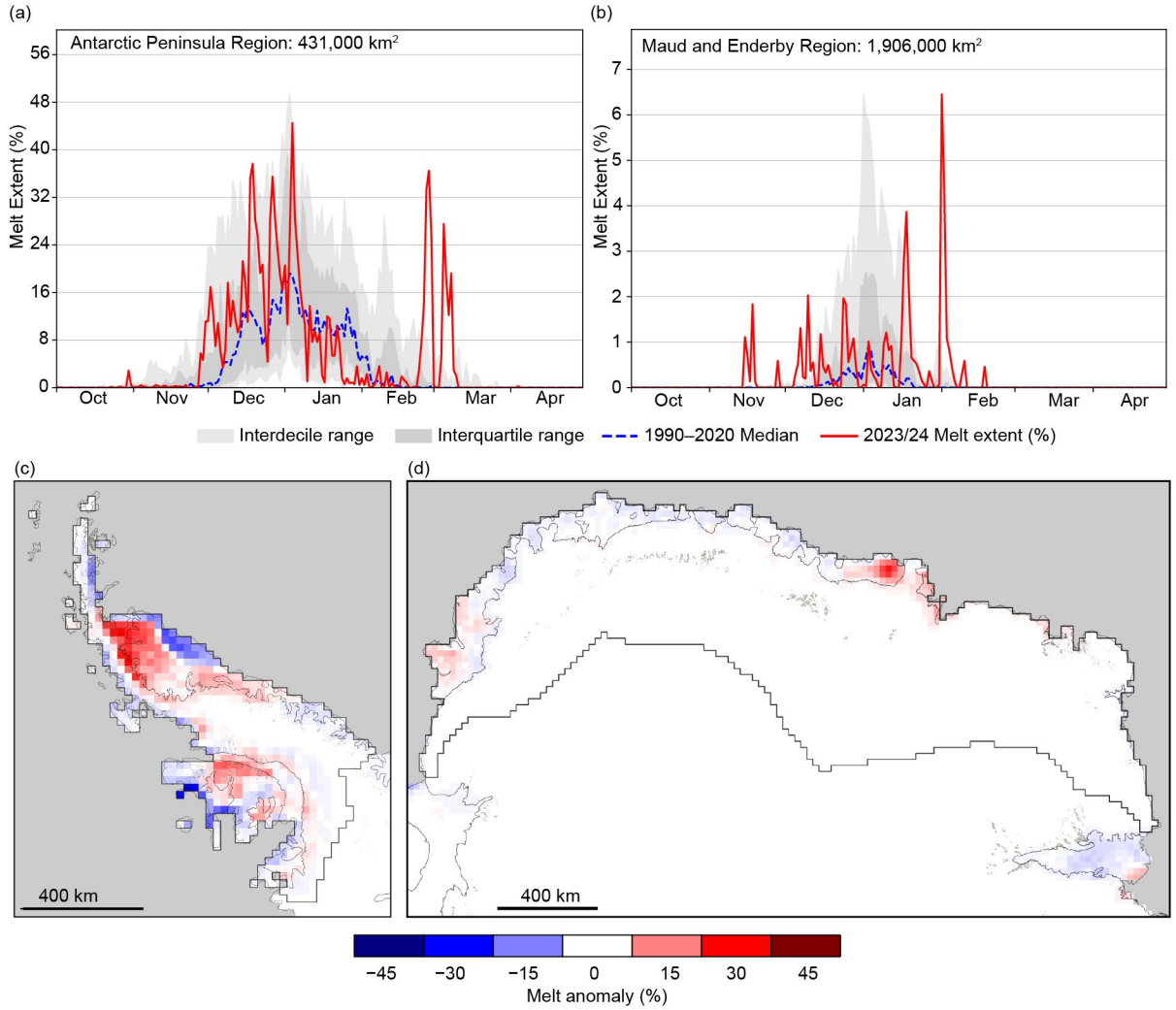

Fig. 6.8. (a),(b) Daily 2023/24 melt extent (%; from National Snow and Ice Data Center [NSIDC]-0001, 0007) over (a) the Antarctic Peninsula region and (b) the Dronning Maud Land and Enderby Land region. (c),(d) Maps of 2023/24 melt anomalies (days) over (c) the Antarctic Peninsula region and (d) the Dronning Maud Land and Enderby Land region.

Unauthenticated | Downloaded 11/21/25 11:34 AM UTC

in the satellite record since 1979, both for the Antarctic Peninsula and the continent as a whole (which is dominated by Peninsula melt; see https://nsidc.org/ice-sheets-today for details on this event).

Like the Peninsula, the Dronning Maud and Enderby Land region of Antarctica also displayed a higher-than-average melt season (Figs. 6.8b,d), recording a total melt index 24.5% more than the baseline period, with several substantial melt events from mid-November through mid-February. The Maud and Enderby region experienced a pair of relatively extensive melt events on 1 February and 18 February 2024 that broke the previous daily records for that region. Melt extent there was concentrated on the Standcomb–Brunt and Riiser–Larsen ice shelves on the eastern side of the region, and the Baudouin and Prince Harald ice shelves on the western side. Portions of the Baudouin Ice Shelf, in particular, experienced more than 30 days melt duration in excess of a median year (Fig. 6.8d).

All other regions of Antarctica experienced a melt index in 2023/24 that was lower than their baseline values, contributing to a relatively modest (8.6% below-average) melt index for the Antarctic continent.

Unauthenticated | Downloaded 11/21/25 11:34 AM UTC

e. Ice sheet mass balance

—S. Adusumilli and H. A. Fricker

The Antarctic Ice Sheet (AIS) stores 58 m of global sea level equivalent. AIS mass balance is the difference between mass gained through accumulation (snowfall minus sublimation) at the surface across the continent and mass lost around margins where ice is delivered to the ocean through its floating ice shelves. For any given time period, the net mass balance for the grounded AIS is the difference between competing processes (mass gain from accumulation and mass loss from dynamic thinning), which depends on the integrated effects of interactions between the ice, ocean, and atmosphere (e.g., Smith et al. 2020). Since 1992, the AIS has experienced overall net mass loss of grounded ice (Otosaka et al. 2023), dominated by trends in the West Antarctic Ice Sheet (WAIS), and its contribution has increased, reaching 0.32 mm of sea level rise per year between 2017 and 2020.

Three complementary techniques track grounded AIS mass changes: 1) satellite altimetry, with elevation changes combined with a firn density model; 2) mass fluxes from synthetic aperture radar (SAR) ice flow rates, ice thickness, and climate models; and 3) gravimetry (e.g., Gravity Recovery and Climate Experiment [GRACE], only for grounded ice). The European Space Agency (ESA)/NASA Ice Mass Balance Intercomparison Exercise (IMBIE) combines all three methods for robust mass change assessments (Otosaka et al. 2023). At the time of writing, there were no published estimates of total AIS mass or height change for 2024. Hence, two different techniques are used: techniques: ICESat-2 satellite laser altimetry and GRACE/GRACE Follow-On (GRACE-FO). Only grounded ice changes are considered, as altimetry-derived height changes over ice shelves at sub-annual time scales are noisy and require further processing, and gravimetry cannot detect mass changes on floating ice.

Following the same approach as used for previous years of this report (e.g., Clem et al. 2023, 2024), estimates of height changes over the grounded ice sheet were derived from NASA's ICESat-2 laser altimeter using all available data for 2024 (until 7 November 2024). The ATLAS/ICESat-2 L3B Slope-Corrected Land Ice Height Time Series, version 6 (Smith et al. 2022), which provides precise estimates of height along repeated ground tracks at 60-m along-track resolution, was used. Along-track height changes between the available data in Cycle 25 (centered around November 2024) and the corresponding data from Cycle 21 (centered around November 2023; Fig. 6.9) were derived. To analyze seasonal variability, height changes over three-month intervals between successive ICESat-2 data acquisition cycles during the November 2023 to November 2024 period (Fig. 6.10) were also derived. The final height change maps were smoothed using a Gaussian filter with a 30-km diameter.

Annual mass anomalies derived from NASA's satellite gravimeter (GRACE-FO; Fig. 6.9b) for 2024 were calculated. Data from the Jet Propulsion Laboratory GRACE and GRACE-FO Ocean, Ice, and Hydrology Equivalent Water Height Coastal Resolution Improvement (CRI) Filtered

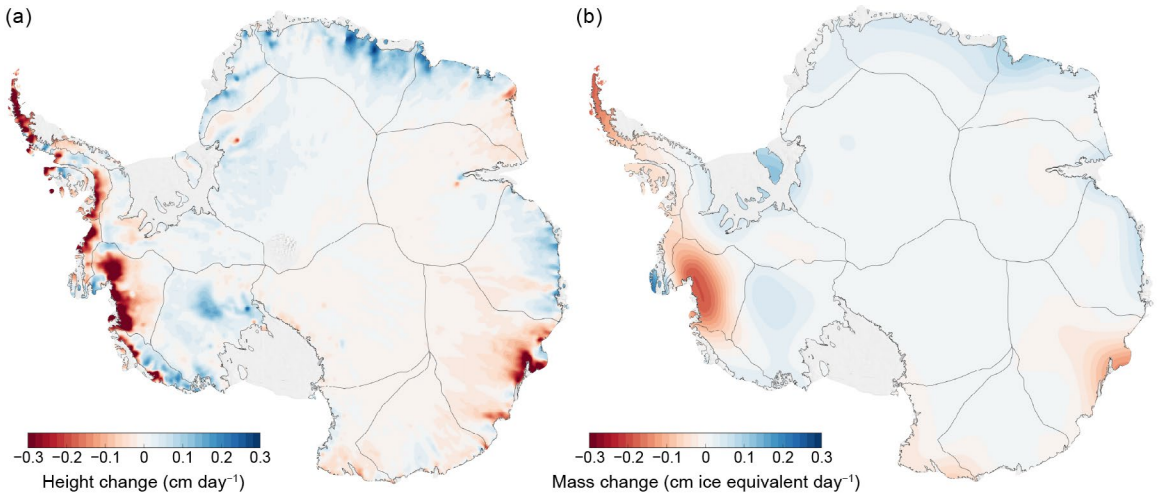

Fig. 6.9. Annual change maps for the Antarctic Ice Sheet from Nov 2023 to Nov 2024. (a) Height change from ICESat-2 (cm day^{-1}); and (b) ice equivalent mass change from Gravity Recovery and Climate Experiment Follow-On (GRACE-FO) (cm ice equivalent day^{-1}).

Unauthenticated | Downloaded 11/21/25 11:34 AM UTC

Release 06 version 02 "mascon data" was used. Mascons (or mass concentration blocks) are 3° × 3° spherical caps placed on an elliptical approximation of Earth's surface over which these data are provided (Wiese et al. 2023a). Gravity-derived mass anomalies were calculated for approximately the same period as used for ICESat-2 (November 2023 to November 2024), with the same three-month averaging. To determine ice sheet mass anomalies, all mascons containing more than 10,000 km^2 of land were identified, according to the provided CRI land mask. The area-averaged rates of change were interpolated using bilinear interpolation according to the location of the geometric center of the land area contained within the mascon. All non-land areas were then masked using the Bedmachine ice mask (Morlighem et al. 2020). Time series of mass changes integrated over the ice sheet (Fig. 6.11) from the Level 4 Antarctica Mass Anomaly Time Series data product (Wiese et al. 2023b) were also retrieved.

The maps of annual change in ice sheet height for November 2023 to November 2024 from ICESat-2 (Fig. 6.9a) and mass from GRACE-FO (Fig. 6.9b) show ongoing losses of ice in the Amundsen Sea sector of WAIS, where losses have been observed since 1992 (e.g., Smith et al. 2020; Clem et al. 2022). Continued ice loss is occurring in the Antarctic Peninsula, particularly the outlet glaciers north of central Larsen C and in the Bellingshausen Sea. In East Antarctica, continued losses at Totten Glacier are found throughout the record (Fig. 6.9b), as well as increases in snowfall/height in the Dronning Maud Land region (Fig.6.9a), especially during August to November 2024 (Fig. 6.10d).

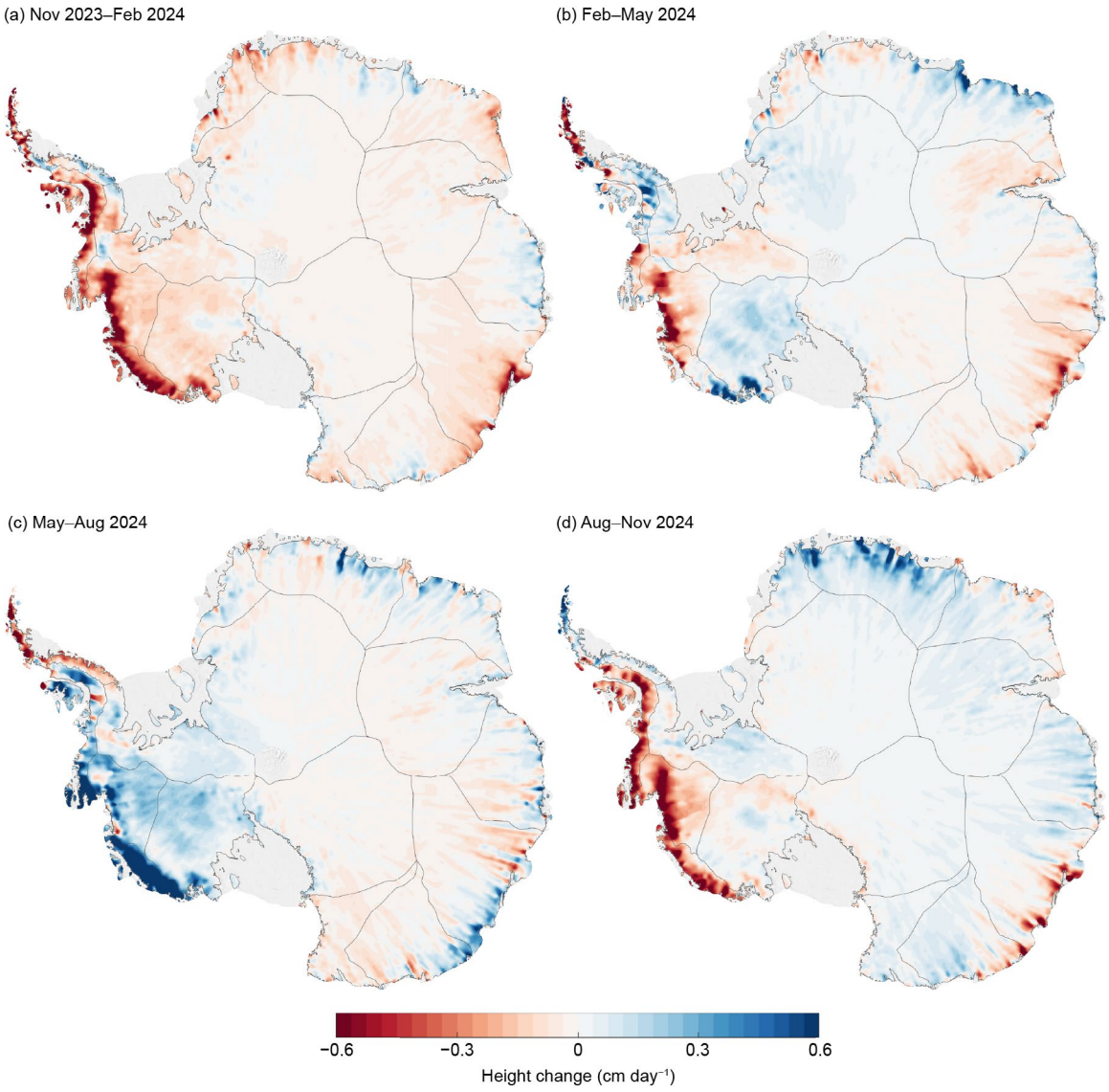

Fig. 6.10. Maps of height change from ICESat-2 shown at three-month intervals for (a) Nov 2023–Feb 2024, (b) Feb–May 2024, (c) May–Aug 2024, and (d) Aug–Nov 2024. Dates represent the central month of each three-month ICESat-2 data acquisition cycle.

Unauthenticated | Downloaded 11/21/25 11:34 AM UTC

The GRACE-FO data show a net mass loss over AIS between January and November 2024 of 125 Gt, which was slightly higher than the average annual mass loss of 100 Gt yr^{-1} between 2003 and 2023 (Fig. 6.11). Mass changes are on a similar trajectory to those in 2023 and reflect continued mass loss since the record-breaking 298 Gt mass gain that occurred in 2022. The ICESat-2 three-monthly maps (Fig. 6.10) enable the constraint of the timing of some of these larger mass fluctuations. For example, they reveal that temporal mass gains in 2023 were in part due to snow accumulation across Dronning Maud Land and a large signal in the Amundsen Sea sector and on the Siple Coast in May to August 2024, which although much lower in density, offset some of the large mass losses in coastal WAIS.

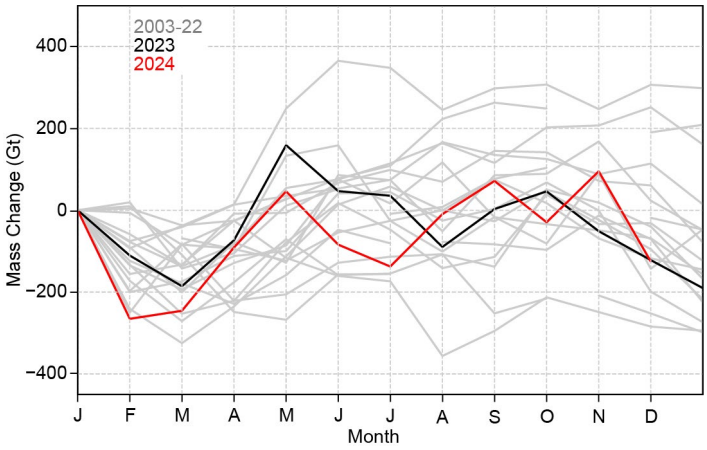

Fig. 6.11. Annual mass change (Gt) from Gravity Recovery and Climate Experiment (GRACE) and GRACE Follow-On (GRACE-FO). Time series of monthly mass changes from GRACE and GRACE-FO, with 2023 and 2024 highlighted by the black and red line, respectively.

Unauthenticated | Downloaded 11/21/25 11:34 AM UTC

f. Sea ice extent, concentration, and seasonality

—P. Reid, S. Stammerjohn, R. A. Massom, S. Barreira, T. Scambos, and J. L. Lieser

Antarctic sea ice—formed from the freezing of the ocean surface—is a critical component of Earth's climate system and biophysical environment, and performs the following functions: moderates solar heating of the ocean and the global energy budget by strongly reflecting incoming solar radiation (Riihelä et al. 2021); modulates ocean–atmosphere interactions (Josey et al. 2024); contributes to the global ocean circulation (Meredith and Brandon 2017); protects ice shelves from potentially destructive wave action (Massom et al. 2018); and serves as a key habitat for a plethora of polar species that are highly adapted to (and dependent on) its presence and seasonal rhythms (Thomas 2017).

Throughout most of 2024, both the net sea ice extent (SIE) and sea ice area (SIA—the product of sea ice extent and concentration) remained well below average or at record-low levels for the satellite time series from 1979 onwards (Fig. 6.12a). However, sea ice coverage rebounded to near-average values towards late December. The record for monthly mean low SIE for November set in 2023 (Reid et al. 2024) was broken in 2024, and several daily record lows were recorded in early September and mid-November (a number of days of record-low SIA also occurred through July to November). Antarctic coastal exposure (Reid and Massom 2022) was at record-breaking high daily values through much of January and February, at times more than twice the long-term (1991–2020) average. Similarly, the areal extent of summertime fast ice (Fraser et al. 2023) crashed to a record low (since its analysis started in 2000) during 2024. Annual daily minimum of both net SIE and SIA was recorded on 18 February (1.97×10^6 km^2 and 1.40×10^6 km^2, respectively); they were, respectively, third and second lowest on record. Annual daily maximum values of net SIE and SIA were recorded on 30 and 21 September, respectively (17.18×10^6 km^2 and 13.55×10^6 km^2), with both being the second lowest on record (behind 2023; Reid et al. 2024).

The well-below-average SIE observed in 2024 marks a continuation of the pattern of low and record-low coverage since 2016. In particular, and as with 2023 (Reid et al. 2024), overall sea ice seasonal growth in 2024 lagged well behind the long-term mean during the autumn–winter advance phase. Changes in upper-ocean conditions may be largely responsible for the increasing persistence in negative Antarctic SIE anomalies and reduced duration observed since 2016 (Cheng et al. 2022; Purich and Doddridge 2023; Raphael et al. 2025). However, the net values of SIE do not capture important regional and seasonal variations, which are outlined below.

In the lead-up to 2024 (October through December 2023), a deep Amundsen Sea Low and a general contraction of circumpolar lows enhanced northward advection of sea ice within the Ross, Amundsen, and Bellingshausen Seas to warmer waters. This led to an unusually early sea ice retreat for 2023/24, and a near-record annual daily SIE minimum that was marginally greater than the previous two summers. From January through March, Antarctic SIE was substantially below average around most of the continent, except for parts of the Amundsen, western Ross, and Weddell Seas, where SIE was slightly above average (Fig. 6.12b); sea ice concentration was anomalously high in the central Weddell Sea (Fig. 6.12c).

Sea ice conditions changed abruptly in April, when development of a zonal wave-3 atmospheric pattern (section 6b) retarded sea ice growth and advection to the east of the central low-pressure systems (~60°E, 150°E, and 60°W) while enhancing SIE to the west. As a result, SIE from April through August remained substantially below average in the Ross and eastern Weddell Seas and across much of the western Pacific (Fig. 6.12b). These regions of relatively low SIE also coincided with regions of high SST (section 6g). In particular, SIE in the eastern Weddell Sea (~10°W–60°E) was greater than five standard deviations below average. Lower sea ice growth in this region was likely influenced by a diminished Winter Water layer—a cold subsurface layer that is a remnant of the previous winter's mixed layer capped by seasonal warming and freshening (see Park et al. 1998; Sabu et al. 2020; Spira et al. 2024)—and enhanced vertical mixing of warmer waters from below. This is somewhat supported by the enhanced ocean–atmosphere heat flux in the Atlantic region of the Southern Ocean in August (Fig. 6.14d). Moreover, the stratospheric warming event in July (sections 6b, 6h) likely contributed to the substantial reductions in SIE (Fig. 6.12b) by increasing monthly averaged near-surface air temperatures across the sea ice zone off Dronning Maud Land (~15°E–30°E) by ~10°C during July–August (section 6b). Sea ice coverage in the eastern Weddell Sea remained much lower than average through to the end of

Unauthenticated | Downloaded 11/21/25 11:34 AM UTC

the year. Conversely, there was a significant expansion of sea ice across the western Pacific and western Ross Sea (~110°E–180°E) and in the Amundsen–Bellingshausen and western Weddell Seas between April and June. This sea ice advance continued in the western Weddell Sea and was particularly rapid in August (Fig. 6.12b); SIE values there exceeded four standard deviations above average, likely due to persistent cold southerly winds beginning in May. A similar albeit less pronounced rapid sea ice advance occurred in the western Ross Sea during early August. The sudden sea ice expansion within these two regions is reflected in the net SIE graph (Fig. 6.12a).

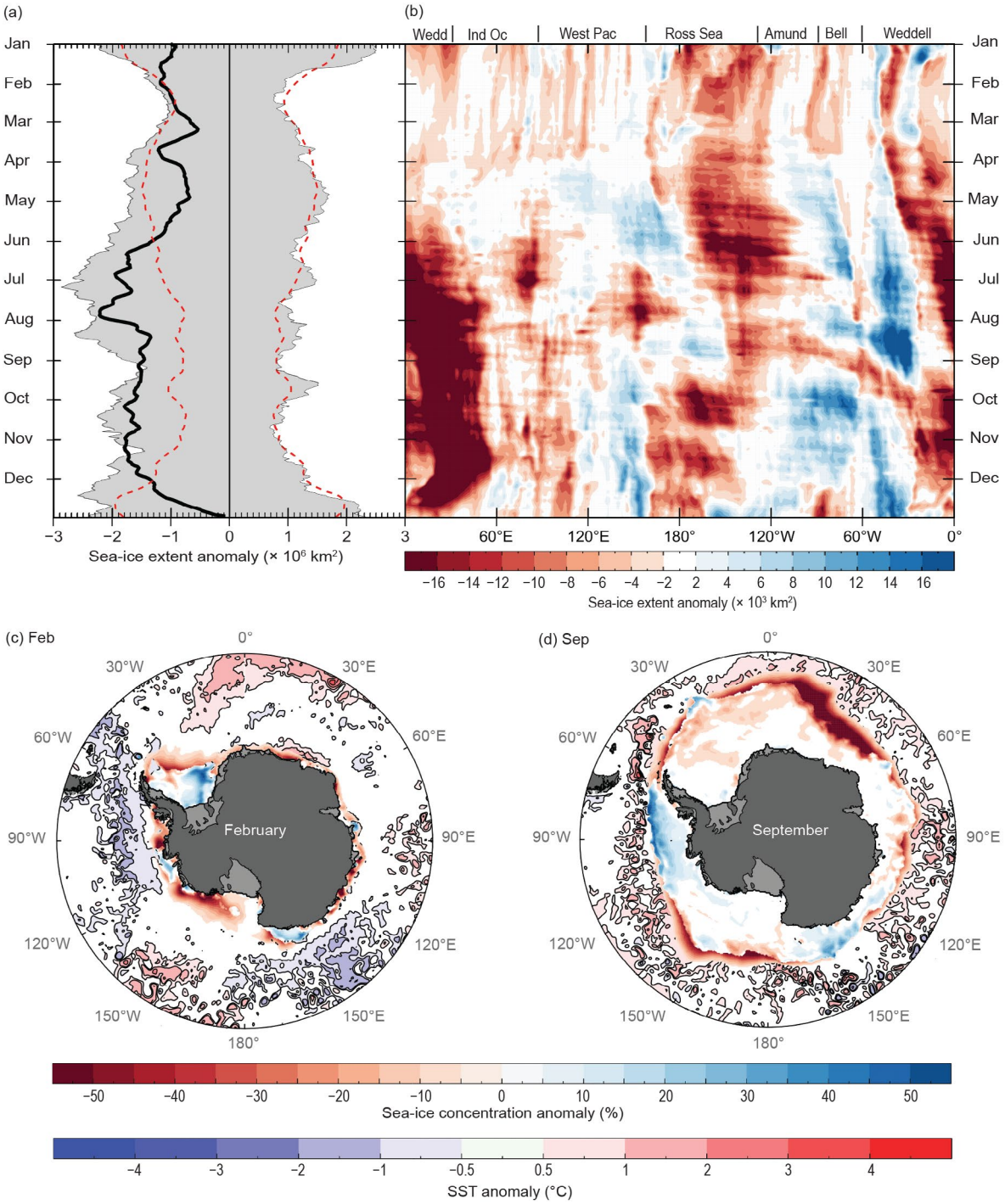

Fig. 6.12. (a) Time series of net daily sea ice extent (SIE) anomalies for 2024 (solid black line; based on a 1991–2020 climatology). Gray shading represents historical (1979–2023) daily SIE anomalies, red dashed line represents ±2 std. dev., and (b) Hovmöller (time–longitude) representation of daily SIE anomaly (× 10³ km² per degree of longitude) for 2024. Maps of sea ice concentration anomaly (%) and sea surface temperature (SST) anomaly (°C; Huang et al. 2021) for (c) Feb 2024 and (d) Sep 2024. Sea ice concentration is based on satellite passive-microwave ice concentration data (Cavalieri et al. 1996, updated yearly for climatology; Maslanik and Stroeve 1999 for the 2024 sea ice concentration). See Fig. 6.1 for relevant place names.

Unauthenticated | Downloaded 11/21/25 11:34 AM UTC

Regional patterns of sea ice coverage changed again in September in response to a marked shift in large-scale atmospheric circulation (section 6b). The formation of the deep low-pressure anomaly over the Antarctic Peninsula and the southwestern Pacific (~150°E) combined with high-pressure systems over the eastern Ross and eastern Weddell Seas (Fig. 6.2e) ushered warmer northerly winds and surface waters into the Ross and western Weddell regions to reduce sea ice coverage there. In the Bellingshausen and Amundsen Seas, as well as north of Victoria Land at ~150°E (Fig. 6.12d), a late surge in seasonal sea ice growth reversed the early September record lows, producing a late annual daily SIE maximum. This positive SIE anomaly in the Amundsen–Bellingshausen Seas intensified in October and persisted into December (Fig. 6.12b).

During November and early December, regional sea ice coverage was strongly influenced by a southward contraction of the circumpolar westerlies associated with the strongly positive Southern Annular Mode (SAM) phase (section 6b), followed by a northward expansion of the westerlies (reflecting a negative SAM) in late December (section 6b). These shifts led to a lack of storm activity along the sea ice edge, which was not conducive to broad-scale sea ice retreat. Although net SIE briefly reached record-low values in early November, it was close to average by the end of December (Fig. 6.12a). This net average, however, comprises the sum of distinctly different regional components (Fig. 6.12b). Notably, the eastern Weddell Sea continued to exhibit greatly reduced sea ice cover (a pattern that began in May) and early annual retreat, along with parts of East Antarctica (~90°E–110°E), the Ross Sea (~160°E–190°W), and the Bellingshausen Sea in late December. Elsewhere, SIE remained above average, most notably in the western part of the western Pacific sector, the western Ross Sea, and the western Weddell Sea (Fig. 6.12b).

In parallel with SIE and SIA, the timings of annual sea ice advance and retreat, and resultant duration of coverage (where a sea ice year here is mid-February 2024 to mid-February 2025 [Stammerjohn et al. 2008]), show distinct regional anomalies (Fig. 6.13) that mirror those of the SIE and SIA records for 2024 (Fig. 6.12b). Annual sea ice advance was delayed by 30 days–60 days (compared to the 1991/92–2020/21 mean) across extensive tracts of the central Weddell Sea, extending eastwards across the Indian and western Pacific Ocean sectors, and the central Ross Sea through the Amundsen Sea (Fig. 6.13a). In contrast, advance was as much as 30 days–60 days earlier in the northwestern Weddell Sea, the western Antarctic Peninsula region, and across an inner band off East Antarctica (east of ~90°E–~170°W; Fig. 6.13a). The retreat pattern was patchier but mostly aligned with the advance pattern, with the

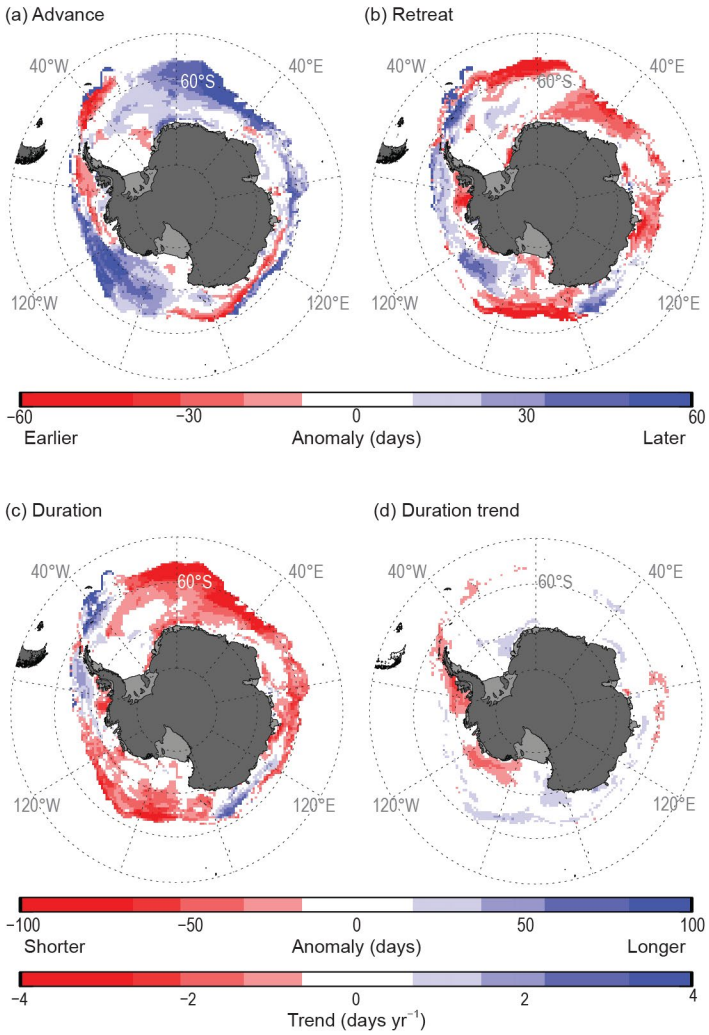

Fig. 6.13. Maps of seasonal sea ice anomaly (days) in 2024 during (a) autumn ice-edge advance, (b) spring ice-edge retreat, and (c) winter ice season duration; together with (d) winter ice season duration trend (days yr^{-1}; Stammerjohn et al. 2008). The seasonal anomalies (a)–(c) are computed against the 1991/92–2020/21 climatology; the trend (d) is computed over 1979/80–2024/25. The climatology (for computing the anomalies) is based on data from Comiso (2017; updated yearly), while the 2024/25 ice-edge retreat duration-year data are from the NASA Team Near-Real-Time Defense Meteorological Satellite Program Special Sensor Microwave Imager Sounder Daily Polar Gridded Sea Ice Concentrations (NRTSI) dataset (Maslanik and Stroeve 1999); the trend is based on the merged dataset containing 1979–2023 data from Comiso (2017) and 2024/25 data from the NASA Team NRTSI dataset (Maslanik and Stroeve 1999).

Unauthenticated | Downloaded 11/21/25 11:34 AM UTC

retreat being earlier (later) by 30 days–60 days where the advance was later (earlier) by 30 days–60 days. The exception was the eastern Ross Sea and outer Amundsen Sea, where the advance and retreat were both later. Seasonality maps show the marked passage of Iceberg A23a (Figs. 6.13a–c; see Sidebar 6.1). Studies have suggested an increase in sea ice concentration and thickness due to iceberg melt, so it is possible that A23a is having an influence (Merino et al. 2016; Haid et al. 2017), although analysis around Iceberg A68 (Meredith et al. 2023) suggests this to be quite localized.

The continuation during 2024 of the recent (post-2016) reduced net sea ice coverage provides further observational support of a transformation in the atmosphere–ocean–sea ice interaction system, which points to an overall decline in sea ice due to a warmer global climate.

Unauthenticated | Downloaded 11/21/25 11:34 AM UTC

Sidebar 6.1: How to train your iceberg: Iceberg A23a drift track in 2024

—T. SCAMBOS, C. SHUMAN, P. REID, A. MEIJERS, M. MEREDITH, AND J. LIESER

Movement of the trillion-ton iceberg A23a in 2024 illustrated several processes that have only recently been appreciated as key drivers of large iceberg drift. Foremost among these are the Taylor Column effects beneath the ice plate (see explanation below), which causes the iceberg's movement to respond to bathymetric features far below the base of the ice (Stern et al. 2019). Another is iceberg spin, related to ocean surface slope oscillations due to the tidal cycle and the variations in thickness across the ice plate (MacAyeal et al. 2008; Scambos et al. 2008).

Iceberg A23a calved in 1986 from the Filchner Ice Shelf ice front, as a large rift named the "Grand Chasm" by explorers in the 1950s finally separated completely, releasing three large icebergs spanning the Filchner front (Ferrigno and Gould 1987), from west to east: A22, A23a, and A24. The much smaller A25 south of the three was also released. Originally, A23a was nearly 4000 km^2 and ~400 m thick. It drifted about 200 km northward and ran aground (Swithinbank et al. 1988; Griggs and Bamber 2011), and for the next 34 years moved very little, before finally drifting free in June 2020 (Barbat et al. 2021). In 2023 it moved northward along the continental slope break to the east of the Antarctic Peninsula, pushed along by the Weddell Gyre.

As 2024 began, A23a was northeast of the tip of the Antarctic Peninsula, about 150 km east of Elephant Island. Drift progressed to the east and northeast, with the iceberg also rotating about once every 25 days, although there were long periods of more rapid eastward transit where the iceberg moved laterally without rotating (NASA Worldview MODIS data, https://worldview.earthdata.nasa.gov).

Around 1 April 2024, A23a entered an area of trapped counterclockwise ocean flow centered over Pirie Bank, north of the South Orkney Islands (Fig. SB6.1). This trapped vortex is characterized as a Taylor Column, a rotating cylinder of water that, under the right flow conditions, can be created above a topographic obstacle in a rotating fluid (Taylor 1922). Such columns are widely known in fluid dynamics experiments and have been observed in atmospheric and oceanic environments above mountains and seamounts, respectively. They are believed to be widespread across the more topographically rugged regions of the Southern Ocean, for example at Maud Rise in the Weddell Sea, but also across various locations including the seamounts that comprise the South Scotia Ridge, one of which is Pirie Bank (Meredith et al. 2015). By early June, A23a had shifted about 75 km to the northwest and began a new pattern of oscillations for the next four months, likely reflecting the impact of time-varying incident ocean flow on the complex shape of the bathymetry.

Still another form of topographic control on iceberg drift can be caused by the keel depth of the iceberg itself in areas of flatter underlying oceanographic terrain. Recent studies have pointed out the strong relationship between sections of iceberg drift tracks and deep bathymetric topography, with the moving iceberg steered in a way that avoids higher ridges or slopes (i.e., conserves potential vorticity in the column of water beneath the iceberg; Neuhaus and MacAyeal 2012; Scambos et al. 2024). Movement of A23a in mid-2023 along the eastern edge of the Antarctic Peninsula's continental slope and around Powell Basin in the northern Weddell Sea was likely guided by this process, as many other icebergs have been (Li et al. 2017).

A further process controlling iceberg flow on a daily to monthly scale is ocean tides. In the open ocean, tides are manifested as a cyclical change in ocean surface slope, typically in the range of a few parts in 10^{-4}. Like a surfboard, the iceberg slides downward on the ocean slope. The net effect of the daily tidal cycle is a circular iceberg movement that varies in amplitude with the bi-weekly tidal cycle, which is observable in the drift tracks of icebergs (Fig. SB6.2) with daily Global Navigation

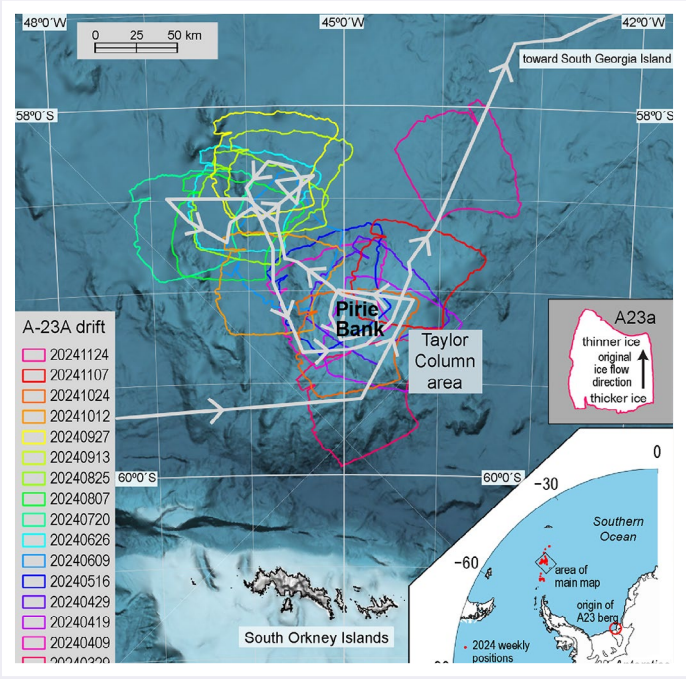

Fig. SB6.1. Bathymetric map of the region near Pirie Bank showing outlines of Iceberg A23a for several dates in 2024. Drift track with weekly positions of A23a shown as a gray line, with arrows showing drift direction. Lower right inset shows weekly positions of A23a for all of 2024 and original calving location of A23a on a regional map of Antarctica and the Southern Ocean; above that is an inset showing A23a outline with original orientation relative to ice flow on the Filchner Ice Shelf.

Unauthenticated | Downloaded 11/21/25 11:34 AM UTC

Satellite System (GNSS) data (MacAyeal et al. 2008; Scambos et al. 2008; Martin et al. 2010). Moreover, as part of this effect, the iceberg can be rotated based on the varying thickness of the ice across it, with the thicker (and therefore heavier) side tending to lead a bit more in the downslope direction. However, the response of large icebergs, like A23a, is generally too slow relative to the pace of tidally-driven ocean slope aspect change to execute daily rotations due to tides. Ocean current gradients and non-tidal sea surface slope variations further affect rotation and drift; thus, the observed rotation is complex and non-steady, particularly in the filamented and eddy-rich Antarctic Circumpolar Current.

Following the extended interaction with the Taylor Column above Pirie Bank, A23a drifted towards South Georgia in early 2025, threatening to run aground on its shoals and potentially disrupt the abundant ecosystems there as A38 did when it grounded there in 2004. Later in its evolution, A23a will succumb to basal thinning, flexure by long-period ocean waves, and meltwater-driven hydrofracture, leading to rapid calving and disintegration.

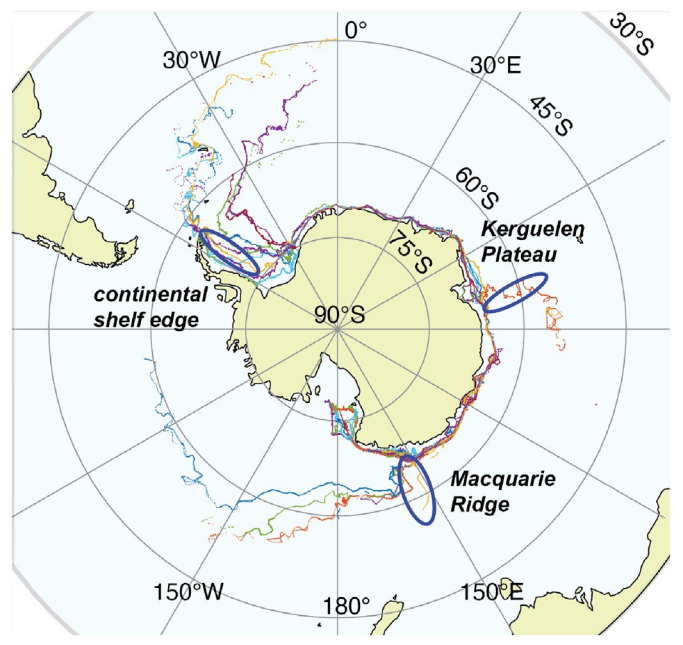

Fig. SB6.2. Map of the drift tracks of all major calved pieces of Icebergs B-15 and C-19—two of the largest icebergs in the historical record that calved from the Ross Ice Shelf front in 2000 and 2002, respectively—serving as an illustration of typical drift paths of Antarctic tabular icebergs. Drift track orientations are affected by deep bathymetry throughout the Southern Ocean; three bathymetric features where icebergs are guided out of westward circumpolar drift are labeled. Drift track data from Budge and Long (2018).

Unauthenticated | Downloaded 11/21/25 11:34 AM UTC

g. Southern Ocean

—S. J. Thomalla, A. M. Hancock, R. L. Beadling, A. Josey, J. Milward, A. Mohamed, L. P. Pezzi, M. du Plessis, T. J. Ryan-Keogh, C. Schulz, J-R. Shi, and E. Souza

The Southern Ocean (SO) plays a disproportionately large role in regulating Earth's climate through the uptake of heat and carbon dioxide (CO_2; Frölicher et al. 2015). The SO drives global ocean circulation and supplies oxygen to the deep ocean and nutrients worldwide (Oschlies et al. 2018; Henley et al. 2020). The SO is undergoing rapid change culminating in substantial warming and record-low sea ice extent, with cascading impacts on ocean biogeochemistry (Beadling et al. 2022; Pezzi et al. 2023; Thomalla et al. 2024). Here, the state of the SO in 2024 is assessed, with focus on a suite of physical and biogeochemical properties that influence SO ventilation and its capacity to take up heat and carbon. In 2024, the SO experienced substantial warming, continuing the warming trend of recent years (Cai et al. 2023) with ocean heat content (OHC) reaching its highest level to date. In some sectors, higher-than-usual salinities and shallower mixed layers were associated with a shift toward a negative Southern Annular Mode (SAM) from August to December (section 6b). Ocean biogeochemistry responded with elevated summer chlorophyll and lower surface oxygen in the Atlantic and eastern Pacific. These findings underscore the consequences of evolving atmosphere–ocean dynamics, reinforcing the SO's critical role in regulating climate.

1. SEA SURFACE TEMPERATURE, SALINITY, AND MIXED-LAYER PROPERTIES

Anomalies for 2024 (relative to a 1991–2020 climatology) were calculated for sea surface temperature (SST) from the NOAA monthly Optimum Interpolation product (Reynolds et al. 2002). Anomalies were calculated for sea surface salinity (SSS) and mixed-layer depth (MLD; according to de Boyer Montegut et al. 2004) from the Argo dataset (Roemmich and Gilson 2009), relative to a 2004–20 climatology. Abnormally warm surface waters prevailed across most of the SO, with positive SST anomalies (+0.4°C to +1.5°C; Fig. 6.14a) persisting throughout the year, following the warming tendency of previous years (Beadling et al. 2022; Pezzi et al. 2023; Thomalla et al. 2024). This was most notable in the western Pacific from February to July (Fig. 6.14e). The exceptions were the eastern Pacific, along the west coast of South America, and Drake Passage, where negative anomalies (−0.3°C to −0.6°C) reveal surface cooling in February and March (Fig. 6.14e). Positive anomalies in SSS (up to 0.20 PSU) dominate large parts of the SO (Fig. 6.14b), especially in spring, with the most extreme (~0.12 PSU) occurring in the Atlantic sector (Fig. 6.14f). These positive SSS anomalies typically occur north of the Subantarctic Front (SAF) and along the southern edge of subtropical gyres (STGs), possibly indicative of a strengthened gyre and enhanced salt import into the SO. A spin up of the STG was expected for the latter half of the year coinciding with the predominantly negative SAM phases. Weak negative anomalies in SSS were observed in summer/autumn (January–May), predominantly due to anomalies in the western Pacific (Fig. 6.14f) north of the SAF (Fig. 6.14b). The pattern of MLD anomalies in the SO is starkly different from recent years (2021–23), where persistent positive anomalies reflected deeper MLDs in the East Pacific (Beadling et al. 2022; Pezzi et al. 2023; Thomalla et al. 2024). In 2024, both Pacific sectors instead show significant shoaling of MLDs with negative anomalies north of the SAF and in the Indian sector south of Australia (Fig. 6.14c). For most sectors the onset of negative MLD anomalies occurred in May/June and peaked in August/September. This seasonal pattern aligns with the timing of positive SSS anomalies when the SAM shifted into a persistent negative phase favoring shallower MLDs when the westerlies shift equatorward into subtropical regions of anomalously positive SSS.

2. AIR–SEA HEAT FLUX

The 2024 net air–sea heat flux anomaly was determined using monthly mean ERA5 reanalysis (Hersbach et al. 2020) relative to the 1991–2020 climatology. Higher-than-average air–sea fluxes occurred across most of the subpolar SO, depicting anomalous ocean heat gain. Negative heat fluxes in the lower latitudes of the Atlantic (Fig. 6.14d) suggest anomalous ocean cooling in winter (Fig. 6.14h). North of the SAF, the imprint of ocean mesoscale variability on the air–sea flux is evident in alternating positive and negative anomalies, particularly in the Algulhas Retroflection region of South Africa extending into the Indian sector along ~60°S (Fig. 6.14d).

Unauthenticated | Downloaded 11/21/25 11:34 AM UTC

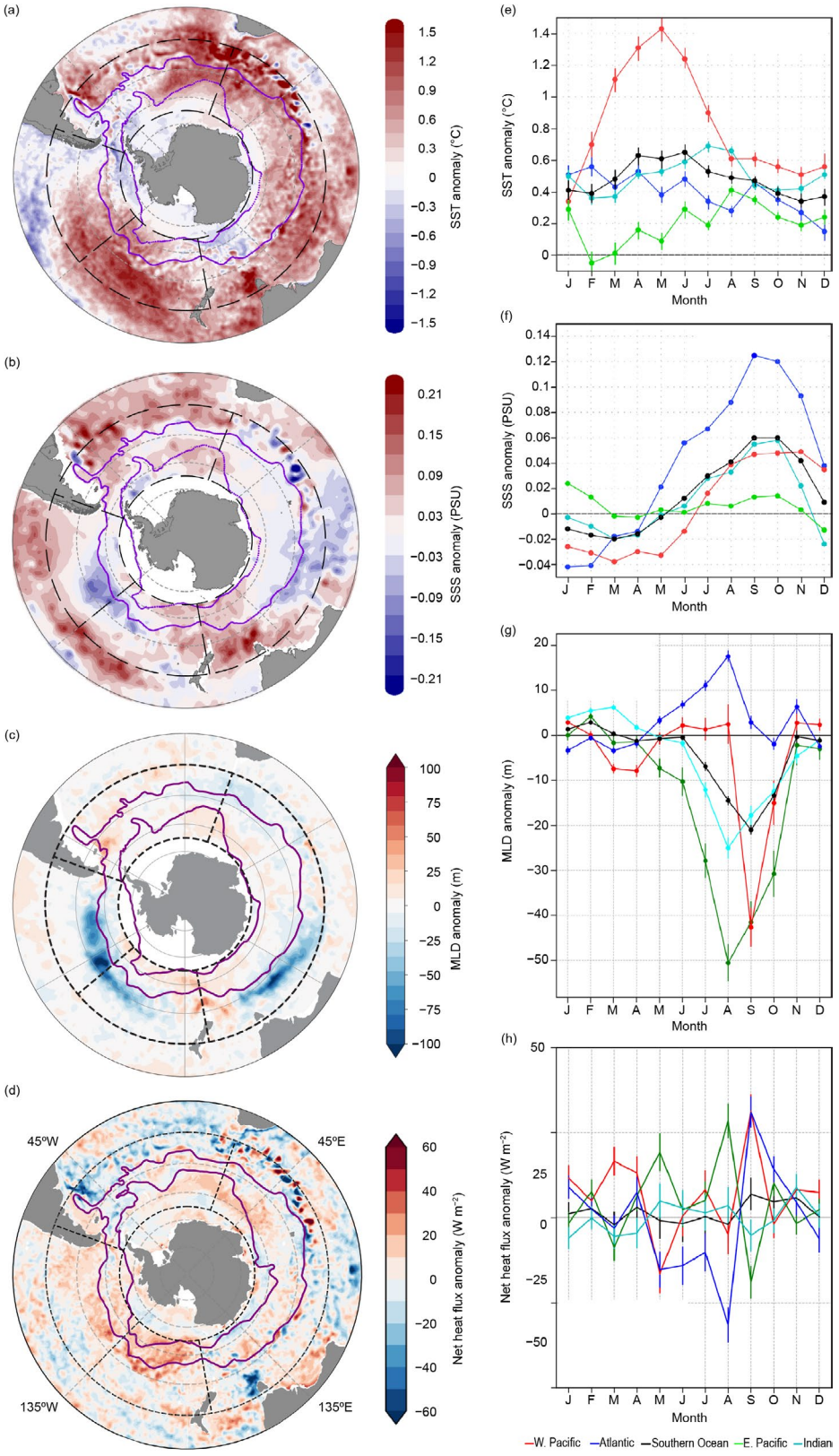

Fig. 6.14. Annual average (Jan–Dec 2024) anomalies of Southern Ocean (a) sea surface temperature (SST; °C; relative to 1991–2020 climatology), (b) sea surface salinity (SSS; PSU), (c) mixed-layer depth (MLD; m; relative to 2004–20 climatology), and (d) net heat flux (W m^{-2}; relative to 1991–2020 climatology). Overlaid are the positions of the Subantarctic and Southern Boundary Antarctic Circumpolar fronts (purple lines) as defined by Orsi et al. (1995). Four distinct sectors between 40°S and 65°S are delineated by black dashed contours corresponding to the Atlantic (70°W–20°E), Indian (20°E–170°E), western Pacific (170°W–120°W), and eastern Pacific (120°W–70°W). The 2024 seasonal cycle of anomalies in (e) SST (°C), (f) SSS (PSU), (g) MLD (m), and (h) net heat flux (W m^{-2}) are separated according to the four sectors defined above. Error bars in (e), (g), and (h) represent the standard error of the climatological mean (i.e., std. dev. divided by √N, where N is the number of years in the climatology).

Unauthenticated | Downloaded 11/21/25 11:34 AM UTC

Additional cooling in winter is also to be expected at high latitudes close to the Antarctic, as ongoing sea ice declines have recently been shown to substantially increase winter ocean heat loss to the atmosphere (Josey et al. 2024). Averaged across the SO, the mean net air–sea heat flux was 1.5 W m^{-2} higher than the climatology, albeit with considerable variability within the different sectors. In particular, the east Pacific and Atlantic sectors displayed large monthly mean heat flux changes in spring that exceed 30 W m^{-2} and 50 W m^{-2}, respectively (Figure 6.14h). The SO heat flux asymmetry index (Josey et al. 2023), which measures the difference in Atlantic–Indian and Pacific sector surface heat exchange, was –0.96 in 2024, which is a slight weakening of the degree of asymmetry relative to the 2023 value of –1.48.

3. UPPER-OCEAN HEAT CONTENT

The 0 m–2000 m upper OHC was retrieved from monthly gridded Argo temperature data (Roemmich and Gilson 2009) with 2024 anomalies determined relative to the 2004–20 climatology. The upper ocean gained heat in 2024 (Fig 6.15a) with positive OHC anomalies mainly north of the SAF. The upper ocean cooling observed in the eastern Pacific in 2023 (Thomalla et al. 2024), became neutral in 2024, with most of the SO exhibiting positive OHC anomalies (increased by 4.1 ZJ compared to 2023). Based on the records from the past two decades, the time series of the OHC anomaly shows long-term warming since 2005, reaching its highest level to date in 2024 (Fig. 6.15b).

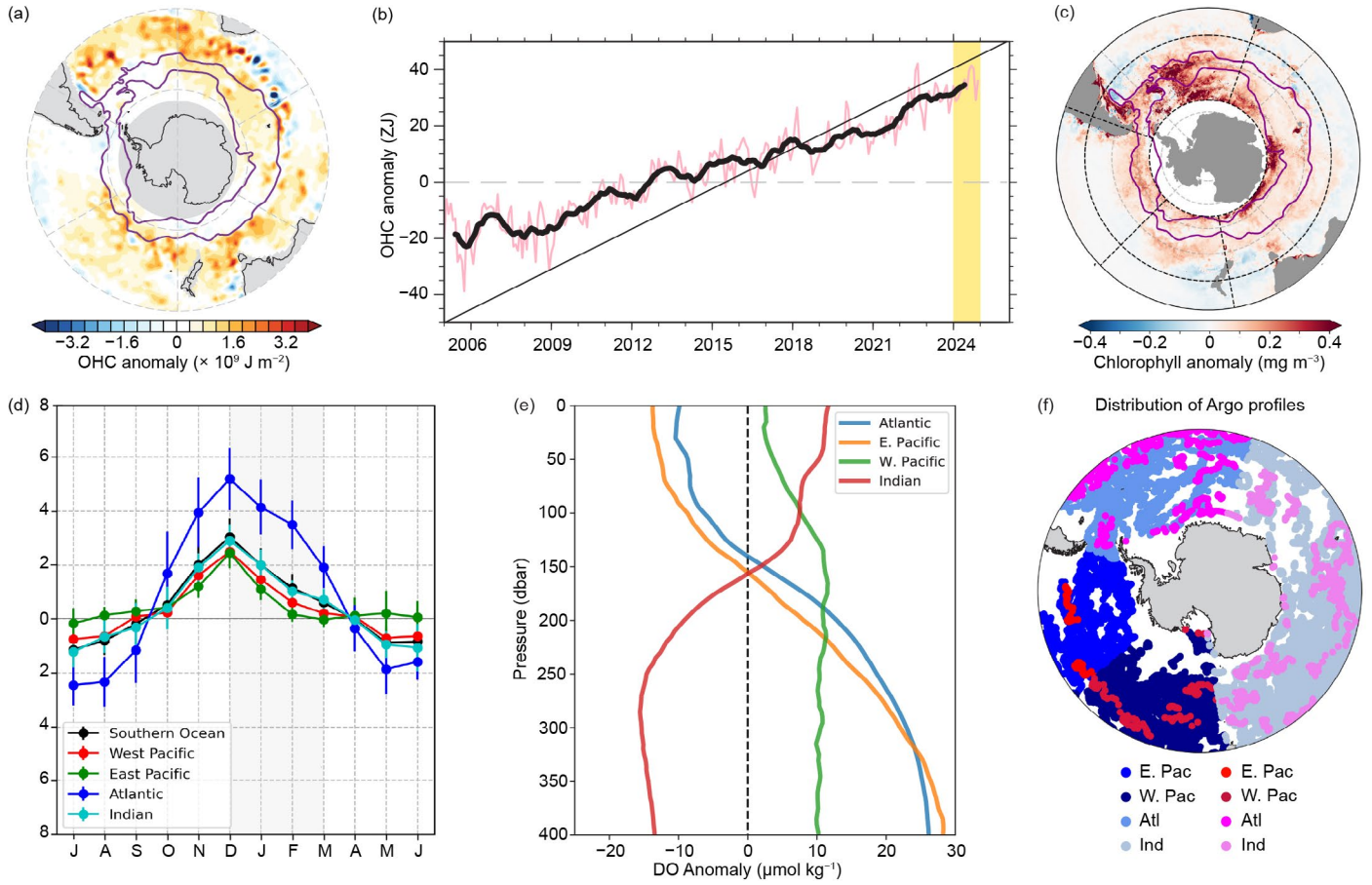

Fig. 6.15. (a) 2024 annual average ocean heat content (OHC; × 10^9 J m^{-2}) anomalies. (b) Time series of monthly average 0 m–2000 m OHC anomaly (ZJ or 10^{21} J) relative to 2004–20 Argo climatology within 40°S–65°S (red line) with 12-month running mean on top (black line) and 2024 highlighted (yellow shading). (c) Annual average (Jul 2023–Jun 2024) anomalies of eight-day, 4-km chlorophyll (mg m^{-3}) relative to 1999–2020 climatology and (d) the 2024 seasonal cycle of anomalies for the Atlantic (70°W–20°E), Indian (20°E–170°E), western Pacific (170°W–120°W), and eastern Pacific (120°W–70°W) between 40°S and 65°S. Error bars represent the standard error of the climatological mean (i.e., std. dev. divided by √N, where N is the number of years in the climatology). Overlaid on (a) and (c) are the Subantarctic and Southern Boundary Antarctic Circumpolar fronts (purple lines) as defined by Orsi et al. (1995). (e) Dissolved oxygen (DO) anomalies (μmol kg^{-1}) with pressure (dbar) for Jul 2023–Jun 2024 relative to the 2004–20 Argo climatology. (f) Distribution of Argo profiles from 2004–20 for the different ocean sectors (blues) relative to the distribution of profiles for the 2023/24 period (pinks and red).

Unauthenticated | Downloaded 11/21/25 11:34 AM UTC

4. OCEAN BIOGEOCHEMISTRY

Chlorophyll data from the eight-day European Space Agency Ocean Colour Climate Change Initiative (OC-CCI) product (v6.0; Sathyendranath et al. 2019) were processed as per Thomalla et al. (2023) with 2024 anomalies computed relative to the 1999–2020 climatology. Positive anomalies dominated the SO south of the SAF (Fig. 6.15c) in austral summer (Fig. 6.15d), most notably in the Atlantic (Weddell Gyre and east coast of South America) and Indian (south of 60°S) sectors, where higher-than-usual chlorophyll concentrations occurred (anomalies up to 0.4 mg m^{-3}). Weaker negative anomalies (<0.2 mg m^{-3}) were more persistent north of the SAF (Fig. 6.15c) in autumn (Fig. 6.15d). Anomalies in dissolved oxygen (DO) for 2024 (relative to 2004–20 climatology) were derived per ocean basin from BGC-Argo (Wong et al. 2020). The Indian sector showed positive DO anomalies from the surface to ~150 m, consistent with 2023 (Fig. 6.15e). In the Atlantic, where positive anomalies in chlorophyll were largest, DO anomalies were instead negative near the surface and positive below 150 m (Fig. 6.15e), indicating that the large positive SST anomalies are more likely driving the surface signal in DO. In the eastern Pacific, DO profiles were biased toward lower latitudes (Fig. 6.15f), where muted chlorophyll anomalies make SST anomalies the likely driver of negative DO anomalies near the surface. In the western Pacific, low positive anomalies persist from the surface to 400 m, likely influenced by positive chlorophyll anomalies or by profiles near the continent (Fig. 6.15f).

Unauthenticated | Downloaded 11/21/25 11:34 AM UTC

h. 2024 Antarctic ozone hole

—L. R. Lait, P. A. Newman, N. A. Kramarova, B. Johnson, M. L. Santee, I. Petropavlovskikh, L. Coy, and J. De Laat

The 2024 Antarctic ozone hole ranked in the lower third in severity (26th largest area over 32 years of observations) during the period of full ozone hole development (1992–present). The 2024 ozone hole had an average of 19.6 million km^2 average area (averaged 7 September–13 October). In 2024 the daily minimum average over 21 September–16 October was 121 Dobson units (DU; 23rd highest), 5 DU higher than the average of the 1992–2023 minimum averages. The 2024 ozone hole appeared later than average and reached 22.4 million km^2 in area on 28 September, in contrast to the record 29.9 million km^2 on 9 September 2000.

The 2024 Antarctic polar vortex evolution was relatively normal in early winter. May 2024 water vapor was higher than average inside the developing vortex because of the January 2022 Hunga volcanic eruption (Fig. 6.16b, purple line). As in 2023 (Kramarova et al. 2024; Santee et al. 2024), in 2024 water vapor abundances started high (Fig. 6.16b), but dehydration led to values only slightly above average by August. Polar cap (60°S–90°S) temperature in the stratosphere (50 hPa)

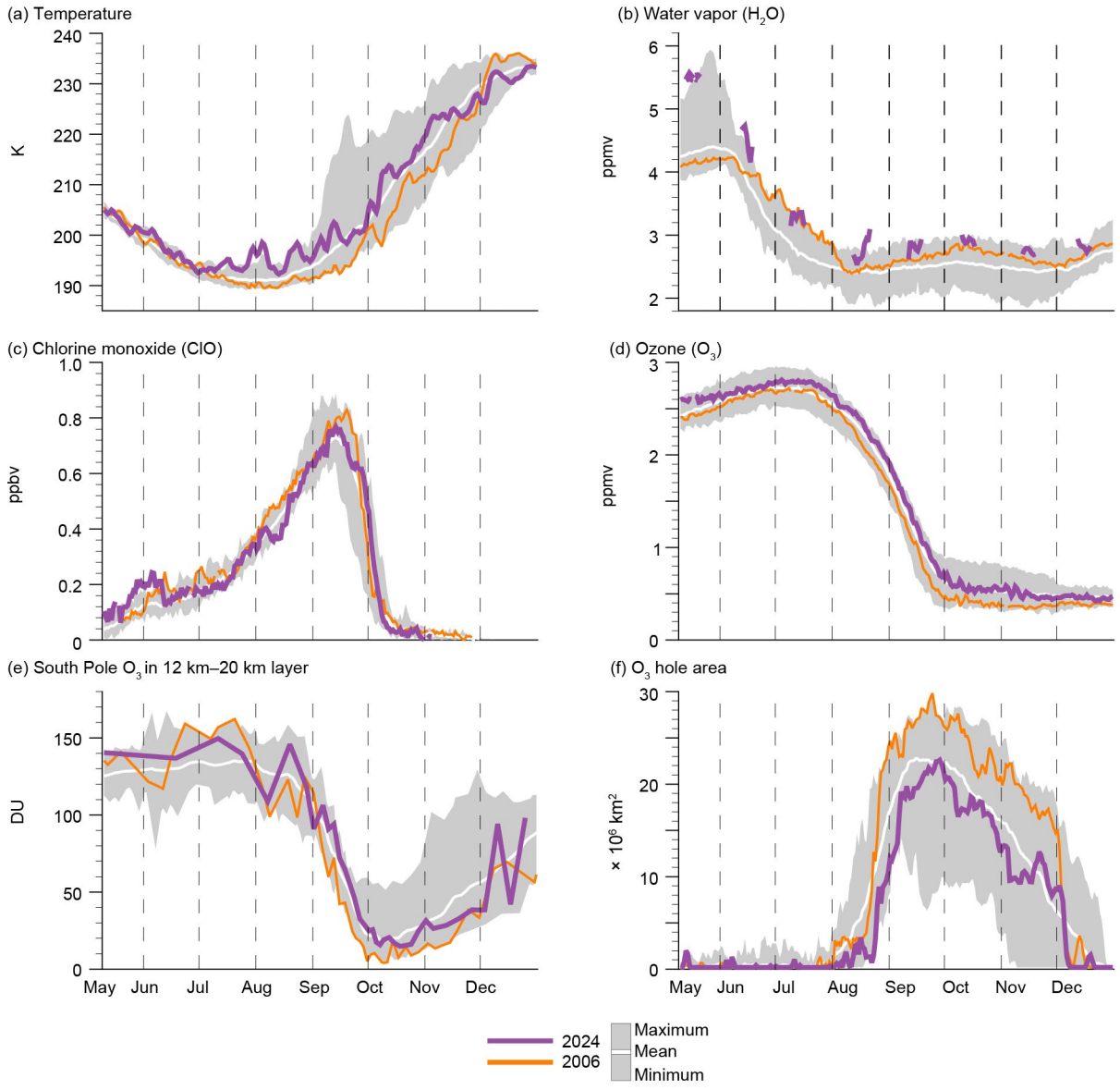

Fig. 6.16. Antarctic (a) polar cap temperature (K) at 50 hPa (~20 km or 60 hPa, averaged 60°S–90°S) from MERRA-2. Aura Microwave Limb Sounder (MLS; updated from Manney et al. 2011) 440-K potential temperature surface (b) water (H_2O; ppmv), (c) chlorine monoxide (ClO; ppbv), and (d) ozone (O_3; ppmv). (e) Lower-stratospheric ozone columns (12 km–20 km; DU) based on sonde measurements at South Pole. (f) Ozone Monitoring Instrument (OMI)/Ozone Mapping and Profiler Suite (OMPS) Antarctic ozone hole area (× 10^6 km^2; area with ozone total column less than 220 DU). Gray shading shows daily Antarctic value ranges for 2005–23 (for [d], the data cover 2006–23). The white lines indicate the 2005–23 long-term means.

Unauthenticated | Downloaded 11/21/25 11:34 AM UTC

was above average during late July and August (Fig. 6.16a). This above-average temperature slightly limited dehydration, resulting in above-average H_2O in June–December. There were no 2024 polar stratospheric cloud (PSC) measurements because the NASA Cloud–Aerosol Lidar and Infrared Pathfinder Satellite Observations (CALIPSO) lidar instrument ceased operation in June 2023.

Stratospheric wave driving from the troposphere (not shown) was anomalously large in mid-winter, warming the vortex and reducing the polar night jet's strength. Stratospheric wave driving is proportional to the eddy heat flux, which was relatively normal until mid-May. An extremely strong wavenumber-2 Rossby wave developed during mid-May to mid-August, increasing the heat flux (not shown). This wavenumber-2 pattern warmed the Antarctic stratosphere from late July to early August 2024 (section 6b). The wave-2 amplitude hit a global daily record high of 1511 geopotential meters (gpm) on 5 August at 10 hPa and exceeded 900 gpm from 25 July to 10 August, resulting in a 5.5 K temperature increase between 24 July and 4 August (Fig. 6.16a). The 4 August temperature was 6.7 K above the 1980–2023 average. Additionally, this wave transported ozone into the polar cap. Polar cap (63°S–90°S) ozone increased 24 DU between 25 July and 5 August 2024, a period when total ozone column typically declines by ~10 DU.

The wave-2 warming event was the proximate cause of the delayed 2024 ozone hole development. The opening of the ozone hole is defined as the date when the area exceeds 7 million km^2. Based on this threshold, the 2024 ozone hole started on 25 August, compared to an average of 18 August between 1992 and the present day. The 2024 delayed formation is consistent with South Pole ozonesonde data (Fig. 6.16e) and vortex-averaged ozone from the Microwave Limb Sounder (MLS; Fig. 6.16d), with both showing higher-than-average mid-winter ozone concentrations.

Ozone depletion rates in August–September 2024 were comparable to previous years, with 2006 being the most severe ozone hole in area and depth. Ozone loss rates were slightly smaller in 2024 than 2006, but both years averaged 40 ppb–50 ppb-per-day losses in early September. PSCs provide surface areas for heterogeneous reactions that convert reservoir chlorine species into active forms (e.g., chlorine monoxide, ClO; Fig. 6.16c). ClO catalytically destroys ozone. While PSC observations were not available in 2024, record-high vortex ClO abundances in May–June (>200 parts per trillion [ppt]) suggest greater early activation and likely greater PSC formation than average (as would be expected because of the Hunga injection of water into the stratosphere). In 2024, chlorine activation generally followed the typical seasonal pattern after early winter.

The ozone hole severity peaked in the late-September to early-October period. The largest single-day area was 22.4 million km^2 (28 September; Fig. 6.16f), the minimum polar cap ozone value was 107 DU on 5 October, the mass deficit was 28.2 million metric tons of ozone (28 September), and the polar cap (63°S–90°S) average ozone was 210 DU (27 September). The South Pole ozone sonde 12 km–20 km column bottomed out in early October and had an absolute 14.8-DU minimum (18 October; Fig. 6.16e).

The ozone hole had near-average September values. Most Antarctic ozone depletion occurs in the August and September period (Figs. 6.16d–f), making September the key period for evaluating the chemical depletion severity. Figure 6.17a displays September average hole area versus year, separated into colder years (lower third, blue triangles), average years (middle third, black dots), and warmer years (upper third, red squares). Year-to-year temperature variability modulates hole severity, with colder (warmer) years leading to greater (lesser) ozone depletion and less (more) ozone advection into the Antarctic polar region (Fig. 6.17b). The 2024 temperature (purple triangle) was near average, leading to a near-zero-hole anomaly. Because of the decreased levels of chlorine and bromine in the Antarctic polar vortex, the 2024 hole was not as deep or extensive as those observed in the early 2000s.

The 2024 ozone hole broke up on 21 December (Fig. 6.17c), two weeks after the 7 December average calculated from the 1992–2024 period (dashed line). The breakup is calculated as the final date with observed total ozone values less than 220 DU in the Antarctic region (Fig. 6.17f). An increasing trend from November to December hole breakup dates is seen from 1979 to 1991 (Fig. 6.17c). As levels of chlorine and bromine decline, the hole breakup should fall back into November. However, there is no apparent breakup trend in the 2000–24 period (Fig. 6.17c), in

Unauthenticated | Downloaded 11/21/25 11:34 AM UTC

remarkable contrast to the recovery in the September hole area (Fig. 6.17a). The November hole area is linearly related to the November 50-hPa polar cap temperature (Fig. 6.17d). Colder- (warmer-) than-average temperatures lead to a larger (smaller) November hole remnant, and therefore a later (earlier) breakup date. The November 2024 temperature was near average, somewhat consistent with the 21 December 2024 breakup. The last five years (2020–24) have seen late breakups, in contrast to the 2013–19 period. These late breakups are not caused by chemically driven loss but rather suggest variability or trends of the stratospheric dynamics in the last five years.

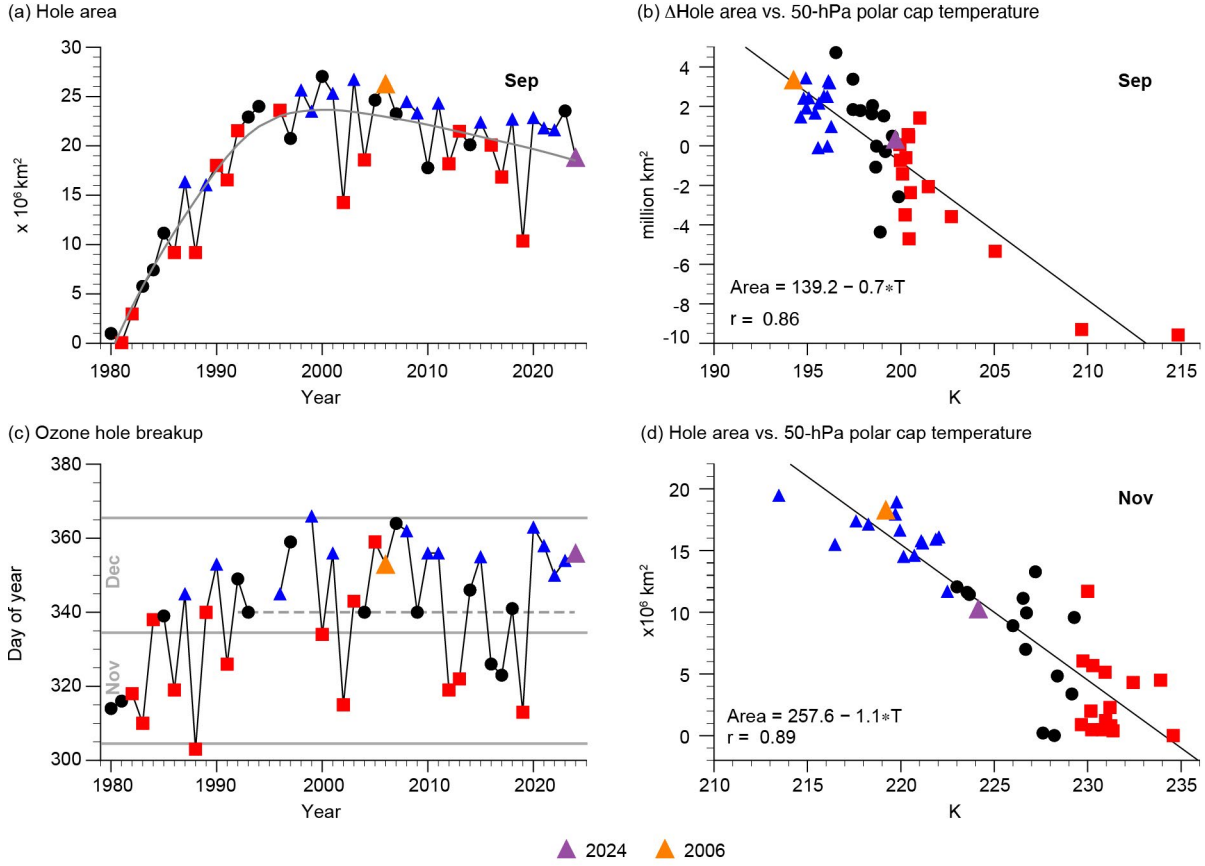

Fig. 6.17. (a) Annual Sep average Antarctic ozone hole area (× 10^6 km^2). (b) Sep ozone hole area anomalies (see text) vs. MERRA-2 Sep 50-hPa temperatures (K) averaged over the polar cap (60°S–90°S). (c) Ozone hole break-up dates, where the horizontal dashed line is the 1992–2024 average. (d) Nov ozone hole areas vs. MERRA-2 Nov 50-hPa temperatures. In (a), the gray curve shows a quadratic fit of effective equivalent stratospheric chlorine with a 5.2-year mean age of air (Newman et al. 2007) to the Sep hole areas. Years with temperatures in the lowest (highest) third are shown as blue triangles (red squares). The years 2006 and 2024 are specifically highlighted in orange and purple, respectively. Ozone data for 1979–92 are from Total Ozone Mapping Spectrometer (TOMS) Nimbus-7; data for 1993/94 are from TOMS Meteor-3; data for 1996–2004 are from TOMS Earth Probe; data for 2005–15 are from Aura Ozone Monitoring Instrument (OMI); and data for 2015–24 are from Suomi National Polar-orbiting Partnership (SNPP) Ozone Mapping and Profiler Suite (OMPS). There are no 1995 satellite mapper total ozone observations.

Unauthenticated | Downloaded 11/21/25 11:34 AM UTC

Acknowledgments

- K. R. Clem and M. N. Raphael would like to acknowledge and thank Samuel Batzli, University of Wisconsin-Madison, for kindly producing the map shown in Fig. 6.1.
- Work at the California Institute of Technology's Jet Propulsion Laboratory was done under contract with NASA. Support was also provided by the NASA Earth Science Division's Modeling and Analysis Program and the Upper Atmospheric Research Program. We are indebted to the many NOAA Corps Officers and Global Monitoring Laboratory technical personnel, who spend the winters at South Pole Station to obtain the ongoing balloon and ground-based data sets. We also acknowledge the logistics support in Antarctica provided by the National Science Foundation (NSF) Office of Polar Programs.

© 2024. All rights reserved.

- P. Reid and J. Lieser were supported through Australia's Bureau of Meteorology, and R. Massom by the Australian Antarctic Division. The work of P. Reid and R. Massom also contributes to the Australian Government's Australian Antarctic Partnership Program (AAPP). For R. Massom, this work was also supported by the Australian Research Council Special Research Initiative of the Australian Centre for Excellence in Antarctic Science (Project Number SR200100008).
- S. Stammerjohn was supported under NSF PLR–1552226; she also thanks the Institute of Arctic and Alpine Research and the National Snow and Ice Data Center, both at the University of Colorado Boulder, for institutional and data support.
- The Southern Ocean Observing System is a joint international initiative of the Scientific Committee on Antarctic Research (SCAR) and the Scientific Committee on Oceanic Research (SCOR).
- L. P. Pezzi acknowledges support from the Brazilian Antarctic Program's (PROANTAR) Antarctic Modeling and Observation System (ATMOS 2) project under the National Council for Scientific and Technological Development (CNPq)/PROANTAR award 440848/2023-7 and PQ 303981/2023-7.
- R. L. Beadling and J. Milward were supported under the NSF Division of Polar Programs Grant NSF2319828.
- S. Thomalla and T. J. Ryan-Keogh were supported through the Council for Scientific and Industrial Research's (CSIR) Southern Ocean Carbon-Climate Observatory (SOCCO) Programme (http://socco.org.za/) funded by the Department of Science and Innovation (DSI/CON C3184/2023), the CSIR's Parliamentary Grant (0000005278), and the National Research Foundation (SANAP23042496681; MCR210429598142).
- K. R. Clem acknowledges support from the Royal Society of New Zealand Marsden Fund grant MFP-VUW2010.

Unauthenticated | Downloaded 11/21/25 11:34 AM UTC

Appendix 1: Acronyms

AIS	Antarctic Ice Sheet
AMRDC	Antarctic Meteorological Research and Data Center
AR	atmospheric river
AWS	automatic weather station
CALIPSO	Cloud–Aerosol Lidar and Infrared Pathfinder Satellite Observations
ClO	chlorine monoxide
CRI	Coastal Resolution Improvement
DMSP	Defense Meteorological Satellite Program
DO	dissolved oxygen
DU	Dobson unit
EPE	extreme precipitation event
ESA	European Space Agency
GNSS	Global Navigation Satellite System
GRACE	Gravity Recovery and Climate Experiment
GRACE-FO	Gravity Recovery and Climate Experiment Follow-On
IMBIE	Ice Mass Balance Intercomparison Exercise
MAR	Model for Surface Mass Balance of the Arctic Ice Sheets
MLD	mixed-layer depth
MLS	Microwave Limb Sounder
NRTSI	Near-Real-Time Defense Meteorological Satellite Program Special Sensor Microwave Imager Sounder Daily Polar Gridded Sea Ice Concentrations
NSIDC	National Snow and Ice Data Center
OC-CCI	Ocean Colour Climate Change Initiative
OHC	ocean heat content
OMI	Ozone Monitoring Instrument
OMPS	Ozone Mapping and Profiler Suite
P–E	total precipitation minus evaporation and sublimation
PSC	polar stratospheric cloud
SAF	Subantarctic Front
SAM	Southern Annular Mode
SAR	synthetic aperture radar
SIA	sea ice area
SIE	sea ice extent
SMB	surface mass balance
SMMR	Scanning Multichannel Microwave Radiometer
SNPP	Suomi National Polar-orbiting Partnership
SO	Southern Ocean
SSM/I	Special Sensor Microwave Imager
SSMIS	Special Sensor Microwave Imager Sounder
SSS	sea surface salinity
SST	sea surface temperature
STG	subtropical gyre
TOMS	Total Ozone Mapping Spectrometer
vIVT	vector-invariant water transport
WAIS	West Antarctic Ice Sheet

Unauthenticated | Downloaded 11/21/25 11:34 AM UTC

Appendix 2: Datasets and sources

Section 6b Atmospheric circulation and surface observations

Sub-section	General Variable or Phenomenon	Specific Dataset or Variable	Source
6b	Geopotential Height	ERA5	https://www.ecmwf.int/en/forecasts/dataset/ecmwf-reanalysis-v5
6b	Modes of Variability	Marshall Southern Annular Mode Index	http://www.nerc-bas.ac.uk/icd/gjma/sam.html
6b	Pressure, Sea Level or Near-Surface	ERA5	https://www.ecmwf.int/en/forecasts/dataset/ecmwf-reanalysis-v5
6b	Pressure, Sea Level or Near-Surface	University of Wisconsin-Madison Automated Weather Stations—Antarctic Meteorological Research and Data Center	https://amrdcdata.ssec.wisc.edu
6b	Pressure, Sea Level or Near-Surface	Staffed Weather Station Data	https://legacy.bas.ac.uk/met/READER/
6b	Temperature, [Near] Surface	ERA5	https://www.ecmwf.int/en/forecasts/dataset/ecmwf-reanalysis-v5
6b	Temperature, [Near] Surface	University of Wisconsin-Madison Automated Weather Stations—Antarctic Meteorological Research and Data Center	https://amrdcdata.ssec.wisc.edu
6b	Temperature, [Near] Surface	Staffed Weather Station Data	https://legacy.bas.ac.uk/met/READER/
6b	Temperature, Upper-Atmosphere	ERA5	https://www.ecmwf.int/en/forecasts/dataset/ecmwf-reanalysis-v5
6b	Wind, Upper-Atmosphere	ERA5	https://www.ecmwf.int/en/forecasts/dataset/ecmwf-reanalysis-v5

Section 6c Ice sheet surface mass balance

Sub-section	General Variable or Phenomenon	Specific Dataset or Variable	Source
6c	Ice Sheet Surface Mass Balance	Polar-Oriented Regional Climate Model (Model for Surface Mass Balance of the Arctic Ice Sheets [MAR])	https://arcticdata.io/catalog/view/doi%3A10.18739%2FA28G8FJ7F
6c	Ice Sheet Surface Mass Balance	ERA5	https://www.ecmwf.int/en/forecasts/dataset/ecmwf-reanalysis-v5

Unauthenticated | Downloaded 11/21/25 11:34 AM UTC

Sub-section	General Variable or Phenomenon	Specific Dataset or Variable	Source
6c	Ice Sheet Surface Mass Balance	MERRA-2	http://gmao.gsfc.nasa.gov/reanalysis/MERRA-2/

Section 6d Ice sheet melt extent and duration

Sub-section	General Variable or Phenomenon	Specific Dataset or Variable	Source
6d	Ice Sheet Surface Melt	Defense Meteorological Satellite Program (DMSP) Special Sensor Microwave Imager/Sounder (SSMIS)	https://nsidc.org/data/nsidc-0001/versions/6
6d	Sea Ice Extent/Area/ Concentration	Nimbus-7 Scanning Multichannel Microwave Radiometer (SMMR) Sea Ice Concentration	https://nsidc.org/data/nsidc-0007

Section 6e Ice sheet mass balance

Sub-section	General Variable or Phenomenon	Specific Dataset or Variable	Source
6e	Ice Sheet Surface Height	Advanced Topographic Laser Altimeter System (ATLAS) Ice, Cloud and Land Elevation Satellite-2 (ICESat-2)	https://nsidc.org/data/atl06/versions/5
6e	Ice Sheet Surface Height	ICESat-2	https://icesat-2.gsfc.nasa.gov/
6e	Ice Sheet Mass	Gravity Recovery and Climate Experiment (GRACE)/GRACE Follow-On (GRACE-FO)	https://podaac.jpl.nasa.gov/dataset/TELLUS_GRAC-GRFO_MASCON_CRI_GRID_RL06_V2

Unauthenticated | Downloaded 11/21/25 11:34 AM UTC

Section 6f Sea ice extent, concentration, and seasonality

Sub-section	General Variable or Phenomenon	Specific Dataset or Variable	Source
6f	Sea Ice Extent and Area	Near-Real-Time Defense Meteorological Satellite Program (DMSP) Special Sensor Microwave Imager/ Sounder (SSMIS) Daily Polar Gridded Sea Ice Concentrations, Version 1	https://arcticdata.io/catalog/view/doi:10.18739/A2B56D64V
6f	Sea Surface Temperature	NOAA OISSTv2.1	https://www.ncei.noaa.gov/products/optimum-interpolation-sst

Section 6g Southern Ocean

Sub-section	General Variable or Phenomenon	Specific Dataset or Variable	Source
6g1	Sea Surface Temperature	NOAA OISSTv2.1	https://www.ncei.noaa.gov/products/optimum-interpolation-sst
6g1	Sea Surface Salinity	Argo Monthly Climatology	https://sio-argo.ucsd.edu/RG_Climatology.html
6g1	Mixed-Layer Depth	Argo Monthly Climatology	https://sio-argo.ucsd.edu/RG_Climatology.html
6g2	Surface Heat flux	ERA5	https://www.ecmwf.int/en/forecasts/dataset/ecmwf-reanalysis-v5
6g3	Ocean Heat Content	Argo Monthly Climatology	https://sio-argo.ucsd.edu/RG_Climatology.html
6g4	Dissolved Oxygen	Biogeochemical Argo (BGC-Argo)	https://biogeochemical-argo.org/
6g4	Ocean Chlorophyll	ESA Ocean Colour Climate Change Initiative (OC-CCI) product Version 6.0	https://www.oceancolour.org/

Section 6h 2024 Antarctic ozone hole

Sub-section	General Variable or Phenomenon	Specific Dataset or Variable	Source
6h	Cloud Volume	CALIPSO	http://www-calipso.larc.nasa.gov
6h	Temperature, [Near] Surface	MERRA-2	http://gmao.gsfc.nasa.gov/reanalysis/MERRA-2/
6h	Temperature, Upper-Atmosphere	MERRA-2	https://gmao.gsfc.nasa.gov/reanalysis/MERRA-2/
6h	Ozone, Total Column and Stratospheric	Aura Microwave Limb Sounder (MLS)	http://disc.sci.gsfc.nasa.gov/Aura/data-holdings/MLS/index.shtml

Unauthenticated | Downloaded 11/21/25 11:34 AM UTC

Sub-section	General Variable or Phenomenon	Specific Dataset or Variable	Source
6h	Ozone, Total Column and Stratospheric	Ozone Mapping Instrument (OMI) Ozone Mapping & Profiler Suite (OMPS), Total Ozone Mapping Spectrum (TOMS), Earth Probe TOMS (EPTOMS)	https://ozoneaq.gsfc.nasa.gov/data/ozone/
6h	Ozone, Lower Stratosphere	Ozonesonde	https://gml.noaa.gov/dv/spo_oz/

Sidebar 6.1: How to train your iceberg: Iceberg A23a drift track in 2024

Sub-section	General Variable or Phenomenon	Specific Dataset or Variable	Source
SB6.1	Iceberg Drift Tracks	NASA Worldview Moderate Resolution Imaging Spectroradiometer (MODIS) data	https://worldview.earthdata.nasa.gov
SB6.1	Iceberg Drift Tracks	Global Navigation Satellite System (GNSS) data	https://cddis.nasa.gov/Data_and_Derived_Products/GNSS/daily_gnss_o.html

Unauthenticated | Downloaded 11/21/25 11:34 AM UTC

References

Agosta, C., and Coauthors, 2019: Estimation of the Antarctic surface mass balance using the regional climate model MAR (1979–2015) and identification of dominant processes. *Cryosphere*, **13**, 281–296, https://doi.org/10.5194/tc-13-281-2019.

AMRDC, 2022: Automatic Weather Station quality-controlled observational data. AMRDC Data Repository, accessed 30 January 2025, https://doi.org/10.48567/1hn2-nw60.

Banwell, A. F., D. R. MacAyeal, and O. V. Sergienko, 2013: Breakup of the Larsen B Ice Shelf triggered by chain reaction drainage of supraglacial lakes. *Geophys. Res. Lett.*, **40**, 5872–5876, https://doi.org/10.1002/2013GL057694.

Barbat, M. M., T. Rackow, C. Wesche, H. H. Hellmer, and M. M. Mata, 2021: Automated iceberg tracking with a machine learning approach applied to SAR imagery: A Weddell sea case study. *ISPRS J. Photogramm. Remote Sens.*, **172**, 189–206, https://doi.org/10.1016/j.isprsjprs.2020.12.006.

Beadling, R. L., N. M. Freeman, G. A. MacGilchrist, M. Mazloff, J.-R. Shi, A. F. Thompson, and E. Wilson, 2022: Southern Ocean [in "State of the Climate in 2021"]. *Bull. Amer. Meteor. Soc.*, **103** (8), S329–S332, https://doi.org/10.1175/BAMS-D-22-0078.1.

Budge, J. S., and D. G. Long, 2018: A comprehensive database for Antarctic iceberg tracking using scatterometer data. *IEEE J. Sel. Top. Appl. Earth Obs. Remote Sens.*, **11**, 434–442, https://doi.org/10.1109/JSTARS.2017.2784186.

Cai, W., and Coauthors, 2023: Southern Ocean warming and its climatic impacts. *Sci. Bull.*, **68** (9), 946–960, https://doi.org/10.1016/j.scib.2023.03.049.

Cavalieri, D. J., C. L. Parkinson, P. Gloersen, and H. J. Zwally, 1996: Sea ice concentrations from Nimbus-7 SMMR and DMSP SSM/I-SSMIS passive microwave data, version 1. NASA National Snow and Ice Data Center Distributed Active Archive Center, accessed 15 February 2025, https://doi.org/10.5067/8GQ8LZQVL0VL.

Cheng, L., and Coauthors, 2022: Past and future ocean warming. *Nat. Rev. Earth Environ.*, **3**, 776–794, https://doi.org/10.1038/s43017-022-00345-1.

Clem, K. R., and Coauthors, 2022: Antarctica and the Southern Ocean [in "State of the Climate in 2021"]. *Bull. Amer. Meteor. Soc.*, **103** (8), S307–S340, https://doi.org/10.1175/BAMS-D-22-0078.1.

—— , and Coauthors, 2023: Antarctica and the Southern Ocean [in "State of the Climate in 2022"]. *Bull. Amer. Meteor. Soc.*, **104** (9), S322–S365, https://doi.org/10.1175/BAMS-D-23-0077.1.

—— , and Coauthors, 2024: Antarctica and the Southern Ocean [in "State of the Climate in 2023"]. *Bull. Amer. Meteor. Soc.*, **105** (8), S331–S370, https://doi.org/10.1175/BAMS-D-24-0099.1.

Comiso, J. C., 2017: Bootstrap sea ice concentrations from Nimbus-7 SMMR and DMSP SSM/I-SSMIS, version 3. NASA National Snow and Ice Data Center Distributed Active Archive Center, accessed 2 February 2024, https://doi.org/10.5067/7Q8HCCWS4I0R.

Davison, B. J., and Coauthors, 2023: Sea level rise from West Antarctic mass loss significantly modified by large snowfall anomalies. *Nat. Commun.*, **14**, 1479, https://doi.org/10.1038/s41467-023-36990-3.

de Boyer Montégut, C., G. Madec, A. S. Fischer, A. Lazar, and D. Ludicone, 2004: Mixed layer depth over the global ocean: An examination of profile data and a profile-based climatology. *J. Geophys. Res.*, **109**, C12003, https://doi.org/10.1029/2004JC002378.

Ferrigno, J. G., and W. G. Gould, 1987: Substantial changes in the coastline of Antarctica revealed by satellite imagery. *Polar Rec.*, **23**, 577–583, https://doi.org/10.1017/S003224740000807X.

Fraser, A. D., and Coauthors, 2023: Antarctic landfast sea ice: A review of its physics, biogeochemistry and ecology. *Rev. Geophys.*, **61**, e2022RG000770, https://doi.org/10.1029/2022RG000770.

Frölicher, T. L., J. L. Sarmiento, D. J. Paynter, J. P. Dunner, J. P. Krasting, and M. Winton, 2015: Dominance of the Southern Ocean in anthropogenic carbon and heat uptake in CMIP5 models. *J. Climate*, **28**, 862–886, https://doi.org/10.1175/JCLI-D-14-00117.1.

Gelaro, R., and Coauthors, 2017: The Modern-Era Retrospective Analysis for Research and Applications, version 2 (MERRA-2). *J. Climate*, **30**, 5419–5454, https://doi.org/10.1175/JCLI-D-16-0758.1.

Gerrish, L., L. Ireland, P. Fretwell, and P. Cooper, 2023: High resolution vector polygons of the Antarctic coastline, version 7.8. UK Polar Data Centre, Natural Environment Research Council, UK Research & Innovation, accessed 8 February 2024, https://doi.org/10.5285/C7FE759D-E042-479A-9ECF-274255B4F0A1.

Gloersen, P., 2006: Nimbus-7 SMMR polar gridded radiances and sea ice concentrations, version 1. Subset: 37 & 19 GHz, h-polarization, 25 km grid, October 1979–April 1987. NASA National Snow and Ice Data Center Distributed Active Archive Center, accessed 5 May 2020, https://doi.org/10.5067/QOZIVYV3V9JP.

Gossart, A., S. Helsen, J. T. M. Lenaerts, S. V. Broucke, N. P. M. Van Lipzig, and N. Souverijns, 2019: An evaluation of surface climatology in state-of-the-art reanalyses over the Antarctic ice sheet. *J. Climate*, **32**, 6899–6915, https://doi.org/10.1175/JCLI-D-19-0030.1.

Griggs, J. A., and J. L. Bamber, 2011: Antarctic ice-shelf thickness from satellite radar altimetry. *J. Glaciol.*, **57**, 485–498, https://doi.org/10.3189/002214311796905659.

Haid, V., D. Iovino, and S. Masina, 2017: Impacts of freshwater changes on Antarctic sea ice in an eddy-permitting sea-ice–ocean model. *Cryosphere*, **11**, 1387–1402, https://doi.org/10.5194/tc-11-1387-2017.

Hanna, E., and Coauthors, 2024: Short- and long-term variability of the Antarctic and Greenland ice sheets. *Nat. Rev. Earth Environ.*, **5**, 193–210, https://doi.org/10.1038/s43017-023-00509-7.

Henley, S. F., and Coauthors, 2020: Changing biogeochemistry of the Southern Ocean and its ecosystem implications. *Front. Mar. Sci.*, **7**, 581, https://doi.org/10.3389/fmars.2020.00581.

Hersbach, H., and Coauthors, 2020: The ERA5 global reanalysis. *Quart. J. Roy. Meteor. Soc.*, **146**, 1999–2049, https://doi.org/10.1002/qj.3803.

Hosking, J. S., A. Orr, T. J. Bracegirdle, and J. Turner, 2016: Future circulation changes off West Antarctica: Sensitivity of the Amundsen Sea Low to projected anthropogenic forcing. *Geophys. Res. Lett.*, **43**, 367–376, https://doi.org/10.1002/2015GL067143.

—— , —— , G. J. Marshall, J. Turner, and T. Phillips, 2013: The influence of the Amundsen–Bellingshausen Seas low on the climate of West Antarctica and its representation in coupled climate model Ssimulations. *J. Climate*, **26**, 6633–6648, https://doi.org/10.1175/JCLI-D-12-00813.1.

Huang, B., C. Liu, V. Banzon, E. Freeman, G. Graham, B. Hankins, T. Smith, and H.-M. Zhang, 2021: Improvements of the Daily Optimum Interpolation Sea Surface Temperature (DOISST) version 2.1. *J. Climate*, **34**, 2923–2939, https://doi.org/10.1175/JCLI-D-20-0166.1.

Unauthenticated | Downloaded 11/21/25 11:34 AM UTC

Josey, S. A., J. P. Grist, J. V. Mecking, B. I. Moat, and E. Schulz, 2023: A clearer view of Southern Ocean air-sea interaction using surface heat flux asymmetry. *Philos. Trans. Roy. Soc.*, **A381**, 20220067, https://doi.org/10.1098/rsta.2022.0067.

—— , A. J. S. Meijers, A. T. Blaker, J. P. Grist, J. Mecking, and H. C. Ayres, 2024: Record-low Antarctic sea ice in 2023 increased ocean heat loss and storms. *Nature*, **636**, 635–639, https://doi.org/10.1038/s41586-024-08368-y.

Kittel, C., and Coauthors, 2021: Diverging future surface mass balance between the Antarctic ice shelves and grounded ice sheet. *Cryosphere*, **15**, 1215–1236, https://doi.org/10.5194/tc-15-1215-2021.

Kolbe, M., R. Bintanja, E. C. van der Linden, and R. R. Cordero, 2025: Vertical structure and surface impact of atmospheric rivers reaching Antarctic sea ice and land. *Atmos. Res.*, **315**, 107841, https://doi.org/10.1016/j.atmosres.2024.107841.

Kramarova, N. A., and Coauthors, 2024: 2023 Antarctic ozone hole [in "State of the Climate in 2023"]. *Bull. Amer. Meteor. Soc.*, **105** (8), S358–S361, https://doi.org/10.1175/BAMS-D-24-0099.1.

Lenaerts, J. T. M., B. Medley, M. R. van den Broeke, and B. Wouters, 2019: Observing and modeling ice sheet surface mass balance. *Rev. Geophys.*, **57**, 376–420, https://doi.org/10.1029/2018RG000622.

Li, T., and Coauthors, 2017: The effect of seafloor topography in the Southern Ocean on tabular iceberg drifting and grounding. *Sci. China Earth Sci.*, **60**, 697–706, https://doi.org/10.1007/s11430-016-9014-5.

MacAyeal, D. R., M. H. Okal, J. E. Thom, K. M. Brunt, Y. J. Kim, and A. K. Bliss, 2008: Tabular iceberg collisions within the coastal regime. *J. Glaciol.*, **54**, 371–386, https://doi.org/10.3189/002214308784886180.

MacFerrin, M., T. Mote, H. Wang, L. Liu, L. Montgomery, and T. Scambos, 2021: Ice sheet seasonal melt extent and duration [in "State of the Climate in 2020"]. *Bull. Amer. Meteor. Soc.*, **102**, S331–S334, https://doi.org/10.1175/BAMS-D-21-0081.1.

—— , —— , A. Banwell, and T. Scambos, 2022: Ice sheet seasonal melt extent and duration [in "State of the Climate in 2021"]. *Bull. Amer. Meteor. Soc.*, **103** (8), S321–S323, https://doi.org/10.1175/2022BAMSStateoftheClimate.1.

—— , —— , —— , and —— , 2023: Ice sheet seasonal melt extent and duration [in "State of the Climate in 2022"]. *Bull. Amer. Meteor. Soc.*, **104** (9), S339–S341, https://doi.org/10.1175/BAMS-D-23-0077.1.

Maclennan, M. L., J. T. M. Lenaerts, C. Shields, and J. D. Wille, 2022: Contribution of atmospheric rivers to Antarctic precipitation. *Geophys. Res. Lett.*, **49**, e2022GL100585, https://doi.org/10.1029/2022GL100585.

Manney, G. L., and Coauthors, 2011: Jet characterization in the upper troposphere/lower stratosphere (UTLS): Applications to climatology and transport studies. *Atmos. Chem. Phys.*, **11**, 6115–6137, https://doi.org/10.5194/acp-11-6115-2011.

Marshall, G. J., 2003: Trends in the Southern Annular Mode from observations and reanalyses. *J. Climate*, **16**, 4134–4143, https://doi.org/10.1175/1520-0442(2003)016<4134:TITSAM>2.0.CO;2.

Martin, S., R. Drucker, R. Aster, F. Davey, E. Okal, T. Scambos, and D. MacAyeal, 2010: Kinematic and seismic analysis of giant tabular iceberg breakup at Cape Adare, Antarctica. *J. Geophys. Res.*, **115**, B06311, https://doi.org/10.1029/2009JB006700.

Maslanik, J., and J. Stroeve, 1999: Near-real-time DMSP SSM/I-SSMIS daily polar gridded sea ice concentrations (updated daily). National Snow and Ice Data Center, accessed 15 February 2025, https://nsidc.org/data/docs/daac/nsidc0081_ssmi_nrt_seaice.gd.html.

Massom, R. A., T. A. Scambos, L. G. Bennetts, P. Reid, V. A. Squire, and S. E. Stammerjohn, 2018: Antarctic ice shelf disintegration triggered by sea ice loss and ocean swell. *Nature*, **558**, 383–389, https://doi.org/10.1038/s41586-018-0212-1.

Medley, B., and E. R. Thomas, 2019: Increased snowfall over the Antarctic Ice Sheet mitigated twentieth-century sea-level rise. *Nat. Climate Change*, **9**, 34–39, https://doi.org/10.1038/s41558-018-0356-x.

Meier, W. N., H. Wilcox, M. A. Hardman, and J. S. Stewart, 2019: DMSP SSM/I-SSMIS daily polar gridded brightness temperatures, version 5. Subset: 37 & 19 GHz, h-polarization, 25 km grid, October 1987–April 2020. NASA National Snow and Ice Data Center Distributed Active Archive Center, accessed 11 February 2021, https://doi.org/10.5067/QU2UYQ6T0B3P.

Meredith, M. P., and M. A. Brandon, 2017: Oceanography and sea ice in the Southern Ocean. *Sea Ice*, D. Thomas, Ed., Wiley, 216–238.

—— , A. S. Meijers, A. C. Naveira Garabato, P. J. Brown, H. J. Venables, E. P. Abrahamsen, L. Jullion, and M. J. Messias, 2015: Circulation, retention, and mixing of waters within the Weddell-Scotia Confluence, Southern Ocean: The role of stratified Taylor columns. *J. Geophys. Res. Oceans*, **120**, 547–562, https://doi.org/10.1002/2014JC010462.

—— , and Coauthors, 2023: Tracing the impacts of recent rapid sea ice changes and the A68 megaberg on the surface freshwater balance of the Weddell and Scotia Seas. *Philos. Trans. Roy. Soc.*, **A381**, 20220162, https://doi.org/10.1098/rsta.2022.0162.

Merino, N., J. Le Sommer, G. Durand, N. C. Jourdain, G. Madec, P. Mathiot, and J. Tournadre, 2016: Antarctic icebergs melt over the Southern Ocean: Climatology and impact on sea ice. *Ocean Modell.*, **104**, 99–110, https://doi.org/10.1016/j.ocemod.2016.05.001.

Morlighem, M., and Coauthors, 2020: Deep glacial troughs and stabilizing ridges unveiled beneath the margins of the Antarctic ice sheet. *Nat. Geosci.*, **13**, 132–137, https://doi.org/10.1038/s41561-019-0510-8.

Mote, T. L., 2007: Greenland surface melt trends 1973–2007: Evidence of a large increase in 2007. *Geophys. Res. Lett.*, **34**, L22507, https://doi.org/10.1029/2007GL031976.

—— , 2014: MEaSUREs Greenland surface melt daily 25km EASE-Grid 2.0, version 1. NASA National Snow and Ice Data Center Distributed Active Archive Center, Accessed 1 December 2024, https://doi.org/10.5067/MEASURES/CRYOSPHERE/nsidc-0533.001.

—— , and M. R. Anderson, 1995: Variations in snowpack melt on the Greenland ice sheet based on passive-microwave measurements. *J. Glaciol.*, **41**, 51–60, https://doi.org/10.3189/S0022143000017755.

Mottram, R., and Coauthors, 2021: What is the surface mass balance of Antarctica? An intercomparison of regional climate model estimates. *Cryosphere*, **15**, 3751–3784, https://doi.org/10.5194/tc-15-3751-2021.

Neuhaus, S. U., and D. R. MacAyeal, 2012: Iceberg drift trajectory follows sea-floor spreading features. 2012 Fall Meeting, San Francisco, CA, Amer. Geophys. Union, Abstract T41B-2596.

Unauthenticated | Downloaded 11/21/25 11:34 AM UTC

Newman, P. A., J. S. Daniel, D. W. Waugh, and E. R. Nash, 2007: A new formulation of equivalent effective stratospheric chlorine (EESC). Atmos. *Chem. Phys.*, **7**, 4537–4552, https://doi.org/10.5194/acp-7-4537-2007.

Norwegian Polar Institute, 2018: Quantarctica v3.0, detailed basemap. Accessed 12 September 2020, https://www.npolar.no/quantarctica/.

Orsi, A. H., T. Whitworth III, and W. D. Nowlin Jr., 1995: On the meridional extent and fronts of the Antarctic Circumpolar Current. *Deep-Sea. Res. I*, **42**, 641–673, https://doi.org/10.1016/0967-0637(95)00021-W.

Oschlies, A., P. Brandt, L. Stramma, and S. Schmidtko, 2018: Drivers and mechanisms of ocean deoxygenation. *Nat. Geosci.*, **11**, 467–473, https://doi.org/10.1038/s41561-018-0152-2.

Otosaka, I. N., and Coauthors, 2023: Mass balance of the Greenland and Antarctic ice sheets from 1992 to 2020. *Earth Syst. Sci. Data*, **15**, 1597–1616, https://doi.org/10.5194/essd-15-1597-2023.

Park, Y.-H., E. Charriaud, and M. Fieux, 1998: Thermohaline structure of the Antarctic surface water/winter water in the Indian sector of the Southern Ocean. *J. Mar. Syst.*, **17**, 5–23, https://doi.org/10.1016/S0924-7963(98)00026-8.

Pezzi, L. P., and Coauthors, 2023: Southern Ocean [in "State of the Climate in 2022"]. *Bull. Amer. Meteor. Soc.*, **104** (9), S351–S355, https://doi.org/10.1175/BAMS-D-23-0077.1.

Purich, A., and E. W. Doddridge, 2023: Record low Antarctic sea ice coverage indicates a new sea ice state. *Commun. Earth Environ.*, **4**, 314, https://doi.org/10.1038/s43247-023-00961-9.

Raphael, M. N., T. J. Maierhofer, R. L. Fogt, W. R. Hobbs, and M. S. Handcock, 2025: A twenty-first century structural change in Antarctica's sea ice system. *Commun. Earth Environ.*, **6**, 131, https://doi.org/10.1038/s43247-025-02107-5.

Reid, P., S. Stammerjohn, R. A. Massom, S. Barreira, T. Scambos, and J. L. Lieser, 2024: Sea ice extent, concentration, and seasonality [in "State of the Climate in 2023"]. *Bull. Amer. Meteor. Soc.*, **105** (8), S351–S354, https://doi.org/10.1175/BAMS-D-24-0099.1.

—— , and R. A. Massom, 2022: Change and variability in Antarctic coastal exposure, 1979–2020. *Nat. Commun.*, **13**, 1164, https://doi.org/10.1038/s41467-022-28676-z.

Reynolds, R. W., N. A. Rayner, T. M. Smith, D. C. Stokes, and W. Wang, 2002: An improved in situ and satellite SST analysis for climate. *J. Climate*, **15**, 1609–1625, https://doi.org/10.1175/1520-0442(2002)015<1609:AIISAS>2.0.CO;2.

Riihelä, A., R. M. Bright, and K. Anttila, 2021: Recent strengthening of snow and ice albedo feedback driven by Antarctic sea-ice loss. *Nat. Geosci.*, **14**, 832–836, https://doi.org/10.1038/s41561-021-00841-x.

Roemmich, D., and J. Gilson, 2009: The 2004–2008 mean and annual cycle of temperature, salinity, and steric height in the global ocean from the Argo Program. *Prog. Oceanogr.*, **82**, 81–100, https://doi.org/10.1016/j.pocean.2009.03.004.

Sabu, P., S. A. Libera, R. Chacko, N. Anilkumar, M. P. Subeesh, and A. P. Thomas, 2020: Winter water variability in the Indian Ocean sector of Southern Ocean during austral summer. *Deep-Sea Res. II*, **178**, 104852, https://doi.org/10.1016/j.dsr2.2020.104852.

Santee, M. L., and Coauthors, 2024: The influence of stratospheric hydration from the Hunga eruption on chemical processing in the 2023 Antarctic vortex. *J. Geophys. Res. Atmos.*, **129**, e2023JD040687, https://doi.org/10.1029/2023JD040687.

Sathyendranath, S., and Coauthors, 2019: An ocean-colour time series for use in climate studies: The experience of the Ocean-Colour Climate Change Initiative (OC-CCI). *Sensors*, **19**, 4285, https://doi.org/10.3390/s19194285.

Scambos, T., R. Ross, R. Bauer, Y. Yermolin, P. Skvarca, D. Long, J. Bohlander, and T. Haran, 2008: Calving and ice-shelf breakup processes investigated by proxy: Antarctic tabular iceberg evolution during northward drift. *J. Glaciol.*, **54**, 579–591, https://doi.org/10.3189/002214308786570836.

—— , E. Berthier, T. Haran, C. A. Shuman, A. J. Cook, S. R. M. Ligtenberg, and J. Bohlander, 2014: Detailed ice loss pattern in the northern Antarctic Peninsula: Widespread decline driven by ice front retreats. *Cryosphere*, **8**, 2135–2145, https://doi.org/10.5194/tc-8-2135-2014.

—— , and Coauthors, 2024: Life cycle of icebergs B-15 and C-19. 2024 Fall Meeting, Washington, D.C., Amer. Geophys. Union, Abstract C21F-0423.

Smith, B., and Coauthors, 2020: Pervasive ice sheet mass loss reflects competing ocean and atmosphere processes. *Science*, **368**, 1239–1242, https://doi.org/10.1126/science.aaz5845.

—— , S. Dickinson, B. P. Jelley, T. A. Neumann, D. Hancock, J. Lee, and K. Harbeck, 2022: ATLAS/ICESat-2 L3B slope-corrected land ice height time series, version 5. NASA National Snow and Ice Data Center Distributed Active Archive Center, accessed 18 February 2024, https://doi.org/10.5067/ATLAS/ATL11.005.

Spira, T., S. Swart, I. Giddy, and M. Du Plessis, 2024: The observed spatiotemporal variability of Antarctic Winter Water. *J. Geophys. Res. Oceans*, **129**, e2024JC021017, https://doi.org/10.1029/2024JC021017.

Stammerjohn, S. E., D. G. Martinson, R. C. Smith, X. Yuan, and D. Rind, 2008: Trends in Antarctic annual sea ice retreat and advance and their relation to El Niño–Southern Oscillation and Southern Annular Mode variability. *J. Geophys. Res.*, **113**, C03S90, https://doi.org/10.1029/2007JC004269.

Stern, A. A., A. Adcroft, and O. Sergienko, 2019: Modeling ice shelf cavities and tabular icebergs using Lagrangian elements. *J. Geophys. Res. Oceans*, **124**, 3378–3392, https://doi.org/10.1029/2018JC014876.

Swithinbank, C., K. Brunk, and J. Sievers, 1988: A glaciological map of Filchner-Ronne ice shelf, Antarctica. *Ann. Glaciol.*, **11**, 150–155, https://doi.org/10.3189/S0260305500006467.

Taylor, G. I., 1922: The motion of a sphere in a rotating liquid. *Proc. Roy. Soc. London*, **102A**, 180–189, https://doi.org/10.1098/rspa.1922.0079.

The Firn Symposium Team, 2024: Firn on ice sheets. *Nat. Rev. Earth Environ.*, **5**, 79–99, https://doi.org/10.1038/s43017-023-00507-9.

The IMBIE Team, 2019: Mass balance of the Greenland Ice Sheet from 1992 to 2018. *Nature*, **579**, 233–239, https://doi.org/10.1038/s41586-019-1855-2.

Thomalla, S., S. Nicholson, T. J. Ryan-Keogh, and M. Smith, 2023: Widespread changes in Southern Ocean phytoplankton blooms linked to climate drivers. *Nat. Climate Change*, **13**, 975–984, https://doi.org/10.1038/s41558-023-01768-4.

—— , and Coauthors, 2024: Southern Ocean [in "State of the Climate in 2023"]. *Bull. Amer. Meteor. Soc.*, **105** (8), S355–S356, https://doi.org/10.1175/BAMS-D-24-0099.1.

Thomas, D. N., Ed., 2017: *Sea Ice.* 3rd ed. Wiley-Blackwell, 664 pp.

Trusel, L. D., J. D. Kromer, and R. T. Datta, 2023: Atmospheric response to Antarctic sea-ice reductions drives ice sheet surface mass balance increases. *J. Climate*, **36**, 6879–6896, https://doi.org/10.1175/JCLI-D-23-0056.1.

Turner, J., and Coauthors, 2004: The SCAR READER project: Toward a high-quality database of mean Antarctic meteorological observations. *J. Climate*, **17**, 2890–2898, https://doi.org/10.1175/1520-0442(2004)017<2890:TSRPTA>2.0.CO;2.

Unauthenticated | Downloaded 11/21/25 11:34 AM UTC

—— , and Coauthors, 2019: The dominant role of extreme precipitation events in Antarctic snowfall variability. *Geophys. Res. Lett.*, **46**, 3502–3511, https://doi.org/10.1029/2018GL081517.

van Wessem, J. M., and Coauthors, 2018: Modelling the climate and surface mass balance of polar ice sheets using RACMO2 – Part 2: Antarctica (1979–2016). *Cryosphere*, **12**, 1479–1498, https://doi.org/10.5194/tc-12-1479-2018.

Wang, H., J. G. Fyke, J. T. M. Lenaerts, J. M. Nusbaumer, H. Singh, D. Noone, P. J. Rasch, and R. Zhang, 2020: Influence of sea-ice anomalies on Antarctic precipitation using source attribution in the Community Earth System Model. *Cryosphere*, **14**, 429–444, https://doi.org/10.5194/tc-14-429-2020.

Wang, Y., D. Zhou, A. Bunde, and S. Havlin, 2016: Testing reanalysis data sets in Antarctica: Trends, persistence properties, and trend significance. *J. Geophys. Res. Atmos.*, **121**, 12 839–12 855, https://doi.org/10.1002/2016JD024864.

Wiese, D. N., D.-N. Yuan, C. Boening, F. W. Landerer, and M. M. Watkins, 2023a: JPL GRACE Mascon ocean, ice, and hydrology equivalent water height RL06.1 CRI filtered version 03. Ver. RL06.1Mv03. PO.DAAC, accessed 10 February 2023, https://doi.org/10.5067/TEMSC-3JC63.

—— , —— , —— , —— , and —— , 2023b: Tellus level-4 ocean mass anomaly time series from JPL GRACE/GRACE-FO Mascon CRI filtered release 06.1 version 03. Ver. RL06.1Mv03. PO.DAAC, accessed 10 February 2023, https://doi.org/10.5067/TEMSC-AT613.

Wille, J. D., and Coauthors, 2021: Antarctic atmospheric river climatology and precipitation impacts. *J. Geophys. Res. Atmos.*, **126**, e2020JD033788, https://doi.org/10.1029/2020JD033788.

Wong, A. P. S., and Coauthors, 2020: Argo data 1999–2019: Two million temperature-salinity profiles and subsurface velocity observations from a global array of profiling floats. *Front. Mar. Sci.*, **7**, 700, https://doi.org/10.3389/fmars.2020.00700.

Unauthenticated | Downloaded 11/21/25 11:34 AM UTC

STATE OF THE CLIMATE IN 2024

REGIONAL CLIMATES

A. Arguez, P. Bissolli, C. Ganter, R. Martinez, A. Mekonnen, L. Stevens, and Z. Zhu, Eds.

Special Online Supplement to the *Bulletin of the American Meteorological Society* Vol. 106, No. 8, August, 2025

https://doi.org/10.1175/2025BAMSStateoftheClimate_Chapter7.1

Corresponding author:
North America: Laura Stevens / Laura.Stevens@noaa.gov
Central America and the Caribbean: Anthony Arguez / Anthony.Arguez@noaa.gov
South America: Rodney Martinez / rmartinez@wmo.int
Africa: Ademe Mekonnen / amekonne@ncat.edu
Europe: Peter Bissolli / Peter.Bissolli@dwd.de
Asia: Zhiwei Zhu / zwz@nuist.edu.cn
Oceania: Catherine Ganter / Catherine.Ganter@bom.gov.au

©2025 American Meteorological Society
For information regarding reuse of this content and general copyright information, consult the AMS Copyright Policy.

Unauthenticated | Downloaded 11/21/25 11:34 AM UTC

STATE OF THE CLIMATE IN 2024
Regional Climates

Editors

Jessica Blunden
James Reagan

Chapter Editors

Anthony Arguez
Josh Blannin
Peter Bissolli
Kyle R. Clem
Howard J. Diamond
Matthew L. Druckenmiller
Robert J. H. Dunn
Catherine Ganter
Nadine Gobron
Gregory C. Johnson
Rick Lumpkin
Rodney Martinez
Ademe Mekonnen
Twila A. Moon
Gary A. Morris
Marilyn N. Raphael
Carl J. Schreck III
Laura Stevens
Richard L. Thoman
Kate M. Willett
Zhiwei Zhu

Technical Editor

Lukas Noguchi

BAMS Special Editor for Climate

Timothy DelSole

American Meteorological Society

Unauthenticated | Downloaded 11/21/25 11:34 AM UTC

Cover Credit:
Aerial view of the city of Canoas in the state of Rio Grande do Sul, Brazil, on 5 May 2024 during what is considered to be the worst flooding event on record to impact the country.
Photo credit: Ricardo Stuckert / PR

How to cite this document:
Regional Climates is one chapter from the *State of the Climate in 2024* annual report and is available from https://doi.org/10.1175/2025BAMSStateoftheClimate_Chapter7.1. Compiled by NOAA's National Centers for Environmental Information, *State of the Climate in 2024* is based on contributions from scientists from around the world. It provides a detailed update on global climate indicators, notable weather events, and other data collected by environmental monitoring stations and instruments located on land, water, ice, and in space. The full report is available from https://doi.org/10.1175/2025BAMSStateoftheClimate.1.

Citing the complete report:
Blunden, J. and J. Reagan, Eds., 2025: "State of the Climate in 2024". Bull. Amer. Meteor. Soc., 106 (8), Si–S513 https://doi.org/10.1175/2025BAMSStateoftheClimate.1.

Citing this chapter:
Arguez, A., P. Bissolli, C. Ganter, R. Martinez, A. Mekonnen, L. Stevens, and Z. Zhu, Eds., 2025: Regional Climates [in "State of the Climate in 2024"]. Bull. Amer. Meteor. Soc., 106 (8), S401–S513, https://doi.org/10.1175/2025BAMSStateoftheClimate_Chapter7.1.

Citing a section (example):
B. Forde, K. Brittain, V. Y. S. Cheng, and M. Beauchemin, 2025: Canada [in "State of the Climate in 2024"]. Bull. Amer. Meteor. Soc., 106 (8), S409–S413, https://doi.org/10.1175/2025BAMSStateoftheClimate_Chapter7.1.

Unauthenticated | Downloaded 11/21/25 11:34 AM UTC

Editor and Author Affiliations (alphabetical by name)

Agyakwah, W., ERT, Inc., College Park, Maryland

Aldeco, Laura S., Servicio Meteorológico Nacional, Buenos Aires, Argentina

Alfaro, Eric J., Center for Geophysical Research, University of Costa Rica, San José, Costa Rica; Center for Research in Marine Sciences and Limnology, University of Costa Rica, San José, Costa Rica; School of Physics, University of Costa Rica, San José, Costa Rica

Allen, Teddy, Caribbean Institute for Meteorology and Hydrology, Bridgetown, Barbados

Alves, Lincoln. M., National Institute for Space Research (INPE), São Paulo, Brazil

Amador, Jorge A., Center for Geophysical Research, University of Costa Rica, San José, Costa Rica; School of Physics, University of Costa Rica, San José, Costa Rica

Andrade, B., Seychelles Meteorological Authority, Mahe, Seychelles

Arguez, Anthony, NOAA/NESDIS National Centers for Environmental Information, Asheville, North Carolina

Asgharzadeh, Parvaneh, Climate Department, Iran National Meteorological Organization, Tehran, Iran

Avalos, Grinia, Servicio Nacional de Meteorología e Hidrología del Perú, Lima, Perú

Bandgar, Arti, India Meteorological Department, Pune, India

Bardin, M. Yu., Yu. A. Izrael Institute of Global Climate and Ecology, Institute of Geography, Russian Academy of Sciences, Moscow, Russia

Basckenstrass, Claire, Meteo France, Direction Interregionale Pour L'Ocean Indien, Réunion

Beauchemin, Marc, Environment and Climate Change Canada, Montreal, Canada

Bekele, E., NOAA/NWS National Centers for Environmental Prediction Climate Prediction Center, College Park, Maryland

Berne, Christine, Météo-France, Toulouse, France

Bilotta, Rocky, NOAA/NESDIS National Centers for Environmental Information, Asheville, North Carolina

Bissolli, Peter, Deutscher Wetterdienst, WMO RA VI Regional Climate Centre Network, Offenbach, Germany

Bochníček, Oliver, Slovak Hydrometeorological Institute, Bratislava, Slovakia

Brittain, Kyle, Environment and Climate Change Canada, Calgary, Canada

Bukunt, Brandon, NOAA/NWS Weather Forecast Office, Tiyan, Guam

Calderón, Blanca, Center for Geophysical Research, University of Costa Rica, San José, Costa Rica

Campbell, Jayaka, Department of Physics, The University of the West Indies, Kingston, Jamaica

Casella, Ana, Instituto Nacional de Meteorología e Hidrología de Venezuela (INAMEH), Caracas, Venezuela

Chandler, Elise, Bureau of Meteorology, Melbourne, Australia

Charlton, Candice S., Department of Physics, The University of the West Indies, Kingston, Jamaica

Chen, Hua, Nanjing University of Information Science and Technology, Nanjing, China

Cheng, Vincent Y. S., Environment and Climate Change Canada, Toronto, Canada

Clarke, Leonardo, Department of Physics, The University of the West Indies, Kingston, Jamaica

Correa, Kris, Servicio Nacional de Meteorología e Hidrología del Perú, Lima, Perú

Costa, Felipe, Centro Internacional para la Investigación del Fenómeno de El Niño (CIIFEN), Guayaquil, Ecuador

Cunha, Ana P., Centro Nacional de Monitoramento e Alertas de Desastres Naturais CEMADEN, São Paulo, Brazil

De Bock, Veerle, Royal Meteorological Institute of Belgium, Brussels, Belgium

Dindyal, S., Mauritius Meteorological Service, Vacoas, Mauritius

Dulamsuren, Dashkhuu, Information Research Institute of Meteorology, Hydrology and Environment, Ulaanbaatar, Mongolia

Echeverría Garcés, Paola, Instituto Nacional de Meteorología e Hidrología de Ecuador (INAMHI), Quito, Ecuador

Ekici, Mithat, Turkish State Meteorological Service, Ankara, Türkiye

ElKharrim, M., General Directorate of Meteorology, Rabat, Morocco

Espinoza, Jhan-Carlo, Université Grenoble Alpes, Institut des Géosciences de l'Environnement, IRD, CNRS, Grenoble INP, Grenoble, France

Fenimore, Chris, NOAA/NESDIS National Centers for Environmental Information, Asheville, North Carolina

Forde, Brendan, Environment and Climate Change Canada, Toronto, Canada

Fuhrman, S., ERT, Inc., College Park, Maryland

Ganter, Catherine, Bureau of Meteorology, Melbourne, Australia

Gevorgyan, Artur, Hydrometeorology and Monitoring Center, Yerevan, Armenia

Gleason, Karin, NOAA/NESDIS National Centers for Environmental Information, Asheville, North Carolina

Hakmi, S., General Directorate of Meteorology, Rabat, Morocco

Hidalgo, Hugo G., Center for Geophysical Research, Center for Research in Pure and Applied Mathematics; University of Costa Rica, San José, Costa Rica; School of Physics, University of Costa Rica, San José, Costa Rica

Jha, B., ERT, Inc., College Park, Maryland

Jumaux, G., Meteo France, Direction Interregionale Pour L'Ocean Indien, Réunion

Kabidi, K., General Directorate of Meteorology, Rabat, Morocco

Kazemi, Amin Fazl, Climate Department, Iran National Meteorological Organization, Tehran, Iran

Kendon, Michael, Met Office Hadley Centre, Exeter, United Kingdom

Kennedy, John, Independent Researcher, Verdun, France

Khalatyan, Yelena, Hydrometeorology and Monitoring Center, Yerevan, Armenia

Khan, Valentina, Hydrometeorological Centre of Russia, World Meteorological Organization (WMO) North EurAsia Climate Center, Moscow, Russia

Khiem, Mai Van, National Center of Hydro-Meteorological Forecasting, Vietnam Meteorological and Hydrological Administration, Hanoi, Vietnam

Korshunova, Natalia N., All-Russia Research Institute of Hydrometeorological Information, World Data Center, Obninsk, Russia

Kowal, K., NOAA/NWS National Centers for Environmental Prediction Climate Prediction Center, College Park, Maryland

Kruger, A. C., Climate Service, South African Weather Service, Pretoria, South Africa

Lakatos, Mónika, Climatology Unit, Hungarian Meteorological Service, Budapest, Hungary

Lam, Hoang Phuc, National Center of Hydro-Meteorological Forecasting, Vietnam Meteorological and Hydrological Administration, Hanoi, Vietnam

Lavado-Casimiro, Waldo, Servicio Nacional de Meteorología e Hidrología del Perú, Lima, Perú

Libonati, R., Federal University of Rio de Janeiro, Rio de Janeiro, Brazil

Liu, Xuefeng, Nanjing University of Information Science and Technology, Nanjing, China

Lu, Rui, Nanjing University of Information Science and Technology, Nanjing, China

Lui, Yuk Sing, Hong Kong Observatory, Hong Kong, China

Lunagomez Cruz, Daniela Paola, National Meteorological Service of Mexico, Mexico City, Mexico

Macara, Gregor, National Institute of Water and Atmospheric Research (NIWA), Lauder, New Zealand

Mamen, Jostein, Climate Division, Norwegian Meteorological Institute, Oslo, Norway

Marengo, Jose A., Centro Nacional de Monitoramento e Alertas de Desastres Naturais CEMADEN, São Paulo, Brazil

Martinez, Rodney, World Meteorological Organization, San Jose, Costa Rica

McBride, C., Climate Service, South African Weather Service, Pretoria, South Africa

Mekonnen, Ademe, North Carolina A&T University, Greensboro, North Carolina

Minney, Caitlin, Bureau of Meteorology, Melbourne, Australia

Mohammadi, Marjan, Climate Department, Iran National Meteorology Organization, Tehran, Iran

Moise, Aurel, Centre for Climate Research Singapore, Meteorological Service Singapore, Singapore

Molina-Carpio, Jorge, Universidad Mayor de San Andrés, La Paz, Bolivia

Unauthenticated | Downloaded 11/21/25 11:34 AM UTC

Editor and Author Affiliations (continued)

Montenegro, Martin, Centro Internacional para la Investigación del Fenómeno de El Niño (CIIFEN), Guayaquil, Ecuador

Moody, Ronald, Meteorological Service of Jamaica, Kingston, Jamaica

Mora, Natali, Center for Geophysical Research, University of Costa Rica, San José, Costa Rica

Morata Gasca, Ana, Agencia Estatal de Meteorología, Madrid, Spain

Mostafa, A. E., Department of Seasonal Forecast and Climate Research, Cairo Numerical Weather Prediction, Egyptian Meteorological Authority, Cairo, Egypt

Nomenjanahary, T., Seychelles Meteorological Authority, Mahe, Seychelles

Pan, Y., International Desks, NOAA/NWS National Centers for Environmental Prediction Climate Prediction Center, College Park, Maryland; ERT, Inc., College Park, Maryland

Pascual Ramírez, Reynaldo, National Meteorological Service of Mexico, Mexico City, Mexico

Rivera, P. P., Servicio Nacional de Meteorología e Hidrología del Perú, Lima, Perú

Robjhon, M., ERT Inc., College Park, Maryland; NOAA/NWS National Centers for Environmental Prediction Climate Prediction Center, NOAA, College Park, Maryland

Roebeling, Maarit, Deutscher Wetterdienst, WMO RA VI Regional Climate Centre Network, Offenbach, Germany

Ronchail, Josyane, Laboratoire LOCEAN-IPSL, Paris, France

Rubek, Frans, Danish Meteorological Institute, Copenhagen, Denmark

Sabeerali, C. T., India Meteorological Department, Pune, India

Salazar, Iliana, Centro Internacional para la Investigación del Fenómeno de El Niño (CIIFEN), Guayaquil, Ecuador

Salinas, Roberto, Dirección de Meteorología e Hidrología, Asunción, Paraguay; Dirección Nacional de Aeronáutica Civil, Asunción, Paraguay

Sato, Hirotaka, Tokyo Climate Center, Japan Meteorological Agency, Tokyo, Japan

Segele, Z. T., NOAA/NWS National Centers for Environmental Prediction Climate Prediction Center, College Park, Maryland

Sensoy, Serhat, Turkish State Meteorological Service, Ankara, Türkiye

Seong, Ji-In, Climate Change Monitoring Division, Korea Meteorological Administration, Seoul, South Korea

Serna Cuenca, Julieta, Instituto de Hidrología, Meteorología y Estudios Ambientales de Colombia (IDEAM), Bogotá, Colombia

Shukla, R., NOAA/NWS National Centers for Environmental Prediction Climate Prediction Center, College Park, Maryland; ERT Inc., College Park, Maryland

Sima, F., Retired, Banjul, The Gambia

Singh, B., University Corporation for Atmospheric Research Cooperative Programs for the Advancement of Earth System Science (CPAESS), College Park, Maryland

Smith, Adam, NOAA/NESDIS National Centers for Environmental Information, Asheville, North Carolina

Spence-Hemmings, Jacqueline, Meteorological Service of Jamaica, Kingston, Jamaica

Spillane, Sandra, Met Éireann, Dublin, Ireland

Sreejith, O. P., India Meteorological Department, Pune, India

Srivastava, A. K., India Meteorological Department, Pune, India

Stella, Jose L., Servicio Meteorológico Nacional, Buenos Aires, Argentina

Stephenson, Tannecia S., Department of Physics, The University of the West Indies, Kingston, Jamaica

Stevens, Laura, Cooperative Institute for Satellite Earth System Studies, North Carolina State University, Asheville, North Carolina

Syafrianno, Alif Akbar, BMKG, Jakarta, Indonesia

Takahashi, Kiyotoshi, Tokyo Climate Center, Japan Meteorological Agency, Tokyo, Japan

Takemura, Kazuto, Tokyo Climate Center, Japan Meteorological Agency, Tokyo, Japan

Taylor, Michael A., Department of Physics, The University of the West Indies, Kingston, Jamaica

Thiaw, W., NOAA/NWS National Centers for Environmental Prediction Climate Prediction Center, College Park, Maryland

Trotman, Adrian, Caribbean Institute for Meteorology and Hydrology, Bridgetown, Barbados

Turňa, Maroš, Slovak Hydrometeorological Institute, Bratislava, Slovakia

van der Linden, Roderick, Deutscher Wetterdienst, Offenbach, Germany

van der Schrier, Gerard, Royal Netherlands Meteorological Institute (KNMI), De Bilt, The Netherlands

Van Meerbeeck, Cédric J., Caribbean Institute for Meteorology and Hydrology, Bridgetown, Barbados

Vazifeh, Ahad, Climate Department, Iran National Meteorological Organization, Tehran, Iran

Virasami, R., Mauritius Meteorological Service, Vacoas, Mauritius

Willems, An, Royal Meteorological Institute, Brussels, Belgium

Yang, Ying, Jiangsu Meteorological Observatory, Nanjing, China

Zhang, Peiqun, Beijing Climate Center, China Meteorological Administration, Beijing, China

Zhu, Zhiwei, Nanjing University of Information Science and Technology, Nanjing, China

Editorial and Production Team

Allen, Jessicca, Graphics Support, Cooperative Institute for Satellite Earth System Studies, North Carolina State University, Asheville, North Carolina

Camper, Amy V., Graphics Support, Innovative Consulting and Management Services, LLC, NOAA/NESDIS National Centers for Environmental Information, Asheville, North Carolina

Carroll, Lauren, Content Team Lead, Communications and Outreach, NOAA/NESDIS National Centers for Environmental Information, Asheville, North Carolina

Haley, Bridgette O., Graphics Support, NOAA/NESDIS National Centers for Environmental Information, Asheville, North Carolina

Love-Brotak, S. Elizabeth, Lead Graphics Production, NOAA/NESDIS National Centers for Environmental Information, Asheville, North Carolina

Ohlmann, Laura, Technical Editor, Innovative Consulting and Management Services, LLC, NOAA/NESDIS National Centers for Environmental Information, Asheville, North Carolina

Noguchi, Lukas, Technical Editor, Innovative Consulting and Management Services, LLC, NOAA/NESDIS National Centers for Environmental Information, Asheville, North Carolina

Riddle, Deborah B., Graphics Support, NOAA/NESDIS National Centers for Environmental Information, Asheville, North Carolina

Veasey, Sara W., Visual Communications Team Lead, Communications and Outreach, NOAA/NESDIS National Centers for Environmental Information, Asheville, North Carolina

Unauthenticated | Downloaded 11/21/25 11:34 AM UTC

7. Table of Contents

Unauthenticated | Downloaded 11/21/25 11:34 AM UTC

7. Table of Contents

Unauthenticated | Downloaded 11/21/25 11:34 AM UTC

7. REGIONAL CLIMATES

A. Arguez, P. Bissolli, C. Ganter, R. Martinez, A. Mekonnen, L. Stevens, and Z. Zhu, Eds.

a. Overview

This chapter provides summaries of the 2024 temperature and precipitation conditions across seven broad regions: North America, Central America and the Caribbean, South America, Africa, Europe and the Middle East, Asia, and Oceania. Summaries of notable weather events are also included at the discretion of the authors. Local scientists provided the annual summary for their respective regions and, unless otherwise noted, the source of the data used is typically the agency affiliated with the authors. The base period used for these analyses is 1991–2020, unless otherwise stated. Please note that on occasion different nations, even within the same section, may use unique periods to define their normal. Section introductions typically define the prevailing practices for that section, and exceptions will be noted within the text. In a similar way, many contributing authors use languages other than English as their primary professional language. To minimize additional loss of fidelity through re-interpretation after translation, editors have been conservative and careful to preserve the voice of the author. In some cases, this may result in abrupt transitions in style from section to section.

Unauthenticated | Downloaded 11/21/25 11:34 AM UTC

b. North America

—L. Stevens, Ed.

Above-average temperatures were recorded across much of Canada, the United States, and the majority of Mexico in 2024. Portions of Mexico experienced near- to below-average temperatures. Averaged as a whole, North America's temperature was 1.32°C above the 1991–2020 base period, making 2024 the warmest year in the 115-year continental record that extends back to 1910. Multiple extreme heat events occurred in all three countries.

Precipitation varied across North America in 2024, and included several dry spells in many locations as well as notable flooding events. Impactful tropical cyclone events occurred in all three countries.

Several other extreme events occurred during the year, including a damaging hailstorm in Canada, wildfires in Canada and Mexico, and a very active tornado season in the United States.

Information in this section relates to the geographic continent of North America. Regions of the United States outside the contiguous United States, and the sections in this report in which they are described, are as follows: Alaska (Chapter 5), Puerto Rico (section 7c1), and Guam and the U.S.-Affiliated Pacific Islands (section 7h2). Limited temperature and precipitation data are available for Hawaii but will be included in the 2025 report. Tropical cyclone events affecting all regions are described in Chapter 4, including sidebars on Hurricanes Helene and Milton.

Anomalies in this section are all with respect to the 1991–2020 base period, unless otherwise noted.

1. CANADA

—B. Forde, K. Brittain, V. Y. S. Cheng, and M. Beauchemin

(i) Temperature

Canada's annual average temperature for 2024 was the highest in the nation's 77-year record, with an average temperature anomaly 2°C above the 1991–2020 average. This value surpassed the now second-warmest year on record set back in 2010 (Fig. 7.1; Vincent et al. 2020). Since national monitoring began in 1948, Canada's average temperature has shown a consistent upward climb. This linear trend represents an average temperature increase of 2.1°C since 1948, where 4 of the 10 warmest years on record have occurred since 2015. For this report, the Canadian Gridded Temperature and Precipitation Anomalies (CANGRD) product—a 50-km gridded temperature dataset—was used.

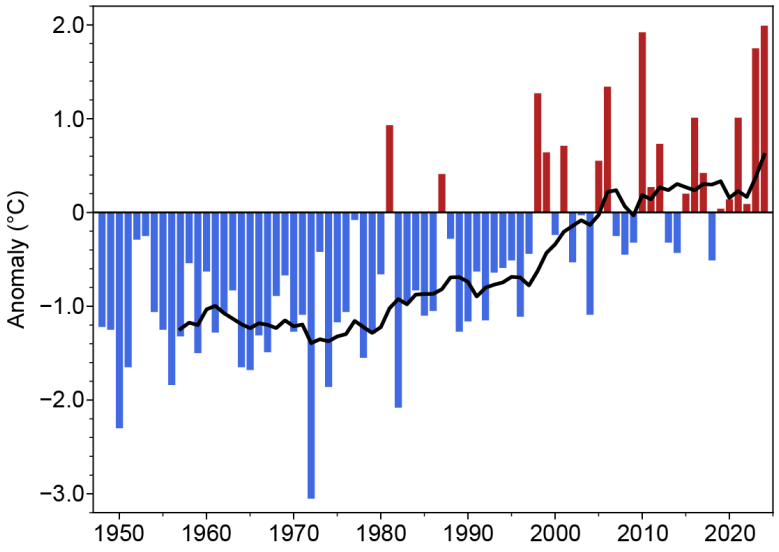

Fig. 7.1. Annual average temperature anomalies (°C; 1991–2020 base period) for Canada for the period 1948–2024. The black lines represent a lagged 10-yr running mean. (Source: Environment and Climate Change Canada.)

In 2024, annual anomalies greater than +1.0°C were recorded across most of Canada, with a clear east–west gradient observed across the nation (Fig. 7.2a). Eastern provinces including Ontario, Quebec, and the Maritimes recorded temperature anomalies exceeding +2.0°C. Four of the 13 provinces and territories (Manitoba, Prince Edward Island, Ontario, and Quebec) recorded their highest annual temperatures on record. Western provinces and territories such as Alberta, British Columbia, and the Yukon recorded annual temperature anomalies closer to the 1991–2020 average.

The winter (December 2023–February 2024) national average temperature was 3.7°C above the 1991–2020 average, making it the warmest winter on record. All Canadian provinces and territories recorded above-average winter temperatures (Fig. 7.2b). Central and eastern Canada experienced temperature anomalies ranging from +3.0°C to +6.0°C, while Nova Scotia and

Unauthenticated | Downloaded 11/21/25 11:34 AM UTC

western Canada recorded anomalies below +3.0°C. Out of the 13 provinces and territories, 3 recorded their warmest winters on record: Ontario (+5.7°C), Manitoba (+5.6°C), and New Brunswick (+3.4°C). The national average temperature for winter has increased by 3.6°C over the past 77 years.

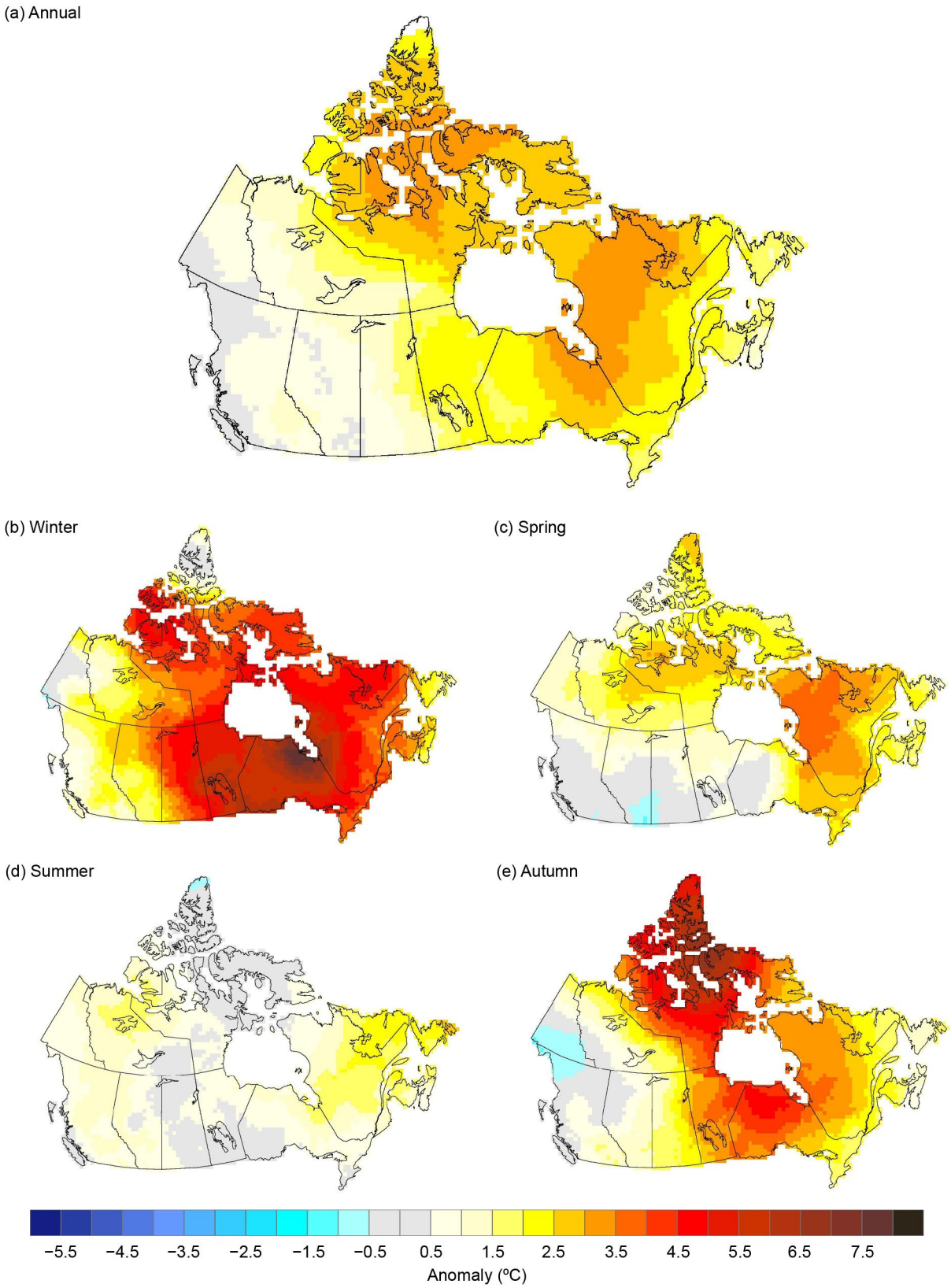

Fig. 7.2. (a) Annual, (b) winter 2023/24, (c) spring 2024, (d) summer 2024, and (e) autumn 2024 average temperature anomalies (°C; 1991–2020 base period) across Canada, using Environment and Climate Change Canada's (ECCC) 50-km gridded temperature analysis. (Source: ECCC.)

Unauthenticated | Downloaded 11/21/25 11:34 AM UTC

The spring (March–May 2024) national average temperature was 1.7°C above average, marking the fourth-warmest spring on record. All Canadian provinces recorded above-average spring temperatures (Fig. 7.2c). Most provinces saw temperature anomalies between +1.0°C and +3.0°C, while western provinces, including British Columbia, Alberta, Saskatchewan, and Manitoba, recorded anomalies below +1.0°C. Out of the 13 provinces and territories, 3 recorded their third-highest spring temperature since nationwide recording began: Newfoundland (+2.7°C), Nunavut (+2.3°C), and Quebec (+3.1°C). The national average temperature for spring has increased by 1.8°C over the past 77 years.

The summer (June–August 2024) national average temperature was 0.9°C above average, marking the fourth-warmest summer on record. All Canadian provinces recorded above-average summer temperatures (Fig. 7.2d). Most of Canada experienced temperature anomalies below +1.5°C, while Newfoundland and Labrador, New Brunswick, and Prince Edward Island recorded anomalies greater than +1.5°C. Out of the 13 provinces and territories, 5 recorded their warmest summer on record since nationwide recording began: Quebec (+1.4°C), New Brunswick (+1.5°C), Nova Scotia (+1.2°C), Newfoundland (+2.1°C), and Prince Edward Island (+1.5°C). The national average temperature for summer has increased by 1.8°C over the past 77 years.

The autumn (September–November 2024) national average temperature was 2.7°C above average, making it the warmest autumn on record. Most of Canada had autumn temperature anomalies that were between +2.0°C and +5.0°C, while British Columbia, Alberta, and the Yukon recorded temperature anomalies below +1.0°C (Fig. 7.2e). With an autumn temperature anomaly of −0.1°C, the Yukon was the only province or territory that recorded a below-average seasonal temperature. Out of the 13 provinces and territories, 5 recorded their warmest average autumn temperature on record: Manitoba (+3.4°C), Ontario (+3.5°C), Quebec (+2.9°C), New Brunswick (+1.9°C), and Nunavut (+4.7°C). The national average temperature for autumn has increased by 2.3°C over the past 77 years.

(ii) Precipitation

Environment and Climate Change Canada (ECCC) completed an extensive data reconciliation effort to link precipitation observations from automatic gauges with long-term historical observations, and developed the first homogenized long-term monthly precipitation station data series and gridded dataset for Canada (Wang et al. 2023). Work is underway to update these precipitation datasets to the most recent year to provide information on trends and variations. Until then, ECCC's 10-km gridded numerical precipitation analysis (10km-CaPA) is being used for this report.

Total precipitation across Canada varied greatly, with most locations experiencing drier-than-average conditions (Fig. 7.3a). Some areas in the Northwest Territories recorded precipitation measuring only 45%–60% of their normal; conversely, parts of the Prairies and Nunavut saw precipitation of up to 120% of normal.

Winter (December 2023–February 2024) saw wetter-than-average conditions in northern Canada, while the Prairies and southern Canadian regions experienced drier-than-average conditions (Fig. 7.3b).

Spring (March–May 2024) brought above-average precipitation to central and southeastern Canada. Western Canada, the Northwest Territories, and parts of the Maritime provinces experienced drier-than-average conditions (Fig. 7.3c).

In summer (June–August 2024), most of Canada experienced drier-than-average conditions with only small areas in the Maritimes and eastern Ontario receiving above-average precipitation (Fig. 7.3d).

In autumn (September–November 2024), eastern Canada experienced drier-than-average conditions while Nunavut and the central Prairies observed wetter-than-average conditions (Fig. 7.3e).

Unauthenticated | Downloaded 11/21/25 11:34 AM UTC

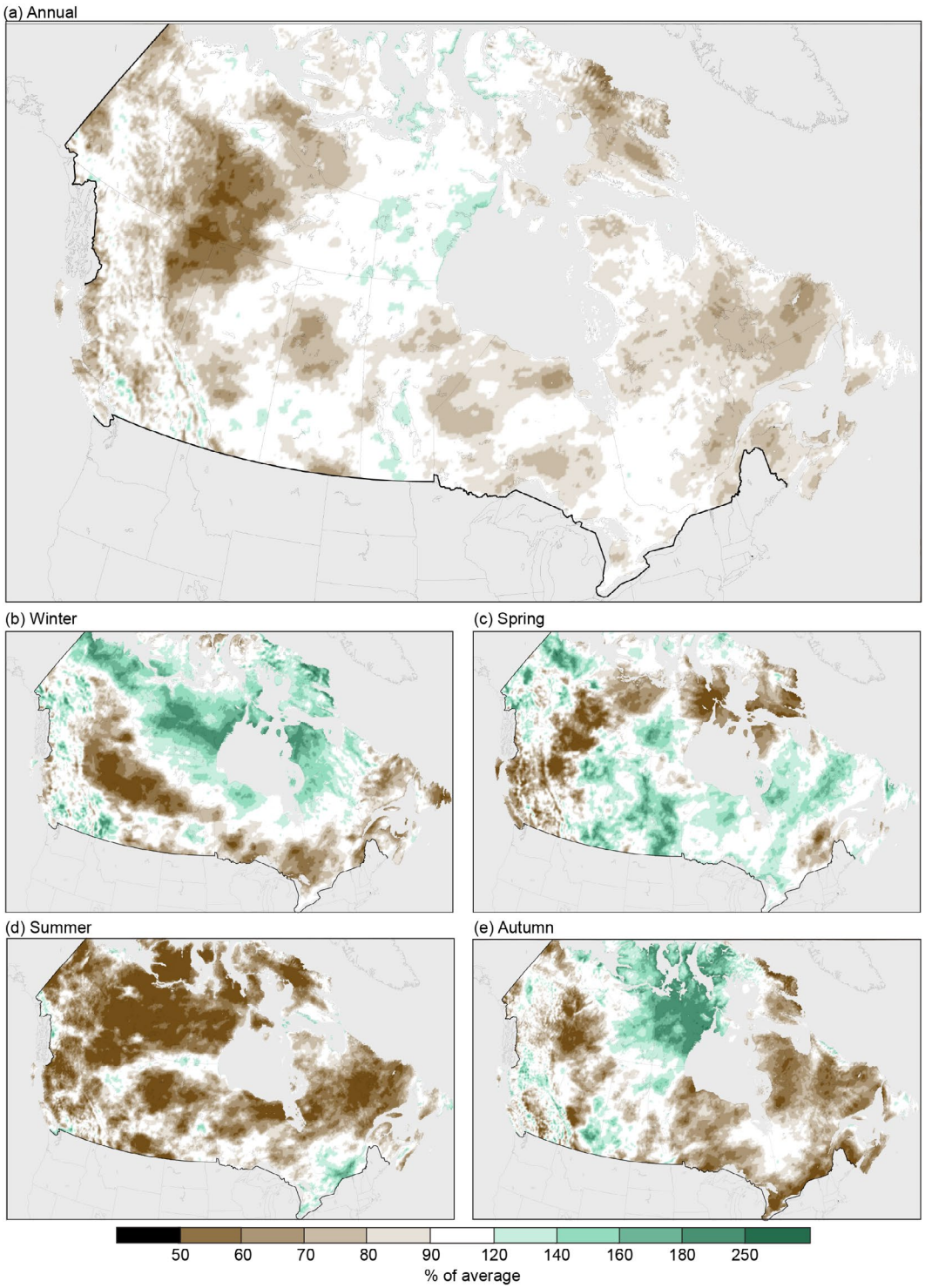

Fig. 7.3. (a) Annual, (b) winter 2023/24, (c) spring 2024, (d) summer 2024, and (e) autumn 2024 total precipitation (% of average; 1991–2020 base period) across Canada, using Environment and Climate Change Canada's (ECCC) 10-km gridded numerical precipitation analysis. (Source: ECCC.)

(iii) Notable events and impacts

Extreme weather events impacted millions of Canadians in 2024, causing destruction to property and resulting in a new all-time annual record in insured losses of over $8.5 billion (Canadian dollars, adjusted for inflation; CatIQ 2025a). In the span of just one month, four summertime events—including flooding events in southern Ontario and Quebec, a wildfire in the iconic Rockies town of Jasper, Alberta, and a $3.25 billion hailstorm in Calgary, Alberta—resulted in over $7.5 billion in damages.

The events of 2024 were also costly in terms of human life, with dozens of western Canada's homeless population perishing during a severe mid-January cold snap. Other fatalities occurred due to flooding events in British Columbia, Quebec, and Nova Scotia (ECCC 2025).

Unauthenticated | Downloaded 11/21/25 11:34 AM UTC

Extreme heatwaves brought record-breaking temperatures to parts of the Canadian Arctic, the Maritime provinces, and western Canada during the summer, which in turn fueled wildfire events that displaced thousands in Labrador and Alberta. Across Canada, wildfires consumed nearly 5.4 million hectares in 2024 (NRCan 2025).

On the afternoon of 22 July, lightning sparked several wildfires across Jasper National Park following a lengthy period of hot and dry weather. Approximately 25,000 people, including residents and visitors, were quickly evacuated from the park as a cluster of fires south of the Jasper Townsite rapidly merged. The wind-driven inferno reached the Jasper Townsite on the evening of 24 July, launching flames tens of meters above the trees and generating its own thunderstorm (ECCC 2025). Showers of embers ignited numerous fires around the townsite, leading to the loss of over 30% of its structures and incurring $1.1 billion (Canadian dollars) in damage (IBC 2025). Tragically, a wildland firefighter lost his life while fighting the fire on 3 August.

Elsewhere, significant urban flooding occurred in several major centers across Canada throughout the year. The remnants of Tropical Cyclone Debby brought flooding rains to eastern Ontario and southern Quebec during 9–10 August. Between 100 mm and 200 mm of rain fell along and north of the densely populated St. Lawrence River Valley, causing flooding that impacted over 1000 homes and damaged 170 roads across southern Quebec. A man lost his life in the Mauricie region when the roadway he was standing on collapsed (ECCC 2025). This flooding event became the costliest weather disaster in Quebec's history, resulting in over $2.7 billion (Canadian dollars) in insured losses (IBC 2025).

On 5 August, large hailstones driven by high winds pelted thousands of homes and vehicles across the northern suburbs of Calgary, Alberta. The storm caused substantial damage, including the collapse of part of a terminal roof at Calgary International Airport. Total insured losses exceeded $3.25 billion (Canadian dollars; CatIQ 2025b), making this the second-costliest disaster in Canadian history. It was also Calgary's second billion-dollar hailstorm in less than five years.

2. UNITED STATES

—K. Gleason, C. Fenimore, R. Bilotta, and A. Smith

(i) Temperature

The annual average temperature for the contiguous United States (CONUS) in 2024 was 13.1°C, which was 1.2°C above the 1991–2020 average, marking the warmest year in the 130-year record (Fig. 7.4a). Regions with the largest positive temperature anomalies were concentrated across portions of the South and from the Upper Midwest to the Mid-Atlantic and into the Northeast (Fig. 7.5a). The annual average temperature across Alaska in 2024 was 0.5°C above average and was the 16th highest on record. Based on a linear regression of data from 1895 to 2024, the annual CONUS temperature is increasing at an average rate of 0.09°C decade^{-1} (0.28°C decade^{-1} since 1970). The annual temperature for Alaska over its 100-year record (1925–2024) is increasing at an average rate of 0.17°C decade^{-1} since 1925 (0.44°C decade^{-1} since 1970).

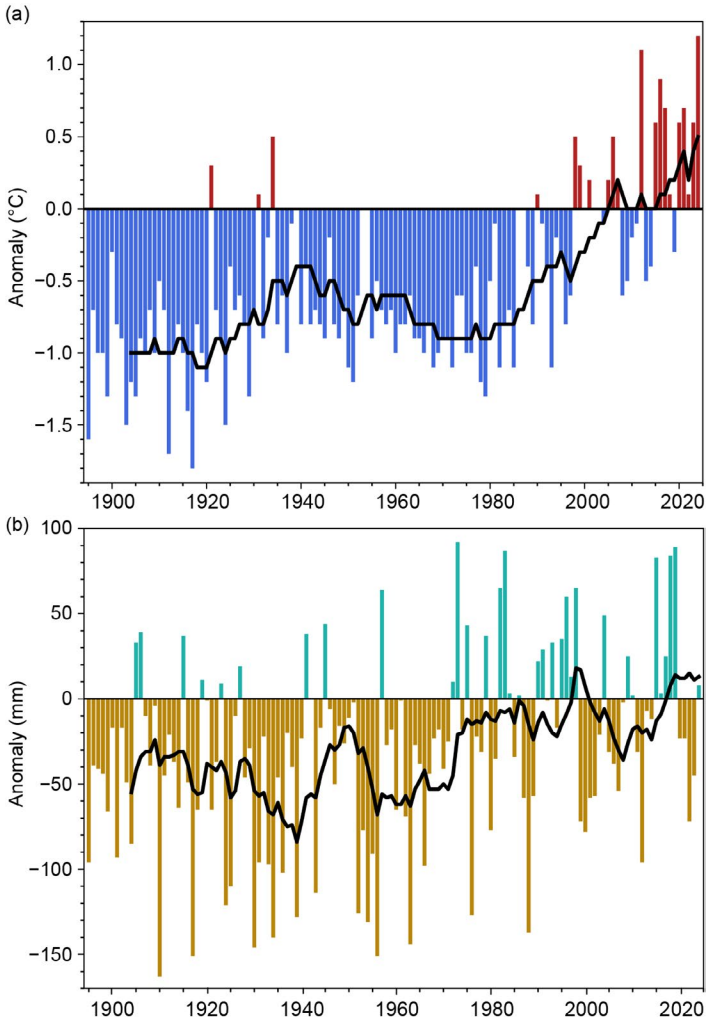

Fig. 7.4. Annual (a) average temperature anomalies (°C) and (b) precipitation anomalies (mm; 1991–2020 base period) for the contiguous United States for the period 1895–2024. The black lines represent a lagged 10-yr running mean. (Source: NOAA/NCEI.)

Unauthenticated | Downloaded 11/21/25 11:34 AM UTC

The winter (December 2023–February 2024) CONUS temperature was record high at 1.9°C above average, with temperature anomalies greater than 2.5°C stretching from the Upper Midwest to the Northeast (Fig. 7.5b). The CONUS spring (March–May) temperature was 0.8°C above average, the seventh highest on record, with above-average temperatures extending across the eastern half of the CONUS (Fig. 7.5c). The summer (June–August) CONUS temperature was fourth highest on record at 0.8°C above average. Record warmth occurred in parts of the West, Northeast, and Florida (Fig. 7.5d). The autumn (September–November) CONUS temperature was record high at 1.7°C above average. Most of the CONUS experienced above-average temperatures with record heat observed across portions of the Rockies, central Plains, Deep South, Great Lakes, and Northeast (Fig. 7.5e).

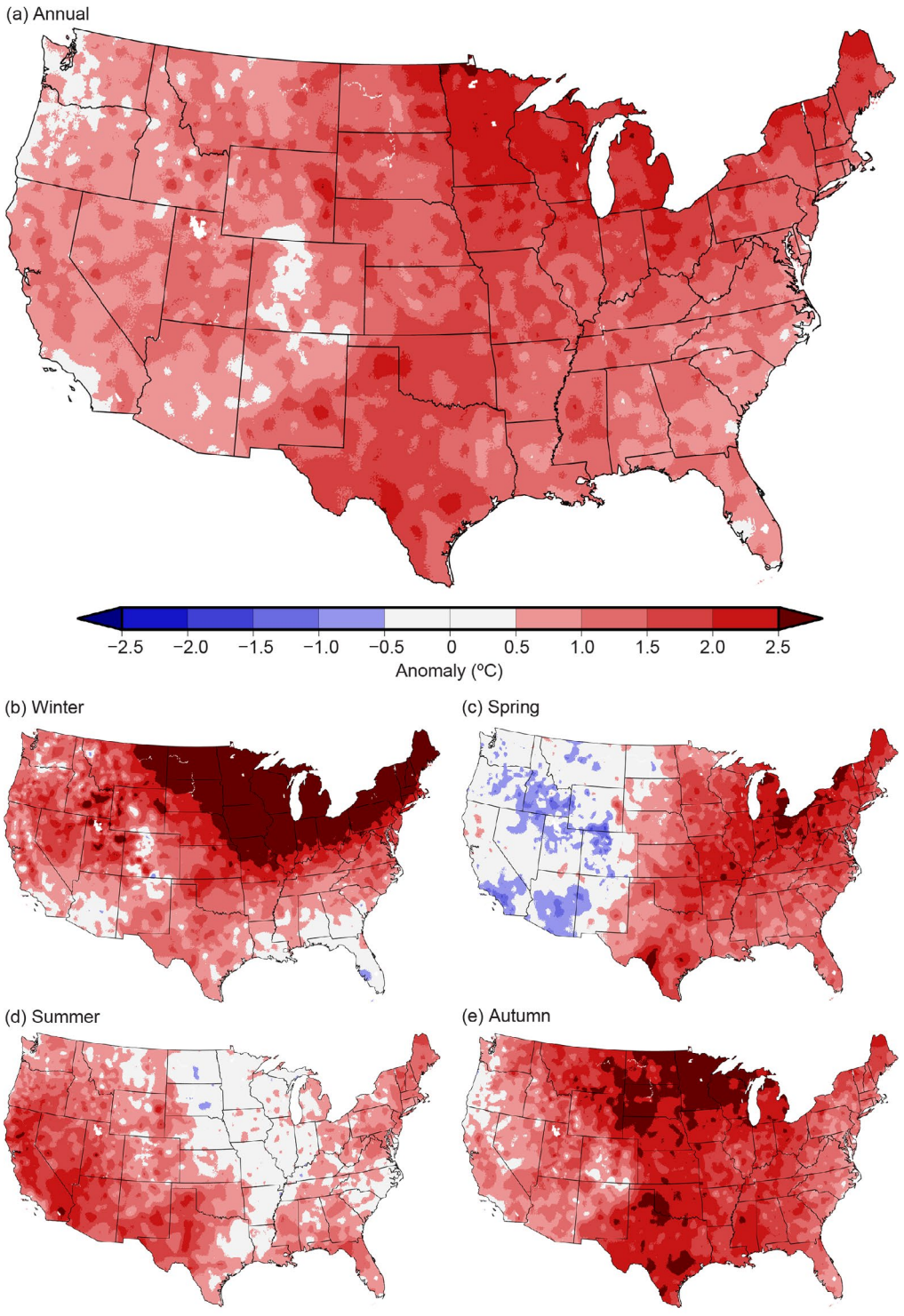

Fig. 7.5. (a) Annual, (b) winter 2023/24, (c) spring 2024, (d) summer 2024, and (e) autumn 2024 average temperature anomalies (°C; 1991–2020 base period) across the contiguous United States. (Source: NOAA/NCEI.)

Unauthenticated | Downloaded 11/21/25 11:34 AM UTC

(ii) Precipitation

Precipitation for the CONUS was near average at 803 mm (Fig. 7.4b). The 2024 total annual precipitation for Alaska (not shown) was equal to its 1991–2020 mean value. The annual precipitation total for the CONUS has been increasing at an average rate of 4 mm decade^{-1} since 1895 (1 mm decade^{-1} since 1970). Precipitation for Alaska is increasing at an average rate of 2 mm decade^{-1} since 1925 (20 mm decade^{-1} since 1970).

Winter precipitation across the CONUS was 113% of the 1991–2020 average, with above-average precipitation observed across much of the Plains and East Coast, as well as in parts of the West and along the Gulf Coast. Dry conditions were concentrated across the northern Rockies and Plains as well as across West Texas (Fig. 7.6b). Spring precipitation was 112% of average.

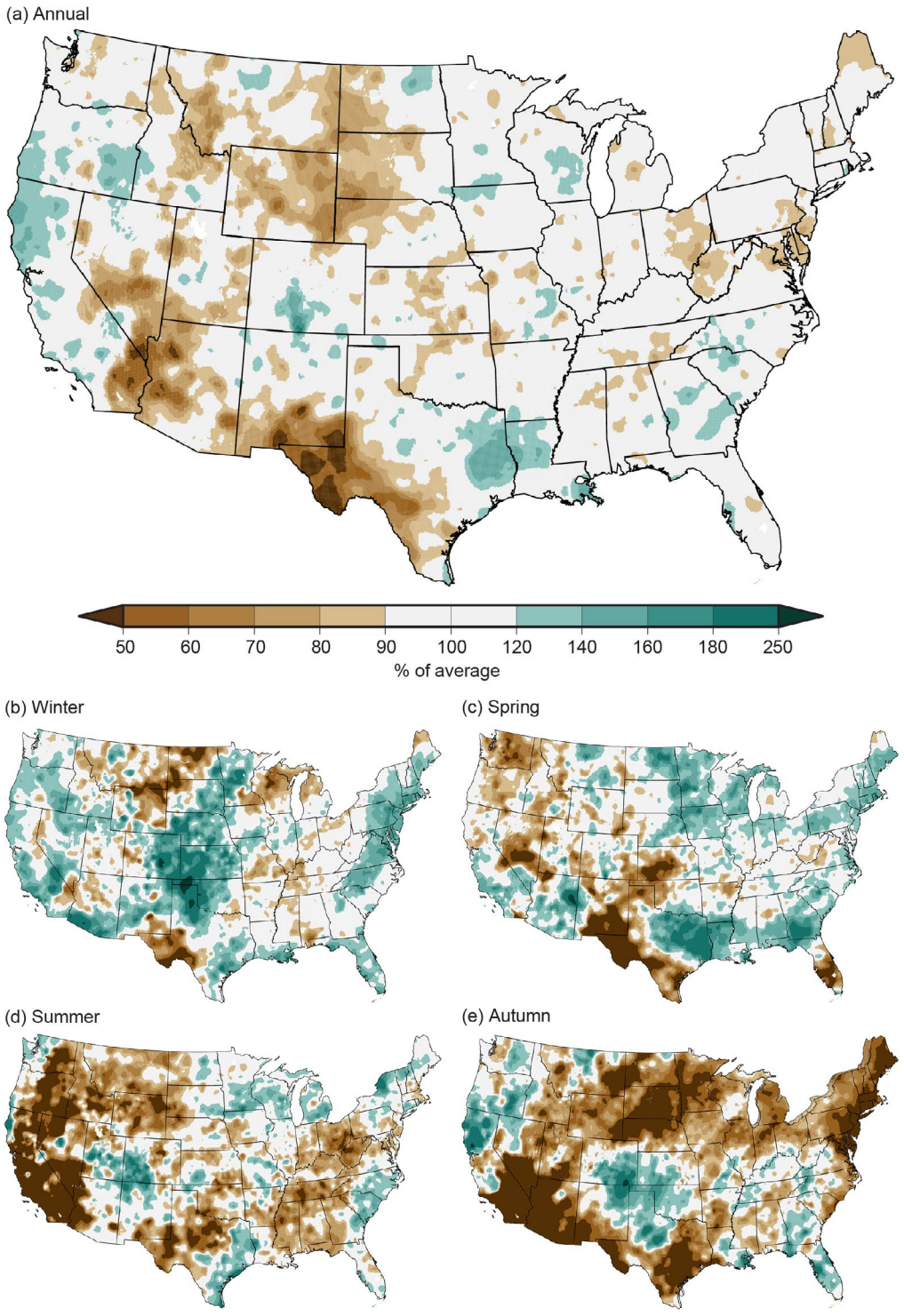

Fig. 7.6. (a) Annual, (b) winter 2023/24, (c) spring 2024, (d) summer 2024, and (e) autumn 2024 total precipitation (% of average; 1991–2020 base period) across the contiguous United States. (Source: NOAA/NCEI.)

Unauthenticated | Downloaded 11/21/25 11:34 AM UTC

Above-average precipitation extended from the northern Plains to the Great Lakes and into the Northeast and was also present across much of the South and Southeast as well as in parts of the Southwest (Fig. 7.6c). Summer precipitation across the CONUS was 96% of average. Conditions were dry across much of the West and northern Rockies, as well as parts of the South and from the central Gulf Coast to the Ohio Valley. Precipitation was above average across parts of the central Rockies, Upper Midwest, Great Lakes, Northeast, Gulf Coast, and Southeast (Fig. 7.6d). The autumn CONUS precipitation total was 86% of average. Precipitation was below average across parts of the South, much of the Southwest, and from the central and northern Rockies to the Great Lakes and into the Northeast, resulting in the driest autumn on record for parts of the Mid-Atlantic and Northeast. Wetter-than-average conditions were concentrated across the central Rockies and the central and southern Plains as well as in parts of the Southeast (Fig. 7.6e).

The year began with approximately 33% of the CONUS in drought. Drought coverage contracted as the year progressed and reached the minimum extent of 12% on 11 June for the year—the smallest CONUS drought footprint since early 2020. As the summer progressed, hot and dry conditions led to the expansion of drought across the Plains, Midwest, Southeast, and Mid-Atlantic. By 29 October, the extent of drought peaked, with more than half of the CONUS (54%) in drought, including significant portions of the Northwest, Southwest, northern and central Rockies, Plains, Great Lakes, and western and central Gulf Coast states, as well as the central Appalachians, the Mid Atlantic, and portions of the Northeast. On 5 November, abnormal dryness and drought covered 87.8% of the CONUS—the greatest such coverage in the U.S. Drought Monitor record (since 2000; NDMC 2025).

(iii) Notable events and impacts

More than 405,000 hectares were consumed by the Smokehouse Creek wildfire in 2024, primarily across the Texas Panhandle during February and March, as dry conditions, warm temperatures, and gusty winds contributed to the rapid spread. This was the largest wildfire on record for Texas, causing two fatalities and destroying more than 100 homes in less than three weeks. The fourth-largest wildfire in California history, known as the Park Fire, consumed nearly 174,000 hectares and destroyed over 600 structures in northern California during the summer and autumn of 2024. For the year, approximately 3.6 million hectares were consumed by fire across the CONUS and Alaska (NIFC 2025).

The tornado count for 2024 was the second highest on record behind 2004 (1817 tornadoes), with 1791 confirmed tornadoes (SPC 2025). With respect to EF-2+ tornadoes, 2024 was the most active year since the historic 2011 season. The highest EF-rated tornadoes observed during 2024 were four EF-4s that occurred in Nebraska, Oklahoma, and Iowa. Overall, there were more than 50 fatalities associated with tornadoes across the United States during 2024, which is below the 1994–2023 average of 72.

Record heat and notable heatwaves impacted the Southwest, Northeast, and Florida in 2024. On 7 July, Las Vegas, Nevada, reported an all-time record high temperature of 49°C, while Palm Springs, California, measured a record high of 51°C on 5 July. An extended heatwave in Phoenix, Arizona, produced 113 consecutive days of 38°C (100°F) or higher temperatures during summer, shattering the previous record of 76 days set in 1993. These persistent and extreme temperatures contributed to more than 600 fatalities in Maricopa County (MCPHD 2025). Across the Northeast and Florida, several cities—including Dulles, Virginia; Caribou, Maine; Hartford, Connecticut; and Fort Lauderdale, Florida—experienced their warmest summer on record.

During 2024, the United States experienced 27 weather and climate disasters each incurring losses that exceeded $1 billion U.S. dollars (adjusted for inflation), which was the second-highest number of billion-dollar disasters to occur in a calendar year (2023 had 28 disasters). These disasters included: 17 severe storms, five tropical cyclones, two winter storms, one flooding event, one drought/heatwave, and one wildfire event (NOAA NCEI 2025). The impacts from the two most costly events of the year—Hurricanes Helene and Milton—were particularly destructive, having caused more than $100 billion (NOAA NCEI 2025) in combined damage across Florida (Helene and Milton), Georgia, South Carolina, North Carolina, Tennessee, and Virginia (Helene) over a two-week period from late September into early October. (See Sidebars 4.1 and 4.2 for details on Hurricanes Helene and Milton, respectfully). Landfalling Category 4 or 5 hurricanes have impacted the CONUS in six of the last eight years.

Unauthenticated | Downloaded 11/21/25 11:34 AM UTC

3. MEXICO

—R. Pascual Ramírez and D. P. Lunagomez Cruz

(i) Temperature

Mexico's annual average temperature in 2024 was 22.9°C, 1.4°C above the 1991–2020 average (Fig. 7.7a). This was the highest temperature since national records began in 1953, exceeding the previous record set in 2023 by 0.2°C. Mexico continued to experience a warming trend, with 2024 marking the 15th consecutive year with an above-average national temperature. Most of the nation saw above-average temperatures, with the exception of parts of the northwest and western regions, which observed near- to below-average temperatures (Fig. 7.8a). While the nation had an above-average temperature anomaly for each month of 2024, only May (+2.9°C) and June (+2.5°C) ranked warmest for their respective months. June 2024 tied July 2023 for the warmest overall month in the historical record, with a national average monthly temperature of 27.6°C. The coolest month of the year was January, which had a national average temperature of 24.4°C, only 0.1°C above average.

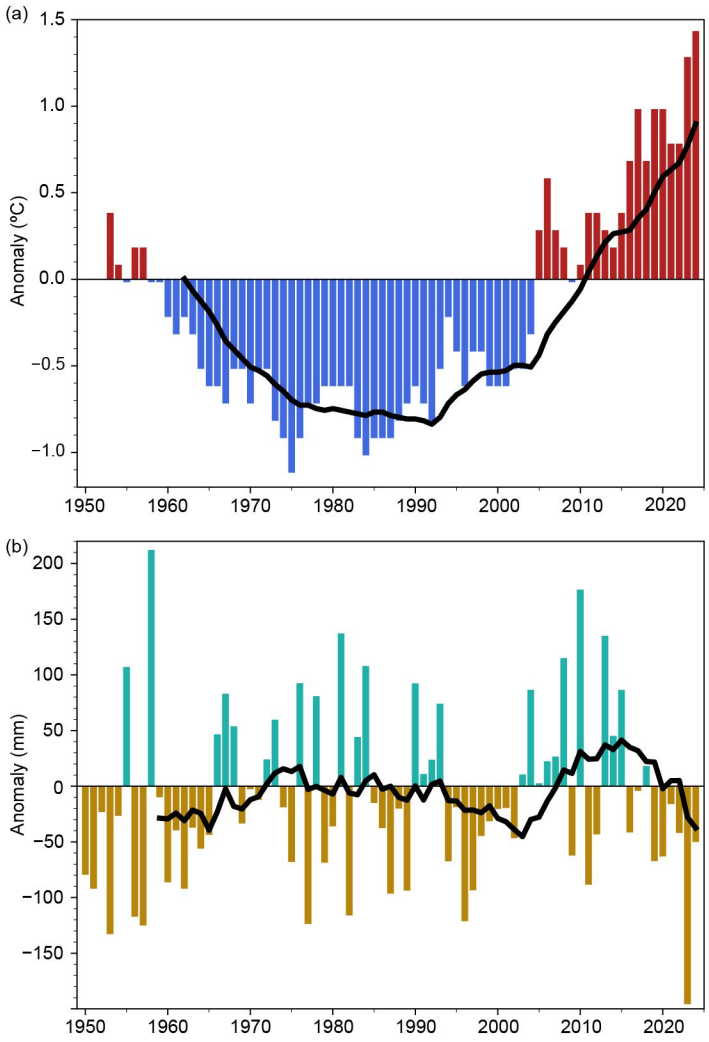

Fig. 7.7. Annual (a) average temperature anomalies for the period 1953–2024 (°C) and (b) precipitation anomalies for the period 1950–2024 (mm; 1991–2020 base period) for Mexico. The black lines represent a 10-yr lagged running mean. (Source: National Meteorological Service of Mexico.)

Mexico has a warm season (spring and summer) and a cool season (autumn and winter). The nation had a winter (December–February) average temperature of 17.3°C, which was 0.1°C above average, marking the 13th-warmest winter on record. Spring (March–May) 2024 saw an average temperature of 23.6°C, which was 1.5°C above the seasonal average, marking the warmest spring on record. Summer (June–August) 2024 ranked as the second-warmest summer on record (behind 2023) with a national average of 27.0°C, which was 2.2°C above average. In autumn (September–November), the national average temperature was 23.2°C, which was 1.5°C above average, marking the second-warmest autumn on record (also behind 2023).

(ii) Precipitation

The national average precipitation in 2024 totaled 735.7 mm, 93.6% of the 1991–2020 average, marking the 25th-driest year on record (Fig. 7.7b). The northeast and the Yucatan Peninsula were the main regions with above-average precipitation during the year (Fig. 7.9a). Central and central-west regions of the Mexican South Pacific saw a combination of above-average, below-average, and near-average rainfall. The largest rainfall deficits were observed in large portions of the Mexican North Pacific, northwest, and north-central regions. Climatologically, September tends to be the rainiest month in the country, contributing 18.8% of the annual rainfall; however, in 2024, June and July were the wettest overall. July contributed 153.8 mm, or 20.9% of the 2024 rainfall, followed by June, which contributed 151.9 mm, or 20.6% of the annual rainfall and marked the wettest June on record. In contrast, March is statistically the driest month, typically contributing 2.1% of the annual rainfall. However, in 2024, April was the driest month of the year, having contributed only 7.8 mm or 1.1% of the annual rainfall, marking the third-driest April on record. May was also drier than average, having contributed 11.0 mm, and ranked as the second-driest May on record. During the January–March quarter, rainfall was

Unauthenticated | Downloaded 11/21/25 11:34 AM UTC

below average across much of the country, with only portions of the northwest, north central, and the Yucatan Peninsula receiving above-average rainfall.

Mexico experiences a rainy season during the summer, which typically commences in June. However, during May 2024, a significant amount of rain fell across the northwest, while the rest of the country showed a dry footprint. Over the summer, there was an improved rainfall contribution mainly due to precipitation from Tropical Storms Alberto (16–20 June) and Chris (29 June–1 July) over the northeast, along with that of Hurricane Beryl (4–6 July) over the Yucatan Peninsula.

For a second consecutive year, the monsoon season was weak, resulting in large parts of the northwest experiencing well-below-average rainfall. The last quarter of the year marks the transition between the end of the rainy season and the beginning of the dry season in Mexico. During this transition period, it is common to observe a combination of tropical and winter systems over the country. Tropical Depression 11E reached the southern Pacific coast in early October, while Tropical Storm Nadine affected southern Mexico during 18–20 October.

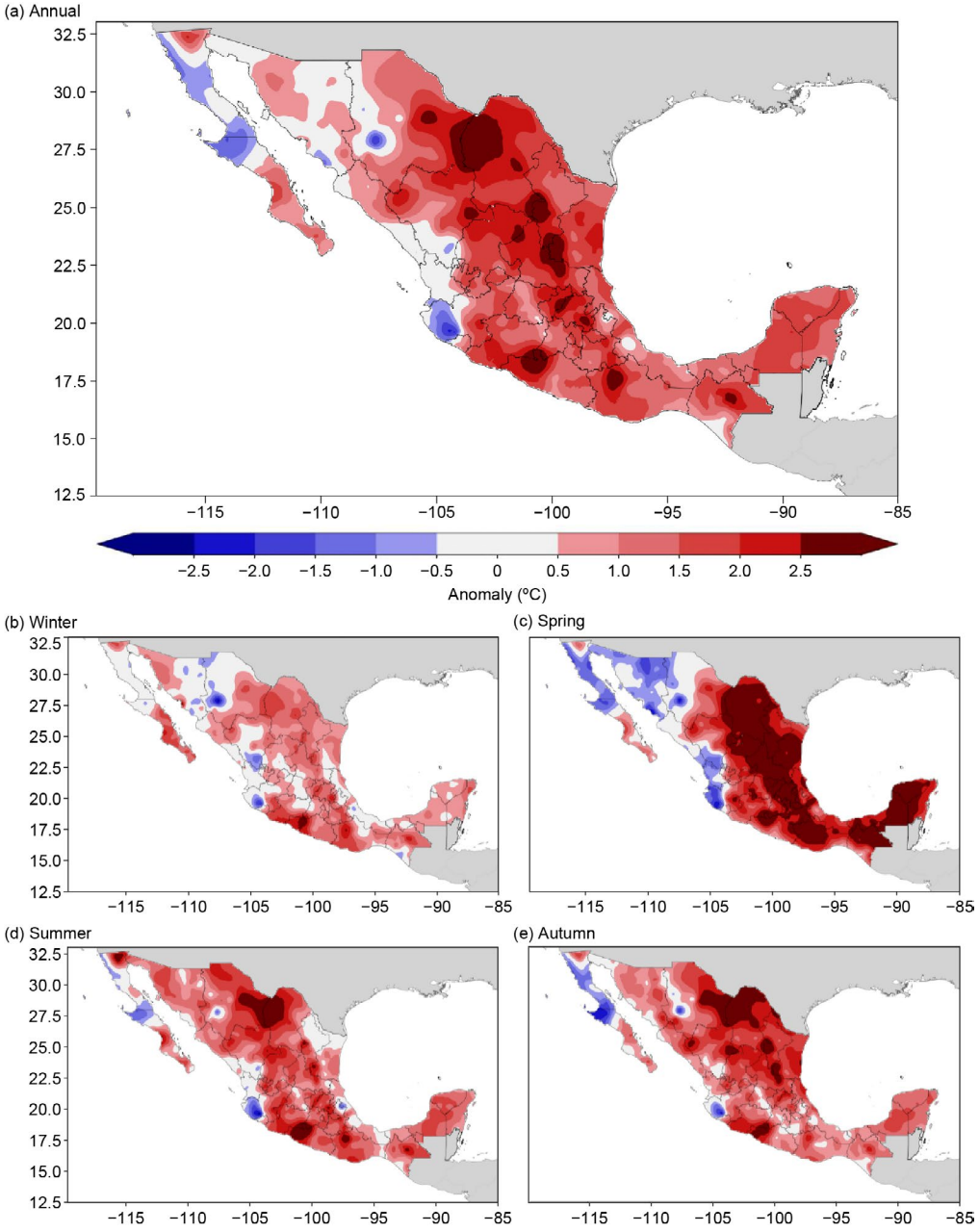

Fig. 7.8. (a) Annual, (b) winter 2023/24, (c) spring 2024, (d) summer 2024, and (e) autumn 2024 average temperature anomalies (°C; 1991–2020 base period) across Mexico. (Source: National Meteorological Service of Mexico.)

Unauthenticated | Downloaded 11/21/25 11:34 AM UTC

Northwest Mexico has been experiencing a prolonged period of drought dating back to September 2023. However, during 2024, drought conditions extended into central Mexico. May saw the highest percentage of drought by area during the year, covering 76% of the country; this also was the fourth-highest monthly percentage overall, less than only June 2011 (85.1%), May 2011 (86.5%), and April 2011 (87.0%), according to data from the Mexican Drought Monitor.

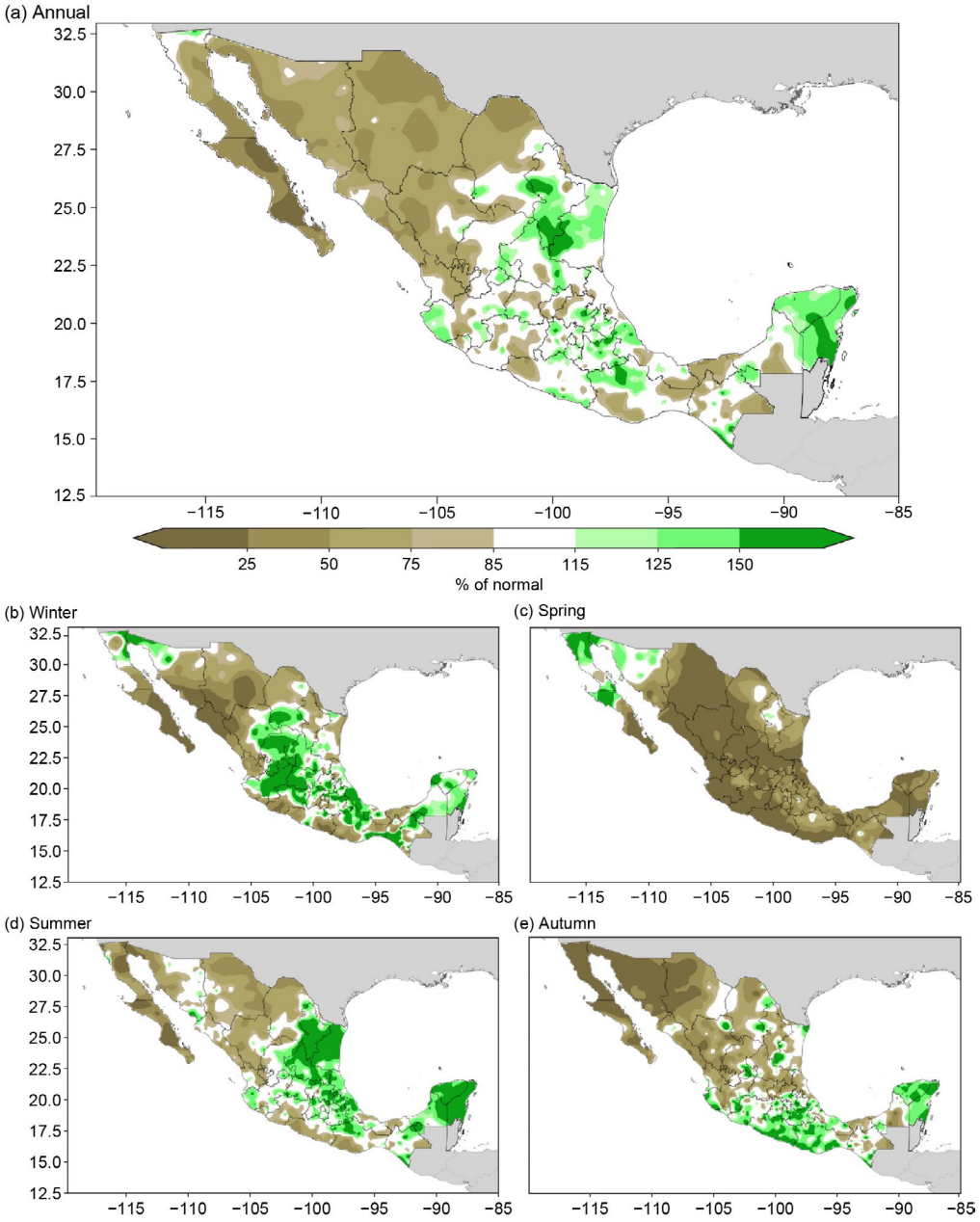

Fig. 7.9. (a) Annual, (b) winter 2023/24, (c) spring 2024, (d) summer 2024, and (e) autumn 2024 precipitation anomalies (% of average; 1991–2020 base period) across Mexico. (Source: National Meteorological Service of Mexico.)

(iii) Notable events and impacts

High temperatures and a lack of rain characterized the months of April and May, along with the first few days of June. During this period, the Mexican Weather Service identified three heatwaves. During the first heatwave (13–19 April), maximum temperatures reached 7°C–9°C above the monthly average across the northern Plateau (Chihuahua, Durango, Coahuila, Nuevo Leon, and Zacatecas). During the second heatwave (3–13 May), maximum temperatures were as much as 8°C–10°C above the May average across a local region in the northeast known as The Huastecas (the joint border of Tamaulipas, San Luis Potosi, Queretaro, Hidalgo, and Veracruz).

Unauthenticated | Downloaded 11/21/25 11:34 AM UTC

During the third heatwave (20 May–4 June), above-average temperatures covered most of the country, with the exception of the northwest and the Baja California Peninsula.

The national maximum temperature for 2024 occurred in Tepache, Sonora (in northwestern Mexico), on 20 June with a value of 52.0°C. This tied the national all-time high temperature record, which was set on 27–28 July 1995 in Mexicali, Baja California.

Several local maximum temperature records were also established in 2024. In Mexico City, for example, the annual maximum temperature record was broken seven times between April and May, ultimately reaching 34.7°C on 25 May. In Hermosillo, Sonora, a record-high temperature of 49.5°C was reached on 12 June, exceeding the previous maximum value of 49.0°C on 25 June 2023.

According to Mexico's National Forestry Commission (CONAFOR), 2024 was classified as the year with the largest area burned by fires, totaling 1,672,216 hectares. This exceeds the previous annual record for total area burned (in 2023) by more than 600,000 hectares.

In September, Hurricane John made landfall in the Acapulco area of the Pacific coast, the same area impacted by Hurricane Otis in 2023. John, which reached Category 3 on the Saffir-Simpson scale, produced 1442 mm of rainfall from 24 to 28 September in Acapulco. The precipitation from this single event exceeded the average annual total rainfall of 1378.5 mm for the town of Acapulco.

Unauthenticated | Downloaded 11/21/25 11:34 AM UTC

c. Central America and the Caribbean

—A. Arguez, Ed.

1. CENTRAL AMERICA

—H. G. Hidalgo, J. A. Amador, E. J. Alfaro, B. Calderón, and N. Mora

Nine stations were analyzed across Central America (see Fig. 7.10 for stations and specific data sources). The station distribution is representative of the relevant seasonal and intraseasonal regimes of precipitation (Amador 1998; Magaña et al. 1999; Amador et al. 2016a,b), wind (Amador 2008), and temperature (Hidalgo et al. 2019) on the Caribbean and Pacific slopes of Central America (CA). Precipitation and temperature data were provided either by Central America National Weather Services (CA-NWS), NOAA, or the University of Costa Rica; however, in some cases, missing 2024 daily precipitation data were filled in with the nearest grid point data from the Climate Hazards and Infrared Precipitation (CHIRPs; Funk et al. 2015). Anomalies are reported using a 1991–2020 base period and were calculated from CA-NWS data. The methodologies used for all variables are described by Amador et al. (2011).

(i) Temperature

The year 2024 was warmer than normal (relative to the 1991–2020 base period) across most of Central America, with the most notable high annual temperature anomalies (Tm; °C) in Guatemala, Belize, and the Caribbean coast of Costa Rica. The stations of Phillip Goldson International Airport (PGIA; Tm1; +0.92°C), Puerto Barrios (Tm2; +1.09°C), Limón (Tm4; +0.72°C), and Montufar (Tm9; +1.79°C) had mean annual temperatures that were statistically significantly ($p \leq 0.05$) higher than the climatology. The Liberia Airport station was the only station analyzed to have a below-normal annual temperature (not significant). The five-day average temperature (Tm; °C) frequency distributions in 2024, as well as the climatology, for all stations analyzed are shown in Fig. 7.10. Annual temperature anomalies for each station are shown in Table 7.1.

Table 7.1. Annual temperature and precipitation anomalies for 2024 with respect to the 1991–2020 averages (normals), calculated from monthly means and accumulations, respectively. Anomalies in the 95% tails of the 1991–2020 (two-tailed) statistical distributions are marked with a star icon (★). Only annual anomalies are presented; seasonal anomalies are not considered as the typical trimester seasons used in mid- and high latitudes are not representative for the tropics.

Station	2024 Annual Temperature Anomaly (°C)	1991–2020 Annual Temperature Normal (°C)	2024 Annual Precipitation Anomaly (mm)	1991–2020 Annual Precipitation Normal (mm)
Phillip Goldson International Airport (PGIA), Belize	+0.92 ★	26.9	+548.7	1963
Puerto Barrios, Guatemala	+1.09 ★	26.6	–483.8	3331
Lempira, Honduras	+1.03	26.7	–1093.5 ★	2699
Limón, Costa Rica	+0.72 ★	25.4	–404.17	3687
Tocumen Airport, Panama	+0.45	27.2	+754.8	1760
David, Panama	+0.19	28.0	+608.6	2196
Liberia Airport, Costa Rica	–0.42	27.1	+660.7	1735
Choluteca, Honduras	+0.48	29.8	+870.8	1963
Montufar, Guatemala	+1.79 ★	27.8	+478.4	1689

Unauthenticated | Downloaded 11/21/25 11:34 AM UTC

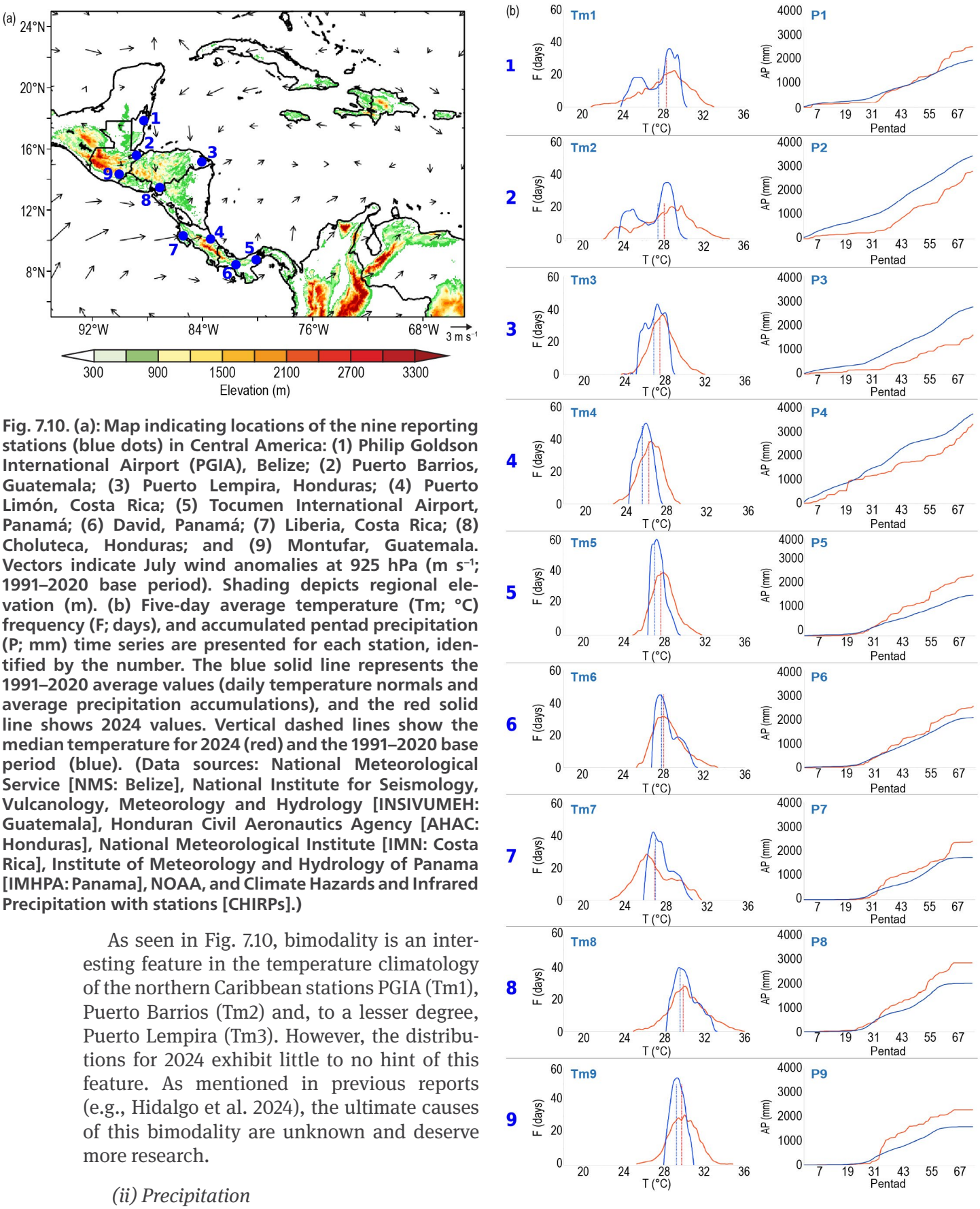

Fig. 7.10. (a): Map indicating locations of the nine reporting stations (blue dots) in Central America: (1) Philip Goldson International Airport (PGIA), Belize; (2) Puerto Barrios, Guatemala; (3) Puerto Lempira, Honduras; (4) Puerto Limón, Costa Rica; (5) Tocumen International Airport, Panamá; (6) David, Panamá; (7) Liberia, Costa Rica; (8) Choluteca, Honduras; and (9) Montufar, Guatemala. Vectors indicate July wind anomalies at 925 hPa (m s^{-1}; 1991–2020 base period). Shading depicts regional elevation (m). (b) Five-day average temperature (Tm; °C) frequency (F; days), and accumulated pentad precipitation (P; mm) time series are presented for each station, identified by the number. The blue solid line represents the 1991–2020 average values (daily temperature normals and average precipitation accumulations), and the red solid line shows 2024 values. Vertical dashed lines show the median temperature for 2024 (red) and the 1991–2020 base period (blue). (Data sources: National Meteorological Service [NMS: Belize], National Institute for Seismology, Vulcanology, Meteorology and Hydrology [INSIVUMEH: Guatemala], Honduran Civil Aeronautics Agency [AHAC: Honduras], National Meteorological Institute [IMN: Costa Rica], Institute of Meteorology and Hydrology of Panama [IMHPA: Panama], NOAA, and Climate Hazards and Infrared Precipitation with stations [CHIRPs].)

As seen in Fig. 7.10, bimodality is an interesting feature in the temperature climatology of the northern Caribbean stations PGIA (Tm1), Puerto Barrios (Tm2) and, to a lesser degree, Puerto Lempira (Tm3). However, the distributions for 2024 exhibit little to no hint of this feature. As mentioned in previous reports (e.g., Hidalgo et al. 2024), the ultimate causes of this bimodality are unknown and deserve more research.

(ii) Precipitation

The annual precipitation accumulations (P; mm) showed statistically significant ($p \leq 0.05$) drier-than-normal conditions in Puerto Lempira (P3; –1093.5mm). The remainder of the stations reported positive anomalies that were not statistically significant, except for Puerto Barrios (P2) and Puerto Limon (P4), which reported non-significant below-normal conditions. The lack of statistically significant annual precipitation accumulations across the Pacific slopes of

Unauthenticated | Downloaded 11/21/25 11:34 AM UTC

Central America coincided with relatively low tropical cyclone activity in the Pacific oceanic basin during 2024. Dry conditions along the central Caribbean coast of Central America, with wetter-than-normal precipitation over the Pacific slope, is a weather pattern typically associated with La Niña and above-normal sea surface temperature anomalies in the Caribbean/Atlantic oceanic basin indexed by the Tropical Northern Atlantic index (TNA; not shown) in a dipole fashion. Such climate teleconnections are referenced in other studies (e.g., Enfield and Alfaro 1999; Durán-Quesada et al. 2020). It is important to note that negative Oceanic Niño Index values were not reported until the July–September trimester of 2024, and that the negative values in the latter half of 2024 were not sufficiently negative or persistent enough to be characterized as a La Niña event (see section 4b for details). However, the TNA was indeed consistently positive throughout 2024 (https://psl.noaa.gov/data/correlation/tna.data), which could suggest that the expected significantly above-normal precipitation pattern was not clearly developed over the Pacific slope. The high-Pacific versus low-Caribbean pressure gradient that produces anomalous westerly flow (shown in the wind anomaly pattern of Fig. 7.10a) is coherent with the aforementioned SST dipole conditions and generally consistent with the above-normal (below-normal) annual precipitation accumulations in the Pacific (Caribbean) slopes observed across Central America in 2024. Annual precipitation anomalies for each station are listed in Table 7.1.

(iii) Notable events and impacts

The 2024 Atlantic tropical cyclone activity was considered to be an above-average season (see section 4g2). In contrast, the eastern tropical Pacific region showed relatively less activity (see section 4g3), with most tropical cyclones developing in the northern part, resulting in relatively low socioeconomic impacts for Central America. There were 96 fatalities due to hydrometeorological events (extreme rainfall and compounding impacts such as winds, mudslides, landslides, floods) in the region for 2024, excluding 26 fatalities due to tropical cyclones and another 26 attributed to lightning strikes (Table 7.2). Hurricane Rafael and Tropical Storm Sara both formed in the Caribbean Sea in November. Rafael caused indirect effects over the southernmost part of the region, leading to five deaths in Panama and two in Costa Rica. Sara caused landslides and floods across most countries in the region and contributed to 19 fatalities (Table 7.2). Due to their broad areas of impact, these two tropical cyclones accounted for most of the socioeconomic impacts in the region in 2024.

Table 7.2. Number of fatalities in several Central American countries due to hydrometeorological events, specific tropical cyclones (Hurricane Rafael and Tropical Storm Sara), and lightning strikes. Data sources: Central American national weather services, regional newspapers, and national emergency committees, including: the National Civil Protection System (SINAPROC; Panama), the National Commission for Risk Prevention and Emergency Response (CNE; Costa Rica), the National System for Civil Protection, Disaster Prevention and Mitigation (El Salvador), the Permanent Contingency Commission of Honduras (COPECO; Honduras), the National Coordination for Disaster Reduction (CONRED; Guatemala), and El Diario de Hoy (Nicaragua).

Country	Hydrometeorological Events	Rafael	Sara	Lightning Strikes
Panamá	7	5	6	12
Costa Rica	5	2	4	1
Nicaragua	16	0	2	5
El Salvador	24	0	0	2
Honduras	12	0	7	3
Guatemala	32	0	0	3
TOTAL	96	7	19	26

Unauthenticated | Downloaded 11/21/25 11:34 AM UTC

2. CARIBBEAN

—T. S. Stephenson, M. A. Taylor, A. Trotman, C. J. Van Meerbeeck, L. Clarke, T. Allen, J. Spence-Hemmings, R. Moody, C. Charlton, and J. Campbell

(i) Temperature

The year 2024 was the warmest year, on average, for the Caribbean region (Figs. 7.11, 7.12) since records begin in 1950 in the ERA5 global reanalysis (Hersbach et al. 2020). The annually averaged 2-m temperature was 26.81°C, which was 0.84°C above the 1991–2020 average. The seasons of December–February (0.65°C above normal) and March–May (+1.05°C) were record warm, while June–August (+0.81°C versus +0.96°C in 2023) and September–November (+0.85°C versus +1.03°C in 2023) were second warmest on record for their respective seasons. Overall, the region has been warming at a rate of 0.13°C decade^{-1} since 1950 (0.19°C decade^{-1} since 1970). Fifteen of 38 stations across Caribbean islands recorded their warmest year on record. Twenty-four stations exceeded their 90th percentile annual mean temperature, while one station recorded an annual mean temperature below its 10th percentile. Record daily minimum temperatures were also observed across several stations (Fig. 7.13). A record-warm tropical North Atlantic was a primary driver of the record-high air temperatures.

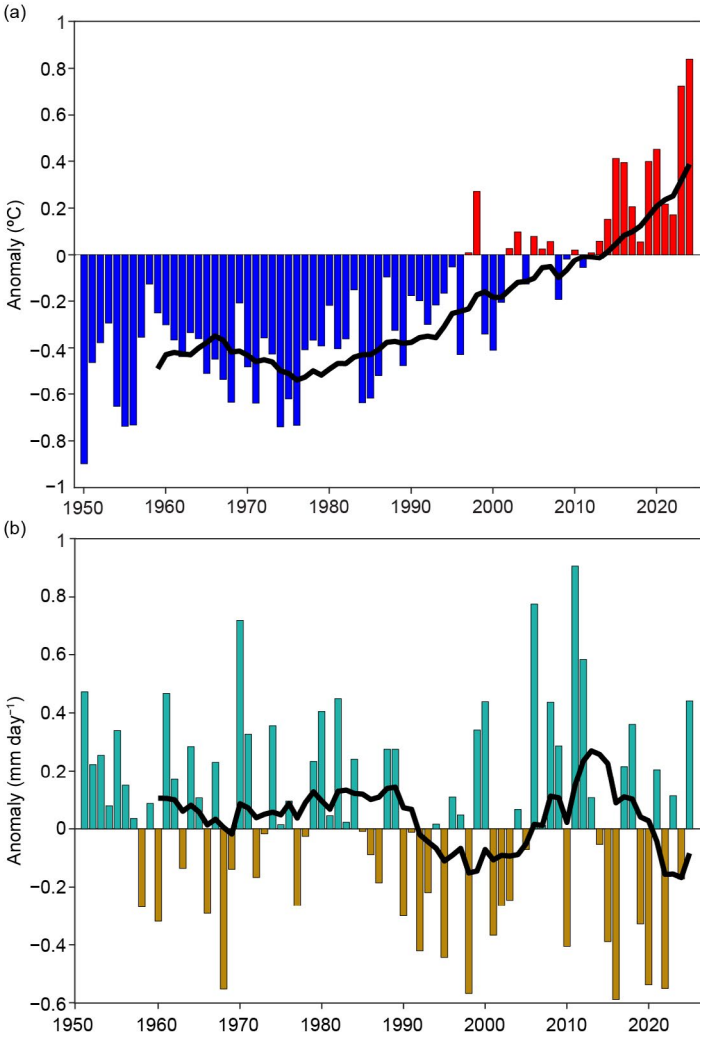

Fig. 7.11. Annually averaged (a) 2-m temperature anomaly (°C) and (b) rainfall anomaly (mm day^{-1}) time series for the Caribbean (9°N–27°N, 58°W–90°W) for the period 1950–2024 relative to the 1991–2020 average. The black line represents the 10-yr running mean. (Source: ERA5 from the Copernicus Climate Data Store.)

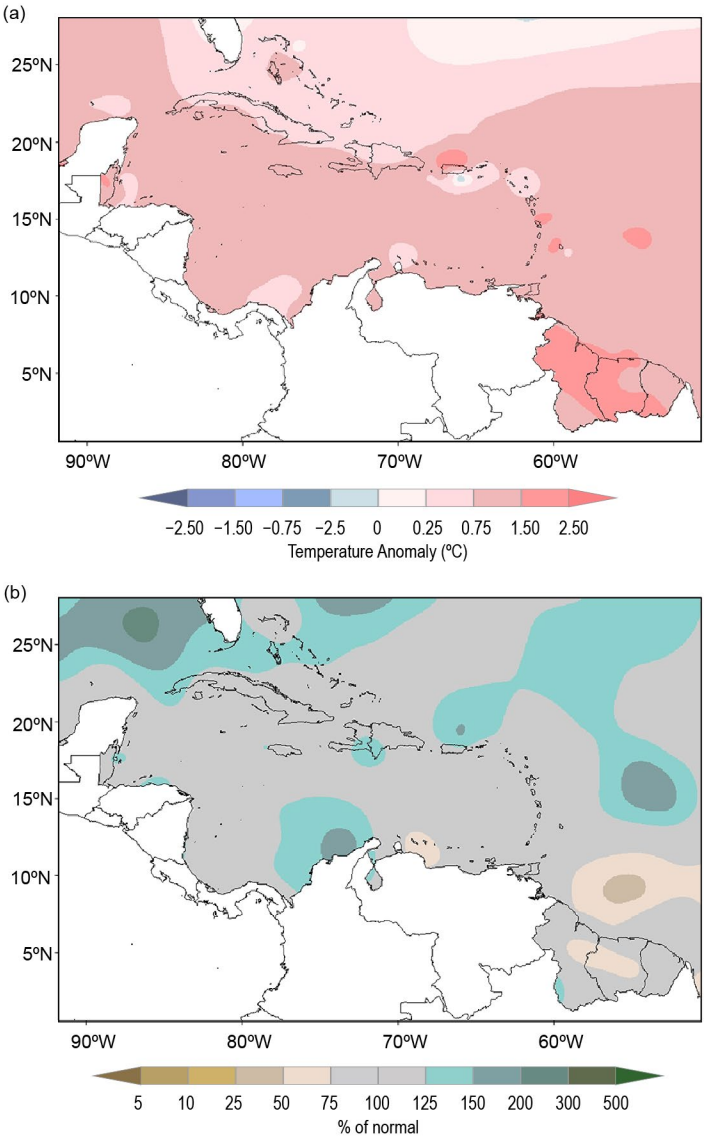

Fig. 7.12. Annual (a) mean temperature anomalies (°C) and (b) total precipitation anomalies (% of normal) relative to 1991–2020. (Source: Caribbean Climate Outlook Forum [CariCOF] and the Caribbean Institute for Meteorology and Hydrology.)

Unauthenticated | Downloaded 11/21/25 11:34 AM UTC

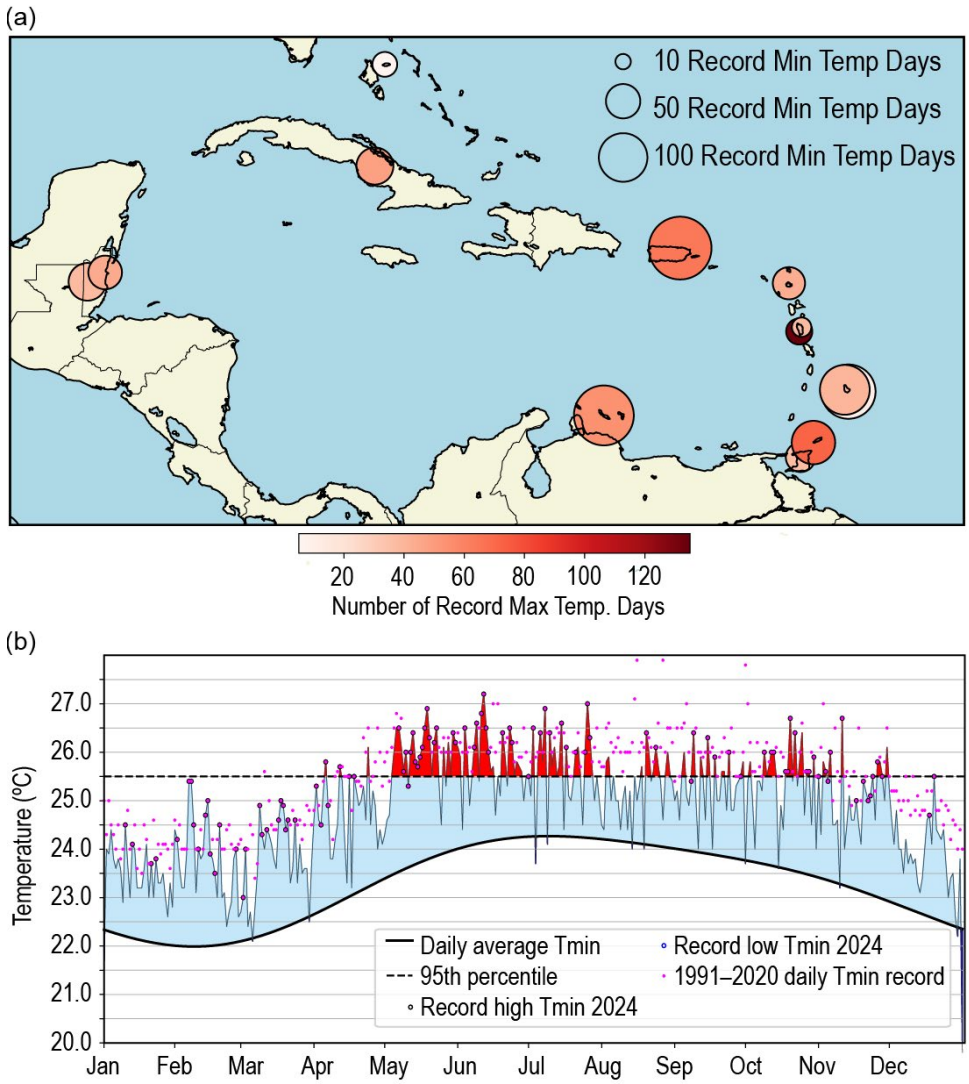

Fig. 7.13. (a) Count of days with record daily temperatures. Shading shows number of record days for maximum temperature and circle size shows number of record days for minimum temperature. (b) Daily minimum temperature for the Caribbean Institute for Meteorology and Hydrology in Barbados relative to the 1991–2020 climatology (thick black curve). Above-normal temperatures are shaded light blue. Values exceeding the 95th percentile (horizontal black line) are shaded red and the daily record from 1971 (magenta dot) and the daily record during 2024 (magenta dot outlined in black) are also shown.

(ii) Precipitation

The 2024 annually averaged rainfall for the Caribbean was the eighth wettest on record (since 1950) at 3.67 mm day^{-1}, which is 114% of the 1991–2020 average (Figs. 7.11, 7.12). The signature December–February Caribbean rainfall pattern associated with a Pacific El Niño, in which the north Caribbean is relatively wet and the south dry (Stephenson et al. 2008), was generally observed, although wetter-than-normal conditions were observed north of Colombia. For March–May, short- and/or long-term drought conditions were noted over the eastern Caribbean, including Barbados, Grenada, St. Lucia, St. Vincent and the Grenadines, Trinidad and Tobago, and the U.S. Virgin Islands, and normal- to above-normal rainfall anomalies were observed largely over the rest of the region. This pattern was consistent with the dissipation of the El Niño in May. The early wet season (June–August) and the late wet season (September–November) yielded normal- to above-normal rainfall over much of the region, concurrent with a record-warm tropical North Atlantic and near-record humid heat in the latter season. The June–August rainfall anomaly for the region was the eighth wettest on record (4.93 mm day^{-1}, 126.9% of normal). Cabrera, Dominican Republic, recorded its wettest year in its 54-year record (3383.3 mm, 205.3% of normal). Eighteen of the 38 stations analyzed recorded annual rainfall above the 90th percentile, and seven stations were below the 10th percentile.

Unauthenticated | Downloaded 11/21/25 11:34 AM UTC

(iii) Notable events and impacts

During 22–25 March, several towns in and around the Cuban province of Artemisa were impacted by floods and hail from severe weather, affecting over 270,000 people (Delforge et al. 2025). Storm surge associated with Major Hurricane Beryl—the earliest Category 5 storm in the Atlantic hurricane season with wind speeds in excess of 270 km h^{-1} (see sections 4g1 and 4g2)—impacted Barbados on 1–2 July, where about 2500 residents were affected. Beryl also impacted Grenada (Union, Carriacou, and Petite Martinique islands) during 1–4 July, causing eight deaths and affecting over 7000 people. Total damage was close to $430 million (U.S. dollars). Beryl impacted St. Vincent and the Grenadines (Union Island, Canouan Island, and Mayrea) over the same period, affecting 15,000 residents and resulting in insured damage of ~$1.8 million (U.S. dollars). Beryl also impacted Jamaica during 3–4 July. While the storm passed just south of the island, it affected about 160,060 residents and caused $1 billion (U.S. dollars; Delforge et al. 2023) in damage. Tropical Storm Ernesto passed the Caribbean Netherlands (Saba and St. Eustatius) on 13 August. The islands mainly experienced heavy rain that led to flooding and falling rocks, along with strong winds that downed trees.

Following an unusual lull in Atlantic hurricanes between mid-August and mid-September, Hurricane Helene tracked east of Cuba as a Category 1 storm on 26–27 September. The storm caused flooding and storm surge for Artemisa and its coastal communities (see Sidebar 4.1 for more details about Helene). Hurricane Oscar made landfall over eastern Cuba during 21–22 October as a Category 1 storm, later weakening to a tropical storm while over the island and causing 10 deaths, $50 million (U.S. dollars) in damage, and impacting more than 320,000 residents. Tropical Storm Rafael passed west of Jamaica on 6 November before rapidly intensifying to a Category 3 hurricane and impacting Artemisa in Cuba on 6 November. The impacts over Jamaica were experienced over four days and resulted in two fatalities and close to $8 million (U.S. dollars) in damage. The impacts over Cuba spanned two days, affecting four million people and causing $1.08 billion (U.S. dollars) in damage. Tropical Cyclone Sara impacted the Dominican Republic and Haiti as a disturbance on 17–18 November and caused three deaths across both countries. On 30 November–4 December and 20–28 December, floods due to heavy rains were experienced in Haiti and caused 30 deaths across the two rain events.

Unauthenticated | Downloaded 11/21/25 11:34 AM UTC

d. South America

1. NORTHERN SOUTH AMERICA

—A. Casella, F. Costa, P. Echeverría, I. Salazar, J. Serna, and M. Montenegro

The northern South America region includes Colombia, Ecuador, French Guiana, Guyana, Suriname, and Venezuela. Throughout this section, 1991–2020 is the base period used for both temperature and precipitation.

Temperature and precipitation patterns in northern South America during the early months of 2024 showed the influence of the 2023/24 El Niño. This event ended in April as a neutral El Niño–Southern Oscillation (ENSO) phase emerged (see section 4b1 for details).

(i) Temperature

Overall, annual maximum temperatures across northern South America were mostly above normal in 2024. In Suriname, maximum recorded values were 2°C to 2.75°C above average, particularly notable from January to March. In Venezuela, the anomalies were between 1°C and 3°C above normal. In Colombia, the average maximum temperatures were particularly high in the first quarter of the year and in September–October at 2°C to 5°C above the average. Conversely, Ecuador had below-normal maximum temperatures with anomalies between –1°C and –3°C (Fig. 7.14a).

Annual minimum temperatures over northern South America were also mainly above normal with positive anomalies between +0.25°C and +2.5°C. The exception was in Venezuela, where minimum temperatures were around 1.5°C below normal (Fig. 7.14b).

The mean temperature over northern South America was also above normal, with anomalies mostly ranging between +0.5°C and +1.25°C (Fig. 7.14c). The above-normal temperatures in most countries across northern South America may be associated with the 2023/24 El Niño in the eastern equatorial Pacific (see section 4b1 for details). Additionally, the global influence derived from the extraordinary warming of surface waters in different oceans, which persisted over the last few months of 2024 (Cheng et al. 2025), is also highlighted.

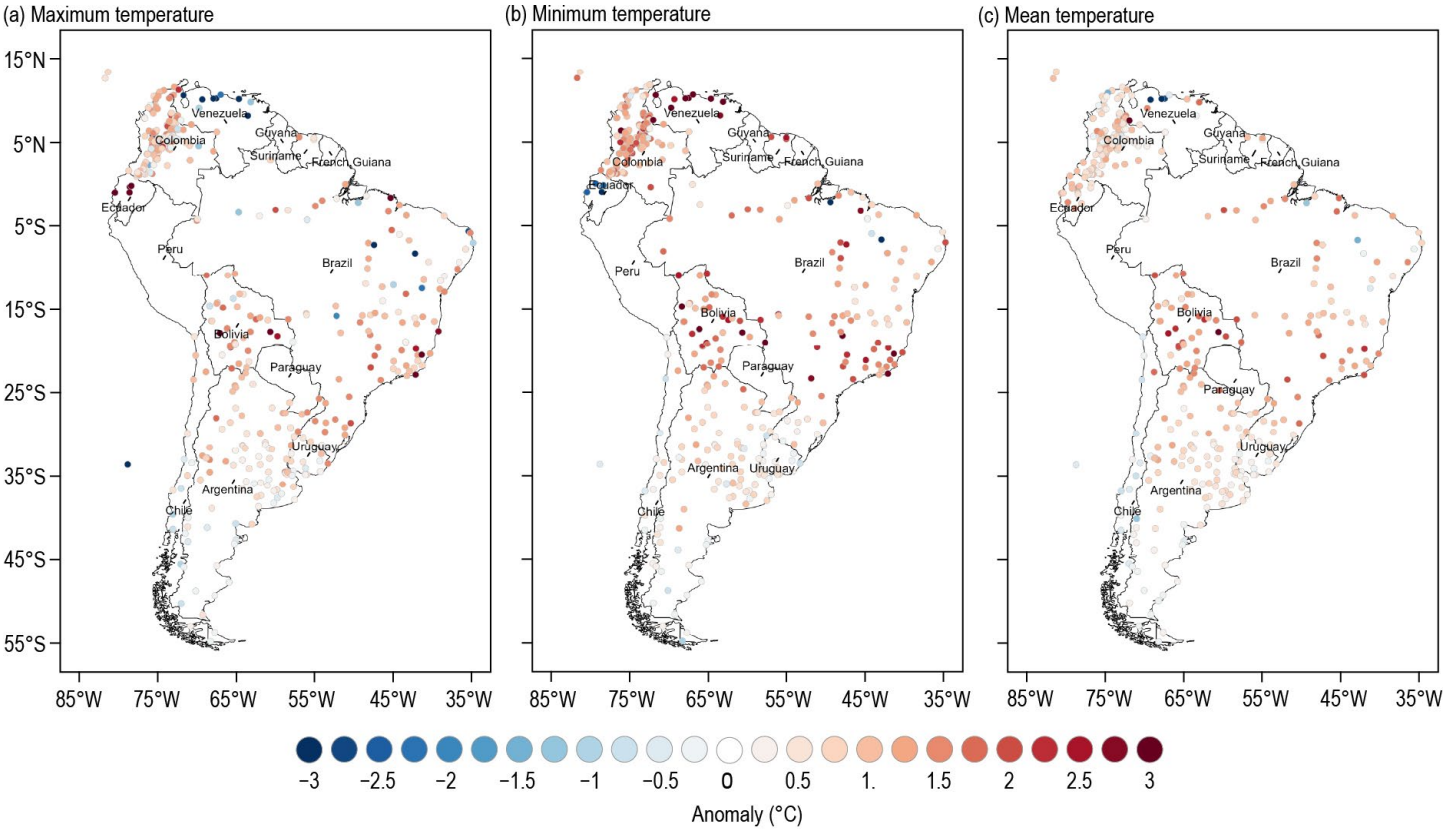

Fig. 7.14. 2024 (a) maximum, (b) minimum, and (c) mean annual temperature anomalies (°C; 1991–2020 base period) for South America. (Sources: station data from the national meteorology and hydrology services of Argentina, Bolivia, Brazil, Chile, Colombia, Ecuador, Paraguay, Suriname, Uruguay, and Venezuela. Processed by the International Center for Research on the El Niño Phenomenon [CIIFEN].)

Unauthenticated | Downloaded 11/21/25 11:34 AM UTC

(ii) Precipitation

Precipitation was variable across northern South America in 2024. Anomalies ranged between 60% above or below normal. Positive anomalies were observed in almost all coastal regions, while the Andes showed negative anomalies (Fig. 7.15). According to station records from the national network of the National Meteorological and Hydrological Service of Venezuela (INAMEH), during January–March, a widespread precipitation deficit was observed throughout the country, with some regions exceeding a 50% deficit compared to normal, which is a typical condition associated with El Niño. During the rainy season from April to November, precipitation exceeding 40% above normal was recorded in some regions of the country.

In Colombia, according to the records from the quasi-real-time network of the National Meteorological and Hydrological Service (IDEAM), above-normal precipitation anomalies of >60% were observed during February, May, June, November, and December across large areas of the country. In January, on the other hand, below-normal precipitation anomalies of around −60% were observed across vast areas of the country. Additionally, in March and from July to October, some subregions had rainfall deficits of –20% to –60% compared to normal. The monthly rainfall behavior showed different patterns with the most probable alterations of the El Niño that causes stronger and longer dry periods, whereas La Niña amplifies rainfall and peak river flows in Colombia (Poveda and Mesa 1996).

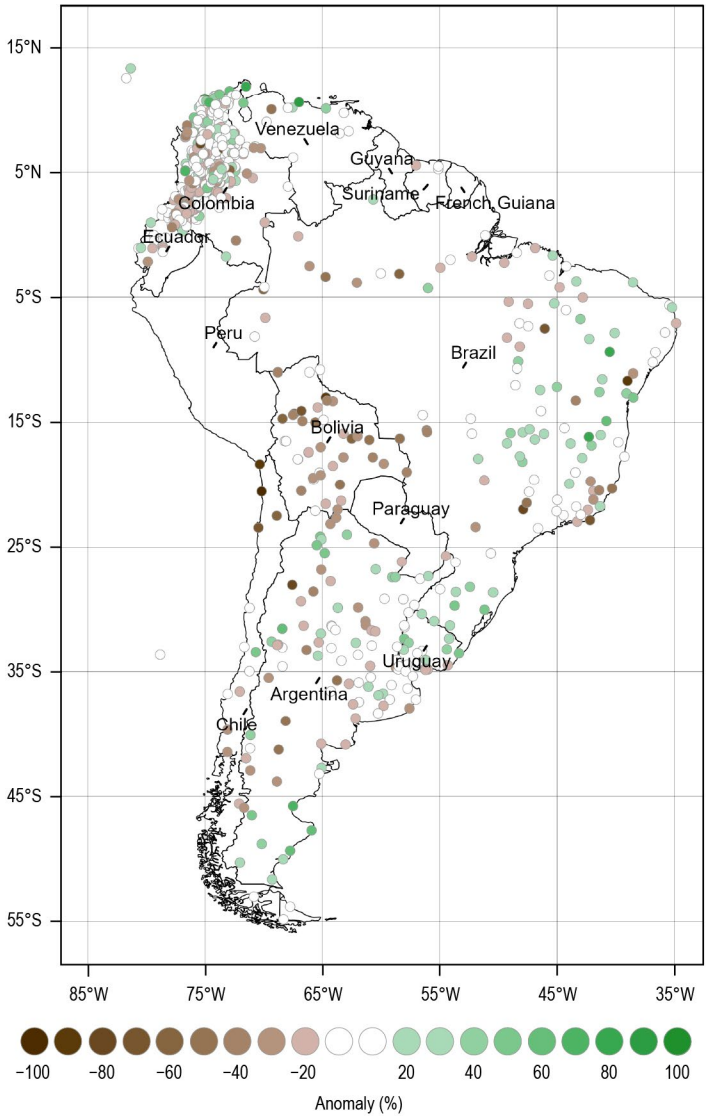

Fig. 7.15. Annual precipitation anomalies (%; 1991–2020 base period) for 2024. (Sources: station data from the national meteorology and hydrology services of Argentina, Bolivia, Brazil, Chile, Colombia, Ecuador, Paraguay, Suriname, Uruguay, and Venezuela. Processed by the International Center for Research on the El Niño Phenomenon [CIIFEN].)

According to station records from the national network of the National Meteorological and Hydrological Service of Ecuador (INAMHI), precipitation was within ±20% of the climatological averages in 2024. The wettest months were January–April, where the coastal region observed precipitation around 50% above normal. In the Andean region, precipitation was around 40% above normal in April, May, and December, and in the Amazon region, positive anomalies of around +60% occurred in May, August, and September.

(iii) Notable events and impacts

Notable events across northern South America highlighted here are mainly associated with heavy precipitation and drought. Additionally, record wildfires—which were associated with high maximum temperatures and long drought periods—are reported. These weather anomalies may be closely related to El Niño conditions in the first months of the year and La Niña-like conditions by the end of the year (see section 4.1 for details).

Suriname was abnormally dry between January and April, which impacted water supplies and led to an increase in wildfires. In Venezuela, severe dry conditions in the first part the year led to a 125% increase in wildfires in January compared to the 2001–23 average, which in turn affected 25,000 hectares (Freitas 2024a). A heatwave also occurred, with 82 days of heat risk

Unauthenticated | Downloaded 11/21/25 11:34 AM UTC

reported (Freitas 2024b). Sahara dust also affected the air quality of several cities. During the second half of the year, precipitation was intensified by tropical waves and by Hurricane Beryl, which caused several rivers to overflow, which in turn contributed to flooding, building damage, and people being displaced from their homes. In 2024, Venezuela also became the first Andes country to register the loss of all glaciers; the general decline has been observed since 1970, but the rate of decline has increased since 2016 (Norberto Paredes 2024).

In Colombia, dry conditions and high temperatures early in the year impacted water supplies, farming, and crops. Nearly 6300 wildfires burned in the National Reserve in the Amazon region as well as in the mountains, including Paramo, a high mountain biome. During the latter half of 2024, the country experienced heavy precipitation, strong winds, and electrical storms, which led to floods, landslides, and building damage, with about 709,000 residents reportedly affected. With the passage of Hurricane Beryl and the onset of the rainy season, the historical maximum 24-hour rainfall record was surpassed in the municipalities of Magdalena, Quindío, and Risaralda (González 2024).

Ecuador was significantly impacted by El Niño in early 2024, the effects of which contributed to heavy precipitation, especially in the coastal region between February and April. The heavy rains resulted in floods, landslides, widespread destruction, and loss of life, with many others injured or displaced. Between July and August, rainfall patterns shifted, with marked deficits and drier conditions than usual. This change increased the risk of wildfires, negatively affected crops, and caused a significant reduction in river flows across various water bodies in the country. The climatic conditions during 2024 significantly impacted important sectors including agriculture, hydroelectric generation, and water supply. The flow rates recorded in the Amazon rivers were among the lowest observed in the past 41 years of record (INAMHI 2024).

2. CENTRAL SOUTH AMERICA

—J. A. Marengo, J. C. Espinoza, J. Ronchail, A. P. Cunha, R. Libonati, L. M. Alves, J. Molina-Carpio, K. Correa, G. Avalos, W. Lavado-Casimiro, R. Salinas, and P. P. Rivera

The central South America region includes Brazil, Peru, Paraguay, and Bolivia. Throughout this section, 1991–2020 is the base period used for both temperature and precipitation unless otherwise specified.

(i) Temperature

The year 2024 was the warmest on record for Brazil and Peru, with annual temperatures above the 1991–2020 average by 0.72°C and 1.11°C, respectively. In central South America as a whole, 2024 was the warmest in the last 50 years (at +1.3°C, Fig. 7.16), surpassing the previous record set in 2023. From January to June, while still under the influence of El Niño, temperatures were about 1°C–2°C above normal in tropical South America. In the Pantanal region between northern Paraguay, southern Bolivia, southern Brazilian Amazonia, and the Bolivian Chiquitania, temperatures were about 1.5°C–2°C above average. From September to November, western Brazil, northern Paraguay, and Bolivia observed anomalies of +2°C. These high temperatures resulted from drought–heat compound events affecting southern Amazonia and the Pantanal, where 10 heatwaves were observed (see *Notable events and impacts* for details).

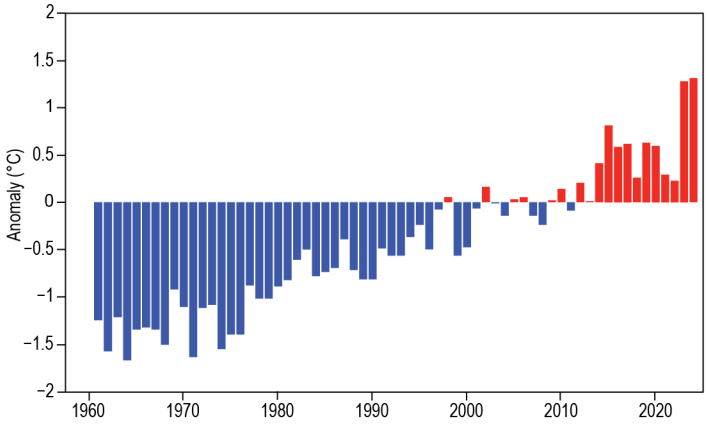

Fig. 7.16. Time series of mean annual temperature anomalies (°C; 1991–2020 base period) for the period 1961–2024 for central South America (Brazil, Bolivia, Paraguay, and Peru). (Source: NOAA/NCEP Global Historical Climatology Network [GHCN] Climate Anomaly Monitoring System [CAMS] data.)

(ii) Precipitation

Below-normal precipitation—and in some regions, drought—was observed in 2024. Rainfall was about 30%–40% below normal across most of central South America and 40%–50% below normal in southern and western Amazonia and Pantanal in the austral winter, triggering drought

Unauthenticated | Downloaded 11/21/25 11:34 AM UTC

in those regions (Marengo et al 2024a). However, in some regions of Brazil and Bolivia, rainfall totals as much as twice the normal were reported during some months (particularly in February, March, and November), along with heavy rainfall events that lasted a few days and generated hydrogeometeorological disasters (see *Notable events and impacts* for details). Rainfall in southern Brazil was about 30%–40% above normal, triggering floods in Rio Grande do Sul in May 2024 (Marengo et al. 2024b; Reboita et al. 2024), which was considered the worst climate disaster in Brazilian history (see Sidebar 7.1 for details). The abundant rainfall in southern Brazil and the drought in the Amazon and Pantanal were associated with El Niño during the first half of 2024.

(iii) Notable events and impacts

Several significant extreme events occurred across central South America in 2024 (Fig. 7.17). During 21–27 February, heavy rainfall affected western Brazil, particularly the Acre State bordering Peru and Bolivia, causing river overflow and floods that resulted in population evacuation and structural damage.

On 26 October, 115 mm of rain in a 24-hour period impacted the city of Belo Horizonte in Brazil, flooding the streets and posing a risk of landslides in the suburbs, according to the National Institute of Meteorology (INMET). On 2 November, heavy rainfall in São Paulo led to power outages that left 70,000 people without electricity.

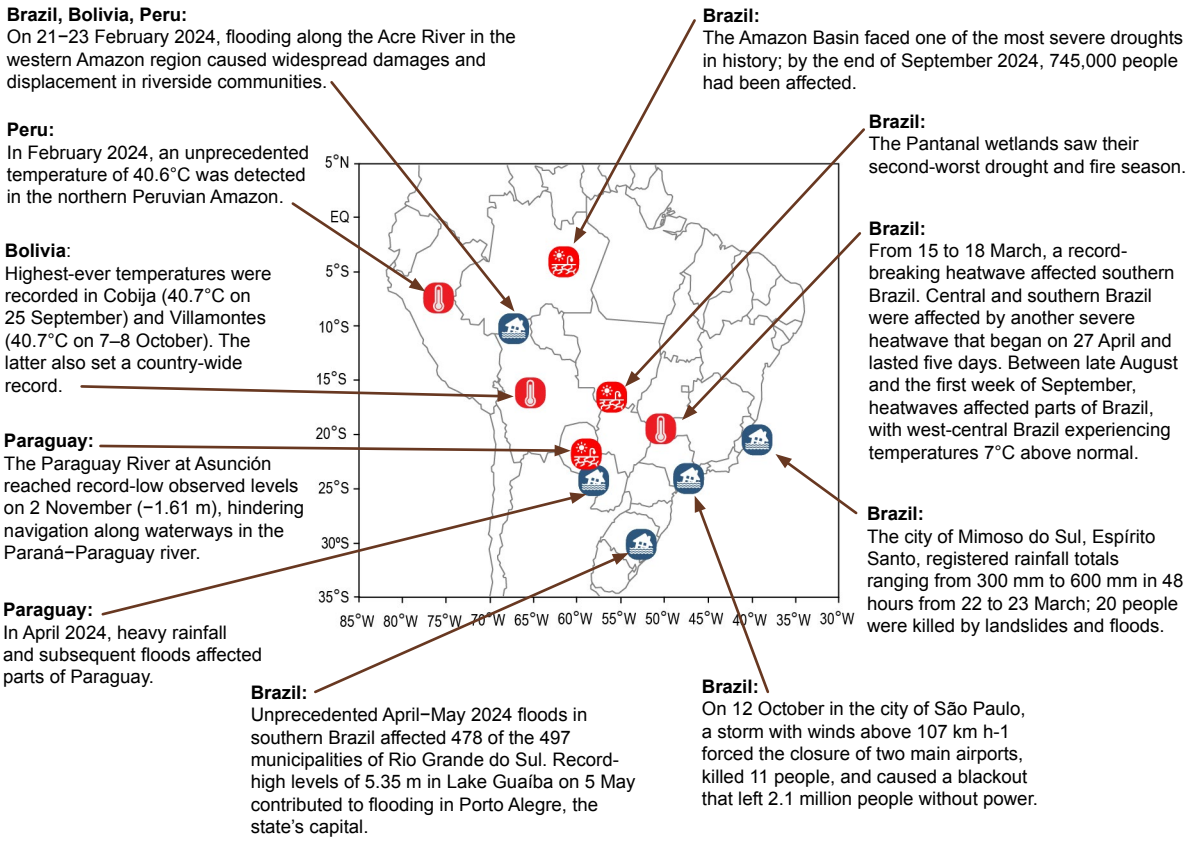

Fig. 7.17. Extreme and notable events across central South America in 2024. (Sources: Peru: National Meteorology and Hydrology Service of Peru [SENAMHI]; Bolivia: National Meteorology and Hydrology Service of Bolivia [SENAMHI]; Paraguay: Directorate of Meteorology and Hydrology [DMH]; Brazil: National Institute of Meteorology [INMET], National Center for Natural Disaster Monitoring and Alerts [CEMADEN], National Institute for Space Research [INPE]; International: UN Office for the Coordination of Humanitarian Affairs, Reliefweb, Flood list.)

Unauthenticated | Downloaded 11/21/25 11:34 AM UTC

Beginning on 20 April, heavy rainfall and ensuing floods affected parts of Paraguay, particularly Asunción and Central in southern Paraguay. Two people were killed in Luque Town, and several roads and houses were flooded, according to Reliefweb and the Ministry of Public Health and Social Welfare. On 11 November, in the department of Huánuco in central Peru, intense rainfall lasting three hours led to devastating floods and landslides, according to the National Institute of Civil Defense (INDECI). Heavy rains in western Bolivia (Andes) in November also caused floods, river overflows, and mudflows.

The Integrated Drought Index (IDI; Fig. 7.18) shows drought conditions in western and southern Amazonia and the Pantanal region between Brazil, Paraguay, and Bolivia during austral summer and autumn. The situation worsened during winter and spring, and, together with heatwaves in those seasons, a record fire season occurred in these regions. Drought also developed in the southern Andes.

In January, late April to early May, and from August to October, several heatwaves affected the Bolivian lowlands. Record-breaking heatwaves affected southern and central Brazil in March and September, with temperatures reaching unprecedented highs for early autumn. In west central Brazil, temperatures were 7°C above normal between late August and the first week of September, according to Belo Horizonte and Brasilia.

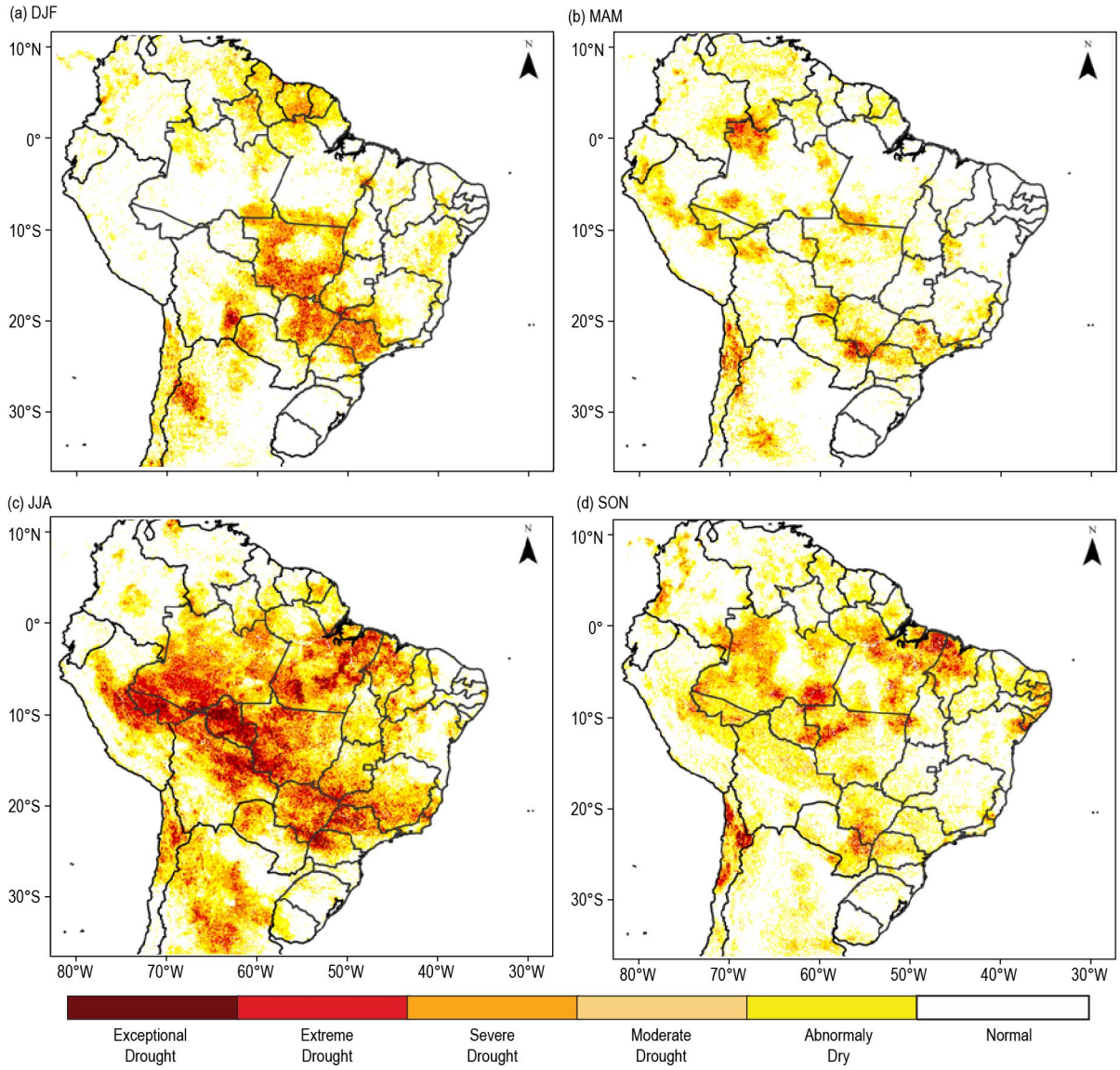

Fig. 7.18. Integrated Drought Index (IDI) maps for central South America during austral (a) summer (Dec–Feb; DJF) 2023/24, (b) autumn (Mar–May; MAM) 2024, (c) winter (Jun–Aug; JJA) 2024, and (d) spring (Sep–Nov; SON) 2024. (Source: National Center for Natural Disaster Monitoring and Alerts [CEMADEN].)

Unauthenticated | Downloaded 11/21/25 11:34 AM UTC

The highest temperature on record (40.7°C) in the northern city of Cobija (Bolivia) was observed on 25 September, breaking the record established in 2023 (40.0°C on 6 October). During 7–8 October, the southern city of Villamontes in the Chaco region recorded 47.0°C, the highest temperature ever recorded in Bolivia (previous maximum: 46.7°C, at the same location).

In 2024, more than 1,025,000 active fires were detected in Latin America, with 47.7% and 20.8% of those in Brazil and Bolivia, respectively. A greater-than-average number of fires reached Bolivia (+197%), Peru (+35%), and Brazil (+20%) during 2024 (https://alarmes.lasa.ufrj.br/).

Despite 2024 being Brazil's warmest year on record, some cold waves occurred in the southern region. At the end of June, several cities in the state of Rio Grande do Sul reported sub-zero temperatures. In Bagé, the temperature dropped to –5.9°C, and in Urupema in the Serra Catarinense region, the temperature fell to –7.2°C. The cities of São Joaquim observed low temperatures of –5.7°C in Urubici and –3.2°C in Bocaina do Sul.

3. SOUTHERN SOUTH AMERICA

—L. S. Aldeco and J. L. Stella

This region includes Argentina, Chile, and Uruguay. Throughout this section, 1991–2020 is the base period used for both temperature and precipitation unless otherwise specified.

(i) Temperature

Above-normal temperatures were observed over much of the region, with the largest anomalies recorded in Argentina north of 40°S. Argentina recorded its second-warmest year on record with an estimated anomaly of +0.54°C (Fig. 7.19a). Uruguay (+0.2°C) and Chile (+0.1°C) were closer to average (Figs. 7.19b,c).

Austral summer (December–February) 2023/24 was extremely warm over most of Argentina and Chile. Temperatures in Uruguay and eastern Argentina were close to normal. Despite being dominated by the effects of El Niño, Argentina experienced an unprecedented heatwave affecting almost all of the country between 21 January and 12 February. Several daily maximum temperatures records were broken during this episode.

Austral autumn (March–May) over southern South America (SSA) was cooler than normal south of 30°S and warmer than normal over northern Argentina and Chile. The largest negative anomalies were recorded over southern Chile and Argentina, especially due to the extremely cold May that affected the region: Esquel (–1.6°C), Paso de Indios (–1.8°C), and Perito Moreno (–2.0°C) in Argentina and Coyhaique (–2.4°C) in Chile each saw their coldest autumn since the start of their records in 1961. This season was characterized by subseasonal variability due to the transition from El Niño to ENSO-neutral conditions.

Winter (June–August) saw near-normal temperatures over most of the region, except for central and southern Chile where below-normal temperatures were predominant. Subseasonal

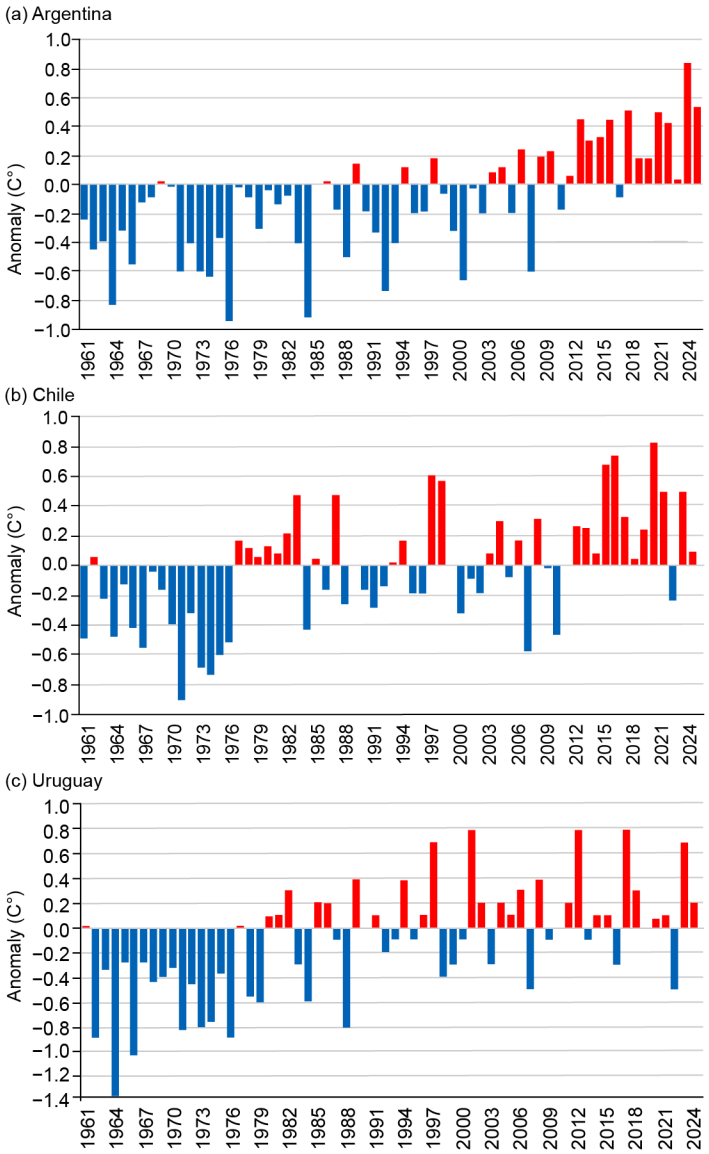

Fig. 7.19. Annual temperature anomalies (°C; 1991–2020 base period) for (a) Argentina, (b) Chile, and (c) Uruguay for the period 1961–2024. (Source: observations from surface meteorological stations.)

Unauthenticated | Downloaded 11/21/25 11:34 AM UTC

and synoptic forcings prevailed during this season, and temperature variability was notable across the three months. Two notable extreme cold events occurred: one at the end of June over southern Patagonia—a region that includes parts of both Chile and Argentina—and another in the first half of July over central and northern Argentina and Uruguay (see *Notable events and impacts* for details).

Austral spring (September–November) was extremely warm over most of SSA. Seasonal anomalies were mostly between +1°C and +3°C and broke several records. In Argentina, 42 locations recorded their warmest spring since the start of the series in 1961. In Uruguay, Carrasco (+1.8°C), Prado (+1.7°C), and Mercedes (+1.6°C) each also set a new seasonal high temperature record.

(ii) Precipitation

During 2024, some regions of southern SSA received above-average annual rainfall, mainly due to precipitation in austral summer and autumn. This was the case for Uruguay and central-eastern Argentina, regions that were influenced by El Niño conditions during those seasons. Below-normal annual rainfall was observed in southern Uruguay, northern Argentina, and in northern and central Patagonia.

During austral summer 2023/24, above-normal precipitation was recorded in northwestern and central-eastern Argentina and Uruguay. In Argentina, Salta and Reconquista each recorded their highest summer precipitation since at least 1961, with Reconquista recording 1069 mm, 596.4 mm above its normal. In Uruguay, precipitation was 50% above normal. The Patagonia region recorded the highest deficits of the season at more than 80% below normal; El Calafate (southern Argentina) recorded no precipitation at all during the summer; this dearth of precipitation has not occurred since at least 1961. In southern Chile, El Tepual station recorded its second-driest summer since 1969, and in central Chile, Pichoy station recorded its third driest since at least 1961.

During austral autumn, El Niño favored above-normal rainfall in eastern Argentina and Uruguay. Seasonal precipitations totals were more than 70% above normal, with some stations setting new daily records. In Argentina, Bolívar recorded 118.9 mm on 15 April and Posadas recorded 160 mm on 1 May; these totals were the highest for their respective stations since they began recording in 1961. In Uruguay, most of the records were set during March: San José recorded a daily precipitation total of 236 mm on 19 March and Florida, Paysandú, and Young each saw their rainiest autumn since 1980. Below-normal rainfall was recorded in central Argentina and Chile and in the northern Patagonia region spanning both countries, with anomalies ranging from –40% to –60%.

During winter, most of the region recorded below-average precipitation with anomalies ranging from –60% to –90%. The greatest deficits were observed in central and northern Argentina and northwestern Patagonia. During July, some stations in Argentina recorded monthly rainfall of less than 1 mm, which were the lowest totals since at least 1961. In Chile, General Freire and Quinta Normal stations set new records for their driest July since 1950 and 1969, respectively. In Uruguay, Puntas del Sauce and Bernabe Rivera recorded their lowest monthly totals for July since 1980. Above-normal rainfall (+60% to +80%) was observed at some stations in central Chile and a southern portion of Patagonia. In Carriel Sur (Chile), a new 72-hour record of 190.2 mm was set during 10–12 June, which was the highest such total since 1966.

During spring, most of Uruguay, central Chile, and central-east Argentina received below-normal rainfall, mainly due to a lack of precipitation in September and October. In October, above-normal rainfall totals were observed in northwestern Argentina and northern Chile, while in November some subseasonal activity favored convection in most parts of this region. Some daily records were set in Argentina: La Rioja recorded 66.9 mm on 8 October, and Sunchales recorded 144 mm on 11 November. These were the highest amounts recorded in those areas since at least 1961. Seasonal records were also set in Argentina: Orán recorded its rainiest spring since at least 1961, while El Calafate recorded its driest spring, also since 1961.

Unauthenticated | Downloaded 11/21/25 11:34 AM UTC

(iii) Notable events and impacts

Figure 7.20 shows several notable events that occurred across the region during 2024. The notable cold waves of June and July are detailed below.

Between the second half of June and the first half of July, two significant cold waves developed over SSA. The first occurred during June and affected the south Patagonia region. A blocking circulation pattern that prevailed for much of the month caused extreme low temperatures and intense snowfall. This led to development of a cold wave with a maximum duration of 10 days in Chile and 8 days in Argentina. Some impacts included ice accumulation and frozen soils, lakes, and lagoons, as well as the suspension of basic services such as water and electricity. The coldest temperatures during this event were recorded in Río Gallegos, Argentina (–17.5°C), and in Punta Arenas, Chile (–14.7°C), on 21 June. During the first half of July, the gradual and persistent entry of cold air favored a marked drop in temperatures, especially in central and northeastern Argentina and Uruguay. Intense frosts occurred in several provinces, with unusually low temperatures ranging between 0°C and –12°C. In the central-eastern region, extreme cold caused water surfaces, such as those of pools, streams, and lagoons, to freeze. The city of Florida, Uruguay, recorded 13 consecutive days with a minimum temperature below 0°C, surpassing its previous record of 8 consecutive days. The city of Paysandú broke its all-time lowest minimum temperature record since 1981 with –5.2°C on 9 July. The city of Buenos Aires, Argentina, recorded four days with temperatures below 0°C, an event that had not occurred since 1980.

Some other locations in Argentina also broke all-time minimum temperature records, including Gualeguaychú (–7.6°C on 9 July), Venado Tuerto (–8.0°C on 10 July), and La Plata (–5.7°C on 10 July). This cold wave was Argentina's most significant since winter 1992.

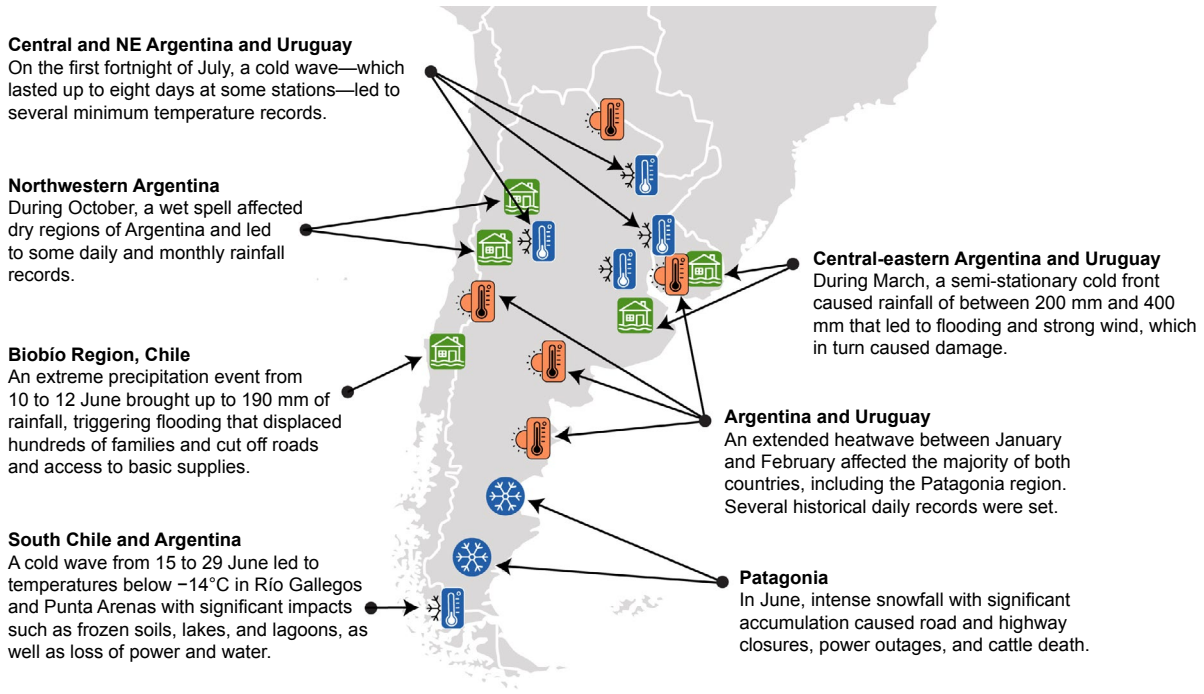

Fig. 7.20. Major extreme events for southern South America during 2024. (Source: national meteorological services of Argentina [National Meteorological Service of Argentina; SMN], Uruguay [Uruguayan Institute of Meteorology; INUMET], and Chile [Meteorological Directorate of Chile; DMC].)

Unauthenticated | Downloaded 11/21/25 11:34 AM UTC

Sidebar 7.1: The worst climate disaster in Brazil: Floods in the state of Rio Grande do Sul —J. MARENGO

In Brazil, flooding and related hydrological hazards are the most common types of weather-related disasters and cause the most significant damage to people and property. Brazil's most extreme disaster on record occurred between late April and early May 2024. Heavy precipitation caused floods in most parts of the state, affecting nearly 2.4 million people and leading to 184 deaths and 21 missing persons. According to the National Center for Monitoring and Early Warning of Natural Disasters (CEMADEN), more than 400 mm of rain fell between 26 April and 5 May; there were several days of uninterrupted rain with daily accumulations above 200 mm. Monthly totals of 667 mm and 803 mm, respectively, were observed in April and May, compared to the average of 151 mm and 137 mm (Marengo et al. 2024b). According to the National Institute for Space Research, three-day accumulated rainfall exceeded 600 mm in some municipalities, and a wide area of the state of Rio Grande do Sul recorded 400 mm totals (Fig. SB.7.1).

This unprecedented rainfall triggered floods in Rio Grande do Sul, affecting 478 of its 497 municipalities. The extreme events occurred in an area from the northwest of the North Region to the east of the Southeast and South Regions. They were caused by the organization of a humidity channel from Amazonia and the presence of the South Atlantic Convergence Zone that feeds severe deep mesoscale convective systems. The Amazon humidity corridor and wind currents helped to form storm clouds. Most notable was the heavy rainfall on 30 April

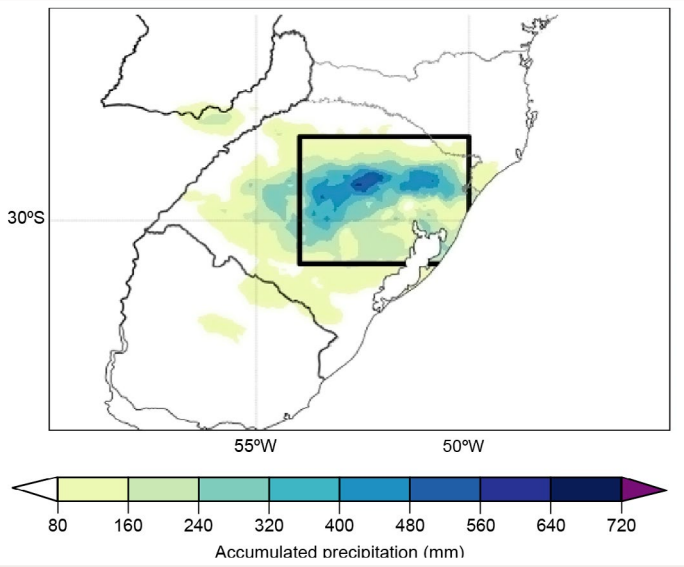

Fig. SB7.1. Accumulated precipitation (mm) between 1200 UTC 29 April and 1200 UTC 2 May. (Source: National Institute for Space Research [INPE].)

in Rio Grande do Sul, with totals of 149.2 mm and 146.6 mm measured in Bento Gonçalves and Rio Pardo, respectively. The highest total for April occurred in Santa Maria with 408.3 mm (climatology is 151.1 mm). Significant rainfall totals were also observed in Santa Maria (213.6 mm) on 1 May and in Soledade (249.4 mm) on 2 May. The highest total for May occurred in Caxias do Sul with 845.3 mm (climatology is 131.4 mm). The rains began in the early hours of 26 April (south of the state), continued uninterrupted for nine days, and accumulated between 300 mm and 600 mm during 29 April to 3 May alone. During 11–12 May, new storms impacted Rio Grande do Sul, with Cambará do Sul recording 154.6 mm, Caxias do Sul 139.2 mm, and Canela 125.8 mm on the 12th (Fig. SB.7.2).

The abundant and persistent accumulated precipitation caused an increase in soil moisture, making water infiltration difficult and consequently triggering flooding in several cities in Rio Grande do Sul. The Taquari, Cai, dos Sinos, and Antas River levels rose by several meters, flooding cities and impacting populations. This rise in turn generated a wave that raised the level of the Guaiba Lake to 5.35 meters on 6 May, which contributed to flooding in several neighborhoods of the capital, Porto Alegre, and culminated in what was considered the worst historical flood in the state in terms of impacts for the city and population.

The intense and long-lasting precipitation led to extreme water levels in mountain regions; the flooding was prolonged, with water remaining high for about 30 days in lower regions. This flood event is ranked highest in Brazil in terms of displaced people as well as damage to property and infrastructure (Collischonn et al. 2025). Total agricultural damage to Rio Grande do Sul from these flooding events was estimated to be approximately $3.7 billion real ($630 million U.S. dollars). The flood in 2024 exceeded the previous extreme record flood of 1941, when the Guaíba River reached the mark of 4.76 m (reference point is 3.00 m at the port pier; Silviera 2020) on 8 May. At that time the Porto Alegre had a population of 272,000 inhabitants, of which approximately 70,000 people had their homes affected by a flood; a third of the commercial establishments and industries were also submerged for approximately 40 days.

A study by World Weather Attribution (WWA 2024) suggests that anthropogenic climate change doubled the likelihood of the historic rainfall that caused the devastating floods in Rio Grande do Sul in 2024. The study also estimates that El Niño increased the probability of the event by a factor of two (twice as likely) and made the rainfall about 3%–10% more intense.

Unauthenticated | Downloaded 11/21/25 11:34 AM UTC

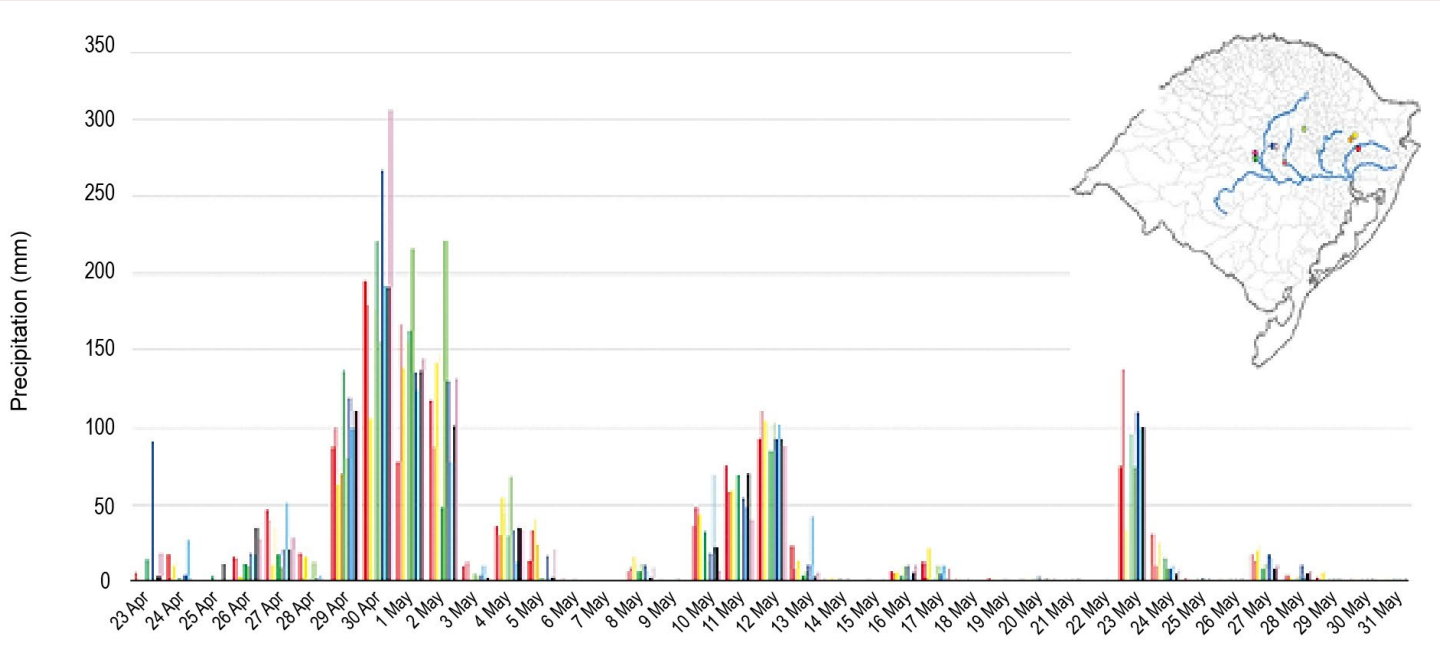

Fig. SB7.2. Daily precipitation totals (mm) for the period 23 April to 31 May 2024 for some stations in the Lake Guaiba basin (highlighted in the top right of the panel) of the state of Rio Grande do Sul (Adapted from Marengo et al 2024b). (Source: National Center for Natural Disaster Monitoring and Alerts [CEMADEN].)

Unauthenticated | Downloaded 11/21/25 11:34 AM UTC

e. Africa

—A. Mekonnen, Ed.

The 2024 analysis for Africa is based on observational records from meteorological and hydrological services, including rainfall from the GPCP and reanalysis products from the National Centers for Environmental Prediction (NCEP)/National Center for Atmospheric Research (NCAR). Notable events were compiled based on reports from government agencies, regional and international organizations, and research and Early Warning organizations. The climatological base period is 1991–2020, and the terms "normal" and "average" are interchangeably used to refer to this climatology.

Figure 7.21a presents the 2024 mean temperature anomalies for Africa. Above-average annual temperature anomalies of more than +2.4°C were observed over northwest Africa and the western part of southern Africa (the Kalahari Desert). Anomalies of between +1.2°C and +2.4°C were also noted over equatorial Africa within 5°S and 5°N (Fig. 7.21a).

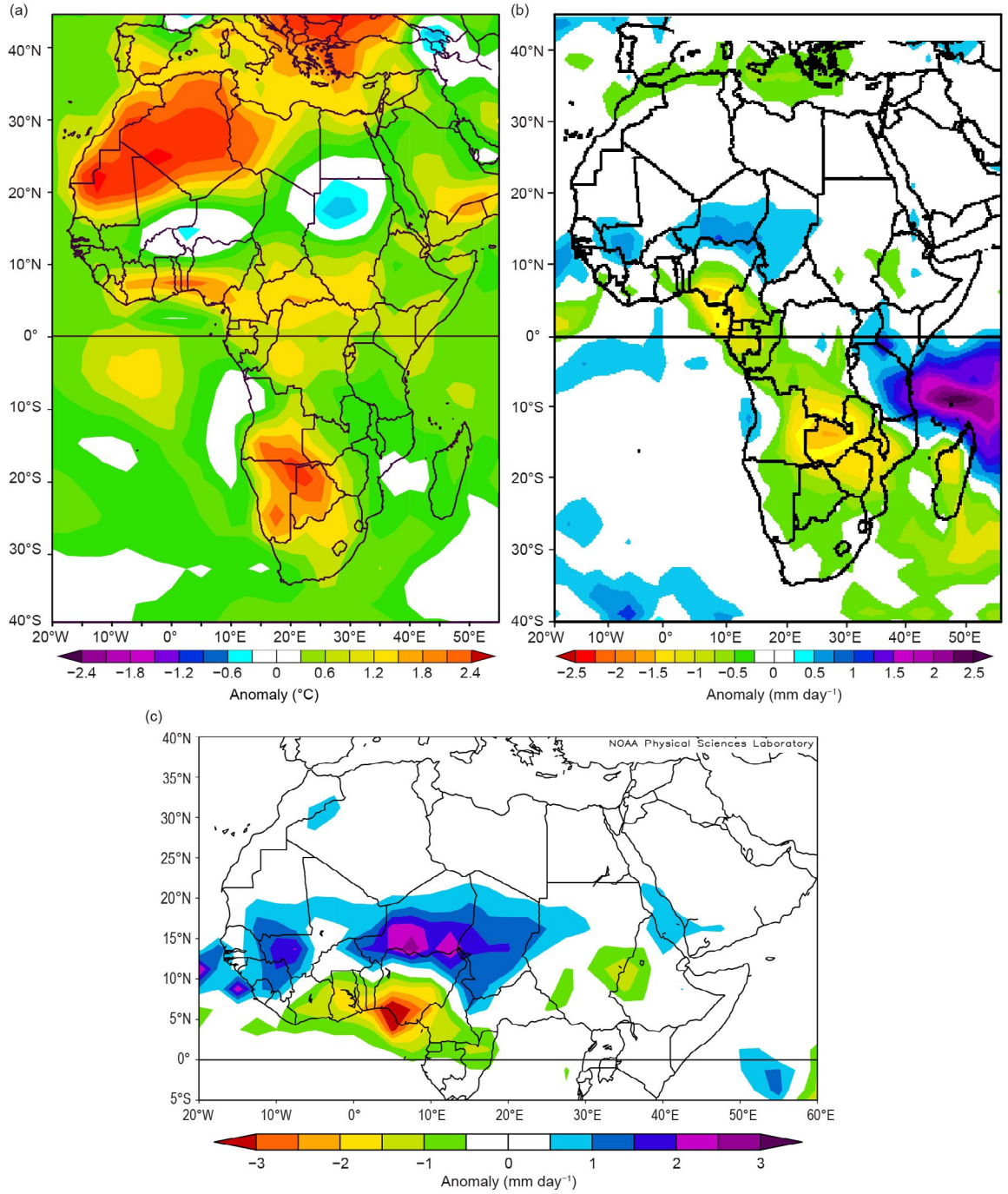

Fig. 7.21. (a) Annual mean surface temperature (°C) and (b) annual mean precipitation (mm day⁻¹) over Africa. (c) Jul–Sep rainfall anomaly (mm day⁻¹) over North Africa. Anomalies are with respect to the 1991–2020 base period. (Sources: National Centers for Environmental Prediction [NCEP]/National Center for Atmospheric Research [NCAR], GPCP.)

Unauthenticated | Downloaded 11/21/25 11:34 AM UTC

Above-average rainfall was observed over the central Sahel region between 10°N and 15°N, extending from Senegal to Chad. The rest of the zone north of 10°N observed near-normal rainfall conditions. Below-average rainfall was also observed over southern Nigeria and adjoining Cameroon, including the Guinea area extending southeastward towards the southern tip of the Democratic Republic of the Congo (DRC), Zambia, and Mozambique. In contrast, above-average rainfall occurred offshore to the north of Madagascar; this event was related to the 2024 tropical cyclones (Fig. 7.21b).

The Sahel region receives most of its annual rainfall during the July–September (JAS) season. As shown in Fig. 7.21c, the Sahel region between 10°N–15°N and 20°W–25°E received above-normal rainfall. Although the main convective zone shifts to the north during JAS, the seasonal rainfall south of 10°N over West Africa was much below normal.

1. NORTHERN AFRICA

—K. Kabidi, M. ElKharrim, S. Hakmi, and A. E. Mostafa

The North Africa subregion is comprised of Mauritania, Morocco, Algeria, Tunisia, Libya, and Egypt. Much of this region is characterized by arid and semi-arid climate, while northern parts exhibit Mediterranean climates. Generally dry conditions prevailed over the region in 2024, which meant a continuation of the recent streak of dry years.

Specific national and local temperature and precipitation information was provided by national meteorological and hydrological organizations.

(i) Temperature

During winter (December 2023–February 2024; DJF), above-normal temperatures were seen over most of the region (Fig. 7.22a). Seasonal anomalies of more than +1.4°C dominated most of Mauritania, Algeria, and Morocco. Mauritania, northern Mali, and southern Algeria experienced anomalies of more than 2°C. In Morocco, the winter average temperature was 2.8°C above normal, while mean minimum and mean maximum temperature were also above normal by 2°C and 3.6°C, respectively. In Algeria, winter temperatures of 1.5°C–2.6°C above normal were recorded. The mean temperature anomalies during January ranged between 1.1°C in Tamanrasset and 4.4°C in Saida (not shown). In Tunisia, temperatures were about 2.3°C above normal in January, marking its warmest January on record (since 1950). Average temperatures ranged from 9.6°C in Thala to 15.6°C in Medenine. Above-normal average temperatures were recorded in

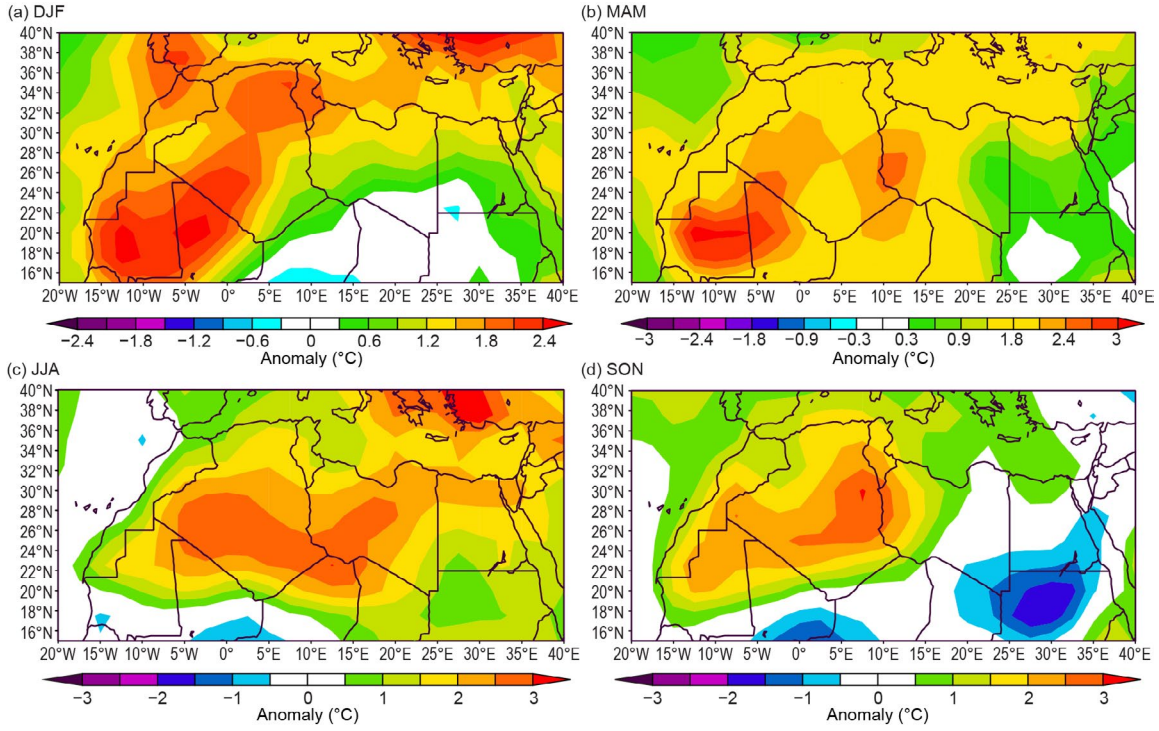

Fig. 7.22. 2024 Seasonal temperature anomalies (°C) over North Africa: (a) winter (Dec 2023–Feb 2024), (b) spring (Mar–May), (c) summer (Jun–Aug), and (d) autumn (Sep–Nov).

Unauthenticated | Downloaded 11/21/25 11:34 AM UTC

February (+2.1°C), March (+2.2°C), April (+0.6°C), and May (+1.6°C). December 2023 and January 2024 temperatures over Egypt were above normal over the northern parts, while below-normal temperatures dominated southern areas during February. Among the notable temperature records, Sharm El-Sheikh was 7.9°C above normal in December 2023, while Asyut was 2.62°C below normal the same month.

In spring (March–May; MAM), the region was dominated by anomalies of more than +1.8°C in Mauritania and northern Mali, while Algeria observed anomalies of more than +2°C (Fig. 7.22b). Algeria was also warmer than normal in March, with anomalies that ranged from +1.6°C (Ghazaouet) to +4.7°C (Medea). May was also warmer than usual over most of the region (+2.9°C for Algeria).

Summer temperatures (June–August; JJA) were above average over North Africa, having been more than 2°C above normal over Algeria extending towards Libya and northern Egypt (Fig. 7.22c). Summer temperatures over Tunisia ranked fourth among the hottest summers since the start of the record in 1950. In August, the monthly average maximum temperature was 4.07°C above normal at Sharm El-Sheikh in Egypt. Aswan registered a maximum temperature for the year of 49.9°C on 7 June 2024.

Autumn temperatures (September–November, SON) over the region were also above average. Western parts of Morocco, northern Mauritania, and Mali extending towards Libya experienced temperatures that were 2°C above average. However, temperatures in southern parts of Egypt were below normal; Luxor, for example, was 2.6°C below normal for November. In Morocco, autumn ranked fourth warmest on record with an average anomaly of +1.18°C (record anomaly of +1.65°C was recorded in 2023). Although September and October had temperatures that were close to normal—with average anomalies of around +0.2°C—November became the warmest November ever recorded for the region with an exceptional anomaly of +3.09°C. In Tunisia, November 2024 was the warmest month in the 75-year record (since 1950), at 2.3°C above normal. An above-normal national temperature was also recorded in October (+2.1°C).

(ii) Precipitation

Figure 7.23 shows seasonal precipitation anomalies in 2024. Summer (JJA) is not normally a precipitation season over the region and therefore is not presented; however, unusual heavy and torrential rains were observed in August in the Red Sea Mountain ranges, including Halaib, Shalateen, Ras Banas, Marsa Alam, and other areas in southern Upper Egypt.

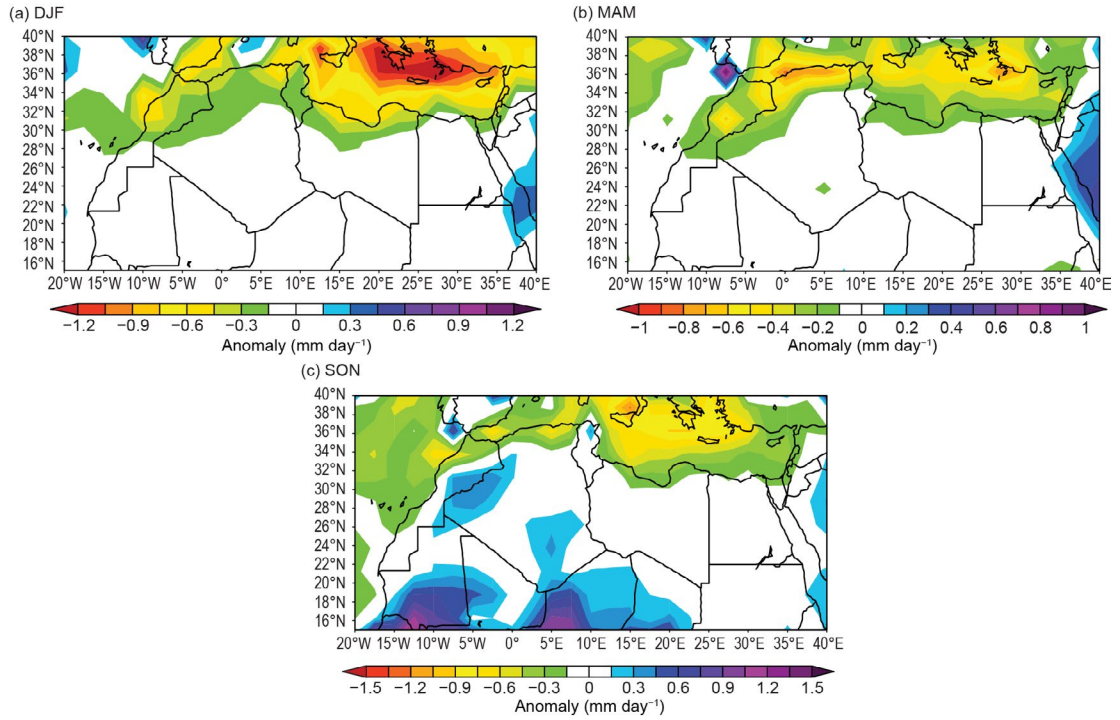

Fig. 7.23. 2024 Seasonal precipitation anomalies (mm day^{-1}) over North Africa: (a) winter (Dec 2023–Feb 2024), (b) spring (Mar–May), and (c) autumn (Sep–Nov).

Unauthenticated | Downloaded 11/21/25 11:34 AM UTC

Winter precipitation was generally below average, ranging between –0.2 mm day^{-1} and –0.6 mm day^{-1} over the region (Fig. 7.23a). Winter precipitation in Morocco was about 25% below normal. In Algeria, January had deficient rainfall, but February was wet, particularly in the north. In Tunisia, the overall average deficit in precipitation was 60% and 20% during January and February, respectively. The first dekad (10 days) of December was very wet for northwest Libya. Most stations in the region recorded high precipitation totals, with Garian recording 297 mm (116 mm of which was recorded on 5 December) and El Khoms recording 213 mm (58 mm on 5 December). Normal to below-normal and normal to above-normal precipitation was observed in Egypt in January and February, respectively. Extremely heavy rainfall of 140 mm was recorded in December 2023 at Alexandria. On 1 February, a 24-hour rainfall total of 37 mm was recorded in Egypt.

Figure 7.23b shows spring precipitation. Below-normal precipitation dominated most of Morocco, northern Algeria, and Tunisia. Most of Egypt and Libya was within –1 mm day^{-1} to 0.1 mm day^{-1} of normal precipitation. In Tunisia, precipitation deficits ranging up to about 60% was observed in March, while up to 20% was reported in April. However, northern and central regions of Morocco received up to 123% of normal precipitation in March.

Autumn precipitation distribution is presented in Fig. 7.23c. While above-average precipitation was noted over eastern Morocco and adjoining Algeria, coastal Morocco, including the Atlas area and northern tip of Algeria, remained under drier-than-normal conditions. September was wetter than average in Morocco. Of particular significance was 229% of normal precipitation at Errachidia, as well as 648% of normal at Ouarzazate in southeast Morocco; these stations are typically characterized climatologically by little rain. However, Moroccan precipitation during autumn generally showed a deficit of 16% of normal. It should be noted that November 2024 was among the driest on record at the national scale, with rainfall 82% below normal. In Tunisia, above-normal precipitation was recorded in September and October, in contrast to November, when the nationally averaged deficit exceeded 40%.

(iii) Notable events and impacts

South and southeast Morocco, as well as parts of the Atlas region, were affected by an extremely unstable tropical air mass over the southern part of the country in September (Knippertz et al. 2003). Humid tropical air masses moved northward and collided with cold air, resulting in the formation of unstable and intense storm clouds. The unusual conditions for these regions caused heavy thunderstorms and significant rainfall, leading to river flooding, according to the Moroccan Government Office. The floods left at least 18 people dead in southern Morocco, especially in the province of Tata. This unstable tropical air mass also impacted southern Algeria, with torrential rains and floods that led to six fatalities.

Nabeul and Hammamet in Tunisia experienced heavy rains accompanied by thunderstorms and intense winds for a few minutes during August. The heavy rainfall caused flooding in many urban areas, leading to significant damage. Heavy rainfall also affected several regions of Tunisia during September and October, causing significant flooding and significant damage.

Heavy rain and flooding occurred in several cities in western Libya during 5–6 December, killing five people and affecting more than 3300 others, according to the United Nations (UN) Office for the Coordination of Humanitarian Affairs (OCHA). The storms caused power outages and swept away vehicles, and many citizens were trapped by floods that inundated businesses and homes.

2. WEST AFRICA

—W. Agyakwah, B. Singh, B. Jha, W. M. Thiaw, and F. Sima

West Africa is a vast region that spans from the Guinean coast in the west to approximately 20°N in the north, and from the eastern Atlantic coast to Niger in the east. It is divided into two distinct subregions. The Sahel, located between 12°N and 17°N, stretches from Senegal and The Gambia in the west to Niger in the east. To the south lies the Gulf of Guinea, which extends from about 4°N to 10°N, covering the Guineas on the western Atlantic coast and reaching eastward to Nigeria and Cameroon.

Unauthenticated | Downloaded 11/21/25 11:34 AM UTC

(i) Temperature

The annual mean temperature over West Africa varied between 22°C and 30°C during 2024 (Fig. 7.24). The highest annual mean temperatures were recorded in Mauritania, central and eastern Senegal, northwestern Mali, southeastern Niger, and northeastern Nigeria. Over northern and central Mauritania, temperatures were 2°C–3°C above the climatological average (Fig. 7.24b). In the Gulf of Guinea region, annual mean temperatures ranged between 24°C and 26°C, which represents anomalies of +0.5°C to +1.5°C (Fig. 7.24b). Most of West Africa, except for parts of the central region covering eastern Mali, southern Niger, and northeastern Burkina Faso, had temperatures that ranked above their 90th percentiles. Notably, countries in the southern parts of the region, including Guinea-Bissau, Sierra Leone, Liberia, much of Ghana, Togo, Benin, southern Nigeria, and far northern Mali and northern Mauritania were near-record warm.

Monthly average temperatures (not shown) across the region displayed significant variability. In January and February, northern Mauritania saw temperatures 2°C–4°C above average, while countries in central West Africa experienced cooler-than-average conditions during the same period. The pre-monsoon months (i.e., MAM) were the warmest, with temperatures 2°C–4°C above normal across most of the region, except for central West Africa, where conditions remained near average. During this time, surface temperatures in much of West Africa ranked above the 90th percentile, except for some countries in central West Africa. Notably, the Gulf of Guinea countries experienced temperatures above the 97th percentile.

During the 2024 monsoon season (June–September), central West Africa recorded temperatures 0.5°C–1.5°C below the climatological average, while the Gulf of Guinea countries experienced warm anomalies of 0.5°C–1.5°C above normal. The consistently dry northern regions of West Africa saw temperatures 2°C–3°C above average. In terms of temperature rankings, southern Mauritania, southern Mali, northern Burkina Faso, and southern Niger experienced some of their coldest seasonal temperatures, with surface temperatures falling below the third percentile.

Following the monsoon season (i.e., October–December [OND]), surface temperatures remained cooler than normal in central West Africa, especially in areas with stronger monsoon rainfall. This cooling in central West Africa aligns with the region's enhanced rainfall during the monsoon season.

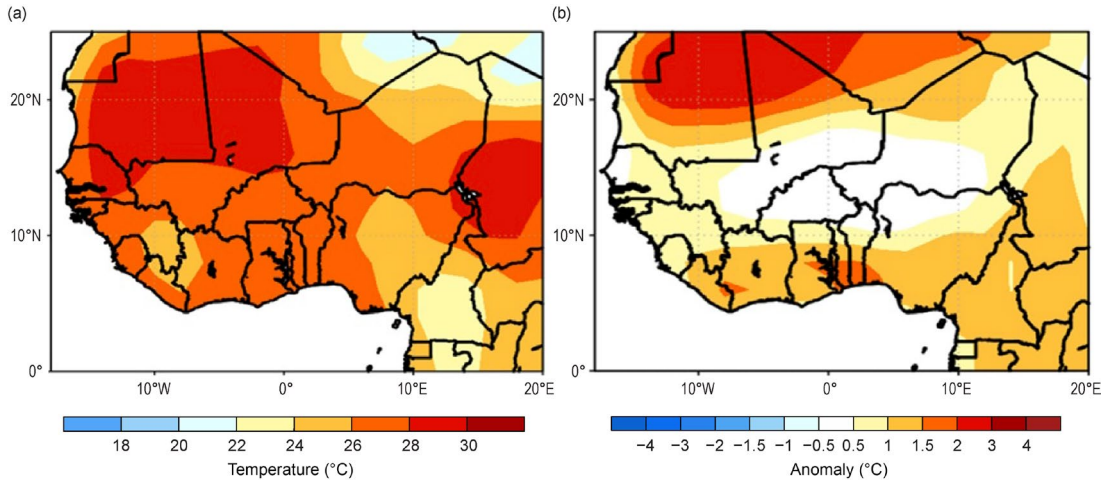

Fig. 7.24. Annual (a) mean temperature (°C) and (b) mean temperature anomalies (°C; 1991–2020 base period) for West Africa in 2024. (Source: NOAA/National Centers for Environmental Prediction [NCEP].)

(ii) Precipitation

In 2024, much of the Sahel region benefited from substantial rainfall surpluses (50 mm–200 mm), with some areas 200 mm–250 mm above average in southern Niger, placing it above the 97th percentile. In contrast, the Gulf of Guinea region faced rainfall deficits in many locations. Nigeria reported significant deficits exceeding 300 mm in central and southeastern regions, which ranked below the third percentile.

From June to October 2024, the Sahel experienced varying levels of rainfall. June saw above-average precipitation in southern Mali, western Burkina Faso, and southeastern Niger

Unauthenticated | Downloaded 11/21/25 11:34 AM UTC

(10 mm to 30 mm), with northern Nigeria receiving 30 mm to 50 mm. July brought even more significant surpluses (50 mm to 100 mm) to southern Mali and northeastern Nigeria. August saw deficits of 10 mm to 50 mm in southern Mauritania and parts of Senegal and Burkina Faso, while the central Sahel experienced surpluses. For the summer overall, the Sahel area's average rainfall was above normal, a trend that has been observed since 2015 and is consistent with past studies that suggest "recovery" of the Sahel region's rainfall (Fig. 7.25d; e.g., Nicholson et al. 2018).

September marked a resurgence with notable above-average rainfall (50 mm to 100 mm) in central Senegal, The Gambia, and other areas. By October, the rainfall receded to the southern Sahel with continued surpluses (10 mm to 100 mm), particularly in Senegal and The Gambia, with significant amounts also observed in southern Mali. Overall, the June–September (JJAS) season recorded above-average rainfall across the Sahel region (Figs. 7.25c,d). Southern Mali, southern Niger, and northeastern Nigeria had over 150 mm of above-average rainfall.

Rainfall during MAM was below average, with 20 mm–100 mm deficits across the region. During the April–June (AMJ) season, deficits continued, with only southern Ghana experiencing 20-mm–40-mm-above-average rainfall (Figs. 7.25a,b). In the May–June season, Guinea-Bissau, Guinea, Sierra Leone, and southern Ghana observed above-average rainfall (20 mm–100 mm), while other countries reported near-average to below-average rainfall. Nigeria faced significant deficits of 40 mm–150 mm from May to October. Overall, the Gulf of Guinea experienced poor rainfall distribution during the major rainy season (March to July; Figs. 7.25a,b), except for October, which saw above-average rainfall and marked the peak of the minor rainy season (i.e., SON). Southern Nigeria also faced severe rainfall deficits from May to November, especially in September, with southeastern areas experiencing deficits exceeding 100 mm. Annual rainfall deficits across the region were more than 300 mm below average in places, underscoring the

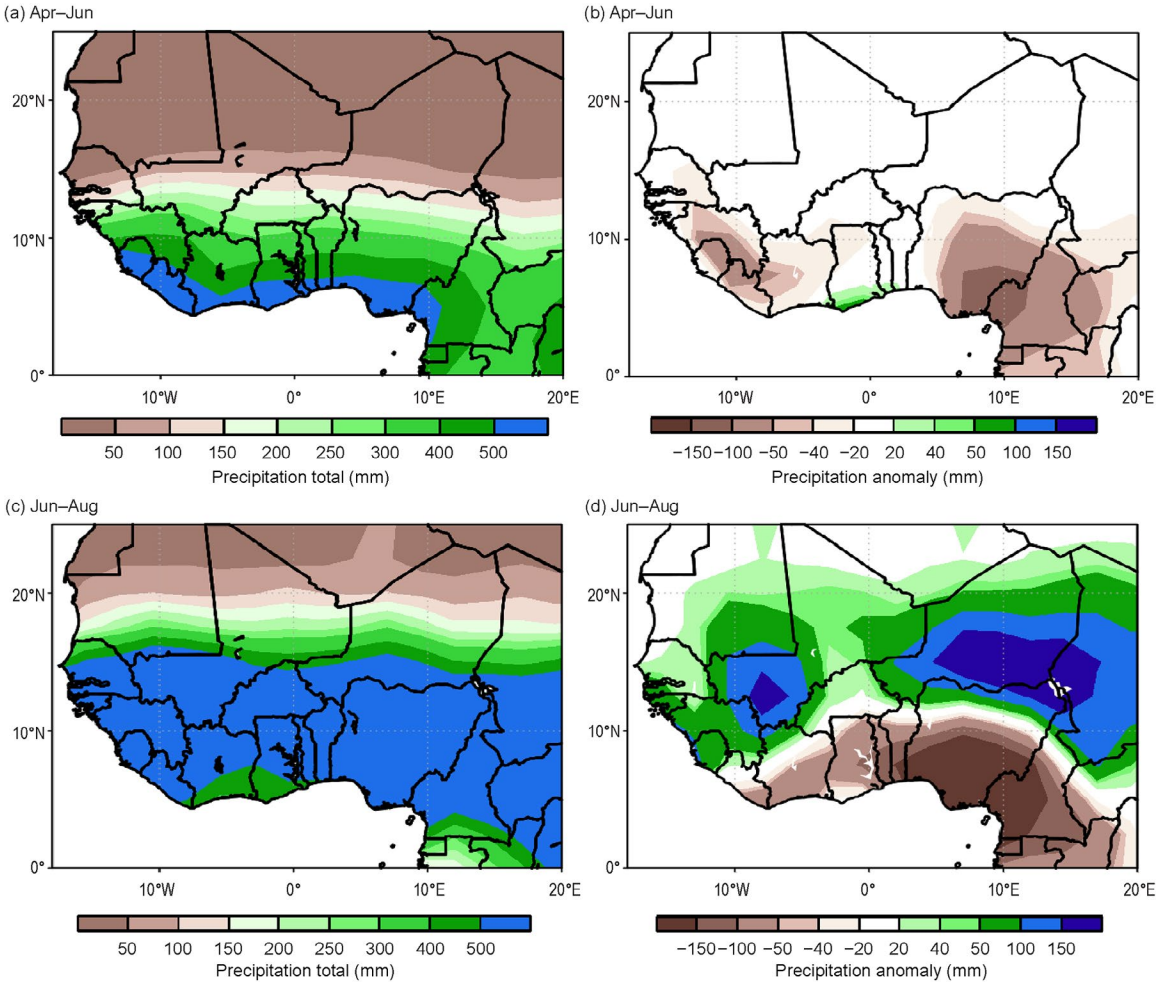

Fig. 7.25. Cumulative Apr–Jun seasonal (a) total precipitation and (b) precipitation anomalies and Jun–Sep seasonal (c) total precipitation and (d) precipitation anomalies in 2024 for West Africa (mm; 1991–2020 base period). (Source: NOAA/National Centers for Environmental Prediction [NCEP].)

Unauthenticated | Downloaded 11/21/25 11:34 AM UTC

inadequate rainfall distribution in the Gulf of Guinea, with the most severe conditions observed in central and southern Nigeria.

(iii) Notable events and impacts

Heavy rainfall impacted multiple towns in Mali in mid-August, leading to significant displacement and damage. The Gao Social Development Department reported that 886 households were displaced and 619 houses destroyed. Flooding since the beginning of the rainy season also led to at least 15 fatalities. According to the Interministerial Committee for Crisis and Disaster Management, more than 30,000 people were affected. By 9 September, the floods worsened in all 19 of Mali's regions. The regions that recorded the highest numbers of people affected were: Ségou (39,245), Timbuktu (36,317), Gao (19,238), Bamako (17,127), and Mopti (1782).

Northern Ghana suffered its worst drought in 40 years, which devastated small-scale farmers without insurance and led to significant crop losses, according to Deutsche Welle. Drought-induced failures reduced yields in half of the country's 16 administrative regions.

Heavy rainfall affected northeastern Nigeria in September; the overflow of the Alau Dam on the Ngadda River flooded Maiduguri city in Borno state on 10 September. By 12 September, at least 30 people died, more than 414,000 were displaced, and approximately 1 million people were affected. Thousands of houses and structures were destroyed.

3. CENTRAL AFRICA

—W. Agyakwah, B. Jha, B. Singh, and W. M. Thiaw

Central Africa spans a vast area across both the Northern and Southern Hemispheres and has a distinct climate system characterized by a pronounced annual cycle. The region stretches from the southern tip of DRC in the south to the central parts of Chad in the north. Longitudinally, it covers approximately 5°E to 35°E. This analysis specifically examines the sub-region that includes Cameroon, Chad, the Central African Republic (CAR), DRC, the Republic of the Congo, Gabon, Equatorial Guinea, and São Tomé and Príncipe.

(i) Temperature

Figure 7.26a shows that the annual average temperature over Central Africa in 2024 varied from 20°C in southeastern DRC to 30°C in northern Chad. Generally, regions north of the equator tend to be warmer on average throughout the year. CAR, southwestern Chad, Equatorial Guinea, Cameroon, as well as central and northern parts of Congo and the northern, central, and western regions of DRC were 1.0°C–1.5°C higher than the 1991–2020 climatological average (Fig. 7.26b). Slightly above-average temperatures (+0.5°C to +1°C) were observed in southeastern DRC, northern and central Angola, southwestern Gabon, and southern Congo. Most of the Central African region surpassed the 90th percentile of the historical record, with the central areas—DRC, Cameroon, Gabon, Congo, Equatorial Guinea, southwestern Chad, and much of CAR—above the 97th percentile, indicating near-record-high temperatures in these regions.

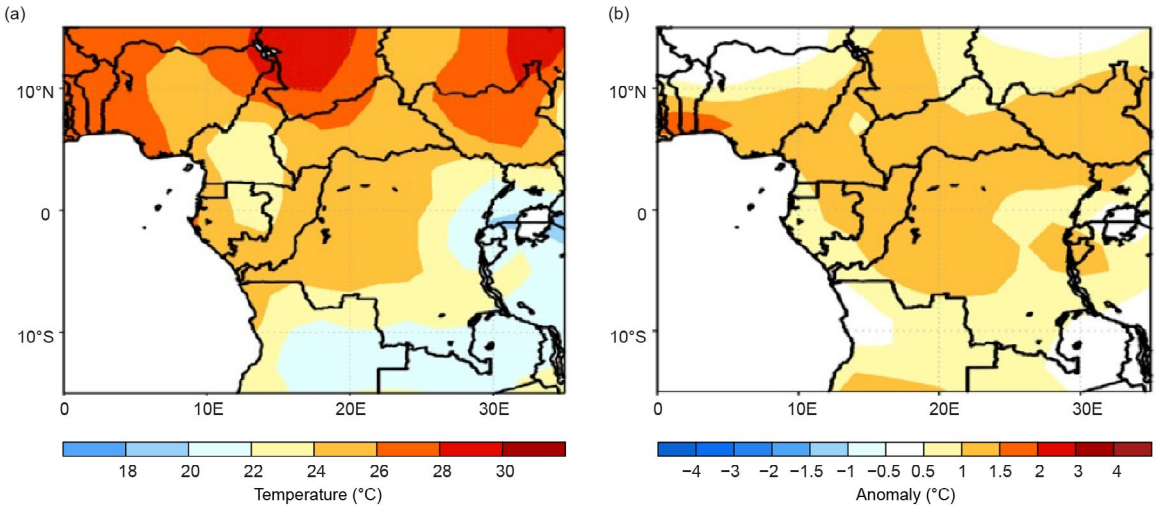

Fig. 7.26. Annual (a) mean temperature (°C) and (b) mean temperature anomalies (°C; 1991–2020 base period) for Central Africa in 2024. (Source: NOAA/National Centers for Environmental Prediction [NCEP].)

Unauthenticated | Downloaded 11/21/25 11:34 AM UTC

Monthly mean temperatures (not shown) in Central Africa were consistently above average throughout 2024. Early in the year, the region experienced warmth, with temperature anomalies of +0.5°C to +4°C. By March, the milder warm anomalies intensified, with northern Cameroon and CAR seeing temperature anomalies exceeding +1.5°C. In April, the warm anomalies expanded southward and became more pronounced, reaching 3°C–4°C above the climatological average in the northern regions of central Africa by May.

From July to September, central DRC experienced above-average temperatures, with anomalies ranging from +2°C to +4°C. These warm conditions persisted through October, when southern DRC also saw higher-than-normal temperatures. November and December, however, were relatively cooler compared to the earlier months, with temperatures returning to near-normal levels across Central Africa.

Throughout the year, the region's monthly mean surface temperatures remained above the 90th percentile. From April to July, most of the region experienced temperatures ranking above the 97th percentile. By the end of the year, the region's temperatures remained slightly above average, with rankings that were above the 70th percentile.

(ii) Precipitation

The rainfall patterns in this area are closely linked to the north–south migration of the Intertropical Convergence Zone (ITCZ) across Africa. The northern part of the region receives rainfall during June–September. In contrast, the southern regions experience dry weather during the boreal summer and receive rainfall from boreal autumn through the winter and early spring. The central area near the equator receives consistent rainfall year-round.

In 2024, northeastern DRC experienced the highest annual rainfall, exceeding 2000 mm, which is significantly above normal. In contrast, western and southern areas of the subregion saw below-average rainfall, with deficits of over 300 mm recorded in parts of Cameroon, Equatorial Guinea, northwestern Gabon, and southern DRC (Fig. 7.27).

In northern Central Africa, rainfall began in June 2024, with precipitation 10 mm to 30 mm above average recorded in northern Cameroon, southern Chad, and southeastern CAR. Surpluses continued until August before a brief decline in September, though southern Chad maintained surplus rainfall. By October, widespread rain surpluses were seen across Central Africa, with southwestern Chad, western CAR, northern and central Congo, and much of the DRC experiencing 50 mm to 100 mm of above-average rainfall (above the 70th percentile).

Meanwhile, the equatorial regions faced low rainfall accumulation during the long rainy season (i.e., MAM), with above-average rainfall only in northern DRC (20 mm to 40 mm) and deficits of up to 100 mm along the eastern borders of Gabon, Congo, and western DRC. Many areas, including Cameroon, Equatorial Guinea, Gabon, Congo, western CAR, and western and central DRC experienced rainfall deficits of 20 mm to 50 mm from May to July 2024.

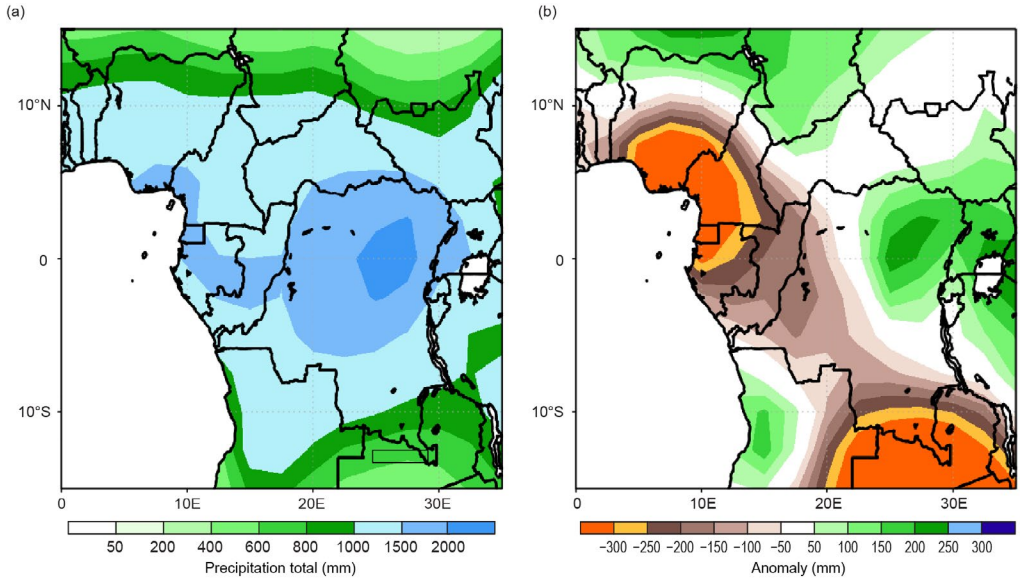

Fig. 7.27. Cumulative annual (a) total precipitation and (b) total precipitation anomalies in 2024 for Central Africa (mm; 1991–2020 base period). (Source: NOAA/National Centers for Environmental Prediction [NCEP].)

Unauthenticated | Downloaded 11/21/25 11:34 AM UTC

During September to November, the northeastern DRC received a significant rainfall surplus, which was over 150 mm. Overall, the annual maximum rainfall exceeded 2000 mm, surpassing the average by 200 mm to 250 mm (Fig. 7.27).

In October, the southern subregion experienced heavy rainfall, with totals ranging from 30 mm to 100 mm. This was followed by additional rains, leading to near-average to above-average precipitation of 20 mm to 100 mm during the October to December period. Areas in western regions—particularly southwestern Cameroon, Equatorial Guinea, and northwestern Gabon—recorded below-average rainfall exceeding 300 mm.

(iii) Notable events

During early January, exceptionally heavy rainfall caused the Congo River to rise by 6.26 m in Kinshasa, according to BBC News, marking its highest level since 1961 and prompting the government to declare a hydrological and ecological catastrophe, according to the Emergency Response Coordination Centre. The disaster devastated 15 of the country's 26 provinces, affecting at least 304,000 families and claiming 300 lives. In the Equateur province alone, 600,000 people were impacted by flooding, while Kinshasa also experienced severe destruction. Reports indicated widespread destruction, including damage to 43,750 homes, 1325 schools, 269 health centers, 41 public markets, and 85 roads.

From mid-July to mid-August, widespread flooding caused by heavy rainfall and strong winds affected central and southwestern Chad. Media reports confirmed at least 54 fatalities, with the Tibesti region in northwestern Chad having been the hardest hit. According to UN OCHA, more than 261,000 people were affected, over 5300 were displaced, and 16,200 houses were damaged or destroyed between 15 July and 15 August.

4. EASTERN AFRICA

—E. Bekele, Z. T. Segele, and W. M. Thiaw

The Greater Horn of Africa (GHA), or Eastern Africa, covers 11 countries and extends from 12°S–24°N to 21°E–52°E. Its northern sector comprises Sudan, South Sudan, Eritrea, Djibouti, northern Somalia, and the northern two-thirds of Ethiopia. Southern and central Somalia, southern and southeastern Ethiopia, Kenya, northern Tanzania, Uganda, Rwanda, and Burundi are in its equatorial sector, while the southern sector encompasses central and southern Tanzania. The region has a complex terrain, with elevation ranging from about 160 m below sea level at Ethiopia's northern exit of the Rift Valley, to more than 5000 m above sea level at glaciated Mount Kilimanjaro. This complex topography is further amplified by the presence of large lakes, and reflects multi-faceted climate zones modulated by local and large-scale forcing such as the deep convective and moisture convergence zone (e.g., Camberlin 2018), the El Niño–Southern Oscillation (e.g., Segele et al. 2009), the Indian Ocean dipole (e.g., MacLeod et al. 2024), the Madden–Julian Oscillation (e.g., Godoshava et al. 2024), and tropical–extratropical interactions (e.g., Bekele-Biratu et al. 2018). Rainfall is bimodal in the equatorial sub-region, with two distinct rainfall seasons in MAM and OND. Seasonal rainfall is unimodal in the northern and southern sectors, spanning November–April in the south and JJAS in the north. The JJAS rainfall over Ethiopia–Eritrea is locally known as "Kiremt" rains.

(i) Temperature

Annual mean temperatures in 2024 exceeded 26°C over northern South Sudan, most of Sudan, Eritrea, northeastern and southeastern Ethiopia, Djibouti, Somalia, far eastern Kenya, and coastal Tanzania (Fig. 7.28a). On the other hand, most of the highlands recorded cooler conditions, with the highlands of Ethiopia averaging annual mean temperatures of 18°C or lower. Annual mean temperatures were 0.5°C to 1.5°C above average over most areas, except over central and northern Sudan and southern Tanzania (Fig. 7.28b). The highest positive annual mean temperature anomalies of +1.0°C to +1.5°C occurred in South Sudan and northeastern Ethiopia (Fig. 7.28b). Recorded annual mean temperatures were above the 97th percentile in southeastern Ethiopia, eastern Kenya, southern and central Somalia, and parts of central South Sudan. Although annual mean temperature anomalies over parts of Sudan were only 0.5°C below average, the observed temperatures were less than 15°C and fell within the lowest 30% (even 15% locally) of historical records. The main contributor to these low temperatures was the

Unauthenticated | Downloaded 11/21/25 11:34 AM UTC

large cooling observed during both January–February and OND 2024, where anomalies were as much as 3°C below average; temperatures ranked in the bottom third in the historical record during OND 2024.

Inspection of the progression of mean maximum monthly temperatures in 2024 shows that a broad region of elevated maximum temperatures exceeding 40°C–42°C appeared in March 2024 over northern South Sudan and southern Sudan and advanced northward, covering most of Sudan and expanding farther east and north into Eritrea, northeast Ethiopia, and Djibouti in June. Maximum temperatures exceeded 46°C in June 2024 but weakened thereafter as the monsoon clouds and rains settled in the region. Accordingly, most of GHA recorded maximum temperatures above the 90th percentile during June and July. High maximum temperatures in the top 3% of historical records were observed along the Red Sea from Djibouti through Ethiopia and Eritrea to northern Sudan, western Sudan, and eastern Kenya (and most of Tanzania) in June (July) 2024. Mean minimum temperatures followed similar patterns, in which a small area of 24°C–26°C emerged in South Sudan in March and rapidly intensified and expanded north and eastward, covering much of Sudan, Eritrea, northeastern Ethiopia, Djibouti, and coastal Somalia in July. Unlike the evolution of maximum temperature, peaks of minimum temperatures extended to Somalia through September. In addition, mean minimum temperatures were above the 97th percentile in central Sudan, coastal areas of Sudan, Eritrea, and Djibouti, and eastern Kenya.

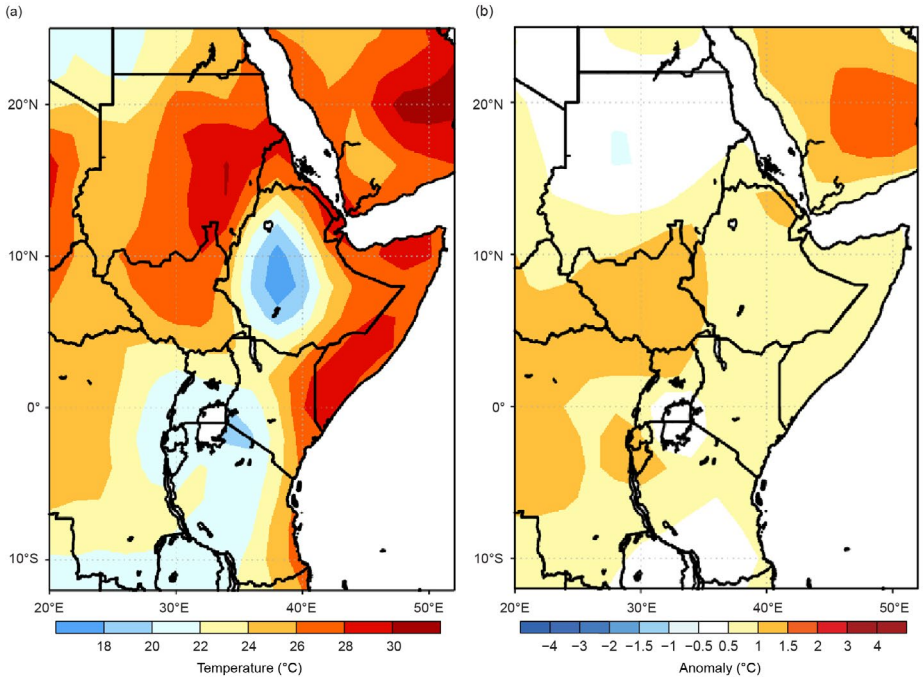

Fig. 7.28. Annual (a) mean temperature (°C) and (b) mean temperature anomalies (°C; 1991–2020 base period) for Eastern Africa for 2024. (Source: NOAA/National Centers for Environmental Prediction [NCEP].)

(ii) Precipitation

Annual rainfall totals in 2024 surpassed 1000 mm in western Ethiopia, South Sudan, most of Uganda, most of Rwanda, Burundi, southwestern Kenya, and most of Tanzania (Fig. 7.29a). Western Uganda and western Rwanda recorded the highest annual totals, which exceeded 1500 mm. Northern South Sudan, southern Sudan, northwestern, central, and southern Ethiopia, northwestern, central, and southeastern Kenya, and central parts of Tanzania received rainfall between 600 mm and 1000 mm. Totals were lower (50 mm–600 mm) over northern Sudan, Eritrea, Djibouti, northeastern and southeastern Ethiopia, northeastern Kenya, and most of Somalia. Overall, annual rainfall totals received in the region were near to above average, except in a few places in western Ethiopia. The highest rainfall anomalies of 300 mm or above (ranking above the 90th percentile) occurred in southeastern Tanzania (Fig. 7.29b). Due to the above-normal rainfall during the monsoon season, the annual rainfall totals in northwestern Sudan were among the top third of the historical record (Fig. 7.29b). Annual rainfall totals in Uganda, southern South Sudan, and eastern Tanzania were above the 90th percentile.

Unauthenticated | Downloaded 11/21/25 11:34 AM UTC

A broad area of monthly rainfall totals between 100 mm and 200 mm progressed from Tanzania and the southern Lake Victoria region in January 2024 to southern Sudan, southern Ethiopia, and southern Somalia in April. It is noted that rainfall in January and April 2024 contributed significantly to the extremity and high ranking of the annual rainfall totals in Tanzania and Uganda. During July–August, the highest rainfall total exceeding 200 mm month^{-1} was recorded in northwestern Ethiopia, although the total monthly/seasonal amounts fell short of the long-term averages for the region. On the other hand, 2024 rainfall totals in Eastern Africa were wetter than average for the year, as well as for the MAM and OND 2024 seasons.

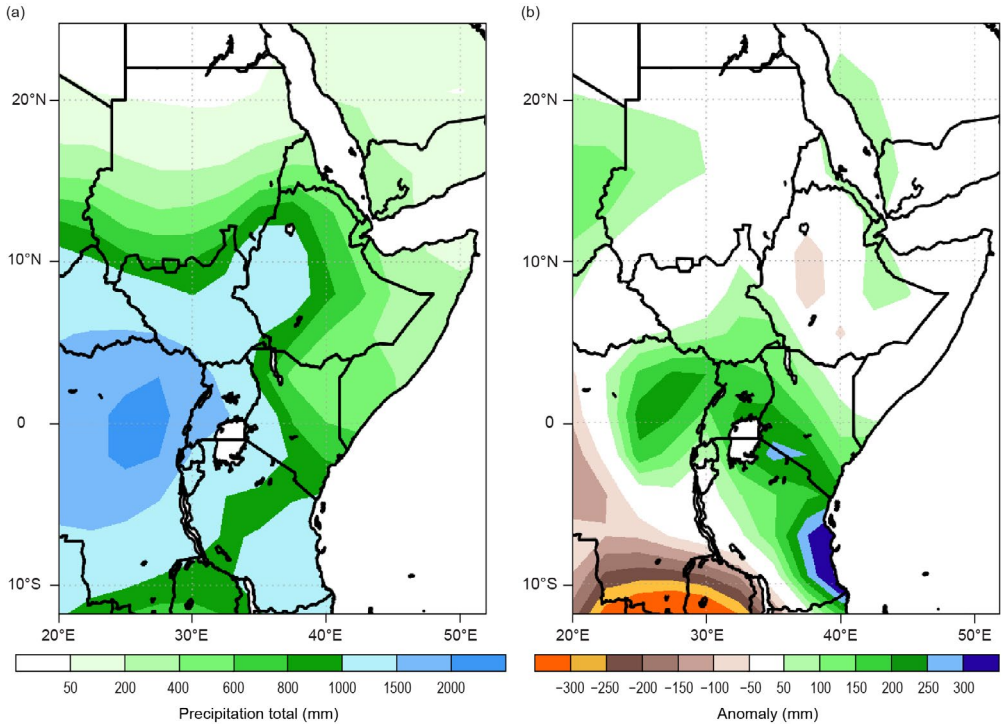

Fig. 7.29. Annual (a) total rainfall (mm) and (b) total rainfall anomalies (mm; 1991–2020 base period) for Eastern Africa for 2024. (Source: GPCP via NOAA/National Centers for Environmental Prediction [NCEP].)

(iii) Notable events and impacts

The El Niño event that began in 2023 continued into the boreal spring of 2024, causing heavy rains and flooding across Eastern Africa, particularly during the long rainy season (i.e., MAM). According to UN OCHA, the floods caused widespread devastation in Burundi, Kenya, Somalia, Rwanda, and Tanzania, affecting over 636,000 people and leading to significant infrastructure damage, crop destruction, and heightened disease risks like cholera.

Cyclone Hidaya, the most intense tropical cyclone in this region on record, struck on 4 May 2024. The storm, a Category 1 equivalent, brought heavy rainfall and strong winds to a region already impacted by extreme weather. Although no casualties were reported, the cyclone caused evacuations in Kenya and led to widespread blackouts and displacement in Tanzania, as reported by earth.org.

5. SOUTHERN AFRICA

—A. C. Kruger, C. McBride, M. Robjhon, S. Fuhrman, and W. M. Thiaw

Southern Africa is a region that covers a wide area in the southern portion of Africa. It extends from about 5°S to 35°S and comprises Angola, Namibia, Zambia, Botswana, Zimbabwe, Malawi, South Africa, Lesotho, Eswatini, and Mozambique. Southern Africa is characterized by two main seasons: the wet and warm season from November of the previous year to April, and the dry and cold season from May to October.

(i) Temperature

Annual mean temperatures ranged from about 16°C to 28°C in Southern Africa, with warmer conditions in the northwest and east along with parts of the central region, and colder conditions across the south (Fig. 7.30a). Annual mean temperatures were above average across the

Unauthenticated | Downloaded 11/21/25 11:34 AM UTC

majority of Southern Africa, especially in the central, southern, and western regions. The largest warm anomalies were observed over northeastern Namibia as well as parts of its southern region, much of Botswana, and parts of central South Africa, where annual mean temperatures were 1.5°C–2°C above average (Fig. 7.30b). Near-average conditions (within 0.5°C of the mean) covered a region encompassing eastern Zambia, Malawi, southwestern Tanzania, central Mozambique as well as parts of the country's northern region, and a portion of northwestern Angola. Annual mean temperatures were not below average anywhere in Southern Africa.

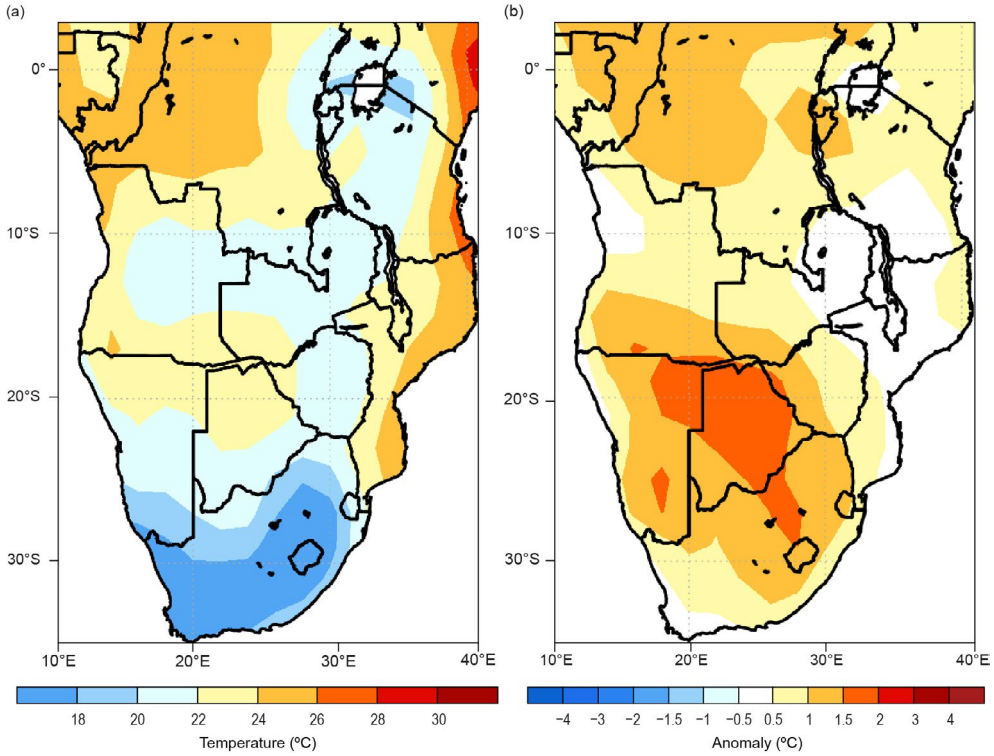

Fig. 7.30. Annual (a) mean temperatures and (b) mean temperature anomalies (°C; 1991–2020 base period) for Southern Africa. (Source: NOAA/National Centers for Environmental Prediction [NCEP].)

South Africa experienced a new record-warm year (since 1951), with hot conditions mainly in the central and northern interior. In the south, however, temperatures were closer to normal. The annual mean temperature anomaly for 2024, based on the data of 26 climate stations, was about 0.9°C above the average of the 1991–2020 base period (Fig. 7.31). A warming trend of approximately 0.17°C decade^{-1} is indicated for the country over the period 1951–2024 and is statistically significant at the 5% level.

Annual maximum temperatures were above average over most areas in Southern Africa, with the warmest conditions in the central and western sectors of the region. Positive anomalies were as high as +3°C to +4.5°C across southern and northeastern Angola, northeastern Namibia, and northwestern Botswana. Positive anomalies corresponded to a rank between the 97th and 98th percentile across most of the region. Portions of northern Mozambique finished the year with maximum temperatures closest to average. Seasonally, maximum temperatures were well above average in the central and eastern parts of southern Africa during the DJF season and above average across southern, western, and some central portions of southern Africa during the SON season.

Annual minimum temperatures were 1°C to 1.5°C above average over central Botswana and eastern Tanzania and 0.5°C to 1°C above average across the remainder of Botswana,

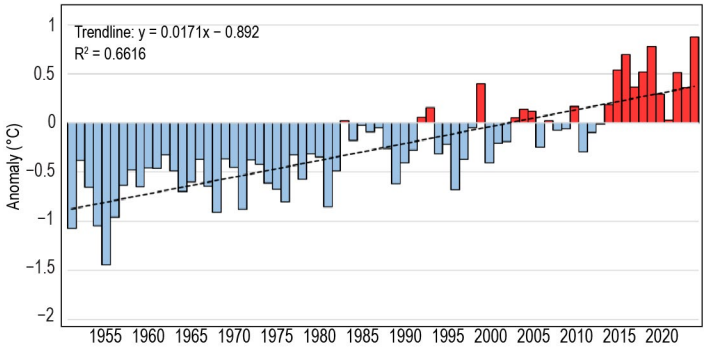

Fig. 7.31. Annual average surface temperature anomalies (°C; 1991–2020 base period) over South Africa based on 26 climate stations for the period 1951–2024. The linear trend is indicated by the black dashed line. (Source: South African Weather Service.)

Unauthenticated | Downloaded 11/21/25 11:34 AM UTC

southern and central Namibia, western Zimbabwe, parts of central and southern South Africa, and northeastern Mozambique. Meanwhile, minimum temperatures were within 0.5°C of average over the other portions of Southern Africa. Minimum temperatures were generally well above average across the region during the MAM season and over the central sector during DJF. Conversely, minimum temperatures were well below average over the southern and western sectors during DJF and over the northwestern sector during the July–August season.

(ii) Precipitation

Annual rainfall totals in 2024 were highly modulated by El Niño, which is typically linked to below-average rainfall in Southern Africa (e.g., Hoell et al. 2021). While central and northern Angola and northern Mozambique saw annual rainfall totals over 1000 mm, a wide area of southern and central Southern Africa received rainfall totals of only between 200 mm and 1000 mm (Fig. 7.32a). Annual rainfall was much below average across central and eastern Southern Africa from eastern Angola to central Mozambique, with eastern Angola, Zambia, northern Zimbabwe, southern Malawi, and central Mozambique experiencing rainfall totals over 300 mm below average, whereas rainfall was above average in western Angola and northeastern Mozambique (Fig. 7.32b). Over the dry portion of Southern Africa stretching from eastern Angola to central Mozambique, 2024 ranked below the third percentile in the historical record that dates to 1991.

In South Africa, the year started with relatively wetter conditions in the central and eastern regions, but was dry in the west. Overall, however, rainfall during 2024 (Fig. 7.33) was near-normal over most of the country. The major exception was the northwestern to central interior, which received well-below-normal rainfall, with some places experiencing extremely dry conditions.

The DJF 2024 rainfall was more than 100 mm below average in eastern Angola, Zambia, northeastern Namibia, northern Botswana, northern Zimbabwe, Malawi, and central Mozambique, while rainfall was 20 mm–100 mm above average in western Angola, Lesotho, and southeastern South Africa. A similarly anomalous rainfall pattern was observed in the region during MAM, with below-average rainfall extending from Namibia, Zambia, Botswana, Zimbabwe, and Malawi to western and northern Mozambique, and above-average rainfall occurring in western Angola, southern Mozambique, and southern South Africa. During JJA and the winter months, rainfall was near-average in most areas of the region except for southern South Africa, which

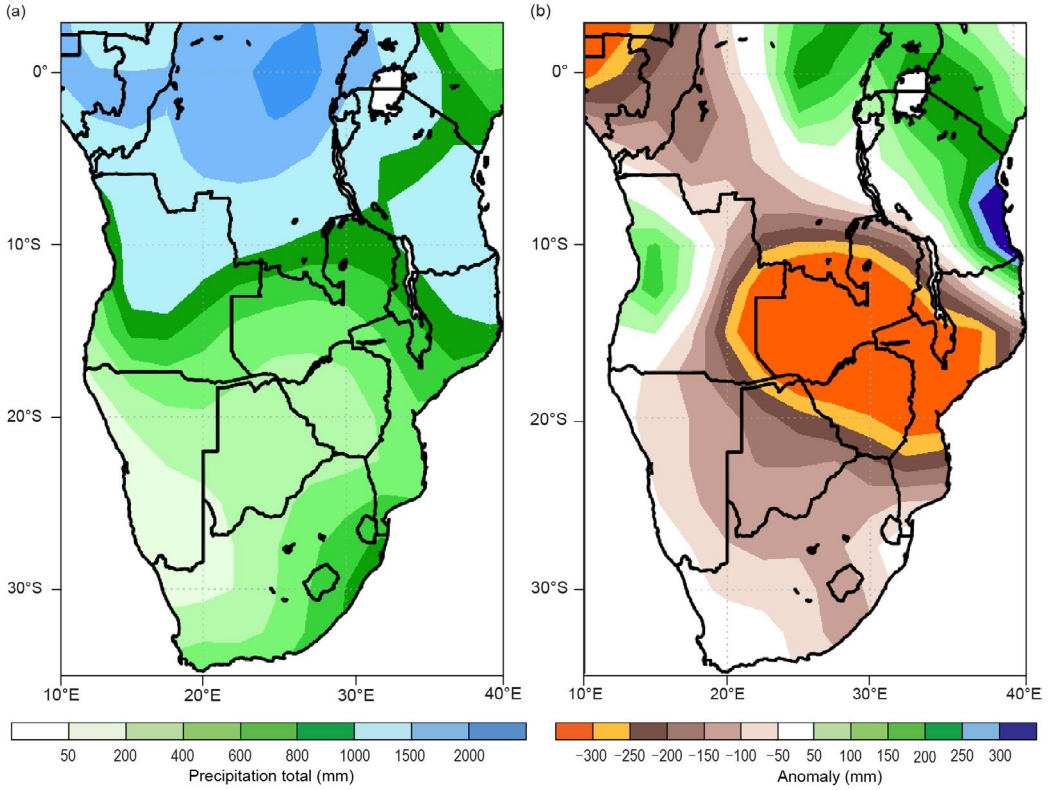

Fig. 7.32. Annual (a) rainfall totals and (b) rainfall anomalies (mm; 1991–2020 base period) for Southern Africa. (Source: GPCP, NOAA/National Centers for Environmental Prediction [NCEP].)

Unauthenticated | Downloaded 11/21/25 11:34 AM UTC

experienced above-average precipitation. During SON, rainfall was 20 mm–50 mm below average in central Southern Africa, including southeastern Angola, northeastern Namibia, southwestern Zambia, Botswana, western Zimbabwe, and northern South Africa, but was 20 mm–40 mm above average in pocket areas of northern Angola, Malawi, western and northern Mozambique, Lesotho, and eastern South Africa.

(iii) Notable events and impacts

The El Niño teleconnection patterns contributed to widespread drought across many countries in Southern Africa. The resulting food and water shortages affected 7.6 million people in Zimbabwe, 6.6 million people in Zambia, 6.1 million people in Malawi, 2.8 million people in Angola, and 1.7 million people in Namibia, according to the Emergency Events Database (EM-DAT), an international disaster database.

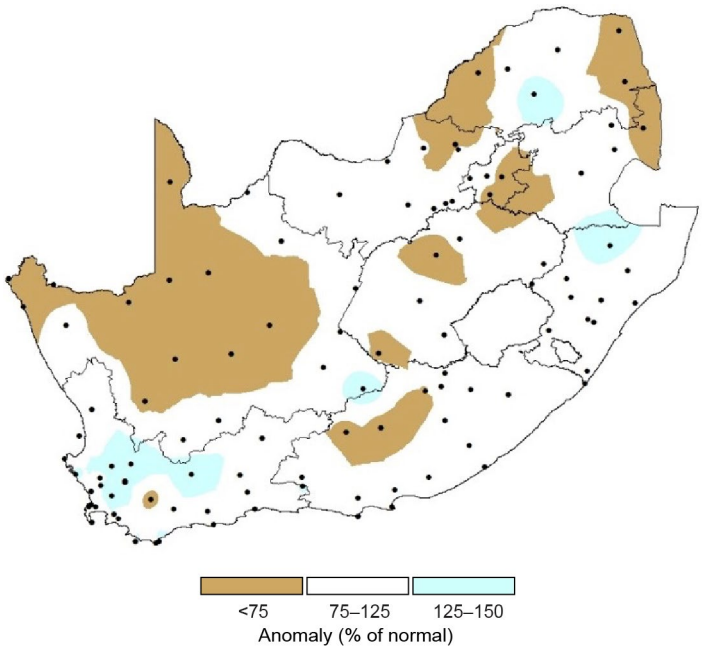

Fig. 7.33. Annual rainfall anomalies (% of 1991–2020 average) for South Africa for 2024. (Source: South African Weather Service.)

Extreme heatwaves affected various parts of Southern Africa throughout the year. Central and western regions were affected during February and March. South Africa was particularly affected in May, and many central and eastern areas were affected during December, resulting in monthly mean temperature anomalies in the range of +3°C to +5°C.

In South Africa, several significant adverse weather events in the east caused flooding, which led to the displacement of many residents and extensive infrastructure damage. On 13 March, heavy rain affected parts of the Zululand region in KwaZulu-Natal after Tropical Storm Filipo made landfall in Mozambique, with reports of flooded and damaged low-lying bridges and roads, as well as fatal accidents. For example, a storm in Margate on the country's east coast on 14 March left five people dead when 250 mm of rain was recorded in 24 hours. May saw dry conditions in the western and central interior. Nearly all of Mozambique was abnormally hot, with maximum temperature anomalies reaching +3°C to +4°C. In June, the south and central parts received more than 200% of normal rainfall. Seven people died and two people were missing after heavy rains resulted in high water levels and severe flooding in parts of Gqeberha and Kariega in the Eastern Cape on 1 June. Additionally, more than 1100 residents were evacuated. In July, the region of heavy rainfall shifted to the west. Infrastructure damage to homes, roads, power supply, and schools were reported in neighborhoods of the Western Cape on 11 July, with residential roofs blown off in Wynberg, 217 schools reporting damage to infrastructure, and at least 10,000 households hit by power cuts. About 100 roads were closed on the same day due to safety concerns. In contrast, the northern parts of the country saw extremely hot conditions during austral winter, which continued to a somewhat lesser degree into August. From November to December, large parts of the eastern half of South Africa observed significantly above-normal temperatures. Many weather stations reported their highest maximum temperature on record for these months, with several heat warnings and heatwaves issued.

On 12 March, Tropical Storm Filipo struck the Vilankulo and Morrumbene districts in Inhambane along with the Gaza, Sofala, and Nampula Provinces of Mozambique with winds of up to 120 km h^{-1}, which led to two fatalities and over 93,000 people affected. In April, central and southern parts of Mozambique received more than double their usual precipitation totals for the month, which led to flooding, loss of life, and infrastructure damage.

Unauthenticated | Downloaded 11/21/25 11:34 AM UTC

During 13–16 December, Tropical Cyclone Chido, with a 24-hour accumulated rainfall of 250 mm and winds of up to 260 km h^{-1}, impacted Mecufi, Metuge, Ancuabe, Meluco, Ilha de Ibo, Quissanga and Pemba City of Cabo Delgado, Memba, Nacala, Nacala Velha, Mossuril, Mongicual, Mozambique Island, Monapo, Meconta, Nacaroa, Erati, Muccate, Nampula City of Nampula, Cuamba, Madimba, Marrupa, Maua, Mecanhelas, Metarica, Nipep of Niassa, and Tete of Mozambique, resulting in 120 deaths and 454,000 people affected. In Malawi, the storm affected the Salima, Kasungu, Machinga, Blantyre, and Lilongwe Districts, causing 13 fatalities and affecting 45,000 people.

6. WESTERN INDIAN OCEAN ISLAND COUNTRIES

—C. Backenstrass, T. Nomenjanahary, B. Andrade, G. Jumaux, R. Virasami, S. Dindyal. M. Robihon, K. Kowal, and W. M. Thiaw

The Western Indian Ocean Island countries consist of Madagascar, Seychelles, Comoros, Mayotte (France), Réunion (France), Mauritius, and Rodrigues (Mauritius). There are two distinct main seasons: a warm and wet period spanning from November of the antecedent year to April, and a cold and dry season lasting from May to October.

(i) Temperature

At Seychelles International Airport in 2024, the annual mean temperature was 0.6°C above normal, the second-highest annual mean temperature since the start of the record in 1972. The year began with its warmest January on record, at 1.5°C above normal. For the period January–March, the temperature anomaly was 1.02°C above normal. This anomaly decreased to +0.44°C during April–June. For July–September, there was a slight increase in temperature to 0.48°C above normal that rose to +0.69°C during October–December. November 2024 was the warmest November on record, with a monthly temperature anomaly of +0.85°C.

The mean annual temperature in Mauritius for 2024 (based on five stations) was 24.3°C, 0.6°C above normal. The highest mean temperature for the year was recorded in January (26.9°C), whereas the lowest mean temperature was observed in July and August (21.3°C). In the first half of the year, the temperature anomaly ranged from +0.1°C to +0.6°C, whereas in the second half, it increased to +0.4°C to +1.2°C.

In 2024, the annual temperature for Réunion island (based on three stations) was 0.72°C above normal, marking the third-highest annual temperature for the island since the start of the record in 1968. The year started with a temperature anomaly of +0.4°C for January–March and increased through the year: + 0.62°C in AMJ, +0.91°C in JAS, and +0.95°C in OND. November 2024 was the warmest November on record, with a monthly temperature anomaly of +1.47°C.

In Mayotte, the annual temperature anomaly was 1.19°C above normal, as measured at Pamandzi airport's weather station. This was the highest annual temperature in the 64-year record and was linked to unusually high sea surface temperatures. Five months (March to June and September) each observed their highest monthly temperatures on record.

In Madagascar, annual mean temperatures in 2024 ranged between 20°C and 28°C (Fig. 7.34a). Higher annual mean temperatures were observed along the west coast and northern part of the island, whereas lower annual mean temperatures were experienced over the central highlands. Annual mean temperatures were 0.5°C–1°C above average over much of the central and northern portions of the country (Fig. 7.34b). These warm anomalies corresponded to the 90th-to-98th-percentile rankings covering most of Madagascar.

Annual maximum temperatures were 0.5°C–1°C above average in the upper half of Madagascar and extending into regions just below 20°S. During September, the highest average maximum temperatures of the year were reached, ranging between 32°C and 34°C, corresponding to anomalies of +1°C to +2°C. In July, although temperatures remained below 30°C, above-average maximum temperatures were widespread over the island, with some eastern regions registering anomalies of +2°C to +2.5°C. Annual minimum temperatures were also generally 0.5°C–1°C above average across the northern two-thirds of Madagascar, and up to +1.5°C in the northwestern subregion. Near- to above-average minimum temperature conditions were observed over many parts of the island in the MAM, JJA, and SON seasons. Above-average minimum temperatures were highest in November, up to +2°C in southeastern Madagascar; however, in October,

Unauthenticated | Downloaded 11/21/25 11:34 AM UTC

minimum temperatures were largely near average and sometimes as cool as 1.0°C below average in southwestern regions of the country.

(ii) Precipitation

In Seychelles, the total annual rainfall (3431.8 mm) was 140% of average, making 2024 the second-wettest year since the start of the record in 1972. Most months experienced above-normal precipitation, except for January, July, and October. January 2024 was the second-driest January in the 53-year record.

In Mauritius, the cumulative observed rainfall for the year 2024 was 2181 mm (108% of normal). January was the wettest month. Hot and sultry conditions prevailed, particularly in January and February. Tropical Cyclone Belal, Moderate Tropical Storm Candice, and Severe Tropical Storm Eleanor influenced weather over the island. April was marked by severe flooding in the capital city. Typical wintry weather was then observed, particularly during the second fortnight of May into June. July was the driest since the start of the record in 1904, and the dry spell persisted into August and September. Despite normal rainfall in October and Intense Tropical Cyclone Bheki bringing above-normal rainfall in November, rainfall totals for the winter season were below normal. During the last week of December, the first thunderstorm event for the 2024/25 summer season was observed. December was also marked by the passage of Intense Tropical Cyclone Chido.

Total annual rainfall in Réunion was 2507 mm (98% of normal) but with large variations through the year. January received more than twice the monthly normal, making this the third-wettest January in the 53-year record. It was followed by a dry period, with only 78% of the normal for the dry season. July 2024 was the driest July on record. Near the end of the year, the rainy season didn't begin as expected (rainfall was 75% below normal for December), causing a drought.

Annual rainfall in Mayotte was normal overall (1428 mm). The year began with above-normal rainfall during January and February. The next months were drier than normal, and the dry season received only half of the normal total, making it the second-driest such season in the 28-year record. The last two months before the start of the wet season again saw above-normal rainfall.

In Madagascar, annual rainfall in 2024 ranged between 600 mm and 1500 mm over the southern two-thirds of the island, but exceeded 1500 mm in the northern regions (Fig. 7.35a). Consequently, most areas of the country registered below-average annual rainfall, with the driest conditions observed across the central highlands and western regions, while the northern

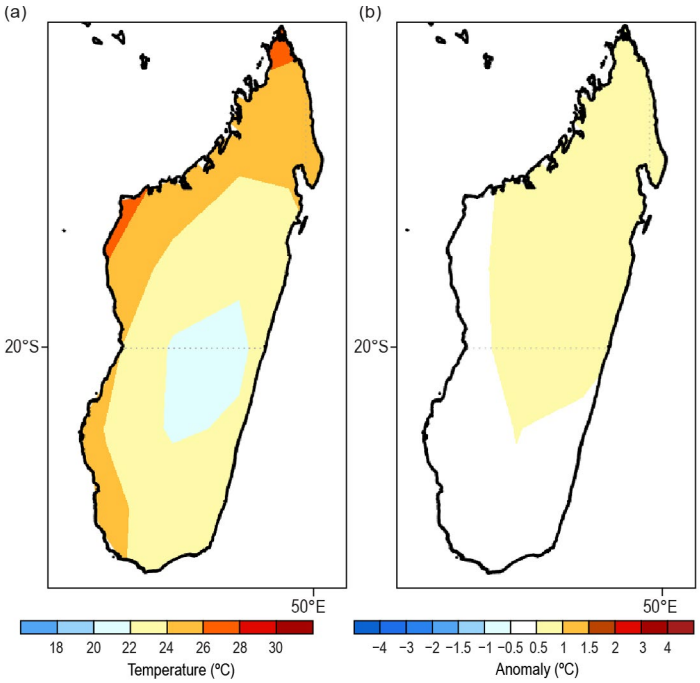

Fig. 7.34. Annual (a) mean temperatures and (b) mean temperature anomalies (°C; 1991–2020 base period) for Madagascar. (Source: NOAA/National Centers for Environmental Prediction [NCEP].)

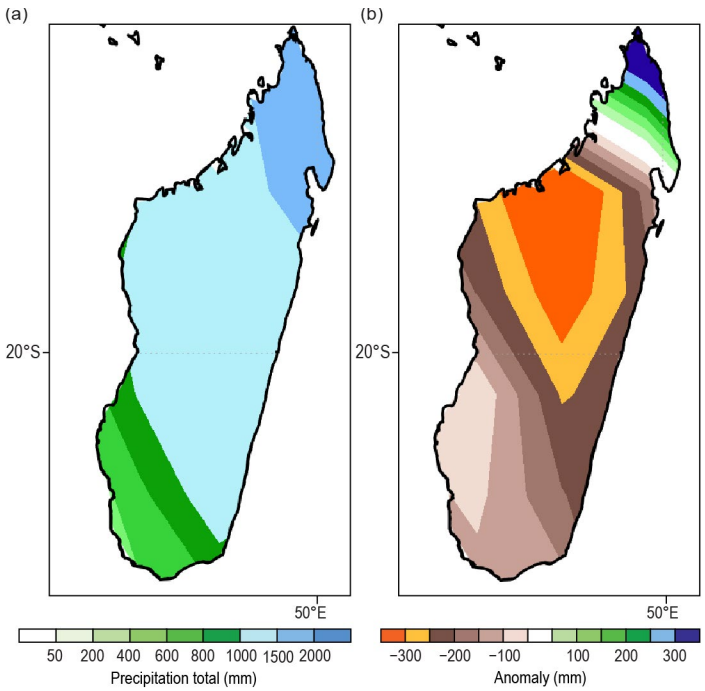

Fig. 7.35. Annual (a) rainfall totals and (b) rainfall anomalies (mm; 1991–2020 base period) for Madagascar. (Source: GPCP, NOAA/National Centers for Environmental Prediction [NCEP].)

Unauthenticated | Downloaded 11/21/25 11:34 AM UTC

tip of the country experienced above-average rainfall (Fig. 7.35b). During DJF, rainfall was below average over much of Madagascar but was above average in the northern regions. During MAM, rainfall was above average in the southwest and north but remained below average in the west. During JJA and SON, below-average rainfall returned over the northern two-thirds of the island and eastern regions, respectively.

(iii) Notable events and impacts

Tropical cyclone Belal impacted Réunion from 13 to 16 January; its center crossed the island on 15 January. This cyclone brought extreme weather conditions, including wind gusts reaching 150 km h^{-1} to 175 km h^{-1}, local rainfall exceeding 1000 mm, and a sea swell on the northern coasts that was 11.6 m high. The storm caused four fatalities, and about 30% of the island's inhabitants experienced water or power cuts in the aftermath.

An active feeder band associated with Belal crossed Mauritius on 15 January, causing heavy rainfall mainly over the western half of the island, including the capital city of Port Louis. The storm's passage near the Mascarene Islands during 15–16 January led to two fatalities and affected 100,000 residents.

Tropical Cyclone Belal passed around 90 km to the south of Mauritius, causing cyclonic conditions during the night of 15 January. The highest gust recorded on the island was 122 km h^{-1} at Nouvelle-Découverte. On 21 November, a moisture convergence associated with Tropical Depression Bheki brought torrential rain over the eastern half of the island. Moderate to heavy rainfall was observed on 21 November and persisted in several regions over the east. More than 100 mm of rain were recorded at Mon Loisir SE, Queen Victoria, and Plaisance. Bheki intensified to an intense tropical cyclone on 17 November. The storm approached Rodrigues along a general west-southwesterly track. Cyclone warnings were issued for the island. Bheki crossed about 55 km to the north of Rodrigues Island on 20 November, causing cyclonic conditions. The highest gust recorded over the island was 122 km h^{-1} at Patate Theophile. This situation led to power outages affecting 64% of the population. Additionally, around 50 families had to seek shelter in refuge centers.

Tropical Cyclone Chido passed over Mayotte between 13 and 16 December. The storm caused 22 deaths, 1373 injuries, and affected 230,000 people. With winds of up to 100 km h^{-1}, Chido impacted the Diana Region of Madagascar and affected over 135,000 people. Earlier in the year, from 26 to 29 March, Tropical Cyclone Gamane—with winds of up to 210 km h^{-1} and rainfall totals between 200 mm and 500 mm—led to flooding, which resulted in 22 fatalities, four injuries, and over 89,000 people affected.

By contrast, the dry season was among the driest recorded in a few decades in Mayotte and Réunion. Combined with high temperatures, droughts affected both islands. Water cuts started early in the dry season and lasted for months in areas where such conditions are highly unusual.

Unauthenticated | Downloaded 11/21/25 11:34 AM UTC

f. Europe and the Middle East

—P. Bissolli, Ed.,
R. van der Linden, M. Roebeling, C. Berne,
O. Bochníček, V. De Bock, M. Ekici, A. Gevorgyan,
M. Kendon, J. R. Kennedy, Y. Khalatyan, V. Khan,
M. Lakatos, J. Mamen, A. Morata Gasca, F. Rubek,
S. Sensoy, S. Spillane, M. Turňa, and A. Willems

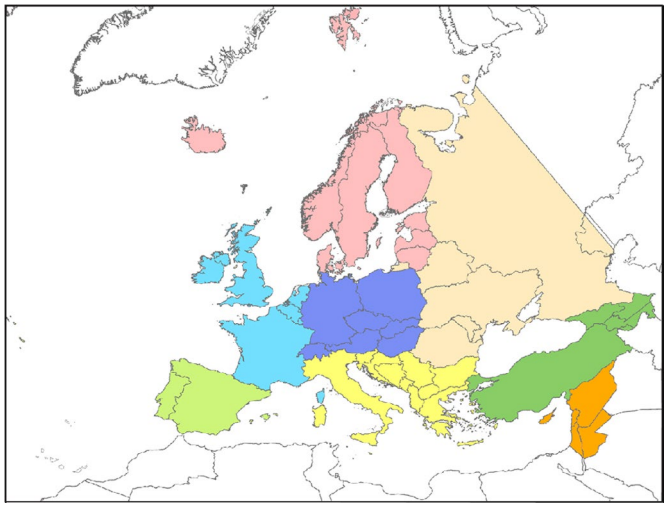

Fig. 7.36. Map of subregions in the World Meteorological Organization (WMO) Regional Association (RA) VI region of Europe.

Throughout this section, 1991–2020 is the base period used for anomalies unless otherwise specified. This base period is referred as "normal" according to the World Meteorological Organization's (WMO) recommendations, although the climate of this period is heavily affected by global warming. It is not associated with a statistical normal (Gaussian) distribution since climate variables may not be normally distributed. Anomalies are consequently described as "above/below normal", implying positive/negative deviations from the so defined normal state (climatological average). All seasons mentioned in this section refer to the Northern Hemisphere; winter refers to the period from December 2023 to February 2024. More detailed information can be found in the Monthly and Annual Bulletin on the Climate in Regional Association (RA) VI–Europe and the Middle East, provided by the WMO RA VI Regional Climate Centre Node on Climate Monitoring (RCC-CM; http://www.dwd.de/rcc-cm). Findings are based on gridded data of interpolated CLIMAT station and ship data for temperature, as well as that of the Global Precipitation Climatology Centre (GPCC) for precipitation (if not otherwise specified); the data were also supplemented by information from National Meteorological and Hydrological Services (NMHSs) where available, as well as information from the WMO (WMO 2025). Spatial averages for subregions displayed in Fig. 7.36 are always based on these gridded data only. More information about the datasets can be found here: https://www.dwd.de/EN/climate_environment/climatemonitoring/europe/maps_node.html.

Anomaly information has been taken from Figs. 7.37–7.41 and from national reports. The length of national temperature and precipitation records, annual anomalies, and rank information for each country are provided in Appendix Table A7.1. A color-coded map of the various subregions of the WMO RA VI Region is shown in Fig. 7.36. Due to the large number of countries in Europe and the limited word space for each subsection, only limited impact information can be provided here. More details about extreme events and impacts across Europe can be found elsewhere, e.g, https://climate.copernicus.eu/esotc/2024/key-events.

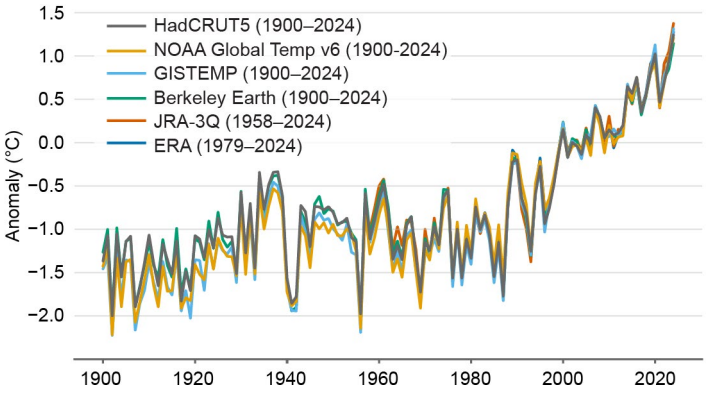

1. OVERVIEW

Based on six different datasets, the year 2024 was the warmest on record over the region (Fig. 7.37). The region is defined as the land areas of the WMO RA VI region as displayed in Fig. 7.36 plus Greenland. The mean temperature anomaly was +1.26°C over land areas, ranging from +1.14°C to +1.37°C depending on the dataset. Based on interpolated climate station and ship data (Fig. 7.38),

Fig. 7.37. Annual regional mean temperature anomaly for the World Meteorological Organization (WMO) Regional Association (RA) VI of Europe (°C; difference from the 1991–2020 average, land areas only) for the period 1900–2024. Data are from the following six datasets: Berkeley Earth, ERA5, GISTEMP, HadCRUT5, JRA-55, and NOAA Global Surface Temperature (NOAAGlobalTemp). For dataset and processing details, see https://www.jkclimate.fr/RegionalDashboard/wmo_ra_vi.html#WMO%20RA%20VI%20Europe (Source: WMO.)

Unauthenticated | Downloaded 11/21/25 11:34 AM UTC

the year was also warmest on record (+0.98°C anomaly; +1.32°C over land only). The year was among the four warmest for all subregions. Central Europe (+1.9°C anomaly), the central Mediterranean region (+1.8°C anomaly), and Eastern Europe (+1.8°C anomaly) each observed their warmest year on record. The largest positive anomalies occurred over eastern parts of Central Europe, western parts of Eastern Europe, and over the Balkan Peninsula. In western parts of the region, generally weaker temperature anomalies prevailed. The year was colder than normal only over Iceland. In terms of annual precipitation, 2024 was close to normal (90% to 110% of normal) over most of the region (Fig. 7.39); however, anomalies varied greatly across the region. The year was mostly wetter than normal over Western Europe, Central Europe, and the Iberian Peninsula. Normal to drier-than-normal conditions dominated across the Nordic and Baltic countries except for Denmark and Norway. The central Mediterranean region saw wetter-than-normal conditions in the north, but drier-than-normal conditions in the east and south. Drier-than-normal conditions also prevailed over Eastern Europe, the Middle East, and Türkiye, while much of the South Caucasus experienced above-normal precipitation.

In winter, below-average 500-hPa geopotential heights prevailed from eastern Greenland to northern European Russia (Fig. 7.40). Farther south, above-average heights dominated. Below-average mean sea level pressure (MSLP) occurred over northern Europe, with the largest negative anomaly occurring over the Baltic Sea (Fig. 7.41). Below-average temperatures occurred in a band from eastern Greenland to northern European Russia, while most other parts saw above-average temperatures. As a result, winter did not rank among the five warmest for the region as a whole, although it ranked among the five warmest over most subregions except for the Nordic and Baltic countries and Eastern Europe. The season was warmest on record over the central Mediterranean region as well as Türkiye and the South Caucasus. Winter was wetter than normal across most parts of Western, Central, and Eastern Europe (120%–150% of normal precipitation). The South Caucasus saw also wetter-than-normal conditions, with the highest anomalies occurring in Azerbaijan (mostly 167%–250% of normal). Drier-than-normal conditions prevailed in the northern and southern parts of the region. The central Mediterranean region (except for the north), Türkiye, Syria, and eastern parts of Spain saw mostly 60%–80% of normal precipitation.

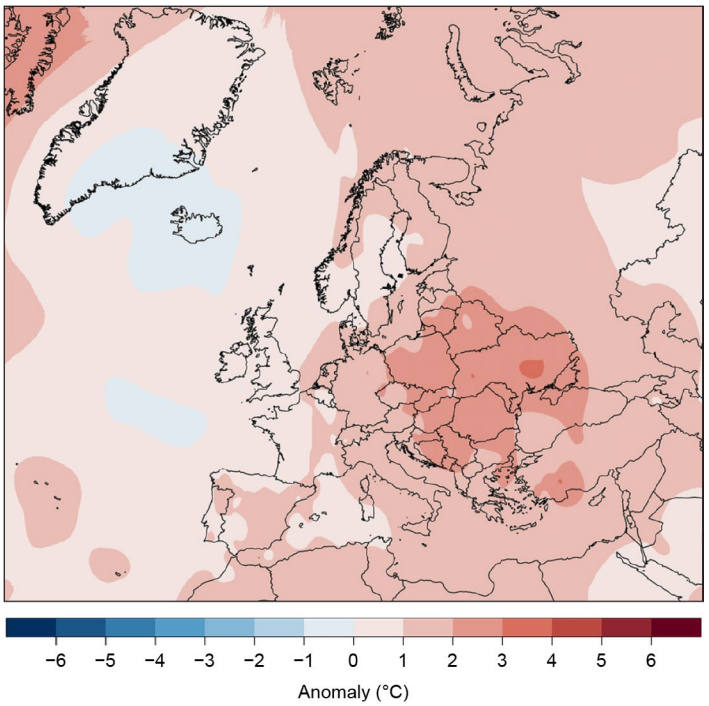

Fig. 7.38. Annual mean temperature anomalies (°C; 1991–2020 base period) for 2024. (Source: interpolated climate station and ship data, Deutscher Wetterdienst [DWD].) The 1991–2020 anomalies were recalculated from 1981–2010 anomalies because the 1991–2020 CLIMAT data were still not available for all countries.

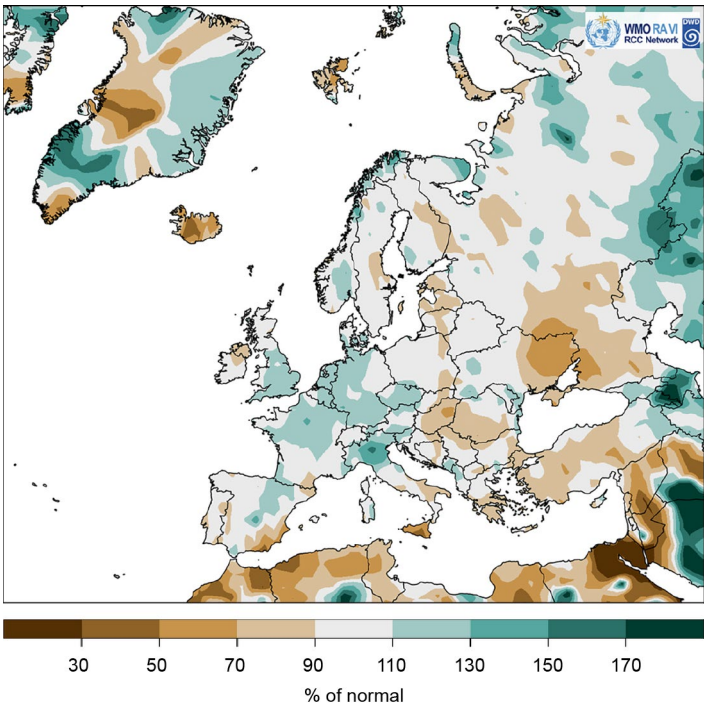

Fig. 7.39. European precipitation totals (% of 1991–2020 normal) for 2024. (Source: Global Precipitation Climatology Centre [GPCC], created by Deutscher Wetterdienst [DWD].)

Unauthenticated | Downloaded 11/21/25 11:34 AM UTC

In the north of the region, drier-than-normal conditions affected parts of Norway, Sweden, Finland, and Iceland (mostly 60%–80% of normal precipitation).

In terms of 500-hPa geopotential height anomalies, spring was characterized by pronounced contrasts. Below-average heights occurred to the west of Ireland and the United Kingdom, as well as over northeastern European Russia. Between these two regions, above-average heights prevailed. Below-average MSLP occurred particularly over Western Europe and over western parts of Central Europe; the largest negative anomaly occurred over Ireland. The season was warmest on record over the region as a whole, and was among the three warmest in Central Europe, the central Mediterranean region, the Middle East, and in Türkiye and the South Caucasus. The seasonal anomalies in these subregions were mostly influenced by warm anomalies in March and/or April, while the anomalies in May were generally weaker. Temperature anomalies in some other subregions were characterized by pronounced month-to-month variations, e.g., in the Nordic and Baltic countries (–0.7°C anomaly in April versus +3.1°C in May), Eastern Europe (+3.2°C anomaly in April versus –1°C in May), and Türkiye and the South Caucasus (+4.4°C anomaly in April versus –0.5°C in May). In spring, wetter-than-normal conditions continued over Western Europe and western Central Europe, Denmark, northern Italy, and Slovenia as well as over the South Caucasus (mostly 125%– 167% of normal precipitation). In contrast, the Nordic and Baltic countries (except for Denmark) saw near-normal to below-normal precipitation (less than 60% of normal over large parts of Norway). The largest deficits occurred

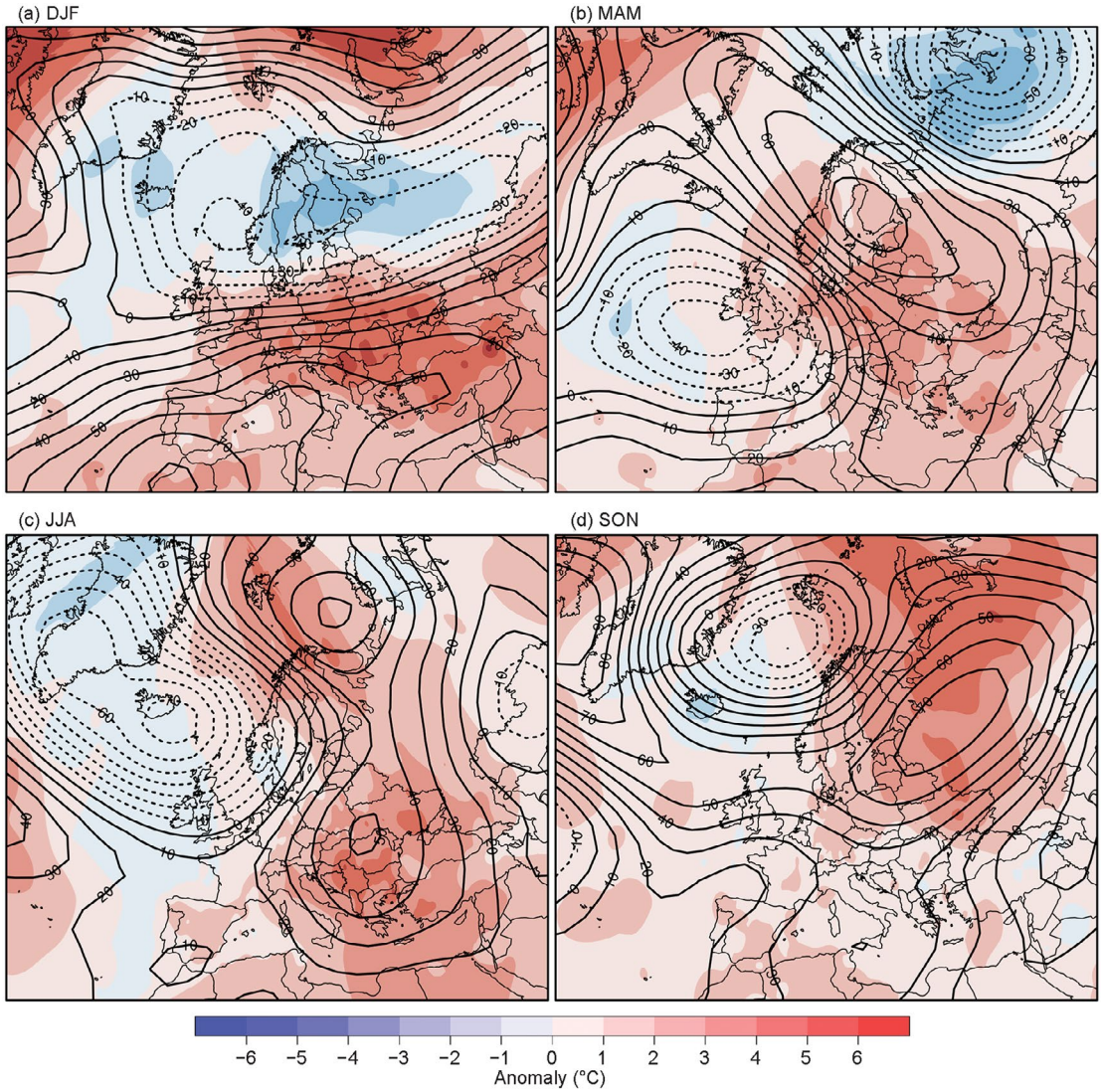

Fig. 7.40. Seasonal anomalies (1991–2020 base period) of 500-hPa geopotential height (contour; m) and surface temperature (shading; °C) using data from the National Centers for Environmental Prediction (NCEP)/National Center for Atmospheric Research (NCAR)reanalysis and Deutscher Wetterdienst (DWD), respectively, for (a) Dec–Feb (DJF) 2023/24, (b) Mar–May (MAM) 2024, (c) Jun–Aug (JJA) 2024, and (d) Sep–Nov (SON) 2024.

Unauthenticated | Downloaded 11/21/25 11:34 AM UTC

over Eastern Europe (less than 40% of normal over eastern Ukraine and southern European Russia) and the Middle East.

In summer, a pronounced contrast in 500-hPa geopotential height anomalies occurred between the west and the east of the region. Over western parts, below-average heights prevailed (minimum over Iceland), while eastern parts saw above-average heights (maxima over the Barents Sea and over Eastern Europe). Below-average MSLP with anomalies larger than –2 hPa occurred over Greenland, Iceland, Ireland, the United Kingdom, and Fennoscandia (largest negative anomaly was over Iceland). Summer was the warmest on record over the region. The season was warmest or second warmest over the central Mediterranean region, Eastern Europe, the Middle East, and Türkiye and the South Caucasus. Summer was fourth warmest over Central Europe and over the Nordic and Baltic countries, mainly due to large positive anomalies in August. Although August was warmest on record over the Iberian Peninsula, the season as a whole was not among the five warmest for that area. Over Western Europe, summer was only slightly warmer than normal (+0.3°C anomaly). Precipitation totals in summer were close to normal over large parts of the region. Over the Balkan Peninsula and around the Black Sea, however, notably drier-than-normal conditions prevailed, while the Iberian Peninsula and Norway saw mostly wetter-than-normal conditions.

In autumn, below-average 500-hPa geopotential heights occurred mainly over the Greenland Sea and Norwegian Sea south of Svalbard, while most other parts of the region—particularly

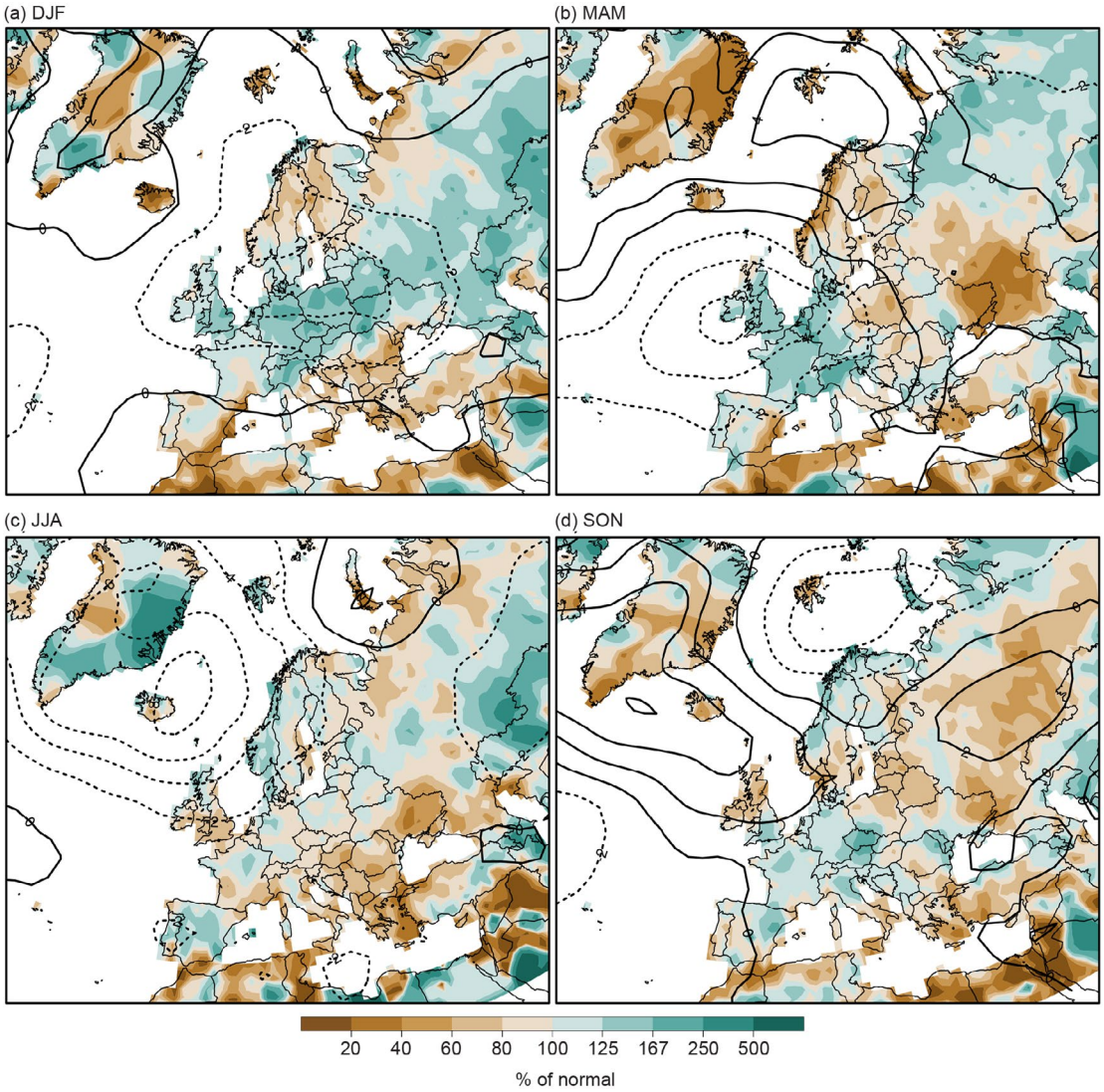

Fig. 7.41. Seasonal anomalies for 2024 (1991–2020 base period) of sea level pressure (hPa) from National Centers for Environmental Prediction (NCEP)/National Center for Atmospheric Research (NCAR) reanalysis for (a) Dec–Feb (DJF) 2023/24, (b) Mar–May (MAM) 2024, (c) Jun–Aug (JJA) 2024, and (d) Sep–Nov (SON) 2024. The colored shading represents the percentage of seasonal mean precipitation for 2024 compared to 1991–2020 (Source data: Global Precipitation Climatology Centre [GPCC], created by Deutscher Wetterdienst [DWD]).

Unauthenticated | Downloaded 11/21/25 11:34 AM UTC

Eastern Europe—saw above-average heights. Below-average MSLP occurred over the Barents Sea, whereas above-average values occurred particularly over Greenland, Iceland, and surrounding sea areas. Autumn was the second warmest on record over the region. The season was warmest on record only over Eastern Europe, mainly due to a record-warm September (+4°C anomaly). The Nordic and Baltic countries saw their fourth-warmest autumn, with a pronounced positive anomaly and second-warmest month in September. Rather weak anomalies well below +1°C occurred over Western Europe, the central Mediterranean region, the Middle East, and over Türkiye and the South Caucasus. In autumn, several heavy precipitation events brought prolonged and intense rainfall, especially to parts of Central and Eastern Europe as well as central Italy and Spain. Norway saw also much above-normal precipitation. Notably drier-than-normal conditions occurred in a band stretching from Ireland and Scotland, over southern Sweden and Denmark, to the Baltic countries, Belarus, and northern Poland. Large parts of Eastern Europe, the eastern Mediterranean region, and southern Italy and Greece were also drier than normal, seeing mostly 60%–80% of normal precipitation.

2. WESTERN EUROPE

This subregion includes Ireland, the United Kingdom, the Netherlands, Belgium, Luxembourg, and France.

(i) Temperature

Over Western Europe, 2024 was 0.8°C higher than normal, ranking as the fourth warmest year on record. The year was also among the five warmest for all countries of the subregion (+0.5°C to +1.3°C anomaly). In De Bilt (Netherlands), 2024 marked the warmest on record since the beginning of measurements in 1901.

Winter was warmer than normal over Western Europe (+1.8°C anomaly; third warmest on record). Nationally, the temperature anomalies were weaker over Ireland and the United Kingdom (+0.5°C and +1.2°C, respectively) and more than +2°C in the remaining countries of the subregion. For the Benelux countries and France, winter was second or third warmest on record. February was particularly warm, marking the warmest February on record for the Benelux countries. For all countries of the subregion, February was among their four warmest.

Spring was 0.9°C warmer than normal over the subregion. For Ireland, the United Kingdom, and the Netherlands, the season was the warmest or second warmest on record, primarily due to an exceptionally warm May (and also a warm March for the Netherlands). Over the subregion as a whole, summer temperatures were much closer to normal than those of the previous two seasons (+0.3°C anomaly). While temperatures were below normal in June (−0.2°C anomaly), July and August were warmer than normal with anomalies of +0.2°C and +1°C, respectively. Moderate temperature anomalies over the subregion continued in autumn (+0.6°C). While September saw slightly below-normal temperatures (−0.4°C anomaly; negative anomalies over France, Ireland, and the United Kingdom), October, November, and December were warmer than normal over the subregion (+1.3°C, +0.8°C, and +0.9°C, respectively).

(ii) Precipitation

Over the year, most of Western Europe received above-normal precipitation. The Netherlands saw a very wet year with 125% of normal in De Bilt, marking its fifth-wettest year on record. The stations Uccle (Belgium) and Findel (Luxembourg) observed their wettest year on record with 140% and 143% of normal, respectively. For France, 2024 was its seventh-wettest year on record with 115% of normal precipitation.

Winter was wetter than normal across most of the subregion (123% of normal precipitation). The season was particularly wet over the Netherlands, which saw 151% of its normal; it was the second-wettest winter on record for the country as a whole and the wettest on record in De Bilt. February was particularly wet across the subregion with 155% of normal. Uccle (Belgium) received almost twice its normal total, making February 2024 its fifth-wettest February on record.

Spring had larger (wet) anomalies than winter and finished with an average 150% of normal precipitation, marking the third-wettest spring on record for the subregion. It was particularly wet over the Benelux countries. With around 170% of normal, it was the second-wettest spring for the Netherlands. Uccle (Belgium) and Findel (Luxembourg) observed their second- and

Unauthenticated | Downloaded 11/21/25 11:34 AM UTC

third- wettest spring on record with 172% and 178% of normal, respectively. May was the wettest on record for the Netherlands with 231% of its normal precipitation.

After two wetter-than-normal seasons, near- or drier-than-normal conditions prevailed in the summer with an average seasonal total of around 70% of normal. For Ireland and the United Kingdom, the summer season started dry with around 70% of normal precipitation in June. For Belgium, France, and the Netherlands, August was the driest summer month with 60%–80% of its normal precipitation.

Due to prevailing low-pressure conditions, autumn saw above-normal precipitation over most parts of the subregion, except for Ireland and the northern United Kingdom. In September, 125%–167% of normal precipitation fell over large areas of the region. De Bilt (Netherlands) and Findel (Luxembourg) received more than twice their normal amounts, marking their fourth- and third-wettest September on record, respectively. November, in contrast, was notably drier than normal with large parts of France, Ireland, and the United Kingdom observing only 60%–80% of their normal totals, and Scotland receiving only half of its normal. December was mostly drier than normal, except for in the United Kingdom, which received mostly above-normal precipitation.

(iii) Notable events and impacts

On 2 January, Storm Henk impacted the United Kingdom with strong winds and heavy rain, leading to widespread flooding. Hundreds of homes, particularly along the Severn River, were flooded. At least one life was lost in England, and there was widespread disruption to the power grid and transportation. Widespread areas of Pas-de-Calais (northern France) were affected by the same storm, with close to 1300 homes damaged.

Between 21 and 23 January, two storms, Isha and Jocelyn, hit Ireland and the United Kingdom in quick succession. Storm Isha brought widespread strong winds and gusts, reaching up to 159 km h^{-1} in the United Kingdom (northern England). Some areas of the United Kingdom were also affected by flooding. There was damage to houses and disruption to transportation, and at least two lives were lost. Storm Isha resulted in at least one fatality and loss of power to around 235,000 homes in Ireland. Storm Jocelyn was less severe but caused difficulties with recovery and clean-up operations from Storm Isha.

Precipitation was exceptionally heavy between 15 and 17 October in some mountainous areas in southeastern France, especially the Cevennes (southeastern Massif Central). Totals of 200 mm–400 mm in 48 hours were widespread in this area with peaks of above 500 mm–600 mm. These totals were more than double the monthly normal and were record-high 48-hour totals for this area since measurements started in the early twentieth century.

Storm Darragh brought strong winds to the United Kingdom (England and Wales) and Ireland in December. Wind gusts at 110 km h^{-1}–150 km h^{-1} were measured at several stations on 6 and 7 December. A few stations in the United Kingdom measured their highest December winds gusts on record in their ~30-year time series. Storm Darragh also brought heavy rain, with 50 mm–100 mm falling across upland areas of Wales that led to flooding. A number of fatalities were reported, and over 2.3 million customers lost power during the storm. The unusual northerly wind direction was likely to have been a significant contributing factor to the number of fallen trees from this storm. Flight cancellations were reported at many airports in the United Kingdom, including Bristol and London Heathrow.

3. CENTRAL EUROPE

This subregion includes Germany, Switzerland, Austria, Poland, Czechia, Slovakia, and Hungary.

(i) Temperature

Central Europe observed its warmest year on record (+1.9°C anomaly). All countries in the subregion also saw their warmest year on record, except for Switzerland, which observed its third-warmest year. On a seasonal basis, winter, spring, and summer were each among the four warmest for the subregion.

Central Europe saw its third-warmest winter on record (+2.9°C anomaly). With an anomaly of +5.6°C, February 2024 was the warmest February on record. At the national scale, February was

Unauthenticated | Downloaded 11/21/25 11:34 AM UTC

also the warmest on record for all countries of the subregion, with anomalies exceeding +5°C in most countries. Above-normal temperatures continued into spring, which marked the warmest spring on record over the subregion (+2.2°C anomaly). Anomalies were most extreme and widespread in March (+3.3°C; warmest on record). Only Switzerland observed a spring that did not rank among its five warmest, with a May temperature that was even slightly colder than normal (−0.1°C anomaly). Summer was fourth warmest on record over the subregion (+1.6°C anomaly), particularly due to an exceptionally warm August (+2.3°C anomaly; second warmest on record). Autumn did not rank among the five warmest over the subregion (+1.1°C), but September was the fifth warmest on record over the subregion (+2.1°C) and second and fifth warmest over Poland and Slovakia, respectively. Temperatures in November were slightly below normal (−0.2°C anomaly). December was warmer than normal, most notably in northeastern Germany and Poland, both of which saw anomalies above +2°C.

(ii) Precipitation

As in 2023, total precipitation was notably above normal in Central Europe (109% of normal). Germany and Austria reported the highest anomalies at 114% of normal. Near- to drier-than-normal conditions prevailed in the eastern parts of the subregion. Hungary was the country with the highest deficit, reaching only 84% of its normal total.

Winter was particularly wet across the subregion, becoming the second wettest on record with an average of around 150% of normal. Many countries of the subregion observed one of their four wettest winters on record, with monthly totals ranging from 146% to 164% of normal: Poland (wettest), Czechia (second wettest), and Austria and Germany (fourth wettest). February was particularly wet with around 160% of normal precipitation for the subregion as a whole. Poland saw its wettest February on record, receiving twice its normal amount.

In spring, wetter-than-normal conditions continued in western parts of the subregion, particularly affecting Germany, Switzerland, and Austria. As in Western Europe, May was also particularly wet in Central Europe with some areas receiving more than double their normal amounts. Germany had its third-wettest May on record with 168% of its normal precipitation. Conversely, in eastern parts of the subregion, near- to drier-than-normal conditions prevailed in spring. The largest deficits occurred over Poland, which received only 72% of its normal.

Summer precipitation was mostly near-normal, except for Hungary and Slovakia, where notably drier-than-normal conditions prevailed. There were, however, large contrasts in precipitation anomalies between the months and across the subregion. In June, persistent heavy rainfall—particularly in southern parts of Central Europe—and locally heavy thunderstorms brought large amounts of precipitation to Germany (119% of normal), Austria (114%), and Slovakia (139%). July and August, in contrast, were drier than normal, especially in southern and northern parts of the subregion.

Precipitation in autumn was above normal across most of the subregion. Czechia (second wettest, 182% of normal) and Austria (15th wettest in a series starting in 1858, 137%) each observed one of their wettest autumns on record. This was mainly due to the low-pressure system Boris, which brought prolonged and intense rainfall in September to Austria, Hungary, Poland, Czechia, and Slovakia (see Sidebar 7.2 for details). Austria and Czechia each reported their wettest September on record with two and three times their normal amounts, respectively. In contrast, December was relatively dry with less than 80% of normal precipitation in most parts.

(iii) Notable events and impacts

In connection with the low-pressure system Katinka, persistent and heavy rain occurred in parts of western Germany, especially during 16–19 May, leading to local flooding at some rivers. In some places, 1 to 1.5 times the average monthly total for May was registered in just 18 to 24 hours. At some stations, new all-time records were observed. Another precipitation event, also with new records, occurred from late May to early June, impacting southern Germany as well as Poland, Czechia, and Austria.

On 20 June, a low-pressure system caused a southerly flow of moist air over the Alpine region. This resulted in storms and heavy rainfall from 21 to 23 June, which caused flooding in several regions of Switzerland, including the River Rhone catchment. In the Valle Mesolcina region (a

Unauthenticated | Downloaded 11/21/25 11:34 AM UTC

valley in southern Switzerland), flooding and mudslides led to extensive damage. The flooding in Switzerland resulted in at least four fatalities.

On 11 July, some intense precipitation episodes occurred in Slovakia, especially stormy downpours. Some of these storms showed signs of a cloudburst that caused flash floods. The largest estimated instantaneous hourly precipitation intensity over the northern slopes of the Monkova valley was 70 mm h^{-1} (with a possible maximum of up to 140 mm h^{-1}).

Due to the very warm and dry summer, a hydrological drought was recorded in Poland. On 10 September, a record-low water level (0.02 m) was recorded at the Warsaw–Bulwary station located at the Vistula River. In total, 26 stations in Poland recorded their absolute minimum water levels on that day.

Extreme precipitation associated with Storm Boris fell in eastern parts of Central Europe. A large area saw at least half a month's worth of rainfall during the five-day period of 12–16 September. Several locations recorded totals of 200 mm–500 mm over this event. The most-affected countries were Austria, Czechia, Slovakia, Poland (specifically its southern region), and Germany (specifically its southeastern region). Boris produced severe river flooding in the upper and middle Danube, Oder, and Elbe basins. The storm caused at least 28 fatalities across the affected countries (see Sidebar 7.2 for more details).

4. IBERIAN PENINSULA

This subregion includes Spain and Portugal (peninsular mainland only). The reference period for Portugal is 1981–2010.

(i) Temperature

Over the Iberian Peninsula, 2024 was 1.1°C above normal, ranking third warmest on record. The year was third and fourth warmest in Spain and Portugal (+1.1°C and +0.9°C anomaly, respectively). On a seasonal basis, only winter ranked among the five warmest over the subregion.

Winter was the third warmest on record over the Iberian Peninsula (+1.5°C anomaly). January and February ranked second and third warmest (+2.0°C and +2.4°C), respectively. Temperature anomalies were much weaker in spring although still positive (+0.7°C). At the monthly timescale, anomalies ranged between +0.3°C in May and +1.2°C in April. Summer as a whole was also not among the five warmest over the subregion (+1.1°C anomaly), although August was the warmest on record (+1.9°C anomaly). Overall, temperature anomalies were weaker (but still positive) over Portugal throughout the summer. Autumn was 1°C warmer than normal averaged over the subregion. Although November was the warmest on record for the area as a whole and in Spain (+2.7°C anomalies), autumn did not rank among the five warmest, nor did December. The subregion even observed below-normal temperatures in September (−0.4°C anomaly).

(ii) Precipitation

In 2024, close-to-normal conditions prevailed over the Iberian Peninsula with an average of 95% of normal (1981–2010 base period) for Portugal and 105% of normal for Spain as a whole; however, southeast Spain only received 60%–80% of its normal precipitation.

Precipitation in winter was close to normal over the Iberian Peninsula with 96% of normal precipitation. Nationally, however, Portugal was wetter than normal (112% of normal), while Spain experienced drier-than-normal conditions (90%).

Overall, spring precipitation totals were above normal over the Iberian Peninsula (109% of normal). Both Portugal and Spain experienced large contrasts between the months. Spring started very wet, with March bringing on average 202% (Spain) and 286% (Portugal, 1981–2010 base period) of their normal totals, marking the sixth- and eighth-wettest March, respectively, since 1961. In contrast, April and May were much drier than normal; April precipitation was only about half the normal total in both countries.

Summer was wetter than normal in both Portugal and Spain with 127% of normal precipitation. This was particularly due to a very wet June, when the passage of several low-pressure systems brought 160% and 149% of normal precipitation, respectively. From July onwards, however, anticyclonic conditions dominated the region, resulting in below-normal precipitation over most parts. For Portugal, the season concluded with the fifth-driest August on record (since 1931) and the driest in the last 35 years (6% of normal).

Unauthenticated | Downloaded 11/21/25 11:34 AM UTC

Autumn was characterized by predominantly wetter-than-average conditions over much of the subregion. With almost twice its normal total (189% of normal), October was record wet in Spain. The largest anomalies (more than 300% of normal) occurred in parts of eastern Spain, which was impacted by heavy rainfall in the last few days of the month. Although heavy precipitation continued over Spain in early November, the month as a whole saw only about half the normal precipitation for both Spain (sixth driest since 1961) and Portugal. The dryness continued in December. Much of the peninsula received less than 40% of its normal precipitation that month, with large areas having even less than 20% and a few places with no precipitation at all. This was far from normal, given that normal values are not below 25 mm in December even in the drier eastern parts of Spain. On country average, Spain received 33% of its normal precipitation that month, which is below the 20th percentile.

(iii) Notable events and impacts

In 2024, high temperatures were frequent in Spain, with three heatwaves affecting both the mainland and the Balearic Islands. The first, occurring from 18 to 20 July, primarily affected northeastern regions and the Comunitat Valenciana. The second, which lasted from 23 July to 1 August, was significant for its duration (10 days) and saw widespread impact across 33 provinces. The third heatwave lasted from 4 to 12 August, affecting 35 provinces with temperatures exceeding 40°C, particularly in central, southern, and western regions. The highest temperatures of the year were measured at Morón de la Frontera (43.5°C on 24 July) and Badajoz airport (43.3°C also on 24 July), as well as at Jerez de la Frontera airport and Granada air base, where 43.2°C was recorded on 24 and 31 July, respectively. Exceptionally high minimum nighttime temperatures were also recorded during these events, setting new records at Zaragoza/Airport (28.1°C, 30 July) and Madrid/Getafe (26.8°C, 25 July).

Heavy rain affected the Balearic Islands (Spain) on 14–15 August, with Menorca Airport setting a local record for the highest daily precipitation for that month at 93.6 mm on 15 August. Other areas of Menorca reported rainfall of up to 200 mm in less than a day, 10 times the average rainfall for the typically dry month of August. Meanwhile, maximum wind gusts of 100 km h^{-1} were recorded in Mallorca. More than 50 flights were cancelled across the Balearic Islands.

From 15 to 20 September, around 1000 wildfires occurred across central and northern Portugal. Approximately 1350 km^2 of land was burnt, and at least nine lives were lost.

Intense precipitation occurred during several periods throughout October in various regions of Portugal, mainly due to thunderstorms. New 24-hour (0900–0900 UTC) records of precipitation extremes were measured on 16 October, with a new local absolute total of 102.3 mm recorded in Mora/Alentejo (southern Portugal).

Locally torrential and persistent rains affected various provinces of eastern and southern Spain, including the Baleares, between 28 October and 4 November. Particularly intense rainfall occurred on 29 October in the Valencia region, setting new historical records with accumulated rainfall totals of 184.6 mm in one hour, 620.6 mm in six hours, and 720.4 mm in twelve hours. This event resulted in severe flooding across 78 municipalities, causing substantial economic losses and significant human impacts, including at least 224 fatalities and damage exceeding 13 billion euros ($14.8 billion U.S. dollars).

5. THE NORDIC AND BALTIC COUNTRIES

This subregion includes Iceland, Norway, Denmark, Sweden, Finland, Estonia, Latvia, and Lithuania.

(i) Temperature

Over the Nordic and Baltic countries, 2024 was 1°C higher than normal, the fourth warmest on record. For all countries except Iceland, the year was also among their four warmest; Latvia and Lithuania observed their warmest year on record. The year was colder than normal over Iceland (–0.8°C anomaly). Spring, summer, and autumn marked the fourth-warmest seasons on record for the subregion.

Winter was colder than normal over the Nordic and Baltic countries (–1.1°C anomaly). The only month with an above-average temperature was February (+1.3°C); January was 2.5°C colder than normal over the subregion. The largest negative anomalies occurred over Estonia and

Unauthenticated | Downloaded 11/21/25 11:34 AM UTC

Finland in January (–3.2°C and –4.3°C). In February, the positive anomalies in Denmark and the Baltic countries were much more pronounced than in the other parts of the subregion, ranging from +2°C in the north to +6°C in the south.

Spring was the fourth warmest on record over the subregion (+1.4°C anomaly). Only Finland and Iceland observed a spring that was not among their five warmest; temperatures were close to normal in Iceland. At the monthly timescale, only April was colder than normal over the subregion (–0.7°C anomaly). The largest positive anomaly for the season occurred in May (+3.1°C), marking the second-warmest May on record for the subregion. Nationally, most countries reported their record-warmest or second-warmest May.

Summer was also fourth warmest over the subregion (+1.3°C anomaly), although only August ranked among its five warmest (fourth warmest; +1.4°C). Summer was colder than normal over Denmark and Iceland (–0.1°C and –0.6°C anomaly). While June and August were colder than normal in Iceland (–0.9°C and –1.1°C anomaly), July was colder than normal in Denmark (–0.7°C).

Autumn was the fourth warmest on record over the subregion (+1.5°C anomaly), mainly due to large positive anomalies exceeding +2°C over Finland and the Baltic countries, which all saw an autumn that was among their four warmest on record. September saw the largest positive anomalies over the subregion (+1.9°C anomaly; second warmest on record), particularly over Finland and the Baltic countries (anomalies exceeding +3°C; warmest or second warmest on record). Anomalies reached +1.6°C in October (fifth warmest over the subregion) and +1.1°C in November over the subregion. The season and all months of the season as well as December were colder than normal over Iceland; however, December was more than 3°C warmer than normal in eastern parts of Latvia and Lithuania.

(ii) Precipitation

In 2024, precipitation varied across the subregion, with above-normal totals in Denmark and Norway and close-to-normal to drier-than-normal conditions in the remaining parts of the subregion. Denmark saw its second-wettest year (122% of normal).

Overall, winter in the Nordic and Baltic countries was drier than normal (90% of normal); however, there were large contrasts between months and across the subregion. In Norway, Sweden, and Finland, winter precipitation was near-normal, with a drier-than-normal December compensating for a wetter-than-normal February. Drier-than-normal conditions prevailed during winter over Iceland and the Svalbard archipelago. In contrast, Denmark, Latvia, and Lithuania had a much wetter-than-normal winter. For Denmark, it was the second-wettest winter on record with about 150% of its normal precipitation. Much of this precipitation came in February, with twice its normal total and marking the fourth-wettest February on record for the country.

Spring was near-normal to drier-than-normal for most parts of the subregion, except for Denmark, which experienced its third-wettest spring on record (150% of normal precipitation). The wet spring in Denmark was mainly due to its record-wettest April, which received more than twice its normal total. April was also very wet in Latvia (197% of normal; fifth wettest on record) and Lithuania (172%; sixth wettest). May, in contrast, had much drier-than-normal conditions over most parts of the subregion (third driest on record). Apart from Denmark, all countries of the subregion received less than 60% of their normal precipitation; Estonia and Finland (both of which experienced their second-driest April on record) had only one-third of their normal totals.

In summer, the subregion saw near-normal or wetter-than-normal conditions. Norway and Denmark were much wetter than normal, having received around 130% of their normal precipitation. For Norway, summer tied with that of 1964 as the wettest in the measurement series dating to 1901. While June was the wettest month within the season in Norway at 140% of normal (fifth wettest on record), July was the wettest month for the rest of the countries (except for Iceland), with the largest anomalies occurring in the Baltic countries and Denmark (170% of normal). For Latvia, July was its third wettest on record.

During autumn and December, there was a contrast between wetter-than-normal conditions over large parts of Norway and Sweden and drier-than-normal conditions over Iceland, Denmark, southern Sweden, and the Baltic countries. Norway experienced its fifth-wettest autumn on record (125% of normal) due to a very wet October. Conversely, October was very dry across the Baltic countries, which received only half their normal precipitation totals.

Unauthenticated | Downloaded 11/21/25 11:34 AM UTC

(iii) Notable events and impacts

The Nordic countries experienced a notable coldwave in early January. On 5 January, Vittangi in northern Sweden reached −44.6°C and Enontekiö in northern Finland −44°C, the lowest temperatures in those countries since 1999. On 4 January, Kautokeino (−43.5°C) registered Norway's lowest January temperature since 1999. Kvikkjokk (Sweden) reported its record lowest temperature in 137 years of data, with −43.6°C on 3 January. On 6 January, Bjørnholt on the northern fringe of Oslo reached −31.1°C, the lowest temperature on record in the Oslo region. Heavy snow caused disruption of transportation, including road, rail, and ferry services across the Nordic countries.

On 1 February, Storm Ingunn affected Norway and Sweden. Wind gusts reached 211 km h^{-1} in the mountainous regions of Sweden. At Sømna, a coastal station in Norway, wind gusts peaked at 224 km h^{-1} and 10-minute mean wind speeds reached 195.8 km h^{-1}. Ten-minute speeds also reached 186.5 km h^{-1} at Stekenjokk, a mountain station in Sweden. Both values surpassed previous national records of 10-minute means at 176.0 km h^{-1} and 172.1 km h^{-1}, respectively. Consequently, Storm Ingunn is regarded as one of the most powerful storms to impact Scandinavia in the past three decades. The storm caused widespread power outages and significant disruptions to transportation, including the suspension of most flights, ferry services, and shipping routes.

In late February, Storm Rolf affected parts of Northern Europe. Denmark experienced gusts as high as 135 km h^{-1}, with sustained winds averaging 101.5 km h^{-1}. Southern Sweden and the Norwegian coast also recorded gusts exceeding 100 km h^{-1}. The storm caused widespread disruption.

In late July, Storm Kirsti developed over the Baltic region, producing intense precipitation, convective thunderstorms, and strong winds. The system subsequently propagated eastward into the Russian Federation. On 29 July, Kalnciems in Latvia recorded 198.3 mm of rain in a 24-hour period—224% of the monthly average for July and 27% of the area's annual precipitation. This event set a new national record for daily rainfall, surpassing the previous high of 160 mm that was recorded in Ventspils on 9 July 1973. Wind gusts during the storm reached speeds of up to 97 km h^{-1}. Similarly, Lithuania experienced substantial rainfall, with more than 80 mm falling within a 12-hour period. In Telšiai, the total accumulation over 24 hours was 117 mm, while in Estonia, rainfall reached up to 90 mm in certain areas.

Monthly mean temperatures at Svalbard Airport reached 11.0°C in August. These are the highest values ever recorded in August at this location. Additionally, for the first time in September, temperatures above 30°C were recorded in Norway.

The first 14 days of November were the warmest ever observed for this time of year at many stations in Iceland. The highest temperature was 23.8°C, the highest ever recorded in Iceland in November. However, temperatures in mid-November cooled down rapidly and were well below average for the rest of the month.

6. CENTRAL MEDITERRANEAN REGION

This subregion includes Italy, Monaco, Malta, Slovenia, Croatia, Serbia, Montenegro, Bosnia and Herzegovina, Albania, North Macedonia, Greece, and Bulgaria.

(i) Temperature

Over the central Mediterranean region, 2024 was the warmest year on record (+1.8°C anomaly), with every country of the subregion also reporting its warmest year. The largest positive anomalies occurred over the Balkan Peninsula, with some anomalies exceeding +2°C in some countries. Winter, spring, and summer were warmest or second warmest on record for the subregion.

Winter was the warmest on record over the central Mediterranean region (+2.7°C anomaly). All months of the season saw above-normal temperatures. February, which was the warmest on record, had the largest positive anomaly among the three months (+4.2°C); the month was also warmest or second warmest for all countries of the subregion.

Spring was the second warmest on record over the subregion (+1.8°C anomaly), with both March and April third warmest (+2.5°C and +2.2°C). May, which was 0.5°C above normal, did not rank among the five warmest Mays.

Unauthenticated | Downloaded 11/21/25 11:34 AM UTC

Summer was warmest on record over the subregion (+2.6°C anomaly), and temperature anomalies exceeded +2°C in each month of the season. Additionally, July and August were the warmest on record for their respective months; June was second warmest. Summer ranked among the five warmest for all countries of the subregion; in fact, all countries were record warm except for Italy, Malta, and Slovenia. Most of the subregion and most of the season had anomalies among the five warmest; only the month of June in Italy and Slovenia was not among their five warmest.

Compared to the other seasons, temperature anomalies were rather weak in autumn over the subregion (+0.6°C anomaly). The largest positive anomalies occurred in October (+1.4°C). Italy, Slovenia, and some parts of the Balkan peninsula (Croatia, Albania, Bosnia and Herzegovina, and Montenegro) all reported between their second- and fifth-warmest October. November was colder than normal for the subregion as a whole (−0.6°C anomaly), and individually for all countries except Italy and Malta. December was again a warm month, with anomalies ranging from near normal in Italy to +3°C in northern Bulgaria.

(ii) Precipitation

In 2024, most of the central Mediterranean region saw near- to drier-than-normal conditions. The largest deficits occurred in Greece and Malta, which reported 80% and 45% of their normal precipitation, respectively. Northern Italy, Slovenia, and Montenegro were wetter than normal.

Winter was drier than normal in the subregion (85% of normal precipitation), especially over the Balkan Peninsula where large parts only received 60% to 70% of their normal totals. February was particularly dry. Serbia and Bulgaria each received only one-third of their normal totals for the month, marking the driest February on record for Serbia. Although dry conditions dominated, Italy observed a very wet February, and Slovenia received between 140% and 160% of its normal in January.

Overall, spring was wetter than normal (113%) in the subregion, especially in the northern parts. Northern Italy, Slovenia, and northern Croatia had a very wet spring, with some areas receiving 150% to 250% of their normal precipitation and locally up to 400%. In these areas, March and May were particularly wet. In contrast, southern parts of the subregion experienced drier-than-normal conditions. Sicily and Malta only received between 20% and 40% of their normal due to dry conditions in March and April.

Summer was drier than normal across the subregion with 75% of normal precipitation. Drier-than-normal conditions dominated in all months of the season. It was driest in North Macedonia and Greece, which received only about half of their normal totals. For Greece, it was the driest June on record with just 20% of normal precipitation. August was wetter than normal in Greece, but was the driest summer month in much of the rest of the subregion.

Autumn saw mostly near- to drier-than-normal conditions. September was very wet, with many countries in the subregion reporting 150% to 200% of their normal precipitation. For Italy (147% of normal) and Croatia (170%), it was the second- and fourth-wettest September on record, respectively. November, in contrast, was mostly much drier than normal, especially in northern parts of the subregion. Italy received only one-third of its normal precipitation, marking the third-driest November on record. December was mostly wetter than normal, but the southern Alpine region (northern Italy and Slovenia) was drier (mostly less than 80% of normal, and locally less than 20% in northwestern Italy).

(iii) Notable events and impacts

Southeastern Europe was affected by some unusually long heatwaves during the summer. During 6–24 July, a heatwave occurred throughout Bulgaria. One station recorded nine consecutive days with maximum temperatures above 40°C. Such a long period with such high maxima has not been recorded there since available measurements at this station began in 1932. Belgrade (Serbia) reported a record 67 days with temperatures at least 3°C above average. On 14 August, record-high temperatures of 40.6°C and 42.7°C were observed in Sombor (Serbia) and Zenica (Bosnia and Herzegovina), respectively. A minimum temperature of 30.6°C at Vrsac on 13 July set a national record for Serbia.

From 3 to 4 October, heavy rain fell across central Bosnia and Herzegovina, causing rapid flooding. The sudden inundation left little time for evacuation, trapping many people in their

Unauthenticated | Downloaded 11/21/25 11:34 AM UTC

homes. More than 1000 homes were damaged, over 700 sections of roads and numerous bridges were impassable or destroyed, electrical outages and water supply disruptions affected multiple municipalities, and farmland across the affected areas was also severely impacted. At least 25 fatalities were reported, mainly due to landslides following heavy rain. Up to 430 mm of precipitation were recorded during this event; at one station, 156 mm fell within a four-hour period on the night of 3–4 October, an amount that was equivalent to its normal monthly average.

Heavy rainfall affected southern Italy from 11 to 13 November—particularly the Catania and Messina provinces in the eastern Sicily region—causing flash floods due to river overflows. One highway and several streets were blocked, and numerous cars were carried away into the sea. Daily totals of up to more than 300 mm were recorded. This was merely the continuation of previous rainfall in the days before. Precipitation totals accumulated up to 700 mm in nine consecutive days; the normal annual rainfall total is 650 mm. This rainfall ended the ongoing drought that existed in Sicily during the previous months.

Storm Bora, a quasi-stationary low-pressure area, persisted over Greece during several days in late November and early December. Strong winds and intense thunderstorms mainly affected the islands of Rhodes and Lemnos. Rhodes had a general traffic ban for 24 hours. Two people died on Lemnos island. Several houses and roads were affected by floods. Extremely high rainfall totals up to 550 mm in three days (30 November to 2 December) were recorded in parts of Macedonia (northern Greece), and also on islands of the Aegean. Rhodes station recorded a 24-hour total of about 230 mm from 30 November to 1 December, an amount that corresponds to typical two-month totals for November and December.

7. EASTERN EUROPE

This subregion includes the European part of Russia, Belarus, Ukraine, Moldova, Romania, and West Kazakhstan.

(i) Temperature

Over Eastern Europe, 2024 was the warmest year on record (+1.8°C anomaly). Nationally, it ranked among the three warmest for all countries of the subregion. The largest positive anomalies—specifically those exceeding +2°C—occurred over Belarus, Moldova, Romania, and Ukraine. Spring, summer, and autumn were among the four warmest on record for the subregion.

Winter was 0.8°C warmer than normal over Eastern Europe. While February was warmer than normal (+2.6°C anomaly), January was colder than normal (–1.1°C). These conditions were largely dominated by anomalies over the European part of Russia that were weakly positive in February and strongly negative in January. On the contrary, the largest positive winter anomalies occurred over Belarus, Moldova, Romania, and Ukraine. In these countries, both February and the season as a whole ranked among the five warmest.

Spring was fourth warmest over the subregion (+1.5°C anomaly), particularly due to a record-warm April (+3.2°C). The only month with below-normal temperatures within this season was May (–1°C anomaly). April ranked among the three warmest for all countries of the subregion.

The subregion experienced its second-warmest summer (+2.1°C anomaly). The seasonal warmth was dominated by June and July, which were warmest and second warmest on record over the subregion (+2.5°C and +2.2°C, respectively). The season, as well as June and July, were each among the five warmest on record for most countries of the subregion.

Autumn was the warmest on record over the subregion (+2.4°C anomaly), mainly due to an exceptionally warm September when anomalies of +4°C were exceeded over the subregion as a whole, as well as in Belarus, the European part of Russia, and Ukraine. Anomalies in October and November were still positive (+1.5°C and +1.7°C), although not as extreme as in September. December was a mild month, having been at least 2°C warmer than normal across most of the subregion.

(ii) Precipitation

Precipitation for the year was slightly lower than normal in Eastern Europe as a whole (94% of normal). The largest deficits occurred over eastern Ukraine and southern European Russia, where only 60%–80% of normal precipitation was registered; in some places, only 40%–60% was

Unauthenticated | Downloaded 11/21/25 11:34 AM UTC

registered. Wetter-than-normal conditions prevailed in Moldova (129%) and West Kazakhstan (151%; its third-wettest year on record).

Overall, winter was wetter than normal in the subregion, especially in Belarus, west Kazakhstan, Ukraine, and European Russia, where 130%–160% of normal precipitation was registered. For Belarus, it was the wettest winter on record (159% of normal); February was its second wettest on record (170%). January was much wetter than normal in west Kazakhstan (203% of normal; third wettest). Although wet conditions prevailed across the subregion, Romania and Moldova saw below-normal precipitation in February, with some parts receiving less than 50% of normal.

Spring precipitation amounts were about 90% of normal on average across Eastern Europe. For eastern Ukraine and southern European Russia, all months of the season were much drier than normal. May was particularly dry across the whole subregion, which received about half of the normal precipitation totals. Belarus observed its second-driest May on record (40% of normal). However, there were also areas with wetter-than-normal conditions during the spring. March brought excessive rainfall to Moldova, which registered twice its normal total. April was very wet over northern European Russia, Belarus, and western Ukraine, with large areas receiving 150% to 250% of their normal precipitation. Belarus observed its second-wettest April on record (218% of normal).

Summer was mostly drier than normal across the subregion with the largest deficits occurring over eastern Ukraine, Moldova, and Romania (70% to 80% of normal precipitation). August was the driest summer month, bringing only around half the normal precipitation in Ukraine, Romania, west Kazakhstan and Belarus, with some areas receiving even less than 20%.

In autumn, drier-than-normal to normal conditions dominated the subregion, except for areas west of the Black Sea, where it was very wet. Moldova had 180% of its normal total in autumn, particularly due to a very wet September (300%–500% of normal; second-wettest September on record). In contrast, September was dry in Belarus (47% of normal), European Russia (37%; its driest September on record), and west Kazakhstan (4% of normal; also its driest September on record). Wetter-than-normal conditions west of the Black Sea continued in December (>150% of normal in southeastern Romania), whereas dryness persisted in Belarus (<80%).

(iii) Notable events and impacts

In April, record precipitation was observed in Ukraine in the Kyiv and Vinnytsia regions, with up to 130 mm of precipitation recorded during the month. These amounts are 4 mm–20 mm more than those of previous records, and two to three times their monthly normal totals.

In May, for the first time since 1961, no precipitation was recorded in many areas of Ukraine in the Kharkiv, Poltava, Lviv, and Volyn regions.

Romania experienced its fifth-driest agricultural year (1 September 2023 to 31 August 2024) due to eight months of below-normal precipitation. Combined with high temperatures, this resulted in a long-lasting soil drought, most notably from May to August, across almost the entire country.

Several heatwaves were particularly outstanding in Eastern Europe during the summer. On 16 and 17 July, maximum temperatures in Moldova rose to around 40°C in most parts of the country. Such high temperatures have only been previously recorded in 2007 and 2012. In Ukraine, several stations reported new local all-time maximum temperature records, with Mykolaiv reaching 41.6°C on 16 July.

Tuapse, a city located at the Russian Black Sea coast, recorded a temperature of 38.8°C on 11 September, which broke not only the September record, but also the record for August. Also in September, Belarus experienced prolonged heatwaves throughout the country. In the central, northern, and northeastern parts, the heatwaves lasted between 9 and 27 days, and in the western, southwestern, and southeastern parts, several heat waves were observed from the end of August to 9 September and from 14 to 27 September, each of which lasted from 6 to 14 days. The maximum temperatures in September reached 27°C across most of the country and were even higher in the south and southeast (28°C–30°C). Normal September maximum temperatures during September in Belarus are 15°C–20°C.

Unauthenticated | Downloaded 11/21/25 11:34 AM UTC

A total of 203 mm fell in a 42-hour period in Sochi at the Russian Black Sea coast on 17–18 December. The heavy rain led to 12 landslides and mudslides that damaged residential buildings and sections of highways.

8. MIDDLE EAST

This subregion includes Israel, Cyprus, Jordan, Lebanon, and Syria.

(i) Temperature

Over the Middle East, 2024 was the second warmest on record (+1.3°C anomaly). The year was among the five warmest for all countries of the subregion. Winter, spring, and summer were each among their three warmest for the subregion.

Winter was the third warmest on record over the Middle East (+2.2°C anomaly; also among the three warmest for all countries of the subregion). January was the second warmest on record for the subregion (+2.5°C) and also warmest or second warmest for most individual countries, except Lebanon.

Spring was also the third warmest on record over the subregion (+1.4°C anomaly; among the four warmest for most countries within the subregion). April was exceptionally warm (+3.3°C; warmest on record for both the subregion and for most countries). Temperatures over the subregion were much closer to normal in March and May (+0.8°C and +0.2°C, respectively).

Summer was warmest on record over the subregion (+2°C anomaly; among the two warmest for all countries). Anomalies were most extreme in June (+3.7°C; warmest June on record for the subregion and for all countries of the subregion). Weaker, albeit still positive anomalies prevailed in July (+1.4°C; fifth-warmest July on record) and in August (+0.9°C).

Temperatures in autumn were near normal over the subregion (+0.3°C anomaly). At the monthly timescale, anomalies ranged from −0.1°C in October to +0.5°C in November. December was also slightly warmer than normal (+0.5°C).

(ii) Precipitation

The year was mostly drier than normal across the Middle East (89% of normal). Parts of Syria, Jordan, and Lebanon received less than 60% of their normal totals, while Israel as a whole saw slightly-wetter-than-normal conditions (106%).

Winter was wetter than normal (110% of normal), but there was substantial variability across the subregion. While January was considerably wetter than normal in northern and central Israel, Lebanon, and Syria (140% to 170% of normal), drier-than-normal conditions prevailed in Jordan and southern Israel (<40% of normal across large areas). February was drier than normal over Cyprus, which received only half its normal precipitation total (1961–1990 base period).

Overall, spring was drier than normal (85%). Parts of Syria and Jordan experienced a continuation of dry conditions (<60% of normal) that had already started during winter.

Summer is the dry season in this subregion, with climatological averages generally not exceeding 1 mm month^{-1} across most of the area. In 2024, summer precipitation totals of more than 10 mm month^{-1} only occurred over northern parts of the subregion, including Cyprus.

Autumn was overall drier than normal (71% of normal), most notably in Jordan (16%) and Israel (53%). The season began with wetter-than-normal conditions in September, especially in Syria and Lebanon, with monthly amounts of between 25 mm and 50 mm (around 300% of normal). October was very dry, with most of the subregion except for the west recording no precipitation at all. Dry conditions continued in November in southern parts of the Middle East, and December was also dry (<20% of normal in much of Syria and eastern Jordan), implying a winter drought during the usually rainy season.

(iii) Notable events and impacts

A prolonged rain event brought 200 mm–400 mm of precipitation to northern and central Israel in late winter. For 15 consecutive days (22 January to 5 February), rain fell each day in the north and center of the country, and even on the least rainy days, a daily total of >20 mm was measured somewhere in the north of the country or in the center. Such a long streak, in which significant rains fall every day in such a wide geographical area, is very unusual. Only in February 1992 was there a longer rain episode (16 days) with a similar spatial extent.

Unauthenticated | Downloaded 11/21/25 11:34 AM UTC

A severe hot and dry spell (locally referred to as Sharav), with temperatures of more than 40°C, occurred in many areas of Israel between 24 and 26 April. In the coastal plain, temperatures were between 40°C and 42°C, and in the Jordan Valley and the Arava, they reached 42°C–45°C. Record high temperatures for April were broken at some stations.

New maximum record temperature records for June were set in Syria at several stations. Damascus recorded 43.2°C on 5 and 6 June, the highest temperature on record for the month. Israel reported a maximum temperature of 48.1°C, breaking a local record for June.

In Cyprus, temperatures reached 40°C every day for a week in mid-June; at least two deaths due to the extreme heat were reported. During that period, of the 52 island automatic weather stations, 43 recorded their most-ever extreme maximum temperature. The highest temperature was 45.3°C in Astromeritis, a village in the Nicosia district.

October was very dry in Israel, with most regions of the country experiencing no precipitation. While October is generally a month with little rainfall, averaging about 15 mm to 30 mm in northern and central parts of the country, an almost completely rainless October across the entire country is unusual. Only four Octobers in the past 100 years of measurements were similar or more extreme in terms of scarcity of rain: 2020, 1992, 1974, and 1964. Also of note: Octobers that are extremely dry in Israel are typically warmer than average. In contrast, October 2024 was notably cooler.

9. TÜRKIYE AND SOUTH CAUCASUS

This subregion includes Türkiye, Armenia, Georgia, and Azerbaijan.

(i) Temperature

Over the subregion of Türkiye and the South Caucasus, 2024 was the second-warmest year on record (+1.6°C anomaly). Nationally, it was the warmest on record for Türkiye (+1.7°C anomaly), third warmest for Azerbaijan, and fifth warmest for Georgia (+1.2°C). Winter, spring, and summer were among the two warmest for their respective seasons for the subregion.

Winter was the warmest on record for Türkiye and the South Caucasus (+3.3°C anomaly). At the monthly timescale, January was also warmest on record (+2.8°C), and February was second warmest (+3.5°C). Nationally, all countries of the subregion observed their warmest or second-warmest winter on record.

Spring was second warmest over the subregion (+1.8°C). The season was characterized by pronounced variations from month to month. The most extreme positive anomalies occurred in April (+4.4°C), marking the warmest April on record over the subregion. In contrast, the anomaly in March was much weaker (+1.3°C) and negative in May (−0.5°C). At the national scale, spring was second warmest for Türkiye (+1.8°C anomaly) and third warmest for Georgia (+1.5°C). April was the warmest on record for all countries of the subregion.

Summer was the warmest on record over the subregion (+1.9°C anomaly). June was the warmest on record (+3.2°C) and July was the third warmest (+1.2°C). Nationally, only Türkiye (for the season and all months) and Georgia (season and June) had such temperatures among their five warmest.

Temperatures in autumn were near normal over the subregion (+0.4°C anomaly). The largest positive monthly anomalies occurred in September (+1.2°C), while temperatures in October and November almost equaled their long-term average. December was warmer than normal over almost the entire subregion (+1.1°C), except for the mountainous region in northeastern Türkiye.

(ii) Precipitation

While 2024 was slightly dry over Türkiye (94% of normal), wetter-than-normal conditions prevailed over the South Caucasus (120%–130% of normal).

In winter, precipitation in the subregion was close to normal (97%) but with drier-than-normal conditions over Türkiye and wetter-than-normal conditions over the South Caucasus. There was a large contrast between the months. January was record wet in Armenia (225% of normal), and Georgia and Azerbaijan reported about 170% and 180% of their normal totals, respectively. February was dry, with only about 60% of normal precipitation over the subregion. Türkiye and Armenia received only about half of their normal precipitation for the month.

Unauthenticated | Downloaded 11/21/25 11:34 AM UTC

Precipitation in spring was also close to normal (104%), as very wet conditions over the South Caucasus and eastern Türkiye compensated for below-normal precipitation occurring over the rest of Türkiye. There were also large contrasts between the months. April was dry across the subregion, receiving only half the normal precipitation. Türkiye observed its third-driest April on record (50% of normal). May, in contrast, brought more than twice the normal amounts to the South Caucasus, with Georgia and Armenia each experiencing their second-wettest May on record.

Summer precipitation totals were mostly near or above-normal, but there were large contrasts between the months and regions. While Türkiye had its fourth-driest June on record with only a third of its normal precipitation, July brought more than twice the normal precipitation amounts to Türkiye and the South Caucasus. July was among the five wettest for all countries of the subregion, except for Georgia.

Autumn precipitation was near normal (95% of normal) and varied regionally from drier-than-normal conditions over most of Türkiye to wetter-than-normal conditions over Georgia (125% of normal). For Türkiye, autumn started with a wet September (136%), whereas October was dry with only half of its normal precipitation. Conversely, in the South Caucasus, September was the driest month in Georgia and Azerbaijan, and was followed by wetter-than-normal conditions during October and November (110%–160% of normal). December brought above-normal precipitation to western Türkiye and western Georgia, but was drier than normal in the eastern parts of the subregion.

(iii) Notable events and impacts

Between 12 and 15 February, a trough extending into the eastern Mediterranean triggered prolonged rainfall and a series of severe thunderstorms, leading to widespread flooding, strong winds, and landslides in southern and eastern Türkiye. The Antalya region experienced the most extreme precipitation, with accumulations of up to 300 mm in 24 hours and more than 400 mm within 48 hours. The normal monthly total for February is around 100 mm. More than 3800 buildings were affected by subsequent flooding, road transportation was disrupted, and one fatality was reported.

A number of stations in Armenia reported 30 mm–50 mm rainfall in less than three hours during the night of 25–26 May. Flash floods developed in the Debed and Aghstev River basins, causing four deaths, destroying roads and homes, and blocking the main communication lines and food supply for thousands of people.

From June to November, a total of 110 floods occurred in the mountain rivers of Azerbaijan, which is a record for this period.

On 5 July, a severe thunderstorm with heavy rain and hail struck Amasya province located inland near the central Black Sea coast in northern Türkiye. As a result, there was damage to homes, businesses, roadways, power lines, vehicles, and agricultural lands. In the highlands of Amasya, dozens of sheep were killed by a lightning strike that also injured a shepherd.

A large forest fire occurred in Türkiye from 15 to 18 August on Mount Yamanlar located in the İzmir region in the west of the country. The fire spread over a wide area due to high temperatures (35°C–41°C), low relative humidity (10%–19%), and strong northerly winds (46 km h^{-1}–57 km h^{-1}).

Intense rain fell in Baku (Azerbaijan) from 21 to 22 October. Over an 18-hour period, 86 mm fell, which is 306% of Baku's monthly climatic norm.

Unauthenticated | Downloaded 11/21/25 11:34 AM UTC

Sidebar 7.2: Storm Boris: Heavy rain over a large area in eastern Central Europe

Storm Boris caused extreme rainfall and flooding in eastern Central Europe in mid-September 2024. The storm developed over the record-warm Mediterranean Sea after cold polar air descended from Western Europe, causing a strong temperature contrast between these two air masses. The storm then followed a so-called Vb track (a path beginning from the north of the western Mediterranean Sea over northern Italy and leading northeastward to eastern Central Europe [MeteoSwiss 2024]). In this track, moist Mediterranean air is transported northward, creating the potential of intense rainfall. Furthermore, due to a blocking high-pressure system over Russia, additional airflow from the southeast pulled water vapor from the Black Sea to eastern Central Europe. The Black Sea had a significantly higher surface temperature than the surrounding land areas (+2°C to +5°C), and thus acted as an additional energy source for the storm.

The storm moved slowly and remained stationary over Slovakia and Czechia for several days, causing persistent and intense rainfall over these regions. Further and more detailed descriptions about the path and the various stages of the development of the storm system have already been published elsewhere (e.g., Greilinger et al. 2024; Gramlich 2024). Combined with the orographic effect of the Alps, this resulted in exceptionally high precipitation totals, particularly in the topographically affected areas. This effect is typical for Vb weather situations, since they are responsible for 45% of extreme precipitation events in northern Austria and Czechia—such as the event in autumn 2024—although only 5% of the low-pressure systems in this region are Vb lows.

Storm Boris was one of the most intense Vb events in recent decades, leading to extreme precipitation and severe flooding across the region and surpassing the magnitudes of previous events. Historical data show that the 50 strongest Vb events in recent decades resulted in 7%–20% more precipitation north of the Alps compared to other weather events. While Vb patterns are not frequent (around 5% of all low-pressure systems over Austria and Czechia), they have historically caused extreme rainfall, for example the events that resulted in floods in 1997 and 2002.

During Storm Boris, many national rainfall records were broken, especially during 12–16 September. The precipitation total exceeded 200 mm in many places (Fig. SB7.3). Some areas of lower Austria received 300 mm–400 mm of rain (Greilinger et al. 2024), doubling previous records in some locations. Most of northern Austria observed its wettest five-day period on record. In Czechia, rainfall exceeded 500 mm in several places, with 130 of 450 measuring stations recording more than 200 mm, including 385.6 mm on 14 September, a national record for daily precipitation. According to Global Precipitation Climatology Centre data (GPCC; Schneider et al. 2022) and the E-OBS dataset (Cornes et al. 2018), this five-day period had the highest such totals in the concerned area compared to any five-day period since 1950 (Fig. SB7.4). The severe weather was classified as a 100-year event, meaning a comparable event could be statistically expected once every 100 years. Also remarkable was the abnormal cooling during this event, which occurred due to a cold airmass coming from the Arctic to central Europe. Snow fell above 600 m altitude in Austria, with record September snow depths at some locations. A station at 2320 m altitude reported a snow depth of 145 cm on 17 September.

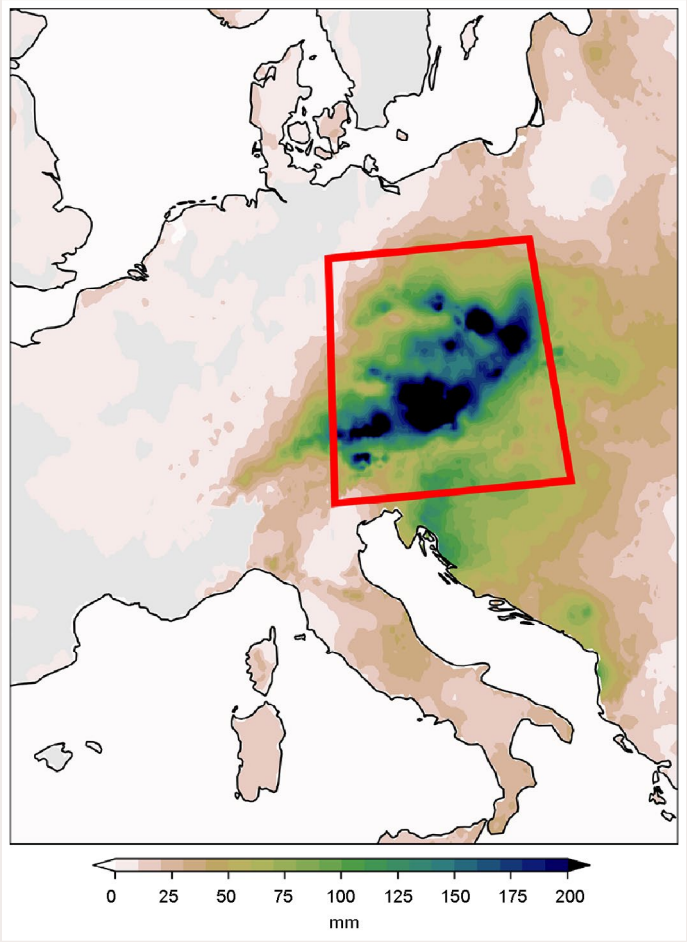

Fig. SB7.3. Five-day precipitations total (mm) in parts of Europe for the period 12–16 September 2024, when Storm Boris occurred. The red box surrounds the most-affected area (southeastern Germany, southern Poland, Czechia, Austria, and Slovakia). (Credit: Royal Netherlands Meteorological Institute [KNMI]/Copernicus Climate Change Service [C3S]; data source: ENSEMBLES daily gridded observational dataset [E-OBS; Cornes et al. 2018].)

Unauthenticated | Downloaded 11/21/25 11:34 AM UTC

This was the largest snowpack ever observed below 2400 m elevation in September in Austria. A station in Vienna reported a maximum temperature of 8.5°C on 13 September (Gramlich 2024).

Widespread severe flooding occurred in several countries, most notably in southeastern Germany, southern Poland, Czechia, Austria, and Slovakia, and also farther southeast in Hungary and Romania. The Danube, Oder, and Elbe River catchments were most affected (Rustemeier et al. 2024). The rainfall and subsequent floods caused power outages, leading to the closure of critical infrastructure. Landslides also occurred in the areas with the heaviest rain, leading to injuries and damage to roads and railways.

The total damage was estimated at several billion U.S. dollars, and over two million people were affected by the storm. At least 27 people were killed; however, the death toll was significantly lower than in past major floods, highlighting the effectiveness of early warning systems and emergency measures (Kimutai et al. 2024).

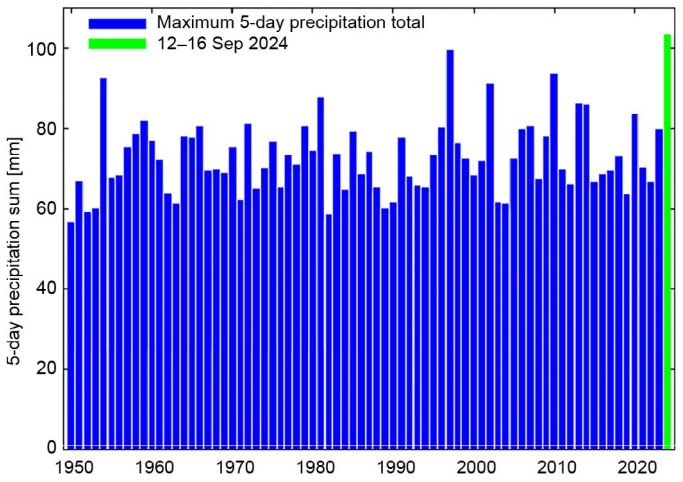

Fig. SB7.4. Annual maximum five-day precipitation totals (mm) averaged over the concerned area displayed in Fig. SB7.3 for the years 1950–2023 (blue bars) and the period 12–16 September 2024 (green bar). (Credit: Royal Netherlands Meteorological Institute [KNMI]/Copernicus Climate Change Service [C3S]; data source: ENSEMBLES daily gridded observational dataset [E-OBS; Cornes et al. 2018].)

Unauthenticated | Downloaded 11/21/25 11:34 AM UTC

g. Asia

—Z. Zhu, Ed.

Throughout this section, the base period for climatological normals and anomalies is 1991–2020 unless otherwise noted. All seasons in this section refer to the Northern Hemisphere, with winter referring to December–February 2023/24, unless otherwise noted.

1. OVERVIEW

—Z. Zhu, P. Zhang, Y.-S. Lui, A. A. Syafrianno, K. Takemura, A. Moise, H. Sato, K. Takahashi, J. I. Seong, D. Dulamsuren, M.-V. Khiem, and H.-P. Lam

Annual mean surface air temperatures during 2024 were above normal across most of Asia, except for parts of eastern Siberia, with anomalies of more than +1.0°C from East Asia to central Siberia, in and around northern India and Afghanistan, and over the Arabian Peninsula (Fig. 7.42). Annual precipitation totals were more than 120% of normal from eastern Mongolia to northern China, in the central part of central Siberia, from western China to Central Asia, in the coastal areas of the Arabian Sea, and over the Arabian Peninsula, while they were less than 80% of normal from northeastern Siberia to south-central Siberia (Fig. 7.43).

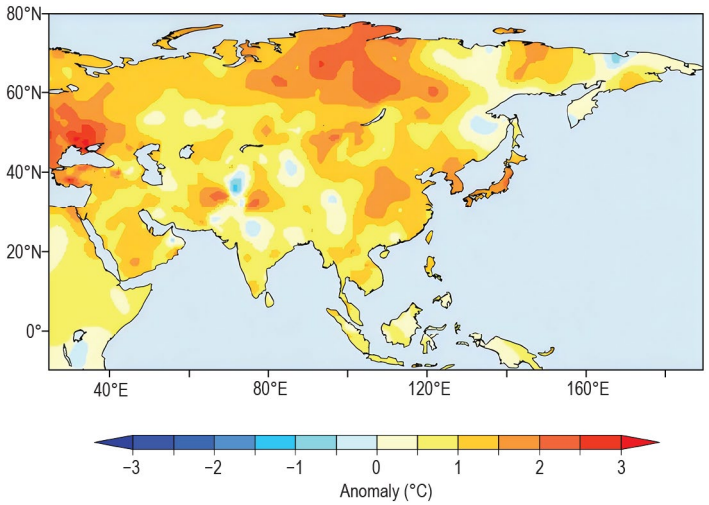

Fig. 7.42. Annual mean surface temperature anomalies (°C; 1991–2020 base period) over Asia in 2024. (Source: Japan Meteorological Agency.)

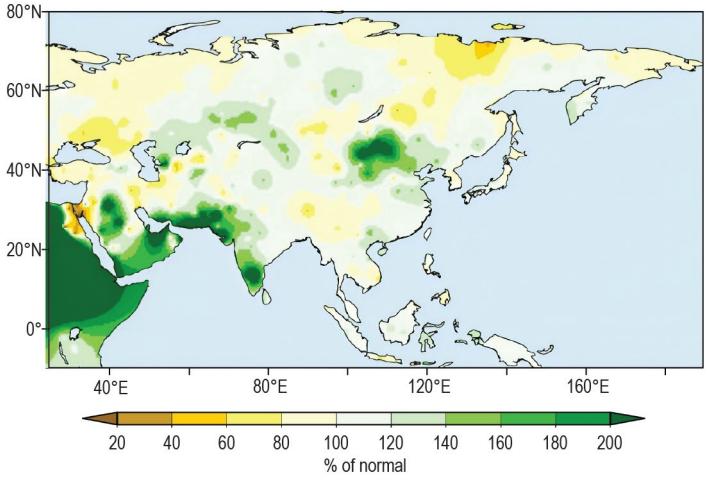

Fig. 7.43. Annual precipitation totals (% of normal; 1991–2020 base period) over Asia in 2024. (Source: Japan Meteorological Agency.)

In winter, seasonal mean temperatures were over 1.0°C above normal from Japan to the Korean Peninsula, in and around the northern Indochina Peninsula, in southern India, in north-central Siberia, and from Central Asia to the Middle East, while they were over 1.0°C below normal from eastern Siberia to northern China, in northern Western Siberia, in parts of western China, and in northern India (Fig. 7.44a). Seasonal mean precipitation was more than 140% of normal from the Korean Peninsula to western Central Asia, from western China to southern India, and in the northern and southern Arabian Peninsula, while it was less than 60% of normal in the Philippines, in the northern Indochina Peninsula, and in and around central Pakistan (Fig. 7.44b).

In spring, temperatures were above normal from eastern Siberia to the Indochina Peninsula and in parts of Central Asia, while they were below normal in northern Western Siberia and from northern Pakistan to the eastern Middle East (Fig. 7.44c). Precipitation was much above normal in parts from eastern to Western Siberia, in central Mongolia, in southern China, in the coastal areas of the Arabian Sea, and in the northern Arabian Peninsula, while it was much below normal in northeastern eastern Siberia, in northern China, and from the northwestern Indochina Peninsula to northern India (Fig. 7.44d).

In summer, temperatures were above normal from Japan to eastern China, and from central Siberia to the Middle East, while they were below normal from eastern to southern eastern Siberia (Fig. 7.44e). Precipitation was much above normal in and around eastern Mongolia, in southern China, the coastal areas of the Arabian Sea, and western Central Asia, while they were

Unauthenticated | Downloaded 11/21/25 11:34 AM UTC

much below normal in west eastern Siberia, northwestern China, southern Central Asia, and the northern Arabian Peninsula (Fig. 7.44f).

In autumn, temperatures were above normal from central to Western Siberia and from Japan to the southern Arabian Peninsula (Fig. 7.44g). Precipitation was much above normal from eastern to western China, in southern India, and parts of the Middle East, while it was below normal in the eastern Middle East, parts of the southern Arabian Peninsula, and Western Siberia (Fig. 7.44h).

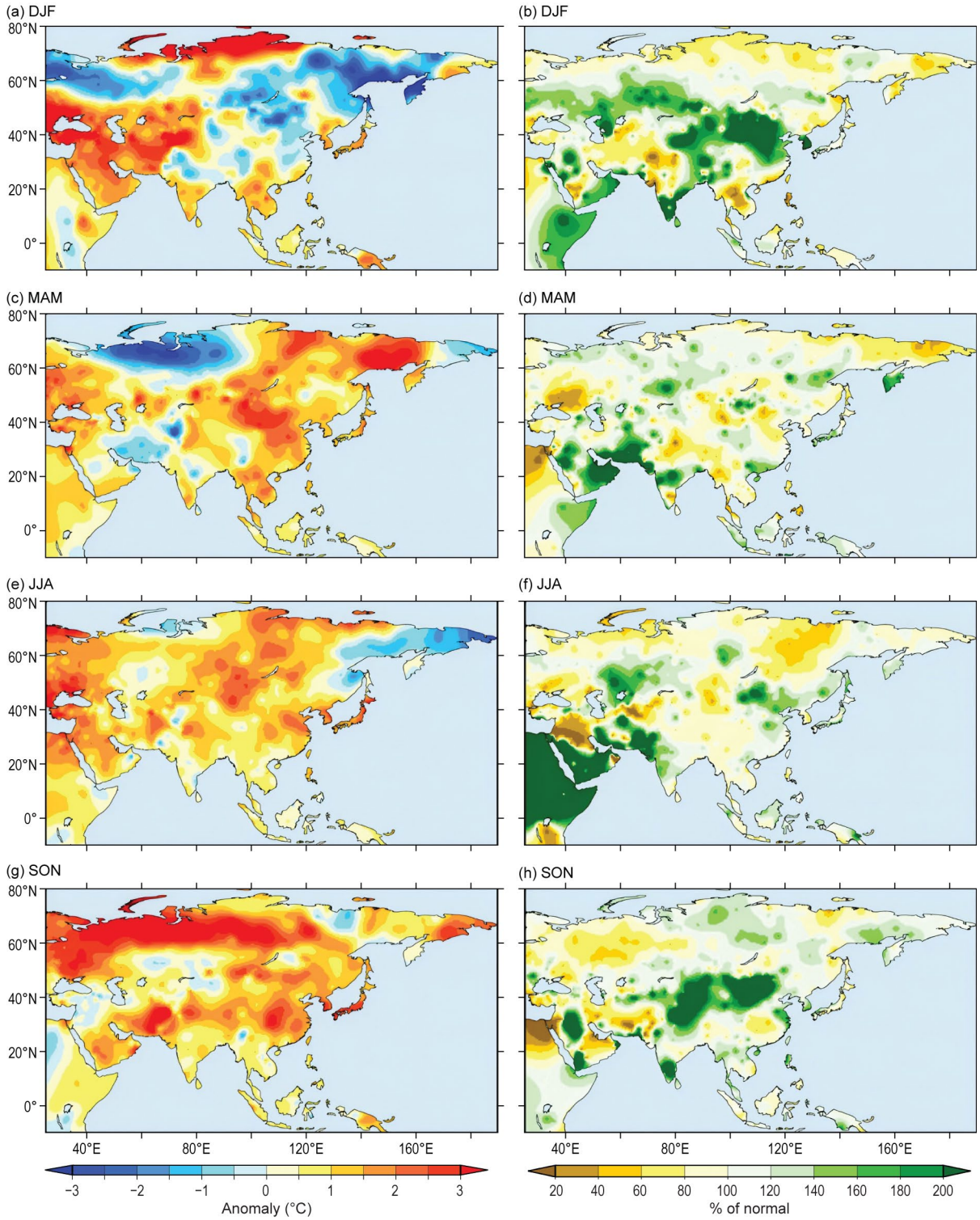

Fig. 7.44. Seasonal mean surface temperature anomalies (°C, left column) and precipitation ratios (% of normal, right column) over Asia in 2024 for (a),(b) winter; (c),(d) spring; (e),(f) summer; and (g),(h) autumn. Anomalies and ratios are relative to 1991–2020. (Source: Japan Meteorological Agency.)

Unauthenticated | Downloaded 11/21/25 11:34 AM UTC

For all seasons, positive mean 500-hPa geopotential height anomalies and mean 850-hPa temperature anomalies were dominant from East Asia to the midlatitude North Pacific (Figs. 7.45a,c,e,g), exhibiting the persistent northward shift of the westerly jet stream over the regions. In winter, convective activity was enhanced over the western Indian Ocean and the equatorial Pacific and suppressed near Southeast Asia (Fig. 7.45b), in association with an El Niño

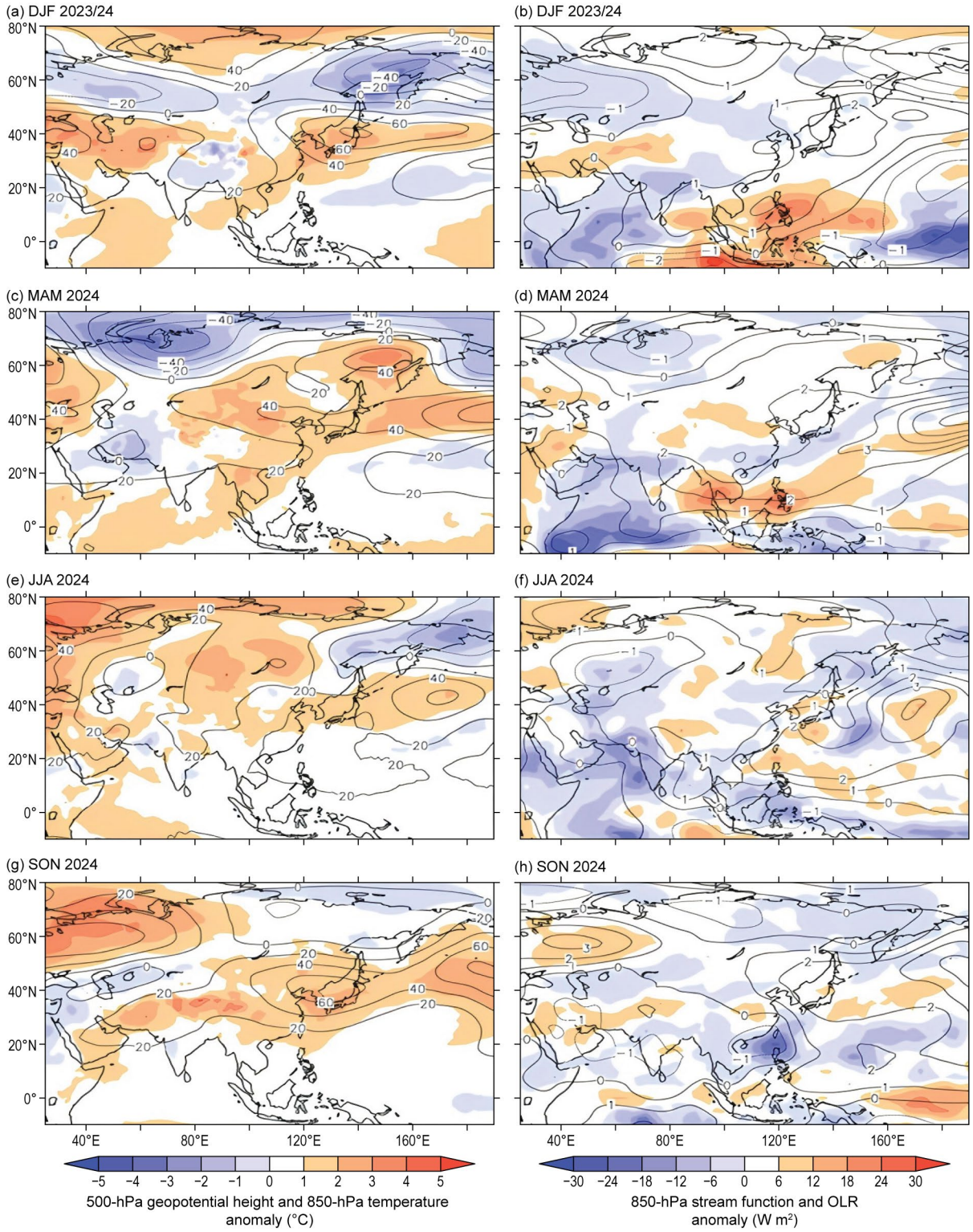

Fig. 7.45. Seasonal mean anomalies of atmospheric circulation variables in 2024 for (a),(b) winter; (c),(d) spring; (e),(f) summer; and (g),(h) autumn. Left column: 500-hPa geopotential height (contour, gpm) and 850-hPa temperature (shading, °C). Right column: 850-hPa stream function (contour, 1×10^6 m^2 s^{-1}) using data from the Japanese Reanalysis for Three Quarters of a Century (JRA-3Q) and Climate Prediction Center's Blended Outgoing Longwave Radiation (OLR; shading, W m^{-2}) using data originally provided by NOAA. Anomalies are relative to 1991–2020. (Source: Japan Meteorological Agency.)

Unauthenticated | Downloaded 11/21/25 11:34 AM UTC

and a remnant impact of a positive Indian Ocean dipole (IOD) that occurred from summer to autumn 2023. In the upper troposphere, a wavy pattern of 500-hPa geopotential height anomalies was observed along the subtropical jet over Eurasia, which was associated with anomalous convection from the Indian Ocean to the Maritime Continent. In the lower troposphere, anticyclonic circulation anomalies straddling the equator were found near Southeast Asia (Fig. 7.45b), corresponding to suppressed convection over the region. In spring, convective activity was enhanced over the western Indian Ocean and suppressed from the Bay of Bengal to the east of the Philippines (Fig. 7.45d), possibly related to the El Niño and the remnant impact of positive IOD mentioned above. In summer, enhanced convective activity extended from the Indian Ocean through Southeast Asia to the Maritime Continent, coinciding with 850-hPa cyclonic anomalies, while suppressed convection over the western tropical North Pacific corresponded to 850-hPa anticyclonic anomalies (Fig. 7.45f). This convection is possibly attributable to the above-normal sea surface temperatures in the Indian Ocean that resulted from remnant impacts of both the El Niño ending in spring and positive IOD from summer to autumn 2023. In the lower troposphere, the southwestward extension of the North Pacific subtropical high (NPSH) was stronger than normal (Fig. 7.45f) in association with the anomalous convection. In addition, the NPSH extended northward near the East China Sea and to the east of Japan, contributing to above-normal temperatures over eastern East Asia. In autumn, convective activity was enhanced from the northern South China Sea to the subtropical western North Pacific and suppressed from the western to central equatorial Pacific (Fig. 7.45h). The enhanced convection was accompanied by 850-hPa cyclonic circulation anomalies near the South China Sea (Fig. 7.45h), as well as above-normal typhoon activity.

2. RUSSIA

—M. Yu. Bardin and N. N. Korshunova

Estimates of climate features for Russia were obtained from hydrometeorological observations of the Roshydromet Observation Network. Anomalies are relative to the 1991–2020 base period, and national rankings and percentiles reflect the 1936–2024 period of record. Note that the temperature database was extended significantly, which in some cases changed previous ranking. The boundary between Asian Russia and European Russia is considered to be 60°E.

(i) Temperature

The year 2024 in Russia was anomalously warm, with the annual mean temperature 0.99°C above normal for Russia as a whole (Fig. 7.46a), marking the second-warmest year on record, and 1.36°C and 1.16°C above normal for the European and Asian parts, respectively.

Anomalies above the 95th percentile were observed at stations all over European Russia and parts of Asian Russia, including south of 50°N in central and eastern Siberia, Transbaikalia, and along the Amur river. The largest anomalies of more than +2°C were located along the Yenisei River.

Winter was the second coldest in the last decade, at 0.31°C below normal (Fig. 7.46b). There were two large areas of negative anomalies of as much as −4°C in European and Asian Russia, along with a warm pool in Western Siberia and the Taimyr peninsula. Principal features of this pattern were formed in January, when anomalies in these cold centers reached −5°C in western European Russia and −8°C in the maritime Far East. The pattern persisted in February, except for strong warming to the north of Siberia (e.g., 9°C above normal in the Taimyr region) and in the North Caucasus region (3.4°C above normal), with temperatures above the 95th percentile in most stations.

Spring was moderately warm, at 0.84°C above normal for all of Russia (Fig. 7.46c). This was the 12th-warmest spring since 1936 and the 10th warmest since 2000. The temperature anomaly pattern in spring was a mirror image of that in winter (Figs. 7.44a,c), with southern European Russia and eastern Asian Russia warmer than normal. All stations in southern European Russia and along the western border recorded temperatures above their 95th percentiles; the average temperature over the Southern Federal District was the highest on record, at 1.85°C above normal. At the same time, northern Siberia, which was warm in winter, was cold in spring, with temperature anomalies of −3°C.

Unauthenticated | Downloaded 11/21/25 11:34 AM UTC

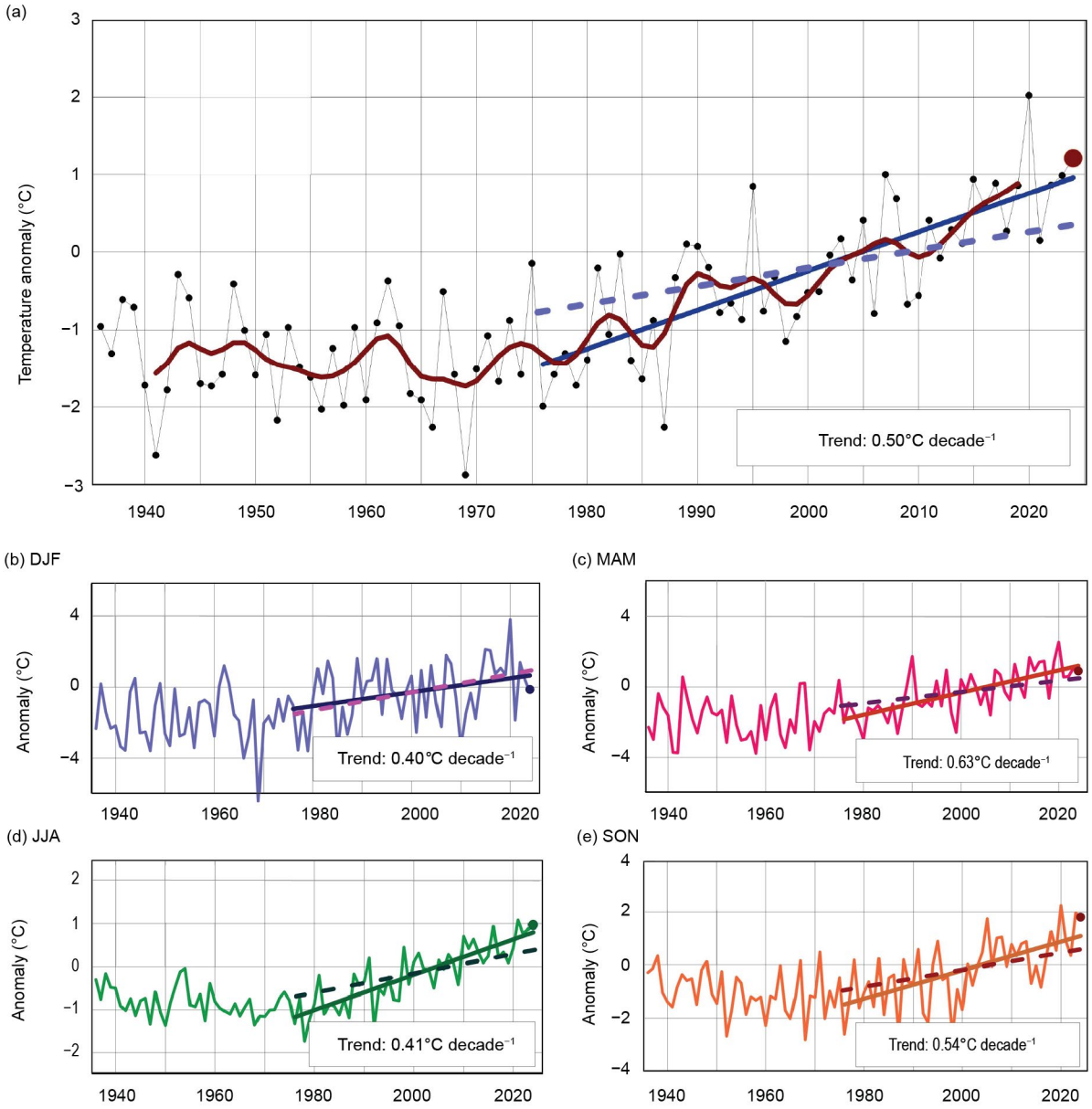

Fig. 7.46. Annual (a) and seasonal (b)–(e) mean temperature anomalies (°C; 1991–2020 base period) averaged over the territory of Russia for the period 1936–2024. The bold red line on the annual mean time series is an 11-point binomial filter. Linear trend b (°C decade^{-1}) is calculated for the period 1976–2024. Significance at 1% slope b is illustrated by dashed lines running through the centers of trend segments.

Summer and autumn were the second and third warmest for Russia as a whole, with seasonal temperatures 0.97°C and 1.80°C above normal, respectively. Asian Russia reported its second-warmest summer (0.78°C above normal), and European Russia observed its warmest autumn on record (2.43°C above normal). Summer temperatures were especially high in the southern part of central Siberia and Transbaikalia, and in southern and northwestern European Russia. In autumn, anomalies of more than +3°C formed a long "tongue" from the western border of Russia to central Siberia, with extremes above the 95th percentile (Fig. 7.44g).

December was record warm—4.22°C above normal—with the Asian part being second warmest on record (+4.71°C). The largest anomalies were observed in the Urals Federal District (the Urals and Western Siberia): +7.46°C. A vast pool of warm air with extremes above the 95th percentile formed in central Western Siberia and lasted for the entire month due to a series of intense Atlantic cyclones. At the Tolka meteorological station, daily temperatures 5°C–10°C above normal persisted throughout the month (Fig. 7.47). Anomalous warm weather associated with the weak Siberian High was observed in the far eastern regions. In the Magadan Region, average

Unauthenticated | Downloaded 11/21/25 11:34 AM UTC

daily temperature anomalies were +8°C to +11°C. At the Susuman weather station, December 2024 was the warmest in the 86-year record.

All seasons in Russia have warmed since the mid-1970s. The average annual rate of 0.5°C decade^{-1} is almost 2.5 times higher than the global warming rate. Annual and seasonal trends, except for winter, are statistically significant at the 1% level in both Asian and European Russia. Due to long-period changes in atmospheric circulation in the Atlantic-European sector (primarily the North Atlantic Oscillation and Scandinavian anticyclonic mode), winters turned cold after the mid-1990s, and then warmed again after mid-2010 (Fig. 7.46), but the trend remained insignificant.

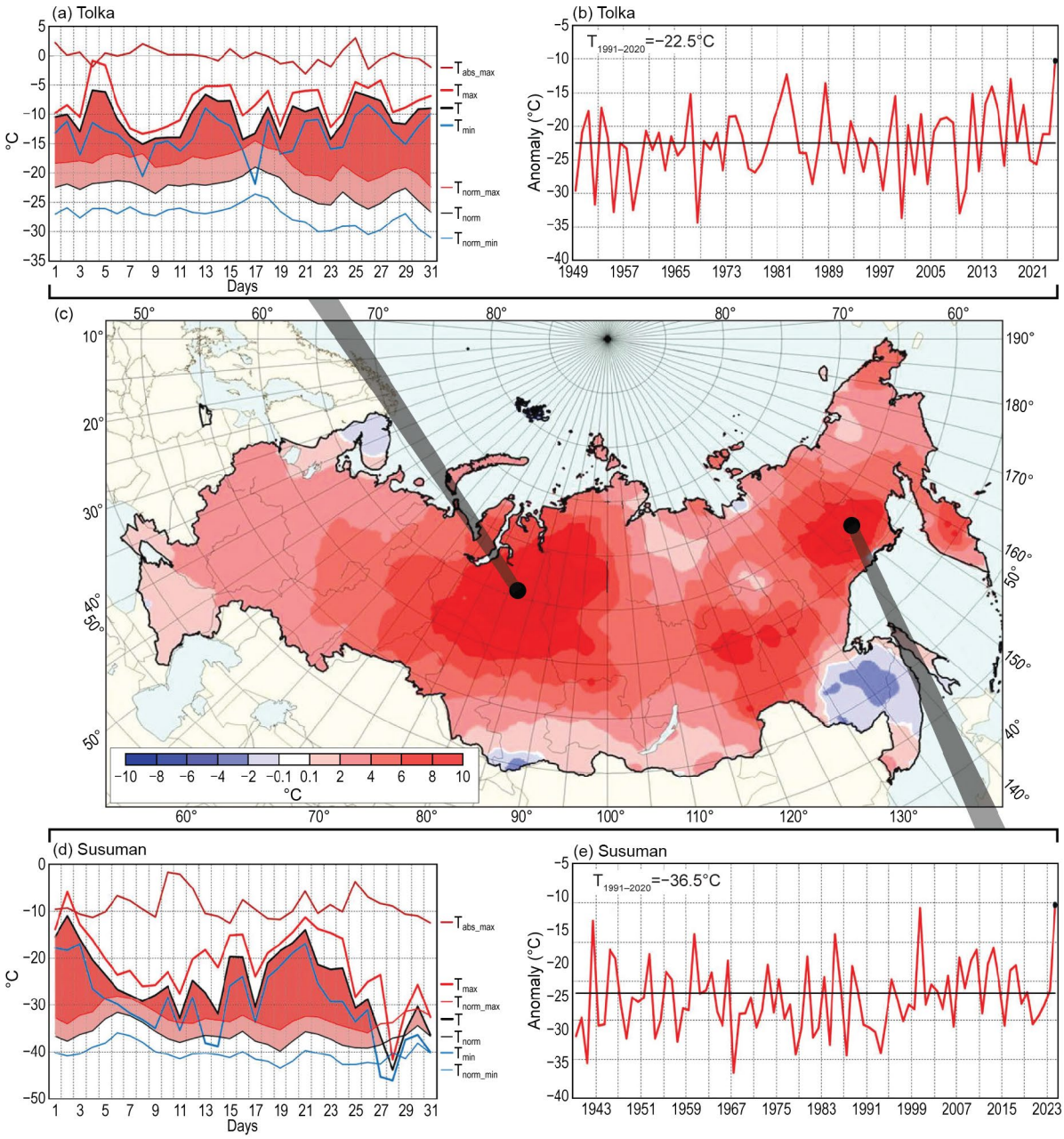

Fig. 7.47. (c) Temperature anomalies across Russia (shading, contour interval is 2°C) in Dec 2024. (b),(e) Monthly mean (red line, °C) and climatological mean temperature (black line, °C) in Tolka (64°N, 82°E; 1949–2024), Susuman (62°N, 148°E; 1939–2024). $T_{1991–2020}$ on plots of monthly temperatures is the 1991–2020 mean. (a),(d) Plots of daily temperature show observed daily mean (T, black line), daily minimum (T_{min}, blue line), and daily maximum (T_{max}, red line) temperatures along with their climatological values (three uppermost curves: T_{norm}, black; T_{norm_min}, blue; T_{norm_max}, red). The area between the normal daily mean curve T_{norm} and the observed daily mean curve is shaded light red where $T > T_{norm}$, and is shaded deep red if T was above the normal daily maximum T_{norm_max}.

Unauthenticated | Downloaded 11/21/25 11:34 AM UTC

(ii) Precipitation

The total precipitation averaged over the Russian territory in 2024 was about 101% of normal (Fig. 7.48) and ranked as the 23rd wettest on record (tied with five other years). Annual precipitation in European Russia was 93% of normal, notably in the southern part, with the Southern Federal District ranking second driest (74% of normal). Conversely, Asian Russia received 106% of its normal precipitation (fourth to sixth wettest). The Siberian Federal District was the wettest on record (114% of normal).

European Russia had below normal precipitation in all seasons except winter (124% of normal). The Southern Federal District received only 38% of normal precipitation in spring, while the Central Federal District saw its largest precipitation in winter (146% of normal) (Figs. 7.44b,d).

Annual total precipitation in Russia has increased since the mid-1970s by about 1.8% decade^{-1}. Increases are most notable in spring, with a rate of 5.1% decade^{-1}; however, a large region in southern European Russia has observed a significant descending trend of precipitation in summer. Precipitation decreases are also noted in all seasons surrounding the Ob' river "guba" (estuary).

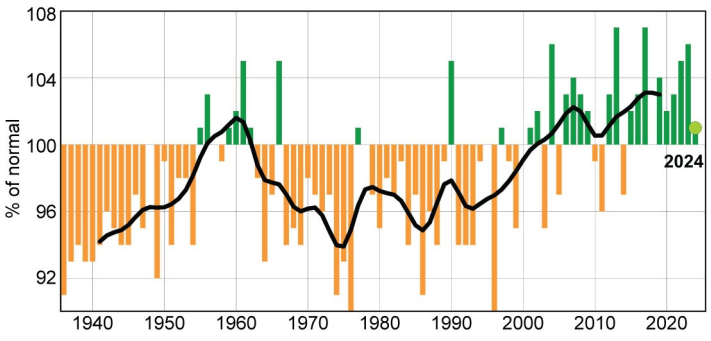

Fig. 7.48. Annual precipitation (% of normal; 1991–2020 base period) averaged over the Russian territory for the period 1936–2024. The smoothed time series (11-point binomial filter) is shown as a bold line. The green dot represents the annual precipitation % of normal for 2024.

(iii) Notable events and impacts

Information on events and impacts is from the Storm telegrams collected, analyzed summarized and archived routinely by the All-Russia Research Institute of Hydrometeorological Information, which acts as the World Data Center.

During 1–7 January, due to severe frosts (–35°C to –41°C) in the Arkhangelsk and Vologda regions, numerous accidents were reported related to heating, electricity, and water supply networks; 139 fires broke out. Twelve people died and eight were injured.

On 5–6 February, as a result of heavy rains (55 mm–130 mm) and waterlogged soil in the district of Sochi, a 14,000-m^3 mud rock flow entered the railroad bed and felled a tree between the Dagomys and Loo stations, damaging the contact line and delaying 44 long-distance trains.

On 4–14 April, rapid snowmelt led to flooding on the Ural River, with the water level 272 cm above the critical value, causing a dam to break in Orsk. Nearly 4500 houses, along with 4510 garden plots, were flooded in the city.

On 31 May in the Karachay-Cherkess Republic, a heavy downpour was accompanied by strong winds of 31 m s^{-1}–33 m s^{-1} and hail 2 cm–4 cm in diameter. Well over 180 structures and 3000 private homes were destroyed, cars were damaged, power lines were torn down, and 160 trees fell. One fatality was reported along with 80 injuries.

On 20 June, in Moscow, strong winds exceeding 26 m s^{-1} caused over 900 trees to topple. Two fatalities and seven injuries were reported along with damage to more than 440 cars.

On 1 July, in the Leningrad Region and St. Petersburg, heavy thunderstorms with 21 mm–30 mm of rain were accompanied by winds as high as 31 m s^{-1}. More than 500 trees and 10 metal structures fell, dozens of cars were damaged, power outages were reported in seven districts, and three people were injured, including one fatality.

3. EAST AND SOUTHEAST ASIA

—P. Zhang, Y. S. Lui, A. Syafrianno, K. Takemura, A. Moise, H. Sato, K. Takahashi, J. I. Seong, D. Dulamsuren, M.-V. Khiem, and H.-P. Lam

Countries/places considered in this section include China, Hong Kong (China), Indonesia, Japan, Korea, Mongolia, Singapore, and Vietnam. Unless otherwise noted, anomalies refer to the 1991–2020 base period.

Unauthenticated | Downloaded 11/21/25 11:34 AM UTC

(i) Temperature

Annual and seasonal mean temperature anomalies for 2024 are shown in Figs. 7.42 and Fig. 7.44, respectively.

In 2024, the annual mean air temperature for China was 1.01°C above normal, the highest since the start of the record in 1951. Temperatures were above normal for all seasons, with large fluctuations in winter, and the highest in spring, summer, and autumn. The number of average high-temperature days (daily maximum temperature >35.0°C) for China was 15.6, the second most since 1961, after 2022.

The annual mean temperature over Japan was significantly above normal nationwide and was the highest on record since 1898. Similarly, the annual mean temperature for the Republic of Korea (ROK) in 2024 was 14.5°C, making this the highest on record since 1973. Monthly mean temperatures were above normal for all 12 months of the year, and 5 months were record warm (April, June, July, August, and September).

The annual mean temperature over Mongolia was 1.9°C (second-warmest year since 1940); the country observed its warmest November on record, with an average temperature that was 3.8°C above normal.

The annual mean temperature over Indonesia was 27.5°C, marking the warmest year since 1981. It was also the warmest year on record for Singapore, equal with 2019 and 2016. July 2024 was the warmest July on record, during which Singapore also experienced a dry spell from 13 to 30 July.

In Vietnam, the temperature in 2024 was 0.5°C–1.5°C above normal. April was particularly warm, with a monthly temperature 4°C above normal in the north and a continuous heatwave lasting 47 days from March 29 to May 14.

(ii) Precipitation

Annual and seasonal precipitation for 2024 are shown in Figs. 7.43 and 7.44, respectively.

The annual precipitation total for China was 697.7 mm, marking the fourth-wettest year since 1951. The total of 8186 station-days of heavy rainfall (stations with daily precipitation higher than 50.0 mm) across the country was 31.3% above normal, the most since 1961. The annual precipitation in Mongolia was 280.6 mm, making 2024 the sixth-wettest year since 1940.

In Japan, annual precipitation totals were significantly above normal in eastern Japan and in Okinawa/Amami. In the Tokai region, precipitation was significantly above normal in spring and summer, and the annual precipitation amount was the highest since 1946, equal with 1998.

In the ROK, precipitation in August was 87.3 mm, just 30.7% of the monthly normal. Precipitation in February was 102.6 mm, which was 287.0% of normal, marking the first time on record that precipitation in February was higher than in August.

It was the third-wettest year since 1991 in Indonesia, with annual rainfall 115% of normal. Rainfall was normal (above normal) for 48.6% (46.1%) of regions in Indonesia. The highest rainfall anomaly was observed in Deiyai Regency, Papua, with an annual total of 5596 mm, 261% of its normal.

Singapore's annual total rainfall averaged over stations island wide was 108.1% of the long-term average of 2534.3 mm, the 12th-highest amount since 1980.

(iii) Notable events and impacts

Information on events and impacts is from the Beijing Climate Centre, Hong Kong Observatory, Japan Meteorological Agency, and Korea Meteorological Administration.

Total precipitation during Meiyu season in China was 480.7 mm rainfall (151% of normal). Heavy rainfall occurred along the Yangtze River from 9 June to 2 July, with totals ranging from 300 mm to 500 mm. The total precipitation exceeded 500 mm in the northern part of Jiangxi, western Zhejiang, and northern Fujian.

A waterspout occurred over Victoria Harbor, Hong Kong, on 28 September, the first occurrence over the harbor since 1959. In November, Tropical Cyclones Yinxing, Toraji, and Man-yi made successive landfalls in Hong Kong, marking the first time since 1946 that three tropical cyclones have struck the region in a single November.

Unauthenticated | Downloaded 11/21/25 11:34 AM UTC

In 2024, Mongolia experienced 95 hazardous disasters and 13 catastrophic disasters. Three people died, more than 3 million livestock were lost, and 13 highways were damaged.

In early September, Typhoon Yagi seriously affected Quang Ninh-Hai Phong in Vietnam. Heavy rain from Yagi caused many rivers to flood. The water level of the lower Red River in Hanoi reached 11.30 m, and Thai Binh River in Pha Lai reached 6.25 m, the highest in the last 20 years.

In eastern and western Japan and Okinawa/Amami, the seasonal mean temperatures in summer and autumn were the highest on record. Among the 153 weather stations nationwide, 80 stations in summer and 120 stations in autumn reported their highest seasonal mean temperatures on record. Heavy rainfall began around 24 July in many parts of northern Japan, including Yamagata Prefecture. In some areas of Yamagata, total precipitation during 23–26 July exceeded 400 mm, far surpassing the normal July average of 200 mm.

In the ROK, the country recorded 30.1 days of heatwaves and 24.5 days of tropical nights (temperatures remain at or above 25°C throughout the night) in 2024, the second highest and the highest on record, respectively. This led to more than 3700 people suffering from heat-related illnesses, with 34 fatalities reported. In November, heavy snow fell in the central region of the ROK and broke the record of maximum daily snowfall total at three observation spots, with Suwon recording a daily total of 32.3 cm.

In Indonesia, the eastern part of Bima Regency, West Nusa Tenggara, saw a dry spell of 214 days, resulting in a drought that triggered a clean water crisis for more than 21,600 people.

4. SOUTH ASIA

—O. P. Sreejith, A. Bandgar, C. T. Sabeerali, and A. K. Srivastava

Countries in this section include Bangladesh, India, Pakistan, Sri Lanka, and Nepal.

(i) Temperature

In 2024, South Asia generally experienced above-normal temperatures. The annual mean surface air temperature averaged over India was 0.65°C above normal (Fig. 7.49), making it the warmest year since 1901. The seasonal mean temperatures averaged over India were above normal for all seasons.

The annual mean temperature for Pakistan was 0.71°C above normal, the ninth highest on record. The annual mean minimum temperature played a large role in this record, being 1.29°C above normal, the second highest on record behind 2022.

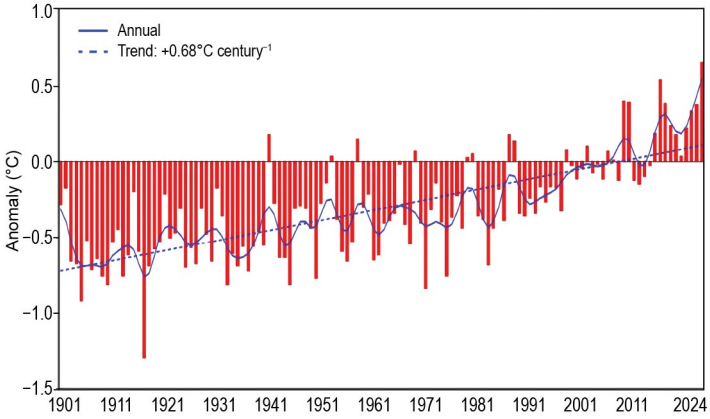

Fig. 7.49. Annual mean temperature anomalies (°C; with respect to 1981–2010 normal) averaged over India for the period 1901–2024. The smoothed time series (9-point binomial filter) is shown as a continuous line. The dashed line indicates the trend, which is statistically significant at the 90% confidence level.

(ii) Precipitation

The 2024 summer monsoon set in over the Indian subcontinent (Kerala, southwestern parts of peninsular India) on 30 May, two days earlier than the climatological onset date of 1 June. The monsoon covered the entire country on 2 July, six days ahead of its normal date (8 July). For India, the long-term average (LTA; 1971–2020) of the summer monsoon rainfall is 869 mm with a standard deviation of about 10% (Fig. 7.50b). During 2024, the summer monsoon rainfall averaged over India (ISMR) was 108% of its LTA value (Fig. 7.50a). During the monsoon season, among the four broad homogenous geographical regions of the country, South Peninsular India, Central India, and Northwest India received seasonal rainfall of 114%, 119%, and 107% of their LTA, respectively, while East and Northeast India received 86% of its LTA (Fig. 7.50c). At the monthly scale, rainfall for the country as a whole was below normal for June and above normal during July, August, and September. Over the core monsoon zone, the southwest monsoon was

Unauthenticated | Downloaded 11/21/25 11:34 AM UTC

active on some days in July, August, and September (Fig. 7.51). During other periods, rainfall over India was below normal (64% of LTA) during the winter season (January–February) of 2024 and near normal (96% and 97% of LTA, respectively) during the pre-monsoon season (March–May) and post-monsoon season (October–December).

The summer monsoon onset in 2024 was two days earlier than normal for Pakistan. The total rainfall for the 2024 monsoon season over Pakistan was 390.0 mm, 31% above the LTA (1961–2010) of 297.6 mm. Both Bangladesh and Sri Lanka received above-normal rainfall during the summer monsoon season (May–September). For Nepal, the 2024 summer monsoon entered eastern Nepal on 10 June, 3 days earlier than the normal onset date, and withdrew on 12 October, 10 days later than normal. Many areas of the eastern half of Nepal received more than 200 mm of rain during 27–29 September, with a peak of 517 mm at Daman. On 28 September, 25 stations, including Kathmandu Airport (239.7 mm), recorded their wettest day on record. The Narayani River at Devghat exceeded its previous record flood level by 3.5 m, and severe flooding occurred in the Kathmandu Valley. At least 250 deaths were reported.

The 2024 northeast/post-monsoon season (October–December) rainfall over India as a whole was near normal (97% of LTA). The seasonal rainfall during the northeast monsoon season over the core region of the south peninsula was above normal (122% of LTA). Sri Lanka received above-normal rain during the northeast monsoon (October–December) season.

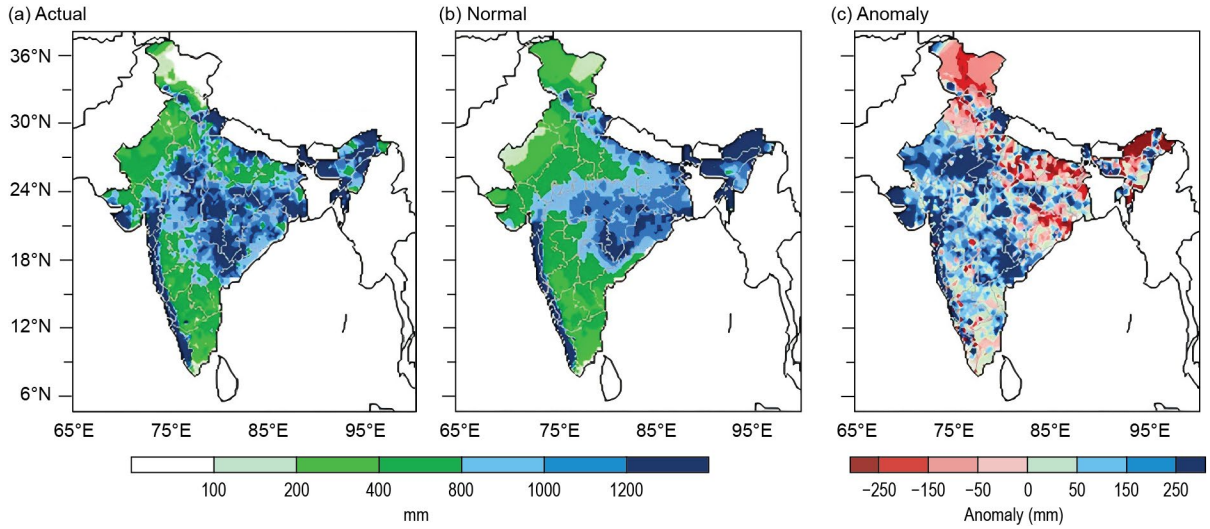

Fig. 7.50. Spatial distribution of monsoon seasonal (Jun–Sep) (a) actual, (b) normal (1971–2020 average), and (c) anomalous rainfall (mm) over India in 2024.

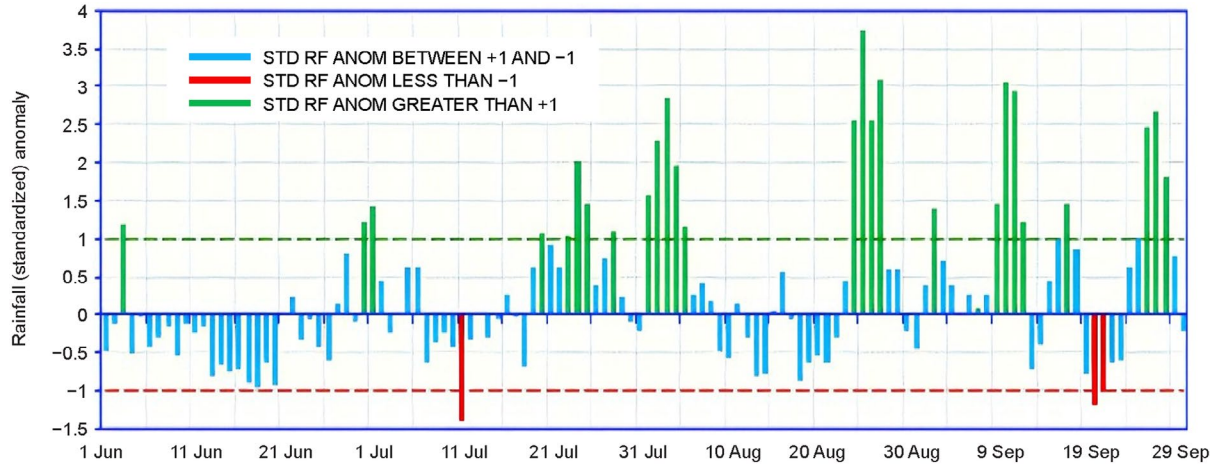

Fig. 7.51. Daily standardized rainfall anomaly time series averaged over the core monsoon zone of India for the period 1 Jun to 30 Sep 2024.

Unauthenticated | Downloaded 11/21/25 11:34 AM UTC

(iii) Notable events and impacts

Information on events and impacts is from the India Meteorological Department.

In 2024, four cyclones formed over the North Indian Ocean (Fig. 7.52; see section 4g5 for details). Severe Cyclonic Storm Remal formed over the north and adjoining east-central Bay of Bengal, leading to 51 fatalities in Mizoram, West Bengal, Assam, Nagaland, Meghalaya, and Manipur in Northeast India. The two districts of Tripura, namely Khowai and West Tripura, were also affected. In Bangladesh, 10 people were killed, 3.75 million people were affected across 19 districts, and more than 150,000 houses were damaged due to the storm.

Severe Cyclonic Storm Dana formed during the post-monsoon season over the east-central Bay of Bengal, claiming four lives from West Bengal. Additionally, about 5800 houses were damaged and 3.5 million people in Odisha were impacted. Cyclonic Storm Fengal also formed in the post-monsoon season over the Bay of Bengal. The storm caused 15 fatalities in Tamil Nadu and Puducherry in southern India. The tracks of these cyclonic storms are shown in Fig. 7.52.

In 2024, thunderstorms and lightning claimed around 1580 lives from different parts of India. Among these, more than 320 deaths occurred in Bihar, along with an estimated 290 in Madhya Pradesh, 220 in Uttar Pradesh, 200 in Odisha, 80 in the Jharkhand and Maharashtra states, and 70 in Telangana.

Heavy rainfall and flood-related incidents claimed around 1320 lives in different parts of India in 2024. Among these, about 425 deaths were reported in Kerala, mainly due to a series of catastrophic landslides in the hills of Meppadi on 30 July. Table 7.3 lists many 24-hour rainfall records that occurred during the 2024 southwest monsoon season.

Extreme rainfall also affected other parts of South Asia. In Nepal, floods and landslides from 26 to 28 September across a wide swath of the country claimed 249 lives and caused almost 27,000 livestock fatalities. Significant damage to infrastructure was also reported, including 26 hydropower facilities and 44 bridges. In Sri Lanka, people were killed due to floods, landslides, and strong winds brought by the southwest monsoon from mid-May to 11 June. Persistent heavy rainfall across Pakistan from 13 to 20 April triggered multiple disasters, resulting in at least 98 fatalities and 89 injuries. Khyber Pakhtunkhwa province, the hardest-hit region, recorded

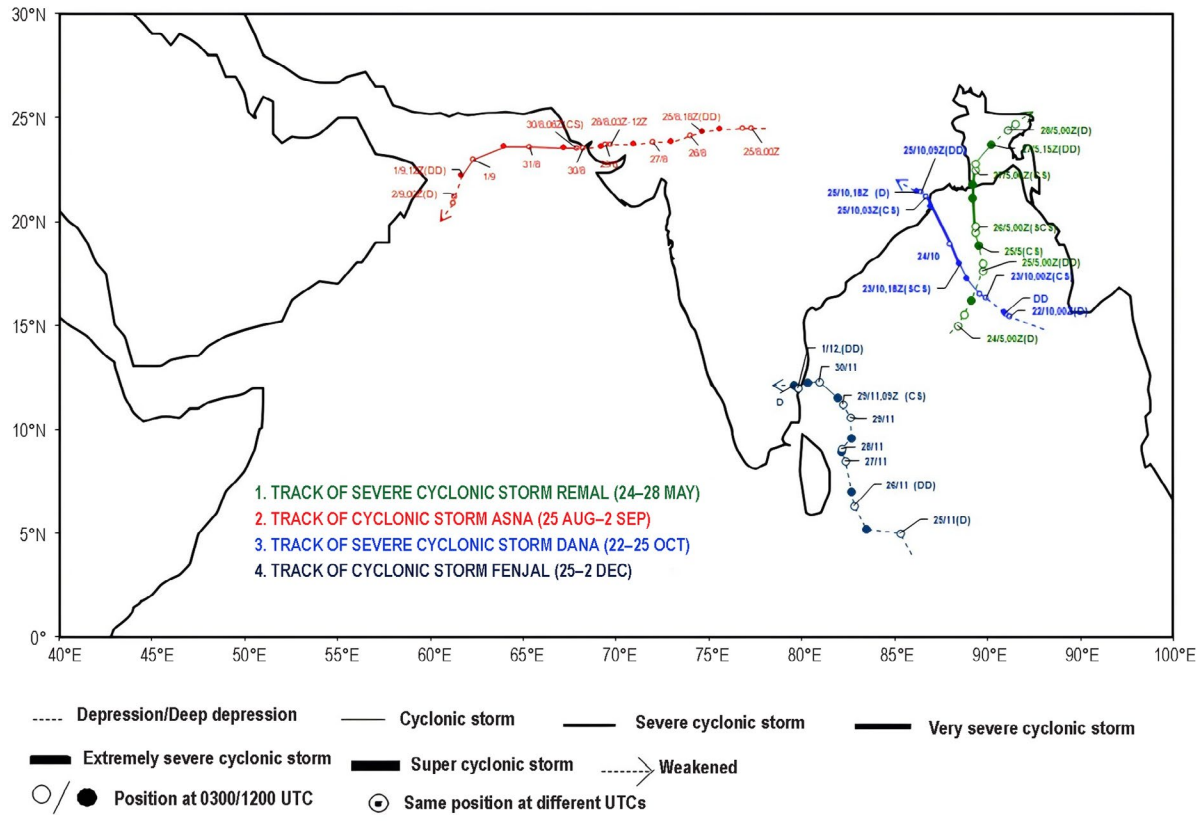

Fig. 7.52. Cyclonic storm tracks during 2024 over the North Indian Ocean.

Unauthenticated | Downloaded 11/21/25 11:34 AM UTC

46 deaths caused by rain-induced hazards. From 1 July to 28 August, an additional 250 people died across Pakistan due to widespread flooding and landslides induced by more heavy rains.

A heatwave claimed more than 455 lives from different parts of India. Pakistan experienced severe heatwave events during the second half of June 2024 that led to more than 560 fatalities, primarily in southern Pakistan. Southeast Asia also experienced extremely hot conditions during the year. In central Myanmar, 47.4°C and 48.2°C were recorded at Chank on 6 April and 28 April, each setting a new national maximum temperature record for the country.

Table 7.3. Record 24-hour rainfall during the 2024 Southwest Monsoon season. Stations marked with a star icon (★) indicate the information is based on real-time available data.

Station	24-hr Total (mm)	Date	Previous Record Total (mm)	Previous Record Date
Bengaluru City	111.1	3 Jun	101.6	16 Jun 1891
Tondi	87.8	7 Jun	68.0	7 Jun 2022
Dwarka	418.6	20 Jul	355.8	7 Jul 1998
Kozhikode ★	241.6	30 Jul	220.6	11 Jul 1997
Palakkad	162.8	30 Jul	157.4	4 Jul 1964
Panjim	360.8	8 Jul	334.7	1 Jul 2009
Porbandar ★	485.8	19 Jul	444.3	16 Jul 2009
Vadodara ★	320.2	25 Jul	297.4	1 Jul 2007
Valparai	305.4	30 Jul	195.6	17 Jul 2007
Visakhapatnam	104.6	19 Jul	94.2	11 Jul 1992
Agatti	195.6	17 Aug	123.0	22 Aug 2014
Churu	124.8	1 Aug	99.0	10 Aug 1964
Gannavaram	122.7	31 Aug	103.1	9 Aug 2008
Karur Paramathi	110.4	15 Aug	80.2	26 Aug 2006
Lengpui	113.6	17 Aug	101.0	25 Aug 2017
Minicoy	218.4	14 Aug	200.7	21 Aug 1930
Naliya	301.2	29 Aug	294.0	12 Aug 1979
Narsaapur	140.7	31 Aug	93.4	22 Aug 1989
Okha	387.4	28 Aug	381.6	6 Aug 2007
Puducherry	155.0	10 Aug	102.2	11 Aug 2011
Ranchi	170.8	3 Aug	122.5	14 Aug 2012
Sriniketan	191.8	2 Aug	159.4	27 Aug 1987
Damoh	215.0	11 Sep	146.4	12 Sep 1992
Forbesganj	310.6	27 Sep	228.6	2 Sep 1960
Gondia	285.4	10 Sep	281.4	2 Sep 1961
Nandigama	172.6	1 Sep	171.2	20 Sep 2005
Pune (Shivajinagar)	133.0	26 Sep	132.3	21 Sep 1938
Rajnandaon	184.4	10 Sep	103.0	5 Sep 1994

Unauthenticated | Downloaded 11/21/25 11:34 AM UTC

5. SOUTHWEST ASIA

—A. Vazifeh, A. F. Kazemi, P. Asgharzadeh, and M. Mohammadi

This section covers the Middle East and Central Asia. Unless otherwise noted, anomalies refer to the 1991–2020 base period in this subsection.

(i) Temperature

Figure 7.53a presents the annual mean temperature anomalies for 2024. Most of the Middle East and Central Asia experienced above-normal temperatures compared to the 1991–2020 base period. The summer of 2024 was particularly warm with the largest temperature anomalies, making it the warmest year on record for many West Asian countries.

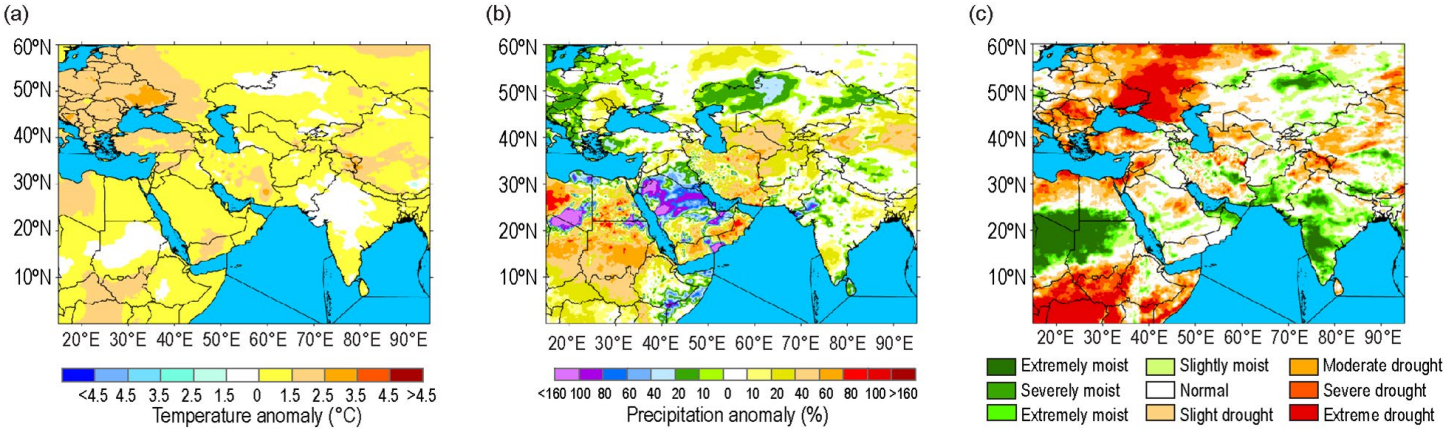

Fig. 7.53. (a) Annual mean air temperature anomaly (°C), (b) annual mean precipitation anomaly (%), and (c) standardized precipitation index in 2024.

(ii) Precipitation

Annual accumulated precipitation anomalies for west-central Asia for 2024 are shown in Fig. 7.53b. The data used to generate these maps primarily come from the ERA5 reanalysis dataset, which provides monthly averaged values. However, for Iran, higher-resolution (3-km) gridded data derived from interpolated observations are used instead. Wetter-than-normal conditions were evident in western and eastern Kazakhstan and the northern and central Arabian Peninsula. Conversely, most of Iran, Afghanistan, and the Central Asian countries experienced drier-than-normal conditions throughout the year. Details are described in the following subsection.

(iii) Notable events and impacts

Information on events and impacts is from the Climate department of the Iran Meteorological Organization, and the United Arab Emirates (UAE) National Center of Meteorology.

Figure 7.53c presents the 12-month Standardized Precipitation Index ending in December 2024. Slight to moderately dry conditions were observed in several areas, including northwest of the Caspian Sea and much of Iran. Conversely, the UAE and Oman experienced slight to severely wet conditions.

Drought conditions affected large parts of Southwest Asia, exacerbating water stress and agricultural challenges. Notably, the eastern and south-central Iranian Plateau experienced precipitation deficits exceeding 30%–50% of the long-term average, compounding multi-year drought conditions. This prolonged aridity severely impacted Iran's agricultural sector in central to southeastern provinces, where reservoir levels dropped to critical lows, triggering water rationing in rural and municipalities in the region. Similarly, Mesopotamia (Iraq) and the Syrian Desert recorded rainfall below normal, worsening food insecurity in regions already strained by conflict and resource mismanagement. Due to prolonged rainfall shortage and drought in the Middle East including Syria, Iraq, and Iran, the number of days with sand and dust storms were above normal and intensified due to parched soils.

While drought-stricken regions like eastern Iran grappled with desertification and groundwater depletion, flood-affected zones faced infrastructure collapse and economic disruption. Prolonged heavy rainfall that began at the end of March extended to April and May across parts

Unauthenticated | Downloaded 11/21/25 11:34 AM UTC

of Southwest Asia. A series of slow-moving weather systems, fueled by anomalously warm waters in the Arabian Sea and persistent troughs over the Persian Gulf, delivered repeated floods to coastal and inland areas. Southern Iran, particularly the provinces of Hormozgan and Sistan-Baluchestan, received two to three times its typical April rainfall in just 72 hours. Flash floods submerged entire villages, displaced over 20,000 people, and damaged critical infrastructure, including the Chabahar port. The southern Persian Gulf coastlines faced similar extremes. Dubai recorded 250 mm of rain in 24 hours—nearly three times its annual average—which submerged highways and paralyzed Dubai International Airport, where floodwaters halted operations for 48 hours. Oman's Dhofar Governorate and the UAE's Al Ain region saw catastrophic flooding, with wadis bursting their banks and sweeping away vehicles. In Balochistan (Pakistan), Quetta and Turbat received 180 mm–220 mm of rain in April alone, triggering landslides that isolated rural communities. In Iran, the provinces of Hormozgan, Sistan-Baluchestan, and Khuzestan faced a second wave of flooding in early May, with rainfall totals greater than the seasonal averages. Southeastern Iraq experienced rare May showers, with 120 mm–150 mm falling over the Maysan and Basra provinces.

6. CENTRAL ASIA

—R. Shukla, Y. Pan, Z. Segele, and W. Thiaw

The climate of Central Asia varies by region and season and is influenced by terrain inhomogeneity. Central Asia is defined as the region encompassing six countries within 20°N–60°N and 40°E–90°E for the purpose of this analysis and includes Afghanistan to the south, Turkmenistan, Uzbekistan, Tajikistan, and Kyrgyzstan (from west to east) in the central part of the region, and Kazakhstan to the north. Central Asia is bordered by the Caspian Sea in the west and exhibits a complex topography ranging from vast plains in Kazakhstan, Uzbekistan, and Turkmenistan to high-elevation mountains in Kyrgyzstan, Tajikistan, and Afghanistan. The NOAA Climate Prediction Center's Global Unified Temperatures and Global Precipitation Climatology Project (GPCP) data are used for this analysis. The climatological base period for both temperature and precipitation is 1991–2020.

(i) Temperature

During 2024, the annual mean temperature in Kazakhstan featured a strong meridional gradient, with temperatures ranging from 0°C to 5°C in northern Kazakhstan and 5°C to 15°C in southern regions (Fig. 7.54a). Annual mean temperatures were the lowest (–5°C to 0°C) in eastern Tajikistan, parts of Kyrgyzstan, and over some high-elevation regions in northeastern Kazakhstan.

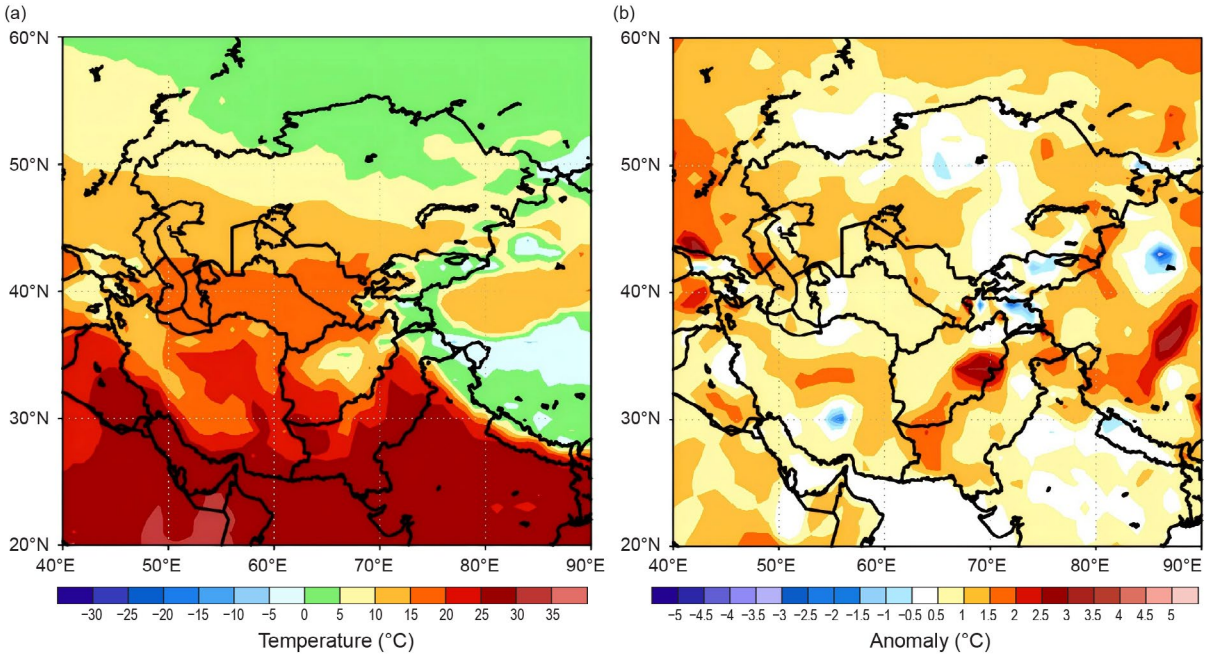

Fig. 7.54. Annual (a) mean temperature (°C) and (b) temperature anomalies for 2024 (°C; 1991–2020 base period) across Central Asia. (Source: NOAA/National Centers for Environmental Prediction.)

Unauthenticated | Downloaded 11/21/25 11:34 AM UTC

Temperatures varied between 10°C and 20°C in much of Uzbekistan, southern Kazakhstan, western Tajikistan, and parts of northern Afghanistan and Turkmenistan, and between 20°C and 30°C in southwestern Afghanistan (Fig 7.54a). The lowest temperatures recorded were –20°C to –10°C in parts of Kazakhstan and Kyrgyzstan in January, while the highest temperatures of 30°C to 40°C occurred in parts of Turkmenistan, Uzbekistan, and Afghanistan in July.

Except for isolated mild cold anomalies over central Kazakhstan, northern Kyrgyzstan, and northern Tajikistan, most of Central Asia recorded positive annual mean temperature anomalies. The largest positive anomalies of +2.5°C to +3°C (>90th percentile) were registered over eastern Afghanistan (Fig. 7.54b). These large positive anomalies were also observed in the maximum and minimum annual temperatures. Isolated areas in northeastern and eastern Kazakhstan and southern Afghanistan recorded positive anomalies of annual mean temperature of +1.5°C to +2°C. Moreover, minimum temperatures were 4°C–7°C above average in Kazakhstan in April, which led to rapid snowmelt and overflow of numerous rivers. In contrast, the lowest anomalies of annual mean temperature ranged from 1.5°C to 2°C below average over northern Tajikistan.

(ii) Precipitation

The annual total precipitation for 2024 showed a large variation across Central Asia (Fig. 7.55a). The largest amounts recorded were 600 mm–800 mm in northern Kazakhstan, while 200 mm–600 mm was received in many parts of Kazakhstan, Kyrgyzstan, Tajikistan, Afghanistan, Uzbekistan, and Turkmenistan. The lowest amounts, 100 mm–200 mm, fell in western Afghanistan, central Turkmenistan, and over isolated areas in northern Uzbekistan (Fig. 7.55a). Most of the precipitation in northern Kazakhstan occurred in January–February and May–August (Figs. 7.44b,d,f), during which near-record precipitation was recorded in each month (>90th percentile), whereas most of the precipitation in Afghanistan, Tajikistan, and western Kyrgyzstan occurred during the peak of their wet season from February to April.

Annual total precipitation was above average (248 mm) by 100 mm–300 mm in most of northern and eastern Kazakhstan (Fig. 7.55b). The annual precipitation was above average by 10 mm–100 mm in the remaining parts of Kazakhstan, Kyrgyzstan, much of Tajikistan, western and northeastern Uzbekistan, northwestern Turkmenistan, and over higher elevation regions in Badakhshan province of Afghanistan. However, the annual precipitation totals were 10 mm–50 mm below average in the northern half of Afghanistan (Fig. 7.55b). Some localized regions in central Afghanistan experienced annual precipitation deficits of up to 100 mm.

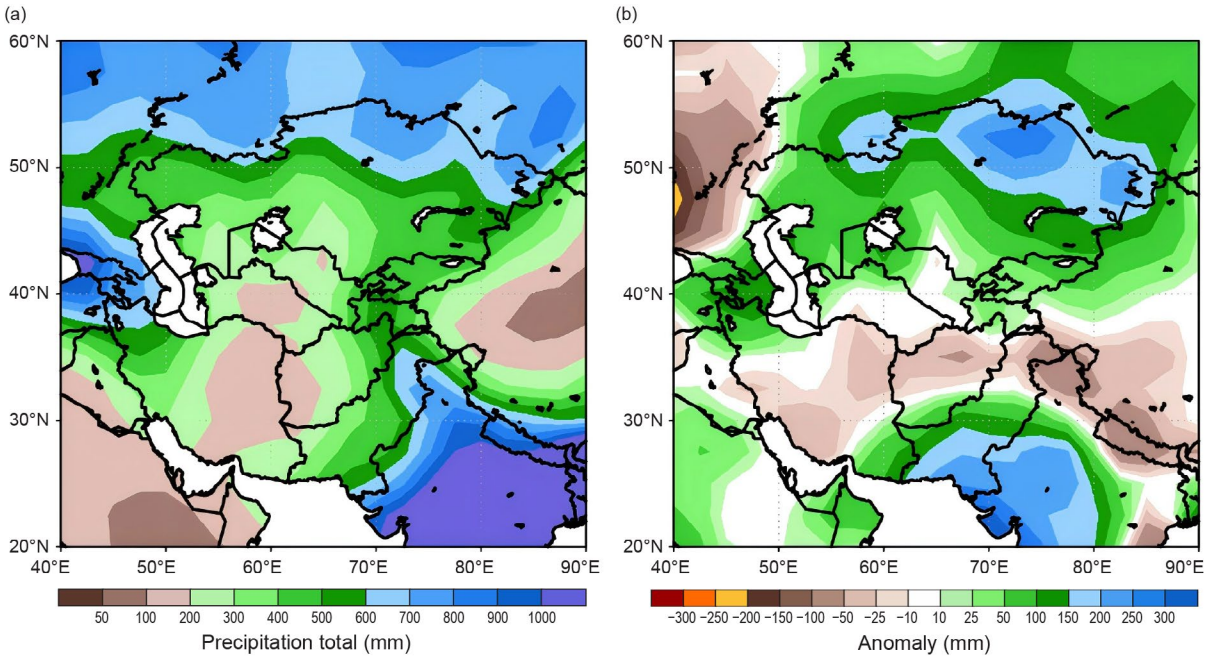

Fig. 7.55. Annual (a) precipitation totals (mm) and (b) precipitation anomalies for 2024 (mm; 1991–2020 base period) across Central Asia. (Source: NOAA/National Centers for Environmental Prediction GPCP data.)

Unauthenticated | Downloaded 11/21/25 11:34 AM UTC

(iii) Notable events and impacts

Information on events and impacts is from the European Civil Protection and Humanitarian Aid Operations Flash, as well as the United Nations Office for the Coordination of Humanitarian Affairs.

Many regions of Afghanistan and Kazakhstan experienced significant impacts from extreme weather events in 2024, mainly due to severe flooding caused by heavy precipitation and rapid snowmelt driven by enhanced above-average temperatures. A heavy snow and rain event during 18–19 February in Nuristan province of northeastern Afghanistan triggered a landslide that led to 25 fatalities and property damage. Heavy precipitation and snowfall during 29 February–3 March in northeastern and eastern parts of Afghanistan killed 39 people and destroyed 637 residential homes and 14,000 livestock. Heavy rainfall across Afghanistan in late March destroyed more than 600 hectares of agricultural land and severely damaged over 540 homes and six bridges. Heavy precipitation in parts of Afghanistan during 12–18 April triggered flash flooding and resulted in 70 fatalities, 56 injuries, and led to the loss of more than 2000 livestock and 38,000 hectares of agricultural land. Similarly, 11 fatalities were reported due to heavy precipitation and flooding in eastern Afghanistan in late April. Heavy precipitation in April and mid-May across Afghanistan triggered flash floods in northeastern regions of the country—especially in the Baghlan, Takhar, and Badakhshan provinces—and resulted in more than 330 fatalities, 1600 injuries, and damage to over 5000 houses. Heavy precipitation and thunderstorms during 14–18 July in parts of eastern and southeastern Afghanistan triggered flash flooding that led to 40 fatalities and 350 injuries. Heavy precipitation in eastern Kyrgyzstan during 17–19 August triggered mudslides and flash floods that resulted in widespread damages.

High minimum temperatures in April (4°C–7°C above average) accelerated snowmelt across Kazakhstan, which—combined with heavy precipitation—triggered rapid river overflow and widespread flooding. This cascade of events caused severe impacts in the Akmola, Kostanay, Atyrau, and North Kazakhstan regions: Seven fatalities, 5500 damaged buildings, displacement of nearly 118,000 people, loss of 5700 livestock, flooding of 180 roads, and the collapse of nine bridges. Ten regions of Kazakhstan declared a state of emergency due to the severity of the disaster. The wetter-than-average conditions during January–March and the above-average minimum temperatures in April across Kazakhstan are shown in Fig. 7.56.

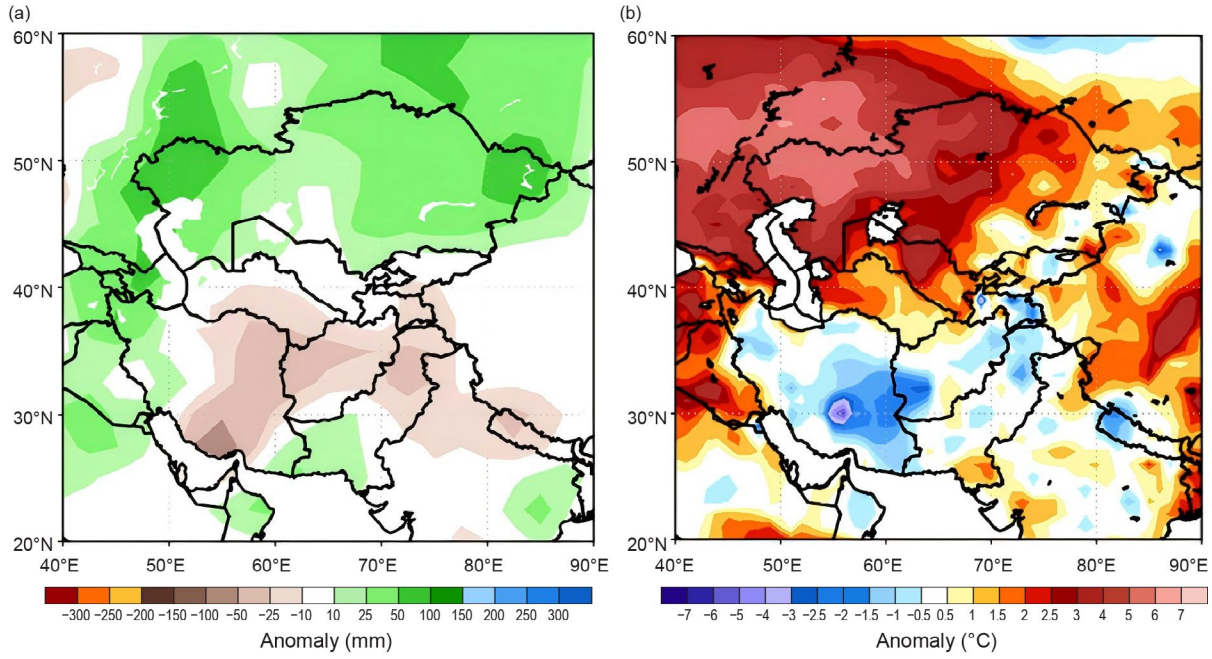

Fig. 7.56. (a) Precipitation anomalies for Jan–Mar 2024 (mm) and (b) mean minimum temperature (°C) for April 2024 for Central Asia. (Source: GPCP for precipitation; NOAA Climate Prediction Center for temperature.)

Unauthenticated | Downloaded 11/21/25 11:34 AM UTC

Sidebar 7.3: **Record-breaking rainfall over South China in April and May 2024**

—Z. ZHU, X. LIU, Y. YANG, K. TAKAHASHI, AND K. TAKEMURA

In April and May 2024, heavy rainstorms swept across South China, resulting in devastating floods. The extreme rainfall caused 53 rivers in Guangdong, Guangxi, and other provinces in southern China to exceed warning water levels. The disaster impacted 2.5 million people and caused direct economic losses of $19.4 billion (U.S. dollars).

The distribution of accumulated rainfall anomalies across South China during April and May 2024 clearly showed remarkable surplus rainfall concentrated over the Guangxi and Guangdong provinces, with maximum anomalies exceeding 600 mm for that period (Fig. SB7.5a). The daily area-mean rainfall over South China (20°N–26°N, 105°E–118°E) largely exceeded the climatology on most days, and the total rainfall was more than twice the climatology and the highest since records began in 1961 (Fig. SB7.5b).

In April and May, East Asia was affected by an anomalous circulation pattern with two anticyclones (high pressure) centered over the Indochina Peninsula and northeast China, respectively (Fig. SB7.5c). To the west of the two southern and northern anticyclones,

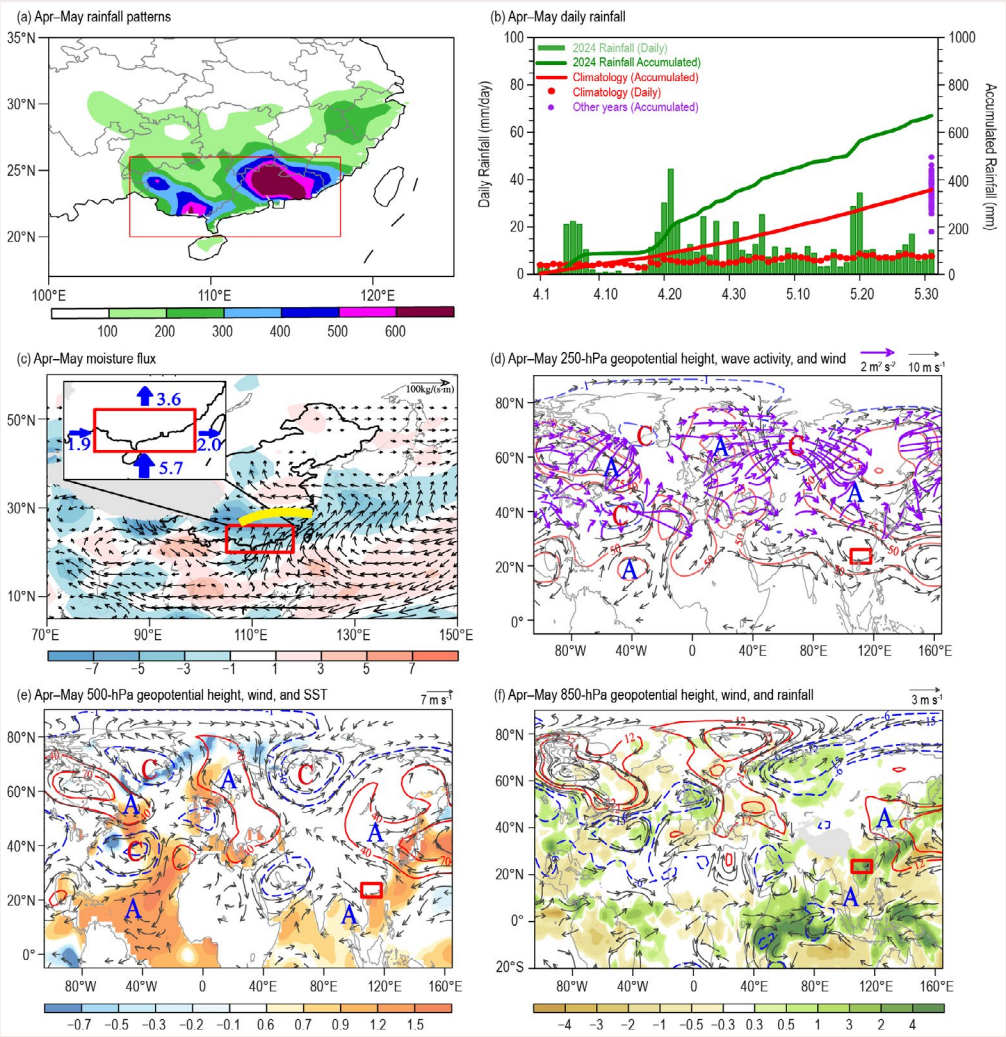

Fig. SB7.5. Top panel: (a) Horizontal distribution of Apr and May 2024 precipitation anomalies (shading; mm). The red box outlines the domain of South China (20°N–26°N, 105°E–118°E). (b) Daily rainfall (bars; mm day^{-1}; left-hand y-axis) and daily accumulated rainfall (green line; mm; right-hand y-axis) over South China during Apr and May 2024. (c) Anomalies of vertically integrated (1000 hPa–700 hPa) vapor flux (vectors; kg m^{-1} s^{-1}) and its divergence (shading; 10–5 kg m^{-2} s^{-1}). The yellow line indicates the horizontal trough. The inset shows the vertically integrated moisture fluxes along north, south, east, and west sides of South China. Bottom panel: Anomalous (d) 250-hPa geopotential height (contours; gpm), wave activity flux (purple vectors; m^2 s^{-2}), and wind (black vectors; m s^{-1}), (e) 500-hPa geopotential height (contours; gpm), wind (vectors; m s^{-1}), and sea surface temperature (shading; °C), and (f) 850-hPa geopotential height (contours; gpm), wind (vectors; m s^{-1}), and precipitation (shading, mm d–1) in Apr and May 2024. The letters "A" and "C" denote the centers of the anticyclonic and cyclonic anomalies, respectively.

Unauthenticated | Downloaded 11/21/25 11:34 AM UTC

a large-scale horizontal trough appeared in between. Steered by the southwesterlies over the northwestern flank of the southern anticyclone, water vapor from the tropical oceans was transported into southern China. Meanwhile, the northern anticyclone hindered the water vapor transportation farther to the north, thereby leading to the enhanced rainfall over southern China.

Associated with the rainfall anomalies were the positive sea surface temperature anomalies (SSTA) over the tropical Indian Ocean and North Atlantic in April and May (Figs. SB7.5d–f). The positive SSTA over the Indian Ocean may induce diabatic heating, which triggered a poleward-declining easterly Kelvin wave and induced the anomalous anticyclone centered over the Indochinese peninsula, thereby transporting sufficient water vapor into eastern China (Figs. SB7.5e,f). The North Atlantic SSTA pattern was linked to a Rossby wave train crossing Eurasia (Fig. SB7.5d), causing an anomalous anticyclone over northeast China (Fig. SB7.5f). The anomalous anticyclone hindered the water vapor from transporting farther to the north, as well as extreme precipitation over southern China.

Unauthenticated | Downloaded 11/21/25 11:34 AM UTC

h. Oceania

—C. Ganter, Ed.

1. OVERVIEW

—C. Ganter

The region of Oceania (Fig. 7.57) began the year with El Niño in place and ended with some possible signs of La Niña (see section 4b for details). However, the rainfall and temperature patterns for the year across the region were not dominated by the El Niño–Southern Oscillation (ENSO) influence.

For Australia, it was the second-warmest year since national records began 1910, while New Zealand reported its 10th warmest since 1909. Both countries were surrounded by very warm ocean waters throughout the year, with a boxed region surrounding Australia (4°S–46°S, 94°E–174°E) observing its warmest year on record, according to NOAA ERSST v5 (Huang et al. 2017) data.

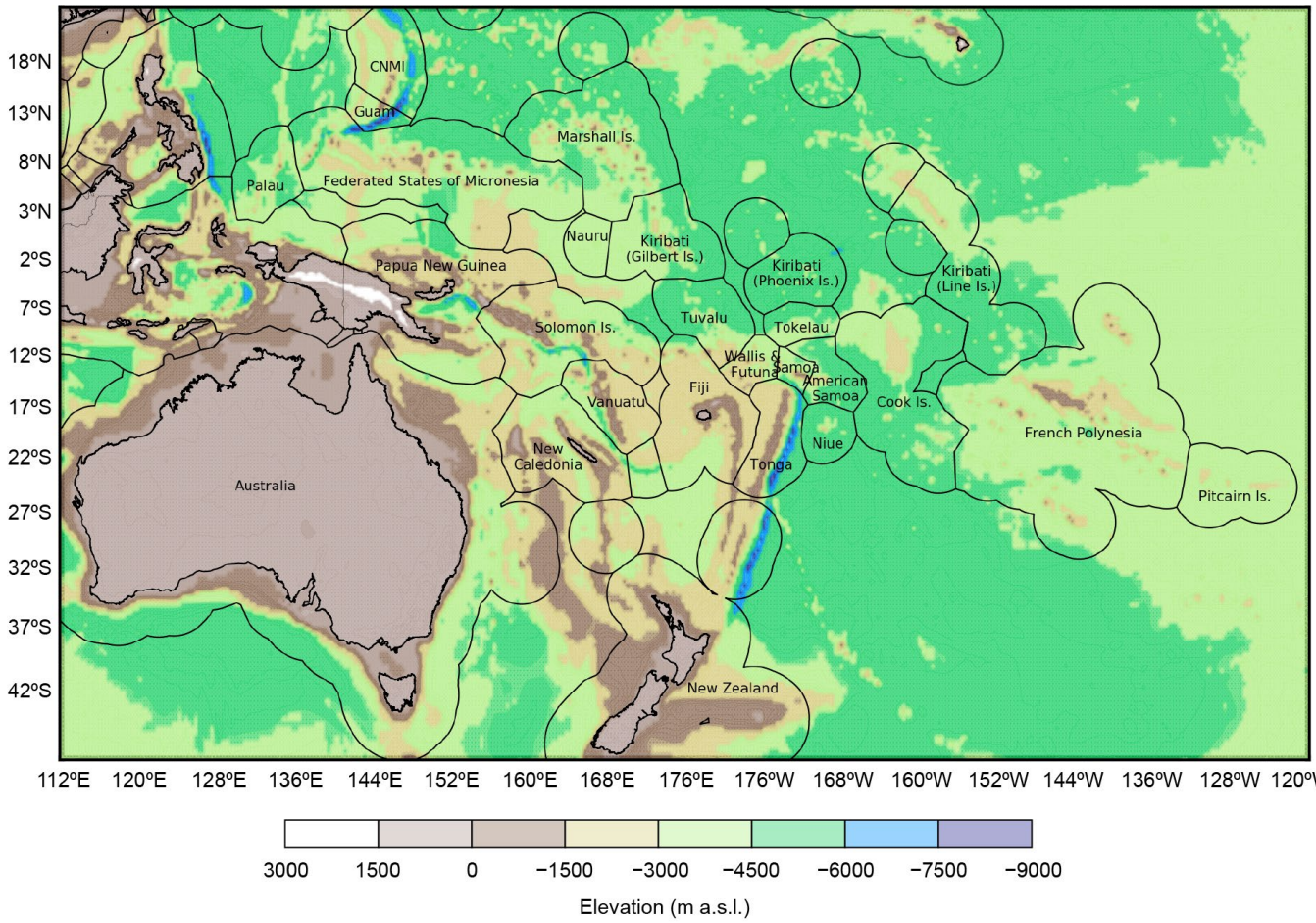

Fig. 7.57. The islands of Oceania. The colors represent topographical heights, with white and brown colors ranging from around 3000 m above sea level (a.s.l) to around –1500 m a.s.l. The yellow, green, and blue indicates greater depths of up to 9000 m below sea level, with blue indicating the lowest depths.

2. NORTHWEST PACIFIC AND MICRONESIA

—B. Bukunt

This assessment covers the area from the dateline west to 130°E, between the equator and 20°N. It includes the U.S.-Affiliated Pacific Islands of Micronesia, but excludes the western islands of Kiribati and nearby northeastern islands of Indonesia (see Fig. 7.57). The temperature analysis is based on data from ERA5 (Hersbach et al. 2020) and scripts developed by NOAA's National Weather Service (NWS). Rainfall data is a combination of NWS station data and the Multi-Source Weighted-Ensemble Precipitation (MSWEP; Beck et al. 2019) analyses as presented by the Bureau of Meteorology (BOM) Pacific Climate Monitoring and the Climate and Oceans Support Program in the Pacific (COSPPac) Online Climate Outlook Forum.

Unauthenticated | Downloaded 11/21/25 11:34 AM UTC

The year 2024 was characterized by a rather atypical, strong El Niño at the beginning followed by a steady progression towards La Niña conditions through the remainder of the year (see section 4b for details). The tropical atmospheric circulation began showcasing La Niña-like attributes as early as September, with continued La Niña growth to round out the year. The Southern Oscillation Index (SOI) returned to positive values in August 2024, in alignment with a typical La Niña-like atmospheric pressure configuration. The interdecadal Pacific oscillation (IPO), which experienced a brief stint of positive values during the 2023/24 El Niño, returned to negative values by May 2024. With the exception of a few El Niño events, the IPO (and similar North Pacific based index known as the Pacific Decadal Oscillation) has been negative since the turn of the twenty-first century. Please refer to this section of the 2023 BAMS *State of the Climate* report for a closer look at the uniqueness of the 2023/24 El Niño.

(i) Temperature

The pattern of surface air temperature anomalies was rather nondescript across Micronesia during 2024, with most areas experiencing temperatures 0.25°C to 1.25°C above normal; however, the far Northern Mariana Islands and waters to their east observed near-normal surface temperatures during the first quarter. Higher sea surface temperature (SST) anomalies linked to the El Niño were evident just east of the dateline during the first quarter, but these SSTs did not stretch into Micronesia during this time.

Temperatures were slightly above normal (0.25°C to 0.75°C) across the Republic of Palau, the Federated States of Micronesia and the Marshall Islands north of 5°N, and the Marianas. Temperature anomalies were 0.75°C–1.25°C above normal in an area generally south of 5°N during the first half of the year, before fragmenting into smaller patches in the second half of the year (Fig. 7.58).

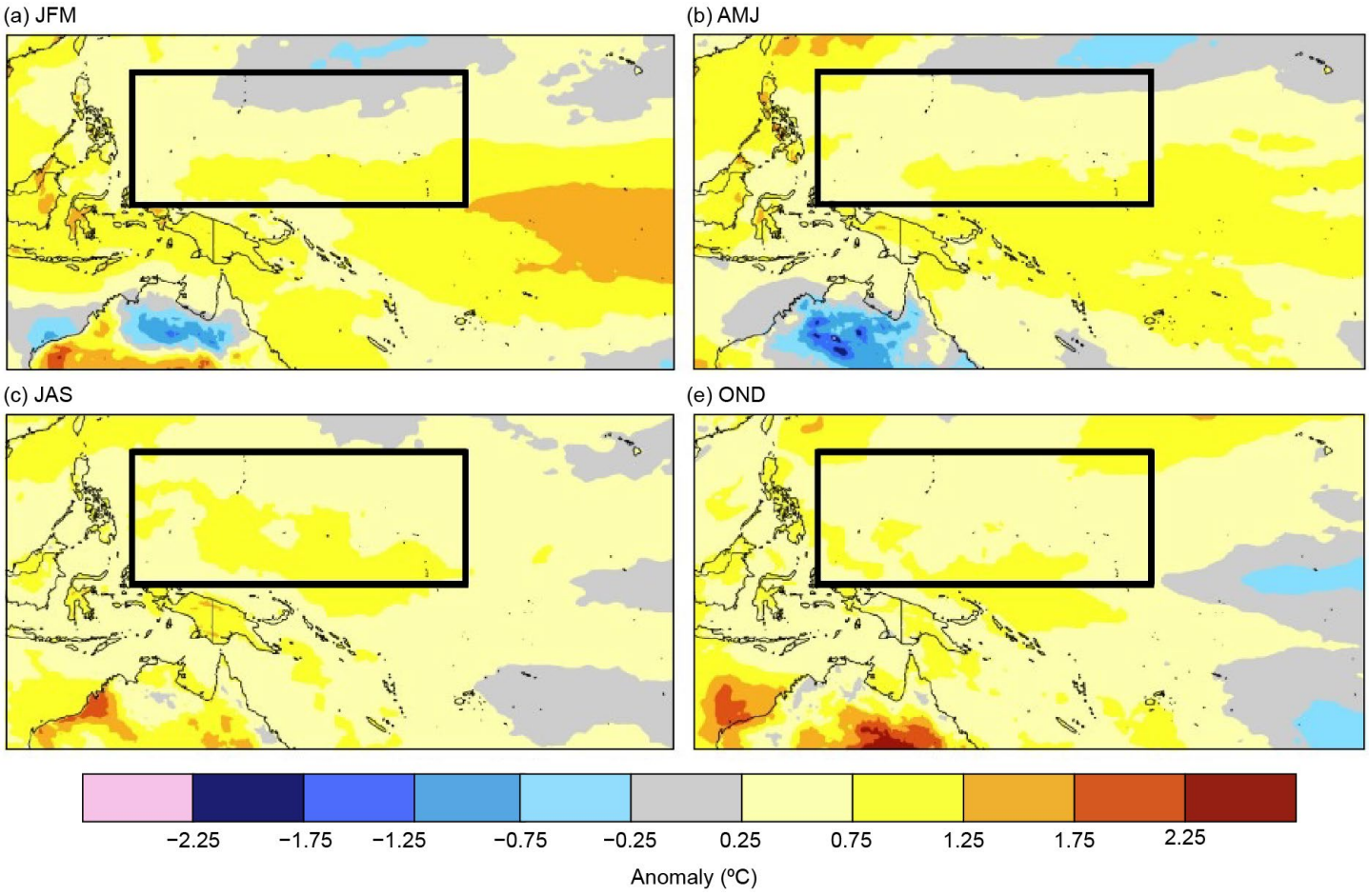

Fig. 7.58. Seasonal air temperature surface anomalies (°C) across the west-central Pacific for (a) Jan–Mar, (b) Apr–Jun, (c) Jul–Sep, and (d) Oct–Dec 2024. The black box in each panel defines the Micronesia region of the northwest Pacific. (Source: ERA5.)

Unauthenticated | Downloaded 11/21/25 11:34 AM UTC

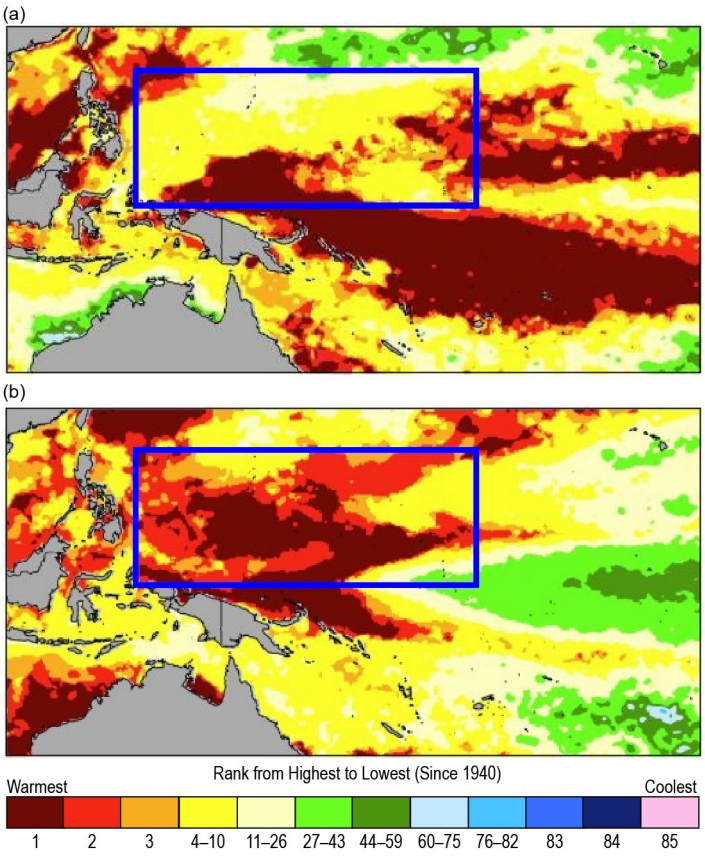

Fig. 7.59. Sea surface temperature rankings in 2024 for (a) Jan–Jun and (b) Jul–Dec. Rankings are based on 84 years of reanalysis data. The blue box in each panel defines the Micronesia region of the northwest Pacific. (Source: ERA5.)

During the first half of 2024, ERA5 reanalysis data highlighted a large area of record-high SSTs extending west-northwestward from the northern islands of French Polynesia and north of Papua New Guinea to islands of Yap State in Micronesia (Fig. 7.59). The record SSTs expanded in coverage across Micronesia during the second half of the year while shrinking in size elsewhere. The NOAA climate sites on Pohnpei and Chuuk observed their highest annual mean temperatures on record, in concert with the aforementioned record-warm ERA5 SST maps.

(ii) Precipitation

Precipitation during the first half of the year generally followed the traditional expectations of a fading El Niño, with slightly drier-than-normal conditions for much of Micronesia (Table 7.4). Although most stations

Table 7.4. Average rainfall total (AVG; mm) compared to rainfall total (mm) and percent of normal values (%) for select Micronesia locations in 2024 (1991–2020 base period) for Jan–Jun, Jul–Dec, and annual (Jan–Dec). Latitudes and longitudes are approximate. "Kapinga" stands for Kapingamarangi Atoll in Pohnpei State, Federated States of Micronesia. Green-filled cells with an up arrow icon (↑) indicate above-average rainfall and yellow-filled cells with a down arrow icon (↓) represent below-average rainfall. (Source: NOAA's National Weather Service.)

Location	Jan–Jun AVG Rainfall (mm)	Jan–Jun 2024 Rainfall (mm)	Jan–Jun % of Normal Rainfall	Jul–Dec AVG Rainfall (mm)	Jul–Dec 2024 Rainfall (mm)	Jul–Dec % of Normal Rainfall	Jan–Dec AVG Rainfall (mm)	Jan–Dec 2024 Rainfall (mm)	Jan–Dec % of Normal Rainfall
Saipan 15°N, 146°E	462.8	424.9 ↓	91.8 ↓	1306.1	1427.2 ↑	109.3 ↑	1768.9	1852.2 ↑	104.7 ↑
Guam 13°N, 145°E	678.7	631.7 ↓	93.1 ↓	1813.6	1917.2 ↑	105.7 ↑	2492.3	2548.9 ↑	102.3 ↑
Palau 7°N, 134°E	1798.1	1698.8 ↓	94.5 ↓	2279.4	2209.0 ↓	96.9 ↓	4077.5	3907.8 ↓	95.8 ↓
Yap 9°N, 138°E	1191.5	601.5 ↓	50.5 ↓	1943.4	2270.5 ↑	116.8 ↑	3134.9	2872.0 ↓	91.6 ↓
Chuuk 7°N, 152°E	1678.2	1456.9 ↓	86.8 ↓	1917.7	1969.8 ↑	102.7 ↑	3595.9	3426.7 ↓	95.3 ↓
Pohnpei 7°N, 158°E	2361.2	2431.0 ↑	103.0 ↑	2308.4	2673.6 ↑	115.8 ↑	4669.6	5104.6 ↑	109.3 ↑
Kapinga 1°N, 155°E	1880.6	2291.1 ↑	121.8 ↑	1485.1	1157.7 ↓	78.0 ↓	3365.7	3448.8 ↑	102.5 ↑
Kosrae 5°N, 163°E	2635.8	2513.1 ↓	95.3 ↓	2354.8	2282.4 ↓	96.9 ↓	4990.6	4795.5 ↓	96.1 ↓
Kwajalein 9°N, 168°E	898.4	842.5 ↓	93.8 ↓	1553.7	1434.1 ↓	92.3 ↓	2452.1	2276.6 ↓	92.8 ↓
Majuro 7°N, 171°E	1459.0	1196.1 ↓	82.0 ↓	1875.0	1961.6 ↑	104.6 ↑	3334.0	3157.7 ↓	94.7 ↓

Unauthenticated | Downloaded 11/21/25 11:34 AM UTC

across Micronesia were drier than normal during the January–June period, they were not overly dry. The one exception was Yap, with only 51% of its normal January–June rainfall. Exceptional drought occurred across Yap State, particularly the islands of western Yap State, such as Yap Proper, Fais, and Ulithi, from early April to early June. MSWEP data (Fig. 7.60) illustrates these rainfall patterns well; however, the signal for below-normal percentiles appear somewhat muted for western Yap State and the accompanying station data and observed drought impacts. This apparent difference is likely tied to the fact that dry conditions peaked during the two-month period from March to April. This March–April period is split between the January–March and April–June figures in the MSWEP data, suppressing the below-normal percentile signal in the maps.

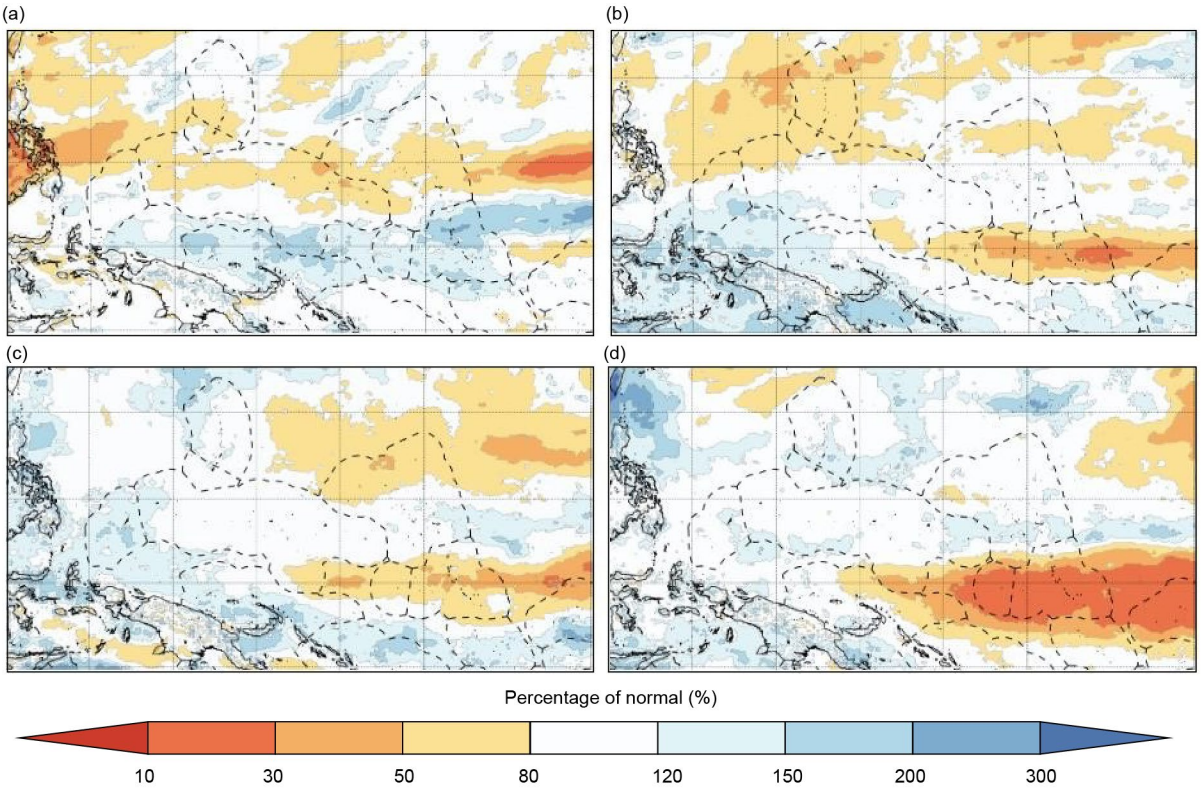

Fig. 7.60. Percent of normal rainfall (%) in 2024 across the central and western Pacific for (a) Jan–Mar, (b) Apr–Jun, (c) Jul–Sep, and (d) Oct–Nov. (Source: Bureau of Meteorology Pacific Climate Monitoring and the Climate and Oceans Support Program in the Pacific [COSPPac]/Multi-Source Weighted-Ensemble Precipitation [MSWEP].)

Station data during the second half of the year also aligned with the general expectations of a transition towards La Niña, with most locations receiving decent rains but not seeing exceptionally wet or dry conditions. Kapingamarangi in the far south of Pohnpei State at 1°N did observe rainfall 78% of normal, a testament of the La Niña-like pattern establishing during the third quarter of 2024.

(iii) Notable events and impacts

An extremely intense North Pacific midlatitude cyclone developed to the north of Micronesia during mid-January. Significant surf-related inundation occurred across Micronesia from eastern Yap State to the Marshall Islands, with major flooding on Kwajalein. Islands of the South Pacific also experienced substantial inundation from this remarkably large, long-period north swell.

The hurricane-force low moved southeastward, with winds of more than 60 kt (51 m s^{-1}) directed towards the Marshall Islands. Seas were well above the wave guidance in overall amplitude and spatial coverage (Fig. 7.61), bringing substantial inundation to coastal areas exposed to swells from a northerly direction; saltwater damaged taro fields in Chuuk and eastern Yap States, and waves damaged homes in Kosrae and Arno Atoll in the Marshall Islands. Much of the islet of Roi Namur, which is located at the north tip of Kwajalein Atoll, was overrun with saltwater.

Unauthenticated | Downloaded 11/21/25 11:34 AM UTC

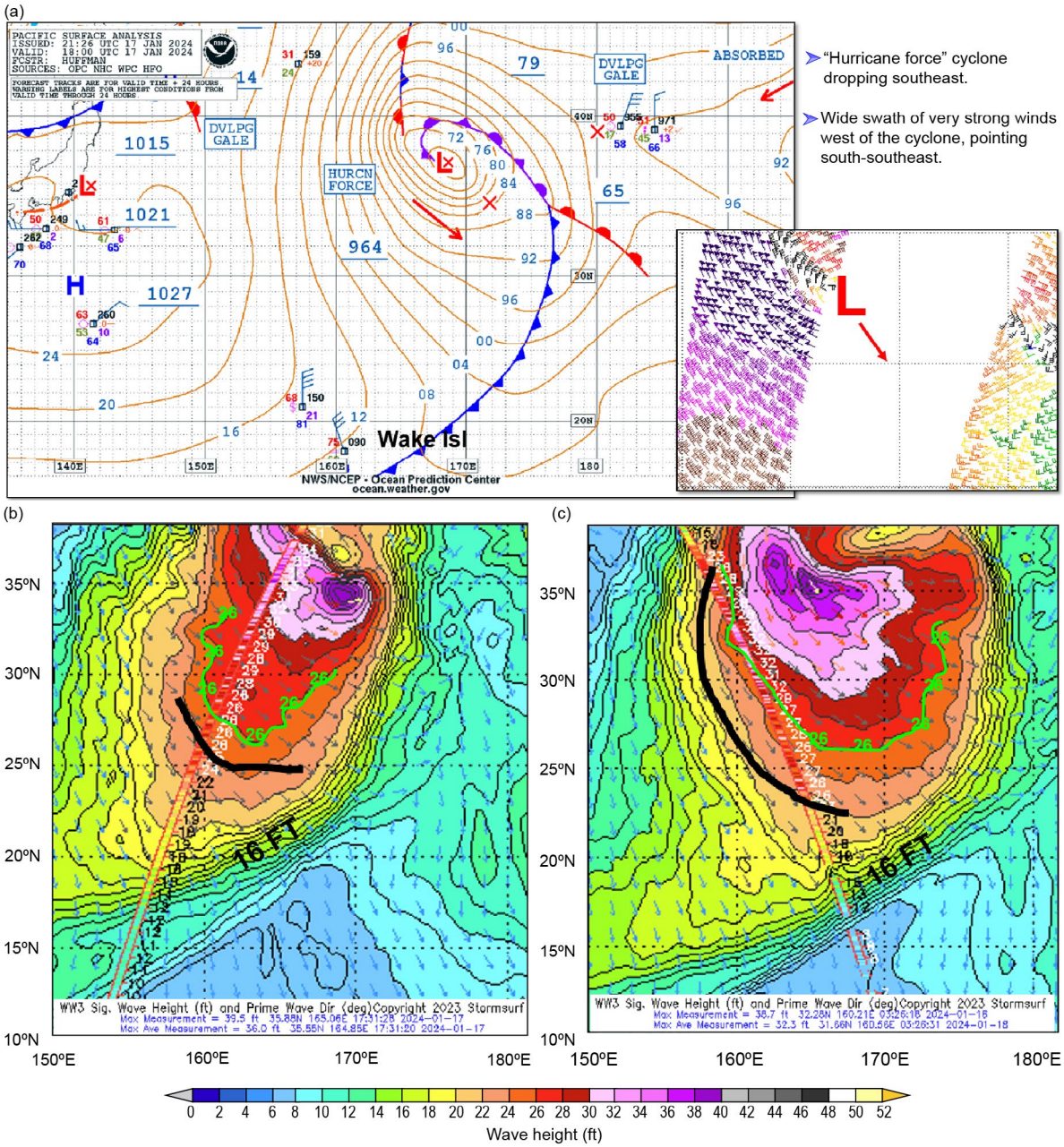

Fig. 7.61. (a) Pacific surface analysis from the National Weather Service Ocean Prediction Center at 1800 UTC on 17 Jan 2024 with corresponding surface wind scatterometer Advanced Scatterometer (ASCAT) data shown in the lower right inset. (b) and (c) show the Global Forecast System-based WaveWatch3 wave model guidance with an overlay of a Jason-3 altimetry pass indicated by a thin strip running top to bottom at (b) 1931 UTC on 17 Jan and (c) 0326 on 18 Jan. The thick green contour indicates the breadth of ~8-m seas based on the wave model guidance, while the thick black contour is the general extent of ~8-m seas assessed from the altimetry data. (Source: [a] NOAA's National Weather Service Ocean Prediction Center, [b] Mark Sponsler).

3. SOUTHWEST PACIFIC

—E. Chandler

Countries considered in this section include American Samoa, the Cook Islands, Fiji, French Polynesia, Kiribati, Nauru, New Caledonia, Niue, Papua New Guinea (PNG), Samoa, the Solomon Islands, Tokelau, Tonga, Tuvalu, Vanuatu, and Wallis and Futuna (Fig. 7.57). The temperature analysis is based on the Climate Anomaly Monitoring System (CAMS) monthly surface air temperature anomalies (https://iridl.ldeo.columbia.edu/maproom/Global/Atm_Temp/Anomaly.html). Anomalies are calculated with respect to the 1991–2020 base period. The precipitation analysis is based on the MSWEP (Beck et al. 2019) monthly analyses as presented for the South Pacific (http://www.bom.gov.au/climate/pacific/outlooks/) and the COSPPac Online Climate Outlook

Unauthenticated | Downloaded 11/21/25 11:34 AM UTC

Forum (https://www.pacificmet.net/products-and-services/online-climate-outlook-forum). The base period for precipitation is 1980–2021.

The year began with a mature El Niño event (see section 4b for details). Atmospheric and oceanic indicators of the event in the Pacific eased through the first quarter of 2024 as they transitioned to ENSO-neutral early in the second quarter. Both sea surface temperatures (SSTs) and air temperatures cooled steadily through the first quarter, eroding the warmth along the equator as the 2023/24 El Niño weakened. Through the second quarter of the year, the equatorial Pacific experienced near-average air temperatures, with a small region of cooler-than-usual temperatures present off the coast of South America along the equator.

Signs of a potential La Niña emerged in the middle of the year as equatorial ocean temperatures continued to cool. However, atmospheric indicators of La Niña lagged the changes in the ocean, with air temperatures, wind, and cloud patterns remaining typical of ENSO-neutral through the third quarter of the year. The rainfall pattern across the Pacific was mixed: while rainfall was suppressed along the equator during the second and third quarters as would be expected with a developing La Niña, the South Pacific Convergence Zone (SPCZ) was persistently located northward of its normal climatological position, resulting in an atypical region of suppressed rainfall between the southern Solomon Islands southeastwards to Tonga during the middle of the year.

While atmospheric patterns showed signs of La Niña emergence in the last quarter of 2024, such as periods of enhanced trade winds, neither atmospheric nor oceanic indicators reached sustained thresholds indicative of a fully coupled event.

(i) Temperature

Along the equator, air temperatures were 1°C above normal on and to the east of the dateline during the first quarter of 2024 (Fig. 7.62a), associated with warmer SSTs in the same region. The region of warm anomalies was at its greatest spatial extent during January, with the warmer-than-normal region shrinking through February and March. A small region of cooler-than-normal air temperatures, with anomalies up to –1°C, was located over French Polynesia during February and March, with air temperatures otherwise near normal across the Pacific overall during the January–March (JFM) period.

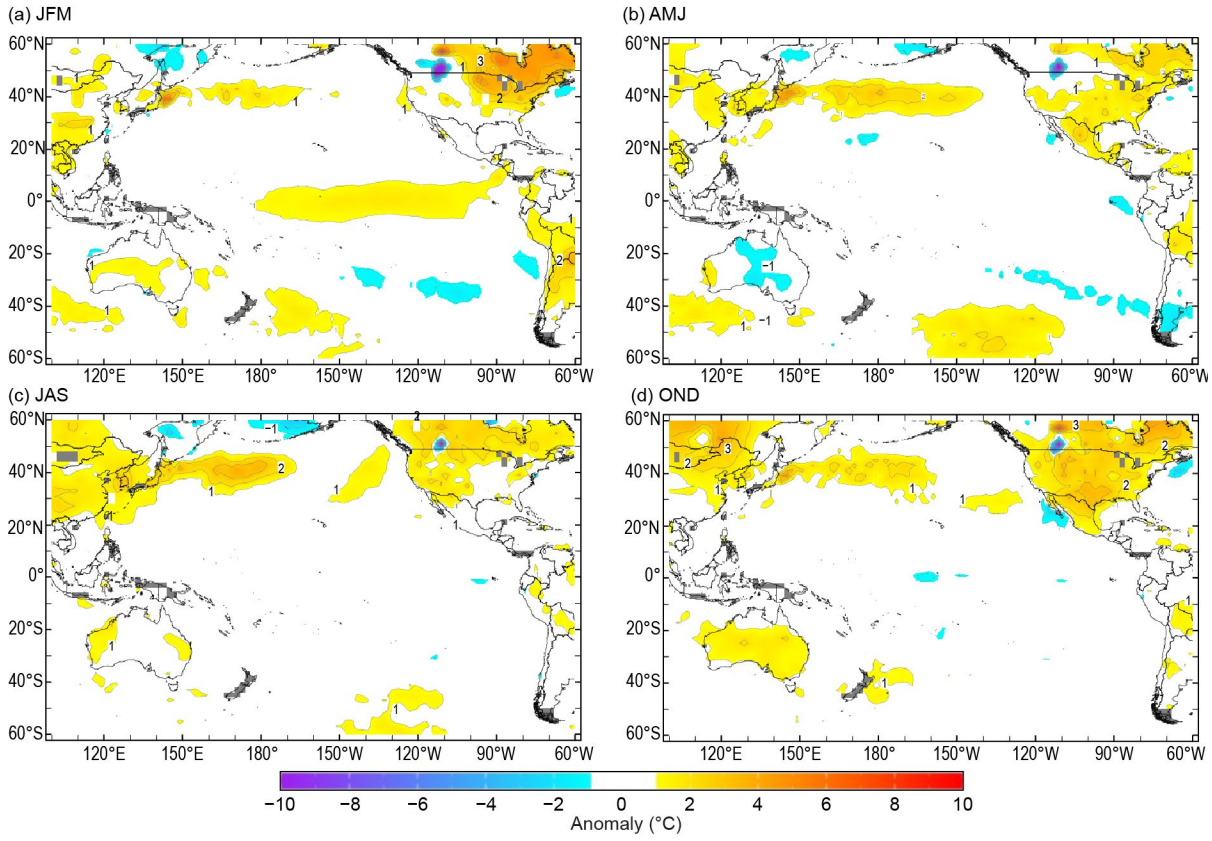

Fig. 7.62. Seasonal air temperature surface anomalies (°C) across the Pacific in 2024 for (a) Jan–Mar, (b) Apr–Jun, (c) Jul–Sep, and (d) Oct–Dec. (Source: Climate Anomaly Monitoring System [CAMS].)

Unauthenticated | Downloaded 11/21/25 11:34 AM UTC

Despite sea surface temperatures remaining relatively warm through the southwest Pacific during April–June (AMJ), air temperatures were near normal across the region (Fig. 7.62b). Small patches of above-normal air temperatures were present during April over Tokelau, central and eastern Kiribati, and the northern Cook Islands; however, these areas of warm anomalies cooled to near normal by May, meaning that AMJ air temperatures overall remained near normal.

During July–September (JAS), near-normal air temperatures persisted across the southwest Pacific (Fig. 7.62c). Small regions of below-normal anomalies were present near eastern Kiribati during October and December, and a region of warmer-than-usual air temperatures was present to the south of Vanuatu during December. Overall, October–December (OND) air temperatures were close to their climatological average across the southwest Pacific (Fig. 7.62d), with the exception of small isolated patches of cool anomalies along the equator.

(ii) Precipitation

As is typical with El Niño events, the Intertropical Convergence Zone (ITCZ) was shifted southward of its usual position at the start of 2024. This shift contributed to enhanced rainfall for the northern Papua New Guinea islands, Nauru, and Kiribati (excluding the southern Line Islands) through the first quarter of the year (Fig. 7.63a). Positive rainfall anomalies were also present over the Solomon Islands, Vanuatu, Fiji, and Tonga, with the largest anomalies occurring in March. Unusually for an El Niño, this second region of atypically persistent positive rainfall anomalies can be attributed to the SPCZ located southward of its normal position, closer to Fiji, as well as two strong Madden–Julian Oscillation (MJO) events impacting the southwest Pacific in mid-January and mid-March. In Fiji, five stations recorded their highest JFM rainfall on record. In Tonga, two stations recorded their wettest JFM, and Vanuatu had one station (Pekoa) that recorded its wettest JFM in the 54-year record with 1724 mm of rainfall.

The rainfall pattern through the southwest Pacific was mixed during the second quarter of the year, associated with the transition to ENSO-neutral (Fig. 7.63b). AMJ rainfall was enhanced in a band near 10°S, stretching from Papua New Guinea eastward through the Solomon Islands, northern Fiji, Tuvalu, Tokelau, and the central and northern Cook Islands. This enhanced rainfall was associated with persistently warm sea surface temperatures in the off-equatorial southwest Pacific during the quarter. Auki (Solomon Islands) recorded its wettest AMJ on record (62 years)

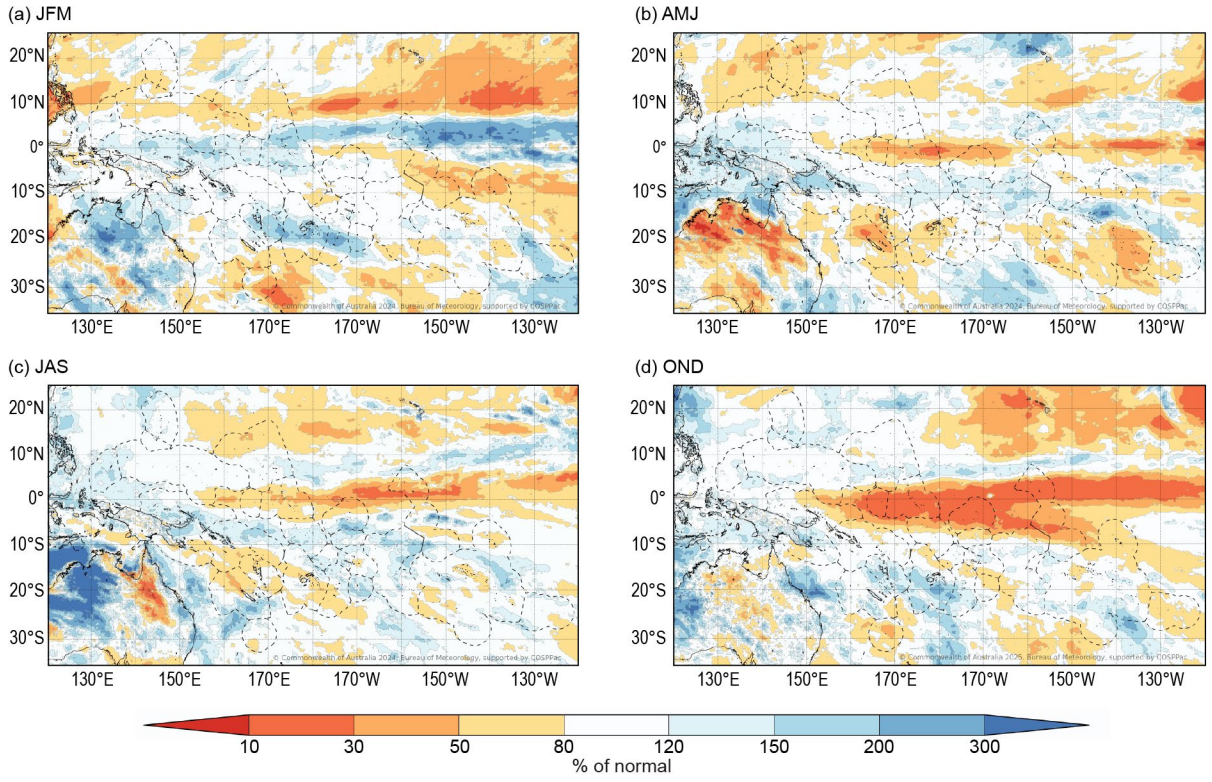

Fig. 7.63. Seasonal percent of normal rainfall (%) across the southwest Pacific in 2024 for (a) Jan–Mar, (b) Apr–Jun, (c) Jul–Sep, and (d) Oct–Dec. (Source: Multi-Source Weighted-Ensemble Precipitation [MSWEP].)

Unauthenticated | Downloaded 11/21/25 11:34 AM UTC

with 1135 mm. Stations in eastern Papua New Guinea and Tuvalu also had rainfall recorded in their top 10% during the season. Conversely, rainfall remained suppressed over Nauru, the Gilbert Islands (Kiribati), and the northern Phoenix Islands (Kiribati) along the equator. Farther south, Vanuatu, New Caledonia, Fiji, Tonga, the southern Cook Islands, and central and southern French Polynesia recorded suppressed rainfall anomalies over the quarter. Stations in both Fiji and Tonga recorded rainfall in their lowest 10% on record.

The rainfall pattern for JAS remained largely unchanged when compared to the second quarter of 2024 (Fig. 7.63c). Suppressed rainfall persisted on and to the east of the dateline along the equator, as well as farther south over the southern Solomon Islands, Vanuatu, northern New Caledonia, Fiji, and Tonga. Butaritari (Kiribati) and Kiritimati (Kiribati) both recorded rainfall in their bottom 10% on record. The band of enhanced rainfall from Papua New Guinea eastwards through the northern Solomon Islands, Tuvalu, Wallis and Futuna, Samoa, and Tokelau also persisted from the second quarter to the third. Nadzab (Papua New Guinea) had its wettest JAS in 49 years of records, with 790 mm.

Rainfall patterns during the last quarter of 2024 reflected a La Niña-like pattern emerging in the Pacific. Rainfall during OND was suppressed over the width of the Pacific extending from South America westward, including Kiribati and Nauru (Fig. 7.63d). Rainfall was also suppressed over Niue, the northern Cook Islands, and patches of northern French Polynesia. Off the equator, rainfall was strongly enhanced over Papua New Guinea, most of Vanuatu, Fiji, and Tonga, particularly during December, associated with a slow-moving MJO event and a tropical disturbance impacting the region. Several stations in Fiji recorded rainfall in their top 10th percentile over the OND period.

(iii) Notable events and impacts

For the South Pacific, the year 2024 was most notable for being the first year since 2009 that did not record a severe tropical cyclone; it was also the least active calendar year since reliable records began in 1979/80. There were only two named tropical cyclones, the most significant being Tropical Cyclone Nat, which reached Category 2 status.

4. AUSTRALIA

—C. Minney

For this section, monthly area-averaged temperatures are based on the Australian Climate Observations Reference Network–Surface Air Temperature (ACORN-SAT) dataset (Trewin 2018), while mapped temperature analyses are based on the Australian Water Availability Project (AWAP) dataset (Jones et al. 2009), both of which begin in 1910. Area-averaged rainfall values and mapped rainfall analyses use the Australian Gridded Climate Data (AGCD) dataset (Evans et al. 2020), which begins in 1900. Anomalies are based on the 1991–2020 average.

(i) Temperature

The year 2024 was Australia's second-warmest on record since national records began in 1910 with the area-averaged mean temperature 0.83°C above the 1991–2020 average (Fig. 7.64). It was the warmest year since national records began for Queensland, with all other states observing one of their five warmest years on record. Nationally, the area-averaged annual mean maximum temperature (Fig. 7.65) was 0.76°C

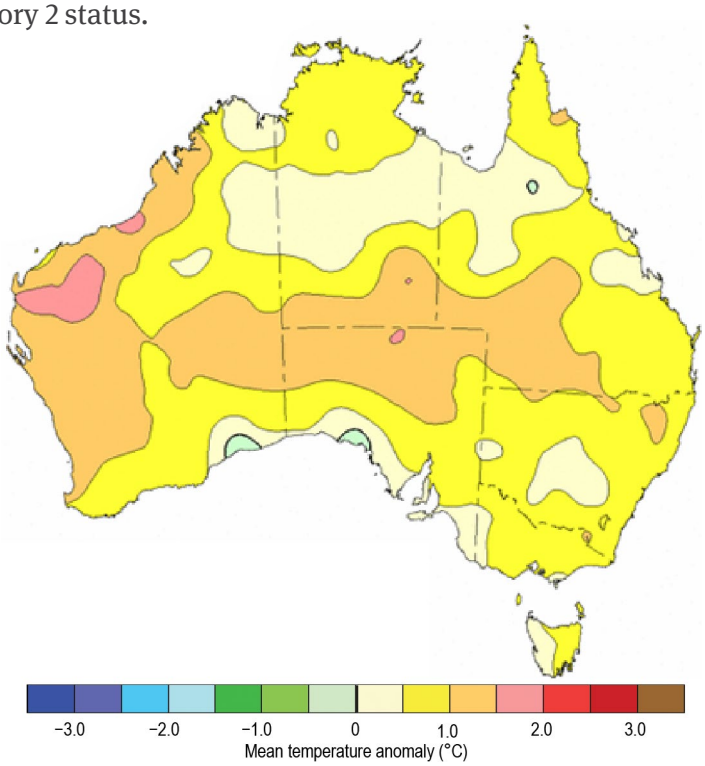

Fig. 7.64. Mean temperature anomalies (°C) for Australia, averaged over 2024, relative to a 1991–2020 base period. Australian States/Territories are as follows, starting in a clockwise fashion from the west: Western Australia, the Northern Territory, Queensland, New South Wales, Victoria, and South Australia, with the island of Tasmania in the southeast. (Source: Australia's Bureau of Meteorology.)

Unauthenticated | Downloaded 11/21/25 11:34 AM UTC

above average. The area-averaged annual mean minimum temperature (Fig. 7.66) was 0.89°C above average, the highest since records began in 1910.

Annual maximum temperature anomalies were positive across most of Australia, excluding some areas across the Northern Territory, northern Western Australia, and western Queensland, where temperatures up to 1°C below average were recorded. Positive anomalies of +1°C to +2°C were recorded across western parts of Western Australia, central and southeast South Australia, southern Northern Territory, central Queensland, and a region covering the New South Wales–Victoria border. Annual minimum temperature anomalies were positive across most of Australia except for some small areas across the southern mainland and central Queensland, where the annual mean minimum temperature was up to 1°C below average. Minimum temperatures were up to 2.5°C above average across northwestern Western Australia and up to 2°C warmer than average across central Australia.

The national mean monthly temperature for the months of January to March and August to December were each among their 10 warmest on record. April and July were the only months where the area-averaged national mean temperature was below the 1991–2020 average.

Nationally averaged, it was the second-warmest winter (June–August; JJA) on record for the country as a whole. It was the warmest winter on record for Western Australia. Persistent high-pressure systems and above-average sea surface temperatures, in addition to warming temperatures globally, contributed to the warmer-than-average conditions throughout most of 2024 in Australia. August 2024 was Australia's warmest August on record (see Sidebar 7.4). However, there were some below-normal temperatures during winter as well. In June, minimum temperatures were below average across large areas of eastern and northern Australia. There was also notable overnight cold at times in July in both northern and southern Australia. On 4 July, Liawenee reached –13.5°C, the second-lowest temperature ever recorded in Tasmania, and on 18 July, Palmerville in northern Queensland observed 0.5°C, the lowest temperature at that location since 1913.

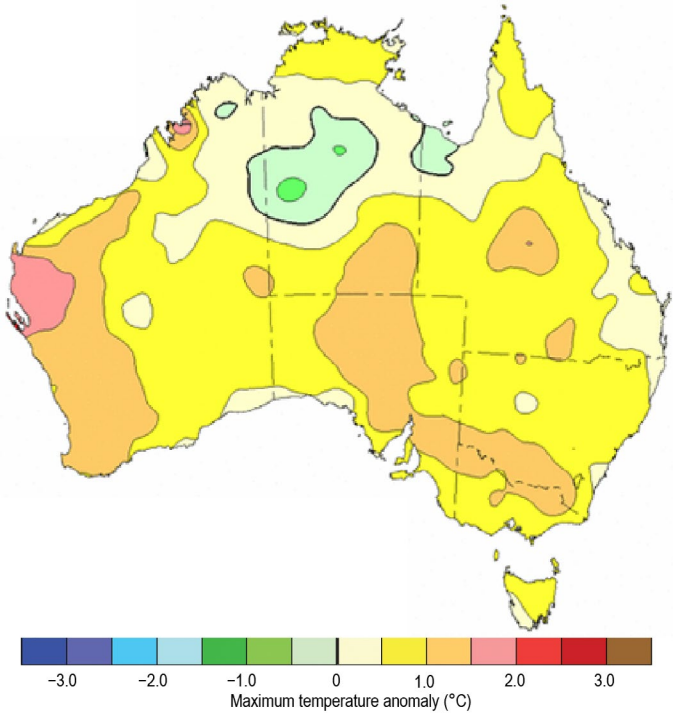

Fig. 7.65. Maximum temperature anomalies (°C) for Australia, averaged over 2024, relative to a 1991–2020 base period. (Source: Australia's Bureau of Meteorology.)

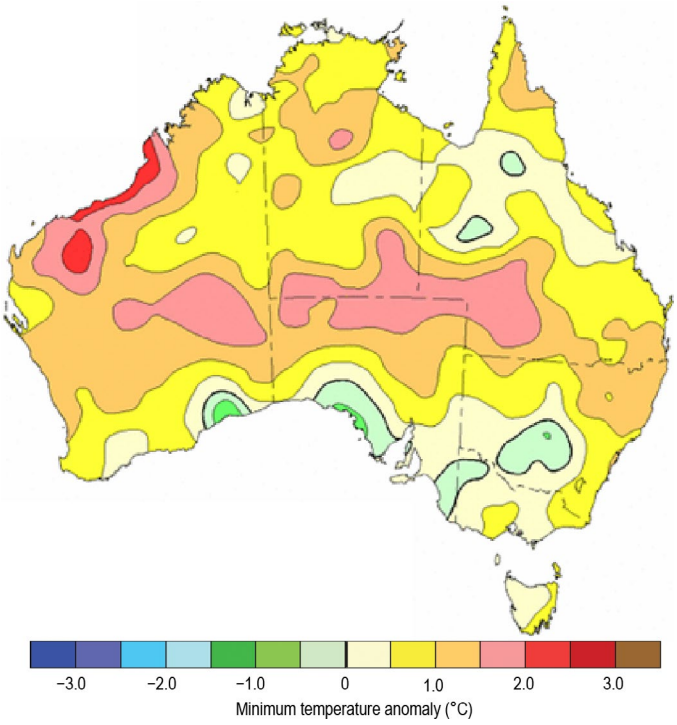

Fig. 7.66. Minimum temperature anomalies (°C) for Australia, averaged over 2024, relative to a 1991–2020 base period. (Source: Australia's Bureau of Meteorology.)

April mean temperatures were below average across much of Australia, attributed to a series of slow-moving high-pressure systems to the south of the mainland that directed southerly airflow over the country and increased nighttime cooling.

Unauthenticated | Downloaded 11/21/25 11:34 AM UTC

Nationally averaged, it was the warmest spring (September–November; SON), driven in part by the second-warmest October on record. It was also the warmest spring on record for Queensland.

(ii) Precipitation

Nationally, the area-average annual rainfall total for Australia during 2024 was 598.7 mm. This was the eighth-wettest year on record, 21.9% above the 1991–2020 average of 491.3 mm.

Compared to the distribution across all 125 years of observations (1900–2024), rainfall in 2024 (Fig. 7.67) was above average (top 30% of records) across most of the Northern Territory, most of Western Australia excluding the west of the state, northern, western, and southern Queensland, central parts of New South Wales, and parts of northern South Australia. It was the fourth-wettest year on record for the Northern Territory, with parts of the central west regions observing their wettest year. Rainfall was below average (bottom 30% of records) across much of the southern mainland, far western Tasmania, and northwestern coastal Western Australia. It was the driest year on record for parts of southern South Australia. Cool-season (April–October) rainfall was below average for much of the southern mainland, impacting water availability during the growing season for much of this region.

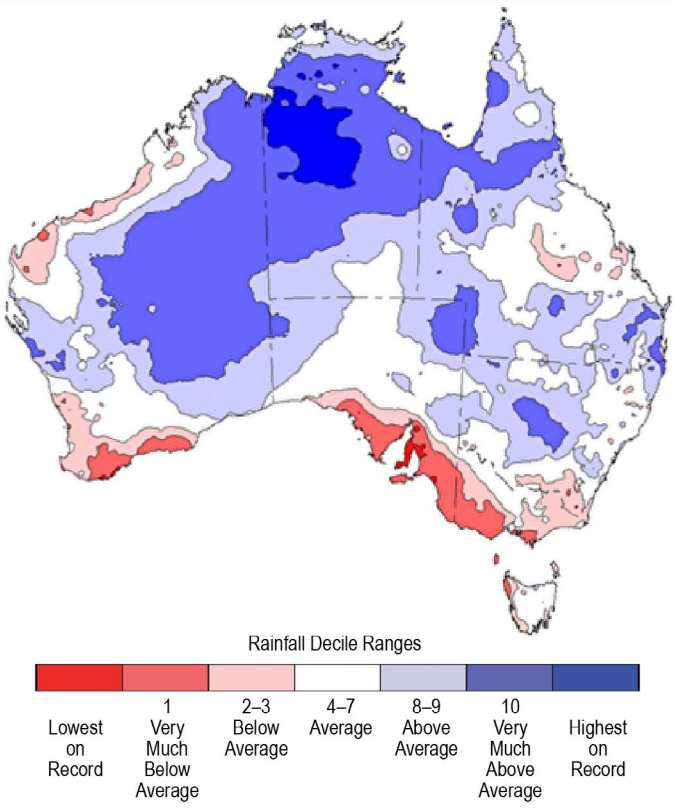

Fig. 7.67. Rainfall deciles for Australia for 2024, based on the 1900–2024 distribution. (Source: Australia's Bureau of Meteorology.)

January 2024 was Australia's ninth-wettest January on record, with drier-than-normal conditions observed only over western parts of Western Australia. February was close to average, and was followed by the third-wettest March on record, with record-high March rainfall for parts of the Northern Territory and Western Australia.

Persistent, slow-moving high-pressure systems were a major feature of atmospheric circulation and subsequent rainfall across Australia in 2024. In April and May, high-pressure systems interacted with low-pressure troughs, bringing persistent and heavy rainfall to coastal New South Wales but below-average rainfall elsewhere across most of southern Australia.

Winter (JJA) rainfall was below average across much of southeastern Australia, with Victoria seeing its driest winter since 2006. Spring (SON) rainfall was above average for much of Western Australia and the Northern Territory, including the wettest spring on record for parts of inland Western Australia. It was a drier-than-average spring for large parts of the southern mainland. The year concluded with above-average rainfall across much of Australia during December, including Tasmania's wettest December since 2005.

There were several significant influences on Australia's climate in 2024. These included the breakdown of the 2023/24 El Niño, followed by a weak La Niña-like pattern that emerged late in 2024. Cooling of SSTs and a subsequent atmospheric response was delayed to late December. Hence, the ENSO is not considered to have been a dominant influence on Australia's climate patterns during 2024. During October and early November, the Indian Ocean dipole (IOD) index was below the negative IOD threshold (–0.4°C) for seven weeks. While not long enough to officially be considered an IOD event, the negative IOD index may have contributed to wet conditions in central and northern Western Australia.

The Southern Annular Mode (SAM) was negative during several periods in 2024. This included an extended negative phase (SAM index less than –1) from late July to mid-August, with significant, record negative values during August associated with a significant stratospheric warming episode. A negative SAM typically increases rainfall over much of southern Australia during

Unauthenticated | Downloaded 11/21/25 11:34 AM UTC

winter (Hendon et al. 2007; Risbey et al. 2009). Rainfall was above average for southwest Western Australia and most of Tasmania but below average across much of southern Australia during August 2024. The SAM briefly returned to a negative phase during late September and again for much of December.

(iii) Notable events and impacts

Tropical Cyclone Kirrily crossed the north Queensland coast in late January, stalling as it moved over Queensland's interior. Its slow progression brought significant humidity, heavy rainfall, and flooding to the region. Its moisture interacted with low-pressure troughs stretching across the state, resulting in severe thunderstorms and heavy rainfall through central and southeastern Queensland and northeastern New South Wales.

Tropical Cyclone Lincoln was a long-lasting system that briefly reached tropical cyclone intensity as it crossed the southern Gulf of Carpentaria coast in mid-February. Tropical Cyclone Megan formed in March, making landfall as a Category 3 system across the southwestern Gulf of Carpentaria in the Northern Territory, close to where Lincoln had crossed several weeks earlier. Heavy rainfall from ex-Tropical Cyclone Megan resulted in record flooding in the McArthur River at Borroloola, where the community was largely evacuated. Heavy rains from both Lincoln and Megan combined with numerous other rain events during the first part of the year to contribute to extensive and long-lived flooding in many parts of the Northern Territory, with a number of remote communities inundated and substantial disruptions to road and rail transport. See sections 4g7 and 4g8 on tropical cyclone activity in the region.

Heatwave conditions impacted Western Australia during February. Record-high temperatures included 49.9°C at Carnarvon and 49.3°C at Geraldton, both on 18 February. The value at Carnarvon was tied with the eighth-highest temperature ever recorded in Australia.

Heatwave conditions were present through much of October across much of northern Australia. Persistent, intense heat continued through November and late December, with heat shifting towards the south of Australia, resulting in high fire danger and the outbreak of fires in parts of western Victoria. Severe thunderstorms impacted Queensland and New South Wales throughout October and December.

5. AOTEAROA NEW ZEALAND

—G. Macara

(i) Temperature

The year 2024 was New Zealand's 10th warmest on record, based on the mean temperature from the National Institute of Water and Atmospheric Research's (NIWA) seven-station series, which began in 1909. The nationwide average temperature for 2024 was 13.25°C, 0.51°C above the 1991–2020 annual average. Annual mean temperatures were above average (0.51°C–1.20°C above the annual average) for much of Northland, northern Waikato, Bay of Plenty, coastal Hawke's Bay, southern Taranaki, Whanganui, eastern and southern Wairarapa, Tasman, inland northern Canterbury, Banks Peninsula, and eastern Otago. Near-average (±0.50°C of average) temperatures occurred elsewhere (Fig. 7.68).

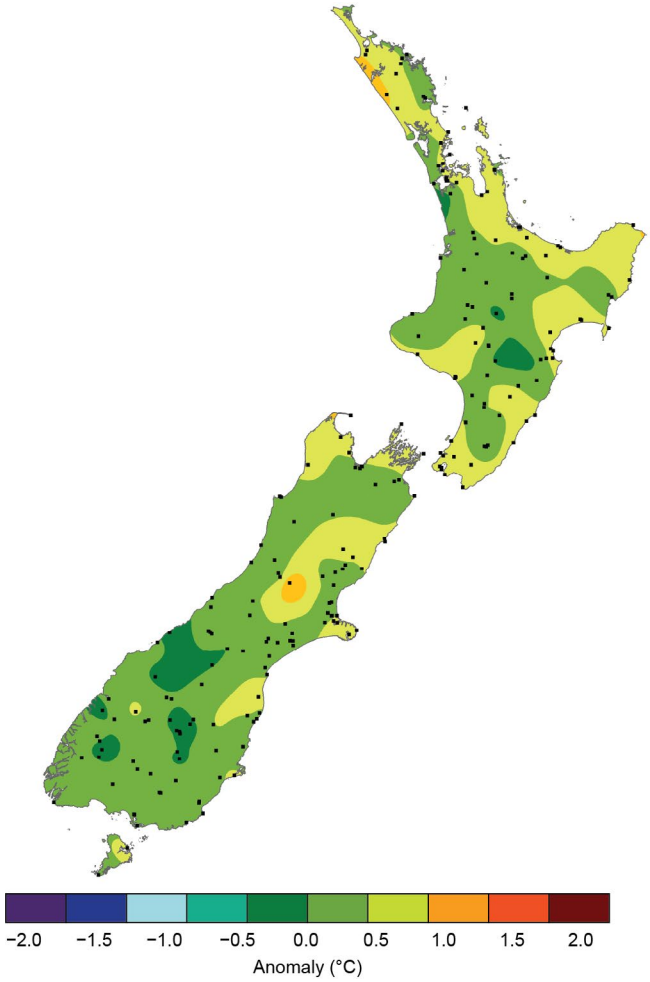

Fig. 7.68. Annual average temperature anomaly (°C) for New Zealand for 2024 relative to the 1991–2020 base period. The black dots represent the locations of climate stations used to create both the temperature and rainfall maps.

Unauthenticated | Downloaded 11/21/25 11:34 AM UTC

Relatively cool conditions took hold during March and May. More frequent southwesterly winds than normal during these months resulted in New Zealand's coolest March in 12 years and coolest May in 15 years. In contrast, regular northerly airflows contributed to the country's third-warmest winter on record. Most notably, Hastings (Hawke's Bay) recorded a maximum temperature of 25.7°C on 10 June—this was New Zealand's highest June temperature on record and second-highest temperature for the austral winter season overall. The highest temperature of 2024 was 37.0°C, recorded on 5 February at Hanmer Forest (Canterbury). The lowest air temperature of the year was –11.8°C, recorded at Lake Tekapo (Canterbury) on 3 August.

(ii) Precipitation

Annual rainfall totals for 2024 were below normal (50%–79% of the annual normal) for much of eastern and northern Canterbury, Tasman, Wairarapa, Bay of Plenty, the Coromandel Peninsula, and Northland. Two locations, both in Northland, observed their driest year on record. Another eight locations observed near-record low annual rainfall totals (in the lowest four on record). Annual rainfall was above normal (120%–149%) for southwestern parts of the South Island, with near-normal annual rainfall (80%–119%) for most remaining areas of the country (Fig. 7.69). Of the regularly reporting rainfall gauges, the wettest location in 2024 was Cropp River in the Hokitika River catchment (West Coast, South Island, 975 m above sea level), with an annual rainfall total of 11,503 mm. The driest of the regularly reporting rainfall sites was Alexandra (Central Otago) and Bromley (eastern Christchurch), which both recorded 354 mm of rainfall.

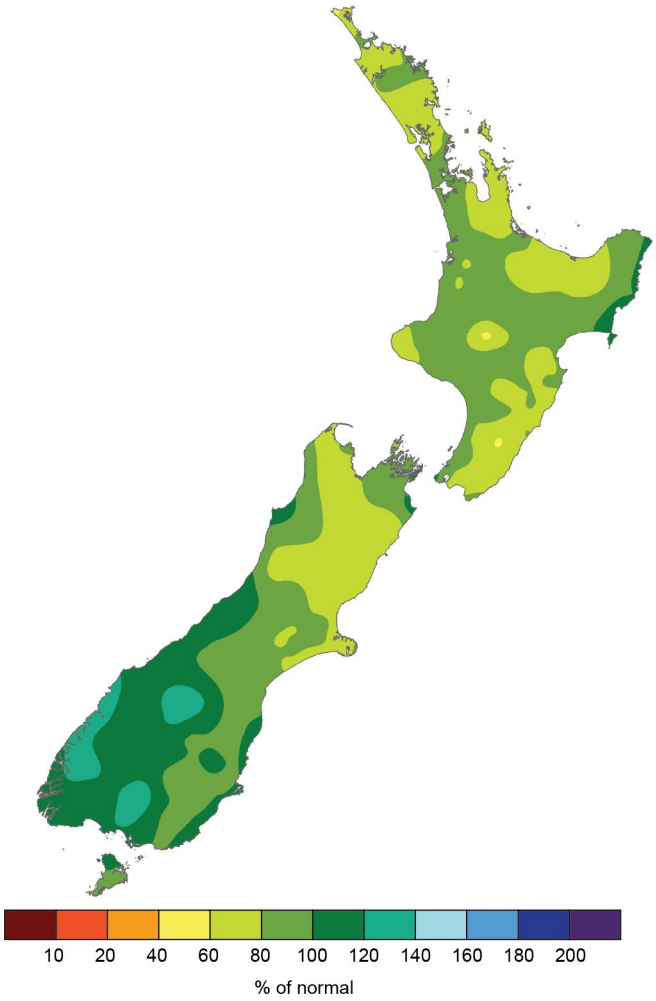

Fig. 7.69. Annual total rainfall (% of normal) for New Zealand for 2024 relative to the 1991–2020 base period.

(iii) Notable events and impacts

After prolonged warmer- and drier-than-usual conditions during the two preceding months, a wildfire ignited in the Port Hills near Christchurch on 14 February. The fire initially required 130 firefighters on the ground and 11 helicopters, and a State of Local Emergency was declared for Christchurch City and the Selwyn District. Around 30 properties were evacuated.

From 25 to 26 June, heavy rainfall associated with a low-pressure system caused severe impacts for much of Gisborne and Hawke's Bay. In Wairoa in the Hawke's Bay region, at least 400 properties were affected by flooding, with hundreds of residents evacuated from their homes. A local state of emergency was declared for Wairoa, with power turned off in the town due to floodwaters putting substations at risk. Farther south, a regional state of emergency was declared for the Heretaunga area of Hastings after high swells and high tide combined to cause inundation of low-lying areas. Numerous roads were affected by flooding and slips including State Highway (SH) 2 from Te Karaka to Waipaoa, SH2 at Wairoa, SH5 from Eskdale to Waipunga, SH35 from Okitu to Tolaga Bay and Tikitiki to Te Araroa, and SH51 at Clive.

From 8 to 21 July, freezing fog and black ice were regularly reported for inland parts of the South Island, especially about the Mackenzie Basin and Central Otago. The icy conditions were associated with an exceptionally strong high-pressure system, which prevailed over the South

Unauthenticated | Downloaded 11/21/25 11:34 AM UTC

Island for nearly two weeks. On the evening of 10 July, Ranfurly recorded a mean sea level pressure of 1046.5 hPa—a record barometric high for the nation.

During 3–4 October, a low-pressure system centered east of the South Island delivered persistent and heavy rain over southeastern parts of the South Island. A state of emergency was declared in Dunedin and the Clutha District. In Dunedin, two welfare centers opened for about 70 residents who evacuated their properties due to flooding. Eleven properties were red-stickered (i.e., access was prohibited), with a further 31 properties yellow-stickered (i.e., access was restricted). Approximately 40 roads in Dunedin were closed due to flooding.

Unauthenticated | Downloaded 11/21/25 11:34 AM UTC

Sidebar 7.4: **Australia's warm end to winter**
—C. MINNEY

August 2024 brought Australia a very warm end to the austral winter. The Australian mean temperature anomaly for August was 2.44°C above the 1991–2020 average; this marked the warmest August on record since national observations began in 1910 and broke the previous record by around 0.5°C.

From 20 August, a slow-moving high-pressure system resulted in persistent clear skies across the interior of Australia, allowing heat to build up to significantly above-average daytime temperatures (Fig. SB7.6). These temperatures were more typical of a month late in the austral spring like November, rather than what would be expected in August. Maximum temperatures of at least 40.0°C were recorded on 20 occasions during the month, including a national August record of 41.6°C on the 26th at Yampi Sound in northern Western Australia. This is also the highest temperature ever recorded in winter Australia-wide. Prior to 2024, 40.0°C had only been reached four times in August.

The previous record-high Australian area-average August daily maximum temperature of 29.9°C (on 31 August 2009) was exceeded on six days in 2024, peaking at 31.3°C on 29 August. This reflects the widespread nature of the warmth across the country. While the peak of the heat mostly affected central Australia, August was warmer than average across almost all of Australia (Fig. SB7.7). Heatwave conditions continued for the remainder of the year; however, the August heat was particularly notable for its magnitude and extent, as well as the unusual time of year.

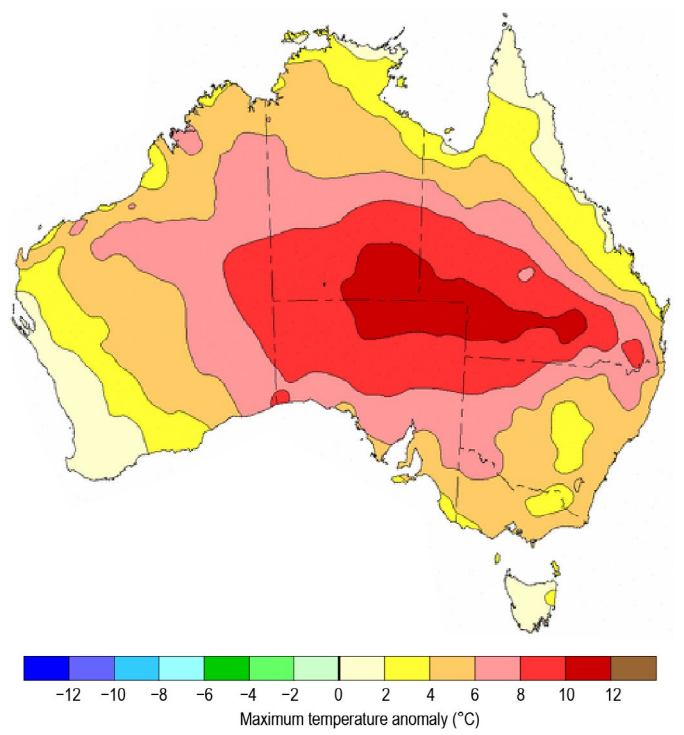

Fig. SB7.6. Maximum temperature anomalies (°C) for Australia relative to the 1991–2020 base period for the week ending on 29 Aug 2024. (Source: Australia's Bureau of Meteorology.)

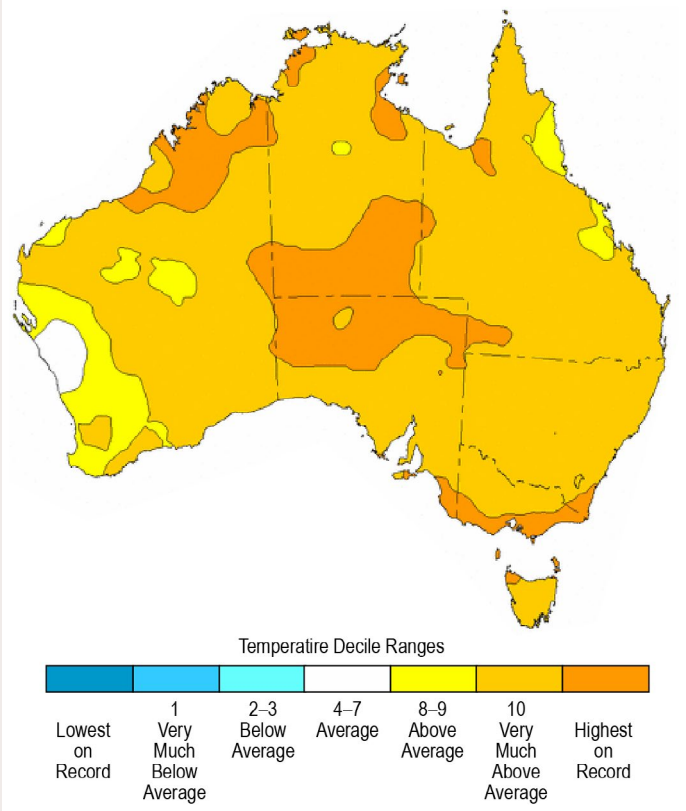

Fig. SB7.7. Maximum temperature deciles for Australia for Aug 2024 based on the 1910–2023 distribution. (Source: Australia's Bureau of Meteorology.)

Unauthenticated | Downloaded 11/21/25 11:34 AM UTC

Acknowledgments

Europe

Much of the information in this section is based on national climate reports kindly provided by the National Meteorological and Hydrological Services (NMHSs) of the World Meteorological Organization (WMO) Regional Association (RA) VI region. The information has been compiled at the WMO RA VI Regional Climate Centre (RCC) Node on Climate Monitoring, located at Deutscher Wetterdienst (DWD) in Germany. National contributions have been made to the cooperation between NMHSs and the RCC. https://rcccm.dwd.de/DWD-RCCCM/EN/products/reports/monthlyreports_national.html?nn=500112

Unauthenticated | Downloaded 11/21/25 11:34 AM UTC

Appendix 1: Acronyms

10km-CaPA	10-km gridded numerical precipitation analysis
ACORN-SAT	Australian Climate Observations Reference Network–Surface Air Temperature
AGCD	Australian Gridded Climate Data
AHAC	Honduran Civil Aeronautics Agency
AWAP	Australian Water Availability Project
BOM	Bureau of Meteorology
C3S	Copernicus Climate Change Service
CA	Central America
CAMS	Climate Anomaly Monitoring System
CANGRD	Canadian Gridded Temperature and Precipitation Anomalies
CA-NWS	Central America National Weather Services
CAR	Central African Republic
CariCOF	Caribbean Climate Outlook Forum
CEMADEN	National Center for Natural Disaster Monitoring and Alerts
CHIRPs	Climate Hazards and Infrared Precipitation
CIIFEN	International Center for Research on the El Niño Phenomenon
CNE	National Commission for Risk Prevention and Emergency Response
CONAFOR	National Forestry Commission (Mexico)
CONRED	National Coordination for Disaster Reduction (Guatemala)
CONUS	contiguous United States
COPECO	Permanent Contingency Commission of Honduras
COSPPac	Climate and Oceans Support Program in the Pacific
DMC	Meteorological Directorate of Chile
DMH	Directorate of Meteorology and Hydrology
DRC	Democratic Republic of the Congo
DWD	Deutscher Wetterdienst
ECCC	Environment and Climate Change Canada
EM-DAT	Emergency Events Database
ENSO	El Niño–Southern Oscillation
F	frequency
GHA	Greater Horn of Africa
GHCN	Global Historical Climatology Network
GPCC	Global Precipitation Climatology Centre
GPCP	Global Precipitation Climatology Project
IDEAM	Institute of Hydrology, Meteorology and Environmental Studies (Colombia)
IDI	Integrated Drought Index
IMHPA	Institute of Meteorology and Hydrology of Panama
IMN	National Meteorological Institute (Costa Rica)
INAMEH	National Meteorological and Hydrological Service of Venezuela
INAMHI	National Meteorological and Hydrological Service of Ecuador
INDECI	National Institute of Civil Defense (Peru)
INMET	National Institute of Meteorology (Brazil)
INPE	National Institute for Space Research (Brazil)
INSIVUMEH	National Institute for Seismology, Vulcanology, Meteorology and Hydrology (Guatemala)
INUMET	Uruguayan Institute of Meteorology
IOD	Indian Ocean dipole
IPO	interdecadal Pacific oscillation
ISMR	summer monsoon rainfall
ITCZ	Intertropical Convergence Zone

Unauthenticated | Downloaded 11/21/25 11:34 AM UTC

KNMI	Royal Netherlands Meteorological Institute
LTA	long-term average
MJO	Madden–Julian Oscillation
MSLP	mean sea level pressure
MSWEP	Multi-Source Weighted-Ensemble Precipitation
NCAR	National Center for Atmospheric Research
NCEP	National Centers for Environmental Prediction
NIWA	National Institute of Water and Atmospheric Research (New Zealand)
NMHS	National Meteorological and Hydrological Services
NMS	National Meteorological Service
NOAAGlobalTemp	NOAA Global Surface Temperature
NPSH	North Pacific subtropical high
NWS	National Weather Service
OCHA	Office for the Coordination of Humanitarian Affairs
OLR	outgoing longwave radiation
P	precipitation
PGIA	Phillip Goldson International Airport
PNG	Papua New Guinea
RA	Regional Association
RCC	Regional Climate Centre
RCC-CM	Regional Climate Centre Node on Climate Monitoring
ROK	Republic of Korea
SAM	Southern Annular Mode
SENAMHI	National Meteorology and Hydrology Service of Bolivia
SENAMHI	National Meteorology and Hydrology Service of Peru
SH	State Highway
SINAPROC	National Civil Protection System (Panama)
SMN	National Meteorological Service of Argentina
SOI	Southern Oscillation Index
SPCZ	South Pacific Convergence Zone
SSA	southern South America
SST	sea surface temperature
SSTA	sea surface temperature anomaly
T	daily mean temperature
Tabs_min	absolute minimum temperature
Tm	mean daily temperature
Tmax	daily maximum temperature
Tmin	daily minimum temperature
TNA	Tropical North Atlantic index
Tnorm	normal temperature
Tnorm_max	normal maximum temperature
Tnorm_min	normal minimum temperature
UAE	United Arab Emirates
UN	United Nations
WMO	World Meteorological Organization
WWA	World Weather Attribution

Unauthenticated | Downloaded 11/21/25 11:34 AM UTC

Appendix 2: Supplemental materials

Table A7.1. The length of national temperature and precipitation records, annual anomalies, and rank information for each country in Europe / World Meteorological Organization (WMO) Regional Association (RA) VI region. Reference period is 1991–2020 unless otherwise specified. For some countries, instead of an area average, only the values at a single station (preferably with a long time series) are given (name of the location in brackets). Nations with a star icon (★) represent cases where national data are not (yet) available, so statistics based on gridded RCC products were used. For the ranking of precipitation, the annual totals were ordered from the wettest to the driest year, unless otherwise stated.

Western Europe

Nation	Temp. Start of Record	Precip. Start of Record	Source	Temp. Anomaly (°C)	Rank (Ordered from Warmest to Coldest)	Precip. Anomaly (Annual Total; % of Normal)	Rank (Ordered from Wettest to Driest)
Belgium (Uccle)	1833	1833	NMHS	+0.9	5	140	1
France	1900	1959	NMHS	+0.9	4	115	7
Ireland	1900	1941	NMHS	+0.5	4	98	44
Luxembourg (Findel)	1838	1854	NMHS	+0.7	5	143	1
Netherlands (De Bilt)	1901	1906	NMHS	+1.3	1	125	5
United Kingdom	1884	1836	NMHS	+0.6	4	107	17

Central Europe

Nation	Temp. Start of Record	Precip. Start of Record	Source	Temp. Anomaly (°C)	Rank (Ordered from Warmest to Coldest)	Precip. Anomaly (Annual Total; % of Normal)	Rank (Ordered from Wettest to Driest)
Austria	1767	1858	NMHS	+1.8	1	106	38
Czech Republic	1961	1961	NMHS	+2.0	1	114	8–9
Germany	1881	1881	NMHS	+1.6	1	114	12
Hungary	1901	1901	NMHS	+2.2	1	84	100
Poland	1951	1951	NMHS	+2.2	1	99	38
Slovakia	1951	1961	NMHS	+2.2	1	96	32
Switzerland	1864	1901	NMHS	+1.4	3	108	32

Iberian Peninsula

Nation	Temp. Start of Record	Precip. Start of Record	Source	Temp. Anomaly (°C)	Rank (Ordered from Warmest to Coldest)	Precip. Anomaly (Annual Total; % of Normal)	Rank (Ordered from Wettest to Driest)
Portugal	1931	1931	NMHS	+0.9[1]	4	95[1]	-
Spain	1961	1961	NMHS	+1.1	3	105	26

[1] reference period 1981–2010

Unauthenticated | Downloaded 11/21/25 11:34 AM UTC

Nordic and Baltic countries

Nation	Temp. Start of Record	Precip. Start of Record	Source	Temp. Anomaly (°C)	Rank (Ordered from Warmest to Coldest)	Precip. Anomaly (Annual Total; % of Normal)	Rank (Ordered from Wettest to Driest)
Denmark	1874	1874	NMHS	+1.1	2	122	2
Estonia	1922	1922	NMHS	+1.7	2	93	53
Finland	1900	1961	NMHS	+1.1	4	103	17
Iceland[2]	1874	1921	NMHS	–0.8	78–79	95	52
Latvia	1924	1924	NMHS	+1.9	1	95	53
Lithuania	1961	1961	NMHS	+2.1	1	90	49
Norway	1901	1901	NMHS	+1.1	3	115	3
Sweden	1858	1880	NMHS	+1.0	3	106	15

[2] precipitation statistics are given for the station of Reykjavík

Central Mediterranean Region

Nation	Temp. Start of Record	Precip. Start of Record	Source	Temp. Anomaly (°C)	Rank (Ordered from Warmest to Coldest)	Precip. Anomaly (Annual Total in % of Normal)	Rank (Ordered from Wettest to Driest)
★ Albania	1981	1901	RCC	+1.9	1	104	73
Bosnia and Herzegovina (Mostar/ Sarajevo)	1961	1961	NMHS	+2.1/+2.2	1/1	71/-	58/49
★ Bulgaria	1981	1901	RCC	+2.1	1	94	89
Croatia	1961	1961	NMHS	+2.0	1	101	28
Greece	1960	1960	NMHS	+1.6	1	78	58
Italy	1961	1961	NMHS	+1.3	1	107	18
★ Malta	1981	1901	RCC	+1.4	1	46	122
Monaco (Jardin Exotique)	1966	1969	NMHS	+1.1	3	128	12
★ Montenegro	1981	1901	RCC	+2.3	1	114	54
North Macedonia	1981	1981	NMHS	+1.5	1	94	28
★ Serbia	1981	1901	RCC	+2.4	1	95	79
Slovenia	1950	1950	NMHS	+1.8	1	111	11

Unauthenticated | Downloaded 11/21/25 11:34 AM UTC

Eastern Europe							
Nation	Temp. Start of Record	Precip. Start of Record	Source	Temp. Anomaly (°C)	Rank (Ordered from Warmest to Coldest)	Precip. Anomaly (Annual Total; % of Normal)	Rank (Ordered from Wettest to Driest)
★ Belarus	1981	1901	RCC	+2.2	1	98	60
Kazakhstan (western part)	1941	1941	NMHS	+1.0	1	151	3
Moldova (Chisinau)	1886	1886	NMHS	+2.2	1	129	9
Romania	1900	1961	NMHS	+2.7	1	83	56
Russia (European part)	1936	1936	NMHS	+1.4	-	94	-
Ukraine	1891	1891	NMHS	+2.5	1	91	82
Middle East							
Nation	Temp. Start of Record	Precip. Start of Record	Source	Temp. Anomaly (°C)	Rank (Ordered from Warmest to Coldest)	Precip. Anomaly (Annual Total; % of Normal)	Rank (Ordered from Wettest to Driest)
Cyprus	1900	1916	NMHS	+1.7	1	88	70
Israel	1950	1950	NMHS	+1.1	2	106	30
★ Jordan	1981	1901	RCC	+1.1	5	61	114
★ Lebanon	1981	1901	RCC	+1.4	2	94	97
★ Syria	1981	1901	RCC	+1.3	2	93	94
Türkiye and South Caucasus							
Nation	Temp. Start of Record	Precip. Start of Record	Source	Temp. Anomaly (°C)	Rank (Ordered from Warmest to Coldest)	Precip. Anomaly (Annual Total; % of Normal)	Rank (Ordered from Wettest to Driest)
Armenia	1935	1935	NMHS	+1.7[3]	7	113[3]	16
Azerbaijan	2000	2000	NMHS	+1.7[3]	-	133[3]	-
Georgia	1956	1956	NMHS	+1.2	5	118	6
Türkiye	1971	1971	NMHS	+1.7	1	94	34

[3] reference period 1961–90

Unauthenticated | Downloaded 11/21/25 11:34 AM UTC

References

Amador, J. A., 1998:A climate feature of the tropical Americas: The trade wind easterly jet. *Tóp. Meteor. Oceanogr.*, **5**, 91–102.

—— , 2008: The Intra-Americas Sea low-level jet: Overview and future research. *Ann. N. Y. Acad. Sci.*, **1146**, 153–188, https://doi.org/10.1196/annals.1446.012.

—— , E. J. Alfaro, H. Hidalgo, and B. Calderon, 2011: Central America and the Caribbean [in "State of the Climate in 2010"]. *Bull. Amer. Meteor. Soc.*, **92** (6), S182–S183, https://doi.org/10.1175/1520-0477-92.6.S1.

—— , E. R. Rivera, A. M. Durán-Quesada, G. Mora, F. Sáenz, B. Calderón, and N. Mora, 2016a: The easternmost tropical Pacific. Part I: A climate review. *Rev. Biol. Trop.*, **64** (Suppl. 1), S1–S22, https://doi.org/10.15517/rbt.v64i1.23407.

—— , A. M. Durán-Quesada, E. R. Rivera, G. Mora, F. Sáenz, B. Calderón, and N. Mora, 2016b: The easternmost tropical Pacific. Part II: Seasonal and intraseasonal modes of atmospheric variability. *Rev. Biol. Trop.*, **64**, 23–57, https://doi.org/10.15517/rbt.v64i1.23409.

Beck, H. E., E. F. Wood, M. Pan, C. K. Fisher, D. G. Miralles, A. I. J. M. Van Dijk, T. R. McVicar, and R. F. Adler, 2019: MSWEP V2 global 3-hourly 0.1° precipitation: Methodology and quantitative assessment. *Bull. Amer. Meteor. Soc.*, **100**, 473–500, https://doi.org/10.1175/BAMS-D-17-0138.1.

Bekele-Biratu, E., W. M. Thiaw, and D. Korecha, 2018: Sub-seasonal variability of the Belg rains in Ethiopia. *Int. J. Climatol.*, **38**, 2940–2953, https://doi.org/10.1002/joc.5474.

Camberlin, P., 2018: Climate of eastern Africa. Oxford Research Encyclopedia of Climate Science, accessed 10 June 2025, https://oxfordre.com/climatescience/view/10.1093/acrefore/9780190228620.001.0001/acrefore-9780190228620-e-512.

CatIQ, 2025a: Canadian insured losses from catastrophic events total CAN $8.5 billion in 2024. Accessed 16 January 2025, https://public.catiq.com/2025/01/13/canadian-insured-losses-from-catastrophic-events-total-can-8-5-billion-in-2024/.

—— ,2025b:CAD 3.253 B — CatIQ discloses updated industry loss for the Calgary hailstorm of August 5, 2024. Accessed 1 May 2025, https://public.catiq.com/2025/02/10/cad-3-253-b-catiq-discloses-updated-industry-loss-for-the-calgary-hailstorm-of-august-5-2024/.

Cheng, L., and Coauthors, 2025: Record high temperatures in the ocean in 2024. *Adv. Atmos. Sci.*, **42**, 1092–1109, https://doi.org/10.1007/s00376-025-4541-3.

Collischonn, W., and Coauthors, 2025: O desastre hidrológico excepcional de abril-maio de 2024 no sul do Brasil. HydroShare,-accessed 01 February 2025, https://www.hydroshare.org/resource/d9e5c2ffb49a4b729b240f3eb3084ff4.

Cornes, R., G. van der Schrier, E. J. M. van den Besselaar, and P. D. Jones, 2018: An ensemble version of the E-OBS temperature and precipitation data sets. *J. Geophys. Res. Atmos.*, **123**, 9391–9409, https://doi/org/10.1029/2017JD028200.

Delforge, D., and Coauthors, 2025:EM-DAT: The Emergency Events Database. *Int. J. Disaster Risk Reduct.*, **124**, 105509, https://doi.org/10.1016/j.ijdrr.2025.105509.

Durán-Quesada, A. M., R. Sorí, P. Ordoñez, and L. Gimeno, 2020: Climate perspectives in the Intra–Americas Seas. *Atmosphere*, **11**, 959, https://doi.org/10.3390/atmos11090959.

ECCC, 2025: Canada's 10 most impactful weather stories of 2024. Accessed 16 January 2025, https://www.canada.ca/en/environment-climate-change/services/ten-most-impactful-weather-stories/2024.html.

Enfield, D., and E. Alfaro, 1999: The dependence of Caribbean rainfall on the interaction of the tropical Atlantic and Pacific Oceans. *J. Climate*, **12**, 2093–2103, https://doi.org/10.1175/1520-0442(1999)012<2093:TDOCRO>2.0.CO;2.

Evans, A., D. Jones, R. Smalley, and S. Lellyett, 2020: An enhanced gridded rainfall analysis scheme for Australia. Bureau of Meteorology Research Rep. 41, 45 pp., https://www.bom.gov.au/research/publications/researchreports/BRR-041.pdf.

Freitas, J. D., 2024a: Venezuela arde sin mitigaciones para el fenómeno de El Niño y el cambio climático. Runrun.es: En defensa de tus derechos humanos, accessed 01 February 2025, https://runrun.es/rr-es-plus/517060/venezuela-arde-sin-mitigaciones-para-el-fenomeno-de-el-nino-y-el-cambio-climatico/.

—— , 2024b: Climate Central: Venezuela tuvo 100 días más calurosos por el cambio climático desde marzo de 2024. Runrun.es: En defensa de tus derechos humanos, accessed 01 February 2025, https://runrun.es/rr-es-plus/558533/climate-central-venezuela-tuvo-100-dias-mas-calurosos-por-el-cambio-climatico-desde-marzo-de-2024/.

Funk, C., and Coauthors, 2015: The climate hazards infrared precipitation with stations—A new environmental record for monitoring extremes. *Sci. Data*, **2**, 150066, https://doi.org/10.1038/sdata.2015.66.

Gramlich, K., 2024: Heavy precipitation, river flooding Central and Eastern Europe, 11–30 September 2024. Karlsruhe Institute of Technology, Institute for Meteorology and Climate Research, https://www.wettergefahren-fruehwarnung.de/Ereignis/20241002_e.html.

Greilinger, M., A. Orlik, A. Tilg, H. Schellander, G. Pistotnik, S. Lehner, M. Schlögl, and R. Koch, 2024: Klimatologische Analyse betreffend des Niederschlagereignisses vom 12. bis 16. September 2024 in Österreich. GeoSphere Austria, https://geosphere.at/de/dokumente/news/klimatologische-analyse-des-niederschlagereignisses-september-2024_final_v2.pdf

González, P. D. M., 2024: Fenómeno de La Niña: Municipios en Colombia alcanzaron máximos históricos de lluvias. *infobae*, 5 July, https://www.infobae.com/colombia/2024/07/06/fenomeno-de-la-nina-municipios-en-colombia-alcanzaron-maximos-historicos-de-lluvias/.

Gudoshava, M., and Coauthors, 2024: Drivers of sub-seasonal extreme rainfall and their representation in ECMWF forecasts during the eastern African March-to-May seasons of 2018–2020. *Meteor. Appl.*, **31**, e70000, https://doi.org/10.1002/met.70000.

Hendon, H. H., D. W. Thompson, and M. C. Wheeler, 2007: Australian rainfall and surface temperature variations associated with the Southern Hemisphere annular mode. *J. Climate*, **20**, 2452–2467, https://doi.org/10.1175/JCLI4134.1.

Hersbach, H., and Coauthors, 2020: The ERA5 global reanalysis. *Quart. J. Roy. Meteor. Soc.*, **146**, 1999–2049, https://doi.org/10.1002/qj.3803.

Hidalgo, H., E. Alfaro, J. Amador, and A. Bastidas, 2019: Precursors of quasi-decadal dry-spells in the Central America Dry Corridor. *Climate Dyn.*, **53**, 1307–1322, https://doi.org/10.1007/s00382-019-04638-y.

—— , J. A. Amador, E. J. Alfaro, B. Calderón, and N. Mora, 2024:Central America [in "State of the Climate in 2023"]. *Bull. Amer. Meteor. Soc.*, **105** (8), S390–S392, https://doi.org/10.1175/2024BAMSStateoftheClimate_Chapter7.1.

Unauthenticated | Downloaded 11/21/25 11:34 AM UTC

Hoell, A., A. E. Gaughan, T. Magadzire, and L. Harrison, 2021: The modulation of daily southern Africa precipitation by El Niño–Southern Oscillation across the summertime wet season. *J. Climate*, **34**, 1115–1134, https://doi.org/10.1175/JCLI-D-20-0379.1.

Huang, B., and Coauthors, 2017: Extended Reconstructed Sea Surface Temperature, version 5 (ERSSTv5): Upgrades, validations, and intercomparisons. *J. Climate*, **30**, 8179–8205, https://doi.org/10.1175/JCLI-D-16-0836.1.

IBC, 2025: 2024 shatters record for costliest year for severe weather-related losses in Canadian history at $8.5 billion. Accessed 16 January 2025, https://www.ibc.ca/news-insights/news/2024-shatters-record-for-costliest-year-for-severe-weather-related-losses-in-canadian-history-at-8-5-billion.

INAMHI, 2024: Technical report presented at the Emergency Operations Committee (COE) meeting, 04 October. National Institute of Meteorology and Hydrology of Ecuador.

Jones, D. A., W. Wang, and R. Fawcett, 2009: High-quality spatial climate data-sets for Australia. *Aust. Meteor. Oceanogr. J.*, **58**, 233–248, https://doi.org/10.22499/2.5804.003.

Kimutai, J., and Coauthors, 2024: Climate change and high exposure increased costs and disruption to lives and livelihoods from flooding associated with exceptionally heavy rainfall in Central Europe. World Weather Attribution, University of Reading Rep., 36 pp., https://doi.org/10.25561/114694.

Knippertz, P., A. H. Fink, A. Reiner, and P. Speth, 2003: Three late summer/early autumn cases of tropical–extratropical interactions causing precipitation in northwest Africa. *Mon. Wea. Rev.*, **131**, 116–135, https://doi.org/10.1175/1520-0493(2003)131<0116:TLSEAC>2.0.CO;2.

MacLeod, D., E. W. Kolstad, K. Michaelides, and M. B. Singer, 2024: Sensitivity of rainfall extremes to unprecedented Indian Ocean dipole events. *Geophys. Res. Lett.*, **51**, e2023GL105258, https://doi.org/10.1029/2023GL105258.

Magaña, V., J. A. Amador, and S. Medina, 1999: The midsummer drought over Mexico and Central America. *J. Climate*, **12**, 1577–1588, https://doi.org/10.1175/1520-0442(1999)012<1577:TMDOMA>2.0.CO;2.

Marengo, J., and Coauthors, 2024a: The drought of Amazonia in 2023–2024. *Amer. J. Climate Change*, **13**, 567–597, https://doi.org/10.4236/ajcc.2024.133026.

——, and Coauthors, 2024b: O maior desastre climático do Brasil: Chuvas e inundações no estado do Rio Grande do Sul em abril-maio 2024. *Estud. Avançados*, **38**, 203–228, https://doi.org/10.1590/s0103-4014.202438112.012.

——, and Coauthors, 2025: Early Warning Services for Disaster Risk Reduction in Brazil: The experience of CEMADEN during the floods of Rio Grande do Sul of May 2024, *Int. Journal Disaster Risk Reduction*, in press.

MCPHD, 2025: 2024 shows first decline in heat deaths in a decade. Accessed 29 April 2025, https://www.maricopa.gov/CivicAlerts.aspx?AID=3222.

MeteoSwiss, 2024: Der aussergewöhnliche Weg des Unwettertiefs «Boris» (Switzerland) (The extraordinary path of the storm "Boris"). Bundesamt für Meteorologie und Klimatologie MeteoSchweiz, https://www.meteoschweiz.admin.ch/ueber-uns/meteoschweiz-blog/de/2024/09/der-aussergewoehnliche-weg-des-unwettertiefs-boris.html.

NDMC, 2025: U.S. drought monitor: Time series. University of Nebraska–Lincoln, accessed 25 March 2025, https://droughtmonitor.unl.edu/DmData/TimeSeries.aspx.

Nicholson, S. E., A. H. Fink, and C. Funk, 2018: Assessing the recovery and change in West Africa's rainfall regime from a 161-year record. *Int. J. Climatol.*, **38**, 3770–3786, https://doi.org/10.1002/joc.5530.

NIFC, 2025: Wildland fire summary and statistics annual report 2024. 57 pp., https://www.nifc.gov/sites/default/files/NICC/2-Predictive%20Services/Intelligence/Annual%20Reports/2024/annual_report_2024.pdf.

NOAA/NCEI, 2025: U.S. billion-dollar weather and climate disasters. Accessed 26 March 2025, https://doi.org/10.25921/stkw-7w73.

Norberto Paredes, 2024: Calentamiento global: "La desaparición del último glaciar de Venezuela es un espejo de lo que pasará en Colombia, Ecuador y Perú". BBC News Mundo, https://www.bbc.com/mundo/articles/cgrrk95jwe6o.

NRCan, 2025: National wildland fire situation report. Accessed 1 May 2025, https://cwfis.cfs.nrcan.gc.ca/report.

Poveda, G., and Ó. J. Mesa, 1996: Las fases extremas del fenómeno ENSO (El Niño y La Niña) y su influencia sobre la hidrología de Colombia. *Tecnol. Cienc. Agua*, **11**, 21–37.

Reboita, M. S., E. V. Mattos, B. C. Capucin, D. O. D. Souza, and G. S. Ferreira, 2024: A multi-scale analysis of the extreme precipitation in southern Brazil in April/May 2024. *Atmosphere*, **15**, 1123, https://doi.org/10.3390/atmos15091123.

Risbey, J. S., M. J. Pook, P. C. McIntosh, M. C. Wheeler, and H. H. Hendon, 2009: On the remote drivers of rainfall variability in Australia. *Mon. Wea. Rev.*, **137**, 3233–3253, https://doi.org/10.1175/2009MWR2861.1.

Rustemeier, E., and Coauthors, 2024: Klimatologische Einordnung der Niederschlagsmengen im östlichen Mitteleuropa Mitte September 2024. Deutscher Wetterdienst, accessed 31 Jan 2025, https://www.dwd.de/DE/leistungen/besondereereignisse/niederschlag/20240923_hochwasser_osteuropa.html?nn=490674.

Schneider, U., P. Finger, E. Rustemeier, M. Ziese, and S. Hänsel, 2022: Global precipitation analysis products of the GPCC. Deutscher Wetterdienst, 17 pp., https://opendata.dwd.de/climate_environment/GPCC/PDF/GPCC_intro_products_lastversion.pdf.

Segele, Z. T., P. J. Lamb, and L. M. Leslie, 2009: Large-scale atmospheric circulation and global sea surface temperature associations with Horn of Africa June–September rainfall. *Int. J. Climatol.*, **29**, 1075–1100, https://doi.org/10.1002/joc.1751.

Silveira, A. L. L., 2020: Chuvas e vazões da grande enchente de 1941 em Porto Alegre/RS. *Bol. Geogr. Rio Grande Sul Porto Alegre*, **35**, 69–90.

SPC, 2025: Tornado totals and related deaths. NOAA/NWS, accessed 14 May 2025, https://www.spc.noaa.gov/climo/torn/STAMTS.txt.

Stephenson, T. S., A. A. Chen, and M. A. Taylor, 2008: Toward the development of prediction models for the primary Caribbean dry season. *Theor. Appl. Climatol.*, **92**, 87–101, https://doi.org/10.1007/s00704-007-0308-2.

Trewin, B., 2018: The Australian Climate Observations Reference Network–Surface Air Temperature (ACORN-SAT) version 2. Bureau of Meteorology Research Rep. 32, 67 pp., https://www.bom.gov.au/research/publications/researchreports/BRR-032.pdf.

Vincent, L. A., M. M. Hartwell, and X. L. Wang, 2020: A third generation of homogenized temperature for trend analysis and monitoring changes in Canada's climate. *Atmos.–Ocean*, **58**, 173–191, https://doi.org/10.1080/07055900.2020.1765728.

Unauthenticated | Downloaded 11/21/25 11:34 AM UTC

Wang, X. L., Y. Feng, V. Y. S. Cheng, and H. Xu, 2023: Observed precipitation trends inferred from Canada's homogenized monthly precipitation dataset. *J. Climate*, **36**, 7957–7971, https://doi.org/10.1175/JCLI-D-23-0193.1.

WMO, 2025: Significant weather and climate events. Supplement to the WMO State of the Climate Rep., 13 pp., https://wmo.int/sites/default/files/2025-03/State%20of%20the%20Global%20Climate%202024_Extremes%20Supplement.pdf.

WWA, 2024: Climate change, El Niño and infrastructure failures behind massive floods in southern Brazil. Accessed 3 January 2025, https://www.worldweatherattribution.org/climate-change-made-the-floods-in-southern-brazil-twice-as-likely/.

Unauthenticated | Downloaded 11/21/25 11:34 AM UTC